R-08-55

Geological discrete fracture network model for the Laxemar site

Site Descriptive Modelling SDM-Site Laxemar

Paul La Pointe, Aaron Fox
Golder Associates Inc

Jan Hermanson, Johan Öhman
Golder Associates AB

October 2008

Svensk Kärnbränslehantering AB
Swedish Nuclear Fuel
and Waste Management Co

Box 250, SE-101 24 Stockholm
Phone +46 8 459 84 00

ISSN 1402-3091
SKB Rapport R-08-55

Geological discrete fracture network model for the Laxemar site

Site Descriptive Modelling SDM-Site Laxemar

Paul La Pointe, Aaron Fox
Golder Associates Inc

Jan Hermanson, Johan Öhman
Golder Associates AB

October 2008

Abstract

The Swedish Nuclear Fuel and Waste Management Company (SKB) is performing site characterization at two different locations, Forsmark and Laxemar, in order to locate a site for a final geologic repository for spent nuclear fuel. The program is built upon the development of Site Descriptive Models (SDMs) at specific timed data freezes. Each SDM is formed from discipline-specific reports from across the scientific spectrum.

This report describes the methods, analyses, and conclusions of the modelling team in the production of the SDM-Site Laxemar geological discrete-fracture network (DFN) model. The DFN builds upon the work of other geological models, including the deformation zone and rock domain models.

The geological DFN is a statistical model for stochastically simulating rock fractures and minor deformation zones at a scale of less than 1,000 m (the lower cut-off of the DZ models). The geological DFN is valid within six distinct fracture domains inside the Laxemar local model subarea: FSM_C, FSM_EW007, FSM_N, FSM_NE005, FSM_S, and FSM_W.

The models are built using data from detailed surface outcrop maps, geophysical lineament maps, and the cored borehole record at Laxemar. The conceptual model for the SDM-Site Laxemar geological DFN model revolves around the identification of fracture domains based on relative fracture set intensities, orientation clustering, and the regional tectonic framework (including deformation zones). A single coupled fracture size/fracture intensity concept (the Base Model) based on a Pareto (power-law) distribution for fracture sizes was chosen as the recommended parameterisation. A slew of alternative size-intensity models were also carried through the fracture analyses and into the uncertainty and model verification analyses.

Uncertainty is modelled by analysing the effects on fracture intensity (P_{32}) that alternative model cases can have. Uncertainty is parameterised as a ratio between the P_{32} of the alternative model and the P_{32} of the recommended Base Model. Alternative model cases are also included in the geological DFN model verification, where they are ranked based on their performance in predicting observed fracture characteristics.

Sammanfattning

Svensk Kärnbränslehantering AB (SKB) genomför platsundersökningar på två platser, Forsmark och Laxemar, med målet att lokalisera ett förvar för använt kärnbränsle. Det genomförda programmet bygger på framtagande av successiva platsbeskrivande modeller (SDM) baserade på datafrysar definierade vid specifika tidpunkter.

Denna rapport beskriver metoder, genomförda analyser och slutsatser kopplade till framstagandet av den geologiska modellen av diskreta spricknätverk (DFN) inom ramen för modellversion SDM-Site Laxemar. DFN-modellen bygger på resultatet av annan geologisk modellering, bl a modeller för bergdomäner och deformationszoner.

Den geologiska DFN är en statistisk modell som möjliggör stokastisk simulering av sprickor och mindre deformationszoner som har en storlek på minder än 1 000 m. (motsvarar den nedre storleken för deterministiskt modellerade deformationszoner). Den geologiska DFN-modellen är tillämpbar inom sex definierade sprickdomäner inom den lokala modellvolymen i Laxemar: FSM_C, FSM_EW007, FSM_N, FSM_NE005, FSM_S, and FSM_W.

Modellen byggs upp med hjälp av data från ytkartor av berghällar, geofysiska kartort och loggar och tolkningar baserade på kärnborrhål i Laxemar. Den konceptuella modellen för geologisk DFN för SDM-Site Laxemar grundas på identifiering av sprickdomäner baserade på relativa skillnder i intesitet hos identifierade sprickset, analys av klustring av sprickorienteringar, samt det övergripande regionala tektoniska ramverket (inklusive deformationszoner). Ett enskilt koncept med kopplad sprickstorlek/sprickintensitet (Basfallet) baserad på en Pareto (potensfunktion) fördelning av sprickstorlek valdes som den rekommenderade parameteriseringen. Ett stort antal alternativa storlek-intensitetsmodeller analyserades också i sprickanalysen och vidare in i osäkerhets- och verifikationsanalyser.

Osäkerhet modelleras genom att analysera de effekter på sprickintensiteten (P_{32}) som de alternativa modellerna har. Osäkerheten parameterisersa som kvoten mellan P_{32} för den alternativa modellen och P_{32} för det rekommenderade Basfallet. De alterantiva modellerna inkluderas också i verifikationen av DFN-modellerna, där dessa rangordnas baserat på deras förmåga att prediktera observerade sprickkarakteristika.

Contents

1 Introduction 9
1.1 Previous modelling work 9
1.2 Project objectives 9
1.3 Model volume, use and applicability 10
1.4 Model location and domain 10
1.5 Acronyms and Terminology 11

2 Data and software used 15
2.1 Data 15
2.1.1 Data freeze version 15
2.1.2 Surface data 15
2.1.3 Borehole data 21
2.1.4 Deformation Zone model 22
2.1.5 Surface lineaments 22
2.1.6 Minor deformation zones 22
2.1.7 Fracture domain models 22
2.1.8 Data used in the definition of fracture domains 22
2.2 Software 24

3 Geological DFN model methodology 27
3.1 Modelling prerequisites, assumptions, limitations, and feedback from other disciplines 27
3.1.1 Strategy for SDM-Site Laxemar geological DFN 27
3.1.2 Modelling prerequisites 28
3.1.3 Model assumptions and limitations 28
3.1.4 Linking of fracture traces 29
3.1.5 Feedback from other disciplines 29
3.2 Fracture domain model methodology 30
3.2.1 Concepts and key assumptions 30
3.2.2 Summary of fracture domain identification methodology 34
3.2.3 Evaluation of fracture domain, rock domain and lithology classifications 34
3.3 DFN orientation model methodology 36
3.3.1 Basic orientation modelling approach 36
3.3.2 Data treatment 37
3.3.3 Identification of pole clusters through soft-sector assignment 38
3.3.4 Fisher distribution parameterisation based on pole clusters 39
3.3.5 Evaluation of Visible/Not Visible in BIPS for fracture orientation set division 41
3.4 DFN size model methodology 42
3.5 Geological DFN intensity model methodology 47
3.5.1 Calculating P_{32} from borehole fracture logs 48
3.6 DFN spatial model methodology 50
3.6.1 Location and scaling model 50
3.6.2 Evaluation of fracture domain, rock domain, and lithology classifications 53
3.6.3 Evaluation of fracture intensity as a function of depth 54
3.6.4 Fracture set termination model 54
3.6.5 Spatial variability of fracture intensity 55

3.7 Uncertainty modelling methodology 56
3.7.1 Identifying uncertainties 56
3.7.2 Quantifying uncertainties 57
3.7.3 Alternative models 57
3.8 Verification and validation of geological DFN model 57
3.8.1 Verification cases 57
3.8.2 Ranking of alternative models: methodology 60
3.8.3 Validation of geological DFN model 61

4 Derivation of SDM-Site Laxemar geological DFN model 63
4.1 Fracture domain model 63
4.1.1 Identifying fracture domains induced by regional and local major deformation zones 63
4.1.2 Identifying fracture domains separated by regional and local major deformation zones 66
4.1.3 SDM-Site Laxemar fracture domain model 68
4.2 Orientation model 75
4.2.1 Analysis of orientation data 75
4.2.2 Set division of data and parameterization of the orientation model 79
4.2.3 Set division of lineament data 80
4.2.4 Fracture orientation and properties as a function of visibility in image logs (BIPS) 84
4.3 Coupled size-intensity model 84
4.3.1 Base Model & alternative model definitions 84
4.3.2 Parameterisation alternatives 87
4.3.3 Preliminary Base Model (BM) 88
4.3.4 Alternative models 96
4.4 Spatial model 129
4.4.1 Borehole mass dimension calculations 129
4.4.2 Outcrop mass dimension calculations 129
4.4.3 Additional investigations of possible fractal/Euclidean scaling transition 132
4.4.4 Fracture domain, rock domain, and lithology classification 137
4.4.5 Fracture intensity as a function of depth 144
4.4.6 Fracture set termination model 154
4.4.7 Spatial variability of fracture intensity within fracture domains 155

5 Verification and validation of the SDM-Site Laxemar geological DFN models 169
5.1 Objectives 169
5.2 Verification of orientation set divisions 169
5.2.1 Evaluation of set-divided data 169
5.2.2 Verification OR-1: Orientation set confidence 175
5.2.3 Verification OR-2: Relative fracture set intensities 178
5.3 Verification SI-1: Outcrop P_{21} 181
5.4 Verification SI-2: Scanline P_{10} 188
5.5 Verification SI-3: Size-intensity model within the MDZ size range 198
5.6 Verification SI-4: Borehole P_{10}. 208
5.7 Verification SI-5: Spatial distribution of fracture intensity as a Gamma or Weibull distribution 219
5.8 Ranking of alternative models based on performance in verification cases 219
5.9 Validation of the geological DFN parameterisation 223

6 Uncertainty 225
6.1 Identification of uncertainties in the geological DFN 225
6.1.1 Conceptual uncertainties 225
6.1.2 Parameter uncertainties 227
6.2 Impact of Uncertainties 228
6.2.1 Quantification 228
6.2.2 Size-intensity dependence on fracture domain 228
6.2.3 Euclidean versus fractal scaling uncertainty 229
6.2.4 Linked versus unlinked traces 229
6.2.5 Size-intensity scaling exponent 232
6.2.6 Open versus sealed fractures 232
6.2.7 Number of lineaments used in size-intensity model 233
6.3 Recommendations for uncertainty propagation to downstream models 237

7 Geological DFN model summary and conclusions 241
7.1 Model summary tables 241
7.1.1 Orientation model 241
7.1.2 Coupled size-intensity model, BMU 241
7.1.3 Spatial model 242
7.2 Modelling Conclusions 242

References 245

Appendix A Linking of fracture traces 249

Appendix G Validation of SDM-Site Laxemar geological DFN model using borehole KLX27A 253

Appendices on CD

Appendix B Contour plots used in identification of fracture domains

Appendix C Contour plots of borehole and outcrop data by fracture domain

Appendix D Fractal mass dimension plots

Appendix E Fracture intensity as a function of depth

Appendix F Spatial variability of fracture intensity as a Gamma or Weibull distribution

1 Introduction

1.1 Previous modelling work

The current modelling version (SDM-Site Laxemar) will result in the concluding site-descriptive model (SDM) as part of the complete site investigations. One of the two investigated sites (Forsmark and Laxemar) will be selected as the site for a final spent-fuel repository. The resulting site-descriptive model for the selected site forms the basis for the license application to design and construct a spent-fuel repository which will be submitted to the regulatory authorities. The geological DFN model presented as part of SDM-Site Laxemar represents the evolution of the DFN modelling process over several generations of site models, and inherently the results of numerous rounds of revision and comment by internal and external reviewers.

The most recent full discrete fracture network model parameterized for Laxemar was an integrated part of the last completed preliminary site description for Laxemar, version 1.2 /SKB 2006/. The version 1.2 of the preliminary site description was the first to contain a complete site-specific DFN parameterization for the Laxemar subarea; previous works had focused either on data inventories (Version 0), localized models of parts of the Äspö HRL, or the Simpevarp subarea /SKB 2002/ and /SKB 2004/.

Previous DFN-specific supporting document reports include:

- Version 1.2 DFN model, Laxemar subarea /Hermanson et al. 2005/.
- Version 1.2 DFN model, Simpevarp subarea /La Pointe and Hermanson 2006/.

1.2 Project objectives

The goal of the Laxemar geological DFN, model version SDM-Site Laxemar, is to produce a model of fracturing within and adjacent to proposed deposition volumes to facilitate hydrogeologic and geomechanical modelling as part of the site descriptive modelling, in support of safety assessment, with reduced and quantified uncertainty, greater transparency, increased confidence, and improved ease-of-use for the intended users of the model.

A key change in the modelling methodology in the geological DFN modelling for version SDM-Site Laxemar is the introduction of parameterization of fractures within specific spatial regions (fracture domains). The technique was first used during the model version 2.2 Forsmark site modelling /Olofsson et al. 2007/, where SKB and SGU jointly produced a model that divided the fracturing into six spatial domains. Subdivision of the model region into fracture domains reduces overall model uncertainty, and makes it easier to identify and exploit predictive modelling relations between geological factors and fracture intensity and fracture orientation, since the "noise" is reduced by dividing data into fracture domains.

The exploration for, recognition and assignment of fracture domains at Laxemar was a key project objective during model version SDM-Site Laxemar. Golder, SKB, and SGU personnel worked together to develop the fracture domain model, using data from cored and percussion boreholes, regional geophysics, and the deformation zone modelling results. The result was a number of rock volumes, largely bounded by regional deformation zone features, within which the background fractures exhibited statistically homogenous trends.

The main objective of the SDM-Site Laxemar analysis efforts was to update the Laxemar discrete fracture network models, using additional data from new surface outcrops, surface trenches, and boreholes, in conjunction with the new model paradigm (fracture domains) developed at Forsmark. The model has been simplified somewhat through the use of global

orientation models and a consistent methodology for describing fracture size and intensity through the use of power laws. To build confidence in the DFN model parameterisations, a series of verification cases using outcrop and borehole fracture data were performed. The verification cases illustrate the limits of applicability of the DFN model parameterization and provide a snapshot of the reproductive capability of the model.

All models have uncertainty. The major impact of these uncertainties is on the volume of rock available for use by the proposed repository, as canister deposition holes intersecting fractures of a certain size or larger will be rejected. Secondary impacts of uncertainty in the geological DFN model include increased or reduced potential for compromising canister safety during future earthquakes, and potential effects on downstream model users, including hydrogeology, transport, and rock mechanics. In the SDM-Site Laxemar geological DFN, the uncertainties that are identified are evaluated as to their possible impacts on the fracture intensity (P_{32}). Uncertainty is expressed as ratios between the P_{32} of the recommended model parameterisation and the P_{32} of the alternative models.

1.3 Model volume, use and applicability

The intended use of the SDM-Site Laxemar geological DFN is as input for hydrogeological and mechanical modelling as part of the site descriptive modelling efforts, and for subsequent analysis in support of repository design, engineering planning, and safety assessment. The model is presented as a mathematical description of the fracturing and not as an implemented model. As such, the model parameters can be implemented in different forms, such as a discrete fracture network (DFN) model for direct stochastic simulation or as upscaled block properties (permeability tensor, porosity, storage volume, and in the ensuing hydraulic DFN in terms of fracture transmissivity) for an equivalent continuum model. The implementation of the mathematical description is a function of the downstream modelling or engineering needs, and is not part of the SDM-Site Laxemar model, although every effort has been made to present the mathematical description in a form that is convenient to the downstream modelling teams and engineers. The goal of this model is to provide downstream users with a means to estimate the fracture orientations, intensity, size, spatial patterns and fracture geology within the Laxemar local model volume, parts of which are currently proposed as a host for a spent nuclear fuel repository, along with the variability of these estimates.

The model is only applicable within the model domains and spatial limits specified in Section 1.4. Applicability outside these limits has not been established nor tested, and users who wish to use the model outside the range of applicability should carefully evaluate the parameters and limitations of the SDM-Site Laxemar geological DFN prior to using the model outside the context for which it was constructed. The SDM-Site Laxemar geological DFN is based upon the data described in Section 2.1, the software versions described in Section 2.2, and the assumptions listed in Chapter 3. Any future data additions or revisions, new conceptual understandings, or changes in assumptions or definitions could require the presented model to be revised.

1.4 Model location and domain

The Laxemar local model area is located in the province of Småland, within the municipality of Oskarshamn and immediately adjacent to the Oskarshamn nuclear power plant (Figure 1-1).

The model is only applicable within the local model boundary (Figure 1-1), from the ground surface to a depth of 1,000 metres. The model size parameterization is presented for fractures within a size range of 0.5 metres up to 564.2 metres, expressed as the radius of an equivalent-area circular disk fracture. If the DFN model is implemented using four-sided square polygons, this size parameterization will produce fractures with side lengths between ~ 0.9 metres and 1,000 metres. In addition, the SDM-Site Laxemar geological DFN is defined only within the

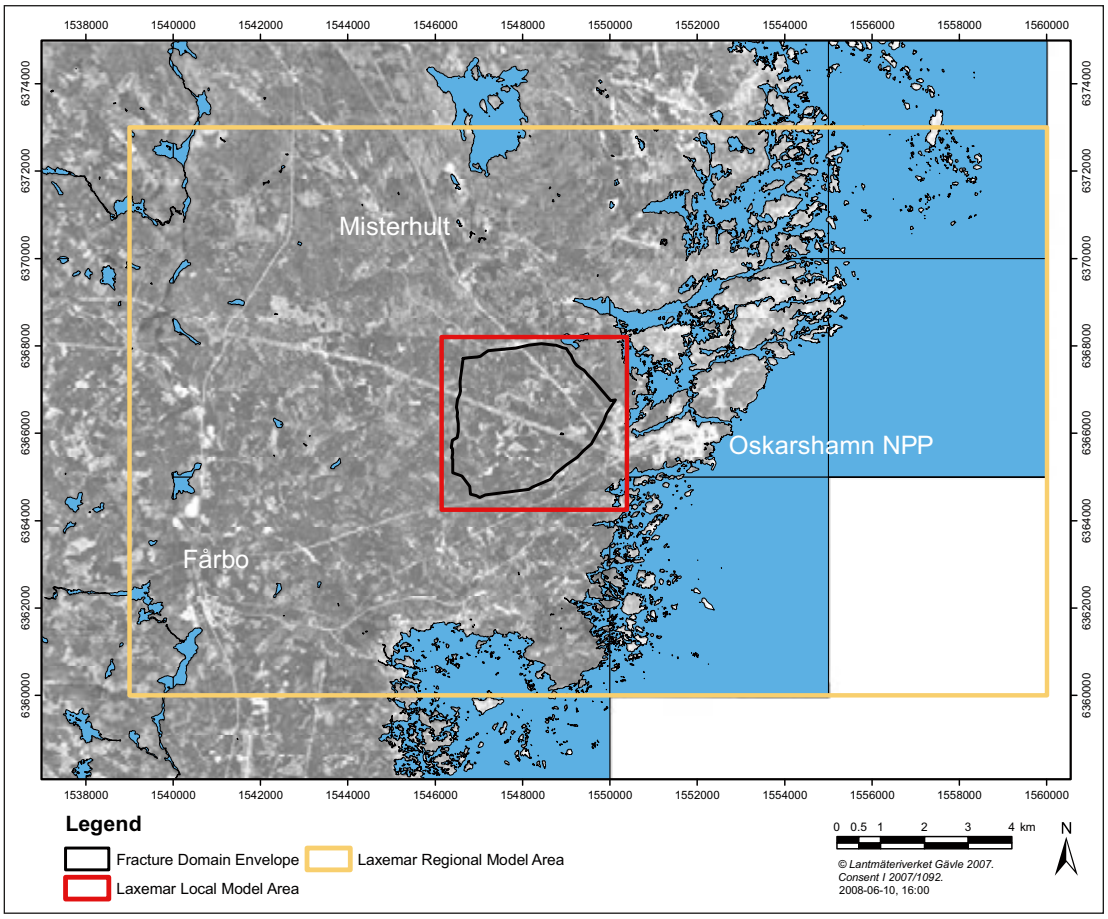

Figure 1-1. *Location of the Laxemar local model area and fracture domain envelope relative to regional landmarks and the Laxemar regional model area limits.*

six identified fracture domains (c.f. Figure 3-2 and Section 3.2); the model is neither defined nor valid inside interpreted deterministic deformation zone volumes, nor outside of the fracture domain envelope (heavy black line in Figure 1-1 below). It is also important to note that, due to a lack of available data (in particular, at depth), fracture domain FSM_S has been largely excluded from the analysis.

1.5 Acronyms and Terminology

CDF – Cumulative Density Function: A function that quantifies the cumulative probability of a distribution. The term is used in this report in the description of fracture trace length and radius distributions. It is the probability that the value of a randomly selected value is less than a specified value.

CCDF – Complementary Cumulative Density Function: A function that quantifies the cumulative probability of a distribution. The term is used in this report in the description of trace length and radius distributions. It is the probability that the value of a randomly selected value is greater than a specified value. The CCDF is equal to 1 minus the CDF.

CCN – Complementary Cumulative Number: A type of plot in which the number of data values greater than or equal to a specific value are plotted as a function of the value. CCN plots are used in this report for estimating the size model for the Tectonic Continuum alternative model.

CFI – Cumulative Fracture Intensity: A type of plot used to identify fractured zones and quantify their characteristic fracture intensity.

DFN – Discrete Fracture Network model: A three-dimensional numerical model in which fractures are represented as finite surfaces with specified mechanical and hydraulic properties.

DZ – Deformation Zone: This notation is employed as a general description of a zone characterised by ductile or brittle deformation, or a combination of the two. Those deformation zones which are possible to correlate between the surface (lineament with a length > 1,000 m) and an interpreted borehole intercept, or alternatively between one or more intercepts, are modelled deterministically, and are thus explicitly accounted for in the 3D RVS model.

Euclidean Scaling, Euclidean Dimension: A scaling behaviour characterised by a first-order relation between the number or density of some object, and the extent of the space in which it is embedded. In this report it is used to describe fracture intensity; a Euclidean scaling model for fracture intensity would be characterised by a linear, first order relation between the number of fractures in a volume of rock and the volume itself. Doubling the volume would lead to a doubling of the number of fractures in a Euclidean scaling model. The Euclidean dimension is a fractal mass dimension that characterises Euclidean scaling. It is 1.0 for line samples, such as borehole fracture data, 2.0 for areal samples, such as outcrop fracture trace data, and 3.0 for volumetric samples, such as rock volumes.

Exfoliation – also **Sheeting**: The development of fractures subparallel to a free surface due to a reduction in stress normal to the free surface. In SDM 2.2, exfoliation or sheeting is thought to have occurred after the last deglaciation, producing new fractures sub-parallel to the present-day rock surface, and possibly causing existing subhorizontal fractures to propagate or enlarge.

Fracture Domain/FSM: A fracture domain refers to a rock volume outside deformation zones in which rock units show similar fracture characteristics. The SDM-Site Laxemar geological DFN model bases the fracture domains largely on differences in relative fracture intensity between different orientation sets. Fracture domains at Laxemar are defined on the basis of the single-hole interpretation (SHI) and its modifications and extensions (ESHI), including the identification of minor deformation zones (MDZ), as presented in /Hermanson et al. 2008/.

The fracture data associated with deformation zones; a) those modelled deterministically in RVS, and b) possible minor local deformation zones (MDZ), the latter which have been identified in the single-hole interpretation but have not been modelled deterministically, are excluded from the fracture domains for the purpose of initial assessment of fracture domain characteristics (e.g. relative fracture intensity). In the ensuing geological DFN analysis the possible minor local deformation zones are reintroduced, but are represented by a single fracture.

The term fracture domain is used in the first instance as a basis for the discrete fracture network modelling work (geological DFN). The different fracture domains at Laxemar are referred to as 'FSM'. The recognition of fracture domains as defined here is also of relevance to colleagues working in the disciplines of hydrogeology, hydrogeochemistry and rock mechanics.

Mass Dimension: A measure of the scaling behaviour of a group of objects. In this report, the mass dimension is used to quantify the scaling behaviour of fracture intensity in boreholes and outcrops.

MDZ – Minor Deformation Zone: A hypothetical thickness-length relationship based on deterministic deformation zones at Laxemar suggests that a deformation zone with a thickness > 10 m has a length > 1,000 m. All possible deformation zones that have been identified in a single borehole (i.e. through ESHI) and have an estimated thickness ≤ 10 m shall be termed minor deformation zones (or MDZ; cf. Local minor deformation zone as stated by /Almén and Thurner 1996/). Minor deformation zones are not modelled deterministically in RVS, but are handled statistically in the geological DFN modelling.

P_{10} – A measure of linear fracture intensity, expressed in this report as the number of fractures per meter (1/m).

P_{20} – A measure of fracture density, expressed in this report as the number of fractures/mapped area in units of the number fractures per square meter ($1/m^2$).

P_{21} – A measure of areal fracture density, expressed in this report as the fracture trace length per unit of mapped area (m/m^2).

P_{30} – A measure of volumetric fracture intensity, expressed in this report as the numbers of fractures per unit of rock volume ($1/m^3$).

P_{32} – A measure of volumetric fracture intensity, expressed in this report as fracture surface area per unit of rock volume (m^2/m^3).

Rock Domain: A rock domain refers to a rock volume in which rock units that show specifically similar composition, grain size, degree of bedrock homogeneity, and degree and style of ductile deformation have been combined and distinguished from each other. The occurrence of early-stage alteration (albitisation) is also used as a help to distinguish rock domains. The term rock domain is used in the 3D geometric modelling work and different rock domains at Laxemar are referred to as RSMxxx. The recognition of rock domains as defined here aims primarily to meet the needs of colleagues working in the disciplines of thermal modelling and rock mechanics. The reader is gently referred to the SDM-Site Laxemar geological description /Wahlgren et al. 2008/ for additional details on rock domain identification, classification, and the subordinate lithologies inside rock domains. The presentation of this material is outside the scope of the DFN report.

SDM – Site Descriptive Model.

SDE – Standard Error.

SSQ – Sum of Squares.

Statistical Significance: This relates to the outcome of a statistical test of a hypothesis. It is the probability of the results of the statistical tests given that the hypothesis is true with reference to a specified value of probability for which the hypothesis is rejected or not rejected. The test of statistical significance does not prove that the hypothesis is true, but rather that the data do or do not reach the probability level of falsifying the hypothesis. Statistical significance is quantified as the parameter α, which represents the probability that the null hypothesis for the statistical test being performed will be rejected when it is in fact true (a Type I error). In general, an α of 0.05 has been used as a level of significance in the Laxemar version 2.2 geological DFN modelling.

Tectonic Continuum Hypothesis: The hypothesis that a fracture population can be analyzed consistently over a large scale range; for example, from metres to kilometres. In the tectonic continuum model, the fractures in outcrop with traces on the scales of metres are part of the same fracture population as lineaments or deformation zones with traces on the scale of kilometres. This model allows for the combination of data sets at multiple scales.

TCM – Tectonic Continuum Model: A coupled size-intensity fracture model based on the tectonic continuum hypothesis.

2 Data and software used

This section of the report describes the specific data sources utilized during the geological DFN modelling process. Where applicable, references to specific tables, queries, or object within approved SKB databases (SICADA, SDE) have been used.

2.1 Data

2.1.1 Data freeze version

In general, the SDM-Site Laxemar fracture domain and geological DFN models have been built atop data available before the data freeze. The data freeze date for the current model version was August 31, 2007. However, due to significant uncertainties regarding the computation of fracture orientation in cored borehole records /Munier and Stigsson 2007/, the data freeze for the SDM-Site Laxemar geological DFN analysis was effectively delayed through late October 2007. In some cases (the deformation zone and rock domain models), interim models in between August 2007 and October 2007 were used so as to encompass the most current geological conceptualization of the project site.

It is important to understand that the rock domain, deformation zone and geological DFN models have all been developed in parallel with each other and not in a consecutive order. This approach has the advantage of multidisciplinary collaborative interpretation while building the models. Of course the drawback is that the geological DFN model, which is dependent on the other models, is forced to use intermediate geological models to be finalized by the same date as the other two models.

2.1.2 Surface data

Surface data, including the fractures mapped in detail on various outcrops across the Laxemar study area, were primarily used to develop the orientation and size models of the geological DFN. In addition, the surface data were used in conjunction with the borehole fracture records to produce the site-specific fracture domain models (FSM), to assess the spatial distribution of fracturing at small (5–10 m) scales, and to determine the scaling properties of fracturing (Euclidean or fractal scaling).

Regional linked lineaments derived from both regional (airborne gravity, magnetic, electrical, and coordinated lineaments) and local (high resolution ground magnetic lineaments) were used as components in the coupled size-intensity DFN models. Unlike the Forsmark 2.2 geological DFN, surface traces of the deformation zone model were not used in the parameterization of the SDM-Site Laxemar geological DFN. Only the linked regional lineaments shorter than one kilometre, clipped to lie inside the fracture domain envelope (Figure 3-2) were used in the construction of the coupled size-intensity models.

Note that this section documents only the raw data sets used in the production of the current geological DFN model; the new outcrop traces from the linking process described in Appendix A are not considered an ‘official’ data source, but as a derived work product, and are treated separately in the data compilation report /Hermanson et al. 2008/.

Detailed fracture mapping of outcrops

Specific data sources for the detailed fracture mapping on outcrops include the following GIS shapefiles exported from SDE. The names listed below are references to feature classes contained in the SKB GIS database (SDE). Locations of the detail-mapped outcrops are presented below in Figure 2-1.

Outcrop Mapping Limits

- SDEADM_GOL_LX_GEO_2347 (ASM000208)
- SDEADM_GOL_LX_GEO_2356 (ASM000209)
- SDEADM_GOL_SM_GEO_3570 (ASM100234)
- SDEADM_GOL_SM_GEO_3690 (ASM100235)

Outcrop Fractures (unlinked)

- SDEADM_GOL_LX_GEO_4125_VIEW (ASM000208)
- SDEADM_GOL_LX_GEO_4126_VIEW (ASM000209)
- SDEADM_GOL_SM_GEO_4224_VIEW (ASM100234)
- SDEADM_GOL_SM_GEO_4641_VIEW (ASM100235)
- SICADA tables p_area_map and p_line_map

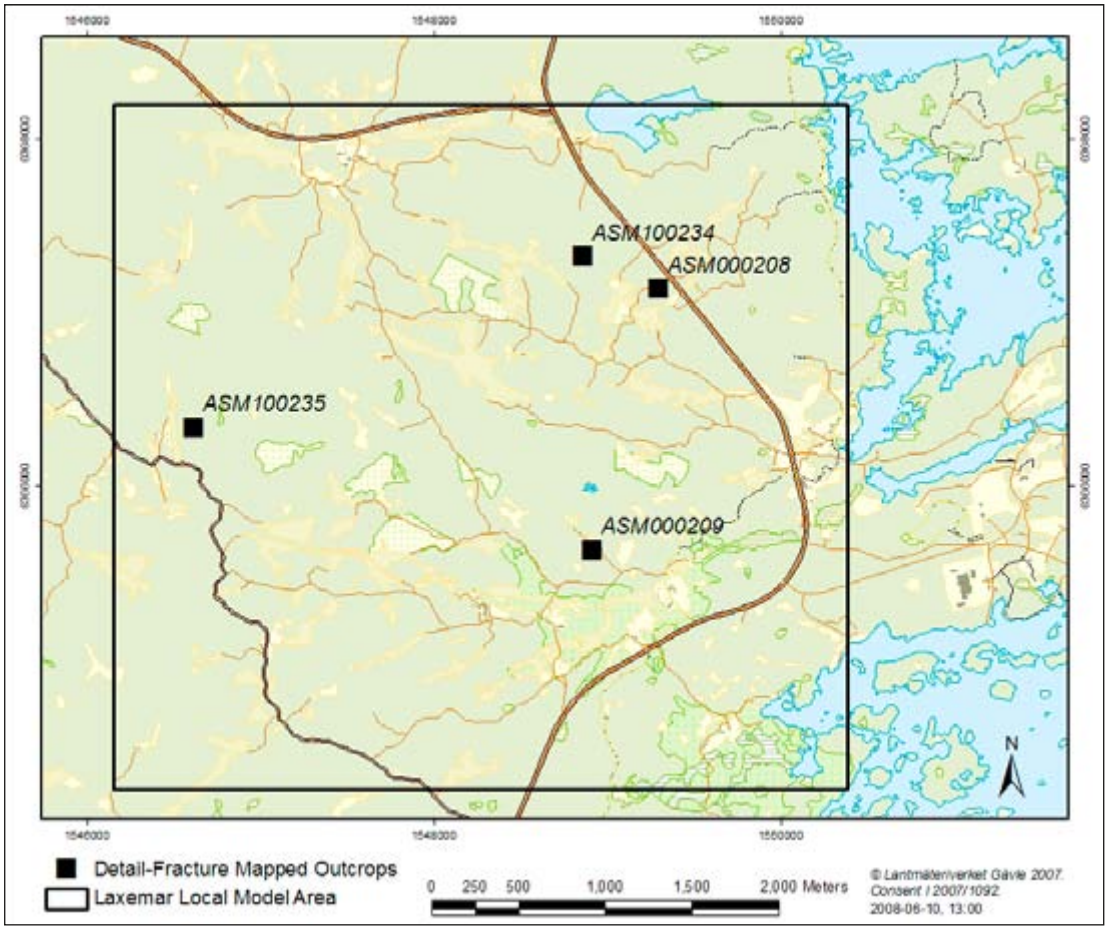

Figure 2-1. *Locations of outcrops on which detailed fracture mapping was performed.*

Outcrop Fractures (linked)

Note that, as of early September 2008, these features had not yet been delivered to SKB and placed in SDE. As such, they represent an interim delivery product.

- ASM000208_hand_linked_Clip.shp
- ASM000209_hand_linked_Clip.shp
- ASM100234_hand_linked_Clip.shp
- ASM100235_hand_linked_Clip.shp
- ASM000208_hand_linked.xls (property tables and set probabilities)
- ASM000209_hand_linked.xls (property tables and set probabilities)
- ASM100234_hand_linked.xls (property tables and set probabilities)
- ASM100235_hand_linked.xls (property tables and set probabilities)

Detailed fracture mapping of trenches

In 2006 and 2007, additional surface mapping was done along narrow strips of cleared land across the Laxemar local model area. The goal was to investigate the surface extent of potential deformation zones identified from LIDAR and regional geophysics, as well as to provide additional data coverage for rock domain and DFN modelling efforts. The mapping results are presented in detail in the data compilation report for Laxemar by /Hermanson et al. 2008/ and by /Forssberg et al. 2007/. The locations of the trenches are displayed below in Figure 2-2.

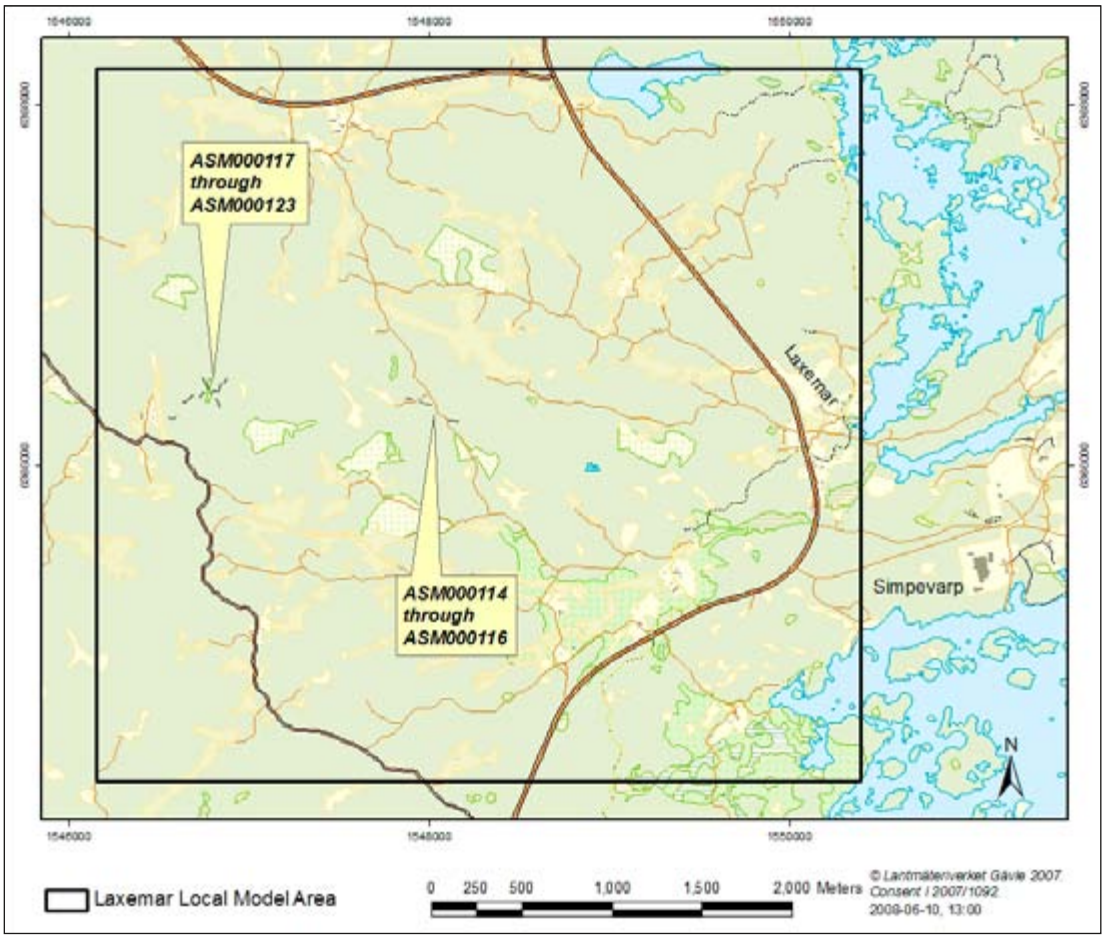

Figure 2-2. *Location of trench outcrops mapped at Laxemar in 2006 and 2007.*

The trench investigation was performed using a similar methodology as for the detailed fracture outcrops. Each trench was cleared of soil and organics, and both the fractures and the bedrock lithology were mapped in detailed. High-resolution digital photographs of each outcrop were taken, orthorectified, and merged into a continuous montage upon which mapped fracture data could be plotted. There are some slight differences in the fracture mapping protocol for the trenches in comparison to the outcrops described in the previous section, however. These differences included:

- Along each strip, fracture traces were measured within a 1 m wide corridor.
- Only traces longer than 1 m were mapped.
- Fractures with trace lengths > 1 m which had at least one end within the 1 m wide band were measured over their full length (including the section of the trace that lay outside the 1 m mapping band).

The illustration in Figure 2-4 shows the 1 m wide mapping strip within which traces > 1 m were mapped. Mapped traces extend outside as far as can be observed or to the boundary of the outcrop. The illustration in Figure 2-3 shows the orthorectified outcrop photographs, with mapped fracture traces (yellow lines) and the 1 m-swath mapping limits (dashed white line). Mapped traces extend outside as far as can be observed or to the boundary of the outcrop.

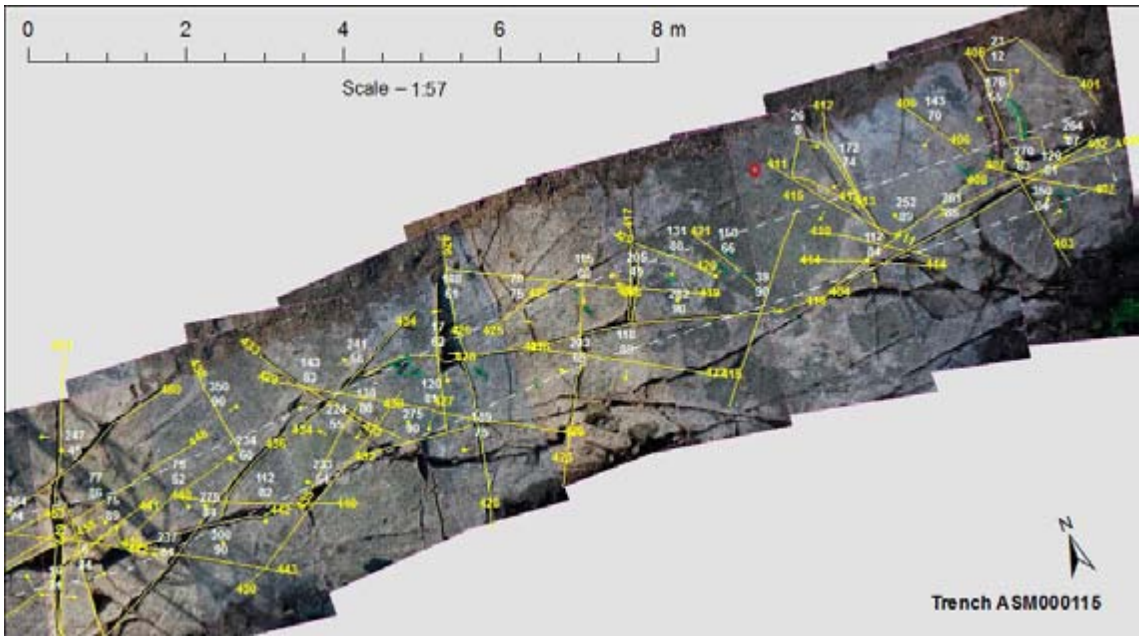

Figure 2-3. *Photographic map of trench ASM000115, illustrating bedrock fractures and extent of the 1 m mapped swath (dashed white line). Yellow text indicates fracture number, while white text indicates the strike (top) and dip (bottom) of the mapped fracture.*

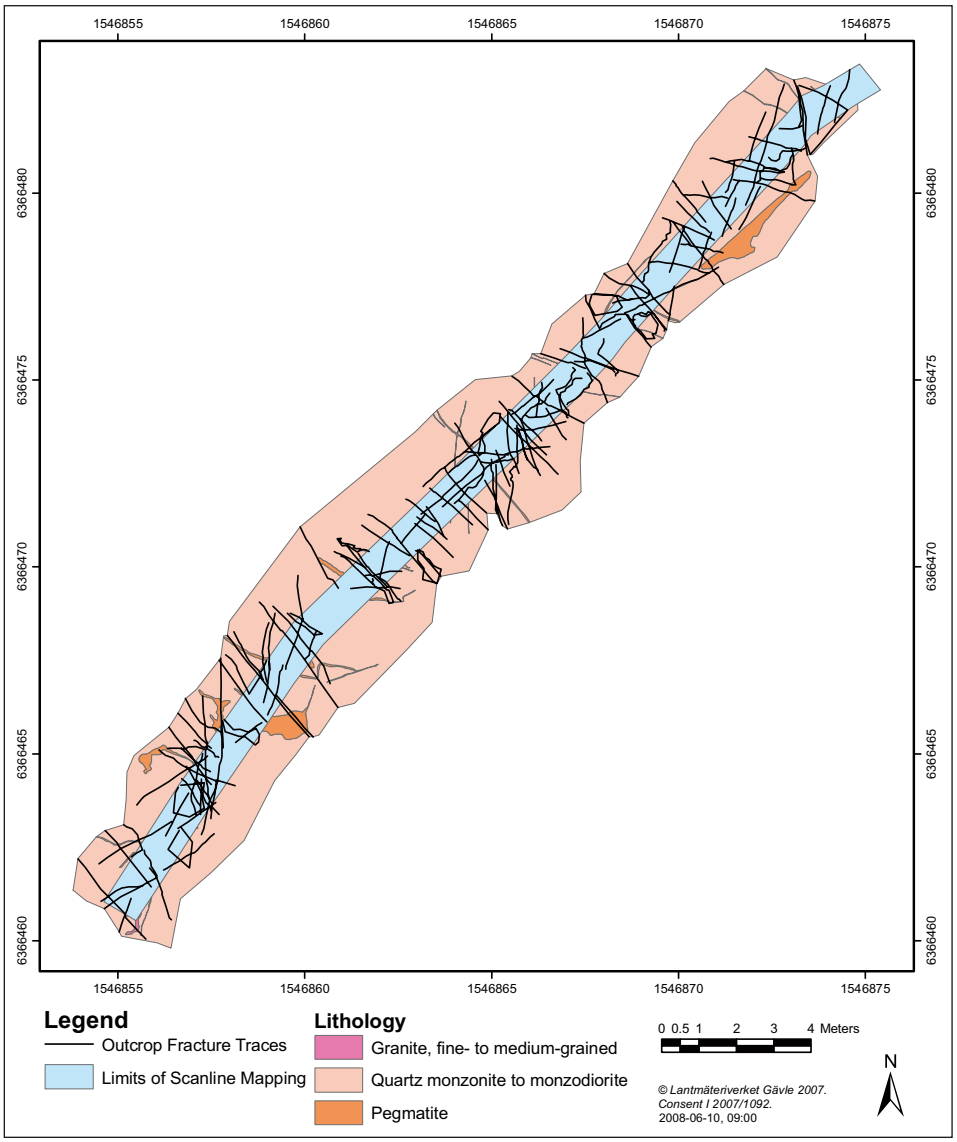

Figure 2-4. *Illustration of a mapping of trench ASM000123 and the mapped 1 m wide band along the strip. Data taken from SDE feature classes SDEADM_GOL_SM_GEO_4739, SDEADM_GOL_SM_GEO_4737, and SDEADM_GOL_SM_GEO_4767_VIEW. Coordinates are given in the RT-90 coordinate system.*

The trench mapping data consist of two basic types: polygon shapefiles delineating rock domain, lithology, or mapped area boundaries, and polyline shapefiles containing the mapped surface fracture traces. The trench data are composed of the following feature classes (with associated attribute tables) exported from SDE:

Trench Mapping Limits/Bedrock Lithology (Polygon shapefiles)

- SDEADM_GOL_SM_GEO_4740 – ASM000114 fracture scanline limits
- SDEADM_GOL_SM_GEO_5343 – ASM000114 outcrop limits and lithology
- SDEADM_GOL_SM_GEO_4742 – ASM000115 fracture scanline limits
- SDEADM_GOL_SM_GEO_4720 – ASM000115 outcrop limits and lithology
- SDEADM_GOL_SM_GEO_4743 – ASM000116 fracture scanline limits
- SDEADM_GOL_SM_GEO_4723 – ASM000116 outcrop limits and lithology
- SDEADM_GOL_SM_GEO_4745 – ASM000117 fracture scanline limits

- SDEADM_GOL_SM_GEO_4725 – ASM000117 outcrop limits and lithology
- SDEADM_GOL_SM_GEO_4746 – ASM000118 fracture scanline limits
- SDEADM_GOL_SM_GEO_4727 – ASM000118 outcrop limits and lithology
- SDEADM_GOL_SM_GEO_4747 – ASM000119 fracture scanline limits
- SDEADM_GOL_SM_GEO_4729 – ASM000119 outcrop limits and lithology
- SDEADM_GOL_SM_GEO_4748 – ASM000120 fracture scanline limits
- SDEADM_GOL_SM_GEO_4731 – ASM000120 outcrop limits and lithology
- SDEADM_GOL_SM_GEO_4749 – ASM000121 fracture scanline limits
- SDEADM_GOL_SM_GEO_4733 – ASM000121 outcrop limits and lithology
- SDEADM_GOL_SM_GEO_4750 – ASM000122 fracture scanline limits
- SDEADM_GOL_SM_GEO_4735 – ASM000122 outcrop limits and lithology
- SDEADM_GOL_SM_GEO_4739 – ASM000123 fracture scanline limits
- SDEADM_GOL_SM_GEO_4737 – ASM000123 outcrop limits and lithology

Fracture Maps (Polyline Shapefiles)

- SDEADM_GOL_SM_GEO_4751_VIEW – ASM000114 outcrop fractures
- SDEADM_GOL_SM_GEO_4752 – ASM000114 fractures with shear indicators
- SDEADM_GOL_SM_GEO_4753_VIEW – ASM000115 outcrop fractures
- SDEADM_GOL_SM_GEO_4754 – ASM000115 fractures with shear indicators
- SDEADM_GOL_SM_GEO_4755_VIEW – ASM000116 outcrop fractures
- SDEADM_GOL_SM_GEO_4756 – ASM000116 fractures with shear indicators
- SDEADM_GOL_SM_GEO_4757_VIEW – ASM000117 outcrop fractures
- SDEADM_GOL_SM_GEO_4758 – ASM000117 fractures with shear indicators
- SDEADM_GOL_SM_GEO_4759_VIEW – ASM000118 outcrop fractures
- SDEADM_GOL_SM_GEO_4760_VIEW – ASM000119 outcrop fractures
- SDEADM_GOL_SM_GEO_4761 – ASM000119 fractures with shear indicators
- SDEADM_GOL_SM_GEO_4762_VIEW – ASM000120 outcrop fractures
- SDEADM_GOL_SM_GEO_4763 – ASM000120 fractures with shear indicators
- SDEADM_GOL_SM_GEO_4764_VIEW – ASM000121 outcrop fractures
- SDEADM_GOL_SM_GEO_4765 – ASM000121 fractures with shear indicators
- SDEADM_GOL_SM_GEO_4766_VIEW – ASM000122 outcrop fractures
- SDEADM_GOL_SM_GEO_4767_VIEW – ASM000123 outcrop fractures
- SDEADM_GOL_SM_GEO_4768 – ASM000123 fractures with shear indicators

2.1.3 Borehole data

More than 18 km of cored borehole data have been utilized in the DFN analysis, c.f. /Hermanson et al. 2008/. Only fracture data from cored boreholes are used during DFN parameterization and fracture domain model development. Data from the following borehole are used (Figure 2-5):

- KLX01, KLX02, KLX03, KLX04, KLX05, KLX06, and KLX08
- KLX07A and KLX07B
- KLX09A, KLX09B, KLX09C, KLX09D, KLX09E, KLX09F, and KLX09G
- KLX10A, KLX10B, and KLX10C
- KLX11A, KLX11B, KLX11C, KLX11D, KLX11E, and KLX11F
- KLX12A, KLX13A, KLX14A, KLX15A, KLX16A, KLX17A, KLX18A, KLX19A, KLX20A, and KLX21B
- KLX22A and KLX22B
- KLX23A and KLX23B
- KLX24A, KLX25A, KLX28A, and KLX29A
- KLX26A and KLX26B

Fracture and geology data in Laxemar cored boreholes were extracted from the following SICADA tables:

- p_object_location (SICADA_07_345)
- p_fract_core_eshi (SICADA_07_350_2 and SICADA_07_410)
- p_fract_eshi (SICADA_07_350_2)

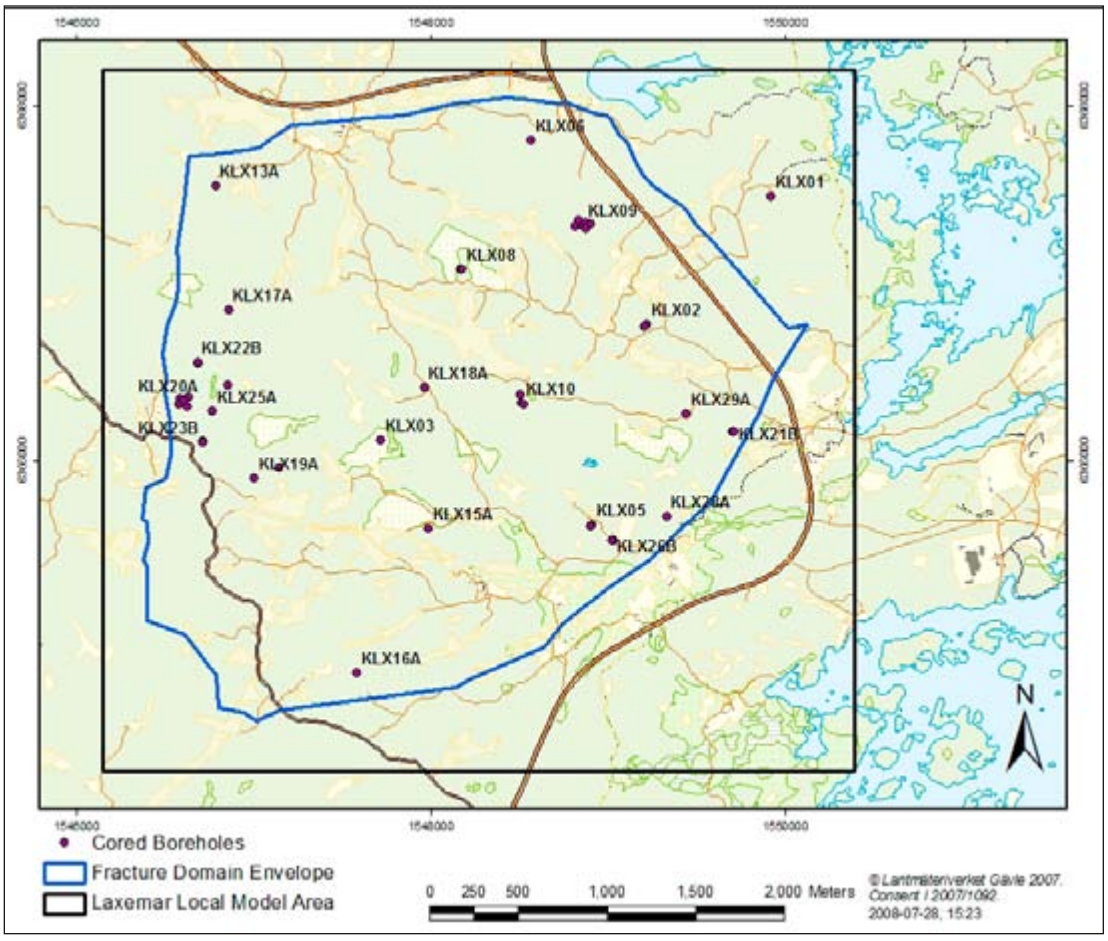

Figure 2-5. *Locations of cored boreholes used in SDM-Site Laxemar geological DFN modelling.*

2.1.4 Deformation Zone model

A draft version (20071211) of the Local SDM Site Laxemar deformation zone (DZ) model is used during the DFN model construction efforts. The draft models were downloaded from the model database SIMON, and consisted of two files:

- SDM_SITE_DZ_LOC_interim071018_nothick.dxf
- SDM_SITE_DZ_LOC_interim071018_thick.dxf

The .DXF files were converted into 3DFace-format DXF meshes using PolyTrans3D, and imported into FracMan. The DZ model is not used for DFN model parameterization; rather, it is used for visualization and verification purposes. The surface expression (traces intersecting at an elevation of 0 m; i.e. sea level) of the DZ model within the Laxemar local model area is presented as Figure 3-1 in Section 3.2.

2.1.5 Surface lineaments

The surface linked lineaments, along with their associated attribute table, are used in the construction of the coupled size-intensity models. Lineament length and orientation data were exported from the attribute table to Microsoft Excel for inclusion in geological DFN models. Data for this analysis were taken from SDE, and consisted of the following feature classes:

- SDEADM_GV_LX_GEO_5567
- SDEADM_GV_LX_GEO_5566

Surface lineaments are illustrated in Figure 3-2 in Section 3.2.

2.1.6 Minor deformation zones

A number of minor deformation zones were identified during site activities leading up to the SDM-Site Laxemar geological modelling efforts. MDZ in the cored borehole array are defined as structures with an apparent thickness of less than 10 m that are only seen in a single borehole (i.e. cannot be projected to intercepts in other boreholes). The MDZ intercepts are used in the size-intensity model verification (Case SI-3). Data for the MDZ at Laxemar are taken directly from Appendix 3 of the SDM-Site Laxemar data compilation report (DCR) /Hermanson et al. 2008/. A detailed discussion of how minor deformation zones fit into the DFN coupled size-intensity model is presented in Section 5.5.

2.1.7 Fracture domain models

A specific RVS model for fracture domains was constructed during the SDM-Site Laxemar geological DFN modelling. The RVS model contains raw geometries that define each fracture domain in three-dimensional space. A two-dimensional projection of the fracture domains at sea level (elevation = 0 MASL) was exported to ArcGIS for inclusion in SKB's SDE database. The files related to the fracture domain model are:

- SDM_SITE_DZ_LOC_interim.rvs
- FD_LX_LOC_V23b.rvs (delivered to SIMON)
- FD_LX_LOC_V23b-topographic_section-2D.shp (delivered to SDE)

Fracture domains are illustrated in Figure 4-6 through Figure 4-9 in Section 4.1.

2.1.8 Data used in the definition of fracture domains

Table 2-1 and Table 2-2 summarize the information used from boreholes and outcrops in the derivation of the fracture domain model during SDM-Site Laxemar geologic modelling.

Table 2-1. Borehole data population, divided in terms of structure visibility in BIPS image logs and fracture aperture interpretation.

	Visible in BIPS					Not visible in BIPS							
IDCODE	Sealed	Open	Partly open	Unidentified	sum	Sealed	Open	Partly open	Unidentified	Sum	Missing orientation	Inside DZs	Borehole total
KLX02	301	471	28		800	187	325	18		530	165	1,575	3,070
KLX03	2,089	284	2		2,375	920	125	1		1,046	110	857	4,388
KLX04	2,309	826	8		3,143	660	291	3		954	103	1,298	5,498
KLX05	1,753	209	1		1,963	1,371	74			1,445	61	70	3,539
KLX06	1,741	388	11		2,140	1,184	135			1,319	247	1,661	5,367
KLX07A	2,182	668	5		2,855	779	200	1		980	108	2,622	6,565
KLX07B	438	226	2		666	114	54	1		169	36	503	1,374
KLX08	1,691	945	2		2,638	728	320	5		1,053		1,605	5,296
KLX09	1,861	546	1		2,408	488	348	2		838	10	1,406	4,662
KLX09B	255	120			375	97	32			129	25	80	609
KLX09C	368	169	3		540	94	42			136	31	64	771
KLX09D	327	164	2		493	132	48	2		182	59	181	915
KLX09E	333	124			457	133	44			177	32	355	1,021
KLX09F	330	123	2		455	219	68	1		288	10	289	1,042
KLX09G	274	88	1		363	121	26			147		318	828
KLX10	1,943	880	4		2,827	958	503	1		1,462	21	1,291	7,947
KLX10B	149	86	3		238	15	10			25	28	341	746
KLX10C	495	131	1		627	56	31			87	30	821	1,784
KLX11A	2,757	368		1	3,126	884	249			1,133	4	1,095	6,860
KLX11B	172	91			263	90	35			125	1	55	660
KLX11C	210	95			305	106	35			141			682
KLX11D	318	131			449	58	18			76		154	886
KLX11E	171	102			273	174	37			211		171	968
KLX11F	194	86			280	88	17			105	5	23	604
KLX12A	851	560	3		1,414	903	514			1,417	49	121	4,981
KLX13A	1,175	702	3		1,880	395	259			654	25	1,177	5,095
KLX14A	259	271			530	261	78			339	48	589	2,116
KLX15A	1,937	871	5		2,813	1,145	447	3		1,595	31	1,079	7,989
KLX16A	1,199	504	5		1,708	549	132			681	22	1,546	5,147
KLX17A	2,174	509	3		2,686	690	156	2	1	849	65	868	5,829
KLX18A	1,179	583	4		1,766	526	218			744		548	4,389
KLX19A	731	295	1		1,027	552	167			719	35	941	3,737
KLX20A	532	243			775	570	150			720	9	794	3,261
KLX21B	2,141	616	4		2,761	805	211			1,016	29	2,094	7,536
KLX22A	326	225			551	102	33			135		8	1,054
KLX22B	313	194			507	101	39			140		22	1,003
KLX23A	97	42			139	26	8			34	3	31	283
KLX23B	40	26			66	14	11			25		24	166
KLX24A	314	238	2		554	173	66			239		91	1,363
KLX25A	143	70			213	85	16			101	1	32	518
KLX26A	188	213	1		402	146	84			230	7	173	1,256
KLX26B	93	223	1		317	13	16			29			599
KLX28A	217	109			326	33	21			54	12	171	726
KLX29A	171	131	1		303	53	9			62	15	83	657

Table 2-2. Outcrop data population; in model parameterization outcrop data are combined with borehole data visible in BIPS, but lacking open/sealed interpretation.

IDCODE	Original data set	Linked data set
ASM000114	249	NA
ASM000115	180	NA
ASM000116	204	NA
ASM000117	188	NA
ASM000118	192	NA
ASM000119	101	NA
ASM000120	255	NA
ASM000121	450	NA
ASM000122	236	NA
ASM000123	160	NA
ASM000208	1,053	870
ASM000209	1,030	923
ASM100234	1,128	905
ASM100235	1,028	757

2.2 Software

Table 2-3. List of software used in the production of the SDM-Site Laxemar geological DFN.

Software Name	Version	Company	Calculation Performed
Excel 2003	11.8120.8122 SP2	Microsoft Corporation One Microsoft Way Redmond, WA 98052 www.microsoft.com	Trace length scaling calculations; general data preparation for other programs, moving-average intensity tables
Analyze-It		Analyze-It Software, Ltd. PO Box 77, Leeds LS12 5XA, England, UK. www.analyse-it.com Tel: +44 (0)113 229 5599	Summary tables for fracture intensity as a function of alteration zones and rock types; variation of fracture intensity with depth
DIPS	5.106	Rocscience, Inc. 31 Balsam Avenue Toronto, Ontario M4E 3B5 +1 416 698-8217 www.rocscience.com	Orientation and display of fracture orientations; calculation of modal poles to fracture sets, Terzaghi weighting of contoured pole plots Trace length scaling calculations; general data preparation for other programs, moving-average intensity tables
GeoFractal	1.2, Build 321	Golder Associates Inc. 18300 NE Union Hill Rd. Redmond, WA 98052 +1 (425) 883-0777 fracman.golder.com	Calculation of fractal mass dimension and box dimension
FracMan	7.00/7.10	Golder Associates Inc. 18300 NE Union Hill Rd. Redmond, WA 98052 +1 (425) 883-0777 fracman.golder.com	Visualization of simulated fracture orientations, conditional sampling of test DFN models
ArcGIS	9.2 SP2 and SP3	ESRI Inc 380 New York St. Redlands, CA 92373 +1 909 793 2853 www.esri.com	Display of fracture and deformation zone traces, creation of new GIS files and metadata to aid data analysis. Visual analysis of outcrop fracturing for set parameterization

Software Name	Version	Company	Calculation Performed
EasyFit XL	4.2 and 4.3	Mathwave Technologies www.mathwave.com	Curve fitting and analysis of statistical significance of P_{32} as a gamma or Weibull distribution
BestFit	4.5.5 Sep. 2005	Palisade Corporation 798 Cascadilla Street Ithaca, NY 14850 (607)-277-8000 www.palisade.com	Curve-fitting and analysis of statistical significance, P_{32} as a gamma distribution
Manifold GIS	8.0	Manifold .Net, Ltd. 1805 North Carson St. Suite 700 Carson City, NV 89701 +1 800 556 5919 www.manifold.net	Extraction of feature data from lineament and deformation zone shapefiles
SPSS	13.0	SPSS, Inc. 11th Floor 233 S. Wacker Dr. Chicago, Illinois 60606 +1 312 651 3000 www.spss.com	Contingency table analyses for relation between alteration, lithology & intensity, hypothesis testing, statistical modelling of spatial patterning and intensity variation of fracture sets
GoLink	N/A	Golder Associates AB P.O. Box 20127 104 60 Stockholm Sweden www.golder.se	Algorithmic linking of 3D fracture traces based on geometrical and morphological properties
SetDivide	N/A	Golder Associates AB P.O. Box 20127 104 60 Stockholm Sweden www.golder.se	Algorithm for parameterising fracture orientation by univariate Fisher distributions and dividing fracture data into sets
ComputeC13	N/A	Golder Associates, Inc. 18300 NE Union Hill Road, Suite 200 Redmond, WA 98052 www.fracturedreservoirs.com	A C++ batch-mode implementation of the Wang C_{13} conversion factor for P_{10}–>P_{32}
PolyTrans 3D	4.3.8	Okino Computer Graphics 3397 American Dr. Unit #1 Mississauga, Ontario L4V 1T8 Canada www.okino.com	Translation of polyface DXF meshes into 3DFace format for use in FracMan

3 Geological DFN model methodology

3.1 Modelling prerequisites, assumptions, limitations, and feedback from other disciplines

3.1.1 Strategy for SDM-Site Laxemar geological DFN

The anticipated users for the geological DFN at Laxemar are expected to be hydrological and mechanical modelling, repository design and engineering planning, and to provide inputs in support of repository safety assessment and licensure. The goal of the geological DFN model is to provide these users with a quantitative basis for specifying fracture orientations, sizes, intensity, spatial variability, and correlation to geological factors at any given location within the Laxemar local scale model volume (Figure 1-1) outside of the footprint of modelled deformation zones.

The model is presented as a mathematical and statistical description of fracturing observed in the Laxemar local model area; it is not implemented as a specific stochastic realization. As such, the model parameterisation can be used in a number of different ways: as a discrete fracture network model for direct stochastic simulation, as fracture network properties that can be upscaled into equivalent continuum models (block permeability tensors, block elastic modulus tensors, porosity, fracture intensity, storage volumes, etc), or as statistical distributions for inclusion in performance-assessment or Monte Carlo-style risk analysis models. The implementation of the statistical and mathematical description of fracturing at Laxemar is a direct function of the needs and limitations of the chosen downstream model; therefore, direct implementation of the GeoDFN model is beyond the scope of the modelling process.

The SDM-Site Laxemar DFN modelling is based on defining and delineating fracture domains in order to reduce the overall uncertainty in the final GeoDFN model. The fracture domain concept, originally suggested in /Munier et al. 2003/, in line with standard practice in structural geology and applied in principal during Forsmark model version 2.2 geological model /Olofsson et al. 2007/ and DFN model /Fox et al. 2007/ modelling, is key to the reduction of uncertainty. Fracture domains are regions of geologically distinct and statistically similar rock fracturing, such that the variability in fracture properties between domains is larger than the variability within a single domain.

The GeoDFN has four distinct sub-models, which together define the statistical behaviour of fractures and minor deformation zones at Laxemar. These sub-models are:

1. **Fracture domain model**: As described in Section 3.2, fracture domains are rock volumes outside of the bounds of modelled deformation zones in which the rocks show similar fracture characteristics. At both Forsmark and Laxemar, fracture orientation and intensity (both total intensity and the relative intensity of different sets) played a major role in the identification of fracture domains. The key objective of the fracture domain assignment is the reduction of the total model uncertainty through the delineation of volumes of rock that possess geological characteristics that correspond to variations in fracture intensity and orientation.
2. **Fracture orientation set model**: Fracture orientation set modelling consists of the identification and parameterisation of fractures into sets as a function of their orientation in space (pole trend and plunge or strike and dip) and possibly of other geological factors. Though orientation is the primary key for classification, other parameters, such as lithology, fracture morphology, aperture, and fracture mineralogy can also be used to divide fractures into sets if they are found to possess statistically-significant differences across the data record. The variability in orientation for each fracture set is defined using univariate Fisher hemispherical probability distributions.

3. **Fracture size/intensity model**: This sub-model describes the size of fractures, expressed as equivalent radius and the intensity, in terms of fracture area per unit volume (P_{32}), which honours the intensity of the fractures observed in cored borehole records and on outcrops at Laxemar. Fracture size and fracture intensity, though separate properties, are mathematically related, since the value of intensity always pertains to a specified size range. Thus, it is appropriate to combine the size and intensity models into one single sub-model. Note that in this report, however, size and intensity modelling are treated in separate chapters for readability.
4. **Fracture spatial model**: The fracture spatial model includes a fairly wide range of analyses of the spatial properties of rock fractures at Laxemar. The spatial model describes how fractures inside fracture domains are distributed spatially, and how their intensity or location scales as a function of model scale. In the SDM-Site Laxemar geological DFN, the spatial model consists of the following parameterisations and analyses.
   – Correlation of fracture intensity to rock domains or host lithology, if possible.
   – Analysis of fracture intensity scaling.
   – Analysis of the spatial variability of fracture intensity.
   – Evaluation of the depth-dependence of fracture intensity.
   – Quantification of the termination relationships between fracture orientation sets.

3.1.2 Modelling prerequisites

The GeoDFN model is built in conjunction with other site descriptive models. In particular, the deterministic deformation zone (DZ) model (Chapter 5 of the SDM-Site geology report /Wahlgren et al. 2008/) is crucial to the geological DFN; the edges of fracture domain volumes (Sections 3.2 and 4.1) are defined at Laxemar by the location and thickness of modelled deformation zones (DZ). This implies that if the DZ model was to change, the GeoDFN model parameterisation could change significantly.

3.1.3 Model assumptions and limitations

The model is intended only to be valid for the rock volume described by the boundaries of the target fracture domains (FSM_N, FSM_W, FSM_C, FSM_NE005, and FSM_EW007, as defined in Section 4.1 and presented in Figure 4-6 through Figure 4-9) and only for the data on which it was based, as described in Section 2.1. This model is not intended for application outside of the target fracture domains. As such, all conclusions and parameters provided in this study should be re-evaluated for any use outside the described volumes.

The key assumptions required to generate the geological DFN for SDM-Site Laxemar are:

- All data retrieved from SICADA are assumed correct. No systematic checking of data validity from this database was carried out by the modelling team. However, the selected SICADA and SDE data were sent to and reviewed by SKB prior to using it for developing the DFN model in order to further minimize data errors or usage of incorrect data.
- The length of a minor deformation zone trace or a linked fracture in outcrop is an accurate and appropriate measure of a single fracture's trace length for the purpose of deriving the radius distribution of geologic structures.
- Deterministic deformation zones constitute a distinct population of fractures different from the "background" fractures and minor deformation zones (MDZ). As such, the mathematical model for the background fractures and MDZ is a distinct model from that describing the deformation zones. The cut-off between DZ and MDZ is made at an equivalent radius of 564.2 m, which corresponds to a square fracture with sides that are 1,000 m long.
- For purposes of modelling size (in terms of surface area), fractures can be approximated as planar, circular discs with a radius that can be described using a probability distribution. The actual fracture shape is not required to be circular; square, rectangular, or polyhedral-shaped fractures are fully acceptable, as long as they are simulated using a one-sided surface area which is equivalent to that of a similarly-sized circular disk. While the real fractures in the rock are probably neither circular nor planar, there are not sufficient data to mathematically

characterise deviations from these two idealizations. In outcrop, the deviations from planarity do not appear to be large. There are also mechanical reasons to suppose that the actual fracture shapes may tend towards being equant, as the mechanical or stratigraphic layering present in sedimentary rocks (which can promote the growth of non-equant fracture shapes) is far less well-developed in the crystalline rocks of the Fennoscandian Shield.

- Fracture sets can be usefully parameterized based only upon orientation. In developing set definitions from outcrops and boreholes, fracture set membership is based only on orientation. However, the identification of orientation sets also relied upon parameters such as length, rock structure, and set termination relationships.
- The geological DFN parameterisation uses a global orientation model that represents the average orientation of sets across the fracture domains. The inherent assumption is that fracture domains at Laxemar differ not in terms of fracture set orientations, but in terms of relative intensities of the identified orientation sets.
- No fracture data from inside mapped deformation zones, sealed fracture networks (zones of very intense sealed fractures too numerous to log or count), or inside areas of crushed rock noted in the cored borehole records are used in the parameterisation of the geological DFN orientation, size, intensity, or fracture domain models.

Additional assumptions relevant to specific model components, such as the size or spatial models, are discussed in the relevant sections.

3.1.4 Linking of fracture traces

During 2007 and early 2008, a re-analysis of fracture traces recorded on detailed fracture outcrops was performed. The re-analysis used geometric and geologic relationships between fracture traces to 'link' them together into larger-scale structures whose geometry may have been lost in the outcrop mapping process. The goal of the linking efforts were to provide a more reasonable definition of fractures at the outcrop scale, where the length of the surface traces directly affects the final size model parameterization in the geological DFN. This is also consistent with the procedure used in lineament interpretation /Triumf and Thunehed 2007/.

The SDM-Site Laxemar geological DFN model is parameterised using both linked and unlinked traces; both cases are carried through the uncertainty analysis (Chapter 6) and model verification (Chapter 5). The trace linking methodology is described in detail in Appendix A.

3.1.5 Feedback from other disciplines

The methodology and implementation for the SDM Laxemar Site geological DFN incorporates many changes and suggestions from expert reviewers of past model versions (including those related to Forsmark). This is a significant advantage of the successive and evolutionary approach to geologic modelling.

Specifically, SDM-Site DFN models incorporate the following changes, based on feedback from both expert reviewers and other modelling teams:

- The DFN implementation has been simplified where possible, so as to make the resulting model easier to understand and use. The fracture domain concept (Section 3.2) first used during the Forsmark Stage 2.2 geological modelling has been introduced at Laxemar to maintain consistency between the two sites and with other geological (RD, DZ) models. In addition, orientation sets were simplified so as to use the minimum number of sets to define fractures in the rock mass.
- More emphasis has been placed on quantifying spatial variability. In particular, the spatial variability of fracture intensity, both over the Laxemar local scale model volume and as a function of depth, has been given special attention based on feedback from expert reviewers.
- More emphasis has been placed on model verification, model uncertainty, and the ranking of alternative size, intensity, and spatial models. This was a request from expert reviewers.

3.2 Fracture domain model methodology

Fracture domains (abbreviated FSM throughout this chapter) provide a large-scale conceptual framework for describing spatial heterogeneity in rock fracturing. The goal behind identifying fracture domains is to find rock volumes with fracture characteristics such that the variability between volumes is larger than the variability within volumes /after Munier 2003/, in line with standard geologic practice. As such, fracture domains should form the basic divisions over which spatial heterogeneity in rock fracturing is characterised; these domains may not necessarily correspond to the limits of other geologically-significant volumes such as those defined in the Rock Domain (RD) model /Wahlgren et al. 2008/.

Within the Laxemar local model area, the fracture orientation set definitions (see Section 3.3) do not possess appreciable spatial variability. Some local-scale variation in the orientation of the mean poles for the sets does exist, but in general, the number and general strike orientations of fracture sets are stable. Rather, the relative intensity of fracture orientation clusters and the location of major regional structural features (DZ) appear to be the controlling factors on fracturing within the Laxemar subarea. As such, these properties are used to delineate the fracture domains during SDM-Site Laxemar geological DFN model development. The fracture domains defined during the construction of the geological DFN combine statistical analysis of relative fracture set intensities with domain boundaries built atop the current understanding of the geologic and tectonic conditions at Laxemar and their evolution through time.

3.2.1 Concepts and key assumptions

The key assumptions behind the fracture domain model are:

- Fracture domains are a valid concept for delineating spatial heterogeneity of fracture intensity at repository scales, i.e. rock volumes with similar fracture patterns at the scale of approximately two square kilometres. A fracture domain was defined as a confined conceptual geological unit with similar general fracture characteristics, such that the fracture population inside a fracture domain are geologically unique when compared to the fracture population outside of the fracture domain.
- The distinction between ‘open’, ‘partly open’, and ‘sealed’ fractures exists only for fractures recorded in cored boreholes. Fracture aperture data recorded on surface outcrops are highly uncertain due to geomorphic effects and weathering. Therefore, when a domain definition is created based on an increase or decrease in sealed or open fracture intensity, the domain definition is based solely on borehole data.
- Data from boreholes KLX01, KLX06, KLX02 inside rock domain RSMBA03, and KLX20A west of regional deformation zone ZSMNS001C were excluded. KLX06 was excluded because it is viewed as being too significantly influenced by the Mederhultszonen (ZSMEW002). KLX02 and KLX20A are outside the limits of the fracture domain envelope. Fracture data from KLX01 did not contain fracture orientations recorded in SICADA; therefore it was impossible to classify data from this borehole into fracture sets. Fracture data from KLX09B was excluded based on the recommendations presented in /Munier and Stigsson 2007/; orientation uncertainty in this borehole is viewed as unacceptably large.
- For applicability to downstream users, pragmatic spatial definitions are used for the fracture domains. Furthermore, the number of fracture domains is minimized.
- The spatial extent of fracture domains (outside boreholes and beyond outcrops) are delimited by geological parameters or by predefined geographical limits where data coverage ends. For example, domains could be delimited as rock volumes bounded by regional deformation zones or lithologic/tectonic structures (such as the Äspö shear zone).

Only outcrop data and data from oriented cored boreholes are used in the identification of potential fracture domains. Only fractures that are visible in the BIPS image logs are used in the analysis of preliminary domain definitions. No data from within modelled deformation zones,

minor deformation zones identified in the ESHI analysis, sealed fracture networks, or zones of crushed rock identified in the single-hole interpretations are included. The linked lineaments from high resolution ground geophysics/LIDAR surveys are also considered during the identification of fracture domains.

For the SDM-Site Laxemar modelling, fracture domains were conceptually constrained by regional and local major deformation zones (Figure 3-1). Fracture domains are identified and bounded using:

a. The orientation and intensity of fractures by type: only sealed fractures, only open fractures, and all fractures combined.

b. The orientation and intensity of regional- and local-scale lineaments derived from airborne laser swath mapping (LIDAR) and high-resolution ground geophysics, c.f. Section 3.8 of the SDM-Site Laxemar geology report /Wahlgren et al. 2008/.

The benefit of the use of lineament data are their spatial extent – the lineament maps provide data coverage over most of the Laxemar local model area. However, the downside to the use of lineament maps is the distinct lack of solid data and proof of their geologic origin and geometry, when compared to structures (fractures, MDZ, and DZ) identified in boreholes and on outcrops. During the analysis, early results indicated that the lineament data did not help to constrain the identification, nor the spatial definition of fracture domains. It was therefore decided to only use the lineament data in the analysis of fracture size and intensity.

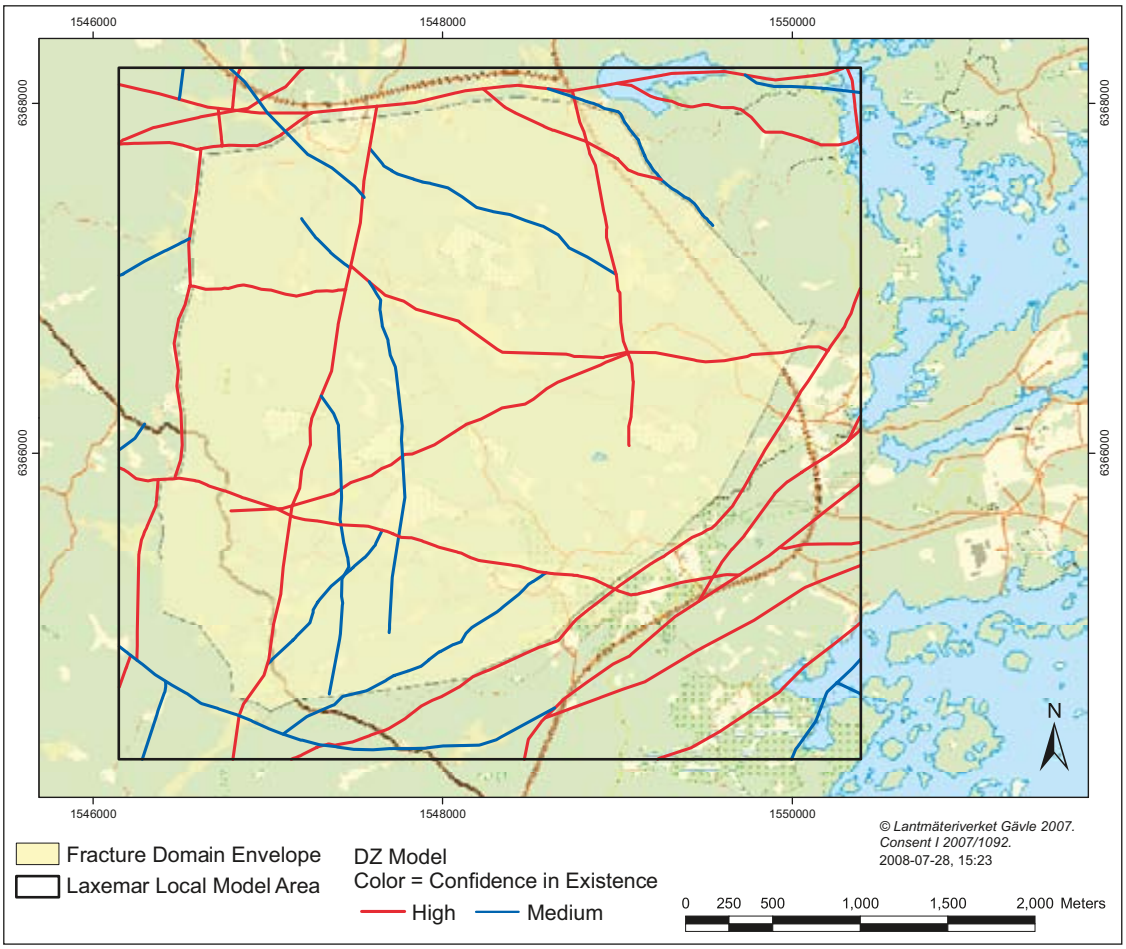

Figure 3-1. *Regional and local major deformation zone traces within the Laxemar local model area. DZ traces are coloured by the confidence in their existence (red = high confidence and blue = medium confidence).*

Spatial definition of potential fracture domains

A key problem in all site-descriptive modelling is the issue of data availability and data density. The problem is particularly acute for the discrete fracture network model, which relies on a wide variety of data types over a fairly large area. Borehole and outcrop data exist only in the central parts of the local model volume, as previously shown in Figure 2-1, Figure 2-2, and Figure 2-5. More importantly, detailed lineaments are only mapped at a high resolution within a certain area (Figure 3-2). Outside of this area, there is little to no data coverage of lineaments in the MDZ size range. This area of high data density (Figure 3-2), hereafter referred to as the fracture domain envelope area, serves as the spatial extent of the fracture domain analysis as well as the boundary of the SDM-Site Laxemar geological DFN model parameterization.

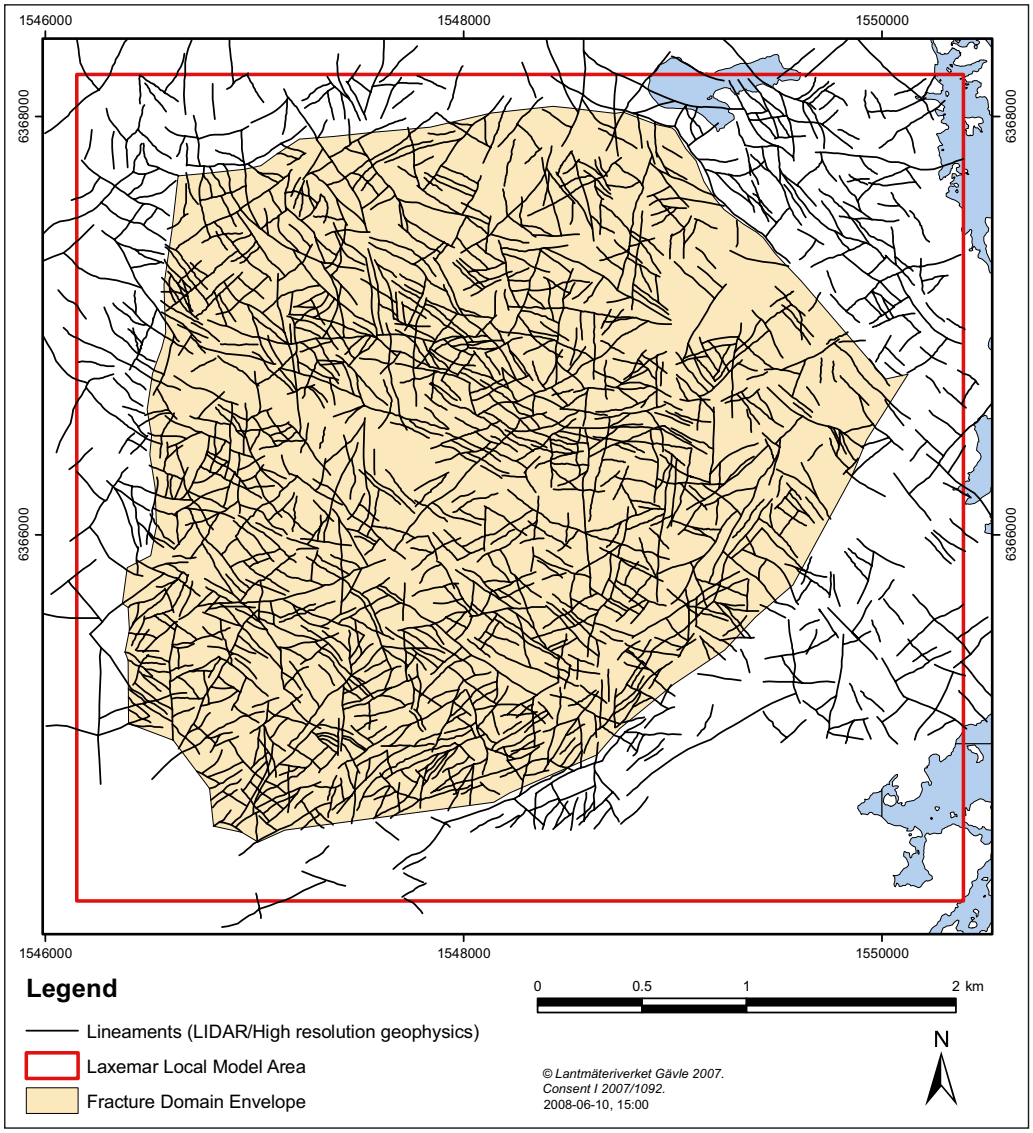

Figure 3-2. *Illustration of the limits of the SDM-Site Laxemar DFN modelling efforts. The fracture domain envelope (yellow area) is assumed to encapsulate the area where surface coverage of detailed lineaments shorter than 1,000 m is of equal resolution.*

A key component of the fracture domain concept is the recognition that regional and local major deformation zones can influence rock fracturing – even at a distance outside the actual zone core, as defined in previous DFN methodology documents, c.f. /Munier et al. 2003, Munier 2006/. A majority of the new boreholes drilled at Laxemar have been oriented to preferentially investigate regional or local deformation zones. In many of these boreholes, the fracture pattern as recorded during borehole mapping suggest that, in many cases, fracture orientation and intensity can be correlated to the presence of a deterministic deformation zone in the borehole. This relationship does not appear to include the possible local minor deformation zones identified during the extended single-hole interpretation process. Figure 3-3 illustrates an example of a borehole where even outside the core of the deformation zone (purple band) an increased frequency of open fractures is evident. These patterns of elevated fracture frequency distal to mapped deformation zones are important keys to identifying fracture domains at Laxemar.

Fracture domains induced by regional and local major deformation zones

The regional and local major deformation zones identified above are assumed to serve two purposes in the identification/definition of fracture domains: either:

- The foundation (base, core) of a fracture domain, or
- A barrier or separation between two fracture domains.

As a starting point, the three largest zones within the local model area, EW007A, EW002A, and NE005A are considered large enough to influence the rock blocks adjacent to them. As such, data from boreholes and outcrops were divided into fracture domains that were conceptualized as centred on the associated deformation zone, and extended a certain distance outwards, after which the dominant influence of the zone ceased.

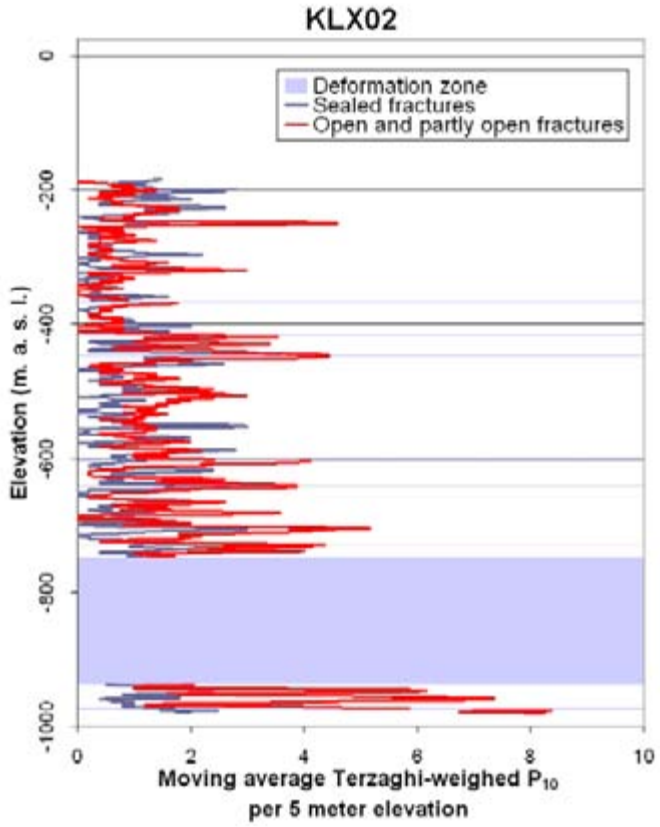

Figure 3-3. *Fracture intensity as a function of elevation (z, in metres) in cored borehole KLX02. Note the increased fracture intensities proximal to the core of the mapped deformation zone (lilac); this supports the conceptual model that DZ can influence the fracture pattern even outside of their mapped (ESHI, DZ model) footprint.*

Fracture domains separated by regional and local major deformation zones

The remaining deformation zones which may have served as indicators for fracture domain transitions (ZSMNS001C, ZSMNS059A, ZSMNW042A, ZSMNE107A, and ZSMNW928A) are hypothesized to have a smaller influence on rock volumes outside of the limits of the zone. For the remaining deformation zones inside the Laxemar local model area, it is difficult to state which zone had the dominant control of fracturing when multiple deformation zones were present (e.g. at zone intersections). However, it is judged geologically reasonable to assume that a rock mass confined between two sub-parallel zones was subject to mechanical influences from both zones, such that the fracturing in the sandwiched rock mass differs from the "global mean" fracturing values.

Therefore, it is assumed that fracture domains can also be formed between two subparallel zones. In other words, the remaining deformation zones could act as barriers between fracture domains and thus be used to define their spatial extent.

3.2.2 Summary of fracture domain identification methodology

The method used to identify and define fracture domains during the SDM-Site Laxemar DFN modelling can be summarized by the following iterative procedure:

1. Individual data sets (fracture orientations from outcrops and cored boreholes, along with lineament strike orientations) are analysed. Anomalous orientations or increased fracture intensities are compared to and associated with adjacent deformation zones where possible. Kamb-contoured stereonets (see /Munier 2006a/ for more details) are used to analyze fracture orientation and relative intensity data mapped on outcrops and in cored boreholes. The stereonets used in this process are presented as Appendix B. Fracture intensity data (P_{10}) from cored boreholes are also used; Figure 3-4 illustrates the set-wise intensity data used in conjunction with the Kamb-contoured stereonet plots. /Kamb 1954/.
2. An initial geological fracture domain hypothesis is formulated by combining relative fracture intensity and the tentative orientation sets with tectonic history, deformation zone geometry, and rock domain volumes from past modelling efforts. The domains are identified using the relative intensities of different fracture pole cluster orientations, the ratio and relative intensity of open versus sealed fractures, and the proximity to deformation zones.
3. The approximate boundaries of the tentative fracture domain are defined using the geometries of regional and local major deformation zones.
4. Fracture data within the tentative fracture domain are combined, evaluated, and compared to the remaining data set. If the difference in the fracture pattern (in terms of orientation and relative set intensity) between the proposed fracture domain and the global population can be considered small, the hypothetical domain is rejected. If the difference in the fracture pattern is relatively large, the hypothetical domain will be accepted as a valid fracture domain for DFN modelling purposes. If elements of the data from the proposed fracture domain are found to deviate significantly from the domain mean as a whole, the fracture domain definitions will be refined by a detailed analysis of alternative data subsets. The refinement involved adjustments of the spatial definitions of the fracture domain (given geometrical and geological constraints) in order to enhance the deviant characteristics of this fracture domain.

3.2.3 Evaluation of fracture domain, rock domain and lithology classifications

Once fracture domains were identified, the next step is to determine whether the identified domains are a statistically appropriate subdivision of the Laxemar local model volume. Statistical stratification of fracture data into groups will reduce the overall uncertainty of the DFN model if the groups are defined such that the variability within the groups is much less than the variability between the groups. On the other hand, if the groups share similar characteristics, then the reduction in uncertainty by adopting the grouping will be small and possibly not worth the additional effort.

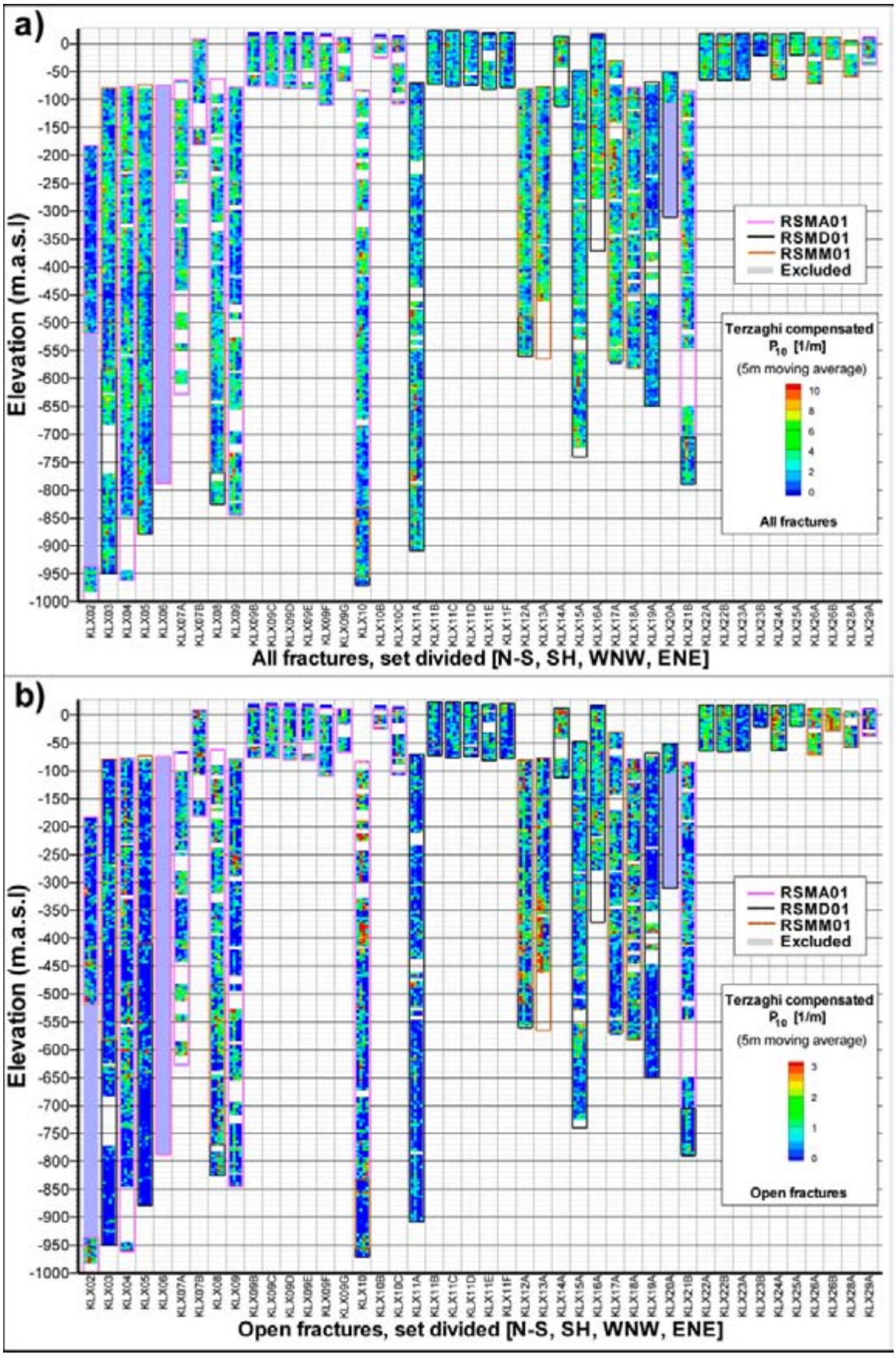

Figure 3-4. *Set-wise linear fracture intensity (P_{10}) shown as a moving average over a 5 m window, as a function of elevation; a) all fractures and b) open fractures. These plot types were instrumental in the identification of fracture domains.*

It is important to note that the identification of fracture domains and the identification of fracture orientation sets occurs simultaneously through an iterative process. Tentative orientation sets based on general grouping of fracture poles to major cardinal directions (NE, NW, WNW, NS, etc) are used to suggest likely areas or trends for further study and potential subdivision into fracture domains. The sets are further refined statistically through the orientation analysis (described below in Section 3.3) for use in the DFN model parameterisation. The final relative set intensities, after the completion of the orientation analysis, are then used to parameterise the fracture domains.

As part of the verification of the fracture domain model, a series of statistical tests are performed on the borehole fracture data to determine whether the fracture domains are statistically different from each other, whether the fracture domains (FSM) or rock domains (RD) are statistically reasonable subdivisions for fracturing, and whether the major rock lithologies have sufficiently different fracture characteristics that there needs to be subdivision by lithology. The statistical tests that are used to address these questions consist of:

- For nominal variables such as roughness, mineral filling, or fracture set designation, cross-tabulation, sometimes referred to as contingency table analysis, is appropriate and widely used /Pearson 1904/. Statistical significance is established using Chi-Squared goodness-of-fit tests.
- For continuous variables such as fracture width, fracture aperture, or fracture length, Linear Discriminant Analysis (LDA) /Davis 2002/ provides a way of assessing whether two groups can be differentiated based on linear combinations of the continuous variables at a prescribed level of statistical significance. Wilk's Lambda test /Shapiro and Wilk 1965/ is used to determine the strength and statistical significance of the separation of continuous variables into linear combinations.
- As fracture intensity is a parameter calculated over a region that may contain more than one fracture set, LDA and cross-tabulation is not an appropriate technique. Instead, standard 1-way ANOVA calculations /Snedecor and Cochran 1980/ is performed on P_{32} values derived for 3 m long intervals in the cored borehole records for each fracture domain. ANOVA calculations examine whether the fracture intensity variation within individual sub groups is less than the fracture intensity variation among groups. In these tests, the Null Hypothesis is that there is no difference. The Null Hypothesis is rejected if the test statistic probability is less than or equal to 0.05.

The hypothesis testing was carried out only using fractures outside of deformation zones.

3.3 DFN orientation model methodology

3.3.1 Basic orientation modelling approach

The purpose of a DFN orientation model is to develop a simplified mechanism for simulating fracture orientations while attempting to reproduce the patterns of fracture strike and dips seen in outcrop and borehole data. A second constraint is to develop a parameterization that utilizes as few distinct fracture sets as possible to produce a simple, easier-to-use model. An important role for the orientation model is the classification of data by sets, for which set-specific properties (fracture size and fracture intensity) are calculated (see Sections 3.4 and 3.5).

The orientation set model is designed to represent the general fracture orientation patterns at the repository scale. At the scale of individual data sets (i.e. outcrop-local or borehole-local), fracture orientation patterns at Laxemar exhibit complex heterogeneity. This heterogeneity is most likely due to localised geological conditions such as variations in lithology, response to local stress regimes induced by localised faulting or intrusion, or rotation and translation due to relative rock block movements over time. It should therefore be emphasised that the orientation model is not expected to reproduce the local-scale observations of clustered fracture orientations in individual data sets.

As a starting point, borehole and outcrop data are analysed in detail in order to obtain a general understanding of fracture orientation characteristics within the SDM-Site Laxemar fracture domain envelope (cf. Figure 1-1 and Figure 4-1). Fracture orientation patterns are examined in all data sets (boreholes, outcrops, and lineaments).

The orientation analysis is performed on a borehole-by-borehole basis, using the fracture aperture interpretation in SICADA, the rock domain (/Wahlgren et al. 2008/, cf. Chapter 4), the preliminary fracture domains (Section 3.2), and the preliminary set divisions suggested by an examination of pole clusters on Kamb-contoured stereonets completed during the fracture domain parameterisation. Data agglomeration as a function of rock domain is used as an initial starting point to evaluate whether a global orientation model (across all domains) is viable, or if a division of fracture set parameterisations by fracture domain would better reduce the spatial variability of fracture orientations.

The results of this evaluation (see Section 4.2.4) supported the concept of a single global orientation model across all fracture domains. Therefore, the SDM-Site Laxemar geological DFN orientation model uses common fracture set divisions across all fracture domains. However fracture intensity and size distributions are treated as fracture-domain and fracture-set specific properties.

The global fracture sets were parameterized in terms of the location of a set mean pole vector (trend, plunge) assuming a lower-hemispherical projection. All fracture sets are assumed to follow a Univariate Fisher spherical probability distribution, described by the orientation of the mean pole vector and a concentration parameter, κ, which represents the degree of clustering of pole vectors around the mean pole. Larger values of κ indicate higher clustering of fracture poles around the mean pole vector.

3.3.2 Data treatment

Only outcrop data and cored borehole fracture data marked ‘Visible in BIPS’ and that are located outside of identified deformation zones and minor deformation zones are used in the parameterization of the orientation model. Fractures not visible in BIPS are assigned to sets after the orientation set model was completed. The reasonableness of this action is evaluated through statistical analysis; borehole fracture data (aperture, morphology, host lithology, mineralogy) for fractures not visible in BIPS are compared to fracture data visible in BIPS through LDA and cross-tabulation, as described in Section 3.3.5. The analysis indicates that, in terms of all fracture properties other than orientation (which was not tested), fractures visible in BIPS and not visible in BIPS are statistically identical.

Fractures without an orientation and fractures not visible in borehole image logs (BIPS) are excluded from the orientation analysis. Fractures without a recorded orientation are excluded not just from the orientation analysis, but from all further analyses. It is important to note that there are relatively few fractures with no orientations; out of the 105,364 fractures in the cored borehole database used for SDM-Site Laxemar, only 164 fractures do not possess an orientation. Most of these are from cored borehole KLX01.

In addition, though fractures inside identified deformation zones are not used to develop the orientation model parameterisation, they are assigned to orientation sets using the same probability model as fractures outside of deformation zones during the DFN modelling.

Lineaments were set-divided by a separate orientation model, as no dip or dip direction information was available for these features. It is important to note that the distinction between open and sealed fractures applies only to borehole data; fractures mapped at surface outcrops are not parameterized in terms of aperture.

Finally, cored boreholes KLX01, KLX06, KLX02 inside rock domain RSMBA03, and those parts of KLX20A which are west of ZSMNS001C are excluded from the orientation model analysis; these boreholes lie outside the fracture domain envelope or the local model boundaries.

3.3.3 Identification of pole clusters through soft-sector assignment

Fracture set assignment for the SDM-Site Laxemar GeoDFN relies on a mix of visual inspection and a quantitative non-linear clustering algorithm. As a first step, the identification of fracture sets is made by visual inspection of contoured plots of cluster significance /Kamb 1959/ and /Robin and Jowett 1986/. Initial fracture set parameters (pole vector orientation and the Fisher concentration parameter) are calculated using a hard sector search /Dershowitz et al. 1998/. In a second step, these hard sectors are transferred into a second subdivision using a Univariate Fisher-distributed soft-sectoring of data /Dershowitz et al. 1998/ through a numerical algorithm (Section 3.3.4). In the final step, fracture set parameterisations are calculated from the soft-sectored data. The reason for including the initial visual approximation of set orientation is to allow for the possibility of including subjective preferences such as the weighting of different data subset characteristics (including outcrop versus borehole data, open versus sealed fractures, rock domains, and fracture domains). These qualitative factors are difficult to include in strictly numerical approaches.

The decision to separate the orientation analysis into two steps is based on the following factors:

- A visual cluster identification based on geological judgment is preferred, as it allows modellers to include their geological understanding and consideration of local geological conditions to the analysis.
- A soft sector division is difficult to do manually; therefore clusters are initially approximated in terms of hard sectors and then numerically adjusted using the method of soft sectoring. After soft-sectoring, the Univariate Fisher distribution parameterisation can be calculated for each set. Figure 3-5 illustrates the practical differences between hard and soft-sectoring.

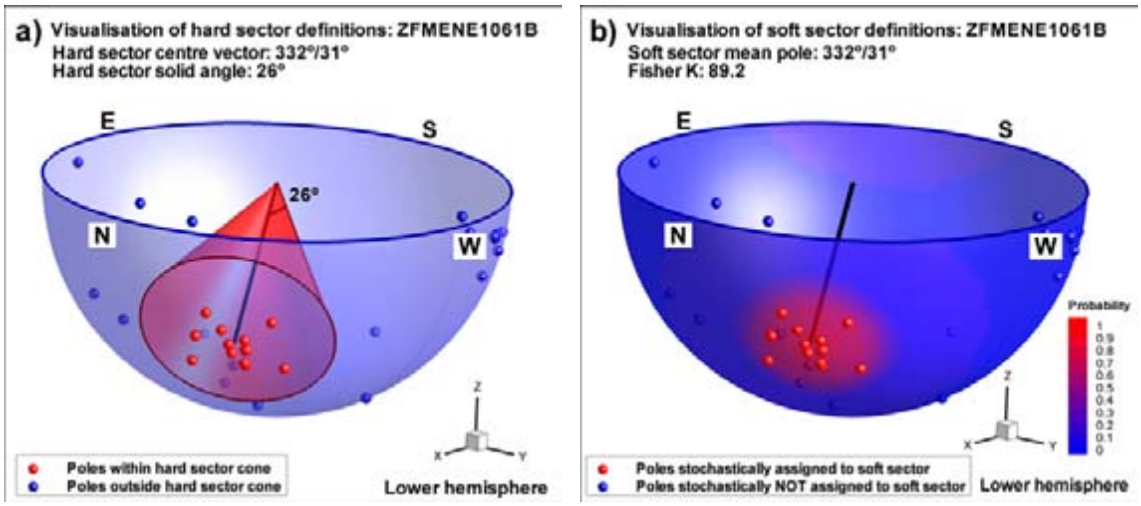

Figure 3-5. *Visualization of principles used; a) a manually hard-sector defined set is transformed into b) a soft sectoring probability field. Note that, for example, the soft sector P=0.5 is defined by the characteristics of the fractures inside the hard sector, and does not necessarily coincide with the initial hard sector solid angle (26°).*

The following procedure was used to compute fracture orientation sets:

1. Fracture orientations are visualized using Kamb-contoured plots of cluster significance.
2. Fracture sets are identified by visual inspection and approximated manually. In this initial step, each cluster is approximated by a Fisher-type hard sector.
3. Fracture poles are calculated for the lower hemisphere, and all poles falling inside a hard sector are used to calculate the mean pole and Fisher κ for the hard-sectored cluster, (to Equation 3-3).
4. Soft sectors (i.e. continuous probability functions for assigning fractures to clusters depending on orientation) are calculated for each cluster, (Equation 3-4 and Equation 3-5) based on the parameterization in Step 3.
5. Fracture poles are again calculated for the lower hemisphere, and poles are stochastically re-assigned according to soft sector probabilities. Finally, the mean pole and Fisher κ are calculated for the soft-sectored clusters.
6. Fractures are assigned to orientation sets based on the highest soft-sector probabilities. Probabilities and set memberships (based on the orientation set models created in Step 5) are assigned to all outcrop and borehole data that posses orientations. This includes fractures not visible in BIPS and fractures inside identified deformation zones.

3.3.4 Fisher distribution parameterisation based on pole clusters

The mean orientation of a cluster of fracture poles is calculated using the eigenvector method /Davis 2002/, while the concentration of clusters is calculated by the resultant vector method /Priest 1993, after others/. Clusters are first approximately defined by hard sectors (Step 3 in Section 3.3.3) and then transformed into corresponding soft sectors (Step 5 in Section 3.3.3) as shown in Figure 3-5. Fracture poles are compensated for sampling bias using Terzaghi weights /Terzaghi 1965/; the sum of Terzaghi weights are used instead of actual fracture pole counts.

The orientation of each fracture i in a fracture cluster can be characterised by its fracture pole $\boldsymbol{n}_i$ (a unit-length vector normal to the fracture plane). This fracture pole is defined by its three vector co-ordinates so that $[\boldsymbol{n}_i] = [n_{ix}, n_{iy}, n_{iz}]^T$. For the calculation of the location of the mean pole, a symmetric matrix T_j is defined for a set of N_j fractures of cluster j by:

$$T_j = \sum_{i=1}^{N_j} w_i \left(\mathbf{n}_i \times \mathbf{n}_i^T \right) \qquad \text{Equation 3-1}$$

where w_i is the Terzaghi weight of each fracture i, and is equal to 1/sin (max(α, 8.2°)). Here, α is the angle between the borehole and the fracture plane. The minimum bias angle is set to 8.2° (for fracture populations larger than 500) to avoid artificially large weights for fracture planes sub-parallel to the borehole orientation; this bias angle produces a maximum Terzaghi weight of approximately 7. The cluster mean pole orientation is obtained from the eigenvector ($\boldsymbol{e}_j$) associated with the largest eigenvalue (λ_j) in the eigenvalue solution /Davis 2002/:

$$T_j e_j = \lambda_j e_j \qquad \text{Equation 3-2}$$

The maximum resultant vector $\mathbf{V}_j$, for the set of N_j poles in cluster j, is then used to calculate the Fisher concentration parameter (κ) of the cluster:

$$\mathbf{V}_j = \sum_{i=1}^{N_j} w_i \, \mathbf{n}_i \qquad \text{Equation 3-3}$$

It should be noted that it is possible to calculate two fracture poles with opposite directions from a fracture plane. Which one of these fracture-pole directions are used to define fracture orientation is generally irrelevant. However, in the calculation of the resultant vector, (1), each fracture-pole direction must be chosen so as to maximize the resultant vector length (i.e. the fracture poles must have the same general direction; see Figure 3-6). Otherwise, the resultant vector will not reflect the overall orientation of the fracture cluster. In this particular case, the maximum resultant is ensured by selecting $\mathbf{n}_j$ such that the scalar product, $\mathbf{n}_j \cdot \mathbf{e}_j$, is not less than zero (i.e. $\mathbf{V}_j$ and $\mathbf{e}_j$ are parallel).

The Fisher concentration in orientation, κ_j, /Fisher 1953/for the cluster *j* is then approximated from the resultant vector by:

$$\kappa_j \approx \frac{W_j}{W_j - \left|\mathbf{V}_j\right|}, \qquad W_j = \sum_{i=1}^{N_j} w_i \qquad \text{Equation 3-4}$$

if $\kappa > 5$ (note that $\kappa < 5$ reflects a cluster with a very large spread in orientation). W_j is the Terzaghi-compensated fracture count of cluster *j*. The univariate Fisher distribution defines the probability density function symmetrically around its cluster mean pole, according to:

$$f_j(\varphi_j, \theta) = \frac{\kappa_j \sin\varphi_j \; e^{\kappa_j \cos\varphi}}{2\pi\left(e^{\kappa_j} - 1\right)}, \quad \varphi_j = \arccos\left|\mathrm{n}_i \; \mathrm{e}_j\right| \qquad \text{Equation 3-5}$$

where φ_{ij} is the solid angle between a fracture pole n_i and the cluster mean pole, e_j, and θ_{ij} is the circumferential angle. The expected value of cluster j, in terms of Terzaghi-compensated fracture count, E[X_j], at some specific orientation (φ_{ij}, θ_{ij}), is calculated by an infinitesimal integration of Equation 3-5 scaled by W_j. In order to enable a comparison of the expectation values of all clusters for a given orientation, this integration area ($d\varphi \; d\theta$) must be constant (i.e. independent of φ_{ij}). This is achieved by setting $d\theta = 1/(2\pi \sin\varphi_{ij})$. Thus, the probability *P* for a given fracture *i* to belong to cluster *j* can be calculated from the expected value for cluster *j*, relative to the total expected value of all clusters:

$$P(x_i \in X_j) = \frac{E\left[X_j\right]}{\sum_j E\left[X_j\right]} = \frac{W_j \; f_j(\varphi_{ij}, \theta_{ij}) / \sin\varphi_{ij}}{\sum_j W_j \; f_j(\varphi_{ij}, \theta_{ij}) / \sin\varphi_{ij}} \qquad \text{Equation 3-6}$$

It is important to note, however, that Terzaghi compensation for orientation bias can have significant limitations. The value of the Terzaghi weight is asymptotic as the α angle (the angle between the borehole axis and the plane of the fracture) approaches zero /Yow 1987/. This has the potential to produce an unacceptably large Terzaghi weight for fractures with orientations very close to that of the borehole axis. It is generally accepted /Yow 1987, Mauldon and Mauldon 1997/, that a 'blind zone' exists between α = 0° and α = 20°. Within this zone the Terzaghi compensation is generally viewed as unreliable. This is important, because for the fracture data derived from the cored borehole array at Laxemar, approximately 17% of the fractures (outside deformation zones, visible in BIPS) possess orientations with a α angle less than or equal to 20°. The standard of practice /Yow 1987, /Priest 1993/ to address the blind zone is to set a maximum value for the Terzaghi correction; a maximum value of 10 is generally used. For the visual descriptions of fracture intensity (borehole P_{10} plots) and the orientation analysis, a bias angle of 8.2 degrees, corresponding to a maximum Terzaghi weight of 7, is used for data sets with more than 500 data points. Approximately 3% of fractures outside of deformation zones and visible in BIPS fall into this category in the Laxemar cored borehole array. For data sets smaller than 500, a bias angle of 15 degrees, corresponding to a maximum Terzaghi weight of 3.8, is used. These numbers implies that, for fractures with a α angle less than 8.2 (or less than 15, for data sets with less than 500 members), the intensity may still be under-estimated even after Terzaghi compensation, due to the limits applied to prevent over-compensation.

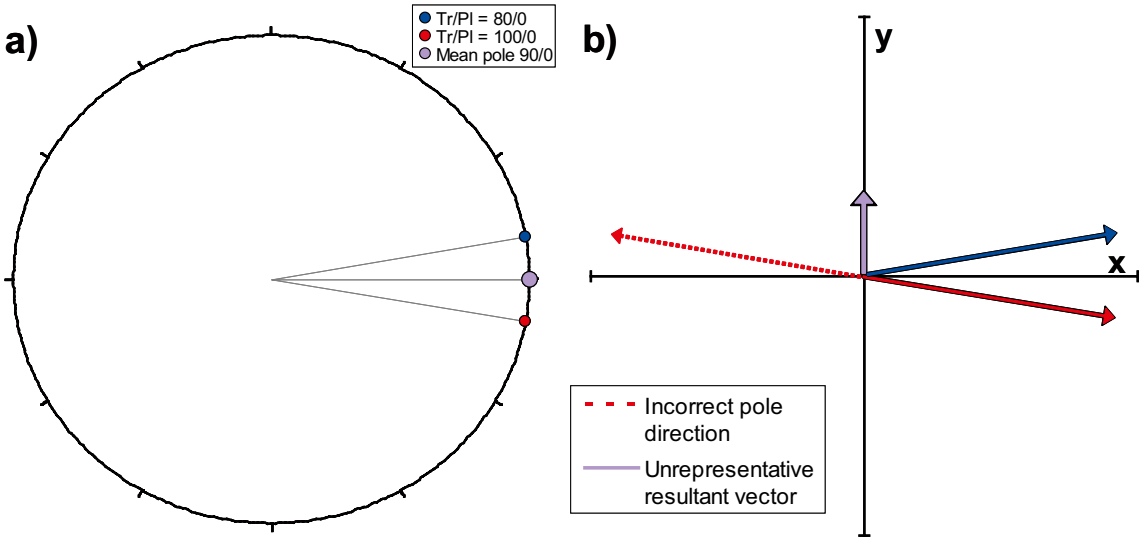

Figure 3-6. *Conceptual figure of mean pole calculation for two vertical fractures with pole vector trends of 80° and 100° respectively); a) the correctly calculated mean pole has a trend of 90°, and b) if poles are incorrectly chosen (red dashed vector) and fail to maximize the resultant vector length (purple vector), both its orientation and magnitude are unrepresentative of the cluster (i.e. erroneous mean pole and Fisher κ).*

In addition, /Davy et al. 2006/ showed that, for fracture networks where fracture size follows a Pareto (power-law) length distribution, the Terzaghi correction will over-estimate the frequency of fractures subparallel to the borehole. Past geological DFN models at Forsmark and Laxemar have demonstrated that a power-law distribution is generally the most appropriate model for fracture sizes at the potential repository sites in Sweden, so this is somewhat of a concern with respect to the DFN model parameterisation.

Due to the limitations described above, Terzaghi compensation is only used during the orientation analysis. Fracture intensity modelling instead relies on the Wang approximation (Section 3.5.1) to transform P_{10} to P_{32} to reduce the orientation bias on observed borehole fracture intensity.

3.3.5 Evaluation of Visible/Not Visible in BIPS for fracture orientation set division

Not all fracture data are visible in the BIPS imagery. The fractures that are poorly imaged in the BIPS data may have a higher degree of uncertainty associated with any interpreted fracture characteristics, such as fracture orientation or aperture. In some analyses for developing the DFN model, it may be preferable to base the parameterization only on the fractures that are visible in BIPS in order to reduce uncertainty. Inherent in this choice, however, is the assumption that the fractures visible in BIPS do not differ from those not visible in any statistically significant way.

Many of the attributes assigned to each fracture are nominal or categorical variables. This type of variable does not have a numerical value associated with it, but rather a name (hence nominal) or category such as rough, northeast set or calcite-filled. Some of the other attributes are continuous variables, such as aperture or width. The statistical tests that can be used to test the hypothesis that the fractures visible in BIPS do not differ from those not visible are specific to the type of variable being tested. For nominal variables, cross-tabulation, sometimes referred to as contingency table analysis, is appropriate and widely used /Pearson 1904/. For continuous variables, linear discriminant analysis (LDA) /Davis 2002/ provides a way of assessing whether two groups can be differentiated based on linear combinations of the continuous variables at a prescribed level of statistical significance.

There are several measures of association that are commonly used in cross-tabulation analyses. These include various forms of Chi-Square tests, Directional and Symmetric Measures. Chi-Square measures may indicate that there is an association between two variables, but the measures do not indicate the strength or the direction of the association. Direction refers to predicting the value of one variable from the other. The ability to predict A from B, for instance, may not be the same as the ability to predict B from A. Directional measures indicate both the strength and direction. Symmetrical measures quantify both the strength and significance of any associations, but are a composite of directions. Common Chi-square tests include Pearson, Likelihood Ratio, Fisher's Exact Test and Linear-by-Linear association. Directional tests include Lambda, Goodman and Kruskal's Tau and the Uncertainty Coefficient. Symmetrical tests include Phi, Cramer's V and the Uncertainty Coefficient. A detailed description of these tests and their interpretations can be found in /Agresti 1994, Goodman and Kruskal 1954, 1959, 1963, 1972, Liebetrau 1983, Rosenberg 1968, SAS 1988/ and /Theil 1972/.

The specified level of probability (α) used for assessing associations in the cross-tabulation analyses was set at 0.05. The Null Hypotheses for these tests is that there is no association or difference between fractures labelled "Visible in BIPS" and fractures labelled as "Not Visible in BIPS". If the reported probability for the specific test statistic is equal to or less than 0.05, then the Null Hypothesis is rejected and the association is deemed to be statistically significant. If the probability was greater than 0.05, then the Null Hypothesis was not rejected and the association was deemed not to be statistically significant. It is important to note that even when the association is statistically significant, the strength of the association may be very weak, so it is important to consider both the significance and the strength in deciding whether fractures visible in BIPS materially differ from those not visible. Since no one measure is adequate to assess the association, in that all have weaknesses and advantages, the final interpretation is made by considering the results of all of the measures.

The objective for LDA is to determine whether a linear combination of continuous variables is adequate to statistically differentiate two or more groups at a desired level of probability. The factors to consider in deciding whether the discrimination is meaningful is to consider the strength and statistical significance of the separation achieved, using Wilk's Lamba test /Shapiro and Wilk 1965/, and also to assess the types of classification errors made. The classification errors indicate the potential bias in the misclassifications using LDA, which can prove valuable in assessing the utility of the attributes for distinguishing visible and not visible fractures. The final decision on the utility is made by considering both the statistical results and the classification errors together.

3.4 DFN size model methodology

Fracture size cannot be directly measured, since there are few techniques that reliably delineate the extent of fracture in three dimensions throughout a volume of rock. One of the most useful indications of fracture size is the trace pattern that the fractures produce when they intersect surfaces. These are more easily measured, and produce data sets such as lineament maps and outcrop fracture trace maps.

A way to avoid the scale limitations that lead to non-uniqueness is to combine data sets at different scales to extend the range of scale coverage from metres to kilometres. Thus, outcrops ranging up to scales of a few tens of metres can be combined with lineament data sets at scales of tens of kilometres. Figure 3-7 illustrates an area-normalised trace length scaling plot; on this type of plot, the size scaling relationship of fracture traces at multiple scales (outcrop fractures at 0–10 m, MDZ lineaments at 10–1,000 m scale, and local, major, and regional deformation zones at greater than 1,000 m scale) can be simultaneously evaluated.

However, it is important to note that in the SDM-Site Laxemar geological DFN, only outcrop fracture and minor deformation zone traces whose length on the ground surface is less than 1,000 m are used in the size model parameterisation. This is a change from past geological DFN models at Laxemar and Forsmark in that deformation zone traces from the DZ model are not used in the size model parameterisation. This is listed as a key assumption in Section 3.1.3.

The probability of a fracture of a given size, where size is the topological measure of a convex polyhedron representing the fracture, intersecting any plane is linearly proportional to this size /La Pointe 2002/. In other words, big fractures have a higher probability of intersecting a plane than do smaller ones. What this means is that the trace patterns observed in outcrop or in lineament patterns are biased in that they preferentially record the trace of the larger fractures. For a power law model of fracture size (Equation 3-9), this means that the scaling exponent of the fracture traces, k_t, is equal to or less than the scaling exponent of the fracture radius, k_r (or diameter) probability distribution /La Pointe 2002/. Thus, an equation that describes the power law distribution of trace lengths can be used to describe the scaling exponent of the parent radius distribution by simply adding 1.0 to the trace length scaling exponent. This result is independent of fracture shape as long as the shape is convex.

One way to estimate fracture size is to find a statistical description of fracture sizes that when quantified as trace length distributions on a surface matches a measured distribution /Dershowitz et al. 1998/. Because of the small scale of outcrop relative to fracture size, this method may be non-unique /La Pointe et al. 1993/. The non-uniqueness is a problem for most data sets, due to their limited scale range.

A way to avoid the scale limitations that lead to non-uniqueness is to combine data sets at different scales to extend the range of scale coverage from metres to kilometres. Thus, outcrops ranging up to scales of a few tens of metres can be combined with lineament data sets at scales of tens of kilometres. To combine data at different scales, however, requires knowledge and incorporation of the spatial/scaling model of the fracture data.

If the spatial model is Euclidean, doubling the area of data coverage should double the number of fractures. Doubling the length of a borehole should double the number of fractures intersecting the borehole. If the scaling is fractal, then doubling the area or length will conform to the mass dimension scaling exponent /La Pointe 1995/. Combining data sets measured at different scales requires knowledge of the mass fractal dimension, in order to properly compensate for the different scales. This leads to the coupling of the fracture sizes, intensity and spatial/scaling model for each set.

If the fractures present in outcrop are part of the same fracture population as the lineaments, then they should share the same statistical parameterization. This implies that the geological processes that created the fractures observed in outcrop are also the same processes that produced the much larger fractures expressed as lineaments. The model in which these conditions are fulfilled is termed a ‘tectonic continuum’.

Certain useful mathematical relations hold for a size model that follows a tectonic continuum in which the spatial/scaling behaviour is fractal or Euclidean. For a Euclidean scaling/spatial model, the number of traces of a given length is linearly proportional to the area or volume over which the data are collected. Thus, it becomes easy to compare fracture trace length data measured over different sized areas by dividing the number of traces of a given length by the area of the outcrop or lineament map. If the traces follow a power law radius distribution, then their traces will follow a power law trace length distribution as previously mentioned. In this case, the cumulative number of fracture traces per unit area greater than or equal to a specified length, x, is:

$$\text{Number/area}(x \geq t_{0n}) = \left(\frac{t_{0n}}{x} \right)^{k_t} \qquad \text{Equation 3-7}$$

The value of t_{0n} corresponds to a trace length of which it is expected that there is only one of them per unit area of this length or longer. Note that the relation does not describe a probability distribution, but rather a cumulative number distribution.

In order to distinguish between the parameters for the various power law distributions that arise from the parameterization of fracture sizes based on normalized cumulative number plots, the following nomenclature is adopted:

Table 3-1. Power-law distribution nomenclature.

Distribution Name	Parameter 1	Parameter 2
Mass dimension	ρ (prefactor)	D_m (mass dimension)
Cumulative number of trace lengths	t_{0n} (coefficient)	k_t (trace length exponent)
Trace length CCDF	x_{0t} (coefficient)	k_t (trace length exponent)
Radius CCDF	r_o (coefficient)	k_r (radius exponent)
Radius size truncation limits	r_{min}	r_{max}

Note that Parameter 2 for both the cumulative number of trace lengths and the trace length CCDF are identical.

To construct the plot, the trace lengths measured in the domain are ordered from shortest to longest. Each trace is numbered according to its cumulative frequency. If there are 50 traces, then the shortest trace would be assigned the number 50, indicating that there are 50 traces greater than or equal to the length of this shortest trace. The second shortest trace would be assigned the number 49, and so on through the longest trace in the data set, which would have a complementary cumulative frequency of 1. More generally, if n_i fracture traces are measured in domain i, then the shortest trace has the cumulative frequency value of n_i, and the next longest has the value of n_{i-1}, and so on such that the longest trace measured has the value of 1. Next, these cumulative frequency numbers are each divided by the appropriate mapped area. The values were plotted with the area-normalized cumulative frequency value on the ordinate (Y-axis), and the trace length value on the abscissa (X-axis) as shown in Figure 3-7. The parameter k_t is the slope of the black line on Figure 3-7, and the parameter t_{0n} is the abscissa value that corresponds to the ordinate value of 1.0.

The equation of the black line shown in Figure 3-7 conforms to a power law. The complementary cumulative number (CCN) plot shown in Figure 3-7 represents the number of traces, per unit area, greater than or equal to a specific trace length.

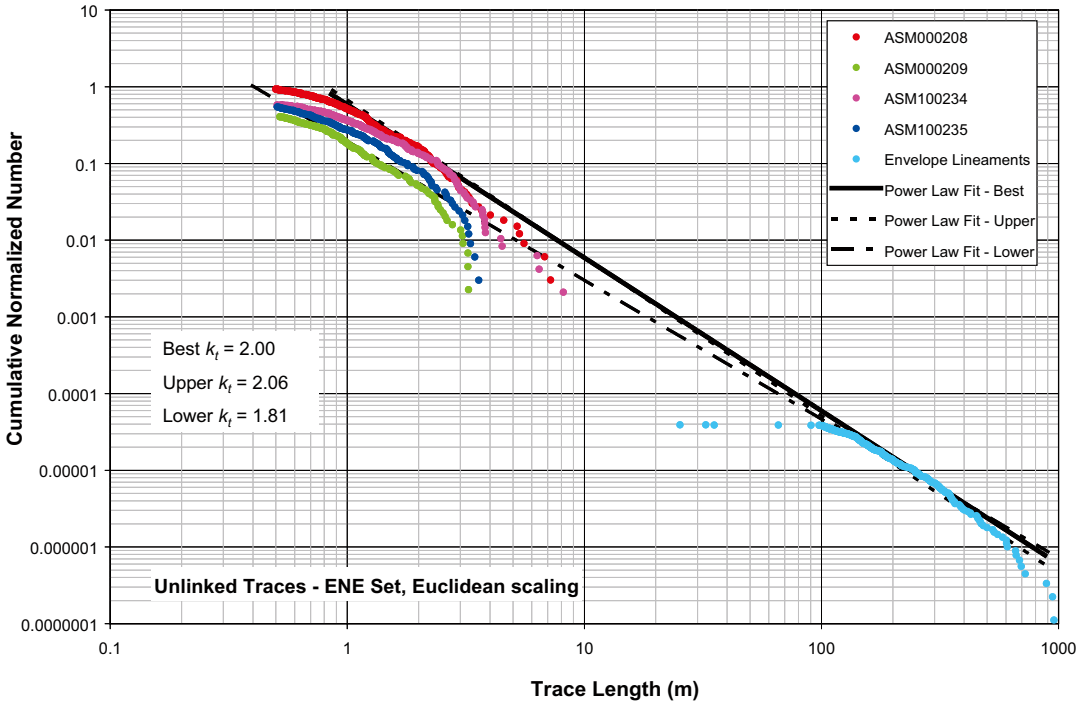

Figure 3-7. *Example area-normalised trace length cumulative frequency plot.*

It is possible to calculate a probability distribution from the cumulative number distribution, but this requires fixing the value of x_{0t} or r_0. This probability density function (PDF) for trace lengths, which is quantified by this line, has the functional form:

$$P(X \geq x) = \left(\frac{x_{ot}}{x} \right)^{k_t}$$ Equation 3-8

where x_{0t} is the minimum trace length;
x is any trace length greater than or equal to x_{0t};
k_t is the trace length dimension, and
$P(X \geq x)$ is the probability that a trace length is greater than or equal to x.

The value of x_{0t} is not the same as t_{0n}. x_{0t} corresponds to a minimum trace length of a probability density function, and is not calculated from t_{0n}. r_0 and x_{0t} are related, however, as are k_r and k_t /La Pointe 2002/, according to Equation 3-9:

$$k_r = k_t + 1$$
$$r_0 = x_{0t} \frac{2}{\pi}$$ Equation 3-9

This equation implies that the exponent describing the radius CCDF can be calculated from the slope of the cumulative number plot by simply adding 1.0 to the slope. The values of r_0 or x_{0t} are not calculated from the cumulative number plot, but are based either on the minimum fracture trace or radius required in the simulation. The methods for calculating P_{32} for a specific combination of minimum fracture size and power-law exponent, as well as a method for re-adjusting P_{32} values for different minimum sizes, are described at the end of this section.

Note also that the exponent of the parent radius distribution is sometimes specified by a parameter, b, often termed the Pareto exponent. This exponent is related to the trace dimension in Equation 3-10 as:

$$k_r = b - 1$$ Equation 3-10

If the scaling/spatial model (see Section 3.6.1) is Euclidean, the area normalization consists of dividing the cumulative number value on the Y-axis by the map area. However, if the fractures conform to a fractal scaling model, then the area normalization is carried out in a different manner. For the fractal scaling case, fracture intensity scales according to the mass dimension (D_m) of the fracture traces. When the mass dimension of the traces has a value of 2.0, the fracture intensity (number of fractures per unit area) scales proportionately to area, and the spatial pattern of traces can be characterised by a Poissonian density function which inherently has no spatial correlation between the fractures.

The process for normalizing for different mapped areas when the spatial/scaling pattern is fractal, using the example of an outcrop data set and traces of the deformation zones, is as follows:

Let the o subscript denote outcrop fractures, the z subscript denote deformation zones, and 1 denote an area equal to 1 m^2. Furthermore, let the variable A denote the area of the outcrop or deformation zone map, and R denote the radius of a circle that has the same area as A. Also, let x represent the trace length of a fracture.

Then, from Equation 3-11 it is possible to calculate the number of fracture traces that would be expected in the deformation zone map area based on what was measured in the outcrop area. The radius (R_1) that corresponds to a circle of area 1 m^2 is:

$$A_1 = \pi R_1^2 = 1.0$$

$$R_1 = \sqrt{\frac{1}{\pi}}$$

$$N(R_1) = \rho\left(\sqrt{\frac{1}{\pi}}\right)^{D_m}$$

Equation 3-11

Alternatively, if the scaling is Poissonian and not fractal, the exponent, D_m, would be equal to 2.0. In this case, the number of fractures in an area of 1 m^2 would be:

$$N(R_1) = \rho\left(\sqrt{\frac{1}{\pi}}\right)^{2}$$

Equation 3-12

A convenient way to adjust the CCN plots for the fractal scaling is to calculate a pseudo-area. For example, the pseudo-area, A^* for an outcrop of A_o is:

$$A^* = A_o \frac{\rho\left(\sqrt{\frac{1}{\pi}}\right)^{2}}{\rho\left(\sqrt{\frac{1}{\pi}}\right)^{D_m}} = A_o\left(\sqrt{\frac{1}{\pi}}\right)^{2-D_m}$$

Equation 3-13

Instead of dividing the cumulative number of traces by A_o, the number is divided by the pseudo-area. The same calculation is repeated for lineaments or any other data sets.

The parameters for the Complementary Cumulative Number (CCN) plots do not directly yield the trace length probability distribution, because they describe the cumulative number of fractures, not the probability of the fractures. The probability distribution will have the same exponent as the radius distribution derived from the CCN plot, but the minimum size value differs from the value calculated from the CCN plot. The minimum size value for the probability distribution can be derived through simulation, however. The simulation steps are as follows, and are based on Equation 3-14:

$$P_{32}(r_{\min}, r_{\max}) = \frac{\left[r_{\min}^{2-k_r} - r_{\max}^{2-k_r}\right]}{r_0^{2-k_r}} P_{32}(r_0, \infty)$$

Equation 3-14

1. For a particular set, specify a size model as a power law distribution using the exponent k_r derived from the cumulative trace number plot, and an assumed minimum size value (r_0). Also assume a value for fracture intensity (P_{32}) chosen to produce enough trace intersections for robust computation of simulation trace length statistics. For the simulations used in this report, a minimum radius of 0.5 m and a P_{32} of 0.1 m^2/m^3 were assumed.
2. Assign the orientation model for the set.
3. Generate the fractures in a volume. If the simulation model volume or area differs from the volume for the data set, then note the ratio of volumes for later plotting adjustment. The volume used in the simulations extends for 50 m in all directions beyond the outcrop limits.
4. Place a surface representing the outcrop surface into the model and compute the fracture intersections with the surface.

5. Export the traces and plot on a CCN plot. If the simulation volume or area differs from the volume or area of the measured data, adjust the Y-value of the simulated data by the ratio so that the volumes or areas are the same.
6. Compare the simulated traces to the measured traces. The ratio of Y-values (cumulative number) for the straight-line portions of the data corresponds to the ratio by which the $P_{32}(r_{min}, r_{max})$ should be adjusted to achieve a match.
7. Make the $P_{32}(r_{min}, r_{max})$ adjustment and re-run for verification that the results match the measured data. Everything in Equation 3-14 is known at this point except r0 and $P_{32}(r_0, \infty)$.
8. Using Equation 3-14, specify a desired value of r_0. Since all other values except $P_{32}(r_0,\infty)$ are known, calculate this value which corresponds to the desired lower limit (r_0) of model applicability.

For the Laxemar Base Model, the size/intensity scaling is assumed to be independent of fracture domain for reasons previously discussed. However, the fracture intensity as measured in boreholes in the various fracture domains for each set is not uniform. The differences in measured borehole intensity can be accounted for by finding a value of minimum fracture radius that matches the borehole data. The assumption of domain independence of the radius scaling exponent (k_r) is tested through the inclusion of an alternative model, within which r_0/r_{min} is fixed, and k_r is calculated from borehole P_{32} data for each fracture set on a domain by domain basis (Section 4.3.4). These models are collectively termed the 'GeoDFN fixed-r_{min}' models; the label was coined during the Forsmark 2.2 geological modelling, and is re-used here for consistency.

The increased P_{32} observed in boreholes represents smaller fractures that were not recorded during the detailed outcrop mapping. The outcrop maps do not record any traces shorter than 0.5 m in length; for outcrop intensity matching, the minimum fracture radius (r_{min}) is set at 0.5 m. Therefore, we can calculate the distribution minimum radius (r_0) by comparing the ratios of the outcrop and borehole P_{32} values through the following steps:

- The borehole P_{32} (P_{32BH}) of a given fracture set in a given fracture domain is calculated using the Wang C_{13} conversion factor (see Section 3.5.1) and 3 m binned P_{10} values.
- Given the minimum radius (r_{minOC}) derived from outcrop trace studies, a value for P_{32} matched to outcrop data (P_{32OC}, described in previous paragraphs) with no imposed maximum fracture sizes, and P_{32BH}, r_{minBH} is adjusted according to Equation 3-15 (which is effect a re-statement of Equation 3-14):

$$r_{min\,BH} = r_{min\,OC}\left(P_{32BH} \Big/ P_{32OC} \right)^{1/(2-k_r)} \qquad \text{Equation 3-15}$$

3.5 Geological DFN intensity model methodology

Fracture intensity can be measured in many different ways. Common intensity measures /Dershowitz et al. 1984/ utilised in past SDM include:

- P_{10}: Linear fracture intensity, defined as the number of intersections of features (either surface traces along a scanline, or fracture intersections in a borehole log) per unit length, in units of 1/m.
- P_{21}: Fracture areal intensity, defined as the total length of all traces created by the intersection of a plane with a set of fractures, divided by the total one-sided surface area of the sampling plane, in units of m/m^2.
- P_{32}: Fracture volumetric intensity, defined as the total one-sided surface area of all features per unit volume, in units of m^2/m^3.

For the SDM-Site Laxemar GeoDFN, coupled size-intensity modelling is based upon P_{32}, as derived from cored borehole records. P_{21}, as computed from the analysis of fracture traces mapped on detailed outcrops across the Laxemar local model area /Hermanson et al. 2008/, is used in conjunction with P_{32} values from boreholes to simultaneously match size and intensity to both outcrop and borehole data, so as to provide a model that is consistent at observational scales.

Though presented in this report as separate model elements, the SDM-Site Laxemar geological DFN is fundamentally a coupled size-intensity model; parameters for one aspect of the model (such as the size, or the P_{32} intensity) cannot be changed without a corresponding change in other parameters. This is a key element of the tectonic continuum assumption. The size-intensity model contains three variables:

1. k_r: The fracture radius scaling exponent, which is determined from fracture and lineament traces. The radius can be treated either as a constant across all fracture domains (the basis for SDM-Site Laxemar geological DFN modelling) or can be treated as a variable between fracture domains (alternative model).
2. r_0/r_{min}: The minimum sized fracture (in terms of equivalent radius) treated by the size model. r_0 represents the minimum value of the PDF, while r_{min} represents a minimum size cut-off that is generally larger than r_0. The SDM-Site Laxemar geological DFN model treats the r_0 value as a variable, which is calculated using the difference in P_{32} intensity between the cored borehole data and the fracture traces from the detail-mapped outcrops. The alternative model, used in conjunction with the concept of the scaling exponent varying as a function of fracture domain, assumes that the minimum fracture size is equal to the diameter of the cored boreholes (76 mm). r_{min} is not used directly in the size-intensity model parameterization, but is used in the uncertainty analysis and model verification.
3. P_{32}: The volumetric fracture intensity, calculated from the cored borehole records using the Wang approximation (Section 3.5.1) and from outcrop trace data through stochastic simulation. There are no alternative size-intensity models based on different interpretations or calculations of P_{32}.

The Forsmark 2.2 geological DFN model established that, in terms of orientation and intensity, there was no statistically significant difference between fractures marked in SICADA as 'Visible in BIPS' or 'Not Visible in BIPS'. This is described in detailed in the Forsmark method-specific geological DFN report /Fox et al. 2007/. This assumption was again tested at Laxemar (Section 4.2.4) and was found to be true. As such, for the calculation of coupled size-intensity models and the analysis of the distribution of fracture intensity during the construction of the Laxemar 2.3 geological DFN, no distinction between the two classes is made. All P_{32} values reported here are assumed representative of the full observed borehole P_{10} outside of identified deformation zones and minor deformation zones, except where an explicit distinction is made between open and sealed fractures. For the same reasons discussed in the fracture domain methodology (Section 3.2.1), boreholes KLX01 and KLX09B are omitted from the intensity analysis.

3.5.1 Calculating P_{32} from borehole fracture logs

Previous geological DFN models have used stochastic simulation to determine the relationship between the one-dimensional fracture intensity measure P_{10} and the three-dimensional fracture intensity measure P_{32}. The approach generally relies on calculating a conversion factor, C_{13}, by which the observed borehole P_{10} is then multiplied to obtain a distribution of P_{32}. The stochastic simulation method is quite versatile, as it allows for the use of different orientation, spatial, and intensity models. However, it can be very sensitive to several simulation parameters, including the fracture size distribution relative to the diameter of the borehole, the size of the simulation region relative to the fracture size, and to the intensity values used in simulation. It is necessary to use very high P_{32} values (in the range of 30–40 m^2/m^3) to obtain stable solutions; it is difficult to model large regions with small fractures in this approach.

The SDM-Site Laxemar geological DFN instead uses an approximate analytical method for the estimation of fracture set intensity distributions; the numerical approximation based on the doctoral research by /Wang 2005/ on stereological relationships between fracture orientation and fracture intensity. This approach was first used in the Forsmark version 2.2 geological DFN modelling during 2006 and 2007.

Wang's C_{13} is an analytical solution, and is subject to several key assumptions:

- The method assumes one-dimensional (line) sampling; i.e. a zero-radius borehole. This implies that every fracture recorded in the SICADA database for a given cored borehole crosses the entire diameter of the core[1]. In situations where the fracture radius is of a comparable size to the borehole radius, this can result in a systematic under-prediction of C_{13}. Previous geological DFN analysis to determine the P_{32} conversion factor through simulation have also used this assumption.
- Wang's C_{13} assumes independence of fracture size, shape, and orientation.
- Wang's C_{13} assumes that the fracture population in a single set follows a Univariate Fisher spherical probability distribution. The method is not suitable for use with other types of probability distributions; it would be inappropriate to use Wang to estimate C_{13} for fractures that appear to follow a girdle distribution (Bingham/Bivariate Normal).

Given a relationship where $C_{13} \times P_{10} = P_{32}$, the conversion factor C_{13} is defined by /Wang 2005/ as:

$$C_{13} = \left[\int_0^{\pi} \left| \cos\alpha \right| f_A(\alpha) d\alpha \right]^{-1} \qquad \text{Equation 3-16}$$

where α is the solid angle between the sampling line and the fracture normal. Assuming line sampling (P_{10}) of fractures distributed according to a univariate Fisher spherical probability distribution, the theoretical probability distribution function given by /Wang 2005/ for α is given by:

$$f_A(\alpha) = \frac{1}{\pi} \int_{R_\delta} \frac{\sin\alpha}{\sqrt{\sin^2\delta \sin^2\rho - (\cos\alpha - \cos\delta\cos\rho)^2}} \frac{\kappa e^{\kappa\cos\delta} \sin\delta}{e^{\kappa} - e^{-\kappa}} d\delta \qquad \text{Equation 3-17}$$

For α in the range $|\delta - \rho| \le \alpha \le \delta + \rho$, where the range of integration of R_δ is given by:

$R_\delta = [\rho - \alpha, \rho + \alpha]$ if $\alpha \le \rho$, or

$R_\delta = [0, \alpha + \rho]$ if $\alpha > \rho$

In the SDM-Site Laxemar geological DFN parameterization, Wang's C_{13} is calculated in the following manner:

1. Borehole coordinate survey data from SICADA table p_object_location are divided into 'bin' intervals of 3 m, 15 m, and 30 m. The bin intervals are based on the borehole length ('ADJUSTED_SECUP', otherwise known as Measured Depth) rather than the true depth or segment elevation (relative to a sea-level datum).
2. SICADA data table p_object_location contains cored borehole centerline coordinates in the RT90-RHB70 coordinate system at 3 m intervals. The start point and endpoint of each section are used to calculate a trend and plunge of each borehole section.
3. For each fracture set in each domain, the mean pole vector orientation (trend, plunge) and Fisher concentration parameter (κ) was obtained from the global orientation model (Section 3.3).

[1] SKB's SICADA database contains the parameter 'centrum_covered', which indicates which fractures cut across the core axis, and would (theoretically) allow for the use of the borehole radius during intensity modelling. However, this parameter has not been applied consistently; boreholes KLX02–KLX07 do not have values assigned in SICADA table p_fract_core for this parameter. The modelling team decided not to introduce additional uncertainty by utilising a parameter not available across the full data set.

4. For each borehole section, in each bin size range, for each fracture set in each fracture domain, the solid angle (θ) between the fracture set mean pole vector and the unit vector representing the orientation of the borehole section is computed.
5. The solid angle and the Fisher concentration parameter are then used as input parameters to a compiled C++ application (ComputeC13.exe). The code uses a numerical integration procedure to approximate the Wang C_{13}. Copies of the executable and/or source code are available upon request; the algorithm will ultimately be included in a future release of FracMan.
6. For all other interval sizes (9 m, 15 m, 21 m, 30 m, and 51 m), C_{13} values are found by taking the arithmetic average of the C_{13} values of the 3 m borehole segments inside the bounds of the larger division. For example, the C_{13} value for a 15 m borehole segment is the average of the C_{13} values of the five (5) 3 m segments inside of it.

The resulting C_{13} values are then input into Microsoft Excel, where the actual P_{10} to P_{32} conversions is performed. The C_{13} value calculated from Wang's method is independent of fracture aperture; the same value is used for calculating the P_{32} of both open and sealed fractures by set and domain.

3.6 DFN spatial model methodology

3.6.1 Location and scaling model

Spatial analysis quantifies how the fracture intensity of each set varies spatially. A spatial model makes it possible to extend local measurements of fracture intensity to other portions of the repository volume where there is no data. It also relates to the scaling of fracture intensity. Certain types of spatial models, such as Poissonian or Fractal, imply that fracture intensity will increase, remain the same or decrease as a function of scale according to particular equations. Scaling behaviour is important to quantify as the scale at which fracture data are obtained may not be the scale at which it is used for subsequent modelling or calculations.

An efficient way to examine the spatial/scaling characteristics of fracture intensity is through the mass dimension. The mass dimension, D_m, describes how intensity varies with scale for fractal data sets. The mass dimension of a fractal data set is given by the equation:

$$N(r) = \rho r^{D_m} \qquad \text{Equation 3-18}$$

where: ρ is a constant,
r is the scale,
D_m is the mass dimension, and
$N(r)$ is the mass, or number of things at the scale r.

The form of this equation indicates that plotting data on doubly-logarithmic axes will produce a straight line if the data conform to this power law representation of intensity versus scale. For the situation in which the scaling exponent or mass dimension D_m equals the Euclidean dimension, the pattern is Poissonian. This means that the intensity is scale-independent. If the area or volume of rock is doubled, the fracture intensity remains constant, but the number of fractures doubles. If the data approximate a straight line but does not have a scaling exponent that equals the Euclidean dimension, then the pattern is fractal and characterised by the constant, ρ, and the scaling exponent, D_m. The scaling exponent is the slope of the line plotted on doubly-logarithmic axes.

There are two sources of data for calculating the mass dimension of fracture intensity: outcrops and boreholes. The borehole data consist of the positions of fractures along the borehole. The borehole has a Euclidean dimension of 1.0 (essentially a line). Borehole data offer the possibility to calculate the mass dimension over scales approaching the length of the borehole. A disadvantage of using borehole data is that it quantifies the scaling behaviour in a particular

direction; it is possible that other directions may have a different scaling exponent or model, and unless boreholes are drilled in a very wide variety of directions, the three-dimensional scaling behaviour may not be well characterised by analyses of borehole fracture data.

Outcrops, on the other hand, provide for a two-dimensional characterization. While this added dimension provides insight into the scaling behaviour, it is limited to the scale of the outcrops, which is something on the order of 30 m for the outcrops studied at Laxemar. Despite this scale limitation, it complements and compensates for one of the weaknesses of the borehole analyses, which is quantification of the scaling behaviour in the horizontal directions. Together, the mass dimension analyses of borehole and outcrop data provide a three-dimensional model for the variation of fracture intensity. Should the data not conform to a power law representation as given in Equation 3-18 then it is necessary to evaluate other types of spatial and scaling models. If Equation 3-18 does approximate the data, then there is no need to investigate further spatial and scaling models.

Lineament maps are not nearly as useful as outcrop maps for carrying out mass dimension calculations. This is because lineaments smaller than a certain size are not included in the database due to detection limitations. Thus, the number of lineaments present at a given scale is not correct; there would be many more lineaments of smaller size had they been detectable. Though this issue of data resolution is a problem at all scales of analysis, the amount of missing mass is generally much smaller at the outcrop or borehole scale than at the lineament scale. As a result, the value of $N(r)$ will be lower than it should be. There is a slight issue with this under-representation for outcrop trace data as well, in that fracture traces less than 0.5 m were not recorded. However, the lack of trace data less than 0.5 m has a much smaller impact than the undercounting that would occur on lineament patterns. The impact of undercounting is greater at smaller scales than at larger, and so values of $N(r)$ at the smaller values of r should be treated as possible minimum values when interpreting the resultant plots.

The methodology for calculating the mass dimension consists of placing a minimal convex covering over the fracture trace data. A covering consists of distributing a number of mathematically convex polyhedra such that all members of the set are enclosed by the polyhedra. The dimension of the covering set, given as r in Equation 3-18 is the maximum size of the covering, essentially the largest chord in the polyhedral set, and $N(r)$ is the minimum number of polyhedrons of this size to completely enclose the set.

In practice, this implies that the mass dimension of the borehole data can be obtained by starting at each fracture location along a borehole, and expanding a circle around this location while counting the number of fractures in the circle as a function of the radius. Starting at existing fracture locations helps insure that the minimum number of polyhedra are required, though it is not a guarantee. A circle superimposed upon a line such as a borehole delineates an interval of a length equal to the circle's diameter. Since the diameter of a circle and its radius are linearly related, the scaling exponent is unchanged whether the radius or the diameter (interval length) is plotted, although the constant will change. By plotting interval length vs. number of fractures for borehole data on log-log axes, it is possible to evaluate whether Equation 3-18 describes the scaling behaviour, and if it does, what the mass dimension is for the data. A slope of 1.0 for borehole data indicates Euclidean scaling.

For the borehole data, fractures inside deformation zones (DZ) and possible local minor deformation zones (MDZ) are excluded. Deformation zones are outside the scope of interest of the geological DFN model, while possible local minor deformation zones are instead treated as single planar features (rather than as a cluster of fractures). Since removal of these zones constitutes a gap in the data record, the mass dimension calculation is only carried out over the contiguous portion of the fracture record in each individual borehole. For example, if a fracture record covers 600 m, but there is a deformation zone between 450 m and 500 m, then the data are broken up into one interval spanning 0.0 m measured depth to 450 m measured depth, and a second interval from 500 m measured depth to 600 m measured depth.

The values selected for the minimum and maximum interval sizes in the cored borehole data set impact the calculation. Only fractures larger than the borehole radius are recorded in the database. Since all of the smaller fractures are not recorded, the number of fractures recorded at interval sizes less than the minimum spacing will only include one fracture, regardless of how much smaller the interval becomes. When intervals become larger than the maximum measured spacing, then the amount of "missed" small fractures is directly proportional to the interval size. This means that for a Poissonian point pattern in which the slope should be a constant value of 1.0, there will be a departure from this slope that begins at the maximum recorded spacing size. The slope will decrease monotonically from this interval size until it reaches the interval size corresponding to the minimum recorded spacing, at which point the slope becomes horizontal. This type of behaviour applies to all types of intensity/spacing distributions.

As shown in Section 4.4.1, the departure from a slope of 1.0 to a horizontal slope occurs in models assuming Poissonian (exponential), uniform and Weibull-distributed spacings. At intervals greater than the largest recorded spacing, the slope for all three spacing distributions is 1.0. There is a monotonic decrease in slope that approaches 0.0 as the interval size approaches the minimum recorded spacing for Poisson- and Weibull-distributed spacings.

The behaviour of spacings that exhibit fractal (power law) spacings is different than for spacings following a Poisson or Weibull distribution (see Section 4.4.1). For a power law spacing distribution, the slope is constant at all interval sizes greater than the minimum spacing, and abruptly becomes equal to 0.0 at intervals smaller than the minimum spacing. There is no monotonic continuous change in slope between the interval sizes corresponding to the maximum and minimum spacing; it is a sharp discontinuity.

For outcrop data, the calculation is similar. A series of random starting points are selected over the outcrop. Circles of increasing radius are expanded from this starting point, and the number of fractures in each circle is recorded. Circles not containing factures are excluded from the calculation, as they violate the minimum coverage requirement. $N(r)$ is the number of fractures in a circle of radius r. A slope of 2.0 in a trace plot indicates Euclidean scaling.

The procedure for calculating the mass dimension for outcrop data is illustrated in Figure 3-8. A data cloud is generated by selecting approximately 100 random points on the outcrop along mapped fracture traces, and then expanding a nested series of concentric circles of increasing radius from each point. The number of fractures for each circle as a function of radius is computed. If a portion of the circle lies outside of the outcrop limits, then the portion of the area outside is subtracted from the circle's total area, and an equivalent radius is calculated. The pairs of radius and number of fractures are then plotted for all of the randomly-selected starting points. These points are the data cloud.

Next, the mean values of the cloud are calculated, and then a non-linear least-square fit of the Pareto equation is fit to the mean. The slope of this line is D_m in Equation 3-18. The value of the prefactor is equal to the ordinate value corresponding to a circle with a radius of 1.0, and can be read directly from the graph. The mass dimension calculations are carried out on each orientation set individually, since each might have unique spatial/scaling behaviour.

The borehole data also make it possible to infer the form of the spatial model from the fracture spacings. If fracture centres are located according to a three-dimensional Poisson point process, then the fracture spacings will be exponentially distributed along a borehole. If the locations of fracture centres are the result of a fractal process then the observed spacings will follow a power-law probability distribution. Other types of spatial mechanisms, for example breakage due to a "weak-link" process, can give rise to fractures that have spacings best described using a Weibull distribution /Iacopino 2006/.

Thus, in order to further reduce uncertainty concerning the spatial model, the spacing distribution of each fracture set is evaluated. Since the complementary cumulative density function (CCDF) for a power law spacing distribution plots as a straight line on a log-log plot, the CCDFs of spacings for each fracture set are plotted. This allows for rapid visual discrimination between fractal spacing distributions and other types.

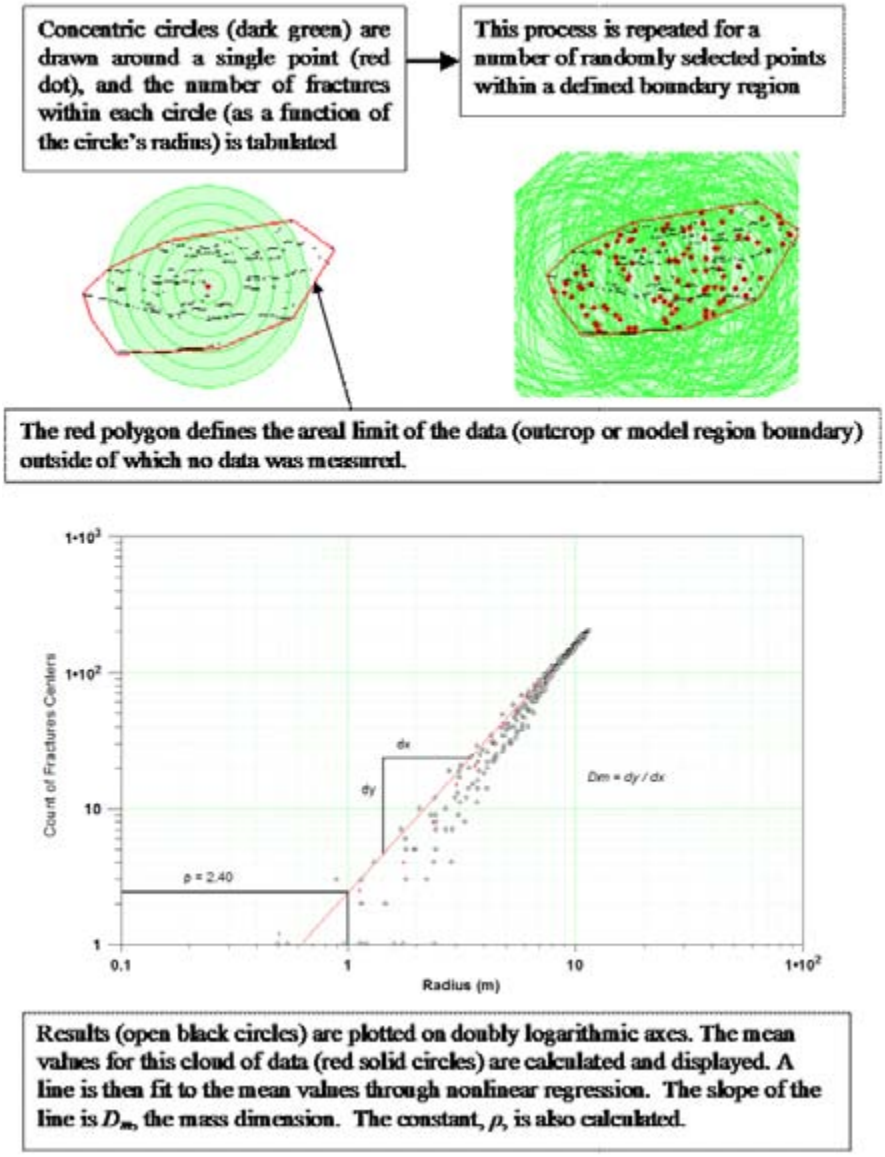

Figure 3-8. *Workflow for calculating the mass dimension from maps of fracture traces.*

3.6.2 Evaluation of fracture domain, rock domain, and lithology classifications

Some of the groupings that need to be assessed for development of the DFN model are the Fracture Domain model (FSM), the Rock Domain model (/Wahlgren et al. 2008/, cf. Chapter 4) and whether the major lithologies have sufficiently different fracture characteristics that there needs to be subdivision by lithology. The statistical tests that are used to address these questions consisted of the cross-tabulation analyses previously described in Section 3.3.5 for the Visible/ Not Visible in BIPS analysis, with additional 1-way ANOVA tests for fracture intensity.

The cross-tabulations are carried out on the data associated with individual fractures, such as their roughness, orientation, mineral fillings and so on. Fracture intensity, which is a parameter calculated over a region that may contain more than one fracture, cannot be included in these types of analyses. In order to assess whether fracture intensity differs among subdivisions, such as fracture domains or rock domains, standard ANOVA calculations /Snedecor and Cochran 1980/ were performed on binned P_{32} fracture intensity data over 3 m-long intervals. ANOVA calculations examine whether the fracture intensity variation within individual sub groups is less than the fracture intensity variation among groups. In these tests, the Null Hypothesis is that there is no difference between the groups being tested. The Null Hypothesis is rejected if the test statistic probability is less than or equal to 0.05.

This analysis was carried out only on fractures outside of deformation zones and inside mapped fracture domains (fractures with a domain assignment of OUTSIDE are discarded).

3.6.3 Evaluation of fracture intensity as a function of depth

Systematic variations of fracture intensity with depth govern how surface fracture data should be used with subsurface borehole fracture data to infer fracture intensity at proposed repository depths. Since the variations may be functions of fracture set, fracture domain and fracture type, it is important to separate out these effects to evaluate possible systematic depth dependences. Borehole orientation effects on the fracture intensity are mitigated by using the volumetric fracture intensity P_{32}. The use of P_{32} requires that fracture intensity be calculated over a finite borehole length. A 3 m borehole length was chosen, as it provides the good depth resolution without producing an unduly high number of intervals with no fractures, which can make it harder to detect systematic depth trends should they exist. Only data and intervals outside of identified deformation zones are included in the depth analysis.

The P_{32} intensity for open and all fractures is first calculated over all 3 m borehole intervals that are entirely outside of any identified deformation zones. The intensity includes both fractures visible in BIPS and those that are not visible. Next, the true vertical depth below the surface (not the elevation or borehole length, i.e. ADJ_SECUP) at the midpoint of the 3 m interval is calculated. A series of 5 m depth intervals are then defined, starting at the surface (0 m) and extending to a vertical depth of 1,000 m. Each 3 m interval P_{32} value is assigned to a 5 m depth increment based on the midpoint depth value of the 3 m interval. The average P_{32} intensity is then calculated from all the 3 m values assigned to the interval as a function of fracture type (open and total), fracture set (ENE, NS, SH & WNW), and fracture domain.

The results are displayed as a histogram with a bar for each 5 m depth increment, as well as a 10-interval moving average that spans five increments (25 m) on either side. The moving average makes it easier to visually detect any systematic changes in intensity with depth, as the higher frequency variations in intensity are smoothed out. This analysis approach does not require any compensation for the number of samples used to calculate the mean intensity, as the number of samples only impacts the confidence on the estimate of the mean intensity, not on the value of the mean.

3.6.4 Fracture set termination model

A final step in the spatial model parameterization is the determination of how DFN features behave when fractures belonging to one orientation set interact with fractures belonging to a different orientation set (see Section 3.3 for details on how orientation sets are defined). Fracture termination relationships have the potential to affect both hydrogeological and rock mechanical models, and as such are an important part of the spatial model parameterization.

Fracture terminations are described through the use of a matrix. The columns (vertical) of the matrix represent the target fracture set (the set that is being terminated against). Each row represents the orientation set being parameterized. An example is illustrated below as Table 3-2. In the sample termination matrix, to determine the percentage of fractures in the ENE Set (row 1) that terminate against the N-S set (column B), one reads the percentage from cell address B1 (25%). The total percentage termination can be interpreted as a proxy for the relative timing of fracturing at a given location; the higher the percentage of fracture terminations, the younger the features observed are likely to be. The percentages can also be interpreted as a probability value; for a given fracture, in a given set, on a given outcrop or in a given fracture domain, where the percentage is considered equivalent to a probability that the fracture will terminate against another fracture.

Table 3-2. Example termination matrix utilizing dummy values.

		A **ENE**	B **N-S**	C **WNW**	D **SH**
1	ENE	0	25%	15%	5%
2	N-S	1%	0	3%	5%
3	WNW	20%	40%	0	20%
3	SH	10%	10%	15%	0

The termination matrices were computed inside ArcGIS using only the four detailed fracture mapped outcrops in the Laxemar local model area. The trench data are excluded from the analysis due to significant directional biases. The methodology for computing fracture termination relationships is as follows:

1. The endpoints of every fracture on a given detail-mapped outcrop are calculated. For multi-segment polyline features, only the start and end points of the polyline (nodes) are used; additional vertices are ignored.
2. A 0.05 m (5 cm) buffer zone surrounding every fracture on the outcrop is created.
3. For a given fracture set, the number of points within the buffer zone of another set was computed using a Select by Location query inside ArcGIS. The results were saved as a point shapefile.
4. For a given fracture set/terminating set relationship, the selected points are examined to determine if the termination made geologic sense. For example, if an endpoint is inside the buffer zone, but the fracture clearly crosses another one, it is not counted as a termination. In addition, the termination data recorded during the detailed fracture mapping field work is also used. If ArcGIS indicates a fracture termination, but the field notes instead indicate that the target fracture ended abruptly inside the rock mass instead of terminating against another fracture, the point is removed from the shapefile.
5. A matrix of termination endpoints is then constructed, with the point counts converted to a percentage.

The results of the analysis are presented as matrices for each detail-mapped fracture outcrop. As there is not an outcrop available in every fracture domain, the recommended usage is to se the global average termination model for domains where data are not available.

3.6.5 Spatial variability of fracture intensity

It has been suggested /Dershowitz 1984/ that, in the absence of other controlling factors such as lithology or deformation zones, P_{32} for a system exhibiting Euclidean scaling behaviour and following a Poisson point process for fracture centres should follow a Gamma (Γ) distribution. Borehole linear fracture intensity (P_{10}) can be taken as the rate parameter (λ) of a Poisson distribution, with Γ as the distribution of the variability of λ within the scale of measurement /Schlaifer and Raiffa, 1972/. The Γ distribution is a two-parameter continuous probability distribution, described by a scale parameter (β) and a shape parameter (α); if α is a positive integer, then the resulting distribution represents the sum of exponentially-distributed random variables, each with a mean of β /NIST 2007b/.

Alternatively, fractures can be modelled as failures following a ‘weakest-link’ type model /Weibull 1951/. Such a model implies that the strength of a material with flaws will decrease with specimen size, as the probability for a weak flaw increases with specimen volume. The failure rate in models of these types follows a Weibull distribution; correspondingly, it is reasonable to assume that the spacing (and potentially the fracture intensity) can be represented through a Weibull distribution.

It is possible to calculate the Gamma or Weibull distributions of P_{32} from borehole data. The method assumes that borehole fracture frequency (P_{10}) has been converted to volumetric fracture intensity (P_{32}), either through simulation or application of the Wang C_{13} factor. Expressing P_{32} as a Gamma or Weibull distribution allows for the implementation of random spatial variability of fracture intensity; this form is most applicable to finite-difference or geocellular-grid style models.

The steps necessary to compute the gamma distribution parameters for a given fracture set within a given fracture domain are:

1. Tabulate fracture frequency (P_{10}) for each fracture set in a given fracture domain for all boreholes. The fracture frequency measurements should be taken from borehole intervals outside of mapped DZ and MDZ, and should not contain sections of rock labelled 'affected by DZ'. The frequency measurements are also relevant to a specific scale; bin sizes of 3 m, 9 m, 15 m, 21 m, 30 m and 51 m are tested. It is possible to have a distribution of fracture intensity that is Gamma at a larger, block scale (30 m), but that can not be well-defined by either a Gamma or a Weibull distribution at local scales (3 m).
2. Convert P_{10} to P_{32} using the Wang approximation (Section 3.5.1).
3. The resulting P_{32} values are copied into BestFit 4.55 or EasyFit 4.3, where a Gamma or Weibull probability distribution was fit to the sample data. For both the Gamma and Weibull distributions, BestFit (and EasyFit) uses a maximum likelihood estimator to estimate distribution parameters, and uses least-squares to then fit the probability distribution to the CDF and PDF /Palisades Corporation 2004/.
4. A goodness-of-fit test of the resulting fitted gamma distribution of P_{32} was performed using BestFit version 4.5.5 and EasyFit 4.3. Goodness-of-fit is determined through the use of the Kolmogorov-Smirnov test /NIST 2007a/, assuming a significance level of $\alpha = 0.05$ (not the same α as in the definition of the Gamma distribution). Goodness-of-fit is also described for the smaller scales (3 m, 9 m, 15 m) using Q-Q and ECDF plots; they were not constructed for the larger scale simulations.

It was not possible to fit a Gamma or Weibull distribution to some fracture set/fracture domain combinations at the chosen level of significance ($\alpha = 0.05$); in those cases, we recommend using the P_{32} median and quartiles to represent spatial variability.

3.7 Uncertainty modelling methodology

The methodology for quantifying uncertainty consists of identifying the uncertainties that could have possibly significant impacts, and then quantifying those impacts using a measure that is relevant to downstream usage of the GeoDFN model.

3.7.1 Identifying uncertainties

There are several types of uncertainty in the GeoDFN model. These different types are a useful way to categorize what is not known precisely about the model, in that each category or type has a different type of impact, and needs to be quantified and incorporated into downstream models or decisions in a different manner.

Conceptual Uncertainty relates to the fundamental geological concepts on which the model is based. An example of a conceptual uncertainty would be whether the fractures measured in one portion of the potential repository volume are part of the same population of fractures measured in a different region. If the fractures are thought to be part of the same population, then the data could be combined and parameterized as a single population; otherwise, the two populations should be parameterized separately. Conceptual uncertainties typically have the greatest impact on model results. Conceptual uncertainties are usually treated as scenarios, in which there is a single Base Case scenario that is believed to be the most likely, and one or more alternative models that represent other possible, though less likely, scenarios. Often, alternative models are explicitly run.

Mathematical Uncertainty concerns the representation of the geological concepts as mathematical equations or computer models. For example, a fracture might be represented as a flat, circular disk, as a rectangular surface, or as something more complex. These mathematical representations can contribute to the overall uncertainty. In general, the mathematical uncertainties are treated as scenarios, although the alternative models are rarely run.

Parameter Uncertainty has to do with the variability of a parameter and the fact that this variability is not fully characterised but only sampled by a relatively small data subset consisting of selected outcrops or boreholes. Parameter uncertainty is usually captured through probability distributions or bounding calculations.

3.7.2 Quantifying uncertainties

The primary impact of the uncertainties identified and described during the geological DFN analysis is likely to be on the intensity of large fractures and minor deformation zones. The intensity of these features controls the volume available and accessible by a potential repository. Also, larger fractures and MDZ in the size range 75 m to 564 m represents the component of fracturing that is of the greatest interest for these safety calculations, as they are large enough to have secondary slip induced during earthquakes that might impact safety, yet are small enough that they may be difficult to detect with 100% reliability during site reconnaissance and construction.

As a result, each uncertainty that is identified will be quantified by comparing the P_{32} of the uncertainty to the P_{32} of the Base Case model. This ratio provides a measure of how much of an impact the uncertainty might have, and whether it would lead to an increased or decreased estimate of P_{32} and any consequences, such as earthquake-related safety, as a result.

3.7.3 Alternative models

Alternative models arise from conceptual uncertainties or mathematical uncertainties. In Chapter 4, the alternative models that were identified during the development of the geological DFN are parameterised. As it turns out, the alternative models all concern the coupled size/intensity parameterization of each set or the intensity scaling. They do not concern set identification or orientation parameterization. As a consequence, the alternative models are presented along with their individual size/intensity and scaling parameterizations. The results from these parameterizations are carried forward into the uncertainty analyses in Chapter 6.

3.8 Verification and validation of geological DFN model

The purpose of verification is to build confidence during model development and to establish the scientific basis and accuracy of the model within its intended scope of use. Verification is also used to evaluate the strengths and weaknesses of various alternative model cases for particular uses, and provides additional insight into the possible importance of the identified uncertainties on downstream model usage.

3.8.1 Verification cases

Verification in the SDM-Site Laxemar geological DFN modelling was conducted by building a series of small-scale DFN models using FracMan /Dershowitz et al. 1998/, conducting simulated sampling using the extent and geometries of actual outcrops, scanlines, and boreholes from the Laxemar local model area. The verification was carried out not only for the Base Model, but also all of the identified alternative models.

The verification efforts consisted of the following test cases:

- Case OR-1: Variability of Fisher distribution mean pole vectors and concentration parameters (κ). This verification is similar to the orientation uncertainty assessments conducted as a part of the SDM Forsmark Stage 2.2 DFN modelling; 95% confidence intervals on the mean pole vector and on the Fisher κ were constructed. Then, for each set, the mean pole and actual κ simulated is recorded. These results are then plotted against the 95% confidence regions for the observed data. More details regarding the specific statistical tests are presented in Section 5.2.
- Case OR-2: Relative fracture set intensities for each fracture domain are calculated using the Terzaghi weight sums for each fracture set. The relative intensity percentages of each fracture set are then compared to the relative P_{32} for each fracture set in the geological DFN model parameterisation. The performance metric is the percent error between the two numbers. Relative intensity of fracture sets is quantified as the sum of the Terzaghi weights (Section 3.3.4) for each set, divided by the sum of Terzaghi weights for all fracture sets.
- Case SI-1: Fracture areal intensity (P_{21}) for simulated fracture traces was compared to P_{21} values derived from fracture traces on detail-mapped outcrops. 20–25 simulations are run for each alternative model case (Table 3-3); the mean P_{21} of all simulations are used for the validation case. There are two comparisons for P_{21}; one within the size range for which the fitted trace length exponent curve and the area-normalized cumulative number plots were collinear (termed the 'fit range'), and a second comparison over the full outcrop size range (0.5 m–564.2 m). Note that fracture traces shorter than 0.5 m were not recorded in the data from the detail-mapped fracture outcrops.
- Case SI-2: Linear fracture intensity (P_{10}) along simulated scan lines is compared to scan line data recorded on drill-pad outcrops; the trench data is not used for this analysis. The simulated scan lines are modelled using Monte Carlo analysis. The verification metric is the percent error between the simulated and observed P_{10} values.
- Case SI-3: Linear fracture intensity (P_{10}) and volumetric fracture intensity (P_{32}) of simulated fractures within the minor deformation zone (MDZ) size range in boreholes is compared to the observed P_{10} of MDZ in the ESHI results. The methodology involved in this verification involves calculating the minimum size (r_{min}) required to match the observed intensity (P_{32}) of MDZ in boreholes for different size-intensity scaling cases. MDZ P_{32} is established by establishing an average Wang C_{13} (Section 3.5.1) for an entire individual borehole, based on the C_{13} values calculated for the 3 m borehole sections. Then, P_{32} is calculated on a set-by-set basis, for each borehole and fracture domain, using the MDZ identified in cored borehole data and discussed in Section 4.3.2 of the Laxemar DCR /Hermanson et al. 2008/. Using Equation 3-14 , the minimum size can be found for the MDZ P_{32} for each of the coupled size-intensity model alternatives. As a check on the minimum size calculated, a second minimum size estimate is made using the length at which the area-normalized cumulative number plot of the surface lineaments begins to 'roll over'.
- Case SI-4: Linear fracture intensity (P_{10}) of simulated fractures in boreholes is compared to observed P_{10} values in a number of borehole sections. The computational time requirements for this test are exceptionally long, due to the need to simulate relatively high numbers of very small fractures. Consequently, verification was completed only for fracture domain FSM_C. FSM_C is the fracture domain most likely to host a proposed HLW repository at Laxemar (SKB, personal communication to DFN team). The verification metric is the percent difference between the mean simulated P_{10} and the mean observed P_{10}.
- Case SI-5: The gamma (α, β) and Weibull (κ, λ) distribution parameters for fracture P_{32} were computed at a number of different scales to determine at what scale ranges the spatial variability of fracture intensity can be described using a Gamma or Weibull probability distribution. The methodology for this analysis is described in Section 3.6.5. The chosen simulation scales are: 3 m, 9 m, 15 m, 21 m, 30 m, and 51 m. Fitting a probability distribution to borehole data at scales larger than 51 m is a difficult task; at that scale, there are very few intervals in the cored borehole array that are not interrupted by a minor deformation

zone or a deterministic deformation zone. As the geological DFN model explicitly excludes fractures inside of deformation zones from the model parameterisation, the inclusion of intervals that cross DZ could dramatically skew the results of the distribution fit. As such, Case SI-5 is capped at a maximum scale of 51 m. Goodness-of-fit is determined through the Kolmogorov-Smirnov test, with ECDF versus CDF and Q-Q plots included as Appendix F.

The results of verification case SI-5 are not presented in Chapter 6; SI-5 is not explicitly 'verification' per se, but rather an extension of the spatial analysis completed during the model parameterisation. The Gamma and Weibull parameters derived during SI-5 are included in Section 4.4.7.

It should be noted that, for verification case OR-1 there are no 'alternative' cases; the orientation model is static across all fracture domains. In addition, verification case SI-5 also does not have any alternative model cases. The calculation of distribution fit is made based on using the cored borehole data available in each domain, and is independent of the size-intensity model. The result is that the ranking of the alternative model cases (AMR) is based on verifications SI-1, SI-2, SI-3, and SI-4. For the remaining verifications, a list of the alternative model cases along with a brief description of each case is presented below in Table 3-3.

Table 3-3. Index of alternative model cases used in the verification of the SDM-Site Laxemar GeoDFN.

Model Case	Case Description	Case Tested in Verification?				
		SI-1 (> 0.5 m)	SI-1 (Fit Range)	SI-2	SI-3	SI-4
BM	Base Model, Linked Traces	Y	Y	Y	Y	Y
EL1	Euclidean Scaling Scaling, Upper k_r, Linked Traces	Y	Y	Y	Y	Y
EL2	Euclidean Scaling, Lower k_r, Linked Traces	Y	Y	Y	Y	Y
BMU	Base Model, Unlinked Traces	Y	Y	Y	Y	Y
EUL1	Euclidean Scaling, Upper k_r, Unlinked Traces	Y	Y	Y	Y	Y
EUL2	Euclidean Scaling, Lower k_r, Unlinked Traces	Y	Y	Y	Y	Y
BMF	Fractal Scaling, Best Fit k_r, Linked Traces	Y	Y	Y	Y	Y
FL1	Fractal Scaling, Upper Fit k_r, Linked Traces	Y	Y	Y	Y	Y
FL2	Fractal Scaling, Lower Fit k_r, Linked Traces	Y	Y	Y	Y	Y
BMUF	Fractal Scaling, Best Fit, k_r, Unlinked Traces	Y	Y	Y	Y	Y
FUL1	Fractal Scaling, Upper Fit k_r, Unlinked Traces	Y	Y	Y	Y	Y
FUL2	Fractal Scaling, Lower Fit k_r, Unlinked Traces	Y	Y	Y	Y	Y
ESL1_N	Euclidean Scaling, Change k_r BestFit, Linked Traces, FSM_N	Y	N/A*	Y	Y	FSM_C**
ESL1_NE005	Euclidean Scaling, Change k_r BestFit, Linked Traces, FSM_NE005	Y	N/A*	Y	Y	FSM_C**
ESL1_W	Euclidean Scaling, Change k_r BestFit, Linked Traces, FSM_W	Y	N/A*	Y	Y	FSM_C**
ESL2_N	Euclidean Scaling, Change k_r Upper, Linked Traces, FSM_N	Y	N/A*	Y	Y	FSM_C**
ESL2_NE005	Euclidean Scaling, Change k_r Upper, Linked Traces, FSM_NE005	Y	N/A*	Y	Y	FSM_C**

Model Case	Case Description	Case Tested in Verification?				
		SI-1 (> 0.5 m)	SI-1 (Fit Range)	SI-2	SI-3	SI-4
ESL2_W	Euclidean Scaling, Change k_r Upper, Linked Traces, FSM_W	Y	N/A*	Y	Y	FSM_C**
ESL3_N	Euclidean Scaling, Change k_r Lower, Linked Traces, FSM_N	Y	N/A*	Y	Y	FSM_C**
ESL3_NE005	Euclidean Scaling, Change k_r Lower, Linked Traces, FSM_NE005	Y	N/A*	Y	Y	FSM_C**
ESL3_W	Euclidean Scaling, Change k_r Lower, Linked Traces, FSM_W	Y	N/A*	Y	Y	FSM_C**
FSL1_N	Fractal Scaling, Change k_r BestFit, Linked Traces, FSM_N	Y	N/A*	Y	Y	FSM_C**
FSL1_NE005	Fractal Scaling, Change k_r BestFit, Linked Traces, FSM_NE005	Y	N/A*	Y	Y	FSM_C**
FSL1_W	Fractal Scaling, Change k_r BestFit, Linked Traces, FSM_W	Y	N/A*	Y	Y	FSM_C**
FSL2_N	Fractal Scaling, Change k_r Upper, Linked Traces, FSM_N	Y	N/A*	Y	Y	FSM_C**
FSL2_NE005	Fractal Scaling, Change k_r Upper, Linked Traces, FSM_NE005	Y	N/A*	Y	Y	FSM_C**
FSL2_W	Fractal Scaling, Change k_r Upper, Linked Traces, FSM_W	Y	N/A*	Y	Y	FSM_C**
FSL3_N	Fractal Scaling, Change k_r Lower, Linked Traces, FSM_N	Y	N/A*	Y	Y	FSM_C**
FSL3_NE005	Fractal Scaling, Change k_r Lower, Linked Traces, FSM_NE005	Y	N/A*	Y	Y	FSM_C**
FSL3_W	Fractal Scaling, Change k_r Lower, Linked Traces, FSM_W	Y	N/A*	Y	Y	FSM_C**

* The Fixed-r_{min} models do not have a 'fit range' as the radius scaling exponent is calculated analytically.

** Due to the time-consuming nature of the simulations required to generate these models, only fracture domain FSM_C is tested in the verifications.

3.8.2 Ranking of alternative models: methodology

In the course of developing the conceptual framework for the SDM-Site Geological DFN, possible alternative models were identified. While one or more of these models appeared to be the most geologically reasonable and self-consistent, and thus served as a preliminary candidate for the preferred Base Model, this does not guarantee that the Base Model will predict the fracture pattern characteristics of interest to performance assessment, repository design and construction better than the alternative models. In order to assess which of the models best predicts the fracturing characteristics of greatest interest, the verification results for the various models and verification cases were statistically compared and ranked.

Each verification case has a value that was to be predicted. The accuracy of the model predictions is quantified by the percentage error made by each model for each verification case. The error is calculated by:

$$V = \frac{\|s - m\|}{m}$$ Equation 3-19

Where V is the error metric,

s is the value predicted by the model, and

m is the measured value.

Within each verification case, the errors for every alternative model can be ranked, with Rank 1 being the most accurate prediction. If the number of alternative models (including the Base Model) is n, and the number of verification cases is k, then this produces an n by k matrix of ranks. Summing across the k verification cases leads to a final rank for each n^{th} alternative model. The model with the overall lowest sum of the verification case ranks is the highest rank model, and has the final rank of 1.

This does not necessarily imply that it is the preferred model, however. For example, a slightly lower ranked model with uniformly low ranks across all verification cases might be preferred to the best-ranked model if this latter model has one rank that is very poor, despite the fact that the sum is still the lowest. Moreover, merely because the sum of one model is slightly lower than another, this may be due to random effects. To test this possibility, the models was tested using the Kruskal-Wallis non-parametric ANOVA tests /Kruskal and Wallis 1952/.

The null hypothesis, H_o, for this test is that the median ranks are the same. The alternative hypothesis, H_a, is that the median ranks differ. The null hypothesis is rejected if the calculated test statistic has a probability value of 0.05 or less.

The Kruskal-Wallis test can be applied to a group of models simultaneously, to determine whether the differences in median rank between models are greater than the differences in rank within an individual model. In this way, it is possible to conclude that two or more models perform statistically the same or not in terms of the verification cases. One conclusion, if the null hypothesis is not rejected, is that regardless of the rankings, any of the group of models tested should perform equally well, and that the tabulated final rank sum differences are more likely due to stochastic variations than actual performance differences. Another conclusion would be that the uncertainties underlying these statistically equivalent models are not likely to be important for performance assessment, repository design and construction to the extent that the verification cases capture the metrics appropriate to these uses of the Geological DFN.

3.8.3 Validation of geological DFN model

Validation of the geological DFN model was performed by using the top five ranked alternative models from ranking case III (Section 5.8) to predict the fracture intensity expected in borehole KLX27A, in domain FSM_W, outside of identified deformation zones and minor deformation zones. The validation compared:

- Mean simulated P_{10} to mean observed P_{10} in KLX27A.
- Distribution of simulated P_{10} to observed P_{10} in KLX27A.
- Simulated number of MDZ versus the actual number of MDZ identified in KLX27A.

The formal methodology and results of the model validation are presented in Appendix G.

4 Derivation of SDM-Site Laxemar geological DFN model

4.1 Fracture domain model

4.1.1 Identifying fracture domains induced by regional and local major deformation zones

In general, the fracture domain model used in the SDM-Site Laxemar DFN modelling is based on a fairly simple tectonic context: three regional deformation zones (ZSMEW002A, ZSMNE005A and ZSMEW007A) are assumed to control fracturing within the Laxemar local model area. These zones are illustrated in Figure 4-1. Note that the discussion of the fracture domain model necessarily involves the simultaneous discussion of fracture orientation sets, which are described in Section 4.2.

A visual inspection of contoured stereo plots from cored borehole logs (Appendix B) reveals that data within approximately 100 m of either side of deformation zone ZSMEW007A have relatively few N-S striking fractures and few open subhorizontal fractures when compared to the rest of the Laxemar local model area as a whole (set nomenclature is specified in Section 4.2.1). Instead, in the zone surrounding ZSMEW007A, most open fractures belong to the WNW set (See Appendix B, Section 4.2, and Figure 4-2). Additional visual inspection suggests that

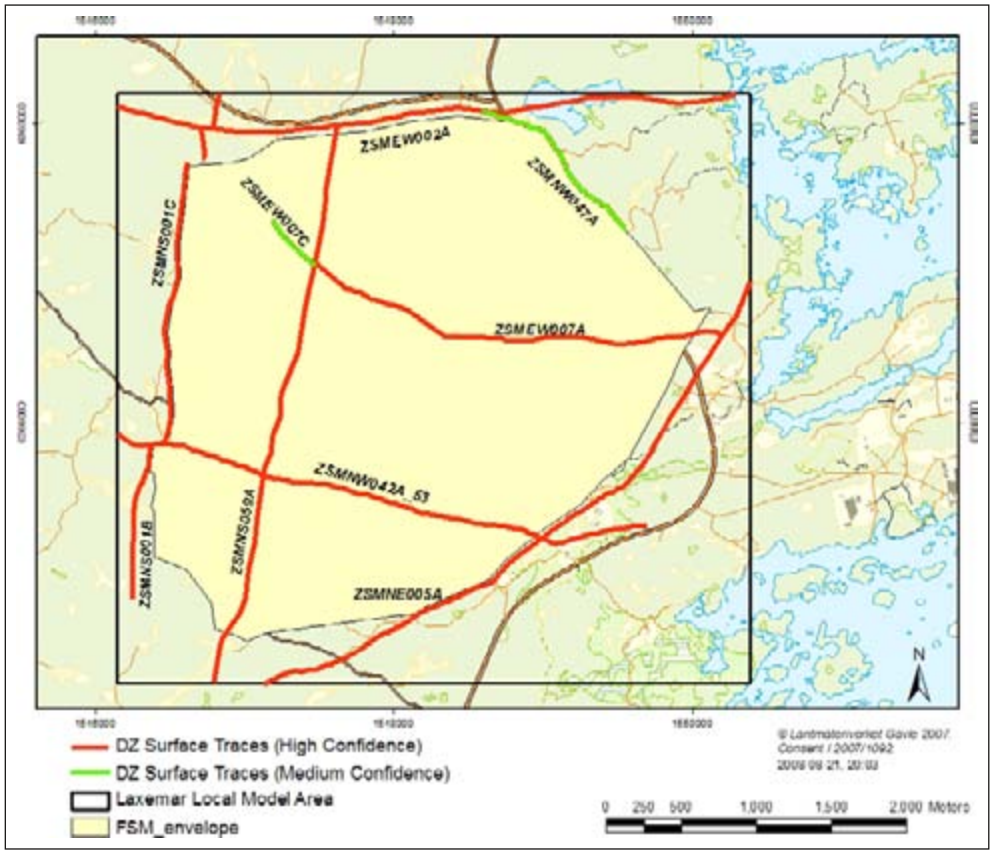

Figure 4-1. *Illustration of deformation zones ZSMEW007A, ZSMEW002A, ZSMNW042A, ZSMNE005A, ZSMNS059A and ZSMNS001C, in the context of the fracture domain envelope used for SDM-Site DFN modelling. These deterministic deformation zones appear to influence the fracture pattern inside the fracture domain envelope (yellow).*

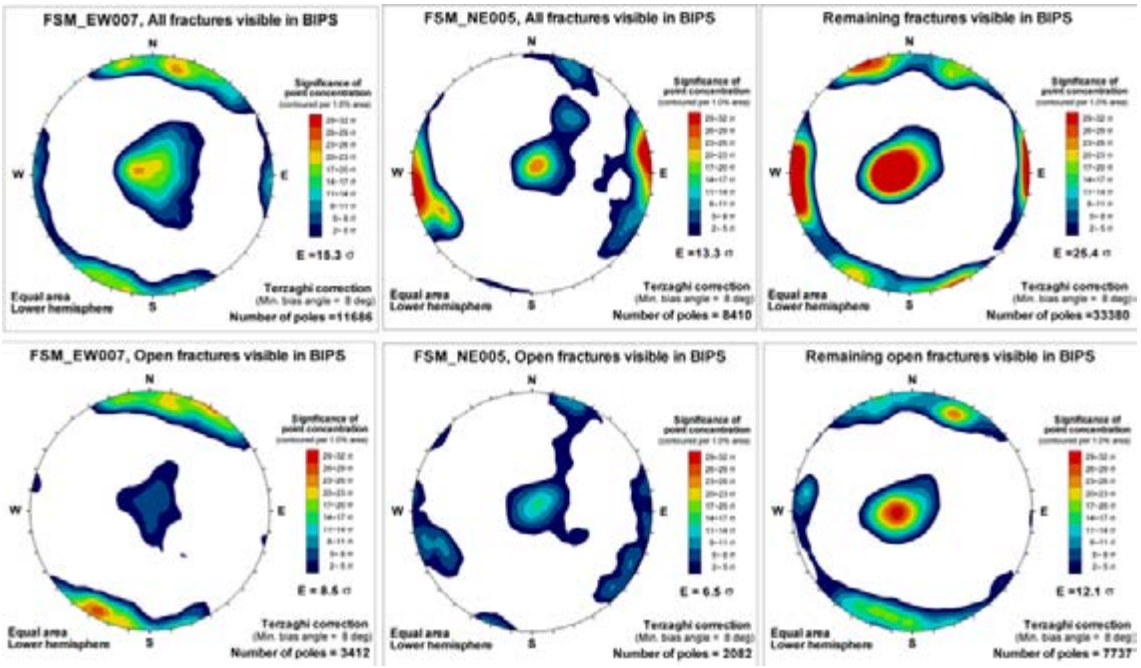

Figure 4-2. *Kamb-contoured polar stereoplots illustrating fracture set orientations from cored boreholes in fracture domains FSM_EW007 and FSM_NE005, relative to fracture orientation from cored boreholes in the remainder of the Laxemar local model area.*

a zone approximately 100 m thick on either side of regional deformation zone ZSMNE005A is dominated by N-S striking fractures. In this zone, the open fractures are predominantly from the SH orientation set (see Section 4.2). Data from boreholes near or cutting through both these zones show similar patterns in set relative intensities.

However, although deformation zone ZSMEW002A is likely to have a regional footprint, only one cored borehole currently intersects this zone (KLX06). This are not enough data to analyze the influence on fracture orientation and relative set intensities that ZSMEW002A might have in the rock volume in the southern half of the Laxemar local model area with any significant statistical power. Therefore, both this zone and data from cored borehole KLX06A are excluded from further fracture domain analysis.

Based on the initial analysis of fracture orientation and intensity data from boreholes near deformation zones ZSMEW007A and NZSME005A, two tentative fracture domains were formed: FSM_EW007 and FSM_NE005 (see Figure 4-3).

The initial definition for FSM_EW007 was set to include a volume extending 250 m from the boundary of ZSMEW007A, with a termination against ZSMNE005 (or the envelope domain) in the east, and a boundary extended to ZSMNS059A in the west. The data coverage in the west of ZSMNS059A is scarce (cored boreholes KLX13A and KLX17A), which precludes stating whether FSM_EW007 in fact terminates at or continues across ZSMNS059A. Due to the lack of contradictory evidence, FSM_EW007 is assumed to terminate at ZSMNS059A, as illustrated in Figure 4-3.

FSM_NE005 was initially assumed to terminate against FSM_EW007 in the north, deformation zone ZSMNE107a in the west, and deformation zone ZSMNW042A to the south (Figure 4-3). Data available west of ZSMNE107A are located relatively far from ZSMNE005A; cored boreholes in this area possess very different characteristics than the boreholes inside the proposed domain FSM_NE005 (see Appendix C). Again, it is impossible to state the exact western boundary of FSM_NE005, but it is assumed unlikely that the fracture control of ZSMNE005 would extend across ZSMNE107A. However, it should be emphasized that ZSMNE005A and ZSMNE107A are semi-parallel and that the rock mass confined by these two are subject to a

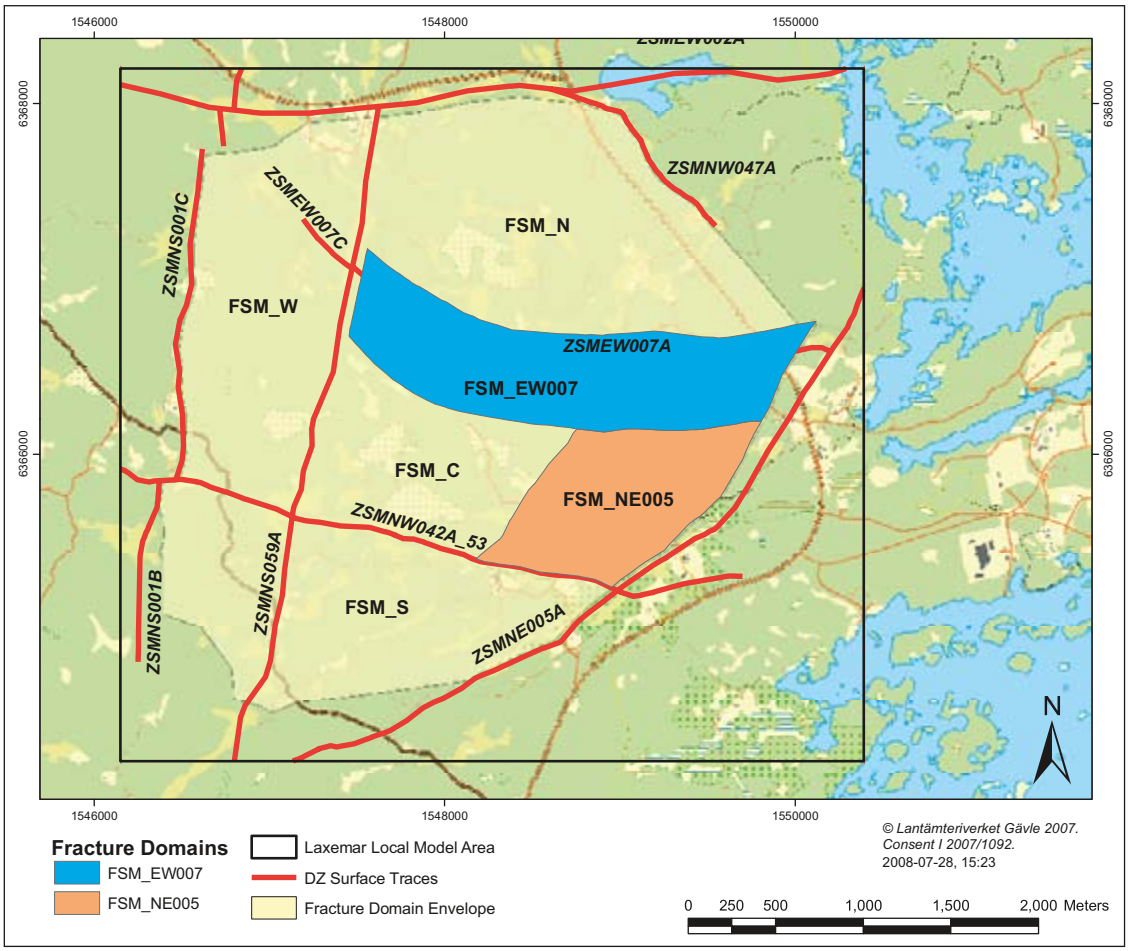

Figure 4-3. *Illustration of fracture domains FSM_EW007 and FSM_NE005.*

combined influence of two "similar" zones; an effect that would cease west of ZSMNE107A (see discussion on zones acting as fracture domain separators, see Section 3.2.1). The reason for terminating FSM_NE005 against ZSMNW042A is lack of supporting data. The only data available south of ZSMNW042A are from cored borehole KLX16A. Furthermore, KLX16A may be unrepresentative for the domain south of ZSMNW042A, as it is suspected to be strongly influenced by ZSMNE107A. Therefore it was decided not to extrapolate any of the central fracture domains south of ZSMNW042A.

Summary – FSM_EW007 and FSM_NE005

In summary, an initial analysis of fracture orientations, relative set intensities, and tectonic histories suggested two fracture domains induced and strongly controlled by regional deformation zones; FSM_EW007 and FSM_NE005. The domains are defined as:

- Domain FSM_EW007: This domain represents a volume of rock, approximately 250 m thick on the south side and 100 m thick on the north side of ZSMEW007A, in which distinct fracture patterns are observed in cored borehole records. This domain features a reduced intensity of both N-S striking fractures and open sub-horizontally-dipping fractures. In this domain, most open fractures appear to belong to the WNW-striking set. Both fracture intensity and orientation have been interpreted as being affected by E-W striking deformation zone ZSMEW007A. FSM_EW007 terminates against deformation zone ZSMNE005 in the east, and is assumed to terminate against ZSMNS059A in the west. The western termination is based on the increase in N-S striking fractures west of ZSMNS059A, as well as the die-out of structure ZSMEW007A into a shorter structure of lower-confidence (ZSMEW007C).

- Domain FSM_NE005: This domain represents a volume of rock west of regional deformation zone ZSMNE005. This deformation zone represents one of several major belts of NE-SW trending ductile deformation belts that appear to have resulted from major crustal shortening in the Oskarshamn region during the waning stages of the Svecokarelian orogeny (/Wahlgren et al. 2008/, cf. Section 5.2.3). These ductile belts form the tectonic backbone of the Laxemar-Simpevarp region. Domain FSM_NE005 is characterised by a significant increase in the relative intensity of N-S striking sealed fractures, relative to the rest of the Laxemar local model area. It is possible that the increased intensity of N-S striking fractures represents brittle reactivation of smaller Riedel conjugate shears originally created in the ductile regime during N-S crustal shortening. FSM_NE005 is terminated against ZSMNE005 on the east, against ZSMNE107A in the west, (based on the patterns of fractures observed in boreholes on the west side of ZSMNE107A), and against ZSMNW042A in the south. The southern termination of FSM_NE005 is the most uncertain, due primarily to a paucity of data south of ZSMNW042A. The current geometry of FSM_NE005 is that it makes up the footwall of ZSMNW042A.

4.1.2 Identifying fracture domains separated by regional and local major deformation zones

A number of different configurations of potential fracture domains in the intermediate rock between zones ZSMNS001C, ZSMNS059A, ZSMNW042A, ZSMNE107A, and ZSMNW928A were explored using the remaining cored borehole and outcrop data (i.e. after exclusion of FSM_EW007 and FSM_NE005). One interesting finding is that fractures west of ZSMNS059A predominantly strike north-south (Figure 4-4). A tentative fracture domain (FSM_W) was therefore defined as the rock between the two sub-parallel zones ZSMNS001C and ZSMNS059A (Figure 4-6). FSM_W is assumed to terminate against ZSMNW042A in the south, as only minute amounts of data are available south of ZSMNW042A. FSM_W is intersected by ZSMEW900A, which potentially could act as a fracture domain boundary. However, the dominating N-S fracture pattern is also seen in two boreholes (KLX13A and KLX17A) north of ZSMEW900A. In this aspect, ZSMEW900A does not appear to act as a domain boundary; therefore the northern boundary for FSM_W is assumed to extend to the northern boundary of the fracture domain envelope (Figure 4-1).

This north-south strike dominance is noted in both subvertically- and subhorizontally-dipping fracture sets (Figure 4-4). The third set of fractures, which strike ENE and roughly parallel the NE-SW striking sinestral shear zones that make up the tectonic fabric of the Laxemar-Simpevarp region, are relatively subdued in intensity when compared to the rest of the Laxemar local model area. This finding (largely from borehole data) is in agreement with surface kinematic investigation results (/Viola et al. 2007/, summarized in /Wahlgren et al. 2008/). The working hypothesis is that domain FSM_W fundamentally represents a crustal block isolated by the major ENE and N-S sinestral tectonic structures.

For the remaining rock mass (after the exclusion of FSM_EW007, FSM_NE005, and FSM_W) three further fracture domains can be identified (Figure 4-5 and Figure 4-6):

- FSM_C: The rock volume south of FSM_EW007, north of ZSMNW042A, and bounded by FSM_W on its western edge and FSM_NE005 on its eastern edge. This fracture domain is dominated by sealed N-S striking fractures (similar to FSM_W), and open WNW striking fractures. It is likely that the open WNW-striking fractures represent either primary fracturing (tension gashes) or brittle reactivation of older fractures in extension due to inferred NW-SE compression during the Caledonian orogeny and the present day /Wahlgren et al. 2008/. This may also explain the prevalence of N-S striking sealed fractures (in compression since ~ 400 Ma).
- FSM_N: This domain represents a volume of rock north of domain FSM_EW007 and east of ZSMNS059A. This fracture domain is dominated by subhorizontally-dipping fractures, but lacks the dominating open WNW fracture set that is observed in FSM_C (Figure 4-5). The domain is bounded on the north by ZSMEW002A and ZSMNW047A.

- FSM_S: This domain represents the rock volume south of ZSMNW042A (i.e. the hanging wall). The definition of this rock volume as a separate fracture domain is highly uncertain due to the lack of data from this are; cored borehole KLX16A represents the only fracture data south of ZSMNW042A. In addition, the data from KLX16A are believed to have been strongly influenced by the adjacent structure ZSMNE107A. This zone is characterised by a relative lack of subhorizontally-dipping fractures. In this domain, the ENE and N-S fracture sets dominate (Figure 4-5). If one views structure ZSMNS059A (and the associated rock block representing FSM_W) as a restraint on the western edge of this domain, then the fracture pattern could be explained as conjugate Riedel R shears (N-S set) combined with the brittle re-activation along NE-SW striking shear bands (ENE set) parallel to the dominant regional tectonic fabric.

The rationale behind fracture domain FSM_S is the suspicion that deformation zone ZSMNW042A may act as a fracture domain boundary, combined with the lack of supporting data for the extrapolation of rock volume fracture characteristics across ZSMNW042A. It is also possible that ZSMNS059A and ZSMNE107A intersect FSM_S and subdivide it into smaller crustal blocks; there is not sufficient data available to make that analysis. It is also possible that these regional deformation zones partition the volume south of ZSMNW042A into additional blocks of FSM_NE005, FSM_W, or FSM_C. It is important to recognize that there is little confidence in the extent or nature of FSM_S; as such, it has been largely excluded from DFN analyses, though it is included in the SDM-Site Laxemar geological DFN parameterisation.

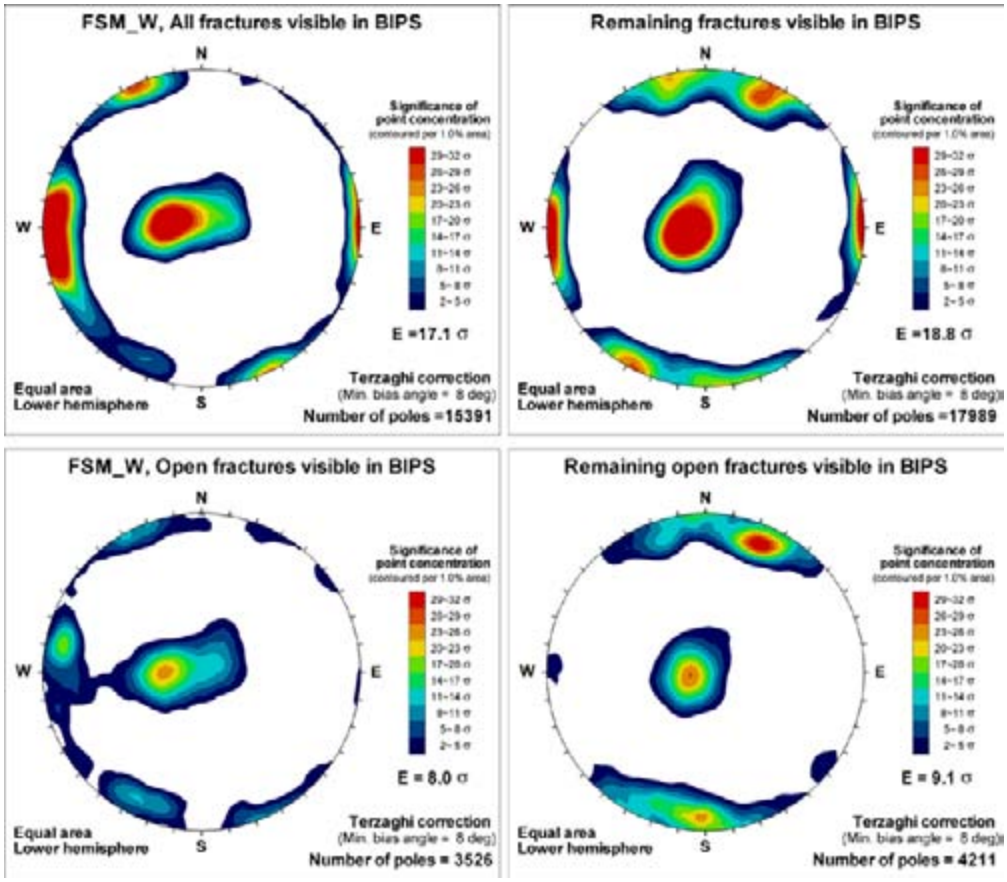

Figure 4-4. *Kamb-contoured polar stereoplots illustrating fracture set orientations from cored boreholes in fracture domain FSM_W, relative to fracture orientations from cored boreholes in the remainder of the Laxemar local model area (FSM_EW007 and FSM_NE005 excluded).*

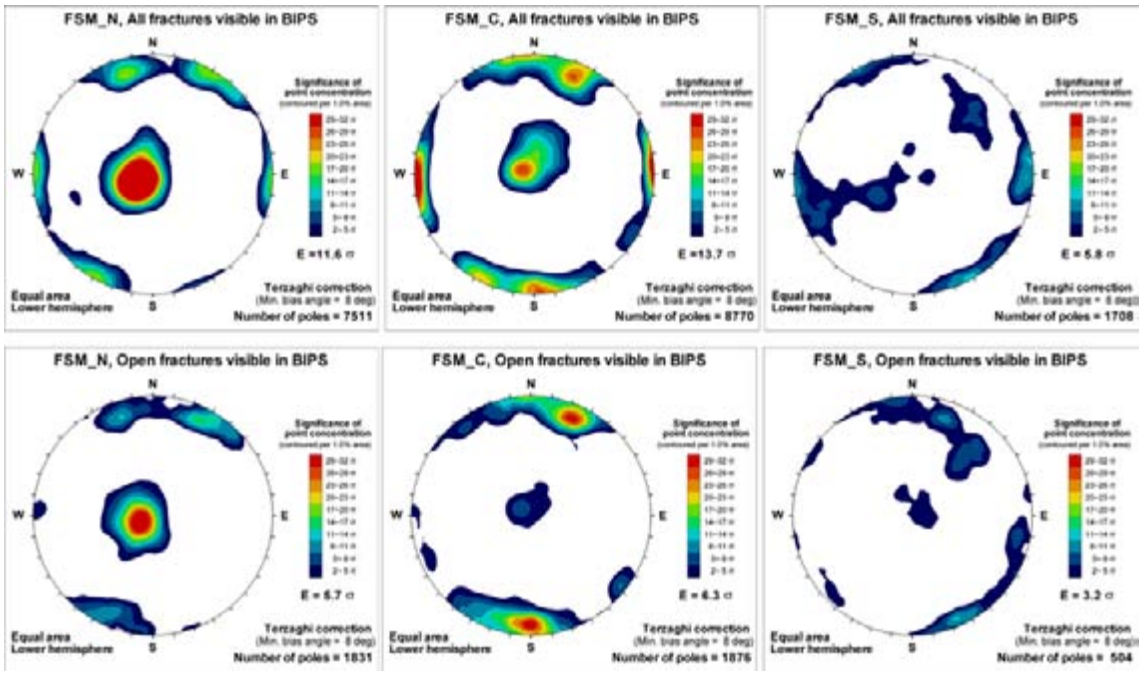

Figure 4-5. *Kamb-contoured polar stereoplots illustrating fracture set orientations from cored boreholes in fracture domains FSM_N, FSM_C, and FSM_S.*

4.1.3 SDM-Site Laxemar fracture domain model

The final fracture domain definitions are summarized in (Figure 4-6 through Figure 4-10, Table 4-1, and Table 4-2). The overall set-wise fracture intensity, in terms of open versus sealed fractures, is shown in Figure 4-11. Dividing the Laxemar local model volume into fracture domains delineates more spatial heterogeneity in the model than through a division solely on the basis of rock domains (see Figure 4-12). Strictly statistically, the variability in data subsets is expected to be somewhat larger than in their parent population, even for random data subset assignment, owing to the reduction in sample size. However, this effect is expected to be small, considering that fracture domain populations are large (the average number of data records in a single fracture domain, excluding FSM_S, is approximately 13,000 fractures). Furthermore, the fact that observed deviant fracture patterns in fracture domains appear related to deformation zones support the rationale in defining fracture domains in terms of regional and local major deformation zones.

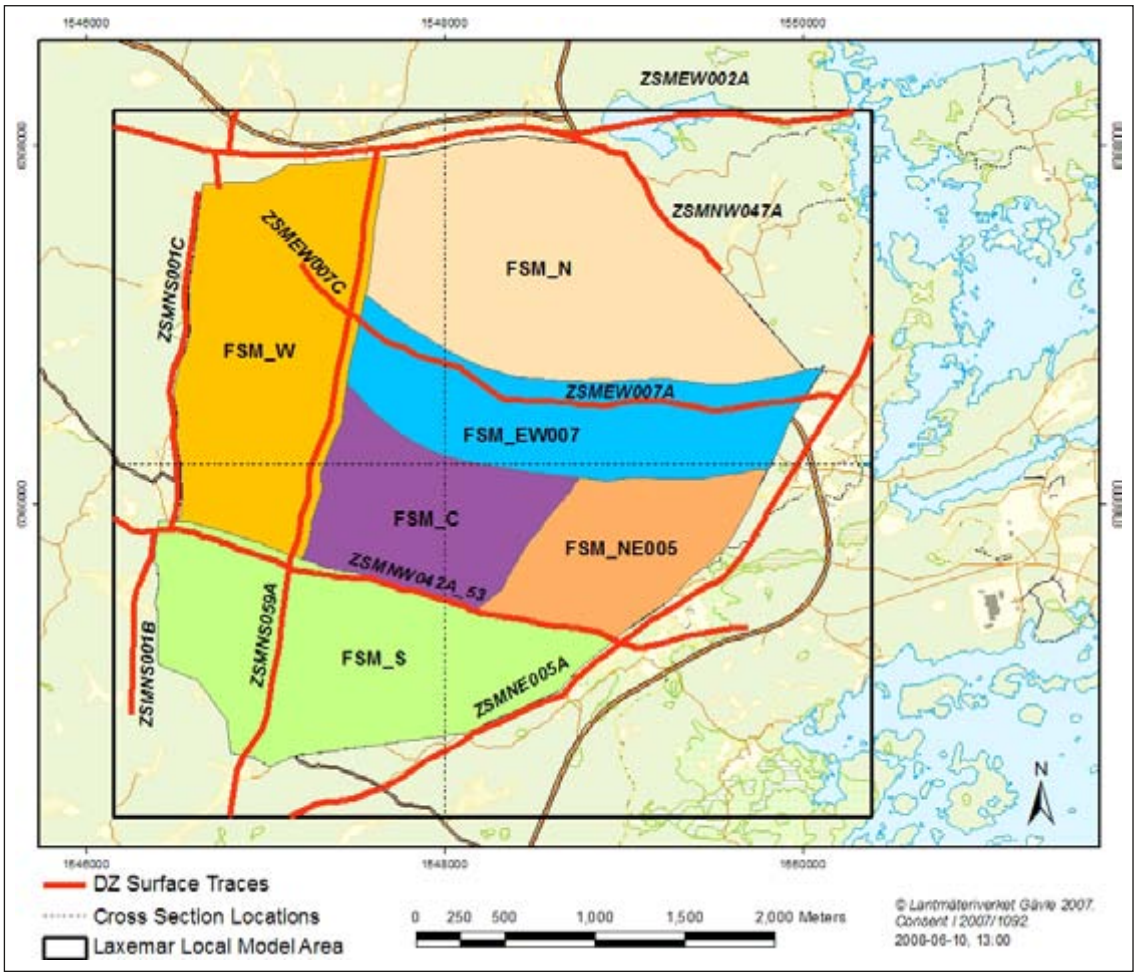

Figure 4-6. *Illustration of the SDM-Site Laxemar Fracture Domain Model.*

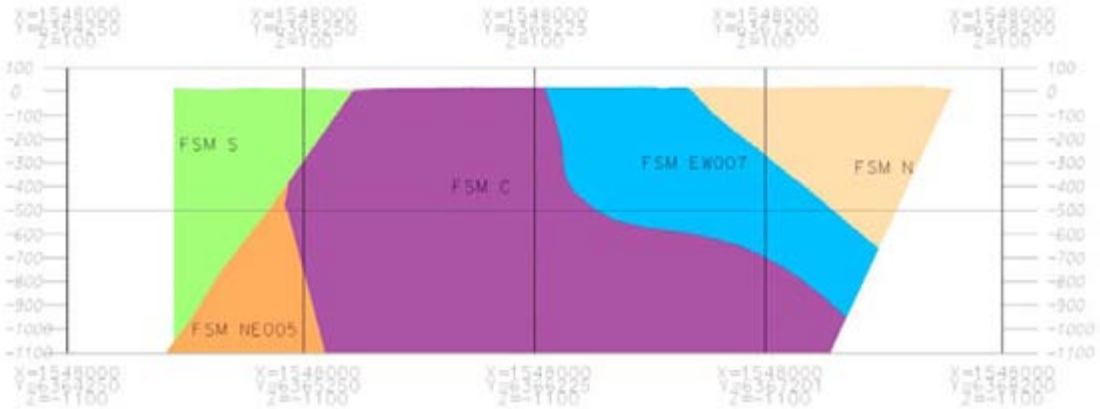

Figure 4-7. *RVS cross-section, oriented north-south through the middle of the Laxemar local model volume, of identified fracture domains.*

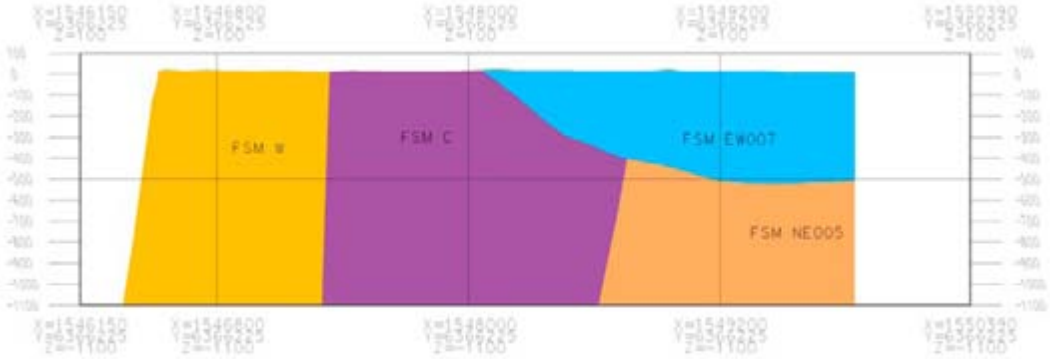

Figure 4-8. *RVS cross-section, oriented east-west through the middle of the Laxemar local model volume, of identified fracture domains.*

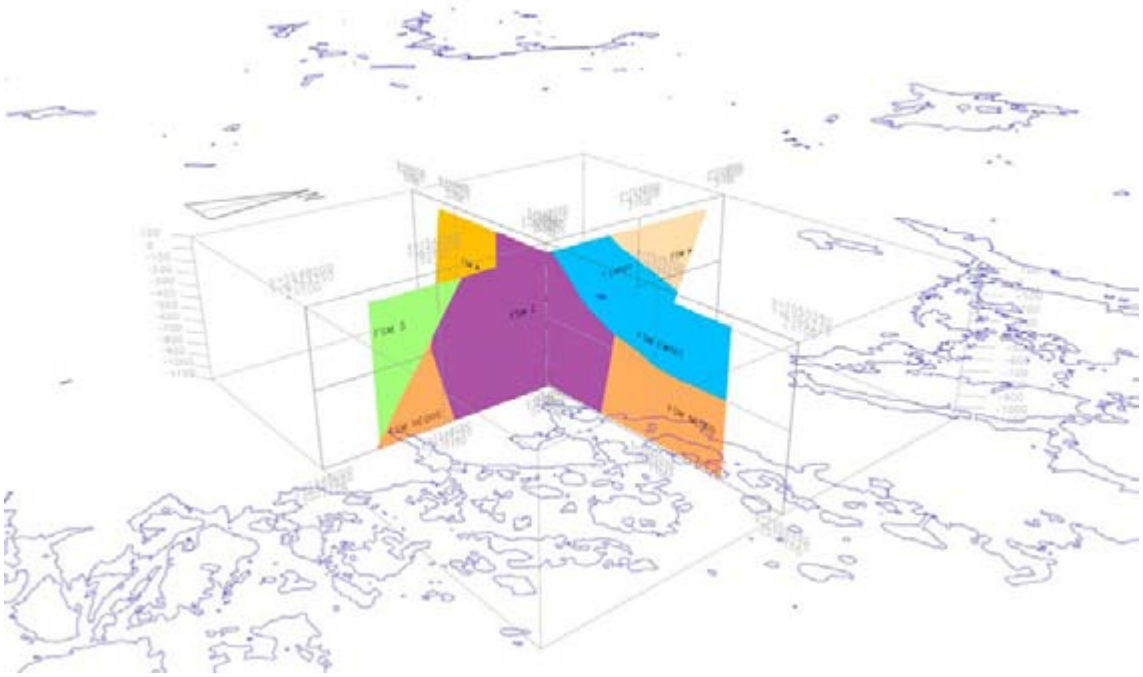

Figure 4-9. *Isometric view, looking NW, of RVS cross section locations relative to Laxemar local model volume and the Baltic coastline.*

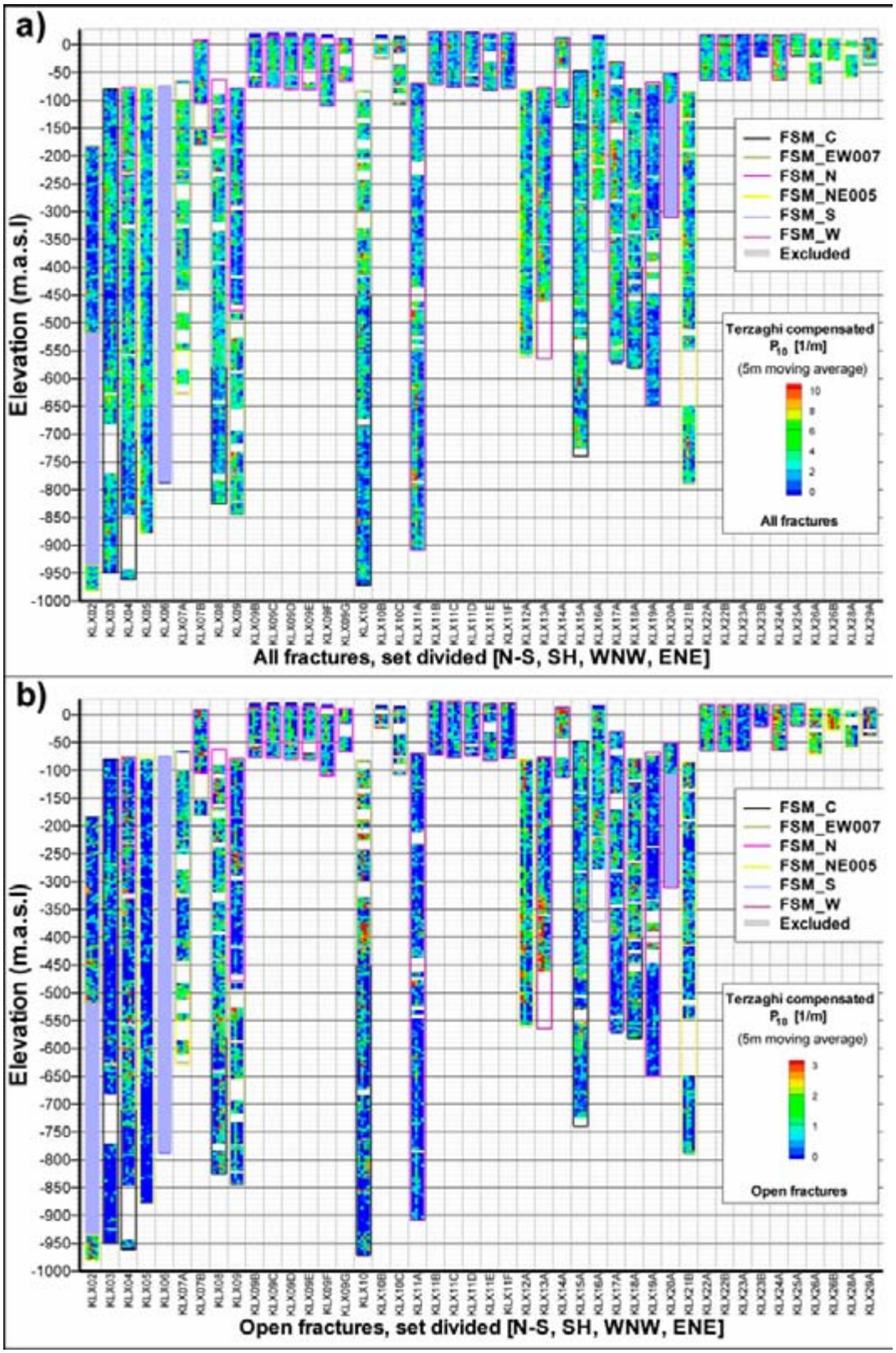

Figure 4-10. *Final fracture domain definitions in cored boreholes, shown as a 5 m moving average of Terzaghi-compensated P_{10} as a function of elevation; a) all fractures and b) open fractures.*

Table 4-1. Final fracture definitions by borehole (following GE-306, October 2007).

IDCODE	Fracture Domain	Start of Domain Vertical Depth (m)	End of Domain Vertical Depth (m)
HLX13	FSM_EW007	12.09	200.20
HLX20	FSM_N	9.12	62.10
HLX21	FSM_EW007	9.10	150.30
HLX22	FSM_EW007	9.10	163.20
HLX23	FSM_EW007	6.11	160.20
HLX24	FSM_EW007	9.10	175.20
HLX25	FSM_EW007	7.10	202.50
HLX26	FSM_S	9.10	60.00
HLX26	FSM_NE005	60.00	151.20
HLX27	FSM_C	6.10	156.00
HLX28	FSM_W	6.10	154.20
HLX30	FSM_EW007	9.11	163.40
HLX31	FSM_EW007	9.10	133.20
HLX32	FSM_S	12.30	104.00
HLX32	FSM_W	114.00	162.60
HLX33	FSM_EW007	9.11	202.10
HLX34	FSM_W	9.10	151.80
HLX35	FSM_W	6.13	151.80
HLX36	FSM_W	6.23	86.20
HLX37	FSM_W	156.20	199.80
HLX38	FSM_W	15.24	163.00
HLX38	FSM_C	163.00	199.50
HLX39	FSM_W	6.10	199.30
HLX40	FSM_W	6.07	199.50
HLX43	FSM_W	6.06	16.50
KLX02	FSM_EW007	201.50	540.00
KLX02	FSM_NE005	960.00	1,125.1
KLX03	FSM_C	101.48	998.21
KLX04	FSM_N	101.48	306.63
KLX04	FSM_EW007	306.63	737.66
KLX04	FSM_C	737.66	991.15
KLX05	FSM_NE005	107.50	995.22
KLX07A	FSM_EW007	101.98	737.90
KLX07A	FSM_NE005	785.00	841.51
KLX07B	FSM_N	9.64	123.84
KLX08B	FSM_EW007	123.84	200.13
KLX08	FSM_N	131.00	211.50
KLX08	FSM_EW007	220.00	702.00
KLX08	FSM_C	702.00	991.87
KLX09	FSM_N	102.02	492.40
KLX09	FSM_EW007	509.00	873.94
KLX09B	FSM_N	11.05	99.91
KLX09C	FSM_N	9.08	119.20
KLX09D	FSM_N	10.01	120.72
KLX09E	FSM_N	9.08	119.70
KLX09F	FSM_N	9.01	151.99
KLX09G	FSM_N	9.31	99.63
KLX10	FSM_EW007	101.86	471.80
KLX10	FSM_C	471.80	996.49
KLX10B	FSM_EW007	8.00	50.24

IDCODE	Fracture Domain	Start of Domain Vertical Depth (m)	End of Domain Vertical Depth (m)
KLX10C	FSM_EW007	9.50	145.34
KLX11A	FSM_W	100.87	990.15
KLX11B	FSM_W	4.00	99.50
KLX11C	FSM_W	4.00	119.43
KLX11D	FSM_W	4.00	119.2
KLX11E	FSM_W	4.02	121.00
KLX11F	FSM_W	4.00	118.83
KLX12A	FSM_NE005	102.01	601.05
KLX13A	FSM_W	102.01	488.00
KLX14A	FSM_W	4.00	174.33
KLX15A	FSM_C	77.59	978.43
KLX16A	FSM_S	2.60	327.00
KLX17A	FSM_W	66.13	696.69
KLX18A	FSM_EW007	100.81	426.81
KLX18A	FSM_C	426.81	610.91
KLX19A	FSM_W	105.76	795.97
KLX20A	FSM_W	100.93	171.38
KLX21B	FSM_NE005	100.83	858.41
KLX22A	FSM_W	4.00	100.37
KLX22B	FSM_W	4.00	100.07
KLX23A	FSM_W	4.00	99.96
KLX23B	FSM_W	4.00	50.25
KLX24A	FSM_W	4.00	99.81
KLX25A	FSM_W	4.00	50.10
KLX26A	FSM_NE005	4.83	99.93
KLX26B	FSM_NE005	4.00	50.30
KLX28A	FSM_NE005	5.24	80.00
KLX29A	FSM_EW007	4.00	59.18

Table 4-2. Final fracture definitions for outcrop data.

IDCODE	Fracture Domain
ASM000114	FSM_C
ASM000115	FSM_C
ASM000116	FSM_C
ASM000117	FSM_W
ASM000118	FSM_W
ASM000119	FSM_W
ASM000120	FSM_W
ASM000121	FSM_W
ASM000122	FSM_W
ASM000123	FSM_W
ASM000208	FSM_N
ASM000209	FSM_NE005
ASM100234	FSM_N
ASM100235	FSM_W

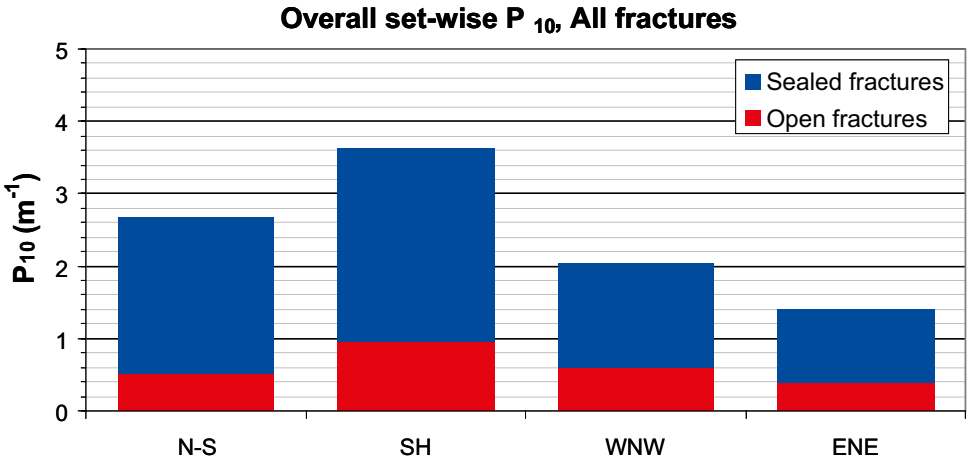

Figure 4-11. *Set-wise Terzaghi-compensated P_{10} within the entire Laxemar SDM-Site model domain, divided into open, respectively, sealed fractures.*

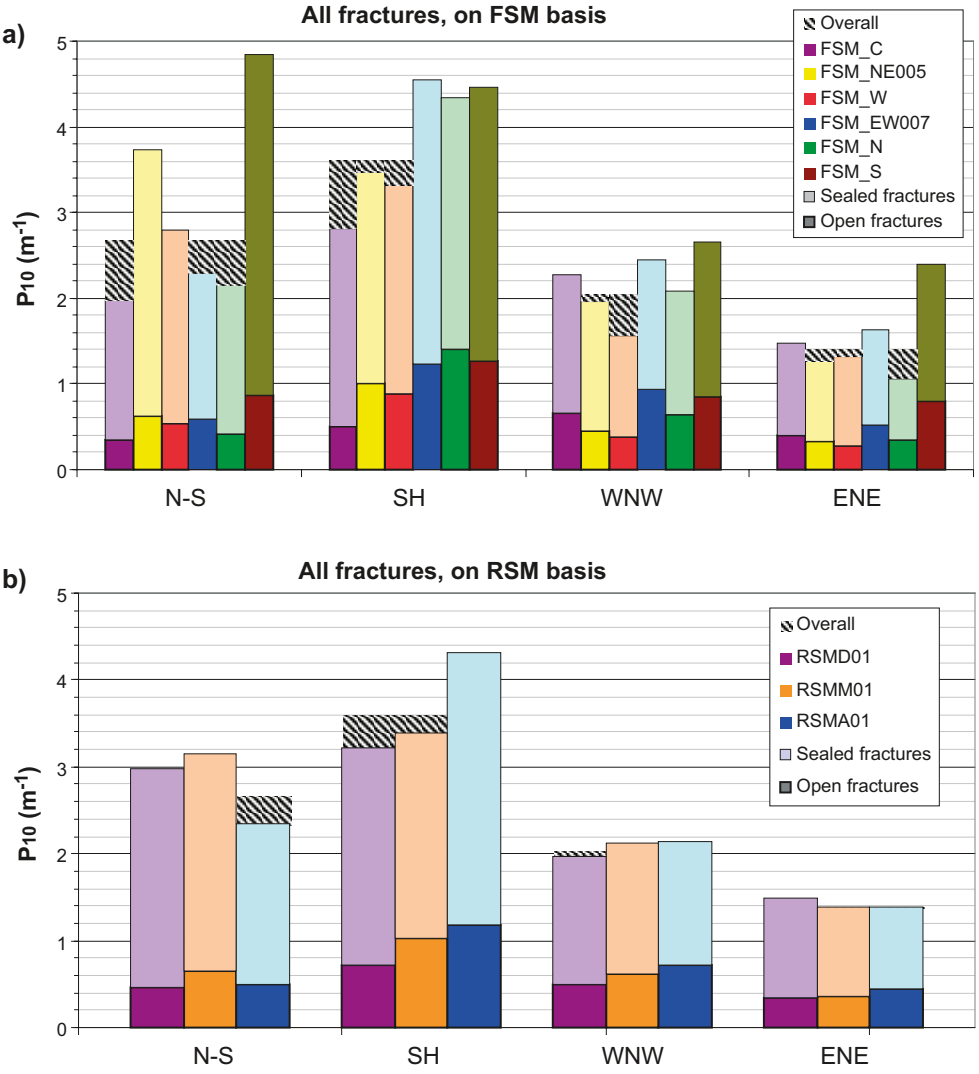

Figure 4-12. *Resolved local deviation in fracture characteristics compared to the overall data set (shaded area) for two conceptual methods; a) fracture domains and b) rock domains. Evaluation made in terms of set-wise Terzaghi-compensated P_{10} for open, respectively, sealed fractures.*

4.2 Orientation model

4.2.1 Analysis of orientation data

Fracture orientation clustering was analyzed to identify global fracture orientation sets. This analysis is done for all fractures possessing a measured orientation in SICADA that were labelled as 'Visible in BIPS'. Fractures in boreholes KLX01, KLX02 (inside rock domain RSMBA03), KLX06, KLX09B, KLX20A west of ZSMNS001C (which lies outside of fracture domain envelope) and fractures inside mapped and modelled deformation zones are omitted from the orientation analysis. The methodology for the orientation analysis is presented in Section 3.3.

On the scale of individual data sets (a single borehole or detail fracture mapped outcrop), fractures generally appear to be separated into highly concentrated clusters (see Appendix B). In most data sets, a subhorizontal cluster is clearly present (notable exceptions are boreholes KLX02, KLX05, and KLX25A), though the pole trend orientation of the subhorizontal structures may vary from borehole to borehole. In comparison, sub-vertical clusters exhibit more variability in both pole trend and plunge orientation between data sets. This variability manifests as different numbers of pole clusters, different mean orientations of the clusters, and different relative intensities between data sets. This observation is partly an outcome of the sampling bias of sub-vertical boreholes; Terzaghi weighting only compensates the intensity of biased fractures, it cannot fully resolve the distribution in orientation of biased fractures, particularly not in small data sets. However, there is considerably less variation in fracture orientation distribution within the two groups of closely-located field measurements. The first group consists of outcrop ASM100234 and boreholes KLX09, KLX09B, KLX09C, KLX09D, KLX09E, and KLX09F. The second group consists of outcrop ASM100235 and boreholes KLX11, KLX11B, KLX11C, KLX11D, KLX11E, and KLX11F.

The cluster of fracture poles with the strongest relative intensity (SH) tends to consist of subhorizontally- to moderately-dipping fractures (generally with dips less than 50°). The SH set generally strikes north-south to north-northwest (260°–280°), and dips are predominantly to the east. However, the strike orientation of the mean pole vector for subhorizontal set can vary significantly between fracture domains, and, in some cases, between boreholes in the same fracture domain.

The next strongest sub-vertically dipping cluster of fracture poles was the N-S set, (Figure 4-13) which strikes roughly north-south with a mean fracture pole trend of 265°. The relative intensity of this fracture set is an important criterion in fracture domain identification. The third and fourth global clusters consist of east-northeast striking (mean pole of 335°–340°) and west-northwest striking (mean pole trend of 25°) fractures, respectively. Dips are predominantly south for the ENE set; in the WNW set, dips are split between north and south. In general, these clusters are less intense than the N-S and SH clusters. However, the intensity of the WNW cluster, specifically in terms of the open-sealed aperture ratio, is also important to the identification of fracture domains.

These fracture clusters were tentatively assumed to represent separate orientation sets, and were labelled WNW, ENE, N-S, and SH. The naming convention used represents the general strike of vertically-dipping fractures in the cluster; the SH represents a set with variations in fracture strikes but with dips close to zero. In numerical definitions, set mean poles are consistently specified by trend and plunge. The clusters WNW, ENE, N-S, and SH are also clearly significant in outcrops (Figure 4-13), although WNW appears rotated to NNW, and less steep.

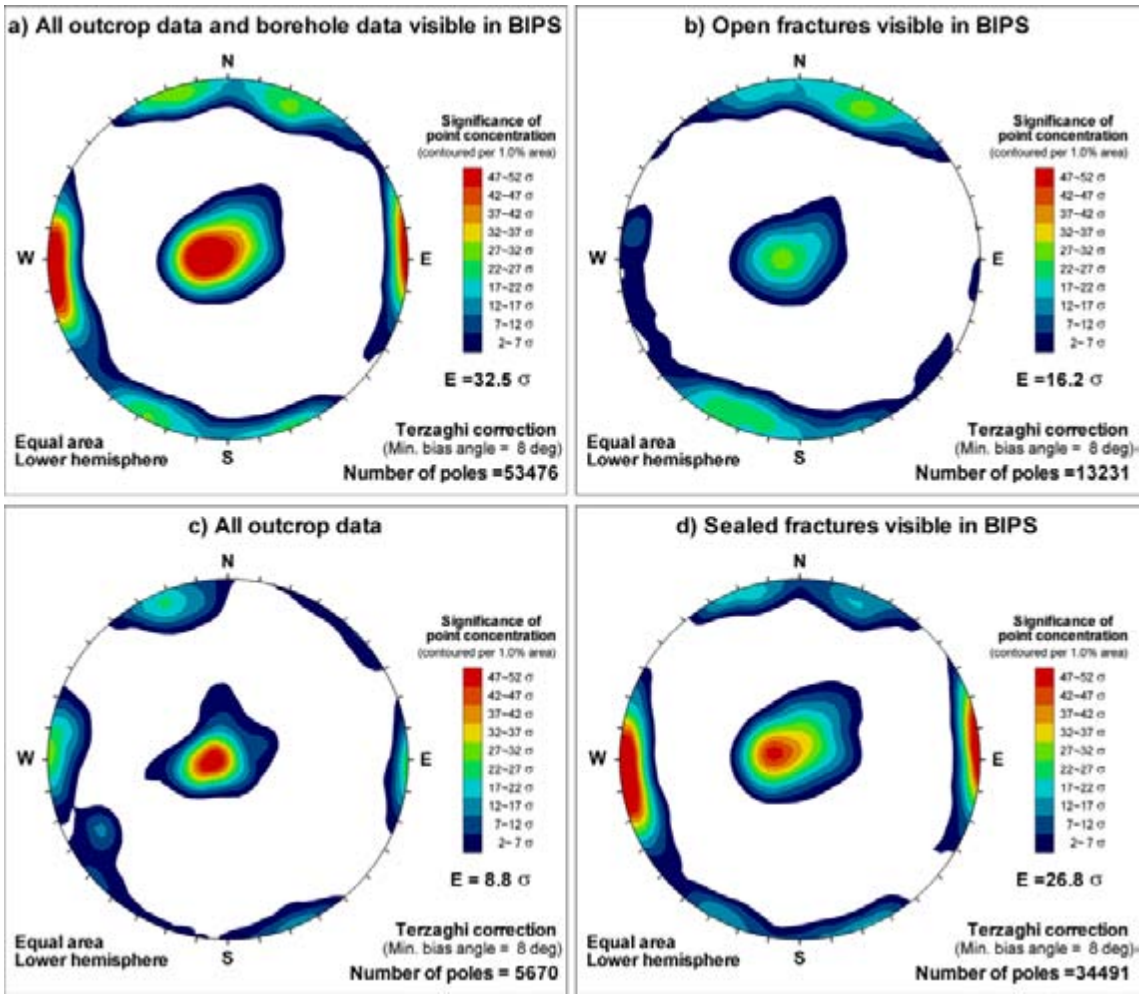

Figure 4-13. *The four data sets used in the parameterization of the orientation model. Note that open and sealed fractures only relate to borehole data.*

The lineament data has a clearly different orientation distribution when compared to borehole and outcrop data (Figure 4-14). WNW is the strongest cluster, while N-S has the weakest cluster significance. This difference can potentially be due to sampling bias and scale effects, or the lineaments and fractures represent structures recording different stress systems (tectonic stresses versus local-scale stress conditions). A particular difficulty in using lineament data for the derivation of the orientation model is that lineaments are fundamentally a 2D feature; they represent the intersection of two planes in space. This means that, relative to the ground surface (the default projection plane), little to no information is available as to the dip direction and angle of the assumed fracture or fault that is responsible for the observed lineament. In addition, we only know the apparent strike It was therefore decided to perform the set division of lineament data separately (see Section 4.2.3).

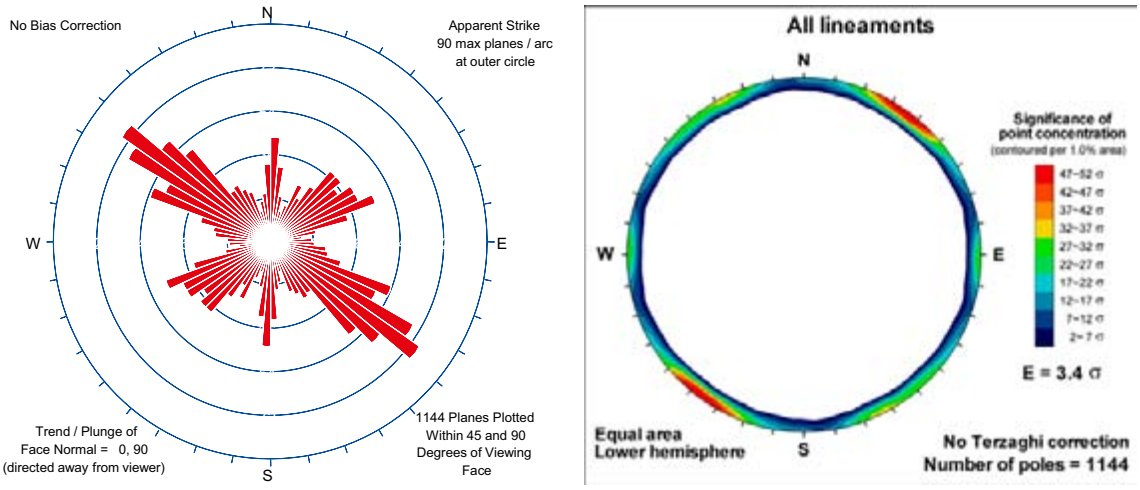

Figure 4-14. *Rose diagram of lineament strike (left) and Kamb-contoured polar stereoplot (right) of all surface lineaments inside the domain. Rose diagram presents lineament strike orientations; contoured stereoplot presents assumed structure mean pole vectors calculated using the right-hand-rule and the lineament strike. Note that the method to evaluate cluster significance through is unsuitable, as we assume that the lineaments represent the surface traces of vertical planes (DZ and MDZ). This violates the underlying expectation in the plot method that data are uniformly distributed /Kamb 1959/.*

When evaluating fracture data at the scale of model rock domains /Wahlgren et al. 2008/, the clusters WNW, ENE, N-S, and SH are seen in all domains except RSMBA03 (Figure 4-15). The orientation distribution of RSMBA03 is girdle shaped and, quite extraordinarily, the frequency of open fractures is higher than that of sealed fractures. RSMBA03 is only found in a 420 m long section of KLX02, which is a borehole cored early in the site investigation program, with a potential lower data quality. It is not possible, however, with the available data to investigate this rock domain further. It does not outcrop at the ground surface and is only seen in one borehole, so its subsurface spatial extent is extremely uncertain. In addition, this rock domain is outside of the volume of interest for SDM-Site Laxemar. Based on these limitations, it was therefore decided to exclude RSMBA03 from further analysis.

Other deviations can also be observed in the fracture orientation data set: the absence of open N-S fractures inside rock domain RSMA01, and possible signs of a fifth NNW-striking cluster in rock domain RSMM01. This potential fifth cluster in RSMM01, with a tentative mean pole vector orientation of (240°, 15°), posed a quandary for the modelling team; should these fractures be treated as a local rotation of the N-S and/or the WNW clusters, or should they be treated as a separate orientation set?

The question of whether or not the apparent NNW cluster should be treated as a fifth fracture set was analyzed by studying the individual data sets in detail (Appendix B). The only grounds for a possible NNW-set were found in the vicinity of ZSMNE005; of particular interest are outcrop ASM000209 and boreholes KLX26B and KLX28. The five-set hypothesis was tested by performing a five set global set-division of all fracture data.

However, the results of this test were unsatisfactory: a general low intensity of NNW, unreasonably split clusters in local datasets, and overall set orientation distributions that clearly deviate from the underlying assumed Fisher distribution. Consequently, with the aim of defining a global orientation model (in terms of fracture domains), it was decided to exclude this vague NNW set in the further analysis.

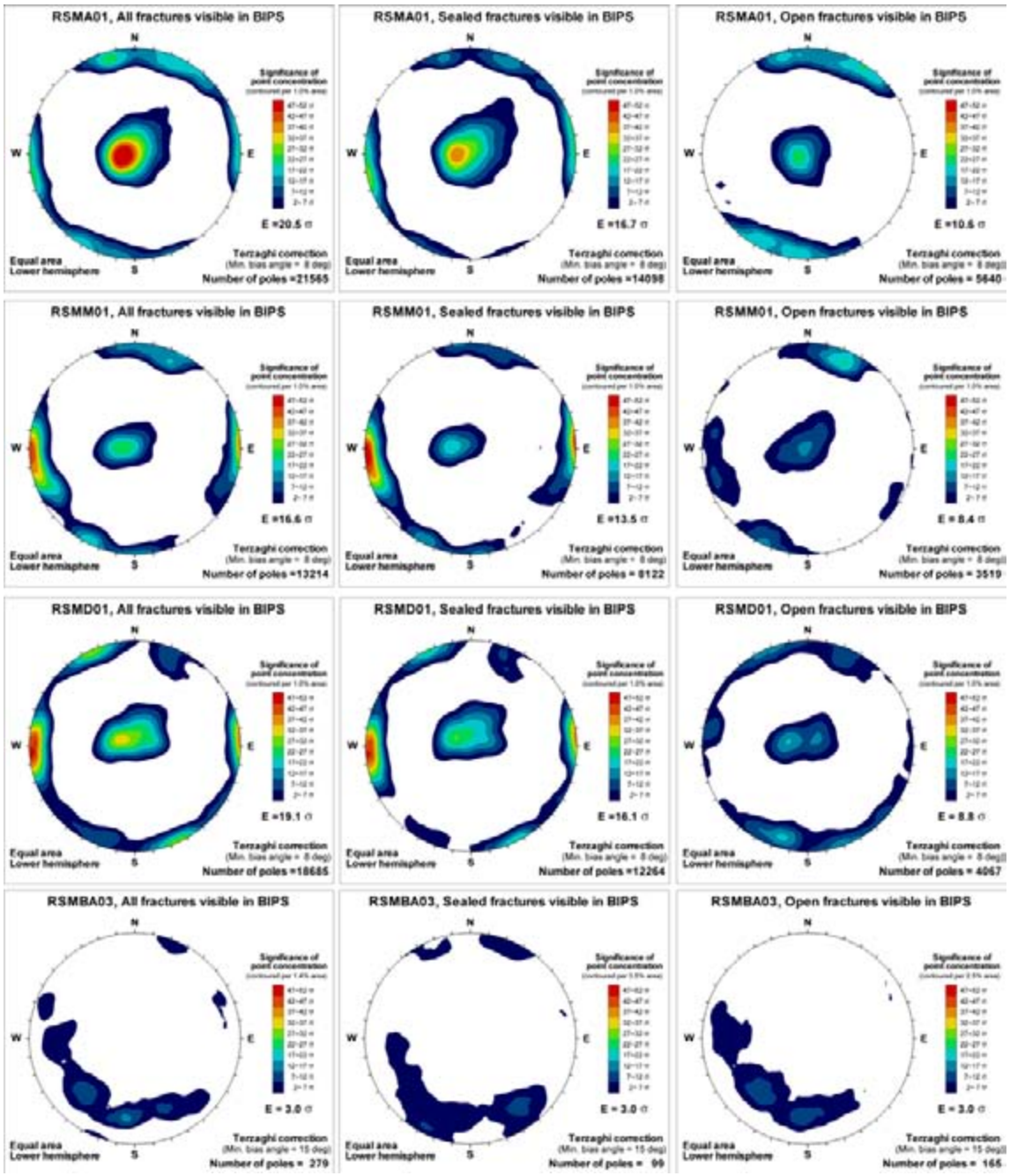

Figure 4-15. *All data, excluding KLX06 and KLX20A west of ZSMNS001, per rock domain and open/sealed interpretation. Note that "All fractures visible in BIPS" also includes linked outcrop data, while open/sealed fractures only relate to borehole data.*

4.2.2 Set division of data and parameterization of the orientation model

The SDM-Site Laxemar geological DFN uses a global (i.e. constant across all fracture domains) orientation model consisting of four sets: ENE, N-S, SH and WNW (Table 4-3; Figure 4-16). Probability of set membership is calculated for all fractures according to Section 3.3. Note that peaks in probability of set-membership (Figure 4-16b) do not necessarily coincide with set mean poles. The reason is that the probability fields are highly influenced by the presence and relative strength of competing sets; the probability of set membership tends to expand into orientations without cluster significance (i.e. lacking competition).It is interesting to note that the probability field of the N-S cluster exhibits an asymmetry that coincides with the (240°, 15°) cluster, which earlier was taken as evidence of a poorly-defined NNW set. This asymmetry signifies a strong soft-sector overlap between the N-S and WNW clusters. This suggests that the apparent fifth set (NNW) is instead an artefact of the overlap of two orientation sets.

In a second step, borehole fractures classified as "Not Visible in BIPS" were assigned set membership according to the probability field obtained in the previous step (Figure 4-16a). In other words, the set definitions obtained from outcrops and borehole fractures labelled "Visible in BIPS" were directly transferred onto fractures not visible in BIPS. It can be noted that the overall orientation statistics (i.e. including fractures not visible in BIPS) show a negligible difference in mean pole orientation when compared to just fractures visible in BIPS, but they also generally show a lower Fisher κ. On average, fractures not visible in BIPS also have slightly lower bias angles (α). These results are evidence supporting the hypothesis that fractures not visible in BIPS are indeed of the same fracture population as those visible in BIPS. The results of the orientation analysis, including the initial set definition guesses, the final DFN orientation model, and the resulting statistics when the model is applied to all data are presented in Table 4-3.

Table 4-3. Summary of global fracture set parameterization.

Initial hard sector definitions
(initial input based on visual inspection and judgment)

Set	Mean Pole		Distribution
	Trend [°]	Plunge [°]	Solid angle [°]
SH	339	87	28
ENE	345	3	24
WNW	23	4	28
N-S	86	0	28

Underlying parameterization of probability fields (*DFN Orientation Model*)
(numerically iterated from the initial hard sector definitions)

Set	Mean Pole		Distribution
	Trend [°]	Plunge [°]	Fisher κ
SH	335.1	87.1	7.2
ENE	340.3	0.5	9.9
WNW	24.1	3.1	7.5
N-S	269.1	1.7	7.3

Overall statistics of all set-divided data
(all outcrops and borehole data, including Not-Visible in BIPS)

Set	Mean Pole		Distribution	Population	
	Trend [°]	Plunge [°]	Fisher κ	# of fractures	Terzaghi weight sum
SH	341.6	87	6.9	36,730	49,916.0
ENE	340.2	0.5	9.8	8,655	22,050.2
WNW	24	2.7	7.4	12,540	31,800.6
N-S	269.4	1.4	7.0	16,056	42,829.6

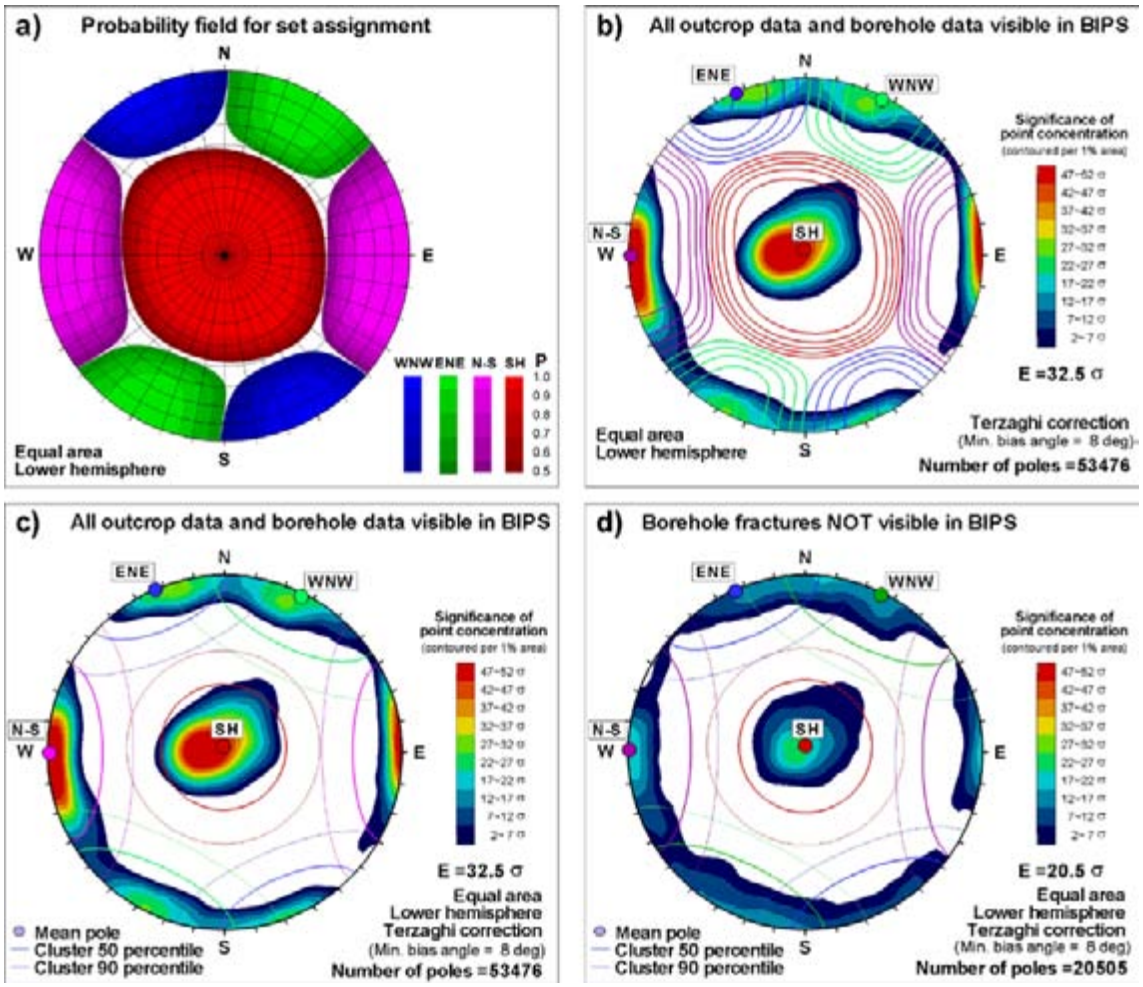

Figure 4-16. *Set assignment of fracture data. Visualization of the probability field for set assignment: a) contours shown for P > 0.5, and b) probability levels P = 0.5, 0.6, 0.7, 0.8, and 0.9 related to fracture orientation clusters. Resulting mean poles and cluster Fisher percentiles visualized for set divided data, c) for outcrops and borehole data visible in BIPS and d) for borehole data not visible in BIPS. KLX02 (RSMBA03), KLX06, and KLX20A west of ZSMNS001 are excluded.*

4.2.3 Set division of lineament data

Fundamentally, a lineament is a line in a plane formed by the intersection of two planes in space. As a lineament is a line, its orientation is defined largely by the orientation of the plane in which it lies. For geologic lineaments such as those identified at Laxemar through LIDAR topographic surveys and high-resolution geophysics, these lineaments are assumed to represent the intersection between a fault or a fracture and the ground surface. The lineaments themselves provide only limited information about the causative geologic structure; generally, lineaments are useful only to estimate sizes based on the length of the surface trace (lineament) and to estimate the strike direction of the underlying faults and fractures. It is not possible to obtain dip angle and dip direction from the lineament data set.

There are two basic options to deal with the lack of dip and dip direction information for structures expressed in the surface lineament data set. First, it is possible to assign an assumed distribution of structure dips and dip directions, based on the orientation model for fracture sets (Table 4-3), or second, simply to assume that the lineaments represent the surface trace of vertically-dipping structures (fractures, MDZ, or DZ). Preliminary analysis of the lineament orientations (Figure 4-14) suggests that the orientation distribution of lineaments may be different than that of fractures. As such, the second alternative (vertical structures) is chosen for modelling purposes.

Strictly speaking, the assumption of vertical lineaments is incompatible with the outcrop trace and borehole fracture set division according to the approach used (described in Section 3.5.4), as data will not conform to the radial-symmetric Fisher distribution. In practice, the lack of dip information for the structures represented by the lineaments has no real significant consequences upon the set division, as the set assignment is largely based on the apparent strike orientation. However, it is important to remember that the parameterized univariate Fisher κ for calculation of probability fields (Table 4-4) assumes a circular distribution of vectors on the hemisphere, and will not reproduce a highly elliptical distribution of vectors (such as those seen in the lineament data set, which are an artefact of the sampling technique). This means that even though the input data are composed solely of vertically-dipping fractures, the final parameterization will produce sub-vertically-dipping structures as well as vertically-dipping structures. This is a desirable outcome; it is far more geologically realistic to have a range of sub-vertically dipping structures than just vertically dipping structures.

No Terzaghi compensation for sampling plane/line orientation bias was used in the lineament set assignment, as the dip of the underlying structures that form the lineament through their intersection with the ground surface are unknown. The lineament mean poles were estimated for the peak concentrations (Figure 4-17) in order to define lineament sets with symmetric distribution in apparent strike.

Table 4-4. Summary of lineament set parameterisation, based on global set definitions.

Initial hard sector definitions
(initial input based on visual inspection and judgment)

Set	Mean Pole		Distribution
	Trend [°]	Plunge [°]	Solid angle [°]
ENE	330	0	24
WNW	33	0	28
N-S	93	0	22

Underlying parameterization of probability fields
(numerically transferred from the initial hard sector definitions)

Set	Mean Pole		Distribution
	Trend [°]	Plunge [°]	Fisher κ
ENE	329.2	0	23.4
WNW	32.8	0	17.5
N-S	92.5	0	8.2

Final statistics of set-divided data
(all outcrops and borehole data visible in BIPS)

Set	Mean Pole		Distribution	Population
	Trend [°]	Plunge [°]	Fisher κ	Number of fractures
ENE	325	0	Not evaluated	381
WNW	35	0	Not evaluated	570
N-S	93	0	Not evaluated	193

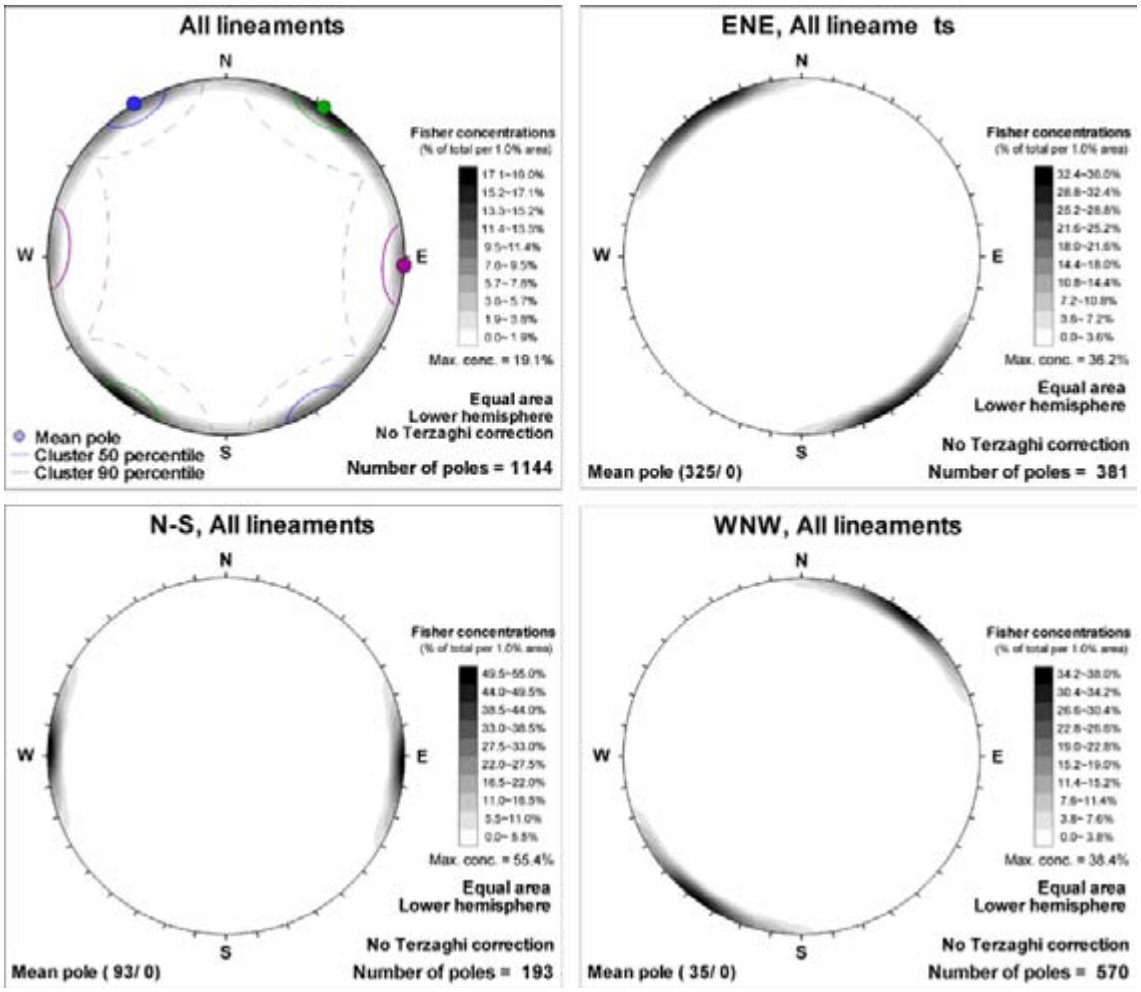

Figure 4-17. *Contoured stereonet plots for lineament sets based on global set definition.*

The mean poles were found to differ somewhat compared to the mean poles of fractures sets (see Table 4-3 and Table 4-4). In addition, it is impossible to classify lineaments into the SH set due to the lack of dip information. However, the general pattern (locations of mean pole vectors relative to each other) of orientation sets is extremely similar to the three vertically-dipping sets (ENE, N-S, and WNW) identified in Section 4.2.2 from borehole and outcrop data. Direct comparisons of lineament strike data to global set strike data from boreholes and outcrops are presented as Figure 4-18. Based on these results, the recommendation is to use a single global orientation model for both outcrop-scale fractures and stochastically-generated lineament-sized features (< 564.2 m in equivalent radius). This is necessarily a modelling simplification, but one that appears most appropriate based on the similarities in the orientation data.

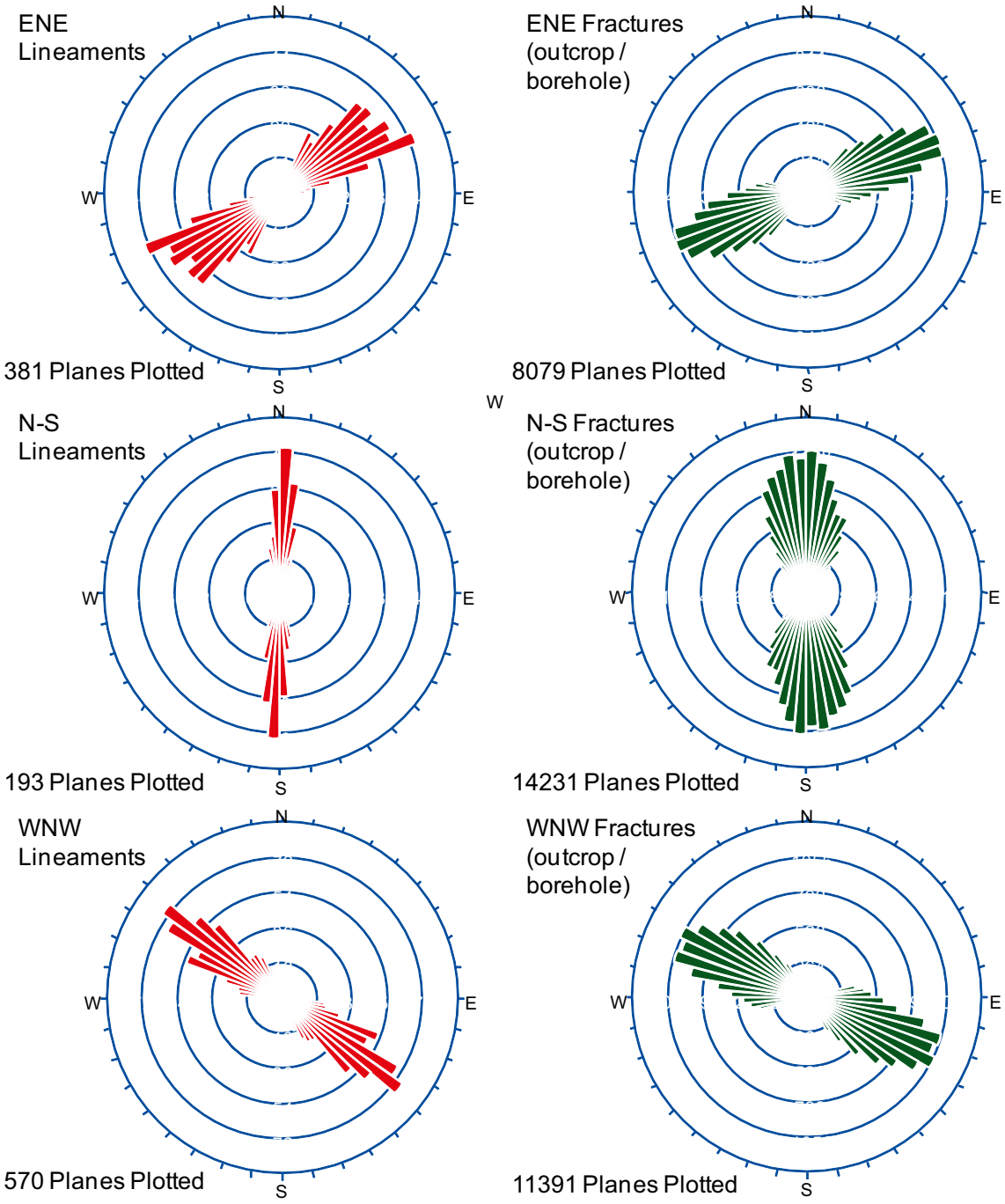

Figure 4-18. *Rose plots of strike of lineaments by set (left) versus strike of fractures from outcrops and boreholes (right) after global set assignment.*

4.2.4 Fracture orientation and properties as a function of visibility in image logs (BIPS)

The results of the statistical tests are voluminous, and are not reproduced in this report. The results and the data on which they are based can be found in the files XTabsBIPS.pdf (cross-tabulation results) and BIPS Discriminant Analyses.pdf (LDA results), both of which are available in the 'Electronic Output Files' folder on the CD that accompanies this report. The specific data used in this analysis are listed in Fracture Data for SPSS Analyses.pdf, in the same folder.

The results for the cross-tabulation are further subdivided for ease in assessment into four subgroups: Fracture Morphology, Lithology & Domains, Fracture Sets and Mineral Fillings. The cross tabulation results for the various attributes are summarized in Table 4-5. The first column identifies the variable being tested; the second column indicates whether there is a difference. There are three possible entries in the second column: "No Difference", "Difference" and "Insufficient Data", the later referring to the case in which the statistical tests lacked sufficient power due to small numbers of data in one or more subcategories.

The LDA results are shown in Table 4-6 through Table 4-9. These tables show that the discrimination is poor, and the misclassification is high. Inspection of the classification function coefficients suggests that the visible fractures have slightly greater apertures, widths and degree of alteration, but the differences are not statistically meaningful.

As these tables show, there are no statistically significant differences between the Visible and Not Visible classes of fractures based upon the categorical attributes tested. Therefore, the geological DFN model assumes that, if fractures Not Visible in BIPS are no different than fractures Visible in BIPS in all other categories, than it is appropriate to assume that they do not differ in terms of their orientation distribution (i.e. they follow the same orientation distribution as the Visible in BIPS fractures.

4.3 Coupled size-intensity model

4.3.1 Base Model & alternative model definitions

The selection of the Base Model consists of two stages: identification of a preliminary Base Model that is the most geologically supported and self-consistent, given the available data; and selection of a final Model as a consequence of the verification cases. During the course of the verification calculations, an alternative model may prove more accurate than the preliminary Base Model and become the final recommended Model.

Alternative models also are supported by data and are also self -consistent, but to a lesser degree than the Base Model. They constitute one or more possible models, but are not the most likely model. Alternative models are treated as uncertainty cases (Chapter 6) and are carried through the model verification and ranking (Chapter 5). The selection of the final Model is important for the uncertainty analyses. The quantification of many of the uncertainties requires a comparison to a standard reference model, and as a consequence, they are carried out using the final Model as the reference case.

The preliminary Base Model size-intensity parameterisation is based upon the following conceptual assumptions:

- The radius exponent (k_r) is not a function of fracture domain, and is constant across the Laxemar local model volume. Conceptually, classes of model variants (including the preliminary Base Model) using this assumption have been referred to colloquially as 'k_r -fixed' models.
- The radius exponent is based on the length-scaling relationship of linked traces.
- Size-intensity scales in a Euclidean manner.
- Fracture intensity is based on all fractures (open and sealed combined).

Table 4-5. Cross-tabulation results for Visible in BIPS versus Not Visible in BIPS.

Fracture Morphology	
FRACT_MAPPED	
FRACT_INTERPRET	No Difference
CONFIDENCE	No Difference
ROUGHNESS	No Difference
SURFACE	No Difference
FRACT_ALTERATION	No Difference
Lithology & Domains	
BEST_ROCK_NAME	No Difference
ROCK_NAME	No Difference
ROCK_DOMAIN	No Difference
FRACTURE_DOMAIN	No Difference
ROCK_UNIT	No Difference
Mineral Fillings	
Adularia	No Difference
Albite	No Difference
Amphibole	No Difference
Biotite	No Difference
Calcite	No Difference
Chalcopyrite	No Difference
Chlorite	No Difference
Clay Minerals	No Difference
Epidote	No Difference
Fluorite	No Difference
Galena	No Difference
Goethite	No Difference
Hematite	No Difference
Hypersthene	No Difference
Kaolinite	No Difference
Laumontite	No Difference
Muscovite	No Difference
Ortho Amphibole	No Difference
Oxidized Walls	No Difference
Plagioclase	No Difference
Potash Feldspar	No Difference
Prehnite	No Difference
Pyrite	No Difference
Quartz	No Difference
Red Feldspar	No Difference
Sericite	No Difference
Sphalerite	No Difference
Sulfides	No Difference
Tourmaline	No Difference
Unknown mineral	No Difference
White Feldspar	No Difference
Zeolites	No Difference
Refractory Minerals	No Difference
Preh_Ep	No Difference
Qtz_Ep_Chl	No Difference
Qtz_Ep	No Difference
Cc_Fl_Py	No Difference
Fracture Orientation Sets	
Sets	No Difference

Table 4-6. Wilk's Lambda test results for LDA results for fracture aperture and fracture width.

Test of Function(s)	Wilks' Lambda	Chi-square	df	Sig.
1	.993	488.074	2	.000

Table 4-7. Classification results for LDA for fracture aperture and fracture width.

Classification Results[b,c]

			Predicted Group Membership		
		VISIBLE_IN_BIPS	0	1	Total
Original	Count	0	15401	7131	22532
		1	30450	20345	50795
		Ungrouped cases	9	0	9
	%	0	68.4	31.6	100.0
		1	59.9	40.1	100.0
		Ungrouped cases	100.0	0	100.0
Cross-validated[a]	Count	0	15401	7131	22532
		1	30450	20345	50795
	%	0	68.4	31.6	100.0
		1	59.9	40.1	100.0

a. Cross validation is done only for those cases in the analysis. In cross validation, each case is classified by the functions derived from all cases other than that case.

b. 48.7% of original grouped cases correctly classified.

c. 48.7% of cross-validated grouped cases correctly classified.

Table 4-8. Wilk's Lambda test results for LDA for fracture alteration.

Test of Function(s)	Wilks' Lambda	Chi-square	df	Sig.
1	.953	1,154.587	1	.000

Table 4-9. Classification results for LDA for fracture alteration.

Classification Results[b,c]

			Predicted Group Membership		
		VISIBLE_IN_BIPS	0	1	Total
Original	Count	0	2674	5363	8037
		1	2263	13673	15936
	%	0	33.3	66.7	100.0
		1	14.2	85.8	100.0
Cross-validated[a]	Count	0	2674	5363	8037
		1	2263	13673	15936
	%	0	33.3	66.7	100.0
		1	14.2	85.8	100.0

a. Cross validation is done only for those cases in the analysis. In cross validation, each case is classified by the functions derived from all cases other than that case.

b. 68.2% of original grouped cases correctly classified.

c. 68.2% of cross-validated grouped cases correctly classified.

4.3.2 Parameterisation alternatives

Section 4.2 shows that the fractures throughout the Laxemar local model area and inside the fracture domain envelope can be assigned to one of four sets – ENE, NS, WNW and SH, and that the orientation parameterization for these sets is not spatially dependent. The analysis of fracture domains in Section 4.1 indicates that the fracture domains are an adequate and useful basis for subdividing the Laxemar site for fracture parameterization. The difference between fracture domains is not in orientation, but rather in the fracture intensity of each set. Thus, the uncertainties related to the parameterisation of the individual fracture sets are related to alternatives that impact the intensity values assigned to each set.

Consideration of the Laxemar data and geological conceptual model suggests that there are several possible alternatives in the parameterisation that could impact intensity. These are:

- Variability of the fracture size scaling exponent among fracture domains.
- Euclidean versus Fractal scaling for scaling up outcrop and borehole data to larger scales.
- Size/intensity based on linked versus unlinked outcrop trace lengths.
- Variability of the fracture size scaling exponent for each set independent of fracture domain.
- Fracture intensity based on all fractures versus only open fractures.

Fracture domain dependence of scaling exponent

Both the geological evolution (/Wahlgren et al. 2008/, cf. Chapter 3) and fracture domain analysis suggest that the major differences in brittle strain are due to differences in the local stress field rather than differences in lithologies. Fracture intensities are relatively homogeneous within individual fracture domains, and these domains represent regions of relatively homogeneous rock deformation, rather than homogeneous lithologies and their attendant mechanical properties. This suggests that given the same stress conditions, the rock within an individual fracture domain will fracture similarly, with the same ratio of large to small fractures and the same overall fracture intensity. The ratio of small to large fractures is described by the size/intensity scaling exponent, and so this exponent is unlikely to change as a function of fracture domain. The intensity of fracturing may change, and indeed does, among the fracture domains, but the ratio of large to small should be independent of fracture domain according to this model.

As a result, the Base Model assumes that the size/intensity scaling exponent (k_r) does not depend upon fracture domain. Instead, the Base Model assumes that the principal difference between domains is in terms of the fracture intensity, P_{32}, and the minimum size (r_0) of fractures generated.

An alternative conceptual model is that the size/intensity scaling exponent does change as a function of fracture domain; as such the minimum size and P_{32} are instead fixed values. The alternative models that follow this conceptual uncertainty are colloquially known as 'r_0-fixed' models; they are conceptually identical to the 'k_r-scaled' alternative model presented in the SDM Forsmark version 2.2 hydrogeological DFN /Follin et al. 2007/.

Scaling

Many published studies of natural fractures in rock indicate that intensity scales according to fractal or Euclidean processes, though a few studies do indicate other types of scaling behaviour. The scaling analysis presented in Section 4.4 suggested that the most likely scaling model for upscaling borehole and outcrop data is a Euclidean model. However, it is possible at scale smaller than 10 m–30 m that a weakly fractal model might be more appropriate. As a result, the Base Model assumes Euclidean scaling, while an alternative model assumes Fractal scaling.

Outcrop fracture trace linking

Appendix A described how fracture traces mapped in outcrop have been linked. The outcrop fracture linking was done in a manner similar to the way in which lineament traces are linked into single features, which may make the linked outcrop traces a more consistent measure

of trace length than unlinked traces. As a consequence, the linked trace lengths are used to parameterize the Base Model. However, the unlinked traces represent a possible alternative to the linked traces, and are a second alternative model.

Scaling exponent variability

Even if the fracture size scaling exponent (k_r) is fracture domain-independent, it is still likely to have some variability. The Base Model, which assumes fracture domain independence of the size/intensity scaling exponent, is based upon the average exponent for each set. Because this exponent is calculated in part from outcrop data, and there are only four outcrops, a rigorous calculation of the mean scaling exponent is not statistically robust. The average exponent is determined qualitatively, as described in Section 4.3. However, other fracture size scaling exponents could be derived from the data scatter. In order to examine these alternatives, two bounding exponents can be defined that represent the minimum and maximum exponents for the available outcrop data. These bounding cases represent a fourth alternative model.

Open versus total fracture intensity

Finally, the intensity parameterization could be based on all fractures, or only on a subset, such as open fractures. It might be argued that open fractures better represent migration pathways for fluids or are weaker and thus more likely to slip during future earthquakes, and thus should be the primary basis for the fracture model intensity. However, open fractures may become sealed, and sealed fractures may be reactivated over the future evolution of the repository. As a result, the Base Model bases the fracture intensity on all fractures. An alternative model, based only on open fractures, is also examined. Table 4-10 summarizes the characteristics of the Base Model in comparison to other potential model alternatives.

The various alternative models and their reference acronyms are presented in Table 4-11. The preliminary Base Model is identified by the acronym ‘BM’.

4.3.3 Preliminary Base Model (BM)

The size/intensity calculations are based on area-normalized Complementary Cumulative Number (CCN) plots (Section 3.4). For Laxemar, these consist of the outcrop traces for each set and the corresponding lineament trace set. The CCN plots for the four fracture sets are shown in Figure 4-21 through Figure 4-24. CCN plots for the alternative models, including unlinked traces and fractal scaling (as discussed in Chapter 6 – Uncertainty) are presented in subsections of Section 4.3.3. The figures in this section show the visual best fit, as well as the bounding fits labelled as “upper” and “lower”. The bounding fits are discussed in Section 4.3.4. The parameters derived from these fits are summarized in Table 4-12.

The value P_{32OC} listed in Table 4-12 is not the borehole P_{32}; rather it is a P_{32} value established through simulation during the size model parameterisation. P_{32OC} was calculated through stochastic simulation. A small-scale (50 m) DFN simulation volume was created in FracMan; the values for the size distribution were taken from the CCN plots (k_r) and the outcrop maps (r_{min}). Models were iterated until the simulated trace pattern was visually deemed an acceptable match to observed outcrop trace data. The P_{32} value produced here (P_{32OC}) represents a first-order estimate of P_{32} for fractures in the size range of 0.5 m–564.2 m. P_{32OC} is used in conjunction with the mean borehole P_{32} (termed P_{32BH} in Chapter 3) value to compute the size probability distribution minimum radius (r_0) through Equation 3-15.

A summary table of the area values used for the normalization is presented as Table 4-13. The area for ‘FSM_envelope’ represents the area of the fracture domain envelope (Figure 3-2), minus the area within which observed lineament density is lower due to the presence of high voltage transmission lines (visible in Figure 3-2 in the centre of the fracture domain envelope as a NW-trending swath with few to no lineaments). The full area of the fracture domain envelope, including the portion covered by high voltage wires, is 9,378,128.0 m^2.

Table 4-10. Summary of the preliminary Base Model & Alternative models.

Base Model	Alternative Model
Total Fracture Intensity	Open Fracture Intensity
Average Fit for All Fracture Domains	Bounding Size Fits
Linked Outcrop Traces	Unlinked Outcrop Traces
Size Scaling Exponent Independent of Fracture Domain	Fracture Domain-Dependent Size Scaling Exponent

Table 4-11. Index to alternative model names and acronyms.

Model Case	Scaling	Outcrop Traces	Scaling Exponent Fit	FSM-Specific Scaling Exponent
BM	Euclidean	Linked	Best	No
EL1	Euclidean	Linked	Upper	No
EL2	Euclidean	Linked	Lower	No
BMU	Euclidean	Unlinked	Best	No
EUL1	Euclidean	Unlinked	Upper	No
EUL2	Euclidean	Unlinked	Lower	No
BMF	Fractal	Linked	Best	No
FL1	Fractal	Linked	Upper	No
FL2	Fractal	Linked	Lower	No
BMUF	Fractal	Unlinked	Best	No
FUL1	Fractal	Unlinked	Upper	No
FUL2	Fractal	Unlinked	Lower	No
ESL1_N	Euclidean	Linked	Best	FSM_N
ESL1_NE005	Euclidean	Linked	Best	FSM_NE005
ESL1_W	Euclidean	Linked	Best	FSM_W
ESL2_N	Euclidean	Linked	Upper	FSM_N
ESL2_NE005	Euclidean	Linked	Upper	FSM_NE005
ESL2_W	Euclidean	Linked	Upper	FSM_W
ESL3_N	Euclidean	Linked	Lower	FSM_N
ESL3_NE005	Euclidean	Linked	Lower	FSM_NE005
ESL3_W	Euclidean	Linked	Lower	FSM_W
FSL1_N	Fractal	Linked	Best	FSM_N
FSL1_NE005	Fractal	Linked	Best	FSM_NE005
FSL1_W	Fractal	Linked	Best	FSM_W
FSL2_N	Fractal	Linked	Upper	FSM_N
FSL2_NE005	Fractal	Linked	Upper	FSM_NE005
FSL2_W	Fractal	Linked	Upper	FSM_W
FSL3_N	Fractal	Linked	Lower	FSM_N
FSL3_NE005	Fractal	Linked	Lower	FSM_NE005
FSL3_W	Fractal	Linked	Lower	FSM_W

Table 4-12. Determination of trace length scaling exponent and associated simulated P_{32} fracture intensity for a minimum radius (r_{min}) of 0.5 m. k_t is the exponent of the traces, while k_r is the exponent of the parent radius distribution.

Scaling	Set	Min Radius (m)	k_t	k_r	P_{32OC}
Euclidean	ENE	0.5	2.03	3.03	1.54
Euclidean	NS	0.5	2.15	3.15	3.27
Euclidean	SH	0.5	1.82	2.82	0.57
Euclidean	WNW	0.5	2.33	3.33	6.34

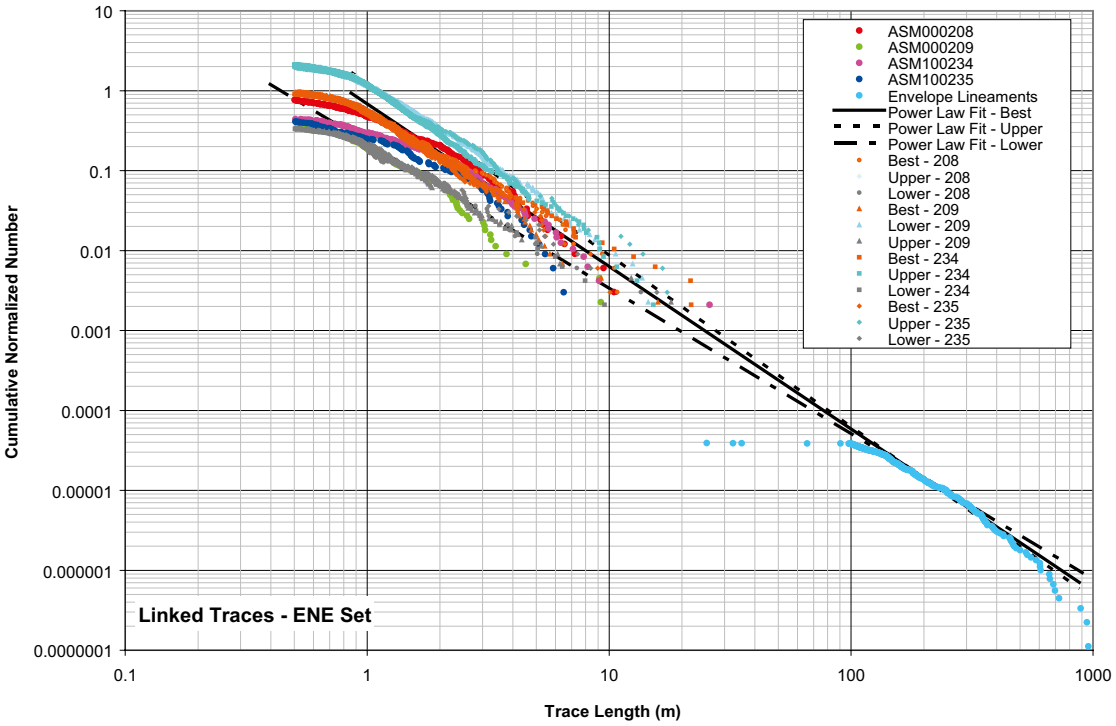

Figure 4-19. *CCN plot illustrating P_{32s} fitting simulation runs; this figure represents the ENE orientation set and the Base Model size-intensity case.*

Table 4-13. Area values used for the CCN area normalizations.

Outcrop/Fracture Domain	GIS Layer Name	Area (m^2)
ASM000208	SDEADM_GOL_LX_GEO_2347	330.70
ASM100234	SDEADM_GOL_SM_GEO_3569	478.60
ASM000209	SDEADM_GOL_LX_GEO_2356	442.10
ASM100235	SDEADM_GOL_SM_GEO_3689	332.60
FSM_EW007	FSM_EW007*	1,065,407.14
FSM_N	FSM_N*	2,159,303.84
FSM_W	FSM_W*	1,579,531.48
FSM_NE005	FSM_NE005*	1,448,762.76
FSM_C	FSM_C*	1,125,064.01
FSM_S	FSM_S*	1,300,219.82
FSM_envelope February 2008	fsm_envelope	9,378,127.97
FSM_envelope December 2007	FD_LX_LOC_V23b_topographic_section-2D	9,415,904.47
FSM_envelope (Dec 2007) – power line areas	N/A	8,968,061.19

* These shapefiles were derived from the December 2007 preliminary fracture domain model, minus the surface area surrounding the deformation zones and the surface area in which high-voltage transmission lines are present.

It is also important to note that the fracture domains used in the area normalizations were early versions; a refinement of the fracture domains was completed in March of 2008, after the size-intensity modelling had been completed. The surface areas of the current fracture domains (Figure 4-6) is slightly different than that used in the area normalization (Figure 4-20); domain FSM_EW007 is slightly larger at the ground surface, while FSM_C and FSM_NE005 are correspondingly smaller. This does not affect the size model parameterisation using the lineament traces, as the lineament traces are normalized only to the total fracture envelope area (fsm_envelope in Table 4-13). There is a small section along the northern side of FSM_W (see Figure 4-20) that was enlarged in the February 2008 model. The total difference in area between

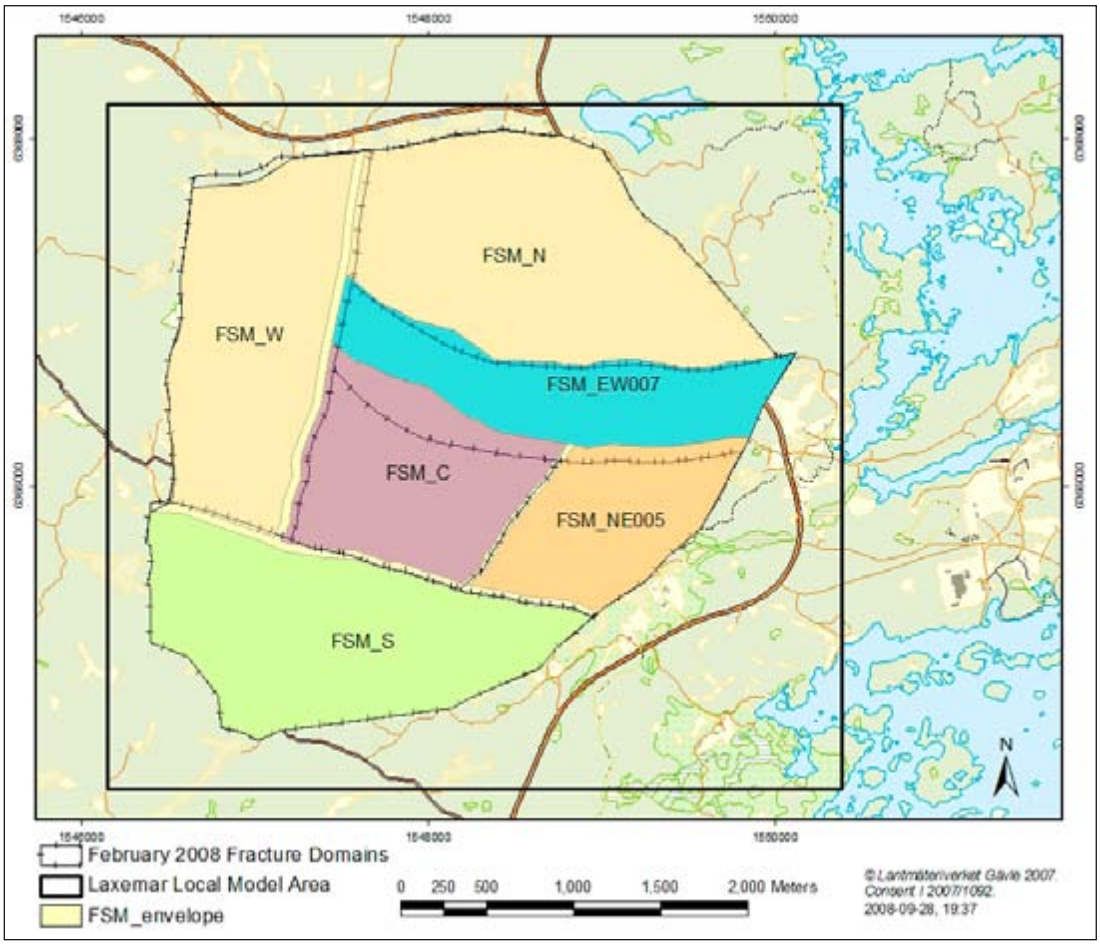

Figure 4-20. *Fracture domain areas (transparent) used for the lineament area re-normalization. Note that the areas around deterministic deformation zones are excluded.*

the December 2007 and February 2008 models is only 0.4%; this is not large enough to have any significant effect on the size-intensity modelling.

The magnitude of the size scaling exponent (k_r) indicates the proportion of the distribution accounted for by large or small fractures. A smaller exponent indicates that a larger proportion of the overall fracture intensity is accounted for by large fractures, while a large scaling exponent indicates a greater relative importance of small fractures. The magnitude of the exponent does not indicate whether one set has a higher or lower overall fracture intensity; it merely describes how the fracture sizes are proportioned.

The area-normalized CCN plots (Figure 4-21 through Figure 4-25) provide some additional support that the scaling exponent is not fracture domain-dependent, which bolsters the preliminary Base Model assumption of domain-independence of the trace length scaling exponent (and therefore the radius scaling exponent). The four outcrops lie in three fracture domains. This makes it possible to evaluate whether there may systematic differences in scaling exponents in at least a few of the fracture domains at Laxemar. For example, ASM000209 is the only outcrop in fracture domain FSM_NE005. If it had a systematically higher or lower scaling exponent than other domains, then it would consistently plot as the highest or lowest set of data for all fracture sets in the CCN plots. Inspection of these four CCN plots shows that it does not. In fact, none of the outcrops plots consistently above or below the other outcrops. This lack of a systematic pattern is consistent with the scaling exponent being independent of fracture domain. As such, the differences among outcrops for a specific fracture orientation set is probably more likely to be a representation of the variability of the scaling exponent that is independent of fracture domain.

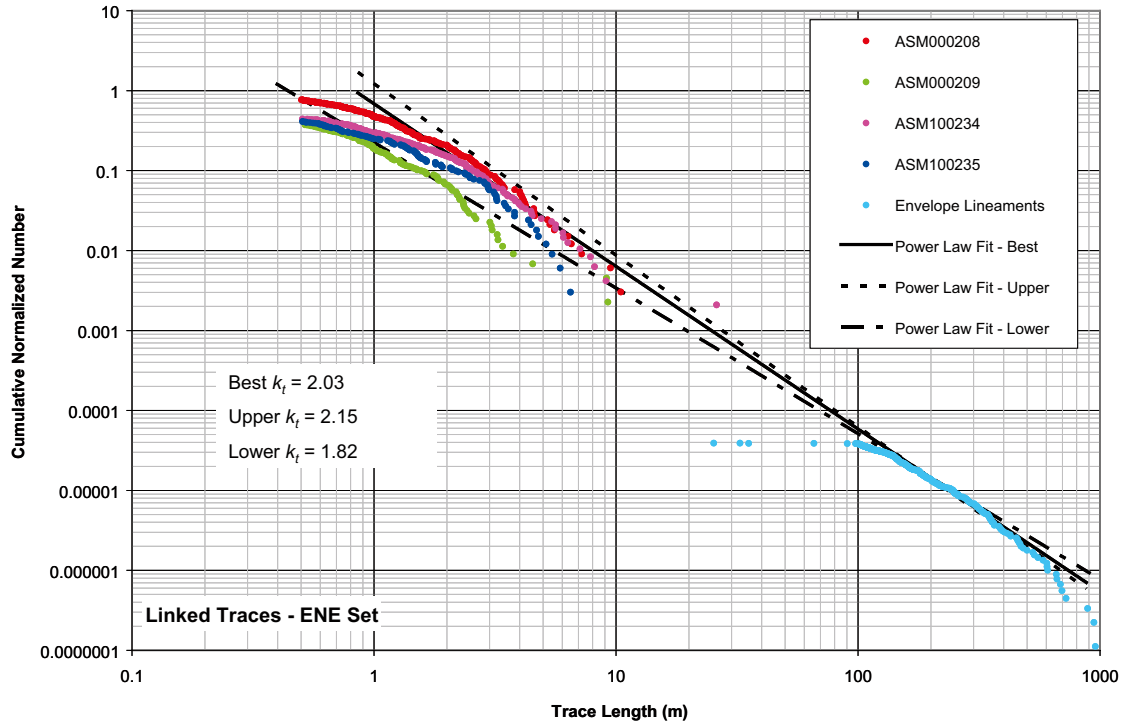

Figure 4-21. *CCN plot for the ENE fracture set, Base Model.*

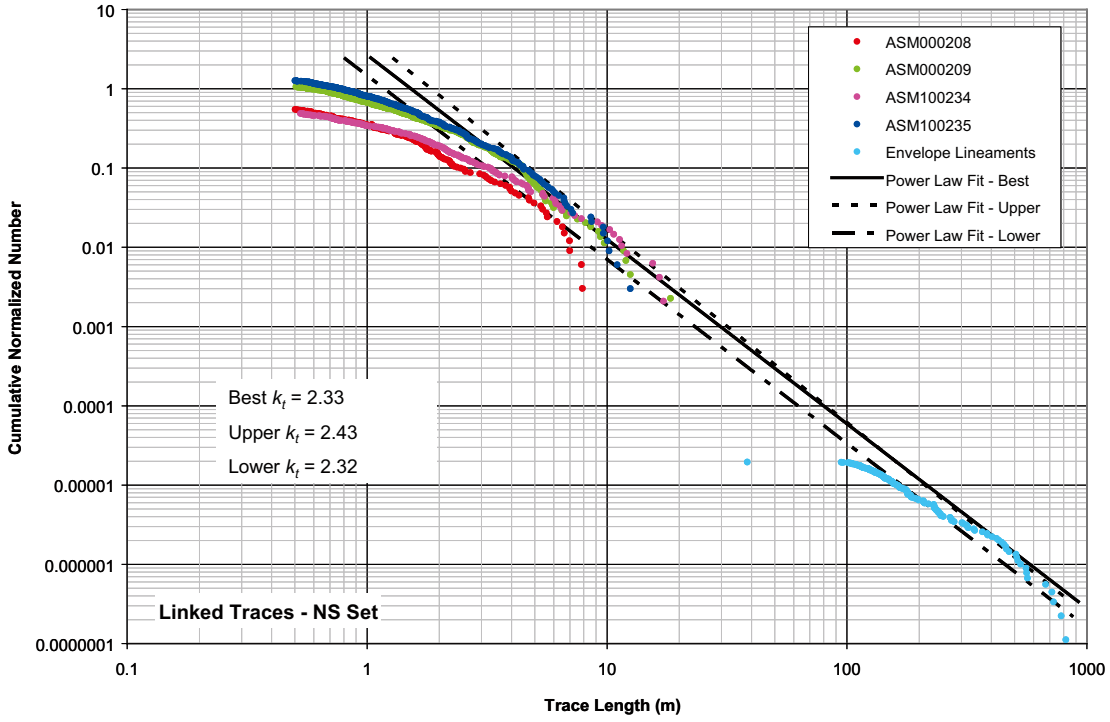

Figure 4-22. *CCN plot for NS fracture set, Base Model.*

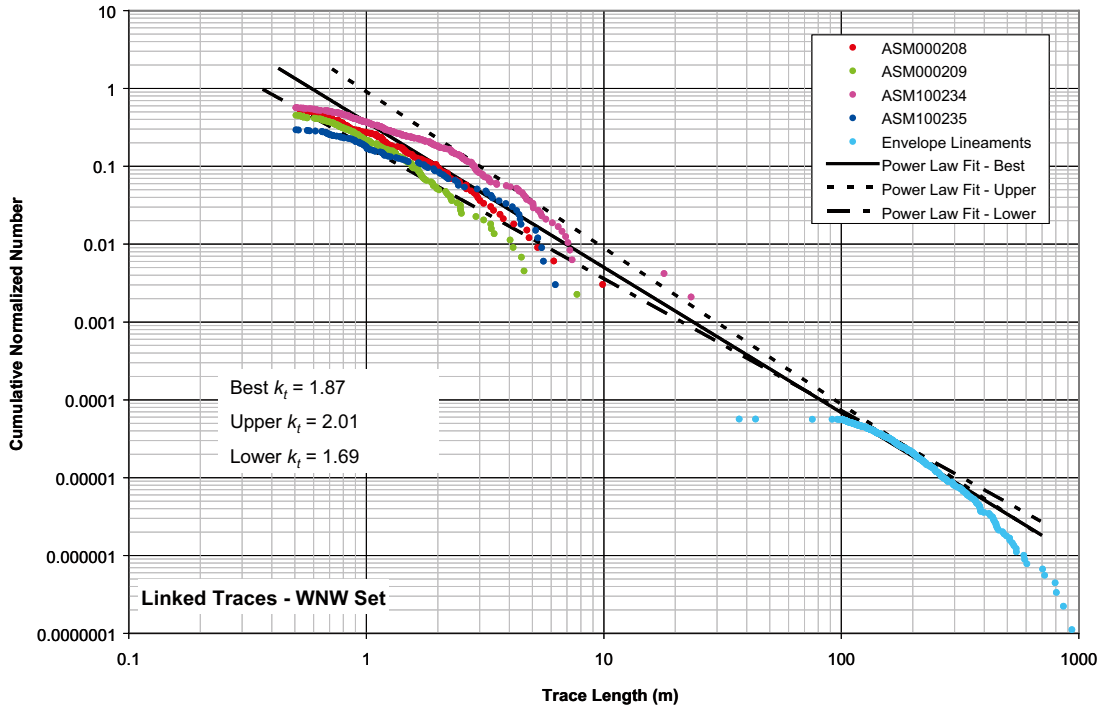

Figure 4-23. *CCN plot for WNW fracture set, Base Model.*

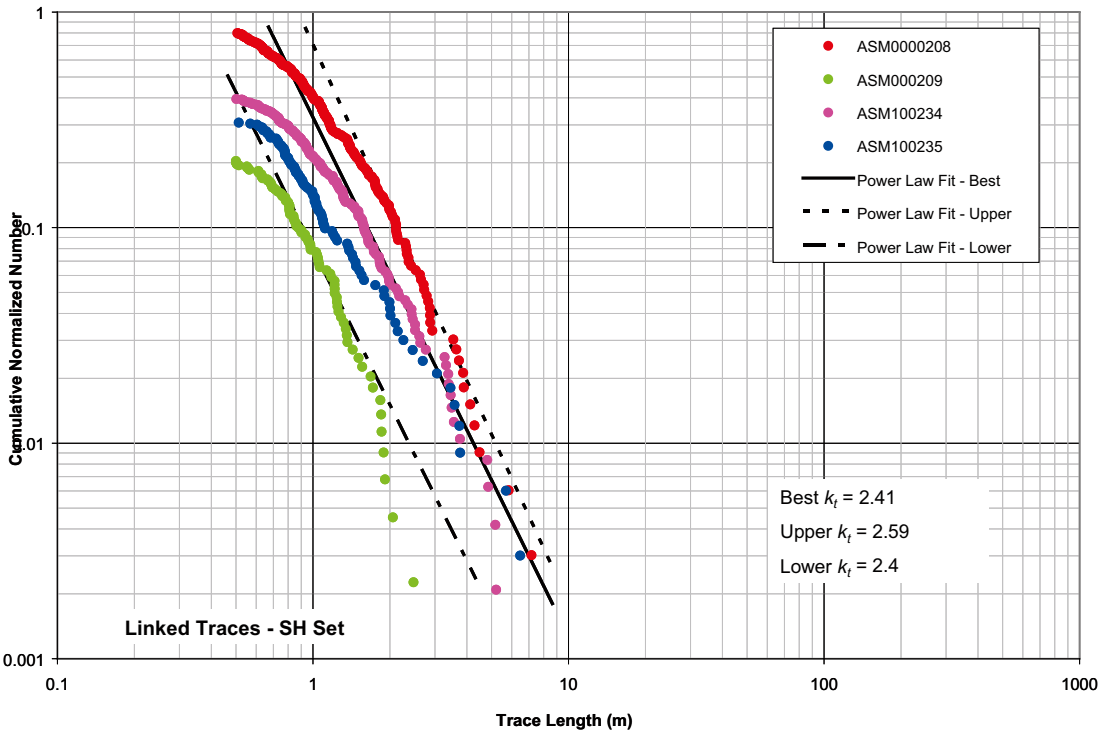

Figure 4-24. *CCN plot for SH fracture set, Base Model.*

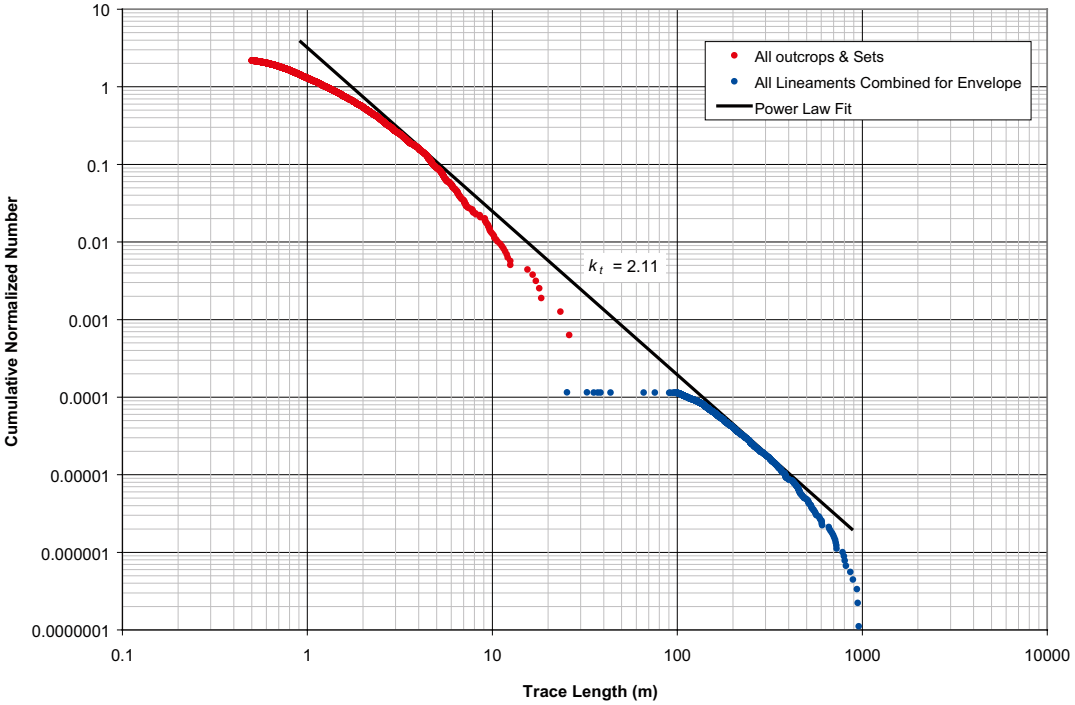

Figure 4-25. *CCN plot for all sets on all outcrops combined, Base Model.*

The next step in the coupled size-intensity preliminary Base Model parameterisation is to calculate a minimum radius value (r_0) that matches the measured fracture intensity in the boreholes. This step allows for a coupled size-intensity model that simultaneously respects the P_{32OC} obtained from outcrop fracture data calculated through simulation and the P_{32} obtained from borehole fracture intensity data (calculated using Wang's approximation). In cases where the borehole P_{32} is higher than the outcrop P_{32OC}, the assumption is that the borehole is encountering fractures smaller than those mapped on the outcrops. In the few cases where the borehole P_{32} is smaller than the simulated outcrop P_{32OC}, the assumption is that the outcrop intensities are anomalous, either due to surficial processes, glacial unloading, surficial stress release, or proximity to deformation zones and minor deformation zones. The borehole P_{32} is viewed as a more accurate representation of the subsurface fracture intensity.

Fracture intensity, quantified as P_{32}, was calculated for each set, fracture domain and fracture type, from the cored borehole data using the method described in Section 3.5.1. Following the methods outlined in Section 3.4, the minimum radius of the size model probability distribution (r_0) was calculated using Equation 3-15, the values of r_{min} and P_{32OC} shown in Table 4-12, and the mean borehole fracture intensity. The results are shown in Table 4-14. The final parameterisations are given in Table 4-15 for the Base Model (labelled as "Best"). The preliminary Base Model size-intensity parameter values again suggest that it is useful in terms of reducing uncertainty to separate the fracture parameterizations by fracture domain; the calculated minimum size (r_0) varies significantly for individual sets across fracture domains.

Table 4-14. Summary of minimum radius by fracture domain, set, fit type and fracture type, Base Model (BM).

Set	Fit Type	FSM_C				FSM_EW007			
		Total Calculated r_0	Total Borehole P_{32}	Open Calculated r_0	Open Borehole P_{32}	Total Calculated r_0	Total Borehole P_{32}	Open Calculated r_0	Open Borehole P_{32}
ENE	Best	0.45	1.72	1.49	0.50	0.39	1.98	1.18	0.64
NS	Best	1.06	2.33	3.64	0.45	0.89	2.96	2.33	0.82
SH	Best	0.39	2.66	1.26	0.51	0.27	4.42	0.70	1.16
WNW	Best	0.15	2.53	0.60	0.77	0.13	2.90	0.40	1.11
Set	**Fit Type**	**FSM_NE005**				**FSM_S**			
		Total Calculated r_0	Total Borehole P_{32}	Open Calculated r_0	Open Borehole P_{32}	Total Calculated r_0	Total Borehole P_{32}	Open Calculated r_0	Open Borehole P_{32}
ENE	Best	0.48	1.60	1.64	0.45	0.19	4.28	0.59	1.30
NS	Best	0.67	4.30	2.43	0.78	0.52	6.09	1.51	1.45
SH	Best	0.34	3.17	0.80	0.96	0.28	4.22	0.58	1.50
WNW	Best	0.17	2.37	0.79	0.61	0.06	5.39	0.31	1.38
Set	**Fit Type**	**FSM_N**				**FSM_W**			
		Total Calculated r_0	Total Borehole P_{32}	Open Calculated r_0	Open Borehole P_{32}	Total Calculated r_0	Total Borehole P_{32}	Open Calculated r_0	Open Borehole P_{32}
ENE	Best	0.56	1.38	1.55	0.48	0.48	1.60	2.01	0.37
NS	Best	0.97	2.63	3.11	0.56	0.77	3.60	2.38	0.79
SH	Best	0.26	4.62	0.58	1.50	0.33	3.40	0.82	0.93
WNW	Best	0.14	2.67	0.55	0.84	0.21	1.97	0.89	0.55

Table 4-15. Couple size/intensity parameters for Base Model (BM).

Set	Fit Type	FSM_C				FSM_EW007			
		k_r	r_0	r_{max}	$P_{32}(k_r,r_0,r_{max})$	k_r	r_0	r_{max}	$P_{32}(k_r,r_0,r_{max})$
ENE	Best	3.03	0.45	564.2	1.72	3.03	0.39	564.2	1.98
NS	Best	3.33	0.88	564.2	2.33	3.33	0.89	564.2	2.96
SH	Best	3.41	0.13	564.2	2.66	3.41	0.27	564.2	4.42
WNW	Best	2.87	1.06	564.2	2.53	2.87	0.13	564.2	2.90
Set	**Fit Type**	**FSM_NE005**				**FSM_S**			
		k_r	r_0	r_{max}	$P_{32}(k_r,r_0,r_{max})$	k_r	r_0	r_{max}	$P_{32}(k_r,r_0,r_{max})$
ENE	Best	3.03	0.48	564.2	1.60	3.03	0.19	564.2	4.28
NS	Best	3.33	0.67	564.2	4.30	3.33	0.52	564.2	6.09
SH	Best	3.41	0.34	564.2	3.17	3.41	0.28	564.2	4.22
WNW	Best	2.87	0.17	564.2	2.37	2.87	0.06	564.2	5.39
Set	**Fit Type**	**FSM_N**				**FSM_W**			
		k_r	r_0	r_{max}	$P_{32}(k_r,r_0,r_{max})$	k_r	r_0	r_{max}	$P_{32}(k_r,r_0,r_{max})$
ENE	Best	3.03	0.56	564.2	1.38	3.03	0.48	564.2	1.60
NS	Best	3.33	0.97	564.2	2.63	3.33	0.77	564.2	3.60
SH	Best	3.41	0.26	564.2	4.62	3.41	0.33	564.2	3.40
WNW	Best	2.87	0.14	564.2	2.67	2.87	0.21	564.2	1.97

4.3.4 Alternative models

EL1 and EL2

The preliminary Base Model was parameterized by visually fitting a line in the CCN plots that appeared to best coincide with the slopes of the outcrop and lineament trace sets, and align most closely between the lineaments and the outcrops. It is an attempt to find a model that is tangent to both the lineament and outcrop data. However, as the plots in Figure 4-21 through Figure 4-24 show, there is some variability in the outcrop trace data, so that there are alternatives to a visual best fit that may provide bounds to the size/intensity parameterization. These results, designated as “upper” (EL1) and “lower” (EL2), are summarized in Table 4-16 through Table 4-18. This alternative model captures some of the variability of the scaling exponent that is independent of the fracture domains, and provide bounds for the (potential) limits of the radius scaling exponent as derived from surface fracture data.

Table 4-16. Determination of trace length scaling exponent and associated simulated P_{32} fracture intensity for a minimum radius (r_{min}) of 0.5 m, upper and lower fits. k_t is the exponent of the traces, while k_r is the exponent of the parent radius distribution.

Fit Type	Set	Min. Radius (m)	k_t	k_r	P_{32OC}
Upper	ENE	0.5	2.15	3.15	3.27
Upper	NS	0.5	2.43	3.43	9.2
Upper	SH	0.5	2.59	3.59	3.7
Upper	WNW	0.5	2.01	3.01	2.02
Lower	ENE	0.5	1.82	2.82	0.57
Lower	NS	0.5	2.32	3.32	2.28
Lower	SH	0.5	2.4	3.4	0.46
Lower	WNW	0.5	1.69	2.69	0.5

Table 4-17. Summary of minimum radius by fracture domain, set, fit type and fracture type, upper and lower fits (EL1 and EL2).

Set	Fit Type	FSM_C				FSM_EW007			
		Total Calculated r_0	Total Borehole P_{32}	Open Calculated r_0	Open Borehole P_{32}	Total Calculated r_0	Total Borehole P_{32}	Open Calculated r_0	Open Borehole P_{32}
ENE	Upper	0.88	1.72	2.56	0.50	0.77	1.98	2.08	0.64
NS	Upper	1.31	2.33	4.11	0.45	1.10	2.96	2.72	0.82
SH	Upper	0.62	2.66	1.74	0.51	0.45	4.42	1.04	1.16
WNW	Upper	0.40	2.53	1.29	0.77	0.35	2.90	0.90	1.11
Set	**Fit Type**	**FSM_NE005**				**FSM_S**			
		Total Calculated r_0	Total Borehole P_{32}	Open Calculated r_0	Open Borehole P_{32}	Total Calculated r_0	Total Borehole P_{32}	Open Calculated r_0	Open Borehole P_{32}
ENE	Upper	0.93	1.60	2.79	0.45	0.40	4.28	1.12	1.30
NS	Upper	0.85	4.30	2.82	0.78	0.67	6.09	1.82	1.45
SH	Upper	0.55	3.17	1.17	0.96	0.46	4.22	0.88	1.50
WNW	Upper	0.43	2.37	1.63	0.61	0.19	5.39	0.73	1.38
Set	**Fit Type**	**FSM_N**				**FSM_W**			
		Total Calculated r_0	Total Borehole P_{32}	Open Calculated r_0	Open Borehole P_{32}	Total Calculated r_0	Total Borehole P_{32}	Open Calculated r_0	Open Borehole P_{32}
ENE	Upper	1.06	1.38	2.65	0.48	0.93	1.60	3.35	0.37
NS	Upper	1.20	2.63	3.56	0.56	0.96	3.60	2.77	0.79
SH	Upper	0.43	4.62	0.88	1.50	0.53	3.40	1.19	0.93
WNW	Upper	0.38	2.67	1.19	0.84	0.51	1.97	1.82	0.55
Set	**Fit Type**	**FSM_C**				**FSM_EW007**			
		Total Calculated r_0	Total Borehole P_{32}	Open Calculated r_0	Open Borehole P_{32}	Total Calculated r_0	Total Borehole P_{32}	Open Calculated r_0	Open Borehole P_{32}
ENE	Lower	0.13	1.72	0.58	0.50	0.11	1.98	0.44	0.64
NS	Lower	0.49	2.33	1.70	0.45	0.41	2.96	1.09	0.82
SH	Lower	0.14	2.66	0.46	0.51	0.10	4.42	0.26	1.16
WNW	Lower	0.05	2.53	0.26	0.77	0.04	2.90	0.16	1.11

Set	Fit Type	FSM_NE005				FSM_S			
		Total Calculated r_0	Total Borehole P_{32}	Open Calculated r_0	Open Borehole P_{32}	Total Calculated r_0	Total Borehole P_{32}	Open Calculated r_0	Open Borehole P_{32}
ENE	Lower	0.14	1.60	0.66	0.45	0.04	4.28	0.18	1.30
NS	Lower	0.31	4.30	1.13	0.78	0.24	6.09	0.70	1.45
SH	Lower	0.13	3.17	0.30	0.96	0.10	4.22	0.22	1.50
WNW	Lower	0.05	2.37	0.37	0.61	0.02	5.39	0.11	1.38
Set	**Fit Type**	**FSM_N**				**FSM_W**			
		Total Calculated r_0	Total Borehole P_{32}	Open Calculated r_0	Open Borehole P_{32}	Total Calculated r_0	Total Borehole P_{32}	Open Calculated r_0	Open Borehole P_{32}
ENE	Lower	0.17	1.38	0.61	0.48	0.14	1.60	0.85	0.37
NS	Lower	0.45	2.63	1.46	0.56	0.35	3.60	1.11	0.79
SH	Lower	0.10	4.62	0.21	1.50	0.12	3.40	0.30	0.93
WNW	Lower	0.04	2.67	0.23	0.84	0.07	1.97	0.44	0.55

Table 4-18. Coupled size/intensity parameters for the upper and lower fits (EL1 and EL2).

Set	Fit Type	FSM_C				FSM_EW007			
		k_r	r_0	r_{max}	P_{32} (k_r,r_0,r_{max})	k_r	r_0	r_{max}	P_{32} (k_r,r_0,r_{max})
ENE	Upper	3.15	0.88	564.20	1.72	3.15	0.77	564.20	1.98
NS	Upper	3.43	1.31	564.20	2.33	3.43	1.10	564.20	2.96
SH	Upper	3.59	0.62	564.20	2.66	3.59	0.45	564.20	4.42
WNW	Upper	3.01	0.40	564.20	2.53	3.01	0.35	564.20	2.90
Set	**Fit Type**	**FSM_NE005**				**FSM_S**			
		k_r	r_0	r_{max}	P_{32} (k_r,r_0,r_{max})	k_r	r_0	r_{max}	P_{32} (k_r,r_0,r_{max})
ENE	Upper	3.15	0.93	564.20	1.60	3.15	0.40	564.20	4.28
NS	Upper	3.43	0.85	564.20	4.30	3.43	0.67	564.20	6.09
SH	Upper	3.59	0.55	564.20	3.17	3.59	0.46	564.20	4.22
WNW	Upper	3.01	0.43	564.20	2.37	3.01	0.19	564.20	5.39
Set	**Fit Type**	**FSM_N**				**FSM_W**			
		k_r	r_0	r_{max}	P_{32} (k_r,r_0,r_{max})	k_r	r_0	r_{max}	P_{32} (k_r,r_0,r_{max})
ENE	Upper	3.15	1.06	564.20	1.38	3.15	0.93	564.20	1.60
NS	Upper	3.43	1.20	564.20	2.63	3.43	0.96	564.20	3.60
SH	Upper	3.59	0.43	564.20	4.62	3.59	0.53	564.20	3.40
WNW	Upper	3.01	0.38	564.20	2.67	3.01	0.51	564.20	1.97
Set	**Fit Type**	**FSM_C**				**FSM_EW007**			
		k_r	r_0	r_{max}	P_{32} (k_r,r_0,r_{max})	k_r	r_0	r_{max}	P_{32} (k_r,r_0,r_{max})
ENE	Lower	2.82	0.13	564.20	1.72	2.82	0.11	564.20	1.98
NS	Lower	3.32	0.49	564.20	2.33	3.32	0.41	564.20	2.96
SH	Lower	3.4	0.14	564.20	2.66	3.4	0.10	564.20	4.42
WNW	Lower	2.69	0.05	564.20	2.53	2.69	0.04	564.20	2.90
Set	**Fit Type**	**FSM_NE005**				**FSM_S**			
		k_r	r_0	r_{max}	P_{32} (k_r,r_0,r_{max})	k_r	r_0	r_{max}	P_{32} (k_r,r_0,r_{max})
ENE	Lower	2.82	0.14	564.20	1.60	2.82	0.04	564.20	4.28
NS	Lower	3.32	0.31	564.20	4.30	3.32	0.24	564.20	6.09
SH	Lower	3.4	0.13	564.20	3.17	3.4	0.10	564.20	4.22
WNW	Lower	2.69	0.05	564.20	2.37	2.69	0.02	564.20	5.39
Set	**Fit Type**	**FSM_N**				**FSM_W**			
		k_r	r_0	r_{max}	P_{32} (k_r,r_0,r_{max})	k_r	r_0	r_{max}	P_{32} (k_r,r_0,r_{max})
ENE	Lower	2.82	0.17	564.20	1.38	2.82	0.14	564.20	1.60
NS	Lower	3.32	0.45	564.20	2.63	3.32	0.35	564.20	3.60
SH	Lower	3.4	0.10	564.20	4.62	3.4	0.12	564.20	3.40
WNW	Lower	2.69	0.04	564.20	2.67	2.69	0.07	564.20	1.97

This alternative model case is parameterised in the exact same manner as the preliminary Base Model (Section 4.3.3). The only difference is in the radius scaling exponent (k_r), the P_{32OC} value found through simulation, and the resulting minimum radius of the probability distribution (r_0); change one of these parameters, and it is necessary to change the other one if P_{32} is to be conserved. The reason why P_{32OC} changes, even when there is no underlying change in the data has to do with the coupling of intensity, scaling exponent, and minimum radius. P_{32OC} is a value calculated through simulation; it is an estimate of the fracture intensity necessary to produce the trace length distributions seen in outcrop and lineaments if one limits the size range for the simulation to that of the data (i.e. 0.5 m–564.2 m). If the slope of the radius exponent changes and r_{min} (0.50 m) and r_{max} (564.2 m) stay constant, than the simulated P_{32OC} must change; it is a fundamental property of the coupled size-intensity model (Section 3.4).

BMF, FL1 and FL2

The fractal scaling alternative model results are shown in Figure 4-26 through Figure 4-29. These results are based on linked traces, and like the Base Model and its bounding cases, on the assumption that the scaling exponent is not a function of fracture domain. The methodologies for calculating P_{32OC} and r_0 are exactly the same as for the Base Model (Section 4.3.3). The only difference between the models is that rather than a straight area re-normalization, in the fractal scaling models the trace length scaling plots are normalized to a pseudo-area. The pseudo-area (A_p) is calculated using Equation 4-1, the area of each outcrop (A), and the mass dimension (D_m) for each outcrop (Section 4.4.2). The lineaments are normalized using the arithmetic mean of the outcrop mass dimensions and the fracture domain envelope area (Table 4-13).

$$A_p = A\sqrt{1/\pi}^{(2-D_m)} \qquad \text{Equation 4-1}$$

The following CCN plots show the visual best fit (BMF), as well as the bounding fits labelled as "upper" (FL1) and "lower" (FL2). The bounding fits are discussed in Section 4.3.3. The parameters derived for the best fit model (BMF) using a minimum radius of 0.5 m is summarized in Table 4-19, while the final parameterisations are presented in Table 4-20 and Table 4-21.

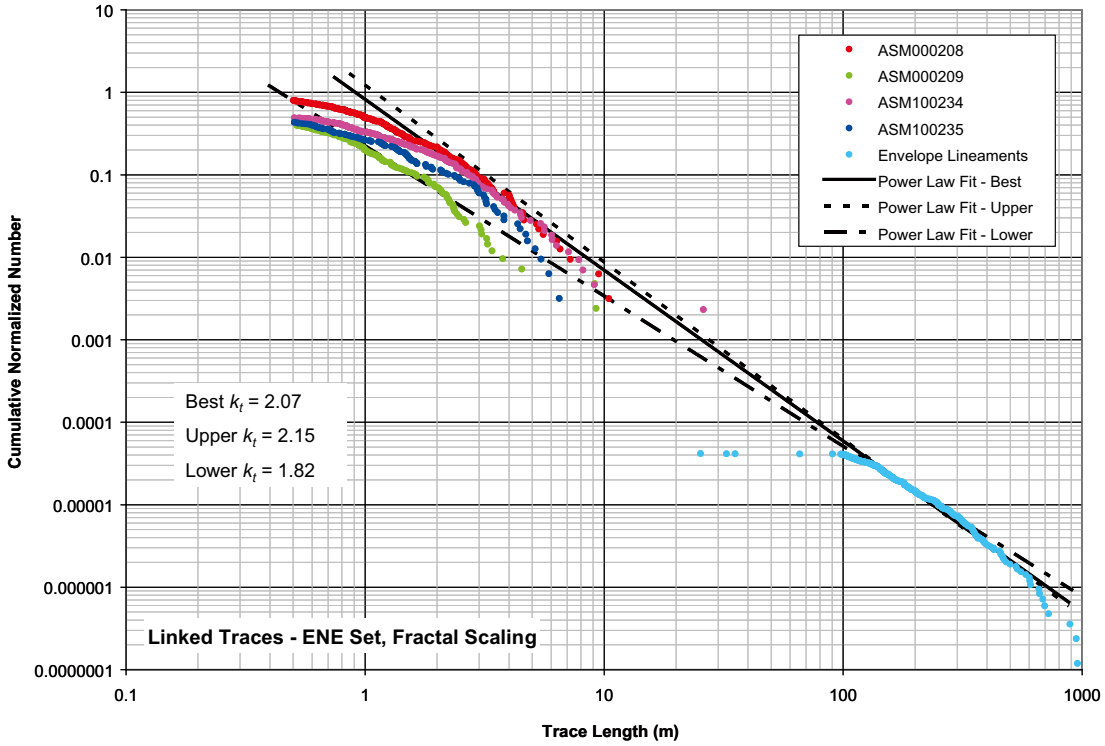

Figure 4-26. *CCN plot for ENE fracture set, fractal scaling alternative model.*

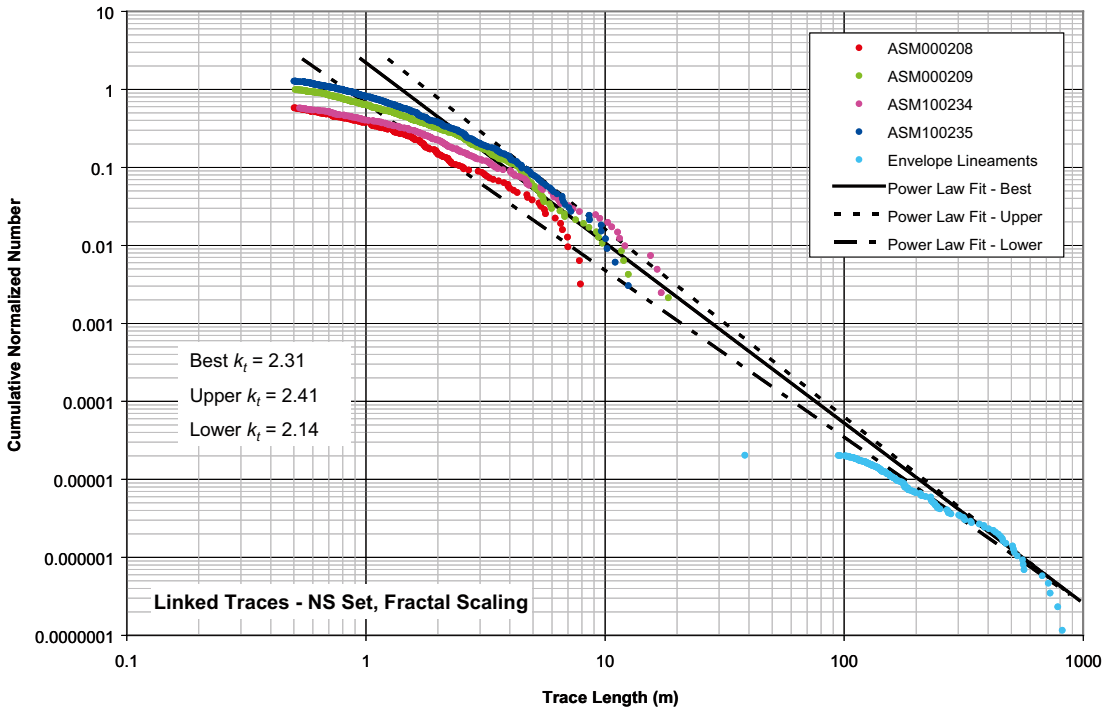

Figure 4-27. *CCN plot for NS fracture set, fractal scaling alternative model.*

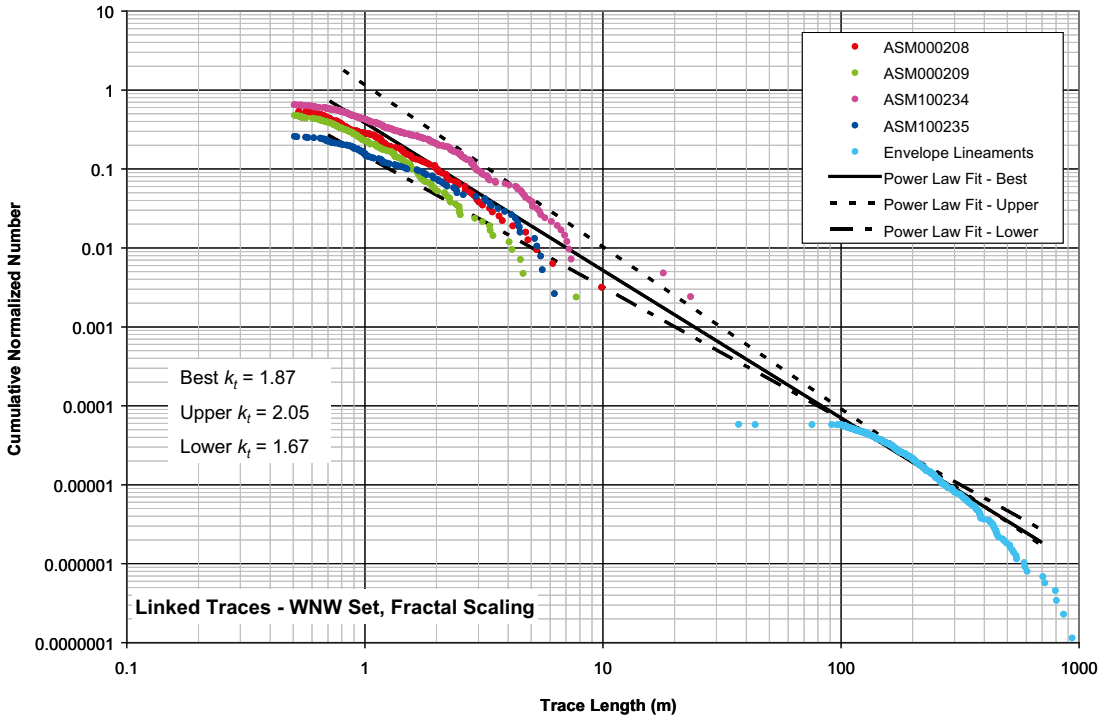

Figure 4-28. *CCN plot for the WNW fracture set, fractal scaling alternative model.*

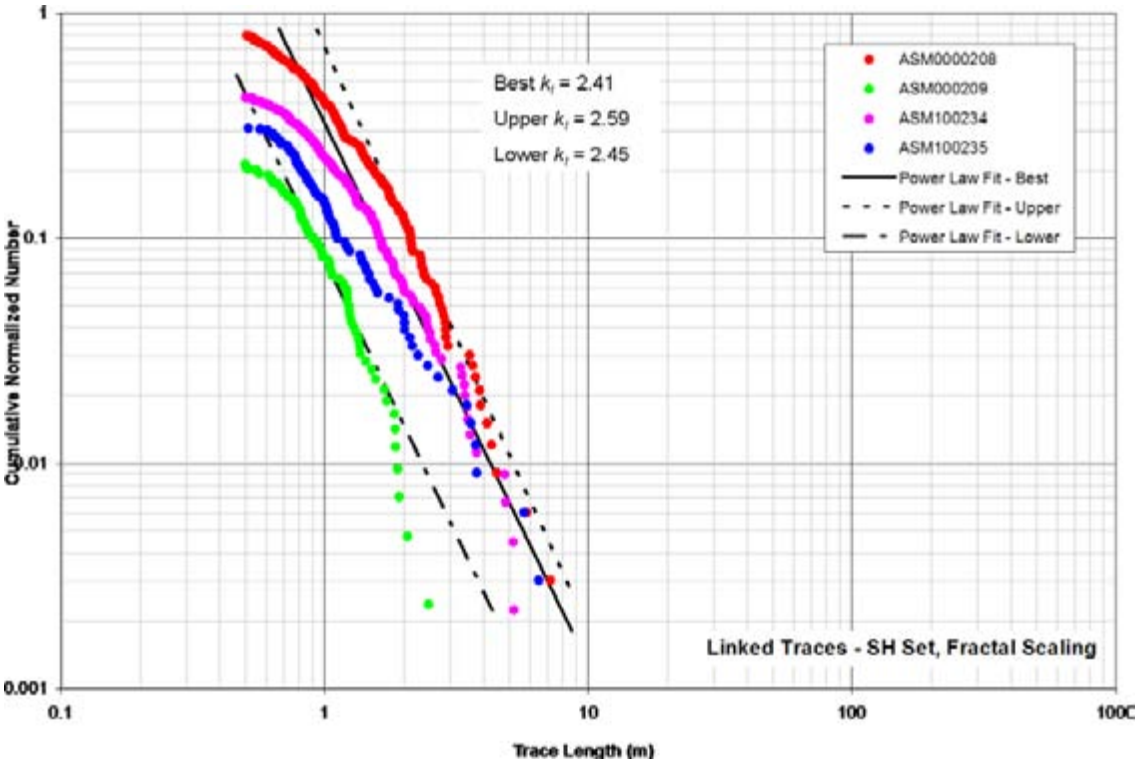

Figure 4-29. *CCN plot for the SH fracture set, fractal scaling alternative model.*

Table 4-19. Determination of trace length scaling exponent and associated simulated P_{32OC} fracture intensity for a minimum radius (r_{min}) of 0.5 m for the fractal alternative scaling model. k_t is the exponent of the traces, while k_r is the exponent of the parent radius distribution.

Scaling	Set	Min. Radius (m)	k_t	k_r	P_{32OC}
Fractal	ENE	0.5	2.07	3.07	2.2
Fractal	NS	0.5	2.31	3.31	5.39
Fractal	SH	0.5	2.41	3.41	1.74
Fractal	WNW	0.5	1.87	2.87	1

Table 4-20. Summary of minimum radius by fracture domain, set, fit type and fracture type, fractal alternative model.

Set	Fit Type	FSM_C				FSM_EW007			
		Total Calculated r_0	Total Borehole P_{32}	Open Calculated r_0	Open Borehole P_{32}	Total Calculated r_0	Total Borehole P_{32}	Open Calculated r_0	Open Borehole P_{32}
ENE	Best	0.63	1.72	1.99	0.50	0.55	1.98	1.59	0.64
NS	Best	0.95	2.33	3.31	0.45	0.79	2.96	2.11	0.82
SH	Best	0.37	2.66	1.19	0.51	0.26	4.42	0.67	1.16
WNW	Best	0.17	2.53	0.67	0.77	0.15	2.90	0.44	1.11
Set	**Fit Type**	**FSM_NE005**				**FSM_S**			
		Total Calculated r_0	Total Borehole P_{32}	Open Calculated r_0	Open Borehole P_{32}	Total Calculated r_0	Total Borehole P_{32}	Open Calculated r_0	Open Borehole P_{32}
ENE	Best	0.67	1.60	2.19	0.45	0.27	4.28	0.82	1.30
NS	Best	0.59	4.30	2.20	0.78	0.46	6.09	1.36	1.45
SH	Best	0.33	3.17	0.76	0.96	0.27	4.22	0.56	1.50
WNW	Best	0.19	2.37	0.88	0.61	0.07	5.39	0.34	1.38
Set	**Fit Type**	**FSM_N**				**FSM_W**			
		Total Calculated r_0	Total Borehole P_{32}	Open Calculated r_0	Open Borehole P_{32}	Total Calculated r_0	Total Borehole P_{32}	Open Calculated r_0	Open Borehole P_{32}
ENE	Best	0.77	1.38	2.07	0.48	0.67	1.60	2.66	0.37
NS	Best	0.86	2.63	2.83	0.56	0.68	3.60	2.16	0.79
SH	Best	0.25	4.62	0.56	1.50	0.31	3.40	0.78	0.93
WNW	Best	0.16	2.67	0.61	0.84	0.23	1.97	1.00	0.55

Table 4-21. Couple size/intensity parameters for fractal alternative model.

Set	Fit Type	FSM_C				FSM_EW007			
		k_r	r_0	r_{max}	P_{32} (k_r,r_0,r_{max})	k_r	r_0	r_{max}	P_{32} (k_r,r_0,r_{max})
ENE	Best	3.07	0.63	564.20	1.72	3.07	0.55	564.20	1.98
NS	Best	3.31	0.95	564.20	2.33	3.31	0.79	564.20	2.96
SH	Best	3.41	0.37	564.20	2.66	3.41	0.26	564.20	4.42
WNW	Best	2.87	0.17	564.20	2.53	2.87	0.15	564.20	2.90
Set	**Fit Type**	**FSM_NE005**				**FSM_S**			
		k_r	r_0	r_{max}	P_{32} (k_r,r_0,r_{max})	k_r	r_0	r_{max}	P_{32} (k_r,r_0,r_{max})
ENE	Best	3.07	0.67	564.20	1.60	3.07	0.27	564.20	4.28
NS	Best	3.31	0.59	564.20	4.30	3.31	0.46	564.20	6.09
SH	Best	3.41	0.33	564.20	3.17	3.41	0.27	564.20	4.22
WNW	Best	2.87	0.19	564.20	2.37	2.87	0.07	564.20	5.39
Set	**Fit Type**	**FSM_N**				**FSM_W**			
		k_r	r_0	r_{max}	P_{32} (k_r,r_0,r_{max})	k_r	r_0	r_{max}	P_{32} (k_r,r_0,r_{max})
ENE	Best	3.07	0.77	564.20	1.38	3.07	0.67	564.20	1.60
NS	Best	3.31	0.86	564.20	2.63	3.31	0.68	564.20	3.60
SH	Best	3.41	0.25	564.20	4.62	3.41	0.31	564.20	3.40
WNW	Best	2.87	0.16	564.20	2.67	2.87	0.23	564.20	1.97

The Fractal best fit model, like the Base Model, was parameterised by visually fitting a line in the CCN plots that appeared to best coincide with the slopes of the outcrop and lineament trace sets, and that aligned most closely between the lineaments and the outcrops. The best fit models are an attempt to find a trace length scaling exponent that is tangent to both the lineament and outcrop data. However, as the plots in Figure 4-26 through Figure 4-29 show, there is some variability in the outcrop trace data, so that there are alternatives to a visual best fit Fractal model that may provide bounds to the size/intensity parameterisation. These results, designated as "upper" (FL1) and "lower" (FL2), are summarized in Table 4-22 through Table 4-24. The bounding case Fractal models are parameterised in the exact same fashion as the best fit Fractal model (using pseudo-areas) and the preliminary Base Model bounding cases (Section 4.3.3). The only difference is in the radius scaling exponent (k_r), the P_{32OC} value found through simulation, and the resulting minimum radius of the probability distribution (r_0); change one of these parameters, and it is necessary to change the other one if P_{32} is to be conserved.

Table 4-22. Determination of trace length scaling exponent and associated simulated P_{32OC} fracture intensity for a minimum radius (r_{min}) of 0.5 m, upper and lower fits, fractal alternative model. k_t is the exponent of the traces, while k_r is the exponent of the parent radius distribution.

Set	Fit Type	Min. Radius (m)	k_t	k_r	P_{32OC}
Upper	ENE	0.5	2.15	3.15	2.4
Upper	NS	0.5	2.41	3.41	8.8
Upper	SH	0.5	2.59	3.59	3.43
Upper	WNW	0.5	2.05	3.05	2.5
Lower	ENE	0.5	1.82	2.82	0.6
Lower	NS	0.5	2.14	3.14	2
Lower	SH	0.5	2.45	3.45	0.51
Lower	WNW	0.5	1.67	2.67	0.39

Table 4-23. Summary of minimum radius by fracture domain, set, fit type and fracture type, upper and lower fits, fractal alternative model.

Set	Fit Type	FSM_C				FSM_EW007			
		Total Calculated r_0	Total Borehole P_{32}	Open Calculated r_0	Open Borehole P_{32}	Total Calculated r_0	Total Borehole P_{32}	Open Calculated r_0	Open Borehole P_{32}
ENE	Upper	0.67	1.72	1.95	0.50	0.59	1.98	1.59	0.64
NS	Upper	1.28	2.33	4.10	0.45	1.08	2.96	2.70	0.82
SH	Upper	0.59	2.66	1.66	0.51	0.43	4.42	0.99	1.16
WNW	Upper	0.49	2.53	1.53	0.77	0.43	2.90	1.08	1.11
Set	**Fit Type**	**FSM_NE005**				**FSM_S**			
		Total Calculated r_0	Total Borehole P_{32}	Open Calculated r_0	Open Borehole P_{32}	Total Calculated r_0	Total Borehole P_{32}	Open Calculated r_0	Open Borehole P_{32}
ENE	Upper	0.71	1.60	2.13	0.45	0.30	4.28	0.85	1.30
NS	Upper	0.83	4.30	2.80	0.78	0.65	6.09	1.79	1.45
SH	Upper	0.53	3.17	1.11	0.96	0.44	4.22	0.84	1.50
WNW	Upper	0.53	2.37	1.91	0.61	0.24	5.39	0.88	1.38
Set	**Fit Type**	**FSM_N**				**FSM_W**			
		Total Calculated r_0	Total Borehole P_{32}	Open Calculated r_0	Open Borehole P_{32}	Total Calculated r_0	Total Borehole P_{32}	Open Calculated r_0	Open Borehole P_{32}
ENE	Upper	0.81	1.38	2.03	0.48	0.71	1.60	2.56	0.37
NS	Upper	1.18	2.63	3.54	0.56	0.94	3.60	2.75	0.79
SH	Upper	0.41	4.62	0.84	1.50	0.50	3.40	1.14	0.93
WNW	Upper	0.47	2.67	1.41	0.84	0.63	1.97	2.12	0.55
Set	**Fit Type**	**FSM_C**				**FSM_EW007**			
		Total Calculated r_0	Total Borehole P_{32}	Open Calculated r_0	Open Borehole P_{32}	Total Calculated r_0	Total Borehole P_{32}	Open Calculated r_0	Open Borehole P_{32}
ENE	Lower	0.14	1.72	0.62	0.50	0.12	1.98	0.46	0.64
NS	Lower	0.44	2.33	1.84	0.45	0.35	2.96	1.10	0.82
SH	Lower	0.16	2.66	0.50	0.51	0.11	4.42	0.28	1.16
WNW	Lower	0.03	2.53	0.18	0.77	0.03	2.90	0.10	1.11

Set	Fit Type	FSM_NE005				FSM_S			
		Total Calculated r_0	Total Borehole P_{32}	Open Calculated r_0	Open Borehole P_{32}	Total Calculated r_0	Total Borehole P_{32}	Open Calculated r_0	Open Borehole P_{32}
ENE	Lower	0.15	1.60	0.70	0.45	0.05	4.28	0.20	1.30
NS	Lower	0.26	4.30	1.15	0.78	0.19	6.09	0.66	1.45
SH	Lower	0.14	3.17	0.32	0.96	0.12	4.22	0.24	1.50
WNW	Lower	0.03	2.37	0.25	0.61	0.01	5.39	0.08	1.38
Set	**Fit Type**	**FSM_N**				**FSM_W**			
		Total Calculated r_0	Total Borehole P_{32}	Open Calculated r_0	Open Borehole P_{32}	Total Calculated r_0	Total Borehole P_{32}	Open Calculated r_0	Open Borehole P_{32}
ENE	Lower	0.18	1.38	0.65	0.48	0.15	1.60	0.91	0.37
NS	Lower	0.39	2.63	1.54	0.56	0.30	3.60	1.12	0.79
SH	Lower	0.11	4.62	0.24	1.50	0.14	3.40	0.33	0.93
WNW	Lower	0.03	2.67	0.16	0.84	0.04	1.97	0.30	0.55

Table 4-24. Coupled size/intensity parameters for the upper and lower fits, fractal alternative model.

Set	Fit Type	FSM_C				FSM_EW007			
		k_r	r_0	r_{max}	P_{32} (k_r,r_0,r_{max})	k_r	r_0	r_{max}	P_{32} (k_r,r_0,r_{max})
ENE	Upper	3.15	0.67	564.20	1.72	3.15	0.59	564.20	1.98
NS	Upper	3.41	1.28	564.20	2.33	3.41	1.08	564.20	2.96
SH	Upper	3.59	0.59	564.20	2.66	3.59	0.43	564.20	4.42
WNW	Upper	3.05	0.49	564.20	2.53	3.05	0.43	564.20	2.90
Set	**Fit Type**	**FSM_NE005**				**FSM_S**			
		k_r	r_0	r_{max}	P_{32} (k_r,r_0,r_{max})	k_r	r_0	r_{max}	P_{32} (k_r,r_0,r_{max})
ENE	Upper	3.15	0.71	564.20	1.60	3.15	0.30	564.20	4.28
NS	Upper	3.41	0.83	564.20	4.30	3.41	0.65	564.20	6.09
SH	Upper	3.59	0.53	564.20	3.17	3.59	0.44	564.20	4.22
WNW	Upper	3.05	0.53	564.20	2.37	3.05	0.24	564.20	5.39
Set	**Fit Type**	**FSM_N**				**FSM_W**			
		k_r	r_0	r_{max}	P_{32} (k_r,r_0,r_{max})	k_r	r_0	r_{max}	P_{32} (k_r,r_0,r_{max})
ENE	Upper	3.15	0.81	564.20	1.38	3.15	0.71	564.20	1.60
NS	Upper	3.41	1.18	564.20	2.63	3.41	0.94	564.20	3.60
SH	Upper	3.59	0.41	564.20	4.62	3.59	0.50	564.20	3.40
WNW	Upper	3.05	0.47	564.20	2.67	3.05	0.63	564.20	1.97
Set	**Fit Type**	**FSM_C**				**FSM_EW007**			
		k_r	r_0	r_{max}	P_{32} (k_r,r_0,r_{max})	k_r	r_0	r_{max}	P_{32} (k_r,r_0,r_{max})
ENE	Lower	2.82	0.14	564.20	1.72	2.82	0.12	564.20	1.98
NS	Lower	3.14	0.44	564.20	2.33	3.14	0.35	564.20	2.96
SH	Lower	3.45	0.16	564.20	2.66	3.45	0.11	564.20	4.42
WNW	Lower	2.67	0.03	564.20	2.53	2.67	0.03	564.20	2.90
Set	**Fit Type**	**FSM_NE005**				**FSM_S**			
		k_r	r_0	r_{max}	P_{32} (k_r,r_0,r_{max})	k_r	r_0	r_{max}	P_{32} (k_r,r_0,r_{max})
ENE	Lower	2.82	0.15	564.20	1.60	2.82	0.05	564.20	4.28
NS	Lower	3.14	0.26	564.20	4.30	3.14	0.19	564.20	6.09
SH	Lower	3.45	0.14	564.20	3.17	3.45	0.12	564.20	4.22
WNW	Lower	2.67	0.03	564.20	2.37	2.67	0.01	564.20	5.39
Set	**Fit Type**	**FSM_N**				**FSM_W**			
		k_r	r_0	r_{max}	P_{32} (k_r,r_0,r_{max})	k_r	r_0	r_{max}	P_{32} (k_r,r_0,r_{max})
ENE	Lower	2.82	0.18	564.20	1.38	2.82	0.15	564.20	1.60
NS	Lower	3.14	0.39	564.20	2.63	3.14	0.30	564.20	3.60
SH	Lower	3.45	0.11	564.20	4.62	3.45	0.14	564.20	3.40
WNW	Lower	2.67	0.03	564.20	2.67	2.67	0.04	564.20	1.97

Unlinked traces alternative models (BMU, EUL1, EUL2, BMUF, FUL1, and FUL2)

This alternative model utilizes the unlinked outcrop traces for the parameterization of the size/intensity scaling model. The hypothesis for this model is that it was inappropriate to link the outcrop traces, and that the unlinked traces truly do represent the actual size distribution of fractures. The unlinked traces alternative models are parameterised identically to the preliminary Base Model (Section 4.3.3), the best-fit Fractal model (Section 4.3.4), and the bounding cases for both the preliminary Base Model (Section 4.3.4, cases EL1 and EL2) and Fractal models (Section 4.3.3, cases BMF, FL1 and FL2). The only difference is that this alternative model substitutes unlinked traces for the linked traces. The trace length scaling plots are shown in Figure 4-30 through Figure 4-37. Values for the trace length scaling exponent for all of the unlinked trace alternative model cases are presented in Table 4-25. The tables summarizing the parameterization for the Euclidean unlinked trace model cases (BMU, EUL1, and EUL2) are presented in Table 4-27 and Table 4-31, while the parameterisation for the fractal unlinked model alternative cases (BMUF, FUL1, and FUL2) are presented in Table 4-29 and Table 4-33.

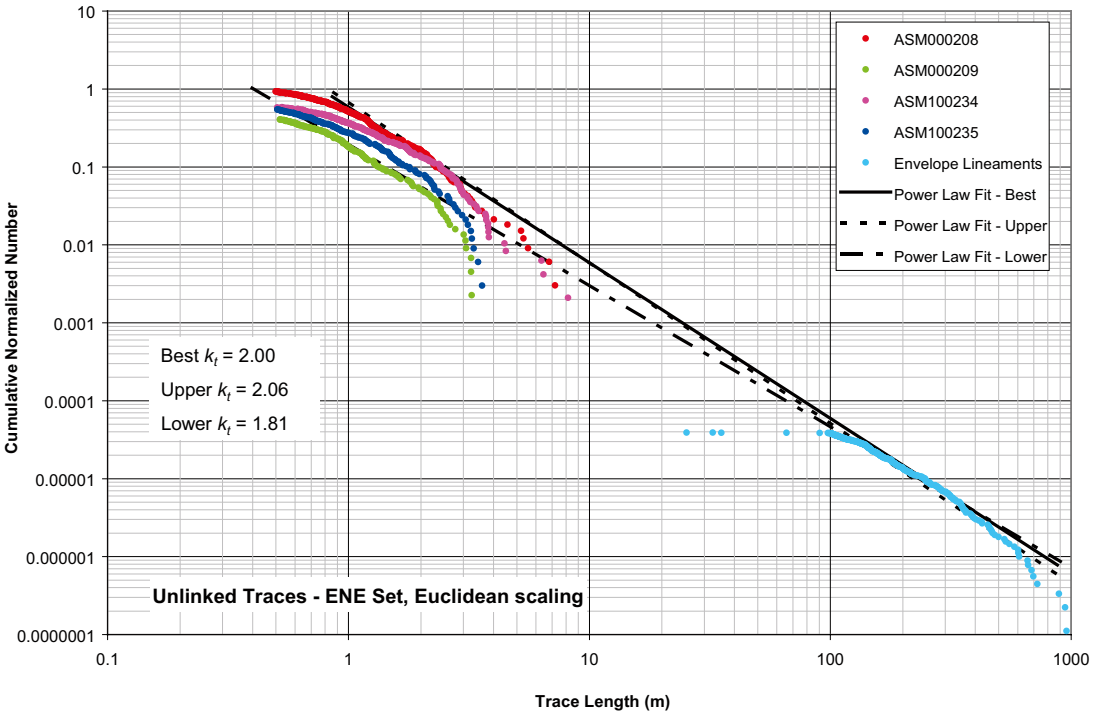

Figure 4-30. *CCN plot for ENE fracture set, unlinked traces alternative model, Euclidean scaling.*

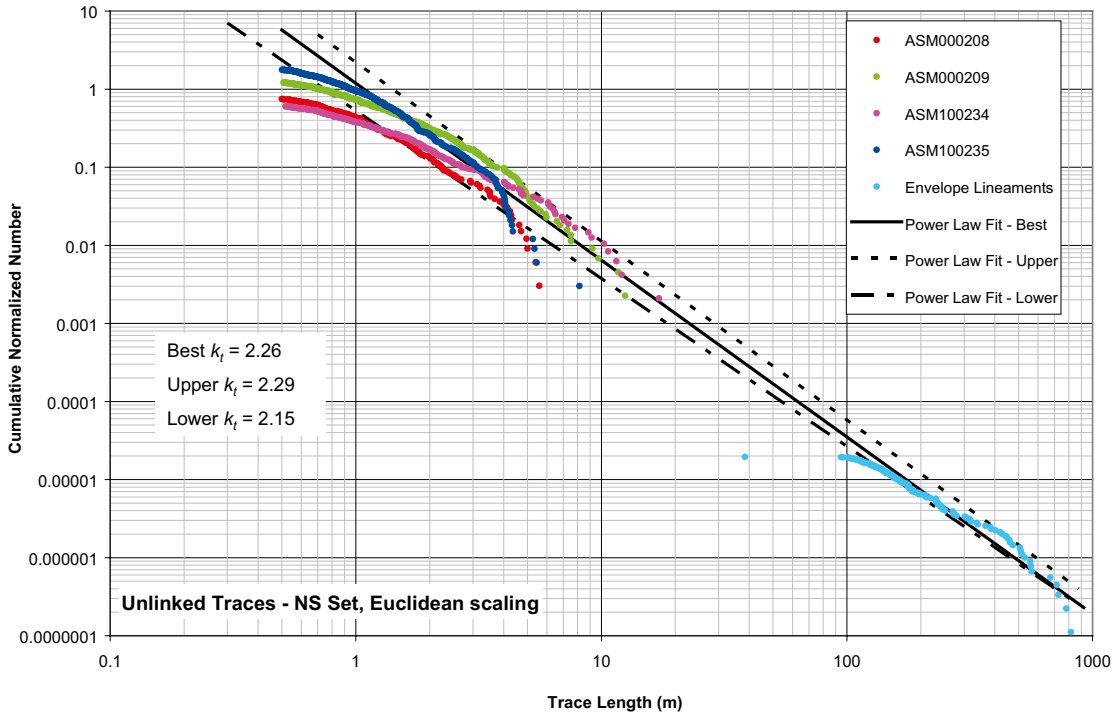

Figure 4-31. *CCN plot for NS fracture set, unlinked traces alternative model, Euclidean scaling.*

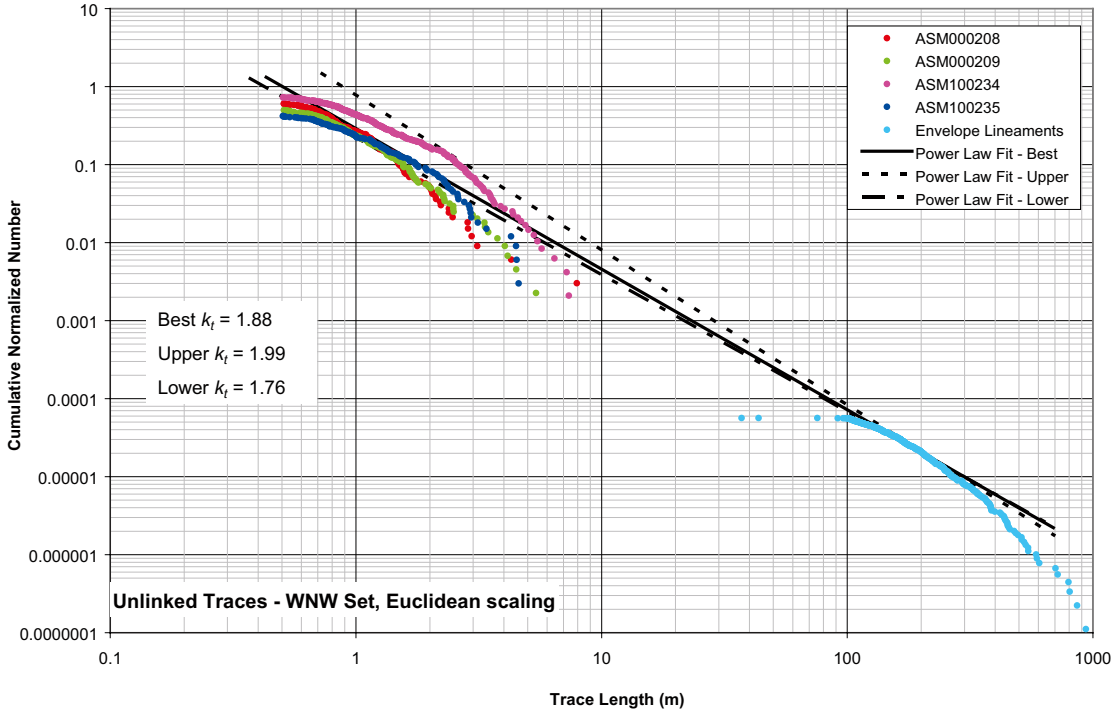

Figure 4-32. *CCN plot for WNW fracture set, unlinked traces alternative model, Euclidean scaling.*

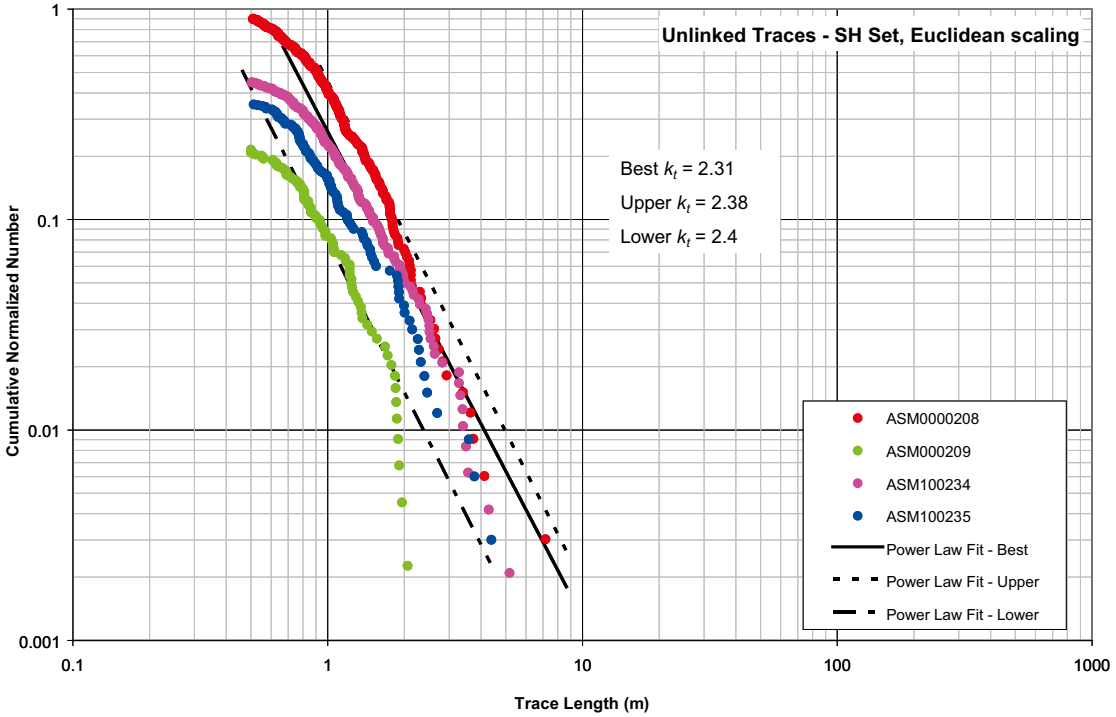

Figure 4-33. *CCN plot for SH fracture set, unlinked traces alternative model, Euclidean scaling.*

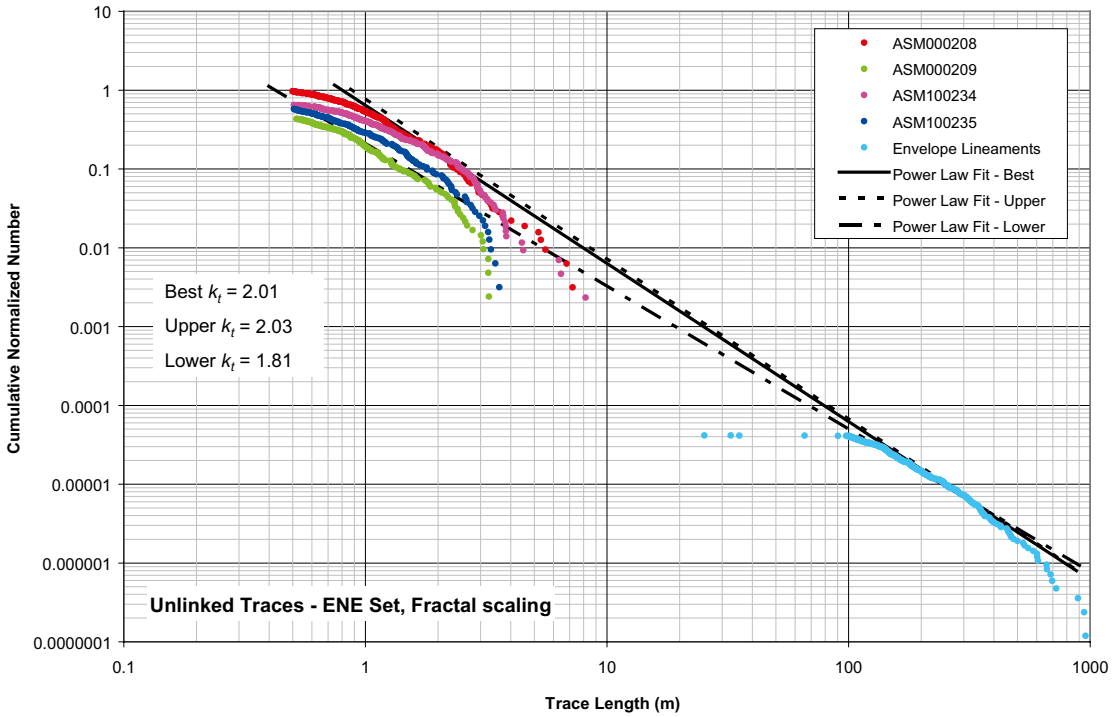

Figure 4-34. *CCN plot for ENE fracture set, unlinked traces alternative model, fractal scaling.*

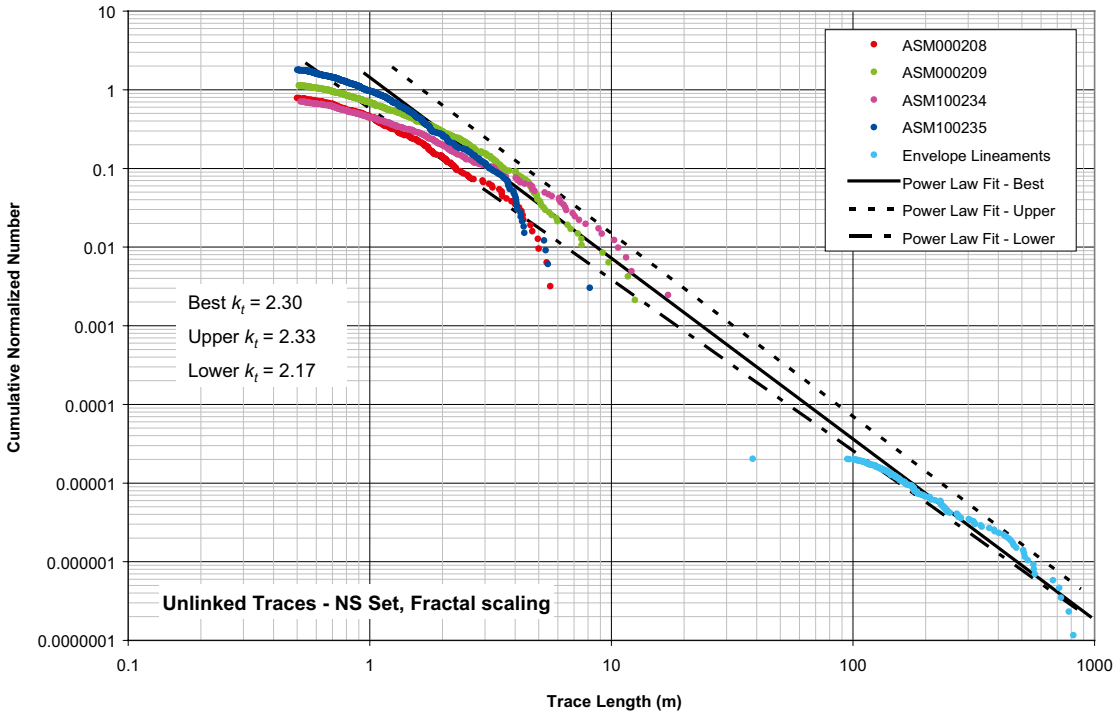

Figure 4-35. *CCN plot for N-S fracture set, unlinked traces alternative model, fractal scaling.*

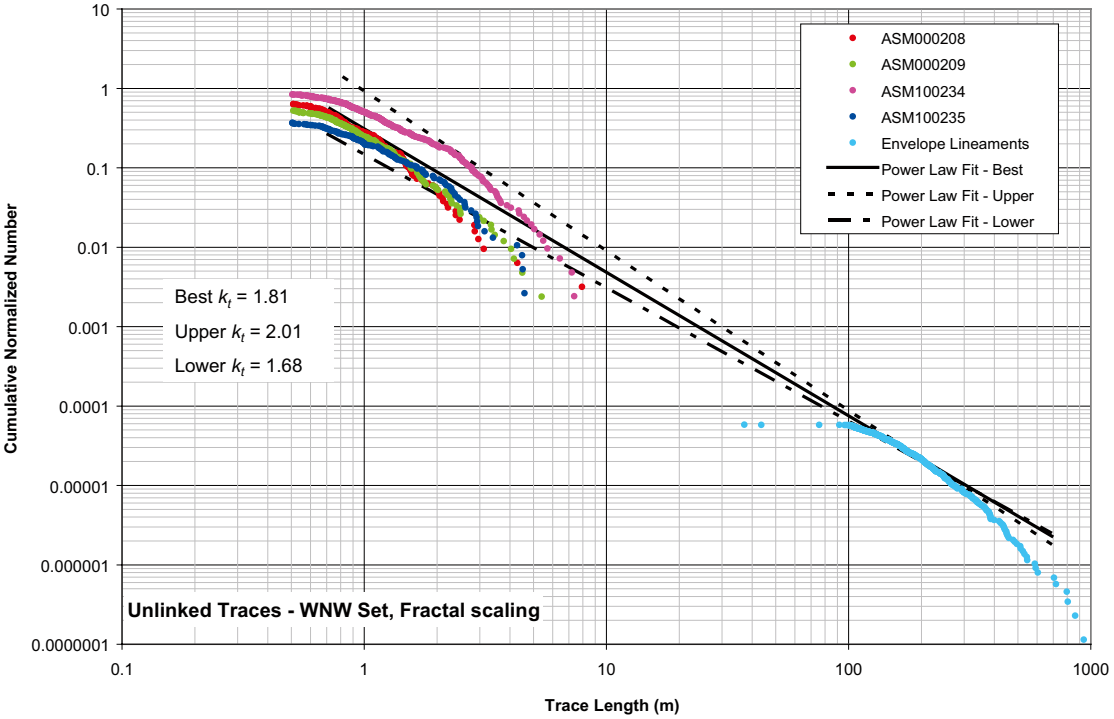

Figure 4-36. *CCN plot for WNW fracture set, unlinked traces alternative model, fractal scaling.*

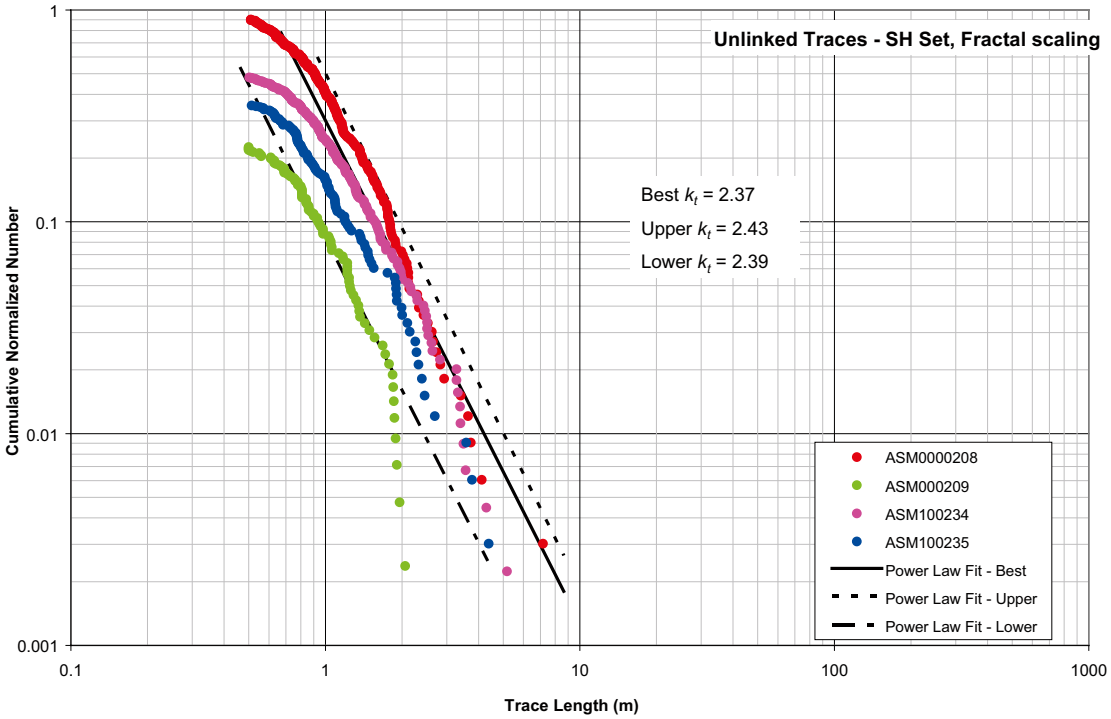

Figure 4-37. *CCN plot for SH fracture set, unlinked traces alternative model, fractal scaling.*

Table 4-25. Determination of trace length scaling exponent and associated simulated P_{32OC} fracture intensity for a minimum radius of 0.5 m for the unlinked traces alternative model. k_t is the exponent of the traces, while k_r is the exponent of the parent radius distribution.

Scaling	Fit Type	Set	Min. Radius (m)	k_t	k_r	P_{32OC}
Euclidean	Best	ENE	0.5	2.00	3.00	1.29
Euclidean	Upper	ENE	0.5	2.06	3.06	1.30
Euclidean	Lower	ENE	0.5	1.81	2.81	0.50
Euclidean	Best	NS	0.5	2.26	3.26	2.85
Euclidean	Upper	NS	0.5	2.29	3.29	6.00
Euclidean	Lower	NS	0.5	2.15	3.15	1.39
Euclidean	Best	SH	0.5	2.31	3.31	1.57
Euclidean	Upper	SH	0.5	2.38	3.38	2.88
Euclidean	Lower	SH	0.5	2.40	3.4	0.39
Euclidean	Best	WNW	0.5	1.80	2.8	0.60
Euclidean	Upper	WNW	0.5	1.99	2.99	1.95
Euclidean	Lower	WNW	0.5	1.76	2.76	0.83
Fractal	Best	ENE	0.5	2.01	3.01	1.40
Fractal	Upper	ENE	0.5	2.03	3.03	1.542
Fractal	Lower	ENE	0.5	1.81	2.81	0.35
Fractal	Best	NS	0.5	2.30	3.3	4.90
Fractal	Upper	NS	0.5	2.33	3.33	8.00
Fractal	Lower	NS	0.5	2.17	3.17	1.91
Fractal	Best	SH	0.5	2.37	3.37	1.38
Fractal	Upper	SH	0.5	2.43	3.43	2.65
Fractal	Lower	SH	0.5	2.39	3.39	0.41
Fractal	Best	WNW	0.5	1.81	2.81	0.75
Fractal	Upper	WNW	0.5	2.01	3.01	1.51
Fractal	Lower	WNW	0.5	1.68	2.68	0.34

Table 4-26. Summary of minimum radius by fracture domain, set, fit type and fracture type, unlinked traces alternative model, best fit, Euclidean scaling (BMU).

Set	Fit Type	FSM_C				FSM_EW007			
		Total Calculated r_0	Total Borehole P_{32}	Open Calculated r_0	Open Borehole P_{32}	Total Calculated r_0	Total Borehole P_{32}	Open Calculated r_0	Open Borehole P_{32}
ENE	Best	0.37	1.72	1.28	0.50	0.32	1.98	1.01	0.64
NS	Best	0.59	2.33	2.16	0.45	0.49	2.96	1.35	0.82
SH	Best	0.33	2.66	1.18	0.51	0.23	4.42	0.63	1.16
WNW	Best	0.08	2.53	0.36	0.77	0.07	2.90	0.23	1.11
Set	**Fit Type**	**FSM_NE005**				**FSM_S**			
		Total Calculated r_0	Total Borehole P_{32}	Open Calculated r_0	Open Borehole P_{32}	Total Calculated r_0	Total Borehole P_{32}	Open Calculated r_0	Open Borehole P_{32}
ENE	Best	0.40	1.60	1.42	0.45	0.15	4.28	0.50	1.30
NS	Best	0.36	4.30	1.41	0.78	0.27	6.09	0.85	1.45
SH	Best	0.29	3.17	0.73	0.96	0.23	4.22	0.52	1.50
WNW	Best	0.09	2.37	0.49	0.61	0.03	5.39	0.18	1.38
Set	**Fit Type**	**FSM_N**				**FSM_W**			
		Total Calculated r_0	Total Borehole P_{32}	Open Calculated r_0	Open Borehole P_{32}	Total Calculated r_0	Total Borehole P_{32}	Open Calculated r_0	Open Borehole P_{32}
ENE	Best	0.46	1.38	1.34	0.48	0.40	1.60	1.75	0.37
NS	Best	0.53	2.63	1.83	0.56	0.42	3.60	1.38	0.79
SH	Best	0.22	4.62	0.52	1.50	0.28	3.40	0.75	0.93
WNW	Best	0.08	2.67	0.33	0.84	0.11	1.97	0.56	0.55

Table 4-27. Couple size/intensity parameters for unlinked traces alternative model, best fit, Euclidean scaling (BMU).

Set	Fit Type	FSM_C				FSM_EW007			
		k_r	r_0	r_{max}	P_{32} (k_r,r_0,r_{max})	k_r	r_0	r_{max}	P_{32} (k_r,r_0,r_{max})
ENE	Best	3.00	0.37	564.20	1.72	3.00	0.32	564.20	1.98
NS	Best	3.26	0.59	564.20	2.33	3.26	0.49	564.20	2.96
SH	Best	3.31	0.33	564.20	2.66	3.31	0.23	564.20	4.42
WNW	Best	2.80	0.08	564.20	2.53	2.80	0.07	564.20	2.90
Set	**Fit Type**	**FSM_NE005**				**FSM_S**			
		k_r	r_0	r_{max}	P_{32} (k_r,r_0,r_{max})	k_r	r_0	r_{max}	P_{32} (k_r,r_0,r_{max})
ENE	Best	3.00	0.40	564.20	1.60	3.00	0.15	564.20	4.28
NS	Best	3.26	0.36	564.20	4.30	3.26	0.27	564.20	6.09
SH	Best	3.31	0.29	564.20	3.17	3.31	0.23	564.20	4.22
WNW	Best	2.80	0.09	564.20	2.37	2.80	0.03	564.20	5.39
Set	**Fit Type**	**FSM_N**				**FSM_W**			
		k_r	r_0	r_{max}	P_{32} (k_r,r_0,r_{max})	k_r	r_0	r_{max}	P_{32} (k_r,r_0,r_{max})
ENE	Best	3.00	0.46	564.20	1.38	3.00	0.40	564.20	1.60
NS	Best	3.26	0.53	564.20	2.63	3.26	0.42	564.20	3.60
SH	Best	3.31	0.22	564.20	4.62	3.31	0.28	564.20	3.40
WNW	Best	2.80	0.08	564.20	2.67	2.80	0.11	564.20	1.97

Table 4-28. Summary of minimum radius by fracture domain, set, fit type and fracture type, unlinked traces alternative model, best fit, fractal scaling (BMUF).

Set	Fit Type	FSM_C				FSM_EW007			
		Total Calculated r_0	Total Borehole P_{32}	Open Calculated r_0	Open Borehole P_{32}	Total Calculated r_0	Total Borehole P_{32}	Open Calculated r_0	Open Borehole P_{32}
ENE	Best	0.41	1.72	1.39	0.50	0.35	1.98	1.09	0.64
NS	Best	0.88	2.33	3.12	0.45	0.74	2.96	1.98	0.82
SH	Best	0.31	2.66	1.03	0.51	0.21	4.42	0.57	1.16
WNW	Best	0.11	2.53	0.48	0.77	0.09	2.90	0.31	1.11
Set	**Fit Type**	**FSM_NE005**				**FSM_S**			
		Total Calculated r_0	Total Borehole P_{32}	Open Calculated r_0	Open Borehole P_{32}	Total Calculated r_0	Total Borehole P_{32}	Open Calculated r_0	Open Borehole P_{32}
ENE	Best	0.44	1.60	1.53	0.45	0.17	4.28	0.54	1.30
NS	Best	0.55	4.30	2.06	0.78	0.42	6.09	1.27	1.45
SH	Best	0.27	3.17	0.65	0.96	0.22	4.22	0.47	1.50
WNW	Best	0.12	2.37	0.64	0.61	0.04	5.39	0.23	1.38
Set	**Fit Type**	**FSM_N**				**FSM_W**			
		Total Calculated r_0	Total Borehole P_{32}	Open Calculated r_0	Open Borehole P_{32}	Total Calculated r_0	Total Borehole P_{32}	Open Calculated r_0	Open Borehole P_{32}
ENE	Best	0.51	1.38	1.44	0.48	0.44	1.60	1.88	0.37
NS	Best	0.81	2.63	2.66	0.56	0.63	3.60	2.03	0.79
SH	Best	0.21	4.62	0.47	1.50	0.26	3.40	0.67	0.93
WNW	Best	0.10	2.67	0.43	0.84	0.15	1.97	0.73	0.55

Table 4-29. Couple size/intensity parameters for unlinked traces alternative model, best fit, fractal scaling (BMUF).

Set	Fit Type	FSM_C				FSM_EW007			
		k_r	r_0	r_{max}	P_{32} (k_r,r_0,r_{max})	k_r	r_0	r_{max}	P_{32} (k_r,r_0,r_{max})
ENE	Best	3.01	0.41	564.20	1.72	3.01	0.35	564.20	1.98
NS	Best	3.30	0.88	564.20	2.33	3.30	0.74	564.20	2.96
SH	Best	3.37	0.31	564.20	2.66	3.37	0.21	564.20	4.42
WNW	Best	2.81	0.11	564.20	2.53	2.81	0.09	564.20	2.90
Set	**Fit Type**	**FSM_NE005**				**FSM_S**			
		k_r	r_0	r_{max}	P_{32} (k_r,r_0,r_{max})	k_r	r_0	r_{max}	P_{32} (k_r,r_0,r_{max})
ENE	Best	3.01	0.44	564.20	1.60	3.01	0.17	564.20	4.28
NS	Best	3.30	0.55	564.20	4.30	3.30	0.42	564.20	6.09
SH	Best	3.37	0.27	564.20	3.17	3.37	0.22	564.20	4.22
WNW	Best	2.81	0.12	564.20	2.37	2.81	0.04	564.20	5.39
Set	**Fit Type**	**FSM_N**				**FSM_W**			
		k_r	r_0	r_{max}	P_{32} (k_r,r_0,r_{max})	k_r	r_0	r_{max}	P_{32} (k_r,r_0,r_{max})
ENE	Best	3.01	0.51	564.20	1.38	3.01	0.44	564.20	1.60
NS	Best	3.30	0.81	564.20	2.63	3.30	0.63	564.20	3.60
SH	Best	3.37	0.21	564.20	4.62	3.37	0.26	564.20	3.40
WNW	Best	2.81	0.10	564.20	2.67	2.81	0.15	564.20	1.97

Table 4-30. Summary of minimum radius by fracture domain, set, fit type and fracture type, unlinked traces alternative model, upper and lower fits, Euclidean scaling (EUL1 and EUL2).

Set	Fit Type	FSM_C				FSM_EW007			
		Total Calculated r_0	Total Borehole P_{32}	Open Calculated r_0	Open Borehole P_{32}	Total Calculated r_0	Total Borehole P_{32}	Open Calculated r_0	Open Borehole P_{32}
ENE	Upper	0.38	1.72	1.23	0.50	0.34	1.98	0.98	0.64
NS	Upper	1.04	2.33	3.71	0.45	0.86	2.96	2.35	0.82
SH	Upper	0.53	2.66	1.75	0.51	0.37	4.42	0.97	1.16
WNW	Upper	0.38	2.53	1.27	0.77	0.34	2.90	0.88	1.11

Set	Fit Type	FSM_NE005				FSM_S			
		Total Calculated r_0	Total Borehole P_{32}	Open Calculated r_0	Open Borehole P_{32}	Total Calculated r_0	Total Borehole P_{32}	Open Calculated r_0	Open Borehole P_{32}
ENE	Upper	0.41	1.60	1.35	0.45	0.16	4.28	0.50	1.30
NS	Upper	0.65	4.30	2.44	0.78	0.49	6.09	1.50	1.45
SH	Upper	0.47	3.17	1.11	0.96	0.38	4.22	0.80	1.50
WNW	Upper	0.41	2.37	1.61	0.61	0.18	5.39	0.71	1.38
Set	**Fit Type**	**FSM_N**				**FSM_W**			
		Total Calculated r_0	Total Borehole P_{32}	Open Calculated r_0	Open Borehole P_{32}	Total Calculated r_0	Total Borehole P_{32}	Open Calculated r_0	Open Borehole P_{32}
ENE	Upper	0.47	1.38	1.28	0.48	0.41	1.60	1.65	0.37
NS	Upper	0.95	2.63	3.16	0.56	0.74	3.60	2.40	0.79
SH	Upper	0.36	4.62	0.80	1.50	0.44	3.40	1.13	0.93
WNW	Upper	0.36	2.67	1.17	0.84	0.50	1.97	1.80	0.55
Set	**Fit Type**	**FSM_C**				**FSM_EW007**			
		Total Calculated r_0	Total Borehole P_{32}	Open Calculated r_0	Open Borehole P_{32}	Total Calculated r_0	Total Borehole P_{32}	Open Calculated r_0	Open Borehole P_{32}
ENE	Lower	0.11	1.72	0.50	0.50	0.09	1.98	0.37	0.64
NS	Lower	0.32	2.33	1.33	0.45	0.26	2.96	0.79	0.82
SH	Lower	0.13	2.66	0.41	0.51	0.09	4.42	0.23	1.16
WNW	Lower	0.12	2.53	0.55	0.77	0.10	2.90	0.34	1.11
Set	**Fit Type**	**FSM_NE005**				**FSM_S**			
		Total Calculated r_0	Total Borehole P_{32}	Open Calculated r_0	Open Borehole P_{32}	Total Calculated r_0	Total Borehole P_{32}	Open Calculated r_0	Open Borehole P_{32}
ENE	Lower	0.12	1.60	0.56	0.45	0.04	4.28	0.15	1.30
NS	Lower	0.19	4.30	0.83	0.78	0.14	6.09	0.48	1.45
SH	Lower	0.11	3.17	0.26	0.96	0.09	4.22	0.19	1.50
WNW	Lower	0.13	2.37	0.75	0.61	0.04	5.39	0.26	1.38
Set	**Fit Type**	**FSM_N**				**FSM_W**			
		Total Calculated r_0	Total Borehole P_{32}	Open Calculated r_0	Open Borehole P_{32}	Total Calculated r_0	Total Borehole P_{32}	Open Calculated r_0	Open Borehole P_{32}
ENE	Lower	0.14	1.38	0.52	0.48	0.12	1.60	0.73	0.37
NS	Lower	0.29	2.63	1.11	0.56	0.22	3.60	0.81	0.79
SH	Lower	0.08	4.62	0.19	1.50	0.11	3.40	0.27	0.93
WNW	Lower	0.11	2.67	0.49	0.84	0.16	1.97	0.86	0.55

Table 4-31. Couple size/intensity parameters for the unlinked traces alternative model, upper and lower fits, Euclidean scaling.

Set	Fit Type	FSM_C				FSM_EW007			
		k_r	r_0	r_{max}	P_{32} (k_r,r_0,r_{max})	k_r	r_0	r_{max}	P_{32} (k_r,r_0,r_{max})
ENE	Upper	3.06	0.38	564.20	1.72	3.06	0.34	564.20	1.98
NS	Upper	3.29	1.04	564.20	2.33	3.29	0.86	564.20	2.96
SH	Upper	3.38	0.53	564.20	2.66	3.38	0.37	564.20	4.42
WNW	Upper	2.99	0.38	564.20	2.53	2.99	0.34	564.20	2.90
Set	**Fit Type**	**FSM_NE005**				**FSM_S**			
		k_r	r_0	r_{max}	P_{32} (k_r,r_0,r_{max})	k_r	r_0	r_{max}	P_{32} (k_r,r_0,r_{max})
ENE	Upper	3.06	0.41	564.20	1.60	3.06	0.16	564.20	4.28
NS	Upper	3.29	0.65	564.20	4.30	3.29	0.49	564.20	6.09
SH	Upper	3.38	0.47	564.20	3.17	3.38	0.38	564.20	4.22
WNW	Upper	2.99	0.41	564.20	2.37	2.99	0.18	564.20	5.39
Set	**Fit Type**	**FSM_N**				**FSM_W**			
		k_r	r_0	r_{max}	P_{32} (k_r,r_0,r_{max})	k_r	r_0	r_{max}	P_{32} (k_r,r_0,r_{max})
ENE	Upper	3.06	0.47	564.20	1.38	3.06	0.41	564.20	1.60
NS	Upper	3.29	0.95	564.20	2.63	3.29	0.74	564.20	3.60
SH	Upper	3.38	0.36	564.20	4.62	3.38	0.44	564.20	3.40
WNW	Upper	2.99	0.36	564.20	2.67	2.99	0.50	564.20	1.97
Set	**Fit Type**	**FSM_C**				**FSM_EW007**			
		k_r	r_0	r_{max}	P_{32} (k_r,r_0,r_{max})	k_r	r_0	r_{max}	P_{32} (k_r,r_0,r_{max})
ENE	Lower	2.81	0.11	564.20	1.72	2.81	0.09	564.20	1.98
NS	Lower	3.15	0.32	564.20	2.33	3.15	0.26	564.20	2.96
SH	Lower	3.40	0.13	564.20	2.66	3.40	0.09	564.20	4.42
WNW	Lower	2.76	0.12	564.20	2.53	2.76	0.10	564.20	2.90
Set	**Fit Type**	**FSM_NE005**				**FSM_S**			
		k_r	r_0	r_{max}	P_{32} (k_r,r_0,r_{max})	k_r	r_0	r_{max}	P_{32} (k_r,r_0,r_{max})
ENE	Lower	2.81	0.12	564.20	1.60	2.81	0.04	564.20	4.28
NS	Lower	3.15	0.19	564.20	4.30	3.15	0.14	564.20	6.09
SH	Lower	3.40	0.11	564.20	3.17	3.40	0.09	564.20	4.22
WNW	Lower	2.76	0.13	564.20	2.37	2.76	0.04	564.20	5.39
Set	**Fit Type**	**FSM_N**				**FSM_W**			
		k_r	r_0	r_{max}	P_{32} (k_r,r_0,r_{max})	k_r	r_0	r_{max}	P_{32} (k_r,r_0,r_{max})
ENE	Lower	2.81	0.14	564.20	1.38	2.81	0.12	564.20	1.60
NS	Lower	3.15	0.29	564.20	2.63	3.15	0.22	564.20	3.60
SH	Lower	3.40	0.08	564.20	4.62	3.40	0.11	564.20	3.40
WNW	Lower	2.76	0.11	564.20	2.67	2.76	0.16	564.20	1.97

Table 4-32. Summary of minimum radius by fracture domain, set, fit type and fracture type, unlinked traces alternative model, upper and lower fits, fractal scaling (FUL1 and FUL2).

Set	Fit Type	FSM_C				FSM_EW007			
		Total Calculated r_0	Total Borehole P_{32}	Open Calculated r_0	Open Borehole P_{32}	Total Calculated r_0	Total Borehole P_{32}	Open Calculated r_0	Open Borehole P_{32}
ENE	Upper	0.45	1.72	1.49	0.50	0.39	1.98	1.18	0.64
NS	Upper	1.26	2.33	4.33	0.45	1.06	2.96	2.78	0.82
SH	Upper	0.50	2.66	1.58	0.51	0.35	4.42	0.89	1.16
WNW	Upper	0.30	2.53	0.97	0.77	0.26	2.90	0.68	1.11
Set	**Fit Type**	**FSM_NE005**				**FSM_S**			
		Total Calculated r_0	Total Borehole P_{32}	Open Calculated r_0	Open Borehole P_{32}	Total Calculated r_0	Total Borehole P_{32}	Open Calculated r_0	Open Borehole P_{32}
ENE	Upper	0.48	1.60	1.64	0.45	0.19	4.28	0.59	1.30
NS	Upper	0.80	4.30	2.89	0.78	0.61	6.09	1.80	1.45
SH	Upper	0.44	3.17	1.02	0.96	0.36	4.22	0.75	1.50
WNW	Upper	0.32	2.37	1.22	0.61	0.14	5.39	0.55	1.38
Set	**Fit Type**	**FSM_N**				**FSM_W**			
		Total Calculated r_0	Total Borehole P_{32}	Open Calculated r_0	Open Borehole P_{32}	Total Calculated r_0	Total Borehole P_{32}	Open Calculated r_0	Open Borehole P_{32}
ENE	Upper	0.56	1.38	1.55	0.48	0.48	1.60	2.01	0.37
NS	Upper	1.15	2.63	3.71	0.56	0.91	3.60	2.84	0.79
SH	Upper	0.34	4.62	0.74	1.50	0.42	3.40	1.04	0.93
WNW	Upper	0.28	2.67	0.89	0.84	0.38	1.97	1.36	0.55
Set	**Fit Type**	**FSM_C**				**FSM_EW007**			
		Total Calculated r_0	Total Borehole P_{32}	Open Calculated r_0	Open Borehole P_{32}	Total Calculated r_0	Total Borehole P_{32}	Open Calculated r_0	Open Borehole P_{32}
ENE	Lower	0.07	1.72	0.32	0.50	0.06	1.98	0.24	0.64
NS	Lower	0.42	2.33	1.71	0.45	0.34	2.96	1.03	0.82
SH	Lower	0.13	2.66	0.43	0.51	0.09	4.42	0.24	1.16
WNW	Lower	0.03	2.53	0.15	0.77	0.02	2.90	0.09	1.11

Set	Fit Type	FSM_NE005				FSM_S			
		Total Calculated r_0	Total Borehole P_{32}	Open Calculated r_0	Open Borehole P_{32}	Total Calculated r_0	Total Borehole P_{32}	Open Calculated r_0	Open Borehole P_{32}
ENE	Lower	0.08	1.60	0.36	0.45	0.02	4.28	0.10	1.30
NS	Lower	0.25	4.30	1.08	0.78	0.19	6.09	0.63	1.45
SH	Lower	0.11	3.17	0.27	0.96	0.09	4.22	0.20	1.50
WNW	Lower	0.03	2.37	0.21	0.61	0.01	5.39	0.06	1.38
Set	**Fit Type**	**FSM_N**				**FSM_W**			
		Total Calculated r_0	Total Borehole P_{32}	Open Calculated r_0	Open Borehole P_{32}	Total Calculated r_0	Total Borehole P_{32}	Open Calculated r_0	Open Borehole P_{32}
ENE	Lower	0.09	1.38	0.34	0.48	0.08	1.60	0.47	0.37
NS	Lower	0.38	2.63	1.43	0.56	0.29	3.60	1.06	0.79
SH	Lower	0.09	4.62	0.20	1.50	0.11	3.40	0.28	0.93
WNW	Lower	0.02	2.67	0.13	0.84	0.04	1.97	0.25	0.55

Table 4-33. Couple size/intensity parameters for the unlinked traces alternative model, upper and lower fits, fractal scaling.

Set	Fit Type	FSM_C				FSM_EW007			
		k_r	r_0	r_{max}	P_{32} (k_r,r_0,r_{max})	k_r	r_0	r_{max}	P_{32} (k_r,r_0,r_{max})
ENE	Upper	3.03	0.45	564.20	1.72	3.03	0.39	564.20	1.98
NS	Upper	3.33	1.26	564.20	2.33	3.33	1.06	564.20	2.96
SH	Upper	3.43	0.50	564.20	2.66	3.43	0.35	564.20	4.42
WNW	Upper	3.01	0.30	564.20	2.53	3.01	0.26	564.20	2.90
Set	**Fit Type**	**FSM_NE005**				**FSM_S**			
		k_r	r_0	r_{max}	P_{32} (k_r,r_0,r_{max})	k_r	r_0	r_{max}	P_{32} (k_r,r_0,r_{max})
ENE	Upper	3.03	0.48	564.20	1.60	3.03	0.19	564.20	4.28
NS	Upper	3.33	0.80	564.20	4.30	3.33	0.61	564.20	6.09
SH	Upper	3.43	0.44	564.20	3.17	3.43	0.36	564.20	4.22
WNW	Upper	3.01	0.32	564.20	2.37	3.01	0.14	564.20	5.39
Set	**Fit Type**	**FSM_N**				**FSM_W**			
		k_r	r_0	r_{max}	P_{32} (k_r,r_0,r_{max})	k_r	r_0	r_{max}	P_{32} (k_r,r_0,r_{max})
ENE	Upper	3.03	0.56	564.20	1.38	3.03	0.48	564.20	1.60
NS	Upper	3.33	1.15	564.20	2.63	3.33	0.91	564.20	3.60
SH	Upper	3.43	0.34	564.20	4.62	3.43	0.42	564.20	3.40
WNW	Upper	3.01	0.28	564.20	2.67	3.01	0.38	564.20	1.97
Set	**Fit Type**	**FSM_C**				**FSM_EW007**			
		k_r	r_0	r_{max}	P_{32} (k_r,r_0,r_{max})	k_r	r_0	r_{max}	P_{32} (k_r,r_0,r_{max})
ENE	Lower	2.81	0.07	564.20	1.72	2.81	0.06	564.20	1.98
NS	Lower	3.17	0.42	564.20	2.33	3.17	0.34	564.20	2.96
SH	Lower	3.39	0.13	564.20	2.66	3.39	0.09	564.20	4.42
WNW	Lower	2.68	0.03	564.20	2.53	2.68	0.02	564.20	2.90
Set	**Fit Type**	**FSM_NE005**				**FSM_S**			
		k_r	r_0	r_{max}	P_{32} (k_r,r_0,r_{max})	k_r	r_0	r_{max}	P_{32} (k_r,r_0,r_{max})
ENE	Lower	2.81	0.08	564.20	1.60	2.81	0.02	564.20	4.28
NS	Lower	3.17	0.25	564.20	4.30	3.17	0.19	564.20	6.09
SH	Lower	3.39	0.11	564.20	3.17	3.39	0.09	564.20	4.22
WNW	Lower	2.68	0.03	564.20	2.37	2.68	0.01	564.20	5.39
Set	**Fit Type**	**FSM_N**				**FSM_W**			
		k_r	r_0	r_{max}	P_{32} (k_r,r_0,r_{max})	k_r	r_0	r_{max}	P_{32} (k_r,r_0,r_{max})
ENE	Lower	2.81	0.09	564.20	1.38	2.81	0.08	564.20	1.60
NS	Lower	3.17	0.38	564.20	2.63	3.17	0.29	564.20	3.60
SH	Lower	3.39	0.09	564.20	4.62	3.39	0.11	564.20	3.40
WNW	Lower	2.68	0.02	564.20	2.67	2.68	0.04	564.20	1.97

Size/Intensity scaling exponent fracture domain dependent alternative model

These alternative models assume that the radius scaling exponent (k_r) depends on the fracture domain; the corollary is that fracture domains differ not in terms of the smallest fracture observed (the assumption of the Base Model), but in terms of the power-law distribution of fracture sizes (k_r). For this hypothesis to be consistent with the use of the Pareto distribution to describe fracture size, then if P_{32} are constant and the probability distribution minimum size (r_0) are constant, k_r must change. The fracture domain dependent model is not based on the calculation of r_0, but k_r. These alternative models are referred to as 'r_0-fixed' models and are similar to that used by the HydroDFN (i.e. the 'k_r-scaled' model) at Forsmark, where the radius scaling exponent of open, hydraulically-significant fractures is calculated entirely from borehole data /Follin et al. 2007/.

Equation 3-14 is used to calculate the values of k_r used in this alternative model. The workflow is as follows:

1. Using the minimum radius for the surface fracture traces (r_{min} = 0.5 m), the radius scaling exponent from the surface fracture traces and lineaments (k_r) and the value of P_{32OC} derived through simulation, Equation 3-14 is used to compute a new value of P_{32}; P_{32lin}. P_{32lin} represents the estimated intensity of lineament-sized features of radius 564.2 m and larger.
2. The minimum radius (r_{min}) for the fracture population in the cored borehole array is deemed to be 0.038 m; this is equal to the diameter of the cored boreholes used at Laxemar. As the geological DFN only makes use of fractures that cut completely across the drill core, this implies that the smallest fracture that is recorded in SICADA is a fracture exactly equal in radius to that of the cored borehole, oriented perpendicular to the core axis. Therefore, we make the assumption that $r_{min} = r_0 = 0.038$ m.
3. P_{32lin} is then used in conjunction with r_0 from the boreholes, along with the observed P_{32} of fractures in the boreholes, to compute the radius scaling exponent k_r, again using a restatement of Equation 3-14.

As the P_{32} of fractures in boreholes varies as a function of fracture domain, so too will the value of k_r calculated using this routine. Table 4-34 through Table 4-41 show the parameterisation for these alternative models as a function of fracture domain. The model acronyms shown below contain a placeholder for the fracture domain name. For example, the best fit model for FSM_N would be 'ESL1_N'. The basis for each of these parameterisations is as follows:

- Table 4-34: Euclidean scaling, linked traces, all fractures, best fit (ESL1_FSM*)
- Table 4-35: Euclidean scaling, linked traces, all fractures, bounding fits (ESL2_FSM* and ESL3_FSM*))
- Table 4-36: Fractal scaling, linked traces, all fractures, best fit (FSL1_FSM*)
- Table 4-37: Fractal scaling, linked traces, all fractures, bounding fits (FSL2_FSM* and FSL3_FSM*)
- Table 4-38: Euclidean scaling, unlinked traces, all fractures, best fit (EUSL1_FSM*)
- Table 4-39: Euclidean scaling, unlinked traces, all fractures, bounding fits (EUSL2_FSM* and EUSL3_FSM*)
- Table 4-40: Fractal scaling, unlinked traces, all fractures, best fit (FUSL1_FSM*)
- Table 4-41: Fractal scaling, unlinked traces, all fractures, bounding fits (FUSL2_FSM* and FUSL3_FSM*)

Table 4-34. Summary of size/intensity parameters for the domain-dependent scaling exponent alternative model, best fit (ESL1_FSM*).

All Fractures			FSM_C				FSM_EW007			
Scaling	Set	Fit Type	k_r	r_0	r_{max}	$P_{32}(k_r,r_0,r_{max})$	k_r	r_0	r_{max}	$P_{32}(k_r,r_0,r_{max})$
Euclidean	ENE	Best	2.76	0.038	564.2	1.72	2.78	0.038	564.2	1.98
Euclidean	NS	Best	2.87	0.038	564.2	2.33	2.89	0.038	564.2	2.96
Euclidean	SH	Best	3.07	0.038	564.2	2.66	3.12	0.038	564.2	4.42
Euclidean	WNW	Best	2.74	0.038	564.2	2.53	2.76	0.038	564.2	2.90
			FSM_N				FSM_NE005			
			k_r	r_0	r_{max}	$P_{32}(k_r,r_0,r_{max})$	k_r	r_0	r_{max}	$P_{32}(k_r,r_0,r_{max})$
Euclidean	ENE	Best	2.74	0.038	564.2	1.38	2.76	0.038	564.2	1.60
Euclidean	NS	Best	2.88	0.038	564.2	2.63	2.93	0.038	564.2	4.30
Euclidean	SH	Best	3.13	0.038	564.2	4.62	3.09	0.038	564.2	3.17
Euclidean	WNW	Best	2.75	0.038	564.2	2.67	2.74	0.038	564.2	2.37
			FSM_S				FSM_W			
			k_r	r_0	r_{max}	$P_{32}(k_r,r_0,r_{max})$	k_r	r_0	r_{max}	$P_{32}(k_r,r_0,r_{max})$
Euclidean	ENE	Best	2.86	0.038	564.2	4.28	2.76	0.038	564.2	1.60
Euclidean	NS	Best	2.97	0.038	564.2	6.09	2.91	0.038	564.2	3.60
Euclidean	SH	Best	3.12	0.038	564.2	4.22	3.09	0.038	564.2	3.40
Euclidean	WNW	Best	3.26	0.038	564.2	5.39	2.72	0.038	564.2	1.97

Table 4-35. Summary of size/intensity parameters for the domain-dependent scaling exponent alternative model, bounding envelope fits (ESL2_FSM* and ESL3_FSM*).

Scaling	Set	Fit Type	FSM_C				FSM_EW007			
			k_r	r_0	r_{max}	$P_{32}(k_r,r_0,r_{max})$	k_r	r_0	r_{max}	$P_{32}(k_r,r_0,r_{max})$
Euclidean	ENE	Lower	2.71	0.038	564.2	1.72	2.73	0.038	564.2	1.98
Euclidean	NS	Lower	2.97	0.038	564.2	2.33	2.99	0.038	564.2	2.96
Euclidean	SH	Lower	3.21	0.038	564.2	2.66	3.26	0.038	564.2	4.42
Euclidean	WNW	Lower	2.67	0.038	564.2	2.53	2.69	0.038	564.2	2.90
Scaling	Set	Fit Type	FSM_N				FSM_NE005			
			k_r	r_0	r_{max}	$P_{32}(k_r,r_0,r_{max})$	k_r	r_0	r_{max}	$P_{32}(k_r,r_0,r_{max})$
Euclidean	ENE	Lower	2.69	0.038	564.2	1.38	2.71	0.038	564.2	1.60
Euclidean	NS	Lower	2.98	0.038	564.2	2.63	3.03	0.038	564.2	4.30
Euclidean	SH	Lower	3.26	0.038	564.2	4.62	3.23	0.038	564.2	3.17
Euclidean	WNW	Lower	2.68	0.038	564.2	2.67	2.67	0.038	564.2	2.37
Scaling	Set	Fit Type	FSM_S				FSM_W			
			k_r	r_0	r_{max}	$P_{32}(k_r,r_0,r_{max})$	k_r	r_0	r_{max}	$P_{32}(k_r,r_0,r_{max})$
Euclidean	ENE	Lower	2.81	0.038	564.2	4.28	2.71	0.038	564.2	1.60
Euclidean	NS	Lower	3.07	0.038	564.2	6.09	3.01	0.038	564.2	3.60
Euclidean	SH	Lower	3.26	0.038	564.2	4.22	3.23	0.038	564.2	3.40
Euclidean	WNW	Lower	2.75	0.038	564.2	5.39	2.65	0.038	564.2	1.97

Scaling	Set	Fit Type	FSM_C				FSM_EW007			
			k_r	r_0	r_{max}	$P_{32}(k_r,r_0,r_{max})$	k_r	r_0	r_{max}	$P_{32}(k_r,r_0,r_{max})$
Euclidean	ENE	Upper	2.77	0.038	564.2	1.72	2.79	0.038	564.2	1.98
Euclidean	NS	Upper	2.90	0.038	564.2	2.33	2.93	0.038	564.2	2.96
Euclidean	SH	Upper	3.13	0.038	564.2	2.66	3.18	0.038	564.2	4.42
Euclidean	WNW	Upper	2.76	0.038	564.2	2.53	2.78	0.038	564.2	2.90
Scaling	**Set**	**Fit Type**	**FSM_N**				**FSM_NE005**			
			k_r	r_0	r_{max}	$P_{32}(k_r,r_0,r_{max})$	k_r	r_0	r_{max}	$P_{32}(k_r,r_0,r_{max})$
Euclidean	ENE	Upper	2.75	0.038	564.2	1.38	2.77	0.038	564.2	1.60
Euclidean	NS	Upper	2.92	0.038	564.2	2.63	2.97	0.038	564.2	4.30
Euclidean	SH	Upper	3.19	0.038	564.2	4.62	3.15	0.038	564.2	3.17
Euclidean	WNW	Upper	2.77	0.038	564.2	2.67	2.76	0.038	564.2	2.37
Scaling	**Set**	**Fit Type**	**FSM_S**				**FSM_W**			
			k_r	r_0	r_{max}	$P_{32}(k_r,r_0,r_{max})$	k_r	r_0	r_{max}	$P_{32}(k_r,r_0,r_{max})$
Euclidean	ENE	Upper	2.87	0.038	564.2	4.28	2.77	0.038	564.2	1.60
Euclidean	NS	Upper	3.00	0.038	564.2	6.09	2.95	0.038	564.2	3.60
Euclidean	SH	Upper	3.18	0.038	564.2	4.22	3.15	0.038	564.2	3.40
Euclidean	WNW	Upper	2.84	0.038	564.2	5.39	2.74	0.038	564.2	1.97

Table 4-36. Summary of size/intensity parameters for the domain-dependent scaling exponent alternative model, fractal scaling, best fit.

All Fractures			FSM_C				FSM_EW007			
Scaling	**Set**	**Fit Type**	k_r	r_0	r_{max}	$P_{32}(k_r,r_0,r_{max})$	k_r	r_0	r_{max}	$P_{32}(k_r,r_0,r_{max})$
Fractal	ENE	Best	2.76	0.038	564.2	1.72	2.77	0.038	564.2	1.98
Fractal	NS	Best	2.87	0.038	564.2	2.33	2.90	0.038	564.2	2.96
Fractal	SH	Best	3.08	0.038	564.2	2.66	3.13	0.038	564.2	4.42
Fractal	WNW	Best	2.73	0.038	564.2	2.53	2.75	0.038	564.2	2.90
			FSM_N				**FSM_NE005**			
			k_r	r_0	r_{max}	$P_{32}(k_r,r_0,r_{max})$	k_r	r_0	r_{max}	$P_{32}(k_r,r_0,r_{max})$
Fractal	ENE	Best	2.74	0.038	564.2	1.38	2.75	0.038	564.2	1.60
Fractal	NS	Best	2.88	0.038	564.2	2.63	2.94	0.038	564.2	4.30
Fractal	SH	Best	3.13	0.038	564.2	4.62	3.09	0.038	564.2	3.17
Fractal	WNW	Best	2.74	0.038	564.2	2.67	2.73	0.038	564.2	2.37
			FSM_S				**FSM_W**			
			k_r	r_0	r_{max}	$P_{32}(k_r,r_0,r_{max})$	k_r	r_0	r_{max}	$P_{32}(k_r,r_0,r_{max})$
Fractal	ENE	Best	2.85	0.038	564.2	4.28	2.75	0.038	564.2	1.60
Fractal	NS	Best	2.97	0.038	564.2	6.09	2.92	0.038	564.2	3.60
Fractal	SH	Best	3.12	0.038	564.2	4.22	3.10	0.038	564.2	3.40
Fractal	WNW	Best	2.81	0.038	564.2	5.39	2.71	0.038	564.2	1.97

Table 4-37. Summary of size/intensity parameters for the domain-dependent scaling exponent alternative model, fractal scaling, bounding envelope fits (FSL2_FSM* and FSL3_FSM*).

Scaling	Set	Fit Type	FSM_C				FSM_EW007			
			k_r	r_0	r_{max}	$P_{32}(k_r,r_0,r_{max})$	k_r	r_0	r_{max}	$P_{32}(k_r,r_0,r_{max})$
Fractal	ENE	Lower	2.71	0.038	564.2	1.72	2.72	0.038	564.2	1.98
Fractal	NS	Lower	2.85	0.038	564.2	2.33	2.88	0.038	564.2	2.96
Fractal	SH	Lower	3.23	0.038	564.2	2.66	3.29	0.038	564.2	4.42
Fractal	WNW	Lower	2.68	0.038	564.2	2.53	2.70	0.038	564.2	2.90
Scaling	**Set**	**Fit Type**	**FSM_N**				**FSM_NE005**			
			k_r	r_0	r_{max}	$P_{32}(k_r,r_0,r_{max})$	k_r	r_0	r_{max}	$P_{32}(k_r,r_0,r_{max})$
Fractal	ENE	Lower	2.69	0.038	564.2	1.38	2.70	0.038	564.2	1.60
Fractal	NS	Lower	2.86	0.038	564.2	2.63	2.91	0.038	564.2	4.30
Fractal	SH	Lower	3.29	0.038	564.2	4.62	3.25	0.038	564.2	3.17
Fractal	WNW	Lower	2.69	0.038	564.2	2.67	2.68	0.038	564.2	2.37
Scaling	**Set**	**Fit Type**	**FSM_S**				**FSM_W**			
			k_r	r_0	r_{max}	$P_{32}(k_r,r_0,r_{max})$	k_r	r_0	r_{max}	$P_{32}(k_r,r_0,r_{max})$
Fractal	ENE	Lower	2.80	0.038	564.2	4.28	2.70	0.038	564.2	1.60
Fractal	NS	Lower	2.95	0.038	564.2	6.09	2.90	0.038	564.2	3.60
Fractal	SH	Lower	3.28	0.038	564.2	4.22	3.26	0.038	564.2	3.40
Fractal	WNW	Lower	2.76	0.038	564.2	5.39	2.66	0.038	564.2	1.97
Scaling	**Set**	**Fit Type**	**FSM_C**				**FSM_EW007**			
			k_r	r_0	r_{max}	$P_{32}(k_r,r_0,r_{max})$	k_r	r_0	r_{max}	$P_{32}(k_r,r_0,r_{max})$
Fractal	ENE	Upper	2.81	0.038	564.2	1.72	2.82	0.038	564.2	1.98
Fractal	NS	Upper	2.89	0.038	564.2	2.33	2.92	0.038	564.2	2.96
Fractal	SH	Upper	3.14	0.038	564.2	2.66	3.19	0.038	564.2	4.42
Fractal	WNW	Upper	2.77	0.038	564.2	2.53	2.78	0.038	564.2	2.90
Scaling	**Set**	**Fit Type**	**FSM_N**				**FSM_NE005**			
			k_r	r_0	r_{max}	$P_{32}(k_r,r_0,r_{max})$	k_r	r_0	r_{max}	$P_{32}(k_r,r_0,r_{max})$
Fractal	ENE	Upper	2.78	0.038	564.2	1.38	2.80	0.038	564.2	1.60
Fractal	NS	Upper	2.91	0.038	564.2	2.63	2.96	0.038	564.2	4.30
Fractal	SH	Upper	3.19	0.038	564.2	4.62	3.16	0.038	564.2	3.17
Fractal	WNW	Upper	2.78	0.038	564.2	2.67	2.76	0.038	564.2	2.37
Scaling	**Set**	**Fit Type**	**FSM_S**				**FSM_W**			
			k_r	r_0	r_{max}	$P_{32}(k_r,r_0,r_{max})$	k_r	r_0	r_{max}	$P_{32}(k_r,r_0,r_{max})$
Fractal	ENE	Upper	2.90	0.038	564.2	4.28	2.80	0.038	564.2	1.60
Fractal	NS	Upper	2.99	0.038	564.2	6.09	2.94	0.038	564.2	3.60
Fractal	SH	Upper	3.19	0.038	564.2	4.22	3.16	0.038	564.2	3.40
Fractal	WNW	Upper	2.85	0.038	564.2	5.39	2.74	0.038	564.2	1.97

Table 4-38. Summary of size/intensity parameters for the domain-dependent scaling exponent alternative model, unlinked traces, best fit (EUSL1_FSM*).

All Fractures			FSM_C				FSM_EW007			
Scaling	Set	Fit Type	k_r	r_0	r_{max}	$P_{32}(k_r,r_0,r_{max})$	k_r	r_0	r_{max}	$P_{32}(k_r,r_0,r_{max})$
Euclidean	ENE	Best	2.76	0.038	564.2	1.72	2.78	0.038	564.2	1.98
Euclidean	NS	Best	2.90	0.038	564.2	2.33	2.93	0.038	564.2	2.96
Euclidean	SH	Best	3.01	0.038	564.2	2.66	3.07	0.038	564.2	4.42
Euclidean	WNW	Best	2.73	0.038	564.2	2.53	2.75	0.038	564.2	2.90
			FSM_N				FSM_NE005			
			k_r	r_0	r_{max}	$P_{32}(k_r,r_0,r_{max})$	k_r	r_0	r_{max}	$P_{32}(k_r,r_0,r_{max})$
Euclidean	ENE	Best	2.74	0.038	564.2	1.38	2.75	0.038	564.2	1.60
Euclidean	NS	Best	2.91	0.038	564.2	2.63	2.96	0.038	564.2	4.30
Euclidean	SH	Best	3.07	0.038	564.2	4.62	3.03	0.038	564.2	3.17
Euclidean	WNW	Best	2.74	0.038	564.2	2.67	2.73	0.038	564.2	2.37
			FSM_S				FSM_W			
			k_r	r_0	r_{max}	$P_{32}(k_r,r_0,r_{max})$	k_r	r_0	r_{max}	$P_{32}(k_r,r_0,r_{max})$
Euclidean	ENE	Best	2.86	0.038	564.2	4.28	2.75	0.038	564.2	1.60
Euclidean	NS	Best	3.00	0.038	564.2	6.09	2.95	0.038	564.2	3.60
Euclidean	SH	Best	3.06	0.038	564.2	4.22	3.04	0.038	564.2	3.40
Euclidean	WNW	Best	2.81	0.038	564.2	5.39	2.71	0.038	564.2	1.97

Table 4-39. Summary of size/intensity parameters for the domain-dependent scaling exponent alternative model, unlinked traces, bounding envelope fits (EUSL2_FSM* & EUSL3_FSM*).

Scaling	Set	Fit Type	FSM_C				FSM_EW007			
			k_r	r_0	r_{max}	$P_{32}(k_r,r_0,r_{max})$	k_r	r_0	r_{max}	$P_{32}(k_r,r_0,r_{max})$
Euclidean	ENE	Lower	2.72	0.038	564.2	1.72	2.74	0.038	564.2	1.98
Euclidean	NS	Lower	2.90	0.038	564.2	2.33	2.92	0.038	564.2	2.96
Euclidean	SH	Lower	3.23	0.038	564.2	2.66	3.28	0.038	564.2	4.42
Euclidean	WNW	Lower	2.67	0.038	564.2	2.53	2.69	0.038	564.2	2.90
Scaling	**Set**	**Fit Type**	**FSM_N**				**FSM_NE005**			
			k_r	r_0	r_{max}	$P_{32}(k_r,r_0,r_{max})$	k_r	r_0	r_{max}	$P_{32}(k_r,r_0,r_{max})$
Euclidean	ENE	Lower	2.70	0.038	564.2	1.38	2.71	0.038	564.2	1.60
Euclidean	NS	Lower	2.91	0.038	564.2	2.63	2.96	0.038	564.2	4.30
Euclidean	SH	Lower	3.28	0.038	564.2	4.62	3.24	0.038	564.2	3.17
Euclidean	WNW	Lower	2.68	0.038	564.2	2.67	2.66	0.038	564.2	2.37
Scaling	**Set**	**Fit Type**	**FSM_S**				**FSM_W**			
			k_r	r_0	r_{max}	$P_{32}(k_r,r_0,r_{max})$	k_r	r_0	r_{max}	$P_{32}(k_r,r_0,r_{max})$
Euclidean	ENE	Lower	2.82	0.038	564.2	4.28	2.71	0.038	564.2	1.60
Euclidean	NS	Lower	3.00	0.038	564.2	6.09	2.94	0.038	564.2	3.60
Euclidean	SH	Lower	3.27	0.038	564.2	4.22	3.25	0.038	564.2	3.40
Euclidean	WNW	Lower	2.75	0.038	564.2	5.39	2.65	0.038	564.2	1.97

Scaling	Set	Fit Type	FSM_C				FSM_EW007			
			k_r	r_0	r_{max}	$P_{32}(k_r,r_0,r_{max})$	k_r	r_0	r_{max}	$P_{32}(k_r,r_0,r_{max})$
Euclidean	ENE	Upper	2.80	0.038	564.2	1.72	2.82	0.038	564.2	1.98
Euclidean	NS	Upper	2.85	0.038	564.2	2.33	2.87	0.038	564.2	2.96
Euclidean	SH	Upper	3.00	0.038	564.2	2.66	3.05	0.038	564.2	4.42
Euclidean	WNW	Upper	2.75	0.038	564.2	2.53	2.77	0.038	564.2	2.90
Scaling	**Set**	**Fit Type**	**FSM_N**				**FSM_NE005**			
			k_r	r_0	r_{max}	$P_{32}(k_r,r_0,r_{max})$	k_r	r_0	r_{max}	$P_{32}(k_r,r_0,r_{max})$
Euclidean	ENE	Upper	2.78	0.038	564.2	1.38	2.80	0.038	564.2	1.60
Euclidean	NS	Upper	2.86	0.038	564.2	2.63	2.91	0.038	564.2	4.30
Euclidean	SH	Upper	3.06	0.038	564.2	4.62	3.02	0.038	564.2	3.17
Euclidean	WNW	Upper	2.76	0.038	564.2	2.67	2.74	0.038	564.2	2.37
Scaling	**Set**	**Fit Type**	**FSM_S**				**FSM_W**			
			k_r	r_0	r_{max}	$P_{32}(k_r,r_0,r_{max})$	k_r	r_0	r_{max}	$P_{32}(k_r,r_0,r_{max})$
Euclidean	ENE	Upper	2.90	0.038	564.2	4.28	2.80	0.038	564.2	1.60
Euclidean	NS	Upper	2.95	0.038	564.2	6.09	2.89	0.038	564.2	3.60
Euclidean	SH	Upper	3.05	0.038	564.2	4.22	3.03	0.038	564.2	3.40
Euclidean	WNW	Upper	2.83	0.038	564.2	5.39	2.73	0.038	564.2	1.97

Table 4-40. Summary of size/intensity parameters for the domain-dependent scaling exponent alternative model, unlinked traces, best fit, fractal scaling (FUSL1_FSM*).

All Fractures			FSM_C				FSM_EW007			
Scaling	**Set**	**Fit Type**	k_r	r_0	r_{max}	$P_{32}(k_r,r_0,r_{max})$	k_r	r_0	r_{max}	$P_{32}(k_r,r_0,r_{max})$
Fractal	ENE	Best	2.76	0.038	564.2	1.72	2.78	0.038	564.2	1.98
Fractal	NS	Best	2.87	0.038	564.2	2.33	2.90	0.038	564.2	2.96
Fractal	SH	Best	3.07	0.038	564.2	2.66	3.12	0.038	564.2	4.42
Fractal	WNW	Best	2.72	0.038	564.2	2.53	2.73	0.038	564.2	2.90
			FSM_N				**FSM_NE005**			
			k_r	r_0	r_{max}	$P_{32}(k_r,r_0,r_{max})$	k_r	r_0	r_{max}	$P_{32}(k_r,r_0,r_{max})$
Fractal	ENE	Best	2.74	0.038	564.2	1.38	2.75	0.038	564.2	1.60
Fractal	NS	Best	2.89	0.038	564.2	2.63	2.94	0.038	564.2	4.30
Fractal	SH	Best	3.13	0.038	564.2	4.62	3.09	0.038	564.2	3.17
Fractal	WNW	Best	2.72	0.038	564.2	2.67	2.71	0.038	564.2	2.37
			FSM_S				**FSM_W**			
			k_r	r_0	r_{max}	$P_{32}(k_r,r_0,r_{max})$	k_r	r_0	r_{max}	$P_{32}(k_r,r_0,r_{max})$
Fractal	ENE	Best	2.86	0.038	564.2	4.28	2.75	0.038	564.2	1.60
Fractal	NS	Best	2.97	0.038	564.2	6.09	2.92	0.038	564.2	3.60
Fractal	SH	Best	3.12	0.038	564.2	4.22	3.10	0.038	564.2	3.40
Fractal	WNW	Best	2.80	0.038	564.2	5.39	2.69	0.038	564.2	1.97

Table 4-41. Summary of size/intensity parameters for the domain-dependent scaling exponent alternative model, unlinked traces, bounding envelope fits. fractal scaling (FUSL2_FSM* & FUSL3_FSM*).

Scaling	Set	Fit Type	FSM_C				FSM_EW007			
			k_r	r_0	r_{max}	$P_{32}(k_r,r_0,r_{max})$	k_r	r_0	r_{max}	$P_{32}(k_r,r_0,r_{max})$
Fractal	ENE	Lower	2.76	0.038	564.2	1.72	2.77	0.038	564.2	1.98
Fractal	NS	Lower	2.84	0.038	564.2	2.33	2.87	0.038	564.2	2.96
Fractal	SH	Lower	3.05	0.038	564.2	2.66	3.10	0.038	564.2	4.42
Fractal	WNW	Lower	2.71	0.038	564.2	2.53	2.72	0.038	564.2	2.90
Scaling	**Set**	**Fit Type**	**FSM_N**				**FSM_NE005**			
			k_r	r_0	r_{max}	$P_{32}(k_r,r_0,r_{max})$	k_r	r_0	r_{max}	$P_{32}(k_r,r_0,r_{max})$
Fractal	ENE	Lower	2.74	0.038	564.2	1.38	2.75	0.038	564.2	1.60
Fractal	NS	Lower	2.86	0.038	564.2	2.63	2.91	0.038	564.2	4.30
Fractal	SH	Lower	3.10	0.038	564.2	4.62	3.06	0.038	564.2	3.17
Fractal	WNW	Lower	2.71	0.038	564.2	2.67	2.70	0.038	564.2	2.37
Scaling	**Set**	**Fit Type**	**FSM_S**				**FSM_W**			
			k_r	r_0	r_{max}	$P_{32}(k_r,r_0,r_{max})$	k_r	r_0	r_{max}	$P_{32}(k_r,r_0,r_{max})$
Fractal	ENE	Lower	2.85	0.038	564.2	4.28	2.75	0.038	564.2	1.60
Fractal	NS	Lower	2.94	0.038	564.2	6.09	2.89	0.038	564.2	3.60
Fractal	SH	Lower	3.09	0.038	564.2	4.22	3.07	0.038	564.2	3.40
Fractal	WNW	Lower	2.78	0.038	564.2	5.39	2.68	0.038	564.2	1.97
Scaling	**Set**	**Fit Type**	**FSM_C**				**FSM_EW007**			
			k_r	r_0	r_{max}	$P_{32}(k_r,r_0,r_{max})$	k_r	r_0	r_{max}	$P_{32}(k_r,r_0,r_{max})$
Fractal	ENE	Upper	2.76	0.038	564.2	1.72	2.78	0.038	564.2	1.98
Fractal	NS	Upper	2.88	0.038	564.2	2.33	2.90	0.038	564.2	2.96
Fractal	SH	Upper	3.21	0.038	564.2	2.66	3.26	0.038	564.2	4.42
Fractal	WNW	Upper	2.79	0.038	564.2	2.53	2.81	0.038	564.2	2.90
Scaling	**Set**	**Fit Type**	**FSM_N**				**FSM_NE005**			
			k_r	r_0	r_{max}	$P_{32}(k_r,r_0,r_{max})$	k_r	r_0	r_{max}	$P_{32}(k_r,r_0,r_{max})$
Fractal	ENE	Upper	2.74	0.038	564.2	1.38	2.76	0.038	564.2	1.60
Fractal	NS	Upper	2.89	0.038	564.2	2.63	2.94	0.038	564.2	4.30
Fractal	SH	Upper	3.27	0.038	564.2	4.62	3.23	0.038	564.2	3.17
Fractal	WNW	Upper	2.80	0.038	564.2	2.67	2.79	0.038	564.2	2.37
Scaling	**Set**	**Fit Type**	**FSM_S**				**FSM_W**			
			k_r	r_0	r_{max}	$P_{32}(k_r,r_0,r_{max})$	k_r	r_0	r_{max}	$P_{32}(k_r,r_0,r_{max})$
Fractal	ENE	Upper	2.86	0.038	564.2	4.28	2.76	0.038	564.2	1.60
Fractal	NS	Upper	2.98	0.038	564.2	6.09	2.92	0.038	564.2	3.60
Fractal	SH	Upper	3.26	0.038	564.2	4.22	3.24	0.038	564.2	3.40
Fractal	WNW	Upper	2.87	0.038	564.2	5.39	2.77	0.038	564.2	1.97

4.4 Spatial model

These analyses consider both borehole and outcrop data. The first step in quantifying the spatial pattern of fracturing is to calculate the mass dimension (Section 3.6.1). The analyses focus on individual sets rather than all sets combined. Borehole results are presented first, followed by outcrop results. The purpose of the mass dimension calculations is to determine if either a Euclidean or a fractal spatial model is appropriate.

Results from the mass dimension calculations indicated that there might be a transition from fractal scaling at scales less than a few tens of meters to Euclidean scaling at larger scales. In order to investigate this possibility, an additional set of analyses was carried out on the borehole data subsequent to the mass dimension calculations. These calculations are described after the mass dimension calculations for both boreholes and outcrops.

4.4.1 Borehole mass dimension calculations

Figure 4-38 through Figure 4-41 show the mass dimension calculations for each of the four sets for borehole data. The individual values for each borehole are plotted in blue, while the mean values of all of the data are shown as red circles. The black dashed line is for reference; it has a slope of 1.0, which represents Euclidean scaling.

The results for individual borehole segments are expressed as aligned chain of blue dots, extending from interval values of around 1 m to about 200 m. Both the mean values and the individual borehole segment values start at slopes somewhat shallower than 1.0, but attain a slope of 1.0 at scales between 10 m and 30 m, particularly for the three vertical sets. The shallower slopes prior to the onset of Euclidean scaling may reflect non-Euclidean scaling at these smaller scales, or it may be due to an artefact related to fracture spacing. For intervals smaller than the smallest spacing between measured fractures, the number of fracture contained in an interval is 1.0, and continues to be 1.0 no matter how much smaller the interval becomes. Thus, for intervals equal to or smaller than the minimum spacing, the number of fractures (the Y-value in the plots) is 1.0 and the points describe a horizontal line. As this minimum spacing is approached, the slope of the data continuously changes from its value at large scales to a slope of 1.0. This type of change is quite evident in the plots. Mean fracture spacing for the borehole fractures is on the order of a few metres, which is consistent with the scales over which the data do not show a constant slope.

The subhorizontal set (Figure 4-41) also shows an orange line fit visually to the data. This line has a slope of around 0.9. The orange line is a better fit to the mean data than the Euclidean line, even at scales greater than 30 m. However, further inspection of this figure also shows that the individual blue lines at interval scales greater than 30 m have a much steeper slope than the orange line, and in fact, are quite close to the black line and Euclidean scaling.

4.4.2 Outcrop mass dimension calculations

The mass dimensions for each set and outcrop were calculated. The mass dimension plots for the detailed fracture outcrop maps are contained in Appendix D. Table 4-42 summarizes the calculations for each set at each of the four Laxemar outcrops. A value of $D_m = 2.0$ indicates Euclidean scaling.

This table shows that many of the sets approximate Euclidean scaling. For example, with the exception of the fractures exposed on outcrop ASM000209, the subhorizontal set has mass dimensions of 2.00, 2.02 and 1.99. The parameters SSQ (Sum of Squares) and SE (Standard Error) are measures of how well the power law model with the given ρ and D_m fit the data.

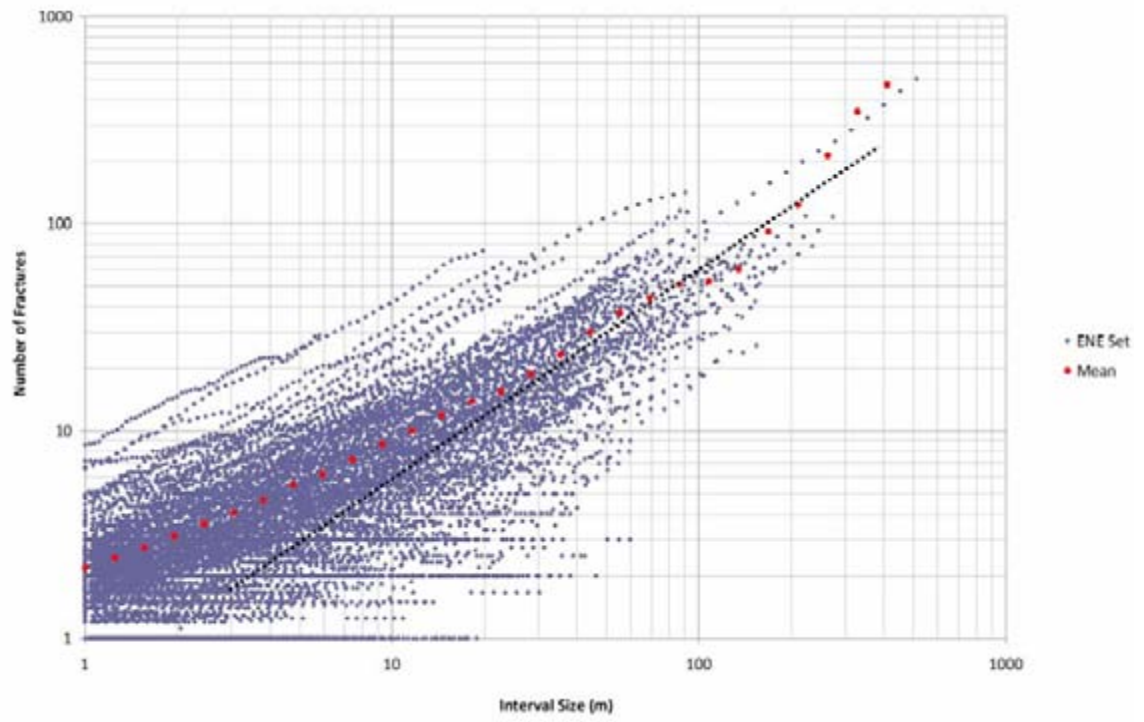

Figure 4-38. *Mass dimension analysis for ENE set from all fracture data outside of mapped deformation zones. Red circles are the mean values; the dashed line has a slope of 1.0.*

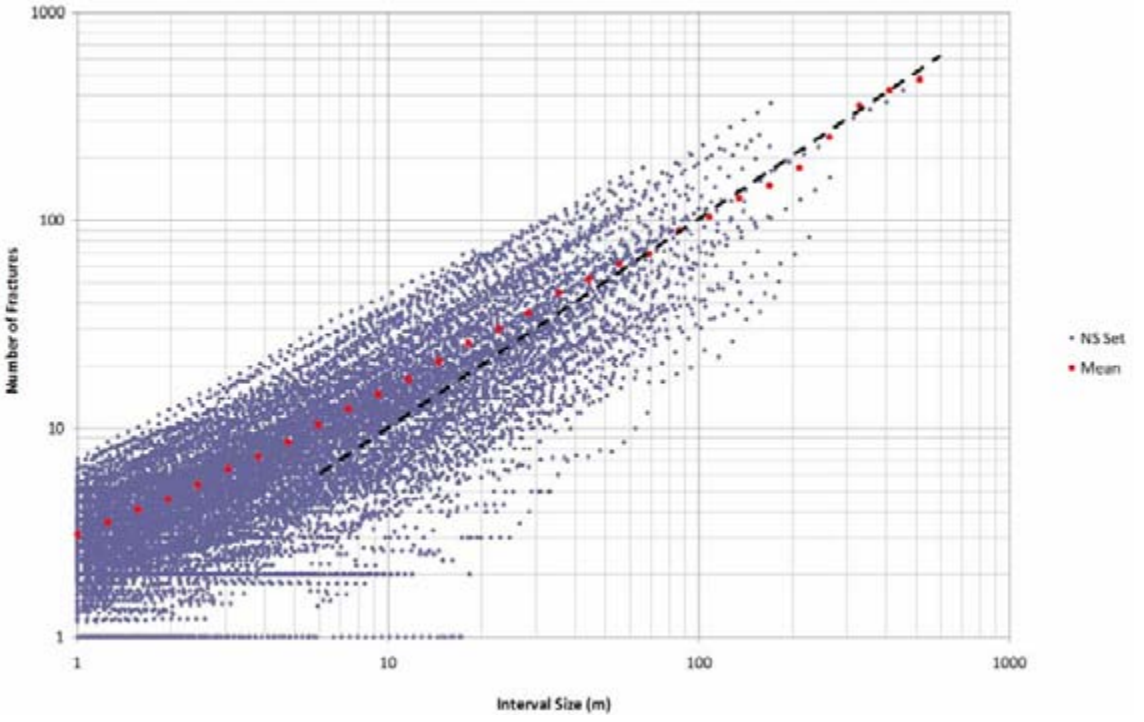

Figure 4-39. *Mass dimension analysis for N-S set from all fracture data outside of mapped deformation zones. Red circles are the mean values; the dashed line has a slope of 1.0.*

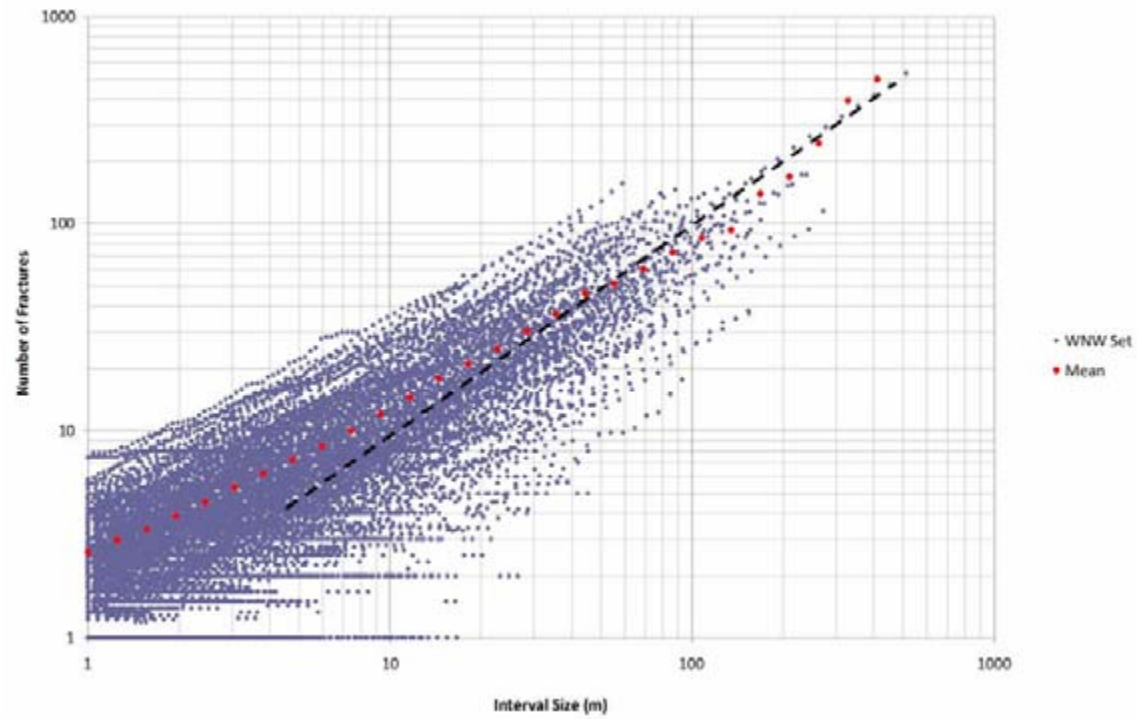

Figure 4-40. *Mass dimension analysis for WNW set from all fracture data outside of mapped deformation zones. Red circles are the mean values; the dashed line has a slope of 1.0.*

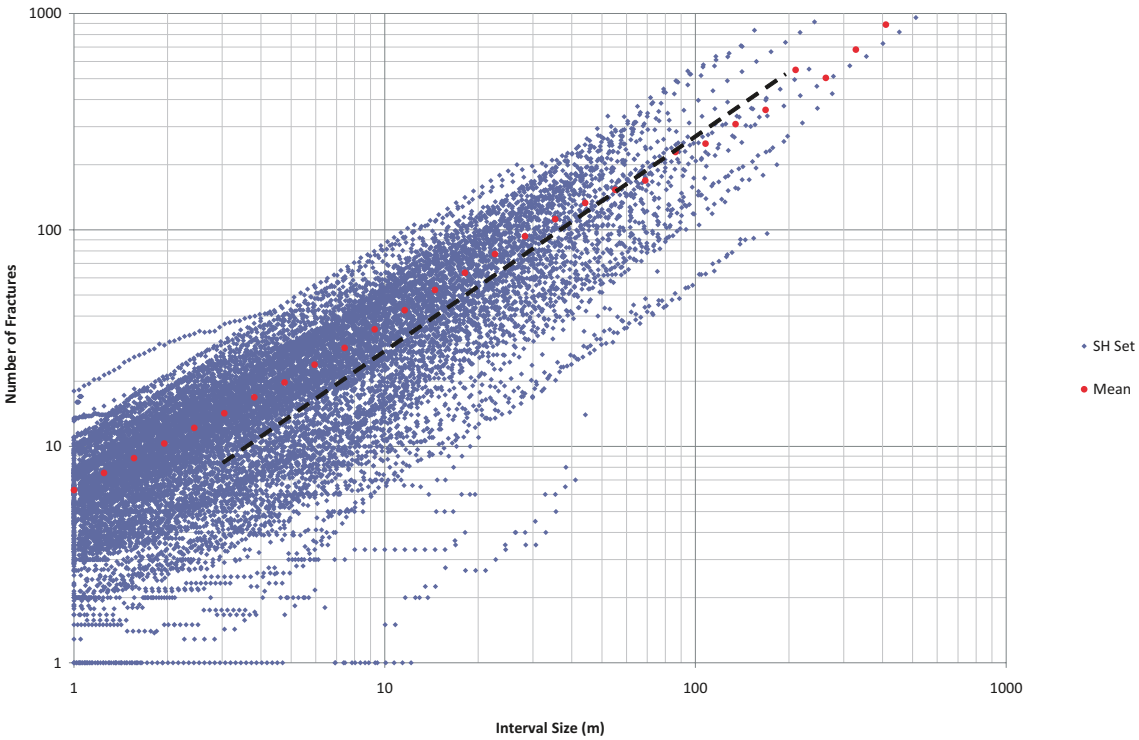

Figure 4-41. *Mass dimension analysis for SH set from all fracture data outside of mapped deformation zones. Red circles are the mean values; the dashed line has a slope of 1.0.*

Table 4-42. Summary of mass dimension calculations for outcrops at Laxemar. SSQ = sum of squares; SE = standard error.

Outcrop	Set	ρ	D_m	SSQ	SE
ASM000208	ENE	9.37	1.93	1.372E+04	44.28
ASM000208	NS	7.90	1.91	3.389E+04	69.59
ASM000208	SH	8.80	2.00	2.160E+04	65.73
ASM000208	WNW	6.10	1.92	1.030E+06	22.55
ASM000209	ENE	8.61	1.76	6.259E+04	6.12
ASM000209	NS	17.20	1.97	7.149E+05	19.90
ASM000209	SH	3.50	1.78	4.246E+04	5.07
ASM000209	WNW	8.44	1.77	4.037E+05	16.00
ASM100234	ENE	12.10	1.95	7.430E+06	60.82
ASM100234	NS	17.89	1.85	6.700E+06	57.02
ASM100234	SH	7.40	2.02	2.058E+07	100.16
ASM100234	WNW	14.47	1.89	1.044E+07	71.19
ASM100235	ENE	13.80	1.91	7.550E+06	62.80
ASM100235	NS	30.12	1.98	4.167E+07	145.62
ASM100235	SH	4.70	1.99	1.710E+06	29.76
ASM100235	WNW	7.02	2.23*	1.930E+07	97.94

* Note that for this outcrop, the mass dimension suggests a fractal dimension exceeding the topological dimension. The mass dimension describes, over a particular range of scales, how mass increases or decreases with scale. There is no inherent reason that mass cannot increase with scale, although the physics of the phenomenon might make this impossible. For fractures, a dimension greater than the Euclidean dimension means that mass, or in this case the number of fractures, increases with scale. Only if the number of fractures decreases will the exponent be less than the Euclidean dimension. While it is true that a mass dimension exponent greater than the Euclidean dimension would render the object non-fractal, it does not violate any mathematical constraint, and it is not obviously violating any physical constraint concerning fracturing that is obvious.

Overall, the mass dimension values for the outcrop data suggest Euclidean or mildly fractal scaling over the scale ranges that were possible to quantify. Scales larger than the outcrops could not be investigated, so the results shown in the table are relevant to scales no larger than a few tens of metres at the most. However, the fact that the mass dimension results are Euclidean or nearly so in this scale range is consistent with the results from the borehole data, and suggest that Euclidean scaling and Poissonian spatial location are adequate models for characterizing the fracture intensity data at scales greater than 10–30 m, and may even be appropriate for smaller scales.

4.4.3 Additional investigations of possible fractal/Euclidean scaling transition

The apparent fractal or non-Euclidean aspect of fracture intensity at scales below a few tens of metres could be due to several causes. One explanation is that the spatial pattern is indeed non-Euclidean below these scales. Another explanation is that it is due to artefacts in the mass dimension calculation methodology. Additional analyses of the fracture spacings in boreholes makes it possible to select from these two alternative explanations, as certain spatial models imply certain spacing probability distributions. For example, a Poisson point process along a line leads to an exponential spacing probability distribution. A fractal process along a line leads to a power law spacing probability distribution.

Figure 4-42 through Figure 4-45 show the spacing distributions for each set and alternative exponential, power law, Gamma and Weibull distributions fit to the data. An examination of fracture spacings by set shows that a power law model is a poor fit to the measured data. Of the remaining three alternative models, the Weibull distribution best matches the measured spacing distributions for each set (Table 4-43).

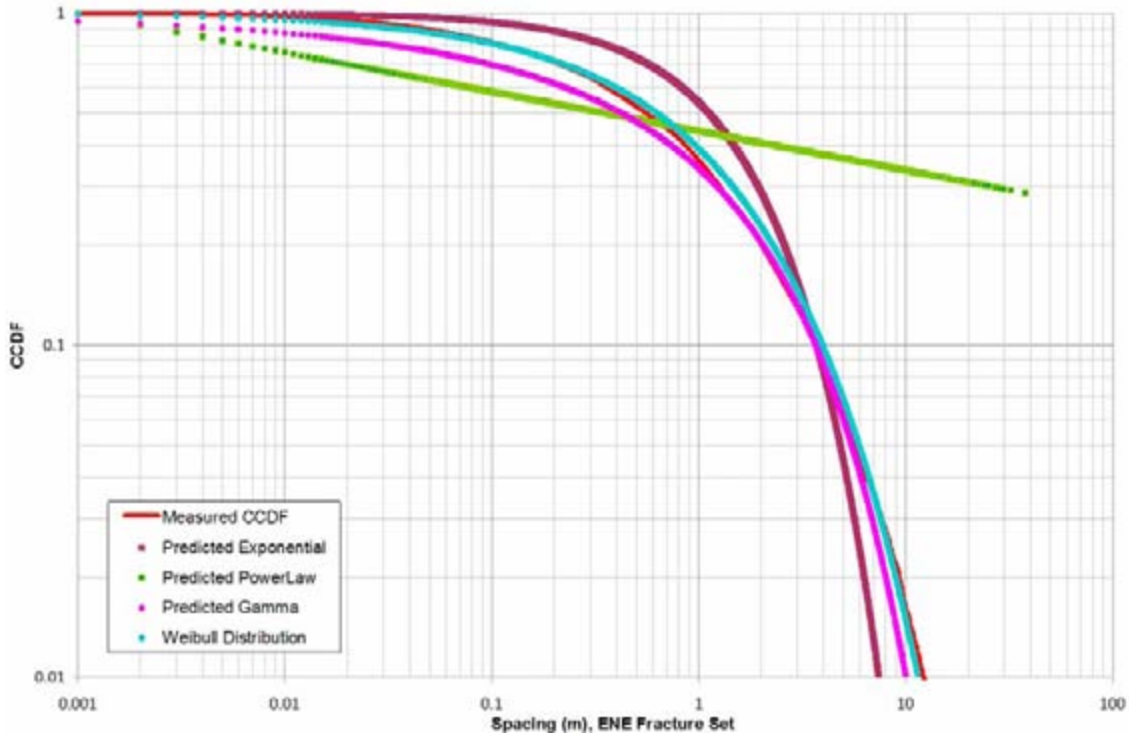

Figure 4-42. *CCDF of spacings for ENE Set.*

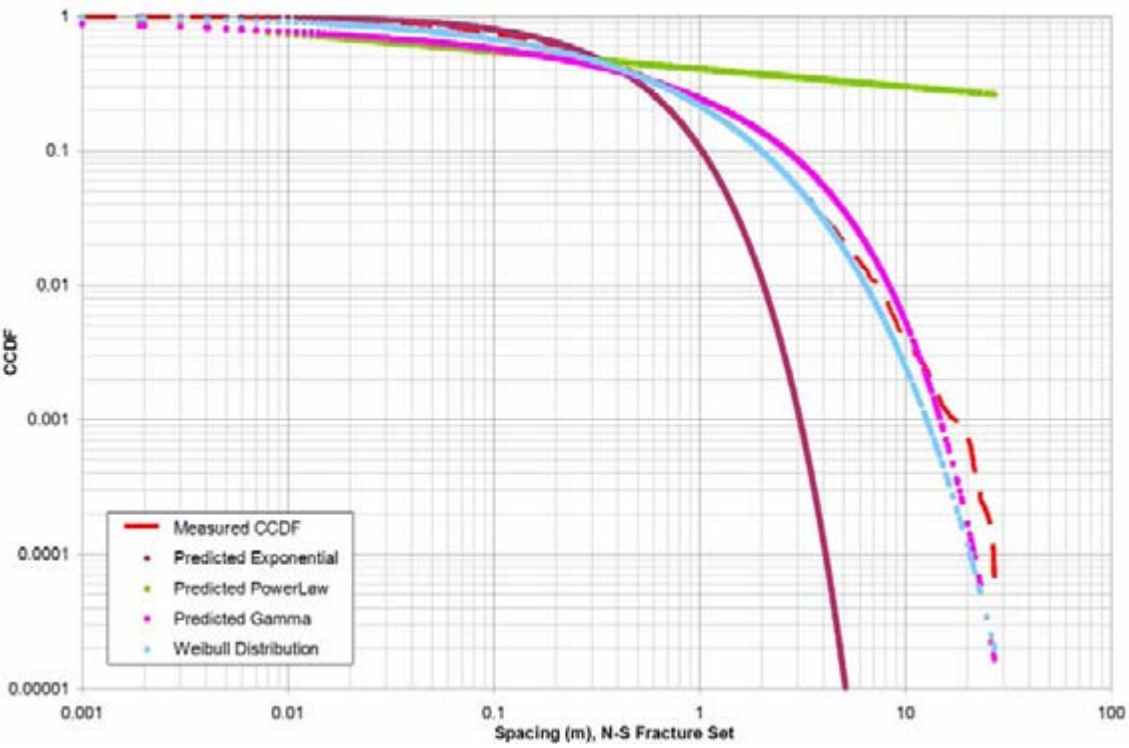

Figure 4-43. *CCDF of spacings for N-S set.*

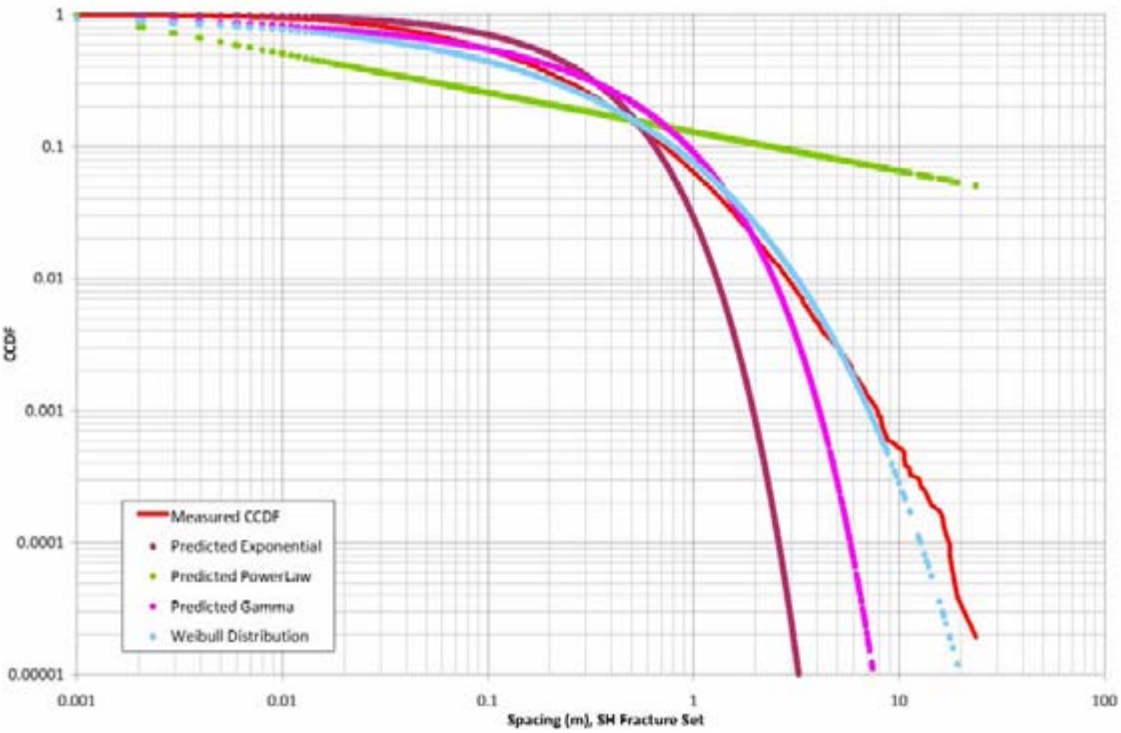

Figure 4-44. *CCDF of spacings for SH Set.*

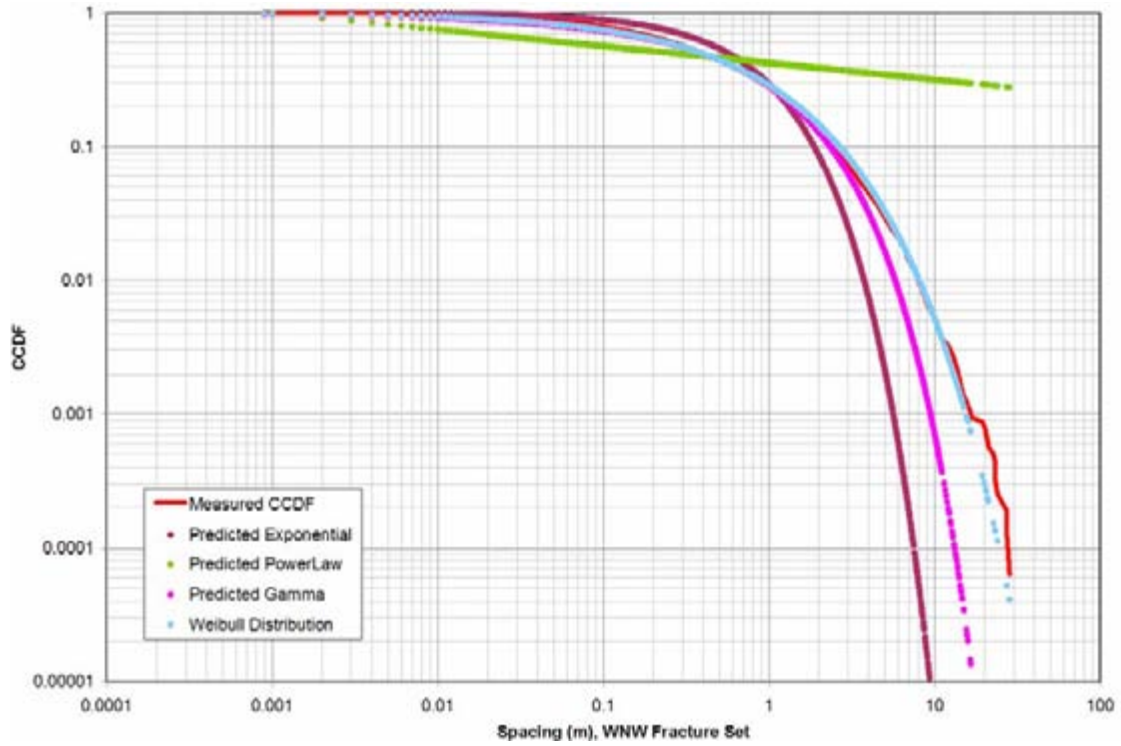

Figure 4-45. *CCDF of spacings for WNW Set.*

Table 4-43. Summary of spacing distribution fits for fracture sets. SSQ is the sums of squares of the deviations between the measured CCDF value and the theoretical fit value.

Set	Exponential (lambda, SSQ)	Power law (minimum size, exponent, SSQ)	Gamma (alpha, beta, SSQ)	Weibull (alpha, beta, SSQ)
ENE	0.62, 1,317.7	0.001, 0.12, 1,813	0.37, 3.46, 587.4	0.65, 1.1, 199.4
NS	2.25, 851.6	0.001, 0.13, 3,315.2	0.27, 3.3, 1,909.5	0.59, 0.49, 723.1
SH	3.54, 181.2	0.001, 0.3, 895.4	0.42, 0.8, 304.5	0.5, 0.15, 249.3
WNW	1.23, 602	0.001, 0.12, 2,733.1	0.49, 1.75, 418.3	0.62, 0.7, 357.3

A Weibull distribution can be produced when a material fails according to a "weakest-link" model /Weibull1951/. Such a model implies that the strength of a material with flaws will decrease with specimen size, as the probability for a weak flaw increases with specimen volume. Many failures of brittle materials forms through a cascade of branching cracks (see, for example, /Brown and Wohletz 1995/, and these cracks form "trees" with scale-invariant or fractal properties. /Iacopino 1996/ showed how the Weibull distribution of failure derives from an assumption that the initial flaws in a material (fracture initiation points, which can be though of as fracture centres, assuming radial symmetric growth) are distributed following a Poisson spatial point process.

Therefore, it is possible for a pattern of flaws (fractures) to have a Poissonian spatial distribution, that, through macroscopic fractal branching processes following a weak-link mechanism, which gives rise to a fracture pattern over time that has 1) Poissonian spatial arrangement; 2) fractal size characteristics; and 3) Weibull spacing characteristics. This overall model is consistent with fracture spatial, size and spacing data obtained at Laxemar, and together with the mass dimension results, indicates that a Poissonian spatial model is probably the most self-consistent model for fracturing at Laxemar over all scales of interest.

Investigation of fracture systems characterised by Weibull spacing distributions, fractal size distributions and Poissonian spatial patterns

The Weibull fracture spacing model might seem inconsistent with the fact that mathematically, the Poissonian point processes in space or time should give rise to gaps whose spacing follows an exponential distribution. It may also seem inconsistent with experiments and theory that show that non-linear self-organizing processes, such as material fracture and failure, have intertwined size, spatial and other characteristics that are all described by power law distributions /Bak et al. 1987/. To further investigate the possibility of a fracture system having a Poissonian spatial distribution, a power law size distribution, and a spacing distribution best described by a Weibull distribution, a series of benchmark simulations were carried out.

The benchmark simulation fracture set consisted of circular planar fractures oriented horizontally. The intensity of the fracture system, expressed as P_{32}, was set to 0.1 m^2/m^3. The fractures size distribution followed a power law, with a radius scaling exponent (k_r) equal to 2.0 (Pareto exponent = 3.0), and a minimum size (r_0) of 1 m. The fractures were generated within a region measuring 2,000 m in horizontal extent, and 200 m in vertical extent. Fracture centres were located randomly within the generation region using the enhanced Baecher model, which is an implementation of a 3D Poisson point process /Dershowitz et al. 1998/. Ten vertical boreholes were constructed inside the simulation region at random locations. The fracture intersections were recorded in the boreholes, and from this the fracture spacing distributions were calculated.

Alternative spacing distribution models were fit to the data. The alternative models and the measured spacing data are expressed as the complementary cumulative probability on doubly logarithmic axes. On this type of graph, a power law spacing distribution will define a straight line, making it very easy to distinguish from other distributions. The results are shown in Figure 4-46.

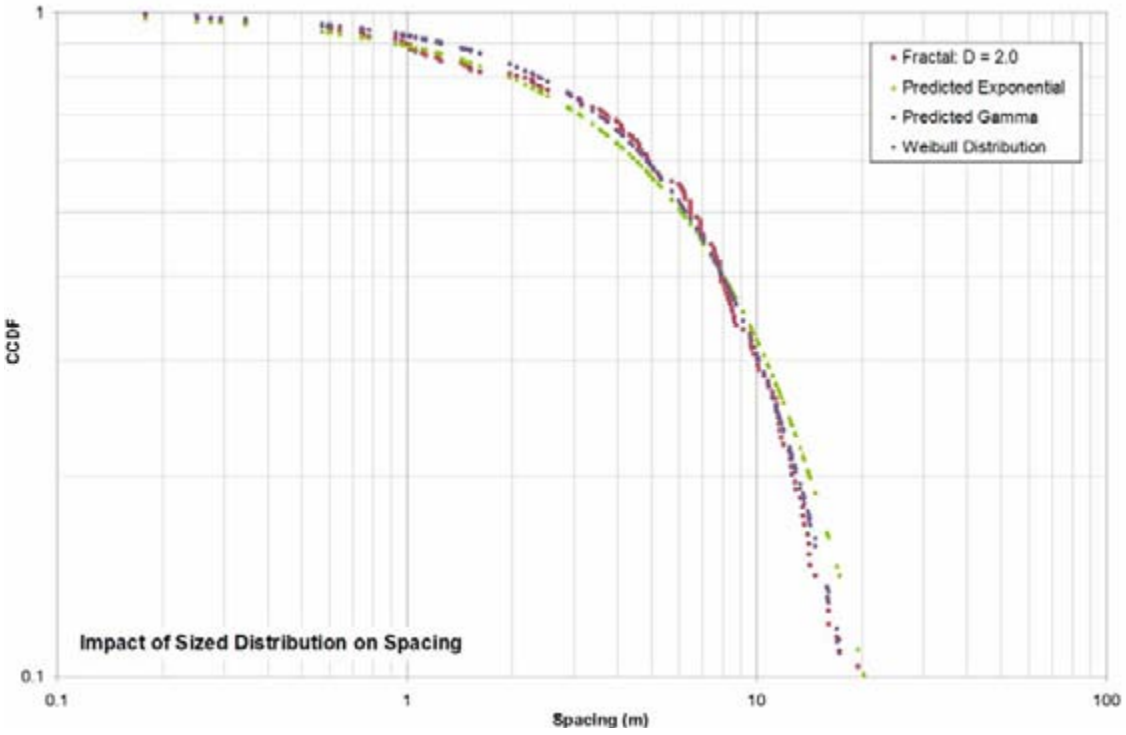

Figure 4-46. *Display of alternative spacing models fit to the measured borehole simulation spacing data.*

Figure 4-42 through Figure 4-44 show that a power law spacing model would be a poor fit to the measured data, as the measured spacing data significantly diverge from a straight line. The other alternative models – exponential, Gamma and Weibull – are all much better fits. The best fit, in terms of the total squared difference between the measured complementary cumulative probability and the model probability is for the Weibull distribution, although both the exponential or Gamma are also good fits.

This simple example illustrates that it is possible to have a system of fractures that have centre points located according to a Poissonian spatial process, with sizes conforming to a power law distribution, and fracture spacings best described by a Weibull distribution.

Investigation of apparent non-Euclidean spatial pattern artefact in mass dimension calculation

It has been previously noted that the apparent transition from a Euclidean spatial pattern to a non-Euclidean spatial pattern at scales of 10 m to 30 m may be due to an artefact in the mass dimension calculation. The artefact might arise for the following reasons:

- Fractures below a certain size (related to the borehole diameter) have not been recorded.
- Fractal calculation methods, like the mass dimension calculations in the report, assume that fractures of all sizes have been measured.

To further investigate this possibility, a series of numerical simulation were carried out.
The parameters for these simulations are as follows:

- 1,000 uniform random numbers were generated.
- They were transformed into Exponential, power law & Weibull distributions.
- The values were assumed to be spacings between successive fractures.
- The coordinates were re-scaled so that the last fracture occurred at 1,000 m measured depth.
- Thus, all models had the same number of fractures, mean spacing, and data range. Moreover, the power law model was given the same scaling exponent (1.0) as the others. The only difference was the spacing distribution form.

The results for these simulations are shown in Figure 4-47.

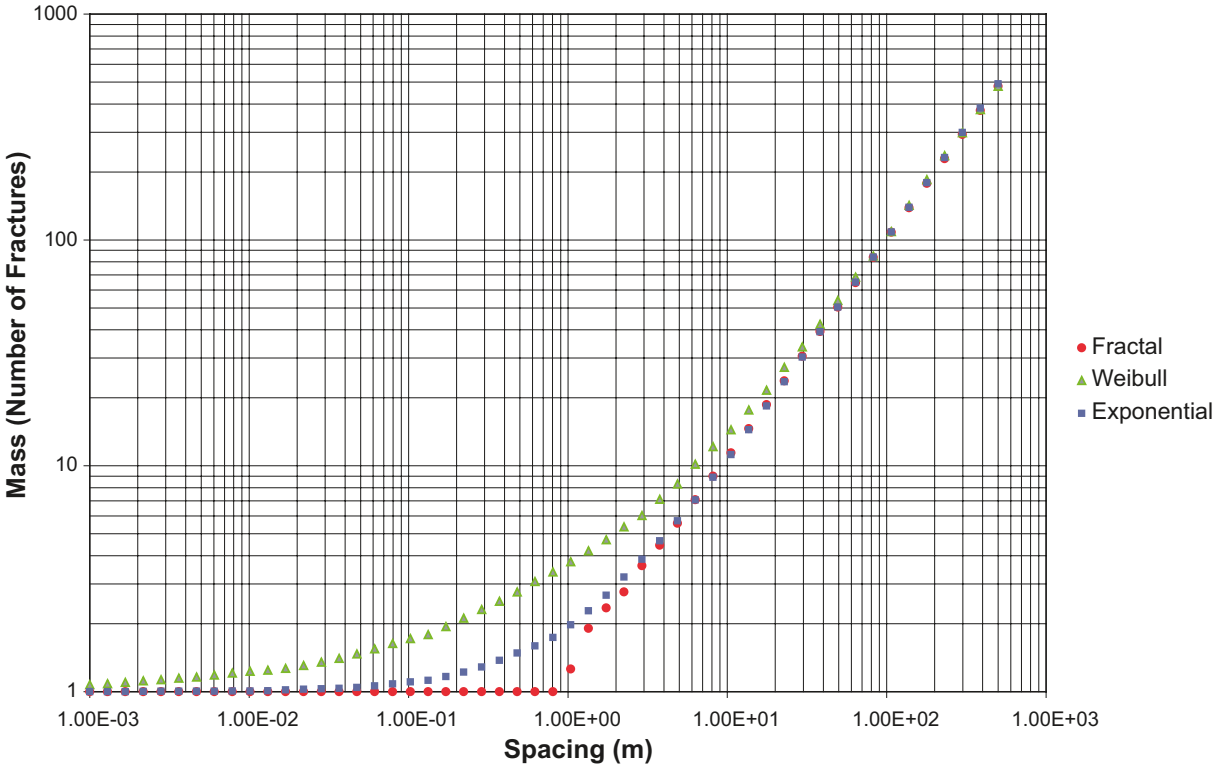

Figure 4-47. *Simulation results for mass dimension calculation for alternative spatial models.*

The results show that the calculation of the mass dimension introduces an artefact due to the lack of inclusion of data below a size threshold (in this case, the borehole diameter) for all spacing models. The artefact manifests itself in the mass dimension calculation as a departure from a straight line at larger scales. For the exponential and Weibull distributions, the slope monotonically decreases from 1.0 to 0.0. The onset of departure from the slope of 1.0 occurs at a value related to the maximum fracture spacing; the scale at which the slope is 0.0 relates to the minimum fracture spacing. Power law spacing distributions appear markedly different from exponential and Weibull distributions. There is no monotonic decrease in slope, but rather a sharp discontinuity from a constant positive slope to a slope of 0.0. Thus, the previous borehole results appear more likely due to the methodological artefact than to an underlying transition from Poissonian to fractal spatial behaviour.

4.4.4 Fracture domain, rock domain, and lithology classification

The results of the statistical tests in this section are voluminous, and are not reproduced in this report. The cross-tabulation results can be found in the files XTabsRD.pdf (Rock domains versus fracture properties), XTabsFD.pdf (fracture properties versus fracture domain), and XTabsLith.pdf (fracture properties as a function of bedrock lithology). All of these files are available in the 'Electronic Output Files' folder on the CD that accompanies this report. The specific data used in this analysis are listed in Fracture Data for SPSS Analyses.pdf, in the same folder.

Differences among fracture domains

The results of the cross-tabulation calculations are shown in Table 4-44. As this table shows, the only statistically significant differences among fracture attributes in the various fracture domains is their lithological association. This is not unexpected, as both rock domains and lithology were taken into account in fracture domain delineations. This table indicates that the fractures in each fracture domain do not have significantly different characteristics, although the differences by set percentage is approaching statistical significance (Table 4-45). This can be seen most clearly by comparing the Expected Count with the Count, which refers to the number of fractures in the category actually measured.

Table 4-44. Cross-tabulation results for fracture domains.

Fracture Morphology	
FRACT_MAPPED	
FRACT_INTERPRET	No Difference
VISIBLE_IN_BIPS	
CONFIDENCE	No Difference
ROUGHNESS	No Difference
SURFACE	No Difference
FRACT_ALTERATION	No Difference
Lithology & Domains	
BEST_ROCK_NAME	Difference
ROCK_NAME	Difference
ROCK_DOMAIN	Difference
ROCK_UNIT	Difference
Mineral Fillings	
Adularia	No Difference
Albite	No Difference
Amphibole	No Difference
Biotite	No Difference
Calcite	No Difference
Chalcopyrite	No Difference
Chlorite	No Difference
Clay Minerals	No Difference
Epidote	No Difference
Fluorite	No Difference
Galena	No Difference
Goethite	No Difference
Hematite	No Difference
Hypersthene	No Difference
Kaolinite	No Difference
Laumontite	No Difference
Muscovite	No Difference
Ortho Amphibole	No Difference
Oxidized Walls	No Difference
Plagioclase	No Difference
Potash Feldspar	No Difference
Prehnite	No Difference
Pyrite	No Difference
Quartz	No Difference
Red Feldspar	No Difference
Sericite	No Difference
Sphalerite	No Difference
Sulfides	No Difference
Tourmaline	No Difference
Unknown mineral	No Difference
White Feldspar	No Difference
Zeolites	No Difference
Refractory Minerals	No Difference
Preh_Ep	No Difference
Qtz_Ep_Chl	No Difference
Qtz_Ep	No Difference
Cc_Fl_Py	No Difference
Fracture Sets	
Sets	No Difference

Table 4-45. Detail of cross-tabulation for fracture set frequency vs. fracture domain.

Fracture Domain		Set				Total
		ENE	NS	SH	WNW	
FSM_C	Count	2,055	2,448	7,374	3,261	15,138
	Expected Count	1,626.2	3,036.6	8,037.1	2,438.0	15,138.0
	% within FRACTURE_DOMAIN	13.6%	16.2%	48.7%	21.5%	100.0%
	% within Set	21.9%	14.0%	15.9%	23.2%	17.4%
	% of Total	2.4%	2.8%	8.5%	3.7%	17.4%
FSM_EW007	Count	2,197	2,866	11,250	3,210	19,523
	Expected Count	2,097.3	3,916.2	10,365.2	3,144.2	19,523.0
	% within FRACTURE_DOMAIN	11.3%	14.7%	57.6%	16.4%	100.0%
	% within Set	23.5%	16.4%	24.3%	22.9%	22.4%
	% of Total	2.5%	3.3%	12.9%	3.7%	22.4%
FSM_N	Count	707	1,590	6,342	1,448	10,087
	Expected Count	1,083.6	2,023.4	5,355.4	1,624.5	10,087.0
	% within FRACTURE_DOMAIN	7.0%	15.8%	62.9%	14.4%	100.0%
	% within Set	7.5%	9.1%	13.7%	10.3%	11.6%
	% of Total	.8%	1.8%	7.3%	1.7%	11.6%
FSM_NE005	Count	1,444	3,948	7,463	2,272	15,127
	Expected Count	1,625.0	3,034.4	8,031.3	2,436.2	15,127.0
	% within FRACTURE_DOMAIN	9.5%	26.1%	49.3%	15.0%	100.0%
	% within Set	15.4%	22.6%	16.1%	16.2%	17.3%
	% of Total	1.7%	4.5%	8.6%	2.6%	17.3%
FSM_S	Count	426	999	1,938	489	3,852
	Expected Count	413.8	772.7	2,045.1	620.4	3,852.0
	% within FRACTURE_DOMAIN	11.1%	25.9%	50.3%	12.7%	100.0%
	% within Set	4.5%	5.7%	4.2%	3.5%	4.4%
	% of Total	.5%	1.1%	2.2%	.6%	4.4%
FSM_W	Count	2,538	5,640	11,927	3,363	23,468
	Expected Count	2,521.1	4,707.6	12,459.7	3,779.6	23,468.0
	% within FRACTURE_DOMAIN	10.8%	24.0%	50.8%	14.3%	100.0%
	% within Set	27.1%	32.2%	25.8%	23.9%	26.9%
	% of Total	2.9%	6.5%	13.7%	3.9%	26.9%

The non-parametric ANOVA results for fracture intensity as a function of fracture set, fracture type and fracture domain show many statistically significant differences. Overall, the intensity differences among the fracture domains are statistically significant for all sets and fracture types (Table 4-46). The magnitude of the F statistic is an indication of the significance; small values of F indicate that the fracture domain grouping makes less difference than when F values are large. Overall, the ENE set shows the least variation by fracture domain, while the SH and N-S sets show the greatest.

Table 4-47 shows pairwise detail. For the ENE set, only the contrasts between FSM_EW007 and FSM_NE005 and FSM_W are statistically significant, suggesting that the intensity of the ENE set is fairly homogeneous in all fracture domains except FSM_EW007. However, the contrast for the NS and SH sets is much stronger between fracture domains; only two of the possible ten pairwise combinations of fracture domains for these sets are not statistically different. Half of the pairs for the WNW are also significantly different. This suggests that the fracture domains are useful for reducing fracture intensity uncertainty.

Table 4-46. ANOVA results for fracture domains as a function of fracture set and fracture type.

Set	Type	F	Probability
ENE	SetP32_open	9.44	< 0.0001
ENE	SetP32_sealed	4.85	0.00067
ENE	SetP32_total	6.42	< 0.0001
N-S	SetP32_open	13.19	< 0.0001
N-S	SetP32_sealed	42.93	< 0.0001
N-S	SetP32_total	43.37	< 0.0001
SH	SetP32_open	54.00	< 0.0001
SH	SetP32_sealed	27.57	< 0.0001
SH	SetP32_total	47.62	< 0.0001
WNW	SetP32_open	26.23	< 0.0001
WNW	SetP32_sealed	6.09	< 0.0001
WNW	SetP32_total	15.99	< 0.0001
Total	Open	28.68	< 0.0001
Total	Sealed	10.20	< 0.0001
Total	P32	19.97	< 0.0001

Table 4-47. ANOVA results for fracture domains as a function of fracture set: pairwise fracture domain contrasts.

Set	Fracture Domain Comparison	Contrast	Result
ENE	FSM_C v FSM_EW007	–0.239	
ENE	FSM_C v FSM_N	0.334	
ENE	FSM_C v FSM_NE005	0.109	
ENE	FSM_C v FSM_W	0.109	
ENE	FSM_EW007 v FSM_N	0.573	(significant)
ENE	FSM_EW007 v FSM_NE005	0.348	(significant)
ENE	FSM_EW007 v FSM_W	0.349	(significant)
ENE	FSM_N v FSM_NE005	–0.225	
ENE	FSM_N v FSM_W	–0.224	
ENE	FSM_NE005 v FSM_W	0.000	
NS	FSM_C v FSM_EW007	–0.589	(significant)
NS	FSM_C v FSM_N	–0.298	
NS	FSM_C v FSM_NE005	–1.979	(significant)
NS	FSM_C v FSM_W	–1.275	(significant)
NS	FSM_EW007 v FSM_N	0.291	
NS	FSM_EW007 v FSM_NE005	–1.391	(significant)
NS	FSM_EW007 v FSM_W	–0.687	(significant)
NS	FSM_N v FSM_NE005	–1.681	(significant)
NS	FSM_N v FSM_W	–0.977	(significant)
NS	FSM_NE005 v FSM_W	0.704	(significant)
SH	FSM_C v FSM_EW007	–1.694	(significant)
SH	FSM_C v FSM_N	–1.950	(significant)
SH	FSM_C v FSM_NE005	–0.518	(significant)
SH	FSM_C v FSM_W	–0.751	(significant)
SH	FSM_EW007 v FSM_N	–0.256	

Set	Fracture Domain Comparison	Contrast	Result
SH	FSM_EW007 v FSM_NE005	1.176	(significant)
SH	FSM_EW007 v FSM_W	0.943	(significant)
SH	FSM_N v FSM_NE005	1.431	(significant)
SH	FSM_N v FSM_W	1.199	(significant)
SH	FSM_NE005 v FSM_W	–0.233	
WNW	FSM_C v FSM_EW007	–0.330	
WNW	FSM_C v FSM_N	–0.144	
WNW	FSM_C v FSM_NE005	0.148	
WNW	FSM_C v FSM_W	0.551	(significant)
WNW	FSM_EW007 v FSM_N	0.186	
WNW	FSM_EW007 v FSM_NE005	0.478	(significant)
WNW	FSM_EW007 v FSM_W	0.881	(significant)
WNW	FSM_N v FSM_NE005	0.292	
WNW	FSM_N v FSM_W	0.694	(significant)
WNW	FSM_NE005 v FSM_W	0.403	(significant)

Differences among rock domains

Rock domains at Laxemar are generally defined by petrography (composition, grain size, igneous texture), the degree of homogeneity (how much mixing of individual rock types), and the frequency of ductile shear zones /Wahlgren et al. 2008/. The rock domains represent mixtures of lithologies, rather than a single homogeneous unit.

The cross-tabulation results for rock domains are shown in Table 4-48. The cross-tabulation results suggest that the fractures in each rock domain differ primarily as a function of lithology and fracture domain, but not on fracture characteristics or set frequency. This is to be expected; different lithologies (granite versus gabbro/diabase) have different mechanical and chemical properties, which have the potential to combine to produce different styles and intensity of rock fracturing.

The principal goal of this analysis is to determine whether the rock domains are a more useful division for reducing uncertainty in the DFN model than the fracture domains. Comparison of the cross-tabulation (Table 4-48) results do not indicate that one is superior to the other. However, a comparison of the ANOVA results suggests that the fracture domain division is likely to reduce uncertainty more than the rock domain division.

Table 4-49 summarizes the ANOVA results for rock domain as a function of fracture set intensity, while Table 4-50 shows the pairwise ANOVA results that indicate which pairs of domains and sets have the greatest contrasts. The rock domains of greatest extent and importance to the repository are RSMA01 and RSMD01, and to a lesser extent RSMM01. While there are many statistically significant differences among the rock domains, the contrasts between RSMA01 and RSMD01, RSMA01 and RSMM01, and RSMD01 and RSMM01 tend not to be significant.

Table 4-50 shows that the fracture intensity contrasts between many pairs of rock domains are not statistically significant. None of the three key domains shows a statistically significant result for the ENE set; half the sets are not significant for RSMA01 versus RSMM01 or RSMD01; three out of four of the sets are not significant for the pairing of RSMD01 and RSMM01. Even when the contrasts among these three important domains are statistically significant, the contrast magnitudes tends to be less then for other statistically- significant contrasts (such as fracture domain or lithology) for the same set. These results suggest that the use of rock domains as the primary division for rock fracturing would be a very inefficient way to reducing fracture intensity uncertainty when compared to the fracture domain classification.

Table 4-48. Cross-tabulation results for rock domains.

Fracture Morphology	
FRACT_MAPPED	No Difference
FRACT_INTERPRET	No Difference
VISIBLE_IN_BIPS	No Difference
CONFIDENCE	No Difference
ROUGHNESS	No Difference
SURFACE	No Difference
FRACT_ALTERATION	No Difference
Lithology & Domains	
BEST_ROCK_NAME	Difference
ROCK_NAME	Difference
FRACTURE_DOMAIN	Difference
ROCK_UNIT	Difference
Mineral Fillings	
Adularia	No Difference
Albite	No Difference
Amphibole	No Difference
Biotite	No Difference
Calcite	No Difference
Chalcopyrite	No Difference
Chlorite	No Difference
Clay Minerals	No Difference
Epidote	No Difference
Fluorite	No Difference
Galena	No Difference
Goethite	No Difference
Hematite	No Difference
Hypersthene	No Difference
Kaolinite	No Difference
Laumontite	No Difference
Muscovite	No Difference
Ortho Amphibole	No Difference
Oxidized Walls	No Difference
Plagioclase	No Difference
Potash Feldspar	No Difference
Prehnite	No Difference
Pyrite	No Difference
Quartz	No Difference
Red Feldspar	No Difference
Sericite	No Difference
Sphalerite	No Difference
Sulfides	No Difference
Tourmaline	No Difference
Unknown mineral	No Difference
White Feldspar	No Difference
Zeolites	No Difference
Refractory Minerals	No Difference
Preh_Ep	No Difference
Qtz_Ep_Chl	No Difference
Qtz_Ep	No Difference
Cc_Fl_Py	No Difference
Fracture Sets	
Sets	No Difference

Table 4-49. ANOVA results for rock domain as a function of fracture set.

Set	F	Probability
ENE	4.26	0.0051
NS	20.02	< 0.0001
SH	52.88	< 0.0001
WNW	9.42	< 0.0001

Table 4-50. ANOVA results for rock domain as a function of fracture set: pair-wise rock domain contrasts.

Pair	ENE		NS		SH		WNW	
	Contrast	Significance	Contrast	Significance	Contrast	Significance	Contrast	Significance
RSMA01 vs.RSMBA03	1.7367	(significant)	2.9369	(significant)	4.2776	(significant)	2.6093	(significant)
RSMA01 vs. RSMD01	0.1353		–0.0905		1.2878	(significant)	0.3718	(significant)
RSMA01 vs. RSMM01	0.0265		–0.8734	(significant)	1.0854	(significant)	0.1736	
RSMBA03 vs. RSMD01	–1.6014	(significant)	–3.0274	(significant)	–2.9899	(significant)	–2.2375	(significant)
RSMBA03 vs. RSMM01	–1.7102	(significant)	–3.8103	(significant)	–3.1922	(significant)	–2.4356	(significant)
RSMD01 vs. RSMM01	–0.1087		–0.7829	(significant)	–0.2023		–0.1982	

Differences among lithologies

Table 4-51 shows the results for the cross-tabulation of fracture lithology and other characteristics. As in the previous calculations concerning fracture and rock domains, the only statistically significant differences are for rock and fracture domains. Overall, fracture characteristics do not vary strongly by lithology.

The ANOVA results (Table 4-52 and Table 4-53) show a very similar result to the rock domain analyses. Table 4-52, which summarizes the overall ANOVA results, indicates that intensity does vary significantly by major rock type for all sets. The pairwise comparisons (Table 4-53), however, show that most of this difference arises from a small percentage of the pairs. Moreover, the major differences come from comparing the major lithologies to "Unknown". When fractures with "Unknown" lithologies are removed from the analyses, the differences are not statistically different for the ENE and N-S sets, and barely so for the WNW and SH sets.

Conclusions regarding the usefulness of dividing fractures by fracture domain, rock domain, or lithology

The ANOVA and cross-tabulation results indicate that the fracture domain division provides the most useful reduction in the geological DFN parameterization. The cross-tabulation results show that there are very few differences in fracture characteristics as a function of fracture domain, rock domain or dominant lithology. The primary difference is in fracture intensity for each set. While both the fracture domain and rock domain divisions produce statistically significant differences among the subgroups, the fracture domain subdivision scheme produces a much higher percentage of pairwise contrasts than do either the rock domain or lithology sub-groupings. In fact, the lithology sub-groupings produce the smallest percentage of statistically significant contrasts.

This implies that while lithology does produce some differences in fracture intensity, the differences arise from a combination of lithology and tectonic deformation. The current fracture domain divisions provide much greater contrasts in intensity than either the rock domain or the lithologic designation. Moreover, the fracture domain division is compact, achieving a greater reduction in fracture parameterization uncertainty with fewer subdivisions than the other alternatives.

4.4.5 Fracture intensity as a function of depth

A series of figures (Appendix E) show the variation in fracture intensity as a function of fracture type, fracture set and fracture domain. There is evidence of changes as a function of all three of these parameters. For example, in domain FSM_C (Appendix E), open fracture intensity appears to not be a systematic function of depth for the ENE set and possible the N-S set, but does appear to systematically decrease for the SH and WNW sets. Total fracture intensity, however, shows not obvious decrease in fracture intensity with depth for FSM_C. Open fracture intensity for the SH set shows a decrease in intensity with depth for some domains, for example FSM_C and FSM_N, but no obvious decrease for other domains, such as FSM_W. Overall, total fracture intensity shows many fewer instances of possible depth dependence, regardless of fracture set or fracture domain.

About the only instances where there appears to be a decrease in total fracture intensity with depth is for FSM_N, although this might be due in part to the fact that there is no fracture data for intervals much deeper than 500 m below the surface. Especially with regards to total fracture intensity, while there is certainly variability in intensity with depth, there does not appear to be a systematic decrease in intensity that overrides the not-spatial variability in intensity with the possible exception of FSM_N.

Table 4-51. Cross-tabulation results for lithology.

Fracture Morphology	
FRACT_MAPPED	No Difference
FRACT_INTERPRET	No Difference
VISIBLE_IN_BIPS	No Difference
CONFIDENCE	No Difference
ROUGHNESS	No Difference
SURFACE	No Difference
FRACT_ALTERATION	No Difference
Lithology & Domains	
ROCK_NAME	Difference
ROCK_DOMAIN	Difference
FRACTURE_DOMAIN	Difference
ROCK_UNIT	Difference
Mineral Fillings	
Adularia	No Difference
Albite	No Difference
Amphibole	No Difference
Biotite	No Difference
Calcite	No Difference
Chalcopyrite	No Difference
Chlorite	No Difference
Clay Minerals	No Difference
Epidote	No Difference
Fluorite	No Difference
Galena	No Difference
Goethite	No Difference
Hematite	No Difference
Hypersthene	No Difference
Kaolinite	No Difference
Laumontite	No Difference
Muscovite	No Difference
Ortho Amphibole	No Difference
Oxidized Walls	No Difference
Plagioclase	No Difference
Potash Feldspar	No Difference
Prehnite	No Difference
Pyrite	No Difference
Quartz	No Difference
Red Feldspar	No Difference
Sericite	No Difference
Sphalerite	No Difference
Sulfides	No Difference
Tourmaline	No Difference
Unknown mineral	No Difference
White Feldspar	No Difference
Zeolites	No Difference
Refractory Minerals	No Difference
Preh_Ep	No Difference
Qtz_Ep_Chl	No Difference
Qtz_Ep	No Difference
Cc_Fl_Py	No Difference
Fracture Sets	
Sets	No Difference

Table 4-52. ANOVA results for lithology as a function of fracture set.

Set	F	Probability
ENE	5.48	< 0.0001
NS	4.17	< 0.0001
SH	20.92	< 0.0001
WNW	6.57	< 0.0001

Table 4-53. ANOVA results for lithology as a function of fracture set: pairwise lithology group contrasts.

Pair	ENE		NS		SH		WNW	
	Contrast	Significance	Contrast	Significance	Contrast	Significance	Contrast	Significance
Fine-grained dioritoid (Metavolcanite_ volcanite) v Granite_ fine- to medium-grained	0.563		–0.115		0.720		0.521	
Fine-grained dioritoid (Metavolcanite_ volcanite) v Granite_ medium- to coarse-grained	0.169		–0.299		0.670		0.332	
Fine-grained dioritoid (Metavolcanite_ volcanite) v Intermediate volanic rock (quartz latite to andesite)	–1.036		–0.614		0.358		0.050	
Fine-grained dioritoid (Metavolcanite_ volcanite) v Mafic rock_ fine-grained	0.577		0.012		0.006		0.366	
Fine-grained dioritoid (Metavolcanite_ volcanite) v Pegmatite	0.514		–0.158		1.149		0.644	
Fine-grained dioritoid (Metavolcanite_ volcanite) v Quartz monzonite to monzodiorite_ equigranular to weakly porphyritic	0.705		0.003		1.474	(significant)	0.723	
Fine-grained dioritoid (Metavolcanite_ volcanite) v Unknown	1.408	(significant)	1.307		3.483	(significant)	1.814	(significant)
Granite to quartz monzodiorite_ generally porphyritic v Granite_ fine- to medium-grained	0.173		–0.033		0.568	(significant)	0.320	
Granite to quartz monzodiorite_ generally porphyritic v Granite_ medium- to coarse-grained	–0.221		–0.217		0.519		0.132	
Granite to quartz monzodiorite_ generally porphyritic v Intermediate volanic rock (quartz latite to andesite)	–1.426		–0.532		0.207		–0.151	
Granite to quartz monzodiorite_ generally porphyritic v Mafic rock_ fine-grained	0.187		0.094		–0.146		0.165	
Granite to quartz monzodiorite_ generally porphyritic v Pegmatite	0.124		–0.076		0.998	(significant)	0.443	
Granite to quartz monzodiorite_ generally porphyritic v Quartz monzonite to monzodiorite_ equigranular to weakly porphyritic	0.315		0.085		1.323	(significant)	0.523	(significant)
Granite to quartz monzodiorite_ generally porphyritic v Unknown	1.018	(significant)	1.389	(significant)	3.331	(significant)	1.614	(significant)

Pair	ENE		NS		SH		WNW	
	Contrast	Significance	Contrast	Significance	Contrast	Significance	Contrast	Significance
Granite_ fine- to medium-grained v Granite_ medium- to coarse-grained	–0.394		–0.184		–0.049		–0.188	
Granite_ fine- to medium-grained v Intermediate volanic rock (quartz latite to andesite)	–1.599		–0.499		–0.361		–0.471	
Granite_ fine- to medium-grained v Mafic rock_ fine-grained	0.014		0.127		–0.714		–0.155	
Granite_ fine- to medium-grained v Pegmatite	–0.049		–0.043		0.430		0.123	
Granite_ fine- to medium-grained v Quartz monzonite to monzodiorite_ equigranular to weakly porphyritic	0.142		0.118		0.755	(significant)	0.202	
Granite_ fine- to medium-grained v Unknown	0.845	(significant)	1.422	(significant)	2.763	(significant)	1.294	(significant)
Granite_ medium- to coarse-grained v Intermediate volanic rock (quartz latite to andesite)	–1.205		–0.315		–0.312		–0.283	
Granite_ medium- to coarse-grained v Mafic rock_ fine-grained	0.408		0.311		–0.665		0.034	
Granite_ medium- to coarse-grained v Pegmatite	0.345		0.141		0.479		0.312	
Granite_ medium- to coarse-grained v Quartz monzonite to monzodiorite_ equigranular to weakly porphyritic	0.537		0.302		0.804		0.391	
Granite_ medium- to coarse-grained v Unknown	1.239	(significant)	1.606	(significant)	2.813	(significant)	1.482	(significant)
Intermediate volanic rock (quartz latite to andesite) v Mafic rock_ fine-grained	1.613		0.626		–0.352		0.316	
Intermediate volanic rock (quartz latite to andesite) v Pegmatite	1.550		0.456		0.791		0.595	
Intermediate volanic rock (quartz latite to andesite) v Quartz monzonite to monzodiorite_ equigranular to weakly porphyritic	1.742		0.617		1.116		0.674	
Intermediate volanic rock (quartz latite to andesite) v Unknown	2.444		1.920		3.125		1.765	
Mafic rock_ fine-grained v Pegmatite	–0.063		–0.170		1.143		0.278	
Mafic rock_ fine-grained v Quartz monzonite to monzodiorite_ equigranular to weakly porphyritic	0.129		–0.009		1.468	(significant)	0.357	
Mafic rock_ fine-grained v Unknown	0.831		1.295		3.477	(significant)	1.448	(significant)
Pegmatite v Quartz monzonite to monzodiorite_ equigranular to weakly porphyritic	0.192		0.161		0.325		0.079	
Pegmatite v Unknown	0.894	(significant)	1.465	(significant)	2.334	(significant)	1.170	(significant)
Quartz monzonite to monzodiorite_ equigranular to weakly porphyritic v Unknown	0.702	(significant)	1.303	(significant)	2.009	(significant)	1.091	(significant)

There is a near-surface (less than 100 m total vertical depth) decrease in total open fracture intensity in domain FSM_NE005. This trend is not seen in any of the other fracture domains, and could represent near-surface unloading or the proximity of this domain to the Äspö shear zone.

This is even more apparent for the total fracture intensity for all sets combined; Figure 4-48 through Figure 4-57 show no systematic patterns of fracture intensity change as functions of depth in the fracture domains.

As an alternative to binned fracture frequency plots, CFI plots can be used to track changes in fracture intensity with depth; breaks in slope on the CFI curve mark potential changes in lithology, stratigraphy, mineralogy through changes in the fracture intensity pattern. A straight line on the CFI plot indicates no significant change in fracture intensity. A curve in the negative y direction of the plot (increasing depth) implies a decrease in fracture intensity as a function of depth, while a curve in the positive y direction implies an increase in fracture intensity as a function of depth. Cumulative-fracture intensity (CFI) plots for the fracture domains at Laxemar again illustrate that, for all fracture domains except FSM_N, there is no systematic change in total fracture intensity (all orientation sets combined) for either open fractures (Figure 4-59) or open + sealed fractures (Figure 4-58). FSM_N appears to be an anomaly; it is not understood at this point why the fracture intensity changes as it does in the lower part of this fracture domain. The trend is also seen in the open fractures in FSM_N.

The CFI plots suggest a near-surface increase in open fracture intensity in domain FSM_NE005; down to ~ 75 m total vertical depth, there is an increased frequency of open fractures in the domain. The plots by set in Appendix E suggest that it is not a single fracture set that is causing this trend; all four orientation sets possess an increased intensity of open fractures in FSM_NE005 at depths shallower than 75 m.

The key message is that though some domains do show variability in fracture intensity as a function of depth, it is not well-defined or systematic. Qualitative judgements can be made, but it is clear from the CFI plots that attempting to assign a depth-intensity relationship to the cored borehole fracture data would largely be a mistake.

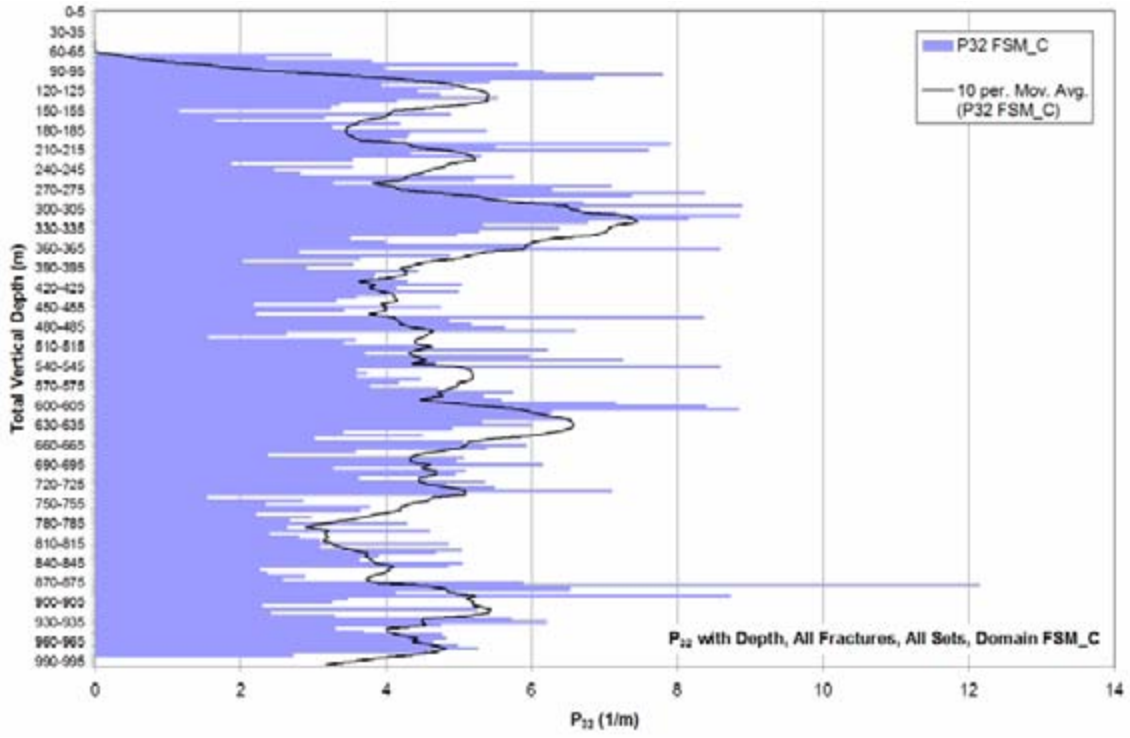

Figure 4-48. *Fracture intensity (P_{32}) for all fractures, all sets combined, Domain FSM_C, as a function of elevation.*

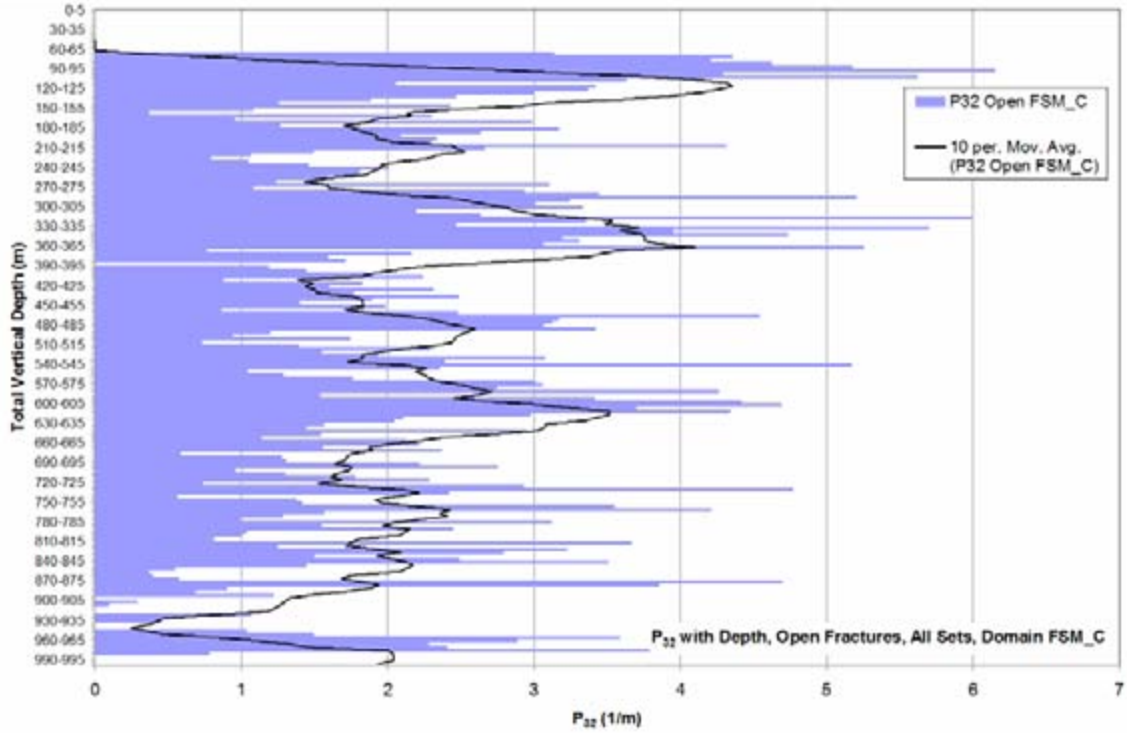

Figure 4-49. *Fracture intensity (P_{32}) for all fractures, all sets combined, Domain FSM_C, as a function of elevation, open fractures only.*

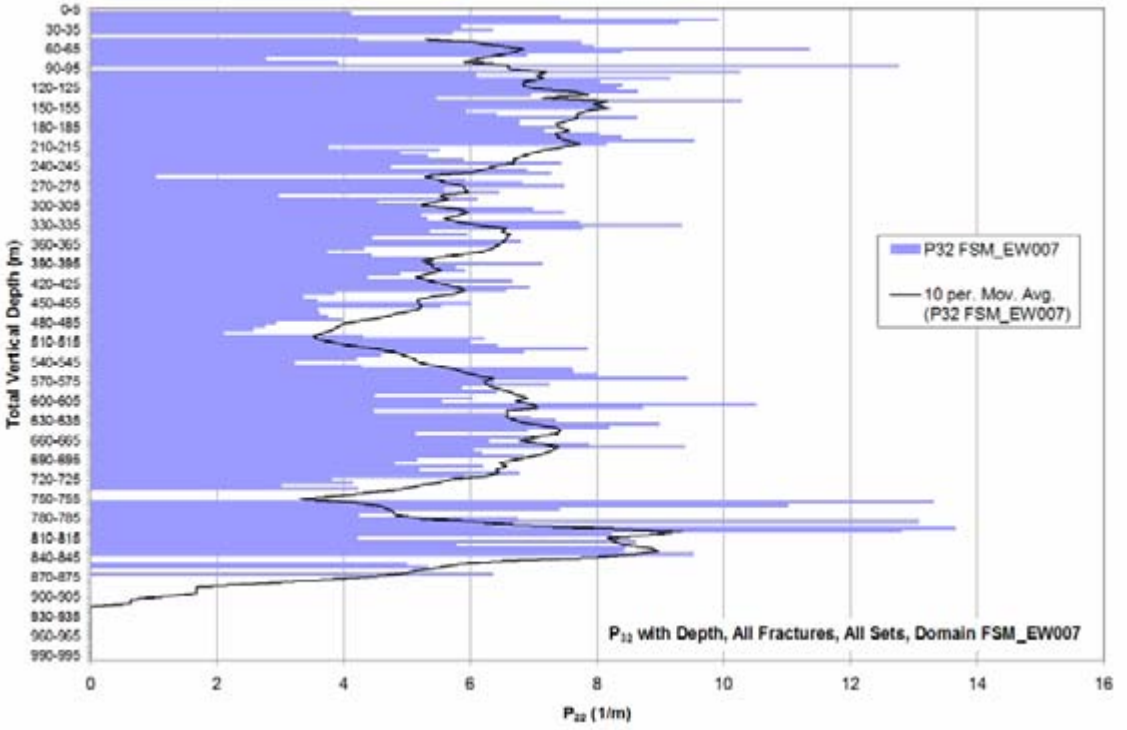

Figure 4-50. *Fracture intensity (P_{32}) for all fractures, all sets combined, Domain FSM_EW007, as a function of elevation.*

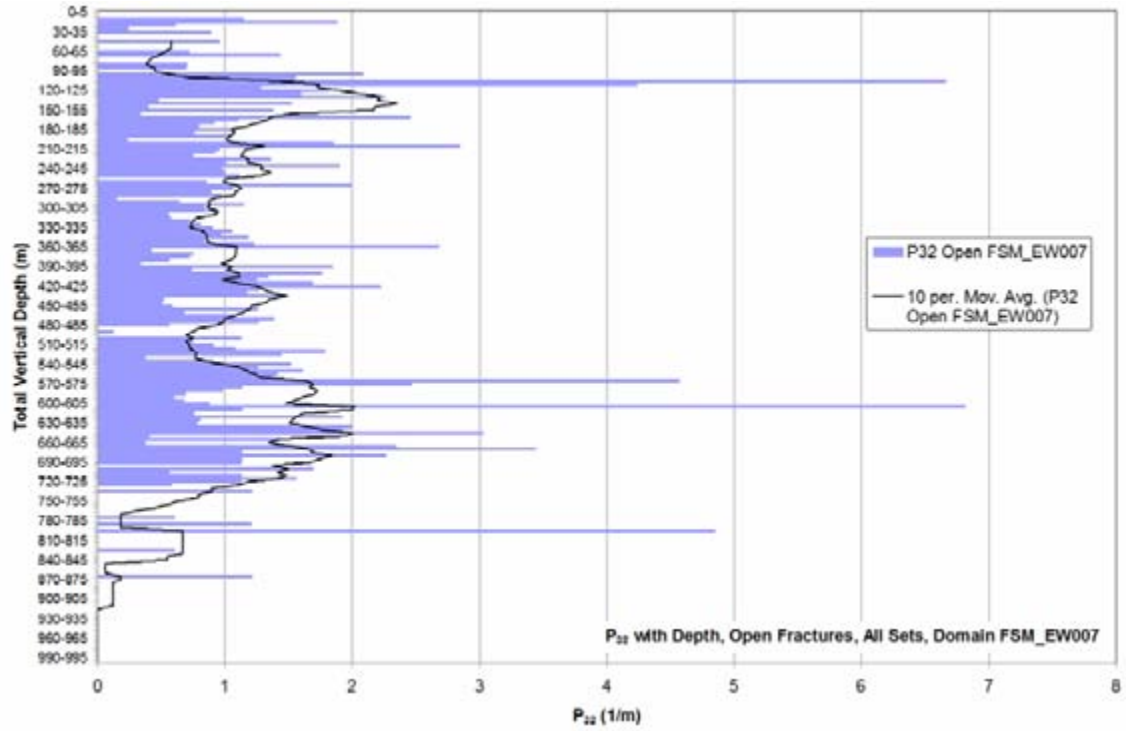

Figure 4-51. *Fracture intensity (P_{32}) for all fractures, all sets combined, Domain FSM_EW007, as a function of elevation, open fractures only.*

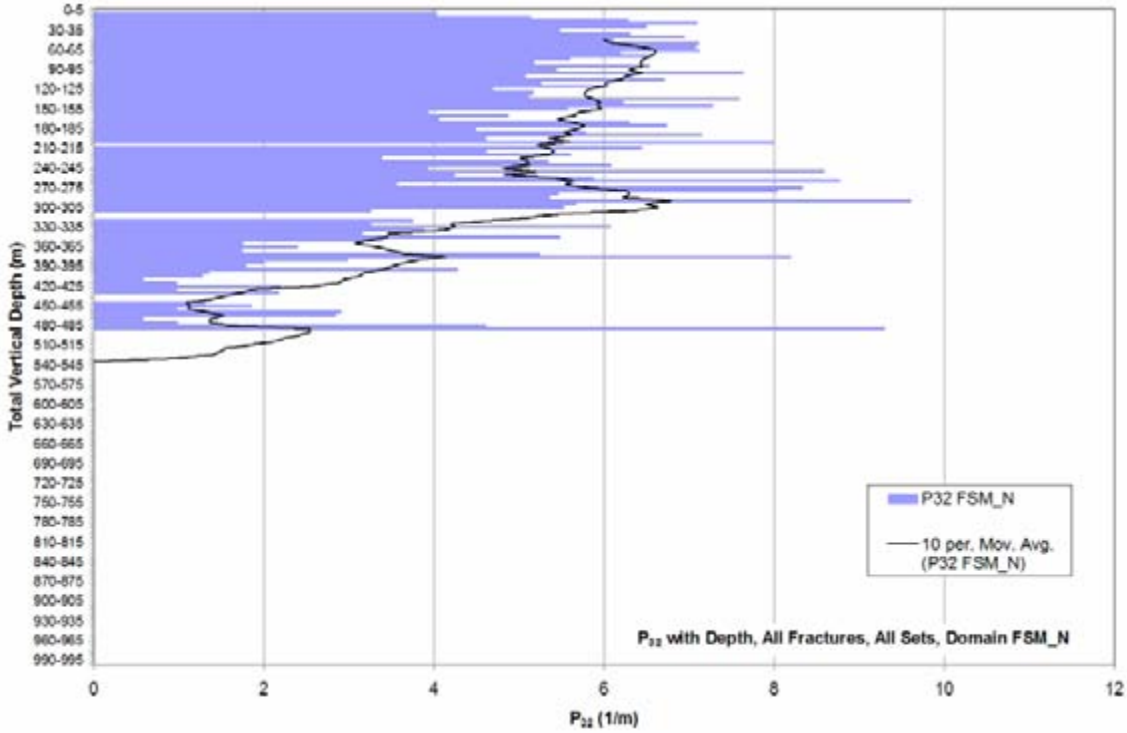

Figure 4-52. *Fracture intensity (P_{32}) for all fractures, all sets combined, Domain FSM_N, as a function of elevation.*

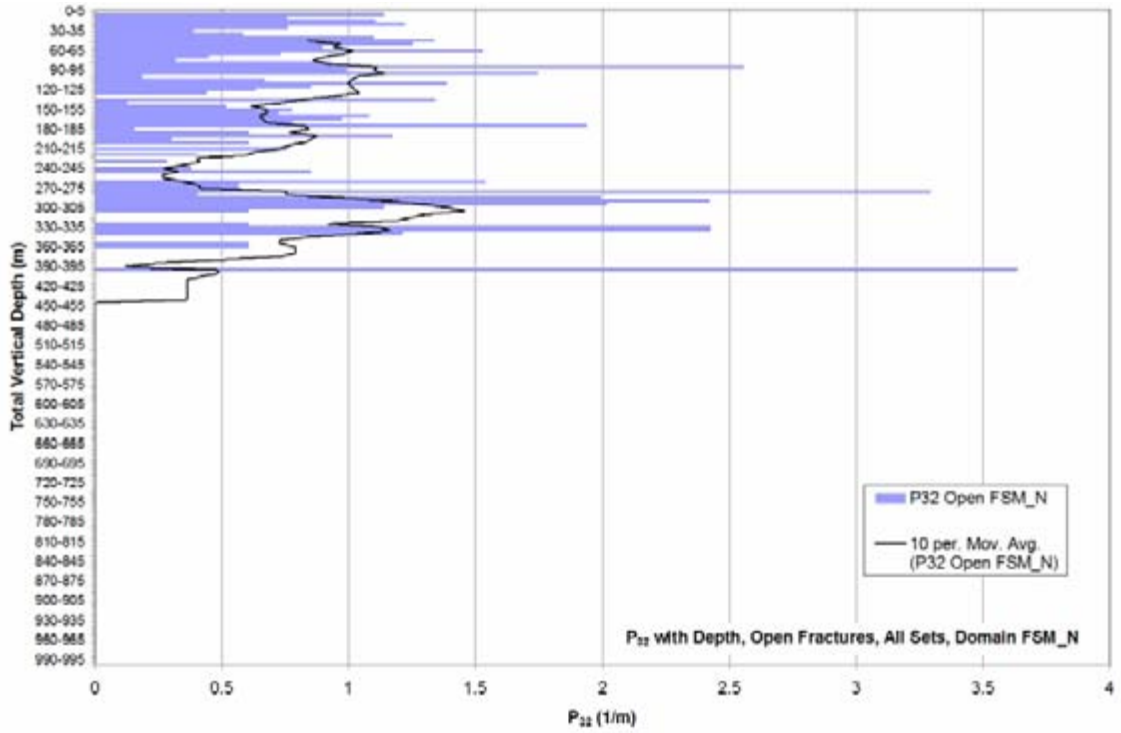

Figure 4-53. *Fracture intensity (P_{32}) for all fractures, all sets combined, Domain FSM_N, as a function of elevation, open fractures only.*

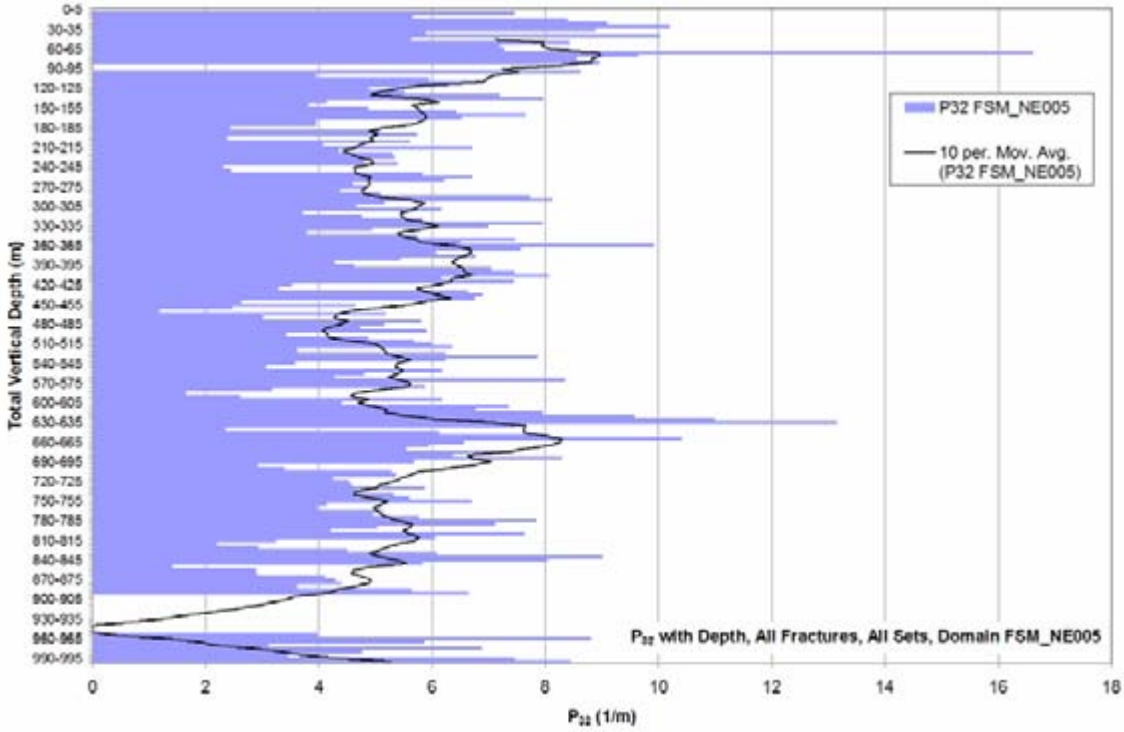

Figure 4-54. *Fracture intensity (P_{32}) for all fractures, all sets combined, Domain FSM_NE005, as a function of elevation.*

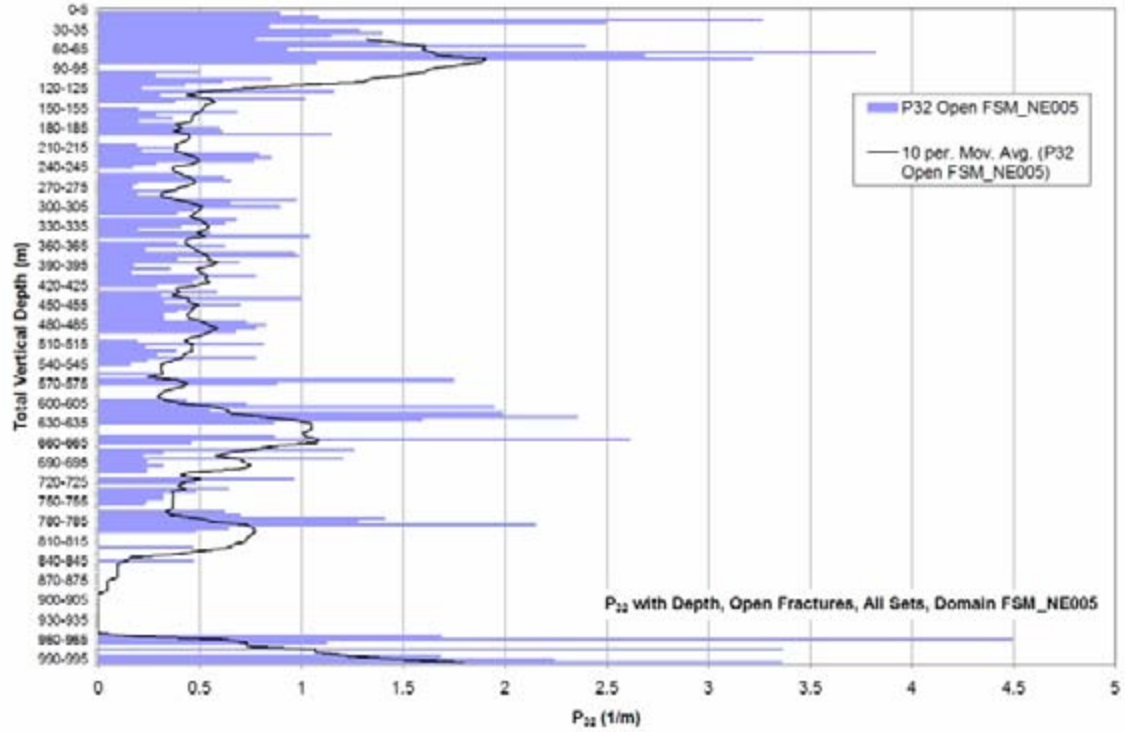

Figure 4-55. *Fracture intensity (P_{32}) for all fractures, all sets combined, Domain FSM_NE005, as a function of elevation, open fractures only.*

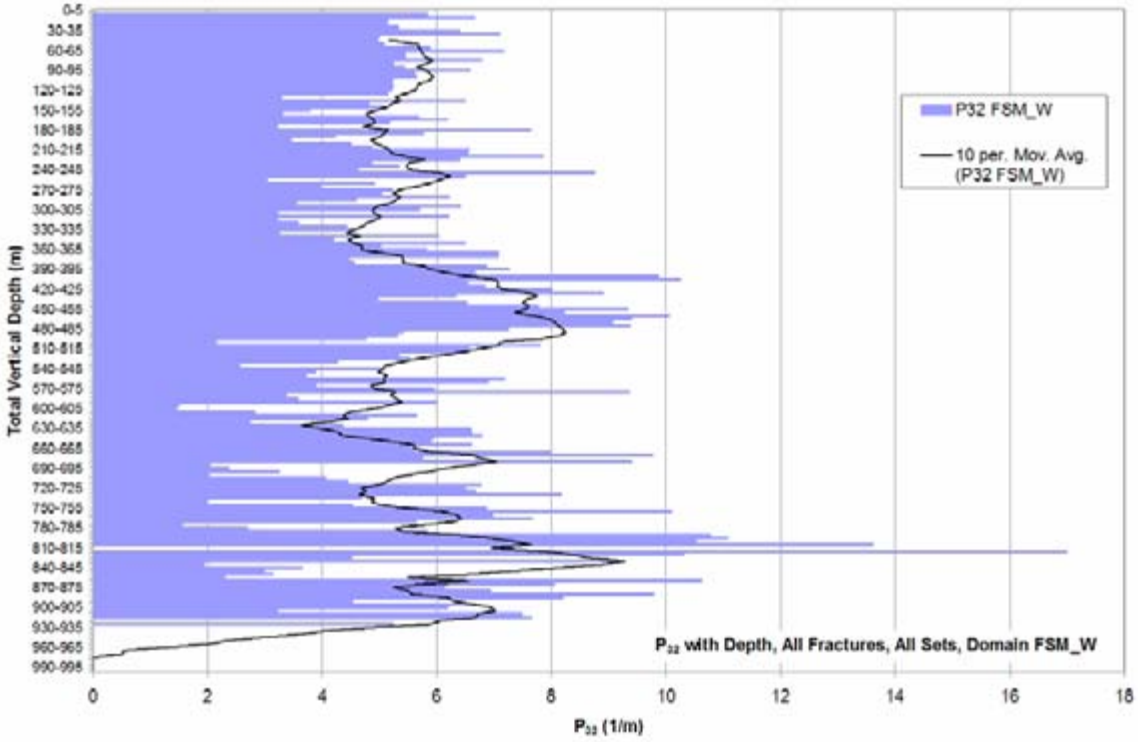

Figure 4-56. *Fracture intensity (P_{32}) for all fractures, all sets combined, Domain FSM_W, as a function of elevation.*

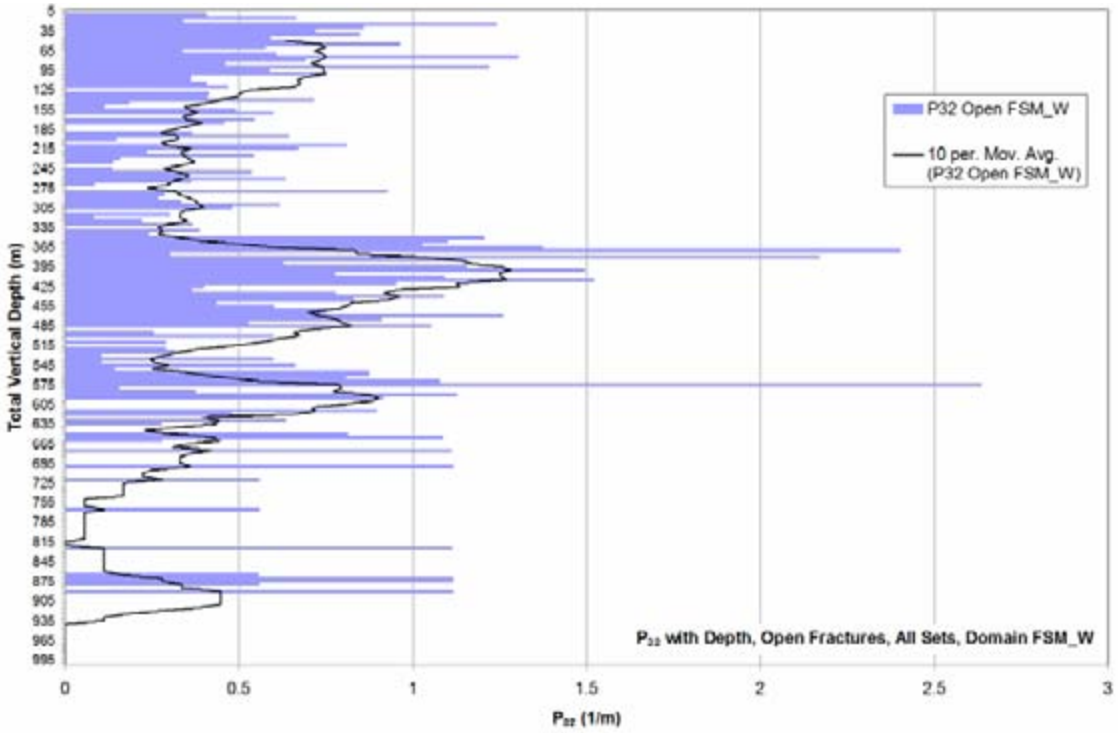

Figure 4-57. *Fracture intensity (P_{32}) for all fractures, all sets combined, Domain FSM_W, as a function of elevation, open fractures only.*

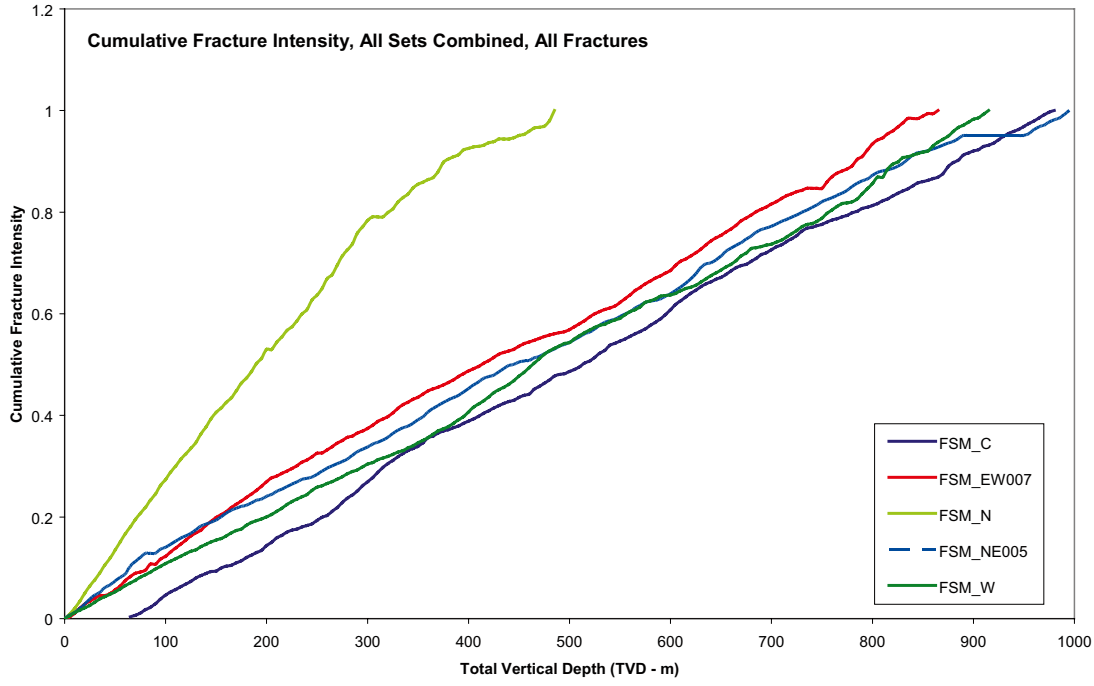

Figure 4-58. *Cumulative fracture intensity (CFI) for all fracture sets combined, all fractures, as a function of fracture domain. Fracture intensity is expressed as P_{32}.*

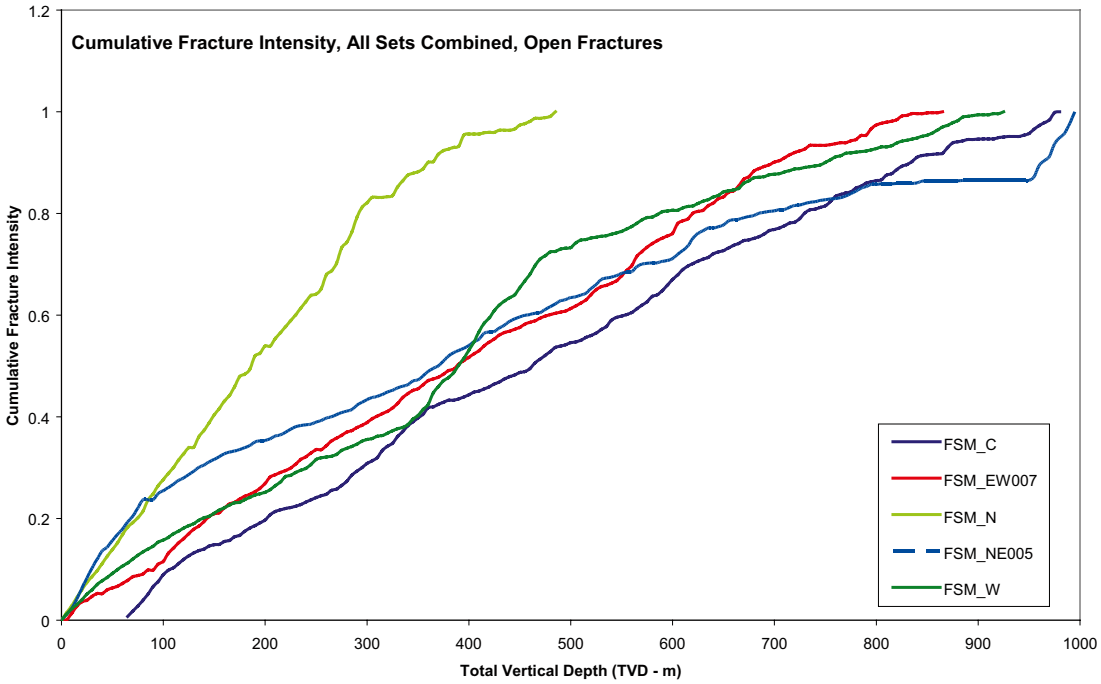

Figure 4-59. *Cumulative fracture intensity (CFI) for all fracture sets combined, open fractures, as a function of fracture domain. Fracture intensity is expressed as* P_{32}.

4.4.6 Fracture set termination model

The results of the fracture termination studies, described in Section 3.6.4, are presented below as Table 4-54 through Table 4-57. The recommended usage is to assume the global average values (Table 4-57) for any regional-scale studies, or for fracture domains in which a detail-mapped fracture outcrop is not available.

Table 4-54. Termination matrices for fracture domain FSM_N.

ASM000208					
		Terminates Against			
Target Set	**ENE**	**N-S**	**WNW**	**SH**	**Bulk Termination**
ENE	0	15.42%	8.12%	9.74%	33.28%
N-S	20.24%	0	13.16%	10.32%	43.72%
WNW	19.25%	20.00%	0	10.50%	49.75%
SH	16.95%	15.94%	9.06%	0	41.95%
ASM100234					
		Terminates Against			
Target Set	**ENE**	**N-S**	**WNW**	**SH**	**Bulk Termination**
ENE	0	20.32%	17.09%	5.40%	42.81%
N-S	12.02%	0	13.94%	3.83%	29.79%
WNW	13.65%	20.55%	0	5.89%	40.09%
SH	12.09%	16.05%	18.60%	0	46.74%

Table 4-55. Termination Matrix for Fracture Domain FSM_W.

ASM100235					
		Terminates Against			
Target Set	ENE	N-S	WNW	SH	Bulk Termination
ENE	0	34.62%	15.38%	5.77%	55.77%
N-S	10.61%	0	10.02%	3.74%	24.36%
WNW	19.29%	32.14%	0	3.57%	55.00%
SH	10.68%	32.48%	8.97%	0	52.14%

Table 4-56. Termination Matrix for Fracture Domain FSM_NE005.

ASM000208					
		Terminates Against			
Target Set	ENE	N-S	WNW	SH	Bulk Termination
ENE	0	41.94%	8.61%	3.33%	53.89%
N-S	8.97%	0	11.21%	2.99%	23.18%
WNW	7.05%	39.32%	0	3.18%	49.55%
SH	7.89%	31.05%	10.53%	0	49.47%

Table 4-57. Global Average Termination Matrix (All Domains).

Global Average					
		Terminates Against			
Target Set	ENE	N-S	WNW	SH	Bulk Termination
ENE	0	25.53%	12.24%	6.54%	44.30%
N-S	11.82%	0	11.58%	4.46%	27.86%
WNW	14.10%	26.87%	0	5.95%	46.92%
SH	13.22%	20.66%	12.12%	0	46.01%

4.4.7 Spatial variability of fracture intensity within fracture domains

Since there is no strong evidence (Appendix E) to support systematic changes in fracture intensity with depth, the variability of fracture intensity (P_{32}) for a given fracture set in a single fracture domain can be quantified through a probability distribution. As discussed in Section 3.6.1 for a Poisson point pattern of fractures in 3D space, the mean fracture intensity variation should follow either a Gamma or a Weibull distribution. The analysis of fracture data during the parameterization of the SDM-Site Laxemar DFN modelling suggests that, at scales larger than 10 m–30 m, the assumption of Euclidean size-intensity scaling and a Poisson fracture location model is appropriate (Section 4.4.2 and 4.4.3), and may well be appropriate for smaller scales.

The workflow for determining whether P_{32} derived from cored borehole data varies spatially according to a Gamma or Weibull distribution is as follows:

1. Wang's C_{13} factor is calculated for a range of borehole section lengths in each fracture domain, for each set in the global orientation model. For sections longer than three metres, an average C_{13} value is used. For example, for a 15 m long borehole segment, C_{13} is calculated as the mean of the five 3 m segments inside that 15 m interval.
2. Using measured borehole P_{10} values for all fractures (open and sealed) with the C_{13} values calculated in Step 1, P_{32} values are computed for every 3 m, 9 m, 15 m, 21 m, 30 m, and 51 m-long segment outside of mapped deformation zones and inside fracture domains. The P_{32} is computed for the total fracture intensity (open, partly open, and sealed); a separate analysis of the variation in intensity of open fractures is not performed.

3. The resulting P_{32} values are copied into BestFit 4.55 or EasyFit 4.3, where a Gamma or Weibull probability distribution was fit to the sample data (P_{32} values, by segment length, fracture set, and fracture domain). A two-parameter Gamma distribution was used, with the lower boundary of the distribution fixed at zero (not possible to have negative fracture intensity). For both the Gamma and Weibull distributions, BestFit and EasyFit use a maximum likelihood estimator to estimate distribution parameters, and uses least-squares to then fit the probability distribution to the CDF and PDF /Palisades Corporation 2004/.
4. Goodness of fit is evaluated qualitatively through the use of comparative cumulative density function (CDF) and quartile-quartile plots (Q-Q). Examples of these plots are presented below as Figure 4-60 and Figure 4-61. Goodness-of-fit is evaluated quantitatively through the Kolomogorov-Smirnov test /NIST 2007a/, assuming a level of significance of $\alpha_{95} = 0.05$.

The results of the analysis are presented below in Table 4-58 through Table 4-67; the results are presented by fracture domain and distribution type. The notation "fail to reject" and "reject" in these tables relates to the decision on the Null Hypothesis for the K-S test, which is that the two distributions are the same. "Fail to reject" implies that there is insufficient evidence in the data to reject the Null Hypothesis, and hence it is concluded that the measured intensities are Gamma- or Weibull-distributed. "Reject" implies that the measured intensities do not appear to be Gamma- or Weibull-distributed.

The associated CDF and Q-Q plots are contained in Appendix F. Note that the α_{95} value referred to in the table is not the level of statistical significance. It is the shape parameter of the gamma distribution, as described in Section 3.6.5. Note that CDF and Q-Q plots were not created for the 21 m, 30 m, and 51 m bins; the plots were only deemed necessary for the marginal bin sizes (3 m, 9 m, 15 m) so as to suggest where and why a distribution did not fit the data.

The results of the analyses suggest that, in general, modelling the spatial variability of P_{32} as a Gamma or Weibull distribution is not possible at 3 m scales. When the total fracture intensity (all sets combined) is used, some domains (FSM_C, FSM_N, FSM_NE005) do fit a Gamma or Weibull distribution at 3 m. However, the geological DFN is based on fractures described both by their host fracture domain and their orientation/set; as such, the model parameterisation has to be completed such that it is possible to simulate sets, not just the total fracture intensity.

The inability to describe the spatial variability of fracture intensity using a Gamma or Weibull distribution at the 3 m scale is largely due to the greater-than-expected number of 3 m intervals with no fractures in them. This may be evidence of the fractal spatial pattern hinted at by the borehole mass dimension plots. A fractal pattern will likely have a larger number of non-fractured intervals than a Poissonian spatial pattern; i.e. the mean non-fractured gap size increases. However, the 9 m interval size approaches the transition between Fractal and Euclidean scaling, and the table shows that the Null Hypothesis is not rejected for any of the fracture domains or sets, indicating that at this scale, the intensity variability is Gamma-distributed. The sole exception is the ENE fracture set; in four of the five domains (FSM_N is the only exception), the ENE set is not well-described by either distribution until scales of 15 m and larger. It should be noted, however, that the null hypothesis is rejected by very small amounts at the 9 m scale; if a slightly smaller confidence interval (90%, instead of 95%) were used, the ENE set could be said to also be appropriate at the 9 m scale.

The results of this analysis are also consistent with the conclusions of the mass dimension results for boreholes and outcrop data; ~ 10 m is the onset of Euclidean scaling. Thus, for scales around 9 m and greater, the variability in mean fracture intensity by set and fracture domain can be well modelled by either a Gamma or a Weibull distribution with the parameters presented in the tables; there are mathematical rationales for using both distributions. At smaller scales, the Gamma and Weibull distributions both appear to underestimate the number of non-fractured intervals.

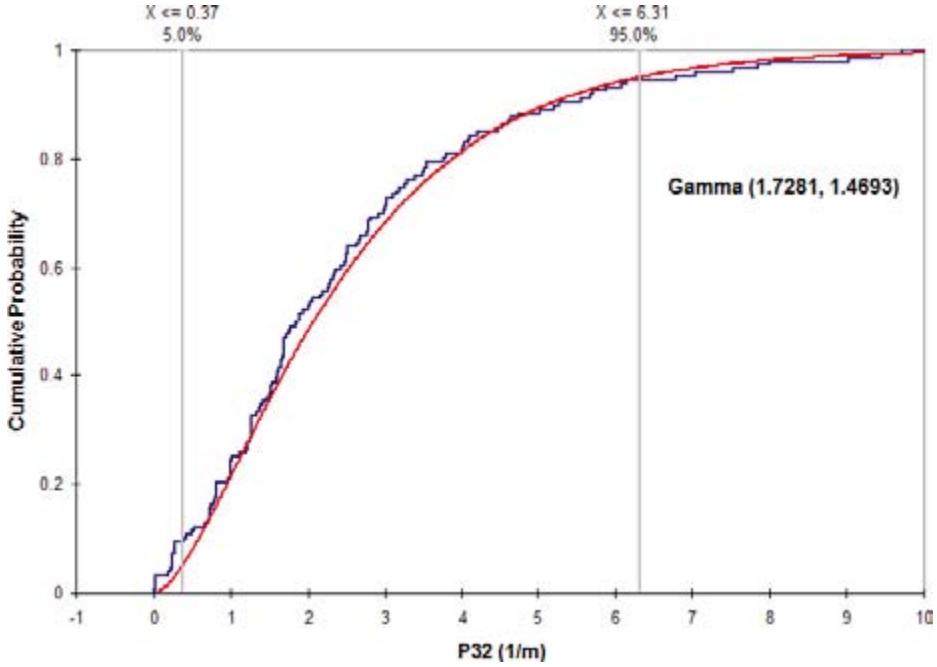

Figure 4-60. *Example of cumulative density function (CDF) for the N-S fracture set in fracture domain FSM_C. Figure is based on P_{32} calculated in 15 m-long borehole segments. The red line represents the empirical PDF for the gamma distribution; the blue line represents the data to which a distribution fit was calculated.*

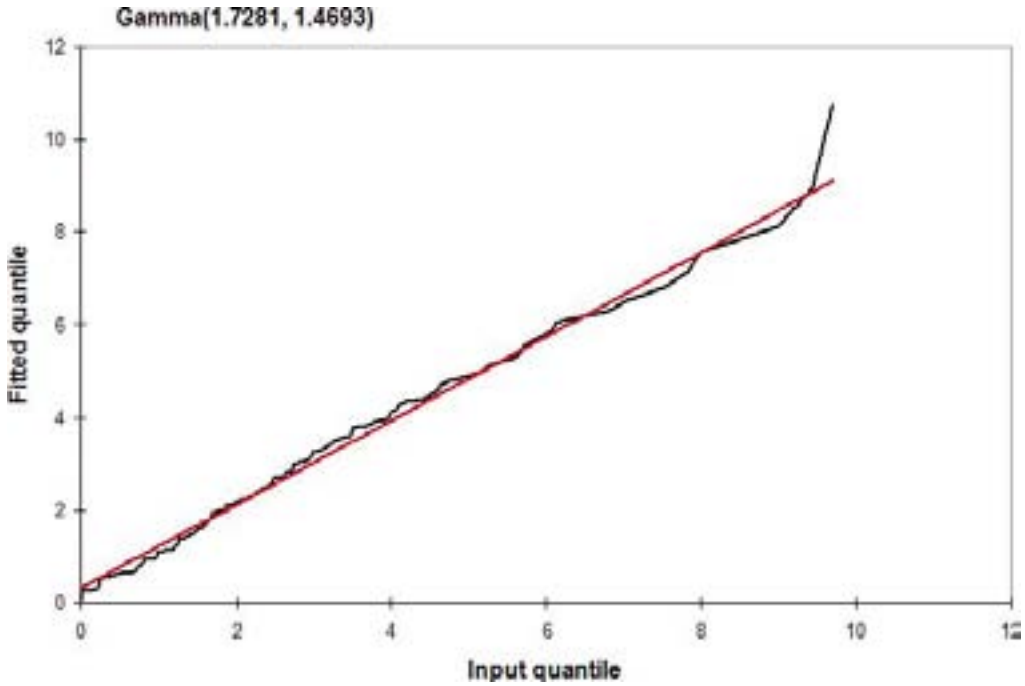

Figure 4-61. *Example quantile-quantile (Q-Q) plot for the N-S fracture set in fracture domain FSM_C. Figure is based on P_{32} calculated in 15 m-long borehole segments. The Q-Q plot is used to graphically determine if two data sets (in our case, the fitted γ distribution and the sample data set) come from populations with a common distribution. The red line represents a 45 degree slope (the data sets come from identical populations); the greater the deviation from the reference line, the less likely it is that the sample data are a good fit to the gamma distribution.*

Table 4-58. Analysis results for Gamma distribution, domain FSM_C.

Fracture Set	Section Length	Test Statistic	Critical Value	Test Result $\alpha_{95} = 0.05$	Distribution Parameters	
					Alpha	Beta
ENE	3 m	0.38	0.05	Reject	2.49	1.08
ENE	9 m	0.12	0.08	Reject	2.12	0.86
ENE	15 m	0.07	0.11	Fail to Reject	2.21	0.75
ENE	21 m	0.08	0.14	Fail to Reject	2.67	0.62
ENE	30 m	0.08	0.17	Fail to Reject	3.52	0.47
ENE	51 m	0.06	0.22	Fail to Reject	4.77	0.36
N-S	3 m	0.36	0.05	Reject	2.01	1.67
N-S	9 m	0.08	0.08	Fail to Reject	1.19	1.92
N-S	15 m	0.05	0.11	Fail to Reject	1.57	1.43
N-S	21 m	0.07	0.14	Fail to Reject	1.98	1.11
N-S	30 m	0.05	0.17	Fail to Reject	1.93	1.14
N-S	51 m	0.11	0.22	Fail to Reject	2.35	0.96
SH	3 m	0.15	0.05	Reject	1.43	2.10
SH	9 m	0.03	0.08	Fail to Reject	1.48	1.77
SH	15 m	0.04	0.11	Fail to Reject	1.85	1.38
SH	21 m	0.05	0.14	Fail to Reject	1.84	1.35
SH	30 m	0.06	0.17	Fail to Reject	2.61	0.94
SH	51 m	0.10	0.22	Fail to Reject	2.93	0.88
WNW	3 m	0.26	0.05	Reject	2.19	1.45
WNW	9 m	0.05	0.08	Fail to Reject	1.87	1.30
WNW	15 m	0.05	0.11	Fail to Reject	2.37	1.04
WNW	21 m	0.05	0.14	Fail to Reject	2.85	0.85
WNW	30 m	0.08	0.17	Fail to Reject	3.57	0.68
WNW	51 m	0.09	0.22	Fail to Reject	4.27	0.56
All Fracs	3 m	0.04	0.05	Fail to Reject	2.02	4.64
All Fracs	9 m	0.06	0.08	Fail to Reject	3.56	2.53
All Fracs	15 m	0.05	0.11	Fail to Reject	4.59	1.95
All Fracs	21 m	0.08	0.14	Fail to Reject	5.51	1.59
All Fracs	30 m	0.07	0.17	Fail to Reject	6.34	1.37
All Fracs	51 m	0.09	0.22	Fail to Reject	6.75	1.32

Table 4-59. Analysis results for Weibull distribution, domain FSM_C.

Fracture Set	Section Length	Test Statistic	Critical Value	Test Result $\alpha_{95} = 0.05$	Distribution Parameters	
					Alpha	Beta
ENE	3 m	0.41	0.05	Reject	2.49	1.08
ENE	9 m	0.10	0.08	Reject	1.17	1.73
ENE	15 m	0.06	0.11	Fail to Reject	1.41	1.81
ENE	21 m	0.07	0.14	Fail to Reject	1.49	1.83
ENE	30 m	0.06	0.17	Fail to Reject	1.89	1.83
ENE	51 m	0.07	0.22	Fail to Reject	2.31	1.88
N-S	3 m	0.32	0.05	Reject	1.36	3.72
N-S	9 m	0.08	0.08	Fail to Reject	1.06	2.26
N-S	15 m	0.06	0.11	Fail to Reject	1.24	2.38
N-S	21 m	0.07	0.14	Fail to Reject	1.41	2.41
N-S	30 m	0.05	0.17	Fail to Reject	1.53	2.37
N-S	51 m	0.11	0.22	Fail to Reject	1.64	2.42
SH	3 m	0.14	0.05	Reject	1.20	3.22
SH	9 m	0.03	0.08	Fail to Reject	1.26	2.83
SH	15 m	0.04	0.11	Fail to Reject	1.35	2.79
SH	21 m	0.04	0.14	Fail to Reject	1.50	2.68
SH	30 m	0.06	0.17	Fail to Reject	1.59	2.71
SH	51 m	0.10	0.22	Fail to Reject	1.76	2.82
WNW	3 m	0.23	0.05	Reject	1.47	3.54
WNW	9 m	0.04	0.08	Fail to Reject	1.41	2.62
WNW	15 m	0.05	0.11	Fail to Reject	1.64	2.68
WNW	21 m	0.05	0.14	Fail to Reject	1.75	2.67
WNW	30 m	0.08	0.17	Fail to Reject	2.06	2.67
WNW	51 m	0.07	0.22	Fail to Reject	2.38	2.60
All Fracs	3 m	0.04	0.05	Fail to Reject	1.55	10.46
All Fracs	9 m	0.04	0.08	Fail to Reject	2.03	10.06
All Fracs	15 m	0.04	0.11	Fail to Reject	2.20	10.06
All Fracs	21 m	0.08	0.14	Fail to Reject	2.48	9.79
All Fracs	30 m	0.09	0.17	Fail to Reject	2.71	9.69
All Fracs	51 m	0.10	0.22	Fail to Reject	2.88	9.78

Table 4-60. Analysis results for Gamma distribution, domain FSM_EW007.

Fracture Set	Section Length	Test Statistic	Critical Value	Test Result $\alpha_{95} = 0.05$	Distribution Parameters	
					Alpha	Beta
ENE	3 m	0.34	0.05	Reject	0.71	2.77
ENE	9 m	0.10	0.09	Reject	1.21	1.59
ENE	15 m	0.06	0.13	Fail to Reject	1.45	1.34
ENE	21 m	0.07	0.16	Fail to Reject	1.64	1.14
ENE	30 m	0.08	0.22	Fail to Reject	2.16	0.92
ENE	51 m	0.08	0.28	Fail to Reject	2.76	0.70
N-S	3 m	0.21	0.05	Reject	0.94	3.14
N-S	9 m	0.07	0.09	Fail to Reject	1.97	1.43
N-S	15 m	0.08	0.13	Fail to Reject	2.57	1.07
N-S	21 m	0.11	0.16	Fail to Reject	3.18	0.82
N-S	30 m	0.07	0.22	Fail to Reject	4.77	0.48
N-S	51 m	0.20	0.28	Fail to Reject	3.99	0.65
SH	3 m	0.08	0.05	Reject	1.55	2.85
SH	9 m	0.09	0.09	Fail to Reject	2.27	1.86
SH	15 m	0.09	0.13	Fail to Reject	2.25	1.88
SH	21 m	0.14	0.16	Fail to Reject	2.73	1.42
SH	30 m	0.15	0.22	Fail to Reject	2.08	1.71
SH	51 m	0.19	0.28	Fail to Reject	3.52	1.13
WNW	3 m	0.20	0.05	Reject	1.00	2.88
WNW	9 m	0.05	0.09	Fail to Reject	1.51	1.89
WNW	15 m	0.06	0.13	Fail to Reject	1.89	1.50
WNW	21 m	0.07	0.16	Fail to Reject	1.85	1.45
WNW	30 m	0.09	0.22	Fail to Reject	2.28	1.15
WNW	51 m	0.08	0.28	Fail to Reject	2.81	1.02
All Fracs	3 m	0.06	0.05	Reject	2.53	4.84
All Fracs	9 m	0.06	0.09	Fail to Reject	3.61	3.28
All Fracs	15 m	0.09	0.13	Fail to Reject	3.69	3.18
All Fracs	21 m	0.11	0.16	Fail to Reject	4.08	2.71
All Fracs	30 m	0.10	0.22	Fail to Reject	3.82	2.73
All Fracs	51 m	0.11	0.28	Fail to Reject	4.76	2.39

Table 4-61. Analysis results for Weibull distribution, domain FSM_EW007.

Fracture Set	Section Length	Test Statistic	Critical Value	Test Result $\alpha_{95} = 0.05$	Distribution Parameters	
					Alpha	Beta
ENE	3 m	0.34	0.05	Reject	0.63	1.48
ENE	9 m	0.10	0.09	Reject	1.02	1.89
ENE	15 m	0.07	0.13	Fail to Reject	1.17	2.00
ENE	21 m	0.08	0.16	Fail to Reject	1.22	1.95
ENE	30 m	0.07	0.22	Fail to Reject	1.35	2.15
ENE	51 m	0.11	0.28	Fail to Reject	1.56	2.08
N-S	3 m	0.21	0.05	Reject	0.67	2.43
N-S	9 m	0.09	0.09	Fail to Reject	1.33	3.04
N-S	15 m	0.08	0.13	Fail to Reject	1.57	3.05
N-S	21 m	0.08	0.16	Fail to Reject	1.63	2.93
N-S	30 m	0.08	0.22	Fail to Reject	2.32	2.49
N-S	51 m	0.20	0.28	Fail to Reject	2.33	2.79
SH	3 m	0.10	0.05	Reject	0.95	4.55
SH	9 m	0.09	0.09	Reject	1.16	4.74
SH	15 m	0.10	0.13	Fail to Reject	1.19	4.72
SH	21 m	0.13	0.16	Fail to Reject	1.21	4.41
SH	30 m	0.10	0.22	Fail to Reject	1.16	3.84
SH	51 m	0.24	0.28	Fail to Reject	1.34	4.54
WNW	3 m	0.20	0.05	Reject	0.72	2.49
WNW	9 m	0.07	0.09	Fail to Reject	1.15	2.95
WNW	15 m	0.07	0.13	Fail to Reject	1.27	3.05
WNW	21 m	0.08	0.16	Fail to Reject	1.33	2.87
WNW	30 m	0.13	0.22	Fail to Reject	1.40	2.84
WNW	51 m	0.10	0.28	Fail to Reject	1.81	3.01
All Fracs	3 m	0.10	0.05	Reject	1.15	14.17
All Fracs	9 m	0.07	0.09	Fail to Reject	1.79	13.45
All Fracs	15 m	0.07	0.13	Fail to Reject	1.77	13.33
All Fracs	21 m	0.09	0.16	Fail to Reject	1.73	12.59
All Fracs	30 m	0.10	0.22	Fail to Reject	1.83	11.56
All Fracs	51 m	0.15	0.28	Fail to Reject	1.95	12.59

Table 4-62. Analysis results for Gamma distribution, domain FSM_N.

Fracture Set	Section Length	Test Statistic	Critical Value	Test Result $\alpha_{95} = 0.05$	Distribution Parameters	
					Alpha	Beta
ENE	3 m	0.40	0.07	Reject	0.60	2.32
ENE	9 m	0.12	0.13	Fail to Reject	1.33	1.04
ENE	15 m	0.10	0.18	Fail to Reject	1.91	0.68
ENE	21 m	0.13	0.25	Fail to Reject	1.50	0.97
ENE	30 m	0.12	0.34	Fail to Reject	2.35	0.54
ENE	51 m	Too few data bins for a reasonable data fit				
N-S	3 m	0.23	0.07	Reject	0.99	2.66
N-S	9 m	0.10	0.13	Fail to Reject	1.77	1.43
N-S	15 m	0.10	0.18	Fail to Reject	1.92	1.26
N-S	21 m	0.08	0.25	Fail to Reject	2.08	1.10
N-S	30 m	0.17	0.34	Fail to Reject	3.50	0.55
N-S	51 m	Too few data bins for a reasonable data fit				
SH	3 m	0.04	0.07	Fail to Reject	2.65	1.74
SH	9 m	0.09	0.13	Fail to Reject	4.87	0.93
SH	15 m	0.11	0.18	Fail to Reject	5.07	0.87
SH	21 m	0.12	0.25	Fail to Reject	6.54	0.63
SH	30 m	0.18	0.34	Fail to Reject	5.78	0.69
SH	51 m	Too few data bins for a reasonable data fit				
WNW	3 m	0.27	0.07	Reject	0.80	3.33
WNW	9 m	0.07	0.13	Fail to Reject	1.50	1.86
WNW	15 m	0.07	0.18	Fail to Reject	1.63	1.60
WNW	21 m	0.11	0.25	Fail to Reject	1.81	1.47
WNW	30 m	0.17	0.34	Fail to Reject	2.21	1.17
WNW	51 m	Too few data bins for a reasonable data fit				
All Fracs	3 m	0.04	0.07	Fail to Reject	2.89	3.91
All Fracs	9 m	0.07	0.13	Fail to Reject	4.74	2.37
All Fracs	15 m	0.10	0.18	Fail to Reject	5.14	2.09
All Fracs	21 m	0.15	0.25	Fail to Reject	6.30	1.67
All Fracs	30 m	0.13	0.34	Fail to Reject	6.07	1.61
All Fracs	51 m	Too few data bins for a reasonable data fit				

Table 4-63. Analysis results for Weibull distribution, domain FSM_N.

Fracture Set	Section Length	Test Statistic	Critical Value	Test Result $\alpha_{95} = 0.05$	Distribution Parameters	
					Alpha	Beta
ENE	3 m	0.40	0.07	Reject	0.76	1.20
ENE	9 m	0.12	0.13	Fail to Reject	1.20	1.40
ENE	15 m	0.11	0.18	Fail to Reject	1.57	1.37
ENE	21 m	0.11	0.25	Fail to Reject	1.48	1.47
ENE	30 m	0.12	0.34	Fail to Reject	1.85	1.30
ENE	51 m	Too few data bins for a reasonable data fit				
N-S	3 m	0.23	0.07	Reject	0.68	2.17
N-S	9 m	0.08	0.13	Fail to Reject	1.24	2.70
N-S	15 m	0.11	0.18	Fail to Reject	1.22	2.63
N-S	21 m	0.10	0.25	Fail to Reject	1.33	2.47
N-S	30 m	0.21	0.34	Fail to Reject	1.29	2.16
N-S	51 m	Too few data bins for a reasonable data fit				
SH	3 m	0.04	0.07	Fail to Reject	1.66	5.15
SH	9 m	0.07	0.13	Fail to Reject	2.25	5.10
SH	15 m	0.10	0.18	Fail to Reject	2.21	4.91
SH	21 m	0.10	0.25	Fail to Reject	2.54	4.55
SH	30 m	0.17	0.34	Fail to Reject	2.31	4.36
SH	51 m	Too few data bins for a reasonable data fit				
WNW	3 m	0.27	0.07	Reject	0.62	2.03
WNW	9 m	0.07	0.13	Fail to Reject	1.14	2.86
WNW	15 m	0.06	0.18	Fail to Reject	1.27	2.77
WNW	21 m	0.10	0.25	Fail to Reject	1.24	2.82
WNW	30 m	0.15	0.34	Fail to Reject	1.28	2.72
WNW	51 m	Too few data bins for a reasonable data fit				
All Fracs	3 m	0.05	0.07	Fail to Reject	1.88	12.58
All Fracs	9 m	0.05	0.13	Fail to Reject	2.29	12.58
All Fracs	15 m	0.08	0.18	Fail to Reject	2.27	11.98
All Fracs	21 m	0.13	0.25	Fail to Reject	2.41	11.71
All Fracs	30 m	0.16	0.34	Fail to Reject	2.21	10.65
All Fracs	51 m	Too few data bins for a reasonable data fit				

Table 4-64. Analysis results for Gamma distribution, domain FSM_NE005.

Fracture Set	Section Length	Test Statistic	Critical Value	Test Result $\alpha_{95} = 0.05$	Distribution Parameters	
					Alpha	Beta
ENE	3 m	0.38	0.05	Reject	0.68	2.36
ENE	9 m	0.12	0.10	Reject	1.21	1.30
ENE	15 m	0.05	0.13	Fail to Reject	1.69	0.91
ENE	21 m	0.06	0.16	Fail to Reject	1.89	0.81
ENE	30 m	0.06	0.20	Fail to Reject	2.27	0.69
ENE	51 m	0.10	0.27	Fail to Reject	2.92	0.54
N-S	3 m	0.12	0.05	Reject	1.53	2.81
N-S	9 m	0.07	0.10	Fail to Reject	2.96	1.44
N-S	15 m	0.09	0.13	Fail to Reject	3.06	1.37
N-S	21 m	0.07	0.16	Fail to Reject	4.05	1.03
N-S	30 m	0.11	0.20	Fail to Reject	4.61	0.89
N-S	51 m	0.14	0.27	Fail to Reject	6.79	0.63
SH	3 m	0.08	0.05	Reject	1.32	2.39
SH	9 m	0.04	0.10	Fail to Reject	1.91	1.61
SH	15 m	0.05	0.13	Fail to Reject	2.05	1.49
SH	21 m	0.08	0.16	Fail to Reject	2.24	1.35
SH	30 m	0.08	0.20	Fail to Reject	2.22	1.33
SH	51 m	0.14	0.27	Fail to Reject	2.10	1.35
WNW	3 m	0.18	0.05	Reject	1.13	2.10
WNW	9 m	0.04	0.10	Fail to Reject	2.65	0.86
WNW	15 m	0.07	0.13	Fail to Reject	2.95	0.79
WNW	21 m	0.05	0.16	Fail to Reject	4.98	0.46
WNW	30 m	0.12	0.20	Fail to Reject	5.53	0.41
WNW	51 m	0.15	0.27	Fail to Reject	10.62	0.21
All Fracs	3 m	0.05	0.05	Fail to Reject	3.37	3.39
All Fracs	9 m	0.07	0.10	Fail to Reject	5.72	1.95
All Fracs	15 m	0.05	0.13	Fail to Reject	6.21	1.80
All Fracs	21 m	0.06	0.16	Fail to Reject	3.09	12.25
All Fracs	30 m	0.08	0.20	Fail to Reject	9.23	1.18
All Fracs	51 m	0.13	0.27	Fail to Reject	13.54	0.81

Table 4-65. Analysis results for Weibull distribution, domain FSM_NE005.

Fracture Set	Section Length	Test Statistic	Critical Value	Test Result $\alpha_{95} = 0.05$	Distribution Parameters	
					Alpha	Beta
ENE	3 m	0.38	0.05	Reject	0.71	1.31
ENE	9 m	0.12	0.10	Reject	1.09	1.56
ENE	15 m	0.06	0.13	Fail to Reject	1.36	1.64
ENE	21 m	0.05	0.16	Fail to Reject	1.40	1.65
ENE	30 m	0.09	0.20	Fail to Reject	1.51	1.69
ENE	51 m	0.13	0.27	Fail to Reject	1.75	1.68
N-S	3 m	0.14	0.05	Reject	0.80	4.24
N-S	9 m	0.06	0.10	Fail to Reject	1.53	4.79
N-S	15 m	0.06	0.13	Fail to Reject	1.64	4.70
N-S	21 m	0.07	0.16	Fail to Reject	1.96	4.70
N-S	30 m	0.10	0.20	Fail to Reject	2.34	4.53
N-S	51 m	0.15	0.27	Fail to Reject	2.70	4.66
SH	3 m	0.07	0.05	Reject	1.04	3.20
SH	9 m	0.03	0.10	Fail to Reject	1.42	3.33
SH	15 m	0.05	0.13	Fail to Reject	1.53	3.32
SH	21 m	0.09	0.16	Fail to Reject	1.69	3.28
SH	30 m	0.08	0.20	Fail to Reject	1.68	3.16
SH	51 m	0.13	0.27	Fail to Reject	1.71	2.94
WNW	3 m	0.18	0.05	Reject	0.86	2.19
WNW	9 m	0.06	0.10	Fail to Reject	1.65	2.53
WNW	15 m	0.06	0.13	Fail to Reject	2.05	2.57
WNW	21 m	0.07	0.16	Fail to Reject	2.49	2.53
WNW	30 m	0.15	0.20	Fail to Reject	2.36	2.54
WNW	51 m	0.16	0.27	Fail to Reject	3.89	2.43
All Fracs	3 m	0.06	0.05	Fail to Reject	1.62	13.12
All Fracs	9 m	0.04	0.10	Fail to Reject	2.38	12.64
All Fracs	15 m	0.05	0.13	Fail to Reject	2.67	12.46
All Fracs	21 m	0.07	0.16	Fail to Reject	9.03	1.22
All Fracs	30 m	0.06	0.20	Fail to Reject	3.25	11.97
All Fracs	51 m	0.14	0.27	Fail to Reject	3.84	11.80

Table 4-66. Analysis results for Gamma distribution, domain FSM_W.

Fracture Set	Section Length	Test Statistic	Critical Value	Test Result $\alpha_{95} = 0.05$	Distribution Parameters	
					Alpha	Beta
ENE	3 m	0.36	0.04	Reject	0.67	2.38
ENE	9 m	0.10	0.08	Reject	1.24	1.22
ENE	15 m	0.06	0.11	Fail to Reject	1.51	1.00
ENE	21 m	0.04	0.14	Fail to Reject	1.87	0.78
ENE	30 m	0.07	0.18	Fail to Reject	1.96	0.74
ENE	51 m	0.12	0.23	Fail to Reject	2.66	0.53
N-S	3 m	0.20	0.04	Reject	0.87	4.14
N-S	9 m	0.04	0.08	Fail to Reject	1.30	2.70
N-S	15 m	0.06	0.11	Fail to Reject	1.70	2.02
N-S	21 m	0.07	0.14	Fail to Reject	1.59	2.00
N-S	30 m	0.08	0.18	Fail to Reject	2.06	1.61
N-S	51 m	0.13	0.23	Fail to Reject	2.14	1.53
SH	3 m	0.09	0.04	Reject	1.16	2.93
SH	9 m	0.04	0.08	Fail to Reject	1.71	1.97
SH	15 m	0.05	0.11	Fail to Reject	1.79	1.83
SH	21 m	0.07	0.14	Fail to Reject	1.93	1.70
SH	30 m	0.07	0.18	Fail to Reject	2.03	1.69
SH	51 m	0.12	0.23	Fail to Reject	2.59	1.26
WNW	3 m	0.27	0.04	Reject	0.84	2.35
WNW	9 m	0.07	0.08	Fail to Reject	1.53	1.23
WNW	15 m	0.09	0.11	Fail to Reject	1.85	0.97
WNW	21 m	0.10	0.14	Fail to Reject	2.14	0.80
WNW	30 m	0.13	0.18	Fail to Reject	3.04	0.55
WNW	51 m	0.07	0.23	Fail to Reject	4.37	0.36
All Fracs	3 m	0.05	0.04	Reject	2.01	5.25
All Fracs	9 m	0.05	0.08	Fail to Reject	2.76	3.72
All Fracs	15 m	0.06	0.11	Fail to Reject	3.17	3.16
All Fracs	21 m	0.07	0.14	Fail to Reject	3.18	3.04
All Fracs	30 m	0.09	0.18	Fail to Reject	3.84	2.57
All Fracs	51 m	0.08	0.23	Fail to Reject	4.36	2.18

Table 4-67. Analysis results for Weibull distribution, domain FSM_W.

Fracture Set	Section Length	Test Statistic	Critical Value	Test Result $\alpha_{95} = 0.05$	Distribution Parameters	
					Alpha	Beta
ENE	3 m	0.36	0.04	Reject	0.72	1.32
ENE	9 m	0.10	0.08	Reject	1.11	1.53
ENE	15 m	0.05	0.11	Fail to Reject	1.34	1.59
ENE	21 m	0.05	0.14	Fail to Reject	1.40	1.56
ENE	30 m	0.07	0.18	Fail to Reject	1.70	1.53
ENE	51 m	0.12	0.23	Fail to Reject	1.79	1.52
N-S	3 m	0.20	0.04	Reject	0.63	2.85
N-S	9 m	0.06	0.08	Fail to Reject	1.08	3.57
N-S	15 m	0.06	0.11	Fail to Reject	1.28	3.66
N-S	21 m	0.06	0.14	Fail to Reject	1.27	3.39
N-S	30 m	0.08	0.18	Fail to Reject	1.44	3.59
N-S	51 m	0.11	0.23	Fail to Reject	1.47	3.51
SH	3 m	0.09	0.04	Reject	0.88	3.23
SH	9 m	0.05	0.08	Fail to Reject	1.24	3.61
SH	15 m	0.03	0.11	Fail to Reject	1.30	3.54
SH	21 m	0.07	0.14	Fail to Reject	1.34	3.57
SH	30 m	0.08	0.18	Fail to Reject	1.62	3.65
SH	51 m	0.14	0.23	Fail to Reject	1.78	3.53
WNW	3 m	0.27	0.04	Reject	0.74	1.64
WNW	9 m	0.07	0.08	Fail to Reject	1.10	1.93
WNW	15 m	0.08	0.11	Fail to Reject	1.23	1.93
WNW	21 m	0.07	0.14	Fail to Reject	1.33	1.87
WNW	30 m	0.14	0.18	Fail to Reject	1.50	1.87
WNW	51 m	0.08	0.23	Fail to Reject	2.19	1.75
All Fracs	3 m	0.07	0.04	Reject	1.10	11.76
All Fracs	9 m	0.03	0.08	Fail to Reject	1.61	11.55
All Fracs	15 m	0.04	0.11	Fail to Reject	1.78	11.24
All Fracs	21 m	0.06	0.14	Fail to Reject	1.74	10.77
All Fracs	30 m	0.08	0.18	Fail to Reject	2.05	10.90
All Fracs	51 m	0.07	0.23	Fail to Reject	2.12	10.51

5 Verification and validation of the SDM-Site Laxemar geological DFN models

5.1 Objectives

The purpose of verification is to build confidence during model development and to establish the scientific basis and accuracy of the model within its intended scope of use. This chapter concentrates on the verification of the base DFN model parameters (referred to as the Base Model) as described in Chapters 3 and 4.

The verification cases for the SDM-Site Laxemar geological DFN consisted of:

- An evaluation of the effect of lumping versus splitting fracture orientation sets.
- An evaluation of the variability of the orientation set mean pole vectors and the Fisher concentration parameter (Case OR-1).
- A verification of the coupled size-intensity model using simulated versus observed outcrop fracture intensity (SI-1).
- A verification of the coupled size-intensity model using P_{10} intensity on simulated and observed scanlines (SI-2).
- A verification of the orientation and size models using a comparison between simulated and observed cored borehole fracture intercepts (SI-3).
- A verification of the coupled size-intensity model for fractures hypothesized to lie within the MDZ size range (SI-4).
- A verification of the DFN spatial model through additional analysis of the Gamma and Weibull distribution fits for fracture intensity (P_{32}).

Table 5-1 presents a list of the alternative models (and their abbreviations) upon with the verification cases were performed; this table is a duplicate of Table 4-11. At the end of the verification, the alternative models are ranked according to their performance.

5.2 Verification of orientation set divisions

5.2.1 Evaluation of set-divided data

It should be kept in mind that the cluster significance observed in the raw data (Figure 4-13) to some extent includes the combined overlap of fracture sets. To demonstrate the significance of isolated fracture sets, the significance of set populations (Table 4-3) is calculated for a case where expected population set equal to the total fracture population (53,476 poles); in other words, the purpose is to demonstrate fracture sets isolated from set overlapping contributions (Figure 5-1). In comparison to the raw data (Figure 4-13), the isolated sets SH and N-S (Figure 5-1) are equally strong, while the isolated sets ENE and WNW appear much weaker. This signifies that the orientation distributions of sets ENE and WNW overlap to a high degree. Nevertheless, even isolated sets prove to be significant.

In terms of distribution of solid angle to set mean pole, the set-divided data conform well to the underlying assumed univariate Fisher distribution, irrespectively of inclusion of borehole data Not Visible in BIPS (Figure 5-2 and Figure 5-3). Minor discrepancies can be observed for the N-S set, which relate to its radial asymmetry (i.e. elliptical shape corresponding to rotation in strike (Figure 5-4, Figure 5-5). Furthermore, a radial asymmetry can be observed in the SH set; the peak concentration deviates slightly from the centre of the cluster. Overall, the underlying assumption of univariate Fisher distributed data, which was the basis for set-division of fracture data, appears reasonable.

Table 5-1. Alternative model cases.

Model Case	Scaling	Outcrop Traces	Scaling Exponent Fit	FSM-Specific Scaling Exponent
BM	Euclidean	Linked	Best	No
EL1	Euclidean	Linked	Upper	No
EL2	Euclidean	Linked	Lower	No
BMU	Euclidean	Unlinked	Best	No
EUL1	Euclidean	Unlinked	Upper	No
EUL2	Euclidean	Unlinked	Lower	No
BMF	Fractal	Linked	Best	No
FL1	Fractal	Linked	Upper	No
FL2	Fractal	Linked	Lower	No
BMUF	Fractal	Unlinked	Best	No
FUL1	Fractal	Unlinked	Upper	No
FUL2	Fractal	Unlinked	Lower	No
ESL1_N	Euclidean	Linked	Best	FSM_N
ESL1_NE005	Euclidean	Linked	Best	FSM_NE005
ESL1_W	Euclidean	Linked	Best	FSM_W
ESL2_N	Euclidean	Linked	Upper	FSM_N
ESL2_NE005	Euclidean	Linked	Upper	FSM_NE005
ESL2_W	Euclidean	Linked	Upper	FSM_W
ESL3_N	Euclidean	Linked	Lower	FSM_N
ESL3_NE005	Euclidean	Linked	Lower	FSM_NE005
ESL3_W	Euclidean	Linked	Lower	FSM_W
FSL1_N	Fractal	Linked	Best	FSM_N
FSL1_NE005	Fractal	Linked	Best	FSM_NE005
FSL1_W	Fractal	Linked	Best	FSM_W
FSL2_N	Fractal	Linked	Upper	FSM_N
FSL2_NE005	Fractal	Linked	Upper	FSM_NE005
FSL2_W	Fractal	Linked	Upper	FSM_W
FSL3_N	Fractal	Linked	Lower	FSM_N
FSL3_NE005	Fractal	Linked	Lower	FSM_NE005
FSL3_W	Fractal	Linked	Lower	FSM_W

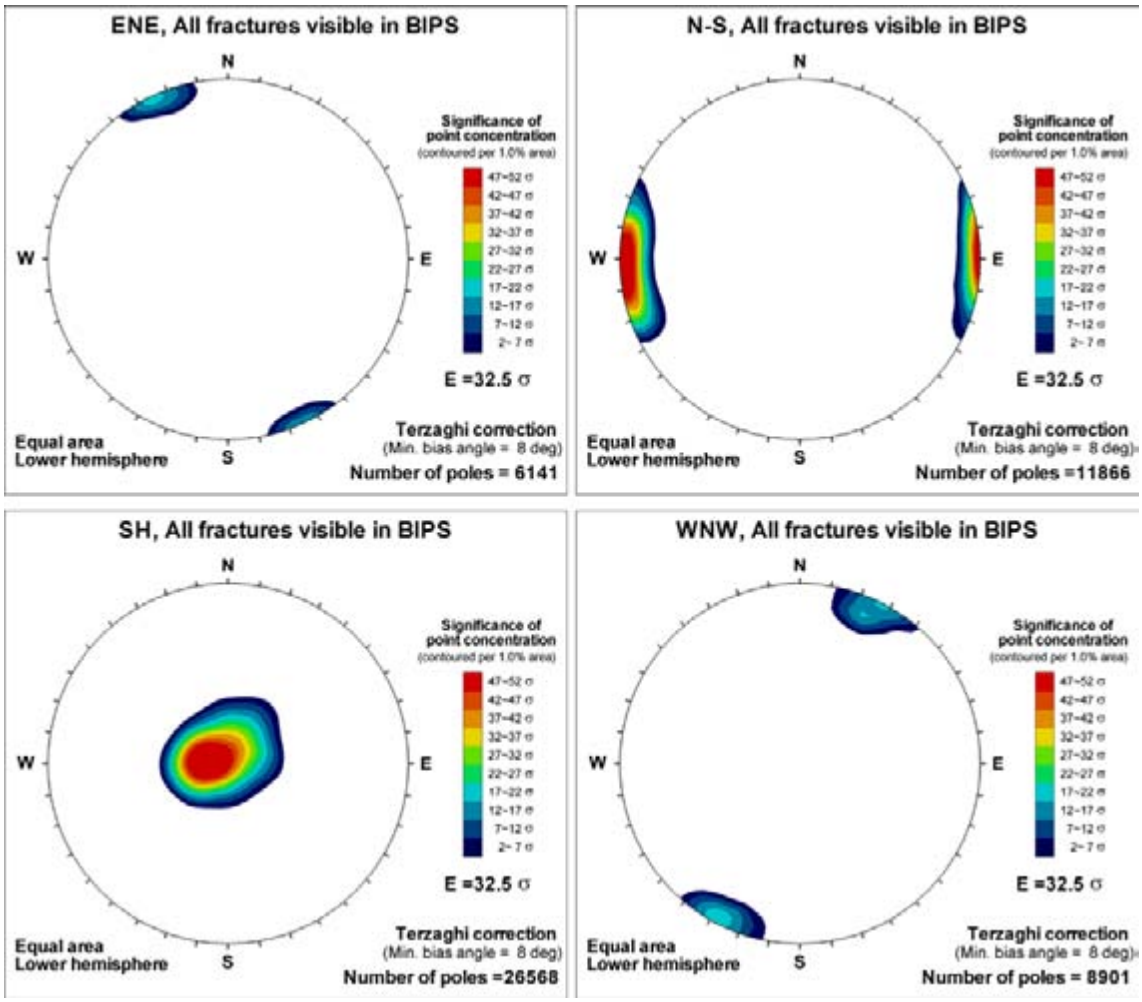

Figure 5-1. *Cluster significance of set-divided outcrop data and borehole data Visible in BIPS. Note that significance is calculated for an expected total fracture population of 53,476 fractures, in order to simplify comparison to Figure 4-13 and Figure 4-16.*

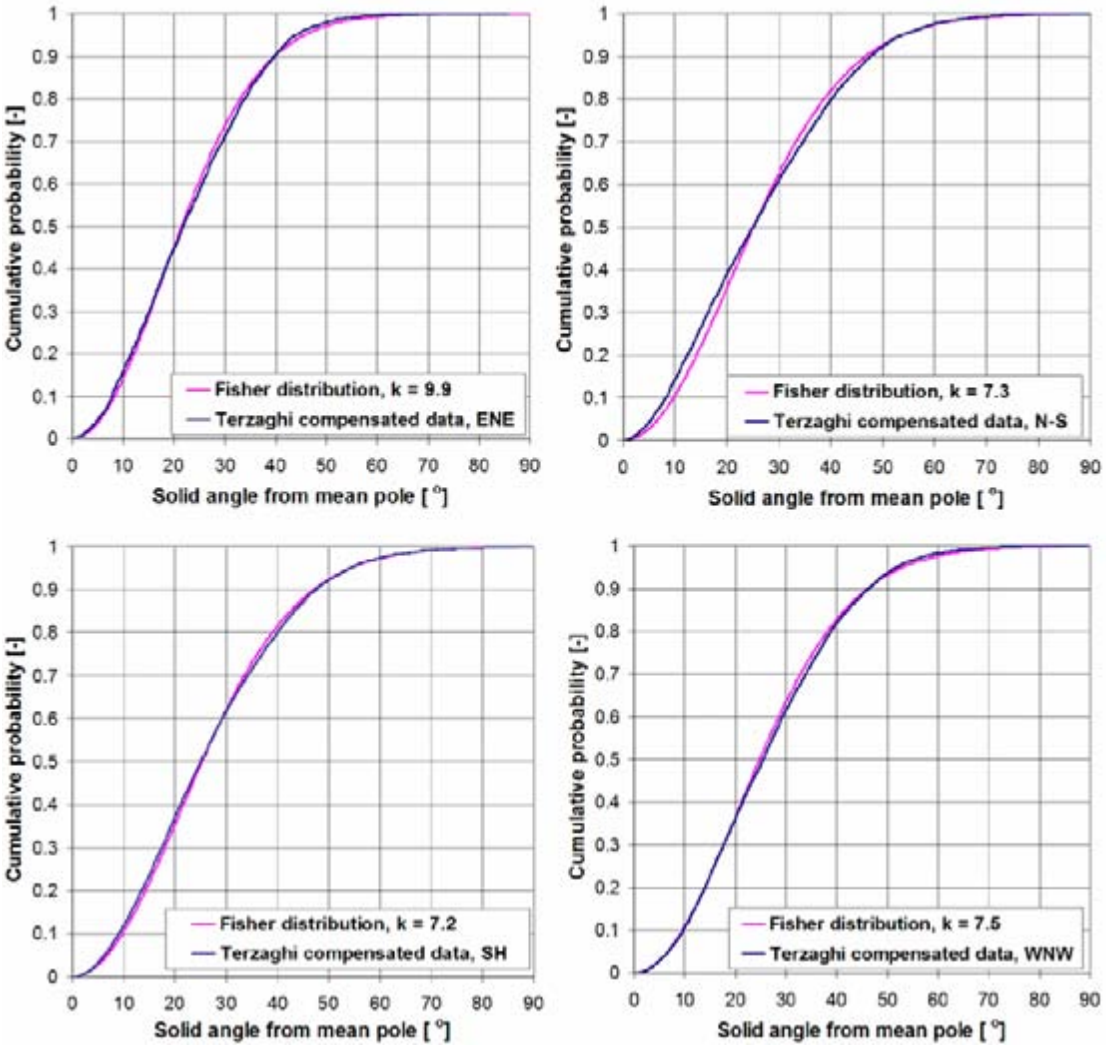

Figure 5-2. *Cumulative density function of solid angle for all outcrop data and borehole data Visible in BIPS; data compared to the analytical Univariate Fisher distribution. KLX02 (RSMBA03), KLX06 and KLX20A west of ZSMNS001 are excluded.*

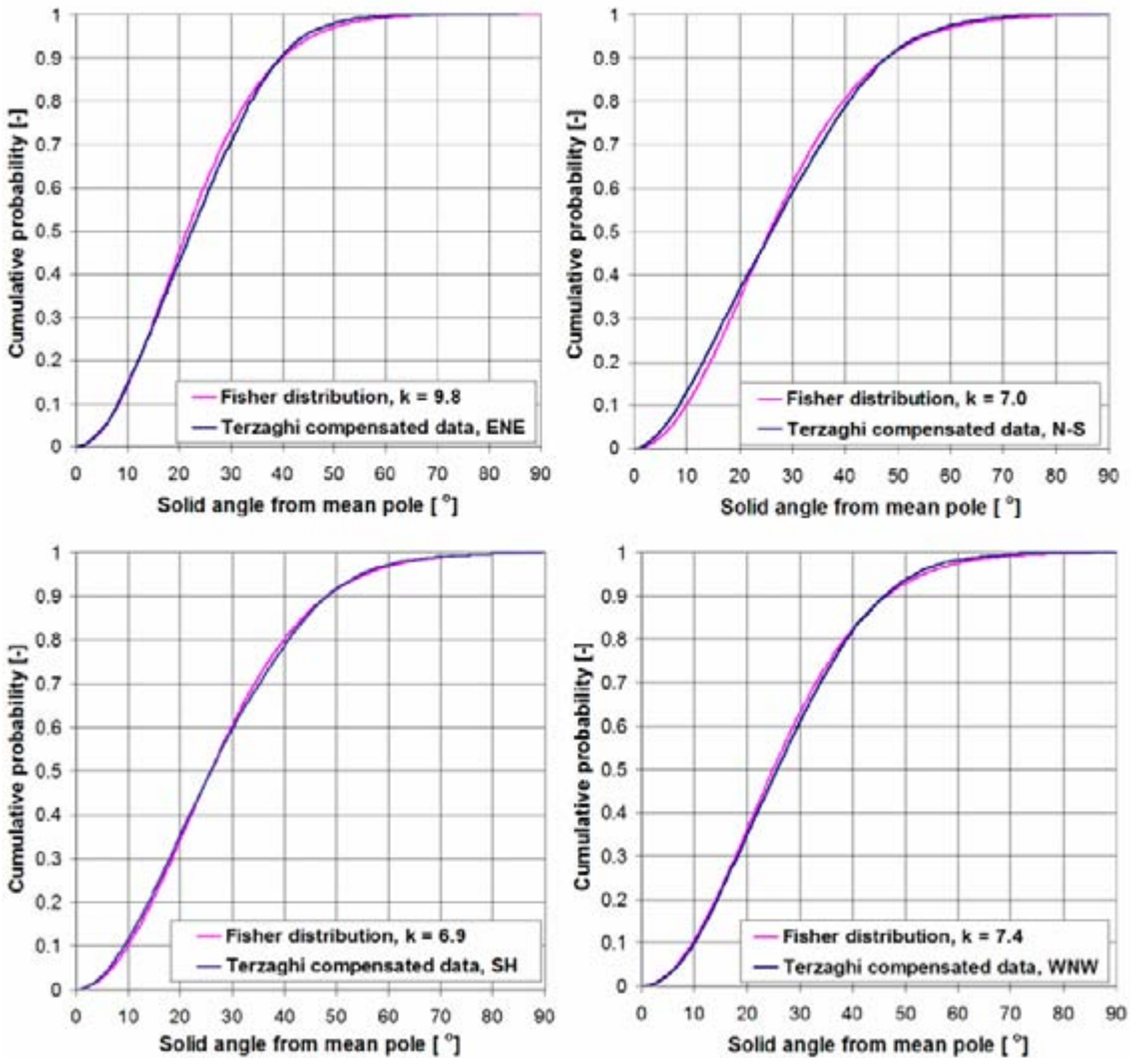

Figure 5-3. *Cumulative density function of solid angle for all set-divided data, even non-Visible in BIPS; data compared to the analytical univariate Fisher distribution. Note that all fractures are included, even those Not Visible in BIPS. However, KLX02 (RSMBA03), KLX09B, KLX06 and KLX20A west of ZSMNS001 are excluded.*

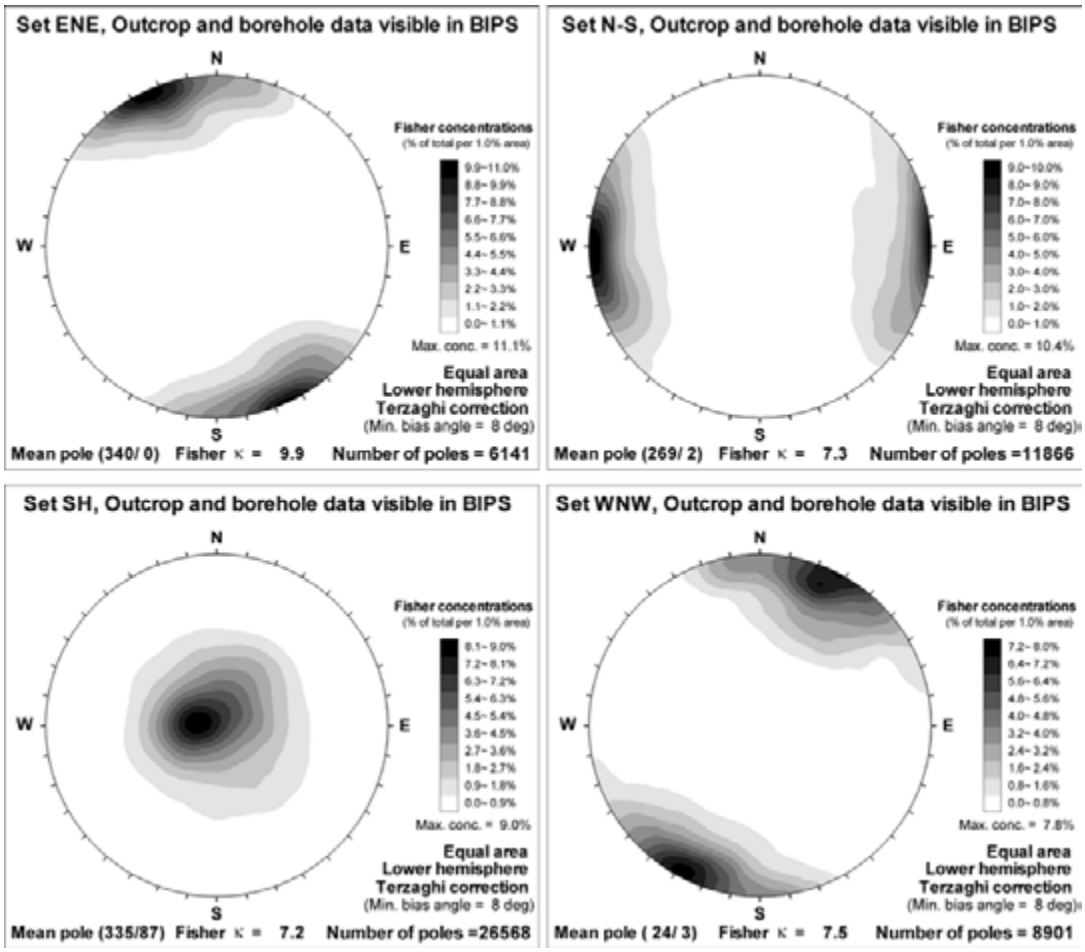

Figure 5-4. *Fracture set distributions divided by set, and including only borehole fractures labelled 'Visible in BIPS'.*

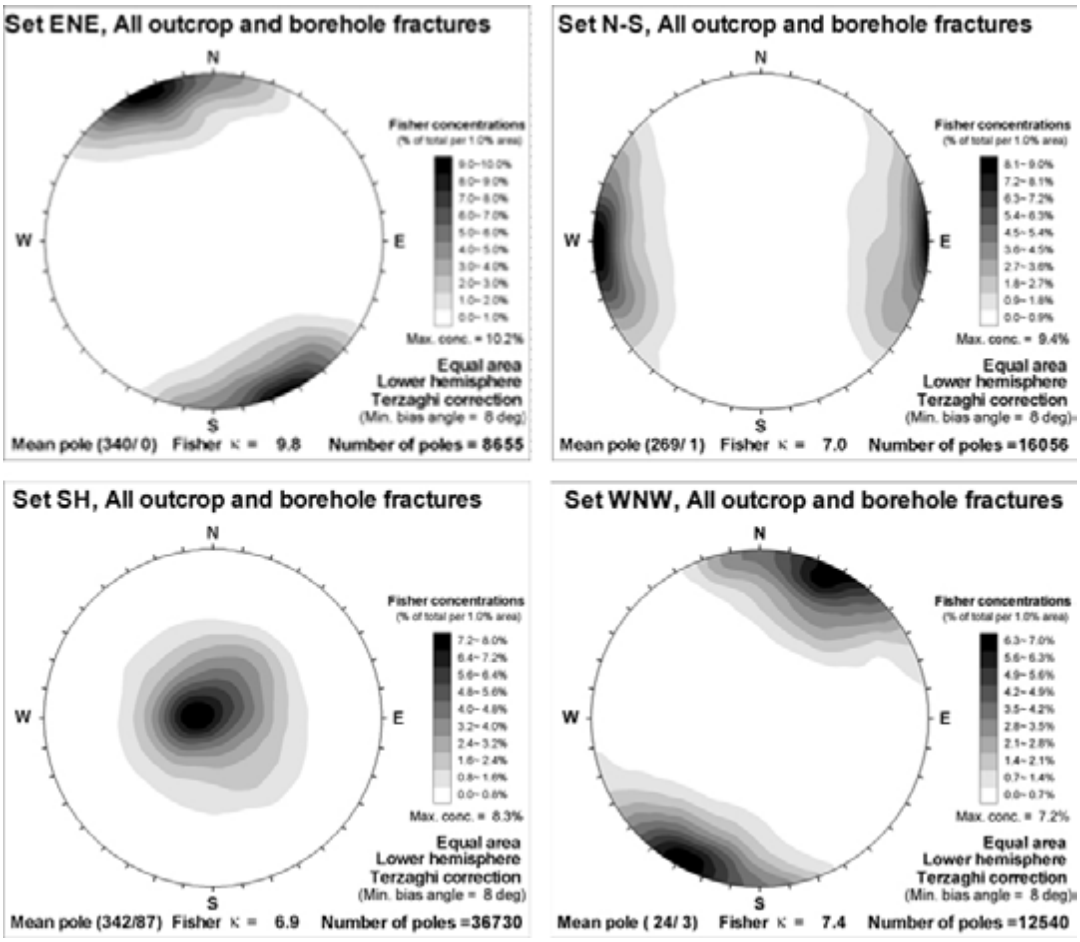

Figure 5-5. *Fracture set distributions set-divided outcrop data and all borehole data (including those fractures labelled 'Not Visible in BIPS').*

5.2.2 Verification OR-1: Orientation set confidence

The analyses conducted in verification case OR-1 are designed to strengthen the support for the Univariate Fisher distributions used in the SDM-Site Laxemar geological DFN orientation model (Sections 3.3 and 4.2), and to quantify orientation model parameter uncertainty. The evaluation of overlapping fracture sets conducted in the previous verification case (Section 5.2.1) suggests that, though there are idiosyncrasies (i.e. the elliptical shape of the N-S trending fracture poles in the Laxemar data versus the circular shape of the parameterised Fisher set) in some elements of the orientation model, the Univariate Fisher distributions fitted during orientation modelling are reasonable and appropriate for site fracture modelling.

Verification OR-1 quantifies uncertainty in the orientation model through the following metrics:

- α_{95}: The 95% confidence cone for the location of the Fisher mean pole, expressed as a radial distance from the mean pole vector /Fisher 1953/, /Fisher et al. 1987/. The uncertainty in the orientation of the dip vector for a fracture can be quantified using the 95% confidence cone.
- β: The strike uncertainty. The strike uncertainty is a function of the dip angle and the dip uncertainty, and is always greater than the dip uncertainty /Cronin 2008, after others/.
- θ_{95}: The angular (two) standard deviations. The Fisher distribution is directly analogous to the normal distribution, projected on the sphere. For a standard normal distributions, standard deviations can be used to quantify the area underneath the probability curve. 95% of observations for a sample from a normally-distributed population will fall within two standard deviations of the mean. The same concepts can be extended to the Fisher distribution on the sphere; if a Fisher distribution is an adequate fit to the observed data, 95% of the fracture poles should fall within two standard deviations.

The 95% confidence cone for the Fisher mean pole is an angular radius, and is defined by the following formula /Fisher et al. 1987/:

$$\alpha_{95} = \arccos\left(1 - \left\{\left(N - R/R\right)\left[\left(\frac{1}{P}\right)^{1/(N-1)} - 1\right]\right\}\right)$$ Equation 5-1

where:

N = number of samples;

R = length of mean resultant vector; and

P = probability (0.05 for a 95% confidence interval)

A convenient approximation of α_{95} has been suggested by /Butler 1992/ for $N \geq 10$ as:

$$\alpha_{95} \approx 140^{\circ}/\sqrt{\kappa N}$$ Equation 5-2

where:

κ = Fisher's concentration parameter

The strike uncertainty for the fracture orientation distributions, assuming no inherited error from sampling, is calculated using Equation 5.3 /Butler 1992/ after /Fisher et al. 1997/. This equation represents a simplification; the assumption is that the uncertainty in the fracture orientation data from Laxemar is carried through the DFN model parameterisation in the Fisher κ value.

$$\beta \approx \arctan\left(\frac{\sin(r_{total})\cos(\theta)}{(\cos(r_{total})\cos(\delta)) - (\sin(r_{total})\sin(\theta)\sin(\delta))}\right)$$ Equation 5-3

where:

$r_{total} = \sqrt{(\alpha_{95})^2 + M^2}$

$\theta = ;\arcsin\left(\frac{\sin(r_{total})\sin(\delta)}{\cos(r_{total})\cos(\delta)}\right)$

M = estimated random measurement error (assumed 0 in this verification); and

δ = plunge of the mean pole vector (degrees).

It is important to note that the strike uncertainty calculation described in Equation 5-3 is a simplified approximation used for the verification. Readers are encouraged to consult /Munier and Stigsson 2007/ and /Stigsson 2007/ for in-depth discussions on SKB's chosen methods for identifying and quantifying uncertainty in the orientation of fractures and borehole axes at Forsmark and Laxemar.

The angular standard two deviations, termed θ_{95}, can be approximated using the following formula /Fisher 1953, Butler 1992/:

$$\theta_{95} \approx 140^{\circ}/\sqrt{\kappa}$$ Equation 5-4

Verification OR-1 was performed by using the global fracture set orientation model (Section 4.2), summarized below in

Table 5-2, to calculate α_{95}, β, and θ_{95}. The calculated α_{95} and β can be used to assess potential set divisions of additional orientation data from new boreholes and outcrops, or can be used as an uncertainty parameter by downstream modellers. α_{95} and β are based on the following data:

- Fracture orientations from cored boreholes outside of deformation zones that were identified as 'Visible in BIPS', were inside the fracture domains, and possessed an orientation.
- Fracture orientations from detail-fracture-mapped outcrops. OR-1 does not include fracture orientations from trench mapping.

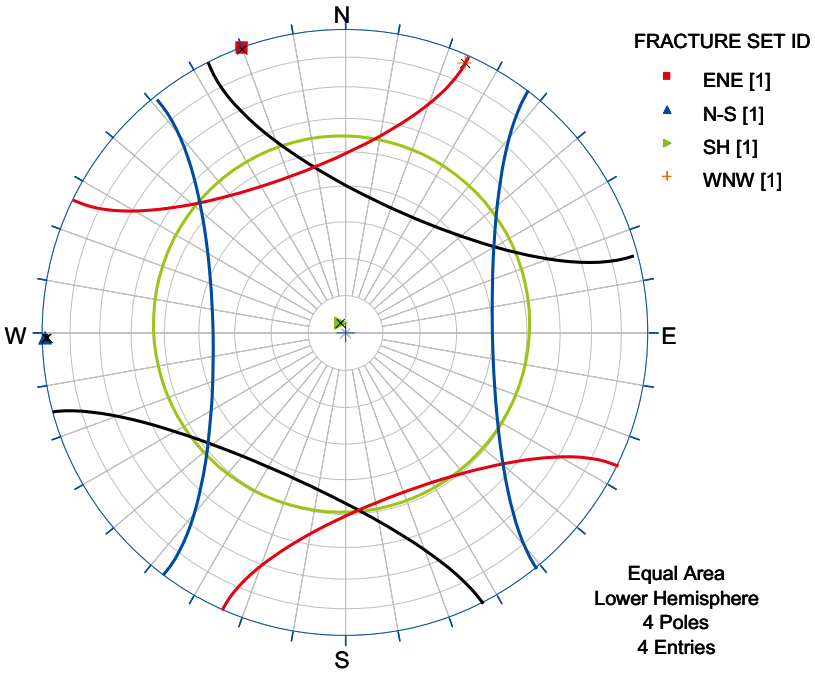

Figure 5-6. *θ_{95} limits for global orientation model by fracture set. The colour of the line represents the set colour (see legend). The cones represent the area within which 95% of the fracture poles should lay.*

Table 5-2. Global orientation model for SDM-Site Laxemar geological DFN model, including estimated values for α_{95}, β, and θ_{95}.

Fracture Set ID	Mean Pole Trend (°)	Plunge (°)	Fisher κ	Number of Poles	Orientation Uncertainty (°) α_{95}	β	θ_{95}
SH	335.1	87.1	7.2	5,881	0.68	13.83	52.17
ENE	340.3	0.5	9.9	11,341	0.42	0.42	44.49
WNW	24.1	3.1	7.5	26,285	0.32	0.32	51.12
N-S	269.1	1.7	7.3	8,538	0.56	0.56	51.82

Equation 5-5 is used to calculate the goodness-of-fit of the Fisher distributions based on the cored borehole fracture data Visible in BIPS. The angle θ between the fracture pole vector and the Univariate Fisher mean pole vector are calculated using Equation 5-5.

$$\vec{n} \cdot \vec{N} = \cos(\theta)$$ Equation 5-5

If the solid angle is greater than θ_{95}, then the pole vector falls outside the 95% confidence cone. The number of pole vectors inside and outside of the confidence cone are tabulated and presented in Table 5-3. The interpretation of 'goodness of fit' is qualitative; it is intended as a guide to downstream users as to the limitations of the assumption of Univariate Fisher distributions for modelling orientations.

Table 5-3 demonstrates that, for three of the four orientation sets, the Univariate Fisher distributions (and specifically the Fisher concentration parameter, κ) fit to the Laxemar cored borehole data, are adequate. The ENE, SH, and WNW set definitions encompass 93%–97% of the fracture poles (two standard deviations), which suggest that the orientation set parameterisation will do an adequate job of simulating the orientation distributions encountered at Laxemar. The N-S set parameterisation is slightly off; only 90% of the fractures fall within the two standard deviation radius. This suggests that the calculated κ value for the N-S orientation set parameterisation may be slightly too high. It is thought that the estimate of κ was biased slightly by using the Terzaghi weight-sums through the resultant-vector method. However, this hypothesis was not tested during the SDM-Site Laxemar geological DFN modelling due to a lack of time.

Table 5-3. Distribution of pole vectors of fractures Visible in BIPS in the Laxemar cored borehole array relative to θ_{95}.

Fracture Set	θ_{95}	Total number of fractures	Number of fractures $\Omega <= \theta_{95}$	Percentage of fractures
ENE	44.49	4,933	4,596	93%
N-S	51.82	9,683	8,710	90%
SH	52.17	25,560	24,573	96%
WNW	51.12	7,630	7,064	93%

5.2.3 Verification OR-2: Relative fracture set intensities

Fracture domains at Laxemar were defined based on a combination of relative fracture orientation set intensities and structural/tectonic boundaries. Terzaghi-compensated borehole fracture frequencies (P_{10}) were used in conjunction with Kamb-contoured stereonets to identify differences between fracture domains. For the geological DFN model to be useful, the model parameterisation must be able to reproduce the distinctive relative set intensities inside each fracture domain.

Verification OR-2 compares the relative percentages of the mean P_{32} values for each fracture domain and fracture set in the DFN model parameterisation to the relative percentages for each fracture domain and fracture set in the cored borehole data. Relative intensities are calculated using the sum of Terzaghi weights (Equation 3-1). The performance metric for verification case OR-2 is expressed as the percent difference between the observed relative fracture intensities and the model parameterisation:

$$\%Difference = \frac{\left|M_1 - M_2\right|}{\left(\frac{M_1 + M_2}{2}\right)} \times 100 \qquad \text{Equation 5-6}$$

where M_1 and M_2 represent the relative fracture intensity ratio calculated from Terzaghi weight sums and mean P_{32}, respectively.

Table 5-4 through Table 5-6 present the results of verification case OR-2. In general, the average P_{32} values calculated as part of the geological DFN model parameterisation produce relative set intensities that are fairly close; the model values are within 10% of the calculated values from cored borehole data. The only significant deviation is for the ENE orientation set in fracture domain FSM_NE005; the relative fracture intensity predicted by the model is approximately 17% higher than the relative set intensity calculated using Terzaghi weighting.

However, the differences in FSM_NE005 are most likely not due to an error in the model predictions, but rather a discrepancy due to the limits of Terzaghi compensation. As discussed in Section 3.3.3, a maximum bias angle of 8.2° is used to prevent overcompensation when Terzaghi weights were calculated. The ENE orientation set, however, possesses a slightly larger number of fractures with dips closer to vertical (this is expressed as a fracture set mean pole vector very close to 90° for the ENE set). This means that the Terzaghi correction will underestimate the intensity (expressed as the sum of Terzaghi weights) for the ENE set. The geological DFN model P_{32} values are calculated using the Wang approximation, which does not suffer from the same problem with fractures oriented sub-parallel to the borehole.

Table 5-4. Relative fracture intensity calculated using sums of Terzaghi weights of fractures Visible in BIPS from cored borehole data.

Fracture Domain	Global Set	Sum of Terzaghi Weights	Relative Intensity
FSM_C	ENE	3,063.02	17.05%
FSM_EW007	ENE	3,024.66	14.68%
FSM_N	ENE	1,709.70	12.58%
FSM_NE005	ENE	1,930.77	11.76%
FSM_W	ENE	3,669.49	14.09%
FSM_C	N-S	4,525.22	25.19%
FSM_EW007	N-S	4,525.15	21.96%
FSM_N	N-S	3,308.43	24.34%
FSM_NE005	N-S	6,331.44	38.57%
FSM_W	N-S	8,853.53	33.99%
FSM_C	SH	5,388.49	29.99%
FSM_EW007	SH	7,985.68	38.76%
FSM_N	SH	5,254.69	38.66%
FSM_NE005	SH	4,981.30	30.35%
FSM_W	SH	9,080.90	34.86%
FSM_C	WNW	4,773.11	26.57%
FSM_EW007	WNW	4,812.46	23.36%
FSM_N	WNW	3,264.04	24.01%
FSM_NE005	WNW	3,132.03	19.08%
FSM_W	WNW	4,326.81	16.61%

Table 5-5. Relative fracture intensity calculated from geological DFN model parameterisation (P_{32}).

Fracture Domain	Total P_{32} (1/m)	ENE		N-S		SH		WNW	
		P_{32} (1/m)	Relative Intensity	P_{32} (1/m)	Relative Intensity	P_{32} (1/m)	Relative Intensity	P_{32} (1/m)	Relative Intensity
FSM_C	9.24	1.72	18.58%	2.33	25.25%	2.66	28.78%	2.53	27.39%
FSM_EW007	12.26	1.98	16.17%	2.96	24.16%	4.42	36.04%	2.90	23.63%
FSM_N	11.31	1.38	12.22%	2.63	23.29%	4.62	40.86%	2.67	23.64%
FSM_NE005	11.43	1.60	13.99%	4.30	37.62%	3.17	27.68%	2.37	20.71%
FSM_S	19.98	4.28	21.44%	6.09	30.46%	4.22	21.14%	5.39	26.96%
FSM_W	10.56	1.60	15.17%	3.60	34.04%	3.40	32.17%	1.97	18.62%

Table 5-6. Verification OR-2: comparison of simulated relative fracture intensities to cored borehole data.

Fracture Domain	ENE Set			N-S set			SH Set			WNW Set		
	Data	Model	% difference	Data	Model	% difference	Data	Model	% difference	Data	Model	% difference
FSM_C	0.17	0.19	8.59%	0.25	0.25	0.25%	0.30	0.29	4.12%	0.27	0.27	3.07%
FSM_EW007	0.15	0.16	9.67%	0.22	0.24	9.54%	0.39	0.36	7.28%	0.23	0.24	1.14%
FSM_N	0.13	0.12	2.88%	0.24	0.23	4.42%	0.39	0.41	5.53%	0.24	0.24	1.57%
FSM_NE005	0.12	0.14	17.30%	0.39	0.38	2.50%	0.30	0.28	9.18%	0.19	0.21	8.18%
FSM_W	0.14	0.15	7.43%	0.34	0.34	0.16%	0.35	0.32	8.04%	0.17	0.19	11.40%

5.3 Verification SI-1: Outcrop P_{21}

The goal of verification case SI-1 is to determine how well the Base Model and the alternative models were able to reproduce fracture trace patterns, as observed on the detail-mapped fracture outcrops. There are two elements to the verification; a qualitative assessment of whether or not the trace patterns produced 'look like' what is observed in the field, and a quantitative element, in which simulated trace length intensities (P_{21}) are directly compared to the values observed during mapping. The goodness-of-fit for verification cases SI-1, SI-2, and SI-4 is expressed as the percent error:

$$\%Error = \left| \frac{T - E}{T} \right| \times 100 \qquad \text{Equation 5-7}$$

where E represents the value derived from simulation and T the theoretical value derived from field data, which, for percent error, is assumed 'correct'.

Trace maps from outcrops inside fracture domains FSM_N, FSM_W, and FSM_NE005 are used for this verification. Unfortunately, detailed fracture-mapped outcrops do not exist for domains FSM_S, FSM_C, and FSM_EW007; as such, these domains are omitted from the verification.

The quantitative verification was performed using simulated sampling of a suite of stochastic DFN realizations; for each combination of fracture set, alternative model, and fracture domain, 20 stochastic realizations were completed. Simulations were performed in a model volume 80 m × 80 m × 30 m; for simulations with very small values of r_0, a smaller volume of 40 m × 40 m × 40 m was used to speed simulation times. Comparison is made using the arithmetic mean simulated P_{21} against the observed outcrop P_{21}. In addition, the standard deviation, maximum simulated P_{21}, and minimum simulated P_{21} are presented for each alternative model case.

It is important to note that though the stochastic DFN realizations contained fractures at all sizes between r_0 and r_{max} (varies by model alternative, and 564.2 m, respectively) , the formal intensity verification only occurs within a limited size range. The outcrop mapping only recorded fractures with trace lengths longer than 0.5 m. As such, traces shorter than 0.5 m are discarded from the model output. In addition, the size-intensity models are based on a power-law size relationship that has been computed from the area-normalized trace length scaling plots (see Section 3.6.1) by fitting a straight line to the linear portions of the trace length cumulative number plots. Only within these straight-line portions (termed the 'trace length match interval') of the data where the scaling exponent was fitted will a trace intensity-size validation be valid. An example of the trace length match interval is displayed below in Figure 5-7.

The trace length limits of the outcrop verification were based on the specific outcrop used to parameterize the minimum radius (r_0) and scaling exponent (k_r) in the Base Model; as such, the trace length match interval varies between alternative model cases. Table 5-7 below presents the trace length match ranges as a function of the particular alternative model case. For the alternative models where the fracture radius scaling exponent varies as a function of the fracture domain (the 'r_0-fixed' models described in Section 4.3), there is no trace length match range; these models are defined based on the borehole P_{32} and the diameter of the borehole. As such, for the r_0-fixed models, the trace length match range is assumed to be the entire range of fracture trace lengths (0.5 m–1,000 m) for which the geological DFN is valid.

The results of Verification SI-1 are presented below as Table 5-8 through Table 5-11, as a function of fracture set and alternative model case. For each set, the alternative model case with the lowest percent error is marked using a black rectangle. There is no one alternative model case that consistently performs the best in this verification. The Base Model and its unlinked counterpart (BM and BMU) perform fairly well for all sets except the SH set.

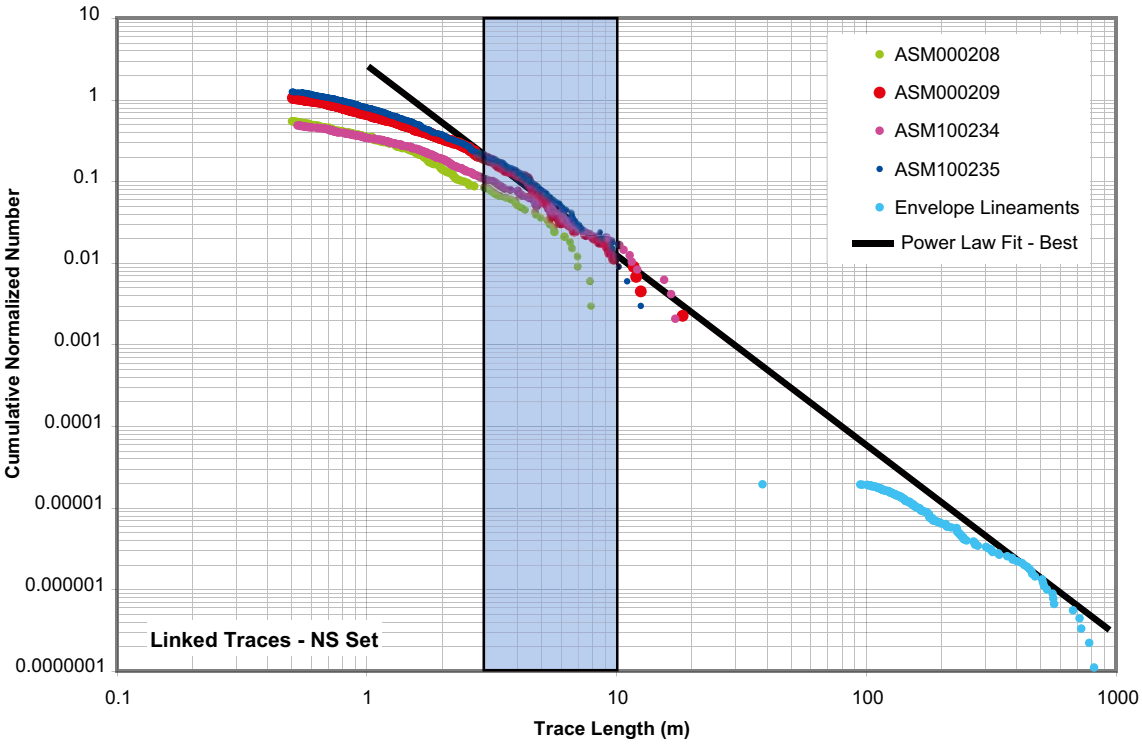

Figure 5-7. *Example of a trace length match interval, N-S Set. The blue bar illustrates the limits of the trace length interval used in the verification, and represents the linear portion of the trace length scaling data to which it was possible to fit a straight line.*

Table 5-7. Trace length match range as a function of alternative model case.

Alternative Model Case	ENE Fracture Set			N-S Fracture Set			SH Fracture Set			WNW Fracture Set		
	Outcrop Matched	Lower Limit (m)	Upper Limit (m)	Outcrop	Lower Limit (m)	Upper Limit (m)	Outcrop	Lower Limit (m)	Upper Limit (m)	Outcrop	Lower Limit (m)	Upper Limit (m)
BM	ASM100234	2	6	ASM000209	3	10	ASM100234	1.5	5	ASM000208	1.5	3
EL1	ASM000208	2.5	4	ASM100235	4	10	ASM000208	1.75	4	ASM100234	2	6
EL2	ASM000209	0.8	2.2	ASM000208	4	7	ASM000209	0.8	2	ASM000209	1.75	2.5
BMU	ASM000208	1	2.75	ASM100235	1.2	3.75	ASM100234	1.2	3.2	ASM100235	1.2	2.4
EUL1	ASM000208	1.75	2.25	ASM000209	2.75	5	ASM000208	0.9	1.75	ASM100234	2	3
EUL2	ASM000209	0.7	2.25	ASM000208	1	4.25	ASM000209	0.75	1.8	ASM000209	0.75	1.7
BMF	ASM100234	2.25	6	ASM000209	2.5	20	ASM100234	1.3	3	ASM000208	2	3
FL1	ASM000208	2	4	ASM100235	3.85	10	ASM000208	1.7	4	ASM100234	2.3	5
FL2	ASM000209	0.8	2.3	ASM000208	1.5	2.5	ASM000209	0.78	1.8	ASM000209	2.2	3.4
BMUF	ASM000208	1.2	2.3	ASM100235	1.5	3.75	ASM100234	1.25	3.3	ASM000208	0.7	1.5
FUL1	ASM000208	1.7	2.1	ASM100234	6	11	ASM000208	1.3	1.8	ASM100234	2	3
FUL2	ASM000209	0.8	2.3	ASM000208	1.3	2.7	ASM000209	0.75	1.85	ASM000209	2.3	3.3
ESL1_N	ASM000208	0.5	1,000	ASM000208	0.5	1,000	ASM000208	0.5	1,000	ASM000208	0.5	1,000
ESL1_NE005	ASM000209	0.5	1,000	ASM000209	0.5	1,000	ASM000209	0.5	1,000	ASM000209	0.5	1,000
ESL1_W	ASM100235	0.5	1,000	ASM100235	0.5	1,000	ASM100235	0.5	1,000	ASM100235	0.5	1,000
ESL2_N	ASM000208	0.5	1,000	ASM000208	0.5	1,000	ASM000208	0.5	1,000	ASM000208	0.5	1,000
ESL2_NE005	ASM000209	0.5	1,000	ASM000209	0.5	1,000	ASM000209	0.5	1,000	ASM000209	0.5	1,000
ESL2_W	ASM100235	0.5	1,000	ASM100235	0.5	1,000	ASM100235	0.5	1,000	ASM100235	0.5	1,000
ESL3_N	ASM000208	0.5	1,000	ASM000208	0.5	1,000	ASM000208	0.5	1,000	ASM000208	0.5	1,000
ESL3_NE005	ASM000209	0.5	1,000	ASM000209	0.5	1,000	ASM000209	0.5	1,000	ASM000209	0.5	1,000
ESL3_W	ASM100235	0.5	1,000	ASM100235	0.5	1,000	ASM100235	0.5	1,000	ASM100235	0.5	1,000
FSL1_N	ASM000208	0.5	1,000	ASM000208	0.5	1,000	ASM000208	0.5	1,000	ASM000208	0.5	1,000
FSL1_NE005	ASM000209	0.5	1,000	ASM000209	0.5	1,000	ASM000209	0.5	1,000	ASM000209	0.5	1,000
FSL1_W	ASM100235	0.5	1,000	ASM100235	0.5	1,000	ASM100235	0.5	1,000	ASM100235	0.5	1,000
FSL2_N	ASM000208	0.5	1,000	ASM000208	0.5	1,000	ASM000208	0.5	1,000	ASM000208	0.5	1,000
FSL2_NE005	ASM000209	0.5	1,000	ASM000209	0.5	1,000	ASM000209	0.5	1,000	ASM000209	0.5	1,000
FSL2_W	ASM100235	0.5	1,000	ASM100235	0.5	1,000	ASM100235	0.5	1,000	ASM100235	0.5	1,000
FSL3_N	ASM000208	0.5	1,000	ASM000208	0.5	1,000	ASM000208	0.5	1,000	ASM000208	0.5	1,000
FSL3_NE005	ASM000209	0.5	1,000	ASM000209	0.5	1,000	ASM000209	0.5	1,000	ASM000209	0.5	1,000
FSL3_W	ASM100235	0.5	1,000	ASM100235	0.5	1,000	ASM100235	0.5	1,000	ASM100235	0.5	1,000

Table 5-8. Verification results, ENE fracture set.

Model Case	Outcrop	ENE Global Set, Traces > 0.5 m						ENE Global Set, Traces in Match Size Range					
		Observed P_{21}	Simulated P_{21}					Observed P_{21}	Simulated P_{21}				
			Mean	Std. Dev.	Max	Min	% Error		Mean	Std. Dev.	Max.	Min.	% Error
BM	ASM100234	0.89	1.29	0.09	1.45	1.15	45.03%	0.41	0.41	0.06	0.54	0.30	1.14%
EL1	ASM000208	1.28	1.43	0.15	1.72	1.17	11.52%	0.25	0.43	0.05	0.51	0.34	70.81%
EL2	ASM000209	0.51	0.54	0.06	0.65	0.40	4.95%	0.27	0.28	0.03	0.32	0.22	1.86%
BMU	ASM000208	1.26	1.18	0.09	1.33	0.96	5.96%	0.70	0.67	0.06	0.79	0.55	5.03%
EUL1	ASM000208	1.26	1.19	0.06	1.33	1.10	5.22%	0.19	0.14	0.02	0.20	0.08	28.42%
EUL2	ASM000209	0.47	0.59	0.07	0.68	0.42	24.98%	0.31	0.10	0.02	0.14	0.05	68.90%
BMF	ASM100234	0.89	1.36	0.11	1.60	1.13	53.38%	0.36	0.51	0.05	0.64	0.41	43.12%
FL1	ASM000208	1.28	1.29	0.09	1.41	1.12	0.57%	0.40	0.49	0.06	0.59	0.33	22.82%
FL2	ASM000209	0.51	0.55	0.05	0.64	0.47	8.19%	0.29	0.31	0.03	0.35	0.26	4.85%
BMUF	ASM000208	1.26	1.33	0.09	1.46	1.14	5.47%	0.48	0.47	0.05	0.55	0.37	0.55%
FUL1	ASM000208	1.26	1.26	0.11	1.47	1.06	0.30%	0.11	0.14	0.03	0.17	0.07	31.33%
FUL2	ASM000209	0.47	0.34	0.05	0.43	0.25	28.37%	0.29	0.18	0.02	0.25	0.13	40.05%
ESL1_N	ASM000208	1.28	0.21	0.03	0.27	0.16	83.33%	N/A	N/A	N/A	N/A	N/A	N/A
ESL1_NE005	ASM000209	0.51	0.22	0.04	0.29	0.16	56.52%	N/A	N/A	N/A	N/A	N/A	N/A
ESL1_W	ASM100235	0.68	0.23	0.04	0.33	0.15	66.42%	N/A	N/A	N/A	N/A	N/A	N/A
ESL2_N	ASM000208	1.28	0.21	0.04	0.33	0.15	83.80%	N/A	N/A	N/A	N/A	N/A	N/A
ESL2_NE005	ASM000209	0.51	0.21	0.04	0.33	0.14	59.34%	N/A	N/A	N/A	N/A	N/A	N/A
ESL2_W	ASM100235	0.68	0.22	0.04	0.30	0.13	68.15%	N/A	N/A	N/A	N/A	N/A	N/A
ESL3_N	ASM000208	1.28	0.22	0.06	0.37	0.11	82.65%	N/A	N/A	N/A	N/A	N/A	N/A
ESL3_NE005	ASM000209	0.51	0.25	0.05	0.40	0.17	51.20%	N/A	N/A	N/A	N/A	N/A	N/A
ESL3_W	ASM100235	0.68	0.25	0.06	0.41	0.16	62.75%	N/A	N/A	N/A	N/A	N/A	N/A
FSL1_N	ASM000208	1.28	0.21	0.04	0.31	0.16	83.36%	N/A	N/A	N/A	N/A	N/A	N/A
FSL1_NE005	ASM000209	0.51	0.23	0.03	0.30	0.16	54.30%	N/A	N/A	N/A	N/A	N/A	N/A
FSL1_W	ASM100235	0.68	0.24	0.04	0.33	0.16	65.36%	N/A	N/A	N/A	N/A	N/A	N/A
FSL2_N	ASM000208	1.28	0.18	0.02	0.21	0.13	85.82%	N/A	N/A	N/A	N/A	N/A	N/A
FSL2_NE005	ASM000209	0.51	0.19	0.04	0.30	0.13	62.54%	N/A	N/A	N/A	N/A	N/A	N/A
FSL2_W	ASM100235	0.68	0.20	0.04	0.29	0.11	70.92%	N/A	N/A	N/A	N/A	N/A	N/A
FSL3_N	ASM000208	1.28	0.24	0.05	0.33	0.13	81.61%	N/A	N/A	N/A	N/A	N/A	N/A
FSL3_NE005	ASM000209	0.51	0.25	0.05	0.35	0.16	51.20%	N/A	N/A	N/A	N/A	N/A	N/A
FSL3_W	ASM100235	0.68	0.25	0.05	0.36	0.17	63.09%	N/A	N/A	N/A	N/A	N/A	N/A

Table 5-9. Verification results, N-S fracture set.

Model Case	Outcrop	N-S Global Set, Traces > 0.5 m						N-S Global Set, Traces in Match Size Range					
		Observed P_{21}	Simulated P_{21}					Observed	Simulated P_{21}				
			Mean	Std. Dev.	Max	Min	% Error	P_{21}	Mean	Std. Dev.	Max.	Min.	% Error
BM	ASM000209	2.09	4.02	0.13	4.37	3.81	91.88%	0.85	0.86	0.08	0.98	0.70	0.72%
EL1	ASM100235	2.41	3.45	0.21	3.80	3.06	43.02%	0.66	0.64	0.09	0.81	0.50	2.65%
EL2	ASM000208	0.99	2.21	0.18	2.52	1.99	123.53%	0.24	0.35	0.07	0.45	0.22	50.16%
BMU	ASM100235	2.36	2.55	0.11	2.80	2.37	7.95%	1.27	1.32	0.08	1.45	1.18	3.99%
EUL1	ASM000209	2.07	4.00	0.11	4.24	3.78	93.36%	0.52	0.68	0.07	0.79	0.56	29.06%
EUL2	ASM000208	1.06	1.31	0.11	1.53	1.14	23.71%	0.71	0.89	0.08	1.01	0.78	25.42%
BMF	ASM000209	2.09	4.07	0.17	4.30	3.74	94.47%	1.17	1.11	0.11	1.31	0.90	4.72%
FL1	ASM100235	2.41	3.49	0.14	3.70	3.24	44.56%	0.71	0.71	0.11	0.90	0.44	0.06%
FL2	ASM000208	0.99	1.80	0.11	1.99	1.57	82.05%	0.27	0.43	0.05	0.53	0.33	59.93%
BMUF	ASM100235	2.36	3.41	0.18	3.94	3.22	44.35%	0.94	1.56	0.09	1.74	1.43	65.24%
FUL1	ASM100234	1.18	2.58	0.13	2.88	2.39	118.72%	0.22	0.29	0.06	0.40	0.21	31.56%
FUL2	ASM000208	1.06	1.73	0.12	1.96	1.48	63.50%	0.40	0.62	0.05	0.71	0.53	53.55%
ESL1_N	ASM000208	0.99	0.59	0.04	0.70	0.52	40.64%	N/A	N/A	N/A	N/A	N/A	N/A
ESL1_NE005	ASM000209	2.09	0.37	0.06	0.53	0.27	82.14%	N/A	N/A	N/A	N/A	N/A	N/A
ESL1_W	ASM100235	2.41	0.32	0.06	0.46	0.17	86.68%	N/A	N/A	N/A	N/A	N/A	N/A
ESL2_N	ASM000208	0.99	0.24	0.04	0.30	0.17	75.73%	N/A	N/A	N/A	N/A	N/A	N/A
ESL2_NE005	ASM000209	2.09	0.24	0.03	0.29	0.19	88.57%	N/A	N/A	N/A	N/A	N/A	N/A
ESL2_W	ASM100235	2.41	0.30	0.07	0.43	0.16	87.71%	N/A	N/A	N/A	N/A	N/A	N/A
ESL3_N	ASM000208	0.99	0.21	0.05	0.31	0.10	78.69%	N/A	N/A	N/A	N/A	N/A	N/A
ESL3_NE005	ASM000209	2.09	0.30	0.07	0.46	0.19	85.55%	N/A	N/A	N/A	N/A	N/A	N/A
ESL3_W	ASM100235	2.41	0.24	0.04	0.32	0.15	90.07%	N/A	N/A	N/A	N/A	N/A	N/A
FSL1_N	ASM000208	0.99	0.26	0.04	0.37	0.19	73.20%	N/A	N/A	N/A	N/A	N/A	N/A
FSL1_NE005	ASM000209	2.09	0.37	0.06	0.53	0.27	82.24%	N/A	N/A	N/A	N/A	N/A	N/A
FSL1_W	ASM100235	2.41	0.32	0.06	0.46	0.17	86.76%	N/A	N/A	N/A	N/A	N/A	N/A
FSL2_N	ASM000208	0.99	0.25	0.04	0.37	0.18	74.81%	N/A	N/A	N/A	N/A	N/A	N/A
FSL2_NE005	ASM000209	2.09	0.36	0.05	0.48	0.26	82.97%	N/A	N/A	N/A	N/A	N/A	N/A
FSL2_W	ASM100235	2.41	0.31	0.07	0.43	0.15	87.16%	N/A	N/A	N/A	N/A	N/A	N/A
FSL3_N	ASM000208	0.99	0.26	0.05	0.34	0.13	73.44%	N/A	N/A	N/A	N/A	N/A	N/A
FSL3_NE005	ASM000209	2.09	0.32	0.06	0.45	0.20	84.55%	N/A	N/A	N/A	N/A	N/A	N/A
FSL3_W	ASM100235	2.41	0.34	0.07	0.53	0.18	86.00%	N/A	N/A	N/A	N/A	N/A	N/A

Table 5-10. Verification results, SH fracture set.

Model Case	Outcrop	SH Global Set, Traces > 0.5 m						SH Global Set, Traces in Match Size Range					
		Observed P_{21}	Simulated P_{21}					Observed	Simulated P_{21}				
			Mean	Std. Dev.	Max	Min	% Error	P_{21}	Mean	Std. Dev.	Max.	Min.	% Error
BM	ASM100234	0.53	0.82	0.06	0.92	0.71	54.05%	0.26	0.30	0.03	0.36	0.23	14.98%
EL1	ASM000208	1.03	1.65	0.08	1.82	1.51	60.03%	0.34	0.78	0.05	0.85	0.65	128.26%
EL2	ASM000209	0.20	0.20	0.03	0.26	0.15	0.29%	0.14	0.13	0.02	0.17	0.11	11.68%
BMU	ASM100234	0.55	0.69	0.06	0.83	0.58	25.11%	0.24	0.34	0.04	0.43	0.30	39.15%
EUL1	ASM000208	1.02	1.22	0.08	1.35	1.11	20.11%	0.48	0.64	0.04	0.75	0.58	34.01%
EUL2	ASM000209	0.22	0.18	0.04	0.27	0.12	18.39%	0.14	0.10	0.02	0.13	0.07	31.67%
BM_F	ASM100234	0.53	0.74	0.07	0.90	0.64	39.20%	0.22	0.30	0.04	0.40	0.23	38.19%
FL1	ASM000208	1.03	1.48	0.10	1.75	1.25	43.72%	0.37	0.37	0.05	0.49	0.30	0.15%
FL2	ASM000209	0.20	0.22	0.03	0.31	0.17	9.72%	0.13	0.13	0.02	0.16	0.11	2.08%
BMUF	ASM100234	0.55	0.61	0.05	0.70	0.52	9.50%	0.24	0.27	0.03	0.34	0.23	13.02%
FUL1	ASM000208	1.02	1.14	0.09	1.40	0.99	11.93%	0.22	0.24	0.03	0.30	0.16	10.52%
FUL2	ASM000209	0.22	0.19	0.03	0.24	0.12	12.54%	0.15	0.11	0.02	0.15	0.08	28.90%
ESL1_N	ASM000208	1.03	0.11	0.03	0.16	0.06	89.73%	N/A	N/A	N/A	N/A	N/A	N/A
ESL1_NE005	ASM000209	0.20	0.84	0.02	0.12	0.06	316.14%	N/A	N/A	N/A	N/A	N/A	N/A
ESL1_W	ASM100235	0.39	0.08	0.02	0.12	0.04	80.47%	N/A	N/A	N/A	N/A	N/A	N/A
ESL2_N	ASM000208	1.03	0.09	0.03	0.15	0.04	91.24%	N/A	N/A	N/A	N/A	N/A	N/A
ESL2_NE005	ASM000209	0.20	0.09	0.02	0.13	0.06	56.03%	N/A	N/A	N/A	N/A	N/A	N/A
ESL2_W	ASM100235	0.39	0.07	0.02	0.13	0.05	83.04%	N/A	N/A	N/A	N/A	N/A	N/A
ESL3_N	ASM000208	1.03	0.07	0.02	0.13	0.04	93.05%	N/A	N/A	N/A	N/A	N/A	N/A
ESL3_NE005	ASM000209	0.20	0.05	0.02	0.10	0.03	74.37%	N/A	N/A	N/A	N/A	N/A	N/A
ESL3_W	ASM100235	0.39	0.06	0.02	0.10	0.03	85.83%	N/A	N/A	N/A	N/A	N/A	N/A
FSL1_N	ASM000208	1.03	0.10	0.02	0.14	0.06	90.15%	N/A	N/A	N/A	N/A	N/A	N/A
FSL1_NE005	ASM000209	0.20	0.08	0.02	0.13	0.06	60.08%	N/A	N/A	N/A	N/A	N/A	N/A
FSL1_W	ASM100235	0.39	0.08	0.02	0.12	0.04	80.09%	N/A	N/A	N/A	N/A	N/A	N/A
FSL2_N	ASM000208	1.03	0.09	0.03	0.14	0.04	91.45%	N/A	N/A	N/A	N/A	N/A	N/A
FSL2_NE005	ASM000209	0.20	0.07	0.02	0.11	0.04	66.04%	N/A	N/A	N/A	N/A	N/A	N/A
FSL2_W	ASM100235	0.39	0.07	0.02	0.13	0.04	82.20%	N/A	N/A	N/A	N/A	N/A	N/A
FSL3_N	ASM000208	1.03	0.07	0.02	0.09	0.04	93.54%	N/A	N/A	N/A	N/A	N/A	N/A
FSL3_NE005	ASM000209	0.20	0.06	0.02	0.09	0.03	72.55%	N/A	N/A	N/A	N/A	N/A	N/A
FSL3_W	ASM100235	0.39	0.05	0.02	0.09	0.02	87.59%	N/A	N/A	N/A	N/A	N/A	N/A

Table 5-11. Verification results, WNW fracture set.

Model Case	Outcrop	WNW Global Set, Traces > 0.5 m						WNW Global Set, Traces in Match Size Range					
		Observed P_{21}	Simulated P_{21}					Observed P_{21}	Simulated P_{21}				
			Mean	Std. Dev.	Max	Min	% Error		Mean	Std. Dev.	Max.	Min.	% Error
BM	ASM000208	0.73	1.48	0.13	1.74	1.26	101.73%	0.23	0.44	0.06	0.52	0.33	90.36%
EL1	ASM100234	1.11	1.85	0.12	2.15	1.62	66.53%	0.51	0.55	0.07	0.64	0.40	8.77%
EL2	ASM000209	0.57	0.46	0.06	0.58	0.34	19.97%	0.09	0.07	0.02	0.11	0.04	26.47%
BMU	ASM100235	0.58	0.54	0.06	0.65	0.46	6.61%	0.23	0.19	0.04	0.27	0.11	18.35%
EUL1	ASM100234	1.12	1.80	0.10	1.98	1.59	61.56%	0.24	0.28	0.04	0.33	0.20	15.80%
EUL2	ASM000209	0.60	0.76	0.07	0.95	0.64	26.83%	0.34	0.31	0.03	0.36	0.26	8.17%
BMF	ASM000208	0.73	0.94	0.07	1.15	0.85	28.27%	0.14	0.13	0.03	0.19	0.08	4.16%
FL1	ASM100234	1.11	2.33	0.12	2.62	2.21	110.09%	0.37	0.46	0.06	0.61	0.36	25.04%
FL2	ASM000209	0.57	0.39	0.05	0.48	0.32	30.89%	0.08	0.06	0.02	0.10	0.03	20.95%
BMUF	ASM000208	0.60	0.69	0.07	0.80	0.58	15.36%	0.39	0.25	0.03	0.32	0.20	34.37%
FUL1	ASM100234	1.12	1.43	0.11	1.67	1.26	28.38%	0.24	0.21	0.03	0.24	0.14	15.08%
FUL2	ASM000209	0.60	0.33	0.04	0.40	0.22	45.49%	0.04	0.04	0.02	0.09	0.01	2.92%
ESL1_N	ASM000208	0.73	0.36	0.06	0.46	0.25	50.39%	N/A	N/A	N/A	N/A	N/A	N/A
ESL1_NE005	ASM000209	0.57	0.35	0.05	0.49	0.24	38.69%	N/A	N/A	N/A	N/A	N/A	N/A
ESL1_W	ASM100235	0.52	0.28	0.04	0.36	0.20	46.09%	N/A	N/A	N/A	N/A	N/A	N/A
ESL2_N	ASM000208	0.73	0.35	0.04	0.42	0.27	51.73%	N/A	N/A	N/A	N/A	N/A	N/A
ESL2_NE005	ASM000209	0.57	0.35	0.05	0.45	0.27	38.69%	N/A	N/A	N/A	N/A	N/A	N/A
ESL2_W	ASM100235	0.52	0.29	0.05	0.37	0.19	44.13%	N/A	N/A	N/A	N/A	N/A	N/A
ESL3_N	ASM000208	0.73	0.43	0.06	0.59	0.35	41.76%	N/A	N/A	N/A	N/A	N/A	N/A
ESL3_NE005	ASM000209	0.57	0.43	0.07	0.53	0.32	24.92%	N/A	N/A	N/A	N/A	N/A	N/A
ESL3_W	ASM100235	0.52	0.36	0.07	0.55	0.26	30.69%	N/A	N/A	N/A	N/A	N/A	N/A
FSL1_N	ASM000208	0.73	0.38	0.07	0.48	0.26	47.84%	N/A	N/A	N/A	N/A	N/A	N/A
FSL1_NE005	ASM000209	0.57	0.35	0.05	0.46	0.27	38.04%	N/A	N/A	N/A	N/A	N/A	N/A
FSL1_W	ASM100235	0.52	0.29	0.05	0.41	0.21	43.17%	N/A	N/A	N/A	N/A	N/A	N/A
FSL2_N	ASM000208	0.73	0.36	0.05	0.49	0.27	50.60%	N/A	N/A	N/A	N/A	N/A	N/A
FSL2_NE005	ASM000209	0.57	0.31	0.06	0.45	0.21	45.68%	N/A	N/A	N/A	N/A	N/A	N/A
FSL2_W	ASM100235	0.52	0.28	0.06	0.38	0.18	44.73%	N/A	N/A	N/A	N/A	N/A	N/A
FSL3_N	ASM000208	0.73	0.43	0.06	0.57	0.32	41.02%	N/A	N/A	N/A	N/A	N/A	N/A
FSL3_NE005	ASM000209	0.57	0.32	0.07	0.46	0.20	44.49%	N/A	N/A	N/A	N/A	N/A	N/A
FSL3_W	ASM100235	0.52	0.34	0.06	0.49	0.25	33.62%	N/A	N/A	N/A	N/A	N/A	N/A

5.4 Verification SI-2: Scanline P_{10}

This verification case involves the comparison of fracture data recorded by scanlines during the detailed fracture outcrop mapping efforts to simulated scanlines inside FracMan. The advantage to using the scanline data set from outcrops is that, unlike the outcrop maps themselves, fractures are mapped down to a smaller minimum trace length (0.2 m, instead of 0.5 m). Theoretically, this allows for a more-accurate assessment of the performance of the size-intensity model. However, the use of scanline data has significant disadvantages; as one-dimensional sampling structures (like boreholes), they are highly susceptible to orientation bias for fracture sets oriented sub-parallel to the scanline axis.

Verification case SI-2 was completed by, for each alternative model case, fracture domain, and fracture orientation set, running 20 stochastic realizations of the SDM-Site geological DFN inside FracMan version 7.10. Simulations were performed in a model volume 80 m × 80 m × 30 m; for simulations with very small values of r_0, a smaller volume of 40 m × 40 m × 40 m was used to speed simulation times. Comparison is made using the arithmetic mean simulated P_{10} against the observed outcrop P_{10}. In addition, the standard deviation, maximum simulated P_{10}, and minimum simulated P_{10} are presented for each alternative model case. The outcrops and scanlines utilized are presented below as Figure 5-8 and Figure 5-9. Two scanlines (LSM000293 and LSM000294) are used from outcrop ASM000208 and one scanline (LSM000296) was used from outcrop ASM000209. The results of the simulations are presented in Table 5-12 through Table 5-15.

The results of verification case SI-2 are anything but clear. Even though Monte-Carlo methods were used in the stochastic simulation, there is still considerable variability in the simulated P_{10} sampled along scanlines. Some scanline-alternative model case combinations produce more than 1,000% error. We believe that the poor performance is primarily due to the short length of the scanlines; most are less than 10 m long. However, it is key to note that, though the percent error value is expressed as a positive number, the tables above show that the alternative models are equally as likely to underestimate P_{10} intensity along scanlines as they are to overestimate P_{10}. At a minimum, this demonstrates that there are no systematic biases or errors in the geological DFN modelling, such that $P_{10observed}$ would always be greater than or less than $P_{10simulated}$.

In terms of model performance, there is quite a bit of spread in terms of which model performed best. Table 5-16 illustrates the top two performing alternative models, ordered by fracture set and scanline. There is not one single model that dominates the ‘top two’ in terms of performance; various versions of the Base Model (BMU, BMF, BM) are consistently one of the top two performing alternative models, especially for predicting the difficult-to-sample SH set. There is also a clear bias for the domain-specific models; outcrop ASM000208 is located inside fracture domain FSM_N; it is not unexpected that models specifically calibrated to fit that fracture domain would prove to be the best performing. This bias can only be eliminated through the inclusion of scanline maps from every fracture domain in the model; only when that is done can a legitimate comparison of the domain-specific size-intensity models be made. This problem also affects verification case SI-1; the uncertainty introduced by the missing data is accounted for during the alternative model ranking (Section 5.8).

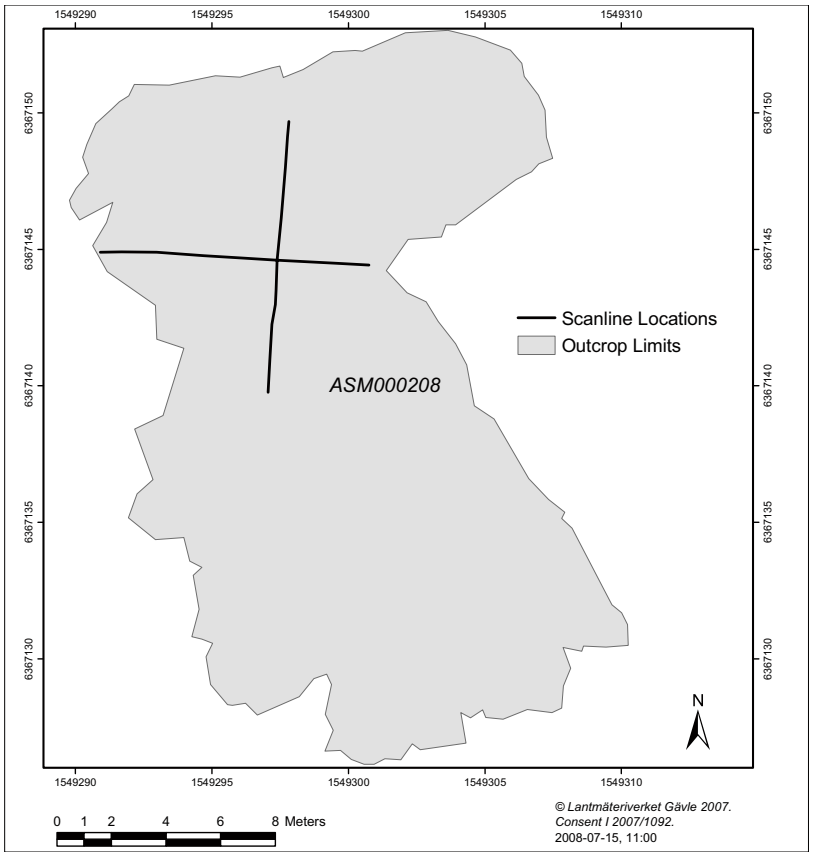

Figure 5-8. *Illustration of scanlines on outcrop ASM000208.*

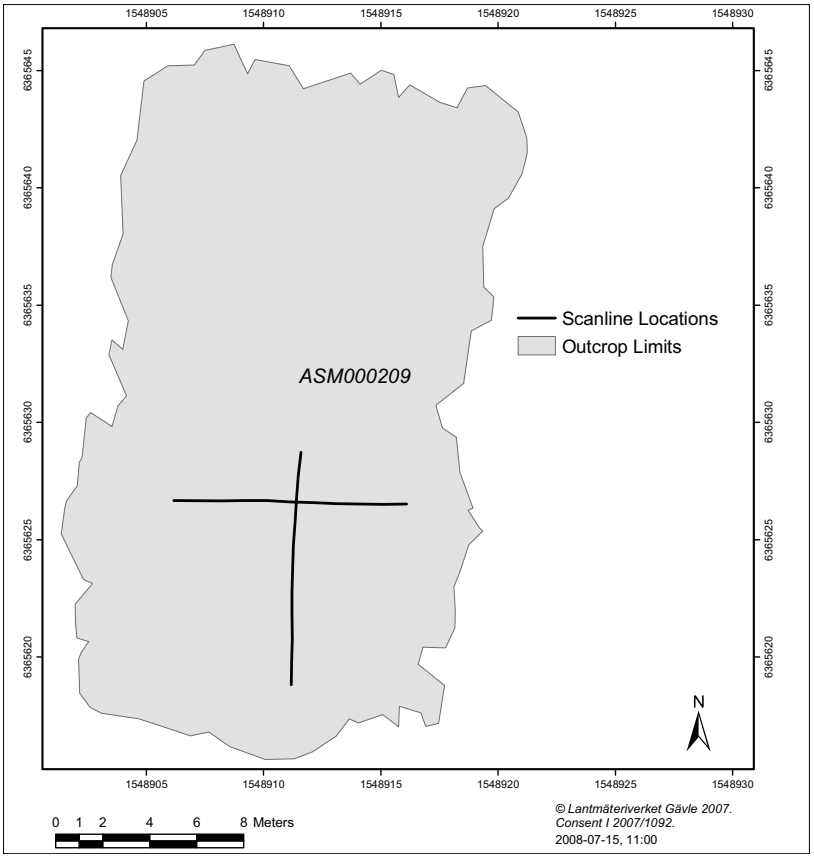

Figure 5-9. *Illustration of scanlines on outcrop ASM000209.*

Table 5-12. Results of scanline P_{10} verification, ENE orientation set.

Case	Set	Outcrop	P_{10} Observed	P_{10} Simulated				
				Mean	Std. Dev.	Max	Min	% Error
BM	ENE	LSM000293	2.12	1.07	0.48	2.12	0.20	49.66%
BM	ENE	LSM000294	0.82	0.54	0.24	1.01	0.10	34.11%
BM	ENE	LSM000296	0.30	0.53	0.22	1.01	0.30	76.00%
BMF	ENE	LSM000293	2.12	1.20	0.37	2.12	0.71	43.10%
BMF	ENE	LSM000294	0.82	0.59	0.26	1.12	0.20	28.12%
BMF	ENE	LSM000296	0.30	0.57	0.24	1.01	0.20	86.67%
BMU	ENE	LSM000293	2.12	1.10	0.29	1.61	0.50	47.86%
BMU	ENE	LSM000294	0.82	0.54	0.31	1.53	0.20	33.75%
BMU	ENE	LSM000296	0.30	0.47	0.30	1.21	0.10	55.00%
BMUF	ENE	LSM000293	2.12	1.07	0.33	1.71	0.50	49.29%
BMUF	ENE	LSM000294	0.82	0.55	0.15	0.92	0.31	33.12%
BMUF	ENE	LSM000296	0.30	0.46	0.19	0.91	0.20	53.33%
EL1	ENE	LSM000293	2.12	1.25	0.30	1.81	0.81	40.71%
EL1	ENE	LSM000294	0.82	0.54	0.17	0.92	0.31	34.37%
EL1	ENE	LSM000296	0.30	0.61	0.18	1.01	0.30	100.00%
EL2	ENE	LSM000293	2.12	0.50	0.21	1.11	0.20	76.43%
EL2	ENE	LSM000294	0.82	0.26	0.19	0.61	0.00	68.12%
EL2	ENE	LSM000296	0.30	0.19	0.13	0.50	0.00	36.67%
ESL1_N	ENE	LSM000293	2.12	0.18	0.12	0.40	0.00	91.43%
ESL1_N	ENE	LSM000294	0.82	0.09	0.10	0.31	0.00	88.75%
ESL1_N	ENE	LSM000296	0.30	0.13	0.13	0.50	0.00	58.33%
ESL1_NE005	ENE	LSM000293	2.12	0.20	0.11	0.40	0.00	90.48%
ESL1_NE005	ENE	LSM000294	0.82	0.11	0.11	0.41	0.00	86.50%
ESL1_NE005	ENE	LSM000296	0.30	0.09	0.13	0.61	0.00	69.33%
ESL1_W	ENE	LSM000293	2.12	0.20	0.10	0.40	0.00	90.48%
ESL1_W	ENE	LSM000294	0.82	0.10	0.12	0.41	0.00	88.12%
ESL1_W	ENE	LSM000296	0.30	0.11	0.14	0.61	0.00	63.33%
ESL2_N	ENE	LSM000293	2.12	0.17	0.11	0.40	0.00	92.14%
ESL2_N	ENE	LSM000294	0.82	0.10	0.10	0.31	0.00	87.50%
ESL2_N	ENE	LSM000296	0.30	0.12	0.15	0.61	0.00	60.00%
ESL2_NE005	ENE	LSM000293	2.12	0.17	0.11	0.40	0.00	92.14%
ESL2_NE005	ENE	LSM000294	0.82	0.10	0.10	0.31	0.00	87.50%
ESL2_NE005	ENE	LSM000296	0.30	0.12	0.15	0.61	0.00	60.00%
ESL2_W	ENE	LSM000293	2.12	0.17	0.11	0.40	0.00	91.90%
ESL2_W	ENE	LSM000294	0.82	0.09	0.11	0.41	0.00	89.37%
ESL2_W	ENE	LSM000296	0.30	0.10	0.14	0.61	0.00	66.67%
ESL3_N	ENE	LSM000293	2.12	0.19	0.13	0.50	0.00	90.95%
ESL3_N	ENE	LSM000294	0.82	0.08	0.10	0.31	0.00	90.00%
ESL3_N	ENE	LSM000296	0.30	0.09	0.10	0.40	0.00	71.67%
ESL3_NE005	ENE	LSM000293	2.12	0.25	0.13	0.50	0.00	88.33%
ESL3_NE005	ENE	LSM000294	0.82	0.14	0.11	0.51	0.00	82.50%
ESL3_NE005	ENE	LSM000296	0.30	0.10	0.10	0.30	0.00	68.33%
ESL3_W	ENE	LSM000293	2.12	0.25	0.13	0.50	0.00	88.33%
ESL3_W	ENE	LSM000294	0.82	0.14	0.11	0.51	0.00	82.50%
ESL3_W	ENE	LSM000296	0.30	0.10	0.10	0.30	0.00	68.33%

Case	Set	Outcrop	P_{10} Observed	P_{10} Simulated				
				Mean	Std. Dev.	Max	Min	% Error
EUL1	ENE	LSM000293	2.12	1.02	0.35	1.81	0.50	51.67%
EUL1	ENE	LSM000294	0.82	0.48	0.31	1.12	0.10	41.25%
EUL1	ENE	LSM000296	0.30	0.49	0.22	0.91	0.10	63.33%
EUL2	ENE	LSM000293	2.12	0.51	0.21	1.01	0.20	75.71%
EUL2	ENE	LSM000294	0.82	0.16	0.15	0.41	0.00	80.00%
EUL2	ENE	LSM000296	0.30	0.26	0.14	0.50	0.00	15.00%
FL1	ENE	LSM000293	2.12	1.12	0.28	1.91	0.60	47.14%
FL1	ENE	LSM000294	0.82	0.48	0.24	0.92	0.00	40.62%
FL1	ENE	LSM000296	0.30	0.50	0.17	1.01	0.30	65.00%
FL2	ENE	LSM000293	2.12	0.52	0.21	0.91	0.20	75.24%
FL2	ENE	LSM000294	0.82	0.25	0.17	0.61	0.00	69.37%
FL2	ENE	LSM000296	0.30	0.22	0.13	0.50	0.00	26.67%
FSL1_N	ENE	LSM000293	2.12	0.19	0.12	0.40	0.00	90.95%
FSL1_N	ENE	LSM000294	0.82	0.10	0.11	0.31	0.00	87.50%
FSL1_N	ENE	LSM000296	0.30	0.11	0.11	0.40	0.00	63.33%
FSL1_NE005	ENE	LSM000293	2.12	0.23	0.12	0.40	0.00	89.29%
FSL1_NE005	ENE	LSM000294	0.82	0.10	0.12	0.41	0.00	88.12%
FSL1_NE005	ENE	LSM000296	0.30	0.11	0.13	0.61	0.00	63.33%
FSL1_W	ENE	LSM000293	2.12	0.23	0.12	0.40	0.00	89.29%
FSL1_W	ENE	LSM000294	0.82	0.10	0.12	0.41	0.00	88.12%
FSL1_W	ENE	LSM000296	0.30	0.11	0.13	0.61	0.00	63.33%
FSL2_N	ENE	LSM000293	2.12	0.17	0.09	0.40	0.00	91.90%
FSL2_N	ENE	LSM000294	0.82	0.09	0.09	0.20	0.00	88.75%
FSL2_N	ENE	LSM000296	0.30	0.09	0.09	0.30	0.00	71.67%
FSL2_NE005	ENE	LSM000293	2.12	0.20	0.16	0.71	0.00	90.48%
FSL2_NE005	ENE	LSM000294	0.82	0.09	0.09	0.31	0.00	89.37%
FSL2_NE005	ENE	LSM000296	0.30	0.09	0.10	0.30	0.00	70.00%
FSL2_W	ENE	LSM000293	2.12	0.20	0.16	0.71	0.00	90.71%
FSL2_W	ENE	LSM000294	0.82	0.09	0.09	0.31	0.00	89.37%
FSL2_W	ENE	LSM000296	0.30	0.10	0.10	0.30	0.00	68.33%
FSL3_N	ENE	LSM000293	2.12	0.20	0.13	0.40	0.00	90.48%
FSL3_N	ENE	LSM000294	0.82	0.09	0.11	0.41	0.00	88.75%
FSL3_N	ENE	LSM000296	0.30	0.11	0.11	0.50	0.00	65.00%
FSL3_NE005	ENE	LSM000293	2.12	0.24	0.14	0.50	0.00	88.81%
FSL3_NE005	ENE	LSM000294	0.82	0.15	0.11	0.51	0.00	81.25%
FSL3_NE005	ENE	LSM000296	0.30	0.09	0.09	0.20	0.00	71.67%
FSL3_W	ENE	LSM000293	2.12	0.24	0.14	0.50	0.00	88.81%
FSL3_W	ENE	LSM000294	0.82	0.15	0.11	0.51	0.00	81.25%
FSL3_W	ENE	LSM000296	0.30	0.09	0.09	0.20	0.00	71.67%
FUL1	ENE	LSM000293	2.12	1.06	0.41	1.81	0.50	49.76%
FUL1	ENE	LSM000294	0.82	0.50	0.24	1.02	0.10	38.12%
FUL1	ENE	LSM000296	0.30	0.60	0.24	1.11	0.20	98.33%
FUL2	ENE	LSM000293	2.12	0.27	0.16	0.60	0.10	87.14%
FUL2	ENE	LSM000294	0.82	0.11	0.10	0.31	0.00	86.25%
FUL2	ENE	LSM000296	0.30	0.15	0.12	0.30	0.00	50.00%

Table 5-13. Results of scanline P_{10} verification, N-S orientation set.

Case	Set	Outcrop	P_{10} Observed	P_{10} Simulated				
				Mean	Std. Dev.	Max	Min	% Error
BM	N-S	LSM000293	0.30	1.22	0.37	2.22	0.40	305.00%
BM	N-S	LSM000294	1.02	3.89	0.68	5.30	2.85	281.50%
BM	N-S	LSM000296	2.42	3.67	0.52	4.54	2.63	51.46%
BMF	N-S	LSM000293	0.30	1.24	0.34	2.32	0.71	311.67%
BMF	N-S	LSM000294	1.02	4.00	0.65	5.20	2.65	292.50%
BMF	N-S	LSM000296	2.42	3.96	0.75	5.45	2.22	63.33%
BMU	N-S	LSM000293	0.30	0.80	0.27	1.31	0.40	165.00%
BMU	N-S	LSM000294	1.02	2.29	0.44	3.16	1.63	124.50%
BMU	N-S	LSM000296	2.42	2.41	0.59	3.64	1.31	0.42%
BMUF	N-S	LSM000293	0.30	1.03	0.27	1.51	0.60	241.67%
BMUF	N-S	LSM000294	1.02	3.24	0.69	4.79	2.04	217.50%
BMUF	N-S	LSM000296	2.42	3.09	0.53	4.04	2.22	27.29%
EL1	N-S	LSM000293	0.30	0.89	0.31	1.51	0.20	195.00%
EL1	N-S	LSM000294	1.02	3.08	0.59	4.08	2.04	202.50%
EL1	N-S	LSM000296	2.42	3.17	0.35	3.94	2.73	30.62%
EL2	N-S	LSM000293	0.30	0.58	0.27	0.91	0.00	93.33%
EL2	N-S	LSM000294	1.02	2.17	0.36	2.96	1.43	113.00%
EL2	N-S	LSM000296	2.42	2.00	0.28	2.83	1.62	17.50%
ESL1_N	N-S	LSM000293	0.30	0.25	0.07	0.40	0.20	18.33%
ESL1_N	N-S	LSM000294	1.02	0.45	0.12	0.61	0.20	56.00%
ESL1_N	N-S	LSM000296	2.42	0.53	0.13	0.81	0.30	78.13%
ESL1_NE005	N-S	LSM000293	0.30	0.12	0.10	0.30	0.00	61.67%
ESL1_NE005	N-S	LSM000294	1.02	0.34	0.20	0.71	0.00	67.00%
ESL1_NE005	N-S	LSM000296	2.42	0.37	0.15	0.61	0.00	84.79%
ESL1_W	N-S	LSM000293	0.30	0.09	0.08	0.30	0.00	71.67%
ESL1_W	N-S	LSM000294	1.02	0.31	0.18	0.71	0.00	69.50%
ESL1_W	N-S	LSM000296	2.42	0.30	0.16	0.71	0.10	87.71%
ESL2_N	N-S	LSM000293	0.30	0.11	0.10	0.40	0.00	63.33%
ESL2_N	N-S	LSM000294	1.02	0.24	0.16	0.61	0.00	76.00%
ESL2_N	N-S	LSM000296	2.42	0.20	0.17	0.71	0.00	91.88%
ESL2_NE005	N-S	LSM000293	0.30	0.11	0.10	0.40	0.00	63.33%
ESL2_NE005	N-S	LSM000294	1.02	0.24	0.16	0.61	0.00	76.00%
ESL2_NE005	N-S	LSM000296	2.42	0.20	0.17	0.71	0.00	91.88%
ESL2_W	N-S	LSM000293	0.30	0.10	0.09	0.30	0.00	66.67%
ESL2_W	N-S	LSM000294	1.02	0.30	0.17	0.61	0.00	70.50%
ESL2_W	N-S	LSM000296	2.42	0.26	0.21	0.81	0.00	89.38%
ESL3_N	N-S	LSM000293	0.30	0.08	0.10	0.40	0.00	75.00%
ESL3_N	N-S	LSM000294	1.02	0.23	0.17	0.51	0.00	77.00%
ESL3_N	N-S	LSM000296	2.42	0.24	0.14	0.50	0.10	90.21%
ESL3_NE005	N-S	LSM000293	0.30	0.14	0.11	0.40	0.00	53.33%
ESL3_NE005	N-S	LSM000294	1.02	0.26	0.15	0.61	0.00	74.50%
ESL3_NE005	N-S	LSM000296	2.42	0.26	0.12	0.50	0.10	89.17%
ESL3_W	N-S	LSM000293	0.30	0.08	0.06	0.20	0.00	75.00%
ESL3_W	N-S	LSM000294	1.02	0.26	0.14	0.41	0.00	74.00%
ESL3_W	N-S	LSM000296	2.42	0.24	0.20	0.81	0.00	90.00%

Case	Set	Outcrop	P_{10} Observed	P_{10} Simulated				
				Mean	Std. Dev.	Max	Min	% Error
EUL1	N-S	LSM000293	0.30	1.12	0.40	1.81	0.50	271.67%
EUL1	N-S	LSM000294	1.02	3.80	0.52	4.59	2.75	273.00%
EUL1	N-S	LSM000296	2.42	3.65	0.62	4.85	2.52	50.42%
EUL2	N-S	LSM000293	0.30	0.45	0.23	0.91	0.20	48.33%
EUL2	N-S	LSM000294	1.02	1.20	0.42	2.14	0.41	18.00%
EUL2	N-S	LSM000296	2.42	1.14	0.33	1.72	0.61	53.13%
FL1	N-S	LSM000293	0.30	1.07	0.46	2.02	0.30	253.33%
FL1	N-S	LSM000294	1.02	3.27	0.42	4.38	2.45	221.00%
FL1	N-S	LSM000296	2.42	3.20	0.59	4.75	2.42	32.08%
FL2	N-S	LSM000293	0.30	0.57	0.24	1.01	0.20	90.00%
FL2	N-S	LSM000294	1.02	2.00	0.44	2.96	1.32	96.00%
FL2	N-S	LSM000296	2.42	1.73	0.42	2.63	0.81	28.54%
FSL1_N	N-S	LSM000293	0.30	0.07	0.08	0.30	0.00	78.33%
FSL1_N	N-S	LSM000294	1.02	0.26	0.17	0.71	0.00	74.50%
FSL1_N	N-S	LSM000296	2.42	0.24	0.13	0.50	0.00	90.21%
FSL1_NE005	N-S	LSM000293	0.30	0.12	0.10	0.30	0.00	61.67%
FSL1_NE005	N-S	LSM000294	1.02	0.34	0.20	0.71	0.00	67.00%
FSL1_NE005	N-S	LSM000296	2.42	0.37	0.15	0.61	0.00	84.79%
FSL1_W	N-S	LSM000293	0.30	0.09	0.08	0.30	0.00	71.67%
FSL1_W	N-S	LSM000294	1.02	0.31	0.18	0.71	0.00	69.50%
FSL1_W	N-S	LSM000296	2.42	0.29	0.16	0.71	0.10	87.92%
FSL2_N	N-S	LSM000293	0.30	0.10	0.10	0.40	0.00	68.33%
FSL2_N	N-S	LSM000294	1.02	0.25	0.15	0.61	0.00	75.00%
FSL2_N	N-S	LSM000296	2.42	0.25	0.21	0.81	0.00	89.79%
FSL2_NE005	N-S	LSM000293	0.30	0.12	0.09	0.40	0.00	61.67%
FSL2_NE005	N-S	LSM000294	1.02	0.36	0.16	0.71	0.10	64.50%
FSL2_NE005	N-S	LSM000296	2.42	0.40	0.21	0.81	0.10	83.54%
FSL2_W	N-S	LSM000293	0.30	0.11	0.10	0.30	0.00	63.33%
FSL2_W	N-S	LSM000294	1.02	0.32	0.14	0.51	0.00	69.00%
FSL2_W	N-S	LSM000296	2.42	0.28	0.19	0.81	0.00	88.33%
FSL3_N	N-S	LSM000293	0.30	0.07	0.06	0.20	0.00	76.67%
FSL3_N	N-S	LSM000294	1.02	0.32	0.14	0.61	0.00	69.01%
FSL3_N	N-S	LSM000296	2.42	0.25	0.15	0.50	0.00	89.58%
FSL3_NE005	N-S	LSM000293	0.30	0.09	0.08	0.30	0.00	71.67%
FSL3_NE005	N-S	LSM000294	1.02	0.31	0.18	0.71	0.00	69.50%
FSL3_NE005	N-S	LSM000296	2.42	0.29	0.16	0.71	0.10	87.92%
FSL3_W	N-S	LSM000293	0.30	0.09	0.10	0.30	0.00	70.00%
FSL3_W	N-S	LSM000294	1.02	0.34	0.20	0.71	0.00	67.00%
FSL3_W	N-S	LSM000296	2.42	0.27	0.15	0.50	0.00	88.96%
FUL1	N-S	LSM000293	0.30	0.75	0.32	1.61	0.30	148.33%
FUL1	N-S	LSM000294	1.02	2.34	0.45	3.26	1.63	129.50%
FUL1	N-S	LSM000296	2.42	2.45	0.46	3.43	1.72	1.04%
FUL2	N-S	LSM000293	0.30	0.55	0.18	1.01	0.20	83.33%
FUL2	N-S	LSM000294	1.02	1.88	0.41	2.55	1.32	84.50%
FUL2	N-S	LSM000296	2.42	1.62	0.40	2.52	0.61	33.13%

Table 5-14. Results of scanline P_{10} verification, SH orientation set.

Case	Set	Outcrop	P_{10} Observed	P_{10} Simulated				
				Mean	Std. Dev.	Max	Min	% Error
BM	SH	LSM000293	0.50	0.62	0.31	1.21	0.10	24.00%
BM	SH	LSM000294	0.51	0.52	0.20	0.82	0.10	2.00%
BM	SH	LSM000296	0.10	0.53	0.26	1.11	0.10	425.00%
BMF	SH	LSM000293	0.50	0.44	0.21	0.91	0.10	12.00%
BMF	SH	LSM000294	0.51	0.58	0.23	0.92	0.10	13.00%
BMF	SH	LSM000296	0.10	0.39	0.19	0.91	0.10	290.00%
BMU	SH	LSM000293	0.50	0.40	0.18	0.71	0.10	20.00%
BMU	SH	LSM000294	0.51	0.51	0.20	0.92	0.10	0.00%
BMU	SH	LSM000296	0.10	0.40	0.22	0.91	0.10	295.00%
BMUF	SH	LSM000293	0.50	0.33	0.20	0.81	0.00	34.00%
BMUF	SH	LSM000294	0.51	0.45	0.25	1.22	0.10	12.00%
BMUF	SH	LSM000296	0.10	0.37	0.19	0.81	0.10	265.00%
EL1	SH	LSM000293	0.50	1.00	0.39	1.81	0.30	99.00%
EL1	SH	LSM000294	0.51	1.01	0.37	1.73	0.31	99.00%
EL1	SH	LSM000296	0.10	1.14	0.34	1.72	0.50	1,025.00%
EL2	SH	LSM000293	0.50	0.16	0.13	0.40	0.00	69.00%
EL2	SH	LSM000294	0.51	0.15	0.12	0.41	0.00	71.00%
EL2	SH	LSM000296	0.10	0.12	0.05	0.20	0.00	20.00%
ESL1_N	SH	LSM000293	0.50	0.07	0.09	0.30	0.00	87.00%
ESL1_N	SH	LSM000294	0.51	0.09	0.11	0.31	0.00	83.00%
ESL1_N	SH	LSM000296	0.10	0.04	0.05	0.10	0.00	65.00%
ESL1_NE005	SH	LSM000293	0.50	0.05	0.08	0.20	0.00	90.40%
ESL1_NE005	SH	LSM000294	0.51	0.07	0.10	0.31	0.00	87.20%
ESL1_NE005	SH	LSM000296	0.10	0.04	0.05	0.10	0.00	64.00%
ESL1_W	SH	LSM000293	0.50	0.06	0.08	0.30	0.00	89.00%
ESL1_W	SH	LSM000294	0.51	0.06	0.10	0.31	0.00	89.00%
ESL1_W	SH	LSM000296	0.10	0.04	0.06	0.20	0.00	60.00%
ESL2_N	SH	LSM000293	0.50	0.06	0.08	0.20	0.00	88.00%
ESL2_N	SH	LSM000294	0.51	0.04	0.07	0.20	0.00	92.00%
ESL2_N	SH	LSM000296	0.10	0.04	0.06	0.20	0.00	60.00%
ESL2_NE005	SH	LSM000293	0.50	0.06	0.08	0.20	0.00	88.00%
ESL2_NE005	SH	LSM000294	0.51	0.04	0.07	0.20	0.00	92.00%
ESL2_NE005	SH	LSM000296	0.10	0.04	0.06	0.20	0.00	60.00%
ESL2_W	SH	LSM000293	0.50	0.04	0.07	0.20	0.00	92.00%
ESL2_W	SH	LSM000294	0.51	0.06	0.09	0.31	0.00	89.00%
ESL2_W	SH	LSM000296	0.10	0.03	0.06	0.20	0.00	70.00%
ESL3_N	SH	LSM000293	0.50	0.04	0.08	0.20	0.00	92.00%
ESL3_N	SH	LSM000294	0.51	0.07	0.10	0.31	0.00	87.00%
ESL3_N	SH	LSM000296	0.10	0.04	0.05	0.10	0.00	65.00%
ESL3_NE005	SH	LSM000293	0.50	0.02	0.04	0.10	0.00	96.00%
ESL3_NE005	SH	LSM000294	0.51	0.03	0.06	0.20	0.00	94.00%
ESL3_NE005	SH	LSM000296	0.10	0.03	0.04	0.10	0.00	75.00%
ESL3_W	SH	LSM000293	0.50	0.03	0.06	0.20	0.00	95.00%
ESL3_W	SH	LSM000294	0.51	0.03	0.06	0.20	0.00	95.00%
ESL3_W	SH	LSM000296	0.10	0.02	0.04	0.10	0.00	80.00%

Case	Set	Outcrop	P_{10} Observed	P_{10} Simulated				
				Mean	Std. Dev.	Max	Min	% Error
EUL1	SH	LSM000293	0.50	0.83	0.35	1.51	0.10	64.00%
EUL1	SH	LSM000294	0.51	0.93	0.24	1.32	0.51	83.00%
EUL1	SH	LSM000296	0.10	0.73	0.33	1.41	0.20	620.00%
EUL2	SH	LSM000293	0.50	0.12	0.10	0.30	0.00	76.00%
EUL2	SH	LSM000294	0.51	0.13	0.10	0.31	0.00	75.00%
EUL2	SH	LSM000296	0.10	0.20	0.14	0.50	0.00	95.00%
FL1	SH	LSM000293	0.50	0.93	0.29	1.71	0.60	84.00%
FL1	SH	LSM000294	0.51	0.98	0.24	1.53	0.51	93.00%
FL1	SH	LSM000296	0.10	0.96	0.31	1.51	0.40	855.00%
FL2	SH	LSM000293	0.50	0.17	0.15	0.60	0.00	66.00%
FL2	SH	LSM000294	0.51	0.18	0.14	0.51	0.00	64.00%
FL2	SH	LSM000296	0.10	0.13	0.11	0.30	0.00	30.00%
FSL1_N	SH	LSM000293	0.50	0.06	0.07	0.20	0.00	89.00%
FSL1_N	SH	LSM000294	0.51	0.09	0.10	0.31	0.00	82.00%
FSL1_N	SH	LSM000296	0.10	0.05	0.07	0.20	0.00	55.00%
FSL1_NE005	SH	LSM000293	0.50	0.05	0.08	0.20	0.00	90.00%
FSL1_NE005	SH	LSM000294	0.51	0.06	0.09	0.20	0.00	88.00%
FSL1_NE005	SH	LSM000296	0.10	0.04	0.05	0.10	0.00	65.00%
FSL1_W	SH	LSM000293	0.50	0.05	0.08	0.30	0.00	91.00%
FSL1_W	SH	LSM000294	0.51	0.06	0.10	0.31	0.00	88.00%
FSL1_W	SH	LSM000296	0.10	0.04	0.05	0.10	0.00	65.00%
FSL2_N	SH	LSM000293	0.50	0.06	0.08	0.20	0.00	89.00%
FSL2_N	SH	LSM000294	0.51	0.05	0.07	0.20	0.00	91.00%
FSL2_N	SH	LSM000296	0.10	0.05	0.06	0.20	0.00	55.00%
FSL2_NE005	SH	LSM000293	0.50	0.02	0.05	0.20	0.00	97.00%
FSL2_NE005	SH	LSM000294	0.51	0.07	0.10	0.31	0.00	87.00%
FSL2_NE005	SH	LSM000296	0.10	0.04	0.08	0.30	0.00	60.00%
FSL2_W	SH	LSM000293	0.50	0.03	0.06	0.20	0.00	94.00%
FSL2_W	SH	LSM000294	0.51	0.05	0.08	0.31	0.00	90.00%
FSL2_W	SH	LSM000296	0.10	0.02	0.04	0.10	0.00	80.00%
FSL3_N	SH	LSM000293	0.50	0.05	0.07	0.20	0.00	91.00%
FSL3_N	SH	LSM000294	0.51	0.04	0.09	0.31	0.00	92.00%
FSL3_N	SH	LSM000296	0.10	0.04	0.08	0.30	0.00	65.00%
FSL3_NE005	SH	LSM000293	0.50	0.03	0.06	0.20	0.00	95.00%
FSL3_NE005	SH	LSM000294	0.51	0.03	0.06	0.20	0.00	94.00%
FSL3_NE005	SH	LSM000296	0.10	0.03	0.04	0.10	0.00	75.00%
FSL3_W	SH	LSM000293	0.50	0.02	0.04	0.10	0.00	96.00%
FSL3_W	SH	LSM000294	0.51	0.03	0.06	0.20	0.00	94.00%
FSL3_W	SH	LSM000296	0.10	0.03	0.04	0.10	0.00	75.00%
FUL1	SH	LSM000293	0.50	0.69	0.24	1.21	0.30	37.00%
FUL1	SH	LSM000294	0.51	0.77	0.26	1.43	0.31	51.00%
FUL1	SH	LSM000296	0.10	0.84	0.31	1.62	0.40	730.00%
FUL2	SH	LSM000293	0.50	0.15	0.11	0.30	0.00	70.00%
FUL2	SH	LSM000294	0.51	0.19	0.12	0.41	0.00	62.00%
FUL2	SH	LSM000296	0.10	0.10	0.10	0.30	0.00	5.00%

Table 5-15. Results of scanline P_{10} verification, WNW orientation set.

Case	Set	Outcrop	P_{10} Observed	P_{10} Simulated				
				Mean	Std. Dev.	Max	Min	% Error
BM	WNW	LSM000293	0.30	1.32	0.38	1.81	0.60	336.67%
BM	WNW	LSM000294	0.31	0.50	0.22	0.92	0.10	63.33%
BM	WNW	LSM000296	0.20	0.68	0.32	1.31	0.20	237.50%
BMF	WNW	LSM000293	0.30	0.83	0.32	1.41	0.10	175.00%
BMF	WNW	LSM000294	0.31	0.51	0.25	1.02	0.00	68.33%
BMF	WNW	LSM000296	0.20	0.40	0.20	0.91	0.10	100.00%
BMU	WNW	LSM000293	0.30	0.50	0.21	0.91	0.20	65.00%
BMU	WNW	LSM000294	0.31	0.26	0.19	0.71	0.00	13.33%
BMU	WNW	LSM000296	0.20	0.24	0.16	0.61	0.00	20.00%
BMUF	WNW	LSM000293	0.30	0.64	0.21	1.11	0.40	111.67%
BMUF	WNW	LSM000294	0.31	0.42	0.22	1.02	0.20	38.33%
BMUF	WNW	LSM000296	0.20	0.35	0.21	1.01	0.10	72.50%
EL1	WNW	LSM000293	0.30	1.71	0.39	2.52	0.91	466.67%
EL1	WNW	LSM000294	0.31	0.86	0.25	1.32	0.41	180.00%
EL1	WNW	LSM000296	0.20	0.76	0.32	1.41	0.20	277.50%
EL2	WNW	LSM000293	0.30	0.35	0.18	0.81	0.10	15.00%
EL2	WNW	LSM000294	0.31	0.17	0.13	0.41	0.00	45.00%
EL2	WNW	LSM000296	0.20	0.19	0.12	0.40	0.00	5.00%
ESL1_N	WNW	LSM000293	0.30	0.30	0.16	0.71	0.10	0.00%
ESL1_N	WNW	LSM000294	0.31	0.19	0.17	0.71	0.00	38.33%
ESL1_N	WNW	LSM000296	0.20	0.18	0.13	0.40	0.00	12.50%
ESL1_NE005	WNW	LSM000293	0.30	0.29	0.13	0.60	0.00	4.00%
ESL1_NE005	WNW	LSM000294	0.31	0.19	0.15	0.71	0.00	37.33%
ESL1_NE005	WNW	LSM000296	0.20	0.17	0.10	0.40	0.00	14.00%
ESL1_W	WNW	LSM000293	0.30	0.21	0.11	0.40	0.00	30.00%
ESL1_W	WNW	LSM000294	0.31	0.14	0.10	0.31	0.00	53.33%
ESL1_W	WNW	LSM000296	0.20	0.13	0.09	0.30	0.00	35.00%
ESL2_N	WNW	LSM000293	0.30	0.27	0.10	0.40	0.10	11.67%
ESL2_N	WNW	LSM000294	0.31	0.20	0.13	0.51	0.00	33.33%
ESL2_N	WNW	LSM000296	0.20	0.19	0.15	0.61	0.00	7.50%
ESL2_NE005	WNW	LSM000293	0.30	0.27	0.10	0.40	0.10	11.67%
ESL2_NE005	WNW	LSM000294	0.31	0.20	0.13	0.51	0.00	33.33%
ESL2_NE005	WNW	LSM000296	0.20	0.19	0.15	0.61	0.00	7.50%
ESL2_W	WNW	LSM000293	0.30	0.24	0.14	0.50	0.00	20.00%
ESL2_W	WNW	LSM000294	0.31	0.13	0.11	0.31	0.00	56.67%
ESL2_W	WNW	LSM000296	0.20	0.11	0.08	0.30	0.00	47.50%
ESL3_N	WNW	LSM000293	0.30	0.42	0.19	0.81	0.00	40.00%
ESL3_N	WNW	LSM000294	0.31	0.26	0.17	0.61	0.00	15.00%
ESL3_N	WNW	LSM000296	0.20	0.24	0.17	0.61	0.00	20.00%
ESL3_NE005	WNW	LSM000293	0.30	0.29	0.15	0.60	0.00	3.33%
ESL3_NE005	WNW	LSM000294	0.31	0.20	0.18	0.61	0.00	33.33%
ESL3_NE005	WNW	LSM000296	0.20	0.23	0.15	0.50	0.00	12.50%
ESL3_W	WNW	LSM000293	0.30	0.29	0.18	0.71	0.00	5.00%
ESL3_W	WNW	LSM000294	0.31	0.17	0.11	0.41	0.00	43.33%
ESL3_W	WNW	LSM000296	0.20	0.18	0.10	0.40	0.00	10.00%

Case	Set	Outcrop	P_{10} Observed	P_{10} Simulated				
				Mean	Std. Dev.	Max	Min	% Error
EUL1	WNW	LSM000293	0.30	1.72	0.39	2.32	1.11	470.00%
EUL1	WNW	LSM000294	0.31	0.72	0.28	1.43	0.20	135.00%
EUL1	WNW	LSM000296	0.20	0.79	0.27	1.31	0.30	290.00%
EUL2	WNW	LSM000293	0.30	0.69	0.25	1.31	0.40	126.67%
EUL2	WNW	LSM000294	0.31	0.36	0.23	0.71	0.00	18.33%
EUL2	WNW	LSM000296	0.20	0.35	0.24	0.91	0.00	75.00%
FL1	WNW	LSM000293	0.30	2.03	0.50	3.02	0.91	570.00%
FL1	WNW	LSM000294	0.31	0.94	0.37	1.63	0.00	206.67%
FL1	WNW	LSM000296	0.20	1.01	0.29	1.72	0.40	400.00%
FL2	WNW	LSM000293	0.30	0.34	0.15	0.60	0.10	11.67%
FL2	WNW	LSM000294	0.31	0.17	0.12	0.51	0.00	45.00%
FL2	WNW	LSM000296	0.20	0.19	0.13	0.50	0.00	5.00%
FSL1_N	WNW	LSM000293	0.30	0.31	0.17	0.71	0.10	1.67%
FSL1_N	WNW	LSM000294	0.31	0.20	0.16	0.61	0.00	35.00%
FSL1_N	WNW	LSM000296	0.20	0.20	0.15	0.40	0.00	2.50%
FSL1_NE005	WNW	LSM000293	0.30	0.28	0.13	0.50	0.00	6.65%
FSL1_NE005	WNW	LSM000294	0.31	0.19	0.12	0.41	0.00	38.33%
FSL1_NE005	WNW	LSM000296	0.20	0.19	0.16	0.61	0.00	7.50%
FSL1_W	WNW	LSM000293	0.30	0.23	0.10	0.40	0.00	23.33%
FSL1_W	WNW	LSM000294	0.31	0.15	0.12	0.41	0.00	51.67%
FSL1_W	WNW	LSM000296	0.20	0.14	0.12	0.50	0.00	30.00%
FSL2_N	WNW	LSM000293	0.30	0.30	0.14	0.50	0.00	0.00%
FSL2_N	WNW	LSM000294	0.31	0.20	0.13	0.41	0.00	35.00%
FSL2_N	WNW	LSM000296	0.20	0.18	0.16	0.61	0.00	10.00%
FSL2_NE005	WNW	LSM000293	0.30	0.26	0.12	0.40	0.00	15.00%
FSL2_NE005	WNW	LSM000294	0.31	0.14	0.11	0.41	0.00	53.33%
FSL2_NE005	WNW	LSM000296	0.20	0.16	0.12	0.50	0.00	22.50%
FSL2_W	WNW	LSM000293	0.30	0.24	0.13	0.40	0.00	21.67%
FSL2_W	WNW	LSM000294	0.31	0.13	0.12	0.41	0.00	58.33%
FSL2_W	WNW	LSM000296	0.20	0.12	0.10	0.30	0.00	42.50%
FSL3_N	WNW	LSM000293	0.30	0.38	0.14	0.60	0.00	26.67%
FSL3_N	WNW	LSM000294	0.31	0.29	0.19	0.71	0.00	5.00%
FSL3_N	WNW	LSM000296	0.20	0.25	0.18	0.61	0.00	22.50%
FSL3_NE005	WNW	LSM000293	0.30	0.26	0.15	0.60	0.00	15.00%
FSL3_NE005	WNW	LSM000294	0.31	0.14	0.14	0.41	0.00	55.00%
FSL3_NE005	WNW	LSM000296	0.20	0.18	0.11	0.40	0.00	10.00%
FSL3_W	WNW	LSM000293	0.30	0.27	0.11	0.40	0.00	10.00%
FSL3_W	WNW	LSM000294	0.31	0.16	0.13	0.51	0.00	46.67%
FSL3_W	WNW	LSM000296	0.20	0.16	0.11	0.50	0.00	20.00%
FUL1	WNW	LSM000293	0.30	1.25	0.35	1.71	0.20	313.33%
FUL1	WNW	LSM000294	0.31	0.62	0.27	1.12	0.10	101.67%
FUL1	WNW	LSM000296	0.20	0.59	0.26	1.21	0.20	192.50%
FUL2	WNW	LSM000293	0.30	0.27	0.11	0.50	0.10	11.67%
FUL2	WNW	LSM000294	0.31	0.12	0.10	0.41	0.00	61.67%
FUL2	WNW	LSM000296	0.20	0.17	0.17	0.61	0.00	17.50%

Table 5-16. List of 'top-two' performing alternative models in verification case SI-2, organised by fracture set and scanline.

Set	Scanline	Case	% Error
ENE	LSM000293	EL1	40.71%
ENE	LSM000293	BMF	43.10%
ENE	LSM000294	BMF	28.12%
ENE	LSM000294	BMUF	33.12%
ENE	LSM000296	EUL2	15.00%
ENE	LSM000296	FL2	26.67%
N-S	LSM000293	ESL1_N	18.33%
N-S	LSM000293	EUL2	48.33%
N-S	LSM000294	EUL2	18.00%
N-S	LSM000294	ESL1_N	56.00%
N-S	LSM000296	BMU	0.42%
N-S	LSM000296	FUL1	1.04%
SH	LSM000293	BMF	12.00%
SH	LSM000293	BMU	20.00%
SH	LSM000294	BMU	0.00%
SH	LSM000294	BM	2.00%
SH	LSM000296	FUL2	5.00%
SH	LSM000296	EL2	20.00%
WNW	LSM000293	ESL1_N	0.00%
WNW	LSM000293	FSL2_N	0.00%
WNW	LSM000294	FSL3_N	5.00%
WNW	LSM000294	BMU	13.33%
WNW	LSM000296	FSL1_N	2.50%
WNW	LSM000296	EL2	5.00%

5.5 Verification SI-3: Size-intensity model within the MDZ size range

Verification case SI-3 is focused on determining the ability of the Base Model and the alternative models to predict the P_{32} intensity of minor deformation zones identified in cored boreholes at Laxemar.

Minor deformation zones, c.f. Section 2.1.6 and /Hermanson et al. 2008/, are structures identified in the ESHI-evaluation of cored borehole records that have the same morphological characteristics as Deformation Zones (DZ), but have a true thickness of less than 10 m and cannot be geometrically matched to structural intercepts in more than one borehole. MDZ structures at Laxemar have the following characteristics:

- MDZ have an apparent thickness of at least 10cm to 20cm and less than or equal to 10 m. Almost half of the identified MDZ have true thicknesses less than 1 m /Hermanson et al. 2008/.
- Rock inside MDZ is interpreted to have a higher fracture intensity than the rock outside of MDZ. A combination of spikes in fracture frequency, borehole geophysical anomalies, flow log anomalies (if present), and rock alteration was how both DZ and MDZ were preliminarily identified during the extended single-hole interpretation.
- MDZ are constrained by the geological DFN model parameterisation to be smaller than 564.2 m in equivalent radius. Any identified structure larger than this is included in the deterministic DZ model /Wahlgren et al. 2008/. As such, the definition for MDZ is a functional relationship rather than a strict geological definition.

- MDZ represent areas of possible stress concentration in the bedrock (in analogy to effects of larger DZ). They may either represent the effects of original ductile or brittle deformation, or the later brittle re-activation of previously-formed ductile structures.
- MDZ may be hydraulically significant as seen through PFL-f data. Overall, 128 of 224 (57%) MDZ are associated with PFL-f features /Rhén et al. 2008/.
- MDZ do not have a well-defined minimum size. This verification case (SI-3) is designed to illustrate some general characteristics of the size-intensity relationships of MDZ-sized structures at Laxemar. However, it is not possible to establish a single categorical minimum size for MDZ at Laxemar.

The observed intensity of MDZ at Laxemar is quantified by their P_{10}: the number of MDZ intersecting a borehole, divided by the length of the borehole. A list of the minor deformation zones in the cored borehole array is presented as Appendix 3 of the SDM-Site Laxemar DCR /Hermanson et al. 2008/; in this appendix, the orientation and locations of MDZ quantified during the ESHI analysis are summarised. The length of the borehole used in the P_{10} calculation is the total length (MD) of the borehole, minus the length of sections of boreholes inside mapped deformation zones (DZ).

Geological DFN modelling, however, relies on P_{32} as the measure of fracture intensity. Therefore, for borehole MDZ intercept data to be useful in geological modelling, it is necessary to transform MDZ P_{10} to MDZ P_{32}. This is accomplished using the Wang approximation (Section 3.5.1). The MDZ intercepts contained in Appendix 3 of /Hermanson et al. 2008/ were assigned to the fracture orientation sets developed for the SDM-Site Laxemar geological DFN. For the purposes of verification case SI-3, each borehole used the average C_{13} value over 3 m long intervals for each fracture set. The P_{32} of MDZ at Laxemar are presented below, organised by orientation set and fracture domain, in Table 5-17. FSM_S is not included in verification case SI-3, as this domain has generally been excluded from analyses due to a distinct lack of data (only a single borehole).

Table 5-17. P_{32} of MDZ in cored boreholes at Laxemar, classified by fracture domain.

Fracture Domain	Borehole IDCODE	Borehole Length	Fracture Set	Number of MDZ	MDZ P_{10}	Average C_{13}	MDZ P_{32}
FSM_C	KLX03	794.76	ENE	0	0.0000	3.88	0.0000
FSM_C	KLX08	264.98	ENE	0	0.0000	2.91	0.0000
FSM_C	KLX15A	813.34	ENE	5	0.0061	2.03	0.0125
FSM_C	KLX18A	152.69	ENE	0	0.0000	4.03	0.0000
FSM_C	KLX03	794.76	N-S	0	0.0000	3.29	0.0000
FSM_C	KLX08	264.98	N-S	0	0.0000	2.91	0.0000
FSM_C	KLX15A	813.34	N-S	4	0.0049	3.25	0.0160
FSM_C	KLX18A	152.69	N-S	0	0.0000	3.24	0.0000
FSM_C	KLX03	794.76	SH	5	0.0063	1.21	0.0076
FSM_C	KLX08	264.98	SH	0	0.0000	1.38	0.0000
FSM_C	KLX15A	813.34	SH	8	0.0098	1.58	0.0156
FSM_C	KLX18A	152.69	SH	2	0.0131	1.18	0.0154
FSM_C	KLX03	794.76	WNW	2	0.0025	3.33	0.0084
FSM_C	KLX08	264.98	WNW	1	0.0038	2.28	0.0086
FSM_C	KLX15A	813.34	WNW	1	0.0012	1.86	0.0023
FSM_C	KLX18A	152.69	WNW	0	0.0000	3.64	0.0000
FSM_EW007	KLX02	376.50	ENE	1	0.0027	3.91	0.0104
FSM_EW007	KLX04	412.26	ENE	1	0.0024	4.04	0.0098
FSM_EW007	KLX07A	445.24	ENE	2	0.0045	1.81	0.0081
FSM_EW007	KLX08	420.60	ENE	0	0.0000	2.91	0.0000
FSM_EW007	KLX09	256.47	ENE	0	0.0000	4.09	0.0000

Fracture Domain	Borehole IDCODE	Borehole Length	Fracture Set	Number of MDZ	MDZ P_{10}	Average C_{13}	MDZ P_{32}
FSM_EW007	KLX10	262.96	ENE	0	0.0000	4.09	0.0000
FSM_EW007	KLX10B	31.20	ENE	0	0.0000	2.17	0.0000
FSM_EW007	KLX10C	86.98	ENE	1	0.0115	2.14	0.0247
FSM_EW007	KLX18A	300.08	ENE	0	0.0000	4.03	0.0000
FSM_EW007	KLX29A	49.35	ENE	0	0.0000	2.21	0.0000
FSM_EW007	KLX02	376.50	N-S	2	0.0053	3.59	0.0191
FSM_EW007	KLX04	412.26	N-S	0	0.0000	3.58	0.0000
FSM_EW007	KLX07A	445.24	N-S	1	0.0022	3.58	0.0080
FSM_EW007	KLX08	420.60	N-S	0	0.0000	2.91	0.0000
FSM_EW007	KLX09	256.47	N-S	1	0.0039	3.38	0.0132
FSM_EW007	KLX10	262.96	N-S	0	0.0000	3.38	0.0000
FSM_EW007	KLX10B	31.20	N-S	1	0.0321	3.56	0.1140
FSM_EW007	KLX10C	86.98	N-S	0	0.0000	3.57	0.0000
FSM_EW007	KLX18A	300.08	N-S	0	0.0000	3.24	0.0000
FSM_EW007	KLX29A	49.35	N-S	0	0.0000	2.82	0.0000
FSM_EW007	KLX02	376.50	SH	0	0.0000	1.17	0.0000
FSM_EW007	KLX04	412.26	SH	7	0.0170	1.17	0.0198
FSM_EW007	KLX07A	445.24	SH	4	0.0090	1.56	0.0140
FSM_EW007	KLX08	420.60	SH	3	0.0071	1.38	0.0098
FSM_EW007	KLX09	256.47	SH	7	0.0273	1.17	0.0320
FSM_EW007	KLX10	262.96	SH	1	0.0038	1.17	0.0045
FSM_EW007	KLX10B	31.20	SH	0	0.0000	1.39	0.0000
FSM_EW007	KLX10C	86.98	SH	4	0.0460	1.32	0.0607
FSM_EW007	KLX18A	300.08	SH	5	0.0167	1.18	0.0196
FSM_EW007	KLX29A	49.35	SH	3	0.0608	1.30	0.0792
FSM_EW007	KLX02	376.50	WNW	0	0.0000	3.38	0.0000
FSM_EW007	KLX04	412.26	WNW	0	0.0000	3.41	0.0000
FSM_EW007	KLX07A	445.24	WNW	1	0.0022	2.14	0.0048
FSM_EW007	KLX08	420.60	WNW	0	0.0000	2.28	0.0000
FSM_EW007	KLX09	256.47	WNW	0	0.0000	3.64	0.0000
FSM_EW007	KLX10	262.96	WNW	1	0.0038	3.64	0.0138
FSM_EW007	KLX10B	31.20	WNW	0	0.0000	2.60	0.0000
FSM_EW007	KLX10C	86.98	WNW	0	0.0000	2.15	0.0000
FSM_EW007	KLX18A	300.08	WNW	0	0.0000	3.64	0.0000
FSM_EW007	KLX29A	49.35	WNW	0	0.0000	2.91	0.0000
FSM_N	KLX04	194.94	ENE	0	0.0000	4.04	0.0000
FSM_N	KLX07B	107.54	ENE	0	0.0000	4.03	0.0000
FSM_N	KLX08	71.82	ENE	0	0.0000	2.91	0.0000
FSM_N	KLX09	362.03	ENE	0	0.0000	4.09	0.0000
FSM_N	KLX09B	91.78	ENE	0	0.0000	4.12	0.0000
FSM_N	KLX09C	110.59	ENE	0	0.0000	2.09	0.0000
FSM_N	KLX09D	109.38	ENE	0	0.0000	3.58	0.0000
FSM_N	KLX09E	88.57	ENE	0	0.0000	2.10	0.0000
FSM_N	KLX09F	127.74	ENE	0	0.0000	3.41	0.0000
FSM_N	KLX04	194.94	N-S	0	0.0000	3.58	0.0000
FSM_N	KLX07B	107.54	N-S	1	0.0093	3.59	0.0334
FSM_N	KLX08	71.82	N-S	0	0.0000	2.91	0.0000
FSM_N	KLX09	362.03	N-S	0	0.0000	3.38	0.0000
FSM_N	KLX09B	91.78	N-S	0	0.0000	3.58	0.0000
FSM_N	KLX09C	110.59	N-S	0	0.0000	3.49	0.0000
FSM_N	KLX09D	109.38	N-S	0	0.0000	2.04	0.0000

Fracture Domain	Borehole IDCODE	Borehole Length	Fracture Set	Number of MDZ	MDZ P_{10}	Average C_{13}	MDZ P_{32}
FSM_N	KLX09E	88.57	N-S	0	0.0000	3.33	0.0000
FSM_N	KLX09F	127.74	N-S	0	0.0000	2.18	0.0000
FSM_N	KLX04	194.94	SH	6	0.0308	1.17	0.0360
FSM_N	KLX07B	107.54	SH	2	0.0186	1.17	0.0218
FSM_N	KLX08	71.82	SH	1	0.0139	1.38	0.0192
FSM_N	KLX09	362.03	SH	8	0.0221	1.17	0.0259
FSM_N	KLX09B	91.78	SH	2	0.0218	1.17	0.0254
FSM_N	KLX09C	110.59	SH	2	0.0181	1.41	0.0255
FSM_N	KLX09D	109.38	SH	2	0.0183	1.34	0.0245
FSM_N	KLX09E	88.57	SH	0	0.0000	1.31	0.0000
FSM_N	KLX09F	127.74	SH	3	0.0235	1.39	0.0326
FSM_N	KLX04	194.94	WNW	1	0.0051	3.41	0.0175
FSM_N	KLX07B	107.54	WNW	0	0.0000	3.63	0.0000
FSM_N	KLX08	71.82	WNW	0	0.0000	2.28	0.0000
FSM_N	KLX09	362.03	WNW	0	0.0000	3.64	0.0000
FSM_N	KLX09B	91.78	WNW	0	0.0000	3.61	0.0000
FSM_N	KLX09C	110.59	WNW	0	0.0000	2.64	0.0000
FSM_N	KLX09D	109.38	WNW	0	0.0000	3.40	0.0000
FSM_N	KLX09E	88.57	WNW	1	0.0113	2.39	0.0270
FSM_N	KLX09F	127.74	WNW	1	0.0078	3.24	0.0254
FSM_NE005	KLX02	45.04	ENE	0	0.0000	3.91	0.0000
FSM_NE005	KLX05	875.61	ENE	1	0.0011	3.29	0.0038
FSM_NE005	KLX12A	488.42	ENE	1	0.0020	3.32	0.0068
FSM_NE005	KLX21B	604.10	ENE	0	0.0000	3.79	0.0000
FSM_NE005	KLX26A	77.97	ENE	2	0.0257	3.52	0.0904
FSM_NE005	KLX28A	56.28	ENE	0	0.0000	2.38	0.0000
FSM_NE005	KLX02	45.04	N-S	0	0.0000	3.59	0.0000
FSM_NE005	KLX05	875.61	N-S	2	0.0023	3.00	0.0069
FSM_NE005	KLX12A	488.42	N-S	1	0.0020	3.11	0.0064
FSM_NE005	KLX21B	604.10	N-S	2	0.0033	2.91	0.0096
FSM_NE005	KLX26A	77.97	N-S	1	0.0128	2.24	0.0288
FSM_NE005	KLX28A	56.28	N-S	1	0.0178	3.46	0.0616
FSM_NE005	KLX02	45.04	SH	1	0.0222	1.17	0.0259
FSM_NE005	KLX05	875.61	SH	3	0.0034	1.31	0.0045
FSM_NE005	KLX12A	488.42	SH	6	0.0123	1.19	0.0147
FSM_NE005	KLX21B	604.10	SH	7	0.0116	1.26	0.0146
FSM_NE005	KLX26A	77.97	SH	1	0.0128	1.36	0.0175
FSM_NE005	KLX28A	56.28	SH	0	0.0000	1.39	0.0000
FSM_NE005	KLX02	45.04	WNW	0	0.0000	3.38	0.0000
FSM_NE005	KLX05	875.61	WNW	0	0.0000	2.64	0.0000
FSM_NE005	KLX12A	488.42	WNW	0	0.0000	3.47	0.0000
FSM_NE005	KLX21B	604.10	WNW	0	0.0000	2.93	0.0000
FSM_NE005	KLX26A	77.97	WNW	0	0.0000	3.22	0.0000
FSM_NE005	KLX28A	56.28	WNW	1	0.0178	2.34	0.0415
FSM_W	KLX11A	790.43	ENE	1	0.0013	3.93	0.0050
FSM_W	KLX11B	91.21	ENE	0	0.0000	4.13	0.0000
FSM_W	KLX11D	99.44	ENE	0	0.0000	3.48	0.0000
FSM_W	KLX11E	86.66	ENE	0	0.0000	2.11	0.0000
FSM_W	KLX13A	375.16	ENE	0	0.0000	4.10	0.0000
FSM_W	KLX14A	115.77	ENE	0	0.0000	2.32	0.0000
FSM_W	KLX17A	558.65	ENE	0	0.0000	2.45	0.0000

Fracture Domain	Borehole IDCODE	Borehole Length	Fracture Set	Number of MDZ	MDZ P_{10}	Average C_{13}	MDZ P_{32}
FSM_W	KLX19A	589.38	ENE	2	0.0034	2.39	0.0081
FSM_W	KLX22A	96.00	ENE	0	0.0000	2.28	0.0000
FSM_W	KLX22B	92.81	ENE	0	0.0000	2.15	0.0000
FSM_W	KLX23A	92.55	ENE	0	0.0000	2.93	0.0000
FSM_W	KLX23B	43.85	ENE	1	0.0228	2.64	0.0602
FSM_W	KLX24A	88.62	ENE	0	0.0000	3.31	0.0000
FSM_W	KLX11A	790.43	N-S	4	0.0051	2.88	0.0146
FSM_W	KLX11B	91.21	N-S	1	0.0110	3.59	0.0393
FSM_W	KLX11D	99.44	N-S	2	0.0201	1.96	0.0394
FSM_W	KLX11E	86.66	N-S	0	0.0000	3.27	0.0000
FSM_W	KLX13A	375.16	N-S	1	0.0027	3.44	0.0092
FSM_W	KLX14A	115.77	N-S	2	0.0173	1.89	0.0326
FSM_W	KLX17A	558.65	N-S	3	0.0054	3.43	0.0184
FSM_W	KLX19A	589.38	N-S	0	0.0000	3.28	0.0000
FSM_W	KLX22A	96.00	N-S	0	0.0000	3.57	0.0000
FSM_W	KLX22B	92.81	N-S	0	0.0000	3.42	0.0000
FSM_W	KLX23A	92.55	N-S	0	0.0000	3.08	0.0000
FSM_W	KLX23B	43.85	N-S	0	0.0000	2.52	0.0000
FSM_W	KLX24A	88.62	N-S	0	0.0000	2.17	0.0000
FSM_W	KLX11A	790.43	SH	11	0.0139	1.24	0.0173
FSM_W	KLX11B	91.21	SH	1	0.0110	1.17	0.0128
FSM_W	KLX11D	99.44	SH	1	0.0101	1.36	0.0137
FSM_W	KLX11E	86.66	SH	3	0.0346	1.31	0.0453
FSM_W	KLX13A	375.16	SH	4	0.0107	1.18	0.0125
FSM_W	KLX14A	115.77	SH	3	0.0259	1.62	0.0420
FSM_W	KLX17A	558.65	SH	5	0.0090	1.33	0.0119
FSM_W	KLX19A	589.38	SH	4	0.0068	1.42	0.0096
FSM_W	KLX22A	96.00	SH	1	0.0104	1.39	0.0144
FSM_W	KLX22B	92.81	SH	1	0.0108	1.30	0.0140
FSM_W	KLX23A	92.55	SH	2	0.0216	1.32	0.0285
FSM_W	KLX23B	43.85	SH	0	0.0000	1.37	0.0000
FSM_W	KLX24A	88.62	SH	4	0.0451	1.39	0.0628
FSM_W	KLX11A	790.43	WNW	0	0.0000	3.33	0.0000
FSM_W	KLX11B	91.21	WNW	0	0.0000	3.62	0.0000
FSM_W	KLX11D	99.44	WNW	0	0.0000	3.39	0.0000
FSM_W	KLX11E	86.66	WNW	1	0.0115	2.46	0.0284
FSM_W	KLX13A	375.16	WNW	1	0.0027	3.60	0.0096
FSM_W	KLX14A	115.77	WNW	0	0.0000	3.61	0.0000
FSM_W	KLX17A	558.65	WNW	0	0.0000	1.99	0.0000
FSM_W	KLX19A	589.38	WNW	3	0.0051	2.17	0.0111
FSM_W	KLX22A	96.00	WNW	0	0.0000	2.41	0.0000
FSM_W	KLX22B	92.81	WNW	0	0.0000	2.35	0.0000
FSM_W	KLX23A	92.55	WNW	0	0.0000	2.03	0.0000
FSM_W	KLX23B	43.85	WNW	0	0.0000	3.63	0.0000
FSM_W	KLX24A	88.62	WNW	0	0.0000	3.30	0.0000

A basic assumption concerning MDZ is that they represent larger structures than most of the fractures exposed in the cored boreholes. The SDM-Site Laxemar geological DFN model considers that all structures (fractures and MDZ) with a equivalent radius less than or equal to 564.2 m are treated stochastically in the geological DFN. However, the true size of the MDZ exposed in the cored borehole record at Laxemar is not known; as none of the MDZ can be traced to intercepts with other boreholes or identified uniquely at the ground surface by geophysics, their true size distribution is unknown. In particular, there are no data on the minimum size of MDZ.

An issue is that the power-law size-intensity scaling models used by the geological DFN model do not discriminate between MDZ and large fractures; the size-intensity model only gives the P_{32} of all structures in a certain size range. Therefore, the radius scaling exponent (k_r), which is derived from outcrop fracture maps and lineament traces, is likely to describe both MDZ and large single fractures.

There are two possible alternatives to deal with the lack of information on the minimum size of MDZ-sized features without collecting additional data:

- Method 1: The P_{32} of MDZ can be used in conjunction with the various size-intensity alternative models to analytically determine a minimum size (r_{min}) of MDZ. This value will vary as a function of the radius scaling exponent (k_r) and the fitted mean P_{32} chosen for the specific size-intensity model alternative. The result of this implies that all structures between the fitted r_{min} value and the maximum size allowed for structures in the stochastic DFN model are MDZ. Data from the surface are only used to establish the radius scaling exponent, and not to determine the intensity of MDZ-sized structures.
- Method 2: One can assume that every surface lineament recorded by the detailed ground magnetic and LIDAR surveys represents an MDZ. The minimum size (r_{min}) of the structures that created the surface lineaments can be estimated using the trace length 'rollover effect' on the area-normalised complementary cumulative number plots; the method is described below. As it is not possible to assign the lineaments to individual fracture domains without incurring substantial truncation effects, Method 2 produces r_{min} values that are global in scope.

Calculating r_{min} from the CCN rollover

The 'rollover' effect alluded to above is a bias peculiar to the DFN methodology of power laws. If fractures are circular discs with area equivalent to that of a polygonal fracture and are of effective radius r, for a given value of r, fracture trace lengths of up to $2r$ can be generated. Therefore, fractures with a radius between 0.5 r_0 (where r_0 is the minimum radius of the probability distribution) and r_0 can theoretically generate traces with lengths between r_0 and $2r_0$. However, since no fractures with a radius less than r_0 are generated in the DFN model, a trace length deficit exists between $2r_0$ and r_0; this deficit is manifested as the apparent 'rollover' in the trace length scaling plots (illustrated in Figure 5-10). The rollover effect is useful as an alternative method for determining the minimum radius cut-off for a particular population of fractures. For example, if the rollover in the trace length scaling plots begins at 1.0 metres in length, then it is likely that the minimum radius of the underlying fracture population is approximately 0.5 metres.

If the minimum radius calculated using the rollover effect matches the minimum radius calculated from the borehole MDZ intercepts, this implies that all the lineaments represent MDZ (Method 2). This increases confidence that the size model alternative chosen provides a 'good fit' to the available data. This would also imply that most of the large structures at Laxemar have the characteristics of deformation zones rather than single planar fractures.

If, however, the r_0 value calculated using the two different methods is significantly different, then a problem exists. Without any additional information, it is impossible to determine with any degree of confidence what the size of the smallest MDZ is likely to be. This therefore makes it very difficult to express a size model exclusively for MDZ; the P_{32} may be known, but the size model is incomplete. In this case, the geological DFN team recommends that the minimum size of an MDZ could generally be given by the functional definition based on earthquake safety criteria, ie. a minimum radius of 75 m /Munier and Hökmark 2004, Munier 2007/.

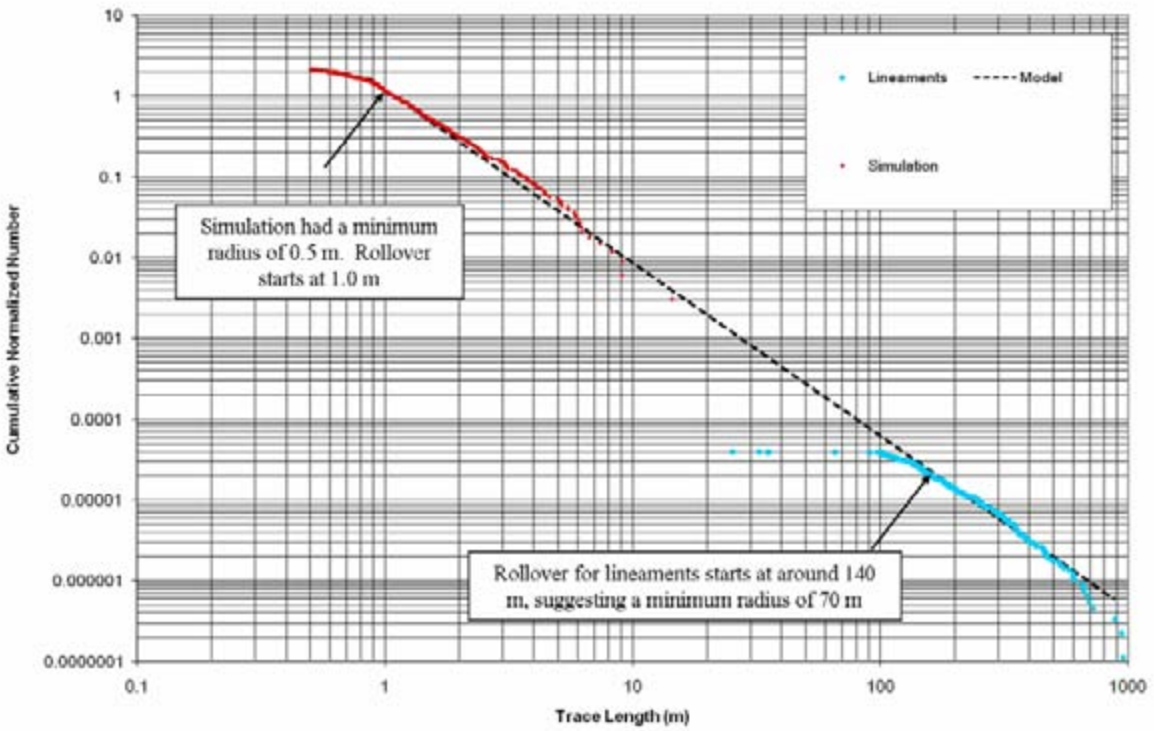

Figure 5-10. *Example of the 'rollover' effect in the area-normalized trace scaling plots.*

A limitation to both methods described above is that they presume that the scaling exponent (k_r) for MDZ is the same as the scaling exponent for fractures exposed on outcrops and in boreholes (i.e. the 'tectonic continuum' hypothesis). Past SDM work has assumed that DZ represent geologically different structures than the so-called 'background fractures'; it is possible that MDZ are also different than the background fractures, and therefore should be modelled using a different radius scaling exponent. However, without the acquisition of additional data on the sizes of MDZ structures (and, in particular, the subhorizontally-oriented MDZ), it is difficult, if not impossible, to test this alternative hypothesis.

Verification case SI-3 utilizes Method 1 to estimate the MDZ minimum size for all size-intensity alternative model cases. Table 5-19 through Table 5-21 present the minimum radius of MDZ calculated using Method 1, as a function of fracture domain, orientation set, and alternative size-intensity model case. The results from Method 1 are then compared to the results derived from the ground magnetic and LIDAR lineaments using Method 2. Minimum radius values calculated using Method 2 are presented below in Table 5-18. The SH orientation set is not included in the verification case, as it is impossible to assign lineaments to the SH set due to the lack of dip and dip direction information. In addition, no MDZ belonging to the ENE orientation set are identified in fracture domain FSM_N.

Table 5-18. Minimum size of MDZ calculated using the trace length rollover effect.

Fracture Set	Start of Rollover (m)	r_{min} (m)
ENE	250	125
NS	125	63
WNW	180	90

Table 5-19. Minimum size of MDZ in the ENE orientation set as a function of fracture domain and alternative size-intensity model. r_{min} calculated using Method 1. Models closest to the value of r_{min} predicted by Method 2 are enclosed by black boxes.

Verification Case	Fracture Set	r_{min} MDZ by Fracture Domain				
		FSM_C	FSM_EW007	FSM_N	FSM_NE005	FSM_W
BM	ENE	154	103	N/A	38	98
EL1	ENE	166	115	N/A	46	110
EL2	ENE	165	105	N/A	32	100
BMU	ENE	151	100	N/A	36	95
EUL1	ENE	121	79	N/A	29	75
EUL2	ENE	155	98	N/A	29	92
BMF	ENE	170	116	N/A	45	110
FL1	ENE	134	91	N/A	36	87
FL2	ENE	172	110	N/A	34	104
BMUF	ENE	155	103	N/A	37	98
FUL1	ENE	154	103	N/A	38	98
FUL2	ENE	114	69	N/A	20	65
ESL1_N	ENE	114	78	N/A	16	58
ESL1_NE005	ENE	103	70	N/A	14	52
ESL1_W	ENE	103	70	N/A	14	52
ESL2_N	ENE	107	73	N/A	15	54
ESL2_NE005	ENE	97	65	N/A	13	49
ESL2_W	ENE	96	65	N/A	13	48
ESL3_N	ENE	160	112	N/A	23	85
ESL3_NE005	ENE	145	101	N/A	21	76
ESL3_W	ENE	145	101	N/A	21	76
FSL1_N	ENE	121	83	N/A	17	62
FSL1_NE005	ENE	109	74	N/A	15	55
FSL1_W	ENE	109	74	N/A	15	55
FSL2_N	ENE	86	58	N/A	12	43
FSL2_NE005	ENE	77	52	N/A	11	38
FSL2_W	ENE	77	51	N/A	11	38
FSL3_N	ENE	165	116	N/A	24	88
FSL3_NE005	ENE	150	105	N/A	22	79
FSL3_W	ENE	150	105	N/A	21	79

Table 5-20. Minimum size of MDZ in the N-S orientation set as a function of fracture domain and alternative size-intensity model. r_{min} calculated using Method 1. Models closest to the value of r_{min} predicted by Method 2 are enclosed by black boxes.

Verification Case	Fracture Set	r_{min} MDZ by Fracture Domain				
		FSM_C	FSM_EW007	FSM_N	FSM_NE005	FSM_W
BM	N-S	116	45	121	39	55
EL1	N-S	105	43	110	37	51
EL2	N-S	59	22	62	19	27
BMU	N-S	85	31	90	26	38
EUL1	N-S	128	49	135	42	60
EUL2	N-S	74	24	79	21	31
BMF	N-S	111	43	117	37	52
FL1	N-S	109	44	114	38	53
FL2	N-S	102	34	108	29	43
BMUF	N-S	108	41	114	35	50
FUL1	N-S	135	53	141	46	64
FUL2	N-S	88	30	93	25	37
ESL1_N	N-S	46	14	56	17	23
ESL1_NE005	N-S	32	10	39	12	17
ESL1_W	N-S	37	12	45	14	19
ESL2_N	N-S	36	11	44	14	19
ESL2_NE005	N-S	26	9	32	10	14
ESL2_W	N-S	29	9	36	11	15
ESL3_N	N-S	24	8	29	9	13
ESL3_NE005	N-S	18	6	21	7	10
ESL3_W	N-S	20	7	24	8	11
FSL1_N	N-S	45	14	55	17	23
FSL1_NE005	N-S	32	10	39	12	17
FSL1_W	N-S	36	11	44	14	19
FSL2_N	N-S	39	12	47	15	20
FSL2_NE005	N-S	28	9	34	11	14
FSL2_W	N-S	31	10	38	12	16
FSL3_N	N-S	52	16	63	19	26
FSL3_NE005	N-S	37	12	45	14	19
FSL3_W	N-S	42	13	51	16	21

The results of verification case SI-3 are, as with cases SI-1 and SI-2, somewhat ambiguous. No one alternative size-intensity model alternative is able to match the r_{min} values derived through Method 2. The only apparent trend is that alternative models utilising fractal scaling appear to perform slightly better than those using Euclidean scaling in this particular verification case. Among the alternative models utilising fractal scaling, alternative FUL1 performed the best. The various Base Model-derived alternatives (BMU, BM, BMUF) perform adequately in most fracture domains; the r_{min} values produced through Method 1 are well within one order of magnitude of the r_{min} values suggested through Method 2.

Table 5-21. Minimum size of MDZ in the WNW orientation set as a function of fracture domain and alternative size-intensity model. r_{min} calculated using Method 1. Models closest to the value of r_{min} predicted by Method 2 are enclosed by black boxes.

Verification Case	Fracture Set	r_{min} MDZ by Fracture Domain				
		FSM_C	FSM_EW007	FSM_N	FSM_NE005	FSM_W
BM	WNW	138	266	92	102	167
EL1	WNW	147	269	102	111	175
EL2	WNW	176	321	116	129	212
BMU	WNW	131	260	84	94	160
EUL1	WNW	155	279	107	117	184
EUL2	WNW	199	341	136	150	235
BMF	WNW	149	279	100	111	180
FL1	WNW	148	267	103	112	175
FL2	WNW	156	299	99	111	190
BMUF	WNW	151	285	100	111	183
FUL1	WNW	118	228	80	88	142
FUL2	WNW	132	270	82	92	163
ESL1_N	WNW	105	248	68	68	104
ESL1_NE005	WNW	114	263	75	75	114
ESL1_W	WNW	130	286	86	86	129
ESL2_N	WNW	91	225	59	59	91
ESL2_NE005	WNW	100	239	65	65	99
ESL2_W	WNW	114	262	75	75	113
ESL3_N	WNW	167	331	114	113	165
ESL3_NE005	WNW	180	346	124	123	179
ESL3_W	WNW	201	367	141	141	200
FSL1_N	WNW	112	259	74	73	111
FSL1_NE005	WNW	122	274	81	80	121
FSL1_W	WNW	139	298	93	92	138
FSL2_N	WNW	87	216	56	56	86
FSL2_NE005	WNW	95	231	62	61	94
FSL2_W	WNW	109	254	71	71	108
FSL3_N	WNW	155	318	105	104	154
FSL3_NE005	WNW	168	333	115	114	167
FSL3_W	WNW	189	355	131	131	188

The only significant anomaly in verification case SI-3 is for the WNW orientation set in fracture domain FSM_EW007. Method 1 predicts r_{min} values that are significantly larger (100 m–300 m) than would be expected from the ground magnetic and LIDAR lineament observations. The reason for this discrepancy is not obvious, but it may be related to the fact that fracture domain FSM_EW007 is defined as a volume around a fairly significant regional deformation zone (ZSMEW007A). It is possible that slip along this deformation zone has historically accommodated enough strain to prevent the growth of new deformation zones or the re-activation of older ones.

5.6 Verification SI-4: Borehole P_{10}.

Verification case SI-4 is designed to test how well the various size-intensity alternatives performed at predicting borehole P_{10} when compared to observed Laxemar data. The verification methodology is fairly straightforward; a number of stochastic DFN realisations are created inside a simulation volume. Simulated boreholes are drilled into each DFN realisation, and the P_{10} of each fracture set is reported. The geometries of sections of actual cored boreholes at Laxemar are used in the verification. The arithmetic average (mean), standard deviation, and extremal values are reported for each fracture domain and alternative model case. The mean fracture intensity from simulation is then compared to the mean fracture intensity for a given borehole, fracture set, and fracture domain combination; percent error is used as the performance metric.

Verification case SI-4 was only performed on fracture domain FSM_C; this is the domain most likely to be selected to host a spent-fuel repository. The DFN simulations are extremely computationally expensive; for alternative models which use the borehole radius as the minimum fracture size, a single round of stochastic simulations for a size-intensity model alternative took a full day (24 hours) to run on a quad-core Pentium-class workstation. Because of the extreme computational loads involved, it was deemed the most effective use of time and resources to simulate only within fracture domain FSM_C.

In verification case SI-4, 20 stochastic realisations inside a 50 m × 50 m × 25 m volume were created for alternative models where the radius scaling exponent is independent of fracture domain. For alternative models where the radius scaling exponent is fracture-domain dependent (i.e. 'Fixed-r_{min}' models), 5 stochastic realisations inside a 10 m × 10 m × 20 m volume were used. Because the Fixed-r_{min} models set the minimum fracture size at the radius of the cored borehole, these alternatives are (as previously mentioned) extremely computationally extensive. Reducing the simulation volume and the number of iterations for SI-4 cases testing Fixed-r_{min} models was judged the most efficient use of time and personnel. Figure 5-11 illustrates an example stochastic model realisation testing a Fixed-r_{min} model; even in this reduced sample volume, several hundred thousand individual fractures were generated. In addition, only the Linked traces versions of the Fixed-r_{min} models were generated; the results of verification cases SI-1 and SI-2 suggest that the differences between the different Fixed-r_{min} models are much larger than the differences between linked and unlinked traces.

Eight 15 m-long sections from six different cored boreholes inside fracture domain FSM_C were chosen for use in verification SI-4. The coordinates and orientation of the target sections are presented as Table 5-22. The borehole sections were chosen to test a wide range of sampling orientations so as to assess how well the global orientation model is able to reproduce borehole observations. Boreholes KLX03 and KLX15A are removed from the simulation for Fixed-r_{min} models.

The results of verification case SI-4 are presented below as Table 5-23 through Table 5-26.

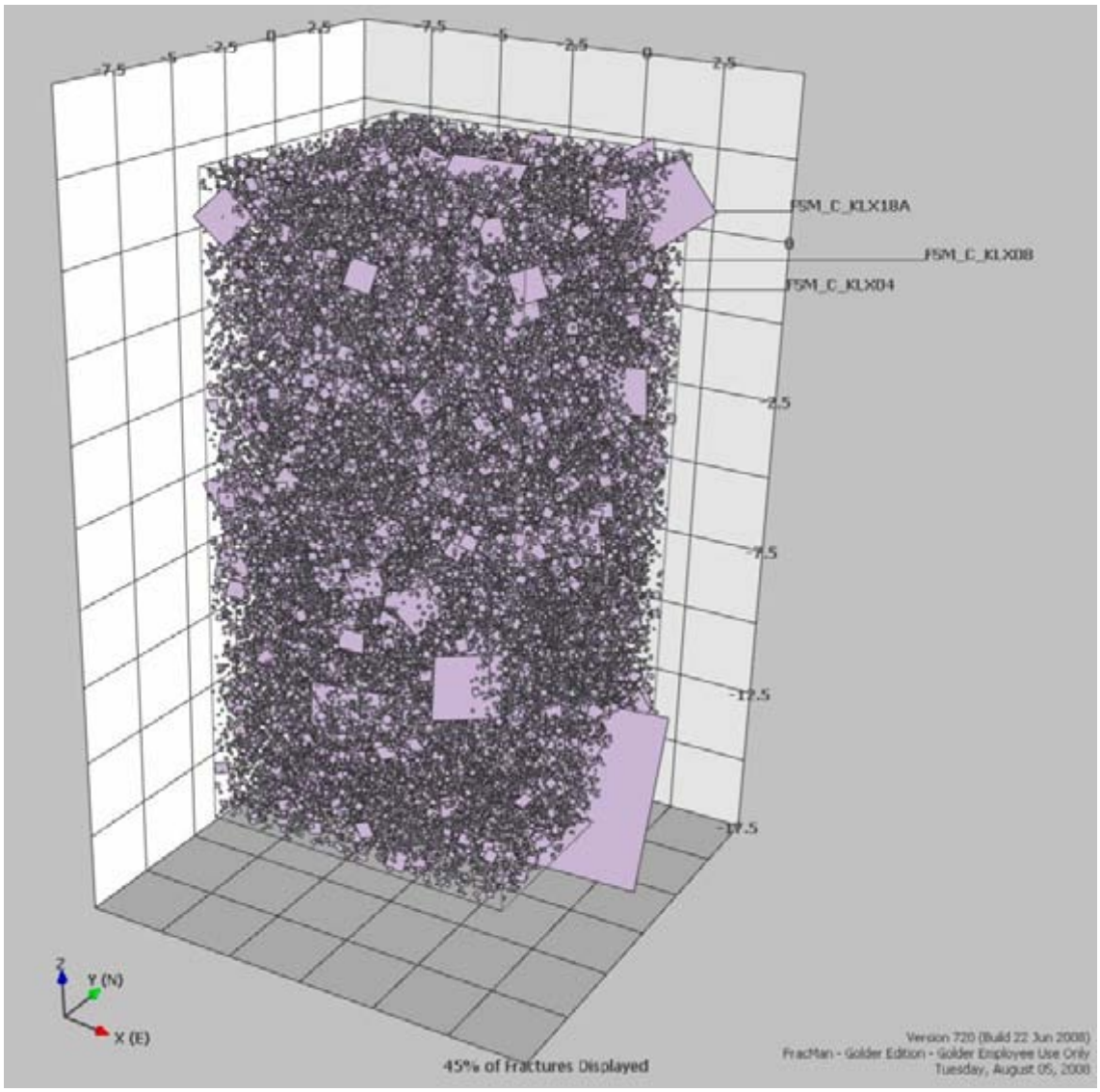

Figure 5-11. *Sample stochastic model realisation, Fixed-r_{min} size-intensity alternative model.*

Table 5-22. Sections of cored borehole array used in verification SI-4. Note that boreholes KLX03 and KLX15A are omitted from verification simulations for Fixed-r_{min} models.

Borehole IDCODE	Elevation (m)		Borehole Orientation	
	Start	End	Trend	Plunge
KLX03	–504.57	–519.15	239.18	76.29
KLX03	–825.30	–839.89	212.67	76.69
KLX04	–766.97	–781.87	38.31	83.45
KLX08	–672.13	–684.88	237.39	58.27
KLX10	–487.95	–502.85	186.86	83.36
KLX15A	–103.48	–115.05	253.41	50.50
KLX15A	–344.32	–355.65	255.91	49.07
KLX18A	–481.92	–496.69	174.37	79.91

Table 5-23. Verification Case SI-4 results, alternative models presuming Euclidean scaling.

Model Case	Fracture Set	Borehole IDCODE	P_{10} Observed	P_{10} Simulated Mean	Std. Dev.	Max.	Min.	Variance	% Error
BM	ENE	KLX03	0.38	0.47	0.21	0.93	0.13	0.044	22.43%
BM	ENE	KLX03	0.38	0.41	0.18	0.73	0.20	0.033	6.69%
BM	ENE	KLX04	0.48	0.43	0.16	0.60	0.13	0.027	11.38%
BM	ENE	KLX08	0.57	0.42	0.20	0.73	0.13	0.039	25.88%
BM	ENE	KLX10	0.37	0.44	0.12	0.67	0.27	0.015	17.99%
BM	ENE	KLX15A	0.98	0.37	0.11	0.60	0.27	0.013	61.91%
BM	ENE	KLX15A	0.98	0.49	0.20	0.93	0.20	0.041	49.67%
BM	ENE	KLX18A	0.38	0.49	0.21	0.93	0.20	0.044	29.50%
BM	N-S	KLX03	0.73	0.79	0.20	1.20	0.53	0.039	9.08%
BM	N-S	KLX03	0.73	0.63	0.26	1.20	0.27	0.069	12.92%
BM	N-S	KLX04	0.21	0.79	0.22	1.07	0.47	0.048	279.29%
BM	N-S	KLX08	0.43	1.00	0.18	1.27	0.73	0.034	135.29%
BM	N-S	KLX10	0.76	0.75	0.17	1.00	0.40	0.029	2.08%
BM	N-S	KLX15A	0.82	1.41	0.26	1.80	0.87	0.066	71.21%
BM	N-S	KLX15A	0.82	1.36	0.20	1.67	1.13	0.040	65.53%
BM	N-S	KLX18A	0.53	0.67	0.20	0.93	0.33	0.042	26.25%
BM	SH	KLX03	2.24	2.26	0.47	2.87	1.53	0.220	0.99%
BM	SH	KLX03	2.24	2.34	0.58	3.27	1.60	0.341	4.56%
BM	SH	KLX04	1.52	2.43	0.48	3.33	1.80	0.233	59.80%
BM	SH	KLX08	0.90	2.14	0.38	2.67	1.60	0.141	137.78%
BM	SH	KLX10	2.50	2.24	0.35	2.93	1.80	0.122	10.25%
BM	SH	KLX15A	0.98	1.95	0.43	2.53	1.33	0.188	98.60%
BM	SH	KLX15A	0.98	1.87	0.37	2.67	1.27	0.139	90.44%
BM	SH	KLX18A	2.66	2.25	0.32	2.80	1.80	0.101	15.45%
BM	WNW	KLX03	0.74	0.72	0.17	1.00	0.47	0.030	3.16%
BM	WNW	KLX03	0.74	0.75	0.19	1.00	0.47	0.035	0.43%
BM	WNW	KLX04	0.40	0.90	0.26	1.33	0.53	0.067	125.00%
BM	WNW	KLX08	0.90	0.99	0.22	1.33	0.73	0.049	9.63%
BM	WNW	KLX10	0.54	0.69	0.17	1.00	0.47	0.029	27.51%
BM	WNW	KLX15A	1.63	1.11	0.23	1.47	0.73	0.051	31.72%
BM	WNW	KLX15A	1.63	0.89	0.22	1.33	0.53	0.048	45.22%
BM	WNW	KLX18A	0.73	0.74	0.27	1.07	0.27	0.073	0.91%
EL2	ENE	KLX03	0.38	0.35	0.15	0.60	0.13	0.024	7.30%
EL2	ENE	KLX03	0.38	0.33	0.07	0.47	0.27	0.005	12.55%
EL2	ENE	KLX04	0.48	0.59	0.21	1.00	0.20	0.045	21.85%
EL2	ENE	KLX08	0.57	0.51	0.19	0.80	0.20	0.036	10.59%
EL2	ENE	KLX10	0.37	0.39	0.14	0.67	0.20	0.019	3.69%
EL2	ENE	KLX15A	0.98	0.40	0.09	0.60	0.33	0.008	59.19%
EL2	ENE	KLX15A	0.98	0.50	0.20	0.73	0.07	0.042	48.99%
EL2	ENE	KLX18A	0.38	0.52	0.15	0.73	0.27	0.024	36.50%
EL2	N-S	KLX03	0.73	0.71	0.19	1.13	0.47	0.038	1.92%
EL2	N-S	KLX03	0.73	0.71	0.22	1.13	0.40	0.051	2.83%
EL2	N-S	KLX04	0.21	0.60	0.24	1.07	0.33	0.058	189.29%
EL2	N-S	KLX08	0.43	1.12	0.23	1.60	0.73	0.051	163.53%
EL2	N-S	KLX10	0.76	0.74	0.29	1.13	0.33	0.086	2.95%
EL2	N-S	KLX15A	0.82	1.23	0.31	1.80	0.73	0.098	50.11%
EL2	N-S	KLX15A	0.82	1.52	0.33	2.20	1.13	0.106	85.00%
EL2	N-S	KLX18A	0.53	0.69	0.22	1.00	0.33	0.049	28.75%
EL2	SH	KLX03	2.24	2.13	0.35	2.67	1.53	0.124	4.97%
EL2	SH	KLX03	2.24	2.21	0.42	2.67	1.47	0.175	1.39%
EL2	SH	KLX04	1.52	2.07	0.42	2.87	1.67	0.180	36.10%
EL2	SH	KLX08	0.90	2.03	0.25	2.40	1.73	0.063	125.93%
EL2	SH	KLX10	2.50	2.09	0.35	2.73	1.60	0.126	16.13%
EL2	SH	KLX15A	0.98	1.81	0.22	2.07	1.53	0.048	85.00%
EL2	SH	KLX15A	0.98	1.60	0.33	2.33	1.27	0.109	63.24%
EL2	SH	KLX18A	2.66	2.25	0.29	2.93	2.00	0.082	15.20%
EL2	WNW	KLX03	0.74	0.73	0.52	2.00	0.00	0.267	1.36%
EL2	WNW	KLX03	0.74	0.53	0.50	1.67	0.00	0.252	28.27%
EL2	WNW	KLX04	0.40	0.77	0.32	1.33	0.33	0.100	91.67%

Model Case	Fracture Set	Borehole IDCODE	P_{10} Observed	P_{10} Simulated Mean	Std. Dev.	Max.	Min.	Variance	% Error
EL2	WNW	KLX08	0.90	1.00	0.63	2.00	0.00	0.395	11.11%
EL2	WNW	KLX10	0.54	0.53	0.17	0.67	0.33	0.030	1.92%
EL2	WNW	KLX15A	1.63	0.60	0.34	1.00	0.00	0.119	63.20%
EL2	WNW	KLX15A	1.63	0.90	0.70	2.00	0.00	0.495	44.81%
EL2	WNW	KLX18A	0.73	0.83	0.79	2.33	0.00	0.623	13.64%
EL1	ENE	KLX03	0.38	0.38	0.10	0.53	0.20	0.010	0.30%
EL1	ENE	KLX03	0.38	0.41	0.10	0.60	0.27	0.010	6.69%
EL1	ENE	KLX04	0.48	0.49	0.19	0.93	0.27	0.038	2.46%
EL1	ENE	KLX08	0.57	0.50	0.12	0.73	0.33	0.015	11.76%
EL1	ENE	KLX10	0.37	0.40	0.17	0.67	0.20	0.028	7.26%
EL1	ENE	KLX15A	0.98	0.47	0.21	0.80	0.13	0.044	51.71%
EL1	ENE	KLX15A	0.98	0.42	0.13	0.60	0.13	0.017	57.15%
EL1	ENE	KLX18A	0.38	0.35	0.17	0.60	0.00	0.028	7.25%
EL1	N-S	KLX03	0.73	0.85	0.14	1.07	0.67	0.019	16.42%
EL1	N-S	KLX03	0.73	0.85	0.27	1.20	0.40	0.071	16.42%
EL1	N-S	KLX04	0.21	0.64	0.16	0.93	0.47	0.026	208.57%
EL1	N-S	KLX08	0.43	1.05	0.28	1.47	0.73	0.077	147.84%
EL1	N-S	KLX10	0.76	0.77	0.16	1.13	0.60	0.026	0.55%
EL1	N-S	KLX15A	0.82	1.45	0.33	2.20	1.00	0.108	76.07%
EL1	N-S	KLX15A	0.82	1.39	0.21	1.73	1.13	0.044	68.77%
EL1	N-S	KLX18A	0.53	0.77	0.16	1.00	0.60	0.025	43.75%
EL1	SH	KLX03	2.24	2.06	0.48	2.93	1.13	0.233	7.95%
EL1	SH	KLX03	2.24	2.45	0.41	3.33	2.00	0.165	9.33%
EL1	SH	KLX04	1.52	2.36	0.44	3.07	1.67	0.195	55.41%
EL1	SH	KLX08	0.90	1.95	0.25	2.60	1.60	0.065	116.30%
EL1	SH	KLX10	2.50	2.45	0.27	2.80	2.07	0.075	1.97%
EL1	SH	KLX15A	0.98	1.77	0.44	2.33	1.00	0.192	80.92%
EL1	SH	KLX15A	0.98	1.95	0.29	2.27	1.33	0.083	98.60%
EL1	SH	KLX18A	2.66	2.28	0.45	3.00	1.80	0.198	14.19%
EL1	WNW	KLX03	0.74	0.74	0.29	1.20	0.27	0.083	0.47%
EL1	WNW	KLX03	0.74	0.85	0.30	1.40	0.67	0.091	14.78%
EL1	WNW	KLX04	0.40	0.71	0.15	0.93	0.40	0.024	78.33%
EL1	WNW	KLX08	0.90	1.11	0.16	1.33	0.80	0.027	22.96%
EL1	WNW	KLX10	0.54	0.83	0.16	1.13	0.67	0.025	53.26%
EL1	WNW	KLX15A	1.63	1.09	0.26	1.73	0.80	0.069	32.95%
EL1	WNW	KLX15A	1.63	1.05	0.23	1.40	0.67	0.053	35.81%
EL1	WNW	KLX18A	0.73	0.77	0.15	1.00	0.53	0.023	4.55%
BMU	ENE	KLX03	0.38	0.49	0.11	0.73	0.33	0.013	27.68%
BMU	ENE	KLX03	0.38	0.45	0.10	0.60	0.27	0.010	17.19%
BMU	ENE	KLX04	0.48	0.47	0.19	0.93	0.33	0.035	3.08%
BMU	ENE	KLX08	0.57	0.49	0.11	0.67	0.33	0.012	12.94%
BMU	ENE	KLX10	0.37	0.41	0.11	0.60	0.27	0.012	9.05%
BMU	ENE	KLX15A	0.98	0.41	0.15	0.67	0.20	0.022	57.83%
BMU	ENE	KLX15A	0.98	0.37	0.14	0.60	0.13	0.021	62.59%
BMU	ENE	KLX18A	0.38	0.55	0.12	0.73	0.33	0.014	45.25%
BMU	N-S	KLX03	0.73	0.81	0.18	1.07	0.53	0.034	10.92%
BMU	N-S	KLX03	0.73	0.80	0.21	1.20	0.53	0.042	10.00%
BMU	N-S	KLX04	0.21	0.59	0.15	0.80	0.33	0.023	182.86%
BMU	N-S	KLX08	0.43	1.23	0.31	1.87	0.87	0.096	188.63%
BMU	N-S	KLX10	0.76	0.57	0.16	0.93	0.40	0.026	25.68%
BMU	N-S	KLX15A	0.82	1.53	0.16	1.73	1.20	0.025	86.62%
BMU	N-S	KLX15A	0.82	1.23	0.23	1.60	0.93	0.052	50.11%
BMU	N-S	KLX18A	0.53	0.59	0.14	0.73	0.27	0.021	10.00%
BMU	SH	KLX03	2.24	2.36	0.53	3.00	1.47	0.279	5.46%
BMU	SH	KLX03	2.24	2.15	0.32	2.73	1.73	0.102	4.08%
BMU	SH	KLX04	1.52	2.16	0.35	2.60	1.60	0.122	42.24%
BMU	SH	KLX08	0.90	2.01	0.41	2.67	1.40	0.170	122.96%
BMU	SH	KLX10	2.50	2.25	0.50	3.20	1.53	0.255	9.72%
BMU	SH	KLX15A	0.98	1.84	0.26	2.27	1.40	0.067	87.72%
BMU	SH	KLX15A	0.98	1.70	0.40	2.60	1.20	0.156	73.44%
BMU	SH	KLX18A	2.66	2.35	0.23	2.80	2.00	0.052	11.68%

Model Case	Fracture Set	Borehole IDCODE	P_{10} Observed	P_{10} Simulated Mean	Std. Dev.	Max.	Min.	Variance	% Error
BMU	WNW	KLX03	0.74	0.75	0.33	1.47	0.40	0.111	0.43%
BMU	WNW	KLX03	0.74	0.83	0.27	1.20	0.40	0.070	11.19%
BMU	WNW	KLX04	0.40	0.81	0.50	1.47	0.13	0.247	103.33%
BMU	WNW	KLX08	0.90	0.97	0.43	1.60	0.27	0.186	8.15%
BMU	WNW	KLX10	0.54	0.68	0.26	1.07	0.40	0.069	25.06%
BMU	WNW	KLX15A	1.63	1.11	0.46	2.00	0.53	0.214	32.13%
BMU	WNW	KLX15A	1.63	0.97	0.36	1.73	0.40	0.131	40.31%
BMU	WNW	KLX18A	0.73	0.81	0.36	1.47	0.13	0.128	10.91%
EUL2	ENE	KLX03	0.38	0.23	0.18	0.53	0.00	0.032	40.53%
EUL2	ENE	KLX03	0.38	0.40	0.24	0.80	0.00	0.055	4.94%
EUL2	ENE	KLX04	0.48	0.43	0.24	0.80	0.13	0.058	11.38%
EUL2	ENE	KLX08	0.57	0.51	0.33	0.93	0.00	0.106	10.59%
EUL2	ENE	KLX10	0.37	0.40	0.23	0.80	0.00	0.051	7.26%
EUL2	ENE	KLX15A	0.98	0.52	0.21	0.93	0.27	0.045	46.95%
EUL2	ENE	KLX15A	0.98	0.48	0.28	0.93	0.00	0.080	51.03%
EUL2	ENE	KLX18A	0.38	0.57	0.25	1.07	0.27	0.063	50.50%
EUL2	N-S	KLX03	0.73	0.79	0.15	0.93	0.47	0.022	9.08%
EUL2	N-S	KLX03	0.73	0.81	0.25	1.27	0.40	0.060	11.83%
EUL2	N-S	KLX04	0.21	0.78	0.20	1.00	0.53	0.041	276.07%
EUL2	N-S	KLX08	0.43	1.06	0.16	1.27	0.73	0.026	149.41%
EUL2	N-S	KLX10	0.76	0.69	0.17	0.93	0.40	0.028	9.95%
EUL2	N-S	KLX15A	0.82	1.37	0.37	2.00	0.67	0.134	66.34%
EUL2	N-S	KLX15A	0.82	1.48	0.23	1.80	1.20	0.052	80.13%
EUL2	N-S	KLX18A	0.53	0.68	0.23	1.07	0.40	0.054	27.50%
EUL2	SH	KLX03	2.24	2.11	0.64	2.93	1.20	0.414	5.86%
EUL2	SH	KLX03	2.24	2.09	0.43	2.67	1.47	0.186	6.46%
EUL2	SH	KLX04	1.52	2.21	0.39	2.67	1.60	0.155	45.76%
EUL2	SH	KLX08	0.90	1.83	0.47	2.67	1.20	0.221	102.96%
EUL2	SH	KLX10	2.50	2.31	0.61	3.20	1.33	0.372	7.58%
EUL2	SH	KLX15A	0.98	1.56	0.65	2.93	0.80	0.419	59.15%
EUL2	SH	KLX15A	0.98	1.79	0.58	2.67	1.07	0.341	82.28%
EUL2	SH	KLX18A	2.66	2.24	0.55	2.93	1.47	0.303	15.70%
EUL2	WNW	KLX03	0.74	0.77	0.25	1.07	0.27	0.062	4.02%
EUL2	WNW	KLX03	0.74	0.77	0.33	1.33	0.27	0.110	4.02%
EUL2	WNW	KLX04	0.40	0.73	0.52	1.47	0.13	0.266	83.33%
EUL2	WNW	KLX08	0.90	0.91	0.34	1.33	0.27	0.118	0.74%
EUL2	WNW	KLX10	0.54	0.77	0.22	1.07	0.53	0.047	42.22%
EUL2	WNW	KLX15A	1.63	1.16	0.22	1.47	0.80	0.048	28.86%
EUL2	WNW	KLX15A	1.63	0.95	0.29	1.33	0.53	0.085	41.94%
EUL2	WNW	KLX18A	0.73	0.80	0.33	1.47	0.40	0.107	9.09%
EUL1	ENE	KLX03	0.38	0.47	0.12	0.67	0.33	0.014	24.18%
EUL1	ENE	KLX03	0.38	0.42	0.08	0.53	0.27	0.006	10.19%
EUL1	ENE	KLX04	0.48	0.47	0.19	0.87	0.20	0.037	1.69%
EUL1	ENE	KLX08	0.57	0.54	0.16	0.87	0.33	0.024	4.71%
EUL1	ENE	KLX10	0.37	0.37	0.11	0.60	0.27	0.013	0.11%
EUL1	ENE	KLX15A	0.98	0.37	0.15	0.60	0.20	0.024	61.91%
EUL1	ENE	KLX15A	0.98	0.39	0.15	0.60	0.13	0.022	60.55%
EUL1	ENE	KLX18A	0.38	0.55	0.12	0.67.	0.33	0.015	43.50%
EUL1	N-S	KLX03	0.73	1.00	0.21	1.20	0.60	0.042	37.50%
EUL1	N-S	KLX03	0.73	0.68	0.14	0.93	0.47	0.021	6.50%
EUL1	N-S	KLX04	0.21	0.66	0.19	1.00	0.40	0.037	218.21%
EUL1	N-S	KLX08	0.43	0.93	0.24	1.40	0.67	0.060	118.04%
EUL1	N-S	KLX10	0.76	0.74	0.16	1.07	0.53	0.026	2.95%
EUL1	N-S	KLX15A	0.82	1.41	0.46	2.07	0.80	0.209	71.21%
EUL1	N-S	KLX15A	0.82	1.41	0.30	1.80	0.80	0.089	71.21%
EUL1	N-S	KLX18A	0.53	0.74	0.27	1.27	0.47	0.071	38.75%
EUL1	SH	KLX03	2.24	2.32	0.41	3.13	1.60	0.169	3.67%
EUL1	SH	KLX03	2.24	2.32	0.54	3.20	1.73	0.294	3.67%
EUL1	SH	KLX04	1.52	2.26	0.58	3.13	1.07	0.338	48.83%
EUL1	SH	KLX08	0.90	2.05	0.40	2.60	1.47	0.157	128.15%
EUL1	SH	KLX10	2.50	2.27	0.37	2.93	1.73	0.133	9.18%

Model Case	Fracture Set	Borehole IDCODE	P_{10} Observed	P_{10} Simulated Mean	Std. Dev.	Max.	Min.	Variance	% Error
EUL1	SH	KLX15A	0.98	1.76	0.46	2.53	1.13	0.210	79.56%
EUL1	SH	KLX15A	0.98	1.69	0.26	2.07	1.20	0.068	72.08%
EUL1	SH	KLX18A	2.66	2.28	0.22	2.60	1.87	0.049	14.19%
EUL1	WNW	KLX03	0.74	0.77	0.39	1.47	0.13	0.149	4.02%
EUL1	WNW	KLX03	0.74	0.81	0.35	1.60	0.40	0.120	9.40%
EUL1	WNW	KLX04	0.40	0.77	0.25	1.20	0.40	0.062	93.33%
EUL1	WNW	KLX08	0.90	0.75	0.35	1.33	0.13	0.119	17.04%
EUL1	WNW	KLX10	0.54	0.61	0.23	0.93	0.27	0.052	12.80%
EUL1	WNW	KLX15A	1.63	1.17	0.43	1.87	0.53	0.181	28.04%
EUL1	WNW	KLX15A	1.63	0.99	0.50	1.73	0.27	0.250	39.49%
EUL1	WNW	KLX18A	0.73	0.81	0.29	1.47	0.53	0.085	10.91%

Table 5-24. Verification Case SI-4 results, alternative models presuming fractal scaling.

Model Case	Fracture Set	Borehole IDCODE	P_{10} Observed	P_{10} Simulated Mean	Std. Dev.	Max.	Min.	Variance	% Error
BMF	ENE	KLX03	0.38	0.53	0.18	0.73	0.27	0.031	38.17%
BMF	ENE	KLX03	0.38	0.54	0.13	0.80	0.40	0.017	41.67%
BMF	ENE	KLX04	0.48	0.45	0.15	0.67	0.20	0.023	5.85%
BMF	ENE	KLX08	0.57	0.50	0.20	0.80	0.20	0.041	11.76%
BMF	ENE	KLX10	0.37	0.50	0.14	0.67	0.20	0.021	34.08%
BMF	ENE	KLX15A	0.98	0.37	0.14	0.60	0.20	0.021	62.59%
BMF	ENE	KLX15A	0.98	0.47	0.16	0.80	0.27	0.025	51.71%
BMF	ENE	KLX18A	0.38	0.42	0.16	0.67	0.20	0.025	10.25%
BMF	N-S	KLX03	0.73	0.88	0.15	1.20	0.60	0.024	21.00%
BMF	N-S	KLX03	0.73	0.77	0.22	1.13	0.40	0.051	5.42%
BMF	N-S	KLX04	0.21	0.71	0.20	1.07	0.40	0.042	240.71%
BMF	N-S	KLX08	0.43	1.12	0.24	1.47	0.73	0.057	163.53%
BMF	N-S	KLX10	0.76	0.75	0.18	1.00	0.47	0.034	1.20%
BMF	N-S	KLX15A	0.82	1.39	0.19	1.67	1.07	0.037	68.77%
BMF	N-S	KLX15A	0.82	1.48	0.21	1.87	1.20	0.046	80.13%
BMF	N-S	KLX18A	0.53	0.69	0.21	1.07	0.40	0.044	28.75%
BMF	SH	KLX03	2.24	2.29	0.51	3.20	1.47	0.263	2.18%
BMF	SH	KLX03	2.24	2.41	0.38	3.20	2.00	0.148	7.54%
BMF	SH	KLX04	1.52	2.38	0.53	3.27	1.53	0.284	56.73%
BMF	SH	KLX08	0.90	1.94	0.47	2.93	1.47	0.219	115.56%
BMF	SH	KLX10	2.50	2.29	0.25	2.80	2.07	0.060	8.11%
BMF	SH	KLX15A	0.98	1.83	0.60	2.87	1.13	0.358	87.04%
BMF	SH	KLX15A	0.98	1.96	0.36	2.53	1.47	0.133	99.96%
BMF	SH	KLX18A	2.66	2.42	0.34	3.13	2.07	0.119	8.92%
BMF	WNW	KLX03	0.74	0.80	0.53	1.67	0.00	0.277	7.60%
BMF	WNW	KLX03	0.74	0.40	0.31	0.67	0.00	0.094	46.20%
BMF	WNW	KLX04	0.40	0.97	0.55	2.00	0.33	0.307	141.67%
BMF	WNW	KLX08	0.90	1.30	0.74	2.67	0.33	0.554	44.44%
BMF	WNW	KLX10	0.54	0.63	0.33	1.00	0.00	0.110	16.48%
BMF	WNW	KLX15A	1.63	1.27	0.77	2.67	0.33	0.588	22.32%
BMF	WNW	KLX15A	1.63	0.90	0.55	2.00	0.00	0.298	44.81%
BMF	WNW	KLX18A	0.73	0.50	0.28	1.00	0.00	0.080	31.82%
FL2	ENE	KLX03	0.38	0.48	0.25	0.80	0.00	0.060	25.93%
FL2	ENE	KLX03	0.38	0.53	0.36	1.33	0.00	0.126	39.92%
FL2	ENE	KLX04	0.48	0.37	0.29	0.80	0.00	0.082	22.46%
FL2	ENE	KLX08	0.57	0.59	0.35	1.33	0.00	0.123	3.53%

FL2	ENE	KLX10	0.37	0.35	0.28	0.80	0.00	0.080	7.04%
FL2	ENE	KLX15A	0.98	0.40	0.29	0.80	0.00	0.083	59.19%
FL2	ENE	KLX15A	0.98	0.51	0.37	1.07	0.00	0.134	48.31%
FL2	ENE	KLX18A	0.38	0.40	0.29	1.07	0.00	0.083	5.00%
FL2	N-S	KLX03	0.73	0.75	0.31	1.40	0.33	0.097	2.67%
FL2	N-S	KLX03	0.73	0.62	0.16	1.00	0.47	0.026	14.75%
FL2	N-S	KLX04	0.21	0.59	0.21	0.93	0.27	0.044	182.86%
FL2	N-S	KLX08	0.43	0.91	0.22	1.20	0.67	0.049	114.90%
FL2	N-S	KLX10	0.76	0.57	0.16	0.80	0.20	0.026	24.81%
FL2	N-S	KLX15A	0.82	1.43	0.21	1.67	0.93	0.044	74.45%
FL2	N-S	KLX15A	0.82	1.42	0.31	2.00	0.87	0.094	72.83%
FL2	N-S	KLX18A	0.53	0.67	0.16	0.93	0.47	0.027	26.25%
FL2	SH	KLX03	2.24	1.73	0.85	3.73	0.53	0.731	22.55%
FL2	SH	KLX03	2.24	2.21	0.59	3.20	1.33	0.348	1.10%
FL2	SH	KLX04	1.52	1.89	0.70	3.47	1.07	0.497	24.68%
FL2	SH	KLX08	0.90	1.95	0.80	2.93	0.80	0.633	116.30%
FL2	SH	KLX10	2.50	2.29	0.79	3.47	1.33	0.619	8.11%
FL2	SH	KLX15A	0.98	1.60	0.74	2.67	0.27	0.553	63.24%
FL2	SH	KLX15A	0.98	1.44	0.49	2.13	0.53	0.240	46.91%
FL2	SH	KLX18A	2.66	2.19	0.93	3.47	0.27	0.866	17.71%
FL2	WNW	KLX03	0.74	0.93	1.00	3.33	0.00	1.007	25.54%
FL2	WNW	KLX03	0.74	0.73	0.49	1.33	0.00	0.242	1.36%
FL2	WNW	KLX04	0.40	0.53	0.69	2.00	0.00	0.474	33.33%
FL2	WNW	KLX08	0.90	1.07	1.05	2.67	0.00	1.106	18.52%
FL2	WNW	KLX10	0.54	0.87	0.95	2.67	0.00	0.894	59.39%
FL2	WNW	KLX15A	1.63	1.27	1.24	3.33	0.00	1.526	22.32%
FL2	WNW	KLX15A	1.63	0.93	0.72	2.00	0.00	0.514	42.76%
FL2	WNW	KLX18A	0.73	0.93	0.84	2.67	0.00	0.711	27.27%
FL1	ENE	KLX03	0.38	0.46	0.16	0.67	0.20	0.026	20.68%
FL1	ENE	KLX03	0.38	0.65	0.22	1.00	0.33	0.048	71.41%
FL1	ENE	KLX04	0.48	0.43	0.19	0.67	0.13	0.038	10.00%
FL1	ENE	KLX08	0.57	0.49	0.21	0.73	0.13	0.043	12.94%
FL1	ENE	KLX10	0.37	0.38	0.16	0.73	0.13	0.025	1.90%
FL1	ENE	KLX15A	0.98	0.37	0.10	0.47	0.20	0.010	62.59%
FL1	ENE	KLX15A	0.98	0.46	0.15	0.73	0.20	0.021	53.07%
FL1	ENE	KLX18A	0.38	0.51	0.22	0.80	0.07	0.049	34.75%
FL1	N-S	KLX03	0.73	0.87	0.25	1.33	0.53	0.060	19.17%
FL1	N-S	KLX03	0.73	0.73	0.29	1.20	0.33	0.085	0.83%
FL1	N-S	KLX04	0.21	0.81	0.29	1.47	0.53	0.087	292.14%
FL1	N-S	KLX08	0.43	1.01	0.18	1.33	0.67	0.032	136.86%
FL1	N-S	KLX10	0.76	0.55	0.12	0.80	0.40	0.016	28.31%
FL1	N-S	KLX15A	0.82	1.40	0.38	1.87	0.60	0.144	70.39%
FL1	N-S	KLX15A	0.82	1.52	0.24	1.93	1.07	0.056	85.00%
FL1	N-S	KLX18A	0.53	0.60	0.17	0.80	0.33	0.030	12.50%
FL1	SH	KLX03	2.24	2.06	0.25	2.47	1.60	0.061	7.95%
FL1	SH	KLX03	2.24	2.44	0.45	3.27	1.93	0.200	9.03%
FL1	SH	KLX04	1.52	2.17	0.47	3.00	1.47	0.217	42.68%
FL1	SH	KLX08	0.90	2.04	0.39	2.73	1.53	0.155	126.67%
FL1	SH	KLX10	2.50	2.23	0.34	3.00	1.93	0.116	10.78%
FL1	SH	KLX15A	0.98	1.61	0.21	1.93	1.27	0.045	64.60%
FL1	SH	KLX15A	0.98	1.65	0.40	2.47	1.00	0.160	68.68%
FL1	SH	KLX18A	2.66	2.13	0.26	2.53	1.73	0.067	19.71%
FL1	WNW	KLX03	0.74	0.75	0.19	1.07	0.47	0.036	1.33%

FL1	WNW	KLX03	0.74	0.72	0.25	1.13	0.40	0.063	3.16%
FL1	WNW	KLX04	0.40	0.76	0.16	1.07	0.60	0.026	90.00%
FL1	WNW	KLX08	0.90	0.96	0.27	1.53	0.60	0.073	6.67%
FL1	WNW	KLX10	0.54	0.73	0.30	1.40	0.40	0.092	34.87%
FL1	WNW	KLX15A	1.63	1.12	0.19	1.47	0.87	0.035	31.31%
FL1	WNW	KLX15A	1.63	1.05	0.17	1.33	0.80	0.027	35.40%
FL1	WNW	KLX18A	0.73	0.71	0.22	1.00	0.40	0.046	2.73%
BMUF	ENE	KLX03	0.38	0.41	0.12	0.67	0.27	0.015	6.69%
BMUF	ENE	KLX03	0.38	0.43	0.13	0.60	0.27	0.016	13.69%
BMUF	ENE	KLX04	0.48	0.53	0.20	0.93	0.20	0.040	10.77%
BMUF	ENE	KLX08	0.57	0.52	0.20	0.87	0.20	0.039	8.24%
BMUF	ENE	KLX10	0.37	0.43	0.13	0.60	0.13	0.016	14.41%
BMUF	ENE	KLX15A	0.98	0.40	0.16	0.73	0.20	0.025	59.19%
BMUF	ENE	KLX15A	0.98	0.35	0.17	0.60	0.13	0.028	63.95%
BMUF	ENE	KLX18A	0.38	0.48	0.23	0.87	0.20	0.051	26.00%
BMUF	N-S	KLX03	0.73	0.81	0.28	1.40	0.47	0.077	10.92%
BMUF	N-S	KLX03	0.73	0.83	0.17	1.13	0.60	0.029	14.58%
BMUF	N-S	KLX04	0.21	0.81	0.27	1.40	0.47	0.072	292.14%
BMUF	N-S	KLX08	0.43	0.96	0.23	1.33	0.60	0.052	125.88%
BMUF	N-S	KLX10	0.76	0.59	0.16	0.87	0.40	0.024	23.06%
BMUF	N-S	KLX15A	0.82	1.35	0.36	1.93	0.87	0.126	64.71%
BMUF	N-S	KLX15A	0.82	1.50	0.29	2.07	1.07	0.083	82.57%
BMUF	N-S	KLX18A	0.53	0.79	0.16	1.13	0.53	0.027	48.75%
BMUF	SH	KLX03	2.24	2.42	0.32	2.87	1.93	0.100	8.14%
BMUF	SH	KLX03	2.24	2.21	0.50	3.07	1.67	0.254	1.39%
BMUF	SH	KLX04	1.52	2.22	0.27	2.80	1.87	0.074	46.20%
BMUF	SH	KLX08	0.90	1.78	0.31	2.20	1.20	0.099	97.78%
BMUF	SH	KLX10	2.50	2.51	0.51	3.73	2.00	0.264	0.43%
BMUF	SH	KLX15A	0.98	1.65	0.32	2.20	1.07	0.104	68.68%
BMUF	SH	KLX15A	0.98	1.78	0.38	2.47	1.40	0.142	81.60%
BMUF	SH	KLX18A	2.66	2.37	0.36	2.93	1.80	0.131	10.93%
BMUF	WNW	KLX03	0.74	0.69	0.42	1.33	0.27	0.173	6.74%
BMUF	WNW	KLX03	0.74	0.89	0.17	1.33	0.80	0.028	20.16%
BMUF	WNW	KLX04	0.40	0.79	0.28	1.20	0.40	0.077	96.67%
BMUF	WNW	KLX08	0.90	0.85	0.38	1.60	0.27	0.147	5.19%
BMUF	WNW	KLX10	0.54	0.57	0.20	0.93	0.27	0.040	5.44%
BMUF	WNW	KLX15A	1.63	0.96	0.29	1.47	0.53	0.086	41.13%
BMUF	WNW	KLX15A	1.63	0.99	0.48	1.73	0.27	0.226	39.49%
BMUF	WNW	KLX18A	0.73	0.77	0.33	1.33	0.40	0.106	5.45%
FUL2	ENE	KLX03	0.38	0.45	0.40	1.07	0.00	0.159	18.94%
FUL2	ENE	KLX03	0.38	0.45	0.31	1.07	0.00	0.096	18.94%
FUL2	ENE	KLX04	0.48	0.51	0.29	1.07	0.00	0.086	5.23%
FUL2	ENE	KLX08	0.57	0.67	0.40	1.07	0.00	0.162	17.65%
FUL2	ENE	KLX10	0.37	0.40	0.29	0.80	0.00	0.083	7.26%
FUL2	ENE	KLX15A	0.98	0.35	0.38	1.07	0.00	0.143	64.63%
FUL2	ENE	KLX15A	0.98	0.48	0.30	1.07	0.27	0.092	51.03%
FUL2	ENE	KLX18A	0.38	0.40	0.40	1.33	0.00	0.162	5.00%
FUL2	N-S	KLX03	0.73	0.71	0.35	1.40	0.33	0.120	2.83%
FUL2	N-S	KLX03	0.73	0.70	0.27	1.20	0.33	0.070	3.75%
FUL2	N-S	KLX04	0.21	0.77	0.14	0.93	0.53	0.020	269.64%
FUL2	N-S	KLX08	0.43	1.26	0.14	1.47	1.07	0.019	196.47%
FUL2	N-S	KLX10	0.76	0.69	0.19	1.00	0.47	0.038	9.95%
FUL2	N-S	KLX15A	0.82	1.25	0.27	1.60	0.73	0.072	52.54%

FUL2	N-S	KLX15A	0.82	1.41	0.26	1.80	1.07	0.070	72.02%
FUL2	N-S	KLX18A	0.53	0.57	0.22	0.93	0.27	0.050	6.25%
FUL2	SH	KLX03	2.24	2.29	0.47	2.93	1.33	0.224	2.48%
FUL2	SH	KLX03	2.24	2.16	0.66	3.20	1.07	0.434	3.48%
FUL2	SH	KLX04	1.52	2.03	0.70	2.93	1.07	0.493	33.46%
FUL2	SH	KLX08	0.90	1.92	1.00	4.00	0.53	0.992	113.33%
FUL2	SH	KLX10	2.50	2.37	0.77	3.20	1.33	0.592	4.91%
FUL2	SH	KLX15A	0.98	1.44	0.59	2.40	0.53	0.351	46.91%
FUL2	SH	KLX15A	0.98	1.76	0.54	2.40	1.07	0.288	79.56%
FUL2	SH	KLX18A	2.66	2.19	0.76	3.20	0.80	0.582	17.71%
FUL2	WNW	KLX03	0.74	0.40	0.47	1.33	0.00	0.217	46.20%
FUL2	WNW	KLX03	0.74	0.60	0.66	2.00	0.00	0.440	19.30%
FUL2	WNW	KLX04	0.40	0.93	0.72	2.00	0.00	0.514	133.33%
FUL2	WNW	KLX08	0.90	1.13	0.89	2.67	0.00	0.795	25.93%
FUL2	WNW	KLX10	0.54	1.07	0.72	2.00	0.00	0.514	96.17%
FUL2	WNW	KLX15A	1.63	0.53	0.53	1.33	0.00	0.277	67.29%
FUL2	WNW	KLX15A	1.63	1.20	1.12	3.33	0.00	1.264	26.41%
FUL2	WNW	KLX18A	0.73	0.47	0.55	1.33	0.00	0.301	36.36%
FUL1	ENE	KLX03	0.38	0.47	0.21	0.93	0.13	0.044	22.43%
FUL1	ENE	KLX03	0.38	0.41	0.18	0.73	0.20	0.033	6.69%
FUL1	ENE	KLX04	0.48	0.43	0.16	0.60	0.13	0.027	11.38%
FUL1	ENE	KLX08	0.57	0.42	0.20	0.73	0.13	0.039	25.88%
FUL1	ENE	KLX10	0.37	0.44	0.12	0.67	0.27	0.015	17.99%
FUL1	ENE	KLX15A	0.98	0.37	0.11	0.60	0.27	0.013	61.91%
FUL1	ENE	KLX15A	0.98	0.49	0.20	0.93	0.20	0.041	49.67%
FUL1	ENE	KLX18A	0.38	0.49	0.21	0.93	0.20	0.044	29.50%
FUL1	N-S	KLX03	0.73	0.73	0.20	1.13	0.47	0.040	0.83%
FUL1	N-S	KLX03	0.73	0.77	0.22	1.13	0.40	0.048	6.33%
FUL1	N-S	KLX04	0.21	0.64	0.16	0.80	0.40	0.025	208.57%
FUL1	N-S	KLX08	0.43	0.99	0.20	1.33	0.67	0.038	132.16%
FUL1	N-S	KLX10	0.76	0.71	0.34	1.47	0.20	0.114	6.45%
FUL1	N-S	KLX15A	0.82	1.33	0.32	2.07	0.93	0.100	61.47%
FUL1	N-S	KLX15A	0.82	1.38	0.32	1.80	0.93	0.104	67.96%
FUL1	N-S	KLX18A	0.53	0.76	0.28	1.27	0.47	0.078	42.50%
FUL1	SH	KLX03	2.24	2.51	0.35	3.13	2.07	0.123	12.01%
FUL1	SH	KLX03	2.24	2.50	0.58	3.53	1.53	0.331	11.71%
FUL1	SH	KLX04	1.52	2.39	0.24	2.67	2.07	0.056	57.17%
FUL1	SH	KLX08	0.90	2.03	0.35	2.73	1.53	0.124	125.19%
FUL1	SH	KLX10	2.50	2.23	0.30	2.67	1.80	0.088	10.52%
FUL1	SH	KLX15A	0.98	1.99	0.17	2.27	1.73	0.029	102.68%
FUL1	SH	KLX15A	0.98	1.87	0.30	2.33	1.27	0.092	91.12%
FUL1	SH	KLX18A	2.66	2.37	0.40	2.93	1.73	0.161	10.93%
FUL1	WNW	KLX03	0.74	0.83	0.19	1.13	0.53	0.038	12.09%
FUL1	WNW	KLX03	0.74	0.76	0.22	1.00	0.47	0.050	2.22%
FUL1	WNW	KLX04	0.40	0.77	0.26	1.27	0.40	0.065	93.33%
FUL1	WNW	KLX08	0.90	1.05	0.33	1.47	0.47	0.109	16.30%
FUL1	WNW	KLX10	0.54	0.72	0.27	1.07	0.27	0.073	32.41%
FUL1	WNW	KLX15A	1.63	0.97	0.21	1.20	0.67	0.044	40.72%
FUL1	WNW	KLX15A	1.63	1.12	0.27	1.47	0.67	0.073	31.31%
FUL1	WNW	KLX18A	0.73	0.66	0.19	0.87	0.40	0.035	10.00%

Table 5-25. Verification Case SI-4 results, Fixed-r_{min} alternative models presuming Euclidean scaling.

Model Case	Fracture Set	Borehole IDCODE	P_{10} Observed	P_{10} Simulated Mean	Std. Dev.	Max.	Min.	Variance	% Error
ESL1	ENE	KLX04	0.48	0.61	0.18	0.87	0.27	0.031	27.38%
ESL1	ENE	KLX08	0.57	0.49	0.18	0.73	0.20	0.033	12.94%
ESL1	ENE	KLX18A	0.38	0.53	0.15	0.73	0.27	0.023	38.25%
ESL1	N-S	KLX04	0.21	0.69	0.28	1.20	0.20	0.076	231.07%
ESL1	N-S	KLX08	0.43	1.06	0.18	1.33	0.73	0.033	149.41%
ESL1	N-S	KLX18A	0.53	0.64	0.14	0.87	0.40	0.019	20.00%
ESL1	SH	KLX04	1.52	2.42	0.31	2.73	1.87	0.096	59.37%
ESL1	SH	KLX08	0.90	1.93	0.20	2.20	1.60	0.041	114.81%
ESL1	SH	KLX18A	2.66	2.38	0.48	3.20	1.80	0.229	10.43%
ESL1	WNW	KLX04	0.40	0.78	0.27	1.27	0.40	0.073	95.00%
ESL1	WNW	KLX08	0.90	0.97	0.25	1.33	0.67	0.063	8.15%
ESL1	WNW	KLX18A	0.73	0.73	0.23	1.07	0.40	0.054	0.00%
ESL3	ENE	KLX04	0.48	0.34	0.09	0.47	0.20	0.007	29.38%
ESL3	ENE	KLX08	0.57	0.51	0.18	0.80	0.27	0.032	9.41%
ESL3	ENE	KLX18A	0.38	0.41	0.12	0.60	0.20	0.015	8.50%
ESL3	N-S	KLX04	0.21	0.67	0.19	1.07	0.47	0.038	221.43%
ESL3	N-S	KLX08	0.43	1.05	0.22	1.47	0.67	0.049	147.84%
ESL3	N-S	KLX18A	0.53	0.60	0.26	1.20	0.27	0.066	12.50%
ESL3	SH	KLX04	1.52	2.27	0.51	2.93	1.47	0.264	49.27%
ESL3	SH	KLX08	0.90	1.91	0.32	2.47	1.47	0.101	112.59%
ESL3	SH	KLX18A	2.66	2.32	0.54	3.07	1.27	0.290	12.69%
ESL3	WNW	KLX04	0.40	0.71	0.16	0.87	0.47	0.025	76.67%
ESL3	WNW	KLX08	0.90	1.03	0.32	1.47	0.53	0.101	14.81%
ESL3	WNW	KLX18A	0.73	0.69	0.18	1.07	0.47	0.031	5.45%
ESL2	ENE	KLX04	0.48	0.49	0.14	0.67	0.27	0.021	1.08%
ESL2	ENE	KLX08	0.57	0.45	0.21	0.87	0.13	0.044	20.00%
ESL2	ENE	KLX18A	0.38	0.49	0.12	0.73	0.27	0.015	29.50%
ESL2	N-S	KLX04	0.21	0.59	0.20	1.00	0.27	0.041	186.07%
ESL2	N-S	KLX08	0.43	0.85	0.41	1.60	0.40	0.172	99.22%
ESL2	N-S	KLX18A	0.53	0.64	0.22	1.13	0.40	0.048	20.00%
ESL2	SH	KLX04	1.52	2.11	0.34	2.53	1.53	0.115	39.17%
ESL2	SH	KLX08	0.90	2.03	0.43	2.73	1.47	0.182	125.19%
ESL2	SH	KLX18A	2.66	2.15	0.25	2.67	1.87	0.063	18.96%
ESL2	WNW	KLX04	0.40	0.87	0.20	1.07	0.33	0.040	116.67%
ESL2	WNW	KLX08	0.90	1.06	0.30	1.67	0.67	0.090	17.78%
ESL2	WNW	KLX18A	0.73	0.65	0.12	0.80	0.40	0.015	11.82%

Table 5-26. Verification Case SI-4 results, Fixed-r_{min} alternative models presuming fractal scaling.

Model Case	Fracture Set	Borehole IDCODE	P_{10} Observed	P_{10} Simulated Mean	Std. Dev.	Max.	Min.	Variance	% Error
FSL1	ENE	KLX04	0.48	0.59	0.21	0.93	0.20	0.046	23.23%
FSL1	ENE	KLX08	0.57	0.46	0.17	0.73	0.20	0.029	18.82%
FSL1	ENE	KLX18A	0.38	0.53	0.17	0.80	0.27	0.029	38.25%
FSL1	N-S	KLX04	0.21	0.75	0.26	1.13	0.33	0.066	260.00%
FSL1	N-S	KLX08	0.43	1.07	0.30	1.53	0.73	0.093	150.98%
FSL1	N-S	KLX18A	0.53	0.63	0.11	0.87	0.47	0.012	17.50%
FSL1	SH	KLX04	1.52	2.34	0.29	2.93	2.00	0.085	54.10%
FSL1	SH	KLX08	0.90	1.92	0.39	2.47	1.33	0.151	113.33%
FSL1	SH	KLX18A	2.66	2.27	0.32	2.87	1.73	0.102	14.70%
FSL1	WNW	KLX04	0.40	0.76	0.15	0.93	0.53	0.022	90.00%
FSL1	WNW	KLX08	0.90	0.92	0.26	1.47	0.47	0.068	2.22%
FSL1	WNW	KLX18A	0.73	0.85	0.14	1.07	0.60	0.019	15.45%
FSL3	ENE	KLX04	0.48	0.39	0.21	0.87	0.13	0.045	18.31%
FSL3	ENE	KLX08	0.57	0.41	0.12	0.60	0.27	0.014	27.06%
FSL3	ENE	KLX18A	0.38	0.47	0.18	0.80	0.27	0.032	22.50%
FSL3	N-S	KLX04	0.21	0.73	0.21	1.13	0.53	0.043	253.57%
FSL3	N-S	KLX08	0.43	1.05	0.22	1.40	0.67	0.049	147.84%
FSL3	N-S	KLX18A	0.53	0.68	0.21	0.93	0.20	0.042	27.50%
FSL3	SH	KLX04	1.52	2.27	0.27	2.60	1.80	0.072	49.71%
FSL3	SH	KLX08	0.90	1.97	0.47	2.80	1.13	0.221	118.52%
FSL3	SH	KLX18A	2.66	2.41	0.43	3.20	1.73	0.182	9.18%
FSL3	WNW	KLX04	0.40	0.83	0.27	1.27	0.40	0.071	108.33%
FSL3	WNW	KLX08	0.90	1.01	0.20	1.33	0.73	0.038	12.59%
FSL3	WNW	KLX18A	0.73	0.75	0.26	1.20	0.40	0.070	1.82%
FSL2	ENE	KLX04	0.48	0.37	0.14	0.53	0.13	0.020	23.85%
FSL2	ENE	KLX08	0.57	0.49	0.15	0.73	0.27	0.023	14.12%
FSL2	ENE	KLX18A	0.38	0.44	0.20	0.87	0.13	0.039	15.50%
FSL2	N-S	KLX04	0.21	0.71	0.13	0.93	0.53	0.017	243.93%
FSL2	N-S	KLX08	0.43	1.05	0.27	1.60	0.73	0.071	147.84%
FSL2	N-S	KLX18A	0.53	0.72	0.19	1.07	0.47	0.034	35.00%
FSL2	SH	KLX04	1.52	2.36	0.50	3.13	1.67	0.245	55.41%
FSL2	SH	KLX08	0.90	2.03	0.29	2.47	1.60	0.085	125.19%
FSL2	SH	KLX18A	2.66	2.24	0.37	2.80	1.67	0.136	15.70%
FSL2	WNW	KLX04	0.40	0.85	0.28	1.47	0.53	0.079	113.33%
FSL2	WNW	KLX08	0.90	1.10	0.34	1.60	0.53	0.114	22.22%
FSL2	WNW	KLX18A	0.73	0.76	0.29	1.33	0.47	0.084	3.64%

5.7 Verification SI-5: Spatial distribution of fracture intensity as a Gamma or Weibull distribution

During the initial model construction, only the Gamma distribution was fit to binned fracture P_{32} data as a method of accommodating spatial variability in DFN models. However, during the revisions process, additional modelling work also suggested that the Weibull distribution could also be an acceptable model for P_{32} variability. In addition, it was desired to test both distributions at a middle scale (9 m) and at larger scales (21 m, 30 m, 50 m). Therefore, SI-5 as a verification case was born.

However, SI-5 is not a true verification case, but an expansion of the original hypothesis testing. As such, its results have been included in the report section documenting the modelling of the spatial distribution of fracturing (Section 4.4). Specifically, the results of the additional Gamma and Weibull distribution fits are presented in Section 4.4.7.

5.8 Ranking of alternative models based on performance in verification cases

Some aspects of the verification cases made it impossible to develop a single ranking model and that includes all verification cases. Verification Case SI-1 consisted of two sub-cases. In Case SI-1a, the measured fracture traces in outcrop longer than 0.5 m were compared to the model predictions. In Case SI-1b, the fracture traces inside the match range (Section 5.3) were compared to predictions from each of the alternative models inside the same match range. The difficulty with Case SI-1b is that outcrop fracture data did not exist for all possible fracture domains (there are only detail-mapped outcrops in three of the six fracture domains exposed at the surface in Laxemar), and thus the fracture domain-specific alternative models could not all be tested for verification Case SI-1b. Moreover, it is questionable whether it is meaningful to compare traces in outcrop outside the match range in a verification, as, by definition, it is already known that outside the range the model departs from the observed data. If all alternative models, including the fracture domain-specific ones are to be tested and ranked, then only verification Cases SI-1a, SI-2 and SI-3 can be included. Likewise, the reduced significance of comparing outcrop trace matches outside of the match range suggests that it may be more meaningful to exclude SI-1a from the rankings and compare the results with a ranking case that includes SI-1a.

The end result is that for the SDM-Site Laxemar geological DFN model, there are two Ranking Cases carried through the verification analysis and alternative model performance ranking:

1. Ranking Case I consists of all alternative models, including the domain-specific ones, but only includes verification cases SI-1a, SI-2 and SI-3.
2. Case II consists of all non-domain-specific alternative models for all possible verification cases (SI-1a, SI-1b, SI-2, SI-3 and SI-4).
3. Case III is the same, except that the comparison of fractures greater than 0.5 m, which is outside the match ranges, is not included. Case III consists of verification cases SI-1b, SI-2, SI-3 and SI-4.

One final consideration concerns verification Case SI-2. Case SI-2 compares the fracture intensity (P_{10}) of simulated scanline data on outcrops to measured data. The mean value of P_{10} calculated for a scanline on an outcrop has much greater uncertainty than the P_{10} calculated from borehole data due to several factors, including significantly less data (scanlines at Laxemar mapped between 10–20 fractures per scanline, as opposed to several hundred to several thousand fractures in the typical cored borehole record) and unfavourable alignments between fracture trace azimuths and the orientation of the scanline.

This leads to the final ranking Case IV:

4. Case IV is identical to Case III except that verification Case SI-2 is not included.

Of all the possible ranking cases, Case III is felt to be the most comprehensive and accurate, and is thus preferred over the others. Together with ranking Case I, which is the only case that includes all domain-specific models, these two ranking cases are best for assessing the performance of the alternative size-intensity models at predicting the field observations chosen for verification.

The rankings for the alternative models and verification cases for ranking Case I are shown in Table 5-27. The ANOVA results are presented in Table 5-28.

For all of the FSM-specific verifications cases, alternative model BMU is the highest ranked overall for the three verification cases considered. This is the original "Base Model" using unlinked, rather than linked traces. It is the top ranked model for verification case SI-1a, and the second-best ranked case for SI-2 and SI-3. Other alternative models that are the highest ranked in an individual verification case have much poorer rankings in the two other verification cases. Using ranking method I, the BMU model is the highest ranked and the most consistently highly ranked of all models.

The Kruskal-Wallis ANOVA analysis of these models shows which ones are statistically similar in pairwise comparisons (Table 5-28). The results in this table show that the unlinked Base model (BMU) differs significantly in its ranking results in ranking Case I from all of the other models except BMUF, FL2 and FUL1. It should be noted that the power for the test for all ranking cases is fairly low due to the small number of samples, and therefore any conclusion to not reject the null hypothesis may be due to lack of statistical power as well as to lack of ranking differences. Alternatively, the rejection of the null hypothesis, which predominates the results, is not due to low power, and thus the ANOVA results strongly indicate that BMU is significantly better than most alternative models.

The results for ranking Cases II–IV, which do not include the domain-specific fracture models, are shown in Table 5-29. The corresponding pairwise comparisons are shown in (Table 5-30). The results show that for ranking Cases II and III, the unlinked Base Model (BMU) is the highest ranked model overall. It is the third highest ranked model for ranking Case IV. When the verification case for SI-1 in which all traces greater than 0.5 m are included is deleted from the rankings, (Ranking Case III), the Base Model is ranked third overall. For all three ranking cases, the pairwise ANOVA results show that there is no statistically-significant difference at the 0.05 probability level between the unlinked Base Model performance and the performance of the other models considered, with the exception of the BMF and EL1 models in ranking Case II and the EL1 model in ranking Case III.

Considering all three of these ranking cases, alternative model BMU has the most consistently low rank values. This implies that the BMU is the best overall model for predicting the verification cases, regardless of the ranking system used. It is also the top-ranked model in the preferred ranking case, Case III. Nonetheless, the BM is also adequate as the rankings performance does not differ significantly from the BMU, especially for Cases III and IV, which do not include the SI-1 case with traces > 0.5 m. Even considering the lack of power, the similarity in rankings between BM and BMU for Ranking Cases III and IV indicates very little real difference between the two models.

Overall, the ranking results and the ANOVA analyses clearly show that the unlinked Base Model (BMU) is the best model in terms of predicting the verification cases, whether it is compared with domain-specific models or not.

Table 5-27. Ranking of alternative models for ranking case I.

Model	SI-1a	SI-2	SI-3	Sum of Ranks	Rank of Sum
BM	28	25	3	56	22
BMF	11	26	10	47	13
BMU	1	2	2	5	1
BMUF	2	10	11	23	4
EL1	8	30	7	45	11
EL2	5	4	15	24	5
ESL1_N	17	5	5	27	6
ESL1_NE005	20	8	19	47	13
ESL1_W	22	17	15	54	18.5
ESL2_N	29.5	11.5	13	54	18.5
ESL2_NE005	14	11.5	25	50.5	17
ESL2_W	24	23	24	71	28
ESL3_N	26	22	27	75	30
ESL3_NE005	13	15	29	57	23.5
ESL3_W	19	21	30	70	27
EUL1	10	28	17	55	20.5
EUL2	3	7	22	32	7
FL1	9	29	9	47	13
FL2	4	1	12	17	2.5
FSL1_N	27	9	4	40	10
FSL1_NE005	12	6	18	36	9
FSL1_W	18	16	14	48	15
FSL2_N	29.5	14	20	63.5	26
FSL2_NE005	16	13	28	57	23.5
FSL2_W	23	24	26	73	29
FSL3_N	25	18	6	49	16
FSL3_NE005	15	20	20	55	20.5
FSL3_W	21	19	23	63	25
FUL1	7	27	1	35	8
FUL2	6	3	8	17	2.5

Table 5-28. Kruskal-Wallis ANOVA results for Ranking Case I.

Model Comparison	K Statistic	Probability
BMU vs. BM	3.97	0.05
BMU vs. BMF	3.97	0.05
BMU vs. BMUF	2.63	0.10
BMU vs. EL1	3.97	0.05
BMU vs. EL2	3.97	0.05
BMU vs. ESL1_N	4.09	0.04
BMU vs. ESL1_NE005	3.97	0.05
BMU vs. ESL1_W	3.97	0.05
BMU vs. ESL2_N	3.97	0.05
BMU vs. ESL2_NE005	3.97	0.05
BMU vs. ESL2_W	4.09	0.04
BMU vs. ESL3_N	3.97	0.05
BMU vs. ESL3_NE005	3.97	0.05
BMU vs. ESL3_W	3.97	0.05
BMU vs. EUL1	3.97	0.05
BMU vs. EUL2	3.97	0.05
BMU vs. FL1	4.09	0.04
BMU vs. FL2	0.81	0.37
BMU vs. FSL1_N	3.97	0.05
BMU vs. FSL1_NE005	3.97	0.05
BMU vs. FSL1_W	3.97	0.05
BMU vs. FSL2_N	3.97	0.05
BMU vs. FSL2_NE005	3.97	0.05
BMU vs. FSL2_W	3.97	0.05
BMU vs. FSL3_N	3.97	0.05
BMU vs. FSL3_NE005	4.09	0.04
BMU vs. FSL3_W	3.97	0.05
BMU vs. FUL1	0.81	0.37
BMU vs. FUL2	3.97	0.05

Table 5-29. Ranking of alternative models for Ranking Cases II–IV.

Model	SI-1a (> 0.5 m)	SI-1b (match range)	SI-2	SI-3	SI-4	Ranking Case II	Ranking Case III	Ranking Case IV
BM	12	2	7	3	10	6	3	2
BMF	11	4	8	10	9	9	7.5	7.5
BMU	1	8	2	2	6	1	1	3
BMUF	2	7	6	11	5	4	6	7.5
EL1	8	9	12	7	12	11	11	10.5
EL2	5	5	4	15	8	7	9	10.5
EUL1	10	6	10	17	4	10	10	9
EUL2	3	12	5	22	7	12	12	12
FL1	9	1	11	9	1.5	5	4	1
FL2	4	3	1	12	3	2	2	4
FUL1	7	10	9	1	11	8	7.5	6
FUL2	6	11	3	8	1.5	3	5	5

Table 5-30. Kruskal-Wallis ANOVA results for Ranking Cases II–IV.

Model Comparison	Case II		Case III		Case IV	
	K Statistic	Probability	K Statistic	Probability	K Statistic	Probability
BMU vs. BM	1.89	0.17	0.35	0.55	0.00	1.00
BMU vs. BMF	4.42	0.04	2.58	0.11	1.19	0.28
BMU vs. BMUF	1.13	0.29	1.05	0.31	0.43	0.51
BMU vs. EL1	5.38	0.02	4.18	0.04	2.33	0.13
BMU vs. EL2	1.60	0.21	1.05	0.31	0.78	0.38
BMU vs. EUL1	3.60	0.06	1.73	0.19	0.20	0.66
BMU vs. EUL2	2.47	0.12	2.11	0.15	2.33	0.13
BMU vs. FL1	0.71	0.40	0.00	1.00	0.43	0.51
BMU vs. FL2	0.18	0.67	0.00	1.00	0.05	0.82
BMU vs. FUL1	2.16	0.14	1.35	0.25	0.43	0.51
BMU vs. FUL2	0.90	0.34	0.19	0.66	0.20	0.66

5.9 Validation of the geological DFN parameterisation

The validation of the SDM-Site Laxemar geological DFN parameterisation involved the comparison of predicted fracture intensities in borehole KLX27A (fracture domain FSM_W) to observed borehole data, using the top five ranked model alternatives from Section 5.8. The methodology and results of the validation are presented in Appendix G. The validation simulations indicated that all five of the top-ranked model alternatives did a good job of predicting total mean fracture intensities in domain FSM_W, but over-predicted fracture intensity in KLX27A. All five size-intensity model alternatives were able to correctly predict the number of MDZ-sized structures intersecting KLX27A.

6 Uncertainty

6.1 Identification of uncertainties in the geological DFN

There are several uncertainties in the SDM-Site Laxemar geological DFN model and its parameterization that downstream modellers need to be aware of. These uncertainties are categorized by their type as to whether they are related to the conceptual models, the mathematical implementation of the conceptual models, or in the data (parameter uncertainty).

The most significant uncertainties in the geological DFN model are related to the coupled size-intensity model parameterization. Uncertainties in the orientation model are fairly well-understood, and have been demonstrated in past SDM reports /Fox et al. 2007/ to have little effect on overall model stability and function. The primary impact of the uncertainties in the coupled size-intensity model is expected to be on the degree of utilisation available for the proposed repository.

The occurrence and spacing of fractures in the size range of the deposition tunnel diameter to the MDZ/DZ radius cut-off (564.2 m) controls the number and spacing of canister deposition holes. /Munier 2006, 2007a, 2007b/. The size range of approximately 2.7 m (which approximately corresponds to the deposition tunnel cross-sectional radius) and larger represent the minimum size for a fracture that would make a full-perimeter intersection (FPI) with a tunnel or shaft oriented normal to the plane of the fracture /Munier 2006a/.

A secondary (but still significant) impact is the intensity of fractures and minor deformation zones larger than 75 m in radius /Munier and Hökmark 2004, SKB 2006, Fälth et al. 2007, Fälth et al. 2008/. Features in this size range represents the component of fracturing that is of greatest interest for subsequent safety calculations, as they are large enough to host secondary slip, induced by nearby earthquakes, that might exceed the failure criterion of the canisters, yet are sufficiently small that they may be difficult to detect with 100% reliability during site reconnaissance and construction /Cosgrove et al. 2006/.

Due to the fact that there are two different size ranges of interest to downstream users of the geological DFN, the uncertainty analysis is carried through for both ranges. The P_{32} intensity values for the various fracture sets, fracture domains and alternative conceptual models are described in Section 4.3. The assessment of the actual impacts of the analysed uncertainties on rock mass mechanical stability, deformation during possible future earthquakes, or radionuclide transport is beyond the scope of this report.

6.1.1 Conceptual uncertainties

There are three main conceptual uncertainties in the SDM-Site Laxemar geologic DFN model. These are:

- Whether or not the fracture size model is independent of the fracture domain.
- Whether fracture intensity scales in a Euclidean manner or exhibits fractal characteristics.
- Whether a size model built atop linked or unlinked traces is a more appropriate description of the rock mass at Laxemar.

Size-Intensity dependence on fracture domain

For each fracture set, is the size model independent of the fracture domain? The uncertainty surrounding this question could be reduced significantly if there were several outcrops in each fracture domain. This would make it possible to calculate a size-intensity relation for each set in each domain that corresponds to the average trace length intensity (P_{21}). However, when there are only one or two outcrops in some domains, and none in others, there is no guarantee that the size-intensity relation derived from outcrop traces accurately portrays the mean trace length intensity, and comparisons among fracture domains could easily be dominated by the variability within a fracture domain as opposed to the variability between fracture domains.

The Base Model (Section 4.3.3, Table 4-14 and Table 4-15) assumes that the size-intensity relation for each fracture set does not depend on the fracture domain. Under this assumption, the slope of the size-intensity and the cumulative normalized number trace length plots (k_r, derived from k_t, see Section 3.4) is constant for each set regardless of fracture domain. The difference in the size-intensity model between fracture domains is in the minimum size (r_0), which is estimated from borehole P_{10}.

A conceptually different modelling assumption (Section 4.3.4, Table 4-34 through Table 4-41) is that the radius scaling exponent (k_r) does vary as a function of fracture domain. Since there are not outcrops available in every fracture domain, the radius scaling exponent is instead back-calculated using the borehole fracture intensity and a constant fixed minimum size (r_0). According to the borehole geologic mapping protocols (Method description for Boremap-Kartering, SKB MD 143.006, version 2.0, SKB internal controlling document), fractures smaller than the borehole radius should not have been recorded in the SICADA database. As such, the measured P_{10} in boreholes represents a minimum fixed size that is related to the borehole radius.

In this alternative conceptual model, the minimum fracture size is judged to be one that completely cuts through the drill core perpendicular to the core axis, and is just large enough to have a full-perimeter intersection. For the idealised case described above, the theoretical minimum size fracture observed has a radius equal to that of the cored boreholes (0.038 m, for the 76 mm diameter hole cut by the N-size core drill barrels used during site investigations). By fixing the minimum size and the associated intensity from the borehole on one end, and the fracture intensity of the ground magnetic lineaments smaller than 1,000 m in length (or any other threshold size for which the intensity is known with confidence) on the other, it is possible to analytically solve for the size-intensity scaling exponent (k_r).

This family of alternative model cases are termed 'r_0-fixed' models; similar approaches have been used by the HydroDFN team at the Forsmark site /Follin et al. 2007/ and in the Forsmark geological DFN /Fox et al. 2007/ for verification purposes. In the hydrogeological DFN models, these types of models are referred to as 'k_r-scaled' models. In terms of alternative size-intensity models, the models consists of cases ESL1, ESL2, ESL3, FSL1, FSL2, and FSL3.

Euclidean versus fractal scaling

The analyses of the mass dimension from both borehole (Section 4.4.1) and outcrop (Section 4.4.2) data suggest that a Euclidean scaling model best characterises the scaling of fracture intensity at scales greater than 10 m to 30 m and may even be the better model at smaller scales. However, the data do not conclusively rule out fractal scaling at larger scales. Fracture data from outcrops are limited to scales not much greater than 30 m. Also, though the cored boreholes offer data records longer than 30 m, they do not adequately test fracture intensity scaling in all directions. The mass dimension for subhorizontally-oriented fracture sets is particularly uncertain. A conceptual alternative to the Base Model, which assumes Euclidean scaling from the scale of the borehole radius to that of the regional lineament maps, is the Fractal scaling model, which hypothesizes that fracture intensity scales according to a fractal process (see Table 4-19 through Table 4-21).

Linked versus unlinked outcrop traces

Fractures may be reactivated due to such geological processes as burial or erosion, changes in the tectonics and associated stresses, or changing thermal or pore fluid conditions. In outcrop, evidence of brittle reactivation can appear as a series of trace segments with similar orientations that appear to define a larger-scale structure. The large faults or fault zones that are expressed as surface lineaments may also have evolved in a similar manner over geologic time. Since the coupled size-intensity models depend upon measurements of fracture trace length in outcrop, whether or not single traces are treated as individual fractures or are linked into larger-scale structures impacts on the reported trace length and affects the area-normalized cumulative trace number, which is used to develop the fracture radius scaling exponent (k_r). One of the problems in the field mapping of outcrop data is that at the outcrop surface, two traces may not be physically connected (i.e. at the surface they appear to be two different fractures), but at a short distance below the ground surface, the fractures representing the traces may anastamose into a single feature. In some cases, there is enough additional evidence to suggest that these traces are part of the same fracture, even though at the outcrop surface the traces appear unconnected.

The Base Model for the SDM-Site Laxemar geological DFN parameterization is founded upon the Linked trace model, in which some traces on the outcrop surfaces have been linked based on the linkage protocol described in Appendix A. The alternative conceptual model, hereafter labelled the Unlinked trace model (Table 4-27 through Table 4-33), is to assume that only traces linked on the outcrop surface are part of the same fracture. In the Unlinked trace model, if there are two traces that are not contiguous on the outcrop surface, regardless of how close their endpoints might be or any other factor, then they are treated as belonging to separate fractures. The Linked trace model will contain fewer traces in outcrop than the Unlinked trace model. Correspondingly, the Linked trace model may contain longer traces than the Unlinked trace model.

6.1.2 Parameter uncertainties

Size-Intensity scaling exponent

The most significant parameter uncertainty in the SDM-Site Laxemar geological DFN model is the fracture radius scaling exponent (k_r) for the size-intensity scaling calculations. In the Base Model, the exponent is based upon fitting a straight line to the area-normalized trace length scaling cumulative number plots constructed from outcrop and lineament trace data. For some sets, there are data from two or more outcrops, and even in the case of a single outcrop, the straight-line portion of the outcrop trace data may not perfectly align with the lineament trace data. In both these situations, it is possible to fit more than just a single line to the data.

The Base Model parameterises k_r as the slope with the best overall "average" fit to all outcrops. There are other slopes that could also have been fit to individual outcrops. In order to estimate the impact of this uncertainty, two bounding lines were also fit to the data, one to represent the "Upper" or largest value of k_r that could be fit to the data, and another to represent the "Lower" or smallest value of k_r. The Upper bound model typically produces the largest fracture intensity, while the Lower bound model typically produces the smallest fracture intensity. Upper and Lower bounds were calculated for the various Base Model derivatives and also for the Fractal and r_0-fixed models.

Open versus total number of fractures

The fracture intensity parameterization includes all fracture types: open, partially open and sealed. In order to assess the difference between using only open fracture intensity, which may relate more to conductive fracture intensity or mechanical weakness and deformation during future earthquakes, the size/intensity values for only open fractures was also calculated as an alternative model. This was carried out by using the open fracture intensity as measured in boreholes, instead of using the total fracture intensity measured in boreholes.

All versus some lineaments

In the SDM-Site Laxemar geological DFN modeling, the radius scaling exponent (k_r) is derived either by fitting a line to outcrop and lineament trace data (the 'k_r-fixed' models) in a complementary cumulative number plot (Figure 3-7, Section 3.4), or by specifying the minimum radius of the size-intensity distribution and back-calculating kr from the fracture intensity data at different scales (the 'r_0-fixed' models). The 'k_r-fixed' series of models, and in particular, the BMU model alternative (Section 4.3.4) are the models recommended to describe the fracturing at Laxemar.

The radius scaling exponent in the 'k_r-fixed' models is calculated using all available outcrop trace data as well as all available lineament data. Every lineament inside the fracture domain envelope (Figure 3-1) shorter than 1,000 m in length is used to parameterize the size-intensity model. However, work performed by other researchers has suggested that some of the lineaments within the model region may not directly correspond to fractures or minor deformation zones; instead, they may represent zones of local rock alteration, low-magnetic dykes, or minor ductile zones. /Olsson et al. 2006/.

Therefore, a limited uncertainty analysis was performed to determine what effect the use of less than 100% of the lineaments might have on the coupled size-intensity model. In theory, the use of fewer lineaments should increase the slope of the trace length scaling exponent (k_t), with a corresponding increase in the value of the radius scaling exponent (k_r). An increase in the radius scaling exponent will generally result in an increase in the percentage of smaller fractures, and a decrease in the percentage of larger fractures and minor deformation zones.

6.2 Impact of Uncertainties

6.2.1 Quantification

The impact of the uncertainties is quantified by comparing the fracture intensity predicted over the fracture radius ranges 75 m to 564.2 m and 2.7 m to 564.2 m (see Section 6.1 for rationale behind size ranges chosen). The Base Model, Unlinked (BMU) case consists of the intensity for all fracture types (open and sealed combined), unlinked outcrop traces, Euclidean scaling and the assumption that the size-intensity scaling is independent of fracture domain.

6.2.2 Size-intensity dependence on fracture domain

The calculation of the intensities for alternative size ranges (r_3,r_4) is based on the following equation:

$$P_{32}(r_3, r_4) = \left(\frac{r_3^{\,2-k_r} - r_4^{\,2-k_r}}{r_1^{\,2-k_r} - r_2^{\,2-k_r}} \right) P_{32}(r_1, r_2) \qquad \text{Equation 6-1}$$

Where r_1 are specified minimum and maximum radius values, and the $P_{32}(r_1,r_2)$ correspond to the fracture intensity in the corresponding size range. Note that the radius scaling exponent (k_r) must be greater than 2.0 for this equation to be valid; this is the case for all current Laxemar size-intensity model alternatives.

The BMU fracture intensity in the ranges 2.7 m to 564 m and 75 m to 564 m does not depend upon the fracture domain, since the minimum radius of 2.7 m is much greater than any of the minimum radii for the fracture domains calculated from the borehole data. Thus, it is possible to use any of the coupled size-intensity pairs for a specified set regardless of the fracture domain. For example, r_1 could be taken from column 4 in Table 4-25, and its counterpart intensity, $P_{32}(r_1, r_2)$ from column 7 for the set of interest. These values of intensity correspond from a minimum radius of r_1= 0.5 m to a maximum radius of r_2 = 564.2 m.

To calculate the intensity over the range 75 m to 564.2 m, r_3 is set to 75 m and r_4 is set to 564.2 m. Using the equation, it is then possible to calculate P_{32}(75 m, 564.2 m). This is the Base Model (Unlinked) intensity to which all other alternative models are compared. The procedure is the same for the 2.7 m to 564.2 m case, with 2.7 m being substituted for 75 m.

The next step is to calculate the intensity over the same size range for the alternative model. Table 4-34 reports the coupled size-intensity for the alternative models where k_r is domain-specific, assuming a minimum radius of 0.038 m, the average borehole radius, and a maximum radius of 564.2 m. The table also reports the scaling exponent and coupled intensity. For the alternative model, r_1 = 0.038 m, $r_2 = r_4$ = 564.2 m, r_3 = 75 m or 2.7 m, P_{32}(0.038, 564.2) comes from column 7 (depending on which variant model is chosen). This leads to values of fracture intensity in the size ranges 75 m to 564.2 m and 2.7 m to 564.2 m as a function of set and fracture domain.

Table 6-1 shows the results of these calculations. The BMU model intensity is given in column 3; the intensity values for the fracture domains using the 'r_0-fixed' alternative model are given in the next six columns. The last six columns present the ratio of the 'r_0-fixed' alternative model intensity to the Base Model Unlinked intensity.

For the ENE, NS and SH sets, the alternative model intensity is lower in the range 75 m to 564.2 m; it is higher for the WNW set in this size range. In the size range 2.7 m to 564.2 m, the intensity for the alternative model is lower for all sets but shows a similar relative pattern. For the size range 75 m to 564 m, the greatest reduction in intensity is in the subhorizontal set, which is about a uniform 15%–17% of the Base Model Unlinked (BMU) intensity. The N-S set shows a reduction across all domains of about 19%–23%, while the ENE set has an intensity equal to about 56% of the base case for most of the fracture domains. The WNW set shows a higher intensity, slightly greater than twice that for BMU There is little variation by fracture domain with the possible exception of FSM-W, which tends to have ratios that differ most from the other domains regardless of set.

There is a similar pattern in the results for the expanded size range. For the range 2.7 m to 564.2 m, all sets in the alternative model have lower intensity than the BMU. For the ENE, NS and SH sets, the reduction is in the range of 15%–30%. The intensity for the WNW is at a higher ratio, very close to the BMU intensity. The ratios in the domain FSM-W show the least consistency with the other domains.

Overall, the domain-specific 'r_0-fixed' alternative models predict fewer fractures for all sets and domains than the BMU with the exception of the WNW set in the size range 75 m to 564.2 m. This is consistent with the lower predicted intensity of the domain-specific models relative to the BMU in the verification cases.

6.2.3 Euclidean versus fractal scaling uncertainty

Table 6-3 and Table 6-4 show the comparison between the intensities for the BMU and for the alternative model (BMUF) when the intensity scales in a fractal as opposed to a Euclidean manner. For both size ranges, the ratio pattern is similar. The intensity of the fractal model is greater for the ENE, NS and WNW sets, and lower for the SH set. There is about a 25% difference in the 75 m to 564.2 m size range, and about a 50% difference in the 2.7 m to 564.2 m size range, with the exception of the SH set in this later size range.

6.2.4 Linked versus unlinked traces

Table 6-5 and Table 6-6 summarize the uncertainty related to the trace linkage method. The ratio between the intensity for the Base Model (BM) and the alternative unlinked model (BMU) varies by set. Intensities for the unlinked and linked models in the size range 75 m to 564.2 m are approximately the same for the ENE and SH sets, but are approximately 50% higher for the NS and WNW sets. In the expanded size range ($r_{min} \approx$ 2.7 m), P_{32} values for the ENE and SH sets are still quite similar, regardless of whether linked or unlinked traces are used. However, in the NS and WNW, fracture intensity can be up to 75% higher if linked traces are used.

Table 6-1. Ratio of P_{32} fracture intensity for alternative r_0-fixed model relative to alternative model case BMU for P_{32} values within the size range 75 m to 564.2 m. The BMU case represents the best-performing model alternative from the DFN model verification (Chapter 5).

Set	Fit Type	P_{32} Intensity – All Fractures							Ratio of Alternative to BMU					
		BMU 75 m to 564.2 m	FSM_C	FSM_EW007	FSM_N	FSM_NE005	FSM_S	FSM_W	FSM_C	FSM_EW007	FSM_N	FSM_NE005	FSM_S	FSM_W
ENE	Best	0.007	0.004	0.004	0.004	0.004	0.005	0.004	0.56	0.56	0.58	0.53	0.55	0.71
NS	Best	0.011	0.002	0.002	0.002	0.002	0.003	0.002	0.19	0.19	0.20	0.19	0.22	0.23
SH	Best	0.007	0.001	0.001	0.001	0.001	0.001	0.001	0.15	0.15	0.17	0.17	0.16	0.17
WNW	Best	0.003	0.007	0.008	0.008	0.007	0.009	0.007	2.28	2.28	2.37	2.32	2.24	2.79

Table 6-2. Ratio of P_{32} fracture intensity for alternative r_0-fixed model relative to alternative model case BMU for P_{32} values within the size range 2.7 m to 564.2 m. The BMU case represents the best-performing model alternative from the DFN model verification (Chapter 5).

Set	Fit Type	P_{32} Intensity – All Fractures							Ratio of Alternative to BMU					
		BMU 2.7 m to 564.2 m	FSM_C	FSM_EW007	FSM_N	FSM_NE005	FSM_S	FSM_W	FSM_C	FSM_EW007	FSM_N	FSM_NE005	FSM_S	FSM_W
ENE	Best	0.237	0.066	0.071	0.058	0.063	0.110	0.063	0.28	0.28	0.30	0.24	0.27	0.46
NS	Best	0.361	0.050	0.057	0.053	0.070	0.085	0.063	0.14	0.14	0.16	0.15	0.19	0.24
SH	Best	0.222	0.035	0.047	0.048	0.039	0.046	0.040	0.16	0.16	0.21	0.22	0.17	0.21
WNW	Best	0.104	0.108	0.117	0.112	0.104	0.166	0.094	1.04	1.04	1.13	1.08	1.01	1.60

Table 6-3. Ratio of P_{32} intensity for the Euclidean versus fractal scaling models for the size range 75 m to 564.2 m. Intensities are based on linked outcrop traces, all fracture types (open and sealed combined), scaling exponent independence of fracture domain, and the Best Fit model for the scaling exponent.

Set	Fit Type	P_{32}		Ratio Fractal to Euclidean
		BMU	Fractal (BMUF)	
ENE	Best	0.007	0.009	1.23
NS	Best	0.011	0.014	1.26
SH	Best	0.007	0.005	0.77
WNW	Best	0.003	0.004	1.35

Table 6-4. Ratio of P_{32} intensity for the Euclidean versus fractal scaling models for the size range 2.7 m to 564.2 m. Intensities are based on linked outcrop traces, all fracture types (open and sealed combined), scaling exponent independence of fracture domain, and the Best Fit model for the scaling exponent.

Set	Fit Type	P_{32}		Ratio Fractal to Euclidean
		BMU	Fractal (BMUF)	
ENE	Best	0.237	0.361	1.52
NS	Best	0.361	0.563	1.56
SH	Best	0.222	0.213	0.96
WNW	Best	0.104	0.174	1.67

Table 6-5. Ratio of P_{32} intensity for the linked (Base Model) and unlinked (BMU) trace reconstruction models for the size range 75 m to 564.2 m. Intensities are based on all fracture types (open and sealed combined), Euclidean scaling, scaling exponent independent of fracture domain, and Best Fit model for the scaling exponent.

Set	Fit Type	P_{32}		Ratio of Linked to Unlinked
		Linked	Unlinked	
ENE	Best	0.008	0.007	1.04
NS	Best	0.018	0.011	1.56
SH	Best	0.007	0.007	0.95
WNW	Best	0.005	0.003	1.45

Table 6-6. Ratio of P_{32} intensity for the linked (Base Model) and unlinked (BMU) trace reconstruction models for the size range 2.7 m to 564.2 m. Intensities are based on all fracture types (open and sealed combined), Euclidean scaling, scaling exponent independent of fracture domain, and Best Fit model for the scaling exponent.

Set	Fit Type	P_{32}		Ratio of Linked to Unlinked
		Linked	Unlinked	
ENE	Best	0.270	0.237	1.14
NS	Best	0.616	0.361	1.71
SH	Best	0.231	0.222	1.04
WNW	Best	0.164	0.104	1.58

6.2.5 Size-intensity scaling exponent

Table 6-7 shows the ratio in fracture intensities for the upper (EUL1) and lower (EUL2) bounding envelopes for the trace length scaling exponent in comparison to the best-performing model alternative (BMU). In all cases but the ENE set, the upper envelope leads to higher fracture intensities, while the lower bounding envelope leads to lower fracture intensities except for the WNW set. The magnitudes vary by set and envelope type. The greatest increase in intensity is for the WNW set, which is approximately three and a half times the intensity in the Best Fit model (BMU).

6.2.6 Open versus sealed fractures

The BMU and all of the other alternative models in the verification suite include all fractures, regardless of whether they are open or sealed, for deriving the set intensities. However, since the lineaments are likely to be "open" fractures, it is possible that the coupled size-intensity parameters for each set should be based on the open fractures only.

Under this assumption, the scaling exponent describing the size-intensity relation for open fractures would differ from that of sealed fractures, or the combination of sealed and open fractures. However, there is not sufficient outcrop data for open fractures to make an independent statistically robust calculation of the scaling exponent. If the scaling exponents are presumed to be the same, and the minimum size of fractures considered is greater than the minimum radius for the radius probability distribution, then the difference in intensity in the 75 m to 564.2 m and 2.7 m to 564.2 m size ranges will be in proportion to the differences in P_{32}.

Independent of fracture domain or outcrop, the fractures designated as open comprise 20% to 30% of all fractures measured in the boreholes outside of the deformation zones, and 5% to 20% of those in outcrop (Table 6-8 and Table 6-9).

These results imply that the open fracture intensities vary from about 5% to 30% of the total. The discrepancy between the outcrop results and the borehole results is contrary to what would be expected if surficial stress relief promoted a higher intensity of open fractures at the surface. Also, if sealed fractures constituted the smaller size fraction of the overall population, then the exclusion of all fractures with fracture traces less than 0.5 m in outcrop would tend to increase the ratio of open to total fracture intensity.

Table 6-7. Ratio of P_{32} intensity for the scaling exponent uncertainty. Intensities are based on all fracture types (open and sealed combined), Euclidean scaling, scaling exponent independent of fracture domain, and unlinked trace reconstruction model.

Ratios	Upper to Best	Lower to Best
ENE	0.96	0.39
NS	1.72	0.61
SH	1.49	0.35
WNW	3.50	1.51

Table 6-8. Percent of open fracture P_{21} as measured in outcrops.

Outcrop	Domain	Total Open Trace Length (m)	Total Trace Length for Open & Sealed (m)	% Open
ASM000208	FSM_N	99.05	1,327.42	7.5%
ASM000209	FSM_NE005	273.58	1,484.41	18.4%
ASM100234	FSM_N	148.29	1,808.07	8.2%
ASM100235	FSM_W	179.94	1,337.35	13.5%

Table 6-9. Percent of open fractures as measured in boreholes outside of deformation zones.

Set	Fit Type	FSM_C	FSM_EW007	FSM_N	FSM_NE005	FSM_S	FSM_W
ENE	Best	29%	31%	35%	27%	30%	23%
NS	Best	19%	27%	21%	18%	24%	22%
SH	Best	18%	26%	32%	30%	35%	27%
WNW	Best	30%	38%	31%	26%	26%	28%

6.2.7 Number of lineaments used in size-intensity model

Analysis methodology

1 Excel's random number generator (RANDBETWEEN function) is used to generate a number between one and one hundred for each lineament trace in the lineament database. For a given percentage (50%, 75%), if the random number was greater than the target percentage, the lineament was discarded from the uncertainty analysis. No weighting is assigned to the function; the decision of inclusion or exclusion is based solely on random chance and not on lineament confidence, length, set membership, or orientation. Since this is a stochastic selection process based on a finite sequence of random numbers, the actual percentage of traces may vary slightly from the specified number.

2 New area-normalized complementary cumulative number (CCN) plots were created utilizing the reduced lineament databases. The trace length scaling exponent was then re-calculated by visually adjusting the slope of the best-fit line to the new data. Where possible, the new slopes were fit to similar sections of the cumulative trace length data. The resulting cases are referred to in the accompanying tables and figures by the applicable percentage: k_r-75% and k_r-50%.

3 Once a new value of the trace length scaling exponent was calculated, it was necessary to re-calculate the fracture intensity needed to reproduce the outcrop traces (P_{32OC}). This was done through stochastic simulation. Simulations were performed within a 50 m × 50 m × 50 m volume centered on the outcrop of interest. The size distribution was truncated to lie between 0.5 m and 564.2 m to speed simulation time; traces shorter than 0.5 m do not exist in the Laxemar detailed outcrop mapping database, and are therefore not useful in the uncertainty calculation.

4 Once a new value of P_{32OC} was obtained, it was possible to re-calculate the minimum radius r_0 using Equation 3-15 and the ratio of intensities between boreholes and outcrops (P_{32OC}/P_{32BH}).

5 The result of steps 1-4 is a new size-intensity parameterization according to the BMU assumptions (Euclidean scaling, unlinked fracture traces, 'best-fit' trace length exponent) for a specific percentage of lineaments representing fracture traces.

6 The uncertainty due to the assumption that not all lineaments represent fractures is quantified by two measures:
   – The ratio of P_{32} in the expanded FPI criterion (EFPC) size range of 3.09 m to 564.2 m for the various lineament alternatives (see below); and
   – The ratio of P_{32} in the functional MDZ size range (assumed to be 75 m–564.2 m) for the various lineament alternatives (see Section 5.5).

The EFPC size range, described in detail in /Munier 2006b/ and /Munier 2007/ represents the range of fracture radii that could conceivably create a full-perimeter intersection (FPI) with a repository access tunnel (assuming a circular tunnel with a radius of 3.09 m). The EFPC criterion may be used to judge whether a specific canister deposition position can be used to host a spent-fuel canister; the intensity of fractures within the EFPC size range has an affect on repository layout and utilization /Munier 2006b/. The MDZ size range represents a functional definition rather than a true break between fractures and deformation zones; a 75 m radius fracture is the largest structure allowed to intersect a canister deposition hole for the hole to be considered 'usable' /Fälth and Hökmark 2006/.

It is important to note that the subhorizontally- to gently-dipping fracture set (SH) is not treated in this uncertainty analysis. There is not enough information available to distinguish between subvertically-dipping and subhorizontally-dipping lineaments in the ground magnetic/LIDAR data. Therefore, the radius scaling exponent for the subhorizontal set is based entirely on data from detail-mapped fracture outcrops.

Results

Figure 6-1 through Figure 6-3 illustrate the differences in the area-normalized cumulative number plots caused by the use of fewer high-resolution ground magnetic/LIDAR lineaments. The black line represents the original best-fit line for the BMU model alternative, the orange line represents the best-fit trace length scaling exponent assuming that only 75% of lineaments represent fractures, and the teal line represents the best-fit k_t assuming that only 50% of lineaments represent fractures.

Figure 6-4 illustrates the simulation volume (a 50 m cube) and an example simulation traceplane. Outcrop ASM000208 was used as the 'best-fit' outcrop for the ENE fracture set, while outcrop ASM100235 was used as the 'best-fit' outcrop for the N-S and WNW fracture sets. This is identical to the parameterization of model alternative BMU. Stochastic DFN models were generated using different P_{32}s for each fracture set until a value was found that would accurately reproduce the outcrop tracelength-cumulative number curve. A simulation result is considered a 'good' fit when the resulting traces are in alignment with the best-fit trace length scaling exponent line (see Figure 6-5). An rmin value of 0.5 m was used for all simulations.

The new size-intensity model parameterizations resulting from the uncertainty simulations for the BMU model alternative in terms of new values for k_r, r_0, and P_{32OC} are presented below in Table 6-10. The values for the 100% case are taken from Table 4-25 for the BMU model alternative. P_{32OC} represents the fracture intensity for a size range of 0.5 m to 564.2 m.

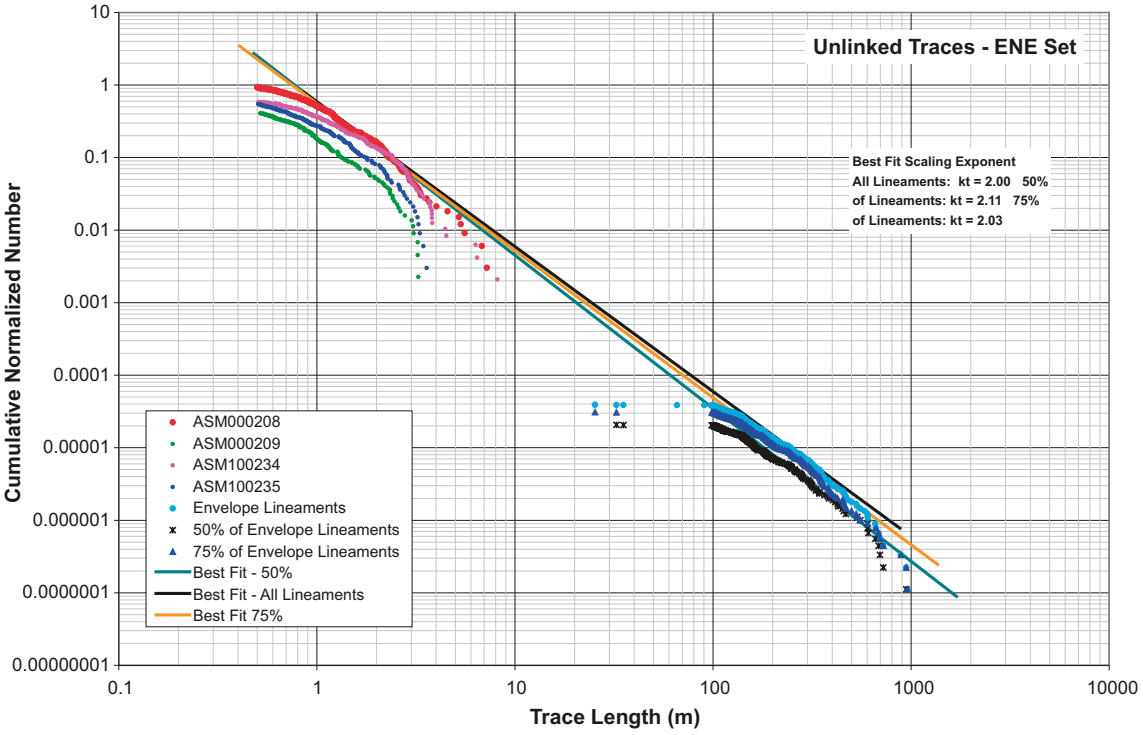

Figure 6-1. *Area-normalized CCN curves for ENE fracture set, BMU model alternative, illustrating the effects of the utilization of 100%, 75%, and 50% of lineaments on the trace length scaling exponent (k_t).*

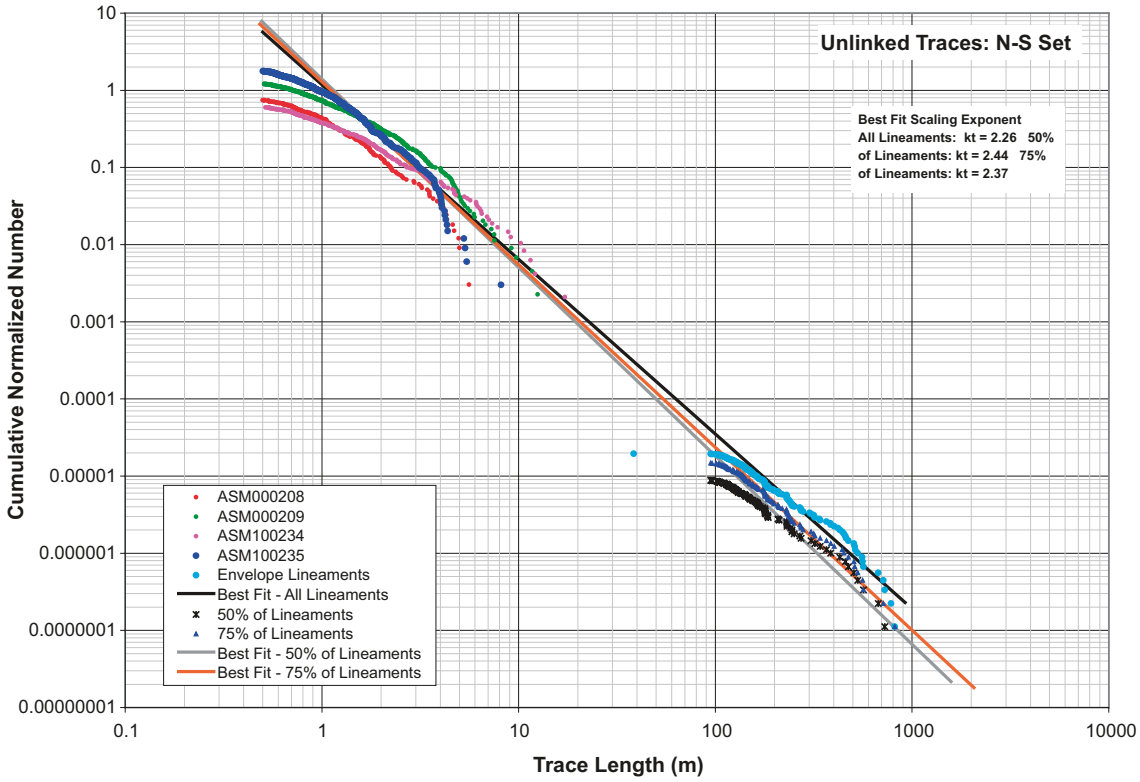

Figure 6-2. *Area-normalized CCN curves for N-S fracture set, BMU model alternative, illustrating the effects of the utilization of 100%, 75%, and 50% of lineaments on the trace length scaling exponent (k_t).*

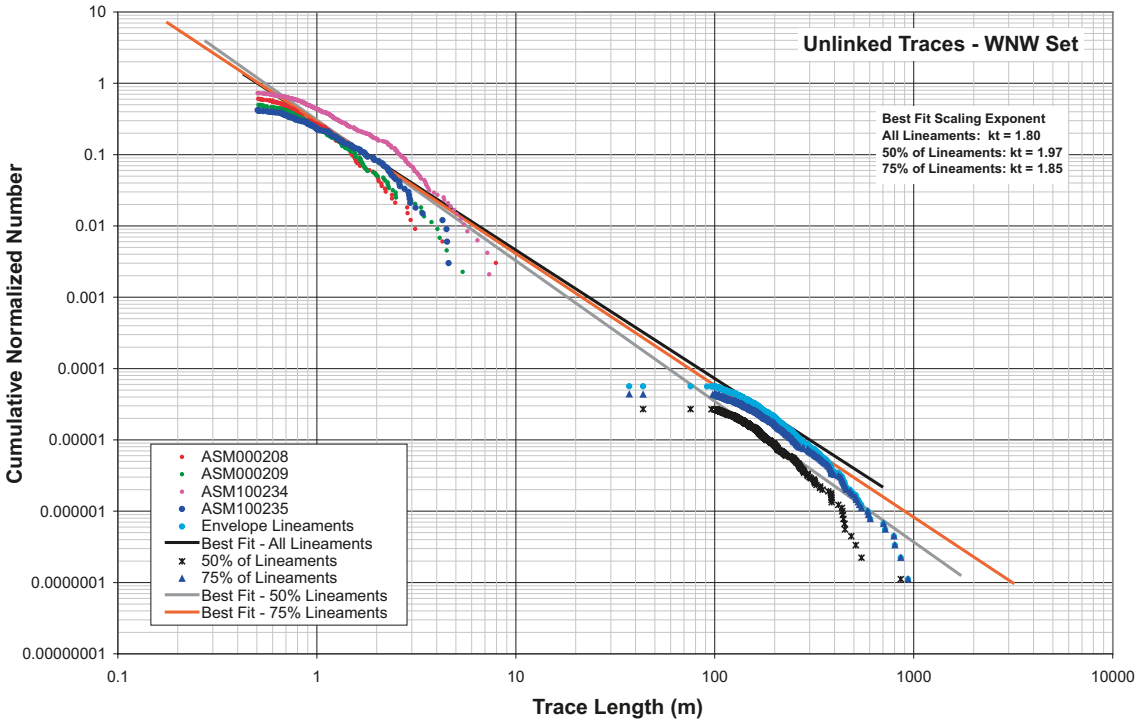

Figure 6-3. *Area-normalized CCN curves for WNW fracture set, BMU model alternative, illustrating the effects of the utilization of 100%, 75%, and 50% of lineaments on the trace length scaling exponent (k_t).*

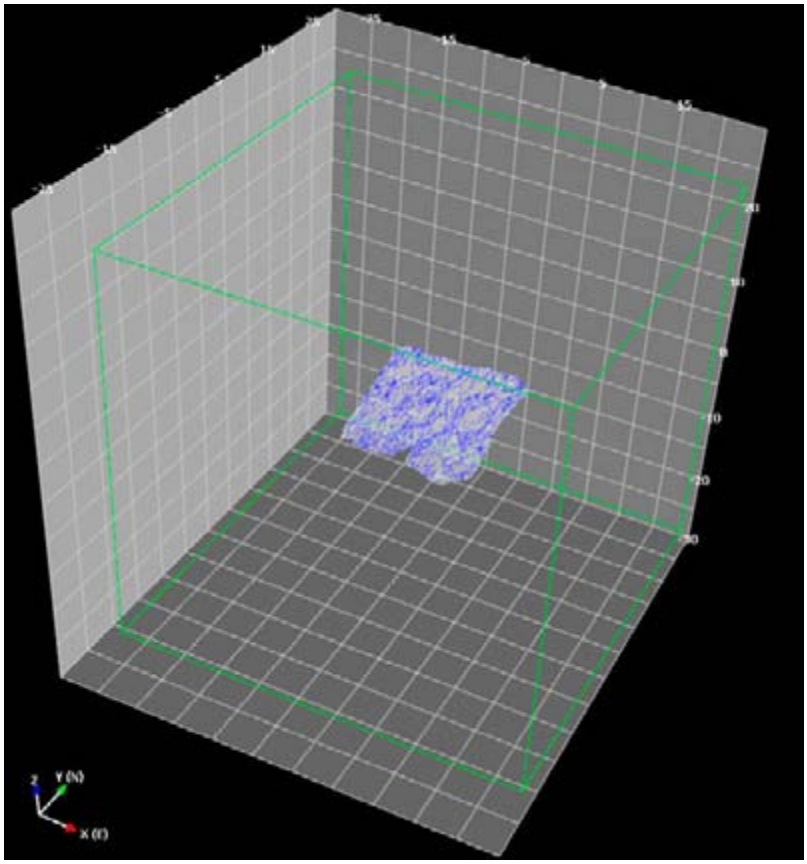

Figure 6-4. *Simulation volume (green) and sampling traceplane (transparent, with blue fracture traces) used to calculate P_{32OC} for 50% and 75% lineament intensity uncertainty cases. This figure illustrates outcrop ASM100235, which was used for the N-S and WNW fracture sets.*

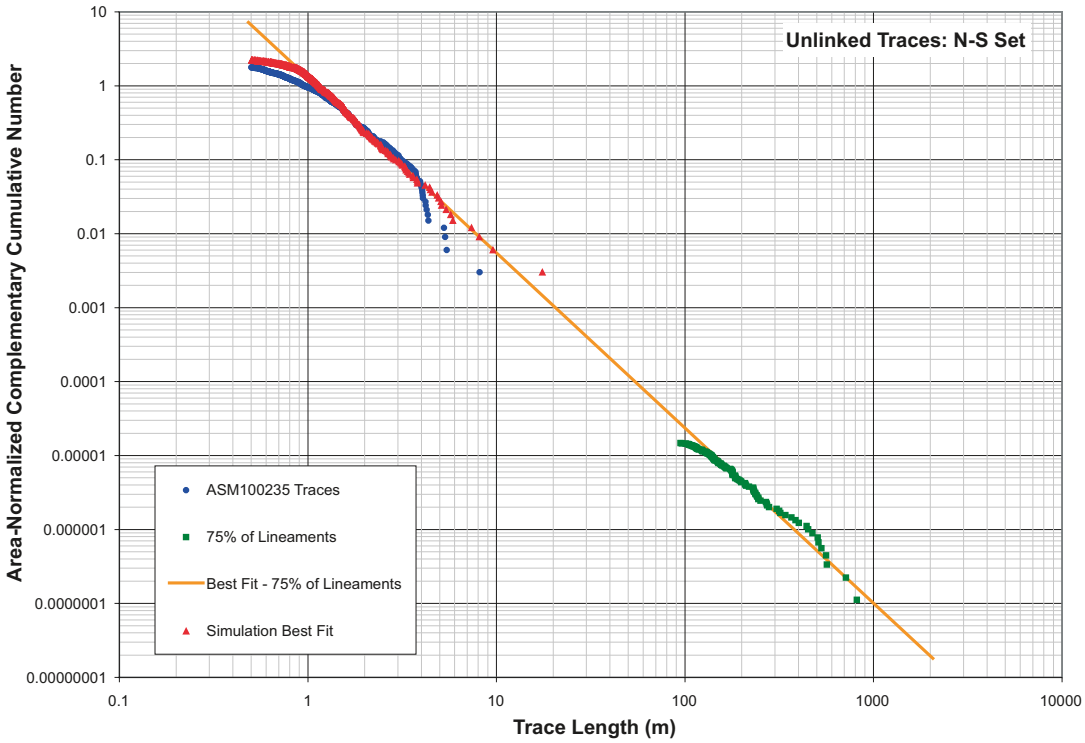

Figure 6-5. *Example of P_{32OC} fitting simulation results for the N-S orientation set. The orange line illustrates the best-fit trace length scaling exponent, the blue circles the original outcrop trace data, and the red triangles the simulated trace data.*

6.3 Recommendations for uncertainty propagation to downstream models

Table 6-10 summarizes the impact of the key uncertainties described in Section 6.1. This table lists the type of uncertainty, the range of its impact on P_{32} relative to the Base Model (BM) or Base Model Unlinked (BMU) and some general comments about how the uncertainty relates to factors like fracture domain and fracture set. The horizontal fractures are the set most likely to intersect vertical canister deposition holes in terms of their geometry, so the uncertainty for that set is also described.

The results shown in Table 6-11 suggest that the best measures to reduce uncertainty in downstream models are to:

- Model each fracture domain separately;
- Model each fracture set within each fracture domain separately; and
- Minimize the scale difference between the scale over which fracture data are collected and the scale to which they are applied. Extrapolating outcrop data to 100 m simulation grid cells produces less uncertainty than extrapolating to 500 m grid cells.

Downstream users of this model must decide upon whether the uncertainty relative to any factor is important to explicitly be taken into account based upon its impact. One conclusion that emerges from the uncertainty quantification is that the Base Model represents a pessimistic estimate of the fracture intensity, since in nearly all cases the alternative models produce lower fracture intensities, especially for the subhorizontal set.

The uncertainties listed in Table 6-10 represent scenarios, with the possible exception of the variation of the scaling exponent parameter, which could also be treated as a continuous variable rather than as a set of bounding values. For scenarios, a useful way to propagate or take into account the uncertainty is to assign a probability that the scenario may occur. If the scenario occurs, then the model would have the parameter values related to the scenario; if not, then the parameter values related to the Base Model would be used. In this way, the uncertainties identified and quantified for the fracture model could be propagated into downstream models or calculations with minimal computational effort.

Table 6-10. Revised size-intensity model parameterizations for k_r-50% and k_r-75%, BMU model alternative.

Fracture Domain	Fracture Set	k_r			P_{32OC} (m^2/m^3)			r_0		
		100%	75%	50%	100%	75%	50%	100%	75%	50%
FSM_C	ENE	3.00	3.03	3.11	1.72	1.34	1.49	0.37	0.39	0.44
FSM_EW007	ENE	3.00	3.03	3.11	1.98	1.34	1.49	0.32	0.34	0.39
FSM_N	ENE	3.00	3.03	3.11	1.38	1.34	1.49	0.47	0.48	0.54
FSM_NE005	ENE	3.00	3.03	3.11	1.60	1.34	1.49	0.40	0.42	0.47
FSM_W	ENE	3.00	3.03	3.11	1.60	1.34	1.49	0.40	0.42	0.47
FSM_C	N-S	3.26	3.37	3.44	2.33	2.80	2.99	0.59	0.57	0.59
FSM_EW007	N-S	3.26	3.37	3.44	2.96	2.80	2.99	0.49	0.48	0.50
FSM_N	N-S	3.26	3.37	3.44	2.63	2.80	2.99	0.53	0.52	0.55
FSM_NE005	N-S	3.26	3.37	3.44	4.30	2.80	2.99	0.36	0.37	0.39
FSM_W	N-S	3.26	3.37	3.44	3.60	2.80	2.99	0.42	0.42	0.44
FSM_C	WNW	2.80	2.85	2.97	2.53	0.73	0.81	0.08	0.12	0.15
FSM_EW007	WNW	2.80	2.85	2.97	2.90	0.73	0.81	0.07	0.10	0.13
FSM_N	WNW	2.80	2.85	2.97	2.67	0.73	0.81	0.08	0.11	0.15
FSM_NE005	WNW	2.80	2.85	2.97	2.37	0.73	0.81	0.09	0.12	0.16
FSM_W	WNW	2.80	2.85	2.97	1.97	0.73	0.81	0.11	0.16	0.20

Table 6-11 and Table 6-12 summarize the effects of the assumption that not all lineaments represent fracture traces. Table 6-11 compares the values of P_{32} for the EFPC fracture size range, while Table 6-12 compares the values of P_{32} for fractures within the functional MDZ size range.

Table 6-11. Comparison of EFPC and MDZ P_{32} values. All values of P_{32} are in units of m^2/m^3.

Fracture Domain	Fracture Set	P_{32} EFPC (3.09 m–564.2 m)			P_{32} (75 m–564.2 m)		
		100%	75%	50%	100%	75%	50%
FSM_C	ENE	0.2070	0.2036	0.1972	0.0074	0.0051	0.0051
FSM_EW007	ENE	0.2070	0.2036	0.1972	0.0074	0.0051	0.0051
FSM_N	ENE	0.2070	0.2036	0.1972	0.0074	0.0051	0.0051
FSM_NE005	ENE	0.2070	0.2036	0.1972	0.0074	0.0051	0.0051
FSM_W	ENE	0.2070	0.2036	0.1972	0.0074	0.0051	0.0051
FSM_C	N-S	0.2871	0.2308	0.2172	0.0048	0.0021	0.0021
FSM_EW007	N-S	0.2871	0.2308	0.2172	0.0048	0.0021	0.0021
FSM_N	N-S	0.2871	0.2308	0.2172	0.0048	0.0021	0.0021
FSM_NE005	N-S	0.2871	0.2308	0.2172	0.0048	0.0021	0.0021
FSM_W	N-S	0.2871	0.2308	0.2172	0.0048	0.0021	0.0021
FSM_C	WNW	0.1376	0.1527	0.1370	0.0087	0.0054	0.0054
FSM_EW007	WNW	0.1376	0.1527	0.1370	0.0087	0.0054	0.0054
FSM_N	WNW	0.1376	0.1527	0.1370	0.0087	0.0054	0.0054
FSM_NE005	WNW	0.1376	0.1527	0.1370	0.0087	0.0054	0.0054
FSM_W	WNW	0.1376	0.1527	0.1370	0.0087	0.0054	0.0054

Table 6-12. P_{32} ratios for kr uncertainty case. Values represent the ratio of the uncertainty case (50% or 75%) to the recommended size-intensity model alternative.

Fracture Set	Fracture Set	EFPC (3.09 m–564.2 m)		MDZ (75 m–564.2 m)	
		50% / BMU	75% / BMU	50% / BMU	75% / BMU
FSM_C	ENE	0.953	0.984	0.690	0.690
FSM_EW007	ENE	0.953	0.984	0.690	0.690
FSM_N	ENE	0.953	0.984	0.690	0.690
FSM_NE005	ENE	0.953	0.984	0.690	0.690
FSM_W	ENE	0.953	0.984	0.690	0.690
FSM_C	N-S	0.756	0.804	0.437	0.437
FSM_EW007	N-S	0.756	0.804	0.437	0.437
FSM_N	N-S	0.756	0.804	0.437	0.437
FSM_NE005	N-S	0.756	0.804	0.437	0.437
FSM_W	N-S	0.756	0.804	0.437	0.437
FSM_C	WNW	0.996	1.110	0.615	0.615
FSM_EW007	WNW	0.996	1.110	0.615	0.615
FSM_N	WNW	0.996	1.110	0.615	0.615
FSM_NE005	WNW	0.996	1.110	0.615	0.615
FSM_W	WNW	0.996	1.110	0.615	0.615

The results of the uncertainty analysis on the sensitivity of the radius scaling exponent (k_r) for the recommended size-intensity model alternative to varying number of lineaments suggest that, within both the EFPC and MDZ size ranges, fracture intensity is relatively insensitive to the differences in the radius scaling exponent. Differences in P_{32} values approach, but are less than, an order of magnitude; this is on the same scale as the other conceptual uncertainties in the geological DFN model. The uncertainty has a larger effect on the MDZ size fraction than on the EFPC size fraction.

As the number of lineaments decreases, the value of k_r increases, while the total fracture intensity as measured in cored boreholes remains constant. The effect is to decrease the relative intensity of larger fractures, and increase the intensity of smaller fractures. A secondary effect is that the minimum size (r_0) of fractures becomes slightly larger (Table 6-10) as the number of lineaments considered to represent fractures decreases.

Table 6-13. Summary of key uncertainties and their expected impacts on downstream modelling.

Uncertainty	Range of the Ratio of Alternative Model Intensity to Base Model Intensity	Comments
Scaling Exponent Dependence on Fracture Domain Conceptual Uncertainty	0.14 to 2.79; generally ~ 0.15–0.22 for subhorizontal sets	Greatest variability is by set, not fracture domain.
Euclidean vs. Fractal Scaling Conceptual Uncertainty	0.77 to 1.67; 0.96 for subhorizontal sets	Varies by set
Linked vs. Unlinked Traces Conceptual Uncertainty	0.63 to 1.03; 1.03 for subhorizontal sets	Fairly minor impact, especially on subhorizontal fractures
Number of lineaments used in size-intensity model parameterisation	0.44 to 1.11; unable to test subhorizontal sets	Smaller than uncertainty in scaling exponent parameter fit
Scaling Exponent Parameter Uncertainty	0.35 – 1.51; 0.35 for subhorizontal sets	Not highly variable among different sets
Open vs. Sealed Parameter Uncertainty	0.05 to 0.10 for outcrops; 0.20 to 0.30 for boreholes; generally around 30% for subhorizontal set (borehole data)	Varies by set and domain

Consider the following example for the subhorizontal (SH) set. The ratios for the uncertainties for the SH set are given in Table 6-11 as a function of the uncertainty listed.

The probability of each uncertainty in this example is arbitrarily set to 5%. The uncertainties are independent of one another, except for the fracture radius scaling exponent cases; the occurrence of one excludes the other. A Monte Carlo simulation using 1,000 realizations was set up in which all uncertainties were independent except for the Scaling Exponent uncertainties. 5% of each realizations used the SH ratio shown in the table; 95% used a ratio of 1.0. The results are shown in Figure 6-1. This figure shows that for about 85% of the realizations, the ratio is approximately 1.0. In about 20% of the realizations it is below 1.0, and in about 5% of the realizations it is above 1.0. The results show that the maximum value is 1.49. Note that the results do not conform to a simple probability distribution model such as a normal or lognormal distribution.

Table 6-14. Example of probability assignment to model uncertainties for a single scenario using the global SH fracture set.

Uncertainty	SH Ratio	Probability
Scaling Exponent Dependence on Fracture Domain Conceptual Uncertainty	0.16	5.0%
Euclidean vs. Fractal Scaling Conceptual Uncertainty	0.77	5.0%
Linked vs. Unlinked Traces Conceptual Uncertainty	0.95	5.0%
Scaling Exponent Parameter Uncertainty – High Case	1.49	5.0%
Scaling Exponent Parameter Uncertainty – Low Case	0.35	5.0%
Open vs. Sealed Parameter Uncertainty	0.28	5.0%

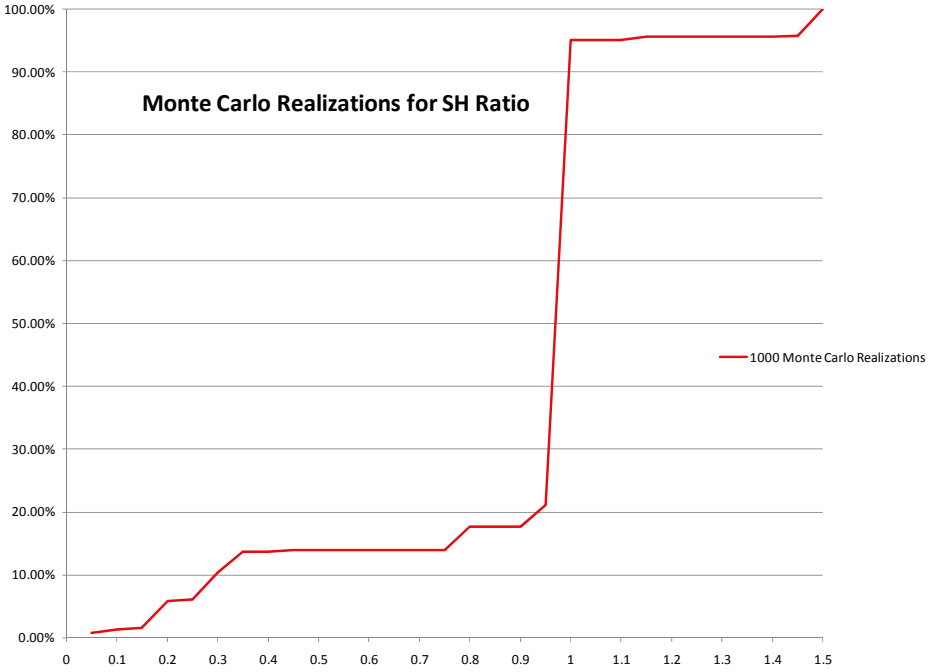

Figure 6-6. *Results of Monte Carlo simulation for SH fracture set scenario.*

7 Geological DFN model summary and conclusions

The recommendations for the parameterisation of the geological DFN model are presented below. The results of the alternative model ranking analysis (Section 5.8) suggest that the most appropriate model, at least in terms of predicting the conditions specified for the DFN verification, is the Base Model variant case using unlinked outcrop traces (BMU). Additional analyses suggest, however, that there is very little effective different between the Base Model (as described in Chapters 3 and 4) and the BMU alternative model. The geological DFN modelling team believes that the concepts behind both of these alternatives are the most consistent and geologically reasonable parameterisation of the fracturing at Laxemar, and that it is appropriate to use either the BM or BMU model variants for DFN simulations.

7.1 Model summary tables

7.1.1 Orientation model

Set	Mean Pole		Distribution
	Trend [°]	Plunge [°]	Fisher κ
SH	335.1	87.1	7.2
ENE	340.3	0.5	9.9
WNW	24.1	3.1	7.5
N-S	269.1	1.7	7.3

7.1.2 Coupled size-intensity model, BMU

Set	Fit Type	FSM_C				FSM_EW007			
		k_r	r_0	r_{max}	P_{32} (k_r,r_0,r_{max})	k_r	r_0	r_{max}	P_{32} (k_r,r_0,r_{max})
ENE	Best	3.00	0.37	564.20	1.72	3.00	0.32	564.20	1.98
NS	Best	3.26	0.59	564.20	2.33	3.26	0.49	564.20	2.96
SH	Best	3.31	0.33	564.20	2.66	3.31	0.23	564.20	4.42
WNW	Best	2.80	0.08	564.20	2.53	2.80	0.07	564.20	2.90
Set	**Fit Type**	**FSM_NE005**				**FSM_S**			
		k_r	r_0	r_{max}	P_{32} (k_r,r_0,r_{max})	k_r	r_0	r_{max}	P_{32} (k_r,r_0,r_{max})
ENE	Best	3.00	0.40	564.20	1.60	3.00	0.15	564.20	4.28
NS	Best	3.26	0.36	564.20	4.30	3.26	0.27	564.20	6.09
SH	Best	3.31	0.29	564.20	3.17	3.31	0.23	564.20	4.22
WNW	Best	2.80	0.09	564.20	2.37	2.80	0.03	564.20	5.39
Set	**Fit Type**	**FSM_N**				**FSM_W**			
		k_r	r_0	r_{max}	P_{32} (k_r,r_0,r_{max})	k_r	r_0	r_{max}	P_{32} (k_r,r_0,r_{max})
ENE	Best	3.00	0.46	564.20	1.38	3.00	0.40	564.20	1.60
NS	Best	3.26	0.53	564.20	2.63	3.26	0.42	564.20	3.60
SH	Best	3.31	0.22	564.20	4.62	3.31	0.28	564.20	3.40
WNW	Best	2.80	0.08	564.20	2.67	2.80	0.11	564.20	1.97

7.1.3 Spatial model

The recommended parameterization for the spatial models at scales greater than or equal to 9 m is to use a Poisson point process model (Baecher or Veneziano) for fracture centre locations, to assume Euclidean scaling for all fracture size/intensity scaling relationships, and, if spatial variability in fracture P_{32} is desired, to use the Gamma or Weibull distribution values presented in Section 4.4.7. At scales smaller than 9 m, a Gamma or Weibull distribution may under-predict the number of completely non-fractured intervals in boreholes, though it will correctly reproduce the mean fracture intensity.

No spatial correlation or fractal clustering appears to be necessary to describe the fracture patterns at Laxemar. Fracture size and intensity patterns are adequately described using fracture domains and fracture sets. Fracture set terminations can be described in terms of probabilities of termination using Table 7-1 (below); if domain-specific termination relationships are required, please utilise the tables in Section 4.4.6.

7.2 Modelling Conclusions

1. The division of the Laxemar site into fracture domains has reduced the overall uncertainty of the model, primarily because the fracture intensity varies more between fracture domains than within fracture domains.
2. The difference among fracture domains is not due to changes in the fracture orientations, but to changes in the intensity of individual sets.
3. Given the above conclusion, scaling exponents should be a function of fracture orientation set, but not of fracture domain, and the size/intensity parameterization should mainly reflect differences in individual set intensity in each domain, not scaling exponent.
4. Fracture termination relationships suggest that the N-S set appears to have formed earliest, while the three remaining sets formed later. The relative chronology of the SH, ENE and WNW sets cannot be distinguished from the termination relations.
5. Analysis of scaling behaviour indicates that intensity scaling is well-modelled by Euclidean scaling at scales greater than 10 m–30 m; evidence exists for fractal scaling at smaller scales, although this is not universal and may be due as well to data limitations. It can also be shown that Euclidean scaling may be appropriate at scales smaller than 10 m–30 m; the apparent departure from Euclidean scaling is most likely an artefact of the analysis method (Section 4.4.1).
6. A Base Model was defined. It had the following properties:
   a. Euclidean scaling;
   b. A radius scaling exponent (k_r) independent of fracture domain;
   c. A radius scaling exponent derived from linked outcrop traces;
   d. The intensity is based on all fractures, not just open; and
   e. The radius scaling exponent is based on the average trace length scaling exponent from outcrop data, rather than extremal values.

Table 7-1. Global Average Termination Matrix (All Domains).

Global Average					
	Terminates Against				
Target Set	ENE	N-S	WNW	SH	Bulk Termination
ENE	0	25.53%	12.24%	6.54%	44.30%
N-S	11.82%	0	11.58%	4.46%	27.86%
WNW	14.10%	26.87%	0	5.95%	46.92%
SH	13.22%	20.66%	12.12%	0	46.01%

7. Several alternative models were identified. Relative to the Base Model, the alternative models feature a combination of conceptual model variants, including:
   a. Fractal scaling instead of Euclidean scaling;
   b. Scaling exponent dependent on fracture domain (the so-called 'r_0-fixed' models, which are roughly equivalent to the 'k_r-scaled' models used in the hydrogeological DFN models at Forsmark and Laxemar);
   c. Based on unlinked traces, instead of linked traces;
   d. Based on open fracture intensity instead of total fracture intensity; and
   e. Based on bounding trace length scaling exponents ('Upper' or 'Lower') instead of the Best Fit exponent.

8. Verification built confidence in the SDM Laxemar Site geological DFN for its intended purposes:
   a. The orientation model parameterisation is adequate and will produce relative fracture set intensity patterns similar to what is seen in field data from Laxemar (see Section 5.2.3).
   b. Visually, the simulated outcrop trace patterns produced using the Base Model resembled the mapped outcrop trace data within the fit limits (see Section 5.3)
   c. Comparisons of outcrop P_{21} between simulations and measured data show reasonable matches (Section 5.3) when the issues related to the departure of the measured data from a power law model (Section 4.4.3) are taken into account.
   d. Comparisons of simulated P_{10} along scanlines to observed scanline data (Section 5.4) are extremely poor; neither the Base Model nor the alternative models are able to successfully predict scanline P_{10} with any confidence. However, the models are as likely to under-predict P_{10} as they are to over-predict P_{10}; this suggests that there are no systematic biases or errors in the geological DFN modelling.
   e. The comparison between the predicted and measured borehole fracture intensities (P_{10}) in fracture domain FSM_C (Section 5.6) is reasonable for most of the validation cases. The domain-specific ('r_0-fixed') models tend to perform the best in these verifications, but this is not a surprise. The r_0-fixed models are specifically calibrated to match mean borehole P_{10}. In most cases, both the Base Model and its variant cases perform reasonably well.
   f. The alternative model ranking suggests that the unlinked Base Model alternative (BMU) is the best model for predicting the verification cases. This model alternative was put forth as the recommended model for geological DFN modelling at Laxemar. However, the ranking also shows that there is very little effective difference between the BM and the BMU cases.
   g. The validation of the SDM-Site Laxemar geological DFN model suggested that the top-five ranked alternative models performed equally well at predicting the mean fracture intensity in FSM_W and the number of MDZ encountered in borehole KLX27A. However, borehole KLX27A and its neighbour KLX19A appear to have total fracture intensities roughly ½ of the average fracture intensity in domain FSM_W. As a result, the recommended parameterisation (BMU) and the four other top-ranked alternative models over-predict total fracture intensity in KLX27A.

9. A validation of the SDM-Site Laxemar geological DFN parameterisation was performed by attempting to predict the intensity of fracturing in borehole KLX27A, which is located inside fracture domains FSM_W and FSM_S.

10. Uncertainty analyses are carried out on the alternative models. Uncertainty is quantified as the ratio in fracture intensity by set for each alternative case relative to the Base Case. The Alternative models tend to produce lower fracture intensities, with maximum reductions to about 10% for the case where the model is based on open fracture intensity rather than total fracture intensity. The impact of each uncertainty typically varies by fracture set and fracture domain, in the cases where the latter consideration is relevant to the model parameterization.

References

Agresti A, 1996. Introduction to categorical data analysis. John Wiley and Sons, New York, New York, USA. ISBN 978-0471113386.

Almén K-E, Thurner E, 1996. Nya bilder av berget inre – djupdykning med ny borrhåls-TV. Svensk Kärnbränslehantering AB.

Bak P, Tang C, Wiesenfeld K, 1987. Self-organized criticality: an explanation of $1/f$ noise. Physical Review Letters, Vol. 59, pp. 381–384.

Brown W K, Wohletz K H, 1995. Derivation of the Weibull distribution based on physical principles and its connection to the Rossin-Rammler and lognormal distributions. Journal of Applied Physics Vol.78, No. 4, pp. 2758–2763.

Butler R, 1992. Paleomagnetism: Magnetic Domains to Geologic Terranes, Blackwell Scientific Publications, reprinted online by University of Arizona, Tuscon, Arizona, USA. http://www.geo.arizona.edu/Paleomag/book/. Last accessed 20080922.

Carlsten S, Mattsson K-J, Stråhle A, Mattsson H, Wahlgren C-H, 2008. Geological single-hole interpretation of KLX27A. Oskarshamn site investigation. SKB P-04-48, Svensk Kärnbränslehantering AB.

Cosgrove J, Stanfors R, Röshoff K, 2006. Geological characteristics of deformation zones and a strategy for their detection in a repository. SKB R-06-39, Svensk Kärnbränslehantering AB.

Cronin V, 2008. Finding the Mean and 95 Percent Confidence Interval of a Set of Strike-and-Dip or Lineation Data. Engineering and Environmental Geoscience, Vol. 54, No.2, Association of Environmental and Engineering Geologists & The Geological Society of America, Denver, Colorado, USA.

Davis J, 2002. Statistics and Data Analysis in Geology, Third Edition. John Wiley and Sons, New York, New York, USA. ISBN 978-0471172758

Davy P, Darcel C, Bour O, Munier R, de Dreuzy J R, 2006. A note on the angular correction applied to fracture intensity profiles along drill core. Journal of Geophysical Research, Vol. 111, No. B11408.

Dershowitz W, 1984. Rock Joint Systems, Doctoral dissertation, Massachusetts Institute of Technology, Cambridge, MA, USA.

Dershowitz W, Lee G, Geier J, Foxford T, La Pointe P, Thomas A, 1998. FRACMAN, Interactive discrete feature data analysis, geometric modelling and exploration simulation. User documentation, version 2.6. Golder Associates, Inc., Redmond, Washington, USA.

Fisher R, 1953. Dispersion on a sphere, Royal Society of London Proceedings 217: 295–305.

Fisher N, Lewis T, Embleton B, 1987. Statistical analysis of spherical data. Cambridge University Press, Cambridge, UK. ISBN 978-0521456999

Follin S, Levén J, Hartley L, Jackson P, Joyce S, Roberts D, Swift B, 2007. Hydrogeological characterisation and modelling of deformation zones and fracture domains, Forsmark modelling stage 2.2. SKB R-07-48, Svensk Kärnbränslehantering AB.

Fox A, La Pointe P, Hermanson J, Öhman J, 2007. Statistical geological discrete fracture network model. Forsmark modelling stage 2.2. SKB R-07-46, Svensk Kärnbränslehantering AB.

Forssberg O, Cronquist T, Vestgård J, Bergkvist L, Hermanson J, Öhman J, Pettersson A, Koyi S, Bergman T, 2007. Detailed outcrop mapping in trenches. Oskarshamn site investigation. SKB P-07-29, Svensk Kärnbränslehantering AB.

Fälth B, Hökmark H, 2006a. Seismically induced shear displacement on repository host rock fractures. Results of new dynamic discrete fracture modelling. SKB R-06-48, Svensk Kärnbränslehantering AB.

Fälth B, Hökmark H, 2006b. Seismically induced slip on rock fractures. Results from dynamic discrete fracture modelling. SKB R-06-48, Svensk Kärnbränslehantering AB.

Fälth B, Hökmark H, Munier R, 2007. Seismically Induced Shear Displacements in Repository Host Rock Fractures. 9th Canadian conference on Earthquake Engineering. Ottawa, Canada.

Fälth B, Hökmark H, Munier R, 2008. Seismically induced slip on rock fractures – expanded study with particular account of large earthquakes. Manuscript accepted at 42nd U.S. Rock Mechanics Symposium. San Francisco 2008.

Goodman L A, Kruskal W H, 1954, 1959, 1963, 1972. Measures for association for cross-classification, I, II, III and IV. Journal of the American Statistical Association. 49: 732–764, 54: 123–163, 58: 310–364, and 67: 415–421 respectively. The 1972 instalment discusses the uncertainty coefficient.

Hermanson J, Forssberg O, Fox A, La Pointe P, 2005. Statistical model of fractures and deformation zones, Laxemar subarea, version 1.2. R-05-45. SKB Svensk Kärnbränslehantering AB.

Hermanson J, Fox A, Öhman J, Rhén I, 2008. Site Descriptive Modelling SDM-Site Laxemar. Compilation of data used for the analysis of the geological and hydrogeological DFN models. SKB P-08-56, Svensk Kärnbränslehantering AB.

Holmén J, Outters N, 2002. Theoretical study of rock mass investigation efficiency, Appendix A. SKB TR-02-21, Svensk Kärnbränslehantering AB.

Iacopino G, 2006. Reliability analysis of mechanical components containing random flaws. Cranfield University, School of Applied Sciences, Ph.D. dissertation, 165 p.

Kamb W B, 1959. Ice petrofabric observations from Blue Glacier, Washington, in relation to theory and experiments, J. Geophys. Res. 64, pp. 1891–1919.

Kruskal W H, Wallis W A, 1952. Use of ranks in one-criterion variance analysis. Jour. Am. Stat. Assoc. v.47, pp. 583–634.

La Pointe P, Wallmann P, Dershowitz W, 1993. Stochastic estimation of fracture size from simulated sampling, Int. Jour. Rock Mech., Min. Sci. & Geomech. Abstr. v. 30, pp. 1611–1617.

La Pointe P, 1995. Estimation of undiscovered hydrocarbon potential through fractal geometry. Chap. 3, Fractals in Petroleum Geology and Earth Processes, Plenum Press, New York, pp. 35–57. ISBN 978-0306448683

La Pointe P, 2002. Derivation of parent fracture population statistics from trace length measurements for fractal fracture populations. International Journal of Rock Mechanics and Mining Sciences, Vol. 39, pp. 381–388.

La Pointe P, Hermanson J, 2006. Statistical model of fractures and deformation zones. Preliminary site description Simpevarp subarea, version 1.2. SKB R-05-28, Svensk Kärnbränslehantering AB.

Liebetrau A M, 1983. Measures of association, Quantitative Applications in the Social Sciences Series No. 32. Sage Publications, Newbury Park, CA, USA. ISBN 978-0803919747.

Mauldon M, Mauldon J G, 1997. Fracture sampling on a cylinder; from scanlines to boreholes and tunnels, Rock Mechanics and Rock Engineering, Vol. 30, No. 3, pp. 129–144.

Munier R, Stenberg L, Stanfors R, Milnes A-G, Hermanson J, Triumf C-A, 2003. Geological Site Descriptive Model; A strategy for the model development during site investigations. SKB R-03-07, Svensk Kärnbränslehantering AB.

Munier R, Hökmark H, 2004. Respect distances. Rationale and means of computation. SKB R-04-17. Svensk Kärnbränslehantering AB.

Munier R, 2004. Statistical analysis of fracture data, adapted for modelling Discrete Fracture Networks-Version 2. SKB R-04-66, Svensk Kärnbränslehantering AB.

Munier R, 2006a. DFN related modelling issues to consider during 2.2 modelling. SKB Project Memorandum, distributed 20060608, Svensk Kärnbränslehantering AB.

Munier R, 2006b. Using observations in deposition tunnels to avoid intersections with critical fractures in deposition holes, SKB R-06-54, Svensk Kärnbränslehantering AB, Stockholm, Sweden.

Munier R, 2007. Demonstrating the efficiency of the EFPC criterion by means of Sensitivity analyses. SKB R-06-115, Svensk Kärnbränslehantering AB.

Munier R, Stigsson M, 2007. Implementation of uncertainties in borehole geometries and geological orientation data in Sicada. SKB R-07-19, Svensk Kärnbränslehantering AB.

NIST, 2007a. Kolmogorov-Smirnov Goodness-of-Fit Test, Chapter 1.3.5.16, NIST/ SEMATECH e-Handbook of Statistical Methods, National Institute of Standards and Technology, United States Department of Commerce, Washington D.C., USA. http://www.itl.nist.gov/div898/handbook/eda/section3/eda35g.htm Last accessed 20070903.

NIST, 2007b. Gamma distribution, Chapter 1.3.6.11, NIST/SEMATECH e-Handbook of Statistical Methods, National Institute of Standards and Technology, United States Department of Commerce, Washington D.C., USA. Last accessed 20070903. http://www.itl.nist.gov/div898/handbook/eda/section3/eda366b.htm

Olofsson I, Simeonov A, Stigsson M, Stephens M, Follin S, Nilsson A-C, Röshoff K, Lindberg U, Lanaro F, Fredriksson L, 2007. A fracture domain concept as a basis for the statistical modelling of fractures and minor deformation zones, and interdisciplinary coordination. Site descriptive modelling Forsmark, stage 2.2. SKB R-07-15, Svensk Kärnbränslehantering AB.

Olsson T, Stanfors R, Sigurdsson O, Erlström M, 2006. Oskarshamn site investigation, Identification and characterization of minor deformation zones based on lineament interpretation, SKB P-06-282, Svensk Kärnbränslehantering AB, Stockholm, Sweden.

Palisades Corporation, 2004. Guide to using BestFit, Version 4.5, September 2004, PDF.

Pearson K, 1904. Mathematical Contributions to the Theory of Evolution XIII: On the theory of contingency and its relation to association and normal correlation. Draper's Company Research Memoirs, Biometric Series, No. 1. Dulau & Company, London, U.K.

Priest S D, Hudson D W, 1981. Estimation of discontinuity spacing and trace length using scanline surveys. International Journal of Rock Mechanics and Mining Science and Geomechanics Abstracts, Vol. 18, pp. 183–197.

Priest S D, 1993. Discontinuity analysis for rock engineering, Chapman & Hall, New York, New York, USA. ISBN 978-0412476006.

Rhén I, Forsmark T, Hartley L, Jackson P, Roberts D, Swan D, Gylling B, 2008. Hydrogeological conceptualisation and parameterisation, Site descriptive modelling SDM-Site Laxemar. SKB R-08-78, Svensk Kärnbränslehantering AB.

Robin P-Y F, Jowett C, 1986. Computerized density contouring and statistical evaluation of oriented data using counting circles and continuous weighing functions, Tectonophysics, 121, pp. 207–223.

Rosenberg M, 1968. The logic of survey analysis. Basic Books, New York, New York, USA. ISBN 978-0465042050.

SAS Institute, 1988. SAS/STAT user's guide. SAS Institute, Cary, North Carolina, USA.

Schlaifer H, Raiffa R, 1972. Applied Statistical Decision Theory, MIT Press, Cambridge, Massachusetts, USA. ISBN 0262680211.

Shapiro S S, Wilk M B, 1965. An analysis of variance test for normality (complete samples), Biometrika, 52, 3 and 4, pages 591–611.

Snedecor G W, Cochran W G, 1980. Statistical methods, 7th edition, Iowa State University Press, Ames, Iowa, USA. ISBN 0813815606.

Stigsson M, 2007. Analysis of uncertainty and changes in orientation of fractures coupled to PFL anomalies. Forsmark site investigation. SKB P-07-178, Svensk Kärnbränslehantering AB.

SKB, 2002. Simpevarp – site descriptive model version 0. SKB R-02-35, Svensk Kärnbränslehantering AB.

SKB, 2004. Preliminary site description Simpevarp area – version 1.1. SKB R-03-25, Svensk Kärnbränslehantering AB.

SKB, 2006. Preliminary site description Laxemar subarea – version 1.2. SKB R-06-10, Svensk Kärnbränslehantering AB.

SKB, 2006b. Long-term safety for KBS-3 repositories at Forsmark and Laxemar – a first evaluation. Main Report of the SR-Can project. SKB TR-06-09, Svensk Kärnbränslehantering AB.

Terzhagi R D, 1965. Sources of error in joint surveys, Geotechnique, Vol. 15, pp. 287–304.

Theil H, 1972. Statistical decomposition analysis. North Holland Publishing Company, Amsterdam, The Netherlands. ISBN 978-0720433142

Triumf C-A, Thunehed H, 2007. Coordinated lineaments longer than 100 m at Laxemar, Identification of lineaments from LIDAR data and co-ordination with lineaments in other topographic and geophysical data, Oskarshamn site investigation. SKB P-06-262, Svensk Kärnbränslehantering AB.

Viola G, Venvik-Ganerod G, 2007. Structural analysis of brittle deformation zones in the Simpevarp-Laxemar area, Oskarshamn, southeast Sweden. Oskarshamn site investigation. SKB P-07-41, Svensk Kärnbränslehantering AB.

Wahlgren C-H, Curtis P, Hermanson J, Forssberg O, Öhman J, Drake H, Fox A, La Pointe P, Triumf C-A, Mattsson H, Thunehed H, 2008. Geology Laxemar, site descriptive modelling, SDM-Site Laxemar. SKB R-08-54, Svensk Kärnbränslehantering AB.

Wang X, 2005. Stereological Interpretation of Rock Fracture Traces on Borehole Walls and Other Cylindrical Surfaces, Virginia Polytechnic Institute and State University, doctoral dissertation.

Weibull W, 1951. A statistical distribution function of wide applicability. Journal of Applied Mechanics 18, pp. 293–305.

Yow J L, 1987. Technical Note: Blind zones in the acquisition of discontinuity orientation data, International Journal of Rock Mechanics and Mining Science and Geomechanics Abstracts, Vol. 24, No. 5, pp. 317–318.

Appendix A

Linking of fracture traces

A.1 Linking of outcrop traces

The fracture trace data provide indispensable information for the parameterization of fracture size distribution in DFN modelling. Past DFN models at Forsmark and Laxemar have assumed that fracture centre locations can be approximated as a three-dimensional Poisson point process. However, some specific trace data reveal spatial patterns in outcrop which deviate from the Poissonian assumption. One such particular spatial pattern may be described as "sequentially located traces (i.e. closely located trace endpoints) with similar orientations" (Figure A-1a). It is possible that such fractures may form a well-connected structure below the ground surface (Figure A-1b), even though the traces are not actually connected in the outcrop surface. Failure to represent this type of possibly connected structures in fracture network modelling may have severe implications on downstream modelling of different processes; x`e.g. resulting in underestimation of the risk of the development of planes of failure or connectivity along flow paths (Figure A-1c).

The goal of the linking efforts were to provide a more reasonable definition of fractures at the outcrop scale, where the length of the surface traces directly affects the final size model parameterization in the geological DFN. This is also consistent with the procedure used in lineament interpretation /Triumf and Thunehed 2007/.

The general approach taken to link traces in the Laxemar outcrops was to divide the problem into two steps. In the first step a computer code (GoLink) is used to link traces strictly based on geometrical criteria. In the second step, the results of the previous step are reviewed in a geologic context by expert judgment, and the results are refined based on the latter evaluation.

The benefits of the numerical algorithm are:

- Efficiency: the trace data set is large and time consuming to interpret; it also facilitates consideration of three-dimensional fracture orientations, which is difficult to assess in a trace map.
- Consistency: as the data set is large, it is difficult to perform a manual linking consistently for all outcrops, for example, to ensure that no links have been overlooked, or to avoid bias.

The drawback of the numerical algorithm is the lack of geologic context; it is difficult to include all structural geologic aspects which are essential to avoid unrealistic links.

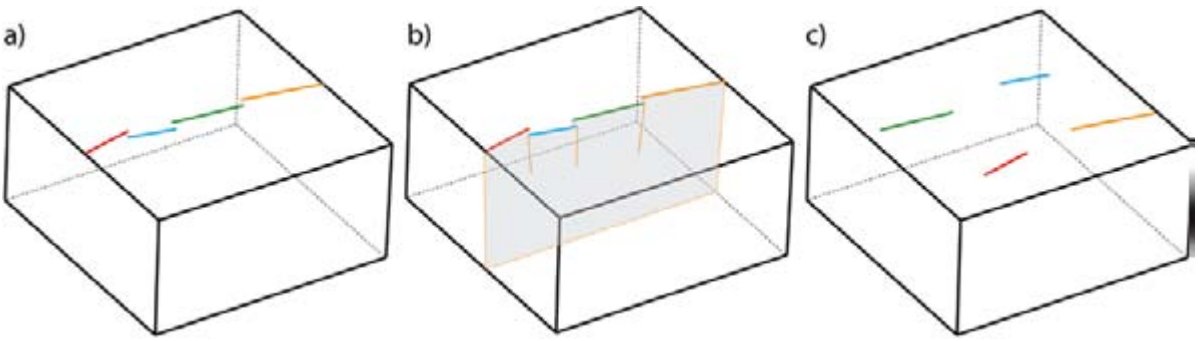

Figure A-1. *Conceptual Figure a) a hypothetical set of sequentially located traces with similar orientations observed in the field, b) possible underground connectivity of fracture planes, with implications for downstream modeling, e.g. hydrological or rock-mechanical properties of the fracture system, and c) illustration of the error resulting from failure to represent this spatial aspect in DFN modeling.*

The GoLink numerical algorithm used the following geometric criteria to determine if two traces from the detailed outcrop mapping results should be linked:

a. The minimum separation distance between the endpoints of two candidate traces must not exceed a specified threshold value, r_{max} (in meters).

b. The difference in orientations of two candidate traces must not exceed a specified maximum polar angle, θ_{max}.

c. The linking must propagate in one general direction.

d. No links are made between traces that are separated by a trace showing shear offset.

Table A-1. Demonstration of criteria used in the linking of trace data

Criterion 1: maximum gap between trace endpoints < r_{max}	
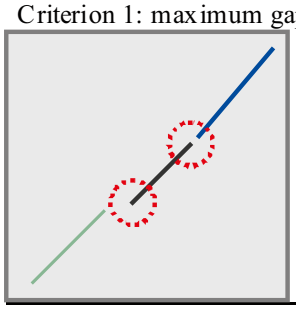	The green trace is not linked to the black trace, as the gap exceeds r_{max} (i.e. neither of its termination points are located within the distance r_{max} of either termination points of the black trace; r_{max} is shown by red circles). The blue trace is linked to the black trace, as the gap between their endpoints is less than r_{max}.
Criterion 2: fractures must be "semi-parallel"	
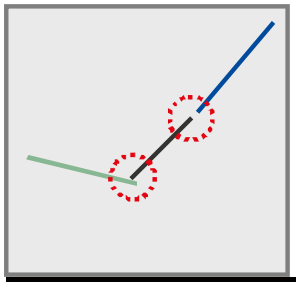	The green trace is not linked to the black trace, as the orientation of their poles deviates more than θ_{max}. The blue trace is linked to the black trace, as their fracture-plane poles are of similar orientation (e.g. the deviation angle < θ_{max}).
Criterion 3: trace linking must propagate in one general direction	
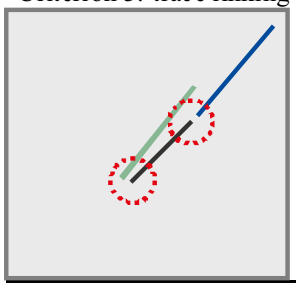	The green trace is not linked to the black trace, although it fulfills the conditions on maximum gap and "semi-parallelity" (see above). Links in the "reverse direction" are avoided by requiring that the distance between endpoints of the linked trace must always increase in every linking step.
Criterion 4: traces separated by shear fractures are not linked	
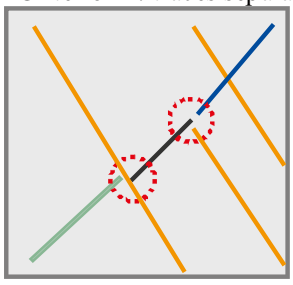	The green trace is not linked to the black trace, as the gap is intersected by a fracture that has signs of shear movement (sheared traces shown as orange lines). The blue trace is linked to the black trace, as: 1) the gap (= distance between endpoints) is not strictly intersected by any shear fracture, and 2) although the blue trace is intersected by a sheared fracture, the trace has been mapped as "intact" in the field.

Once the results of the GoLink process were integrated into GIS, an expert review of the linked traces was performed. The goal of the expert review was to assess the difference between what a trained field geologist would link to what a fully algorithmic approach would link.

As previously discussed, the advantage of using an algorithm to link traces is repeatability. The process is transparent, repeatable, and largely free of observer-induced bias. It is entirely possible that three different geologists, mapping the same outcrop, would come up with three different sets of linked traces, based on their judgment of the conditions and relationships observed. A computer program has the potential to eliminate this observer bias. However, the simple algorithm-based approach taken here cannot match the human brain when it comes to combining optical pattern analysis with experiences from past work at other field sites. In particular, a trained professional is much better at looking at the 'big pictures', i.e. the relationship of the trace not only to other traces, but to the outcrop as a whole.

A wide variety of parameters were investigated during the expert review to determine whether two traces should be linked together. Of particular importance were the following characteristics:

1. Do the traces cross or end at or near a lithologic boundary? What is the relationship between the trace and the outcrop geology (does the trace represent a break along a geological contact such as a vein or dike)?
2. Do the traces bend near a shear structures, or do they show clean shear offset?
3. Do the traces terminate against other traces? What are the termination relationships?
4. Do groups of traces appear to represent a larger-scale single feature? For example, closely-spaced parallel traces with identical orientations and morphologies may represent the results of a single fracture propagating towards a free surface.

The expert analysis noted that GoLink had problems linking the correct traces in the following specific cases:

- When there are several small traces, all of which strike in the same direction at roughly the same dip. The algorithm picks the trace closest to the endpoint of the currently-selected analysis trace. This may not necessarily be the correct trace; the results may be stereologically correct but are incorrect to the trained eye.
- When there are complex geologic structures. GoLink is designed to include a search neighbourhood around each fracture, specifically to search for parallel structures that might represent larger-scale features (minor deformation zones). However, this functionality was not used during the linking efforts. The result was that GoLink performed poorly at linking structures with any width (i.e. 2–3 parallel, closely spaced joints that represent the possible interaction of a single fracture near a free surface).
- Linking across sheared structures. GoLink has been programmed not to link structures across a shear boundary. In cases like this, geometry alone is not sufficient to match up traces, and human input is required.
- Linking very long (> 10 m) traces.

The end result of the linking process was a set of GIS files containing the linked fracture traces for each detail-mapped outcrop at Laxemar, along with a modified attribute table listing the orientations, sizes, and SICADA identification numbers of the smaller traces used to create the new linked fractures.

The orientation of a linked trace was estimated from the orientations of its individual trace components. The resultant-vector method was used for this calculation, and the relative contribution from each trace component was weighted by its trace length. The reason for weighing orientations by trace length was that larger trace exposures to the surface are assumed to be more representative of the structure that is formed in the linking procedure.

The orientation of each component fracture, i, can be characterized by its fracture pole n_i (a unit-length vector normal to the fracture plane). This fracture pole is defined by its three vector co-ordinates so that $[n_i] = [n_{ix}, n_{iy}, n_{iz}]$. The maximum resultant vector V, for a given set of N trace components, is calculated to estimate the mean pole orientation of the linked structure using the following relationship:

$$\mathbf{V} = \sum_{i=1}^{N} w_i \mathbf{n}_i \qquad \text{Equation A-1}$$

where w_i is the weight of each fracture component i, and is set equal to its trace length in meters. It should be noted it is possible to calculate two fracture poles with opposite directions from a fracture plane. Which one of these fracture-pole directions are used to define fracture orientation is generally irrelevant. However, in the calculation of the resultant vector, each fracture-pole direction must be chosen so as to maximize the resultant vector length (i.e. the fracture poles must have the same general direction). Otherwise, the resultant vector will not reflect the overall orientation of the fracture components. The default for vectors has been to choose those oriented in the lower hemisphere (i.e. standard geologic convention).

For more information on the fracture trace linking project for SDM-Site Laxemar, please see the data compilation report /Hermanson et al. 2008/.

Appendix G

Validation of SDM-Site Laxemar geological DFN model using borehole KLX27A

G.1 Introduction

The verification presented in Chapter 6 demonstrated that the DFN model has been implemented as intended, and that it quantified the predictive accuracy of the model and other conceptual alternative models. Verification is taken as a check both of the numerical implementation of the model and the predictive uncertainty inherent in the model. It does not assess the model's capability and accuracy in predicting fracturing at locations not used to develop the model. Validation, on the other hand, involves determining whether the DFN model adequately predicts the fracturing at locations (boreholes) not used to develop the model. The model is valid to the extent that it predicts the fracture pattern within the uncertainty inherent in the model itself. At the conclusion of the SDM-Site Laxemar geological site description, model validation was carried out. Borehole KLX27A, which was drilled after the SDM-Site Laxemar data freeze, was chosen as the target for the validation. The validation was performed only for the portion of KLX27A that was within fracture domain FSM_W. There were two validation metrics selected which are relevant to the DFN model's intended use:

- Borehole fracture intensity (P_{10}) over 3 m and 15 m long intervals (bins).
- Total count of minor-deformation zones (MDZ).

G.2 Description of KLX27A

Cored borehole KLX27A is located in the southwest corner of the Laxemar local model area (Figure G-1). The borehole trends approximately north-south and is inclined to the north at approximately 65°. The borehole begins in fracture domain FSM_S, intersects deformation zone ZSMNW042A at an elevation of approximately –170 m, and proceeds into fracture domain FSM_W. The borehole is approximately 649 m long, of which 209 m is inside FSM_S, 47 m is inside ZSMNW042A, and 393 m is inside FSM_W.

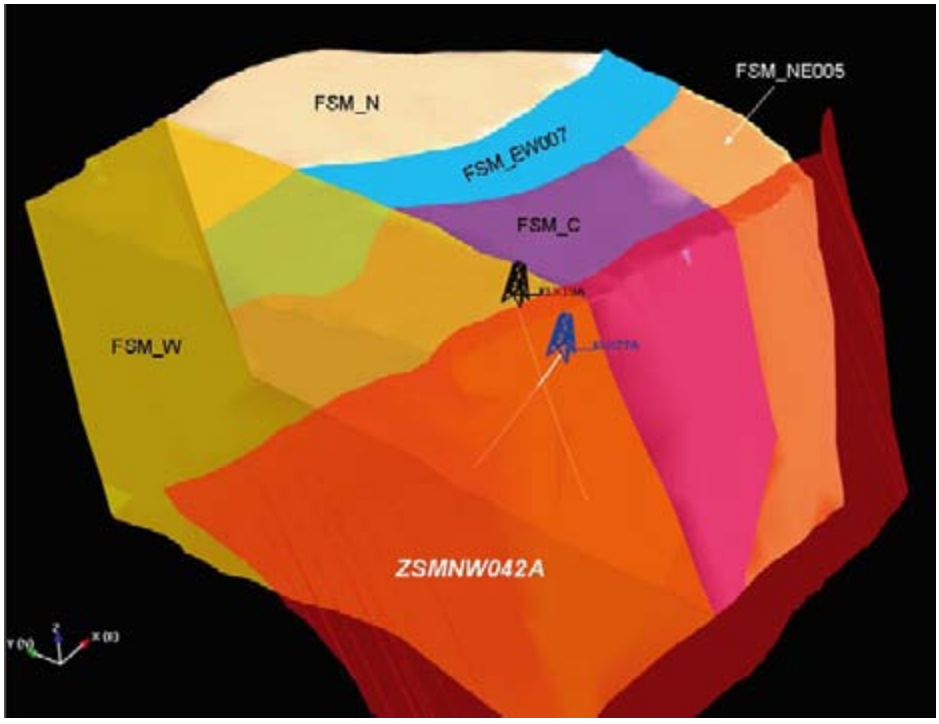

Figure G-1. *Location of cored boreholes KLX19A and KLX27A with respect to SDM Laxemar fracture domains. Note that fracture domain FSM_S has been removed to better illustrate the relationship between the two boreholes and ZSMNW042A.*

The extended single-hole interpretation of KLX27A /Carlsten et al. 2008/ suggests that the borehole lies entirely within rock domain RSMD01. Nine possible deformation zones or minor deformation zones were mapped in KLX27A; only one of them (ZSMNW042A) has been matched to a structure included in the SDM-Site Laxemar deterministic deformation zone (DZ) model.

All interpretation made from the fractures in KLX27A utilise fractures inside fracture domain FSM_W and outside DZ and MDZ identified during the extended single-hole interpretation. Fractures not visible in BIPS are included in the analysis as this is a validation based primarily on fracture intensity and not on fracture set orientations.

Fracture orientations are similar to those found elsewhere in the Laxemar local scale model volume. There are four general classes of fracture orientations visible in the data from KLX27A; ENE and WNW-striking, N-S striking, and subhorizontally- to moderately-dipping fractures that generally strike N-S. However, there are a few key differences between fracture orientations in KLX27A and the fracture sets parameterised in the SDM-Site Laxemar geological DFN global orientation model for domain FSM_W (Figure G-2):

- The mean pole vector of north-south striking fractures appears to be rotated approximately 20°–30° clockwise, relative to the rest of fracture domain FSM_W.
- The relative intensity of subhorizontally-dipping fractures is dramatically less than in the rest of fracture domain FSM_W.
- The relative intensity of west-northwest striking fractures is significantly higher in KLX27A than in the rest of fracture domain FSM_W. Also, fractures with this strike in KLX27A are slightly more likely to be north-northeast dipping than the rest of domain FSM_W.

The patterns of fracture orientations and relative set intensity in KLX27A are very similar to those seen in cored borehole KLX19A (Figure G-3), which is also located in the southern half of fracture domain FSM_W in the footwall of deformation zone ZSMNW042A. Both boreholes show a decrease in the relative intensity of the SH set and a corresponding increase in the intensity of the WNW-striking set. The WNW set in KLX19A is predominantly north-dipping, while in KLX27A it is predominantly south-dipping. The relative set intensity patterns in both boreholes are significantly different from the average values for domain FSM_W; this suggests that the zone of influence surrounding deformation zone ZSMNW042A may extend a substantial distance into FSM_W, that the rock volume just north of ZSMNW042A may be different enough to warrant inclusion as a separate fracture domain, or that the variability in fracture orientations inside domain FSM_W is larger than previously thought.

Fractures intersecting KLX27A were assigned to orientation sets using the methodology described in Section 3.3. A summary of the set parameters and probability field are presented below in Figure G-4. An examination of the location of the mean pole vector for the fitted fracture sets (Table G-1 and Figure G-4) suggests that the ENE, WNW, and SH sets are fairly close to the global orientation model (given the uncertainty in determining strike for subhorizontally-dipping fractures for the SH set), but that the mean pole vectors of fractures in the N-S set in KLX27A are somewhat different than the global orientation model values.

Relative fracture intensities in KLX27A and KLX19A differ somewhat from the average values for domain FSM_W. The average values of relative set intensities for fracture domain FSM_W were computed using the arithmetic average P_{10} of all fractures (open and sealed, Visible in BIPS and Not Visible in BIPS) over 3 m long borehole intervals. As observed P_{10} is the verification metric, we have not corrected either the average values of P_{10} for FSM_W nor the sampled P_{10} values for KLX19A or KLX27A for orientation bias using Terzaghi's method; the goal of the validation is to see whether predicted P_{10}s (sampling bias and all) can be predicted by the geological DFN model.

The total borehole fracture intensity (P_{10}) for all sets combined differs significantly in KLX27A and KLX19A from the average value in FSM_W (Table G-2); in these boreholes total P_{10} is approximately one-half the average value in FSM_W.

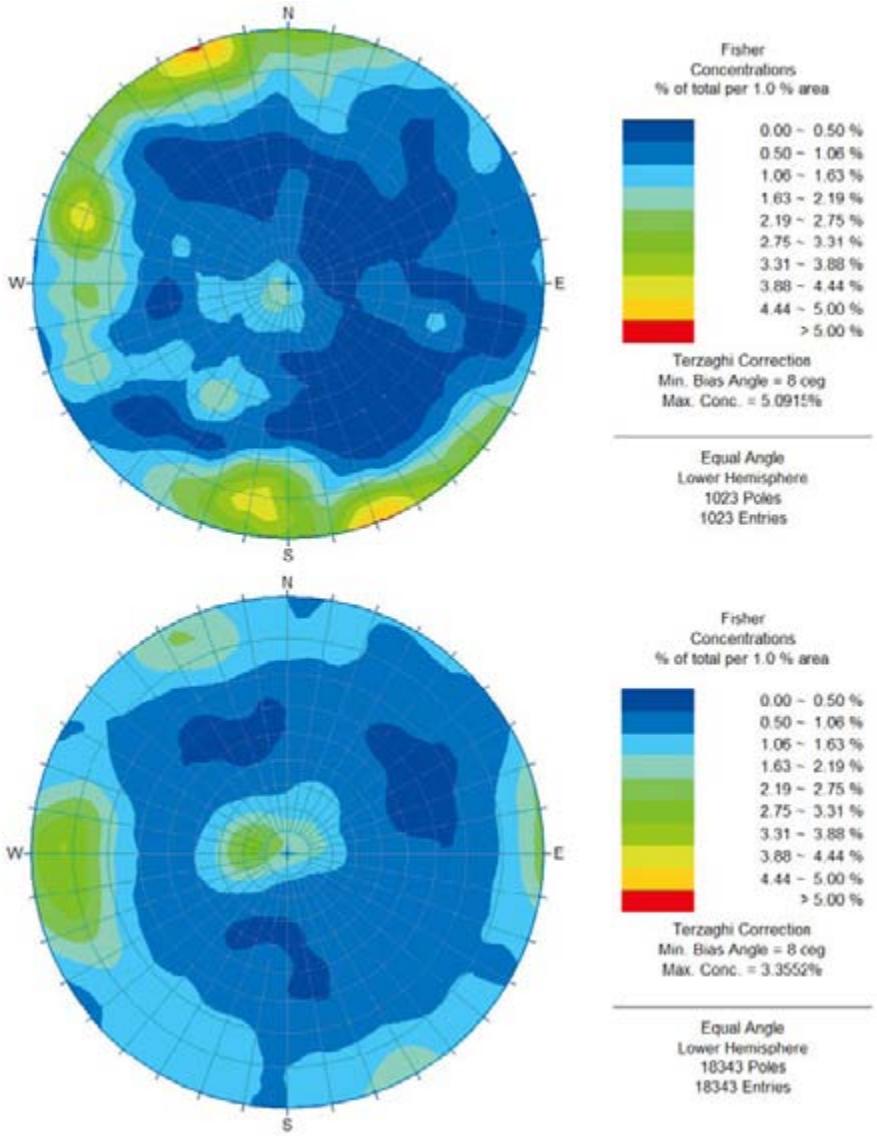

Figure G-2. *Comparison of fracture orientations in FSM_W inside KLX27A (top) to domain FSM_W as a whole (bottom). Note the reduced prominence of subhorizontally-dipping fractures and the apparent rotation of the N-S orientation set by ~30° clockwise).*

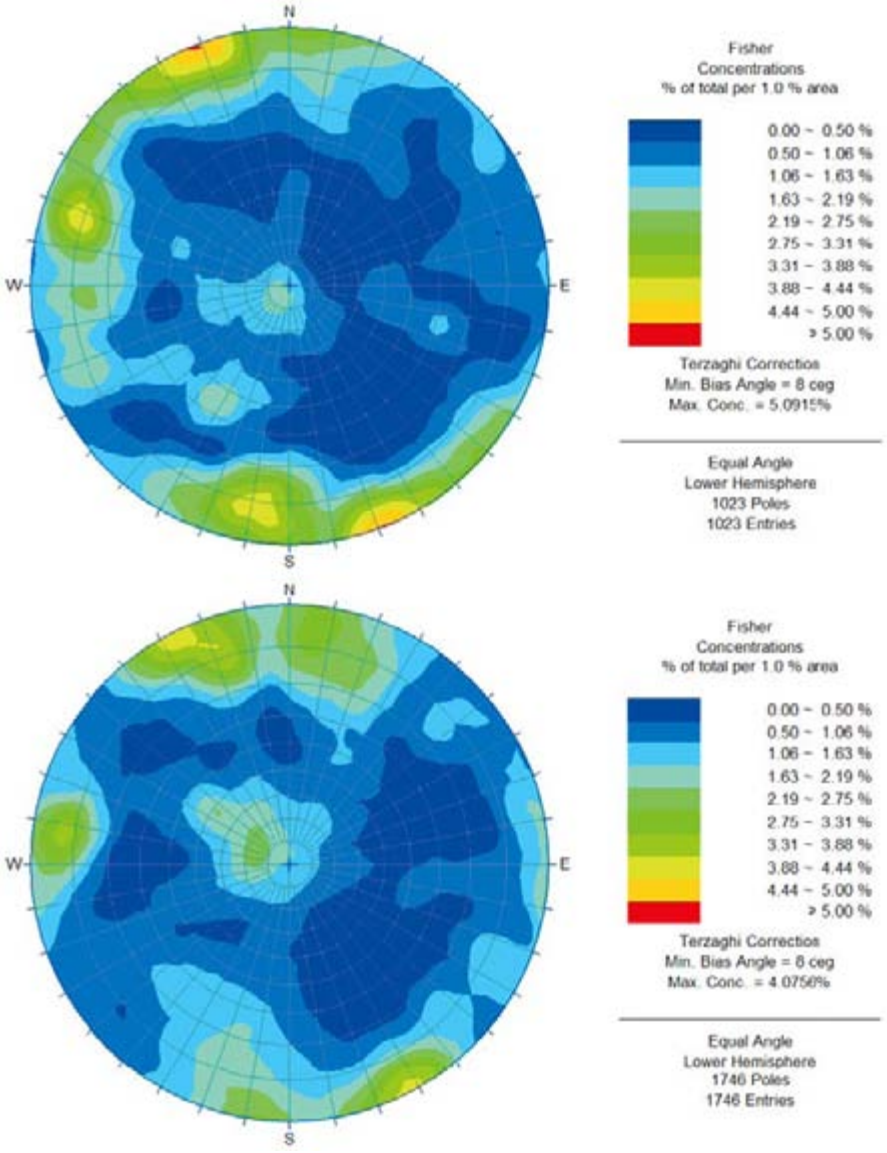

Figure G-3. *Comparison of fracture orientations in KLX27A (top) and KLX19A (bottom). Both boreholes have significant portions of their length inside the footwall of ZSMNW042A.*

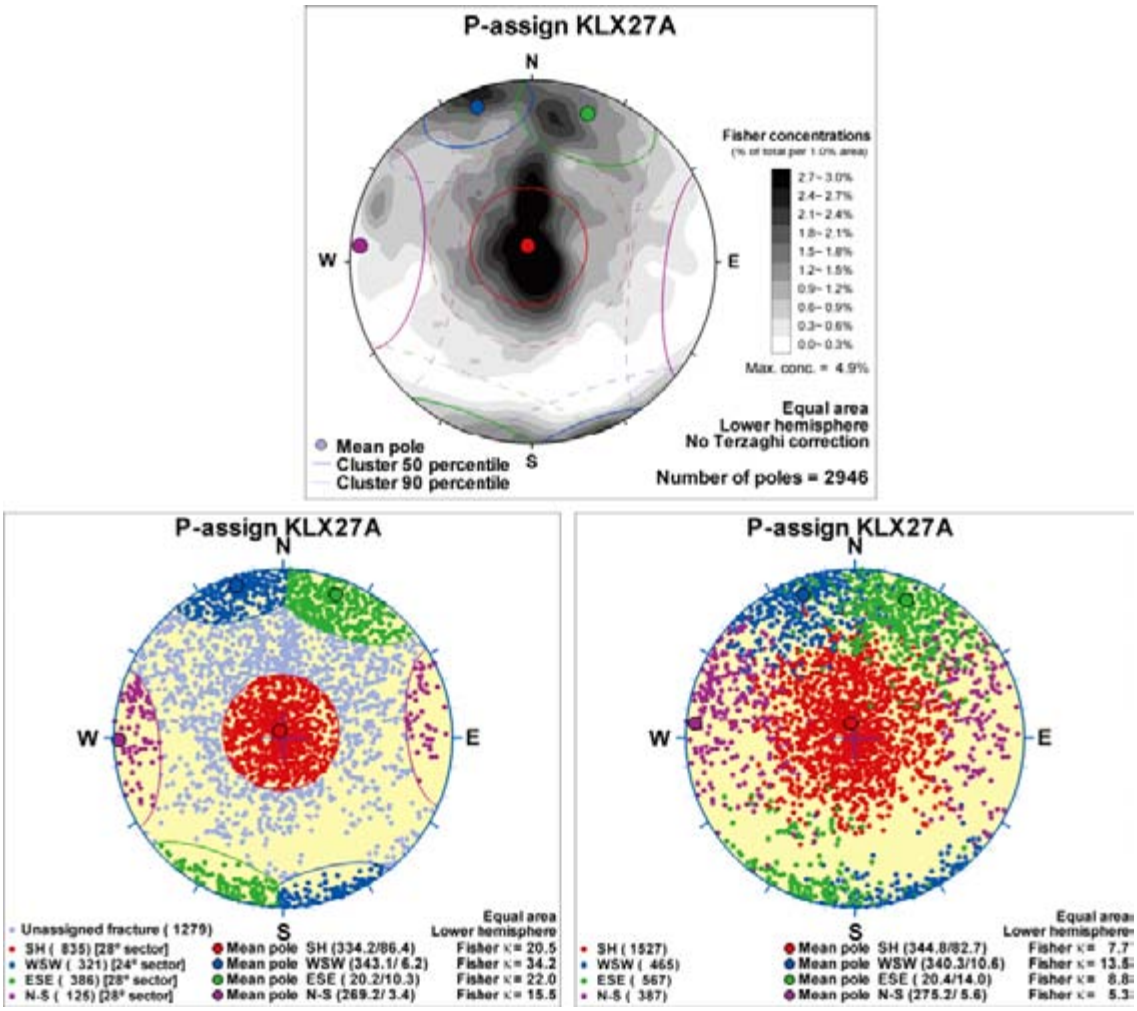

Figure G-4. *Assignment of fractures in KLX27A to orientation sets. Note that these figures illustrate fractures in both FSM_W and FSM_S; the SDM-Site Laxemar geological DFN model utilises a global orientation model.*

Table G-1. Comparison of mean pole vector orientation for fracture sets in FSM_W and KLX27A. Mean pole vector orientation calculated using the resultant vector method (Section 3.3) after fractures were divided into orientation sets using soft-sectoring.

Orientation Set	Global Set Mean Pole		KLX27A Set Mean Pole		Solid Angle
	Trend (°)	Plunge (°)	Trend (°)	Plunge (°)	(°)
ENE	340.30	0.50	339.60	5.50	5.05
NS	269.10	1.70	275.00	11.90	11.76
SH	335.10	87.10	285.80	82.50	6.02
WNW	24.10	3.10	18.90	5.80	5.84

Table G 2. P10 fracture intensity in KLX19A, KLX27A, and FSM_W, calculated using 3 m long borehole intervals. Note that this data is not Terzaghi-corrected.

Fracture Set	Statistic	Borehole P_{10} KLX19A	KLX27A	FSM_W
ENE	Mean	0.466	0.531	0.553
ENE	Median	0.333	0.333	0.333
ENE	Std. Dev.	0.660	0.531	0.685
ENE	Min	0.000	0.000	0.000
ENE	Max	4.000	2.333	5.000
NS	Mean	0.427	0.507	1.209
NS	Median	0.333	0.333	0.667
NS	Std. Dev.	0.579	0.745	1.298
NS	Min	0.000	0.000	0.000
NS	Max	2.667	3.667	9.000
SH	Mean	1.256	1.014	2.604
SH	Median	0.667	0.667	2.000
SH	Std. Dev.	1.681	1.150	2.446
SH	Min	0.000	0.000	0.000
SH	Max	11.333	3.667	14.333
WNW	Mean	0.702	0.528	0.732
WNW	Median	0.333	0.333	0.333
WNW	Std. Dev.	0.912	0.585	0.826
WNW	Min	0.000	0.000	0.000
WNW	Max	4.000	2.333	6.333
Total	Mean	2.850	2.580	5.098

An analysis of fracture intensity as a function of depth in KLX27A (Figure G-5) suggests that the borehole can be divided into three distinct mechanical layers. The boundary appears to be a zone of rock between elevation ~ –350 m and ~ –410 m; the fractures on either side of this zone display different intensity patterns (different slope of the CFI plot). The mechanical layer boundaries do not line up with known rock domain, fracture domain, or deformation zone boundaries, and do not show a strong correlation to any observed changes in rock type in the core logs. The cause of this zone of unusually good-quality rock between elevation ~ –350 m and –410 m is unknown.

To rule out the question of whether the differences in observed relative fracture intensity patterns are due to orientation bias, P_{32} values for fractures over 3 m long borehole intervals in KLX27A were computed, and compared to values derived from 3 m long intervals in all other boreholes inside domain FSM_W using Wang's C_{13}. The P_{32} values show the same patterns in terms of relative intensity as the P_{10} values, which indicates that the differences between KLX27A and the rest of FSM_W are not due to sampling orientation bias.

G.3 Methodology

The validation methodology involved Monte Carlo-style simulation of discrete fracture networks at two intensity scales: full-model intensity, which represents fracture sizes from r_0 to 564.2 m, and at a reduced intensity representing the MDZ size range (Section 5. For each alternative model case, ten simulations were run. Model case FUL2 was interrupted after eight Monte Carlo runs by a power failure on the modelling server. The eight completed runs were judged a suitable sample to characterise stochastic variability; the remaining two runs were not completed.

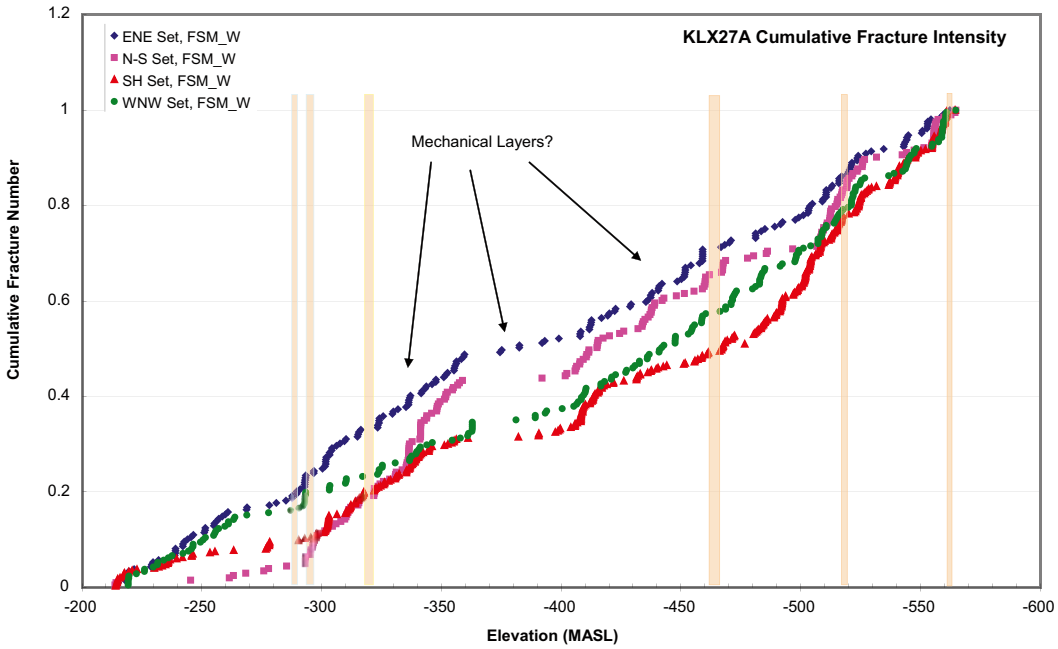

Figure G-5. *Cumulative fracture intensity (CFI) plot as a function of fracture orientation set, borehole KLX27A. Tan bars indicate locations of mapped DZ and MDZ.*

Table G-3. P_{32} fracture intensity by set in KLX27A and FSM_W, calculated using the Wang approximation for all boreholes over 3 m long intervals.

Statistic	ENE FSM_W	KLX27A	N-S FSM_W	KLX27A	SH FSM_W	KLX27A	WNW FSM_W	KLX27A
Mean	1.70	1.34	3.88	1.82	3.33	1.27	2.08	1.26
Median	1.19	0.84	2.54	1.20	2.50	0.84	1.36	0.79
Std. Dev.	2.10	1.34	4.21	2.67	3.09	1.44	2.29	1.39
Min.	0.00	0.00	0.00	0.00	0.00	0.00	0.00	0.00
Max.	14.75	5.90	31.54	13.16	17.46	6.28	14.70	5.56

For the full-model intensity, a 70 m by 30 m by 45 m simulation volume (Figure G-6) was chosen to minimize computational time. Borehole KLX27A was divided into nine sections (KLX27A1 through KLX27A9 in below), each 45 m long, along which P_{10} was computed over 3 m long borehole intervals. The size model parameterisation for alternative model case FL2 includes small values for the minimum size (r_0) parameter. This results in the generation of lots of small fractures that do not intersect the target borehole, but consume considerable simulation time. To reduce simulation time to reasonable lengths (2–3 days), case FL2 was generated within a sub-region of the simulation volume in which only three borehole sections were used (KLX27A4 through KLX27A6).

For the MDZ-size range, a rectangular volume 4,690 m by 4,500 m by 2,500 m was used in the validation simulations (Figure G-7). The simulation volume was designed to be large enough to include FSM_S, FSM_W, and the lateral extents of ZSMNW042A. In these simulations, the complete length of KLX27A in FSM_W was used, and the total count of MDZ was tracked. The total count of MDZ, rather than MDZ P_{10}, was used in the validation because a formal analysis of MDZ-fracture orientations and a corresponding MDZ set division has not yet been performed for data from KLX27A. Without knowing which set the observed MDZ 'belong to', it is not possible to directly compare simulated MDZ P_{10} to observed MDZ P_{10}.

The minimum size of MDZ was taken directly from Verification Case SI-3 (Section 5.5) and utilized the surface trace rollover method (Table 5-18). The minimum radius for SH-oriented MDZ was set at the functional cut-off of 75 m (Section 5.5). The P_{32} of fractures within the MDZ size range was calculated using Equation 6-1.

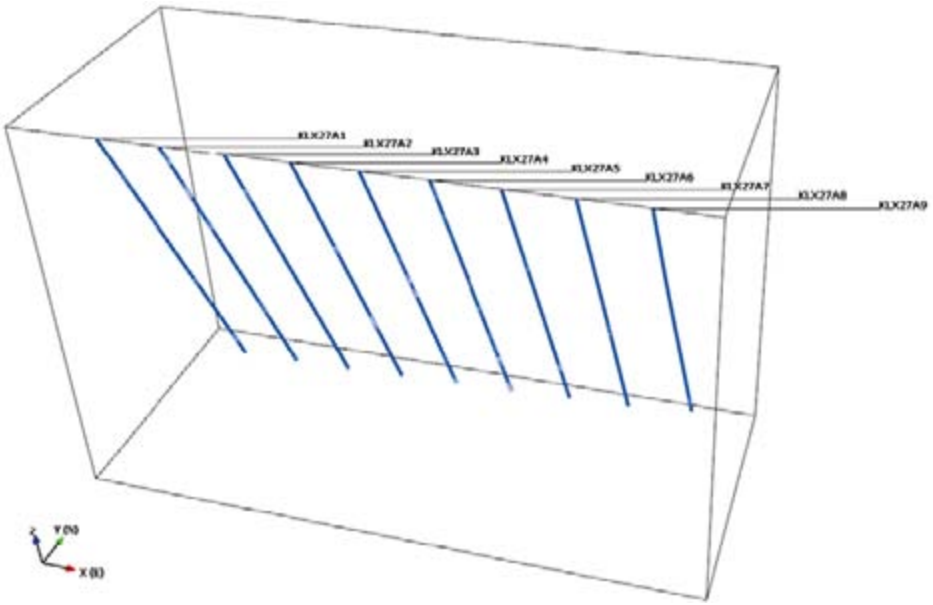

Figure G-6. *Simulation region and boreholes used for full-intensity case simulations. Each borehole represents a 45 m long section of KLX27A, with the exact same borehole trend and plunge, as recorded in SICADA table p_object_location.*

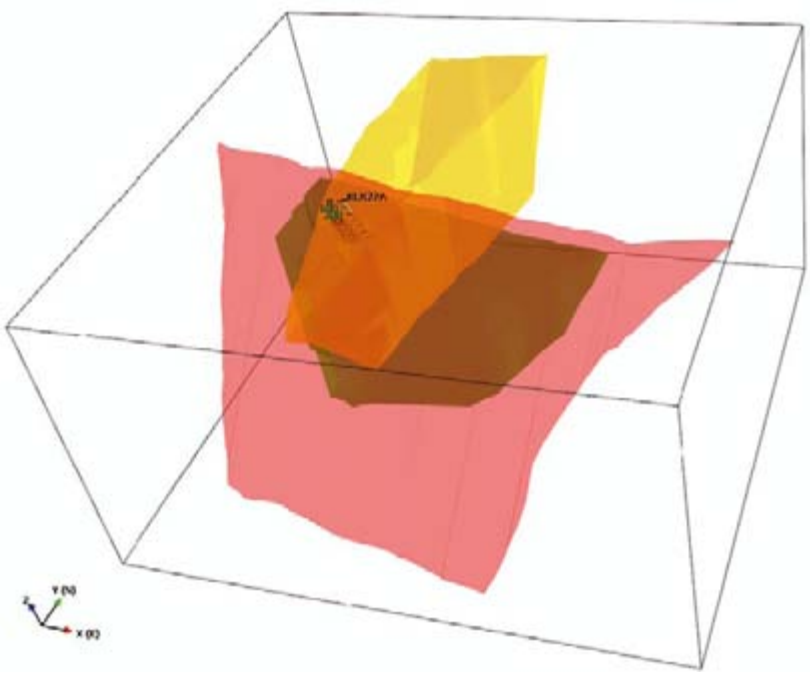

Figure G-7. *Simulation volume for MDZ size-range cases.*

G.4 Validation results

G.4.1 Inherent model uncertainty

Verification case SI-4 was used to calculate the inherent model uncertainty for predicting borehole fracture intensity. Verification case SI-4 consisted of generating 20 realizations of each size-intensity model alternative, sampling the resulting stochastic DFN realisations, and comparing the simulated borehole P_{10} to measured P_{10} values.

Using the means and standard deviations for the simulated P_{10} results (Table 5-23 through Table 5-26) and assuming that the differences between the simulated P_{10} and the measured P_{10} are normally distributed (the Central Limit Theorem), the upper and lower 95% confidence intervals were calculated for each borehole and alternative model in Verification Case SI-4. Example results of this calculation for the BMU model are shown in Table G-4. The confidence limits are estimated from the standard deviations for SI-4, assuming a population of ten. Values of minimum, maximum, mean and median confidence interval width are reported for each set based upon all of the boreholes simulated in SI-4.

Table G-4. 95% confidence limits on borehole P_{10} from verification case SI-4, BMU alternative model.

Model Alternative	Fracture Set	Borehole	P_{10} Simulated	Std. Dev.	95% CL	Min	Max	Mean	Median
BMU	ENE	KLX03	0.447	0.100	0.062				
BMU	ENE	KLX03	0.487	0.114	0.070				
BMU	ENE	KLX04	0.467	0.186	0.115				
BMU	ENE	KLX08	0.493	0.110	0.068				
BMU	ENE	KLX10	0.407	0.111	0.069				
BMU	ENE	KLX15A	0.413	0.147	0.091				
BMU	ENE	KLX15A	0.367	0.145	0.090				
BMU	ENE	KLX18A	0.553	0.118	0.073	0.06	0.12	0.08	0.07
BMU	N-S	KLX03	0.800	0.206	0.128				
BMU	N-S	KLX03	0.807	0.184	0.114				
BMU	N-S	KLX04	0.587	0.150	0.093				
BMU	N-S	KLX08	1.227	0.310	0.192				
BMU	N-S	KLX10	0.567	0.161	0.100				
BMU	N-S	KLX15A	1.233	0.227	0.141				
BMU	N-S	KLX15A	1.533	0.157	0.097				
BMU	N-S	KLX18A	0.587	0.143	0.089	0.09	0.19	0.12	0.11
BMU	SH	KLX03	2.147	0.319	0.197				
BMU	SH	KLX03	2.360	0.528	0.327				
BMU	SH	KLX04	2.160	0.349	0.216				
BMU	SH	KLX08	2.007	0.413	0.256				
BMU	SH	KLX10	2.253	0.505	0.313				
BMU	SH	KLX15A	1.700	0.395	0.245				
BMU	SH	KLX15A	1.840	0.260	0.161				
BMU	SH	KLX18A	2.347	0.228	0.142	0.14	0.33	0.23	0.23
BMU	WNW	KLX03	0.747	0.334	0.207				
BMU	WNW	KLX03	0.827	0.265	0.164				
BMU	WNW	KLX04	0.813	0.497	0.308				
BMU	WNW	KLX08	0.973	0.431	0.267				
BMU	WNW	KLX10	0.680	0.263	0.163				
BMU	WNW	KLX15A	1.107	0.462	0.286				
BMU	WNW	KLX15A	0.973	0.361	0.224				
BMU	WNW	KLX18A	0.813	0.358	0.222	0.16	0.31	0.23	0.22

G.4.2 Results of full-intensity cases

The results of the full-intensity validation cases are presented below in Table G-6 and Table G-7. For the 3 m bins, the P_{10} of the ENE fracture set is well-predicted by all five alternative models, with a slight over-estimation of borehole P_{10} by approximately 30%. The prediction results of the remaining three sets are a bit poorer; all five alternative model cases predict twice the observed intensity of the N-S set, and nearly three times the intensity of the SH-set. The WNW set falls between the ENE and N-S/SH sets; it over-predicts fracturing in KLX27A by approximately 75%.

In all cases, the difference between alternative models is on the order of 10%, which is much smaller than the difference between any individual model and the data observed in borehole KLX27A. The results for 15 m bins are very similar to the results for the 3 m bins, though the average intensities in the observed data do decrease slightly.

The upper and lower 95% confidence limits on the mean are shown in Table G-4. The Mean Upper (UCL) and Lower (LCL) confidence limits are calculated by using the mean and average confidence limits calculated from verification case SI-4 (see Table G-4 for an example). The mean or maximum value for a given alternative model case is either added (UCL) or subtracted (LCL) from the predicted P_{10} value for that case to determine the upper and lower confidence intervals. All confidence intervals are based on a sample size of ten Monte-Carlo runs, except for model FUL1, which is based on a sample size of eight runs.

Table G-6 and Table G-7 show that the confidence limits derived the mean confidence interval width predict fairly accurately the set intensity for FSM_W, but over-predict the intensity for KLX27A. However, if the confidence limits are based on the maximum value, under the assumption that KLX27A is not a representative sample of domain FSM_W but rather an extremal value, then the predicted values are fairly close to the measured values with the exception of the SH set.

The validation results suggest that all five top alternative models over-predict P_{10} in borehole KLX27A. However, as discussed in Section G.3, borehole KLX27A does not show fracturing typical of what is seen elsewhere in domain FSM_W. The total P_{10} of KLX27A is about one-half of the average value of total P_{10} for FSM_W, and the relative fracture intensity patterns are significantly different. As a check of the reasonableness of the DFN model at predicting the average values within a single fracture domain, a quick model verification using P_{10} was performed (Table G-8). It tested the observed average values of P_{10} in domain FSM_W against the simulation results. The verification shows that the mean values of P_{10} for domain FSM_W are well-characterised by all five of the top-ranked alternative models; the maximum error between observed and simulated P_{10} is only 25%. This is well inside the uncertainty ranges documented in Chapter 6.

The solution would not improve significantly through the use of the Gamma or Weibull distributions (Sections 3.6 and 4.4.7) to simulate the distribution of fracture intensity in FSM_W. The assumption behind using these models is that intensity variability is uncorrelated in space, and that the Gamma or Weibull distribution will reproduce the variability of P_{32} over the entire fracture domain. It will not account for localized conditions where a sizeable volume of rock is significantly different from the domain as a whole.

G.4.3 Results of MDZ size range cases

The results of the validation simulations for fractures within the MDZ size range are presented below in Table G-9 and Table G-10. There is very little difference in terms of MDZ P_{32} between the various alternative model cases. In addition, all five cases (the recommended BMU and four other alternative models) do an excellent job of predicting the total number of MDZ-sized fractures that intersect KLX27A. Figure G-8 through Figure G-11 illustrate the results from a single iteration of the BMU alternative; fractures are generated within the MDZ simulation region described in Section G.3 and illustrated in Figure G-7.

Table G-5. 95% confidence intervals for borehole P_{10} for the top five size-intensity model alternatives.

Model Alternative	Fracture Set	Mean	Median	Max	Predicted P_{10}	LCL Mean	UCL Mean	LCL Max	UCL Max	KLX27A	FSM_W
BM	ENE	0.108	0.117	0.131	0.697	0.589	0.805	0.566	0.828	0.531	0.553
BM	N-S	0.131	0.125	0.163	1.074	0.943	1.205	0.911	1.237	0.507	1.209
BM	SH	0.262	0.251	0.362	2.726	2.464	2.988	2.364	3.088	1.014	2.604
BM	WNW	0.134	0.136	0.167	0.861	0.727	0.995	0.694	1.028	0.528	0.732
BMU	ENE	0.080	0.072	0.115	0.694	0.614	0.774	0.579	0.809	0.531	0.553
BMU	N-S	0.119	0.107	0.192	1.045	0.926	1.164	0.853	1.237	0.507	1.209
BMU	SH	0.232	0.231	0.327	2.653	2.421	2.885	2.326	2.980	1.014	2.604
BMU	WNW	0.230	0.223	0.308	0.873	0.643	1.103	0.565	1.181	0.528	0.732
FL1	ENE	0.142	0.135	0.202	0.681	0.539	0.823	0.479	0.883	0.531	0.553
FL1	N-S	0.127	0.124	0.183	1.069	0.942	1.196	0.886	1.252	0.507	1.209
FL1	SH	0.191	0.194	0.288	2.760	2.569	2.951	2.472	3.048	1.014	2.604
FL1	WNW	0.161	0.158	0.248	0.914	0.753	1.075	0.666	1.162	0.528	0.732
FL2	ENE	0.164	0.165	0.220	0.685	0.521	0.849	0.465	0.905	0.531	0.553
FL2	N-S	0.165	0.177	0.226	1.093	0.928	1.258	0.867	1.319	0.507	1.209
FL2	SH	0.293	0.278	0.530	2.733	2.440	3.026	2.203	3.263	1.014	2.604
FL2	WNW	0.479	0.474	0.652	0.908	0.429	1.387	0.256	1.560	0.528	0.732
FUL2	ENE	0.238	0.236	0.279	0.686	0.448	0.924	0.407	0.965	0.531	0.553
FUL2	N-S	0.159	0.169	0.240	0.996	0.837	1.155	0.756	1.236	0.507	1.209
FUL2	SH	0.476	0.471	0.690	2.700	2.224	3.176	2.010	3.390	1.014	2.604
FUL2	WNW	0.490	0.478	0.779	0.867	0.377	1.357	0.088	1.646	0.528	0.732

Table G-6. Validation results for 3 m bins, full-intensity cases.

Fracture Set	Alternative Model (Rank / Name)						Data KLX27A	Average FSM_W	Simulation Results versus KLX27A Data Percent Error				
	Rank	1	2	3	4	5							
	Statistic	BMU	FL2	BM	FL1	FUL2			BMU	FL2	BM	FL1	FUL2
ENE	Mean	0.694	0.685	0.697	0.681	0.686	0.531	0.553	30.6%	29.0%	31.1%	28.2%	29.1%
ENE	Median	0.667	0.667	0.667	0.667	0.667	0.333	0.333	100.0%	100.0%	100.0%	100.0%	100.0%
ENE	Std. Dev.	0.471	0.519	0.486	0.492	0.506	0.531	0.685	11.3%	2.2%	8.4%	7.4%	4.7%
ENE	Min	0.000	0.000	0.000	0.000	0.000	0.000	0.000	n/a	n/a	n/a	n/a	n/a
ENE	Max	3.333	3.333	2.667	3.333	3.333	2.333	5.000	n/a	n/a	n/a	n/a	n/a
NS	Mean	1.045	1.093	1.074	1.069	0.996	0.507	1.209	106.2%	115.7%	112.0%	110.9%	96.6%
NS	Median	1.000	1.000	1.000	1.000	1.000	0.333	0.667	200.0%	200.0%	200.0%	200.0%	200.0%
NS	Std. Dev.	0.616	0.590	0.599	0.588	0.589	0.745	1.298	17.3%	20.7%	19.6%	21.1%	20.9%
NS	Min	0.000	0.000	0.000	0.000	0.000	0.000	0.000	n/a	n/a	n/a	n/a	n/a
NS	Max	3.667	3.333	3.667	3.000	3.333	3.667	9.000	n/a	n/a	n/a	n/a	n/a
SH	Mean	2.653	2.733	2.726	2.760	2.700	1.014	2.604	161.8%	169.7%	169.0%	172.3%	166.4%
SH	Median	2.667	2.667	2.667	2.667	2.667	0.667	2.000	300.0%	300.0%	300.0%	300.0%	300.0%
SH	Std. Dev.	0.937	1.014	0.961	1.014	0.936	1.150	2.446	18.5%	11.9%	16.4%	11.8%	18.6%
SH	Min	0.333	0.000	0.000	0.000	0.000	0.000	0.000	n/a	n/a	n/a	n/a	n/a
SH	Max	6.667	6.000	6.333	6.667	6.667	3.667	14.333	n/a	n/a	n/a	n/a	n/a
WNW	Mean	0.873	0.908	0.861	0.914	0.867	0.528	0.732	65.2%	71.8%	63.0%	72.9%	64.1%
WNW	Median	0.667	1.000	0.667	1.000	0.667	0.333	0.333	100.0%	200.0%	100.0%	200.0%	100.0%
WNW	Std. Dev.	0.557	0.540	0.547	0.554	0.541	0.585	0.826	4.9%	7.7%	6.5%	5.4%	7.5%
WNW	Min	0.000	0.000	0.000	0.000	0.000	0.000	0.000	n/a	n/a	n/a	n/a	n/a
WNW	Max	3.667	3.000	3.000	3.000	3.333	2.333	6.333	n/a	n/a	n/a	n/a	n/a

Table G-7. Validation results for 15 m bins, full-intensity cases.

Fracture Set	Alternative Model (Rank / Name)					Data KLX27A	Average FSM_W	Simulation Results versus KLX27A Data Percent Error				
	Rank	1	2	3	4	5						
	Statistic	BMU	FL2	BM	FL1	FUL2		BMU	FL2	BM	FL1	FUL2
ENE	Mean	0.694	0.685	0.697	0.681	0.676	0.495	0.517	40.1%	38.4%	40.6%	37.5%	36.6%
ENE	Median	0.667	0.667	0.667	0.667	0.667	0.533	0.400	25.0%	25.0%	25.0%	25.0%	25.0%
ENE	Std. Dev.	0.195	0.226	0.218	0.217	0.225	0.224	0.430	12.9%	1.2%	2.6%	2.8%	0.5%
ENE	Min	0.133	0.200	0.267	0.067	0.200	0.133	0.000	n/a	n/a	n/a	n/a	n/a
ENE	Max	1.333	1.200	1.333	1.467	1.533	0.933	3.067	n/a	n/a	n/a	n/a	n/a
NS	Mean	1.045	1.093	1.074	1.069	0.993	0.460	1.135	127.0%	137.5%	133.4%	132.2%	115.8%
NS	Median	1.067	1.100	1.067	1.067	1.000	0.267	0.833	300.0%	312.5%	300.0%	300.0%	275.0%
NS	Std. Dev.	0.262	0.248	0.275	0.243	0.271	0.464	0.890	43.5%	46.5%	40.8%	47.6%	41.6%
NS	Min	0.267	0.467	0.400	0.533	0.333	0.000	0.000	n/a	n/a	n/a	n/a	n/a
NS	Max	1.667	1.867	2.000	1.733	1.733	1.800	4.000	n/a	n/a	n/a	n/a	n/a
SH	Mean	2.653	2.733	2.726	2.760	2.692	0.895	2.523	196.4%	205.3%	204.5%	208.3%	200.7%
SH	Median	2.600	2.667	2.733	2.800	2.667	0.733	2.000	254.5%	263.6%	272.7%	281.8%	263.6%
SH	Std. Dev.	0.441	0.429	0.429	0.471	0.461	0.632	1.923	30.2%	32.1%	32.2%	25.5%	27.0%
SH	Min	1.467	1.667	1.667	1.467	1.400	0.000	0.000	n/a	n/a	n/a	n/a	n/a
SH	Max	4.200	3.733	4.067	4.400	3.800	2.000	9.600	n/a	n/a	n/a	n/a	n/a
WNW	Mean	0.873	0.908	0.861	0.914	0.867	0.483	0.691	80.9%	88.2%	78.5%	89.4%	79.8%
WNW	Median	0.867	0.900	0.867	0.933	0.867	0.533	0.533	62.5%	68.7%	62.5%	75.0%	62.5%
WNW	Std. Dev.	0.255	0.236	0.234	0.249	0.257	0.223	0.540	14.2%	5.9%	4.8%	11.4%	15.5%
WNW	Min	0.200	0.333	0.267	0.267	0.333	0.067	0.000	n/a	n/a	n/a	n/a	n/a
WNW	Max	1.600	1.467	1.600	1.800	1.667	0.933	3.133	n/a	n/a	n/a	n/a	n/a

Table G-8. Comparison of validation results for 3 m bins to average values for domain FSM_W, full-intensity cases.

Fracture Set	Alternative Model (Rank / Name)					Data KLX27A	Average FSM_W	Simulation Results versus FSM_W Data Percent Error				
	Rank	1	2	3	4	5						
	Statistic	BMU	FL2	BM	FL1	FUL2			BMU	FL2	BM	FL1	FUL2
ENE	Mean	0.694	0.685	0.697	0.681	0.686	0.531	0.553	25.4%	23.9%	25.9%	23.1%	24.0%
ENE	Median	0.667	0.667	0.667	0.667	0.667	0.333	0.333	100.0%	100.0%	100.0%	100.0%	100.0%
ENE	Std. Dev.	0.471	0.519	0.486	0.492	0.506	0.531	0.685	31.3%	24.2%	29.0%	28.2%	26.2%
ENE	Min	0.000	0.000	0.000	0.000	0.000	0.000	0.000	n/a	n/a	n/a	n/a	n/a
ENE	Max	3.333	3.333	2.667	3.333	3.333	2.333	5.000	n/a	n/a	n/a	n/a	n/a
NS	Mean	1.045	1.093	1.074	1.069	0.996	0.507	1.209	13.5%	9.5%	11.1%	11.6%	17.5%
NS	Median	1.000	1.000	1.000	1.000	1.000	0.333	0.667	50.0%	50.0%	50.0%	50.0%	50.0%
NS	Std. Dev.	0.616	0.590	0.599	0.588	0.589	0.745	1.298	52.6%	54.5%	53.9%	54.7%	54.6%
NS	Min	0.000	0.000	0.000	0.000	0.000	0.000	0.000	n/a	n/a	n/a	n/a	n/a
NS	Max	3.667	3.333	3.667	3.000	3.333	3.667	9.000	n/a	n/a	n/a	n/a	n/a
SH	Mean	2.653	2.733	2.726	2.760	2.700	1.014	2.604	1.9%	5.0%	4.7%	6.0%	3.7%
SH	Median	2.667	2.667	2.667	2.667	2.667	0.667	2.000	33.3%	33.3%	33.3%	33.3%	33.3%
SH	Std. Dev.	0.937	1.014	0.961	1.014	0.936	1.150	2.446	61.7%	58.6%	60.7%	58.5%	61.7%
SH	Min	0.333	0.000	0.000	0.000	0.000	0.000	0.000	n/a	n/a	n/a	n/a	n/a
SH	Max	6.667	6.000	6.333	6.667	6.667	3.667	14.333	n/a	n/a	n/a	n/a	n/a
WNW	Mean	0.873	0.908	0.861	0.914	0.867	0.528	0.732	19.2%	24.0%	17.6%	24.8%	18.5%
WNW	Median	0.667	1.000	0.667	1.000	0.667	0.333	0.333	100.0%	200.0%	100.0%	200.0%	100.0%
WNW	Std. Dev.	0.557	0.540	0.547	0.554	0.541	0.585	0.826	32.6%	34.6%	33.7%	33.0%	34.4%
WNW	Min	0.000	0.000	0.000	0.000	0.000	0.000	0.000	n/a	n/a	n/a	n/a	n/a
WNW	Max	3.667	3.000	3.000	3.000	3.333	2.333	6.333	n/a	n/a	n/a	n/a	n/a

G.5 Conclusions

The use of cored borehole KLX27A as a validation case for the SDM-Site Laxemar geological DFN model was an interesting exercise. The validation suggested that the model makes accurate predictions of the average fracture intensity characteristics of FSM_W, but over-predicts the intensity for cored borehole KLX27A, especially the subhorizontal set. Further analysis indicated that borehole KLX27A (and its neighbour KLX19A) sample a volume of rock that is noticeably different than the rest of domain FSM_W; the total P_{10} value in KLX27A is roughly half that of the average value for FSM_W, and the fractures exhibit a different pattern of relative set intensities than the fracture domain FSM_W as a whole.

The performance of the model at predicting the intensity of MDZ is very encouraging; all of the top 5 model alternatives predict the same number (on average) of MDZ as were mapped in the cored borehole data. This also supports the use of the trace-length rollover point suggested in Verification Case SI-3 to parameterize the minimum size of MDZ.

Table G-9. P_{32} of fractures in MDZ size range.

Alternative Model	Envelope Set	Size Distribution Parameters k_r	r_{min}	r_{max}	P_{32}-MDZ
BMU	ENE	3	125	564.2	0.0040
BMU	NS	3.26	63	564.2	0.0060
BMU	SH	3.31	75	564.2	0.0021
BMU	WNW	2.8	90	564.2	0.0072
FL2	ENE	2.82	125	564.2	0.0046
FL2	NS	3.14	63	564.2	0.0074
FL2	SH	3.45	75	564.2	0.0003
FL2	WNW	2.67	90	564.2	0.0085
BM	ENE	3.03	125	564.2	0.0041
BM	NS	3.33	63	564.2	0.0096
BM	SH	3.41	75	564.2	0.0015
BM	WNW	2.87	90	564.2	0.0079
FL1	ENE	3.15	125	564.2	0.0035
FL1	NS	3.41	63	564.2	0.0092
FL1	SH	3.59	75	564.2	0.0011
FL1	WNW	3.05	90	564.2	0.0092
FUL2	ENE	2.81	125	564.2	0.0028
FUL2	NS	3.17	63	564.2	0.0061
FUL2	SH	3.39	75	564.2	0.0004
FUL2	WNW	2.68	90	564.2	0.0071

Table G-10. Results of validation simulations for fractures in MDZ size range.

Fracture Set	Number of MDZ Rank Case	1 BMU	2 FL2	3 BM	4 FL1	5 FUL2	Observed KLX27A
Total	Mean	5	6	6	7	5	6
Total	Median	5	6	5	7	5	n/a
Total	Std. Dev.	2.07	2.39	2.22	2.10	2.07	n/a
Total	Min	3	1	1	2	3	n/a
Total	Max	10	10	10	10	10	n/a

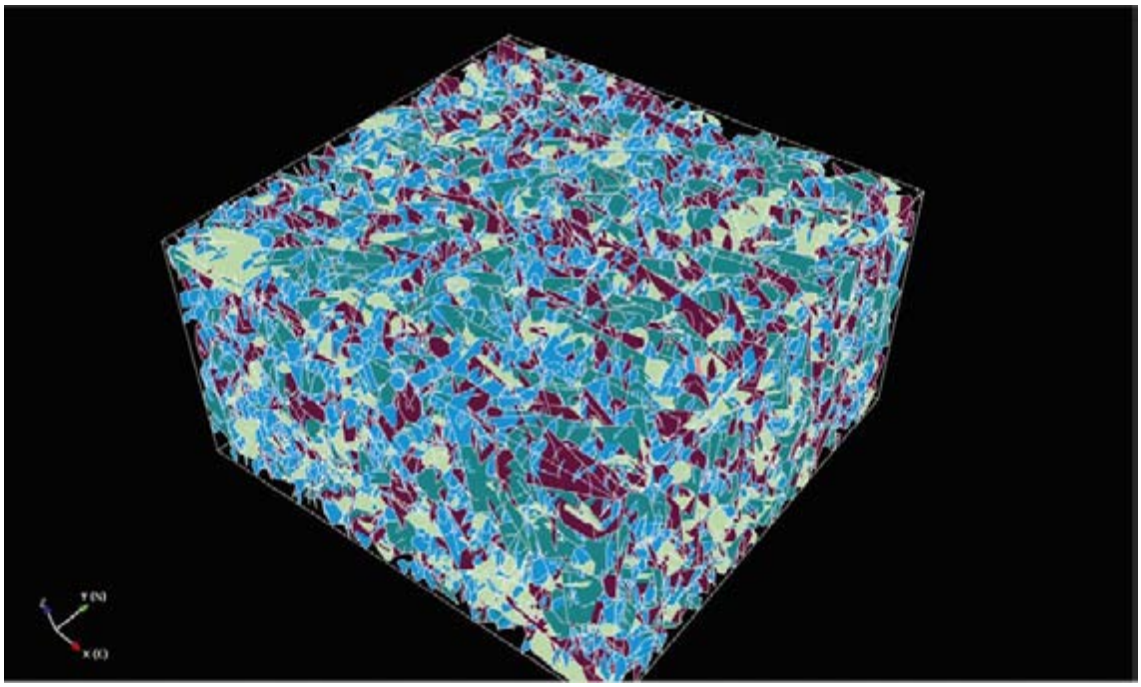

Figure G-8. *Stochastic MDZ-sized fractures from one Monte-Carlo run, BMU alternative. Simulation region is 4,690 m (east-west) by 4,500 m (north-south) by 2,500 m (vertical).*

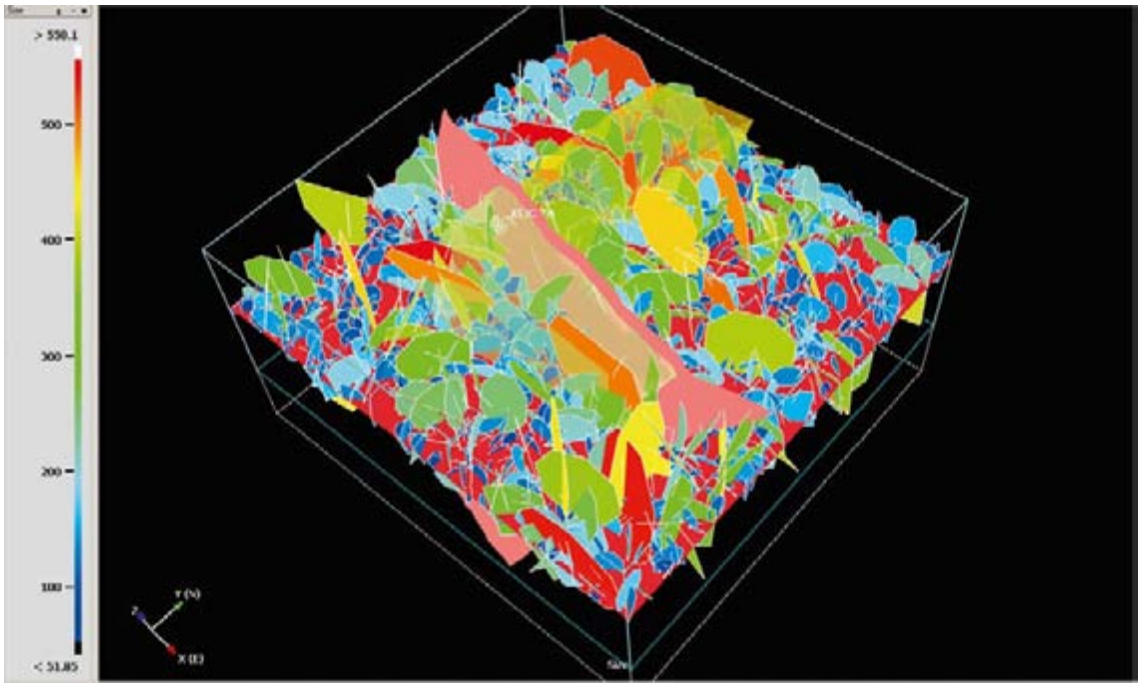

Figure G-9. *MDZ-sized fractures (BMU alternative) intersecting a traceplane inserted at repository depth of –450 m.a.s.l. Fractures are coloured by their size (radius); the scale (in meters) is located on the left side of the image.*

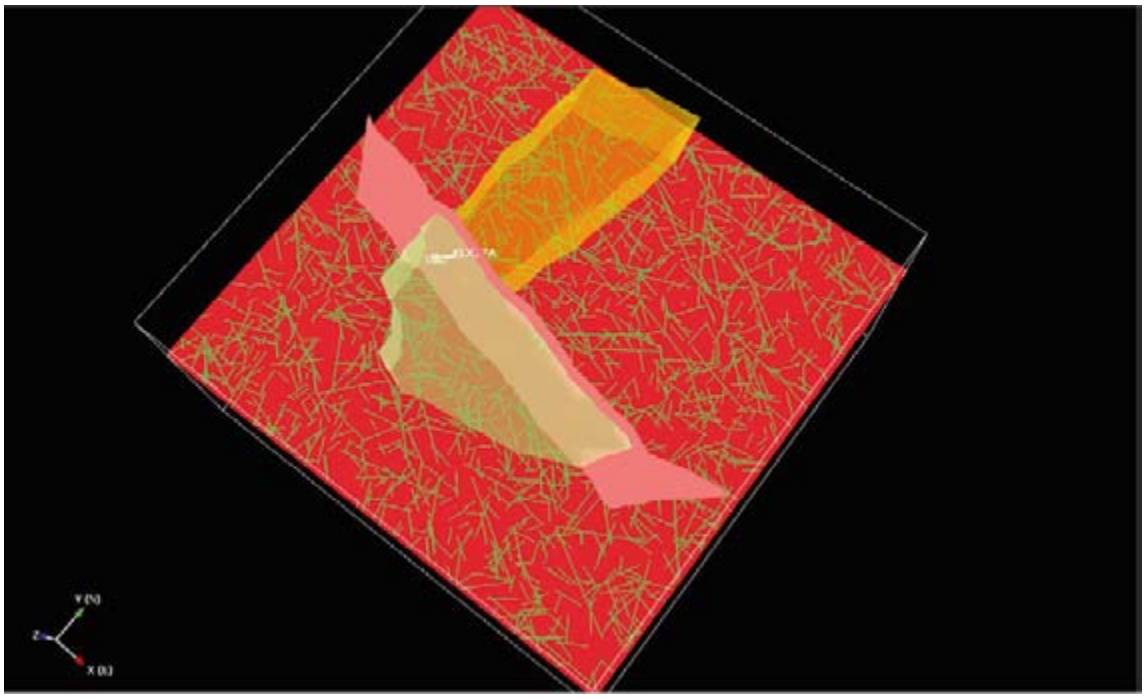

Figure G-10. *Trace map of MDZ-sized fractures (BMU alternative) intersecting a traceplane at repository depth of elevation –450 m.*

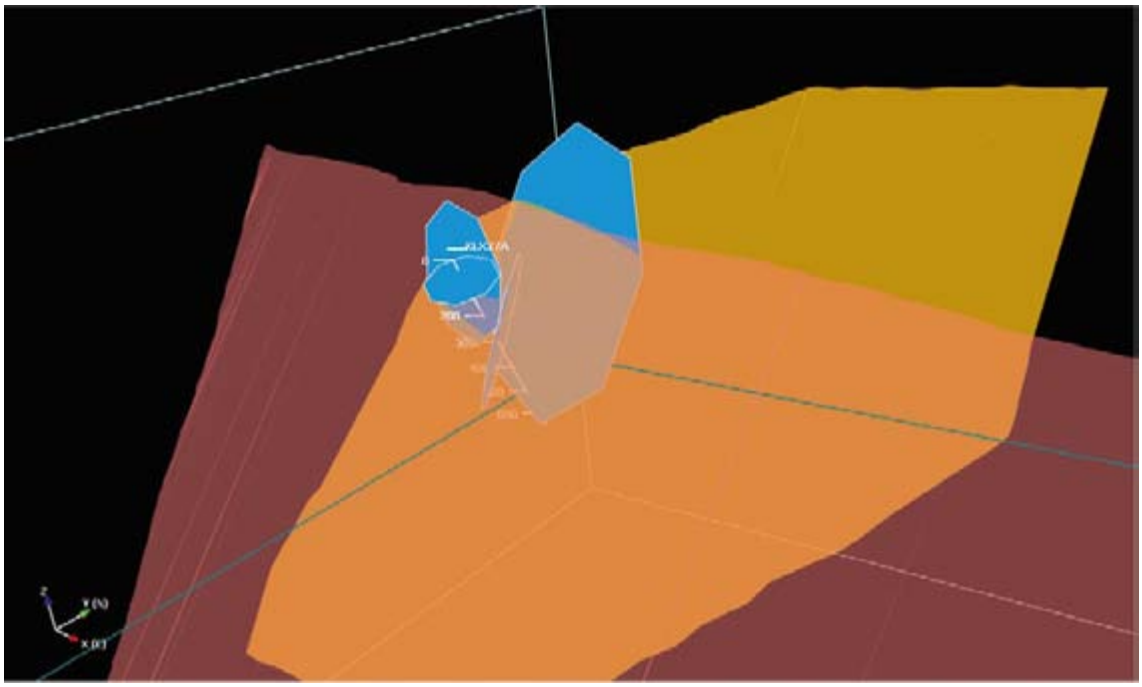

Figure G-11. *Stochastic MDZ-sized fractures (BMU alternative) intersecting KLX27A in one Monte-Carlo run. Orange volume is FSM_W, while the red transparent structure is ZSMNW042A. View is from the southeast.*

Appendix B

Contour plots used in the identification of fracture domains

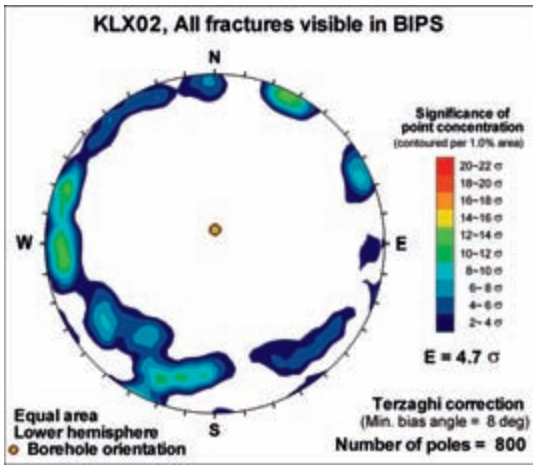

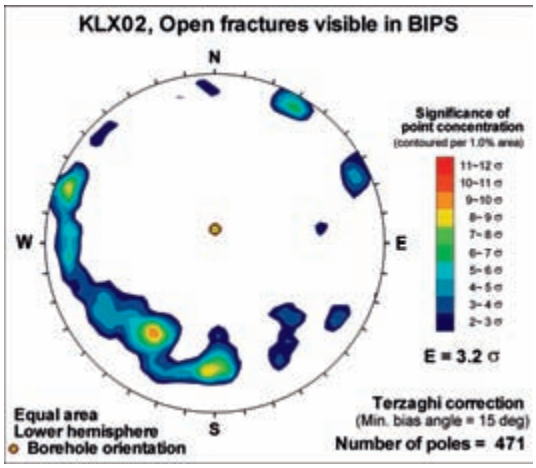

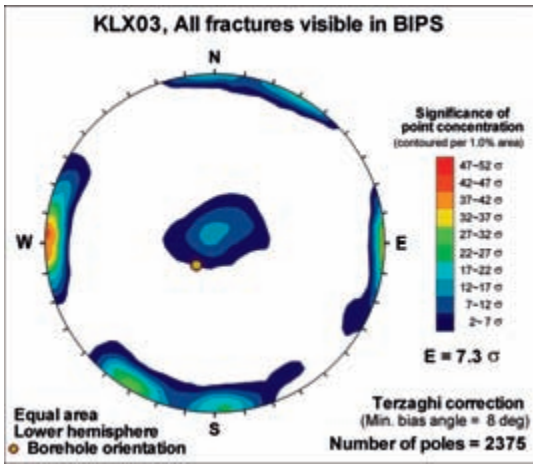

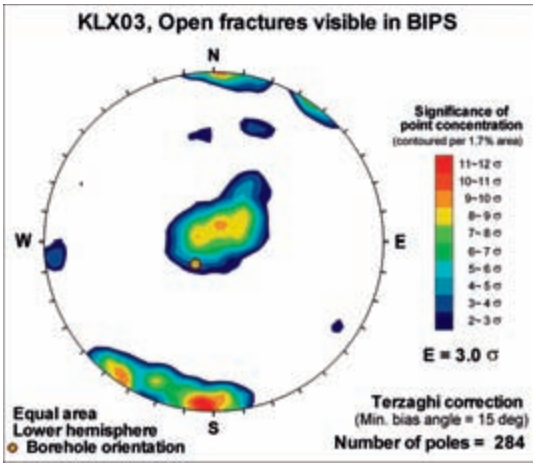

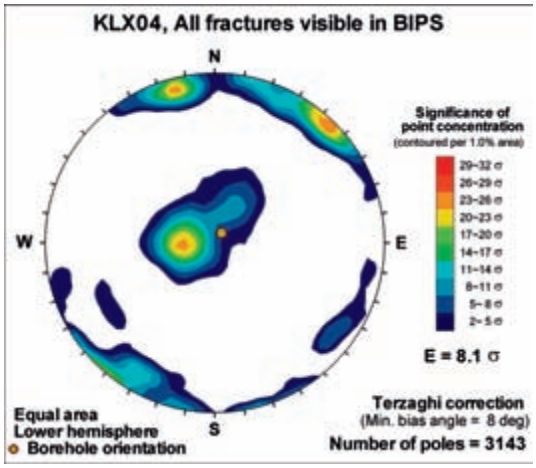

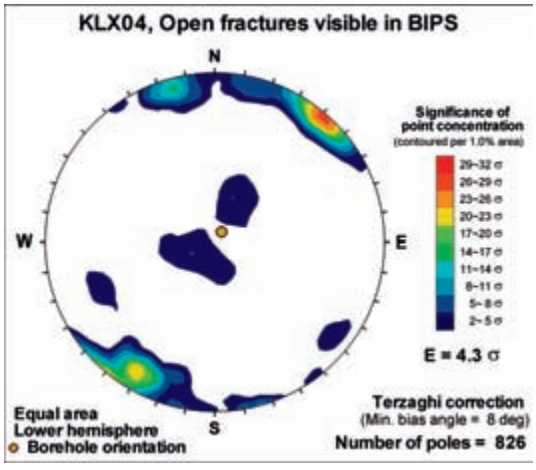

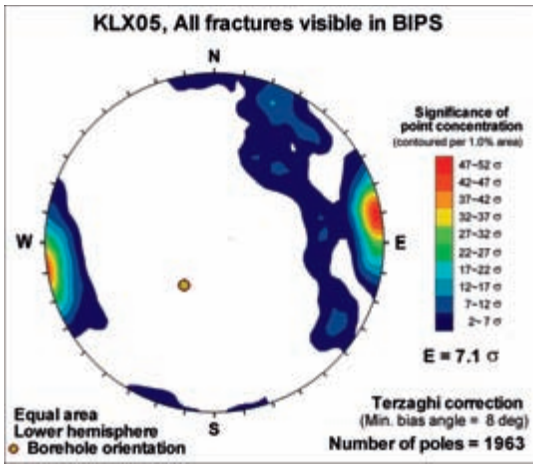
KLX05, All fractures visible in BIPS
N
W
E
S
Significance of point concentration
(contoured per 1.0% area)
47–52 σ
42–47 σ
37–42 σ
32–37 σ
27–32 σ
22–27 σ
17–22 σ
12–17 σ
7–12 σ
2–7 σ
E = 7.1 σ
Equal area
Lower hemisphere
Borehole orientation
Terzaghi correction
(Min. bias angle = 8 deg)
Number of poles = 1963

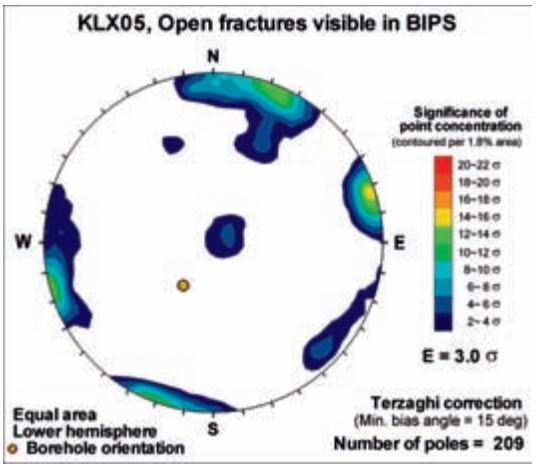
KLX05, Open fractures visible in BIPS
N
W
E
S
Significance of point concentration
(contoured per 1.8% area)
20–22 σ
18–20 σ
16–18 σ
14–16 σ
12–14 σ
10–12 σ
8–10 σ
6–8 σ
4–6 σ
2–4 σ
E = 3.0 σ
Equal area
Lower hemisphere
Borehole orientation
Terzaghi correction
(Min. bias angle = 15 deg)
Number of poles = 209

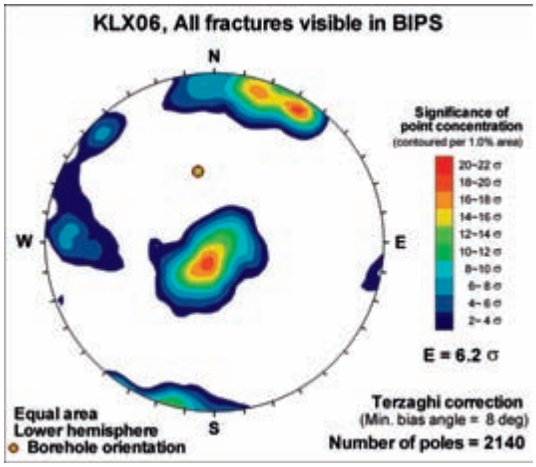
KLX06, All fractures visible in BIPS
N
W
E
S
Significance of point concentration
(contoured per 1.0% area)
20–22 σ
18–20 σ
16–18 σ
14–16 σ
12–14 σ
10–12 σ
8–10 σ
6–8 σ
4–6 σ
2–4 σ
E = 6.2 σ
Equal area
Lower hemisphere
Borehole orientation
Terzaghi correction
(Min. bias angle = 8 deg)
Number of poles = 2140

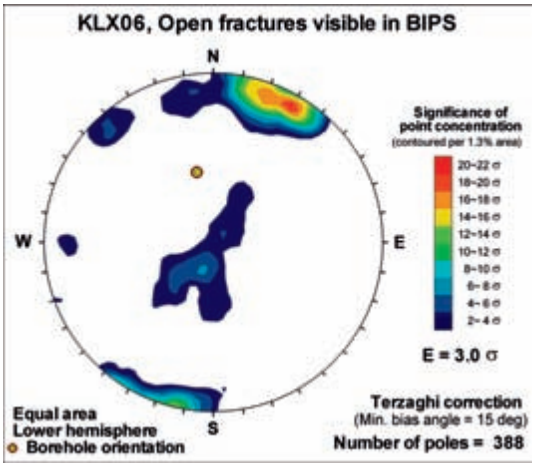
KLX06, Open fractures visible in BIPS
N
W
E
S
Significance of point concentration
(contoured per 1.3% area)
20–22 σ
18–20 σ
16–18 σ
14–16 σ
12–14 σ
10–12 σ
8–10 σ
6–8 σ
4–6 σ
2–4 σ
E = 3.0 σ
Equal area
Lower hemisphere
Borehole orientation
Terzaghi correction
(Min. bias angle = 15 deg)
Number of poles = 388

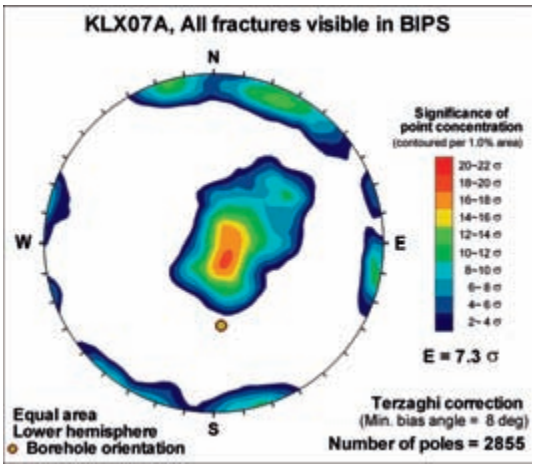
KLX07A, All fractures visible in BIPS
N
W
E
S
Significance of point concentration
(contoured per 1.0% area)
20–22 σ
18–20 σ
16–18 σ
14–16 σ
12–14 σ
10–12 σ
8–10 σ
6–8 σ
4–6 σ
2–4 σ
E = 7.3 σ
Equal area
Lower hemisphere
Borehole orientation
Terzaghi correction
(Min. bias angle = 8 deg)
Number of poles = 2855

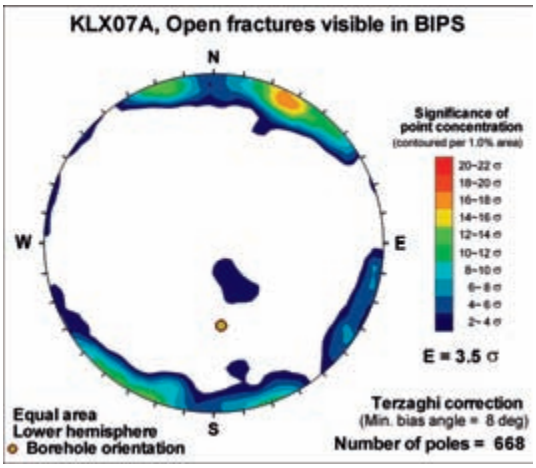
KLX07A, Open fractures visible in BIPS
N
W
E
S
Significance of point concentration
(contoured per 1.0% area)
20–22 σ
18–20 σ
16–18 σ
14–16 σ
12–14 σ
10–12 σ
8–10 σ
6–8 σ
4–6 σ
2–4 σ
E = 3.5 σ
Equal area
Lower hemisphere
Borehole orientation
Terzaghi correction
(Min. bias angle = 8 deg)
Number of poles = 668

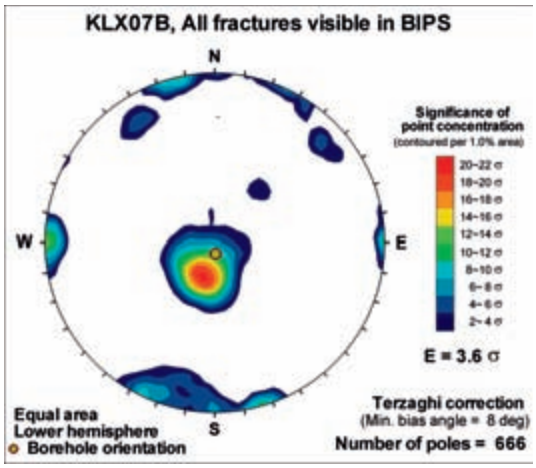
KLX07B, All fractures visible in BIPS
N
W
E
S
Significance of point concentration
(contoured per 1.0% area)
20–22 σ
18–20 σ
16–18 σ
14–16 σ
12–14 σ
10–12 σ
8–10 σ
6–8 σ
4–6 σ
2–4 σ
E = 3.6 σ
Equal area
Lower hemisphere
Borehole orientation
Terzaghi correction
(Min. bias angle = 8 deg)
Number of poles = 666

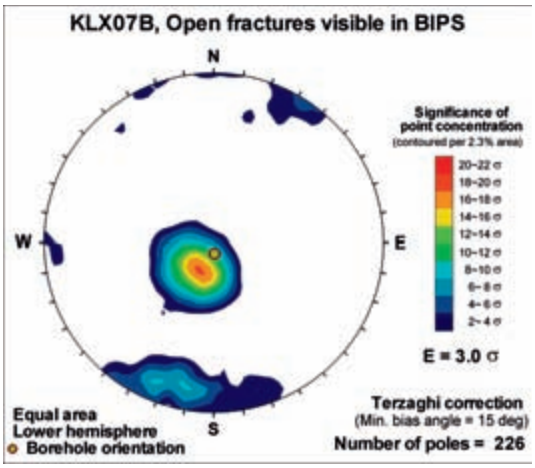
KLX07B, Open fractures visible in BIPS
N
W
E
S
Significance of point concentration
(contoured per 2.3% area)
20–22 σ
18–20 σ
16–18 σ
14–16 σ
12–14 σ
10–12 σ
8–10 σ
6–8 σ
4–6 σ
2–4 σ
E = 3.0 σ
Equal area
Lower hemisphere
Borehole orientation
Terzaghi correction
(Min. bias angle = 15 deg)
Number of poles = 226

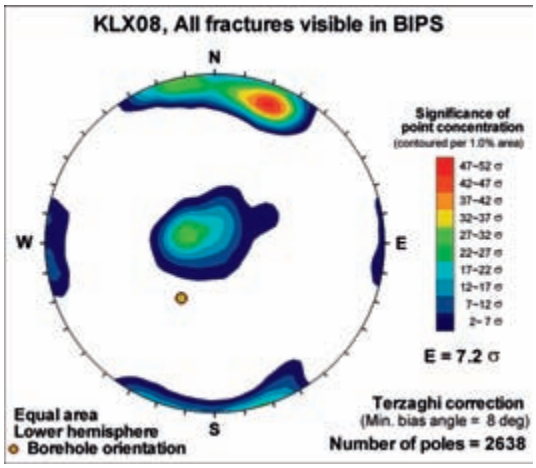
KLX08, All fractures visible in BIPS
N
W
E
S
Significance of point concentration
(contoured per 1.0% area)
47–52 σ
42–47 σ
37–42 σ
32–37 σ
27–32 σ
22–27 σ
17–22 σ
12–17 σ
7–12 σ
2–7 σ
E = 7.2 σ
Equal area
Lower hemisphere
Borehole orientation
Terzaghi correction
(Min. bias angle = 8 deg)
Number of poles = 2638

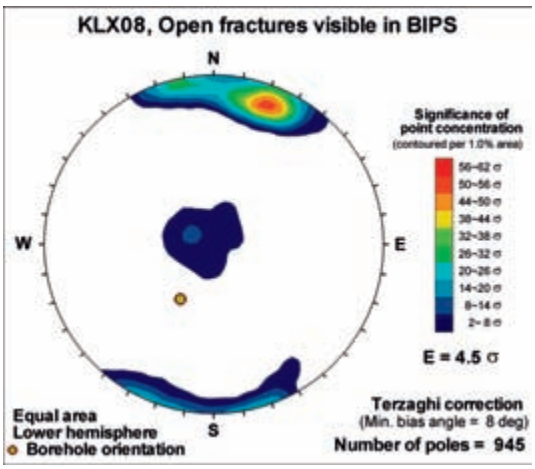
KLX08, Open fractures visible in BIPS
N
W
E
S
Significance of point concentration
(contoured per 1.0% area)
56–62 σ
50–56 σ
44–50 σ
38–44 σ
32–38 σ
26–32 σ
20–26 σ
14–20 σ
8–14 σ
2–8 σ
E = 4.5 σ
Equal area
Lower hemisphere
Borehole orientation
Terzaghi correction
(Min. bias angle = 8 deg)
Number of poles = 945

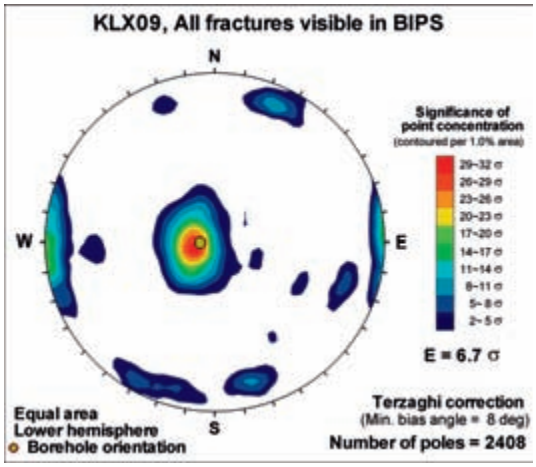
KLX09, All fractures visible in BIPS
N
W
E
S
Significance of point concentration
(contoured per 1.0% area)
29–32 σ
26–29 σ
23–26 σ
20–23 σ
17–20 σ
14–17 σ
11–14 σ
8–11 σ
5–8 σ
2–5 σ
E = 6.7 σ
Equal area
Lower hemisphere
Borehole orientation
Terzaghi correction
(Min. bias angle = 8 deg)
Number of poles = 2408

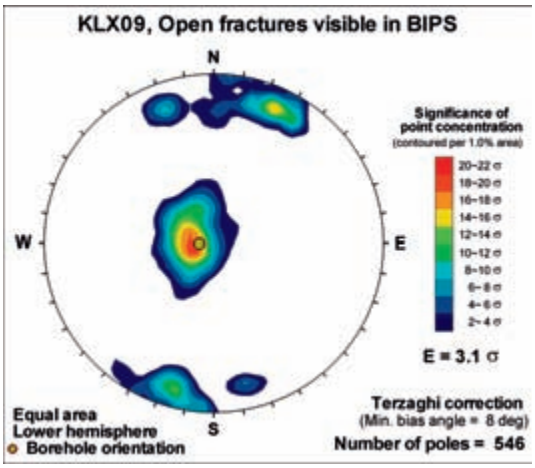
KLX09, Open fractures visible in BIPS
N
W
E
S
Significance of point concentration
(contoured per 1.0% area)
20–22 σ
18–20 σ
16–18 σ
14–16 σ
12–14 σ
10–12 σ
8–10 σ
6–8 σ
4–6 σ
2–4 σ
E = 3.1 σ
Equal area
Lower hemisphere
Borehole orientation
Terzaghi correction
(Min. bias angle = 8 deg)
Number of poles = 546

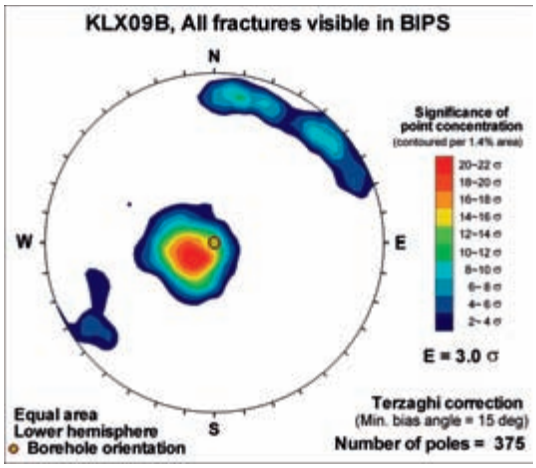
KLX09B, All fractures visible in BIPS
N
W
E
S
Significance of point concentration
(contoured per 1.4% area)
20-22 σ
18-20 σ
16-18 σ
14-16 σ
12-14 σ
10-12 σ
8-10 σ
6-8 σ
4-6 σ
2-4 σ
E = 3.0 σ
Equal area
Lower hemisphere
Borehole orientation
Terzaghi correction
(Min. bias angle = 15 deg)
Number of poles = 375

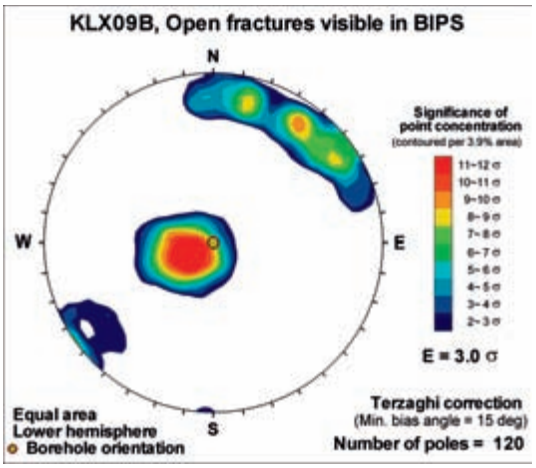
KLX09B, Open fractures visible in BIPS
N
W
E
S
Significance of point concentration
(contoured per 3.9% area)
11-12 σ
10-11 σ
9-10 σ
8-9 σ
7-8 σ
6-7 σ
5-6 σ
4-5 σ
3-4 σ
2-3 σ
E = 3.0 σ
Equal area
Lower hemisphere
Borehole orientation
Terzaghi correction
(Min. bias angle = 15 deg)
Number of poles = 120

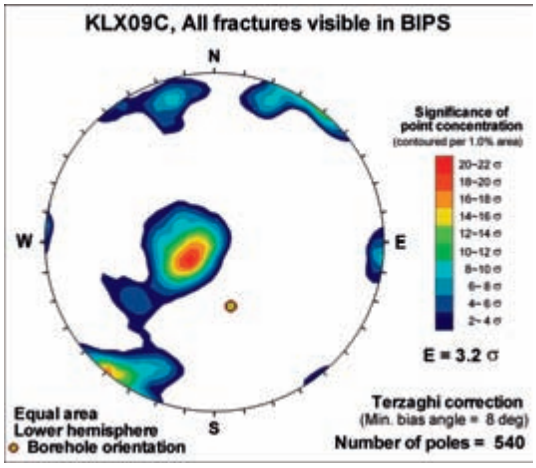
KLX09C, All fractures visible in BIPS
N
W
E
S
Significance of point concentration
(contoured per 1.0% area)
20-22 σ
18-20 σ
16-18 σ
14-16 σ
12-14 σ
10-12 σ
8-10 σ
6-8 σ
4-6 σ
2-4 σ
E = 3.2 σ
Equal area
Lower hemisphere
Borehole orientation
Terzaghi correction
(Min. bias angle = 8 deg)
Number of poles = 540

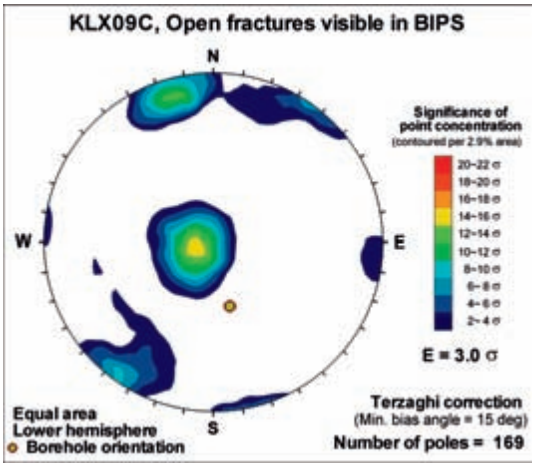
KLX09C, Open fractures visible in BIPS
N
W
E
S
Significance of point concentration
(contoured per 2.9% area)
20-22 σ
18-20 σ
16-18 σ
14-16 σ
12-14 σ
10-12 σ
8-10 σ
6-8 σ
4-6 σ
2-4 σ
E = 3.0 σ
Equal area
Lower hemisphere
Borehole orientation
Terzaghi correction
(Min. bias angle = 15 deg)
Number of poles = 169

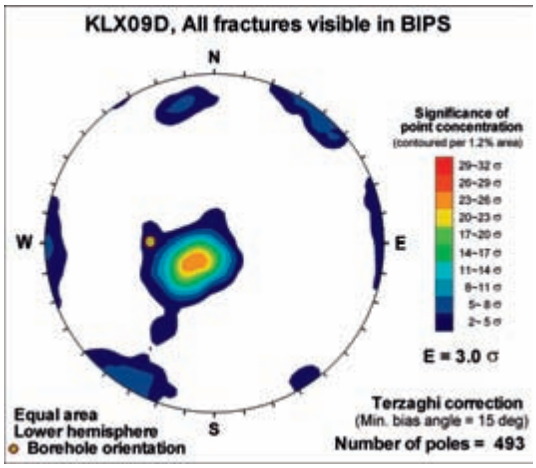
KLX09D, All fractures visible in BIPS
N
W
E
S
Significance of point concentration
(contoured per 1.2% area)
29-32 σ
26-29 σ
23-26 σ
20-23 σ
17-20 σ
14-17 σ
11-14 σ
8-11 σ
5-8 σ
2-5 σ
E = 3.0 σ
Equal area
Lower hemisphere
Borehole orientation
Terzaghi correction
(Min. bias angle = 15 deg)
Number of poles = 493

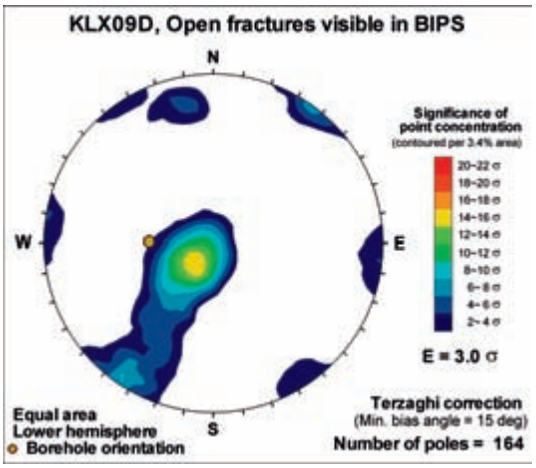
KLX09D, Open fractures visible in BIPS
N
W
E
S
Significance of point concentration
(contoured per 3.4% area)
20-22 σ
18-20 σ
16-18 σ
14-16 σ
12-14 σ
10-12 σ
8-10 σ
6-8 σ
4-6 σ
2-4 σ
E = 3.0 σ
Equal area
Lower hemisphere
Borehole orientation
Terzaghi correction
(Min. bias angle = 15 deg)
Number of poles = 164

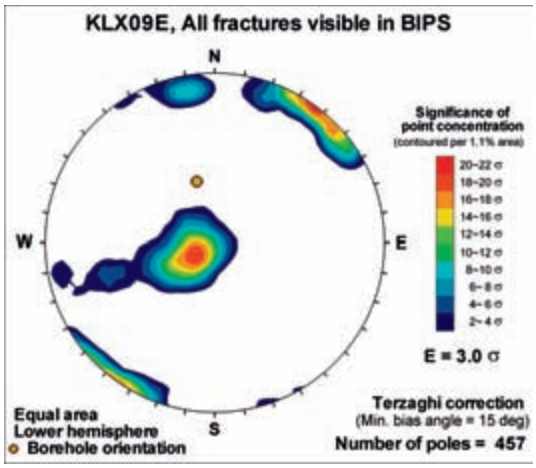
KLX09E, All fractures visible in BIPS
N
W
E
S
Significance of point concentration
(contoured per 1.1% area)
20–22 σ
18–20 σ
16–18 σ
14–16 σ
12–14 σ
10–12 σ
8–10 σ
6–8 σ
4–6 σ
2–4 σ
E = 3.0 σ
Terzaghi correction
(Min. bias angle = 15 deg)
Number of poles = 457
Equal area
Lower hemisphere
Borehole orientation

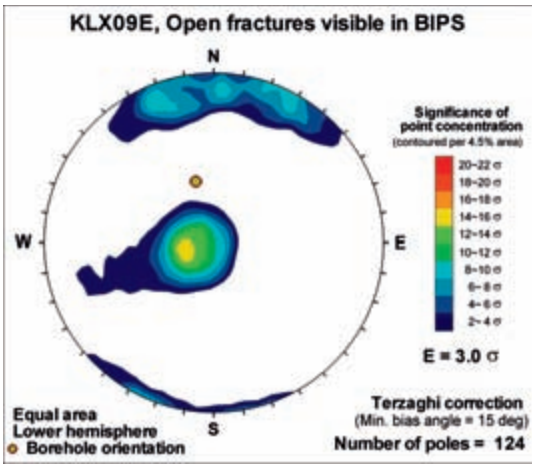
KLX09E, Open fractures visible in BIPS
N
W
E
S
Significance of point concentration
(contoured per 4.5% area)
20–22 σ
18–20 σ
16–18 σ
14–16 σ
12–14 σ
10–12 σ
8–10 σ
6–8 σ
4–6 σ
2–4 σ
E = 3.0 σ
Terzaghi correction
(Min. bias angle = 15 deg)
Number of poles = 124
Equal area
Lower hemisphere
Borehole orientation

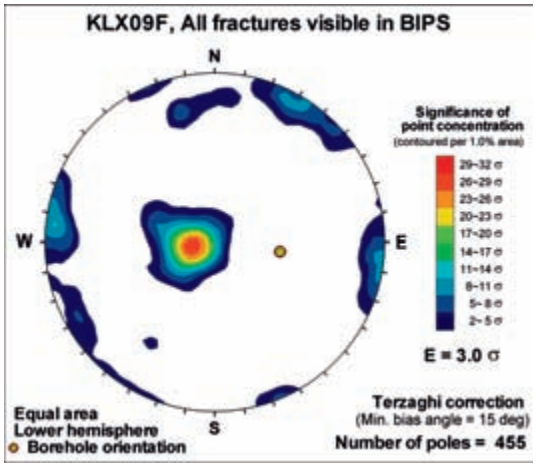
KLX09F, All fractures visible in BIPS
N
W
E
S
Significance of point concentration
(contoured per 1.0% area)
29–32 σ
26–29 σ
23–26 σ
20–23 σ
17–20 σ
14–17 σ
11–14 σ
8–11 σ
5–8 σ
2–5 σ
E = 3.0 σ
Terzaghi correction
(Min. bias angle = 15 deg)
Number of poles = 455
Equal area
Lower hemisphere
Borehole orientation

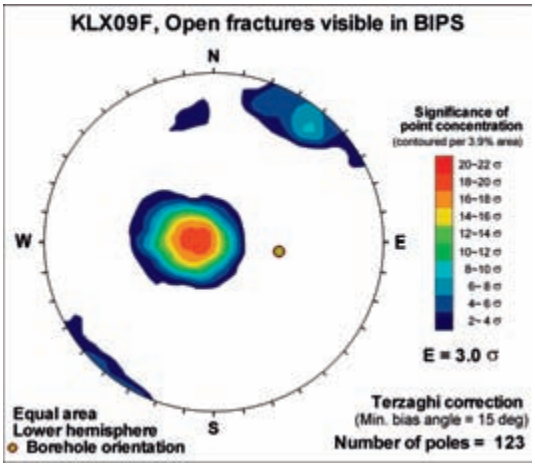
KLX09F, Open fractures visible in BIPS
N
W
E
S
Significance of point concentration
(contoured per 3.9% area)
20–22 σ
18–20 σ
16–18 σ
14–16 σ
12–14 σ
10–12 σ
8–10 σ
6–8 σ
4–6 σ
2–4 σ
E = 3.0 σ
Terzaghi correction
(Min. bias angle = 15 deg)
Number of poles = 123
Equal area
Lower hemisphere
Borehole orientation

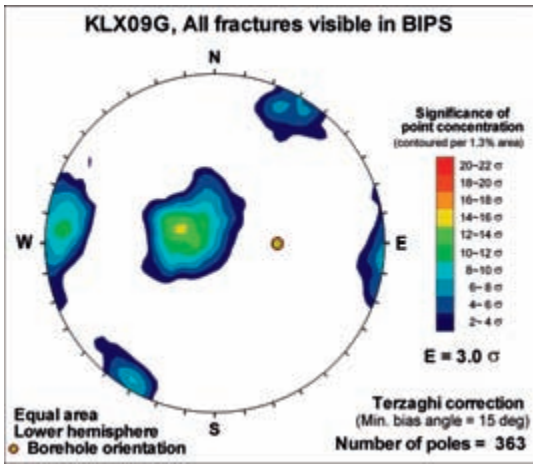
KLX09G, All fractures visible in BIPS
N
W
E
S
Significance of point concentration
(contoured per 1.3% area)
20–22 σ
18–20 σ
16–18 σ
14–16 σ
12–14 σ
10–12 σ
8–10 σ
6–8 σ
4–6 σ
2–4 σ
E = 3.0 σ
Terzaghi correction
(Min. bias angle = 15 deg)
Number of poles = 363
Equal area
Lower hemisphere
Borehole orientation

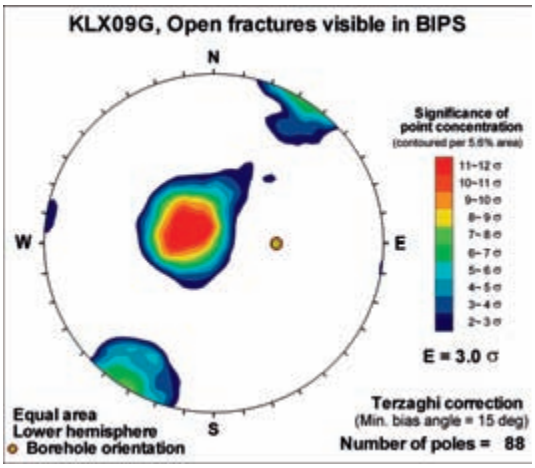
KLX09G, Open fractures visible in BIPS
N
W
E
S
Significance of point concentration
(contoured per 5.6% area)
11–12 σ
10–11 σ
9–10 σ
8–9 σ
7–8 σ
6–7 σ
5–6 σ
4–5 σ
3–4 σ
2–3 σ
E = 3.0 σ
Terzaghi correction
(Min. bias angle = 15 deg)
Number of poles = 88
Equal area
Lower hemisphere
Borehole orientation

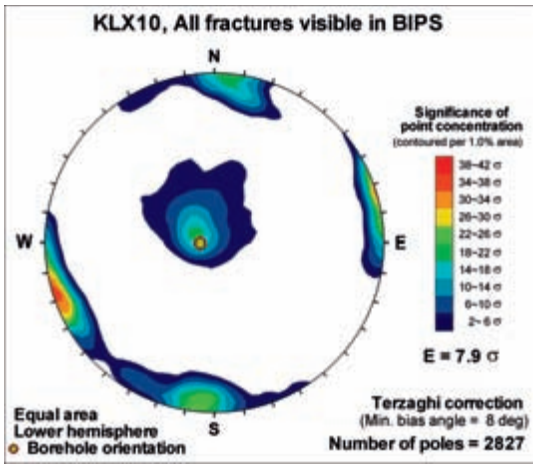
KLX10, All fractures visible in BIPS
N
W
E
S
Significance of point concentration
(contoured per 1.0% area)
38-42 σ
34-38 σ
30-34 σ
26-30 σ
22-26 σ
18-22 σ
14-18 σ
10-14 σ
6-10 σ
2-6 σ
E = 7.9 σ
Equal area
Lower hemisphere
Borehole orientation
Terzaghi correction
(Min. bias angle = 8 deg)
Number of poles = 2827

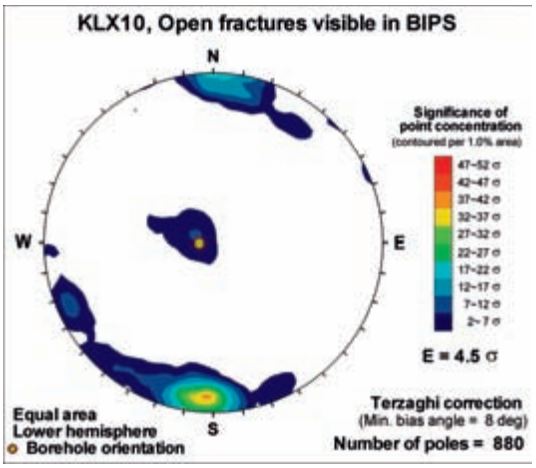
KLX10, Open fractures visible in BIPS
N
W
E
S
Significance of point concentration
(contoured per 1.0% area)
47-52 σ
42-47 σ
37-42 σ
32-37 σ
27-32 σ
22-27 σ
17-22 σ
12-17 σ
7-12 σ
2-7 σ
E = 4.5 σ
Equal area
Lower hemisphere
Borehole orientation
Terzaghi correction
(Min. bias angle = 8 deg)
Number of poles = 880

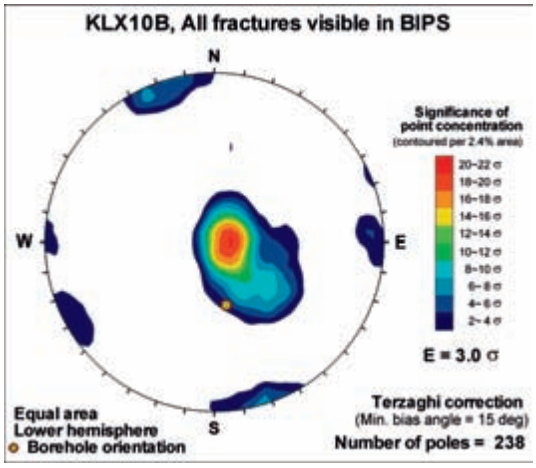
KLX10B, All fractures visible in BIPS
N
W
E
S
Significance of point concentration
(contoured per 2.4% area)
20-22 σ
18-20 σ
16-18 σ
14-16 σ
12-14 σ
10-12 σ
8-10 σ
6-8 σ
4-6 σ
2-4 σ
E = 3.0 σ
Equal area
Lower hemisphere
Borehole orientation
Terzaghi correction
(Min. bias angle = 15 deg)
Number of poles = 238

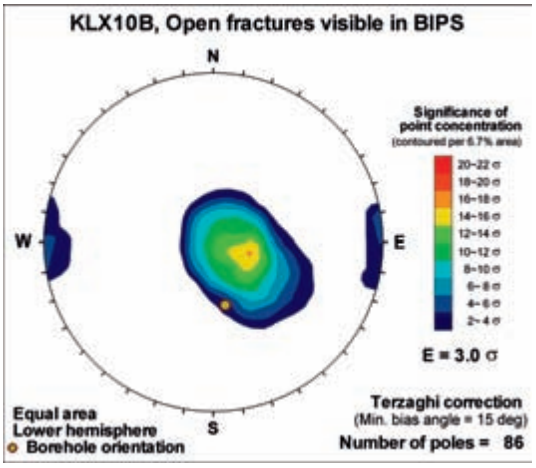
KLX10B, Open fractures visible in BIPS
N
W
E
S
Significance of point concentration
(contoured per 6.7% area)
20-22 σ
18-20 σ
16-18 σ
14-16 σ
12-14 σ
10-12 σ
8-10 σ
6-8 σ
4-6 σ
2-4 σ
E = 3.0 σ
Equal area
Lower hemisphere
Borehole orientation
Terzaghi correction
(Min. bias angle = 15 deg)
Number of poles = 86

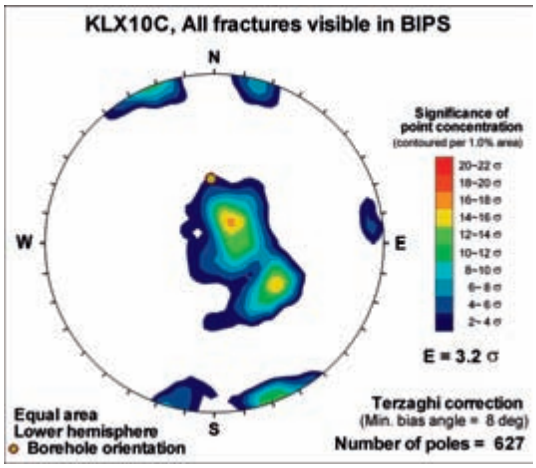
KLX10C, All fractures visible in BIPS
N
W
E
S
Significance of point concentration
(contoured per 1.0% area)
20-22 σ
18-20 σ
16-18 σ
14-16 σ
12-14 σ
10-12 σ
8-10 σ
6-8 σ
4-6 σ
2-4 σ
E = 3.2 σ
Equal area
Lower hemisphere
Borehole orientation
Terzaghi correction
(Min. bias angle = 8 deg)
Number of poles = 627

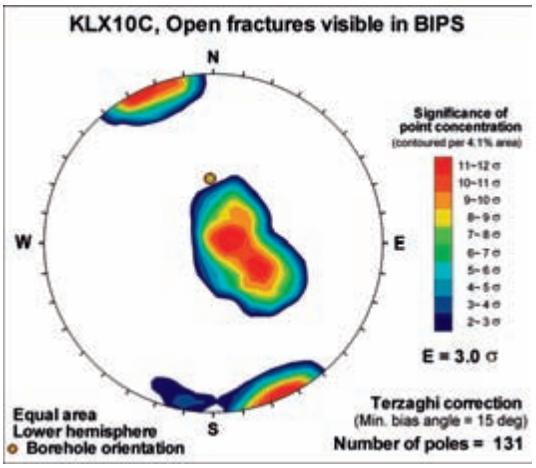
KLX10C, Open fractures visible in BIPS
N
W
E
S
Significance of point concentration
(contoured per 4.1% area)
11-12 σ
10-11 σ
9-10 σ
8-9 σ
7-8 σ
6-7 σ
5-6 σ
4-5 σ
3-4 σ
2-3 σ
E = 3.0 σ
Equal area
Lower hemisphere
Borehole orientation
Terzaghi correction
(Min. bias angle = 15 deg)
Number of poles = 131

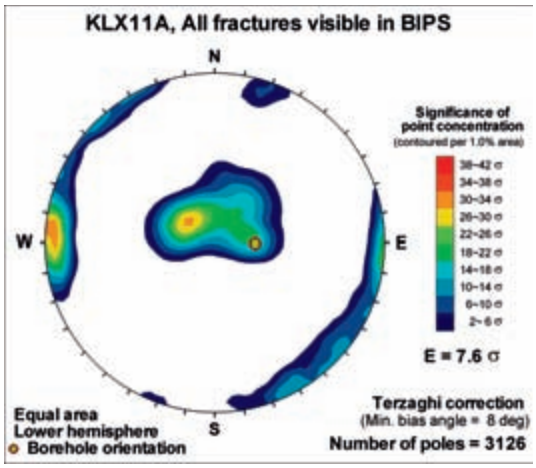
KLX11A, All fractures visible in BIPS
N
W
E
S
Significance of point concentration
(contoured per 1.0% area)
38–42 σ
34–38 σ
30–34 σ
26–30 σ
22–26 σ
18–22 σ
14–18 σ
10–14 σ
6–10 σ
2–6 σ
E = 7.6 σ
Equal area
Lower hemisphere
Borehole orientation
Terzaghi correction
(Min. bias angle = 8 deg)
Number of poles = 3126

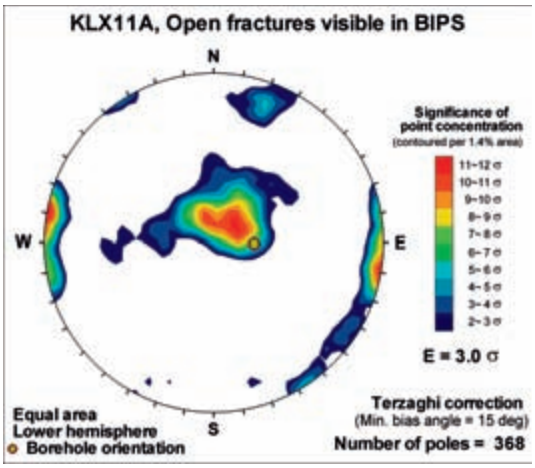
KLX11A, Open fractures visible in BIPS
N
W
E
S
Significance of point concentration
(contoured per 1.4% area)
11–12 σ
10–11 σ
9–10 σ
8–9 σ
7–8 σ
6–7 σ
5–6 σ
4–5 σ
3–4 σ
2–3 σ
E = 3.0 σ
Equal area
Lower hemisphere
Borehole orientation
Terzaghi correction
(Min. bias angle = 15 deg)
Number of poles = 368

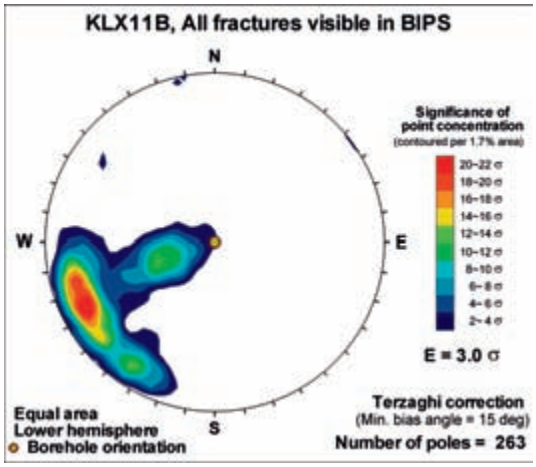
KLX11B, All fractures visible in BIPS
N
W
E
S
Significance of point concentration
(contoured per 1.7% area)
20–22 σ
18–20 σ
16–18 σ
14–16 σ
12–14 σ
10–12 σ
8–10 σ
6–8 σ
4–6 σ
2–4 σ
E = 3.0 σ
Equal area
Lower hemisphere
Borehole orientation
Terzaghi correction
(Min. bias angle = 15 deg)
Number of poles = 263

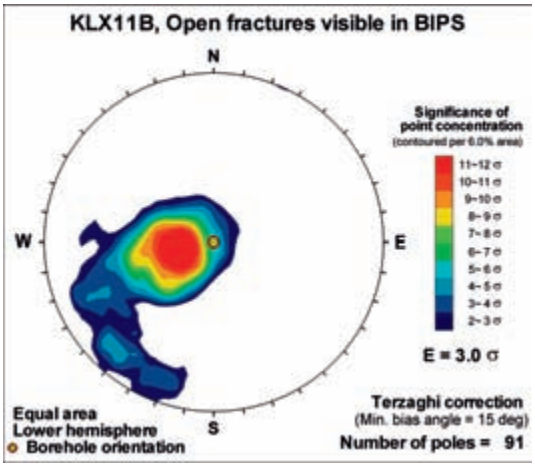
KLX11B, Open fractures visible in BIPS
N
W
E
S
Significance of point concentration
(contoured per 6.0% area)
11–12 σ
10–11 σ
9–10 σ
8–9 σ
7–8 σ
6–7 σ
5–6 σ
4–5 σ
3–4 σ
2–3 σ
E = 3.0 σ
Equal area
Lower hemisphere
Borehole orientation
Terzaghi correction
(Min. bias angle = 15 deg)
Number of poles = 91

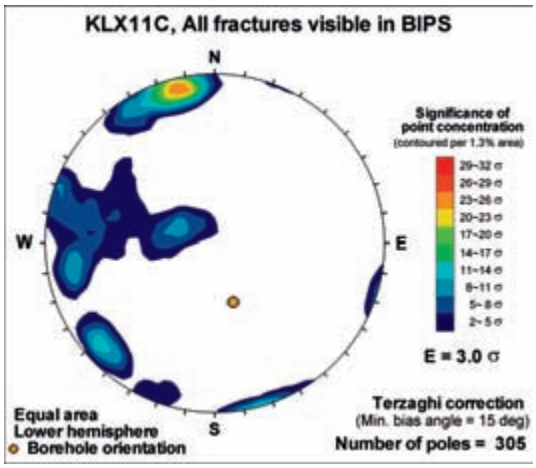
KLX11C, All fractures visible in BIPS
N
W
E
S
Significance of point concentration
(contoured per 1.3% area)
29–32 σ
26–29 σ
23–26 σ
20–23 σ
17–20 σ
14–17 σ
11–14 σ
8–11 σ
5–8 σ
2–5 σ
E = 3.0 σ
Equal area
Lower hemisphere
Borehole orientation
Terzaghi correction
(Min. bias angle = 15 deg)
Number of poles = 305

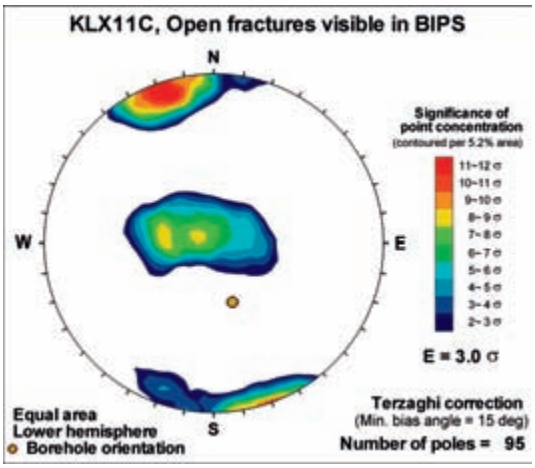
KLX11C, Open fractures visible in BIPS
N
W
E
S
Significance of point concentration
(contoured per 5.2% area)
11–12 σ
10–11 σ
9–10 σ
8–9 σ
7–8 σ
6–7 σ
5–6 σ
4–5 σ
3–4 σ
2–3 σ
E = 3.0 σ
Equal area
Lower hemisphere
Borehole orientation
Terzaghi correction
(Min. bias angle = 15 deg)
Number of poles = 95

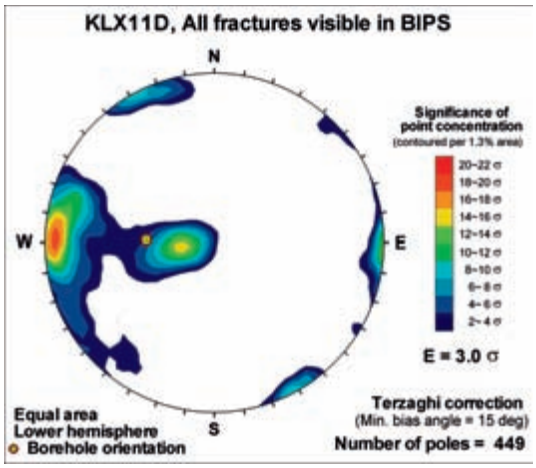
KLX11D, All fractures visible in BIPS
N
W
E
S
Significance of point concentration
(contoured per 1.3% area)
20–22 σ
18–20 σ
16–18 σ
14–16 σ
12–14 σ
10–12 σ
8–10 σ
6–8 σ
4–6 σ
2–4 σ
E = 3.0 σ
Equal area
Lower hemisphere
Borehole orientation
Terzaghi correction
(Min. bias angle = 15 deg)
Number of poles = 449

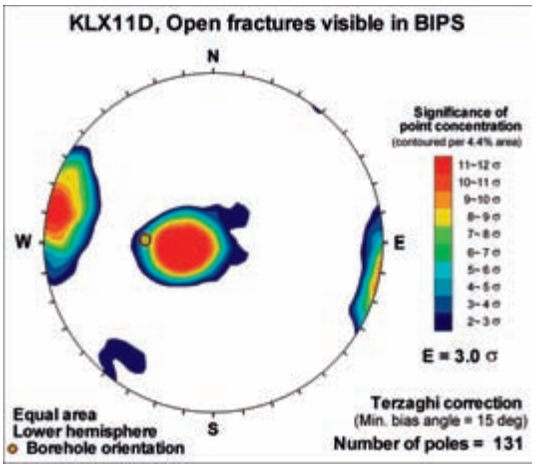
KLX11D, Open fractures visible in BIPS
N
W
E
S
Significance of point concentration
(contoured per 4.4% area)
11–12 σ
10–11 σ
9–10 σ
8–9 σ
7–8 σ
6–7 σ
5–6 σ
4–5 σ
3–4 σ
2–3 σ
E = 3.0 σ
Equal area
Lower hemisphere
Borehole orientation
Terzaghi correction
(Min. bias angle = 15 deg)
Number of poles = 131

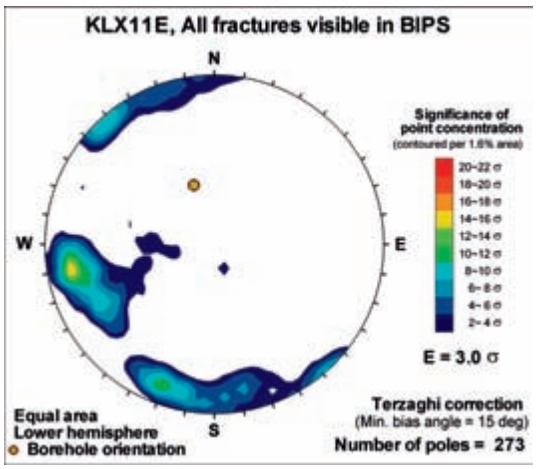
KLX11E, All fractures visible in BIPS
N
W
E
S
Significance of point concentration
(contoured per 1.6% area)
20–22 σ
18–20 σ
16–18 σ
14–16 σ
12–14 σ
10–12 σ
8–10 σ
6–8 σ
4–6 σ
2–4 σ
E = 3.0 σ
Equal area
Lower hemisphere
Borehole orientation
Terzaghi correction
(Min. bias angle = 15 deg)
Number of poles = 273

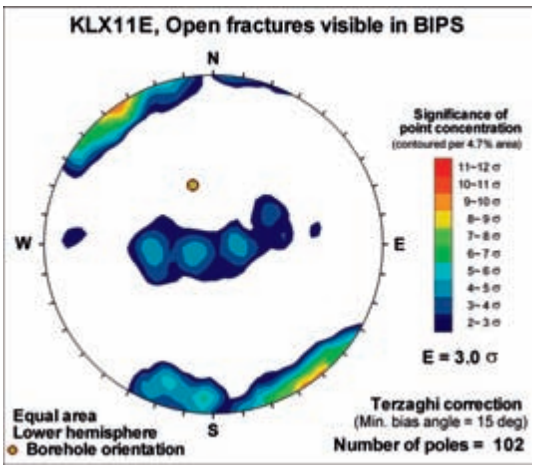
KLX11E, Open fractures visible in BIPS
N
W
E
S
Significance of point concentration
(contoured per 4.7% area)
11–12 σ
10–11 σ
9–10 σ
8–9 σ
7–8 σ
6–7 σ
5–6 σ
4–5 σ
3–4 σ
2–3 σ
E = 3.0 σ
Equal area
Lower hemisphere
Borehole orientation
Terzaghi correction
(Min. bias angle = 15 deg)
Number of poles = 102

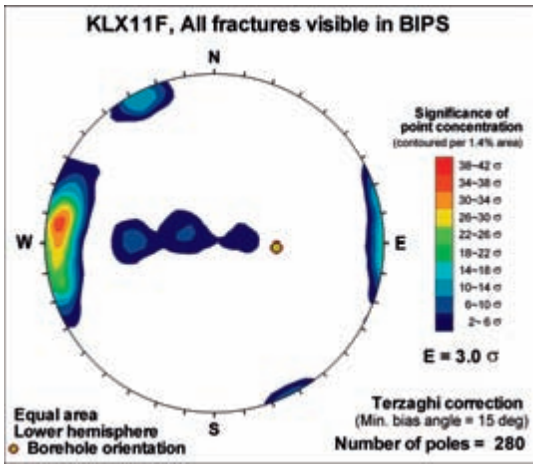
KLX11F, All fractures visible in BIPS
N
W
E
S
Significance of point concentration
(contoured per 1.4% area)
38–42 σ
34–38 σ
30–34 σ
26–30 σ
22–26 σ
18–22 σ
14–18 σ
10–14 σ
6–10 σ
2–6 σ
E = 3.0 σ
Equal area
Lower hemisphere
Borehole orientation
Terzaghi correction
(Min. bias angle = 15 deg)
Number of poles = 280

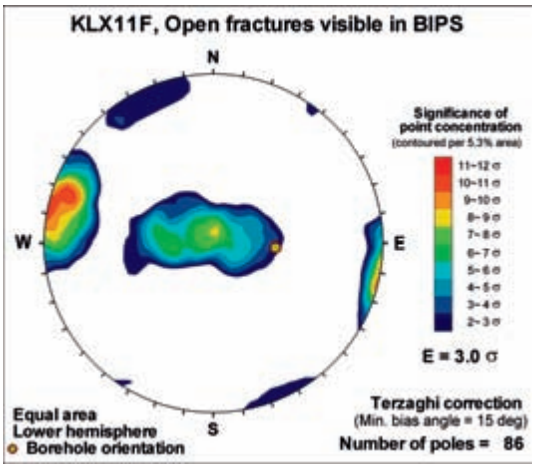
KLX11F, Open fractures visible in BIPS
N
W
E
S
Significance of point concentration
(contoured per 5.3% area)
11–12 σ
10–11 σ
9–10 σ
8–9 σ
7–8 σ
6–7 σ
5–6 σ
4–5 σ
3–4 σ
2–3 σ
E = 3.0 σ
Equal area
Lower hemisphere
Borehole orientation
Terzaghi correction
(Min. bias angle = 15 deg)
Number of poles = 86

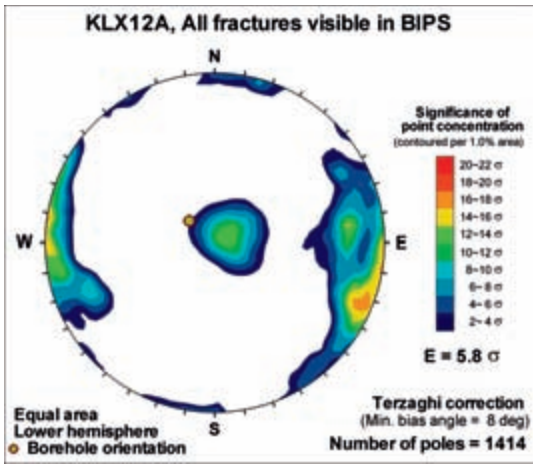
KLX12A, All fractures visible in BIPS
N
W
E
S
Significance of point concentration
(contoured per 1.0% area)
20–22 σ
18–20 σ
16–18 σ
14–16 σ
12–14 σ
10–12 σ
8–10 σ
6–8 σ
4–6 σ
2–4 σ
E = 5.8 σ
Equal area
Lower hemisphere
Borehole orientation
Terzaghi correction
(Min. bias angle = 8 deg)
Number of poles = 1414

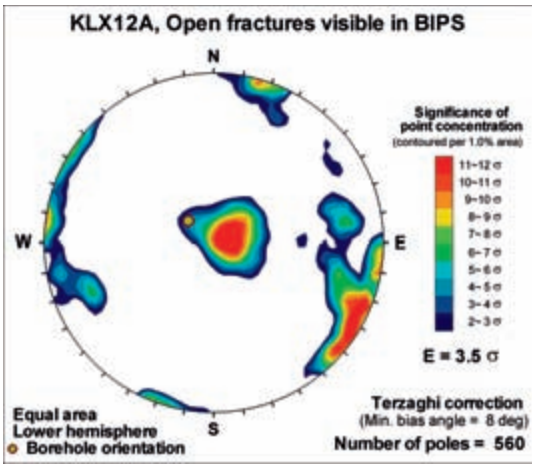
KLX12A, Open fractures visible in BIPS
N
W
E
S
Significance of point concentration
(contoured per 1.0% area)
11–12 σ
10–11 σ
9–10 σ
8–9 σ
7–8 σ
6–7 σ
5–6 σ
4–5 σ
3–4 σ
2–3 σ
E = 3.5 σ
Equal area
Lower hemisphere
Borehole orientation
Terzaghi correction
(Min. bias angle = 8 deg)
Number of poles = 560

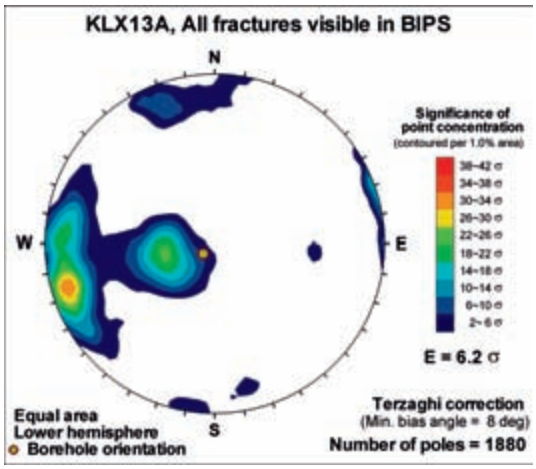
KLX13A, All fractures visible in BIPS
N
W
E
S
Significance of point concentration
(contoured per 1.0% area)
38–42 σ
34–38 σ
30–34 σ
26–30 σ
22–26 σ
18–22 σ
14–18 σ
10–14 σ
6–10 σ
2–6 σ
E = 6.2 σ
Equal area
Lower hemisphere
Borehole orientation
Terzaghi correction
(Min. bias angle = 8 deg)
Number of poles = 1880

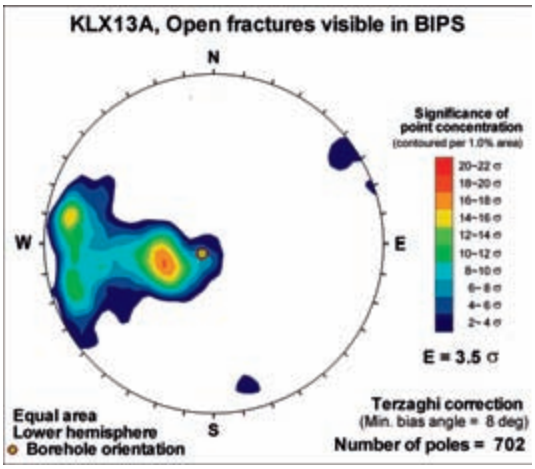
KLX13A, Open fractures visible in BIPS
N
W
E
S
Significance of point concentration
(contoured per 1.0% area)
20–22 σ
18–20 σ
16–18 σ
14–16 σ
12–14 σ
10–12 σ
8–10 σ
6–8 σ
4–6 σ
2–4 σ
E = 3.5 σ
Equal area
Lower hemisphere
Borehole orientation
Terzaghi correction
(Min. bias angle = 8 deg)
Number of poles = 702

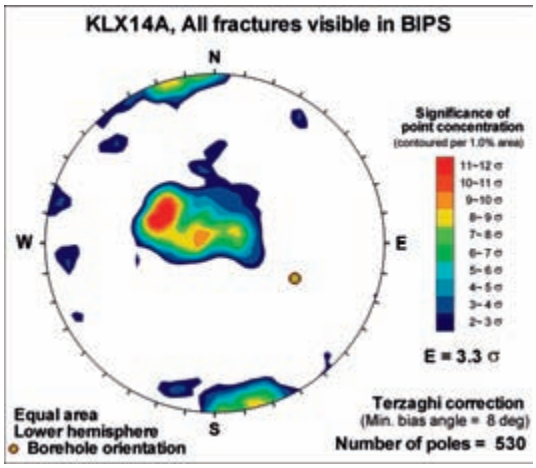
KLX14A, All fractures visible in BIPS
N
W
E
S
Significance of point concentration
(contoured per 1.0% area)
11–12 σ
10–11 σ
9–10 σ
8–9 σ
7–8 σ
6–7 σ
5–6 σ
4–5 σ
3–4 σ
2–3 σ
E = 3.3 σ
Equal area
Lower hemisphere
Borehole orientation
Terzaghi correction
(Min. bias angle = 8 deg)
Number of poles = 530

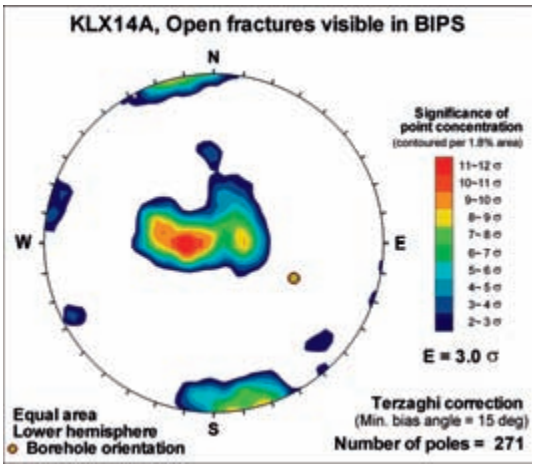
KLX14A, Open fractures visible in BIPS
N
W
E
S
Significance of point concentration
(contoured per 1.8% area)
11–12 σ
10–11 σ
9–10 σ
8–9 σ
7–8 σ
6–7 σ
5–6 σ
4–5 σ
3–4 σ
2–3 σ
E = 3.0 σ
Equal area
Lower hemisphere
Borehole orientation
Terzaghi correction
(Min. bias angle = 15 deg)
Number of poles = 271

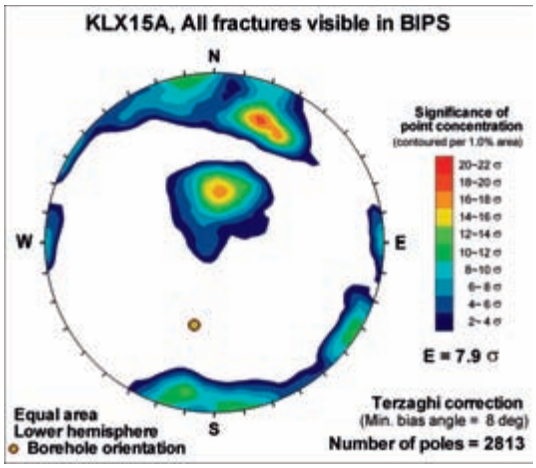
KLX15A, All fractures visible in BIPS
N
W
E
S
Significance of point concentration
(contoured per 1.0% area)
20-22 σ
18-20 σ
16-18 σ
14-16 σ
12-14 σ
10-12 σ
8-10 σ
6-8 σ
4-6 σ
2-4 σ
E = 7.9 σ
Terzaghi correction
(Min. bias angle = 8 deg)
Number of poles = 2813
Equal area
Lower hemisphere
Borehole orientation

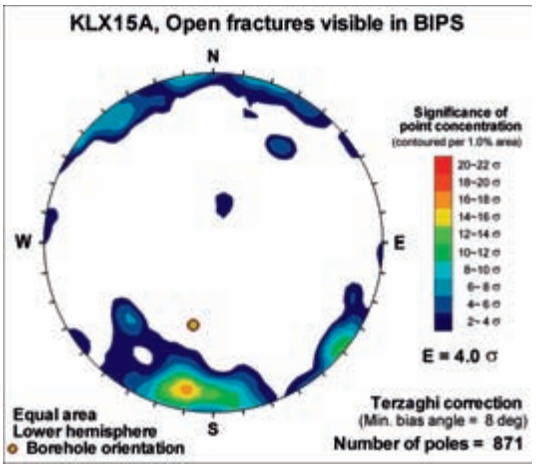
KLX15A, Open fractures visible in BIPS
N
W
E
S
Significance of point concentration
(contoured per 1.0% area)
20-22 σ
18-20 σ
16-18 σ
14-16 σ
12-14 σ
10-12 σ
8-10 σ
6-8 σ
4-6 σ
2-4 σ
E = 4.0 σ
Terzaghi correction
(Min. bias angle = 8 deg)
Number of poles = 871
Equal area
Lower hemisphere
Borehole orientation

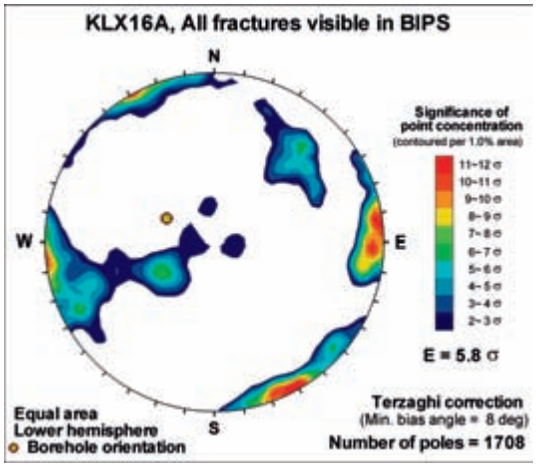
KLX16A, All fractures visible in BIPS
N
W
E
S
Significance of point concentration
(contoured per 1.0% area)
11-12 σ
10-11 σ
9-10 σ
8-9 σ
7-8 σ
6-7 σ
5-6 σ
4-5 σ
3-4 σ
2-3 σ
E = 5.8 σ
Terzaghi correction
(Min. bias angle = 8 deg)
Number of poles = 1708
Equal area
Lower hemisphere
Borehole orientation

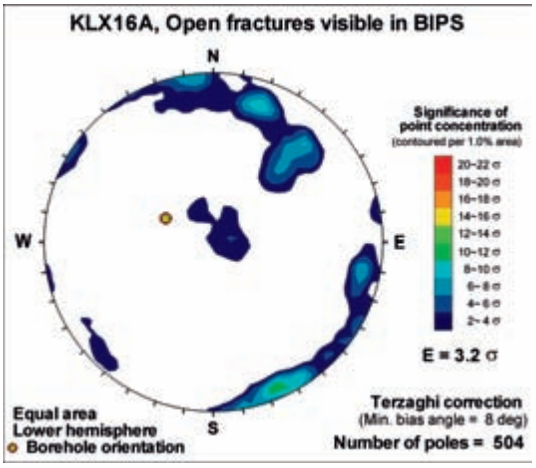
KLX16A, Open fractures visible in BIPS
N
W
E
S
Significance of point concentration
(contoured per 1.0% area)
20-22 σ
18-20 σ
16-18 σ
14-16 σ
12-14 σ
10-12 σ
8-10 σ
6-8 σ
4-6 σ
2-4 σ
E = 3.2 σ
Terzaghi correction
(Min. bias angle = 8 deg)
Number of poles = 504
Equal area
Lower hemisphere
Borehole orientation

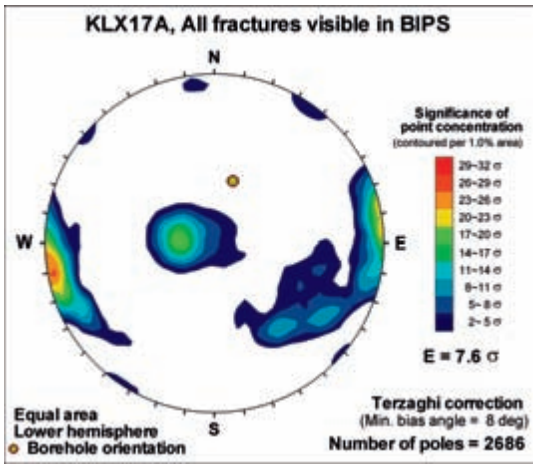
KLX17A, All fractures visible in BIPS
N
W
E
S
Significance of point concentration
(contoured per 1.0% area)
29-32 σ
26-29 σ
23-26 σ
20-23 σ
17-20 σ
14-17 σ
11-14 σ
8-11 σ
5-8 σ
2-5 σ
E = 7.6 σ
Terzaghi correction
(Min. bias angle = 8 deg)
Number of poles = 2686
Equal area
Lower hemisphere
Borehole orientation

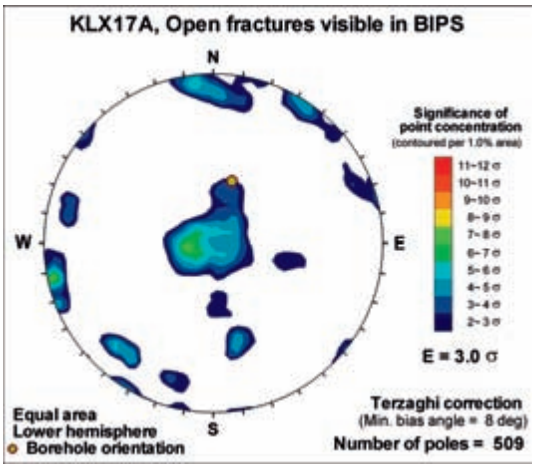
KLX17A, Open fractures visible in BIPS
N
W
E
S
Significance of point concentration
(contoured per 1.0% area)
11-12 σ
10-11 σ
9-10 σ
8-9 σ
7-8 σ
6-7 σ
5-6 σ
4-5 σ
3-4 σ
2-3 σ
E = 3.0 σ
Terzaghi correction
(Min. bias angle = 8 deg)
Number of poles = 509
Equal area
Lower hemisphere
Borehole orientation

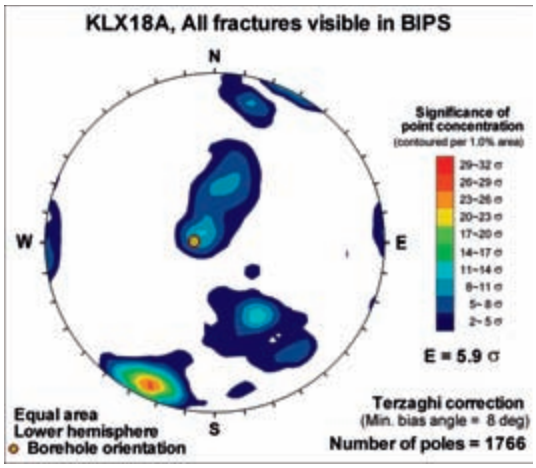
KLX18A, All fractures visible in BIPS
N
W
E
S
Significance of point concentration
(contoured per 1.0% area)
29–32 σ
26–29 σ
23–26 σ
20–23 σ
17–20 σ
14–17 σ
11–14 σ
8–11 σ
5–8 σ
2–5 σ
E = 5.9 σ
Equal area
Lower hemisphere
Borehole orientation
Terzaghi correction
(Min. bias angle = 8 deg)
Number of poles = 1766

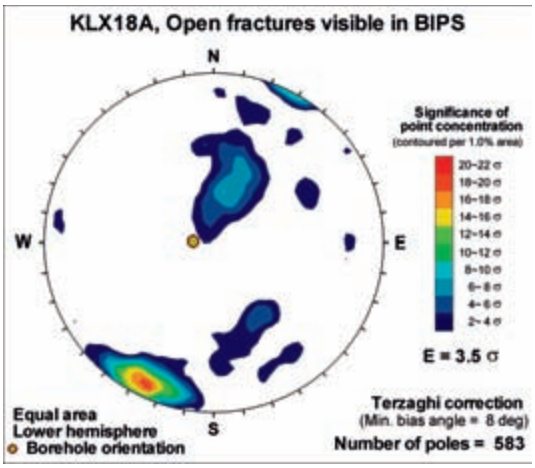
KLX18A, Open fractures visible in BIPS
N
W
E
S
Significance of point concentration
(contoured per 1.0% area)
20–22 σ
18–20 σ
16–18 σ
14–16 σ
12–14 σ
10–12 σ
8–10 σ
6–8 σ
4–6 σ
2–4 σ
E = 3.5 σ
Equal area
Lower hemisphere
Borehole orientation
Terzaghi correction
(Min. bias angle = 8 deg)
Number of poles = 583

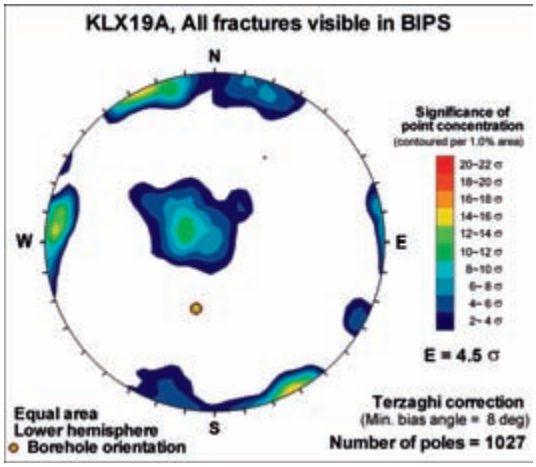
KLX19A, All fractures visible in BIPS
N
W
E
S
Significance of point concentration
(contoured per 1.0% area)
20–22 σ
18–20 σ
16–18 σ
14–16 σ
12–14 σ
10–12 σ
8–10 σ
6–8 σ
4–6 σ
2–4 σ
E = 4.5 σ
Equal area
Lower hemisphere
Borehole orientation
Terzaghi correction
(Min. bias angle = 8 deg)
Number of poles = 1027

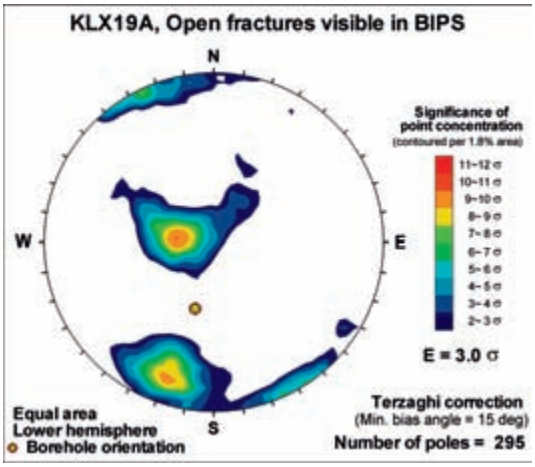
KLX19A, Open fractures visible in BIPS
N
W
E
S
Significance of point concentration
(contoured per 1.8% area)
11–12 σ
10–11 σ
9–10 σ
8–9 σ
7–8 σ
6–7 σ
5–6 σ
4–5 σ
3–4 σ
2–3 σ
E = 3.0 σ
Equal area
Lower hemisphere
Borehole orientation
Terzaghi correction
(Min. bias angle = 15 deg)
Number of poles = 295

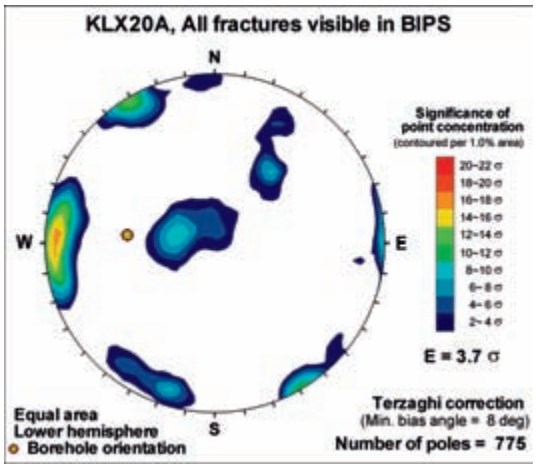
KLX20A, All fractures visible in BIPS
N
W
E
S
Significance of point concentration
(contoured per 1.0% area)
20–22 σ
18–20 σ
16–18 σ
14–16 σ
12–14 σ
10–12 σ
8–10 σ
6–8 σ
4–6 σ
2–4 σ
E = 3.7 σ
Equal area
Lower hemisphere
Borehole orientation
Terzaghi correction
(Min. bias angle = 8 deg)
Number of poles = 775

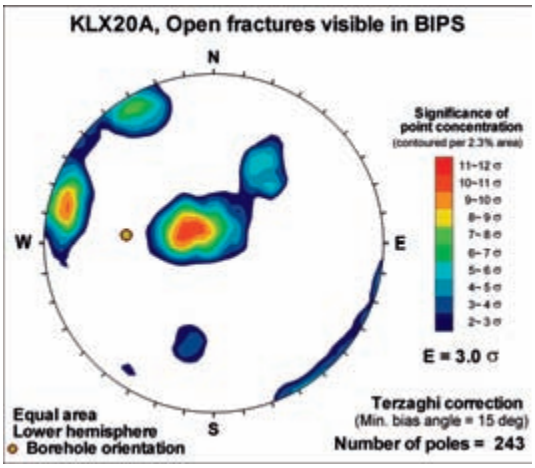
KLX20A, Open fractures visible in BIPS
N
W
E
S
Significance of point concentration
(contoured per 2.3% area)
11–12 σ
10–11 σ
9–10 σ
8–9 σ
7–8 σ
6–7 σ
5–6 σ
4–5 σ
3–4 σ
2–3 σ
E = 3.0 σ
Equal area
Lower hemisphere
Borehole orientation
Terzaghi correction
(Min. bias angle = 15 deg)
Number of poles = 243

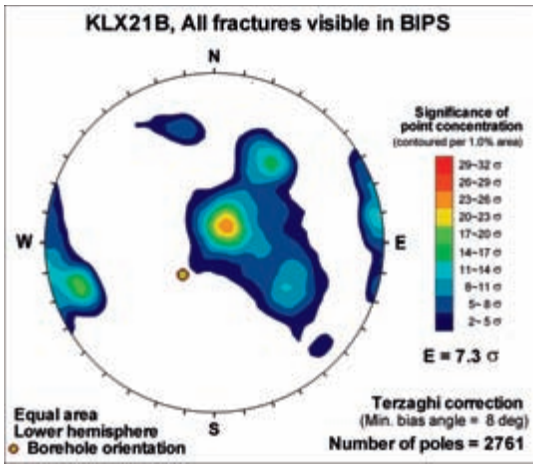
KLX21B, All fractures visible in BIPS
N
W
E
S
Significance of point concentration
(contoured per 1.0% area)
29-32 σ
26-29 σ
23-26 σ
20-23 σ
17-20 σ
14-17 σ
11-14 σ
8-11 σ
5-8 σ
2-5 σ
E = 7.3 σ
Equal area
Lower hemisphere
Borehole orientation
Terzaghi correction
(Min. bias angle = 8 deg)
Number of poles = 2761

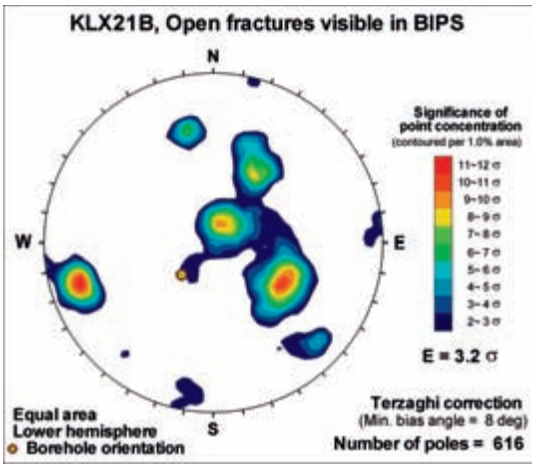
KLX21B, Open fractures visible in BIPS
N
W
E
S
Significance of point concentration
(contoured per 1.0% area)
11-12 σ
10-11 σ
9-10 σ
8-9 σ
7-8 σ
6-7 σ
5-6 σ
4-5 σ
3-4 σ
2-3 σ
E = 3.2 σ
Equal area
Lower hemisphere
Borehole orientation
Terzaghi correction
(Min. bias angle = 8 deg)
Number of poles = 616

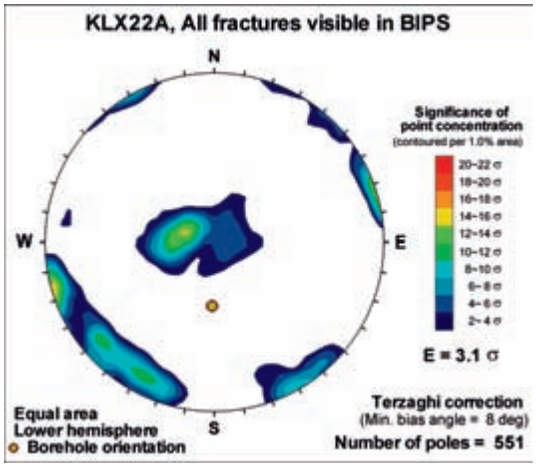
KLX22A, All fractures visible in BIPS
N
W
E
S
Significance of point concentration
(contoured per 1.0% area)
20-22 σ
18-20 σ
16-18 σ
14-16 σ
12-14 σ
10-12 σ
8-10 σ
6-8 σ
4-6 σ
2-4 σ
E = 3.1 σ
Equal area
Lower hemisphere
Borehole orientation
Terzaghi correction
(Min. bias angle = 8 deg)
Number of poles = 551

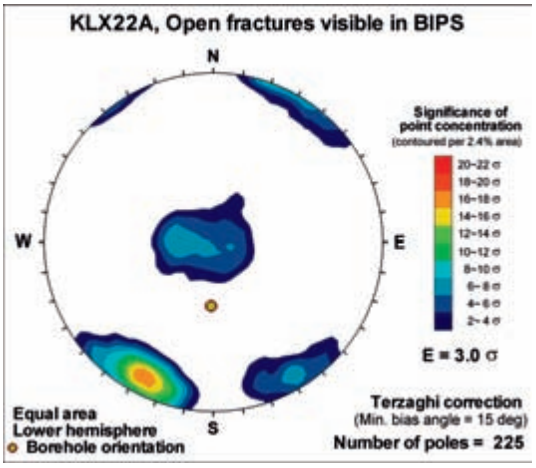
KLX22A, Open fractures visible in BIPS
N
W
E
S
Significance of point concentration
(contoured per 2.4% area)
20-22 σ
18-20 σ
16-18 σ
14-16 σ
12-14 σ
10-12 σ
8-10 σ
6-8 σ
4-6 σ
2-4 σ
E = 3.0 σ
Equal area
Lower hemisphere
Borehole orientation
Terzaghi correction
(Min. bias angle = 15 deg)
Number of poles = 225

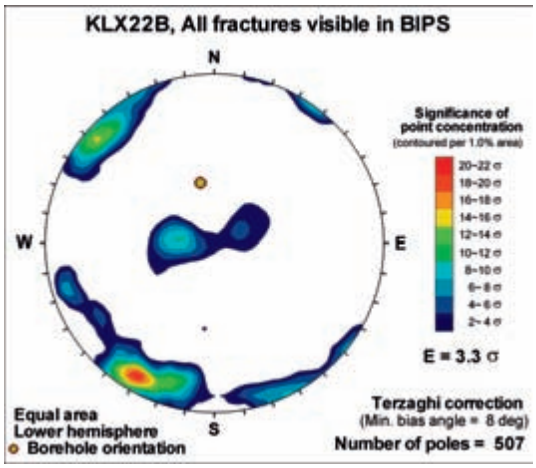
KLX22B, All fractures visible in BIPS
N
W
E
S
Significance of point concentration
(contoured per 1.0% area)
20-22 σ
18-20 σ
16-18 σ
14-16 σ
12-14 σ
10-12 σ
8-10 σ
6-8 σ
4-6 σ
2-4 σ
E = 3.3 σ
Equal area
Lower hemisphere
Borehole orientation
Terzaghi correction
(Min. bias angle = 8 deg)
Number of poles = 507

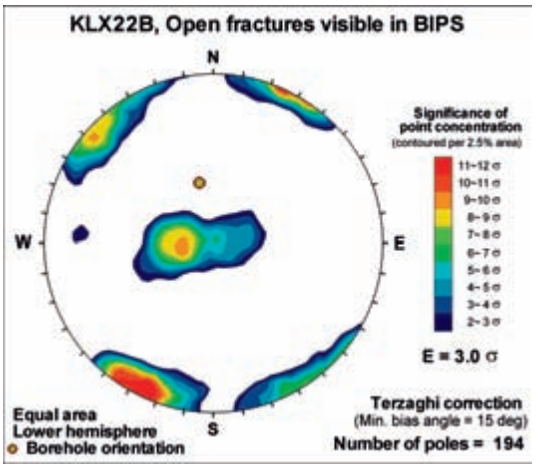
KLX22B, Open fractures visible in BIPS
N
W
E
S
Significance of point concentration
(contoured per 2.5% area)
11-12 σ
10-11 σ
9-10 σ
8-9 σ
7-8 σ
6-7 σ
5-6 σ
4-5 σ
3-4 σ
2-3 σ
E = 3.0 σ
Equal area
Lower hemisphere
Borehole orientation
Terzaghi correction
(Min. bias angle = 15 deg)
Number of poles = 194

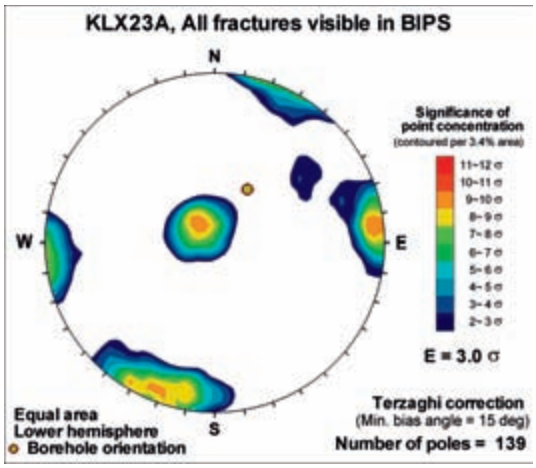
KLX23A, All fractures visible in BIPS
N
W
E
S
Significance of point concentration
(contoured per 3.4% area)
11-12 σ
10-11 σ
9-10 σ
8-9 σ
7-8 σ
6-7 σ
5-6 σ
4-5 σ
3-4 σ
2-3 σ
E = 3.0 σ
Equal area
Lower hemisphere
Borehole orientation
Terzaghi correction
(Min. bias angle = 15 deg)
Number of poles = 139

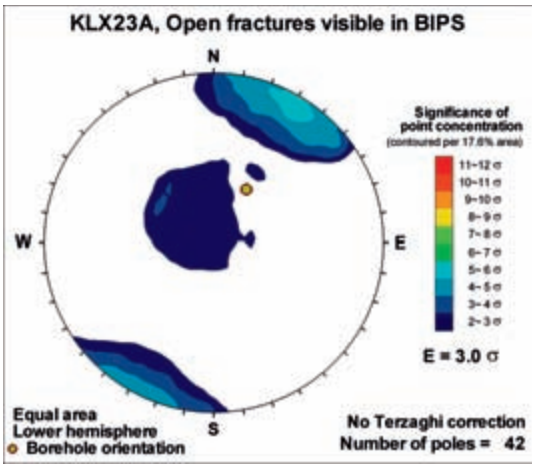
KLX23A, Open fractures visible in BIPS
N
W
E
S
Significance of point concentration
(contoured per 17.6% area)
11-12 σ
10-11 σ
9-10 σ
8-9 σ
7-8 σ
6-7 σ
5-6 σ
4-5 σ
3-4 σ
2-3 σ
E = 3.0 σ
Equal area
Lower hemisphere
Borehole orientation
No Terzaghi correction
Number of poles = 42

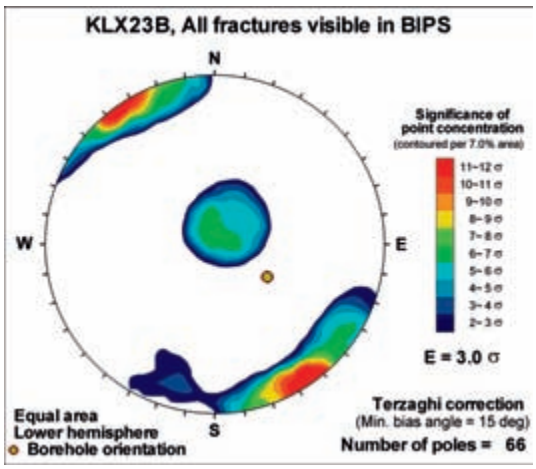
KLX23B, All fractures visible in BIPS
N
W
E
S
Significance of point concentration
(contoured per 7.0% area)
11-12 σ
10-11 σ
9-10 σ
8-9 σ
7-8 σ
6-7 σ
5-6 σ
4-5 σ
3-4 σ
2-3 σ
E = 3.0 σ
Equal area
Lower hemisphere
Borehole orientation
Terzaghi correction
(Min. bias angle = 15 deg)
Number of poles = 66

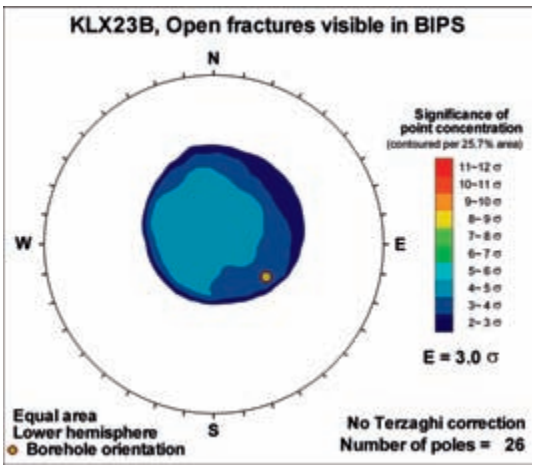
KLX23B, Open fractures visible in BIPS
N
W
E
S
Significance of point concentration
(contoured per 25.7% area)
11-12 σ
10-11 σ
9-10 σ
8-9 σ
7-8 σ
6-7 σ
5-6 σ
4-5 σ
3-4 σ
2-3 σ
E = 3.0 σ
Equal area
Lower hemisphere
Borehole orientation
No Terzaghi correction
Number of poles = 26

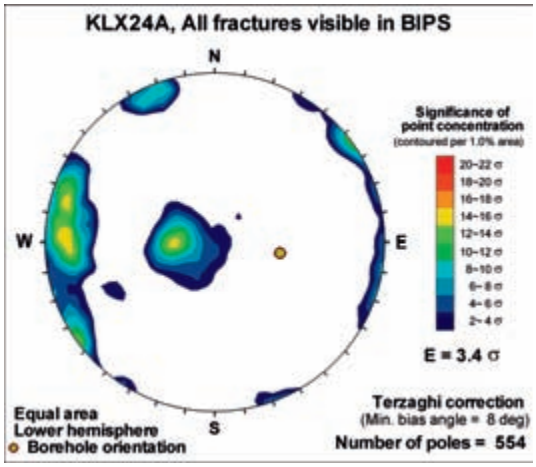
KLX24A, All fractures visible in BIPS
N
W
E
S
Significance of point concentration
(contoured per 1.0% area)
20-22 σ
18-20 σ
16-18 σ
14-16 σ
12-14 σ
10-12 σ
8-10 σ
6-8 σ
4-6 σ
2-4 σ
E = 3.4 σ
Equal area
Lower hemisphere
Borehole orientation
Terzaghi correction
(Min. bias angle = 8 deg)
Number of poles = 554

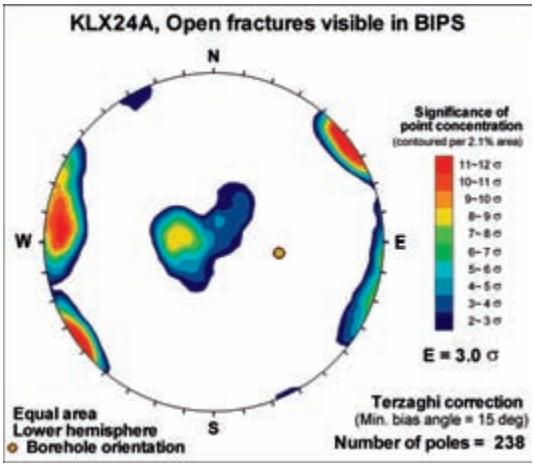
KLX24A, Open fractures visible in BIPS
N
W
E
S
Significance of point concentration
(contoured per 2.1% area)
11-12 σ
10-11 σ
9-10 σ
8-9 σ
7-8 σ
6-7 σ
5-6 σ
4-5 σ
3-4 σ
2-3 σ
E = 3.0 σ
Equal area
Lower hemisphere
Borehole orientation
Terzaghi correction
(Min. bias angle = 15 deg)
Number of poles = 238

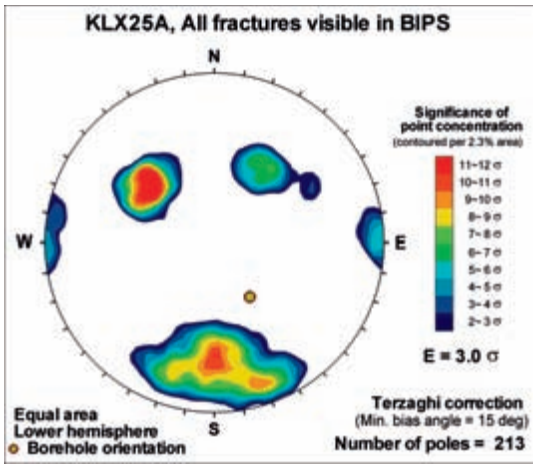
KLX25A, All fractures visible in BIPS
N
W
E
S
Significance of point concentration
(contoured per 2.3% area)
11-12 σ
10-11 σ
9-10 σ
8-9 σ
7-8 σ
6-7 σ
5-6 σ
4-5 σ
3-4 σ
2-3 σ
E = 3.0 σ
Equal area
Lower hemisphere
Borehole orientation
Terzaghi correction
(Min. bias angle = 15 deg)
Number of poles = 213

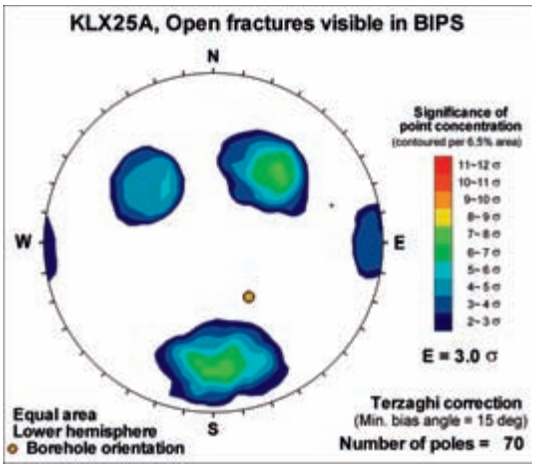
KLX25A, Open fractures visible in BIPS
N
W
E
S
Significance of point concentration
(contoured per 6.5% area)
11-12 σ
10-11 σ
9-10 σ
8-9 σ
7-8 σ
6-7 σ
5-6 σ
4-5 σ
3-4 σ
2-3 σ
E = 3.0 σ
Equal area
Lower hemisphere
Borehole orientation
Terzaghi correction
(Min. bias angle = 15 deg)
Number of poles = 70

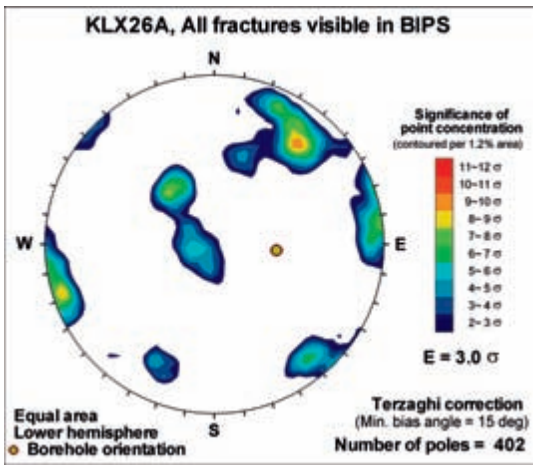
KLX26A, All fractures visible in BIPS
N
W
E
S
Significance of point concentration
(contoured per 1.2% area)
11-12 σ
10-11 σ
9-10 σ
8-9 σ
7-8 σ
6-7 σ
5-6 σ
4-5 σ
3-4 σ
2-3 σ
E = 3.0 σ
Equal area
Lower hemisphere
Borehole orientation
Terzaghi correction
(Min. bias angle = 15 deg)
Number of poles = 402

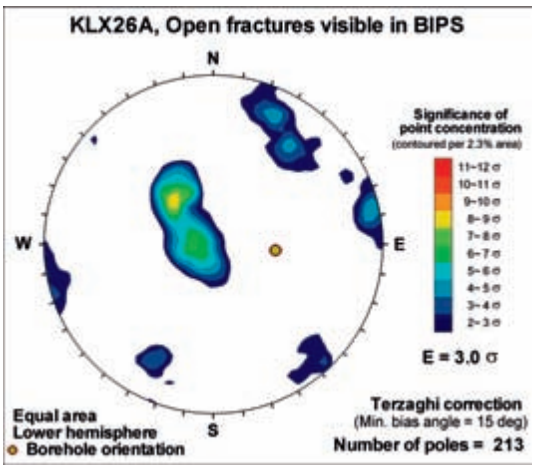
KLX26A, Open fractures visible in BIPS
N
W
E
S
Significance of point concentration
(contoured per 2.3% area)
11-12 σ
10-11 σ
9-10 σ
8-9 σ
7-8 σ
6-7 σ
5-6 σ
4-5 σ
3-4 σ
2-3 σ
E = 3.0 σ
Equal area
Lower hemisphere
Borehole orientation
Terzaghi correction
(Min. bias angle = 15 deg)
Number of poles = 213

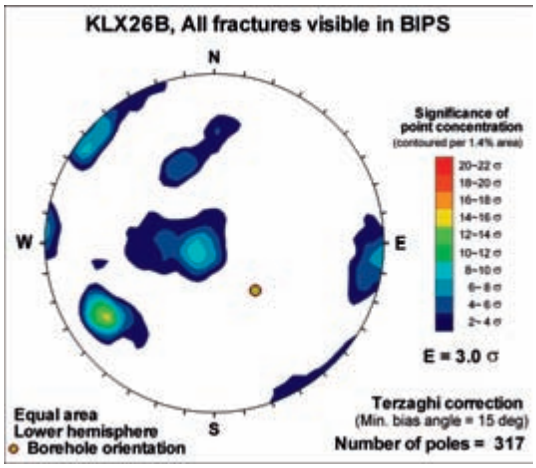
KLX26B, All fractures visible in BIPS
N
W
E
S
Significance of point concentration
(contoured per 1.4% area)
20-22 σ
18-20 σ
16-18 σ
14-16 σ
12-14 σ
10-12 σ
8-10 σ
6-8 σ
4-6 σ
2-4 σ
E = 3.0 σ
Equal area
Lower hemisphere
Borehole orientation
Terzaghi correction
(Min. bias angle = 15 deg)
Number of poles = 317

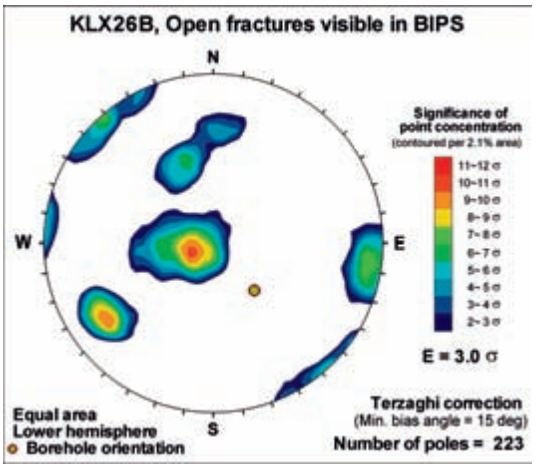
KLX26B, Open fractures visible in BIPS
N
W
E
S
Significance of point concentration
(contoured per 2.1% area)
11-12 σ
10-11 σ
9-10 σ
8-9 σ
7-8 σ
6-7 σ
5-6 σ
4-5 σ
3-4 σ
2-3 σ
E = 3.0 σ
Equal area
Lower hemisphere
Borehole orientation
Terzaghi correction
(Min. bias angle = 15 deg)
Number of poles = 223

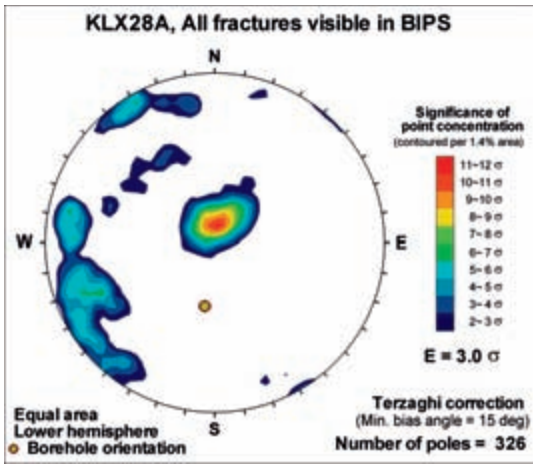
KLX28A, All fractures visible in BIPS
N
W
E
S
Significance of point concentration
(contoured per 1.4% area)
11-12 σ
10-11 σ
9-10 σ
8-9 σ
7-8 σ
6-7 σ
5-6 σ
4-5 σ
3-4 σ
2-3 σ
E = 3.0 σ
Equal area
Lower hemisphere
Borehole orientation
Terzaghi correction
(Min. bias angle = 15 deg)
Number of poles = 326

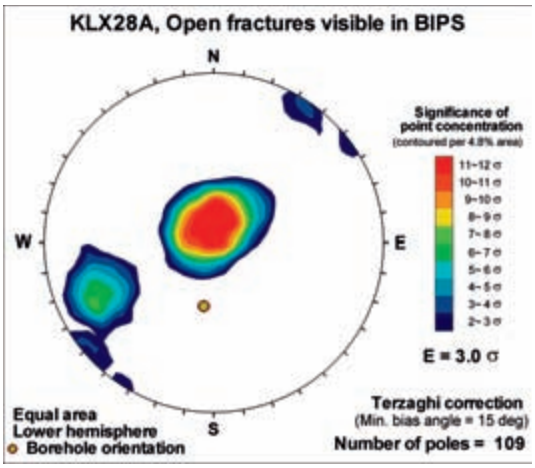
KLX28A, Open fractures visible in BIPS
N
W
E
S
Significance of point concentration
(contoured per 4.8% area)
11-12 σ
10-11 σ
9-10 σ
8-9 σ
7-8 σ
6-7 σ
5-6 σ
4-5 σ
3-4 σ
2-3 σ
E = 3.0 σ
Equal area
Lower hemisphere
Borehole orientation
Terzaghi correction
(Min. bias angle = 15 deg)
Number of poles = 109

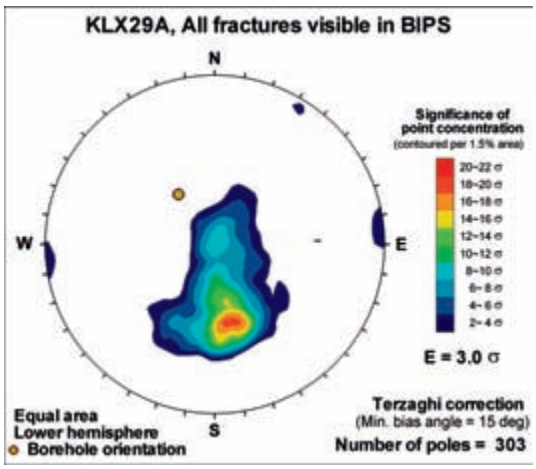
KLX29A, All fractures visible in BIPS
N
W
E
S
Significance of point concentration
(contoured per 1.5% area)
20-22 σ
18-20 σ
16-18 σ
14-16 σ
12-14 σ
10-12 σ
8-10 σ
6-8 σ
4-6 σ
2-4 σ
E = 3.0 σ
Equal area
Lower hemisphere
Borehole orientation
Terzaghi correction
(Min. bias angle = 15 deg)
Number of poles = 303

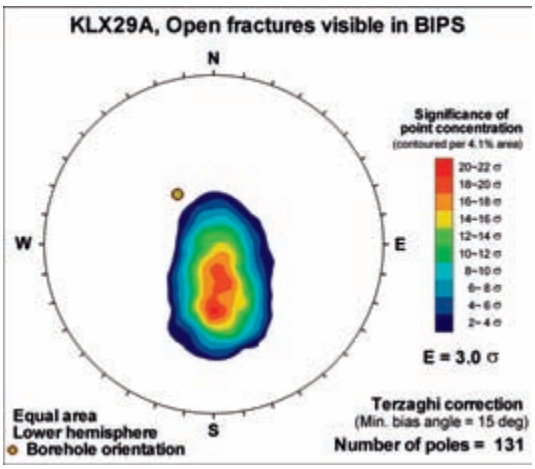
KLX29A, Open fractures visible in BIPS
N
W
E
S
Significance of point concentration
(contoured per 4.1% area)
20-22 σ
18-20 σ
16-18 σ
14-16 σ
12-14 σ
10-12 σ
8-10 σ
6-8 σ
4-6 σ
2-4 σ
E = 3.0 σ
Equal area
Lower hemisphere
Borehole orientation
Terzaghi correction
(Min. bias angle = 15 deg)
Number of poles = 131

Appendix C

Contour plots of borehole and outcrop data by fracture domain

This appendix contains stereonet plots of fracture orientations within fracture domains; the record consists of both the total data population and individual data sets, grouped by fracture domain.

Key to plots:

- All fractures = all oriented borehole data visible in BIPS combined with outcrop data within a fracture domain.
- Sealed fractures = all oriented sealed borehole fractures visible in BIPS within a fracture domain.
- Open fractures = all oriented open borehole fractures visible in BIPS within a fracture domain.
- Lineaments = all lineaments strictly inside a fracture domain (lineaments extending across two or more domains are excluded).

Individual data sets: In the Figure legend, it is specified if the entire borehole belongs to a fracture domain (FSM), or just a section of the borehole, defined in terms of measured length along the borehole (ADJ_SECUP and ADJ_SECLOW from SICADA).

Fracture domain: FSM_C

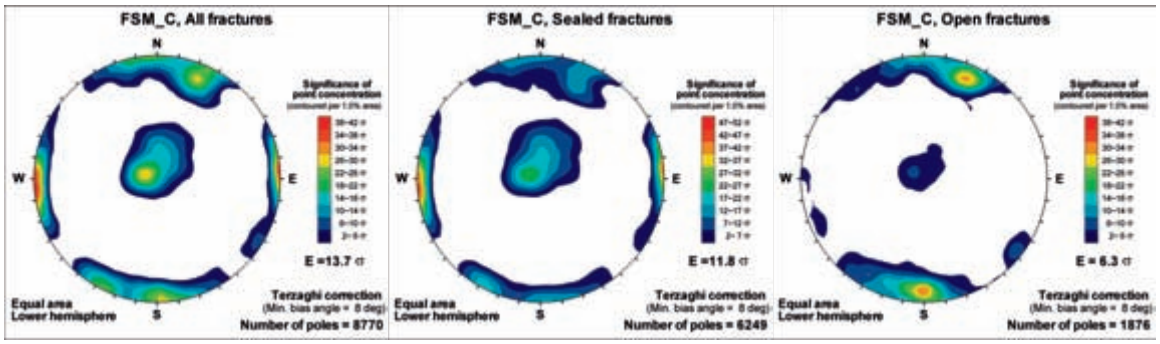

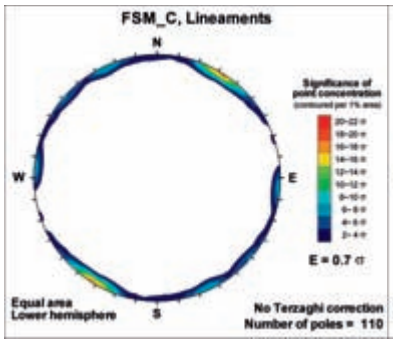
FSM_C, Lineaments
N
W
E
S
Significance of pole concentration
E = 0.7 σ
Equal area
Lower hemisphere
No Terzaghi correction
Number of poles = 110

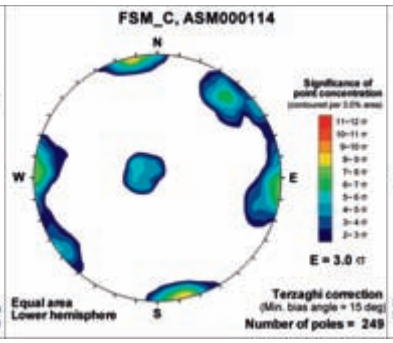
FSM_C, ASM000114
N
W
E
S
Significance of pole concentration
E = 3.0 σ
Equal area
Lower hemisphere
Terzaghi correction
(Min. bias angle = 15 deg)
Number of poles = 249

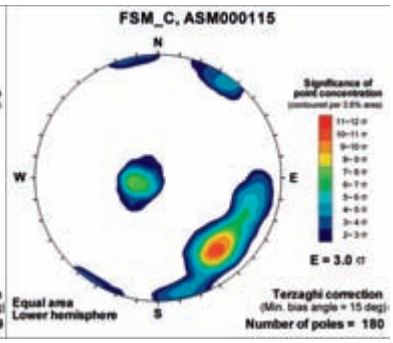
FSM_C, ASM000115
N
W
E
S
Significance of pole concentration
E = 3.0 σ
Equal area
Lower hemisphere
Terzaghi correction
(Min. bias angle = 15 deg)
Number of poles = 180

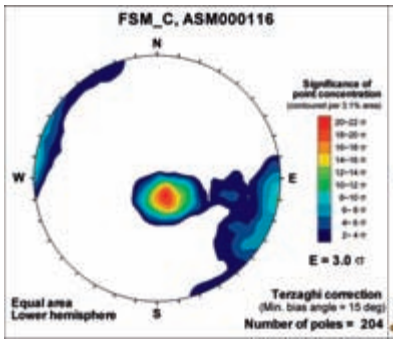
FSM_C, ASM000116
N
W
E
S
Significance of pole concentration
E = 3.0 σ
Equal area
Lower hemisphere
Terzaghi correction
(Min. bias angle = 15 deg)
Number of poles = 204

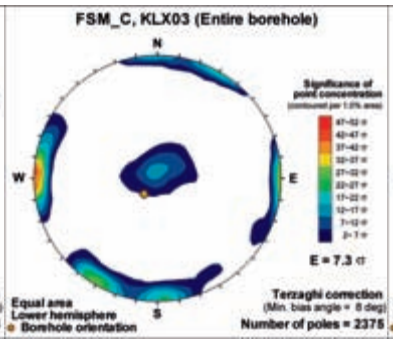
FSM_C, KLX03 (Entire borehole)
N
W
E
S
Significance of pole concentration
E = 7.3 σ
Equal area
Lower hemisphere
Borehole orientation
Terzaghi correction
(Min. bias angle = 8 deg)
Number of poles = 2375

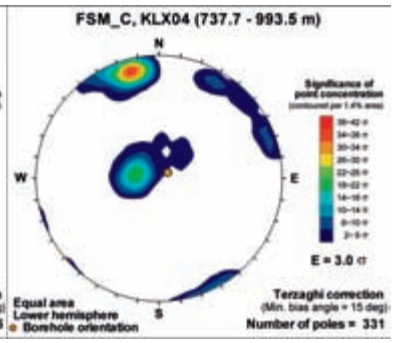
FSM_C, KLX04 (737.7 - 993.5 m)
N
W
E
S
Significance of pole concentration
E = 3.0 σ
Equal area
Lower hemisphere
Borehole orientation
Terzaghi correction
(Min. bias angle = 15 deg)
Number of poles = 331

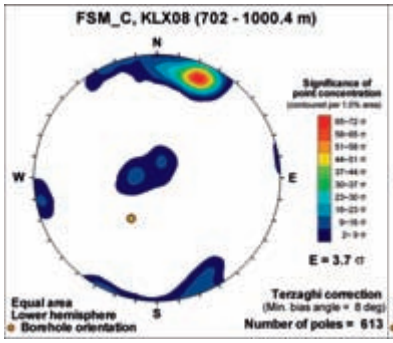
FSM_C, KLX08 (702 - 1000.4 m)
N
W
E
S
Significance of pole concentration
E = 3.7 σ
Equal area
Lower hemisphere
Borehole orientation
Terzaghi correction
(Min. bias angle = 8 deg)
Number of poles = 613

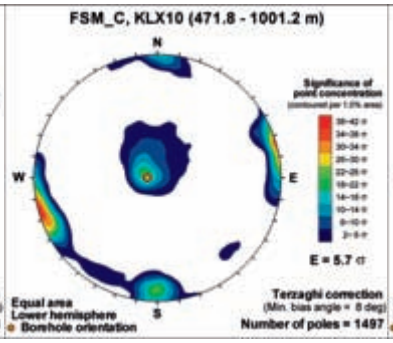
FSM_C, KLX10 (471.8 - 1001.2 m)
N
W
E
S
Significance of pole concentration
E = 5.7 σ
Equal area
Lower hemisphere
Borehole orientation
Terzaghi correction
(Min. bias angle = 8 deg)
Number of poles = 1497

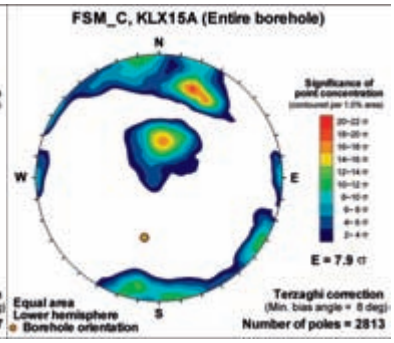
FSM_C, KLX15A (Entire borehole)
N
W
E
S
Significance of pole concentration
E = 7.9 σ
Equal area
Lower hemisphere
Borehole orientation
Terzaghi correction
(Min. bias angle = 8 deg)
Number of poles = 2813

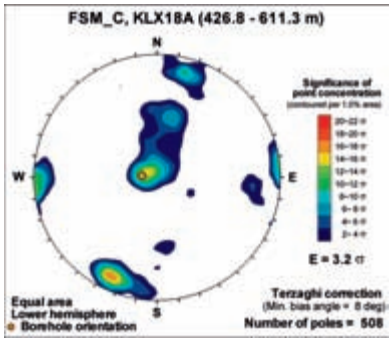
FSM_C, KLX18A (426.8 - 611.3 m)
N
W
E
S
Significance of pole concentration
E = 3.2 σ
Equal area
Lower hemisphere
Borehole orientation
Terzaghi correction
(Min. bias angle = 8 deg)
Number of poles = 508

Fracture domain: FSM_EW007

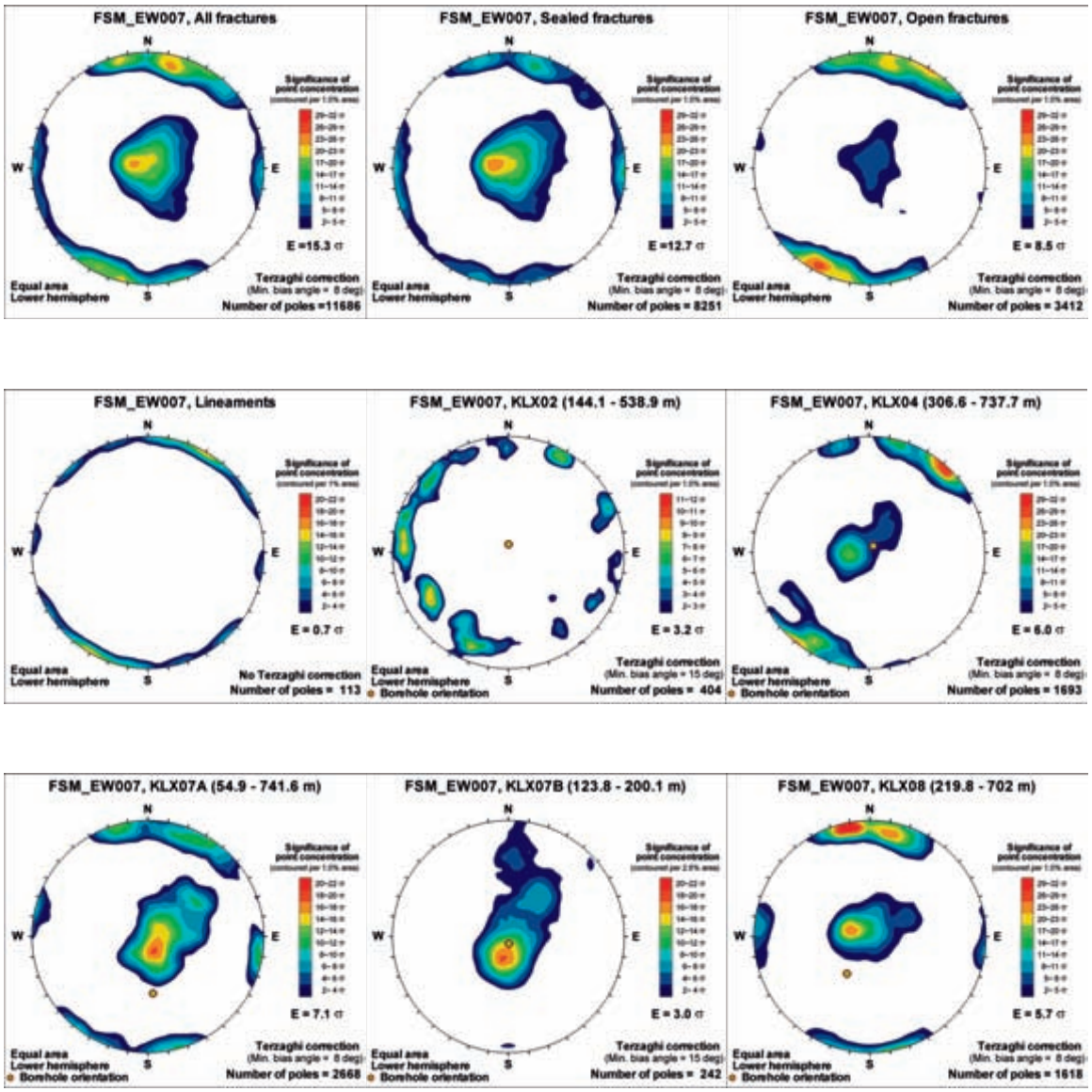

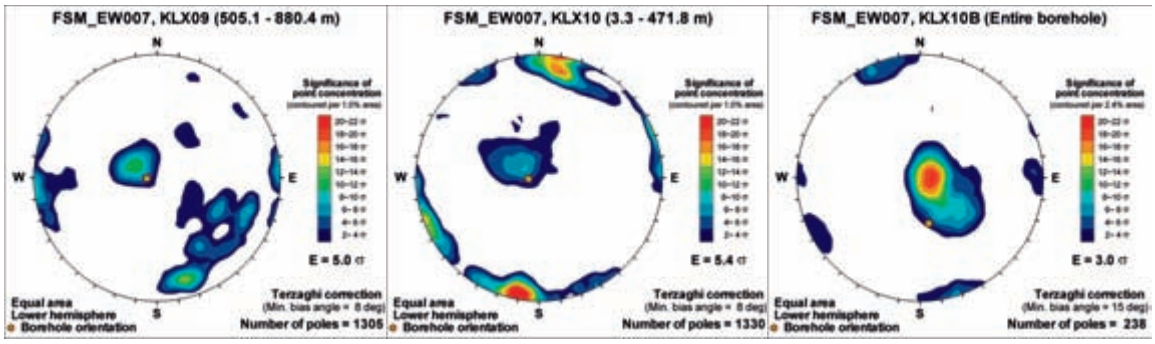
FSM_EW007, KLX09 (505.1 - 880.4 m)
N
W
E
S
Significance of pole concentration
E = 5.0 σ
Equal area
Lower hemisphere
Borehole orientation
Terzaghi correction
Number of poles = 1305
FSM_EW007, KLX10 (3.3 - 471.8 m)
N
W
E
S
Significance of pole concentration
E = 5.4 σ
Equal area
Lower hemisphere
Borehole orientation
Terzaghi correction
Number of poles = 1330
FSM_EW007, KLX10B (Entire borehole)
N
W
E
S
Significance of pole concentration
E = 3.0 σ
Equal area
Lower hemisphere
Borehole orientation
Terzaghi correction
Number of poles = 238

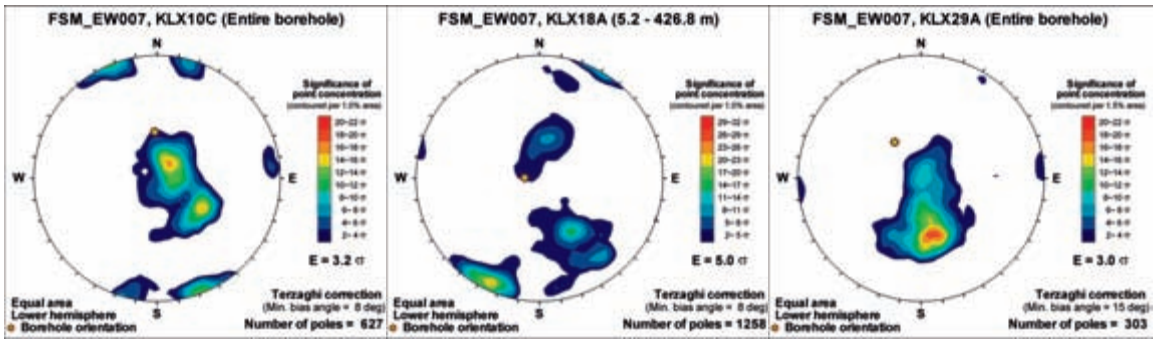
FSM_EW007, KLX10C (Entire borehole)
N
W
E
S
Significance of pole concentration
E = 3.2 σ
Equal area
Lower hemisphere
Borehole orientation
Terzaghi correction
Number of poles = 627
FSM_EW007, KLX18A (5.2 - 426.8 m)
N
W
E
S
Significance of pole concentration
E = 5.0 σ
Equal area
Lower hemisphere
Borehole orientation
Terzaghi correction
Number of poles = 1258
FSM_EW007, KLX29A (Entire borehole)
N
W
E
S
Significance of pole concentration
E = 3.0 σ
Equal area
Lower hemisphere
Borehole orientation
Terzaghi correction
Number of poles = 303

Fracture domain: FSM_N

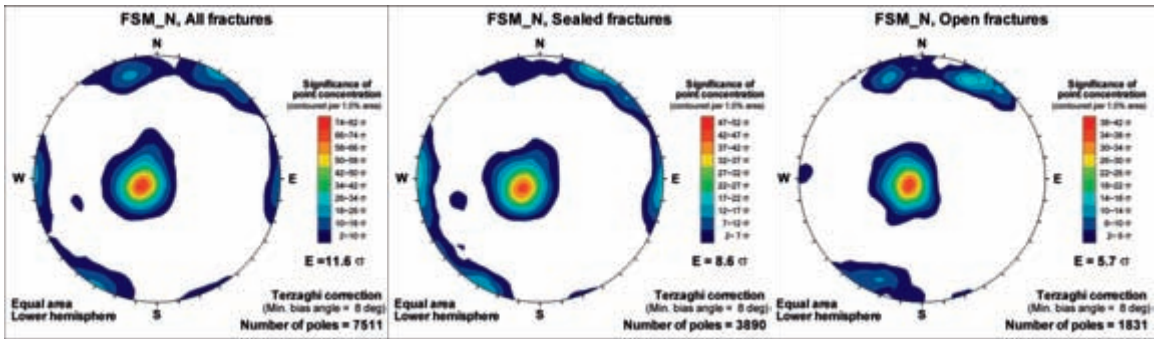

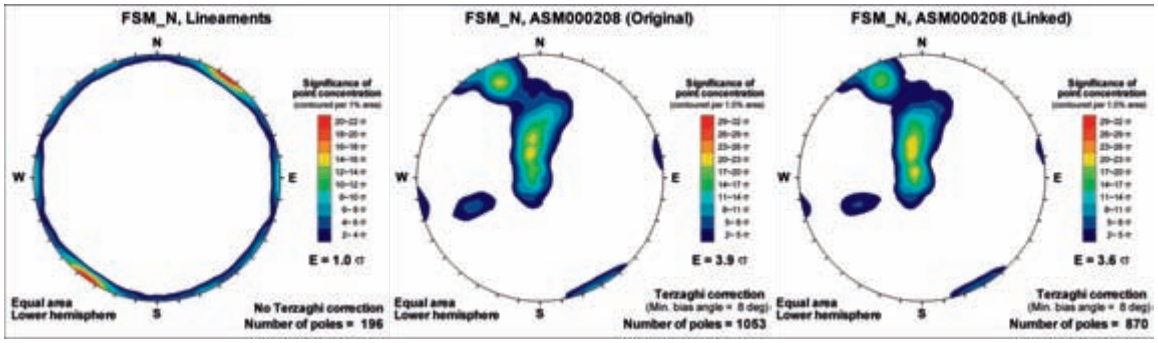

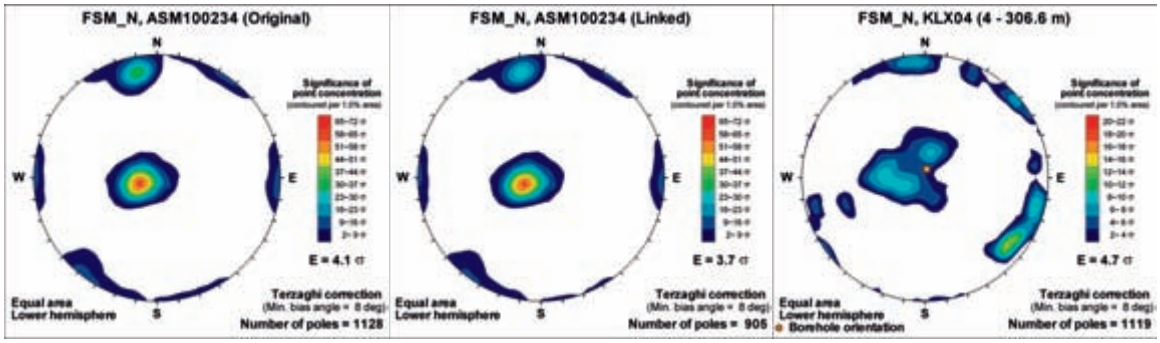

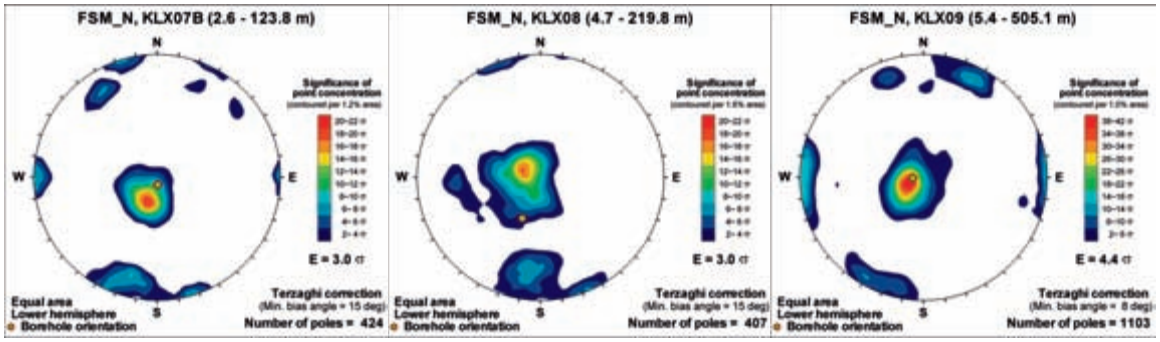

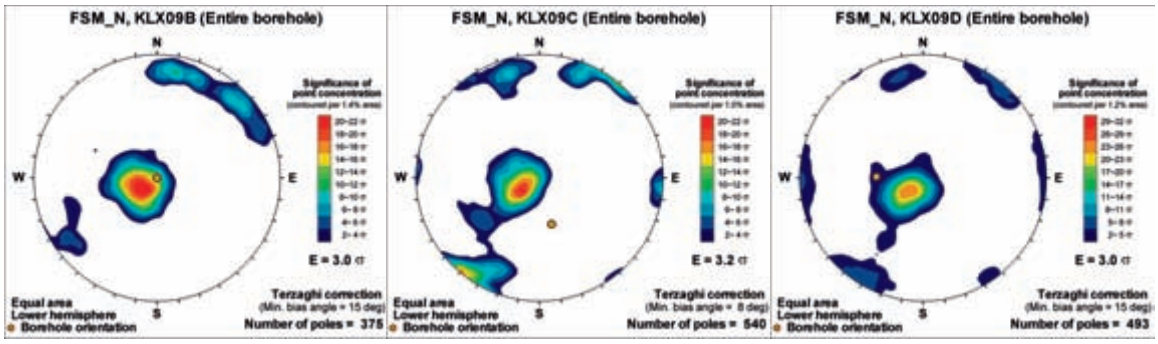
FSM_N, KLX09B (Entire borehole)
N
W
E
S
Significance of pole concentration
E = 3.0 σ
Equal area
Lower hemisphere
Borehole orientation
Terzaghi correction
(Min. bias angle = 15 deg)
Number of poles = 375
FSM_N, KLX09C (Entire borehole)
N
W
E
S
Significance of pole concentration
E = 3.2 σ
Equal area
Lower hemisphere
Borehole orientation
Terzaghi correction
(Min. bias angle = 8 deg)
Number of poles = 540
FSM_N, KLX09D (Entire borehole)
N
W
E
S
Significance of pole concentration
E = 3.0 σ
Equal area
Lower hemisphere
Borehole orientation
Terzaghi correction
(Min. bias angle = 15 deg)
Number of poles = 493

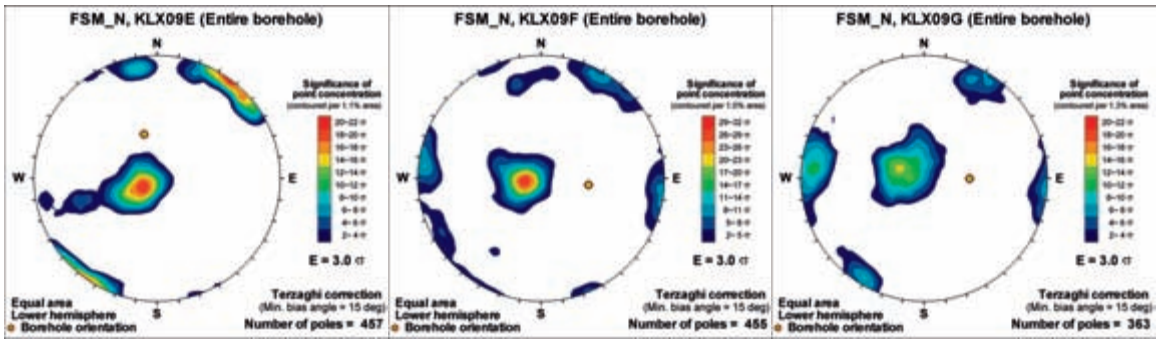
FSM_N, KLX09E (Entire borehole)
N
W
E
S
Significance of pole concentration
E = 3.0 σ
Equal area
Lower hemisphere
Borehole orientation
Terzaghi correction
(Min. bias angle = 15 deg)
Number of poles = 457
FSM_N, KLX09F (Entire borehole)
N
W
E
S
Significance of pole concentration
E = 3.0 σ
Equal area
Lower hemisphere
Borehole orientation
Terzaghi correction
(Min. bias angle = 15 deg)
Number of poles = 455
FSM_N, KLX09G (Entire borehole)
N
W
E
S
Significance of pole concentration
E = 3.0 σ
Equal area
Lower hemisphere
Borehole orientation
Terzaghi correction
(Min. bias angle = 15 deg)
Number of poles = 363

Fracture domain: FSM_NE005

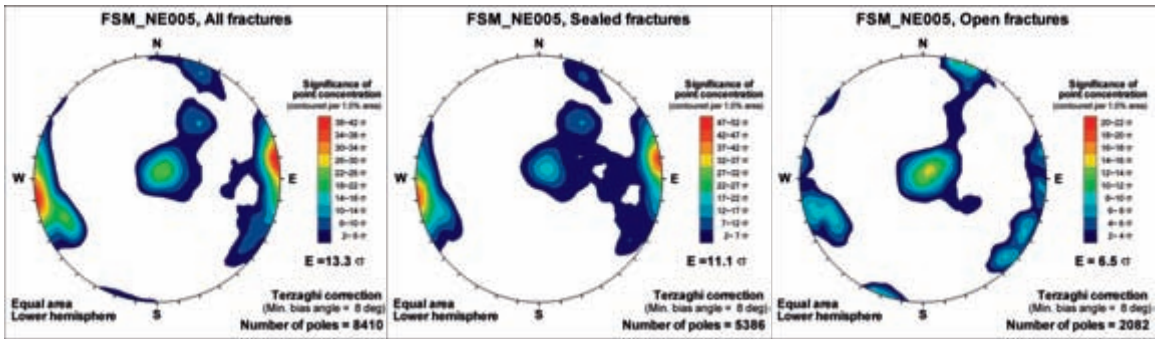

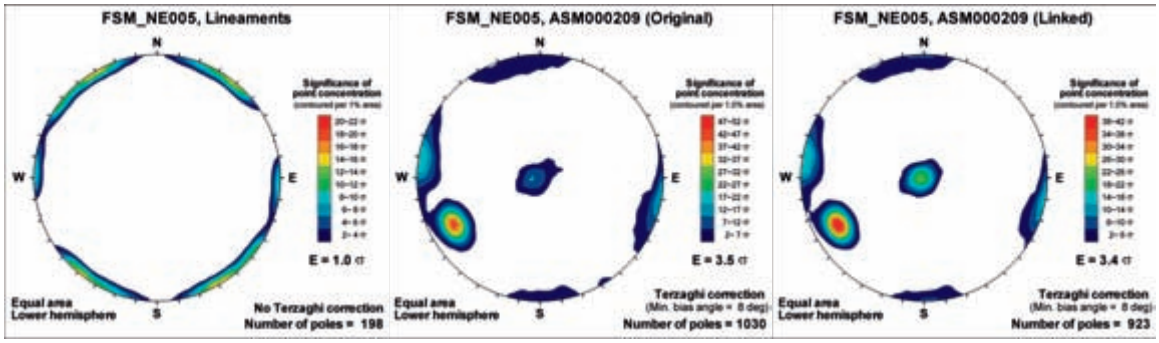

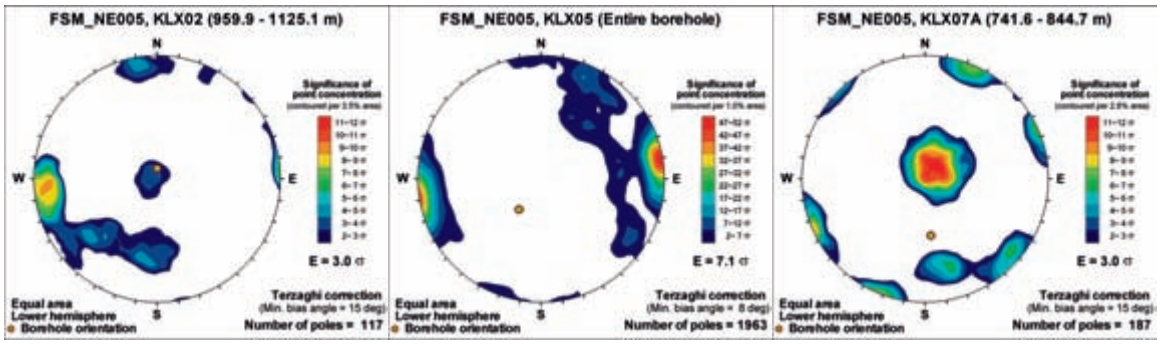

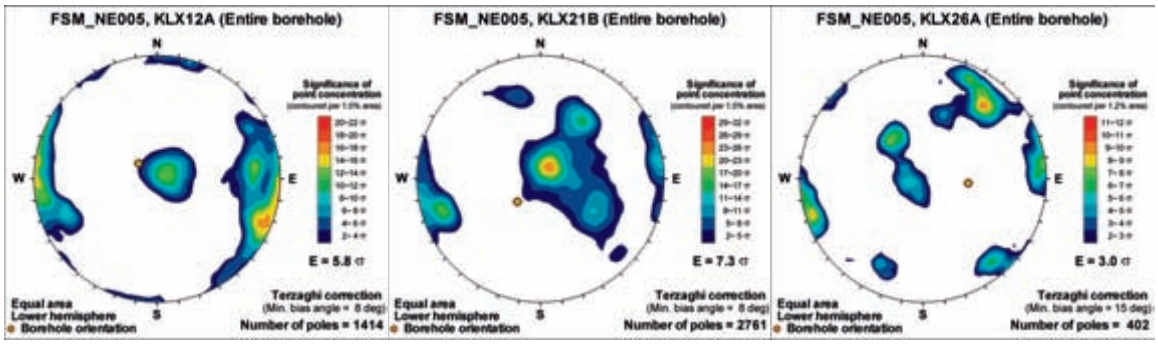

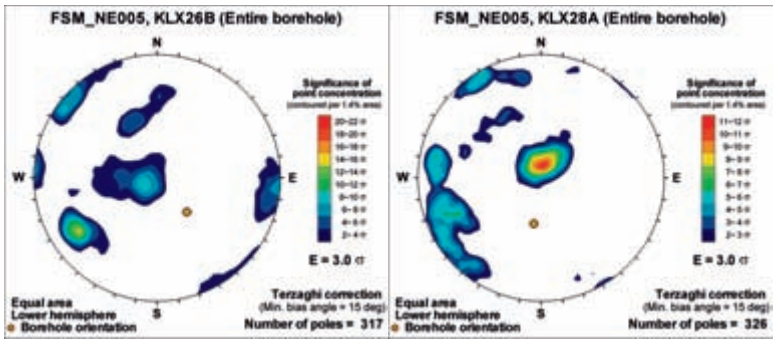
FSM_NE005, KLX26B (Entire borehole)
N
W
E
S
Significance of point concentration
E = 3.0 σ
Equal area
Lower hemisphere
Borehole orientation
Terzaghi correction
(Min. bias angle = 15 deg)
Number of poles = 317
FSM_NE005, KLX28A (Entire borehole)
N
W
E
S
Significance of point concentration
E = 3.0 σ
Equal area
Lower hemisphere
Borehole orientation
Terzaghi correction
(Min. bias angle = 15 deg)
Number of poles = 326

Fracture domain: FSM_W

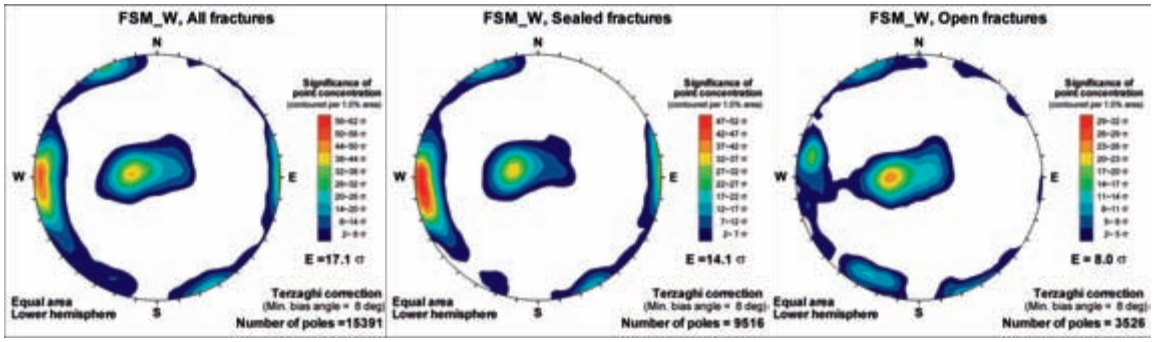

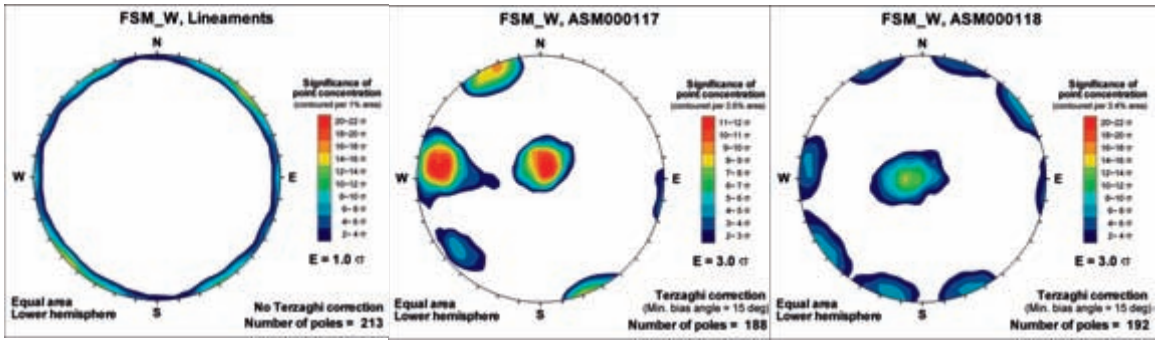

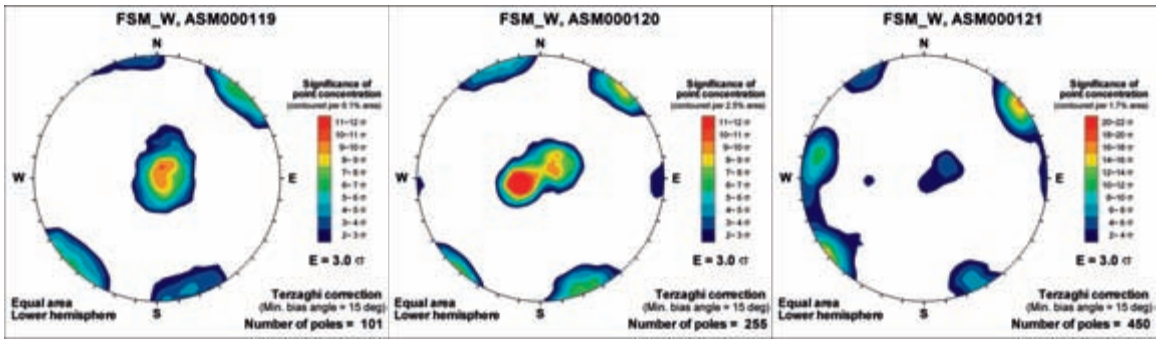

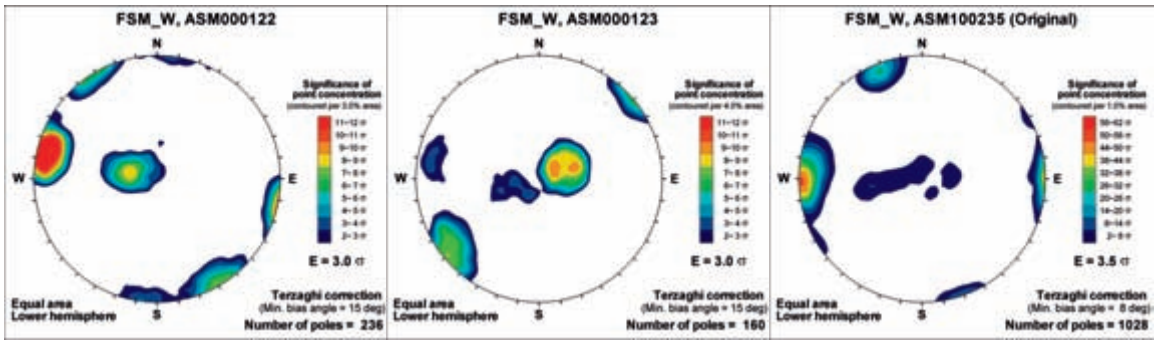

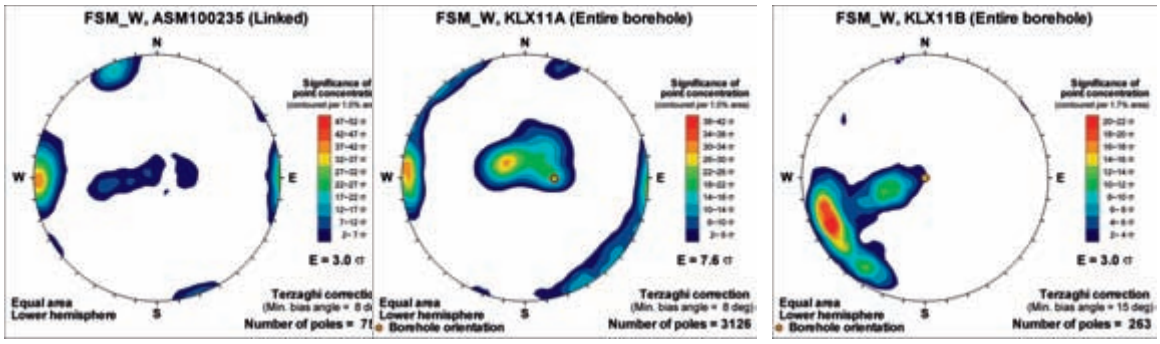
FSM_W, ASM100235 (Linked)
FSM_W, KLX11A (Entire borehole)
FSM_W, KLX11B (Entire borehole)
N
W
E
S
Significance of point concentration
E = 3.0 σ
E = 7.6 σ
E = 3.0 σ
Equal area
Lower hemisphere
Borehole orientation
Terzaghi correction
(Min. bias angle = 15 deg)
Number of poles = 3126
Number of poles = 263

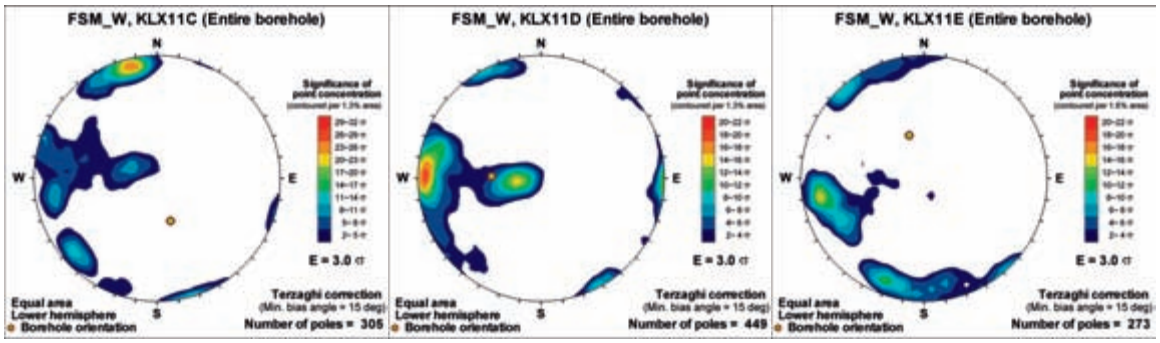
FSM_W, KLX11C (Entire borehole)
FSM_W, KLX11D (Entire borehole)
FSM_W, KLX11E (Entire borehole)
N
W
E
S
Significance of point concentration
E = 3.0 σ
E = 3.0 σ
E = 3.0 σ
Equal area
Lower hemisphere
Borehole orientation
Terzaghi correction
(Min. bias angle = 15 deg)
Number of poles = 305
Number of poles = 449
Number of poles = 273

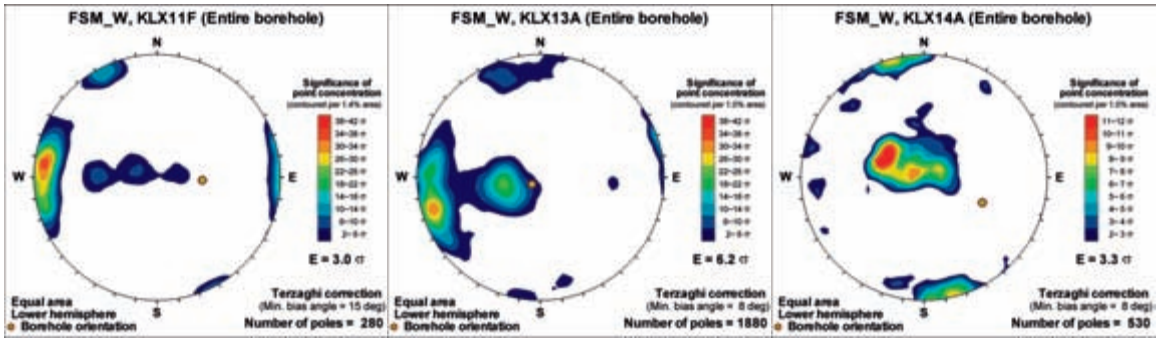
FSM_W, KLX11F (Entire borehole)
FSM_W, KLX13A (Entire borehole)
FSM_W, KLX14A (Entire borehole)
N
W
E
S
Significance of point concentration
E = 3.0 σ
E = 6.2 σ
E = 3.3 σ
Equal area
Lower hemisphere
Borehole orientation
Terzaghi correction
(Min. bias angle = 15 deg)
(Min. bias angle = 8 deg)
Number of poles = 280
Number of poles = 1880
Number of poles = 530

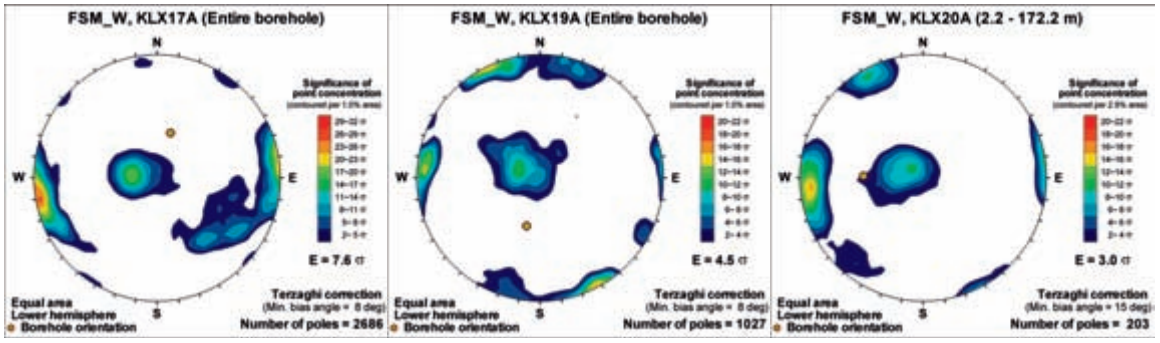
FSM_W, KLX17A (Entire borehole)
FSM_W, KLX19A (Entire borehole)
FSM_W, KLX20A (2.2 - 172.2 m)
N
W
E
S
Significance of point concentration
E = 7.6 σ
E = 4.5 σ
E = 3.0 σ
Equal area
Lower hemisphere
Borehole orientation
Terzaghi correction
(Min. bias angle = 8 deg)
(Min. bias angle = 15 deg)
Number of poles = 2686
Number of poles = 1027
Number of poles = 203

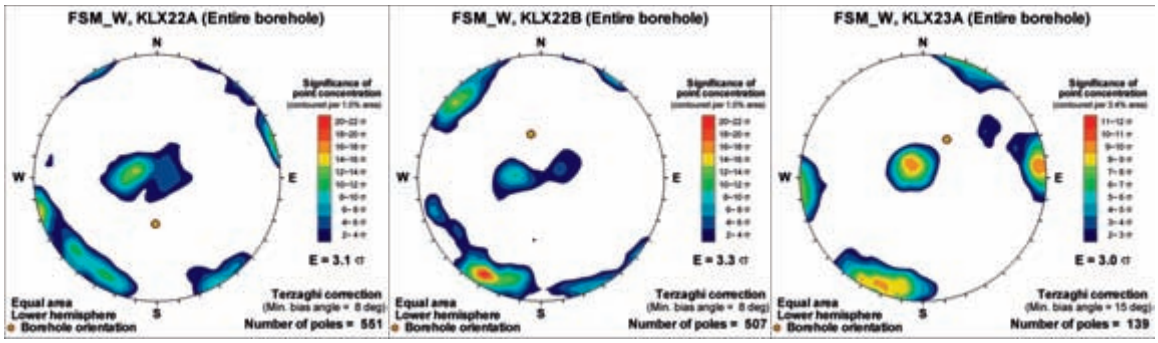
FSM_W, KLX22A (Entire borehole)
N
W
E
S
Significance of point concentration
E = 3.1 σ1
Equal area
Lower hemisphere
Borehole orientation
Terzaghi correction
(Min. bias angle = 8 deg)
Number of poles = 551
FSM_W, KLX22B (Entire borehole)
N
W
E
S
Significance of point concentration
E = 3.3 σ1
Equal area
Lower hemisphere
Borehole orientation
Terzaghi correction
(Min. bias angle = 8 deg)
Number of poles = 507
FSM_W, KLX23A (Entire borehole)
N
W
E
S
Significance of point concentration
E = 3.0 σ1
Equal area
Lower hemisphere
Borehole orientation
Terzaghi correction
(Min. bias angle = 15 deg)
Number of poles = 139

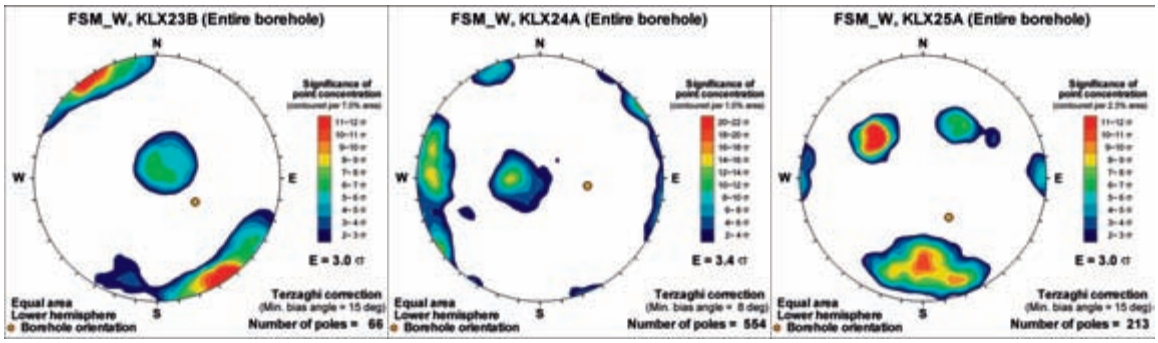
FSM_W, KLX23B (Entire borehole)
N
W
E
S
Significance of point concentration
E = 3.0 σ1
Equal area
Lower hemisphere
Borehole orientation
Terzaghi correction
(Min. bias angle = 15 deg)
Number of poles = 66
FSM_W, KLX24A (Entire borehole)
N
W
E
S
Significance of point concentration
E = 3.4 σ1
Equal area
Lower hemisphere
Borehole orientation
Terzaghi correction
(Min. bias angle = 8 deg)
Number of poles = 554
FSM_W, KLX25A (Entire borehole)
N
W
E
S
Significance of point concentration
E = 3.0 σ1
Equal area
Lower hemisphere
Borehole orientation
Terzaghi correction
(Min. bias angle = 15 deg)
Number of poles = 213

Fracture domain: FSM_S

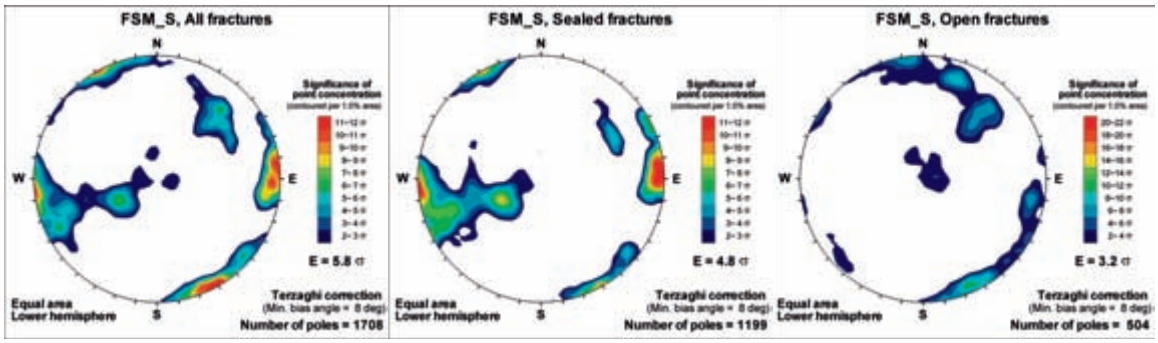

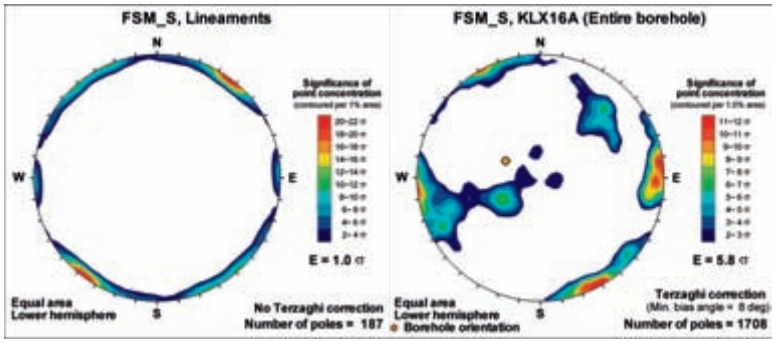

Appendix D

Fractal mass dimension plots

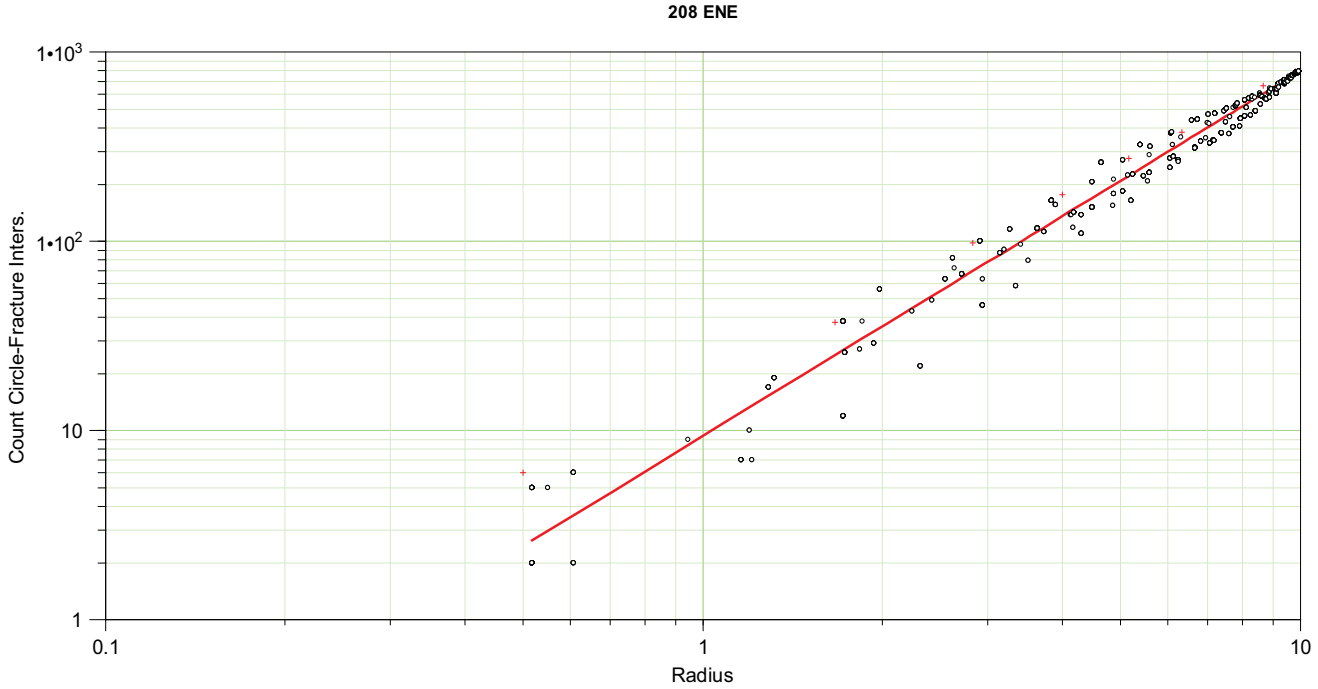

Power Law function: Parameters selected by user
Exponent = 1.93 Coefficient = 9.37
SSQ (sum of sq. errors) = 13724.6
Std.Deviaton Error = 44.2794
Locus Set has been fitted

Figure D-1. *Outcrop ASM000208, ENE fracture set.*

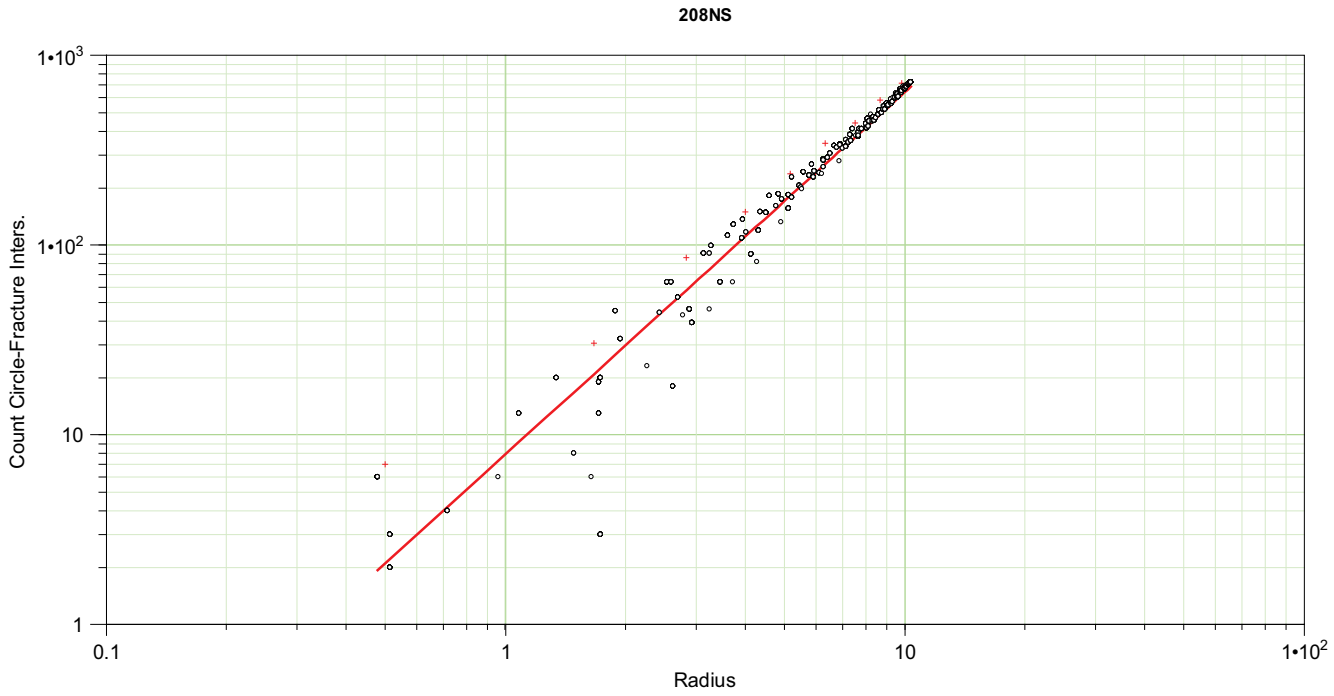

Power Law function: Parameters selected by user
Exponent = 1.91 Coefficient = 7.9
SSQ (sum of sq. errors) = 33894.8
Std.Deviaton Error = 69.5853
Locus Set has been fitted

Figure D-2. *Outcrop ASM000208, NS fracture set.*

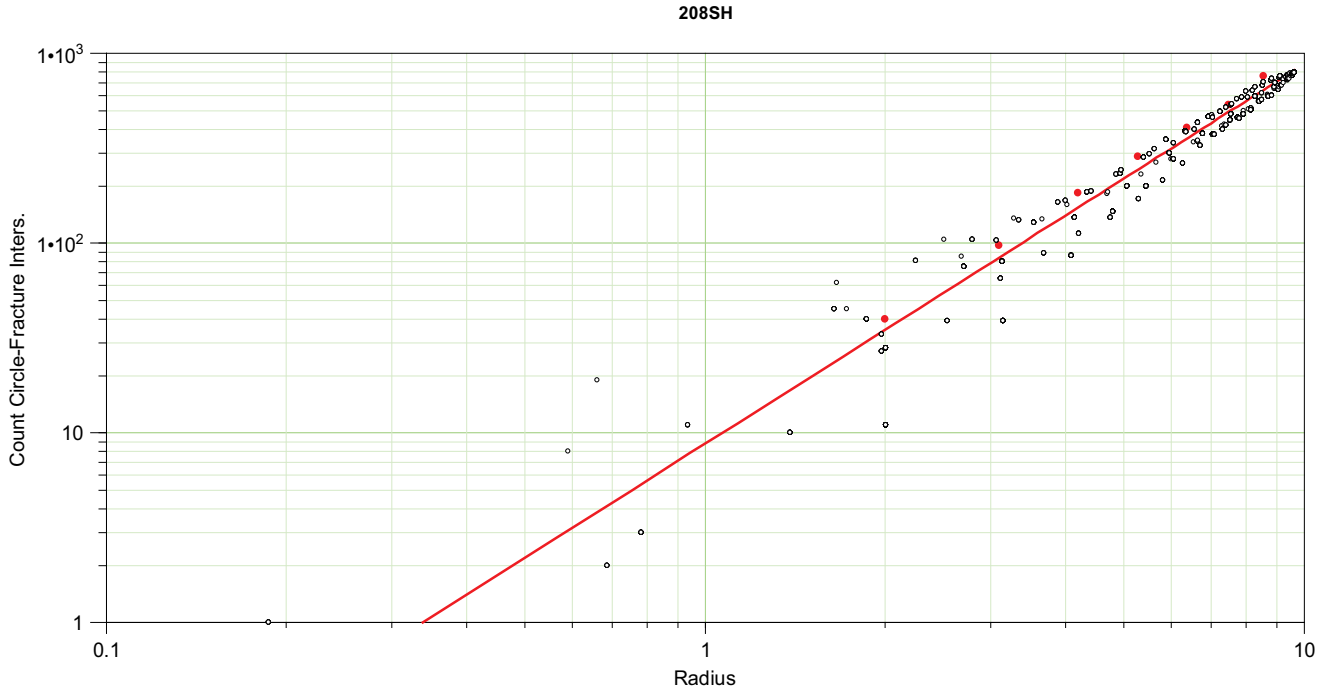

Power Law function: Parameters selected by user
Exponent = 1.99826 Coefficient = 8.8
SSQ (sum of sq. errors) = 21601.1
Std.Deviaton Error = 65.7284
Locus Set has been fitted

Figure D-3. *Outcrop ASM000208, SH fracture set.*

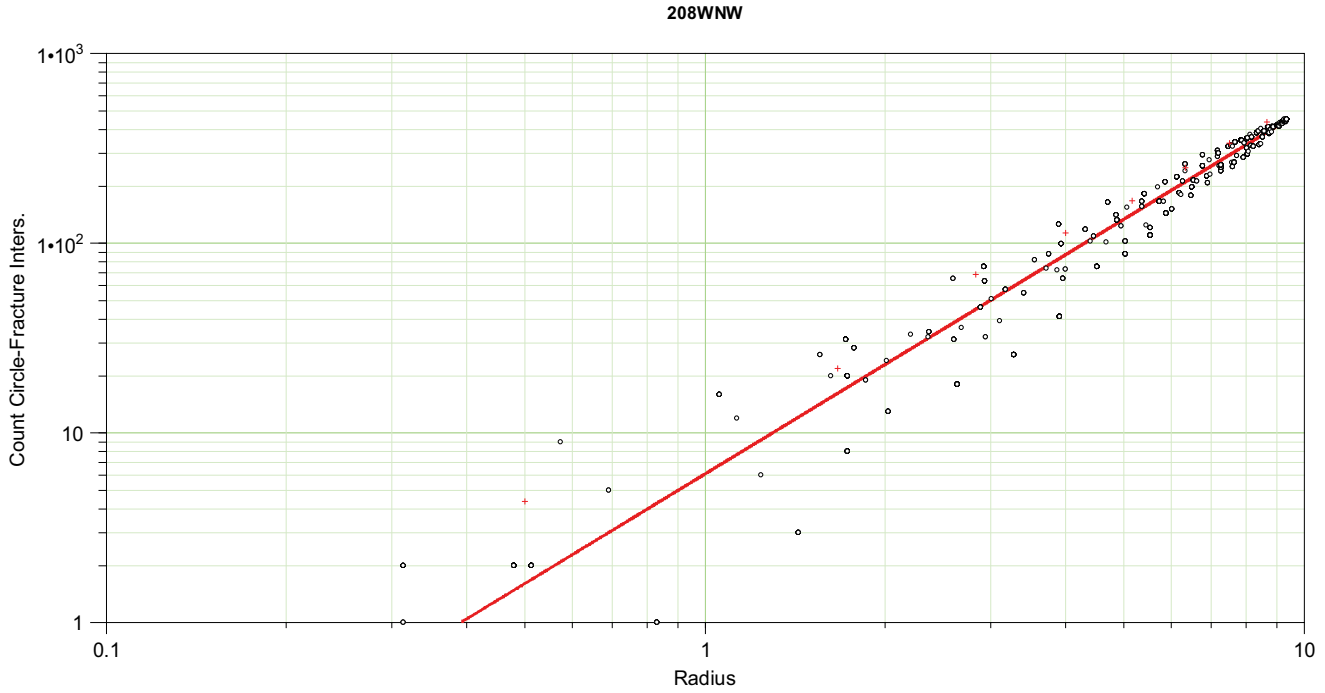

Power Law function: Parameters selected by user
Exponent = 1.92 Coefficient = 6.1
SSQ (sum of sq. errors) = 1.03285e+006
Std.Deviaton Error = 22.5509
Primary Set has been fitted

Figure D-4. *Outcrop ASM000208, WNW fracture set.*

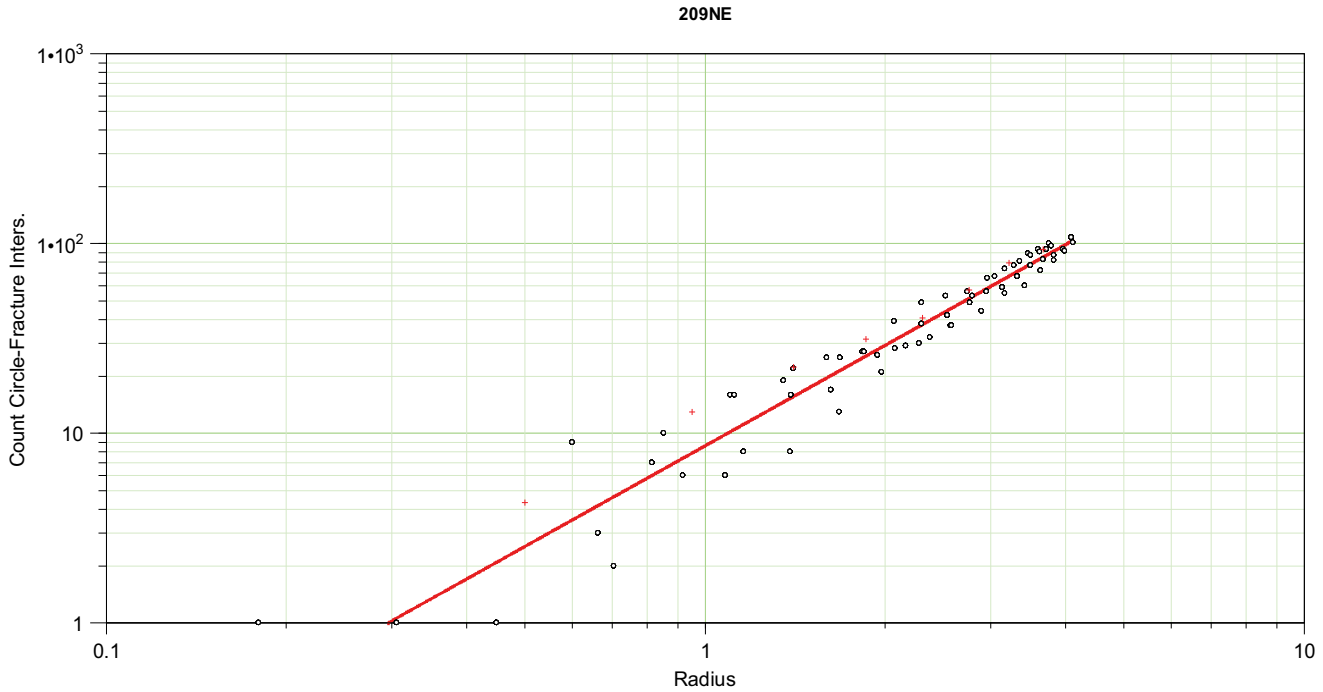

Power Law function: Least Squares method
Exponent = 1.76257 Coefficient = 8.60598
SSQ (sum of sq. errors) = 62587.8
Std.Deviaton Error = 6.12007
Primary Set has been fitted

Figure D-5. *Outcrop ASM000209, ENE fracture set.*

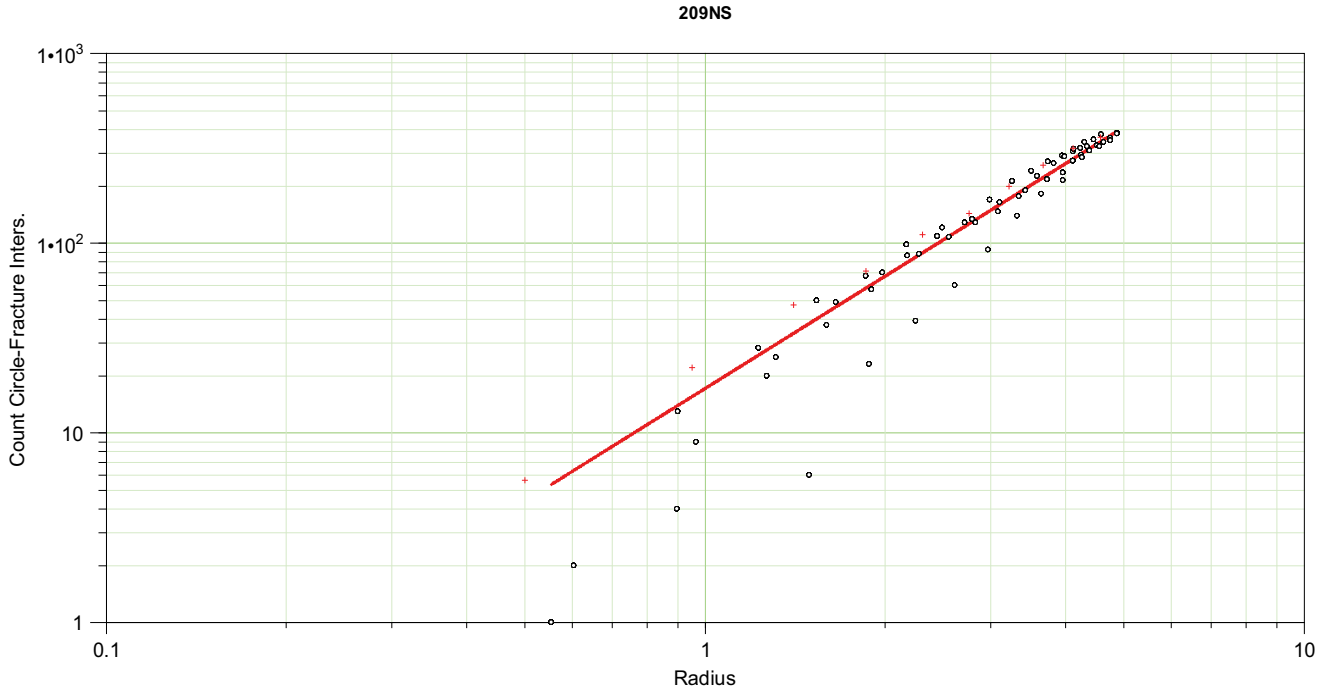

Power Law function: Parameters selected by user
Exponent = 1.97 Coefficient = 17.2
SSQ (sum of sq. errors) = 714864
Std.Deviaton Error = 19.8954
Primary Set has been fitted

Figure D-6. *Outcrop ASM000209, NS fracture set.*

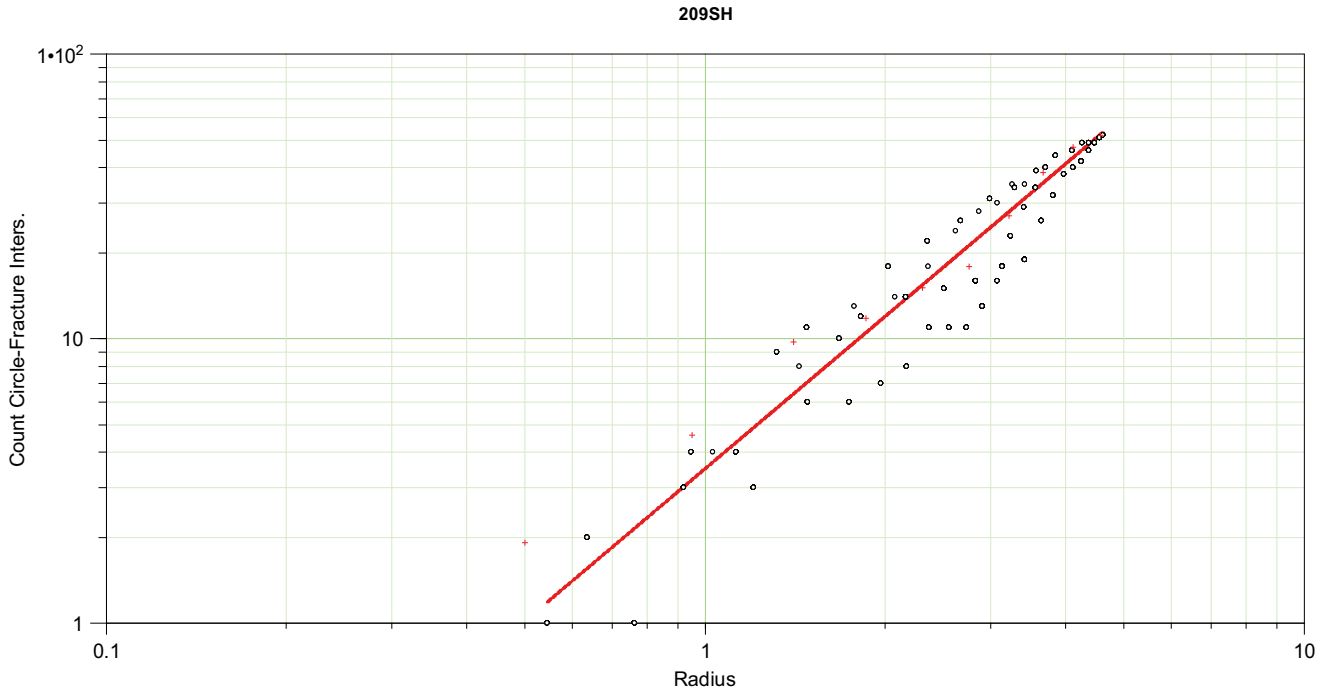

Power Law function: Parameters selected by user
Exponent = 1.77947 Coefficient = 3.5
SSQ (sum of sq. errors) = 42458.3
Std.Deviaton Error = 5.06657
Primary Set has been fitted

Figure D-7. *Outcrop ASM000209, SH fracture set.*

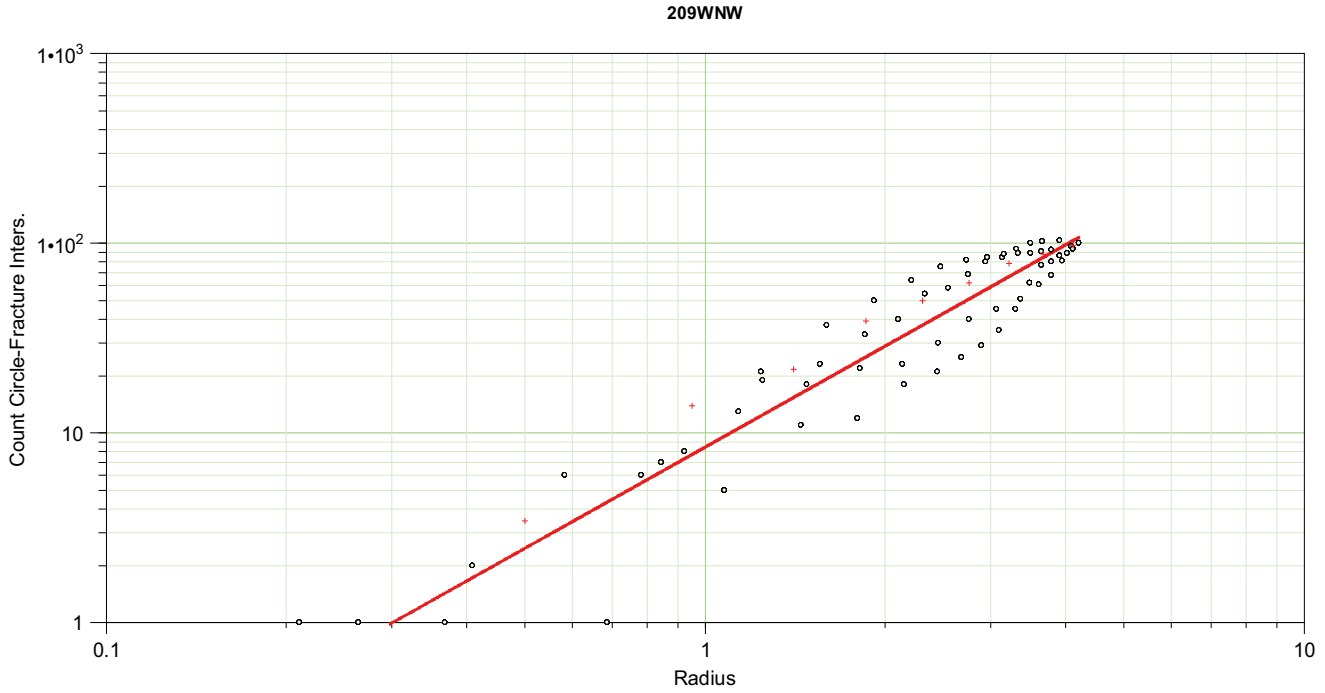

Power Law function: Least Squares method
Exponent = 1.77184 Coefficient = 8.43761
SSQ (sum of sq. errors) = 403687
Std.Deviaton Error = 16.0046
Primary Set has been fitted

Figure D-8. *Outcrop ASM000209, WNW fracture set.*

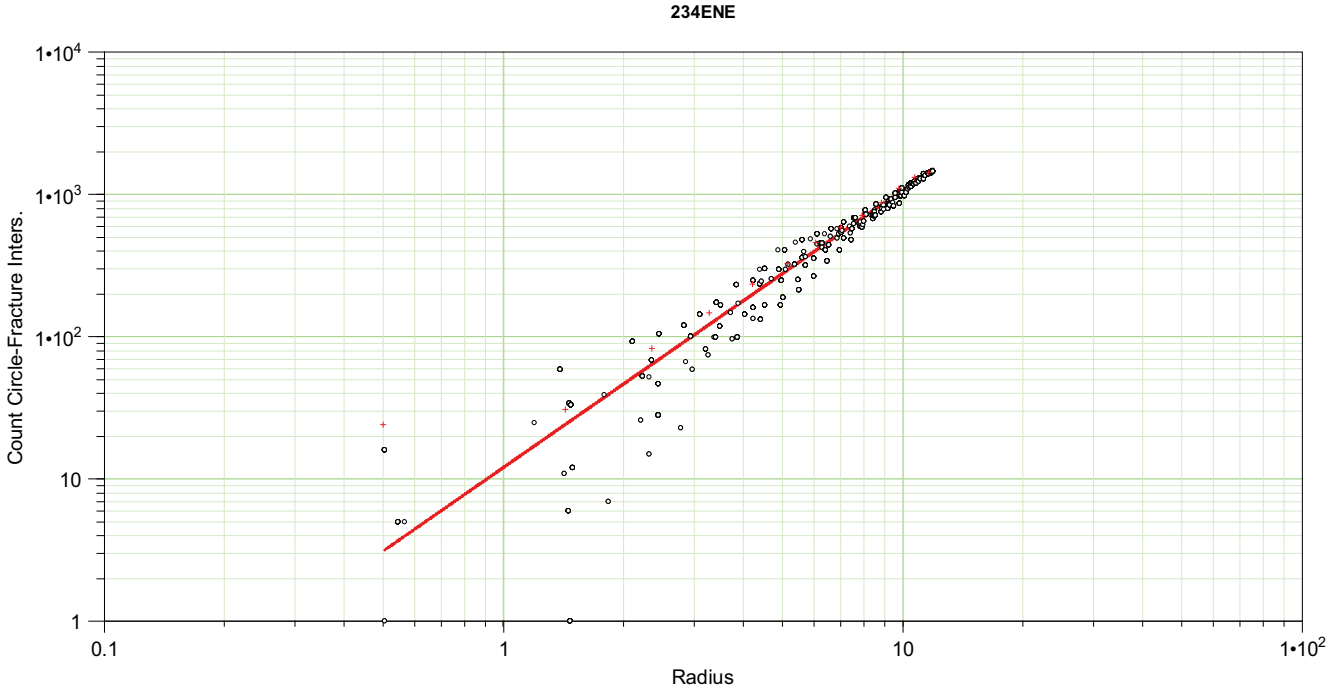

Power Law function: Parameters selected by user
Exponent = 1.95 Coefficient = 12.1
SSQ (sum of sq. errors) = 7.43133e+006
Std.Deviaton Error = 60.8196
Primary Set has been fitted

Figure D-9. *Outcrop ASM100234, ENE fracture set.*

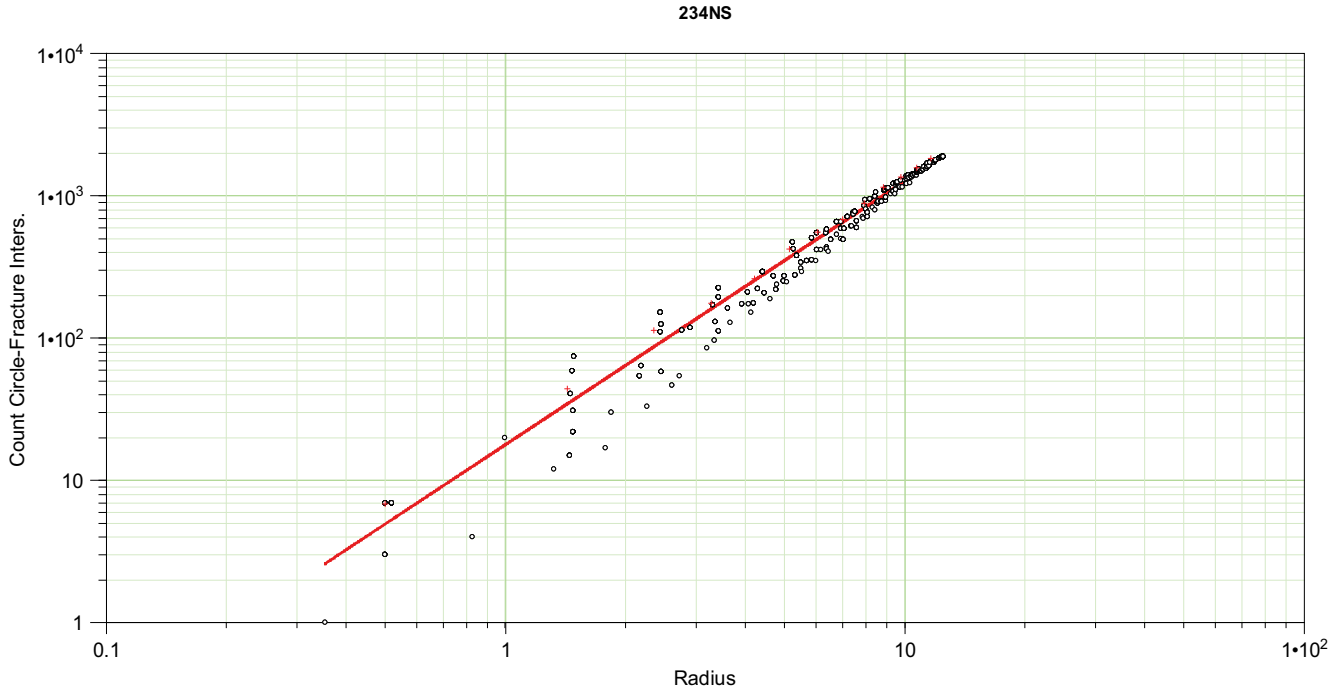

Power Law function: Least Squares method
Exponent = 1.85143 Coefficient = 17.8905
SSQ (sum of sq. errors) = 6.70412e+006
Std.Deviaton Error = 57.0199
Primary Set has been fitted

Figure D-10. *Outcrop ASM100234, NS fracture set.*

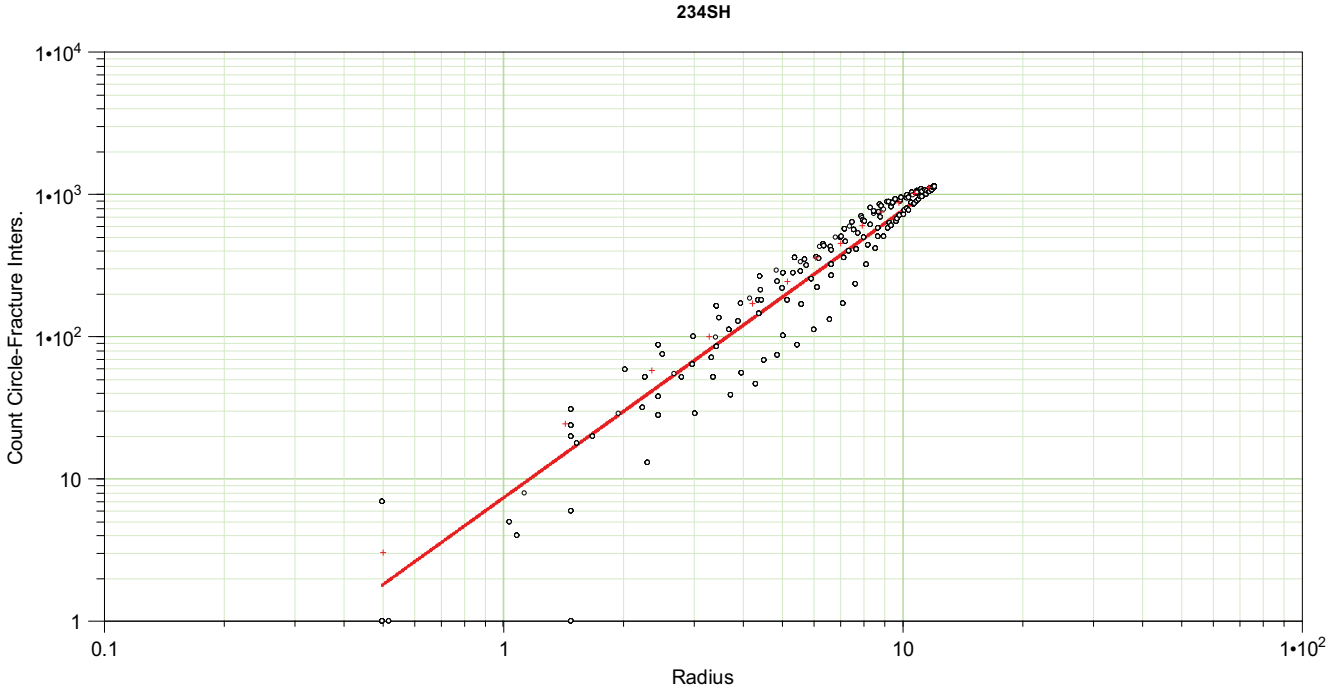

Power Law function: Parameters selected by user
Exponent = 2.02 Coefficient = 7.4
SSQ (sum of sq. errors) = 2.05774e+007
Std.Deviaton Error = 100.164
Primary Set has been fitted

Figure D-11. *Outcrop ASM100234, SH fracture set.*

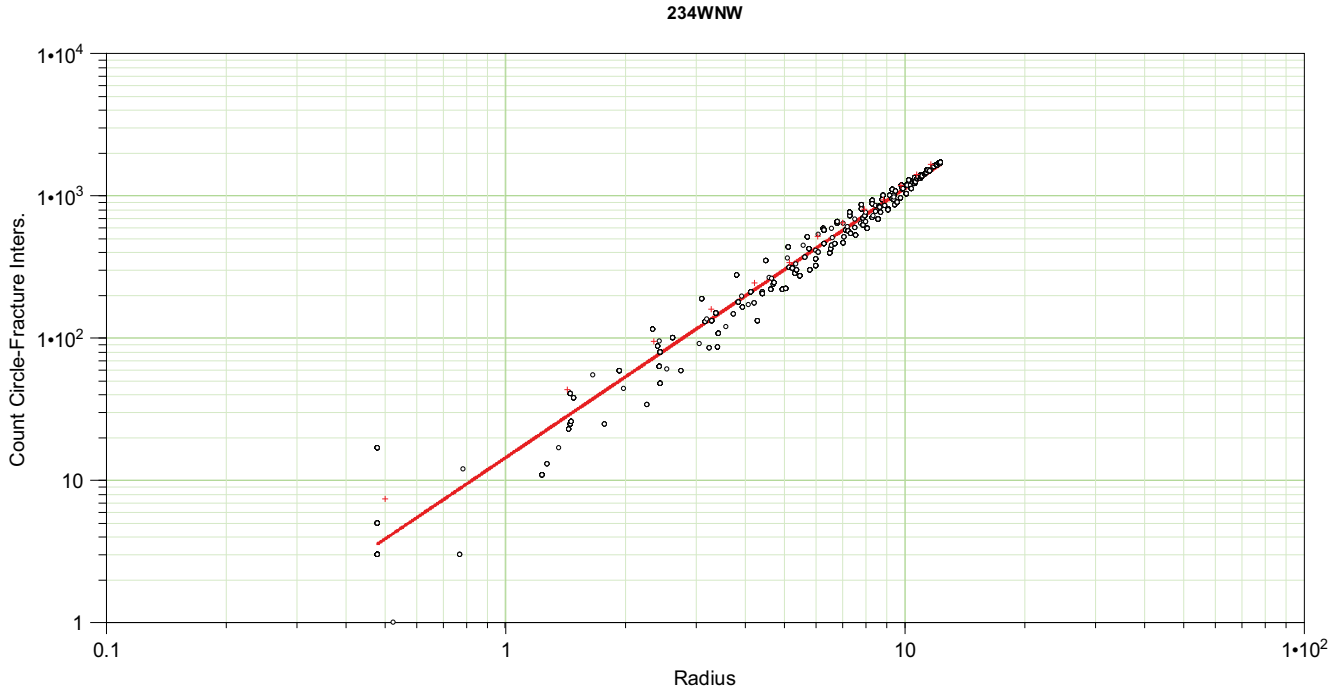

Power Law function: Least Squares method
Exponent = 1.89283 Coefficient = 14.4737
SSQ (sum of sq. errors) = 1.04498e+007
Std.Deviaton Error = 71.1886
Primary Set has been fitted

Figure D-12. *Outcrop ASM100234, WNW fracture set.*

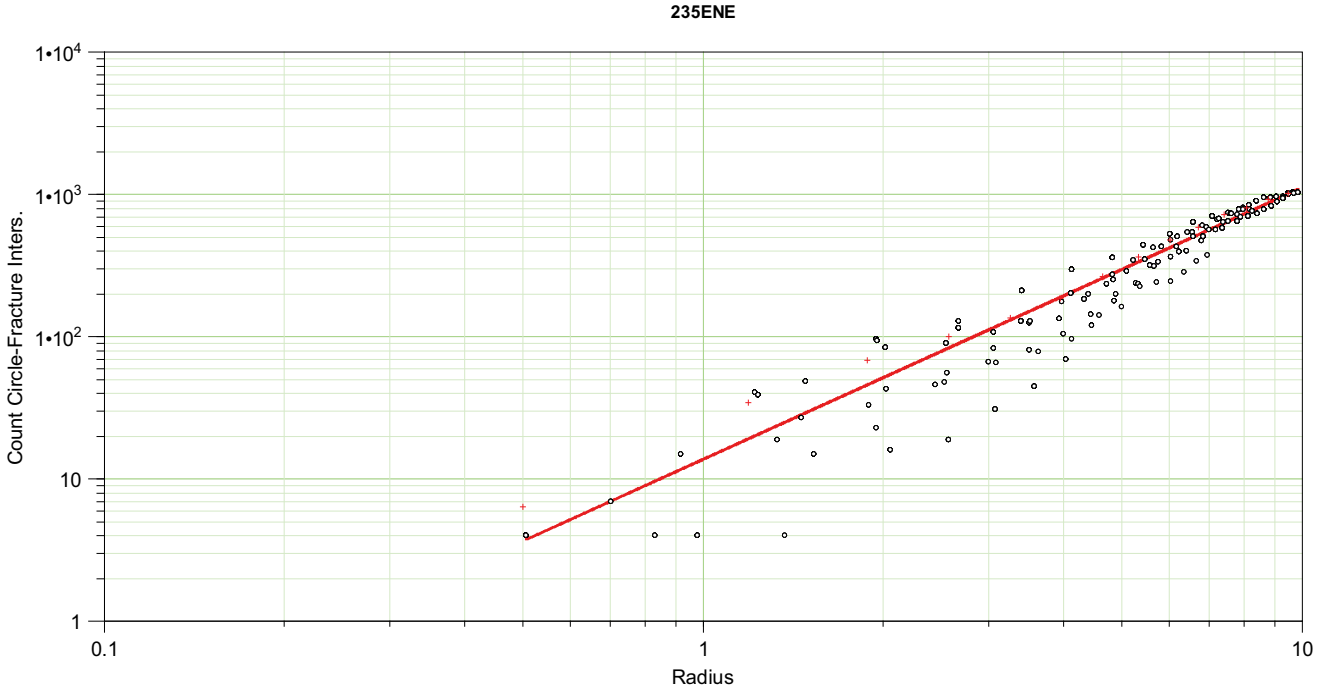

Power Law function: Least Squares method
Exponent = 1.9093 Coefficient = 13.7993
SSQ (sum of sq. errors) = 7.55203e+006
Std.Deviaton Error = 62.7982
Primary Set has been fitted

Figure D-13. *Outcrop ASM100235, ENE fracture set.*

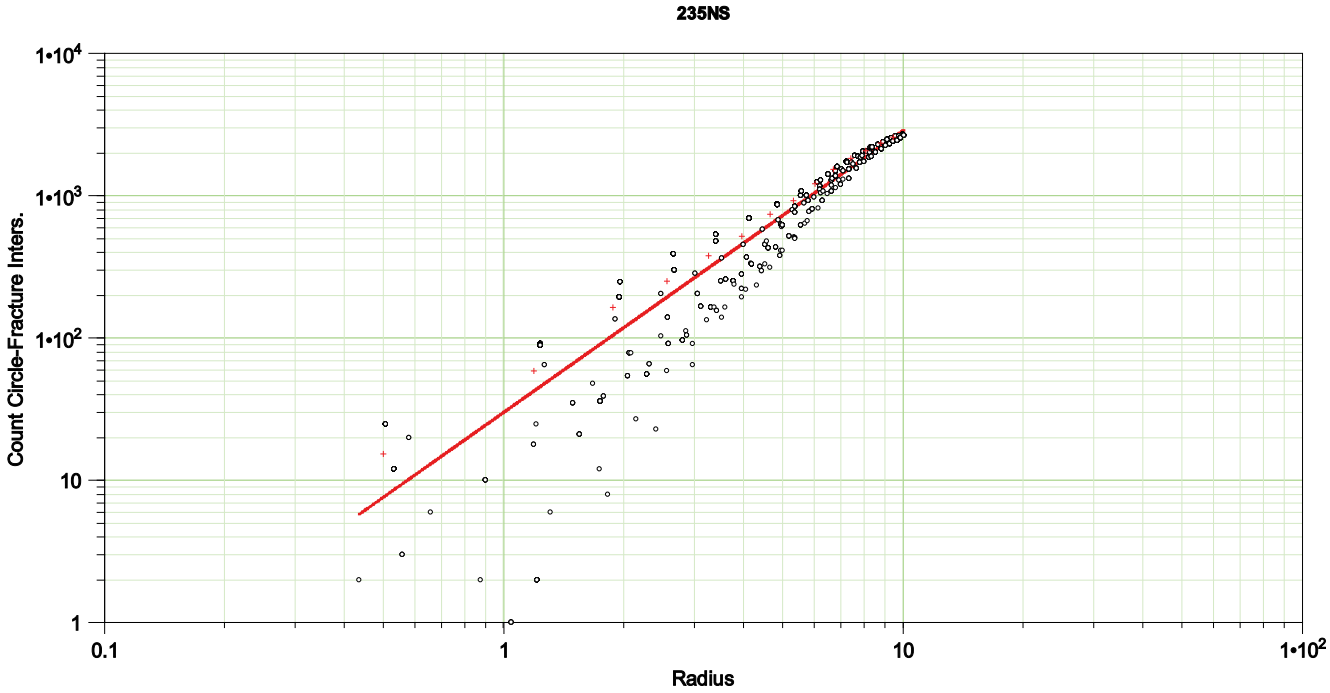

Power Law function: Parameters selected by user
Exponent = 1.98 Coefficient = 30.12
SSQ (sum of sq. errors) = 4.16678e+007
Std.Deviaton Error = 145.619
Primary Set has been fitted

Figure D-14. *Outcrop ASM100235, NS fracture set.*

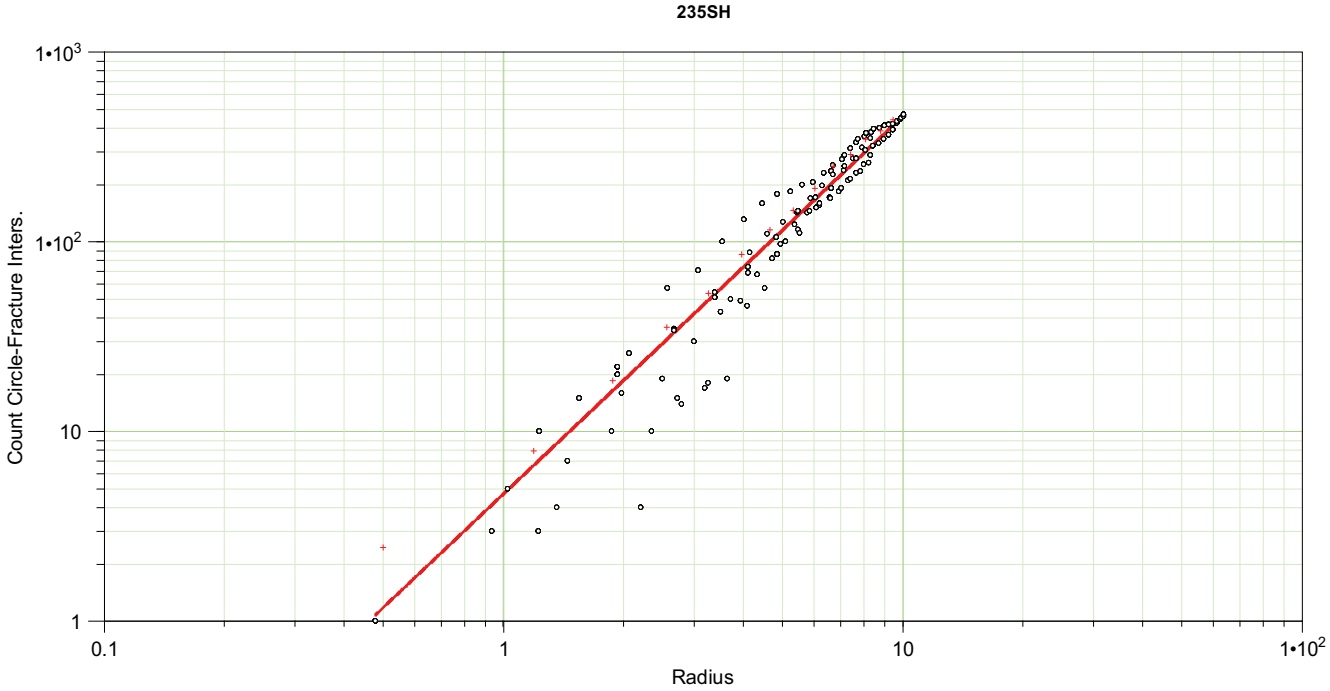

Power Law function: Parameters selected by user
Exponent = 1.99 Coefficient = 4.7
SSQ (sum of sq. errors) = 1.70682e+006
Std.Deviaton Error = 29.7614
Primary Set has been fitted

Figure D-15. *Outcrop ASM100235, SH fracture set.*

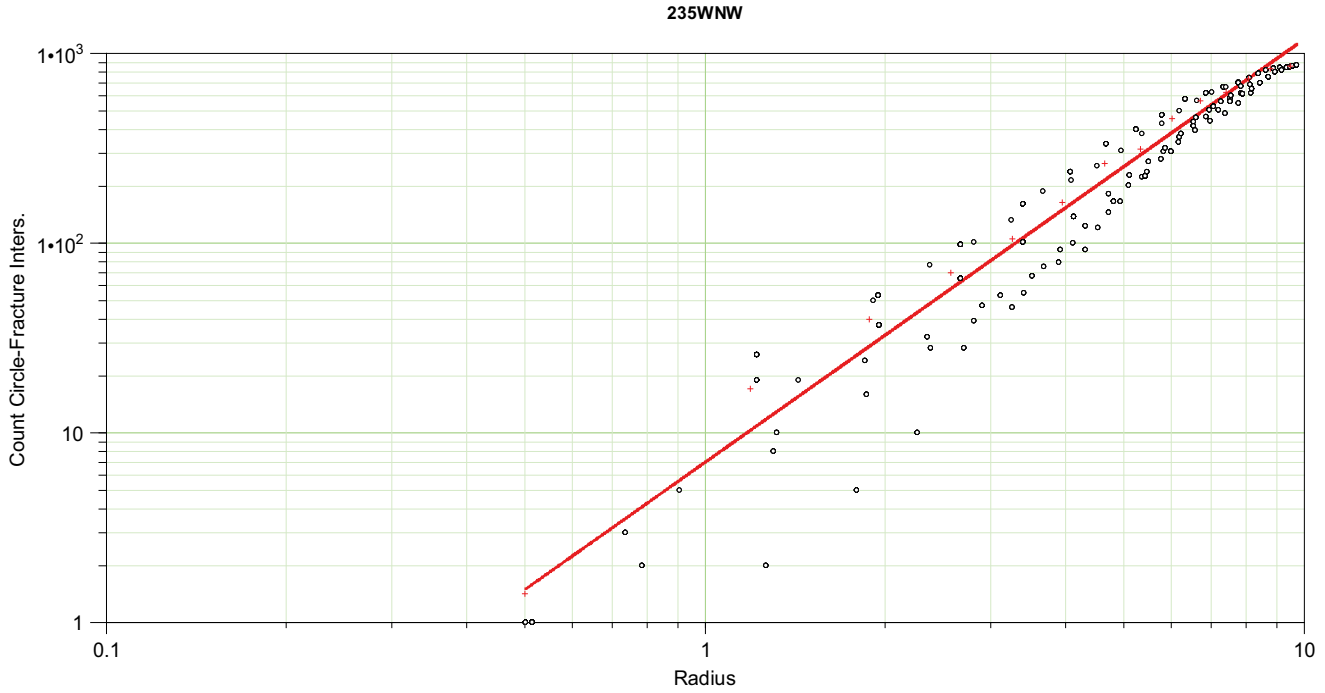

Power Law function: Parameters selected by user
Exponent = 2.22939 Coefficient = 7.02281
SSQ (sum of sq. errors) = 1.92978e+007
Std.Deviaton Error = 97.9354
Primary Set has been fitted

Figure D-16. *Outcrop ASM100235, WNW fracture set.*

Appendix E

Fracture intensity as a function of depth

E.1 Data population in fracture domains with depth

The following six figures illustrate the availability and distribution of borehole data inside the fracture domains at Laxemar. The plots illustrate, for 1 m elevation bins, the total length of boreholes outside of deformation zones. The bins are colored by individual borehole name, such that one can quickly glance at the chart and determine which borehole is contributing to the total data population at what depth. For a given borehole at a given elevation, the length outside deformation zones is controlled by the plunge of the boreholes. Vertical boreholes will have a length of 1 m for a 1 m elevation interval outside of DZ; an inclined borehole will have a length greater than 1 m for a 1 m interval outside DZ. For example, in Figure E-1 below, the plunge of borehole KLX15A shallows between z = –100 m.a.s.l. and z = –400 m.a.s.l.. This can be seen by the gentle increase in length of the brown column between those elevations.

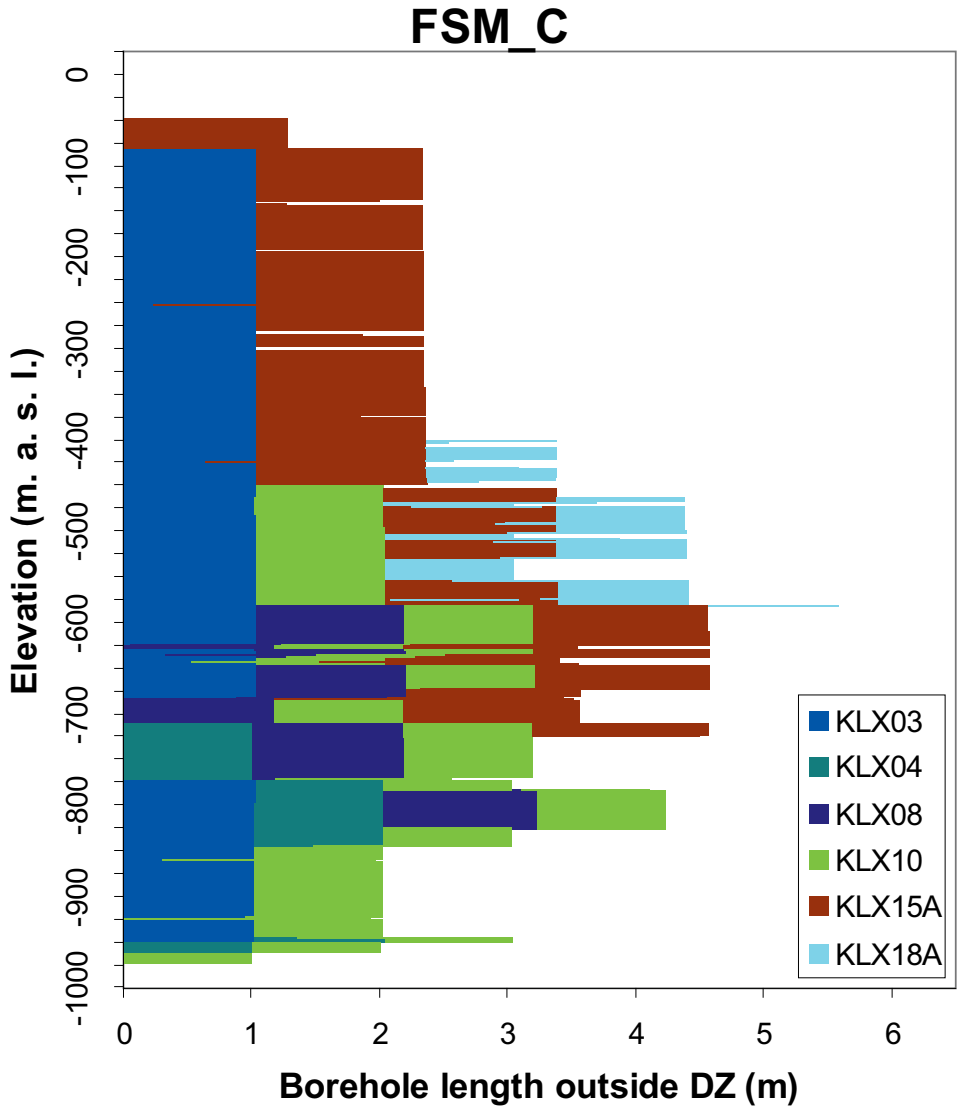

Figure E-1. *Data population in FSM_C.*

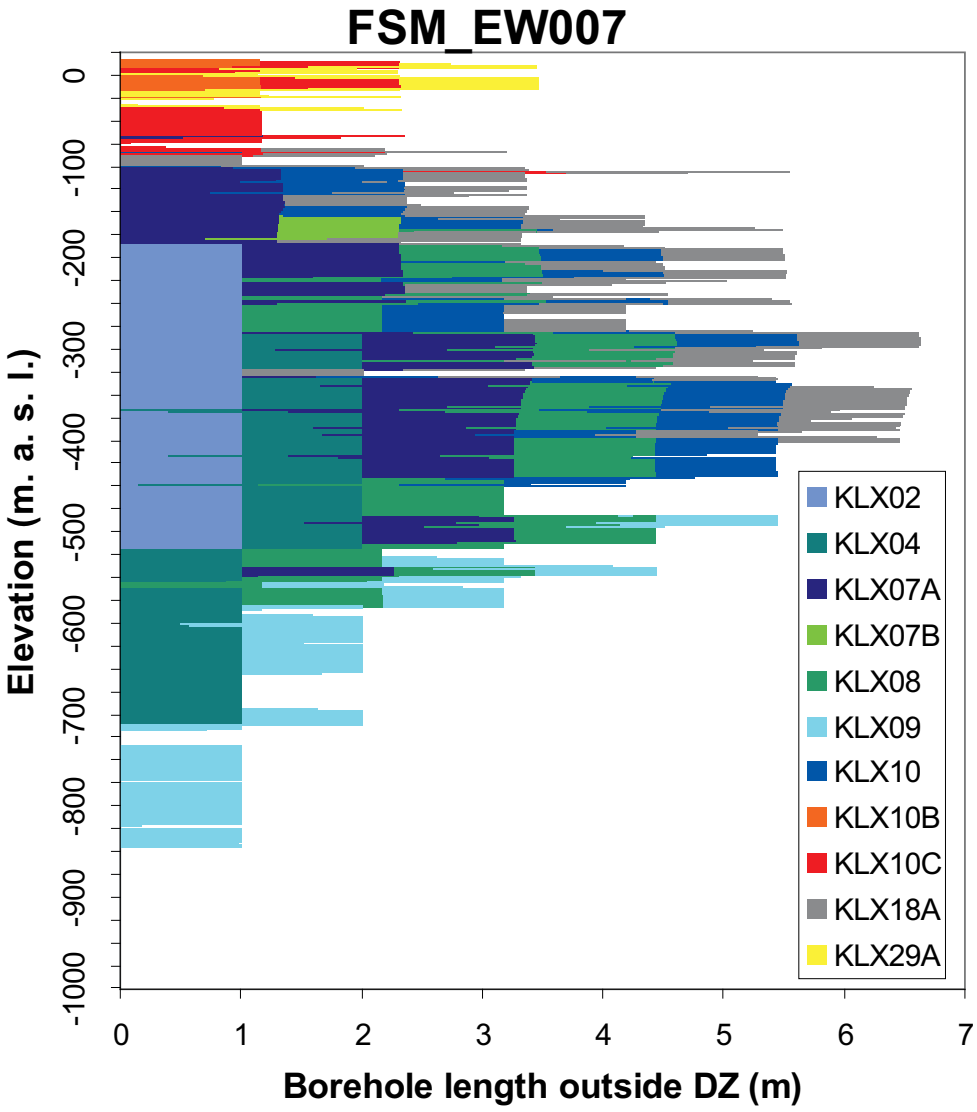

Figure E-2. *Data population in FSM_EW007.*

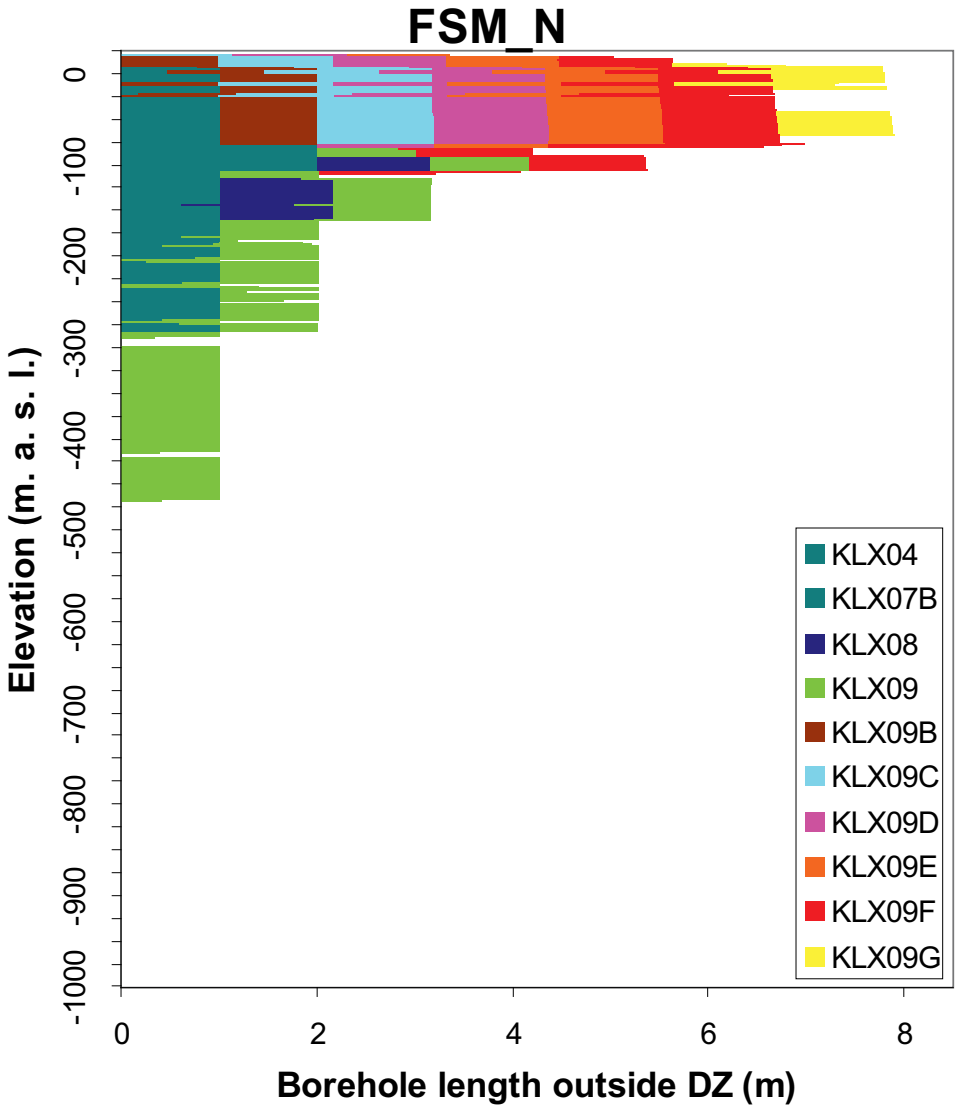

Figure E-3. *Data population in FSM_N.*

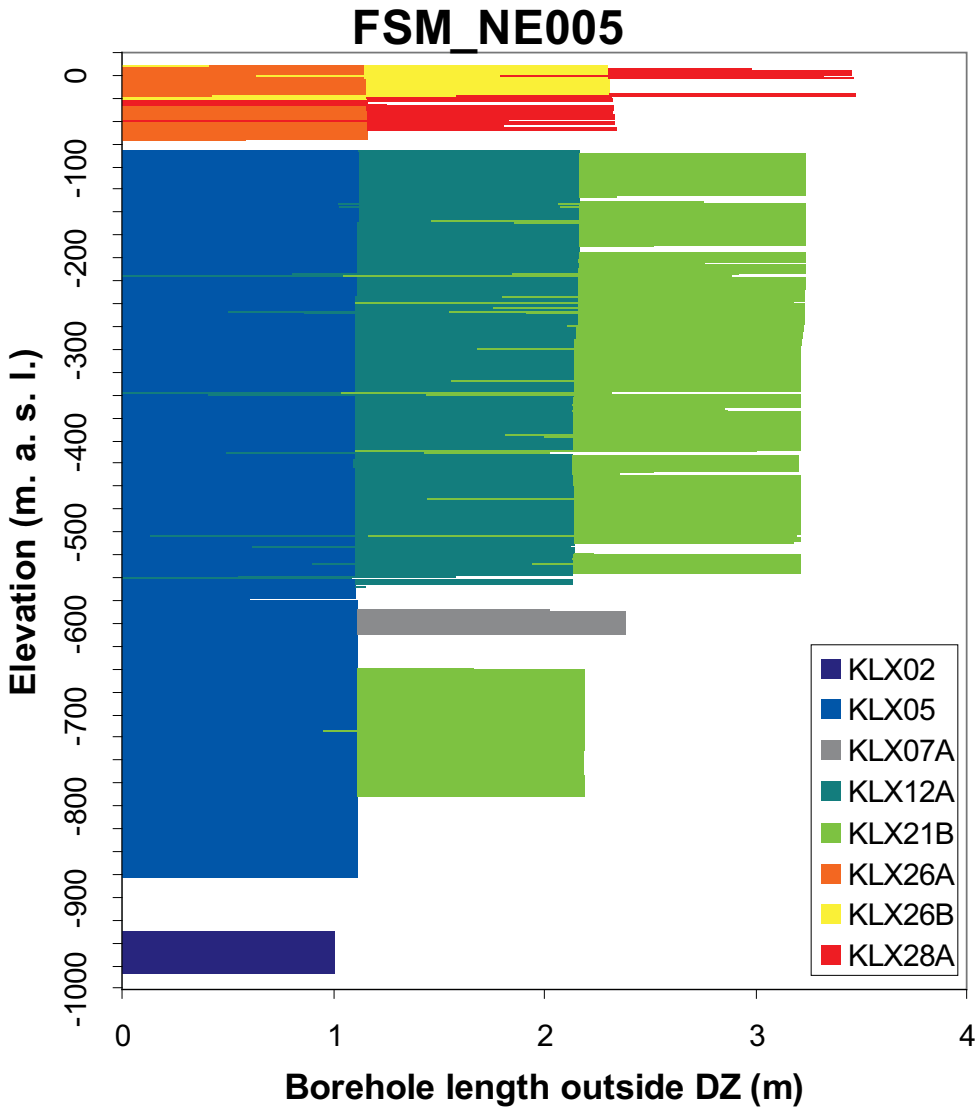

Figure E-4. *Data population in FSM_NE005.*

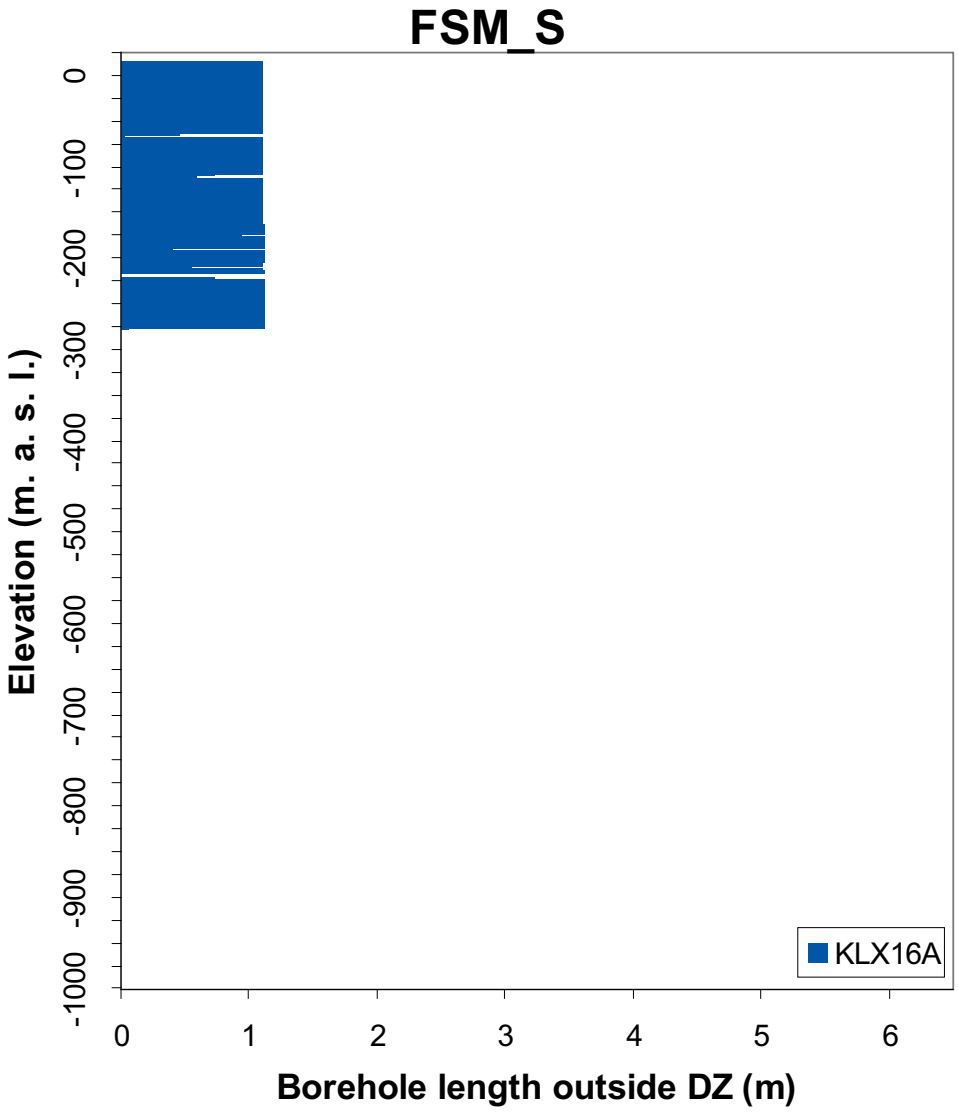

Figure E-5. *Data population in FSM_S.*

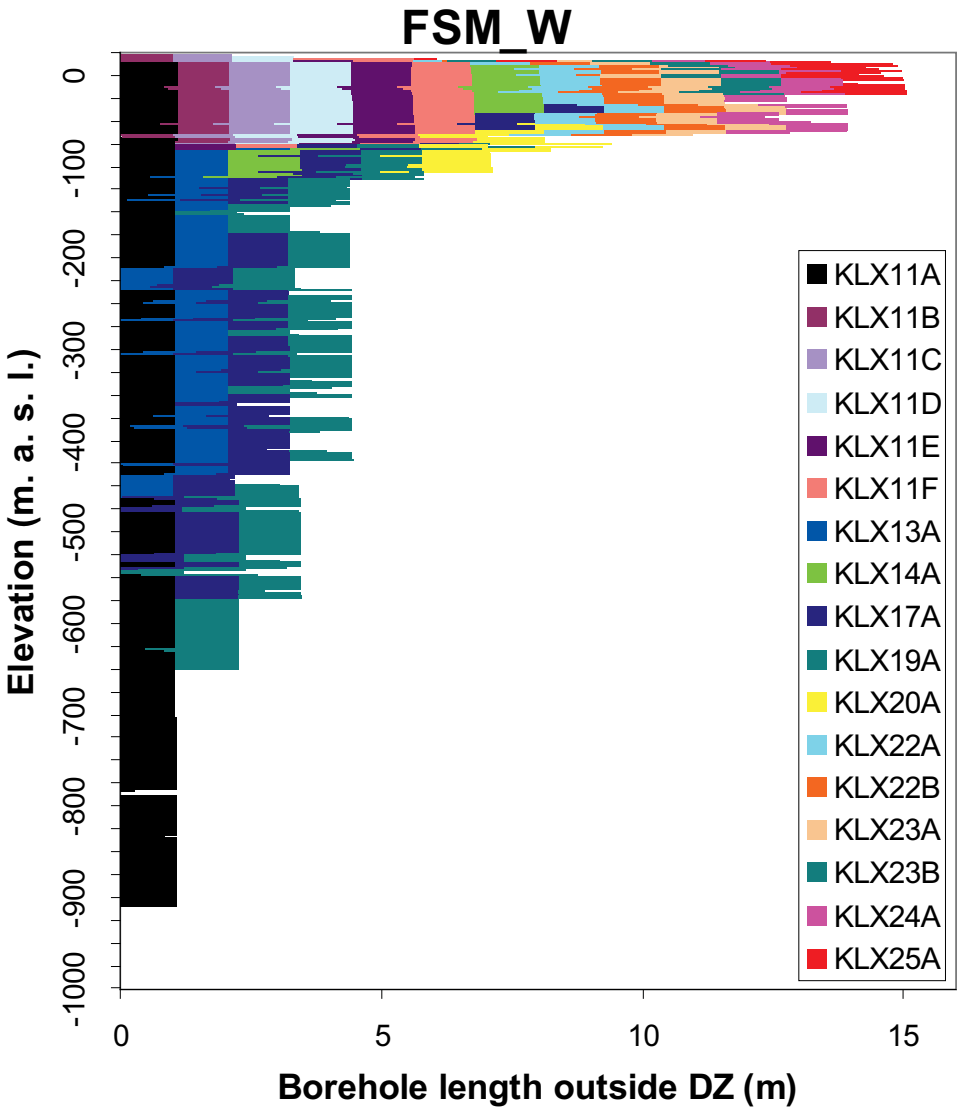

Figure E-6. *Data population in FSM_W.*

E.2 P_{32} fracture intensity as a function of fracture set, fracture domain, and total vertical depth (TVD).

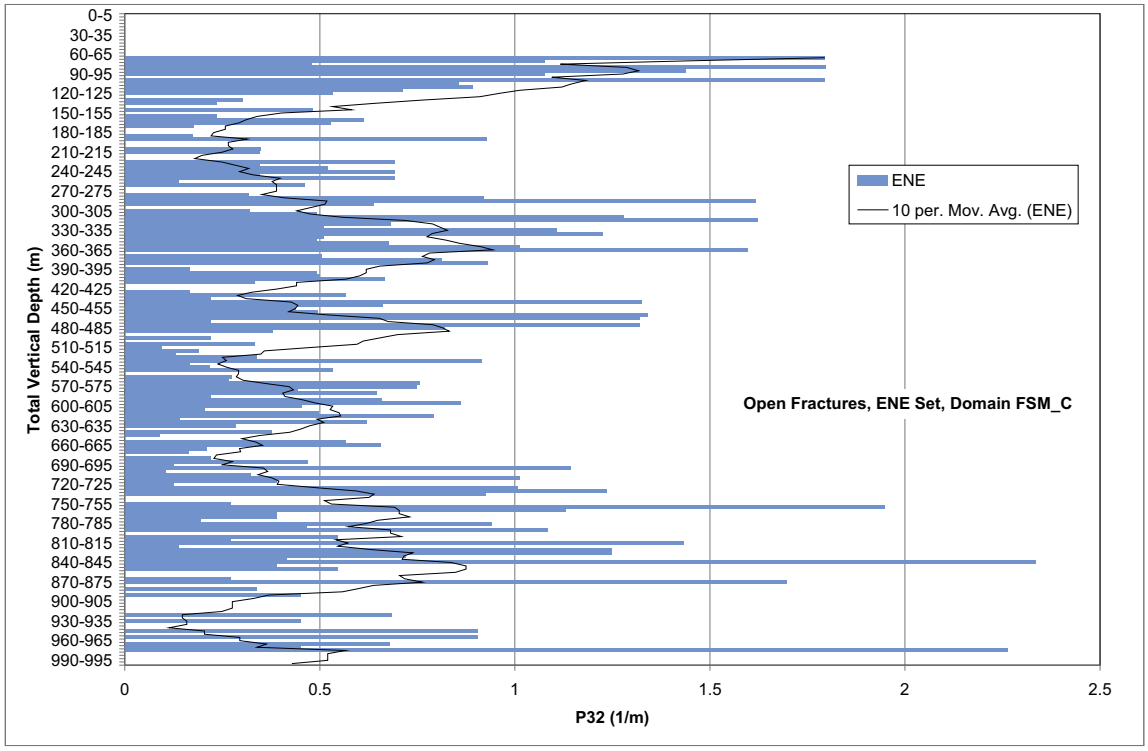

Figure E-7. *P_{32} as a function of total vertical depth, open fractures, ENE set, domain FSM_C.*

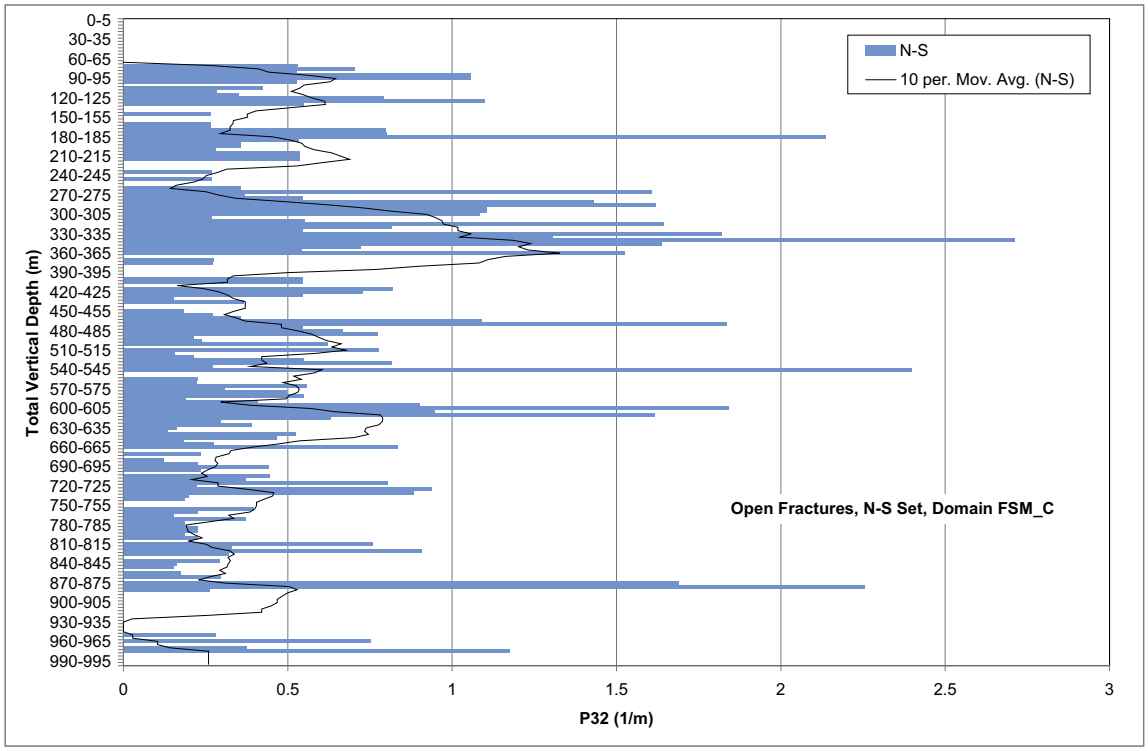

Figure E-8. *P_{32} as a function of total vertical depth, open fractures, N-S set, domain FSM_C.*

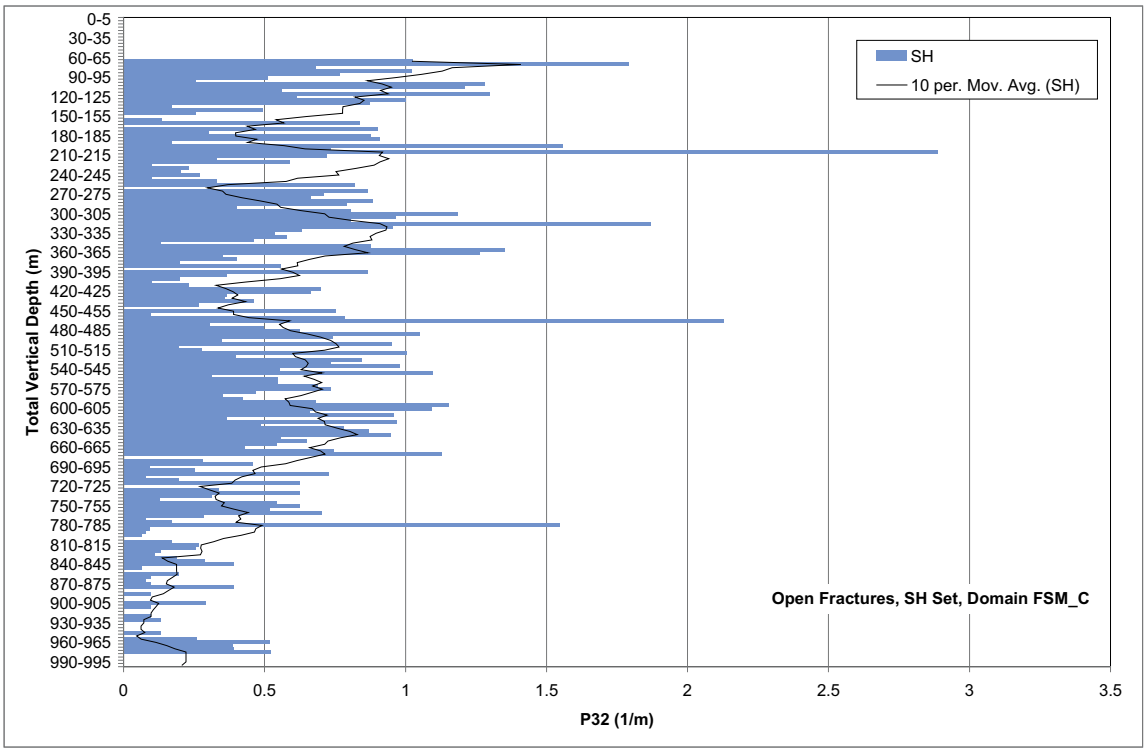

Figure E-9. *P_{32} as a function of total vertical depth, open fractures, SH set, domain FSM_C.*

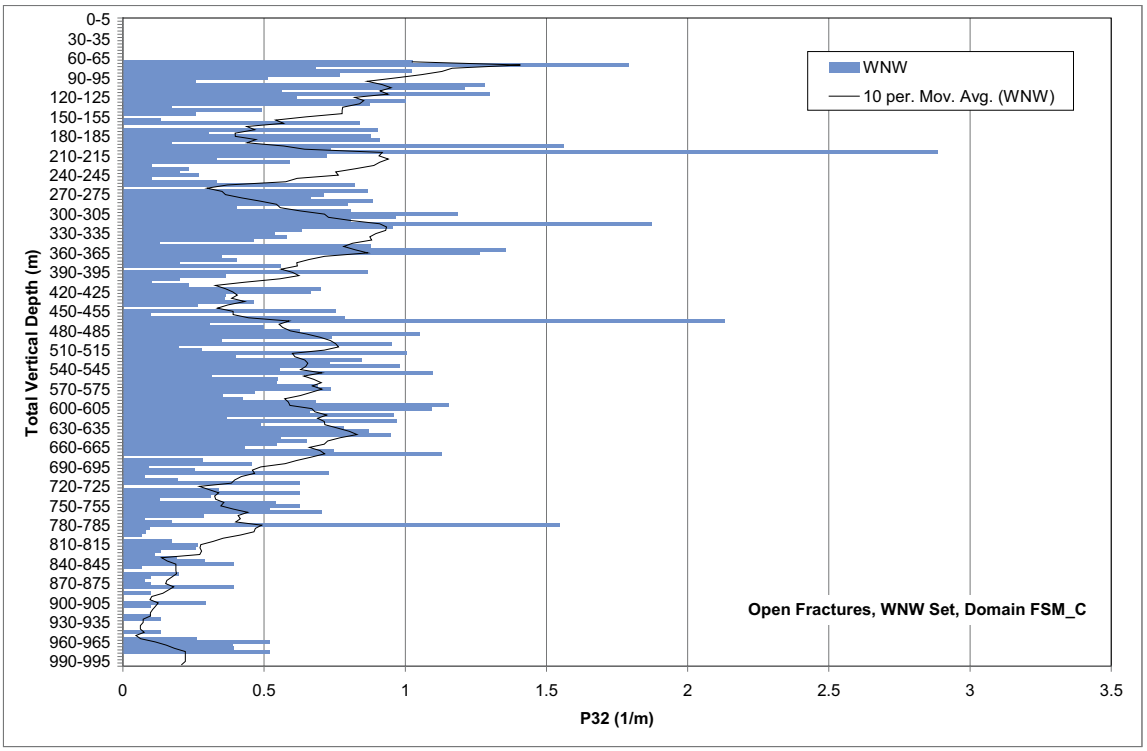

Figure E-10. *P_{32} as a function of total vertical depth, open fractures, WNW set, domain FSM_C.*

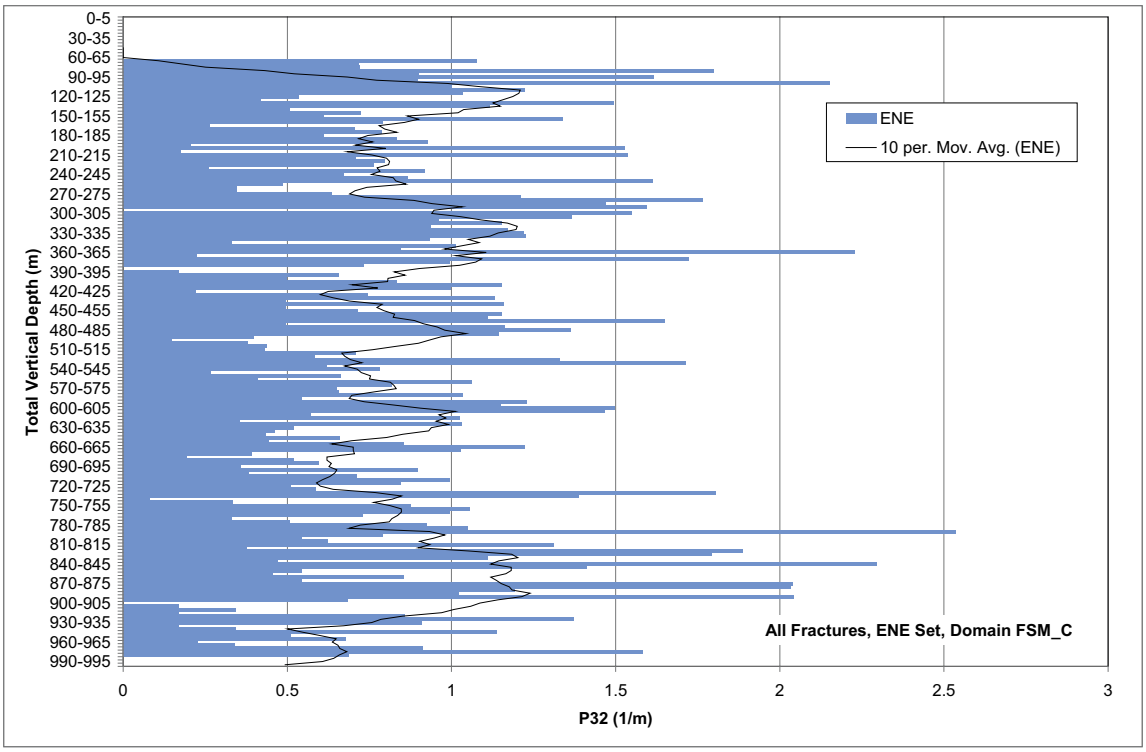

Figure E-11. *P_{32} as a function of total vertical depth, all fractures, ENE set, domain FSM_C.*

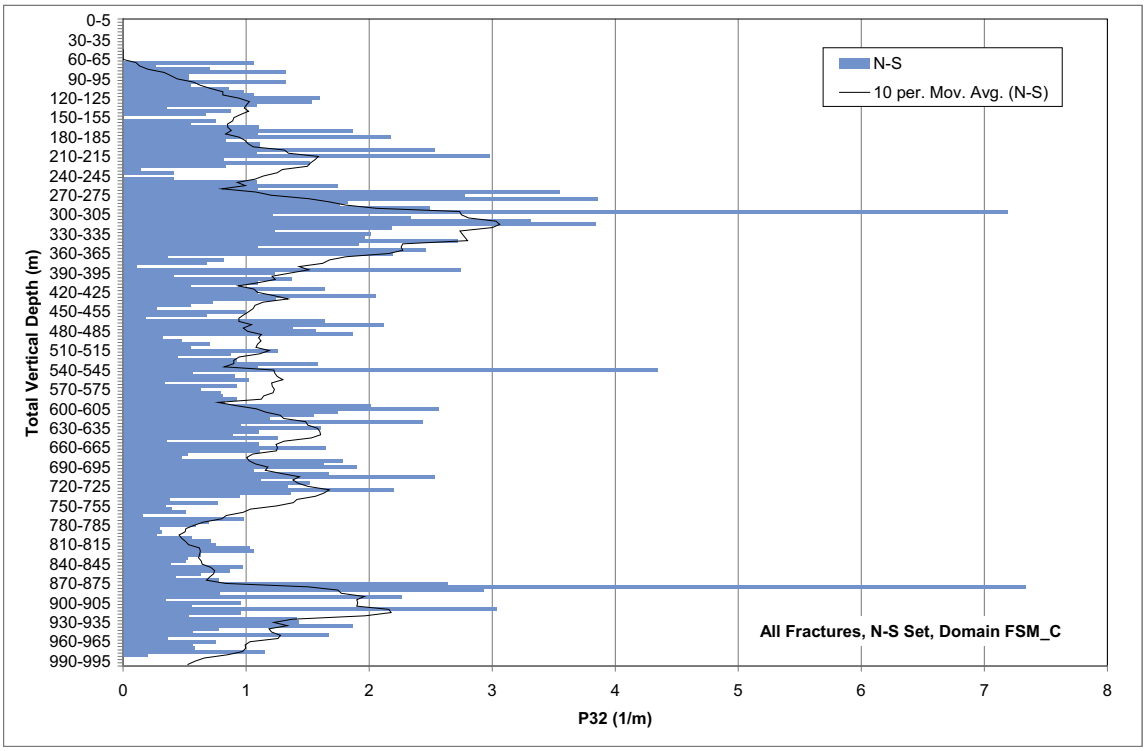

Figure E-12. *P_{32} as a function of total vertical depth, all fractures, N-S set, domain FSM_C.*

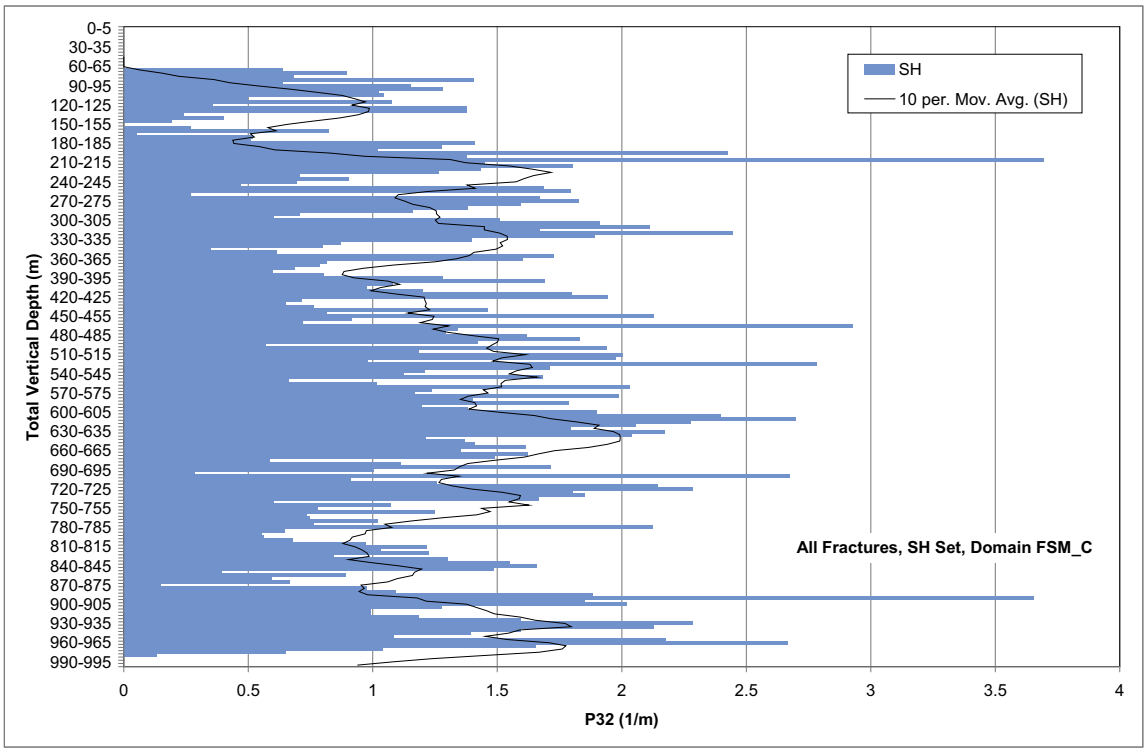

Figure E-13. *P_{32} as a function of total vertical depth, all fractures, SH set, domain FSM_C.*

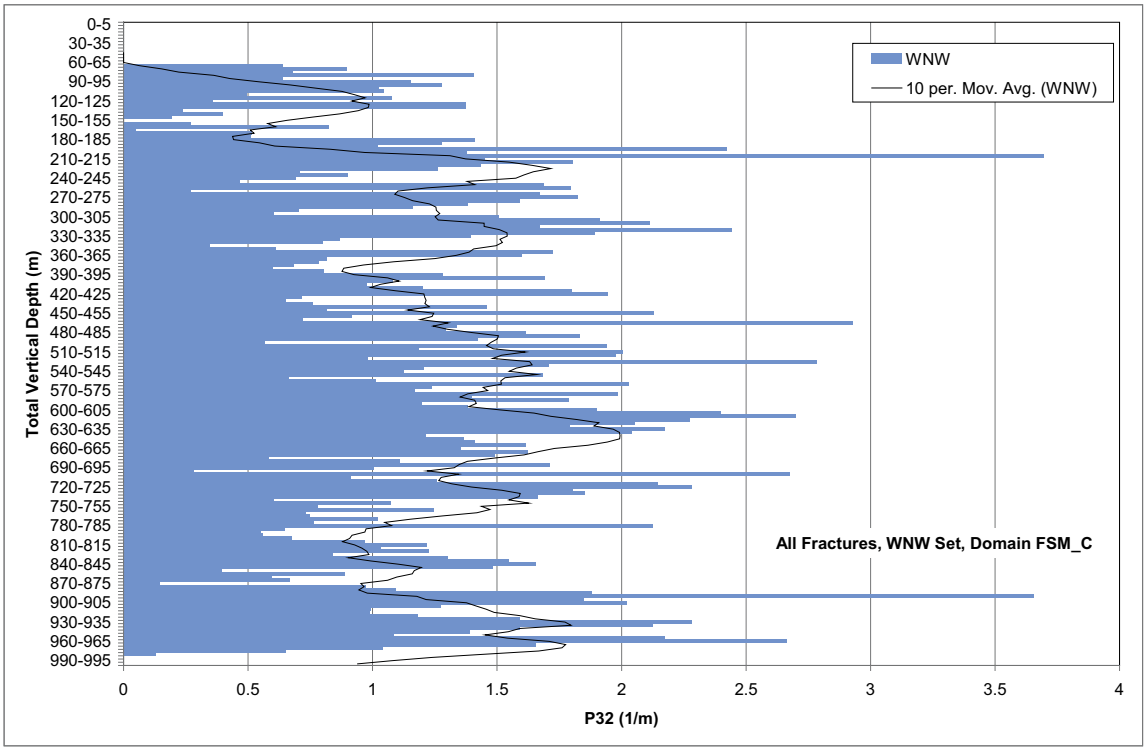

Figure E-14. *P_{32} as a function of total vertical depth, all fractures, WNW set, domain FSM_C.*

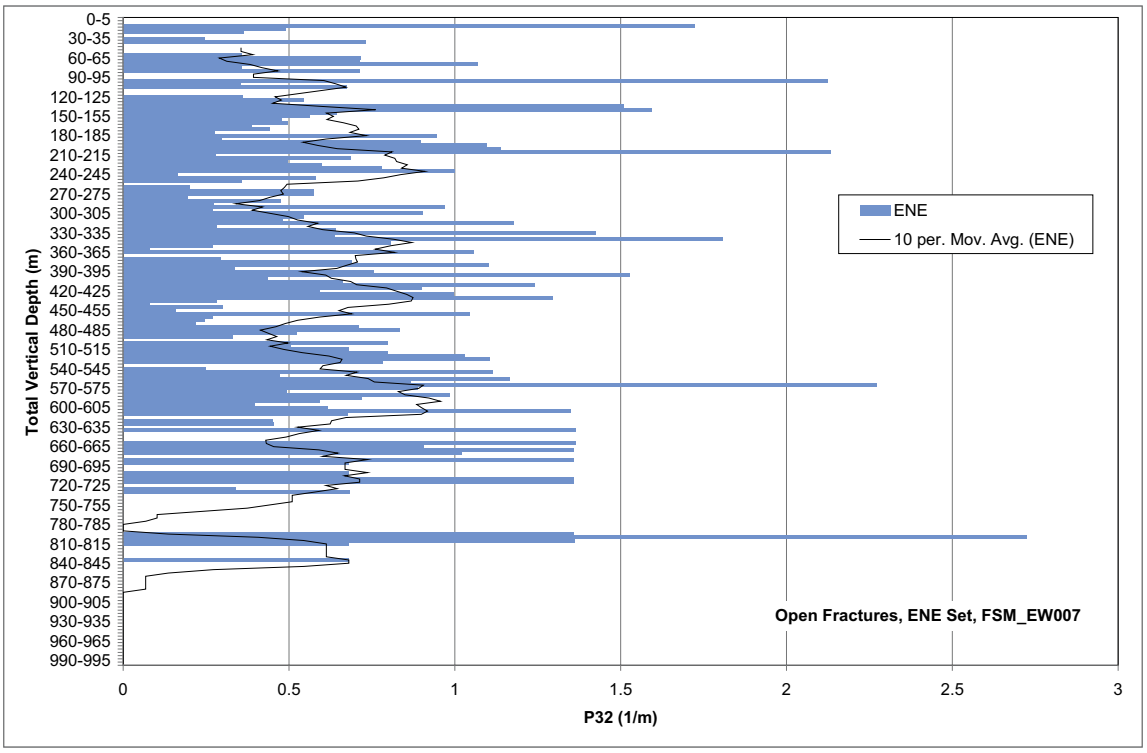

Figure E-15. *P_{32} as a function of total vertical depth, open fractures, ENE set, domain FSM_EW007.*

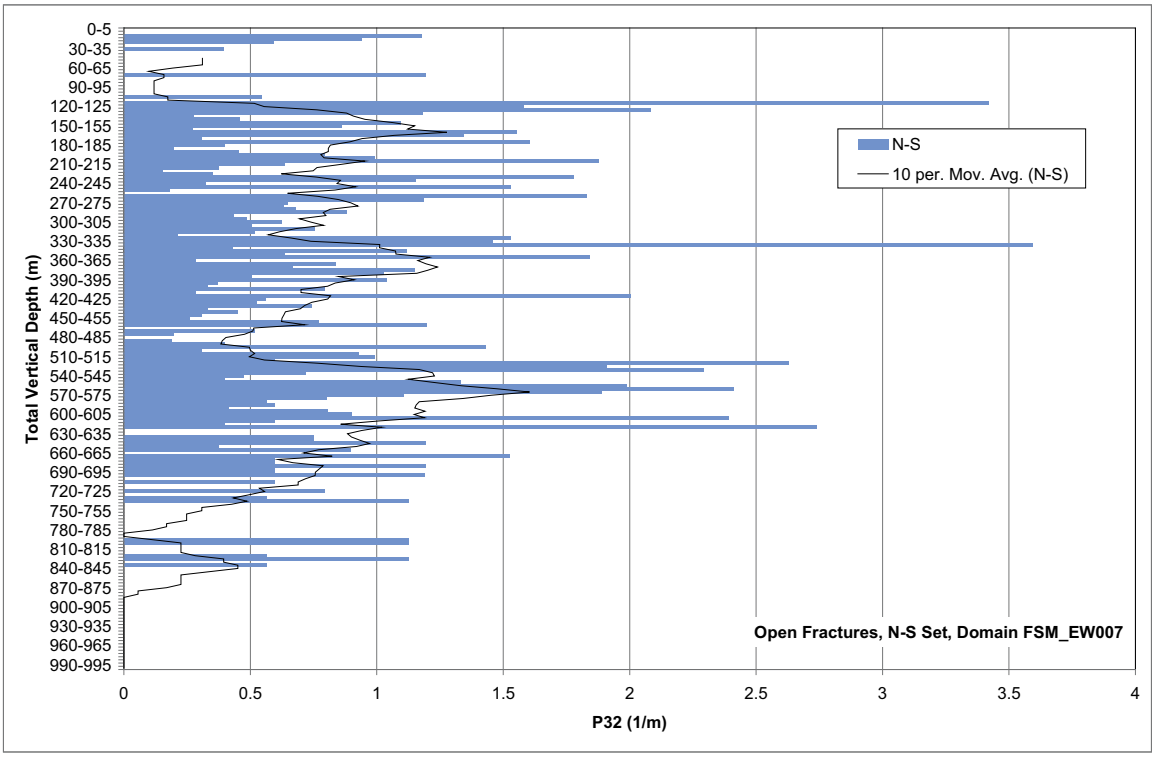

Figure E-16. *P_{32} as a function of total vertical depth, open fractures, N-S set, domain FSM_EW007.*

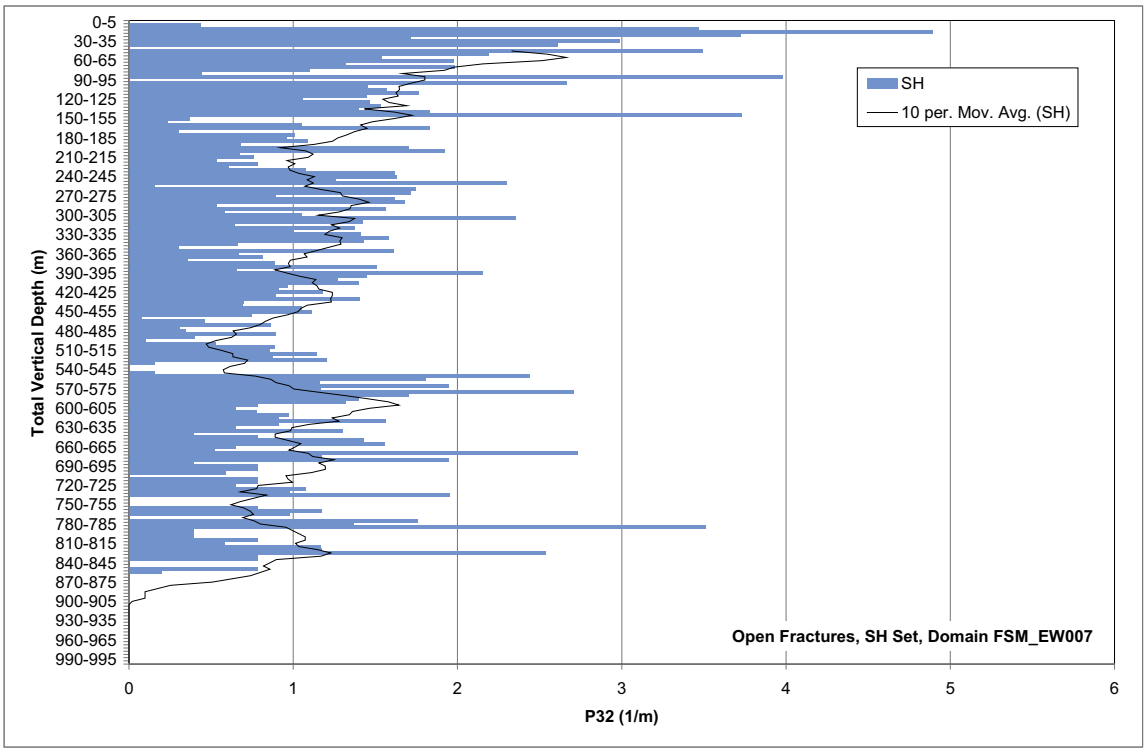

Figure E-17. *P_{32} as a function of total vertical depth, open fractures, SH set, domain FSM_EW007.*

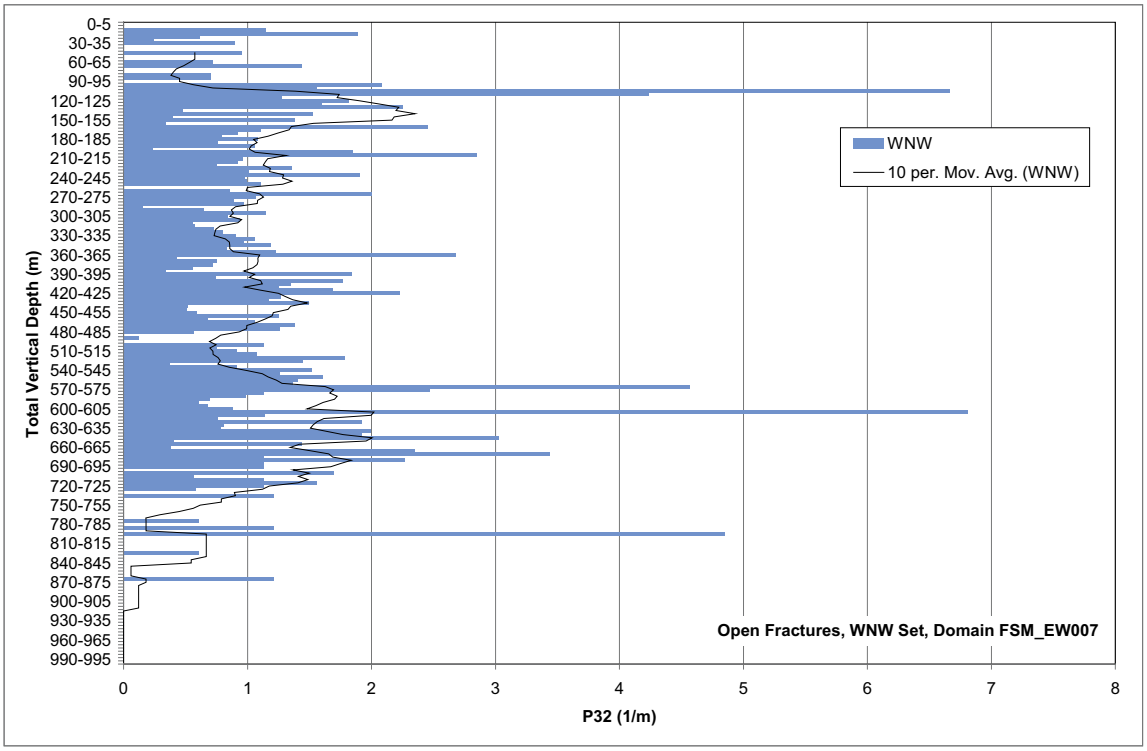

Figure E-18. *P_{32} as a function of total vertical depth, open fractures, WNW set, domain FSM_EW007.*

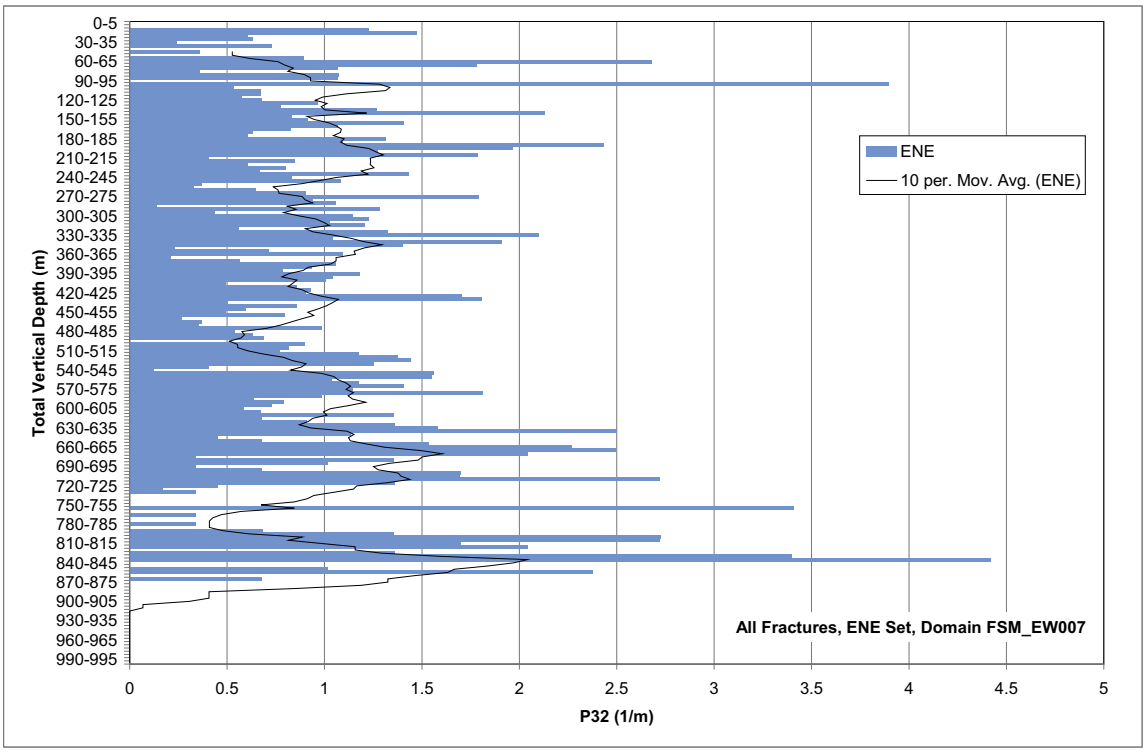

Figure E-19. *P_{32} as a function of total vertical depth, all fractures, ENE set, domain FSM_EW007.*

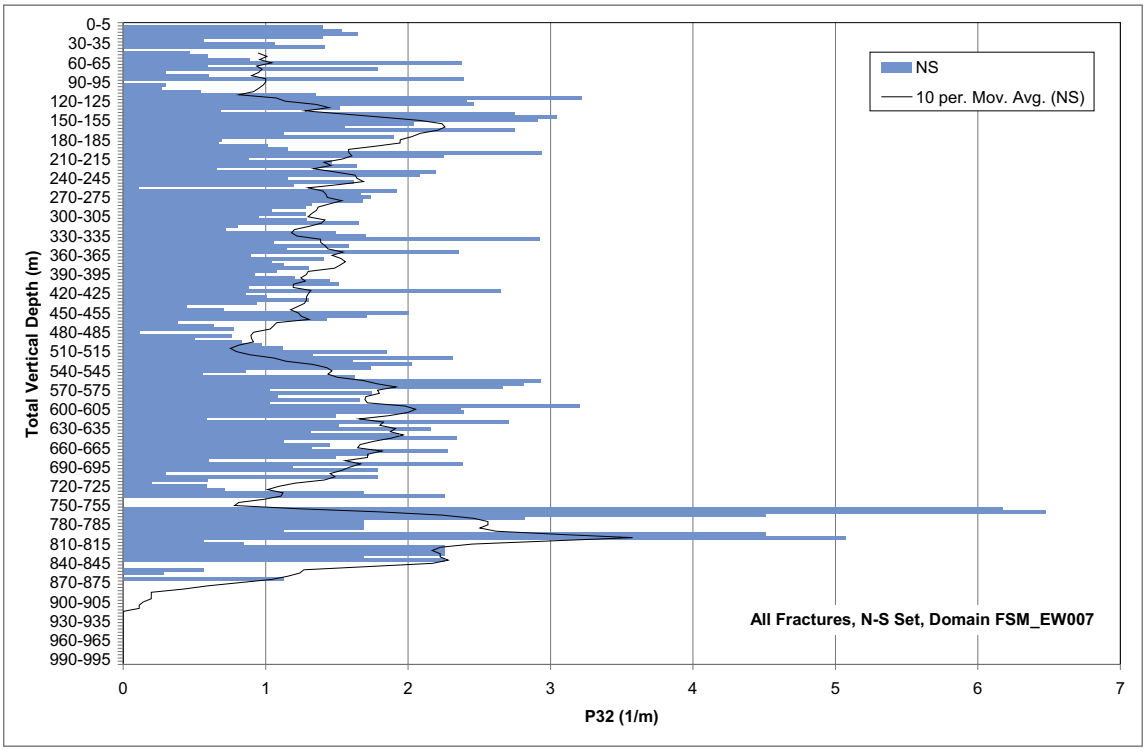

Figure E-20. *P_{32} as a function of total vertical depth, all fractures, N-S set, domain FSM_EW007.*

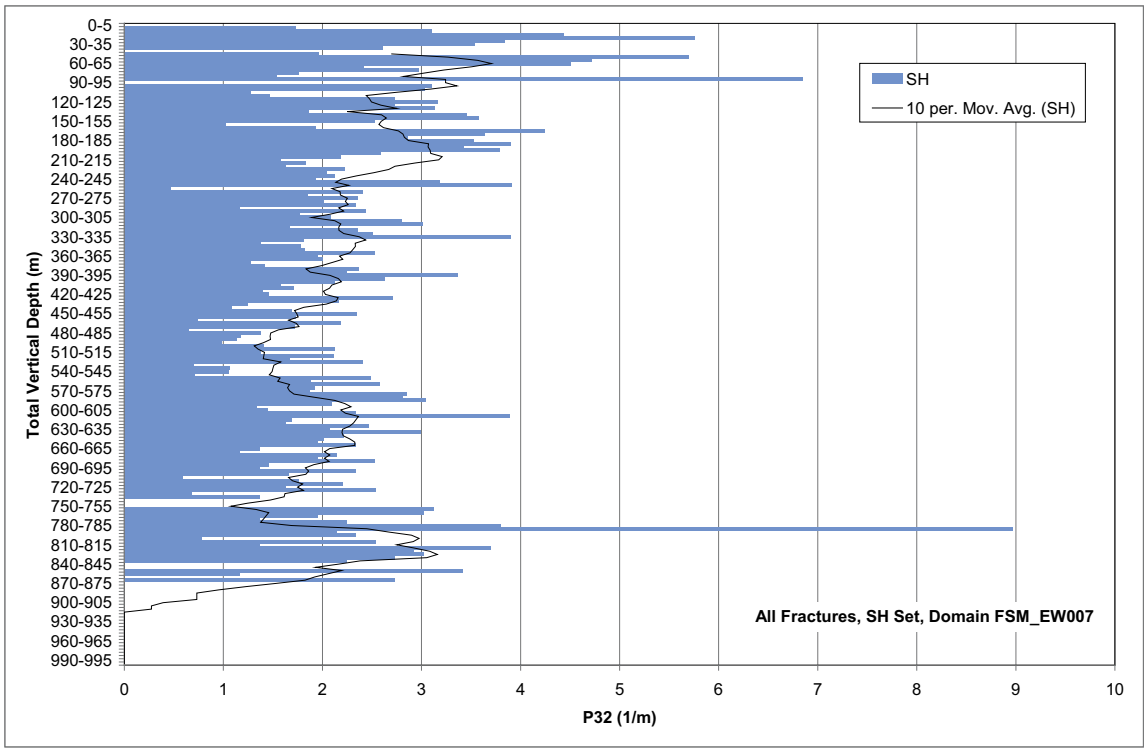

Figure E-21. *P_{32} as a function of total vertical depth, all fractures, SH set, domain FSM_EW007.*

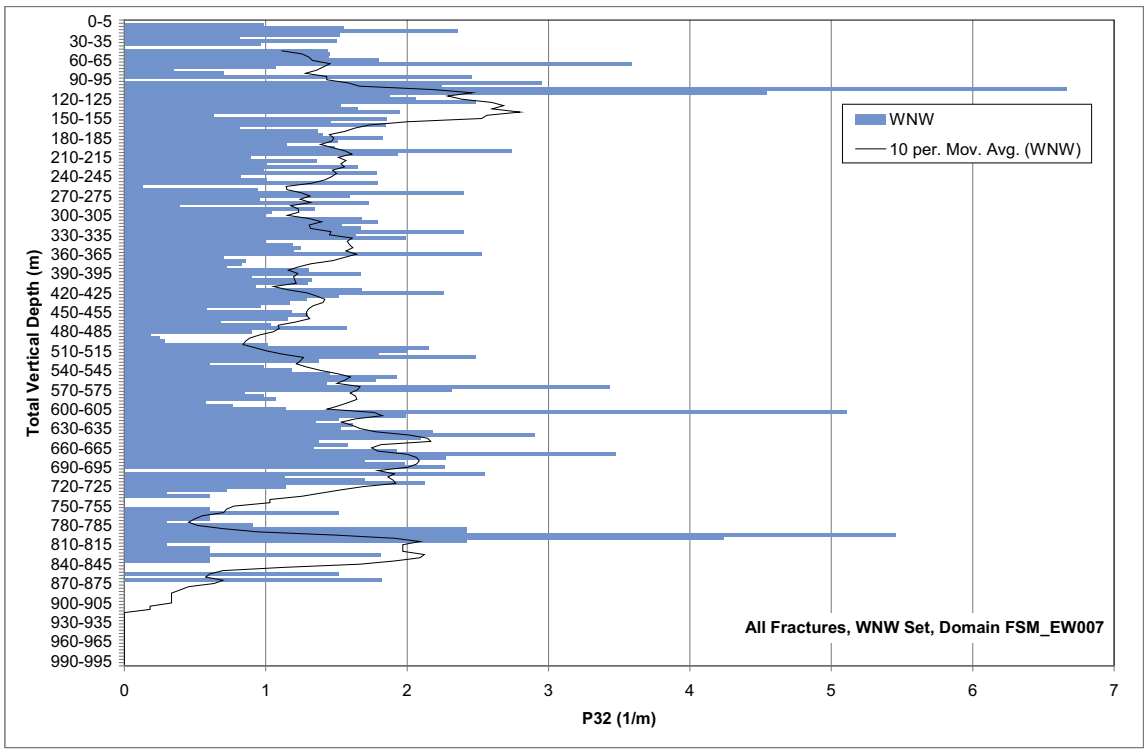

Figure E-22. *P_{32} as a function of total vertical depth, all fractures, WNW set, domain FSM_EW007.*

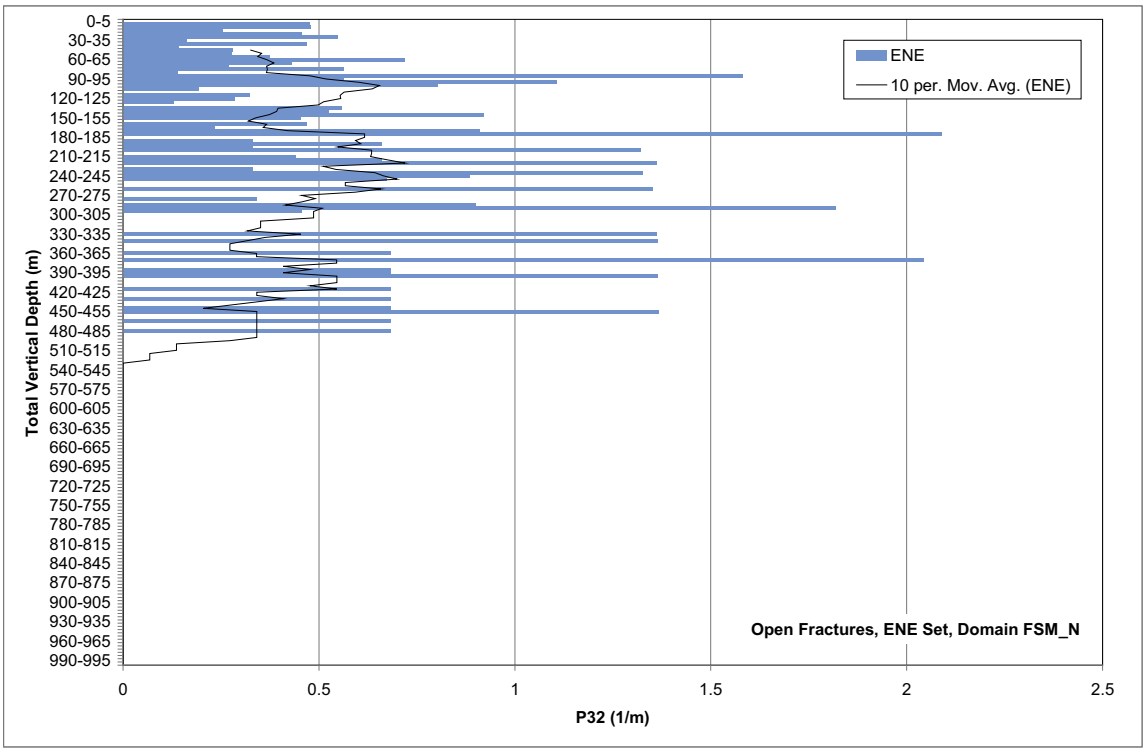

Figure E-23. *P_{32} as a function of total vertical depth, open fractures, ENE set, domain FSM_N.*

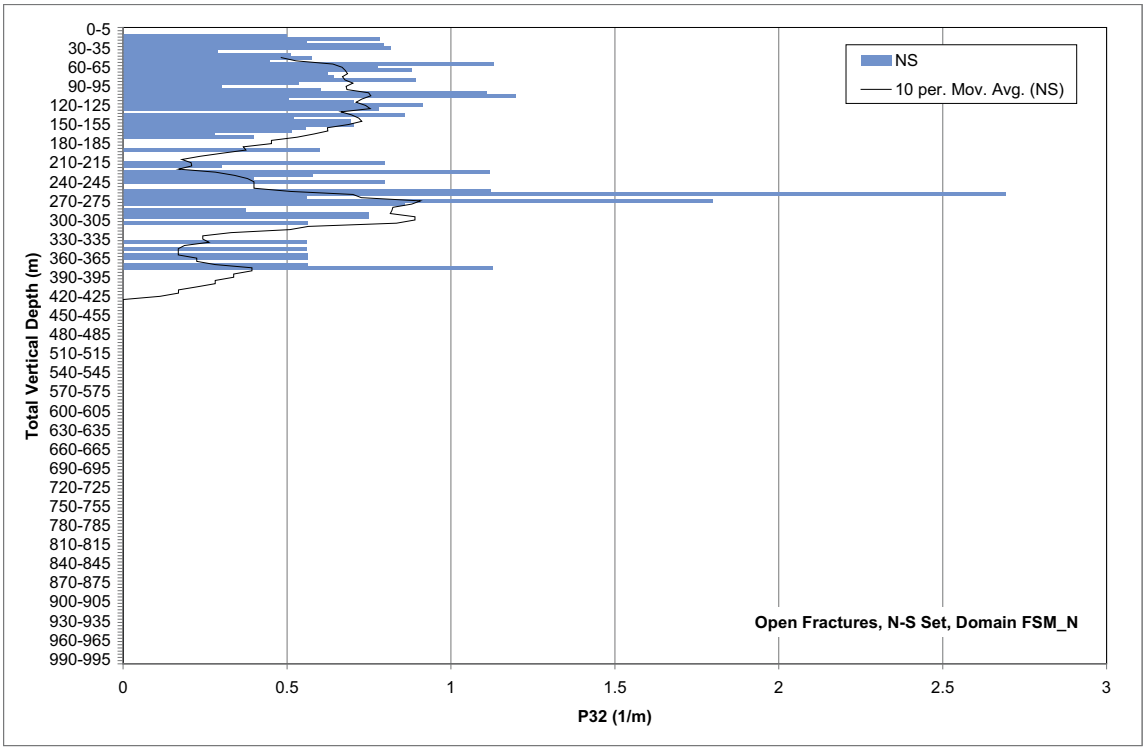

Figure E-24. *P_{32} as a function of total vertical depth, open fractures, N-S set, domain FSM_N.*

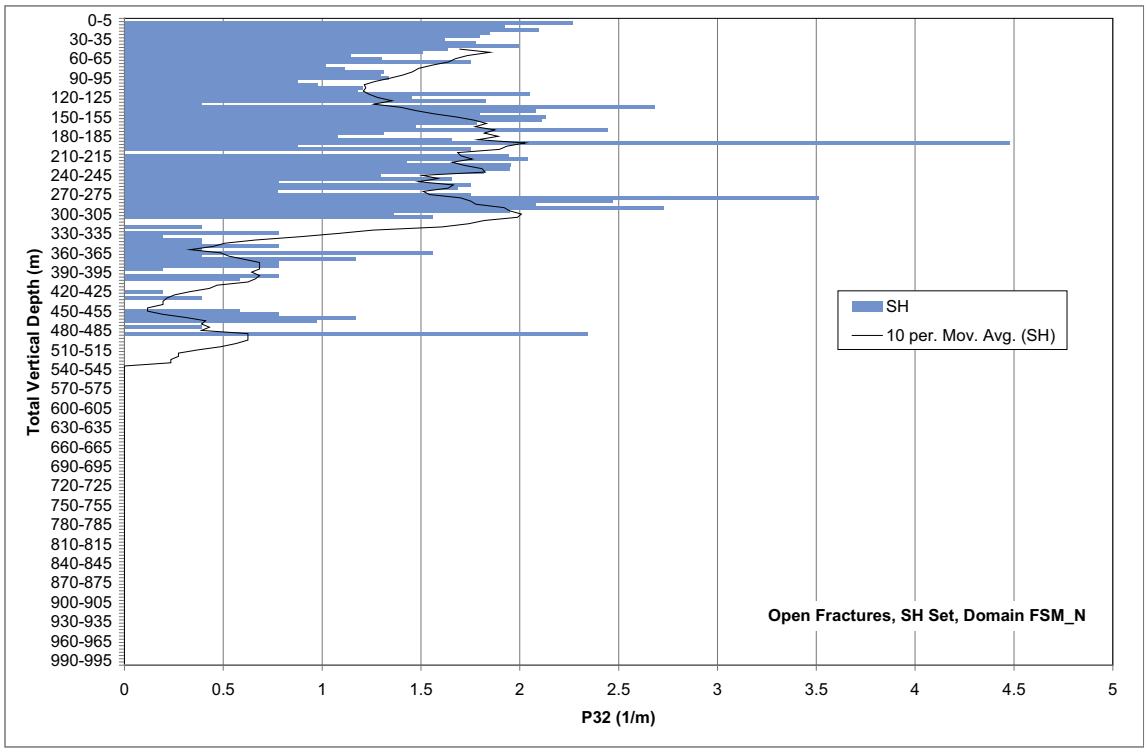

Figure E-25. *P_{32} as a function of total vertical depth, open fractures, SH set, domain FSM_N.*

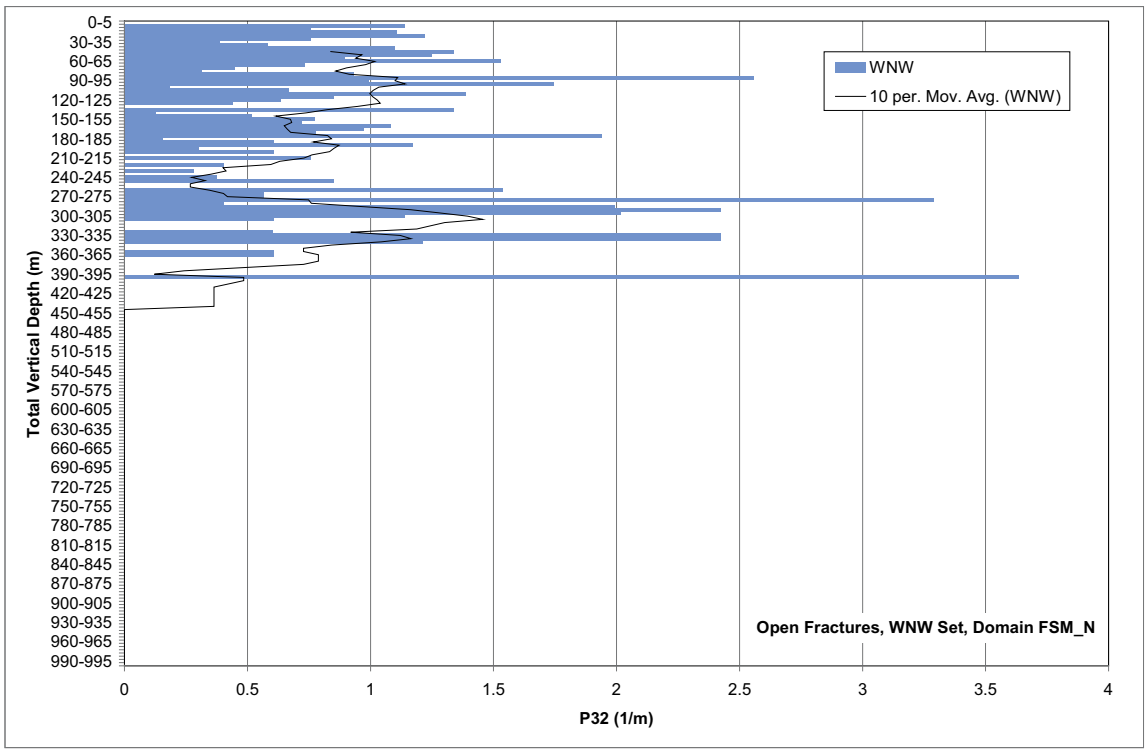

Figure E-26. *P_{32} as a function of total vertical depth, open fractures, WNW set, domain FSM_N.*

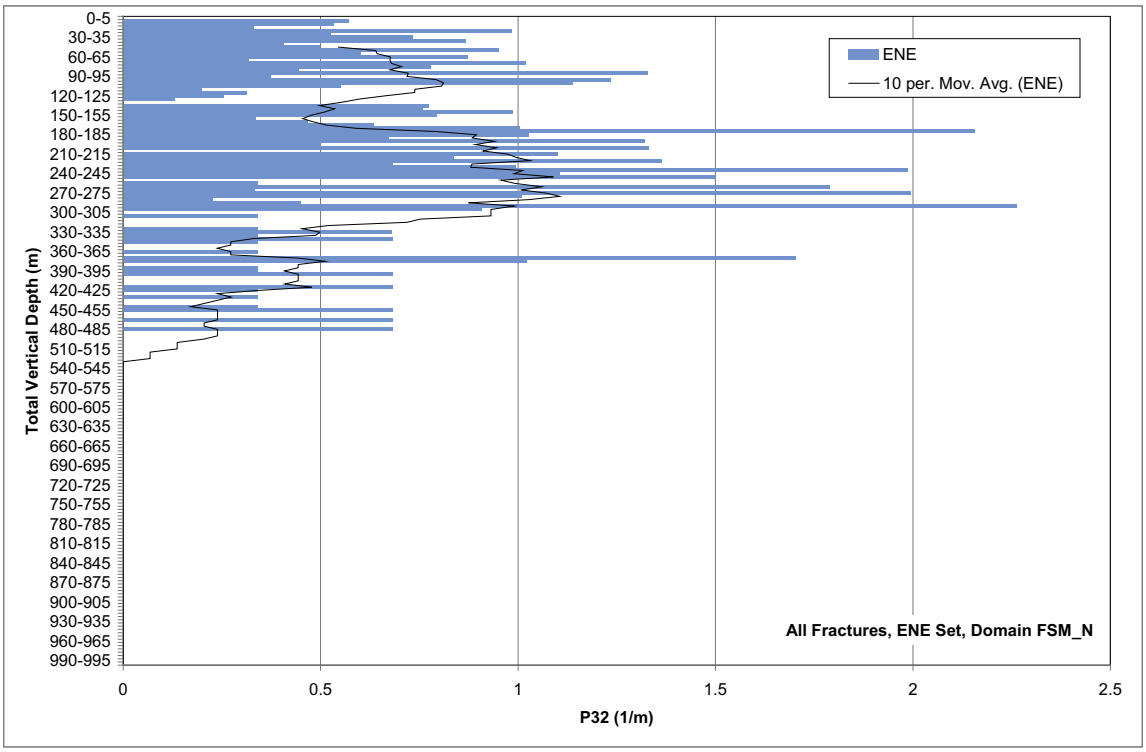

Figure E-27. *P_{32} as a function of total vertical depth, all fractures, ENE set, domain FSM_N.*

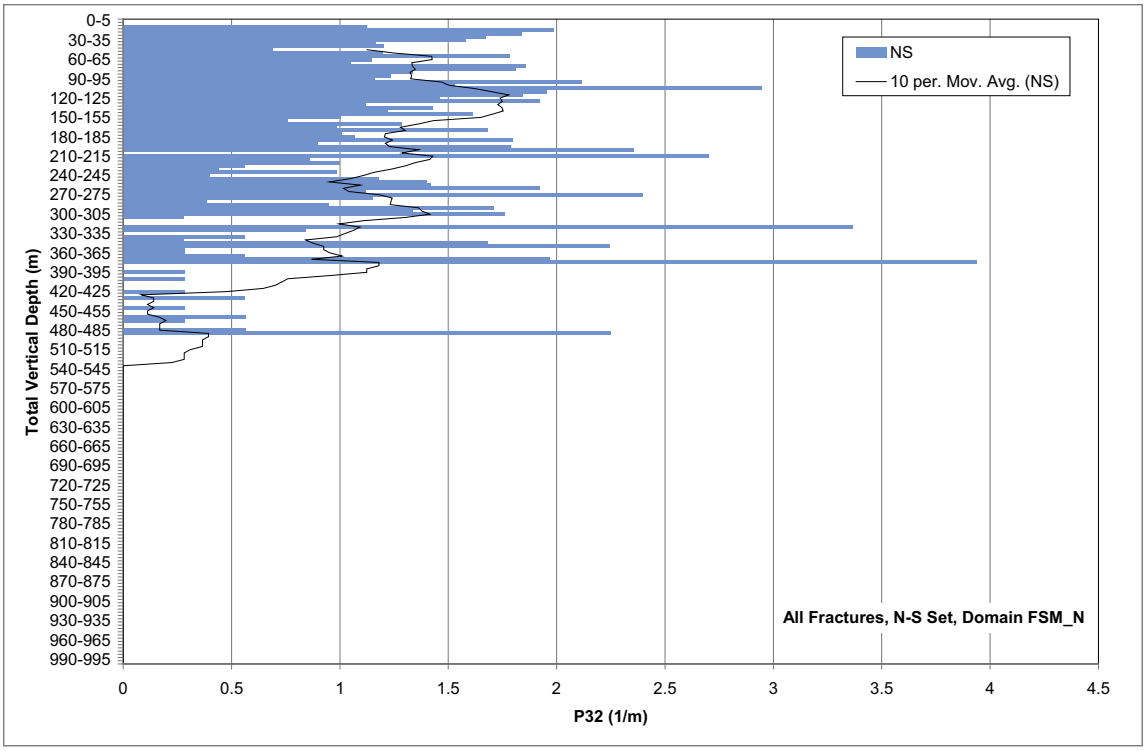

Figure E-28. *P_{32} as a function of total vertical depth, all fractures, N-S set, domain FSM_N.*

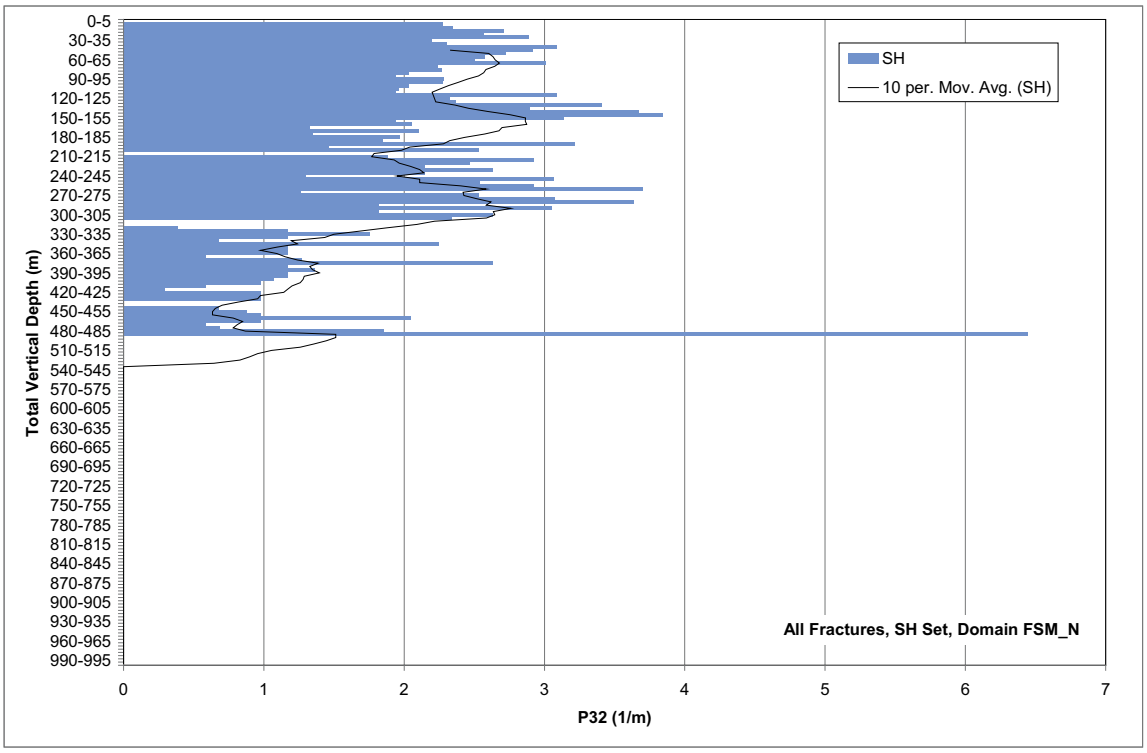

Figure E-29. *P_{32} as a function of total vertical depth, all fractures, SH set, domain FSM_N.*

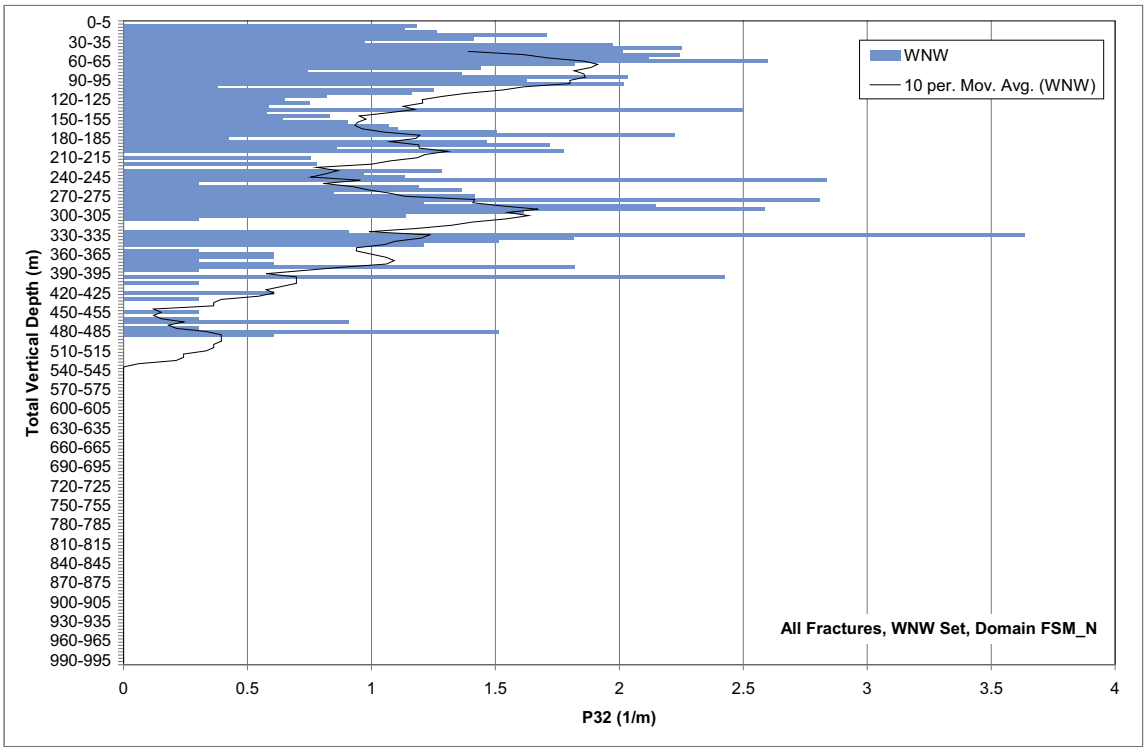

Figure E-30. *P_{32} as a function of total vertical depth, all fractures, WNW set, domain FSM_N.*

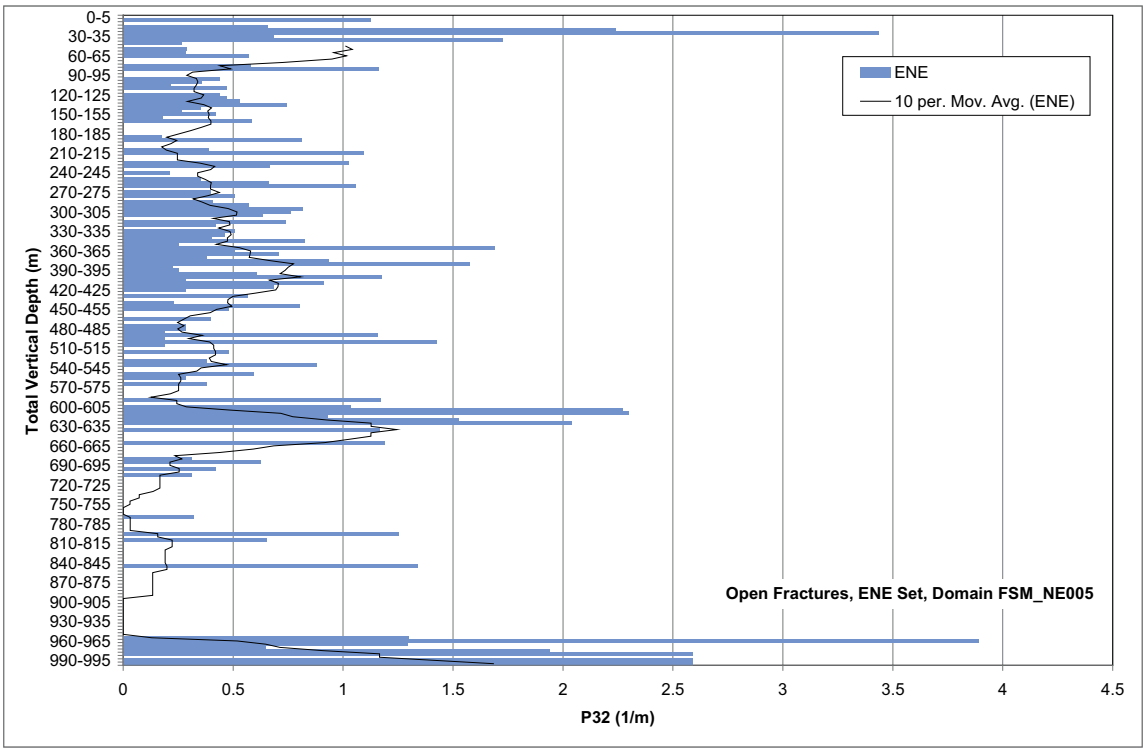

Figure E-31. *P_{32} as a function of total vertical depth, open fractures, ENE set, domain FSM_NE005.*

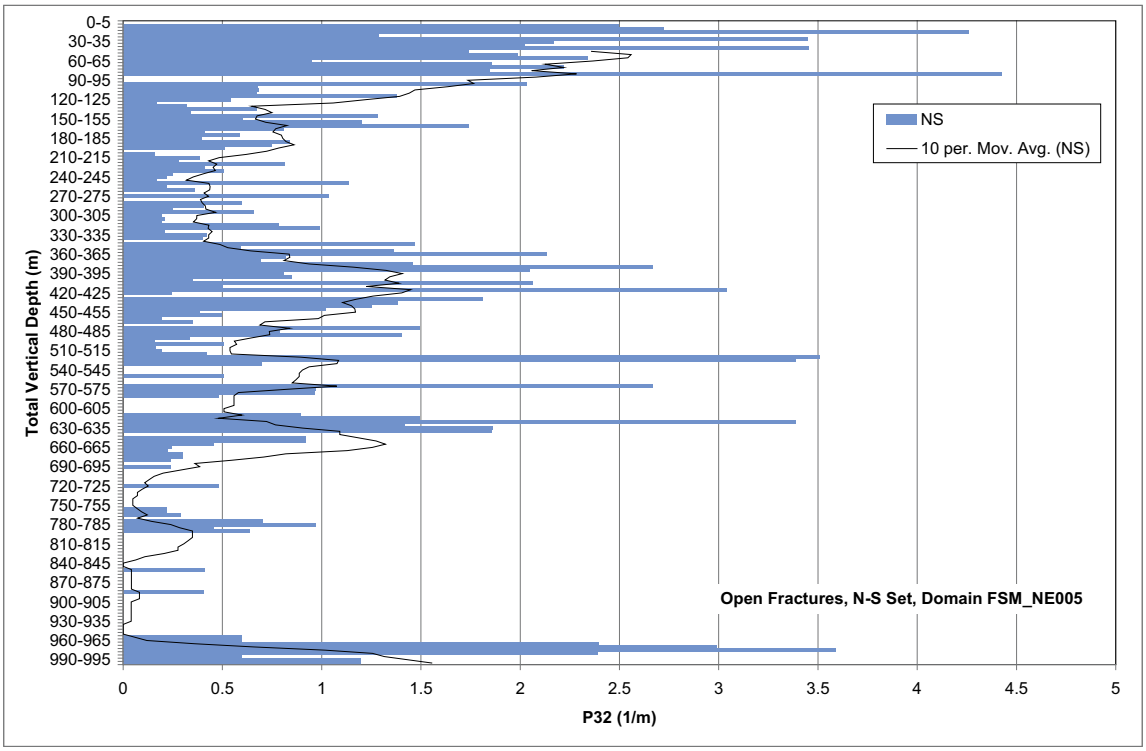

Figure E-32. *P_{32} as a function of total vertical depth, open fractures, N-S set, domain FSM_NE005.*

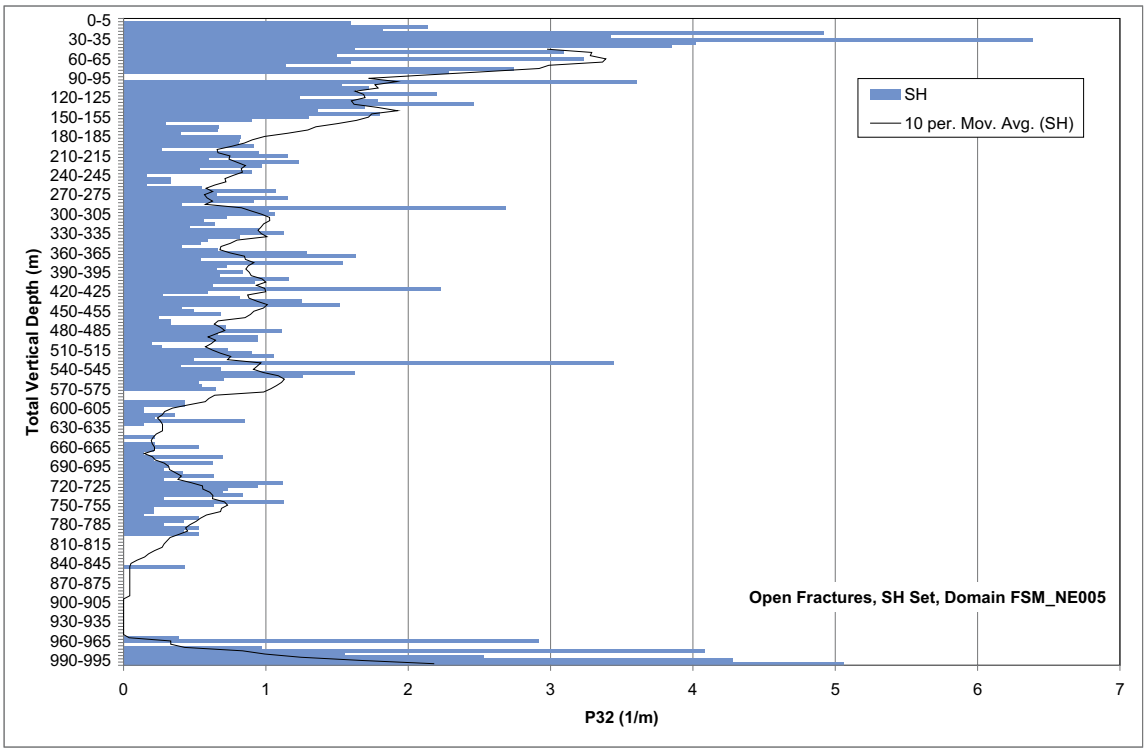

Figure E-33. *P_{32} as a function of total vertical depth, open fractures, SH set, domain FSM_NE005.*

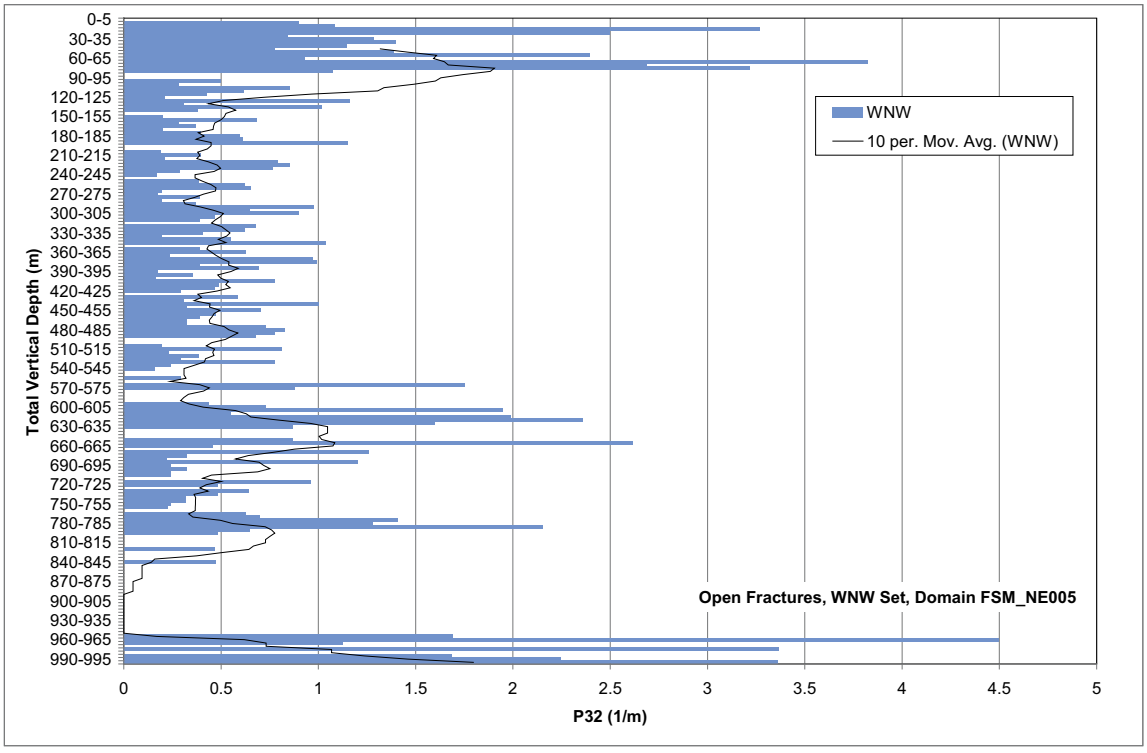

Figure E-34. *P_{32} as a function of total vertical depth, open fractures, WNW set, domain FSM_NE005.*

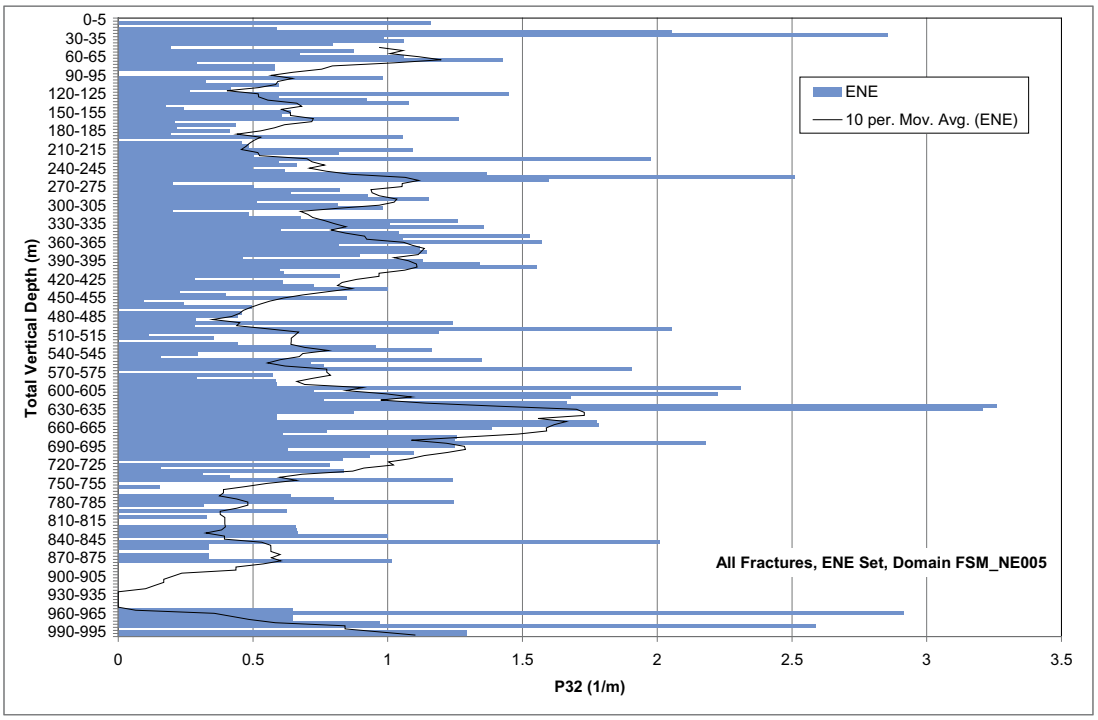

Figure E-35. *P_{32} as a function of total vertical depth, all fractures, ENE set, domain FSM_NE005.*

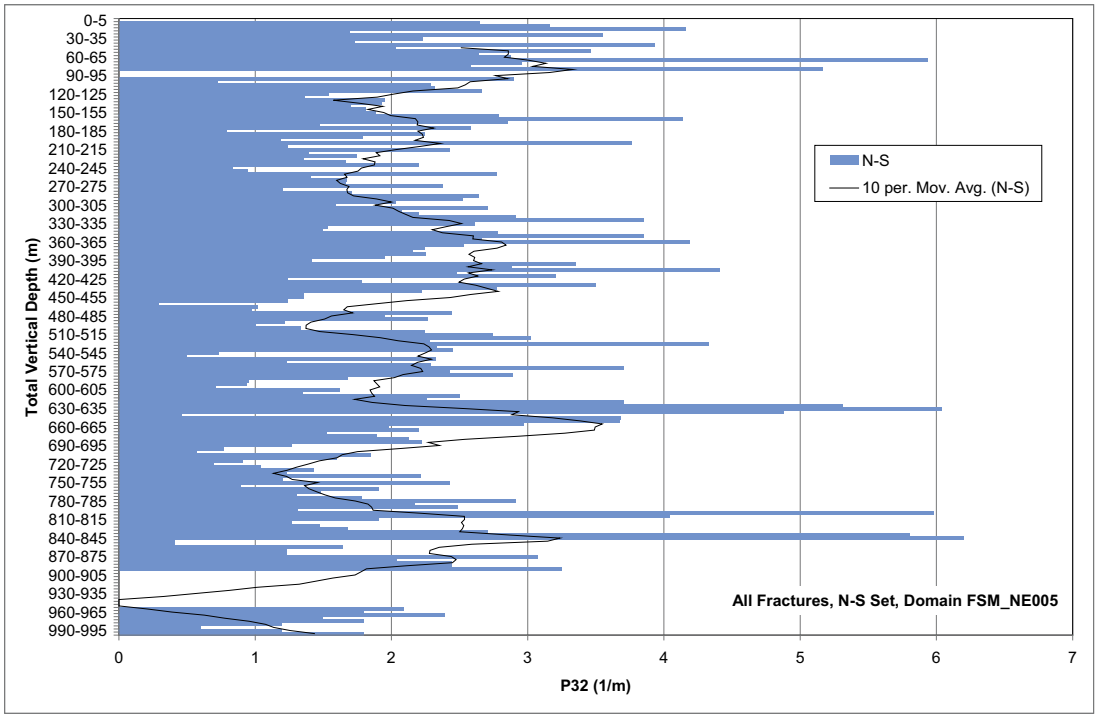

Figure E-36. *P_{32} as a function of total vertical depth, all fractures, N-S set, domain FSM_NE005.*

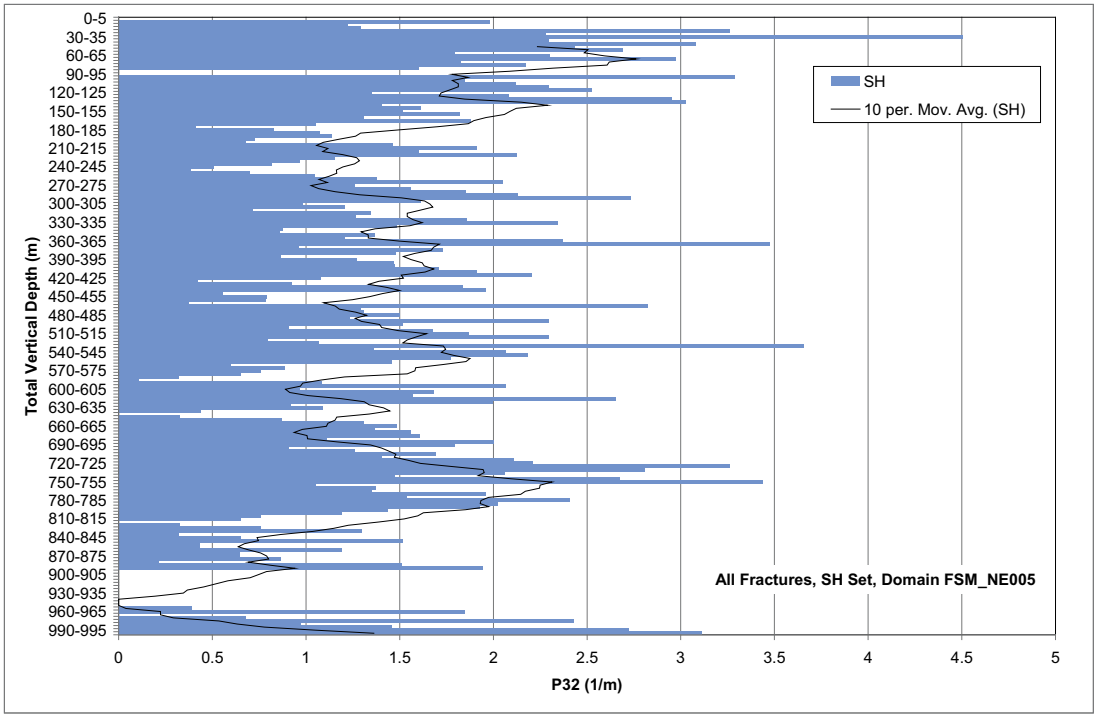

Figure E-37. *P_{32} as a function of total vertical depth, all fractures, SH set, domain FSM_NE005.*

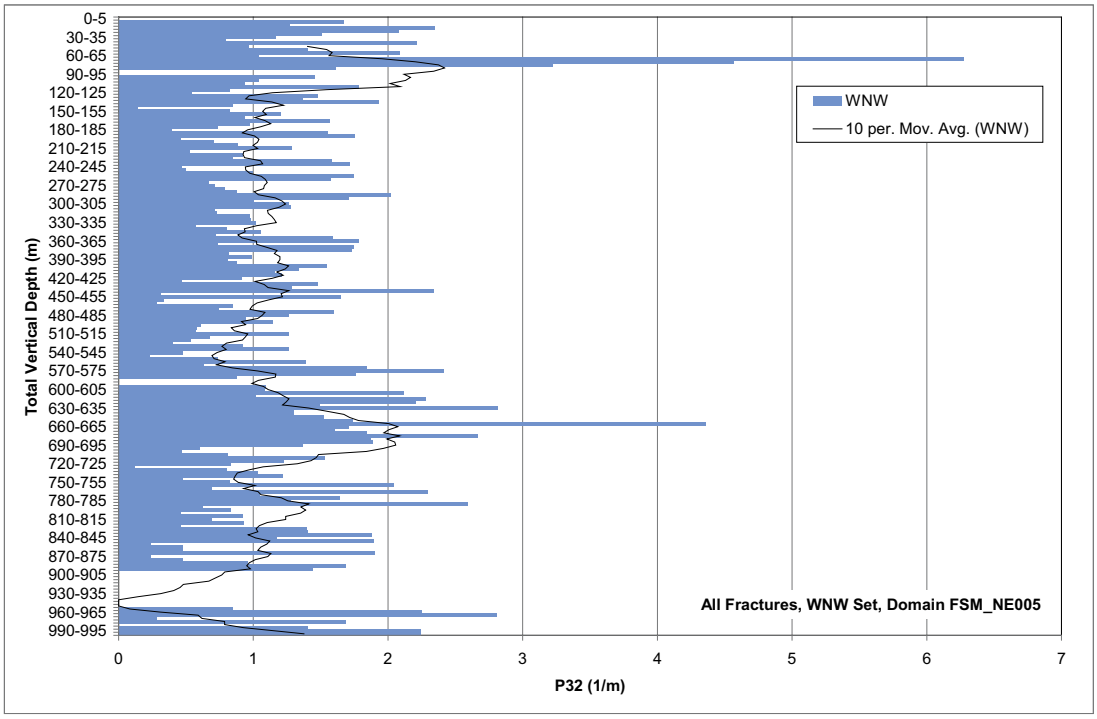

Figure E-38. *P_{32} as a function of total vertical depth, all fractures, WNW set, domain FSM_NE005.*

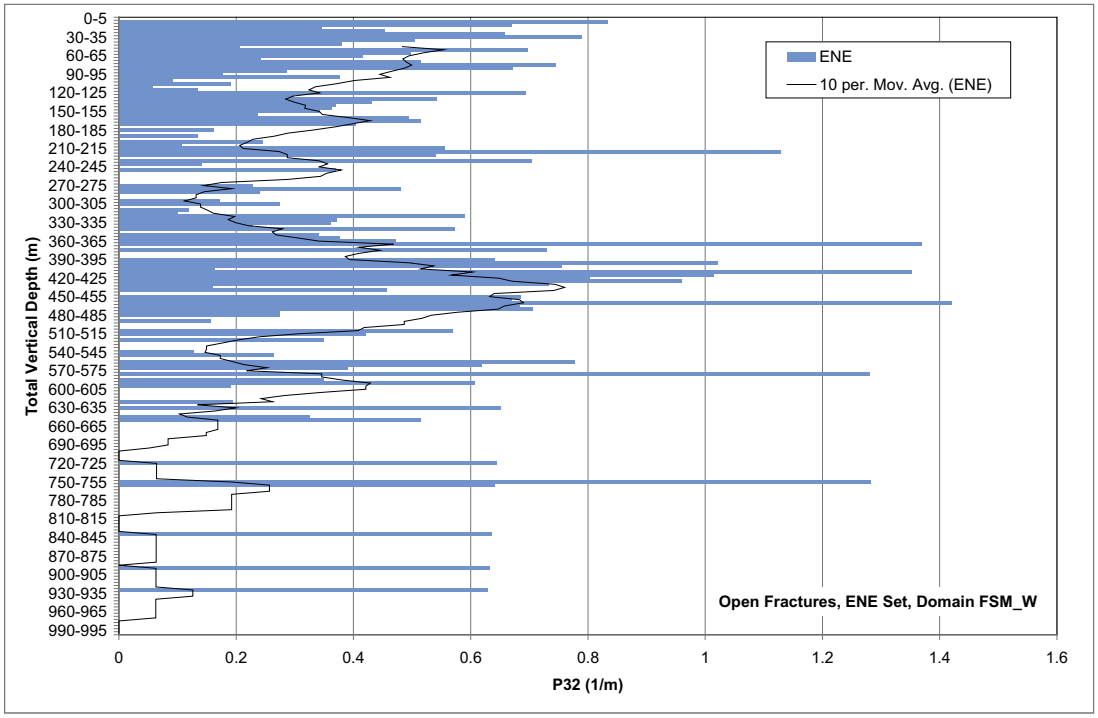

Figure E-39. *P_{32} as a function of total vertical depth, open fractures, ENE set, domain FSM_W.*

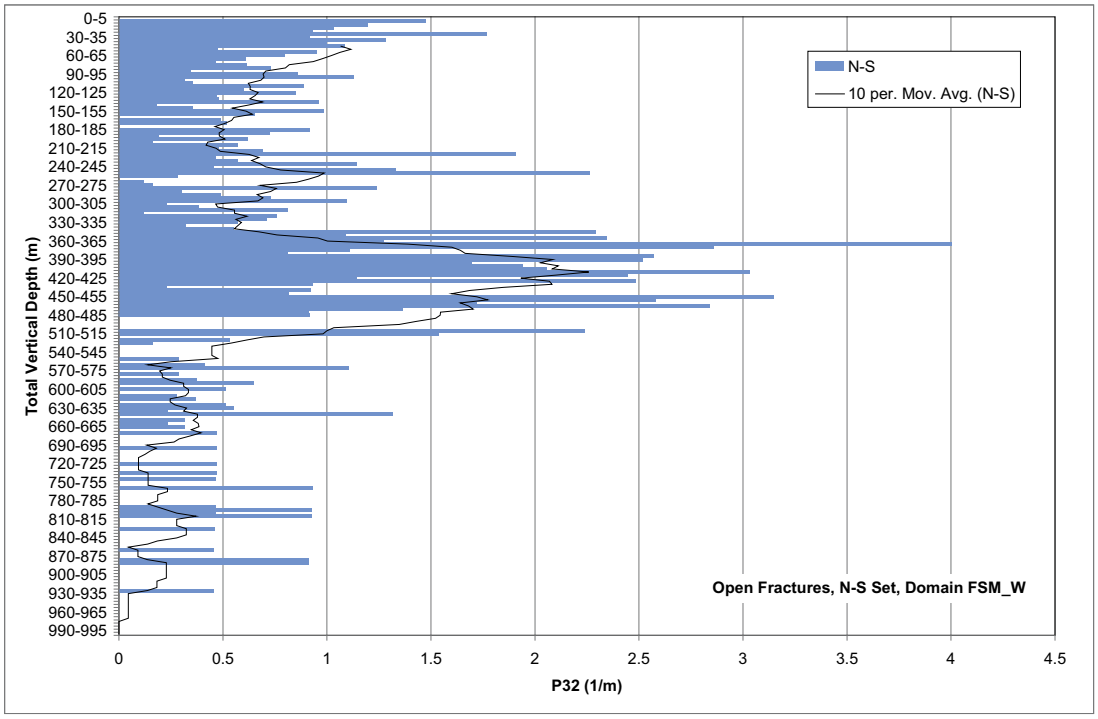

Figure E-40. *P_{32} as a function of total vertical depth, open fractures, N-S set, domain FSM_W.*

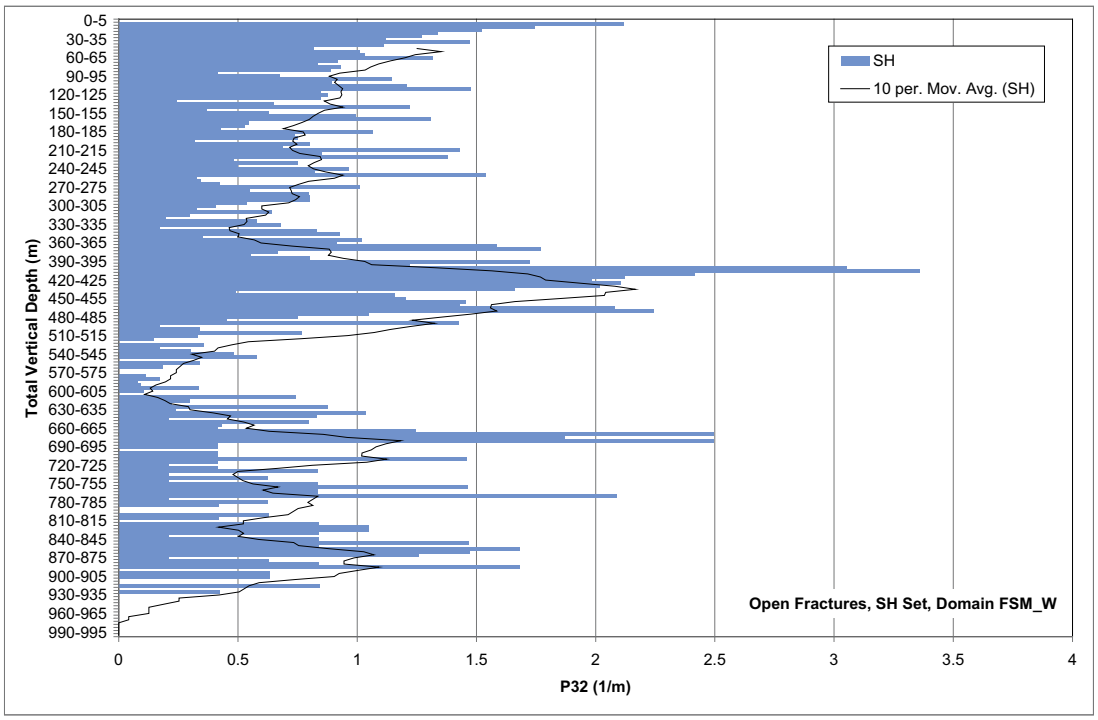

Figure E-41. *P_{32} as a function of total vertical depth, open fractures, SH set, domain FSM_W.*

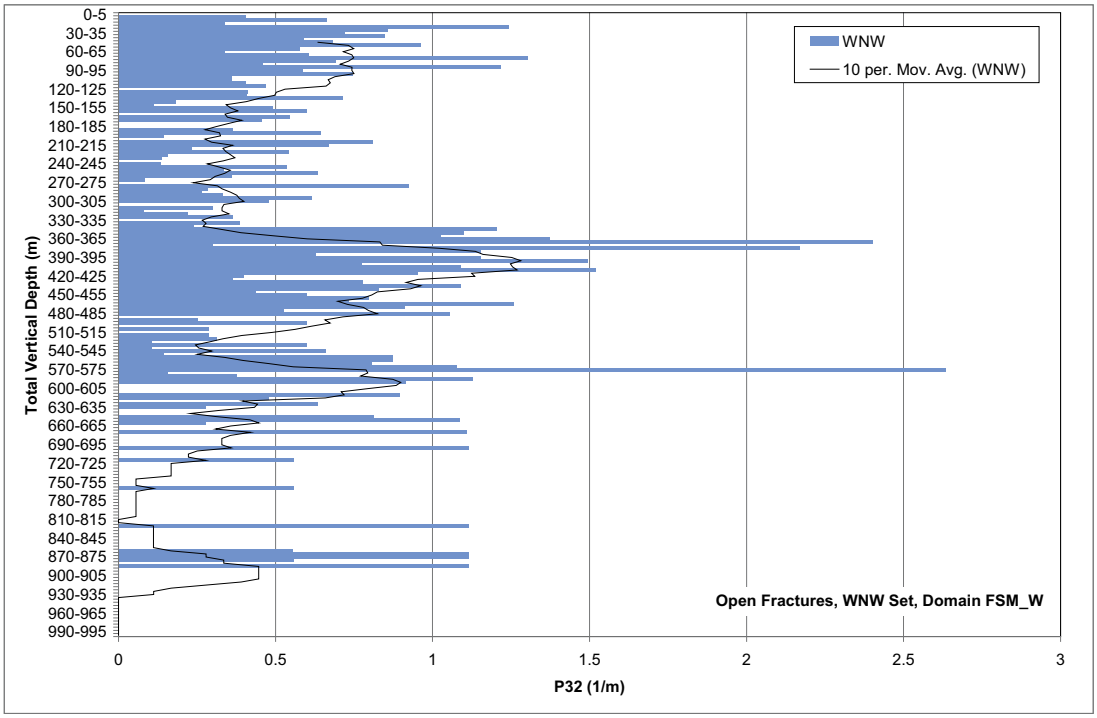

Figure E-42. *P_{32} as a function of total vertical depth, open fractures, WNW set, domain FSM_W.*

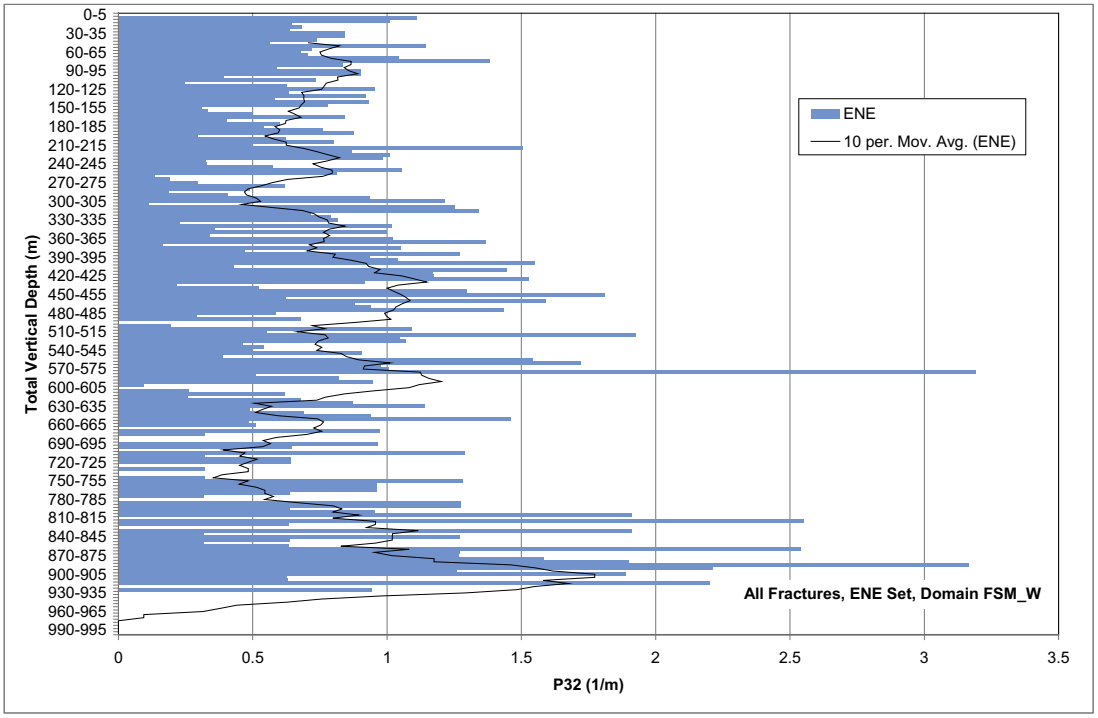

Figure E-43. *P_{32} as a function of total vertical depth, all fractures, ENE set, domain FSM_W.*

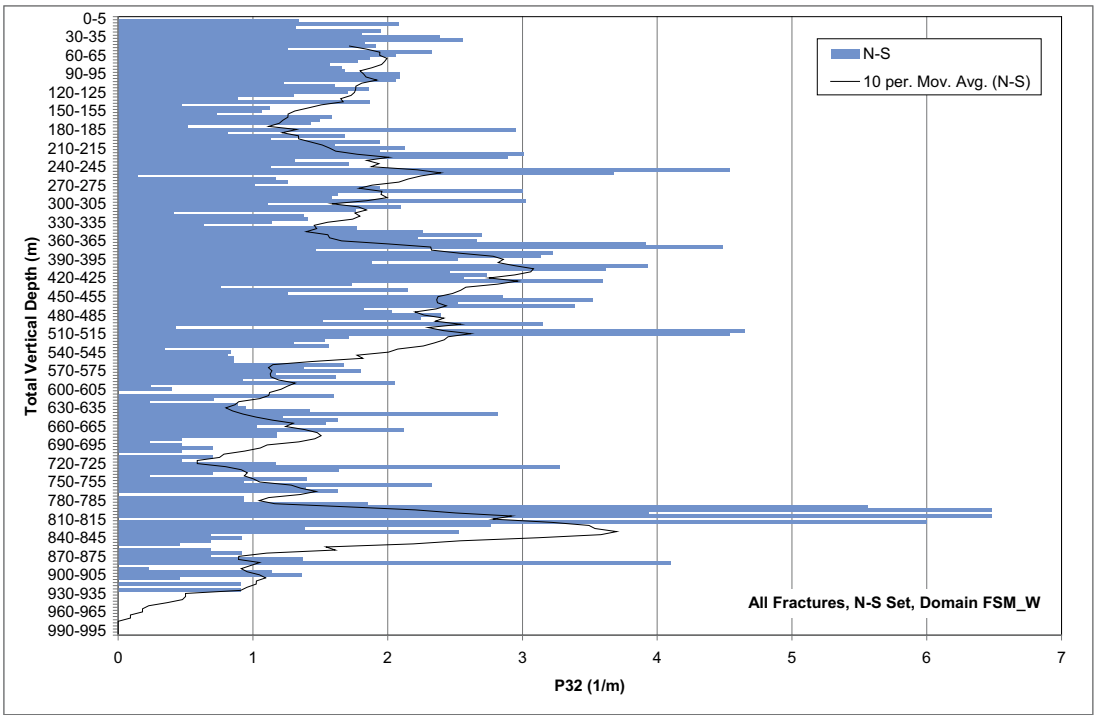

Figure E-44. *P_{32} as a function of total vertical depth, all fractures, N-S set, domain FSM_W.*

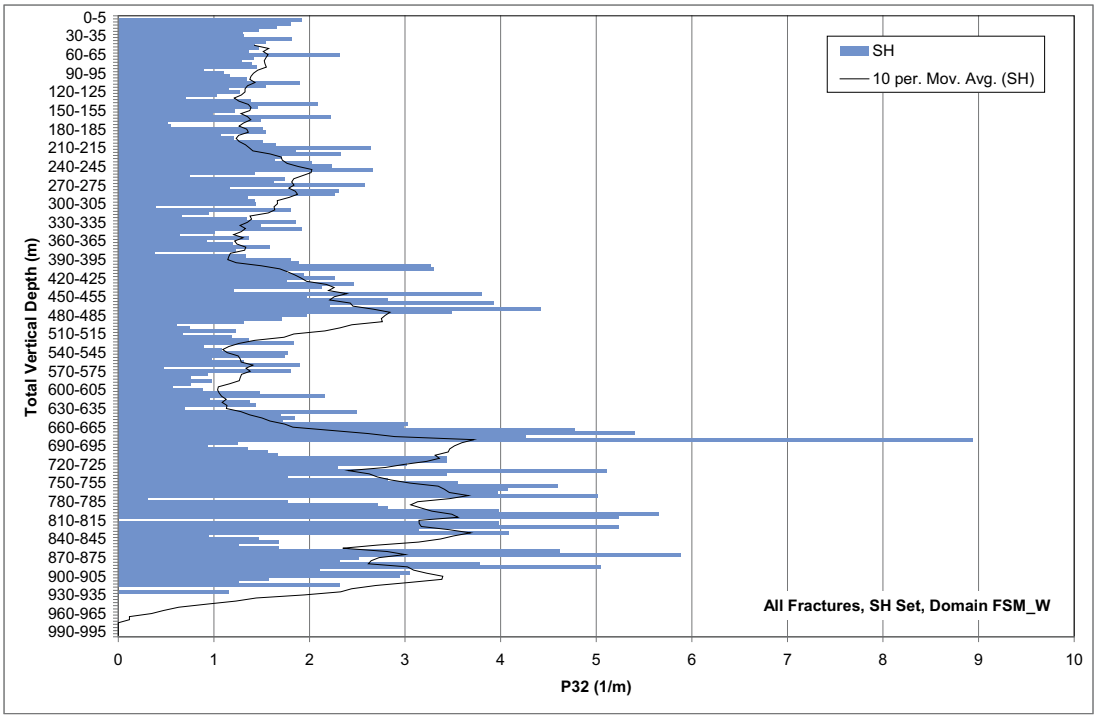

Figure E-45. *P_{32} as a function of total vertical depth, all fractures, SH set, domain FSM_W.*

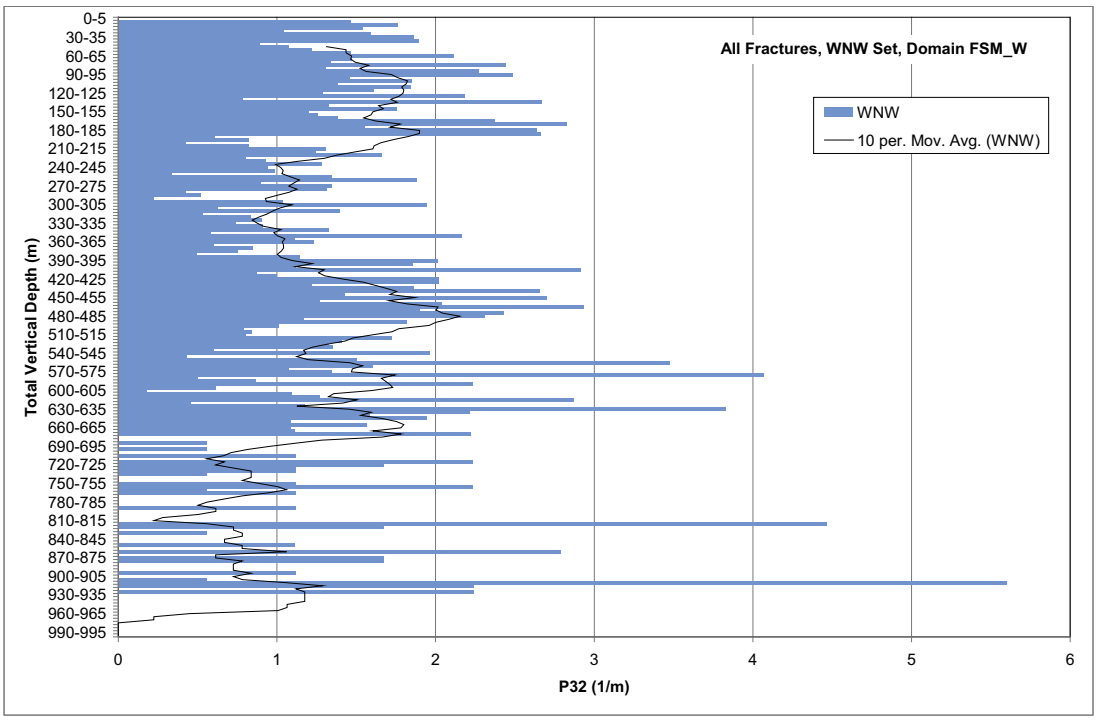

Figure E-46. *P_{32} as a function of total vertical depth, all fractures, WNW set, domain FSM_W.*

Appendix F

Spatial variability of fracture intensity as a Gamma or Weibull Distribution

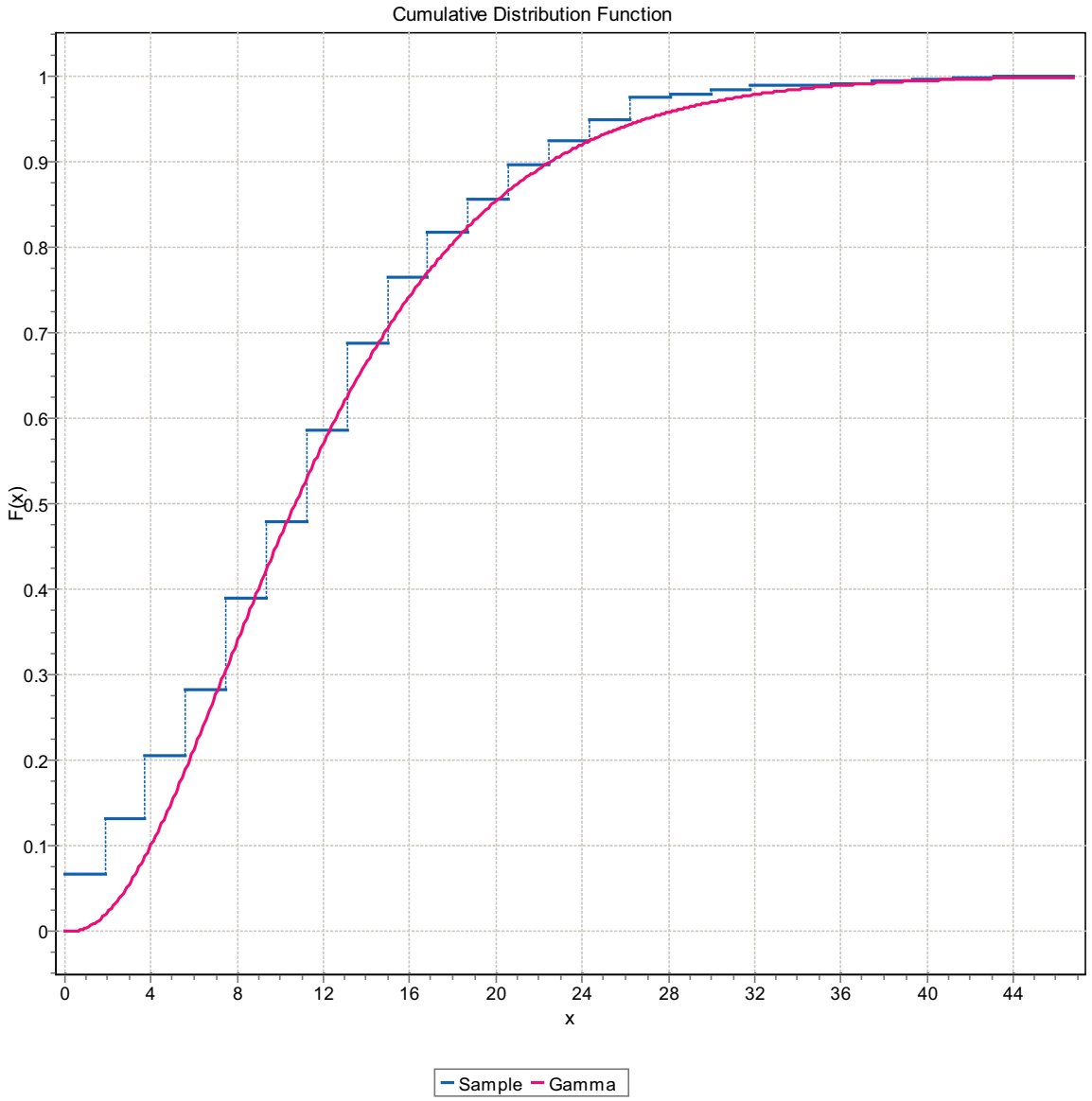

Figure F-1. *CDF, Domain FSM_EW007, 3 m bins, Gamma Distribution.*

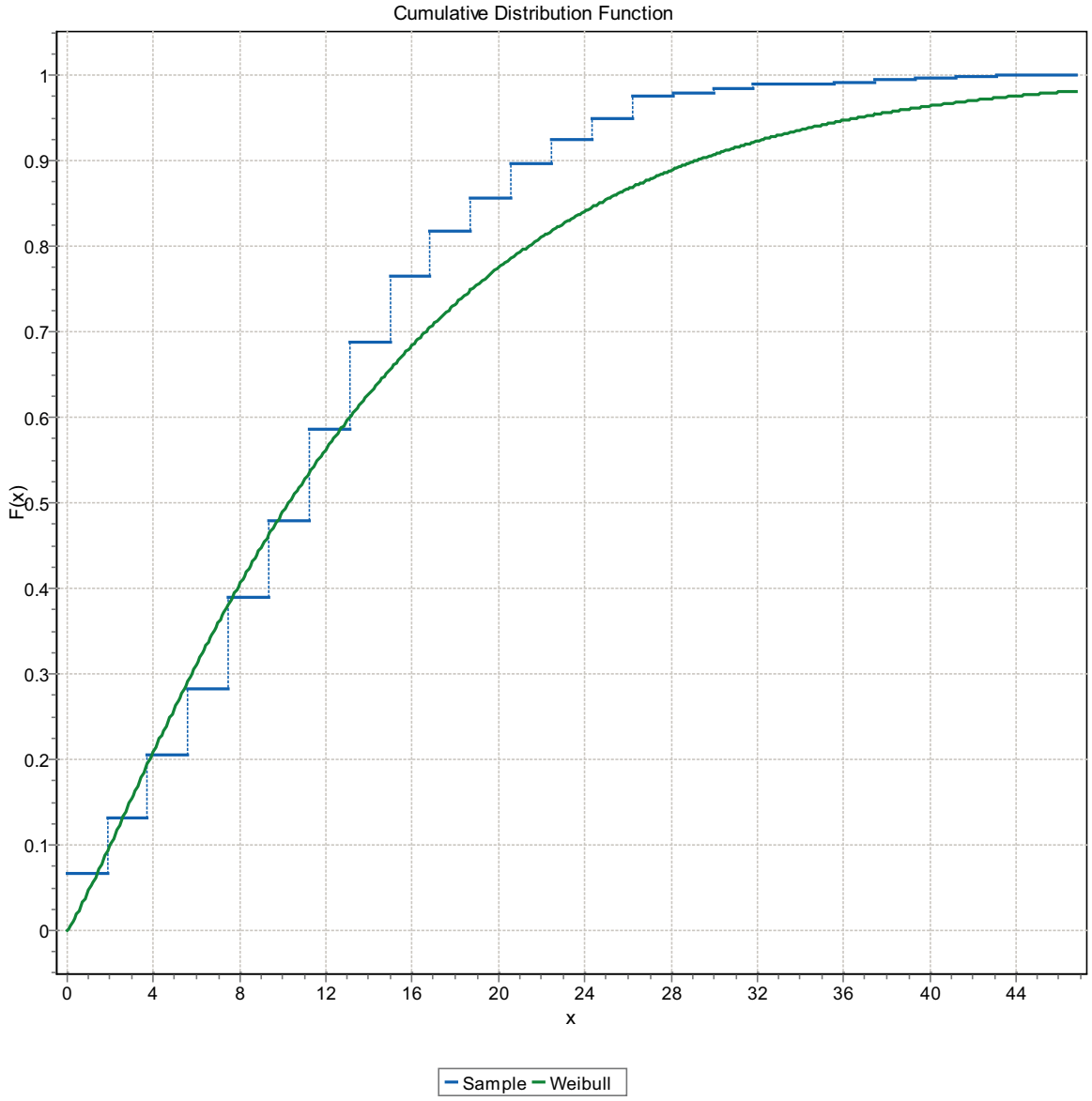

Figure F-2. *CDF, Domain FSM_EW007, 3 m bins, Weibull Distribution.*

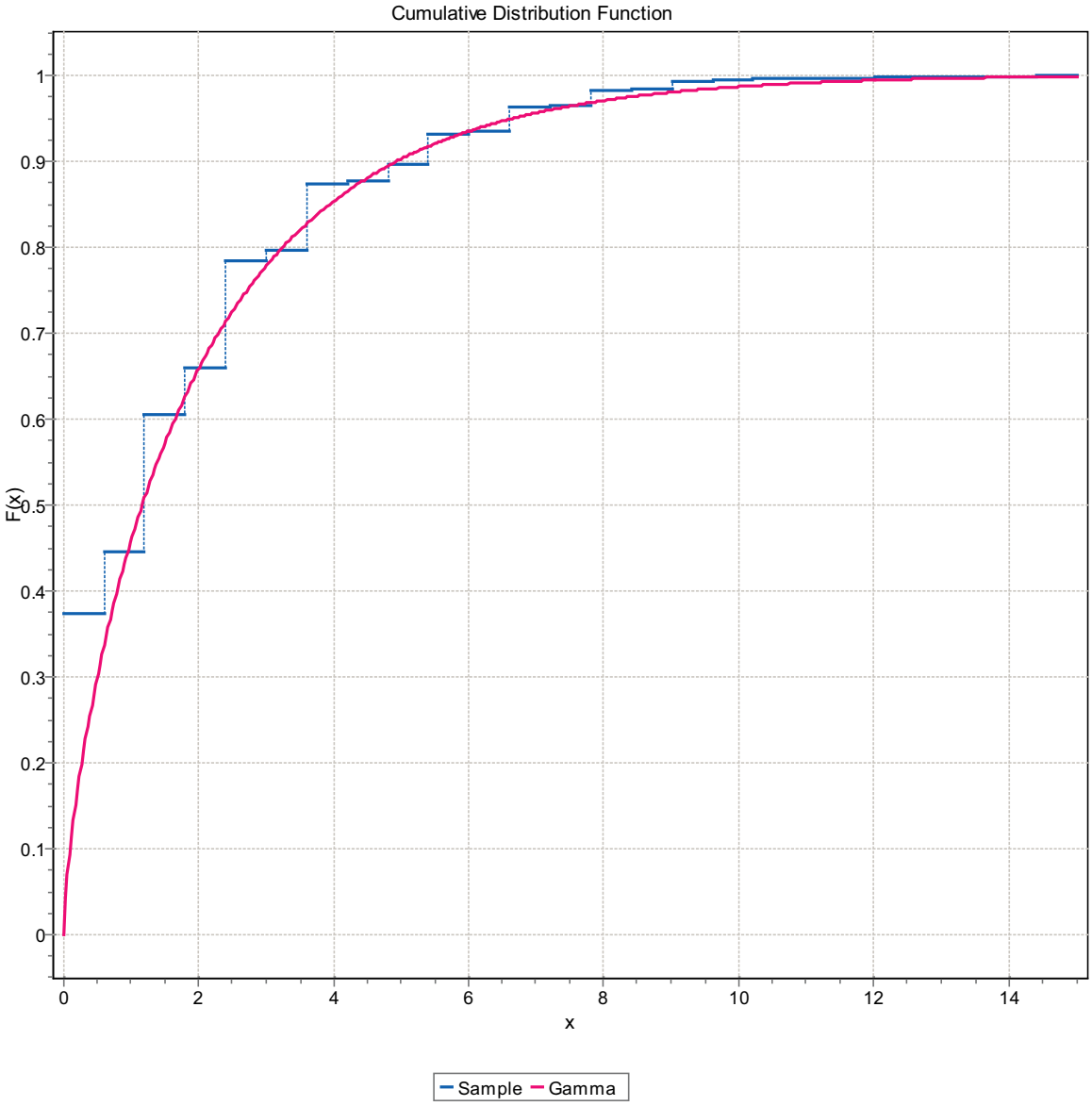

Figure F-3. *CDF, Domain FSM_EW007, 3 m bins, Gamma Distribution.*

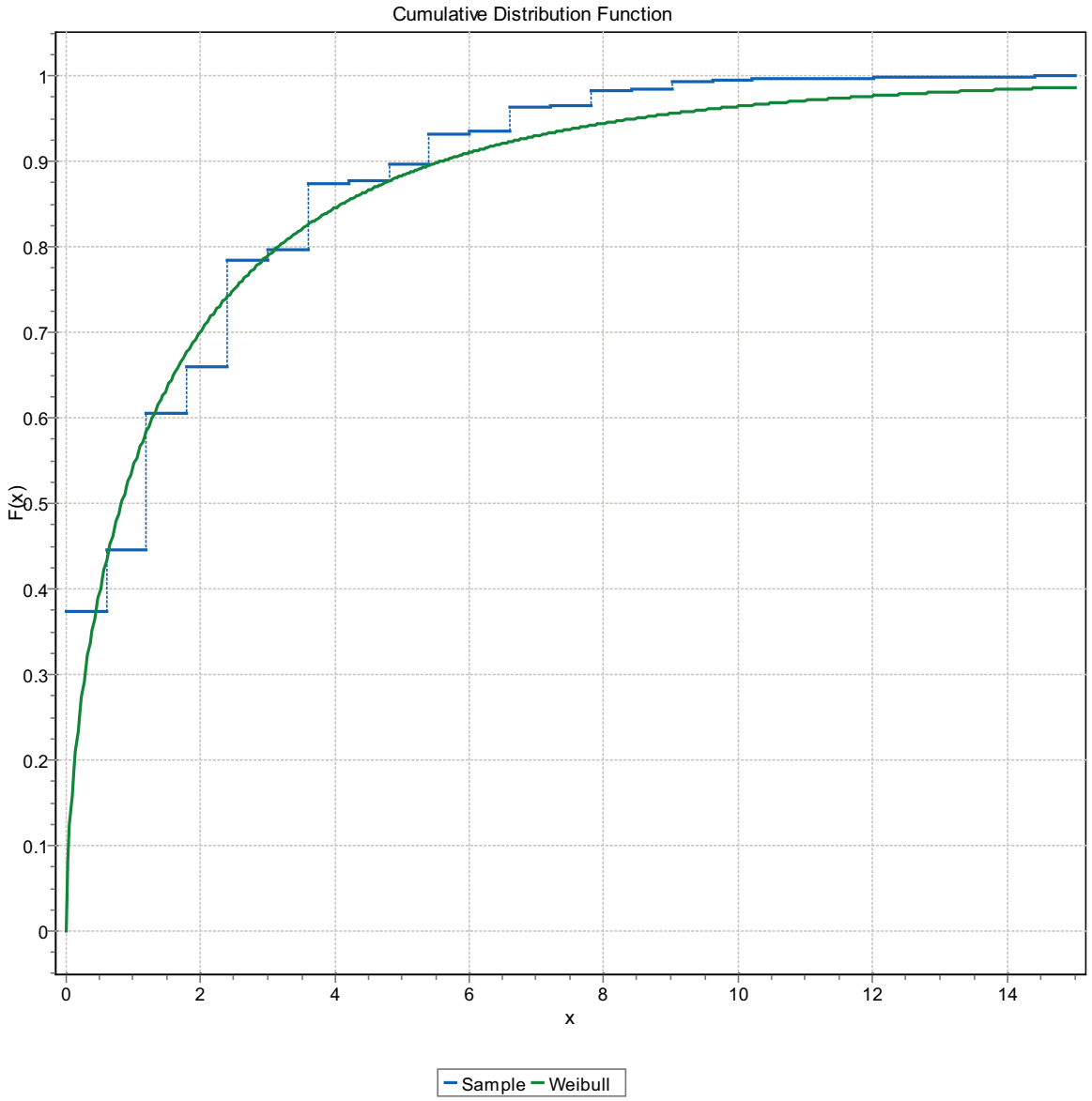

Figure F-4. *CDF, Domain FSM_EW007, 3 m bins, Weibull Distribution.*

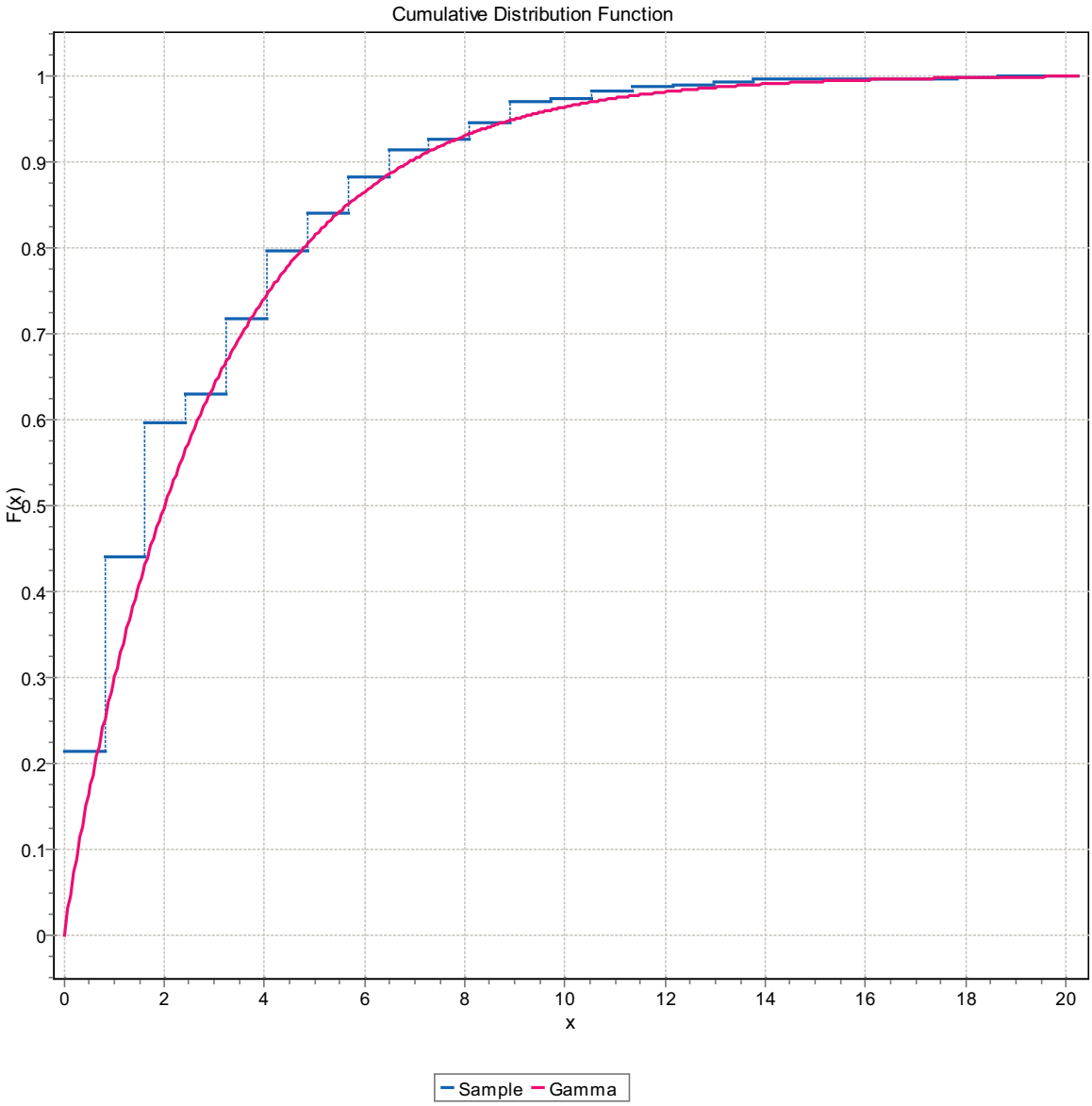

Figure F-5. *CDF, Domain FSM_EW007, 3 m bins, Gamma Distribution.*

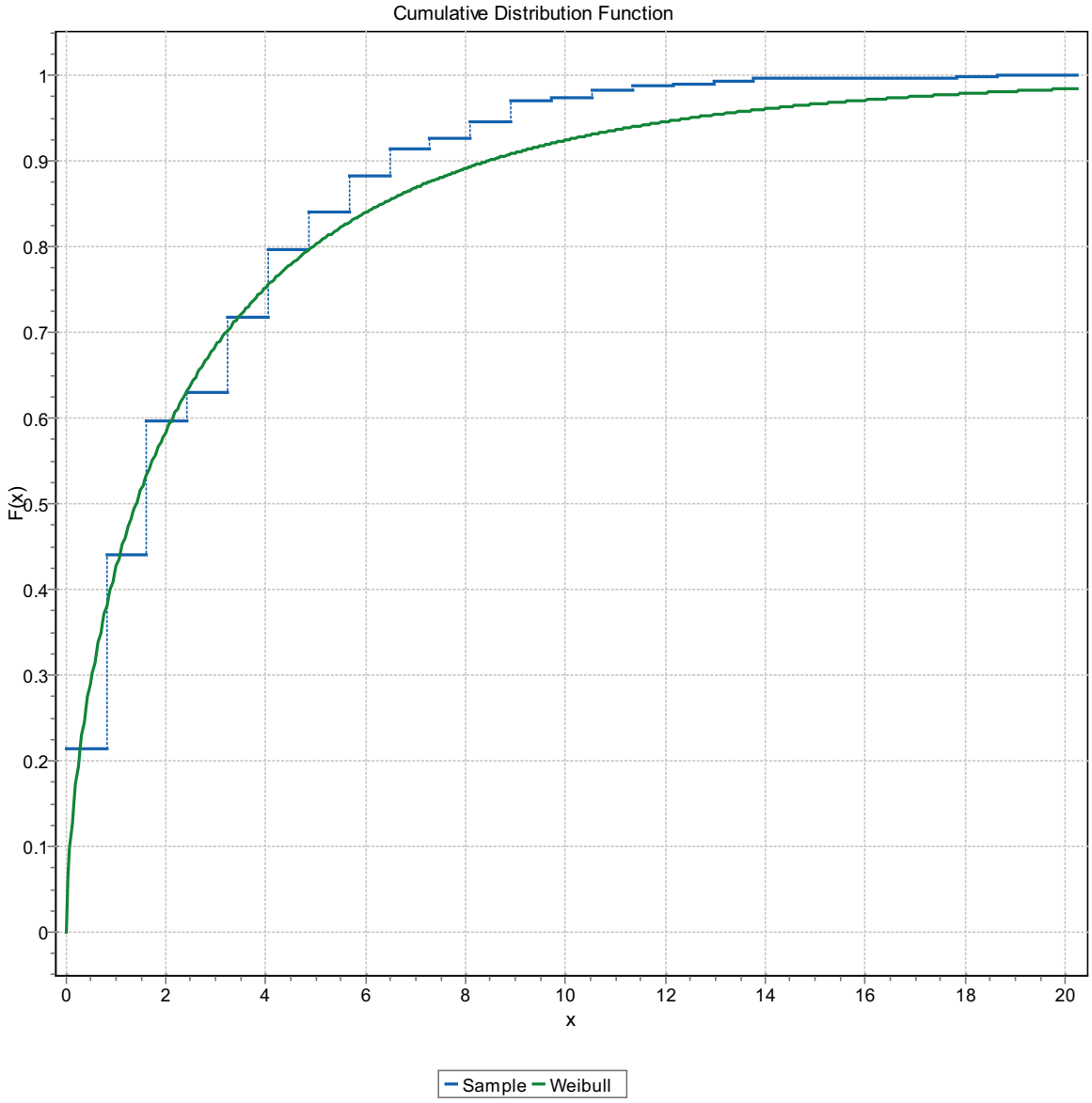

Figure F-6. *CDF, Domain FSM_EW007, 3 m bins, Weibull Distribution.*

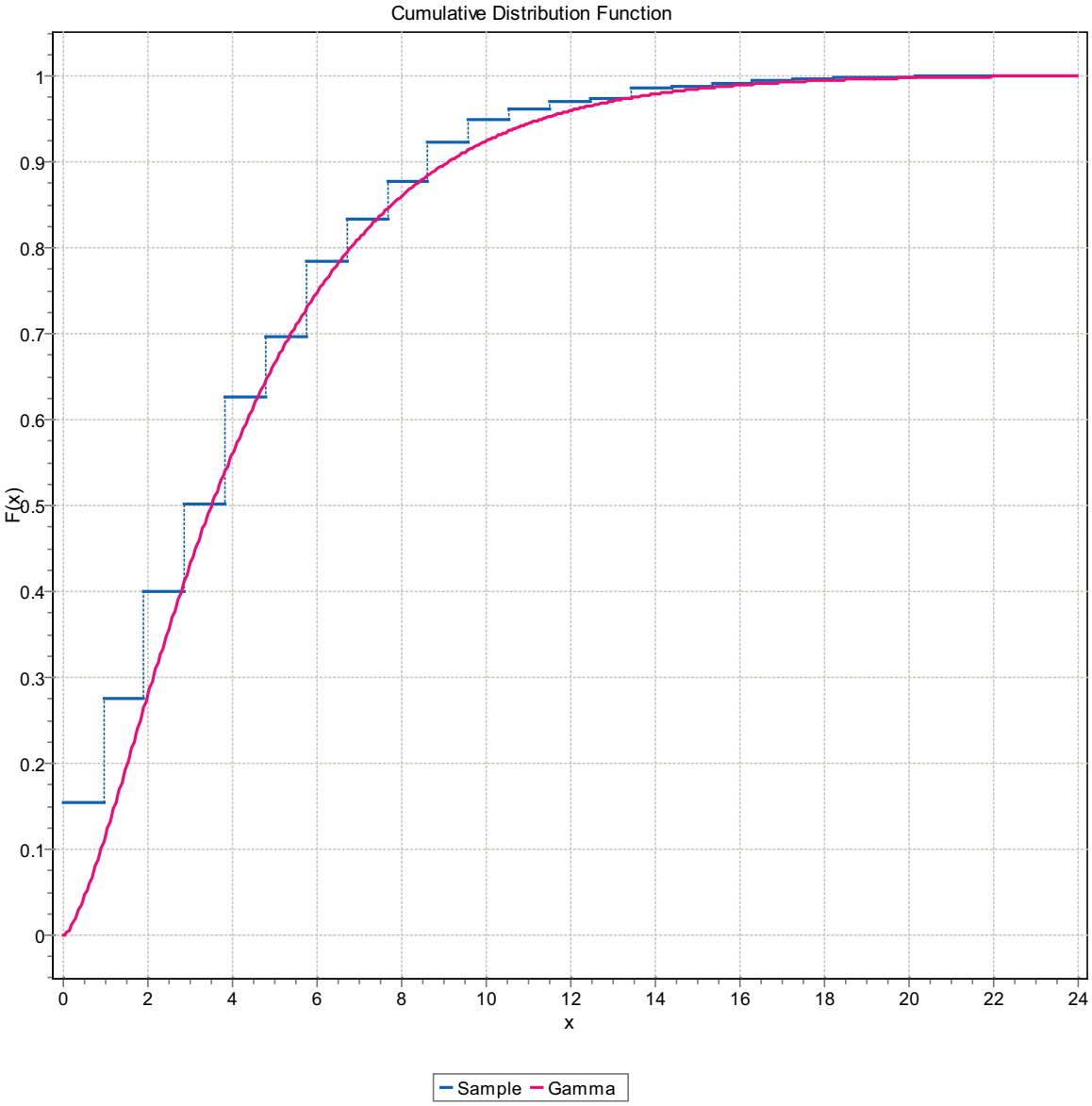

Figure F-7. *CDF, Domain FSM_EW007, 3 m bins, Gamma Distribution.*

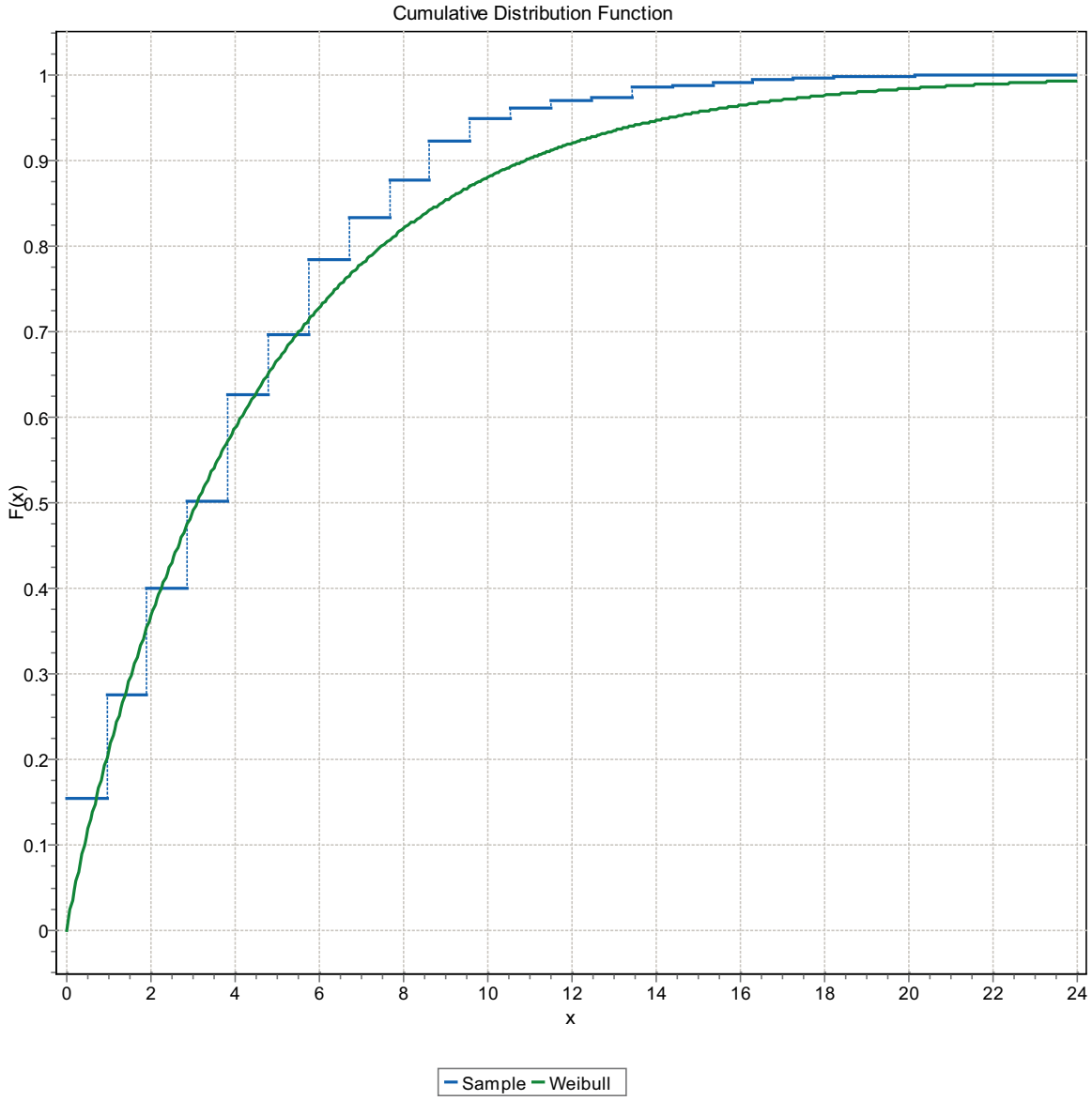

Figure F-8. *CDF, Domain FSM_EW007, 3 m bins, Weibull Distribution.*

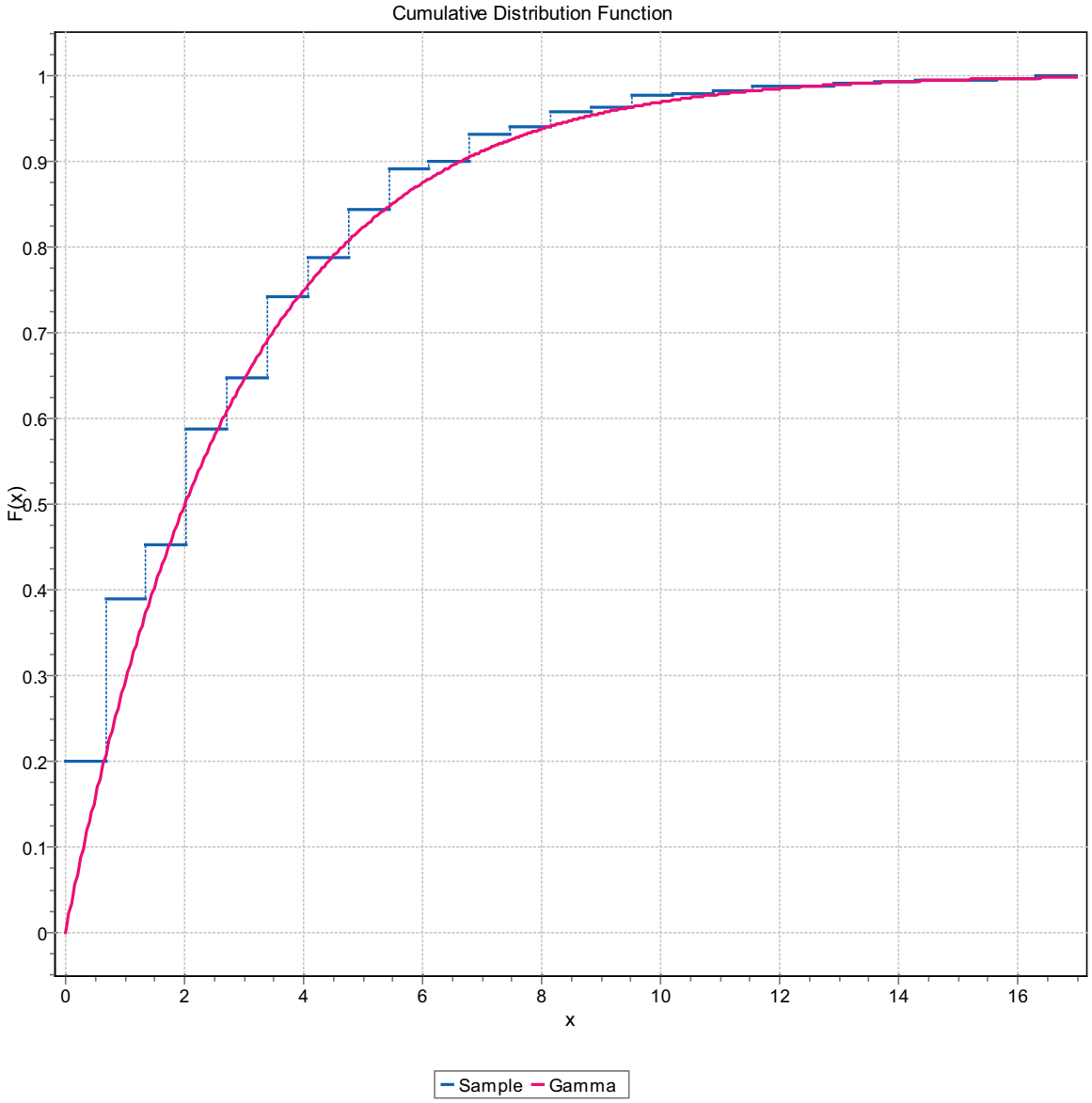

Figure F-9. *CDF, Domain FSM_EW007, 3 m bins, Gamma Distribution.*

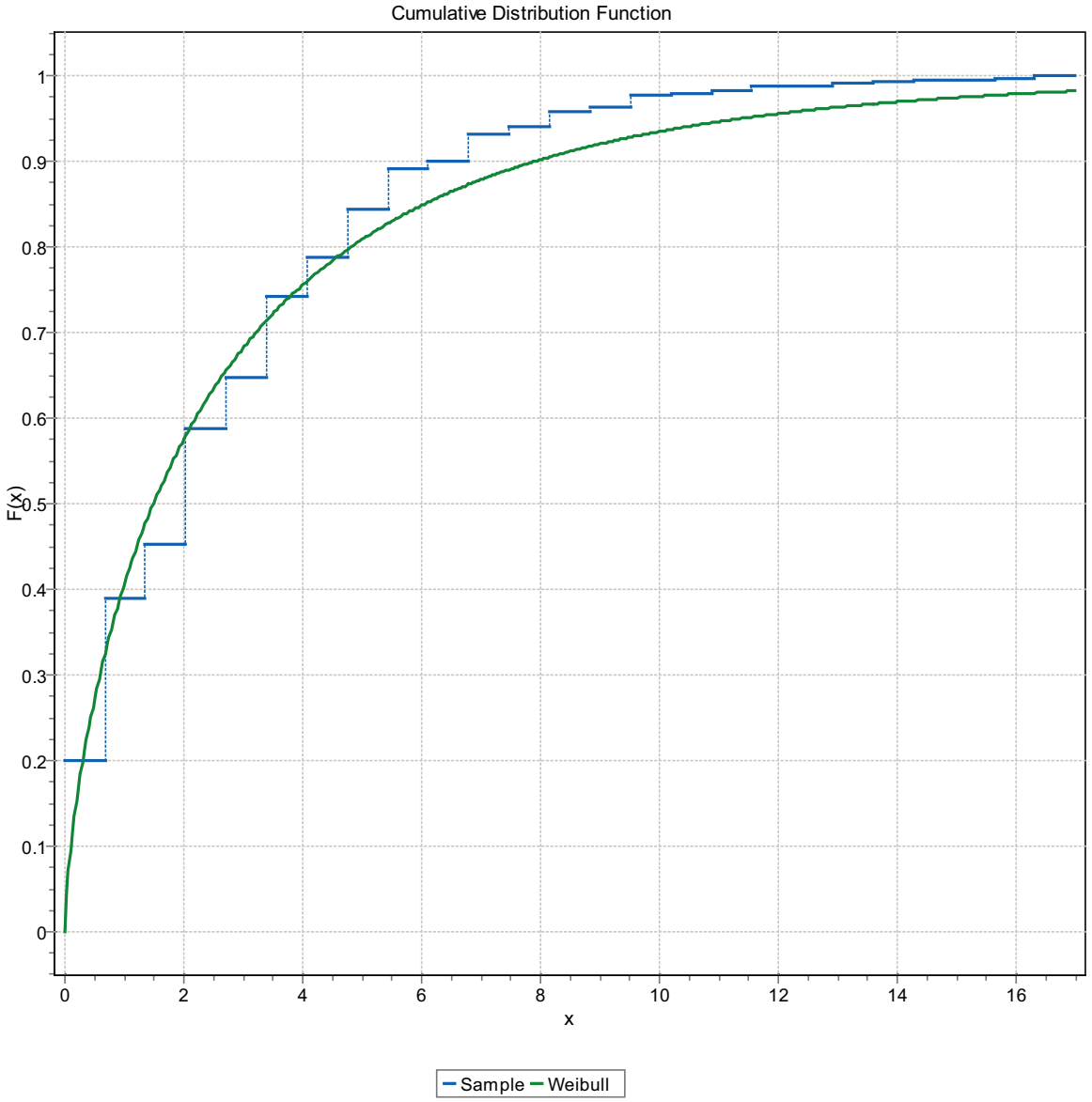

Figure F-10. *CDF, Domain FSM_EW007, 3 m bins, Weibull Distribution.*

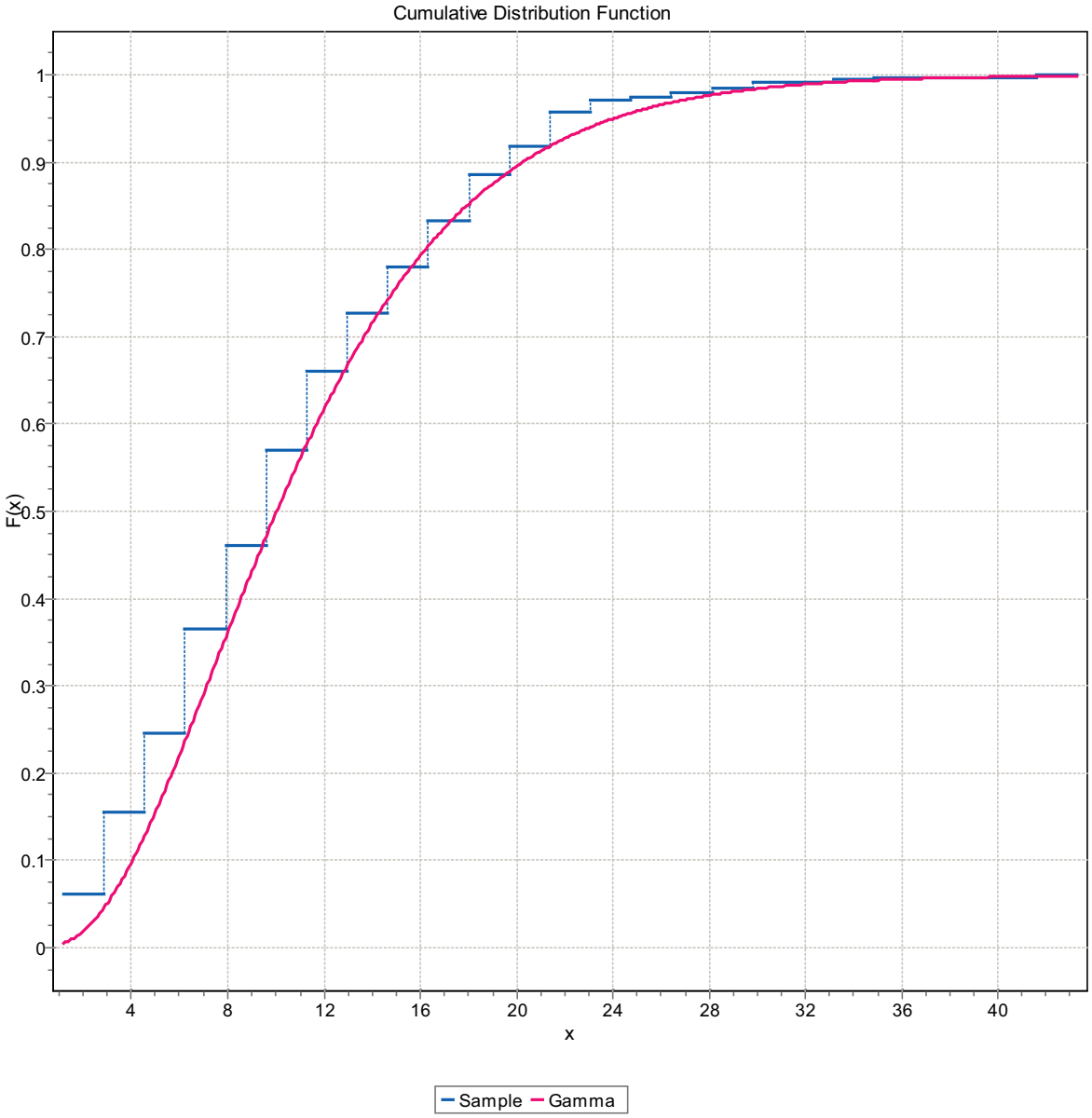

Figure F-11. *CDF, Domain FSM_NE005, 3 m bins, Gamma Distribution.*

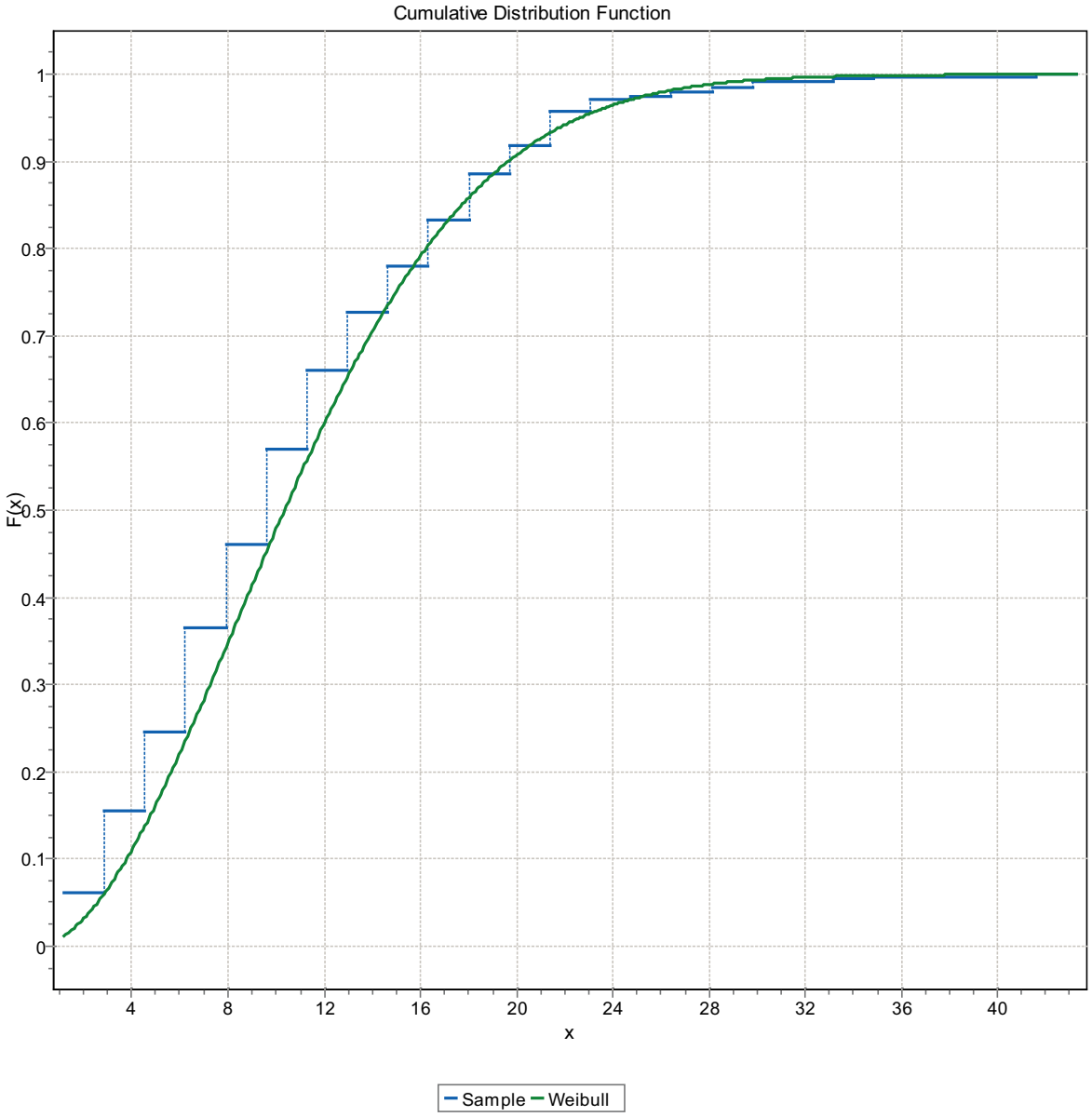

Figure F-12. *CDF, Domain FSM_NE005, 3 m bins, Weibull Distribution.*

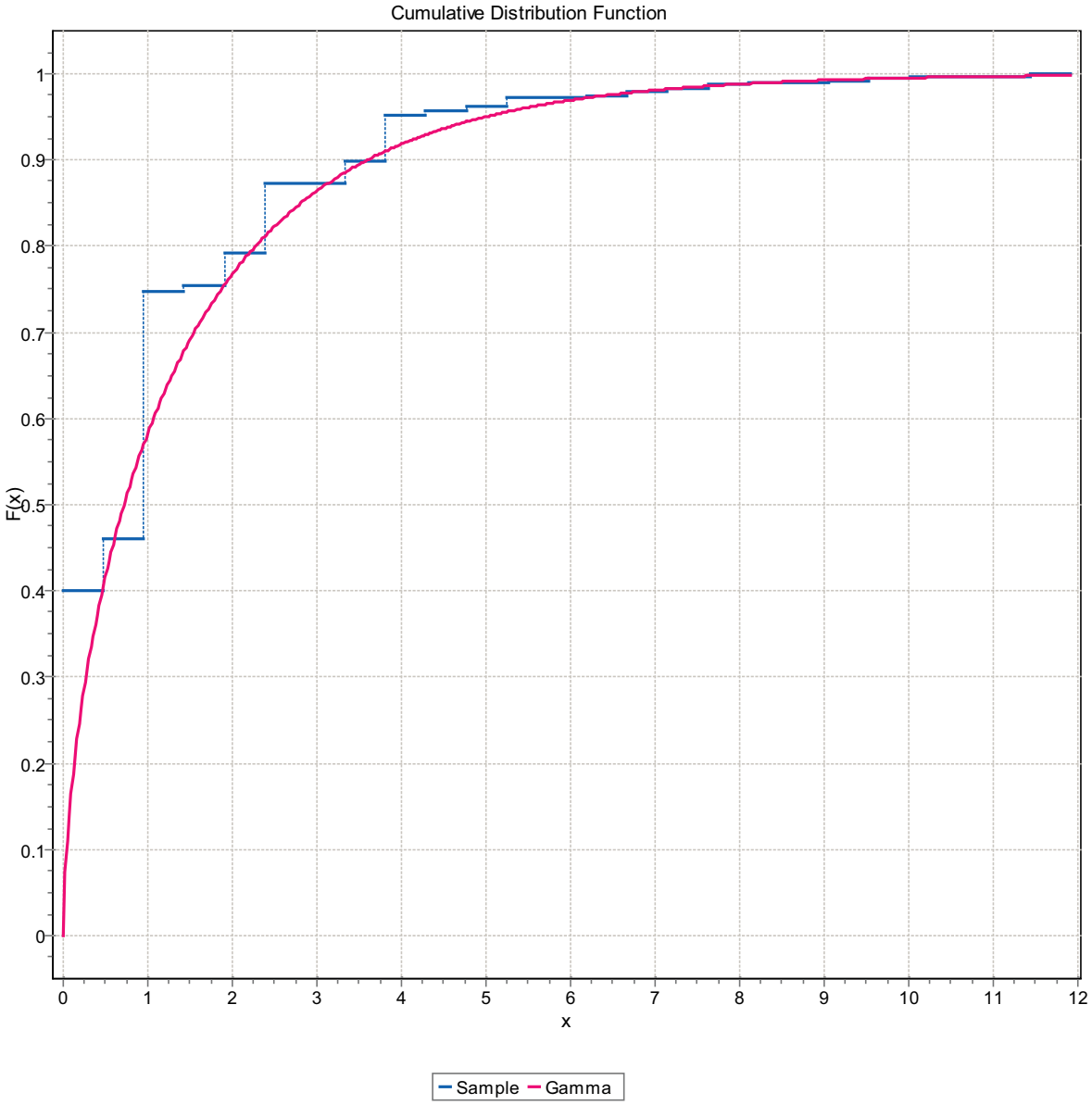

Figure F-13. *CDF, Domain FSM_NE005, 3 m bins, Gamma Distribution.*

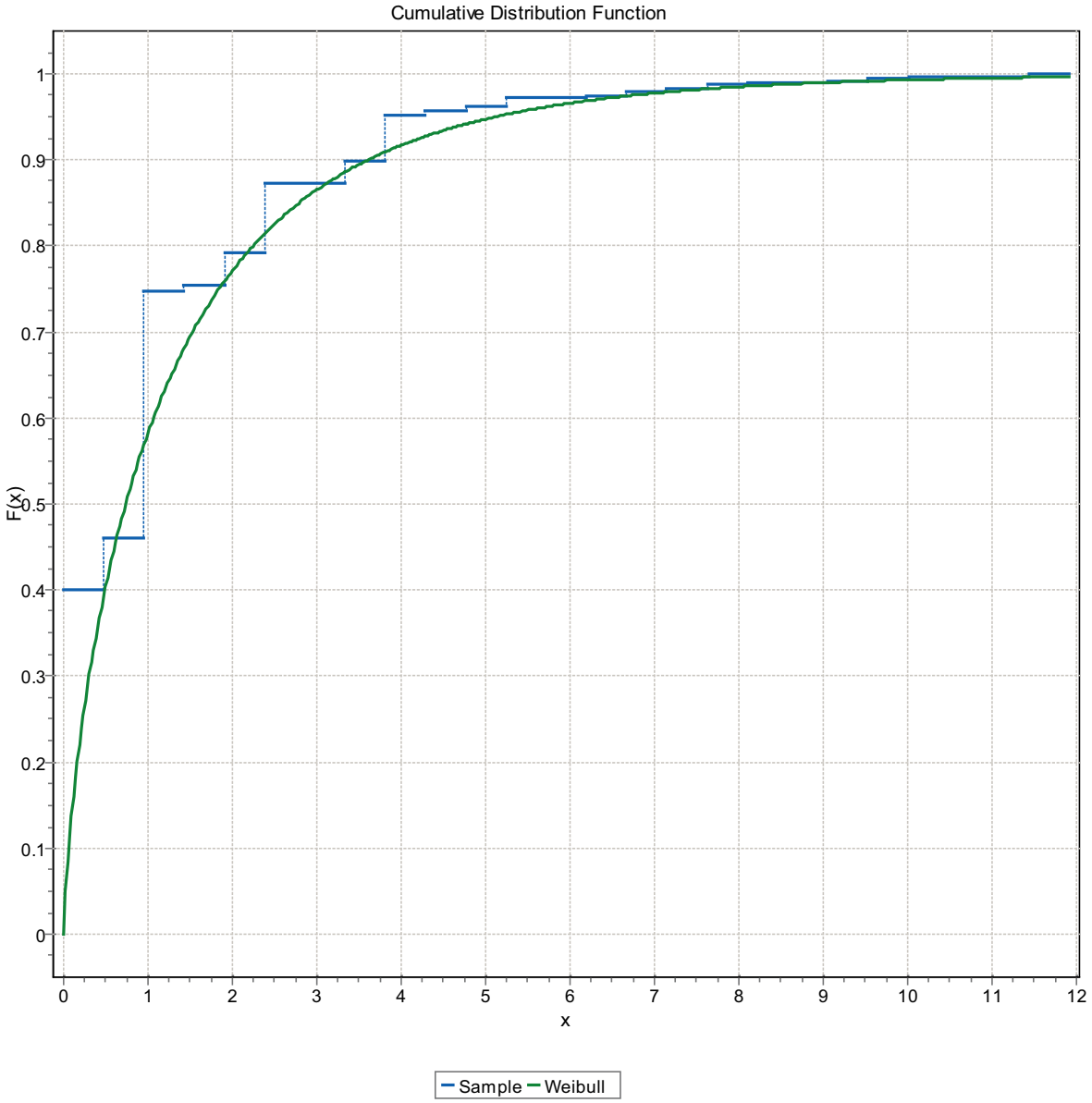

Figure F-14. *CDF, Domain FSM_NE005, 3 m bins, Weibull Distribution.*

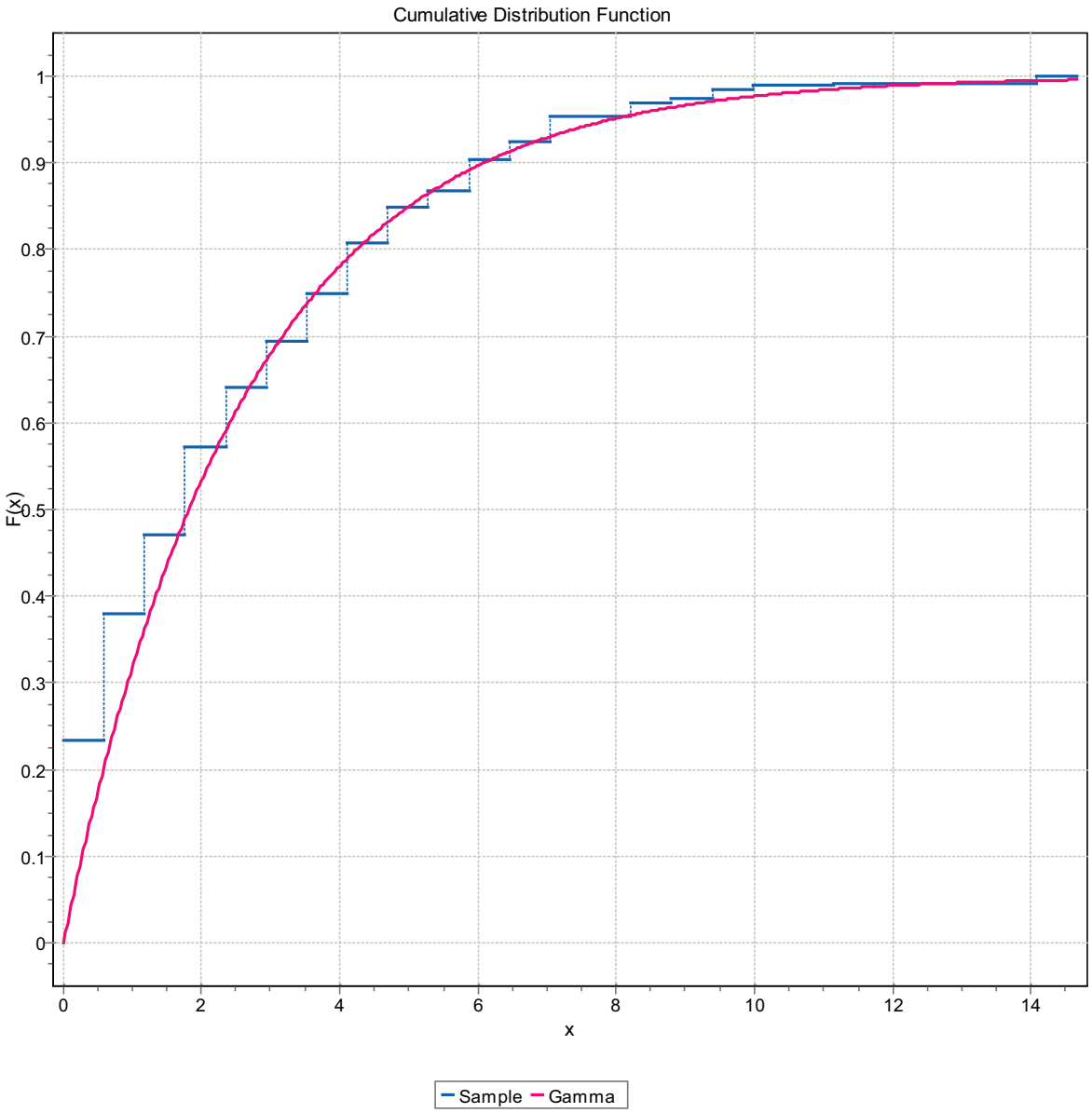

Figure F-15. *CDF, Domain FSM_NE005, 3 m bins, Gamma Distribution.*

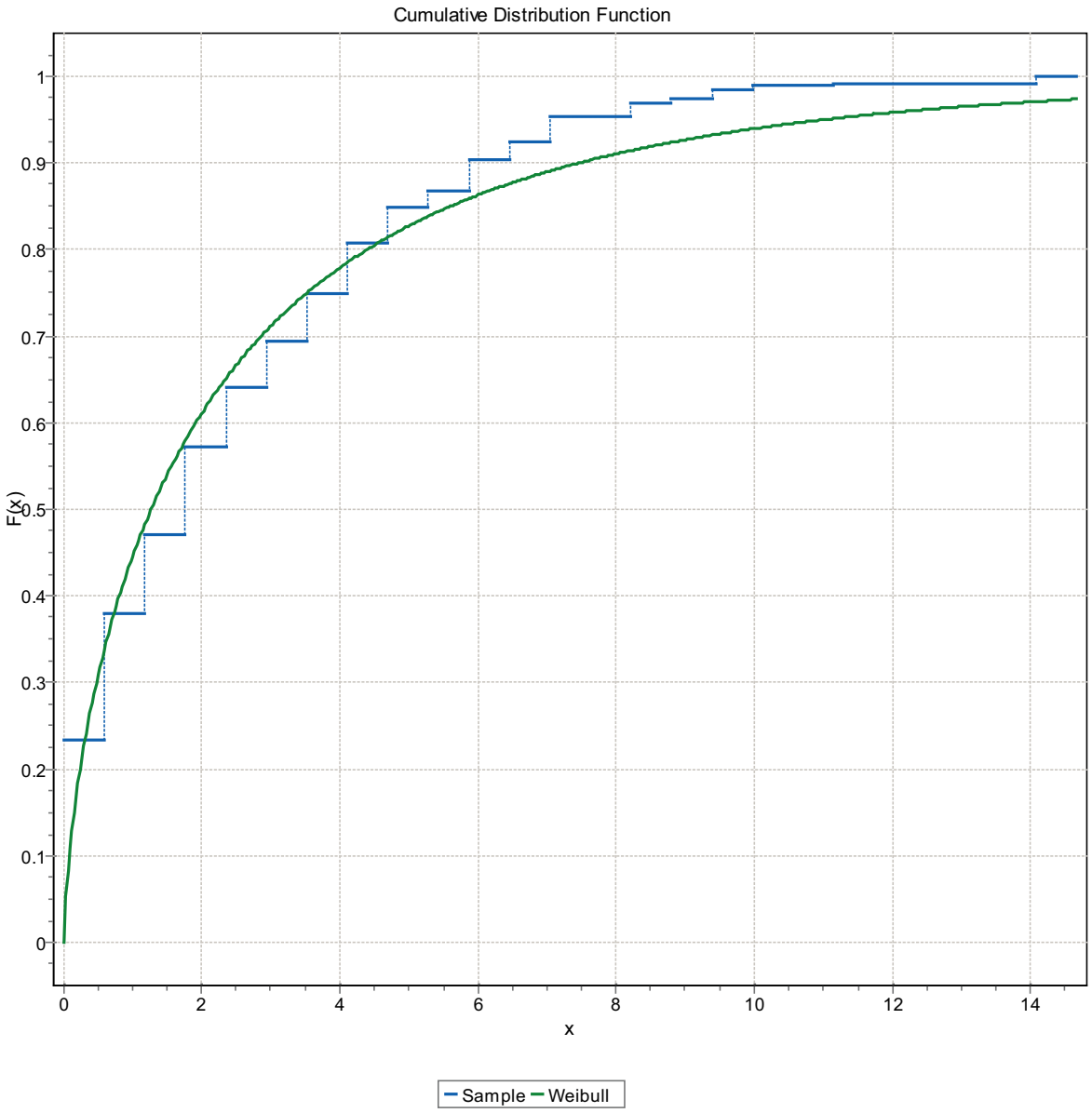

Figure F-16. *CDF, Domain FSM_NE005, 3 m bins, Weibull Distribution.*

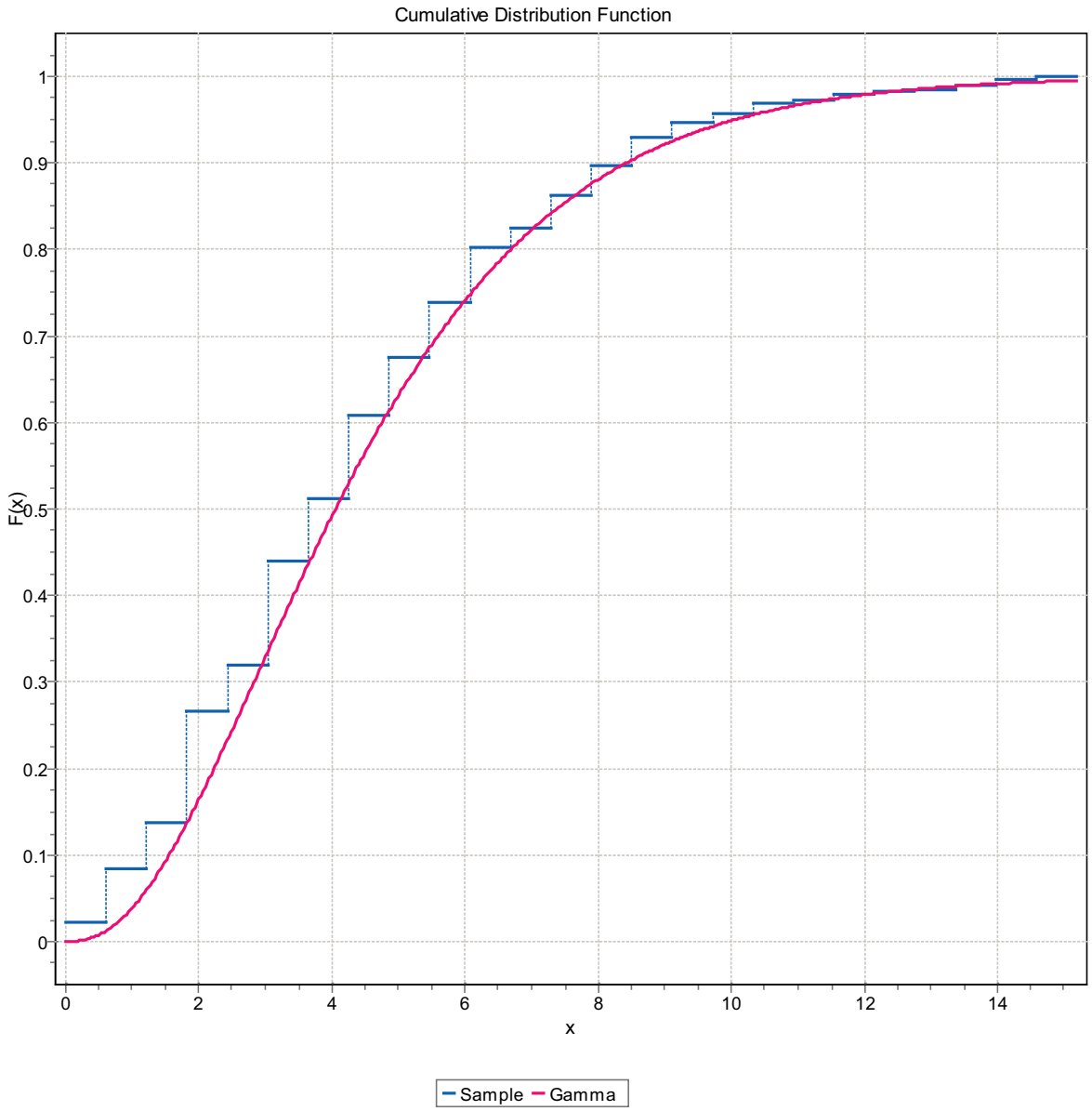

Figure F-17. *CDF, Domain FSM_NE005, 3 m bins, Gamma Distribution.*

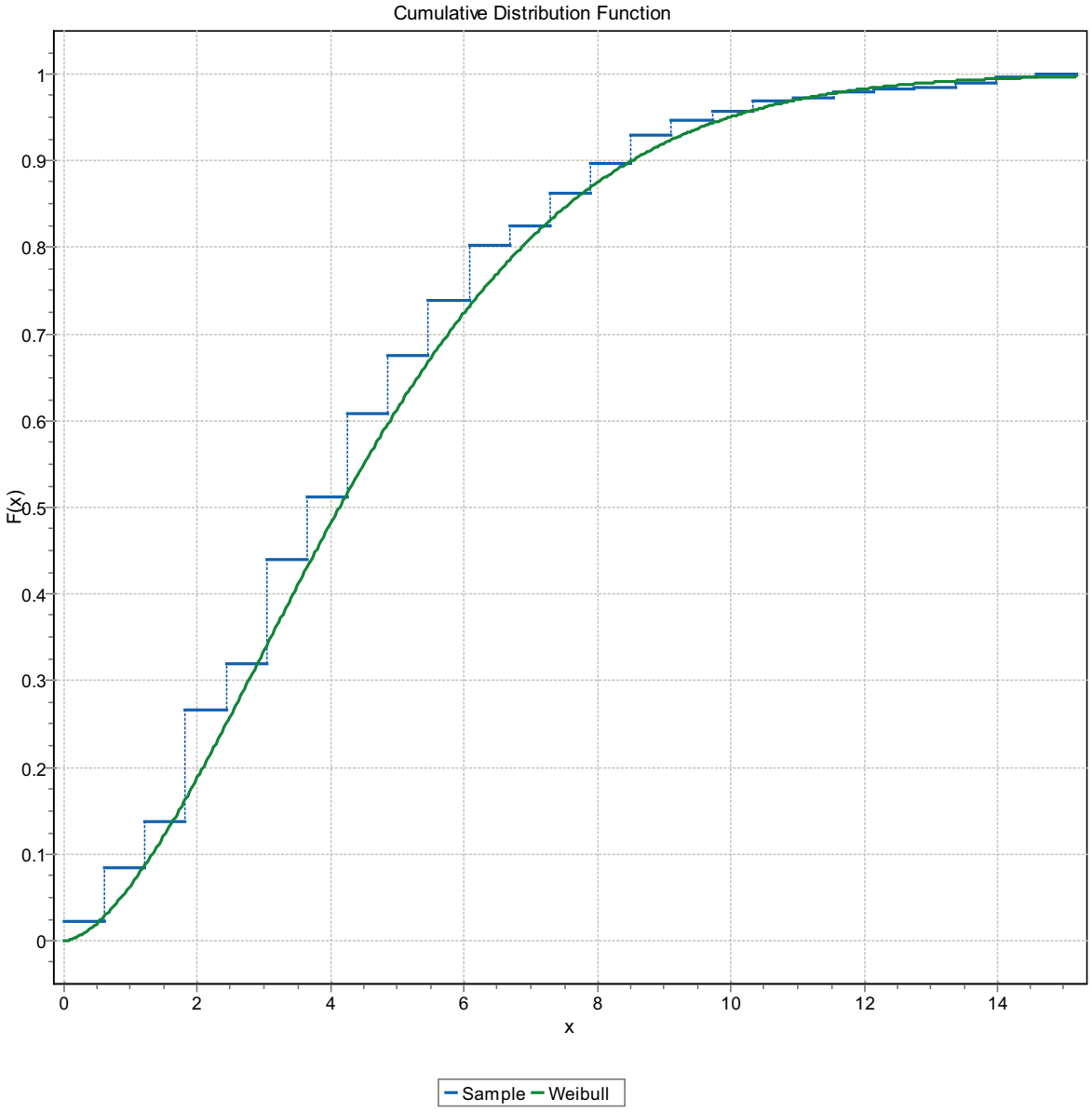

Figure F-18. *CDF, Domain FSM_NE005, 3 m bins, Weibull Distribution.*

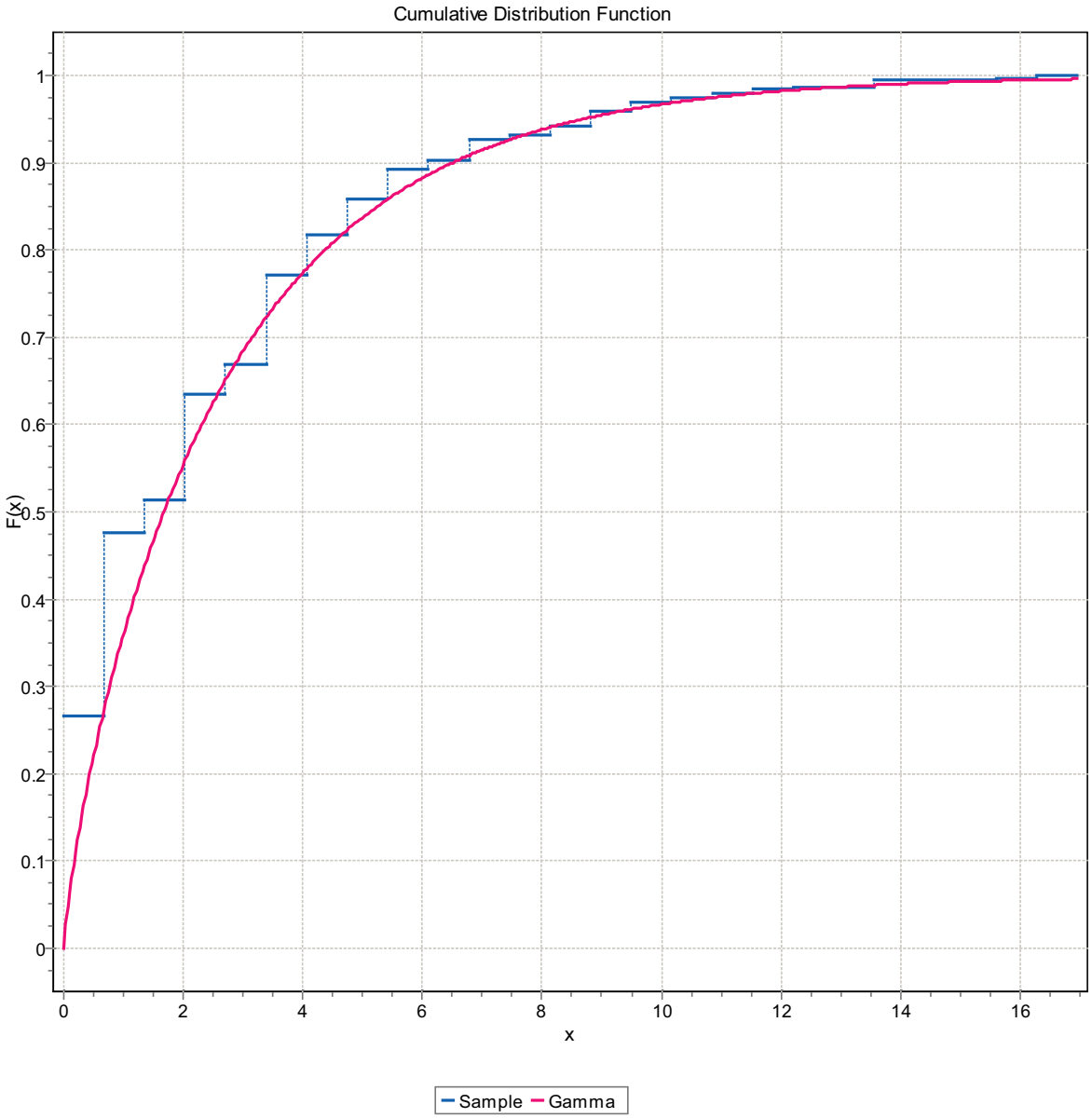

Figure F-19. *CDF, Domain FSM_NE005, 3 m bins, Gamma Distribution.*

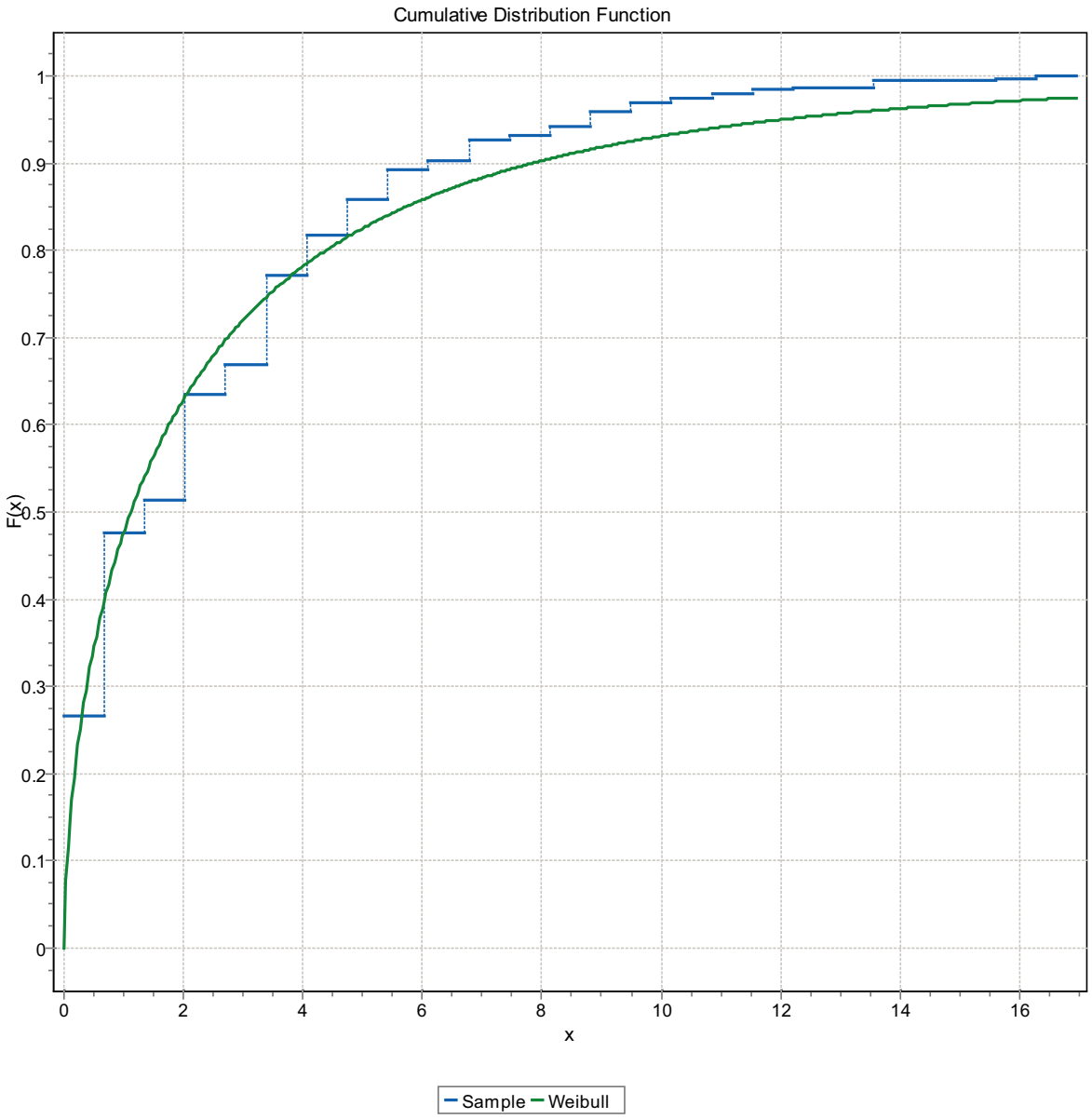

Figure F-20. *CDF, Domain FSM_NE005, 3 m bins, Weibull Distribution.*

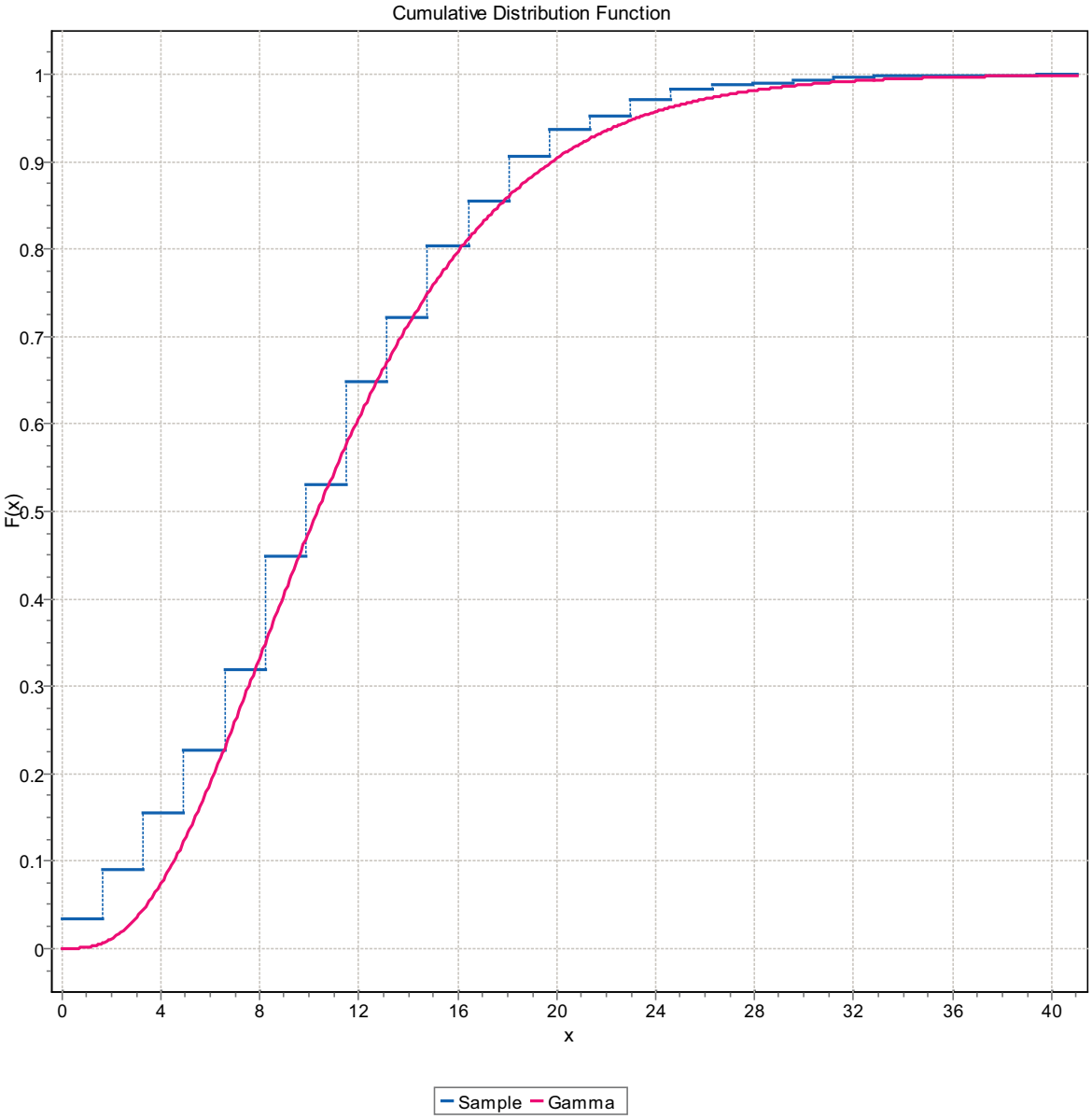

Figure F-21. *CDF, Domain FSM_N, 3 m bins, Gamma Distribution.*

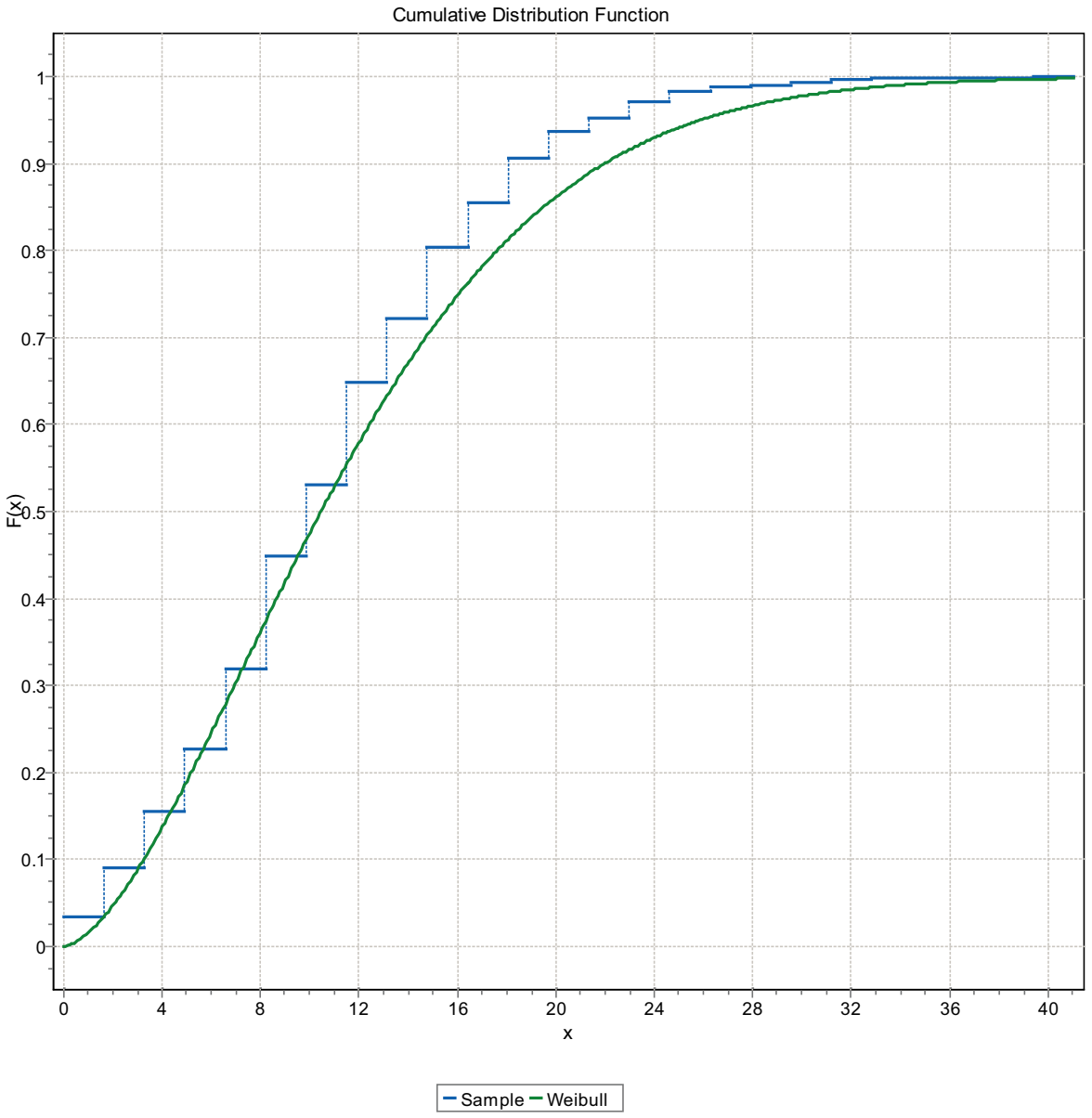

Figure F-22. *CDF, Domain FSM_N, 3 m bins, Weibull Distribution.*

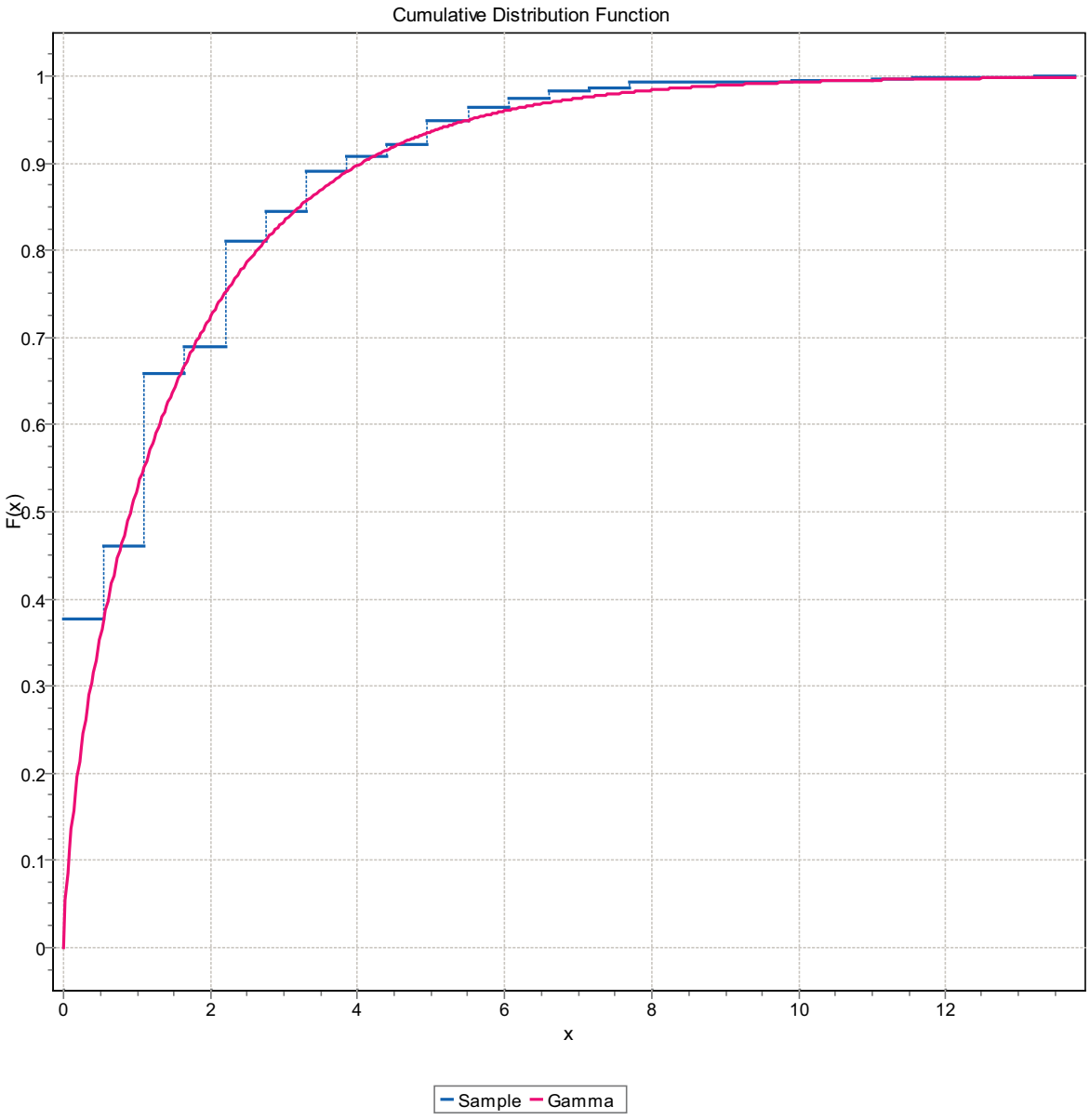

Figure F-23. *CDF, Domain FSM_N, 3 m bins, Gamma Distribution.*

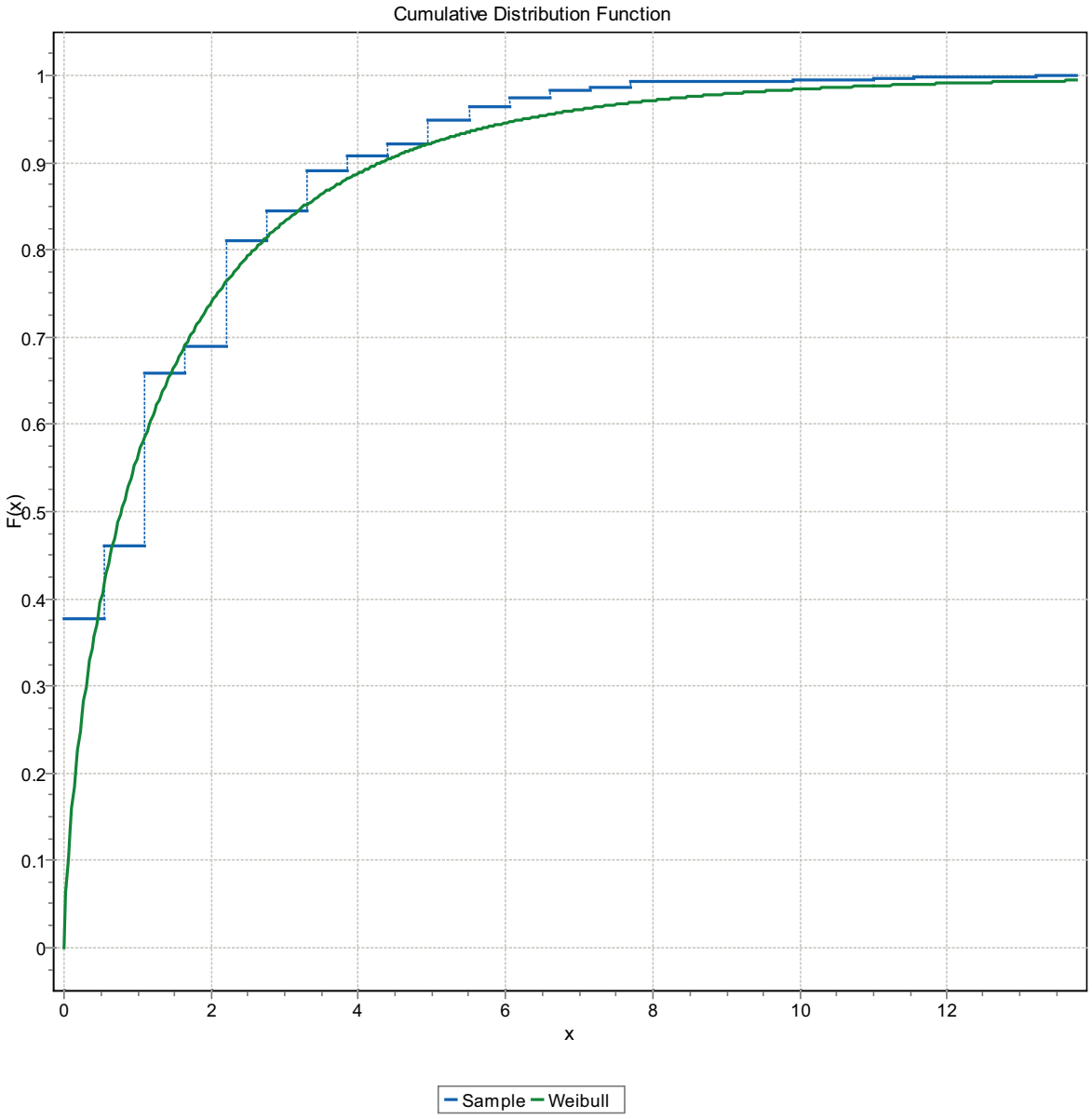

Figure F-24. *CDF, Domain FSM_N, 3 m bins, Weibull Distribution.*

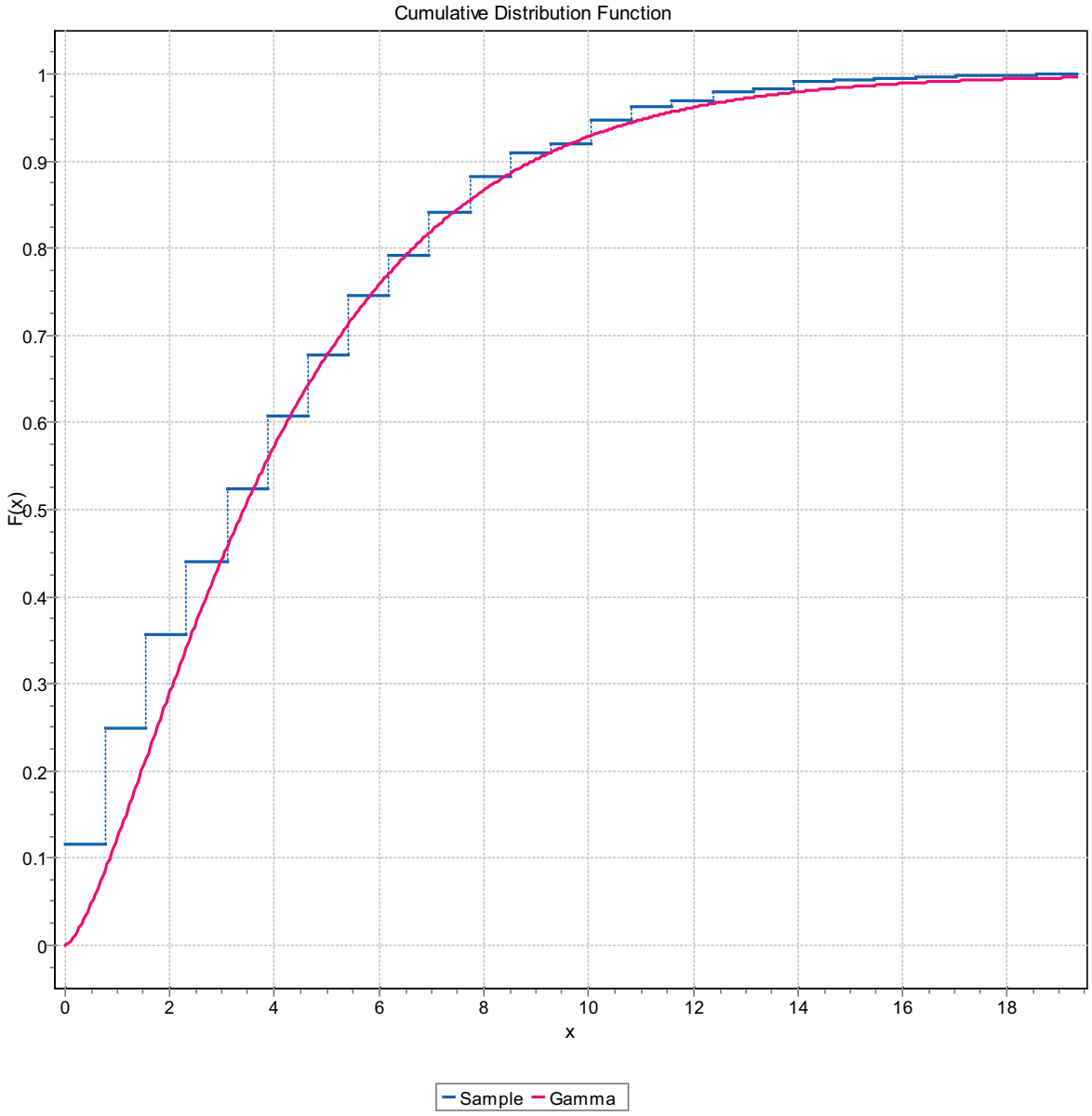

Figure F-25. *CDF, Domain FSM_N, 3 m bins, Gamma Distribution.*

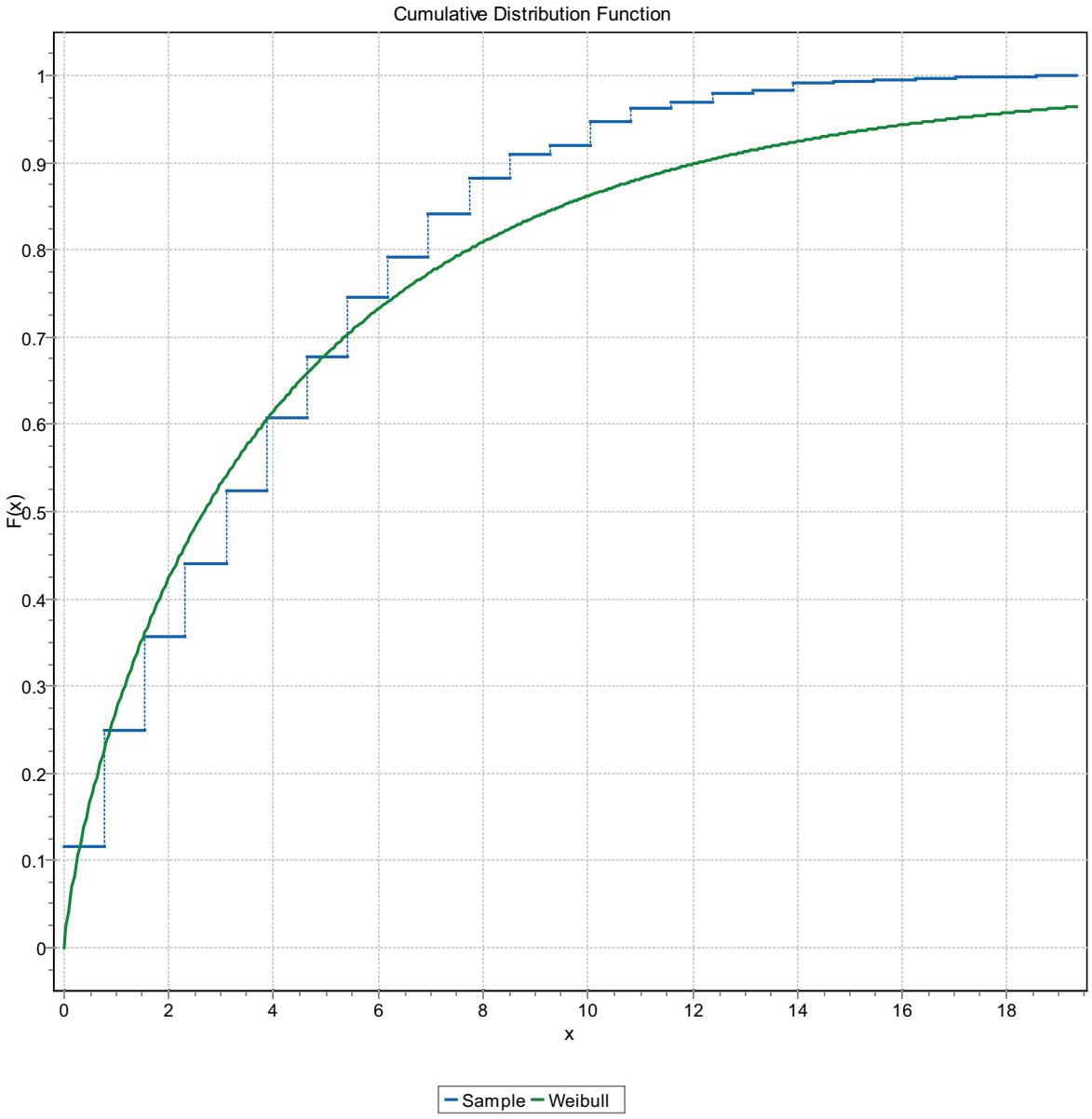

Figure F-26. *CDF, Domain FSM_N, 3 m bins, Weibull Distribution.*

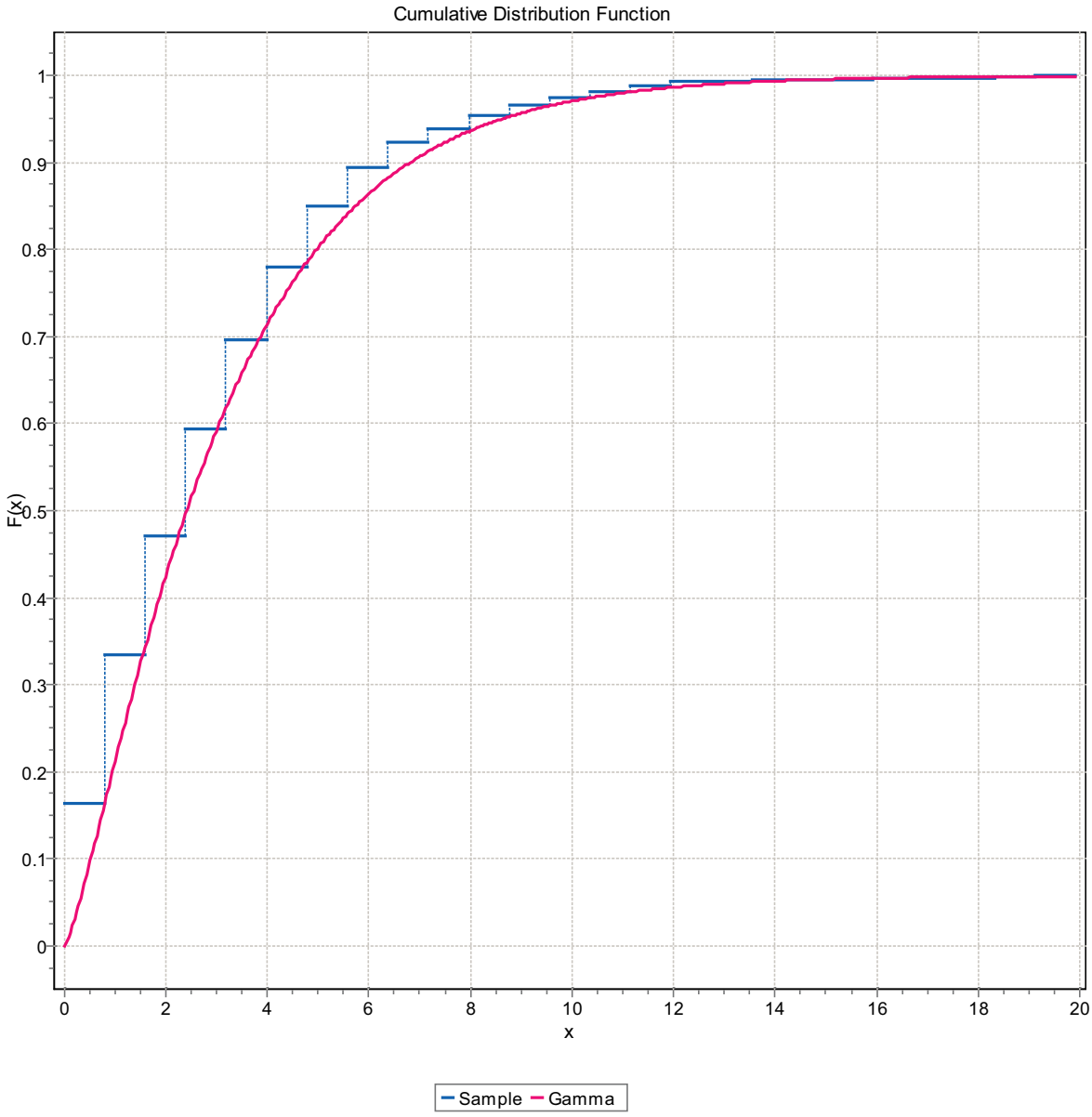

Figure F-27. *CDF, Domain FSM_N, 3 m bins, Gamma Distribution.*

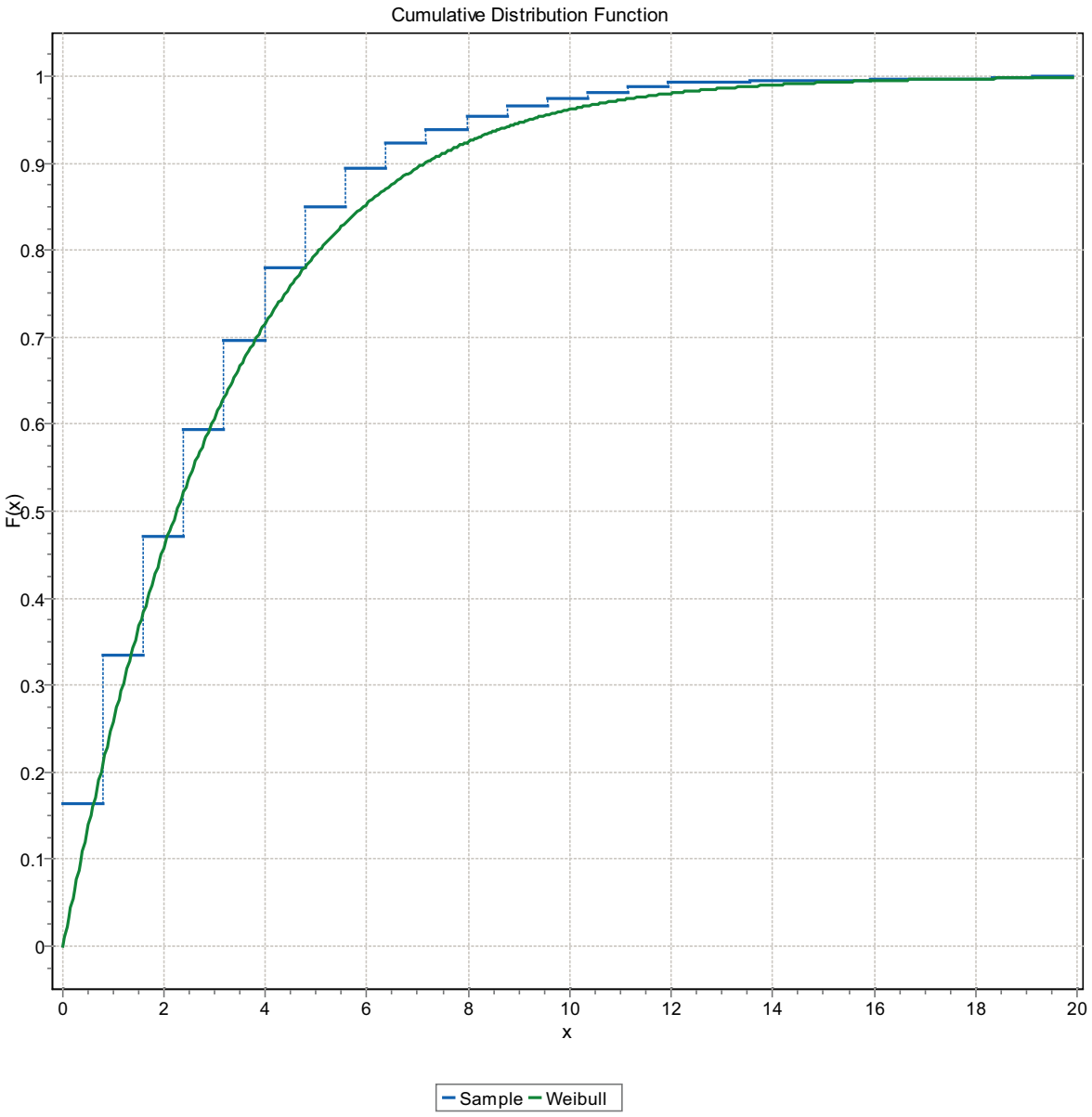

Figure F-28. *CDF, Domain FSM_N, 3 m bins, Weibull Distribution.*

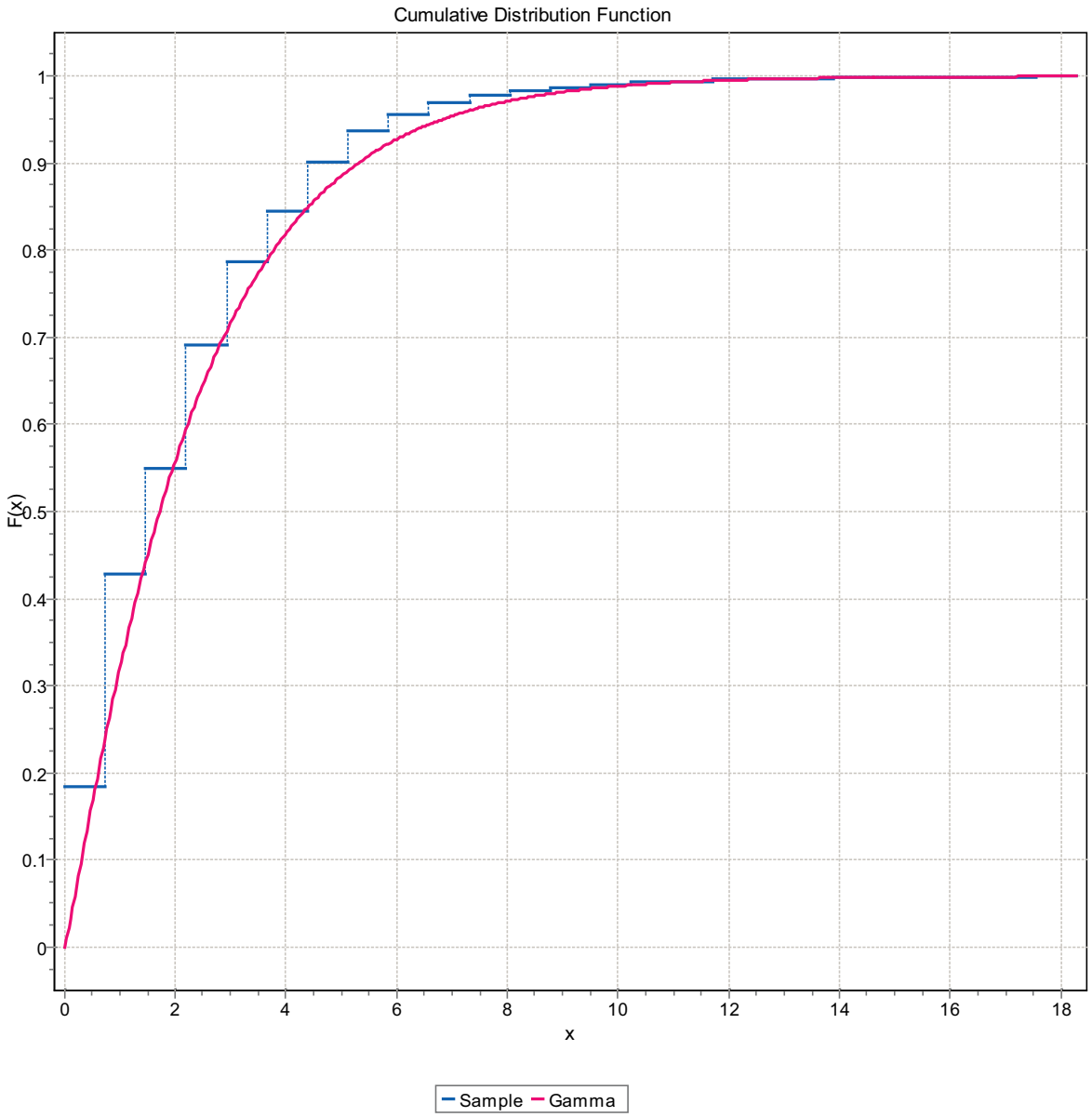

Figure F-29. *CDF, Domain FSM_N, 3 m bins, Gamma Distribution.*

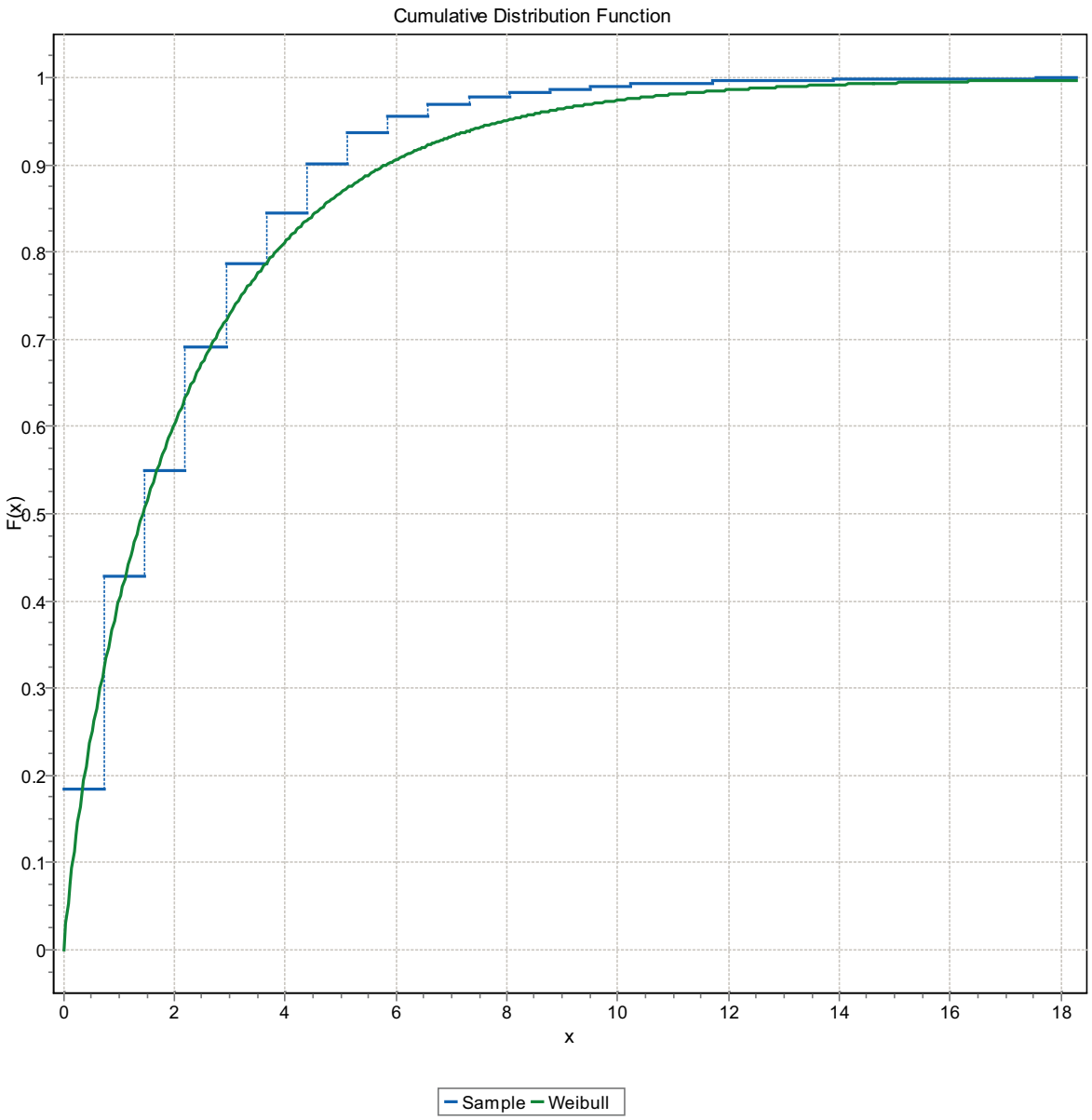

Figure F-30. *CDF, Domain FSM_N, 3 m bins, Weibull Distribution.*

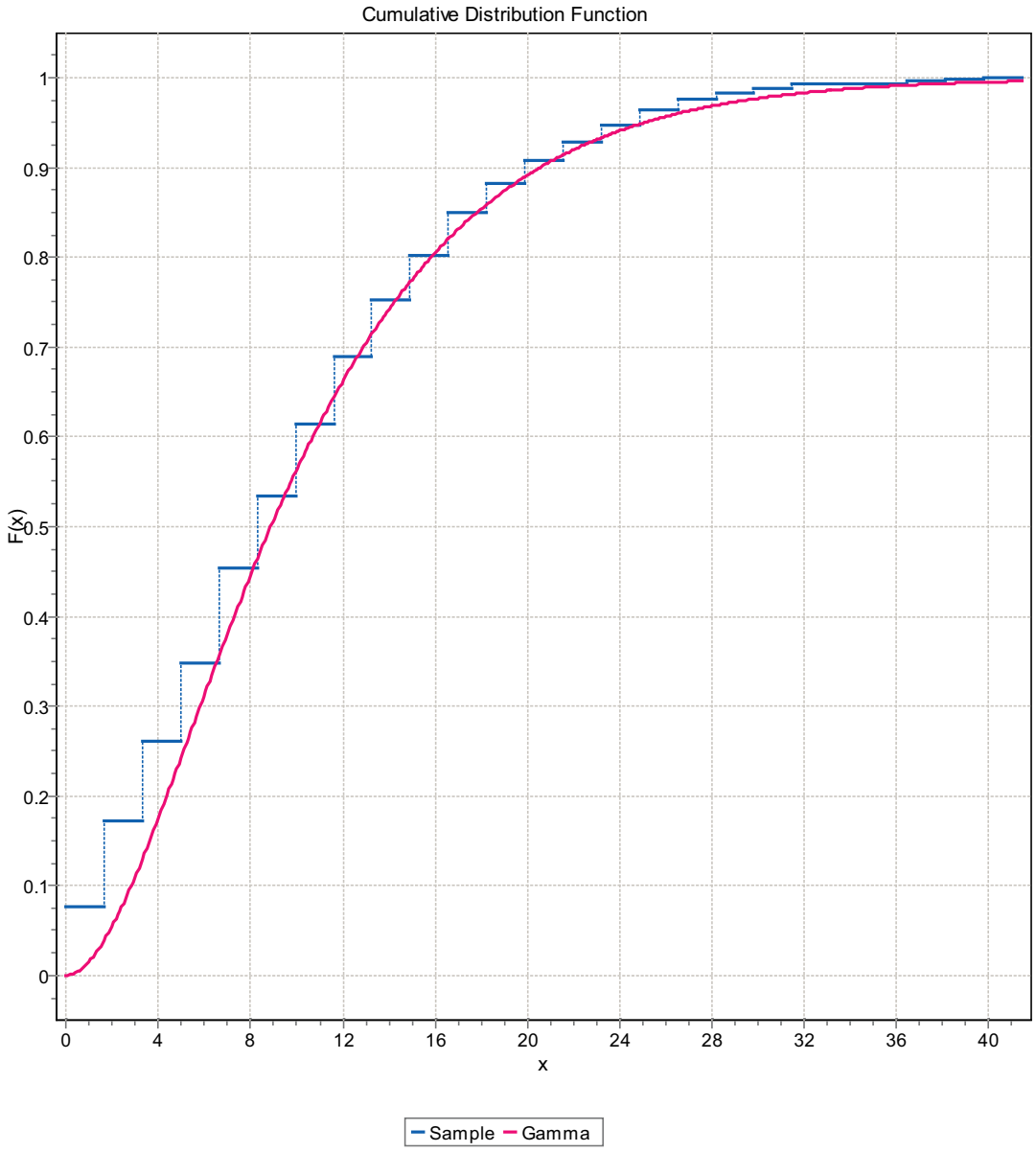

Figure F-31. *CDF, Domain FSM_W, 3 m bins, Gamma Distribution.*

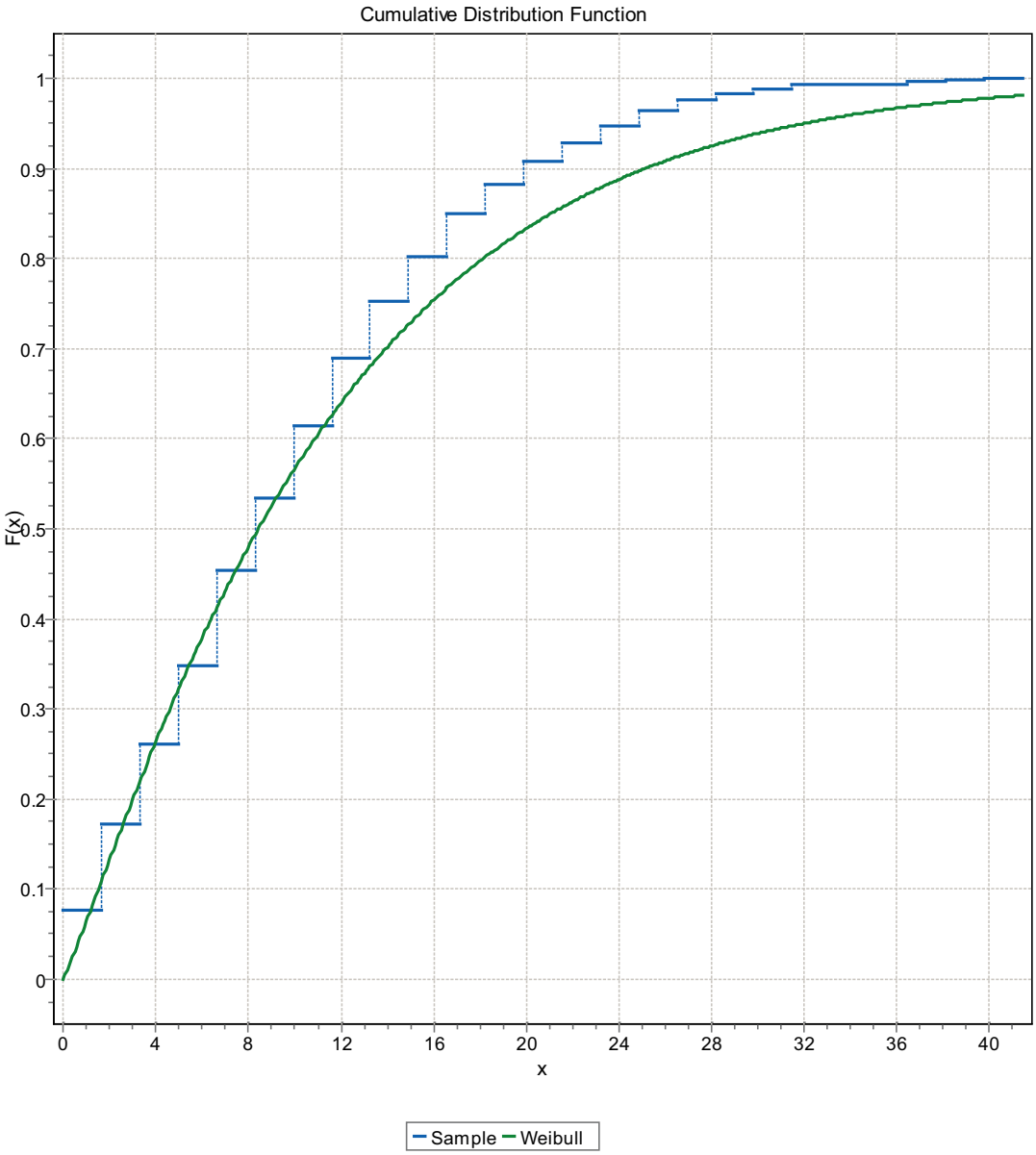

Figure F-32. *CDF, Domain FSM_W, 3 m bins, Weibull Distribution.*

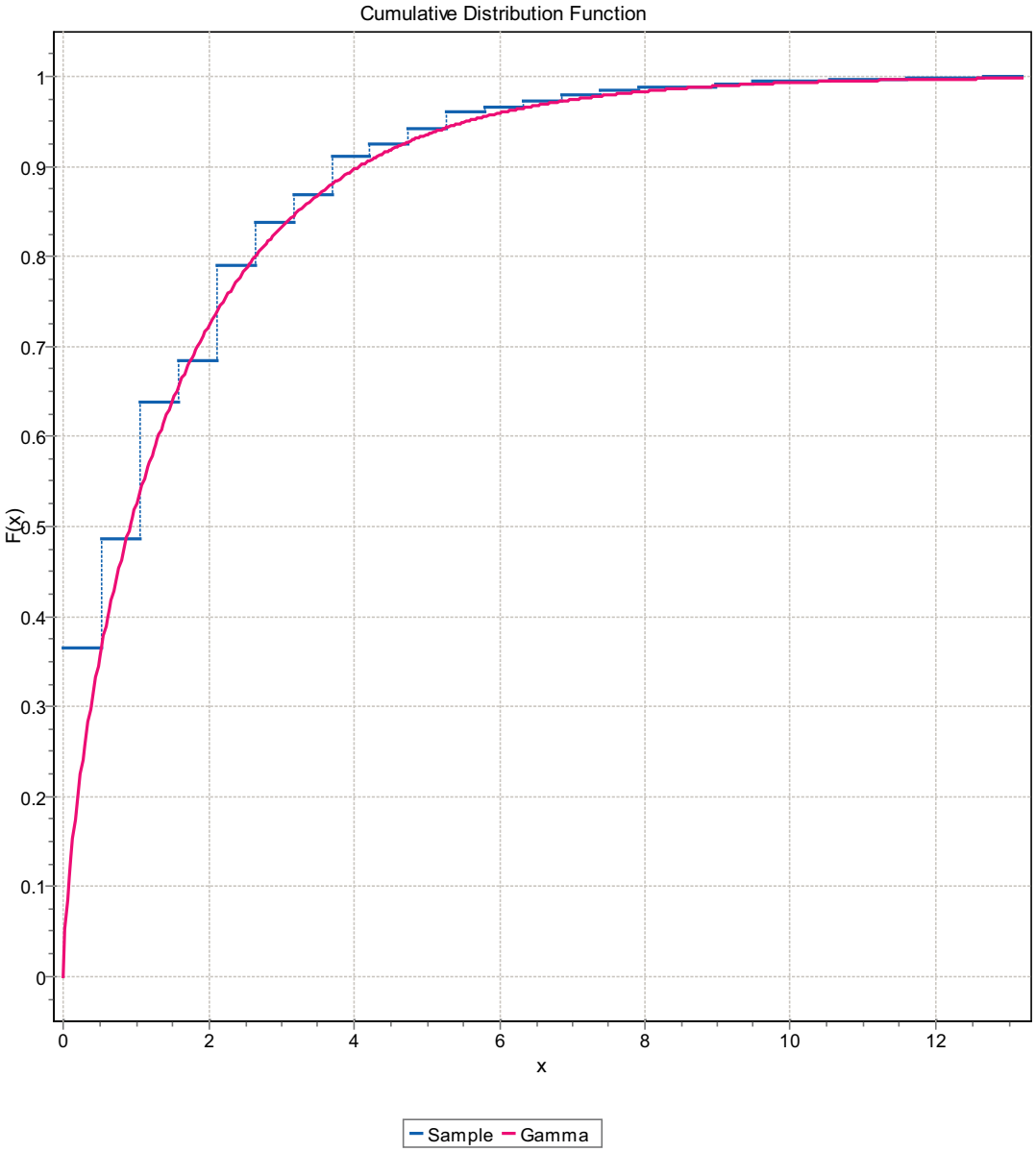

Figure F-33. *CDF, Domain FSM_W, 3 m bins, Gamma Distribution.*

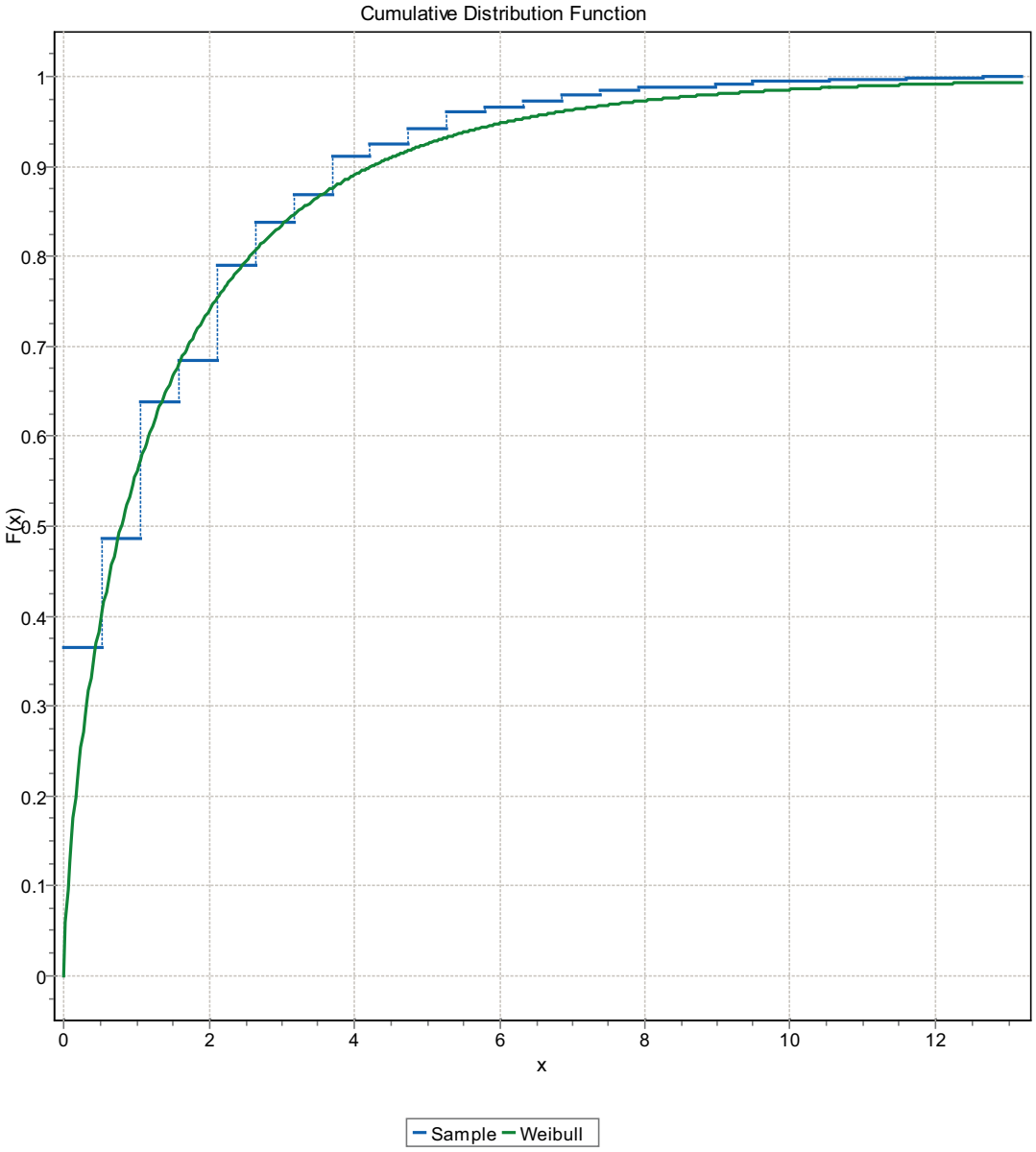

Figure F-34. *CDF, Domain FSM_W, 3 m bins, Weibull Distribution.*

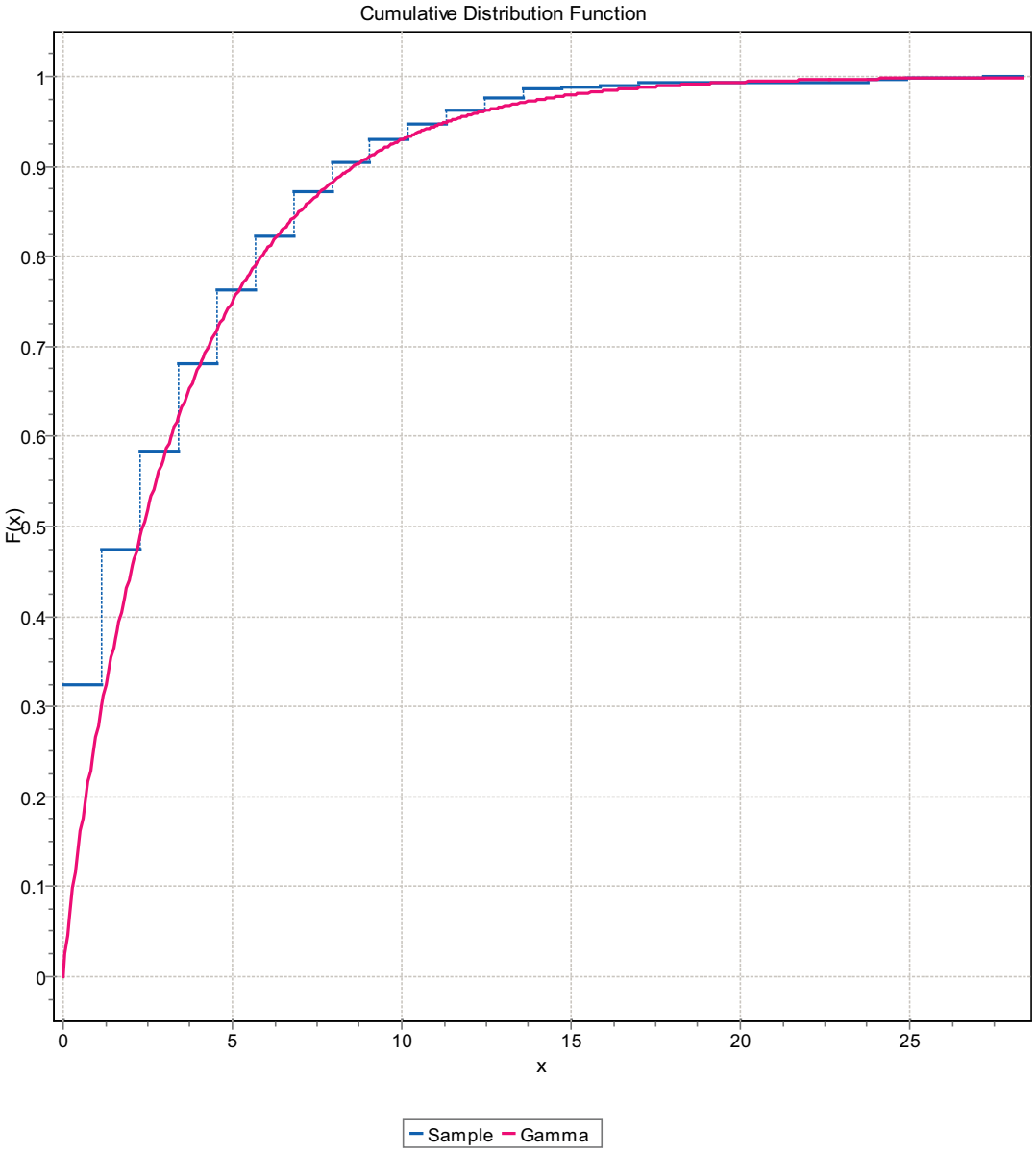

Figure F-35. *CDF, Domain FSM_W, 3 m bins, Gamma Distribution.*

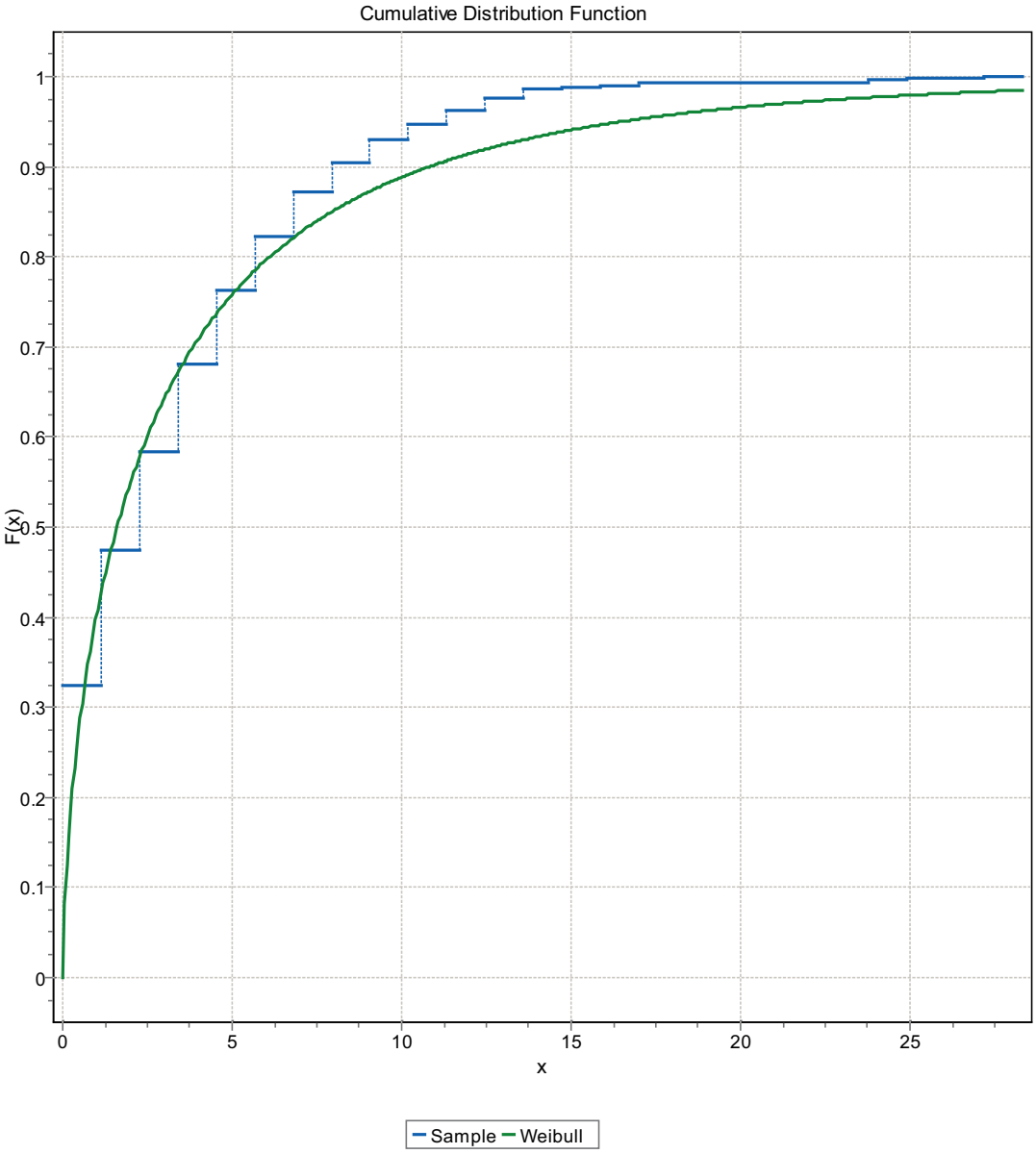

Figure F-36. *CDF, Domain FSM_W, 3 m bins, Weibull Distribution.*

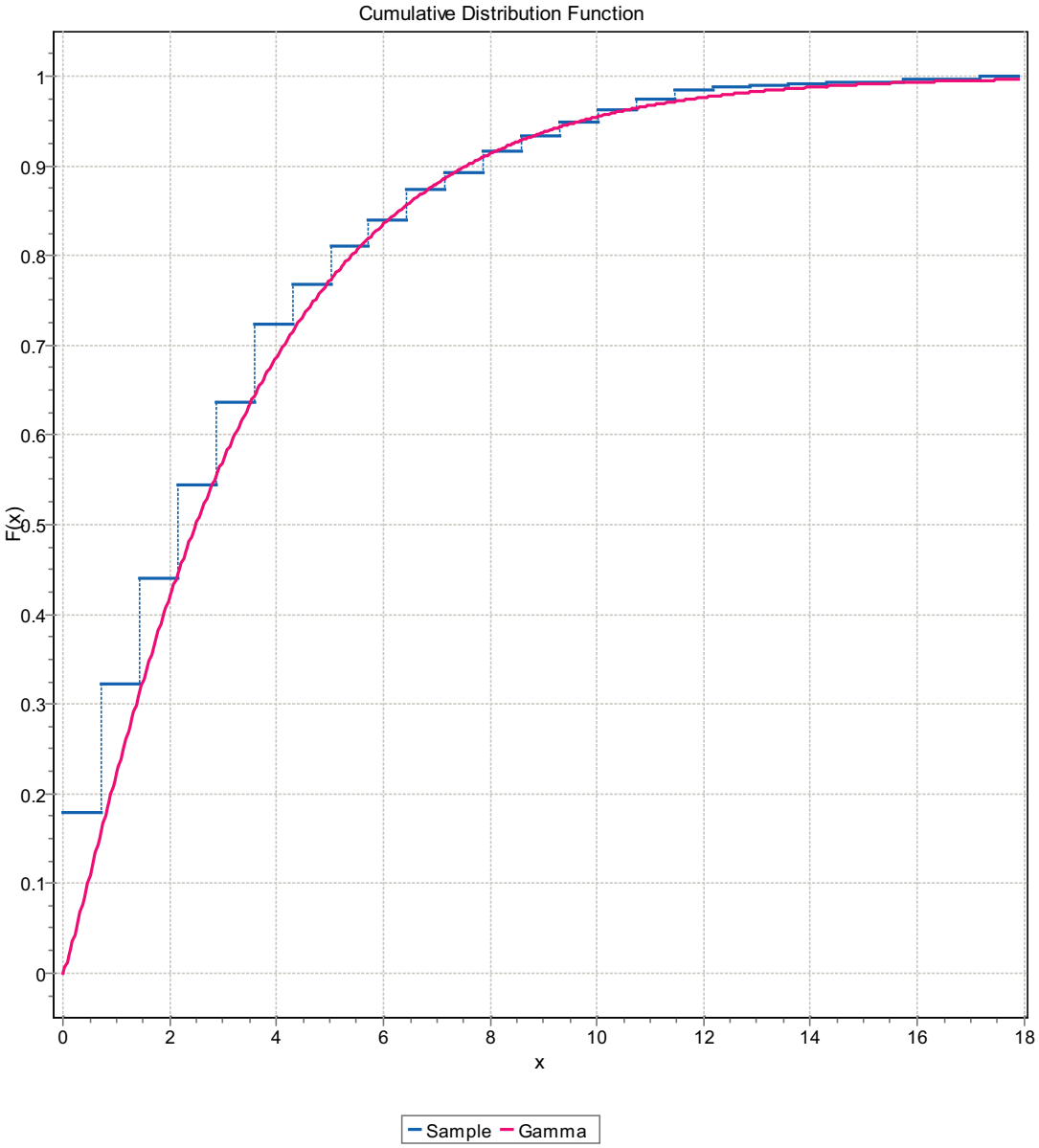

Figure F-37. *CDF, Domain FSM_W, 3 m bins, Gamma Distribution.*

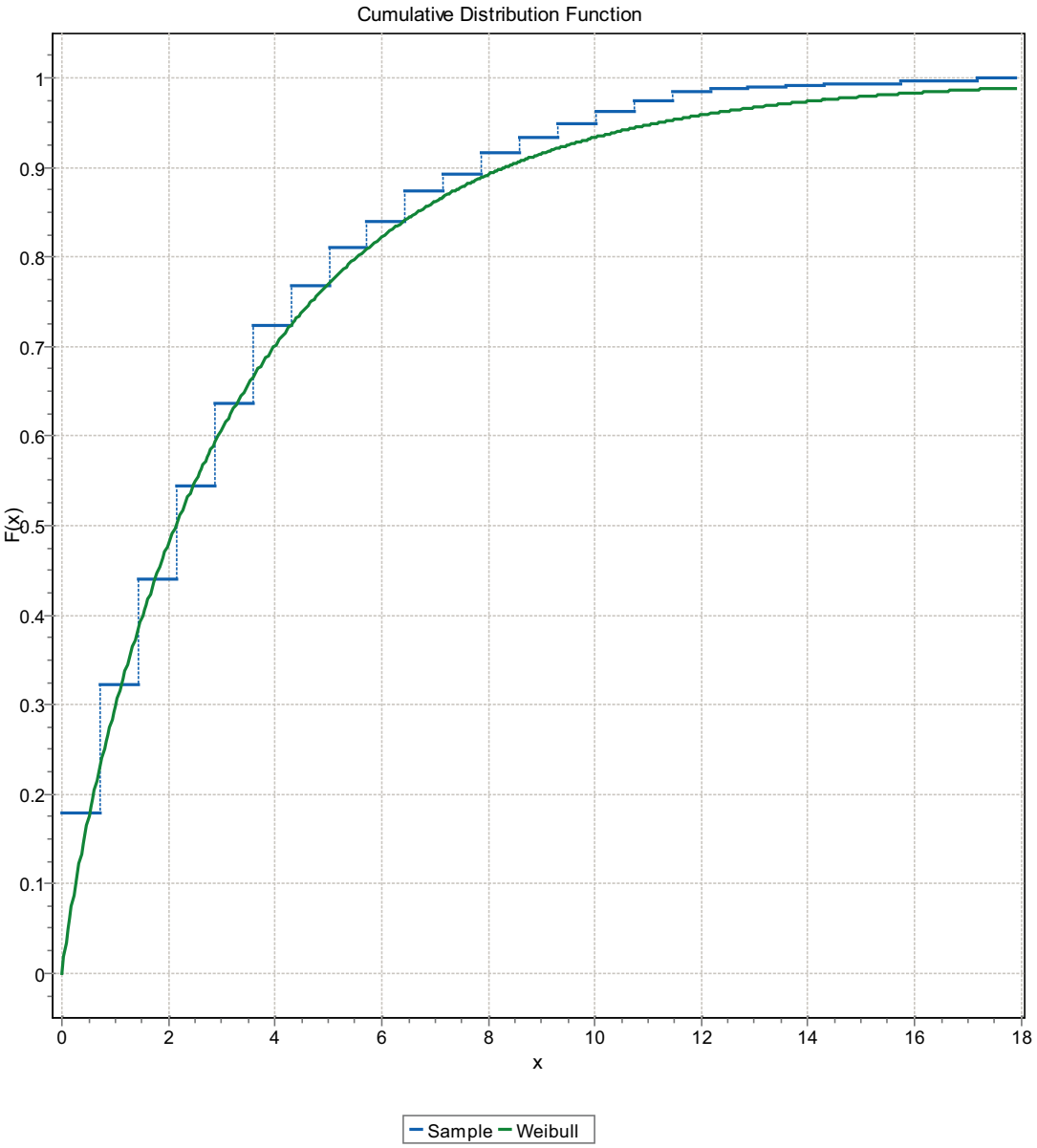

Figure F-38. *CDF, Domain FSM_W, 3 m bins, Weibull Distribution.*

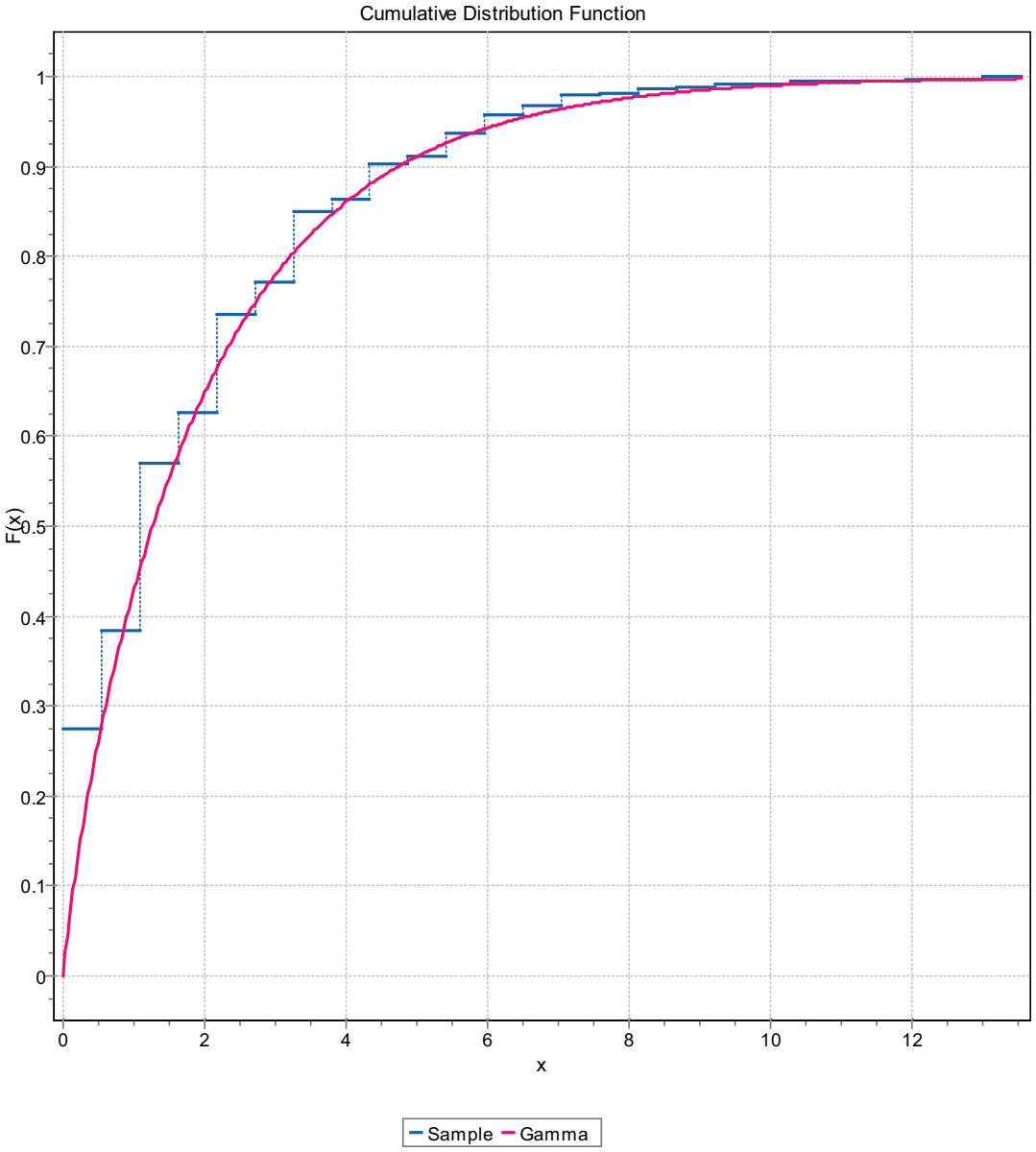

Figure F-39. *CDF, Domain FSM_W, 3 m bins, Gamma Distribution.*

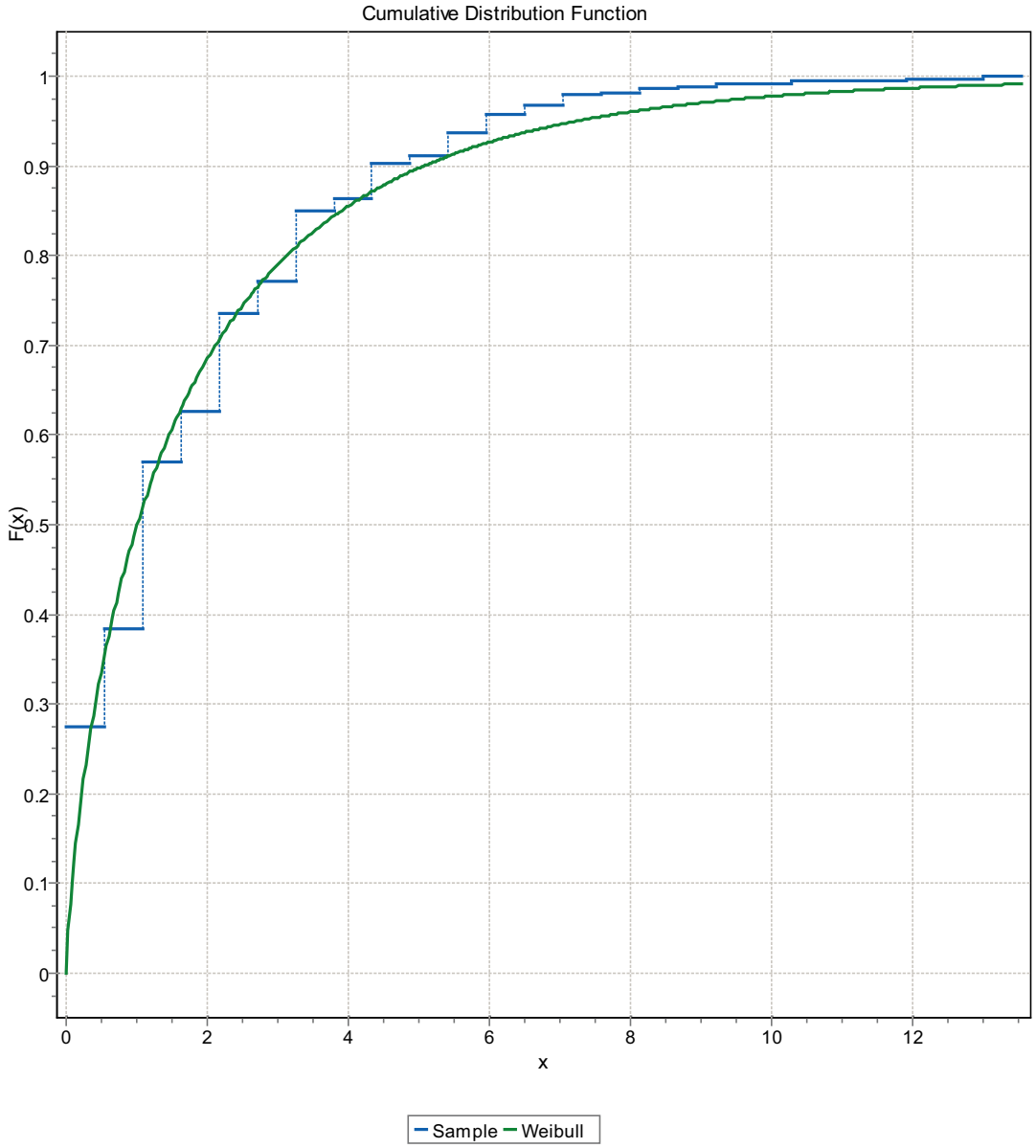

Figure F-40. *CDF, Domain FSM_W, 3 m bins, Weibull Distribution.*

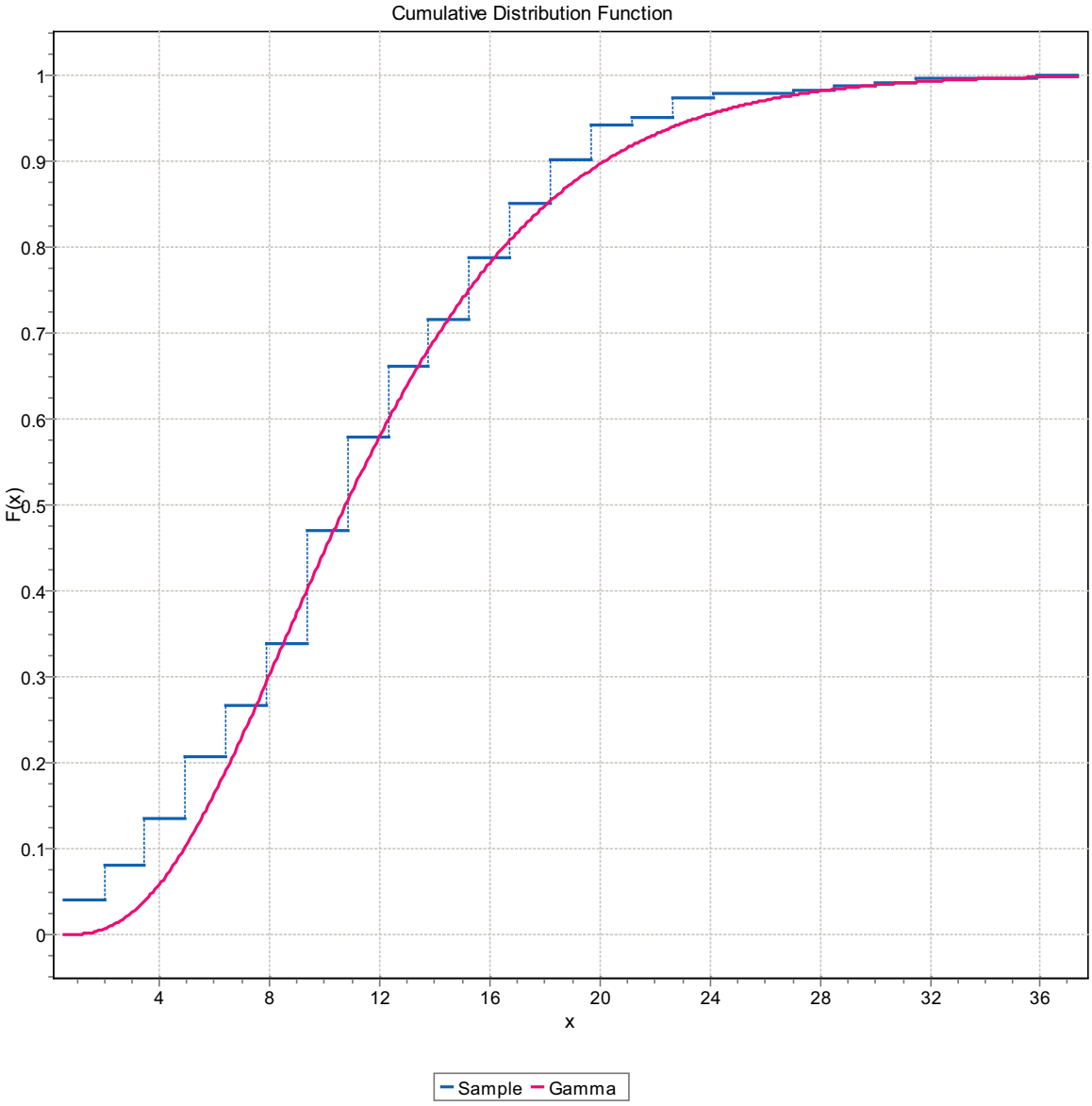

Figure F-41. *CDF, Domain FSM_EW007, 9 m bins, Gamma Distribution.*

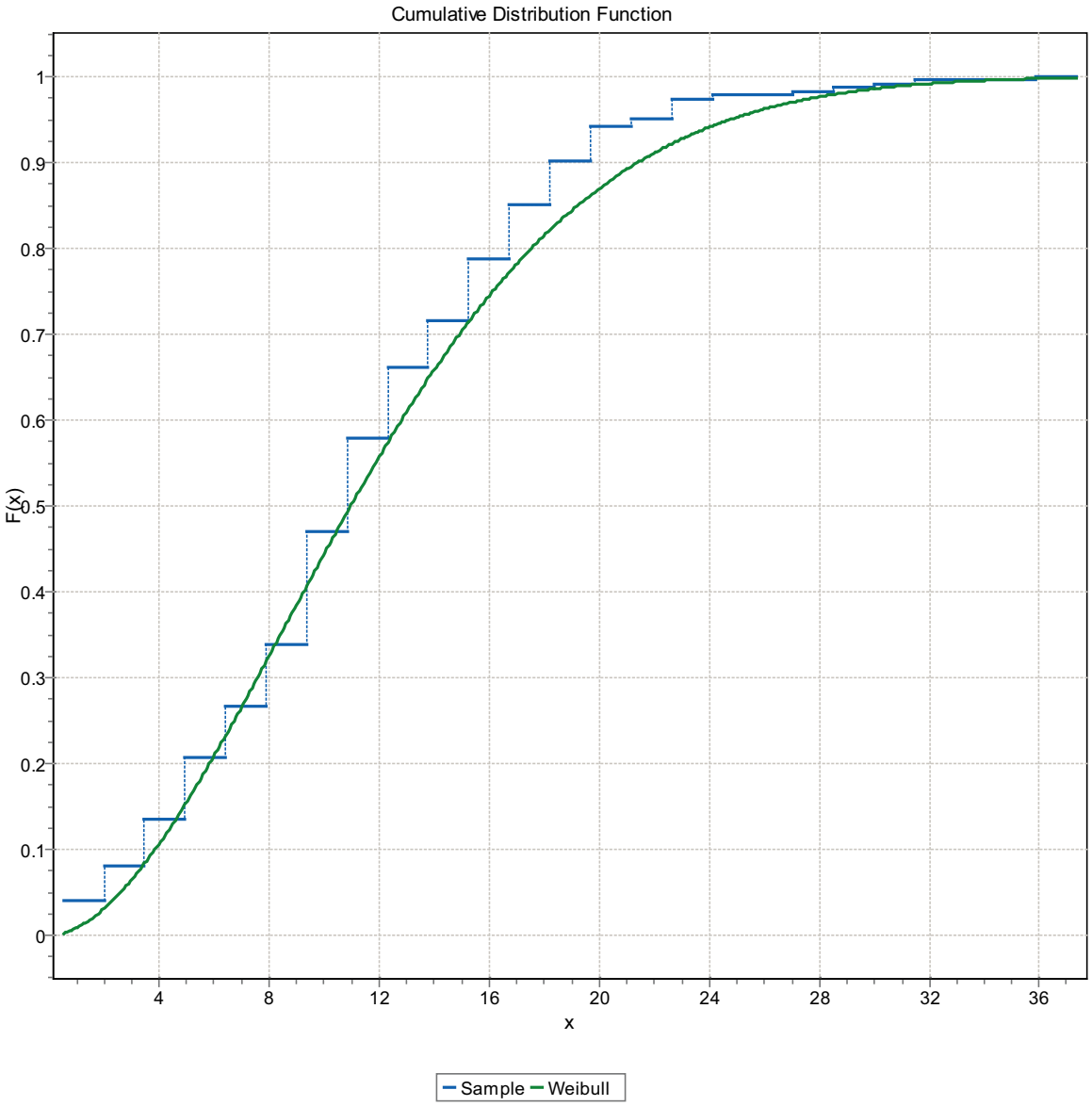

Figure F-42. *CDF, Domain FSM_EW007, 9 m bins, Weibull Distribution.*

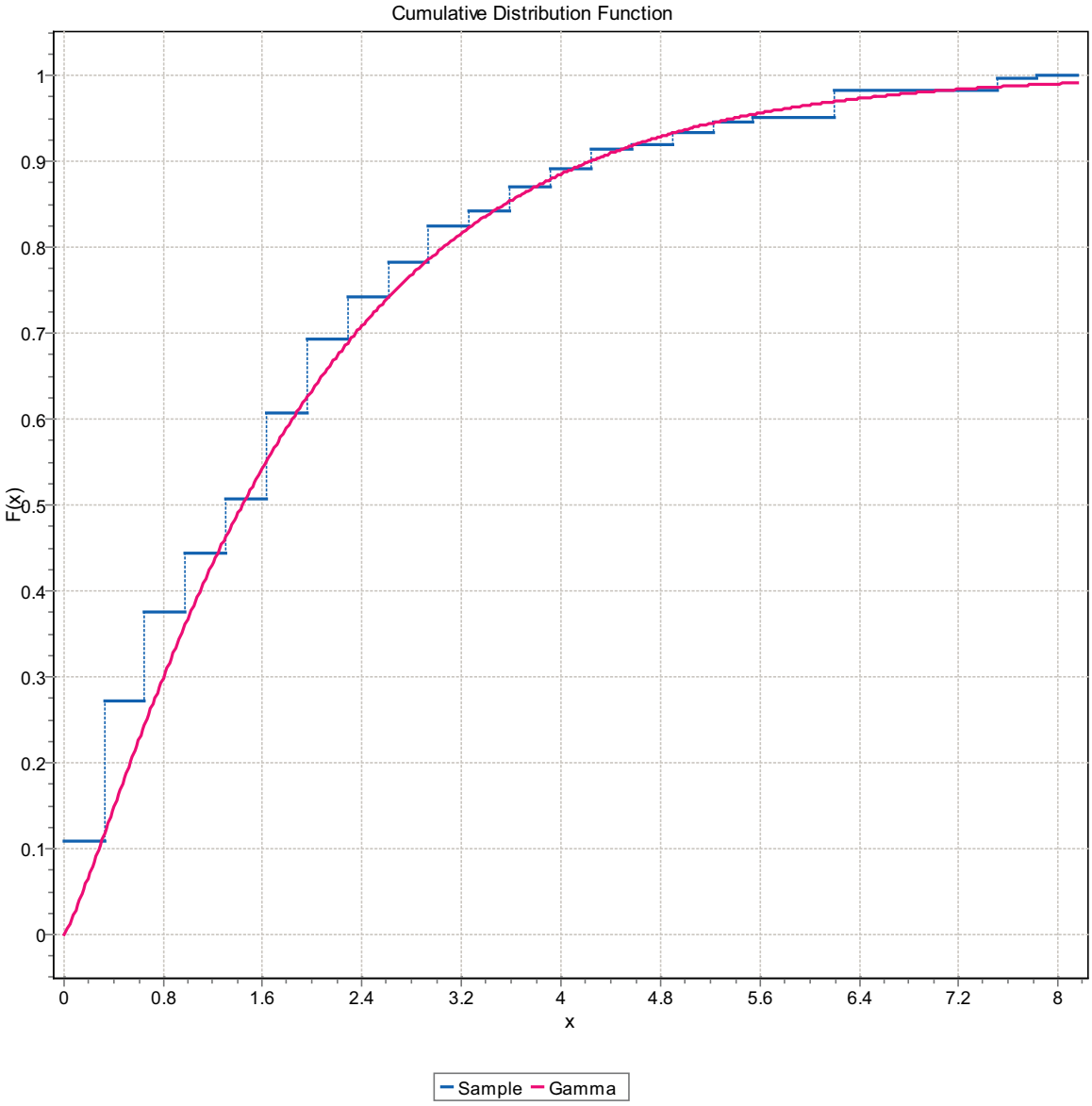

Figure F-43. *CDF, Domain FSM_EW007, 9 m bins, Gamma Distribution.*

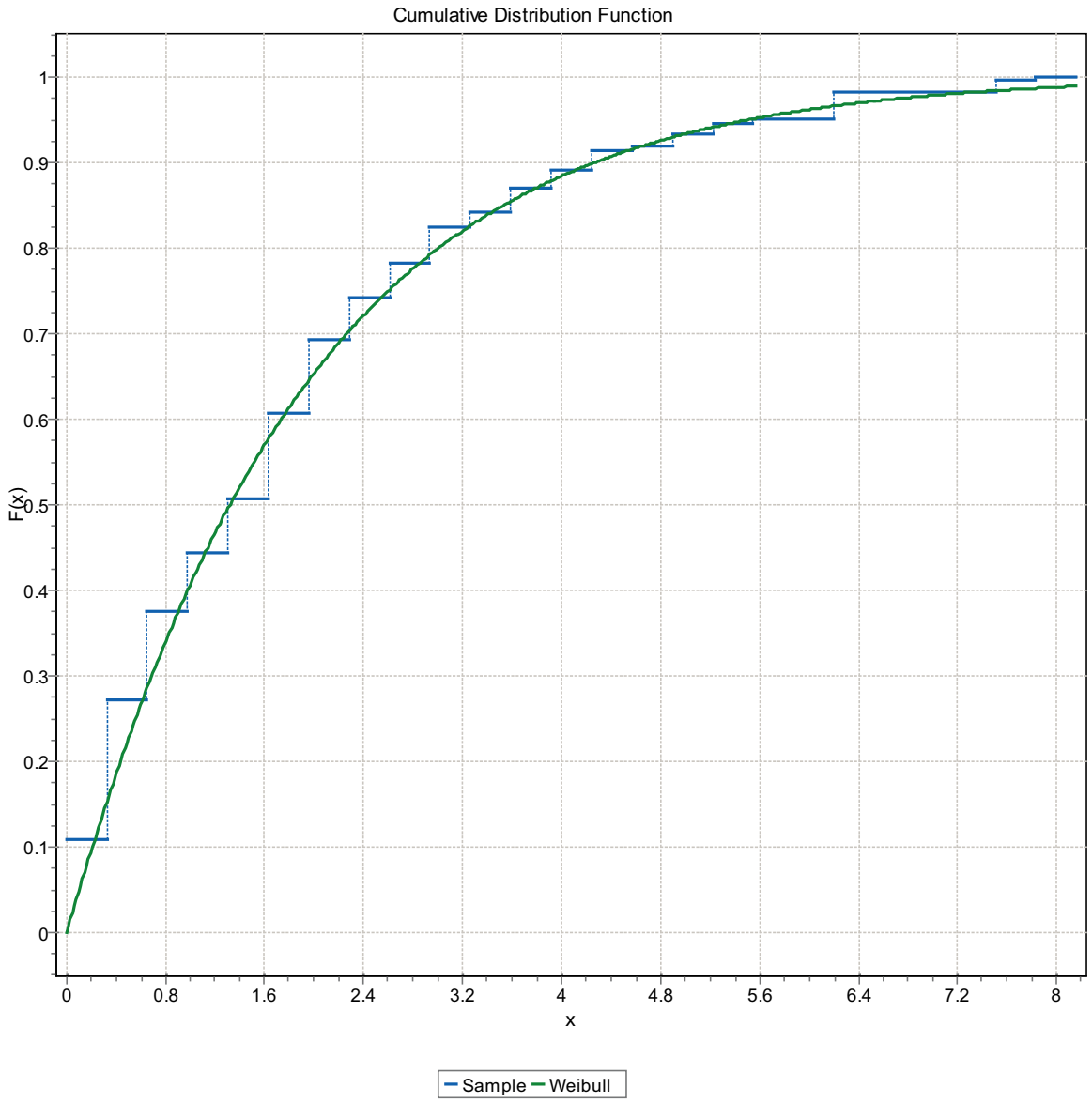

Figure F-44. *CDF, Domain FSM_EW007, 9 m bins, Weibull Distribution.*

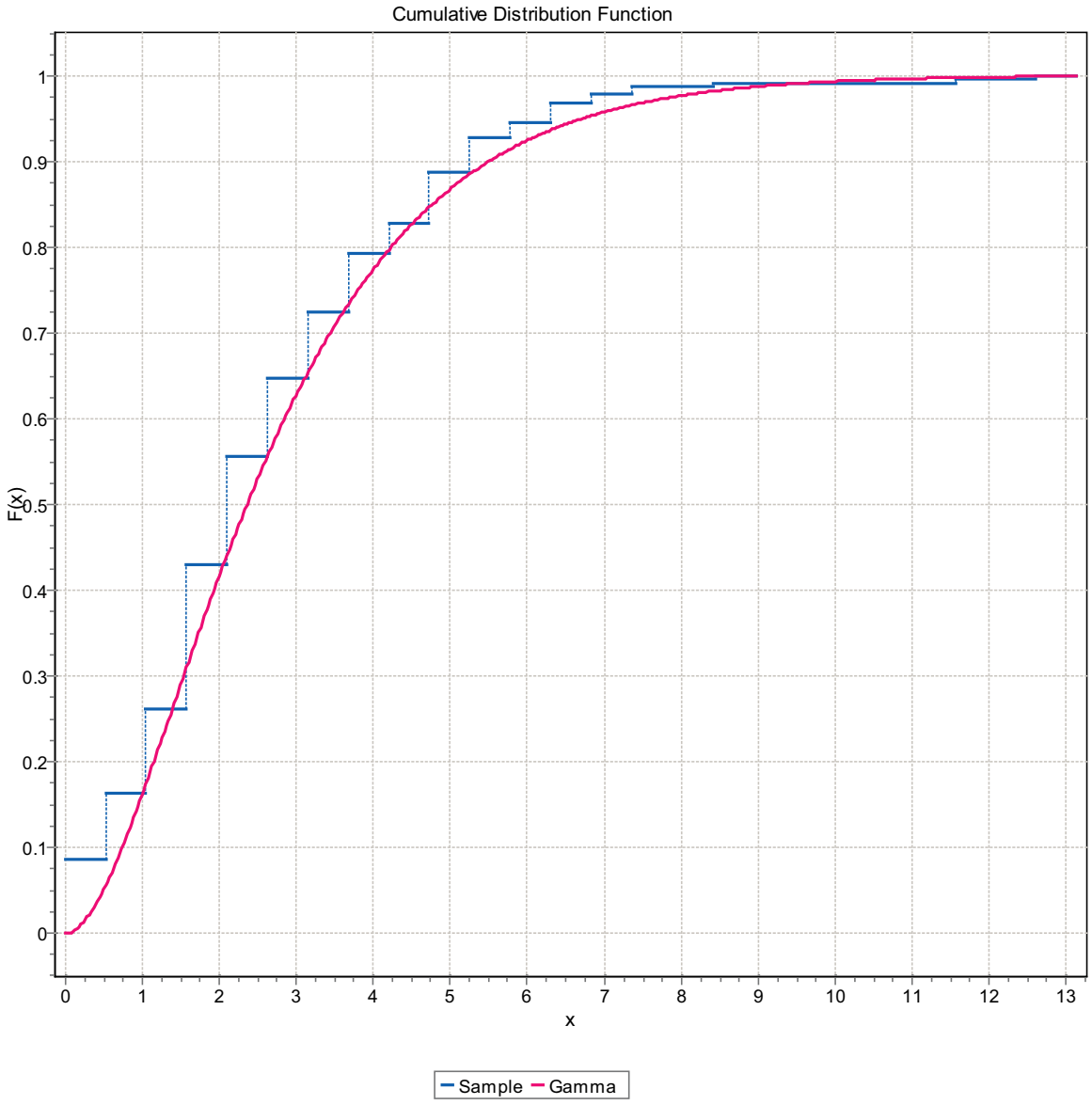

Figure F-45. *CDF, Domain FSM_EW007, 9 m bins, Gamma Distribution.*

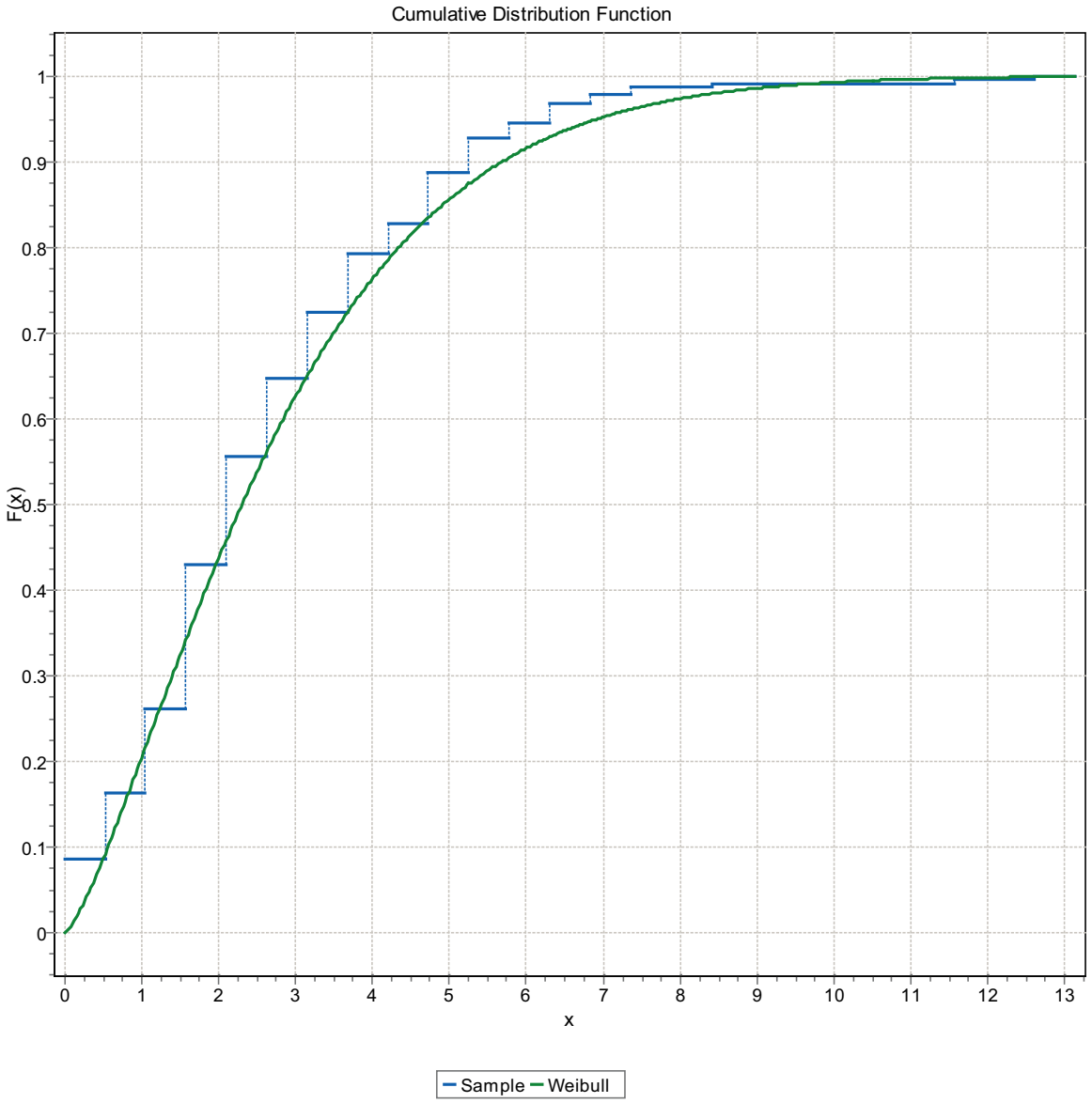

Figure F-46. *CDF, Domain FSM_EW007, 9 m bins, Weibull Distribution.*

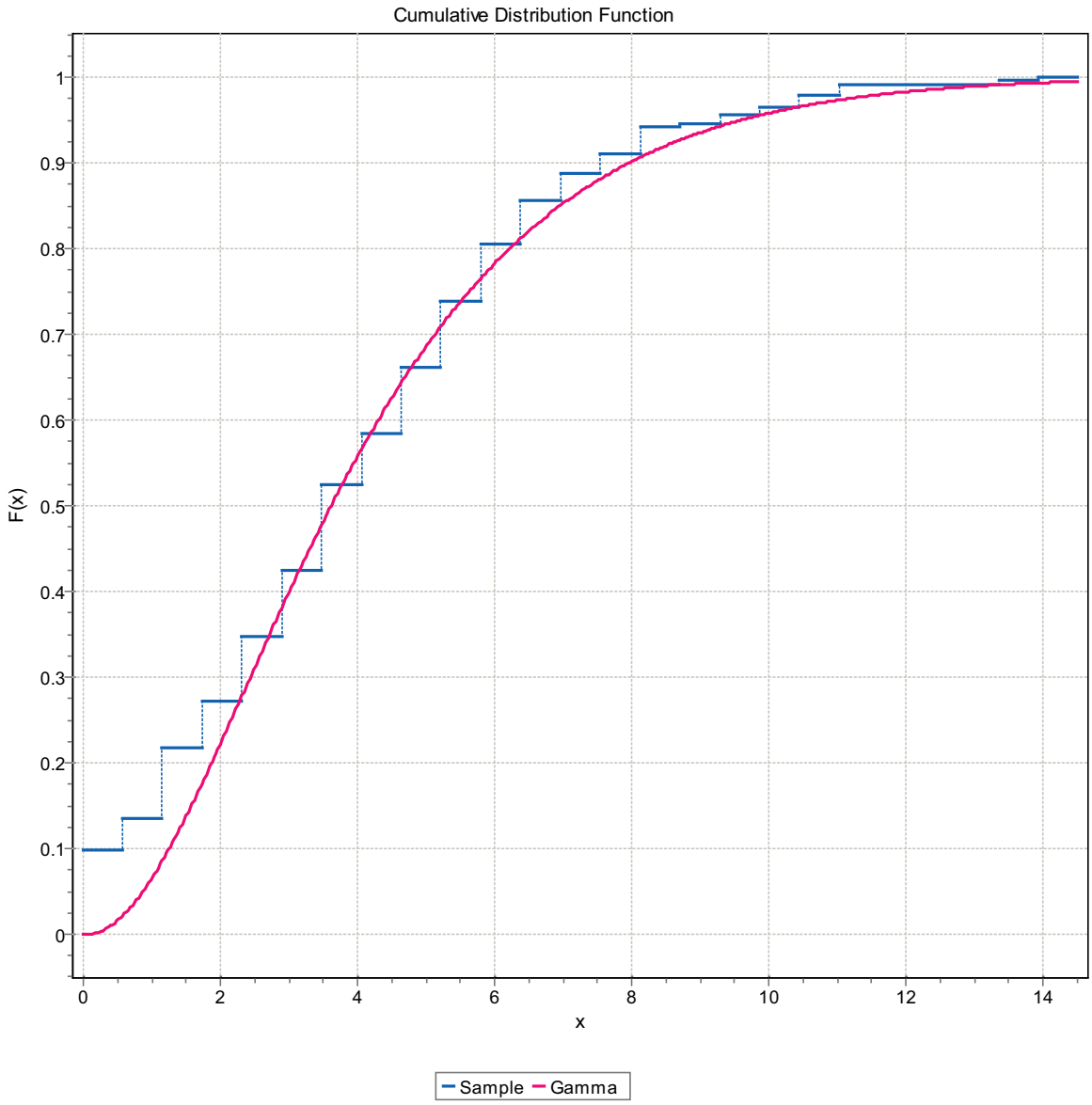

Figure F-47. *CDF, Domain FSM_EW007, 9 m bins, Gamma Distribution.*

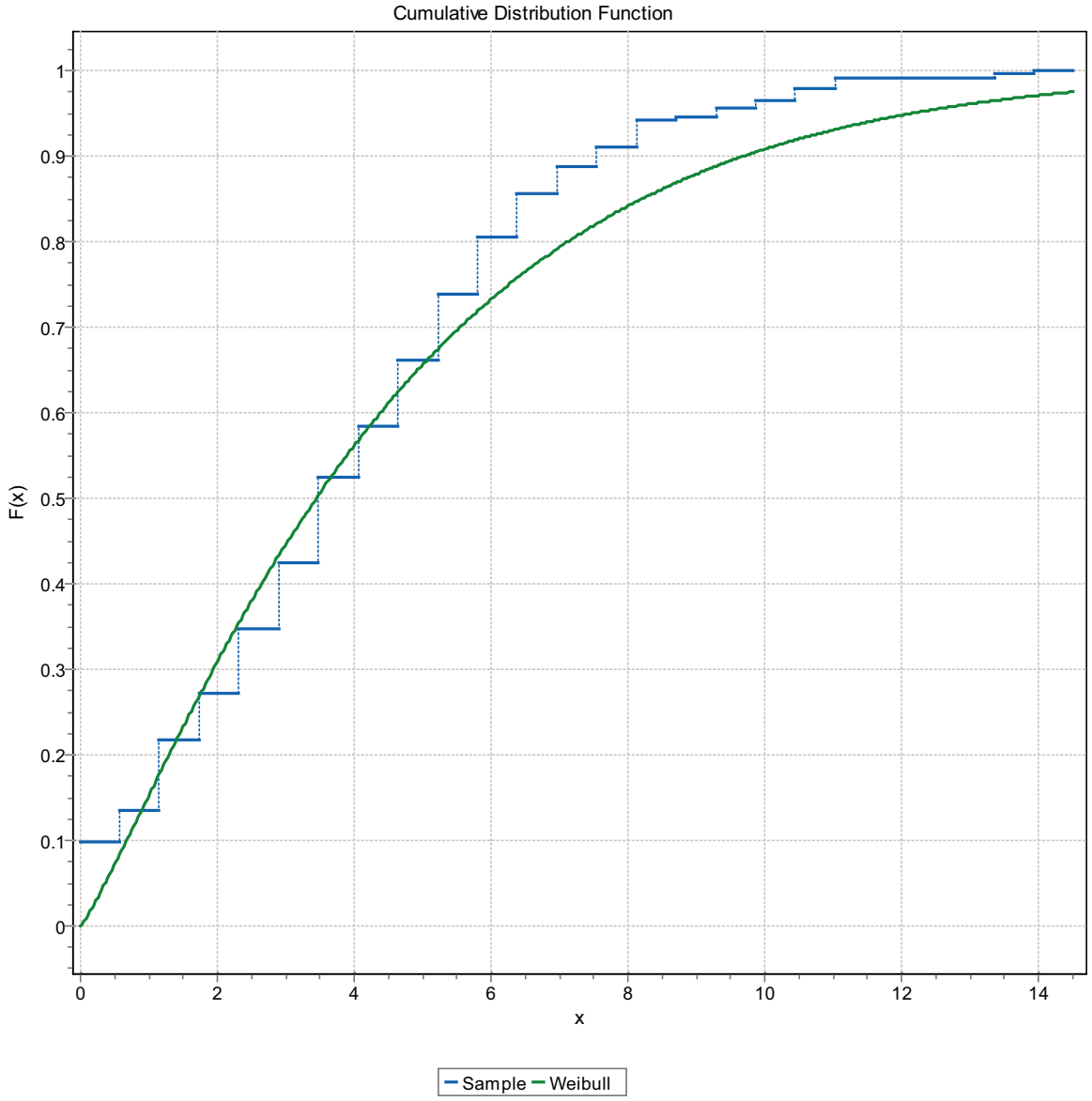

Figure F-48. *CDF, Domain FSM_EW007, 9 m bins, Weibull Distribution.*

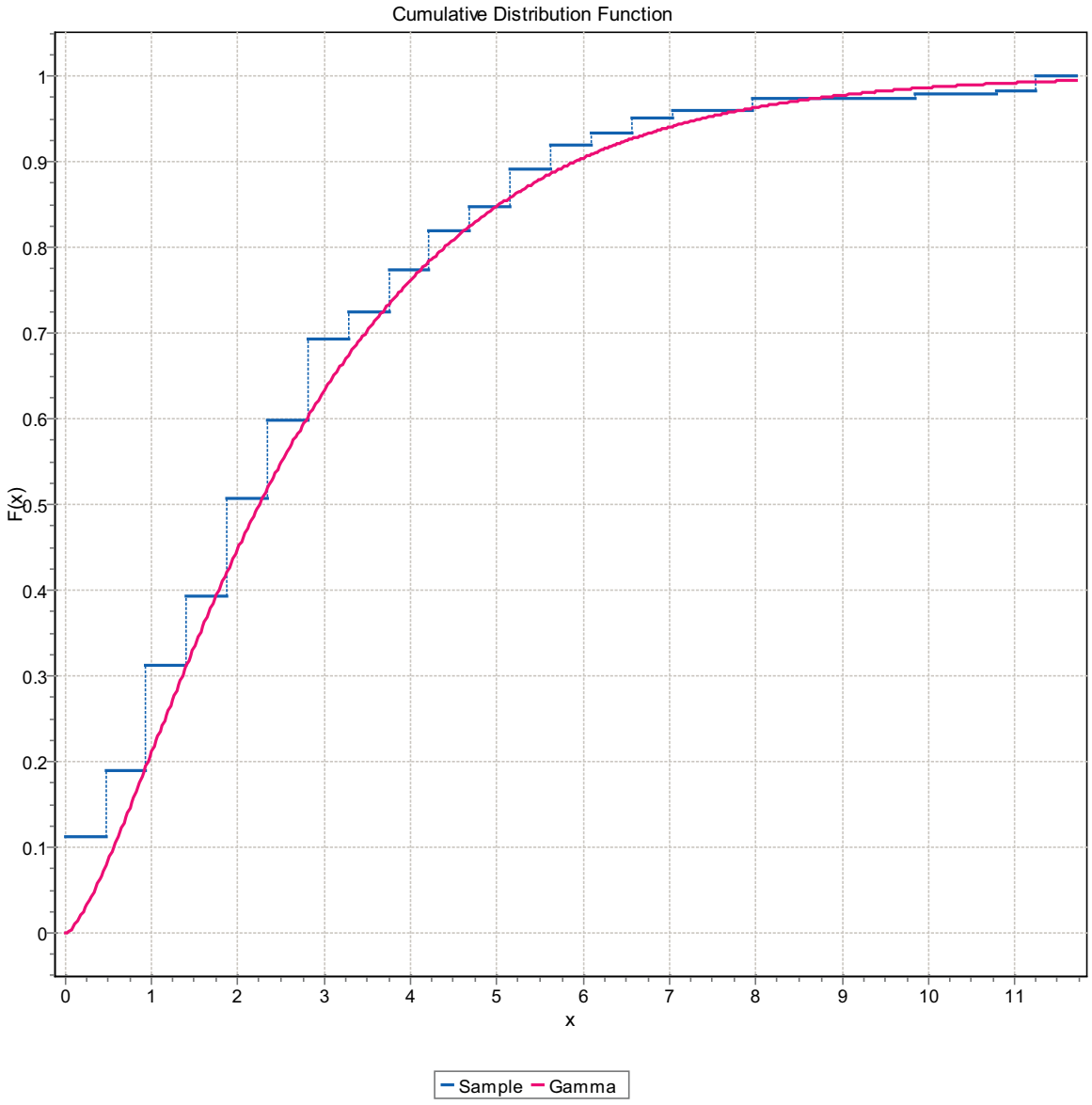

Figure F-49. *CDF, Domain FSM_EW007, 9 m bins, Gamma Distribution.*

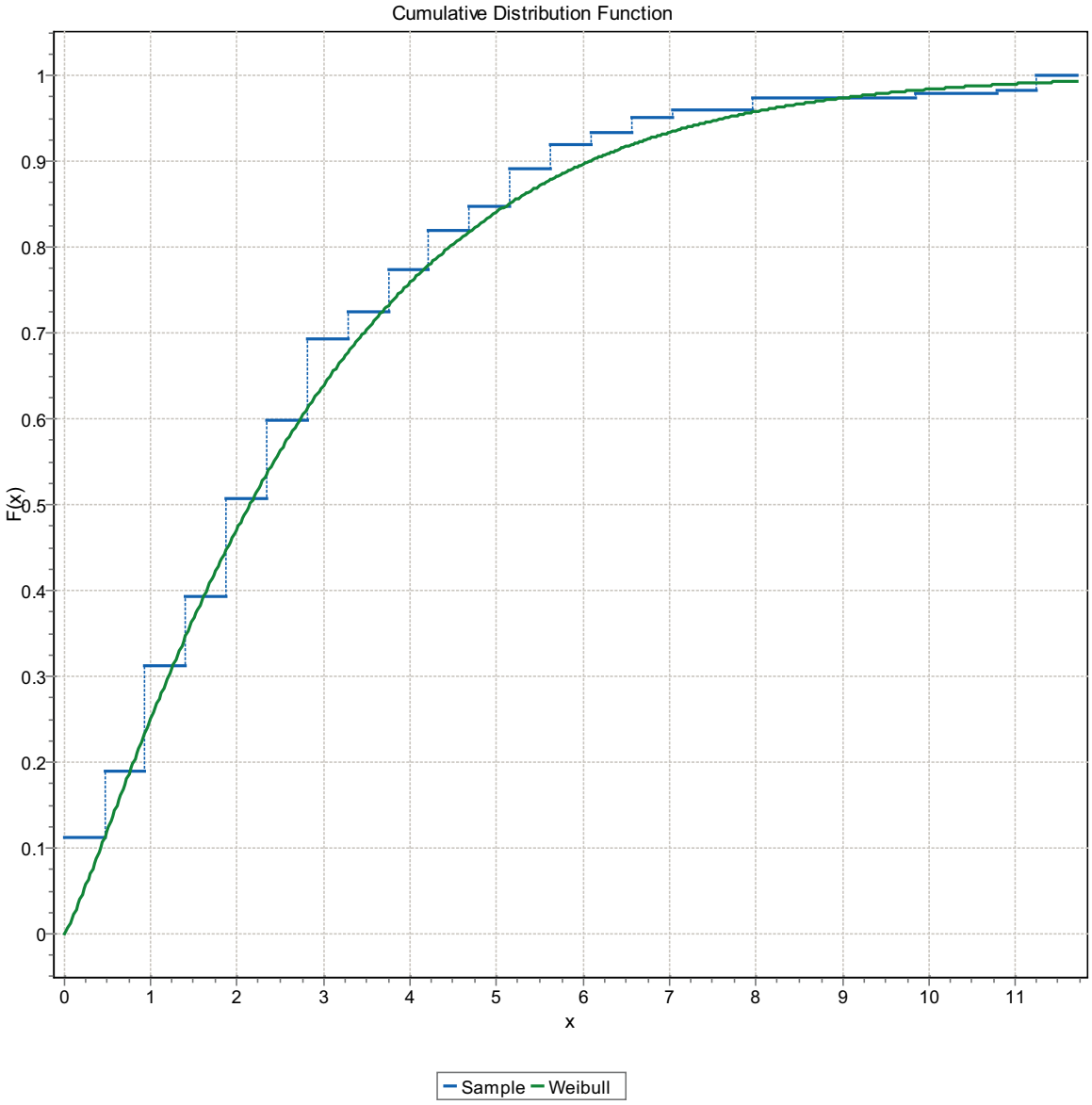

Figure F-50. *CDF, Domain FSM_EW007, 9 m bins, Weibull Distribution.*

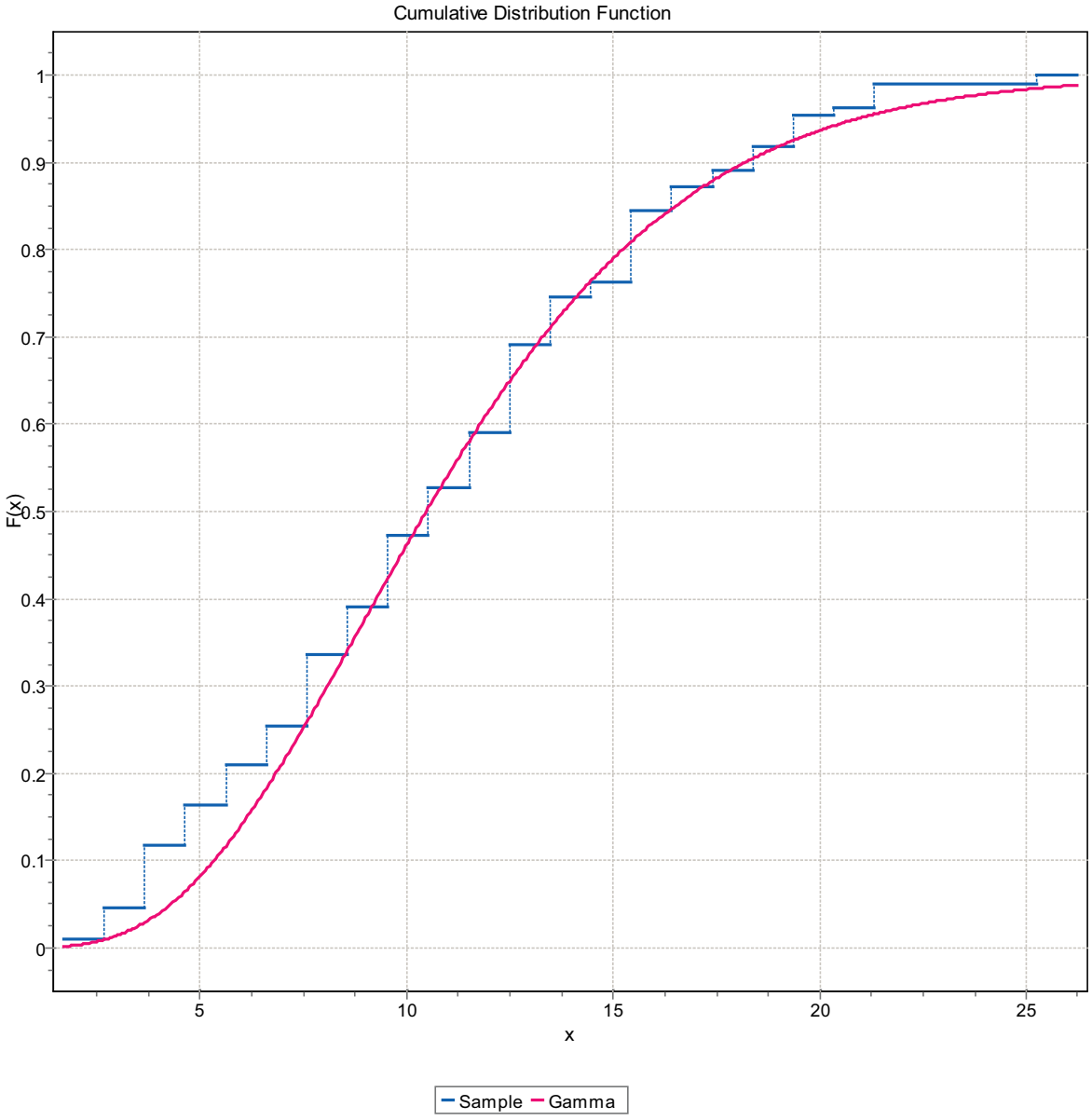

Figure F-51. *CDF, Domain FSM_NE005, 9 m bins, Gamma Distribution.*

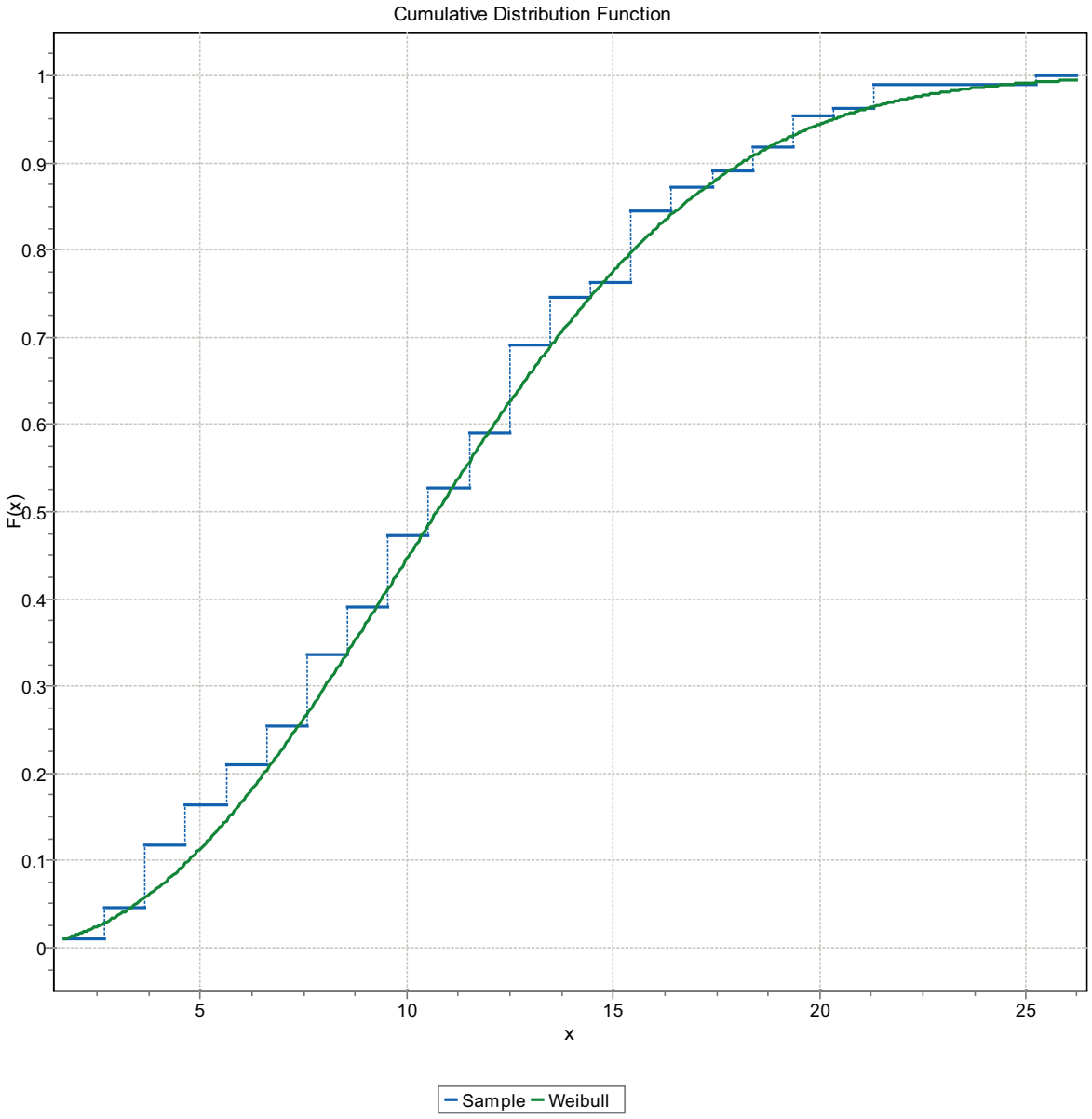

Figure F-52. *CDF, Domain FSM_NE005, 9 m bins, Weibull Distribution.*

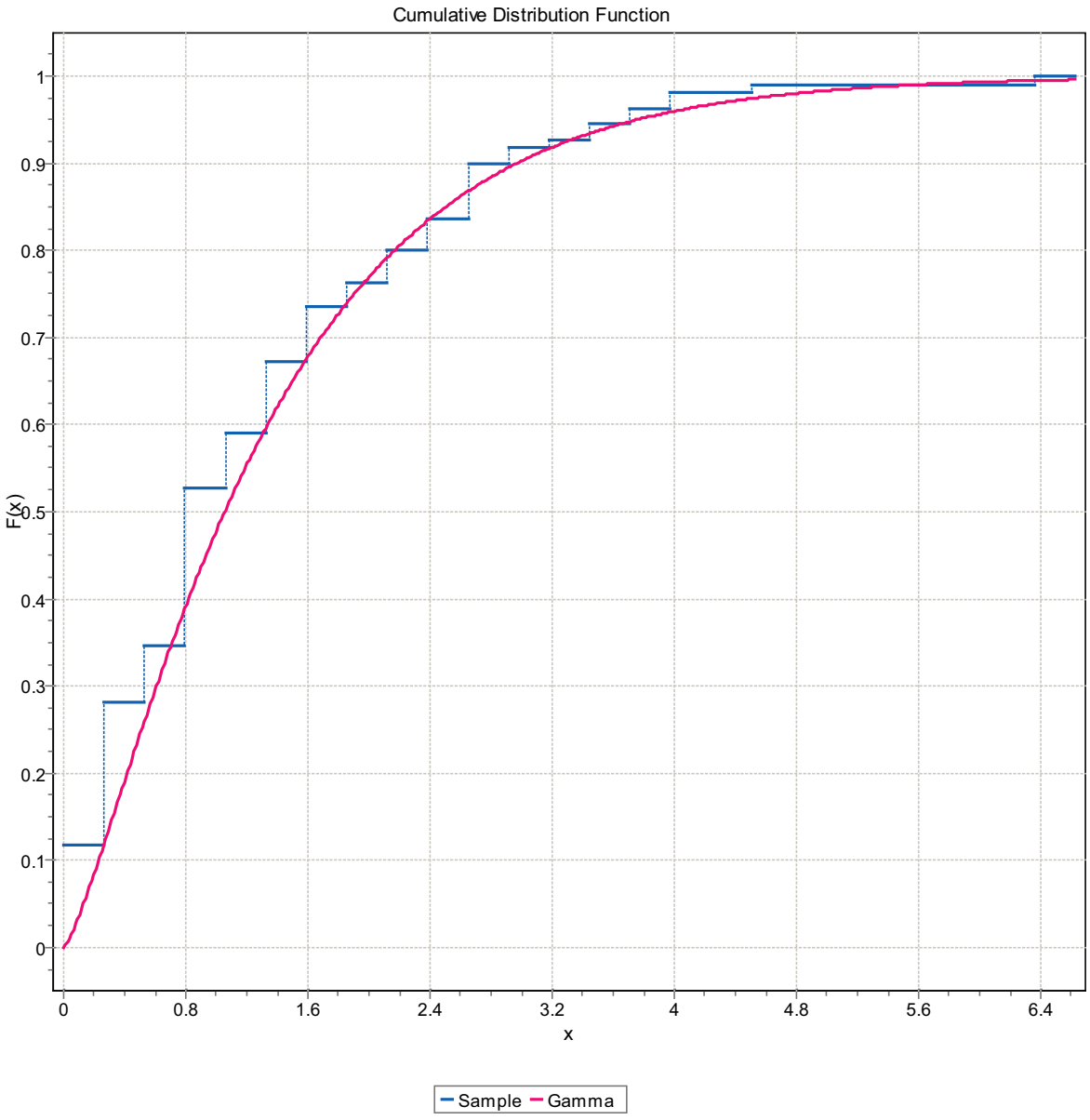

Figure F-53. *CDF, Domain FSM_NE005, 9 m bins, Gamma Distribution.*

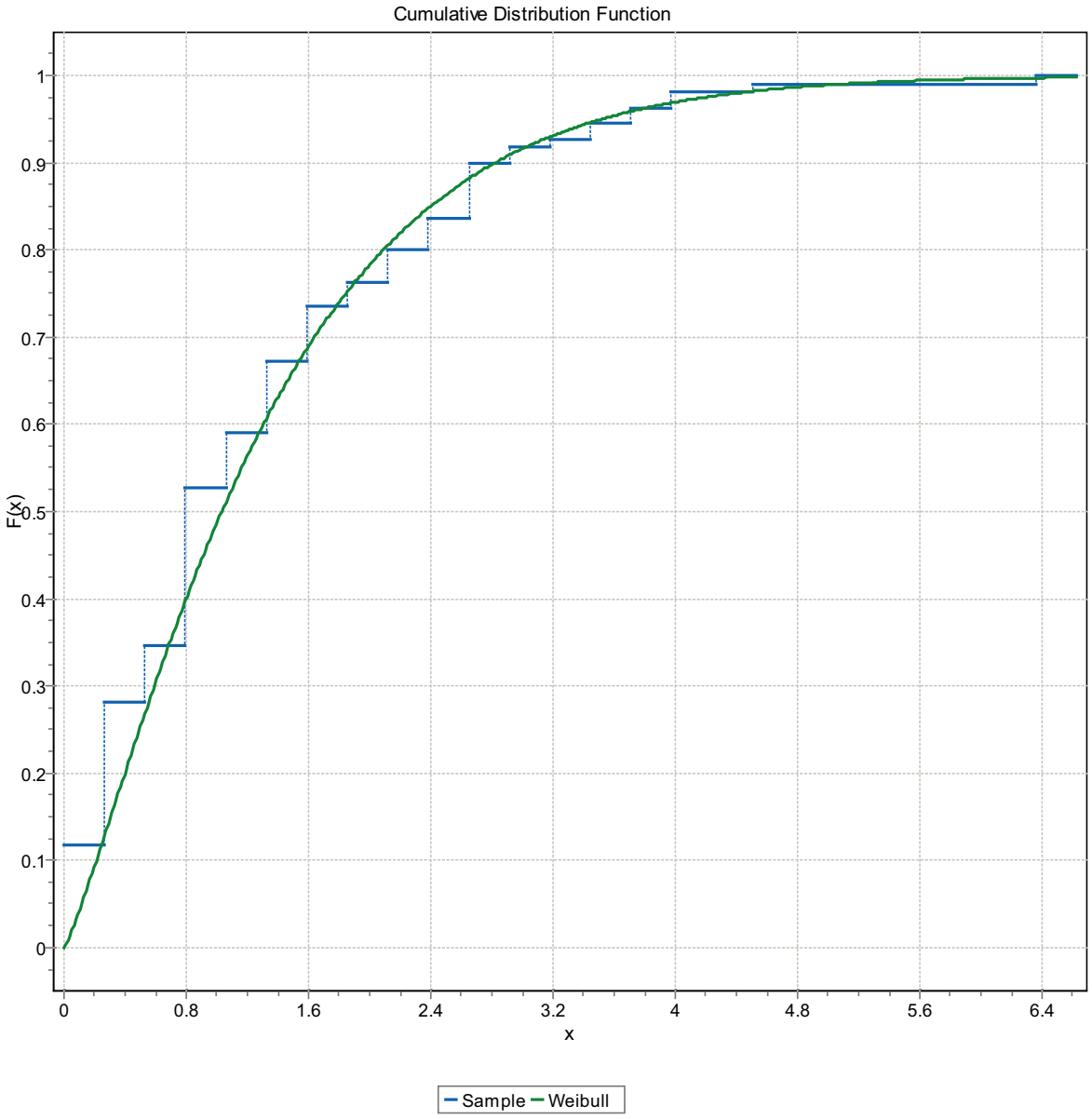

Figure F-54. *CDF, Domain FSM_NE005, 9 m bins, Weibull Distribution.*

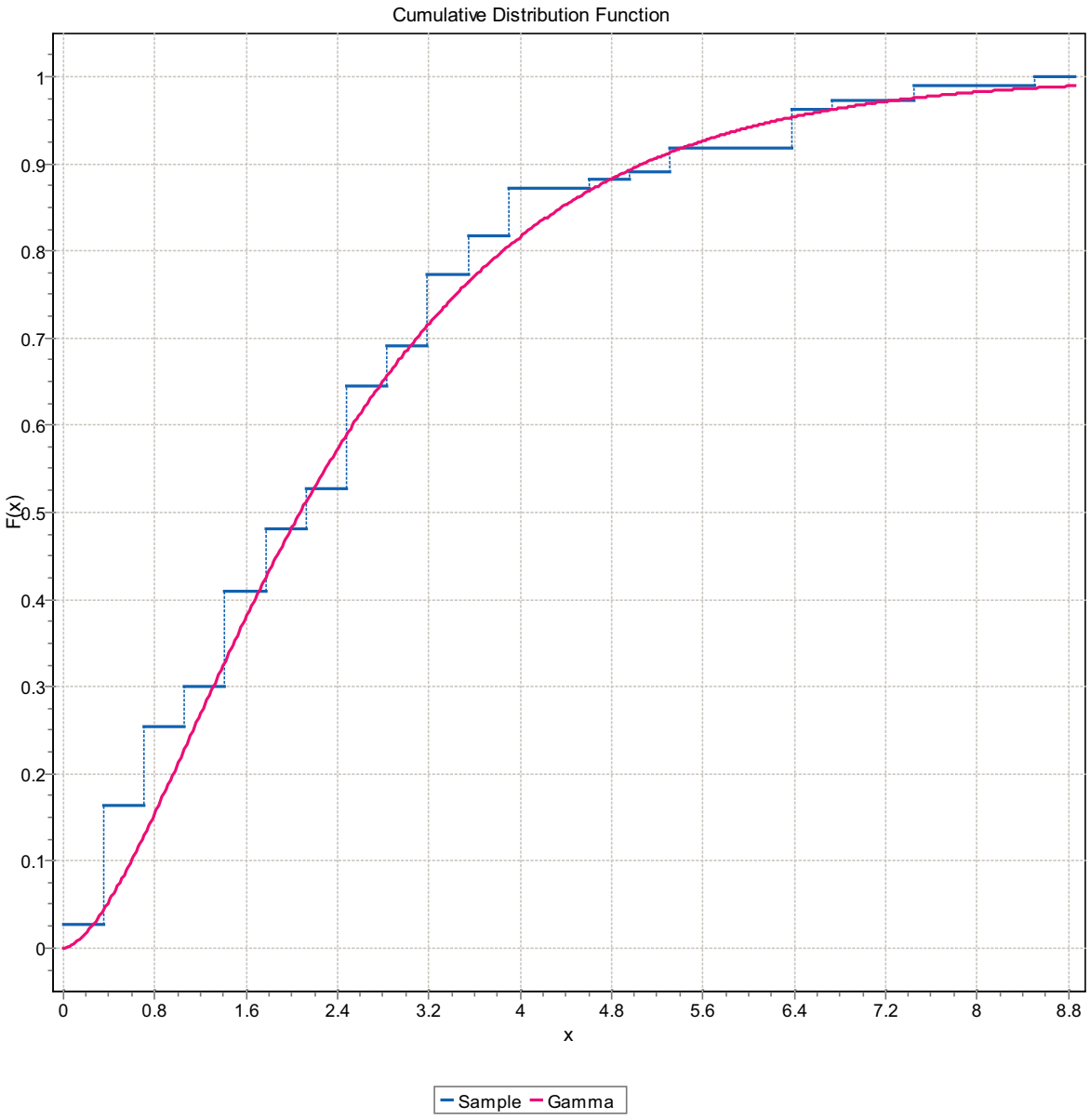

Figure F-55. *CDF, Domain FSM_NE005, 9 m bins, Gamma Distribution.*

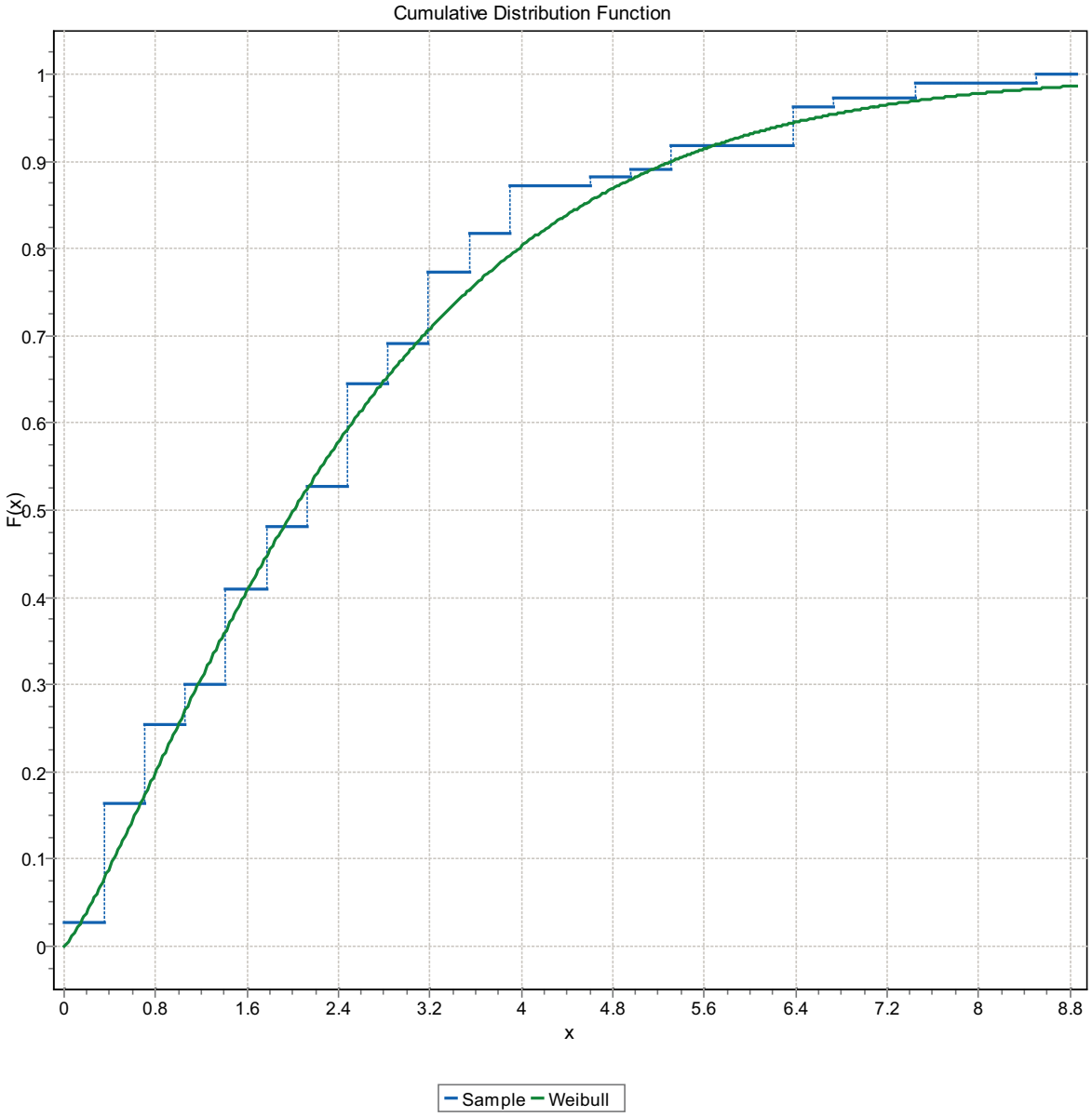

Figure F-56. *CDF, Domain FSM_NE005, 9 m bins, Weibull Distribution.*

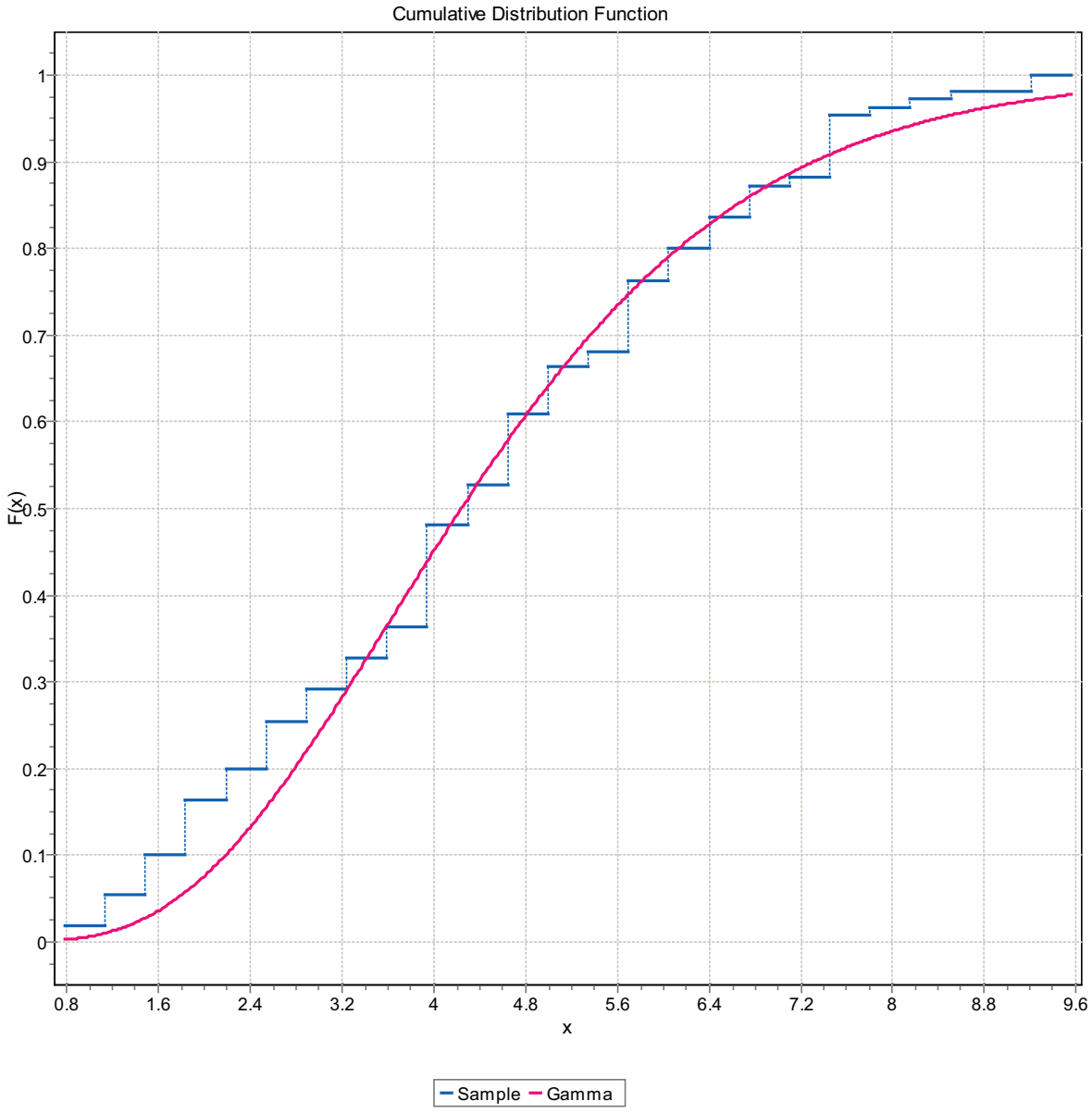

Figure F-57. *CDF, Domain FSM_NE005, 9 m bins, Gamma Distribution.*

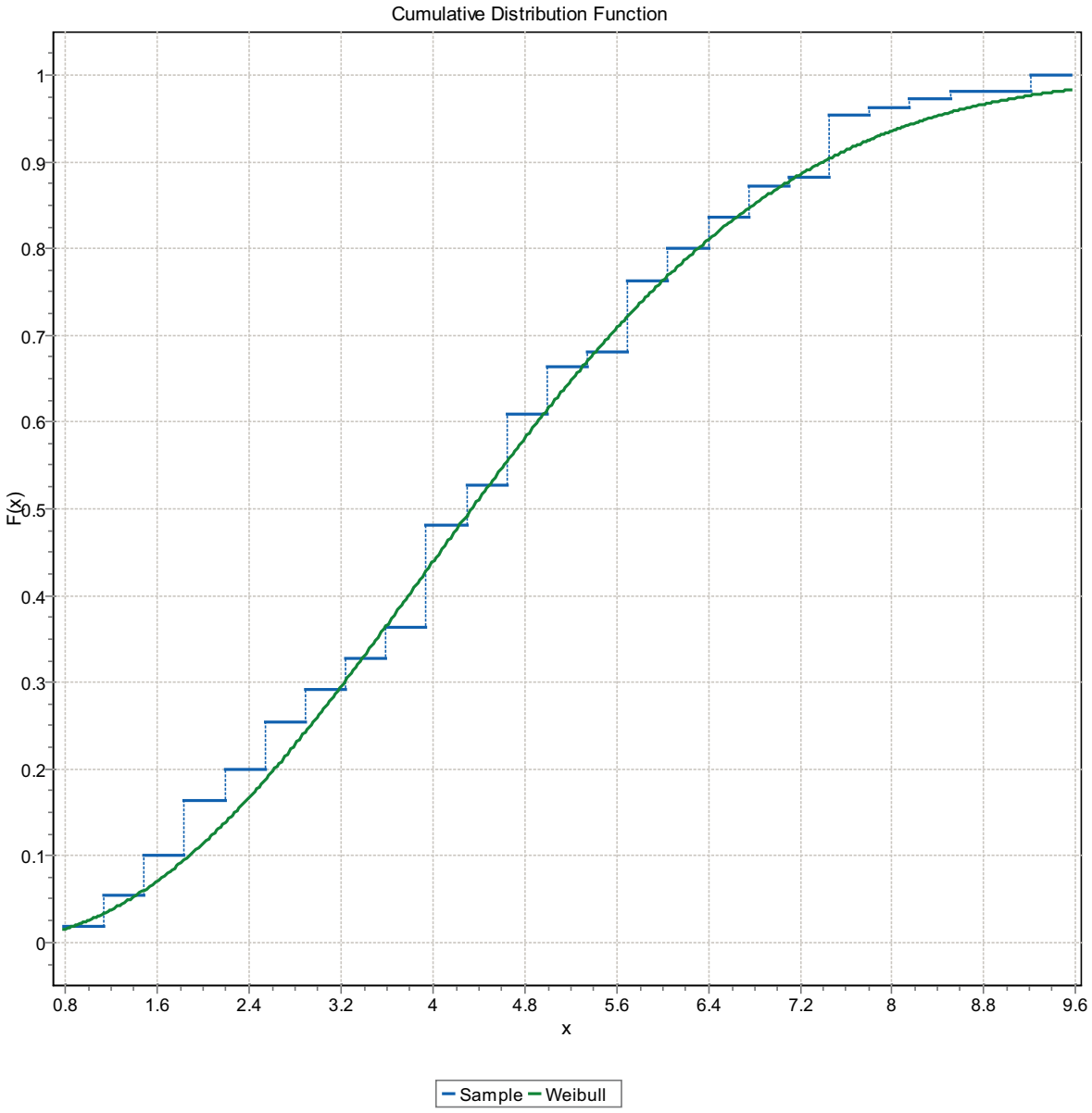

Figure F-58. *CDF, Domain FSM_NE005, 9 m bins, Weibull Distribution.*

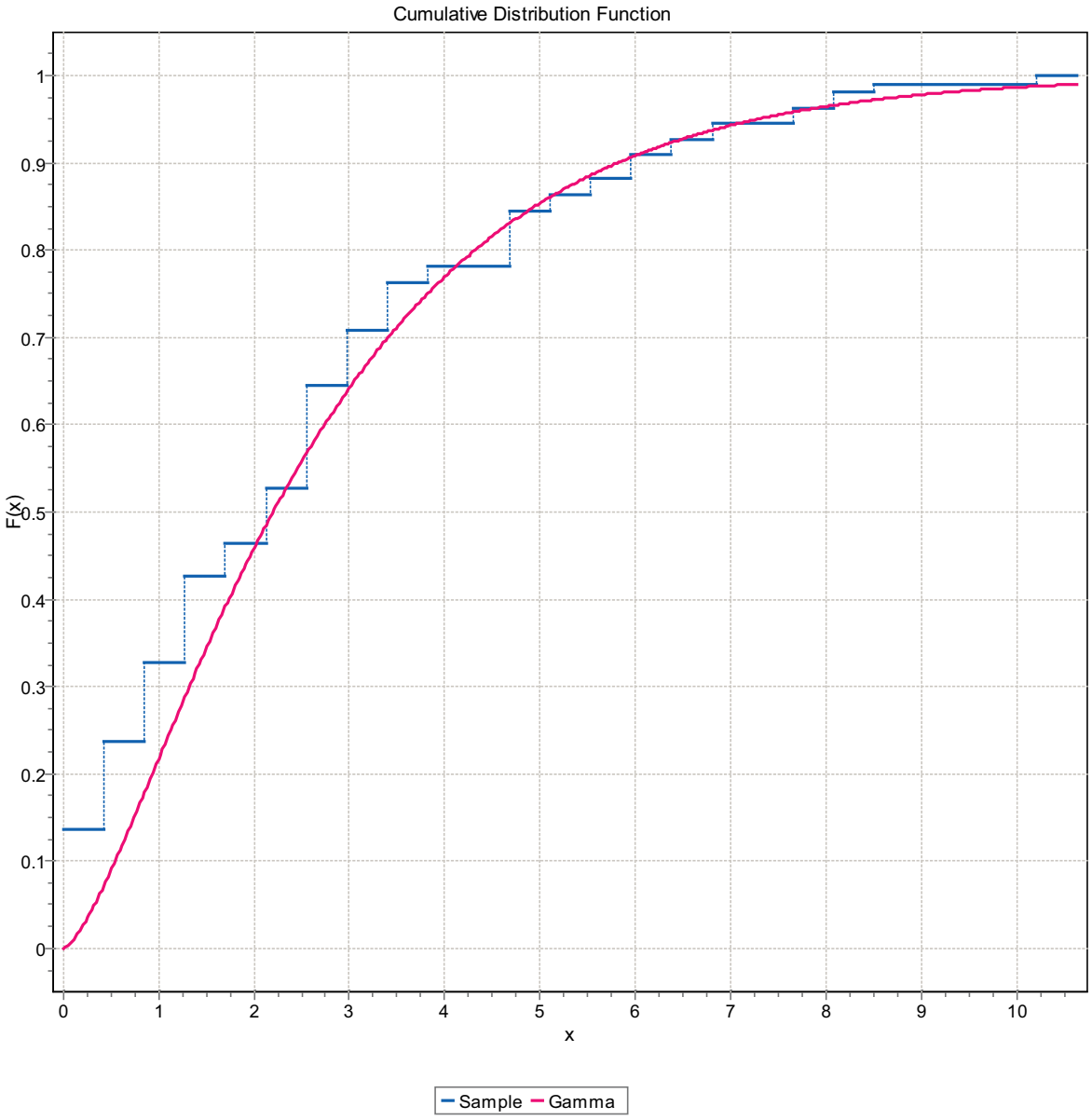

Figure F-59. *CDF, Domain FSM_NE005, 9 m bins, Gamma Distribution.*

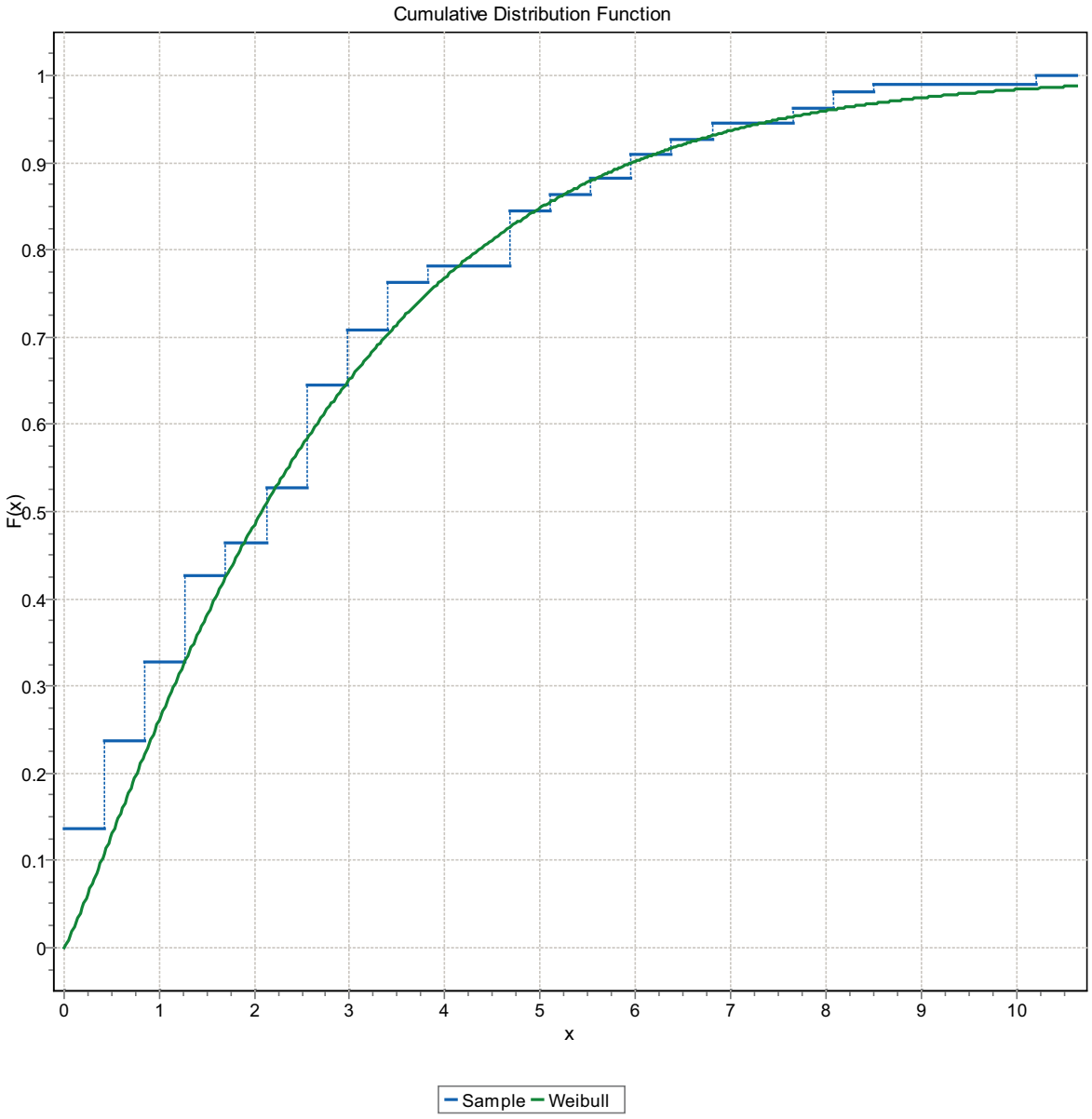

Figure F-60. *CDF, Domain FSM_NE005, 9 m bins, Weibull Distribution.*

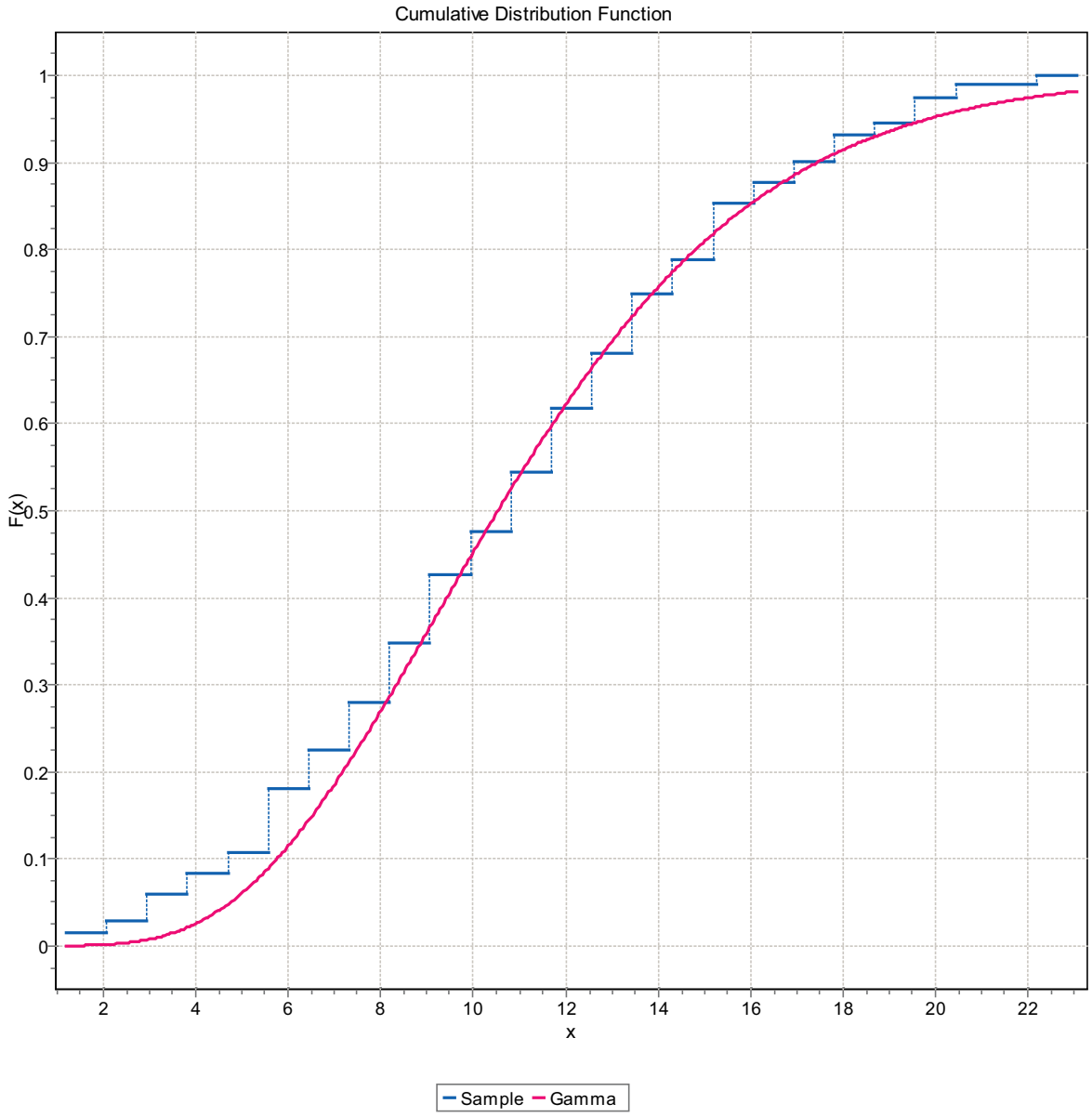

Figure F-61. *CDF, Domain FSM_N, 9 m bins, Gamma Distribution.*

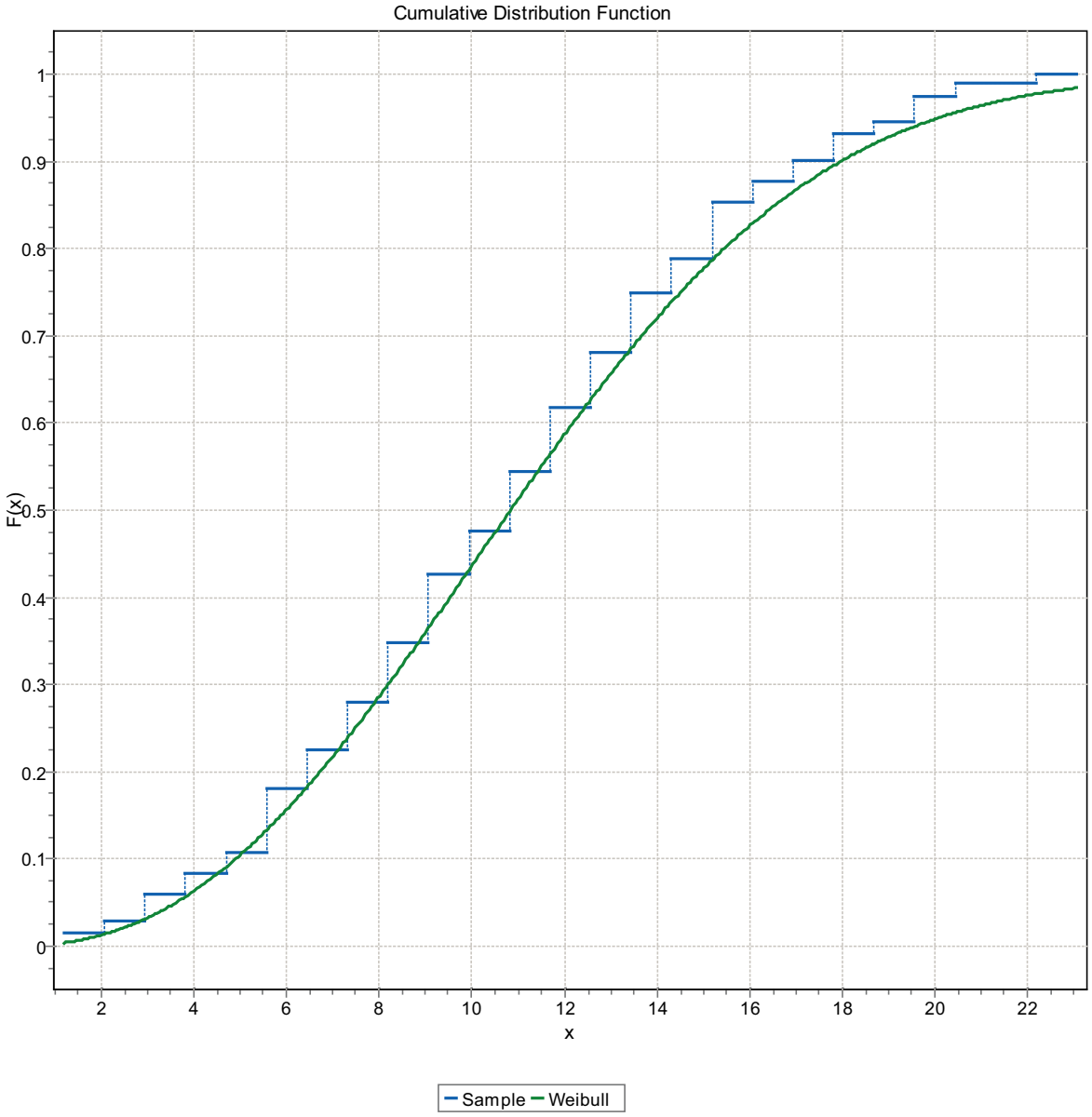

Figure F-62. *CDF, Domain FSM_N, 9 m bins, Weibull Distribution.*

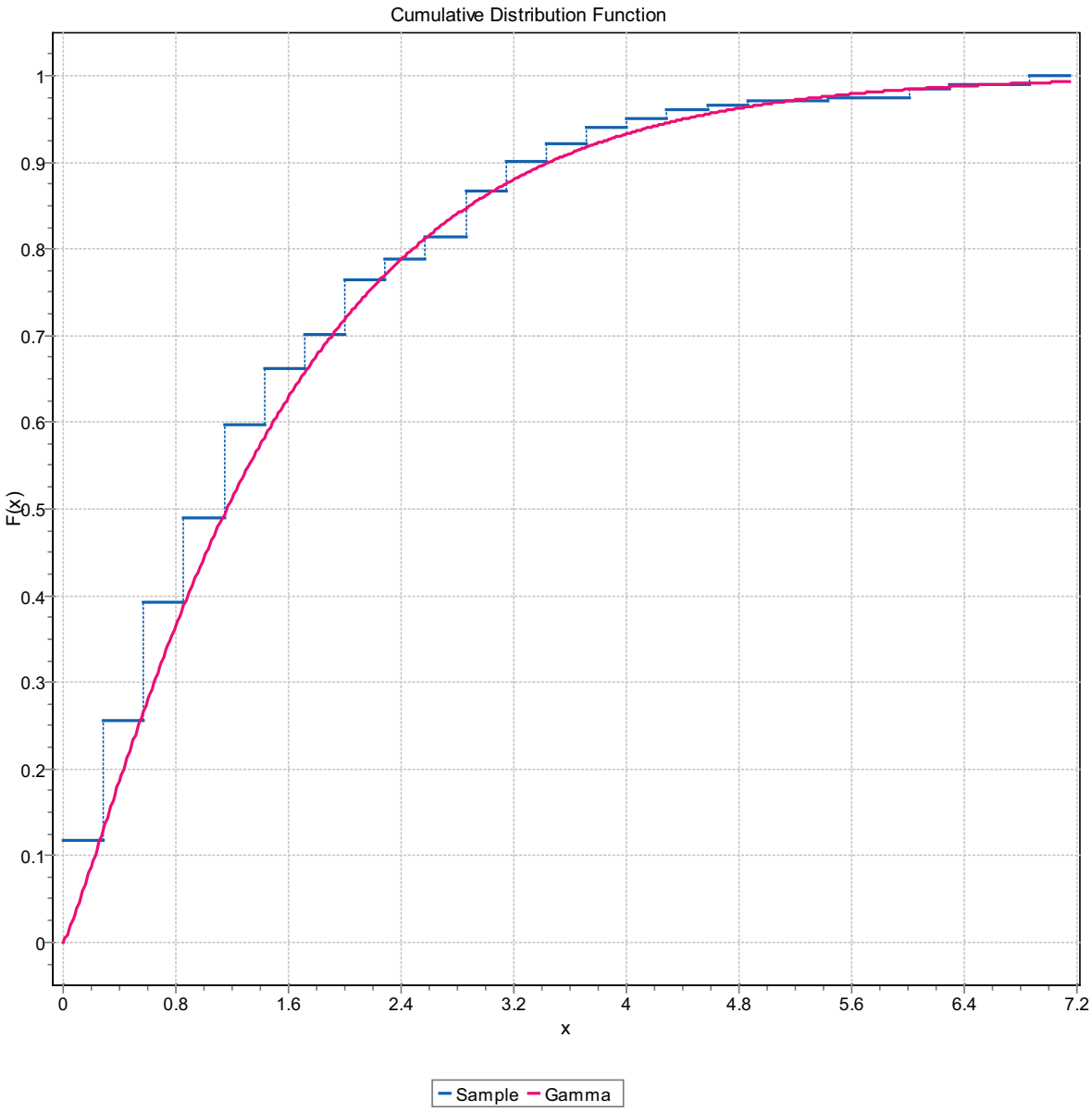

Figure F-63. *CDF, Domain FSM_N, 9 m bins, Gamma Distribution.*

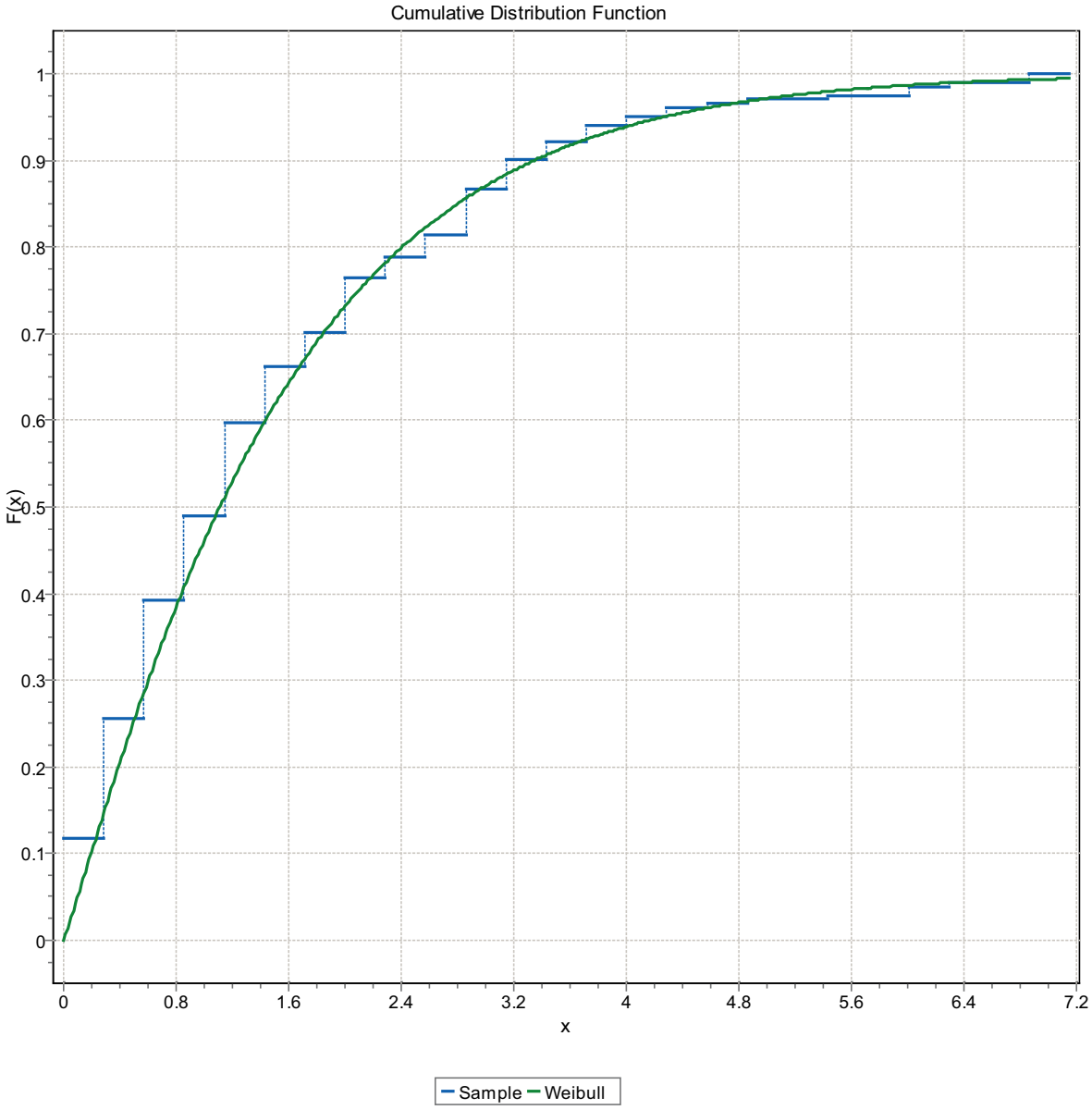

Figure F-64. *CDF, Domain FSM_N, 9 m bins, Weibull Distribution.*

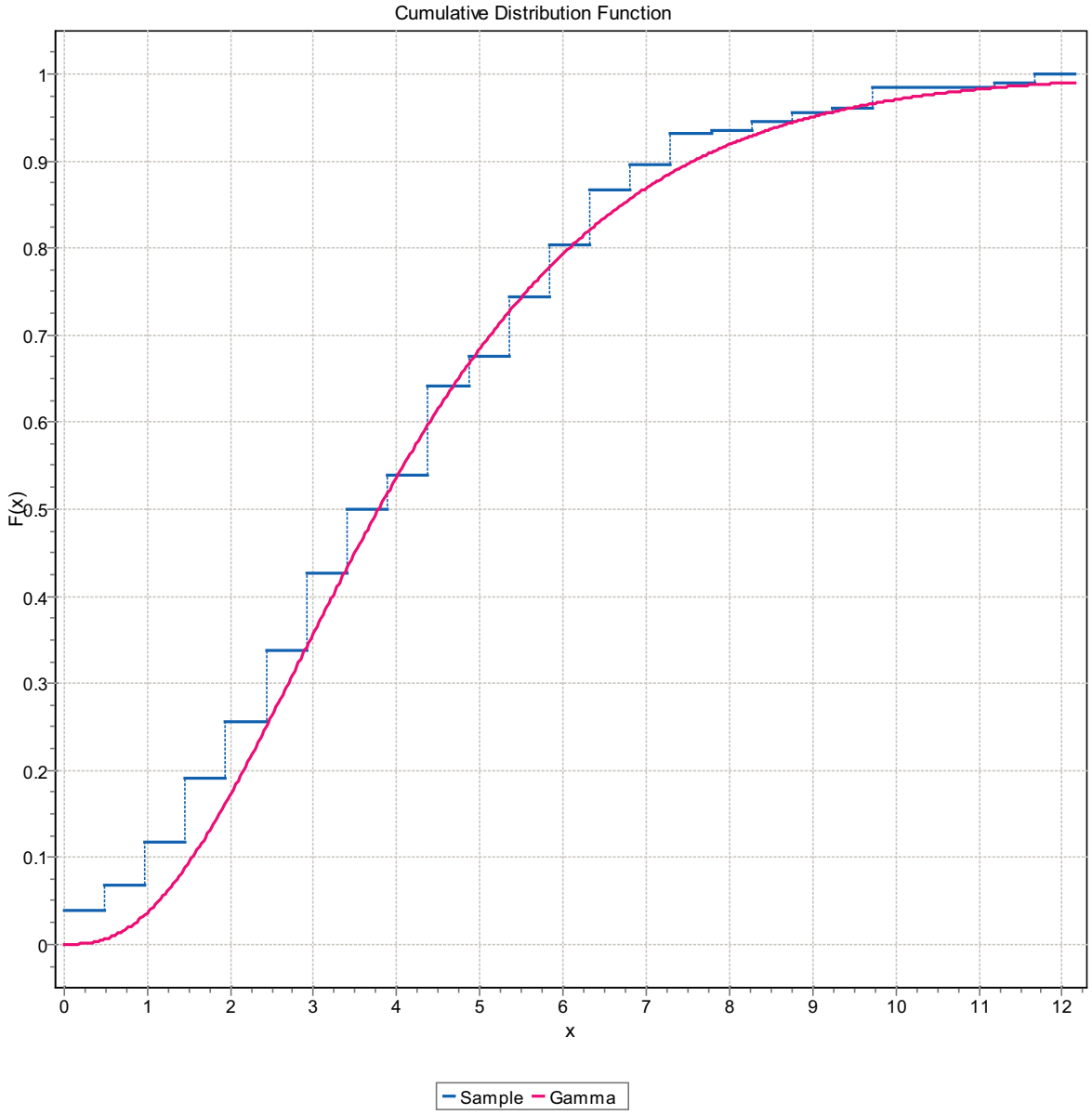

Figure F-65. *CDF, Domain FSM_N, 9 m bins, Gamma Distribution.*

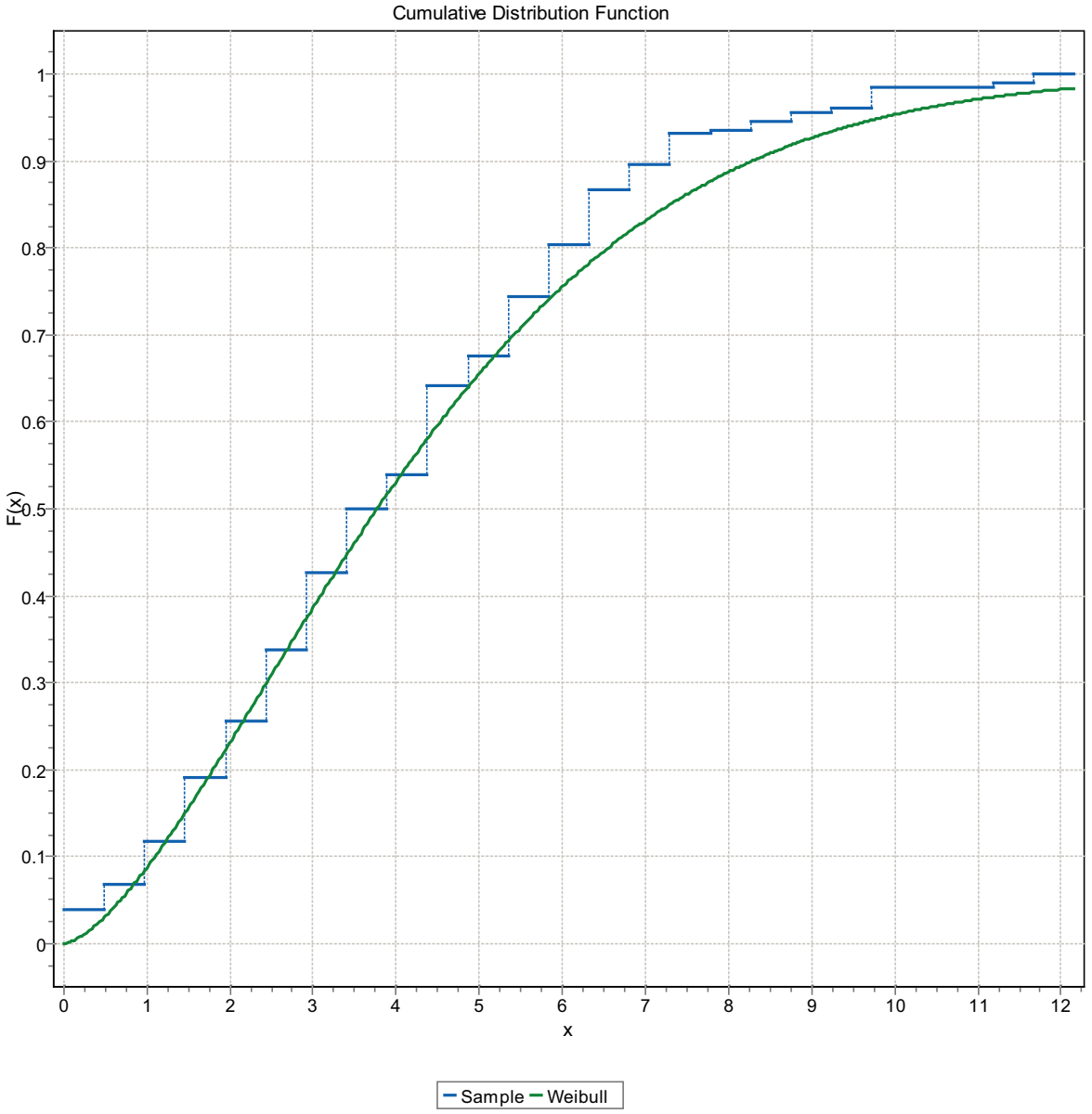

Figure F-66. *CDF, Domain FSM_N, 9 m bins, Weibull Distribution.*

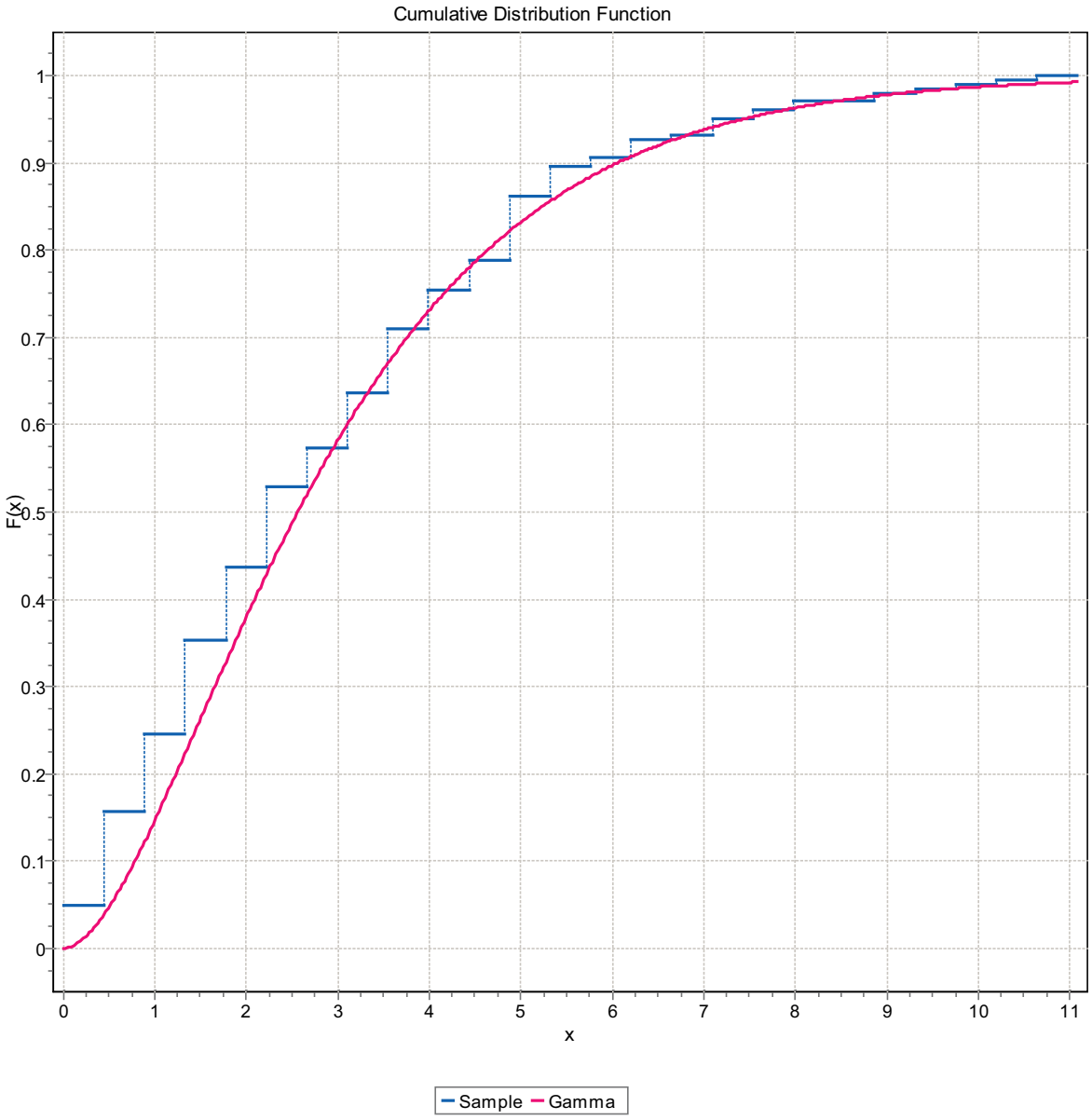

Figure F-67. *CDF, Domain FSM_N, 9 m bins, Gamma Distribution.*

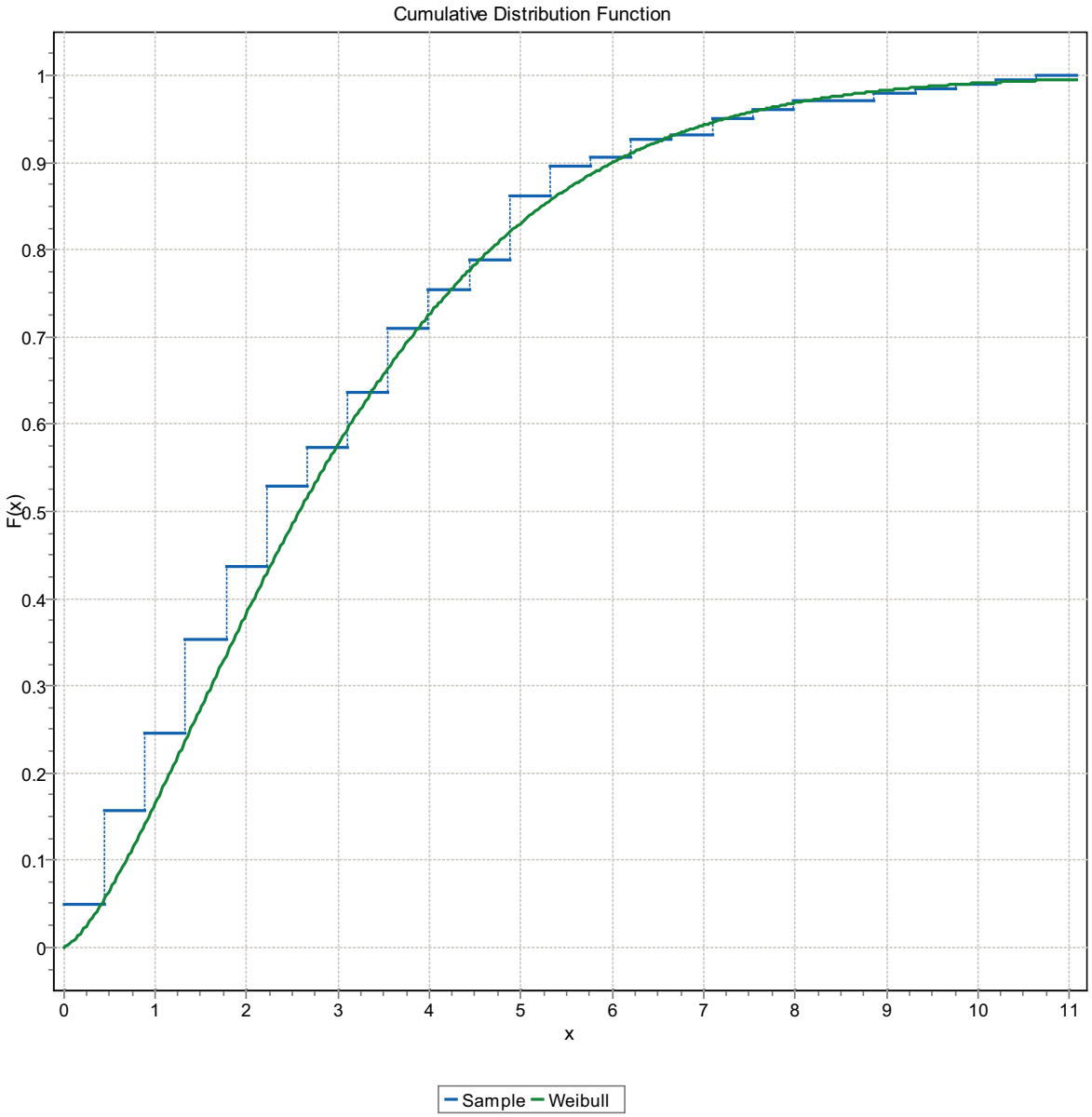

Figure F-68. *CDF, Domain FSM_N, 9 m bins, Weibull Distribution.*

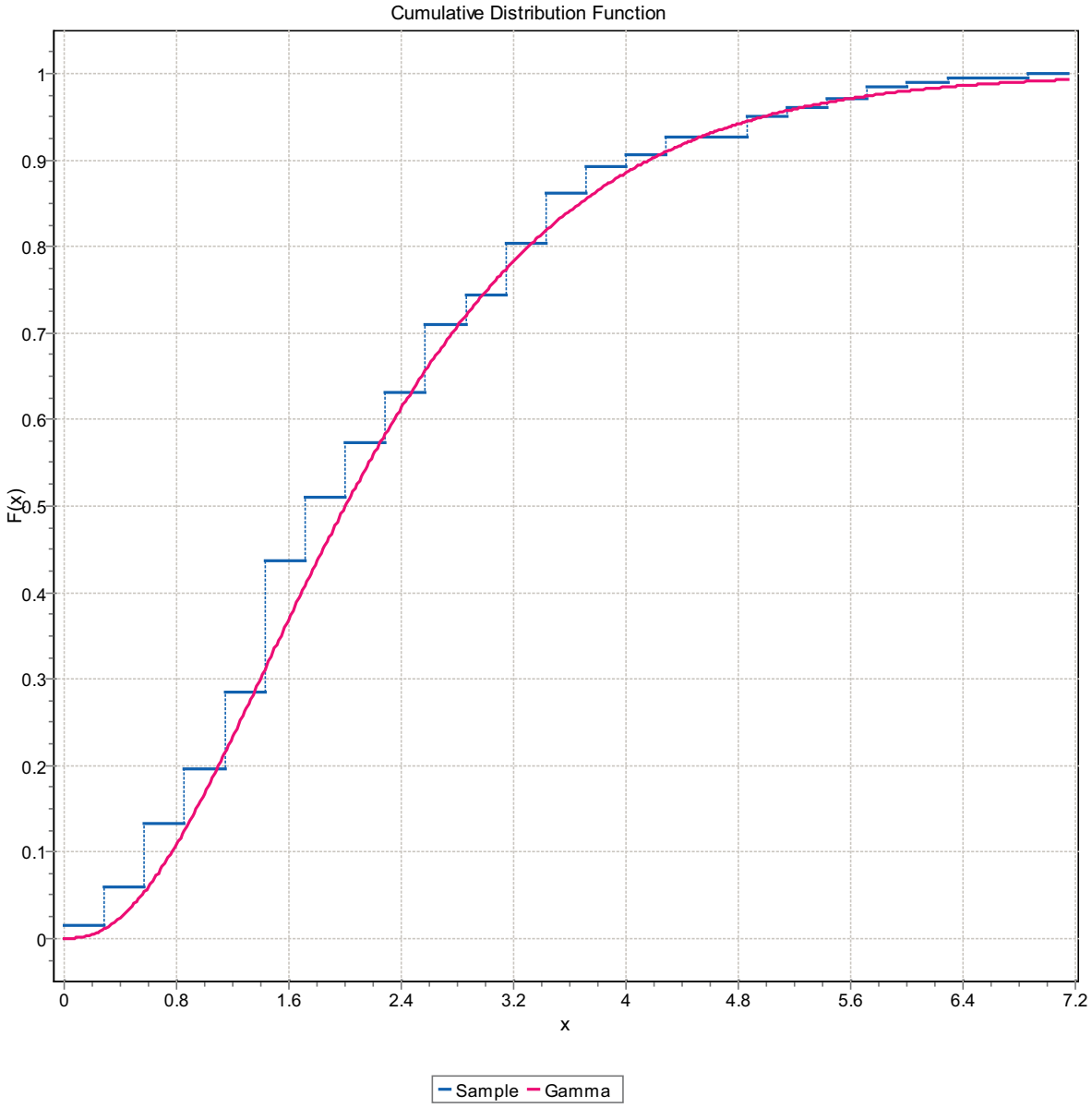

Figure F-69. *CDF, Domain FSM_N, 9 m bins, Gamma Distribution.*

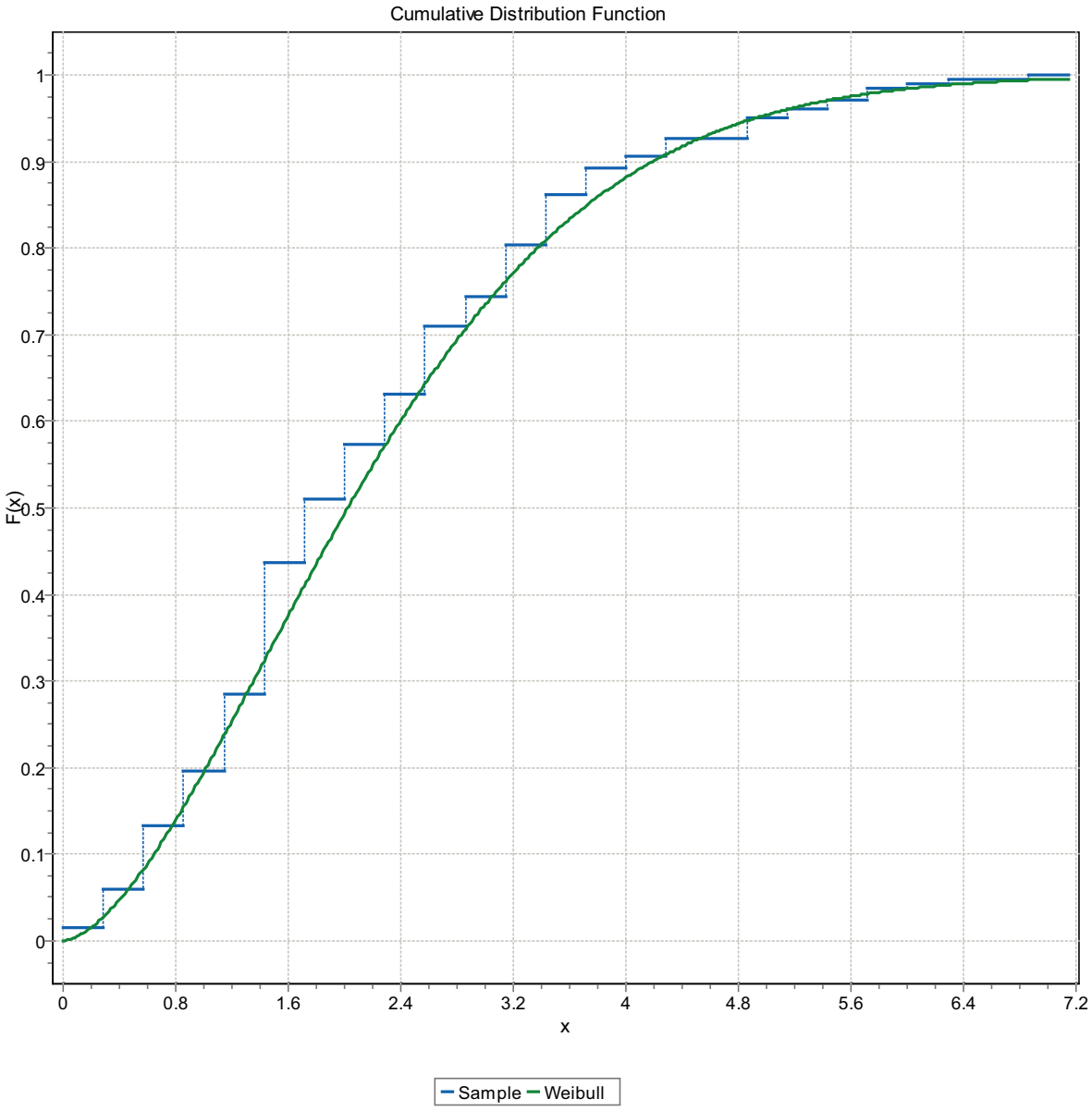

Figure F-70. *CDF, Domain FSM_N, 9 m bins, Weibull Distribution.*

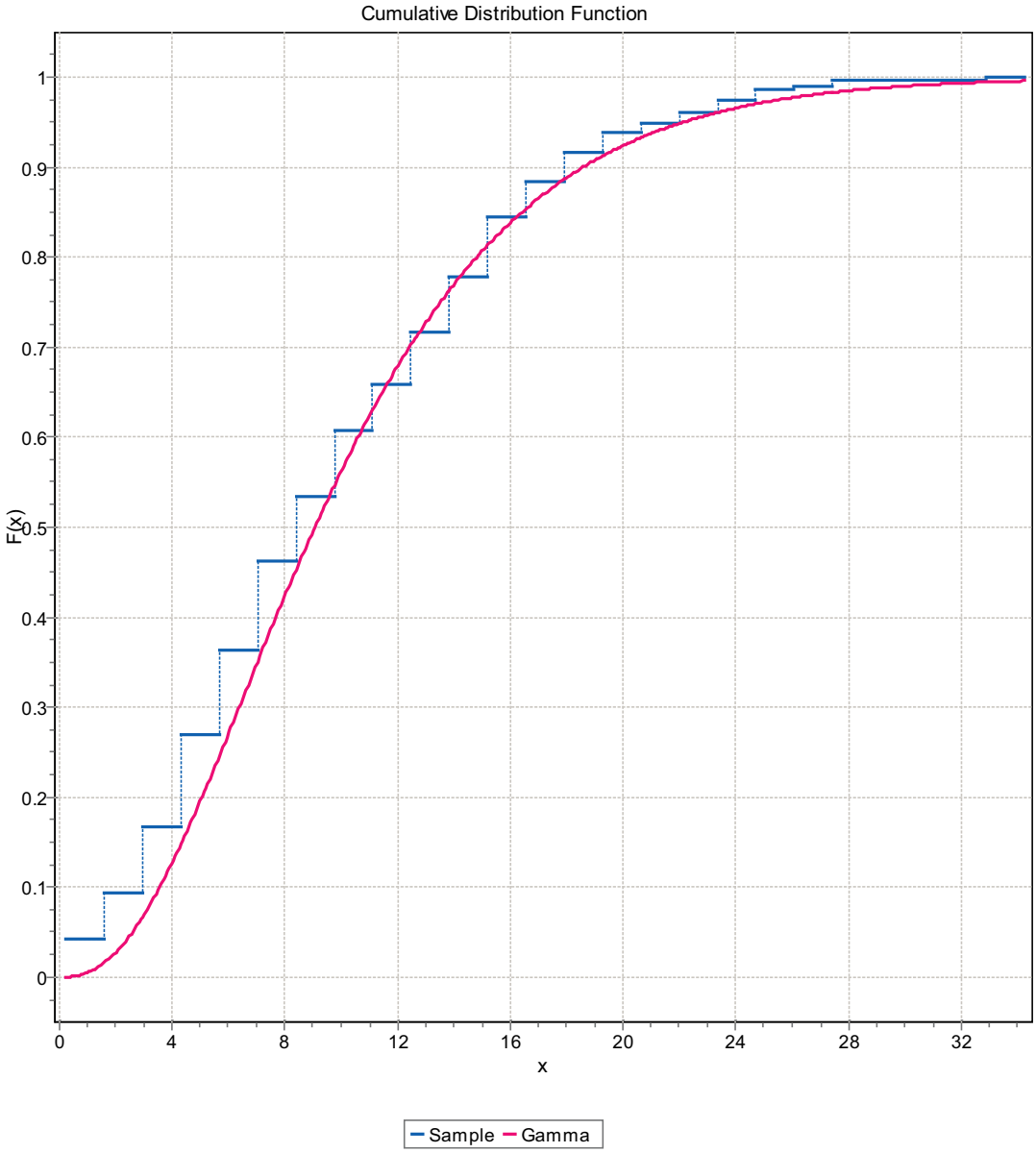

Figure F-71. *CDF, Domain FSM_W, 9 m bins, Gamma Distribution.*

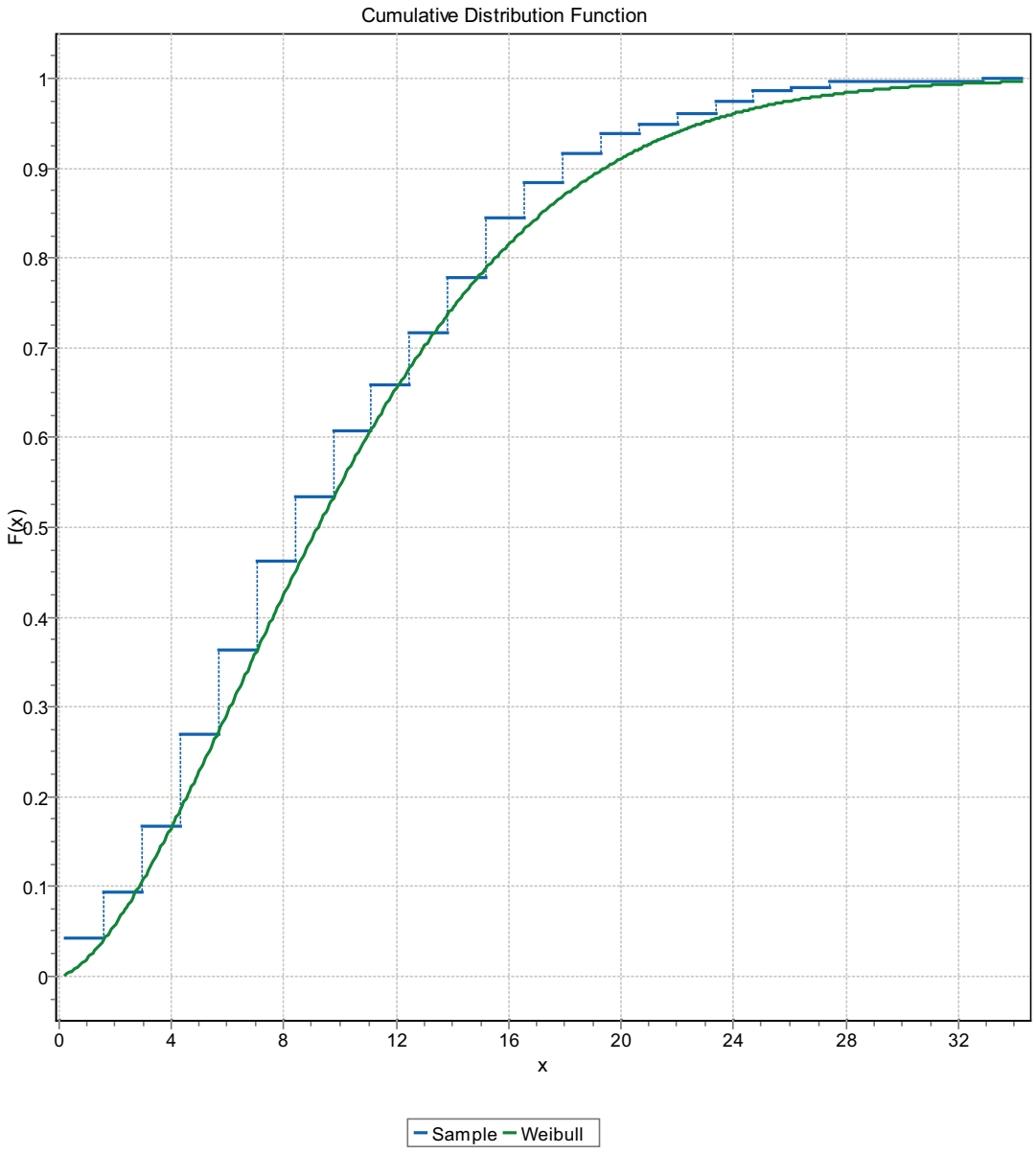

Figure F-72. *CDF, Domain FSM_W, 9 m bins, Weibull Distribution.*

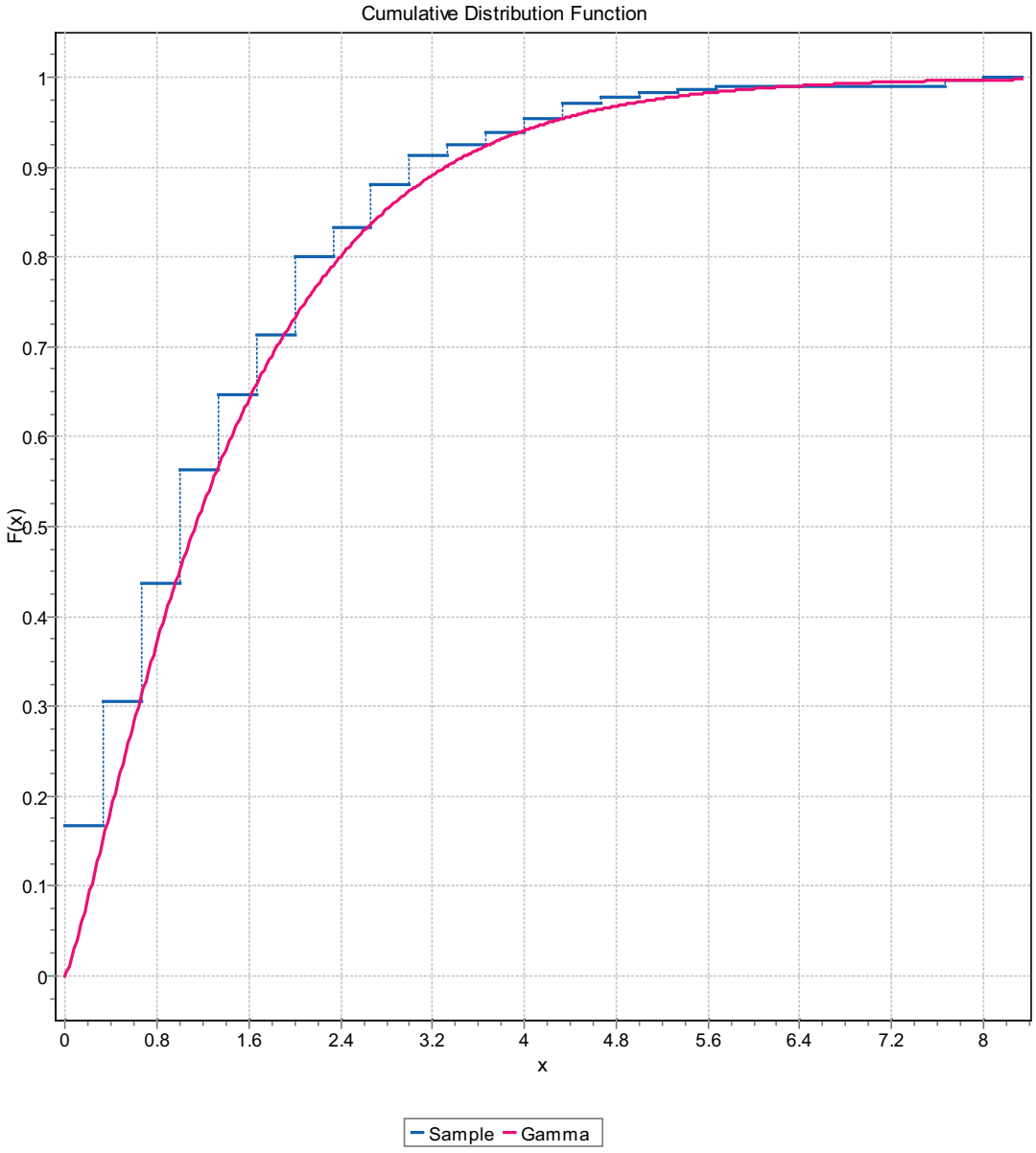

Figure F-73. *CDF, Domain FSM_W, 9 m bins, Gamma Distribution.*

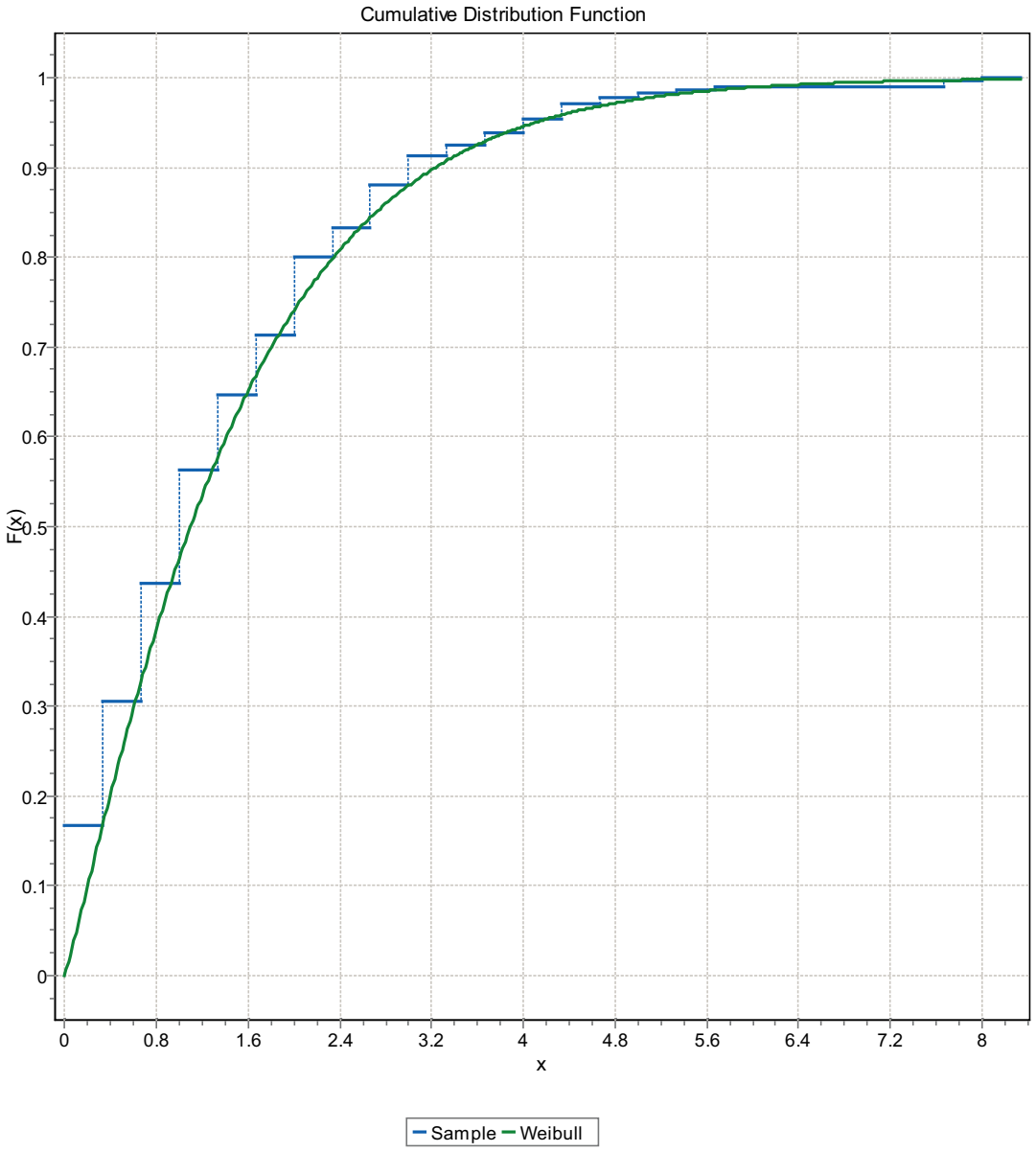

Figure F-74. *CDF, Domain FSM_W, 9 m bins, Weibull Distribution.*

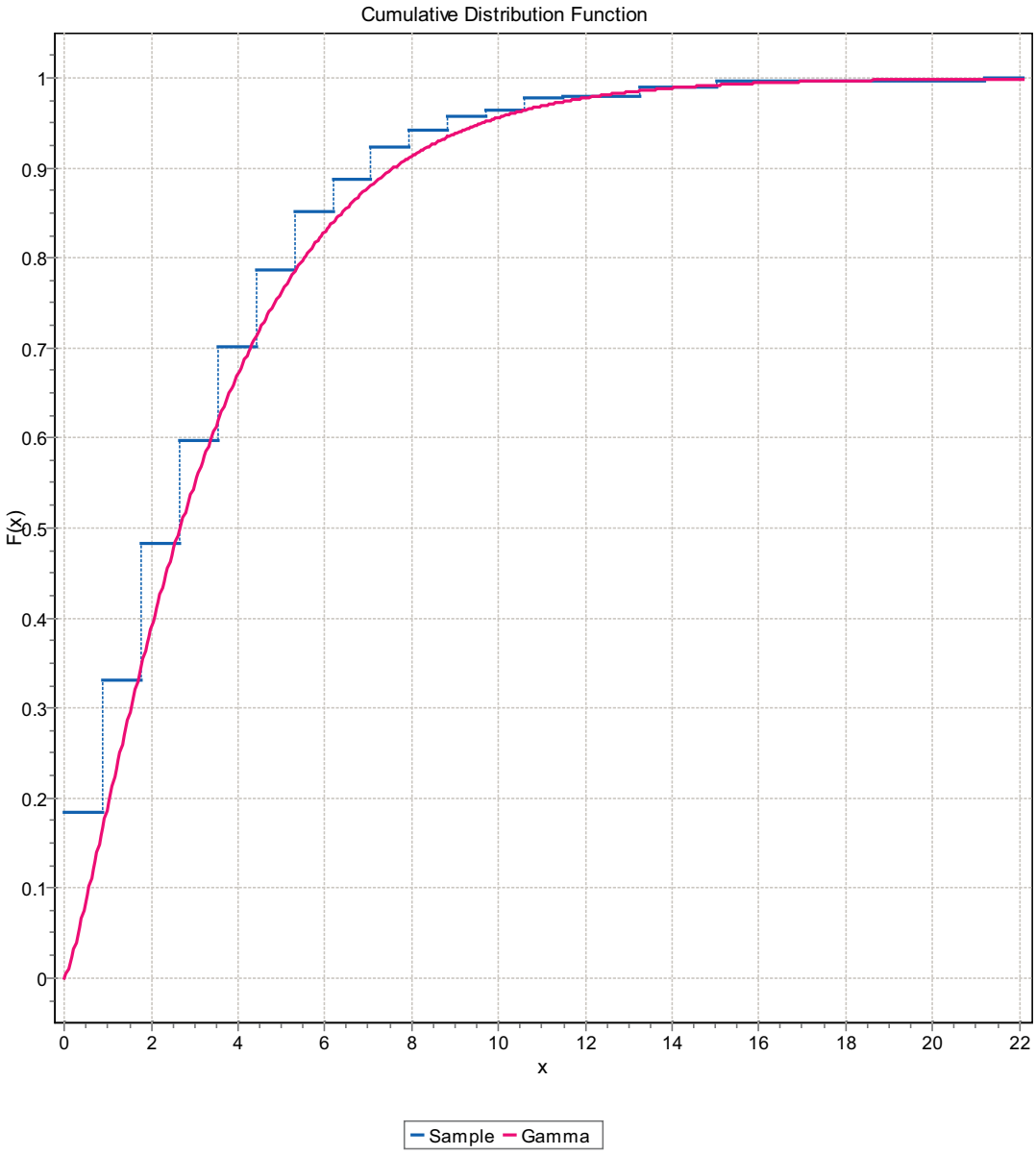

Figure F-75. *CDF, Domain FSM_W, 9 m bins, Gamma Distribution.*

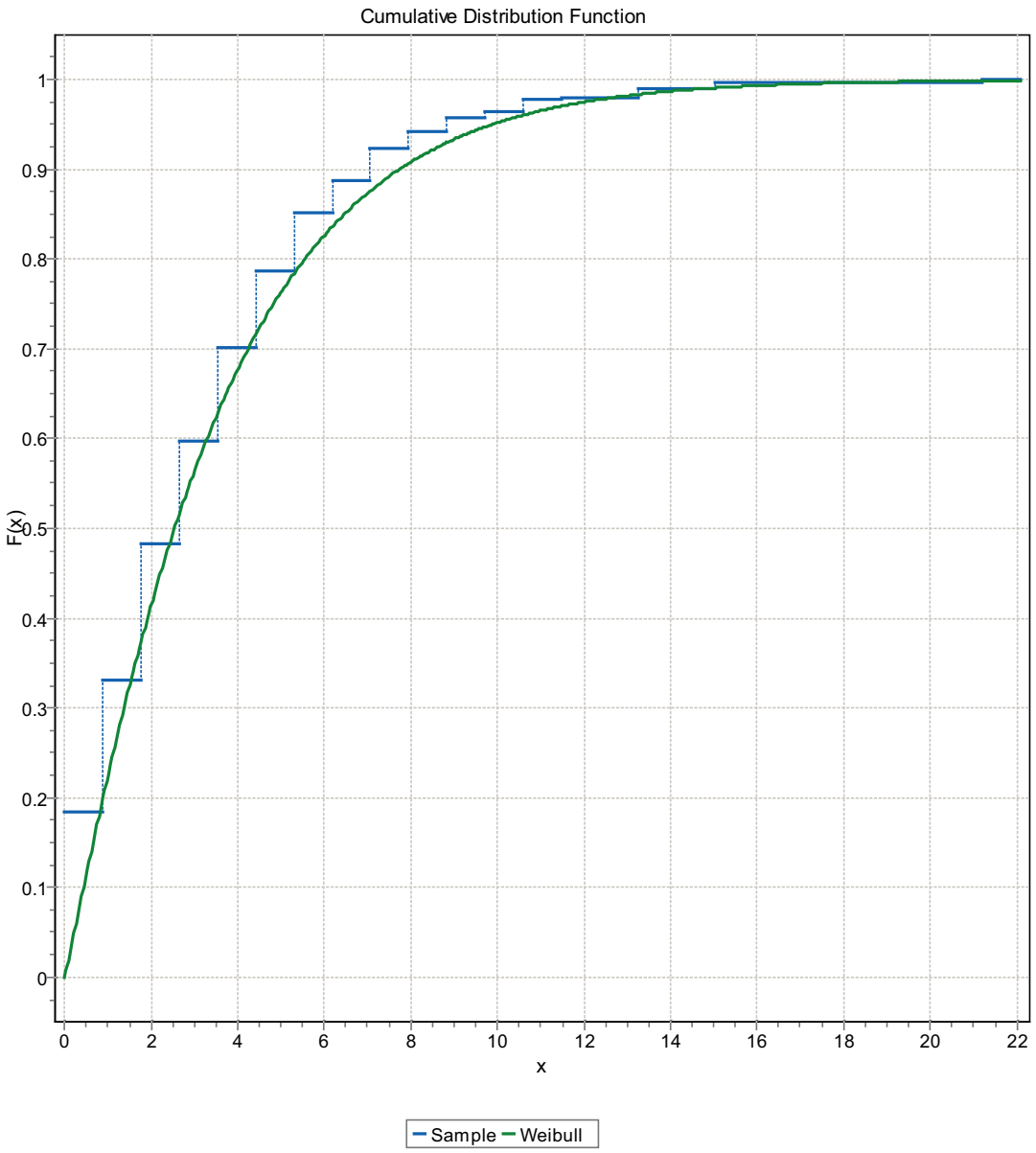

Figure F-76. *CDF, Domain FSM_W, 9 m bins, Weibull Distribution.*

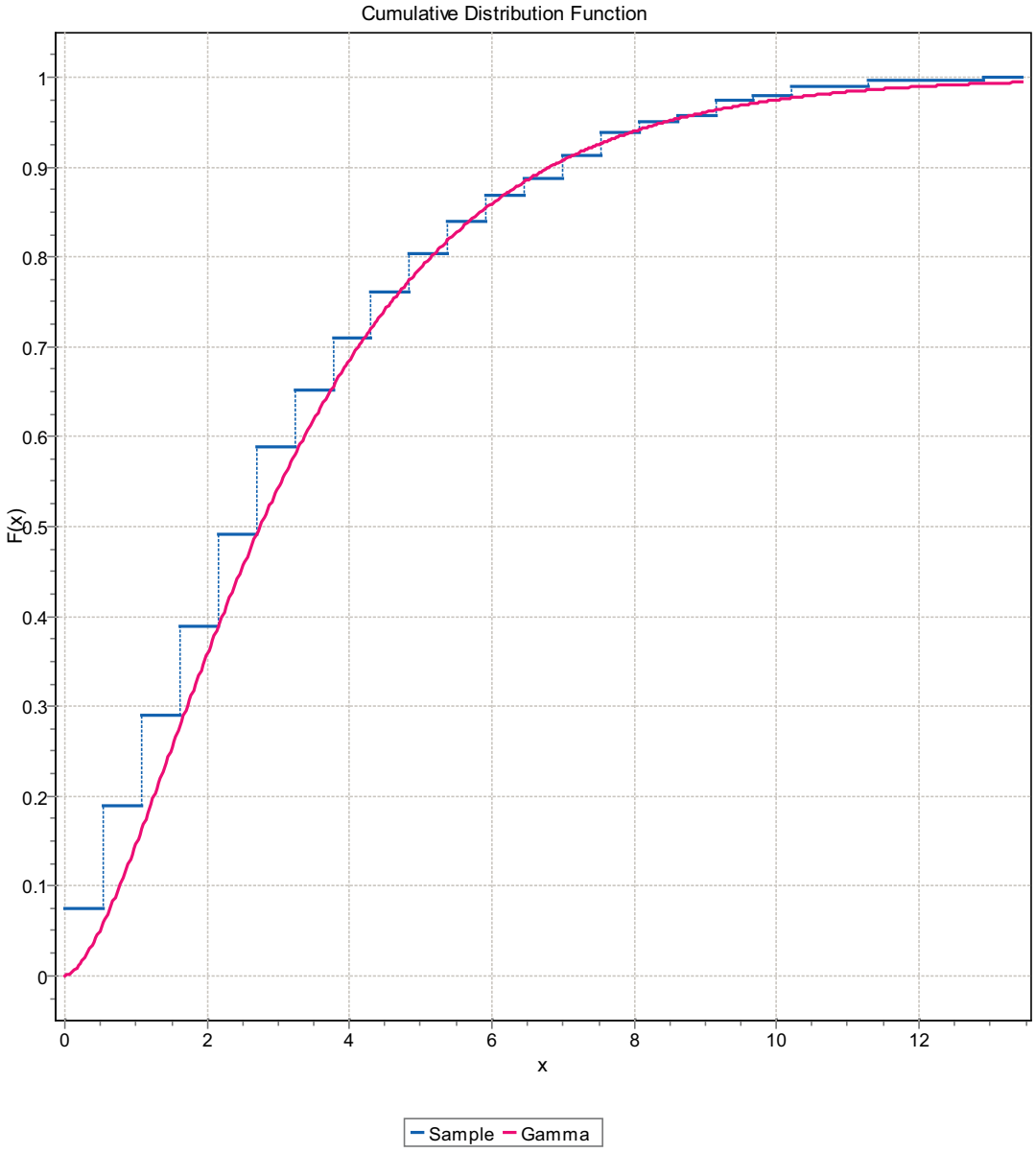

Figure F-77. *CDF, Domain FSM_W, 9 m bins, Gamma Distribution.*

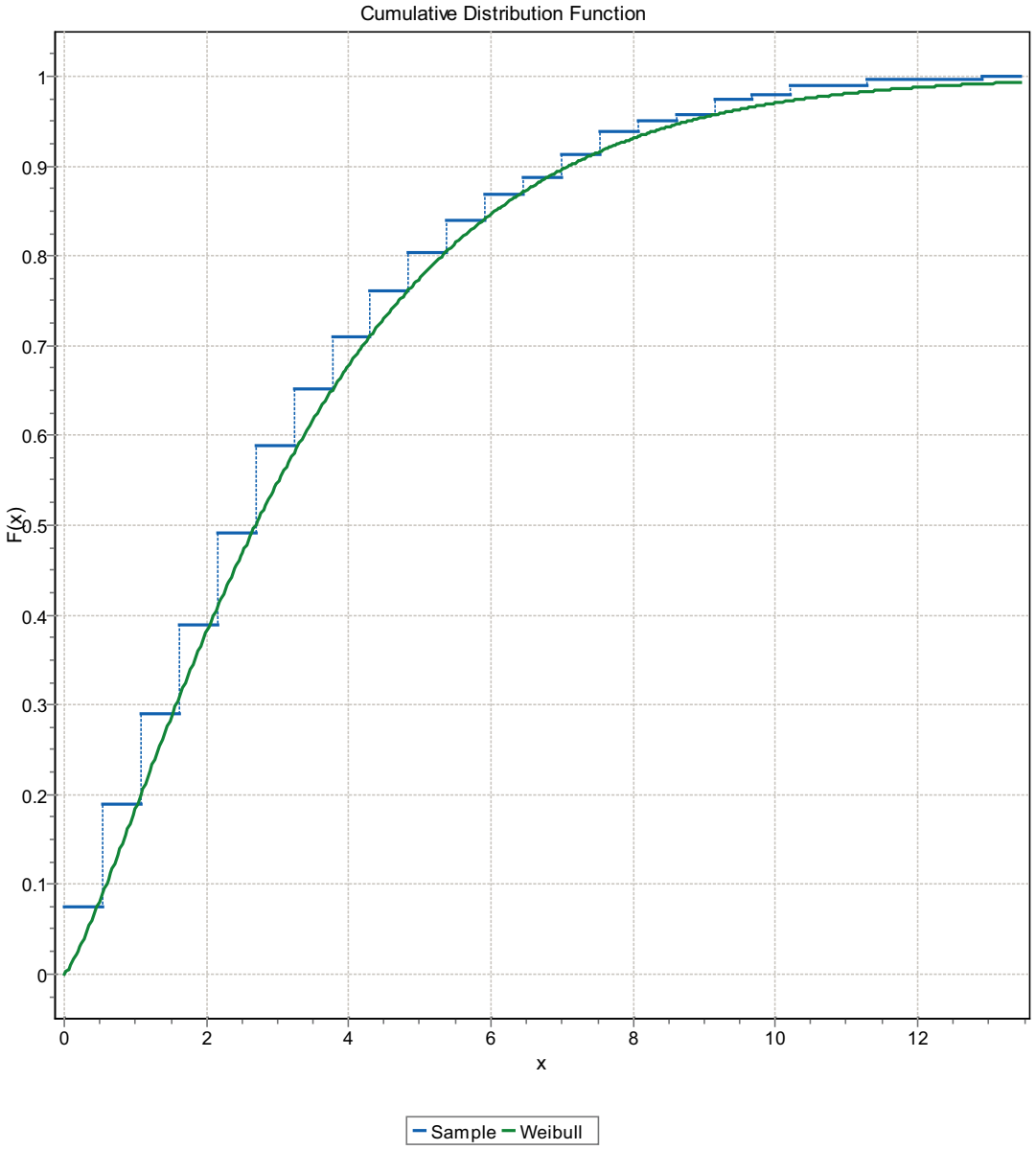

Figure F-78. *CDF, Domain FSM_W, 9 m bins, Weibull Distribution.*

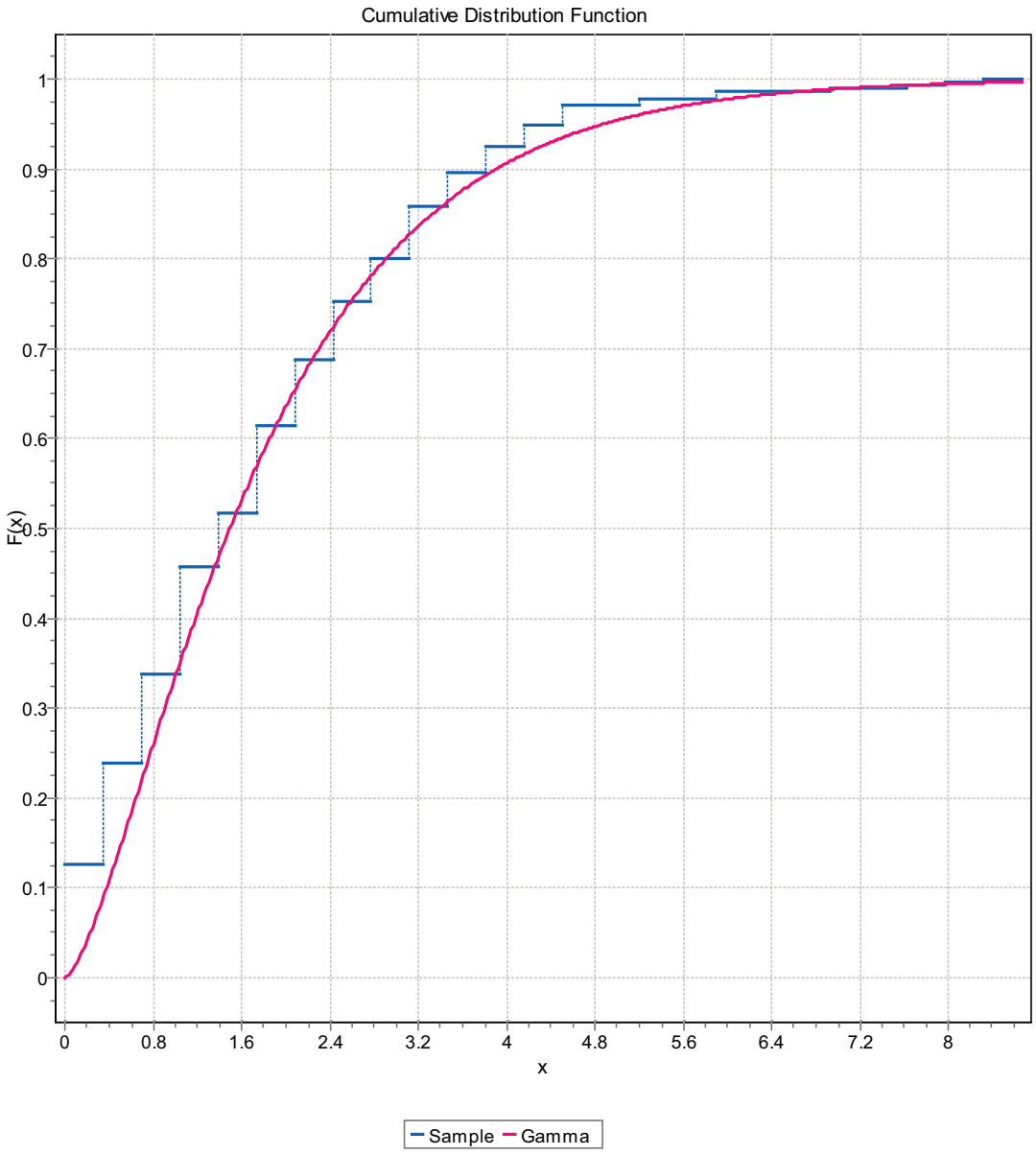

Figure F-79. *CDF, Domain FSM_W, 9 m bins, Gamma Distribution.*

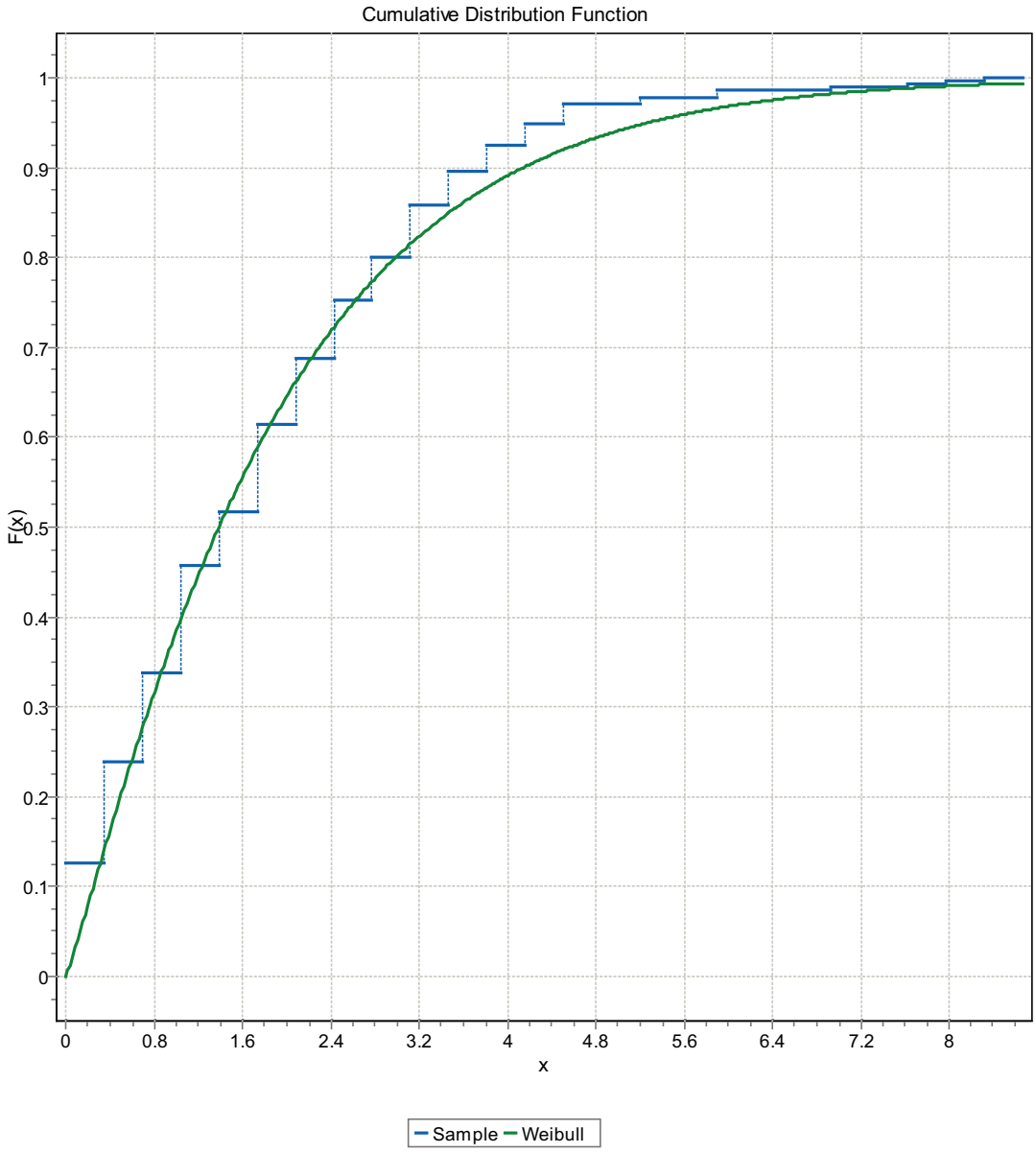

Figure F-80. *CDF, Domain FSM_W, 9 m bins, Weibull Distribution.*

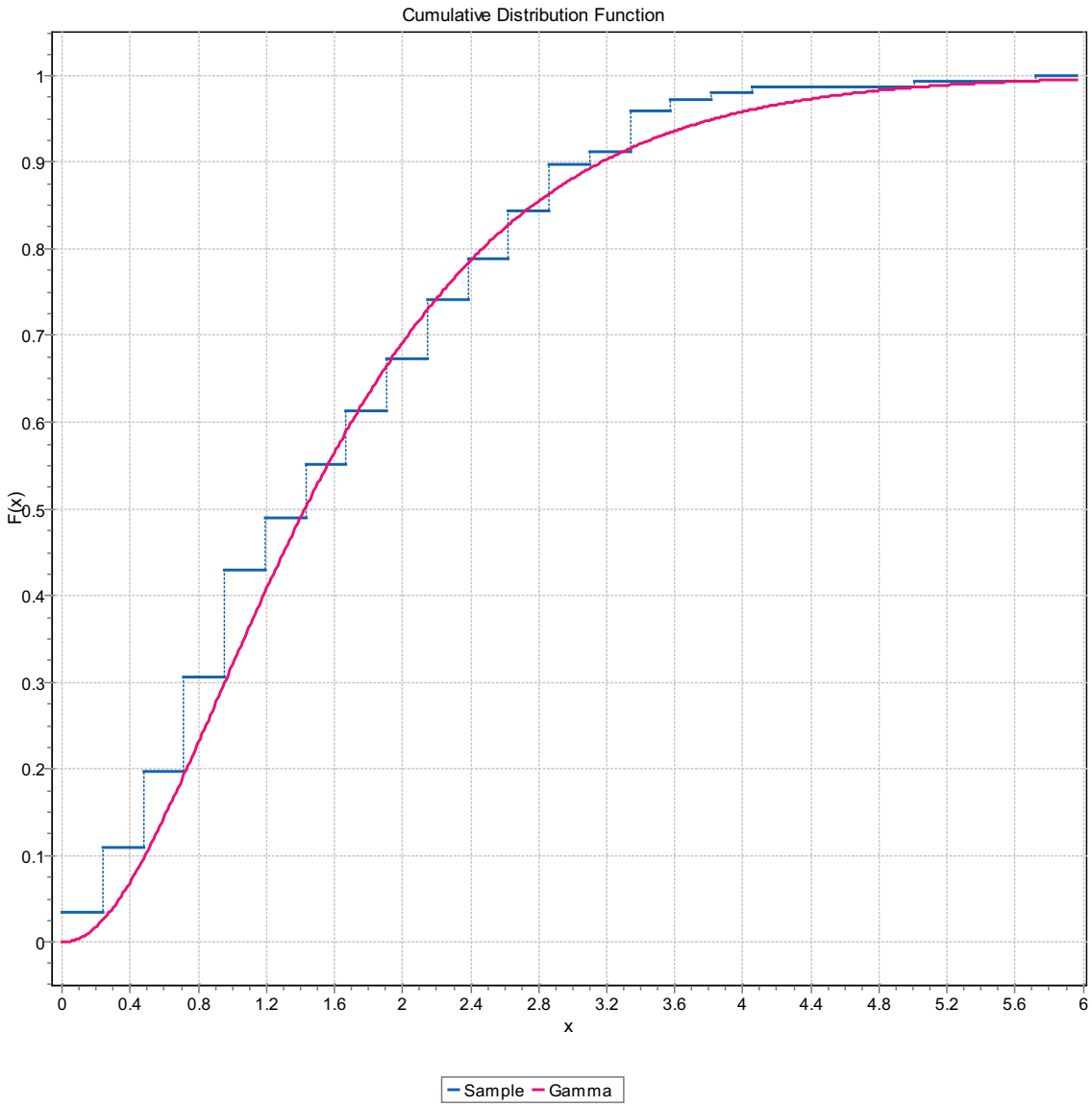

Figure F-81. *CDF, Domain FSM_C, 15 m bins, Gamma Distribution.*

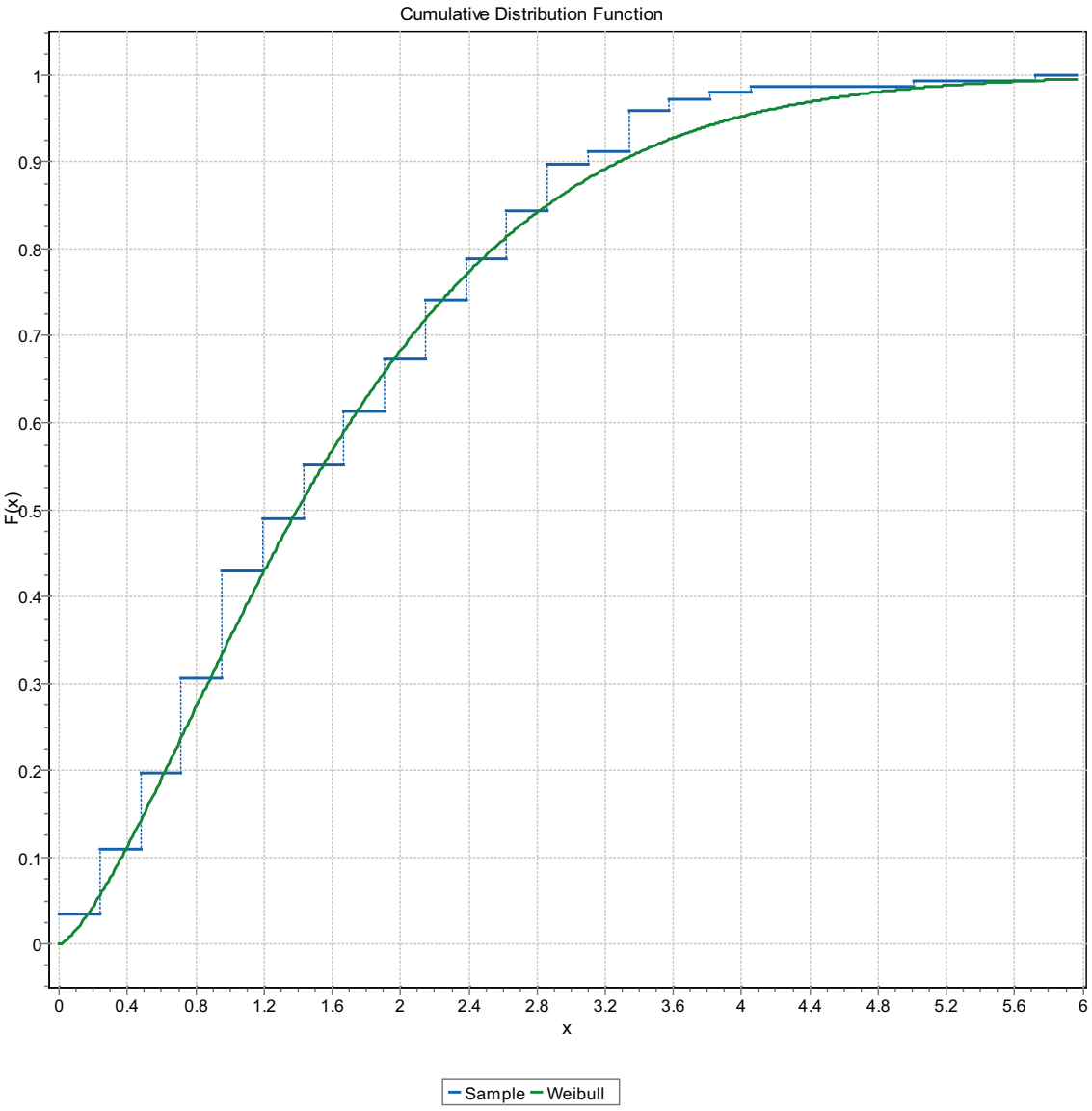

Figure F-82. *CDF, Domain FSM_C, 15 m bins, Weibull Distribution.*

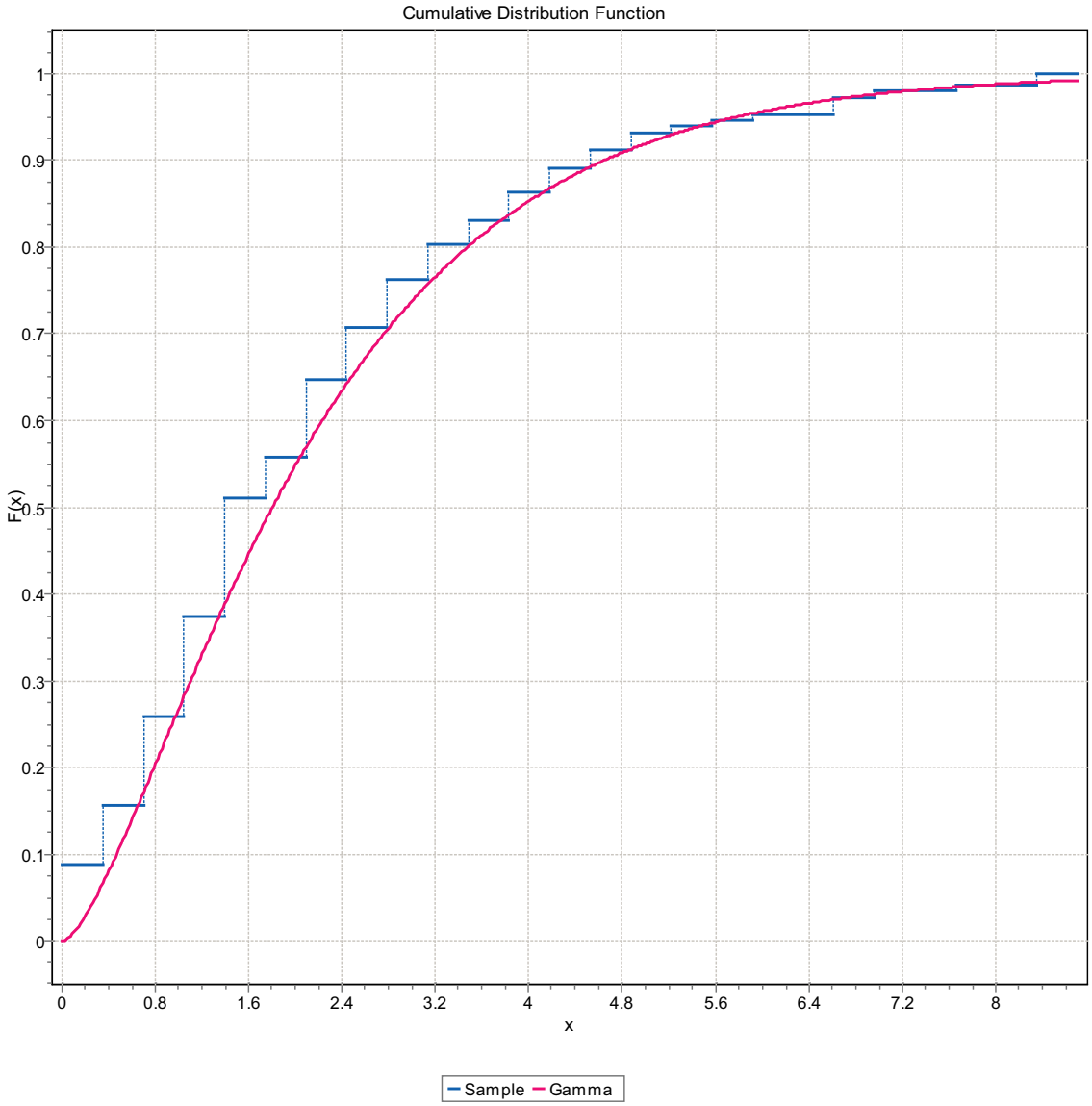

Figure F-83. *CDF, Domain FSM_C, 15 m bins, Gamma Distribution.*

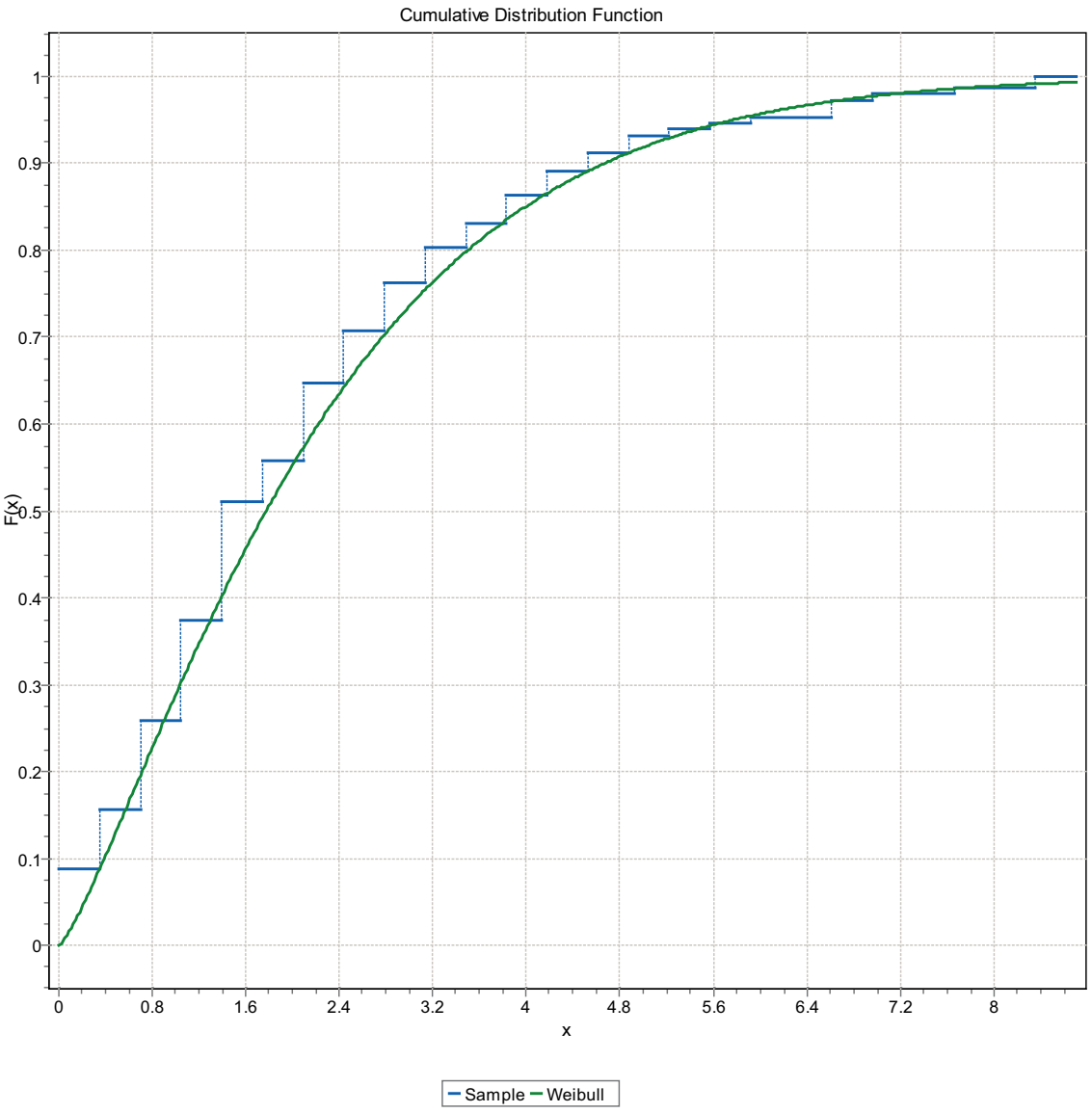

Figure F-84. *CDF, Domain FSM_C, 15 m bins, Weibull Distribution.*

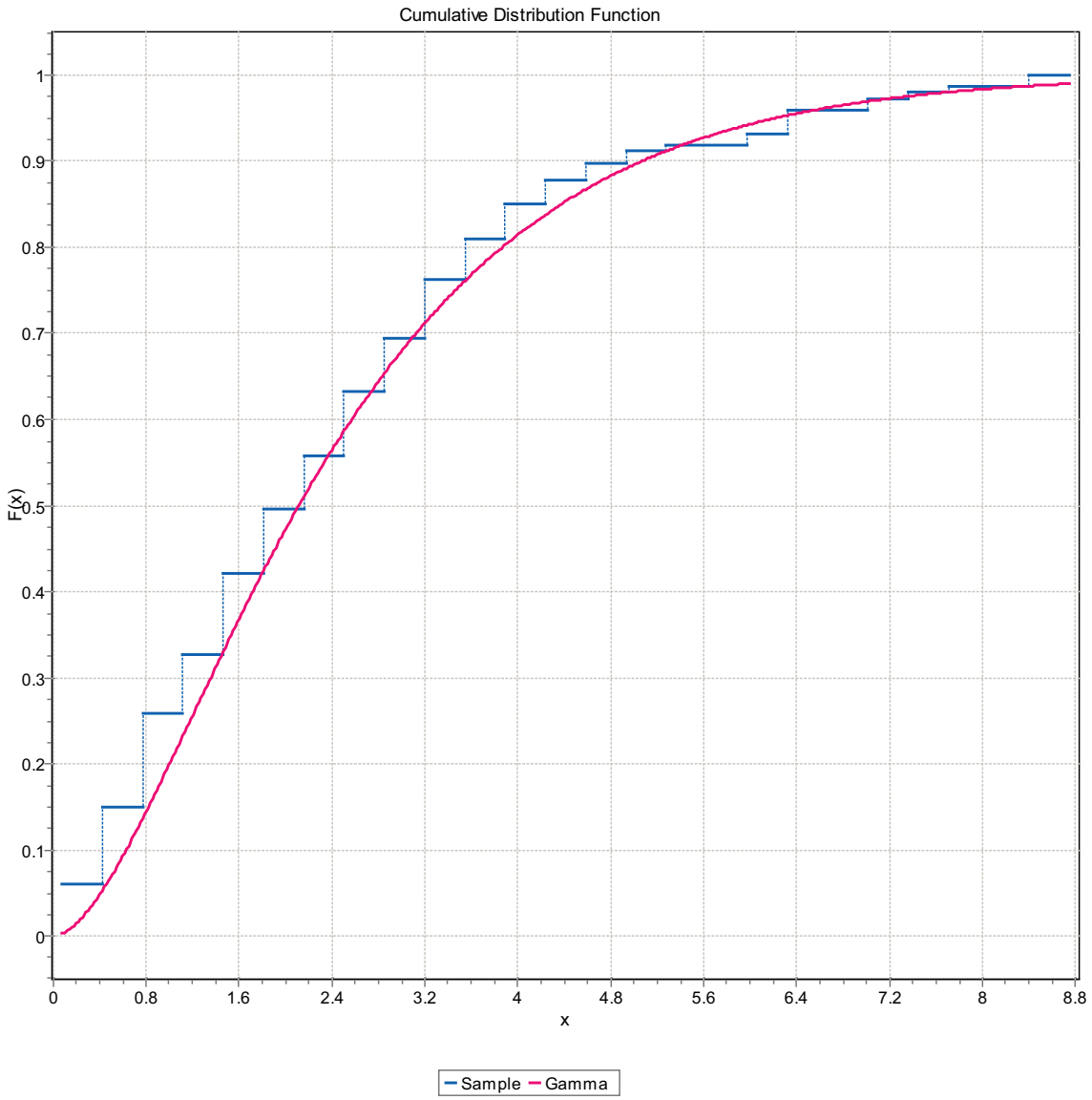

Figure F-85. *CDF, Domain FSM_C, 15 m bins, Gamma Distribution.*

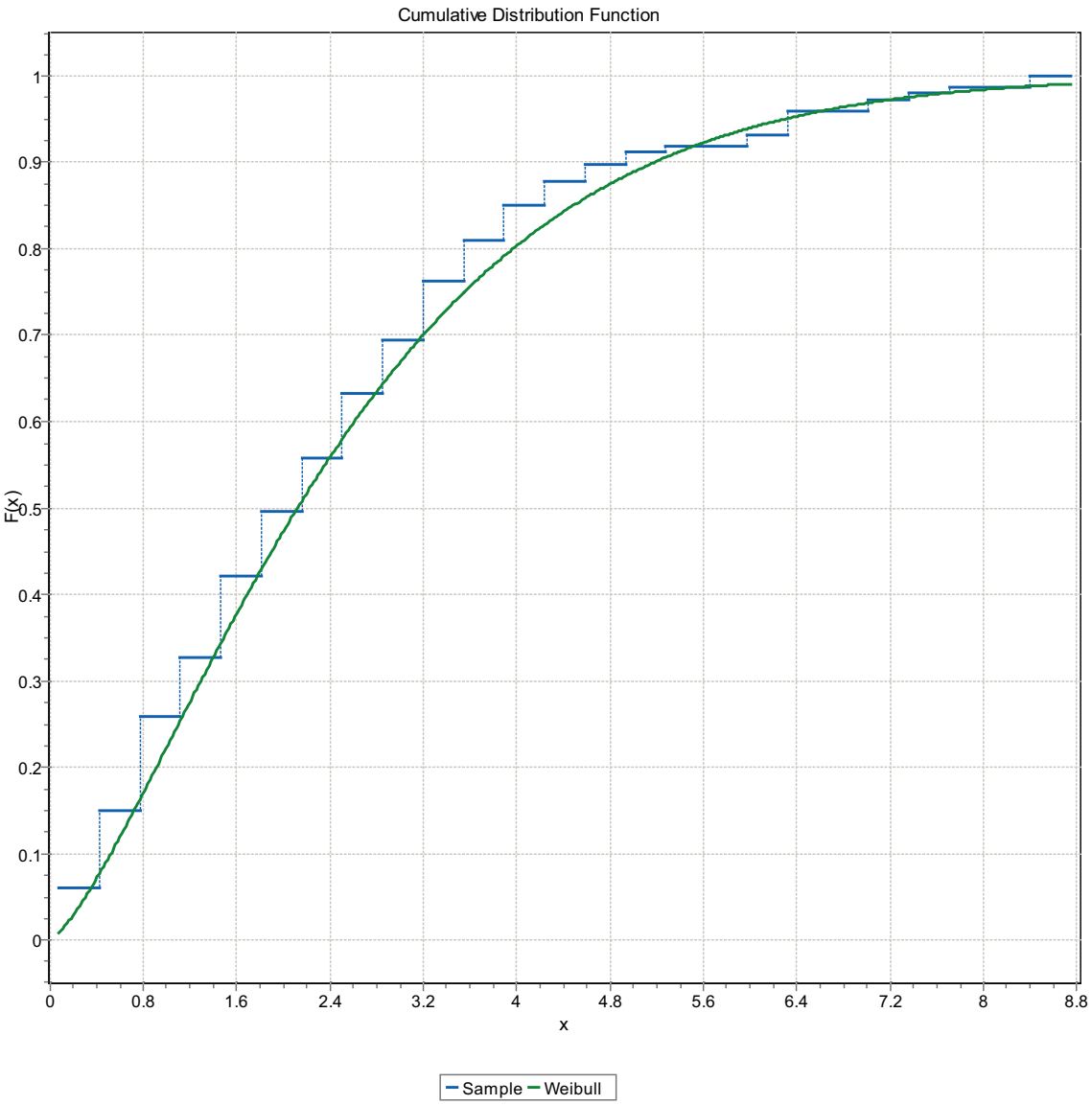

Figure F-86. *CDF, Domain FSM_C, 15 m bins, Weibull Distribution.*

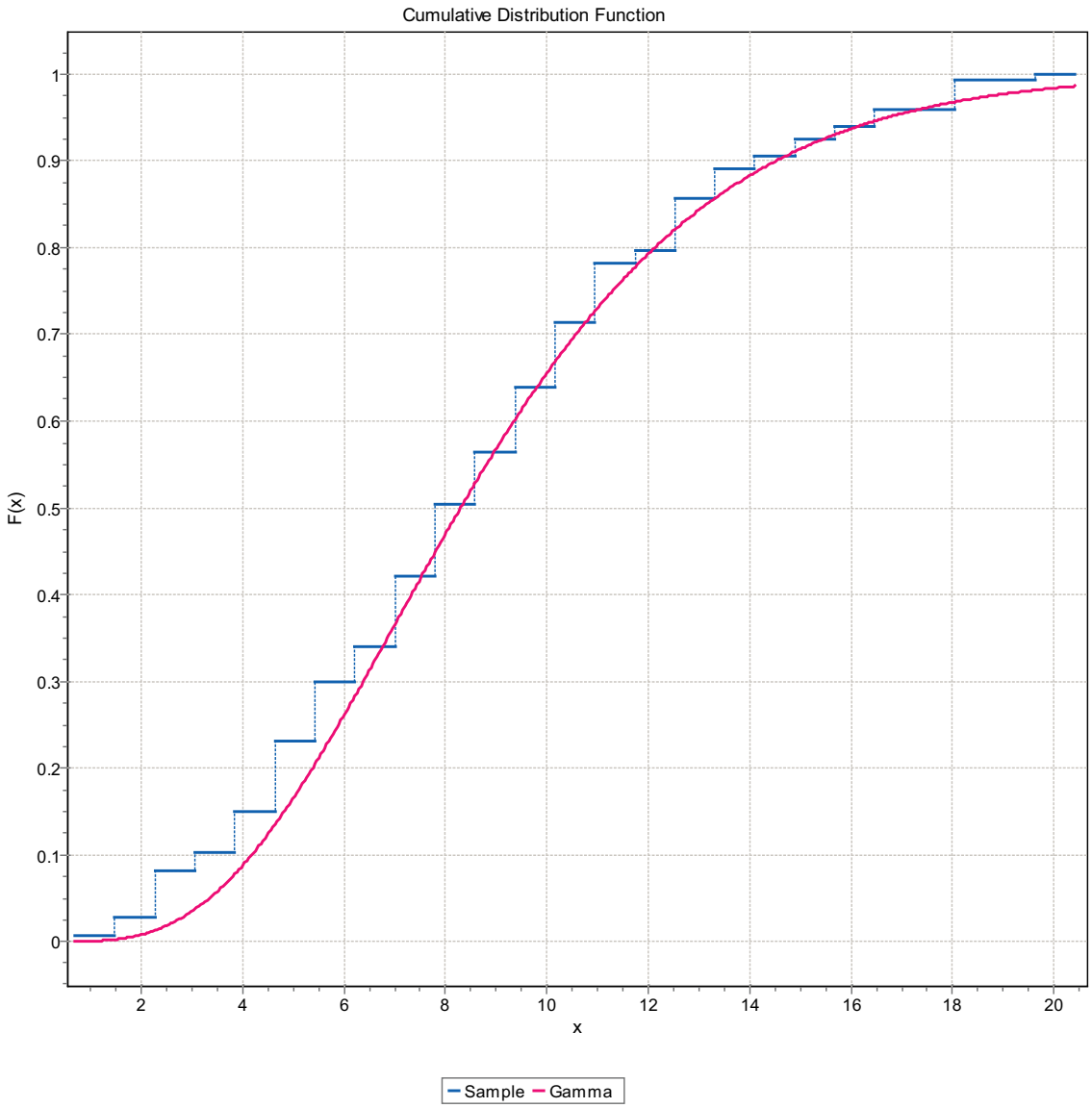

Figure F-87. *CDF, Domain FSM_C, 15 m bins, Gamma Distribution.*

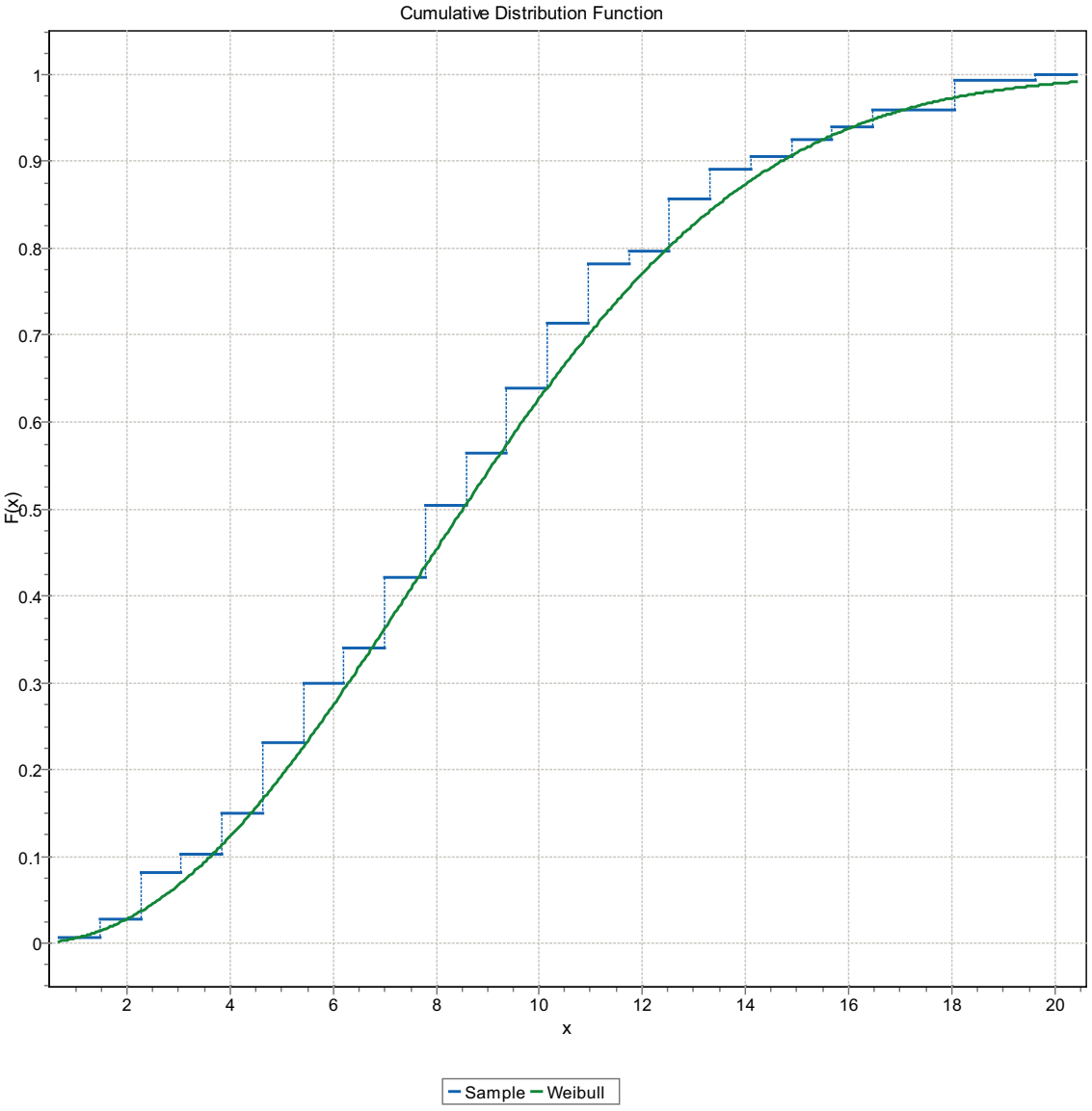

Figure F-88. *CDF, Domain FSM_C, 15 m bins, Wiebull Distribution.*

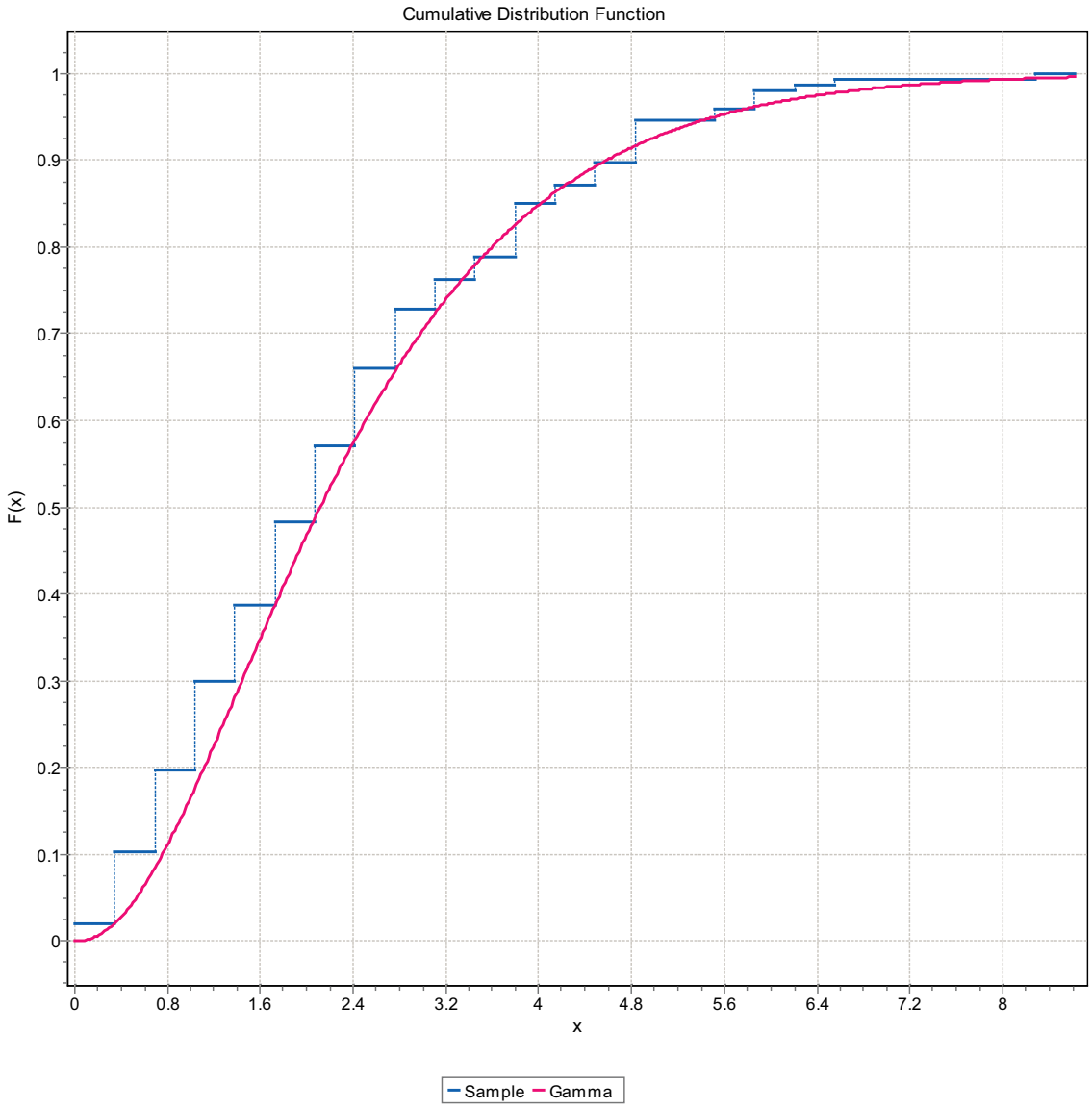

Figure F-89. *CDF, Domain FSM_C, 15 m bins, Gamma Distribution.*

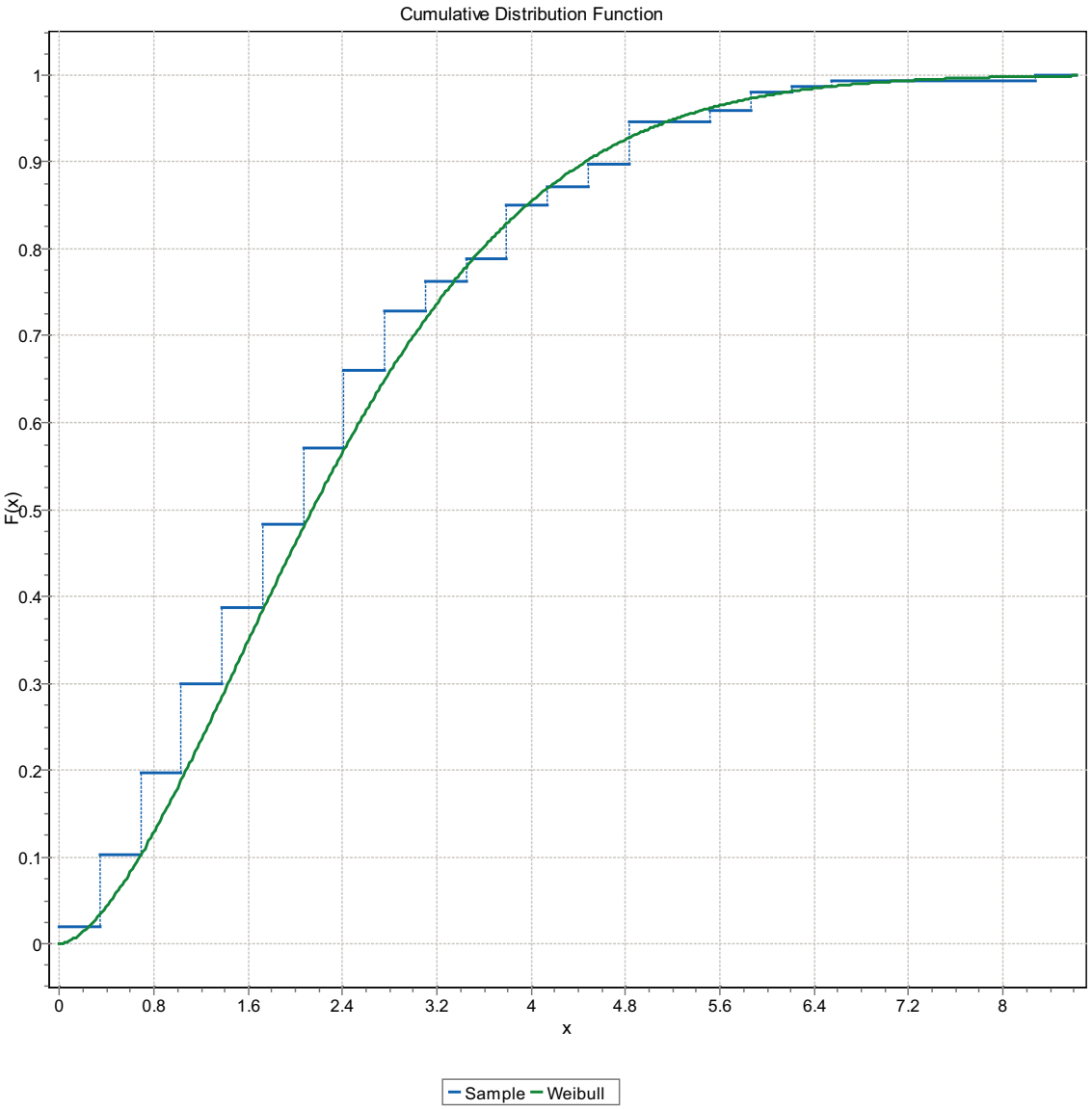

Figure F-90. *CDF, Domain FSM_C, 15 m bins, Weibull Distribution.*

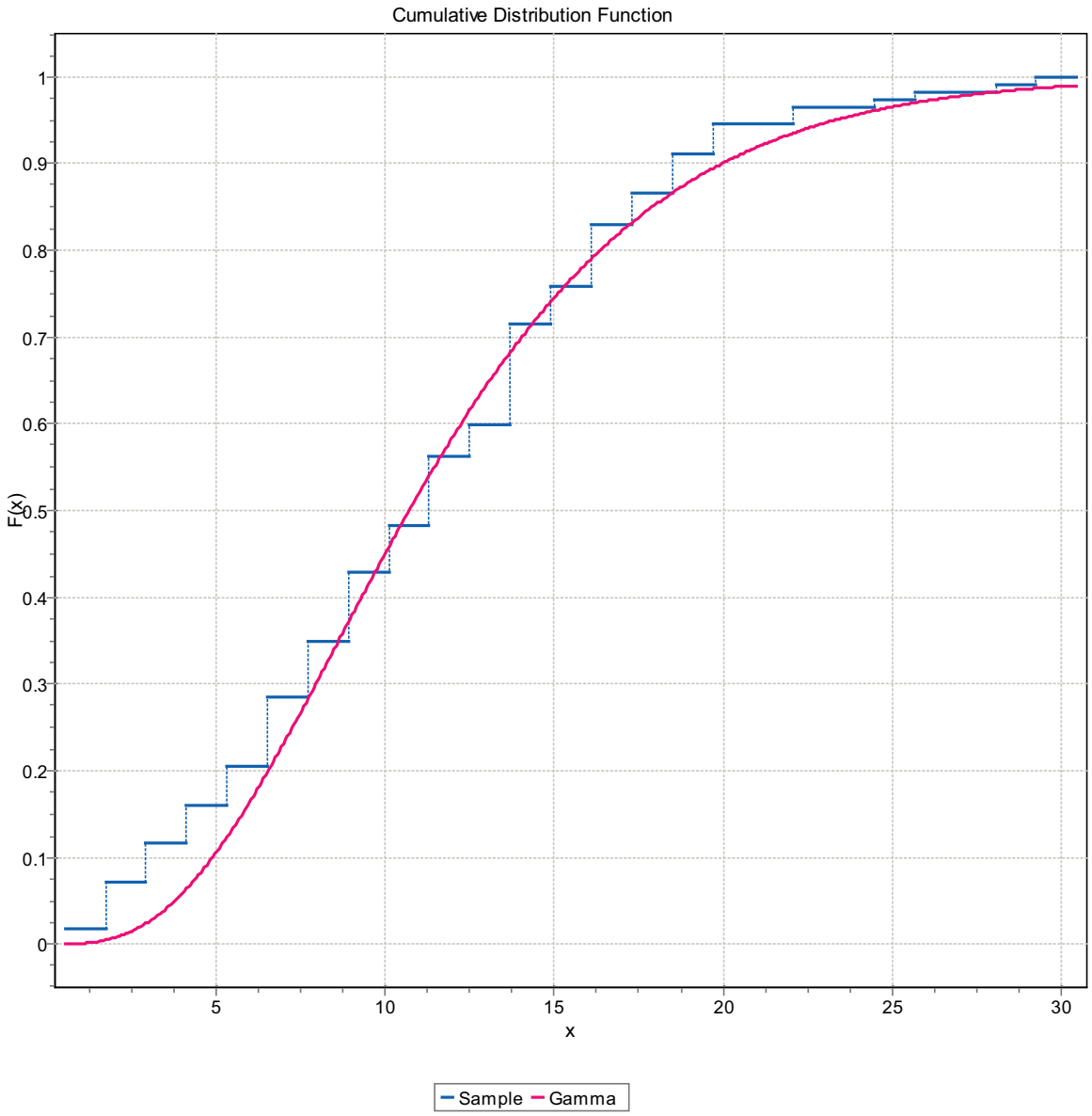

Figure F-91. *CDF, Domain FSM_EW007, 15 m bins, Gamma Distribution.*

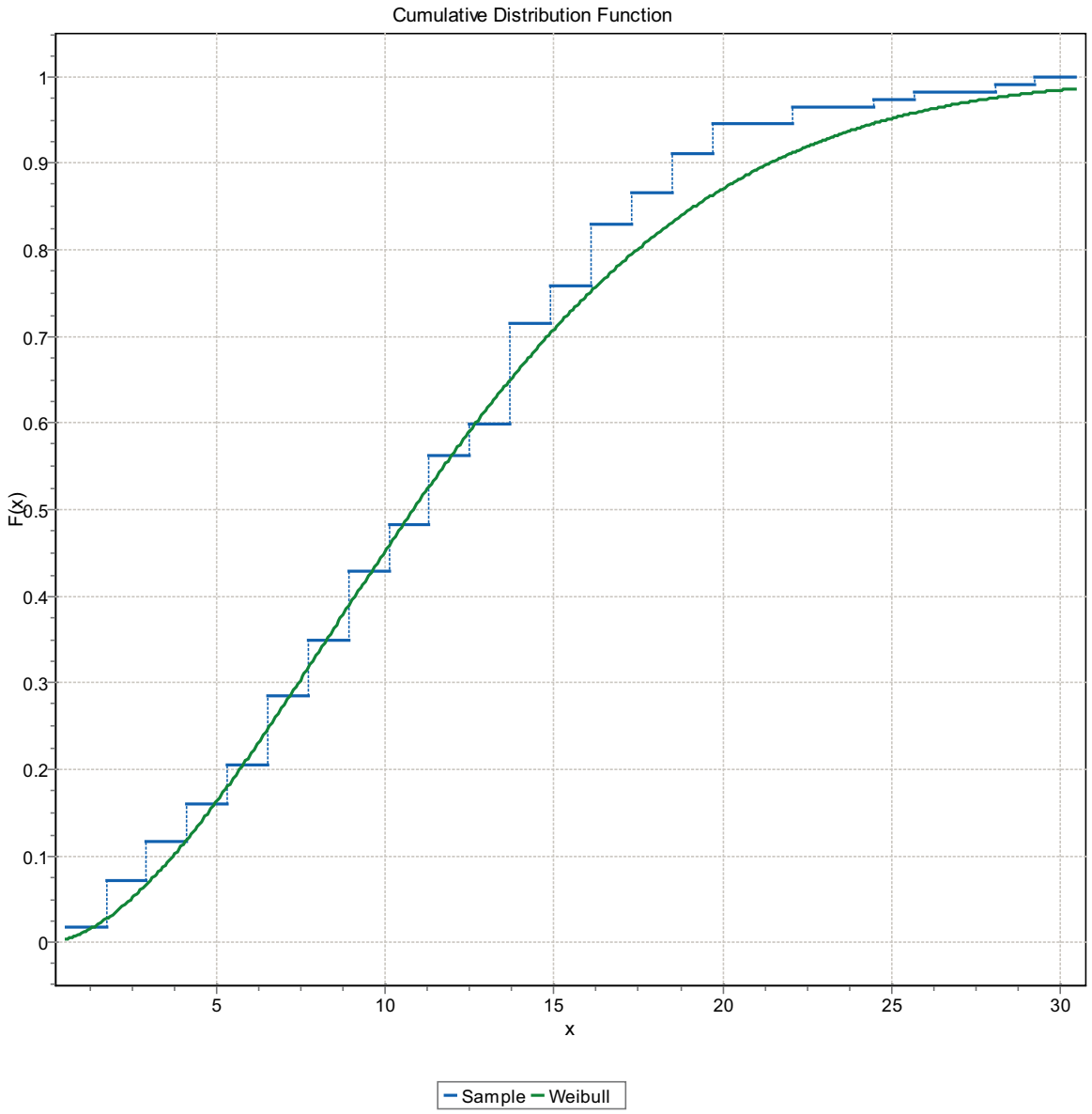

Figure F-92. *CDF, Domain FSM_EW007, 15 m bins, Weibull Distribution.*

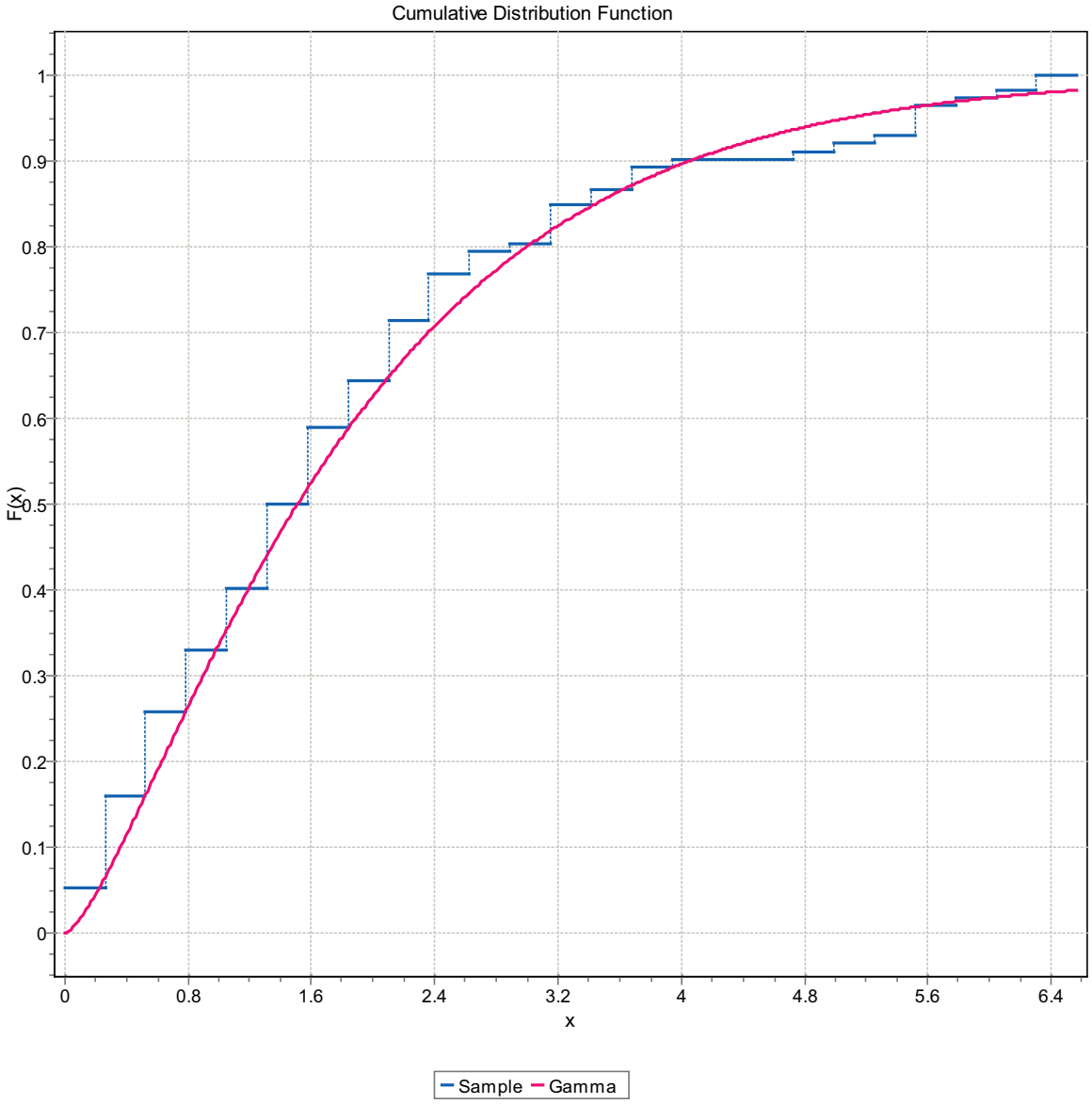

Figure F-93. *CDF, Domain FSM_EW007, 15 m bins, Gamma Distribution.*

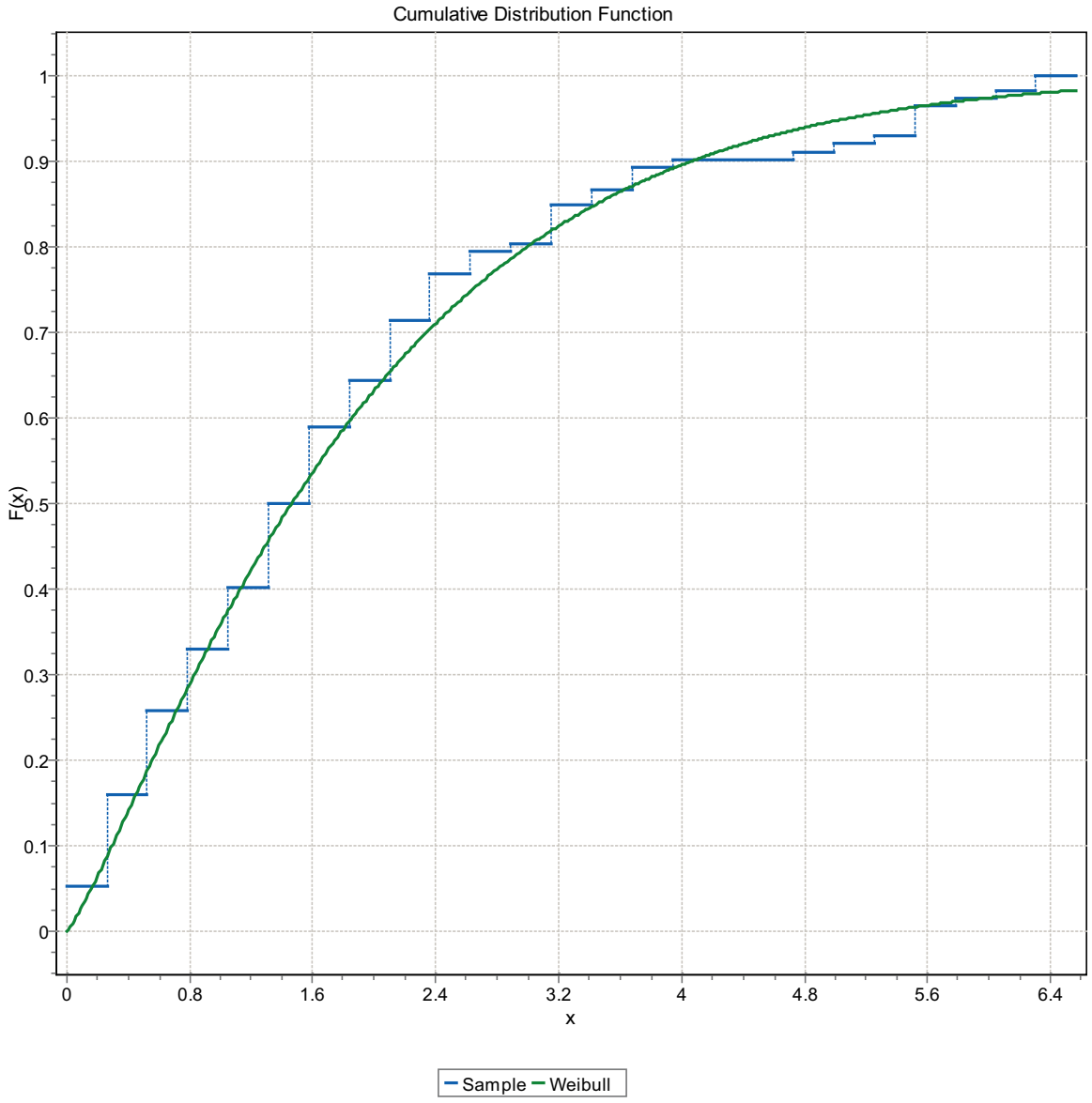

Figure F-94. *CDF, Domain FSM_EW007, 15 m bins, Weibull Distribution.*

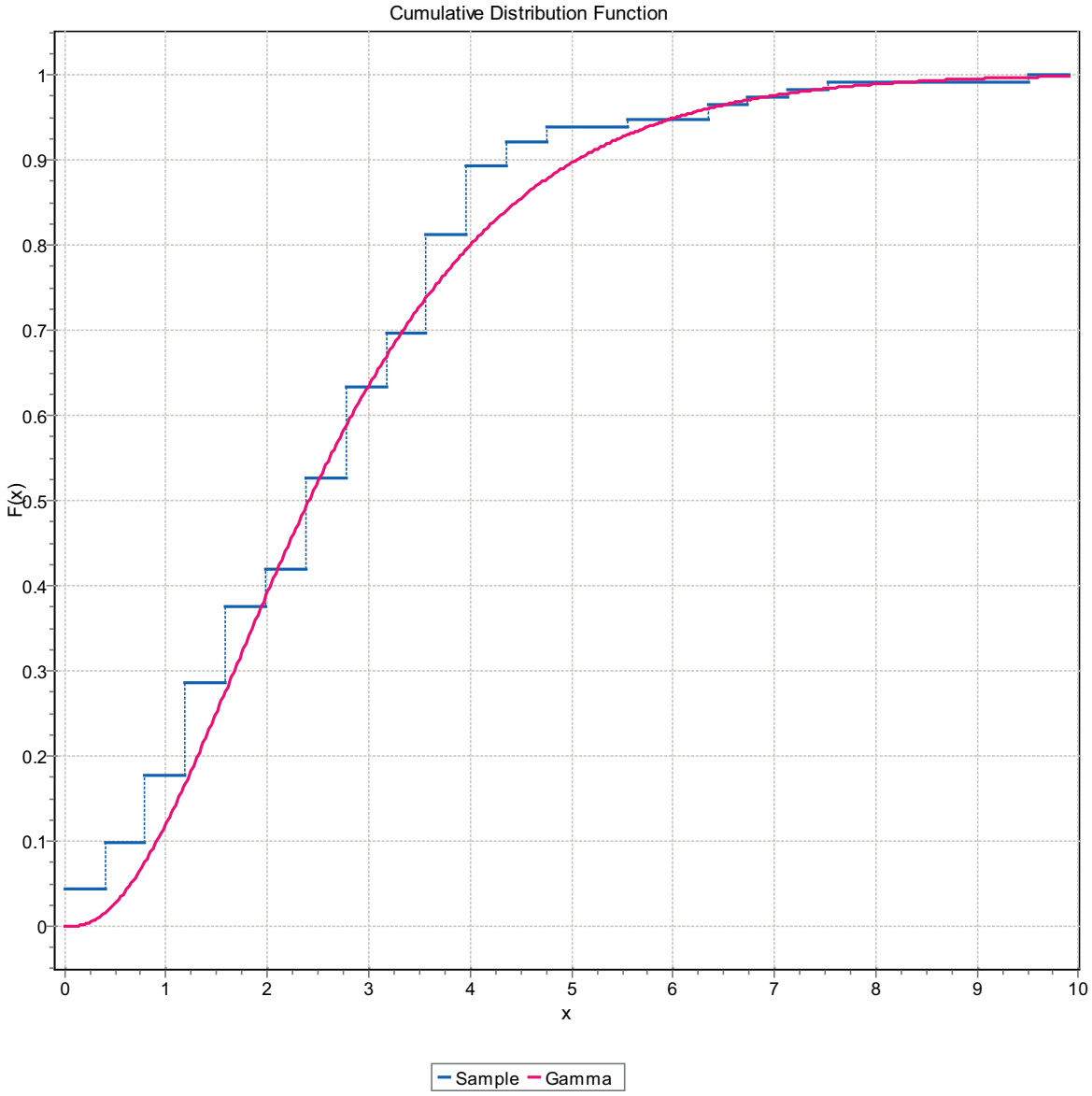

Figure F-95. *CDF, Domain FSM_EW007, 15 m bins, Gamma Distribution.*

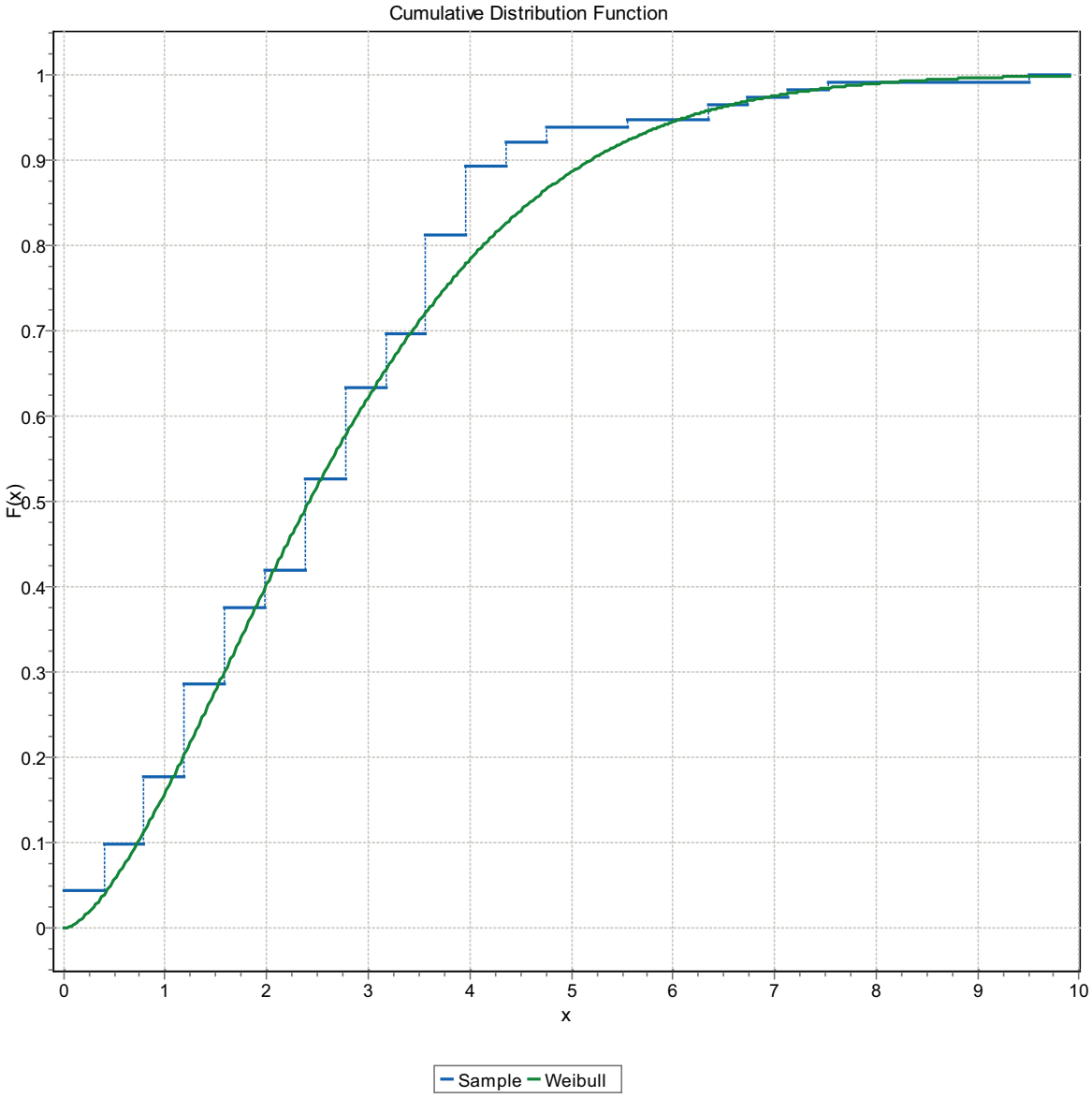

Figure F-96. *CDF, Domain FSM_EW007, 15 m bins, Weibull Distribution.*

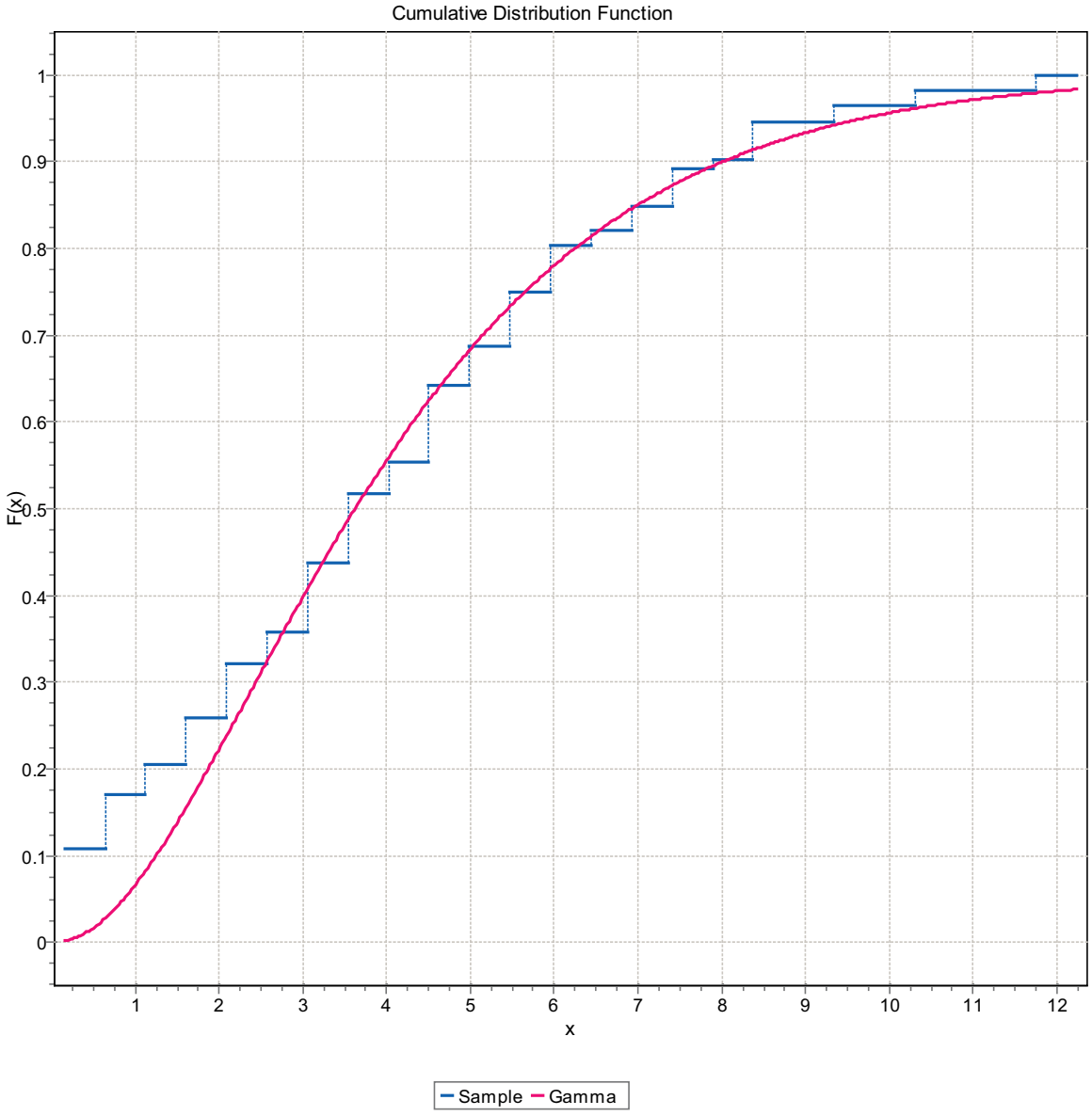

Figure F-97. *CDF, Domain FSM_EW007, 15 m bins, Gamma Distribution.*

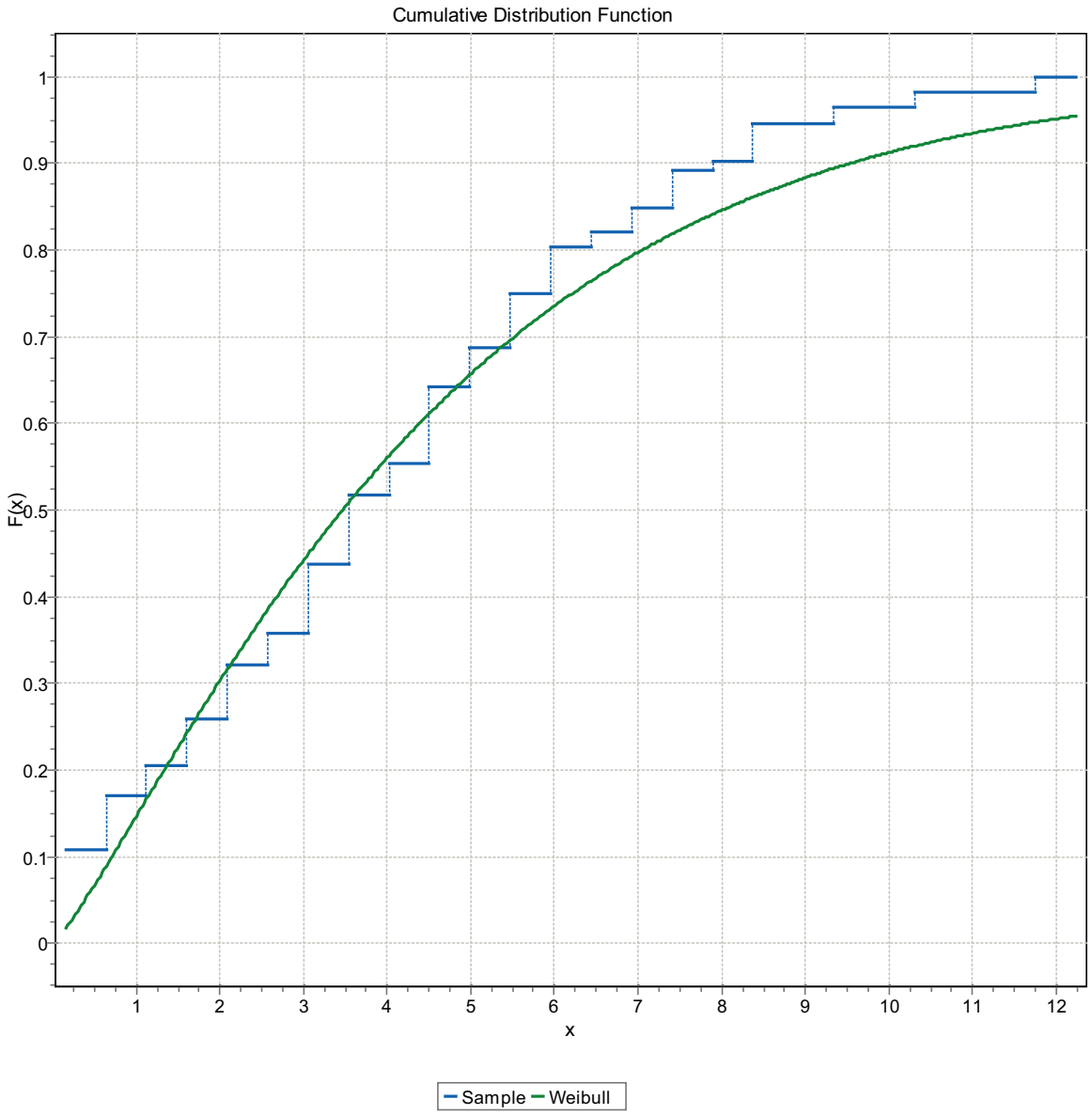

Figure F-98. *CDF, Domain FSM_EW007, 15 m bins, Weibull Distribution.*

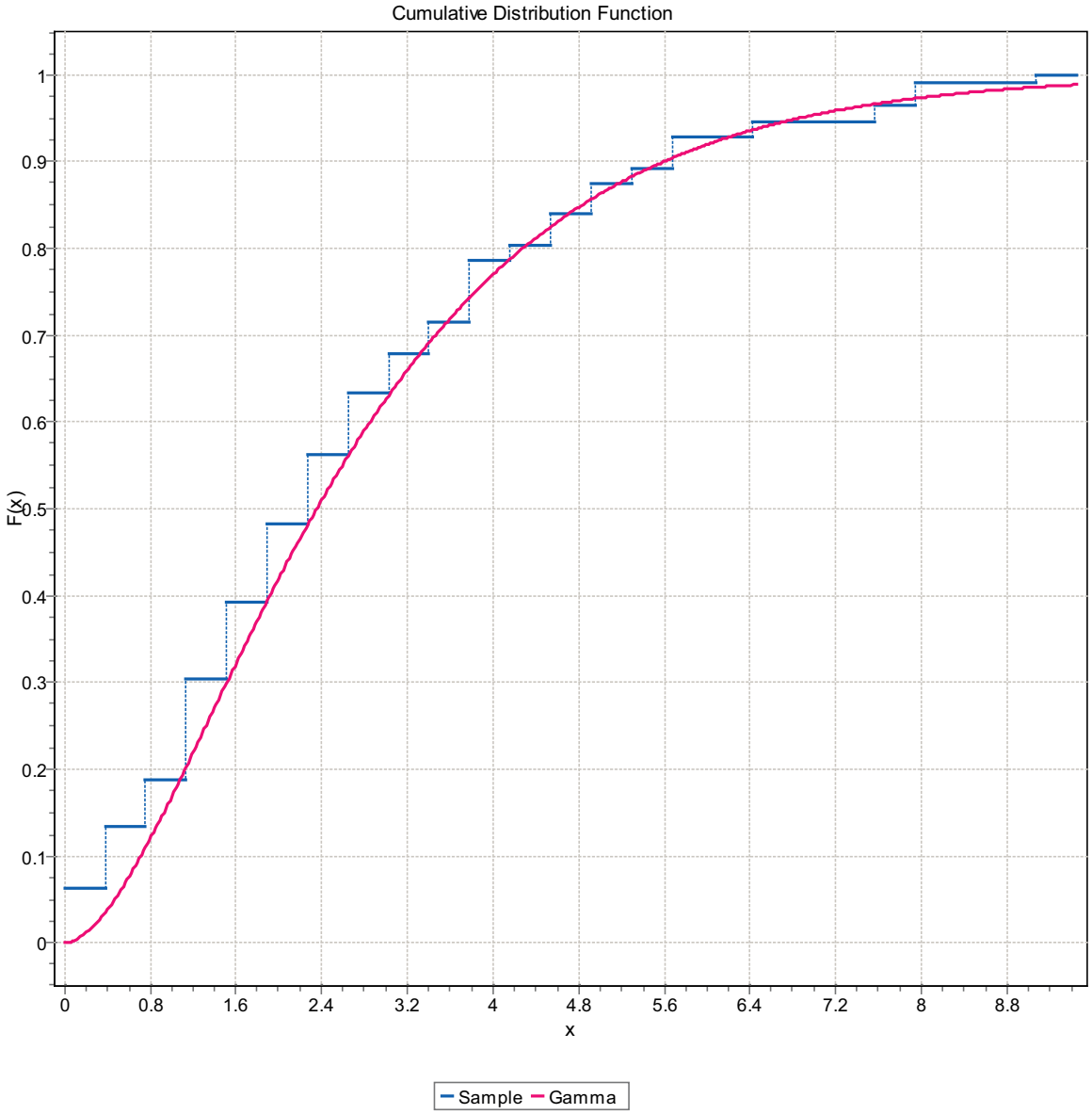

Figure F-99. *CDF, Domain FSM_EW007, 15 m bins, Gamma Distribution.*

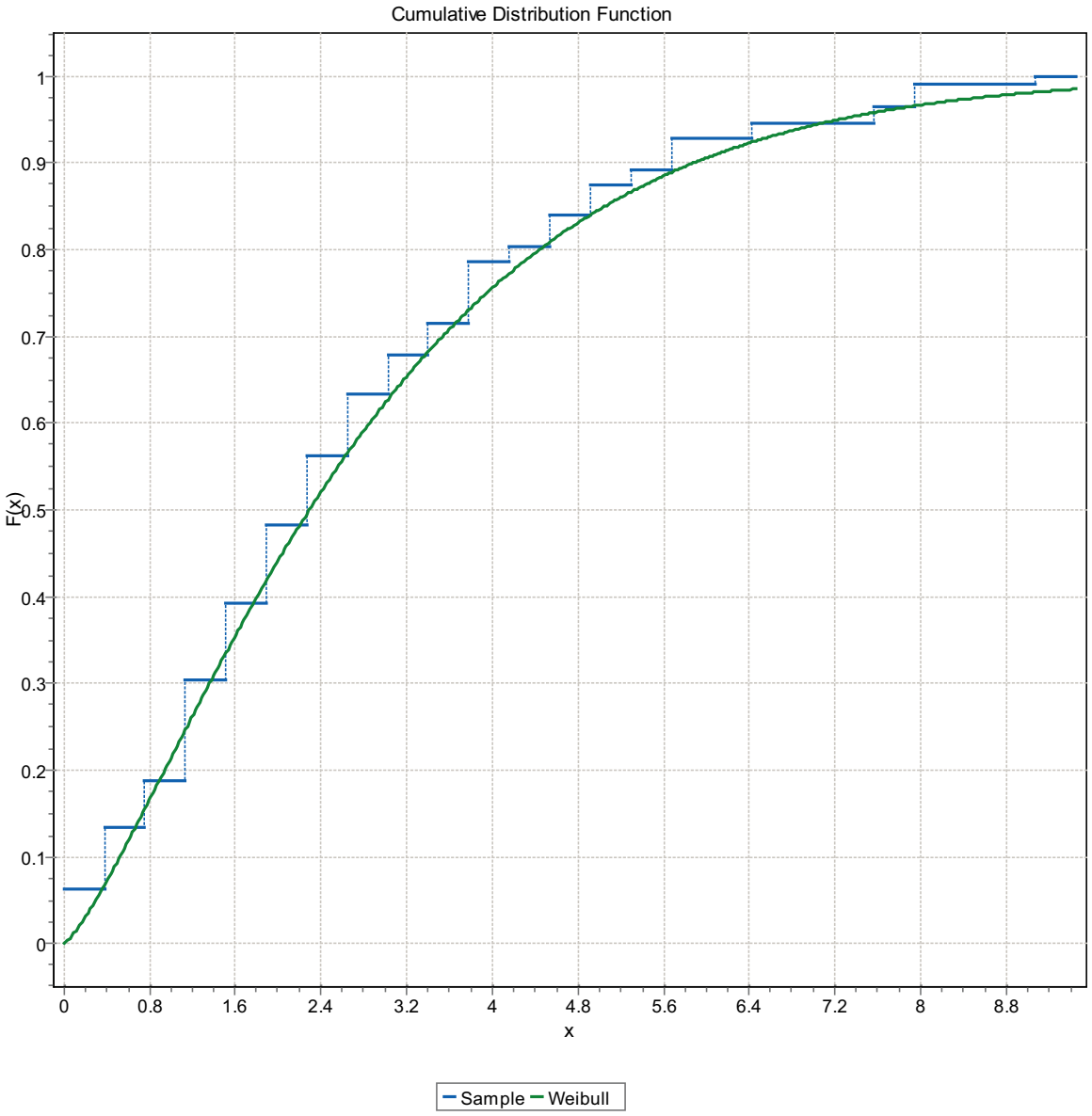

Figure F-100. *CDF, Domain FSM_EW007, 15 m bins, Weibull Distribution.*

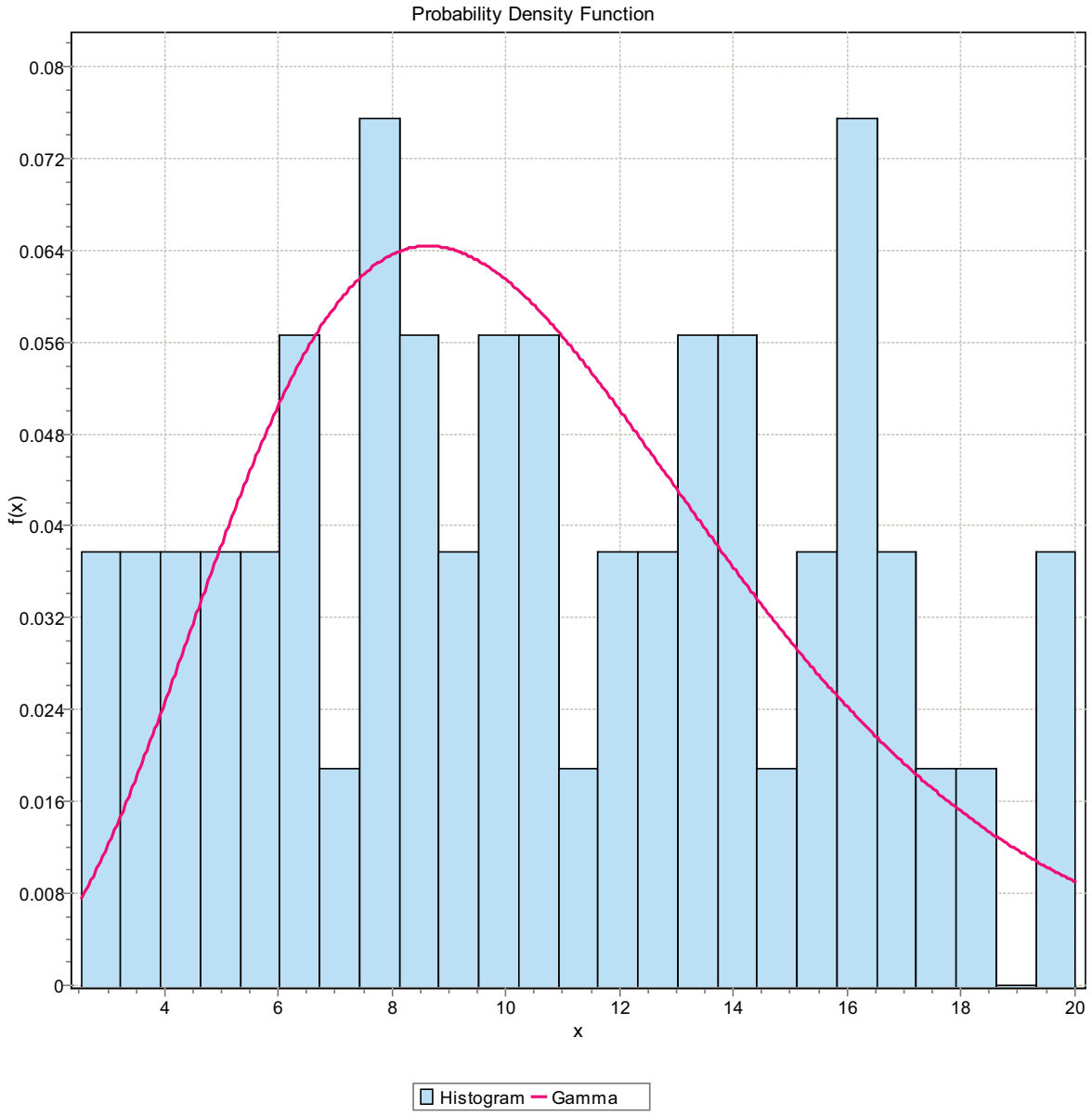

Figure F-101. *CDF, Domain FSM_NE005, 15 m bins, Gamma Distribution.*

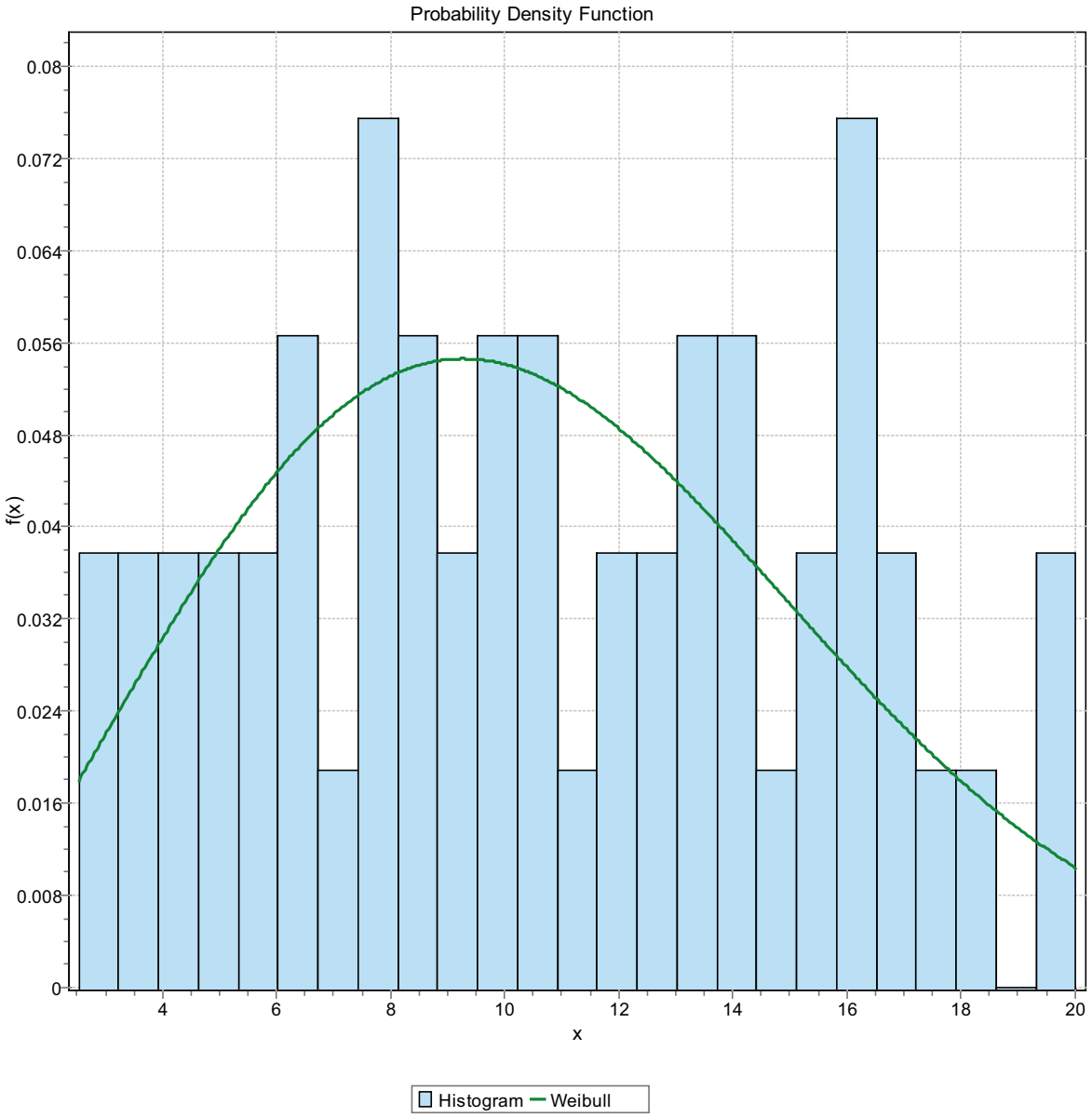

Figure F-102. *CDF, Domain FSM_NE005, 15 m bins, Weibull Distribution.*

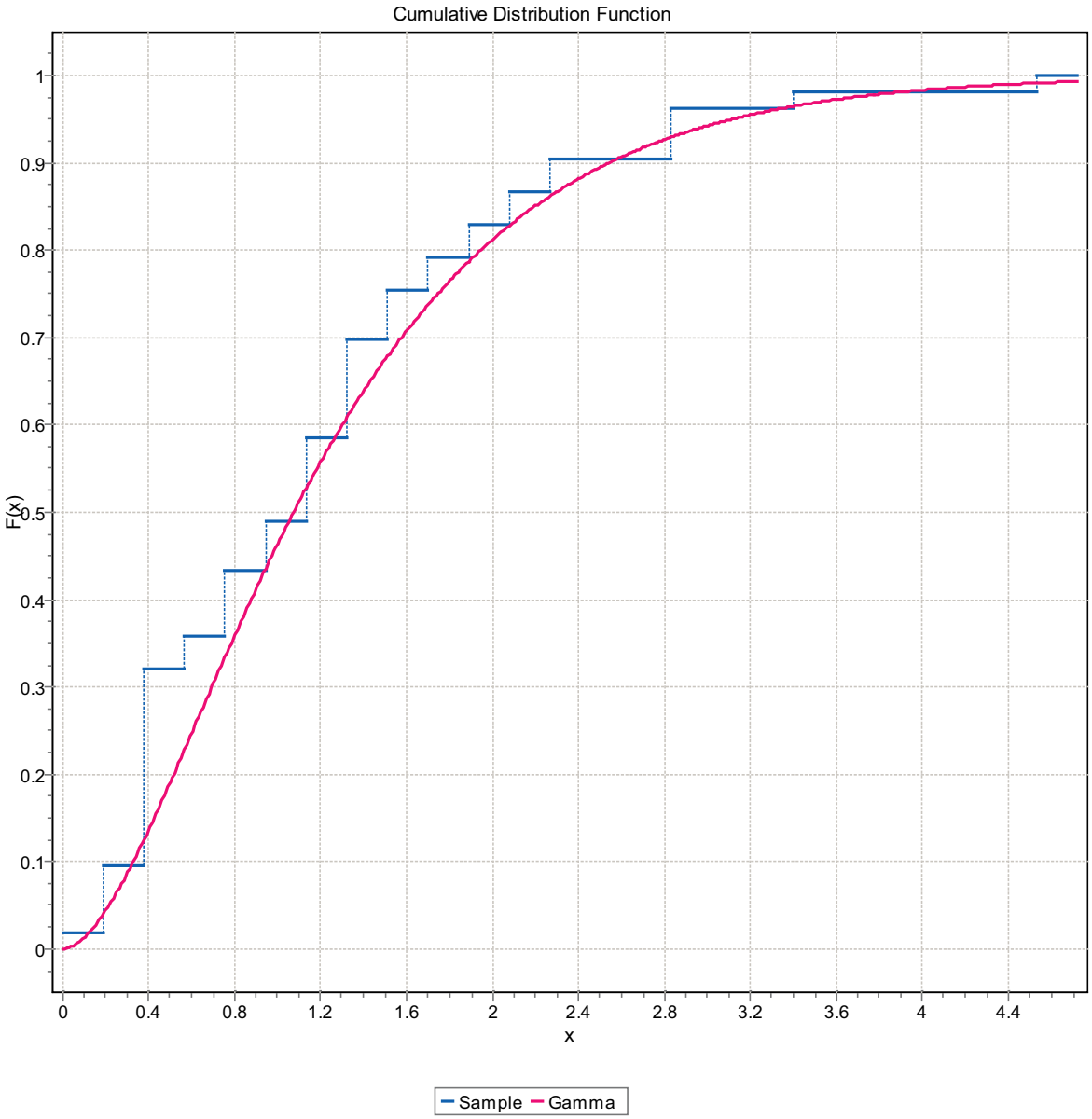

Figure F-103. *CDF, Domain FSM_NE005, 15 m bins, Gamma Distribution.*

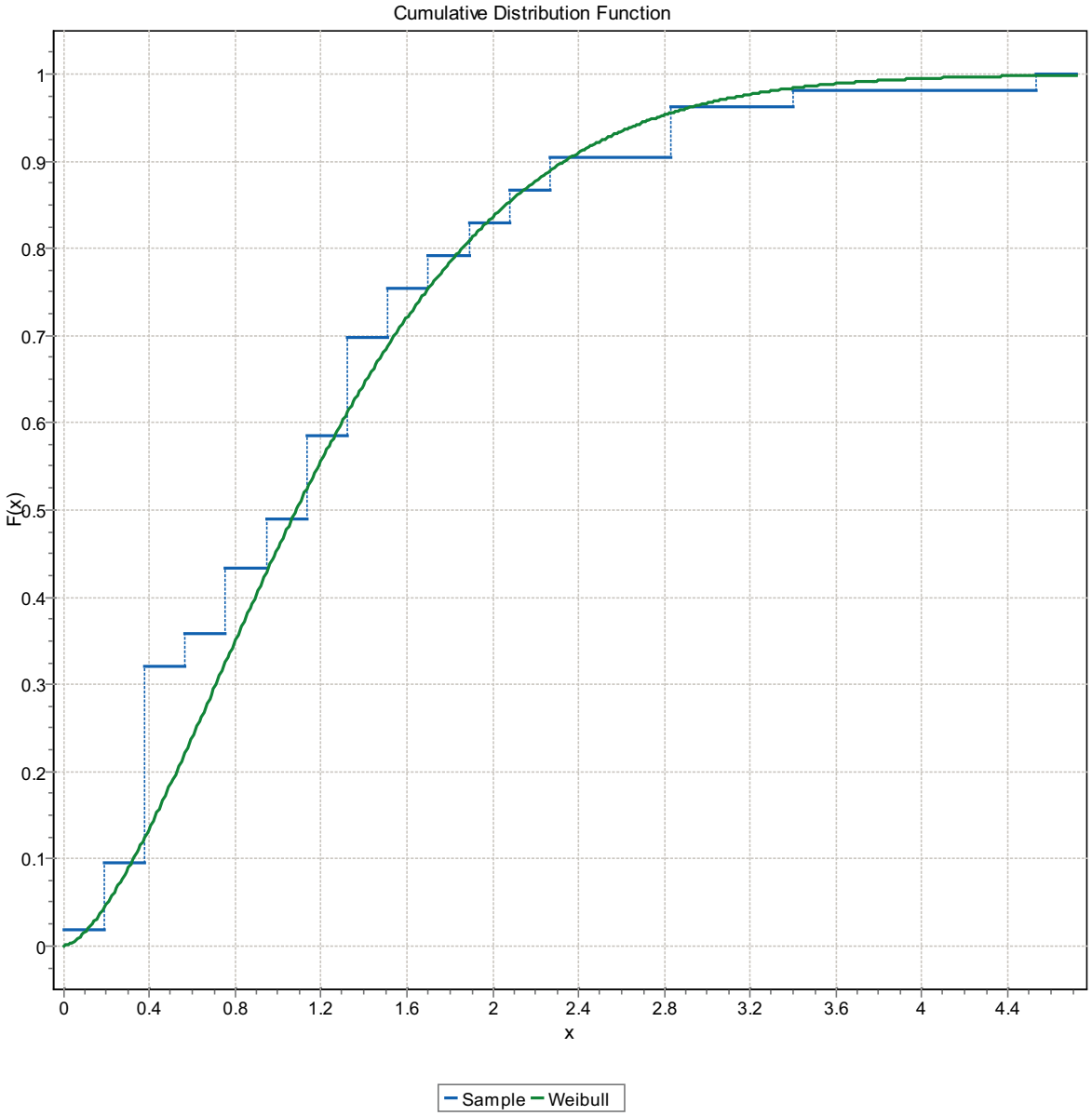

Figure F-104. *CDF, Domain FSM_NE005, 15 m bins, Weibull Distribution.*

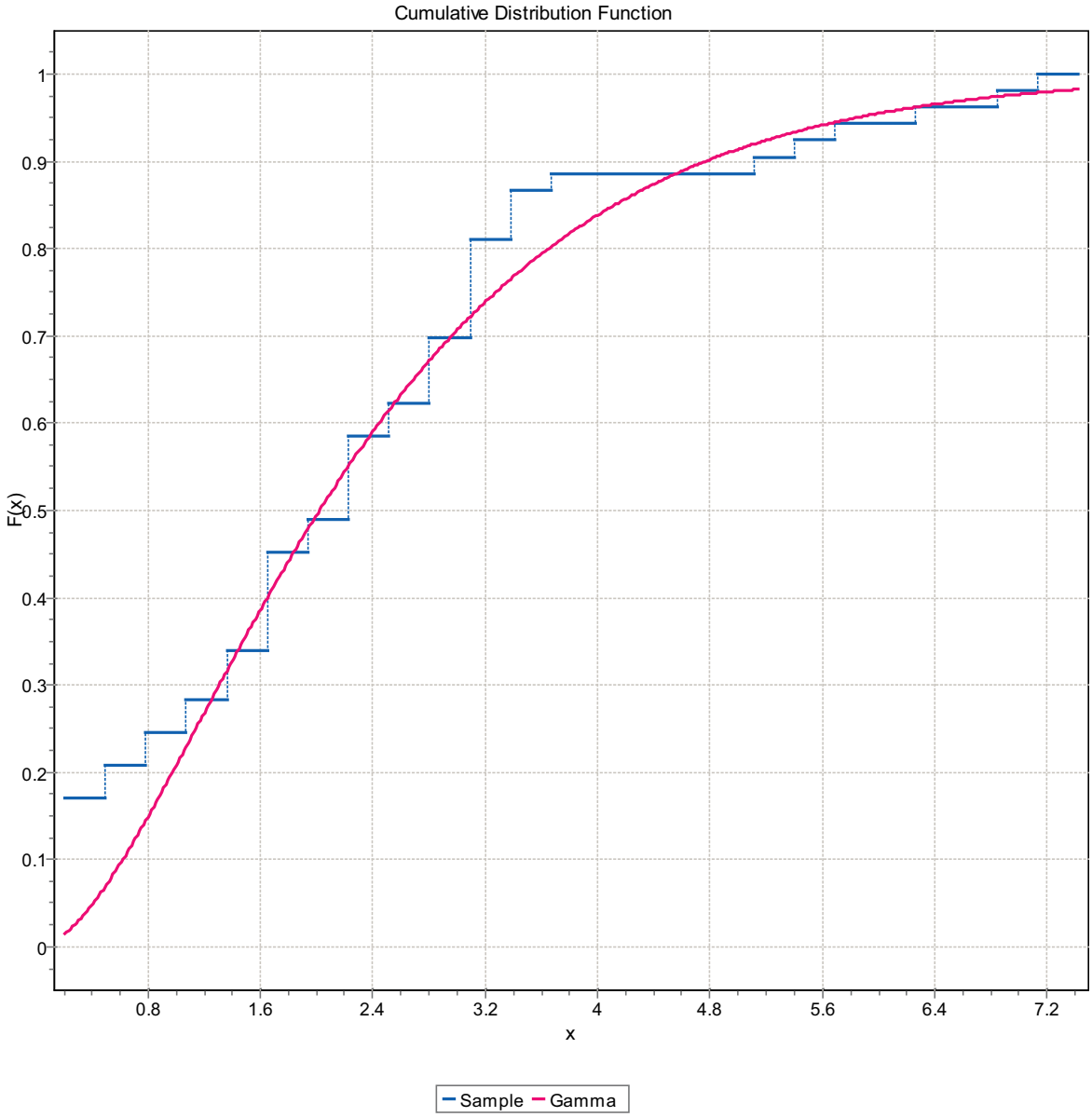

Figure F-105. *CDF, Domain FSM_NE005, 15 m bins, Gamma Distribution.*

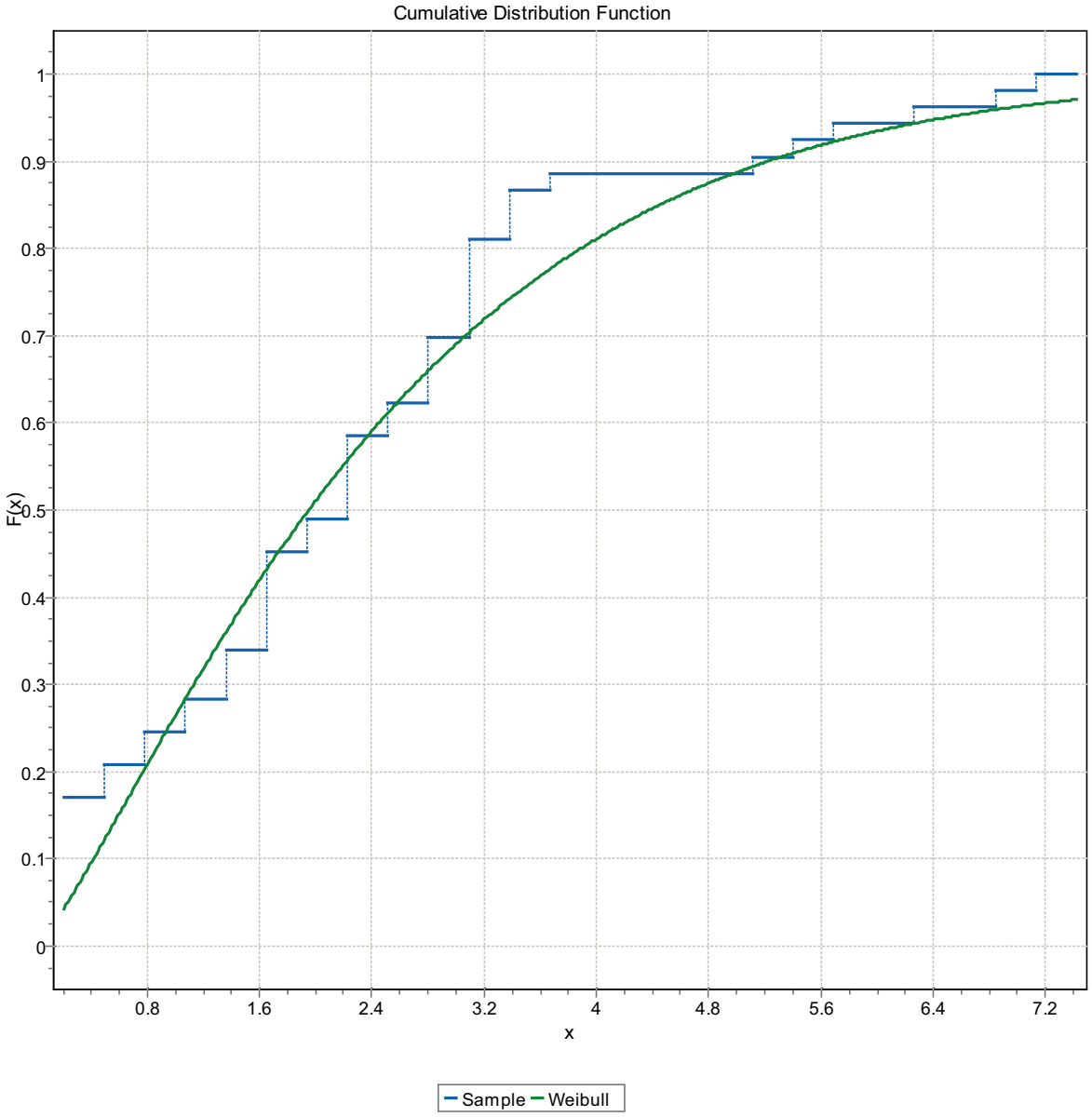

Figure F-106. *CDF, Domain FSM_NE005, 15 m bins, Weibull Distribution.*

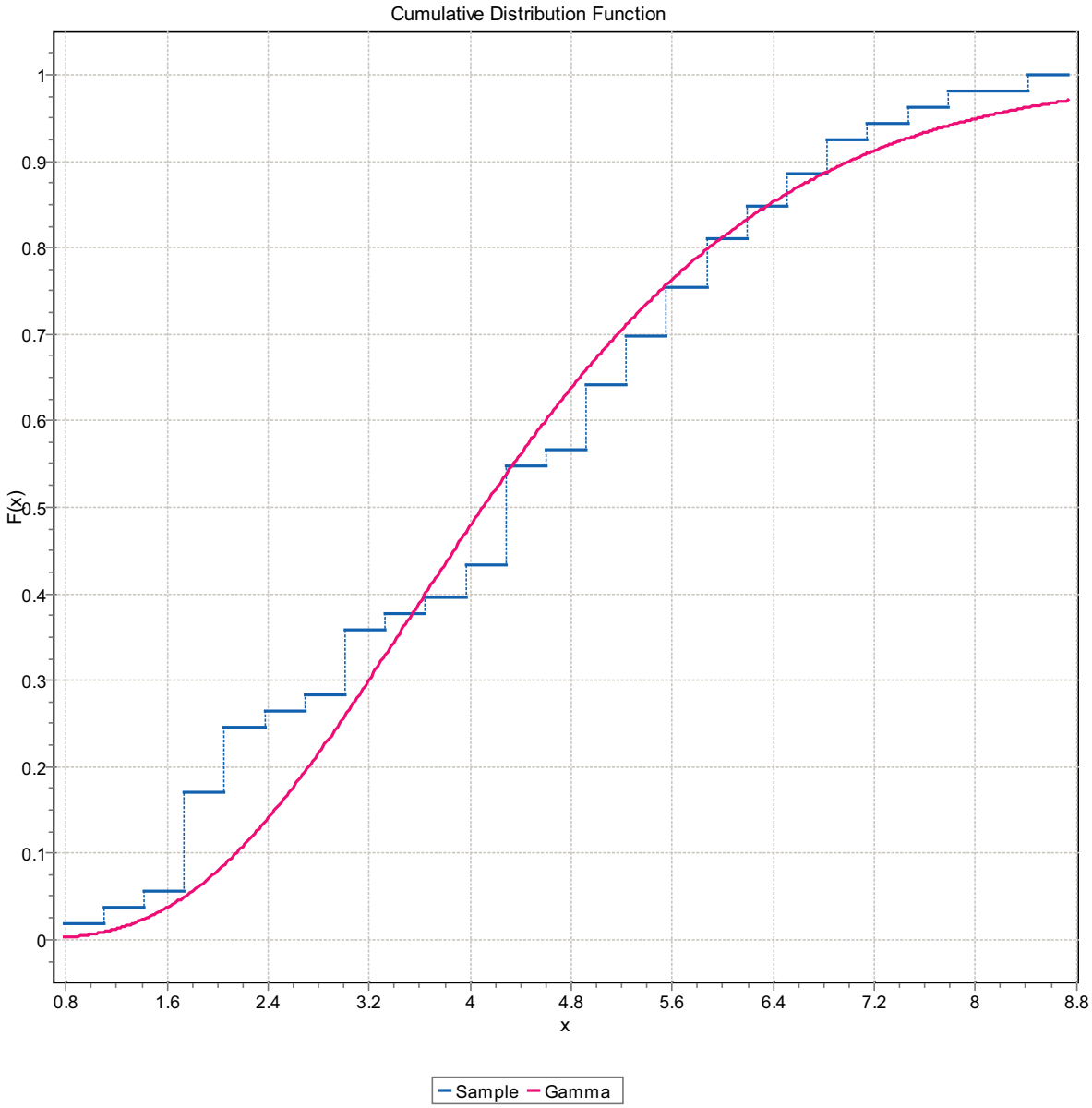

Figure F-107. *CDF, Domain FSM_NE005, 15 m bins, Gamma Distribution.*

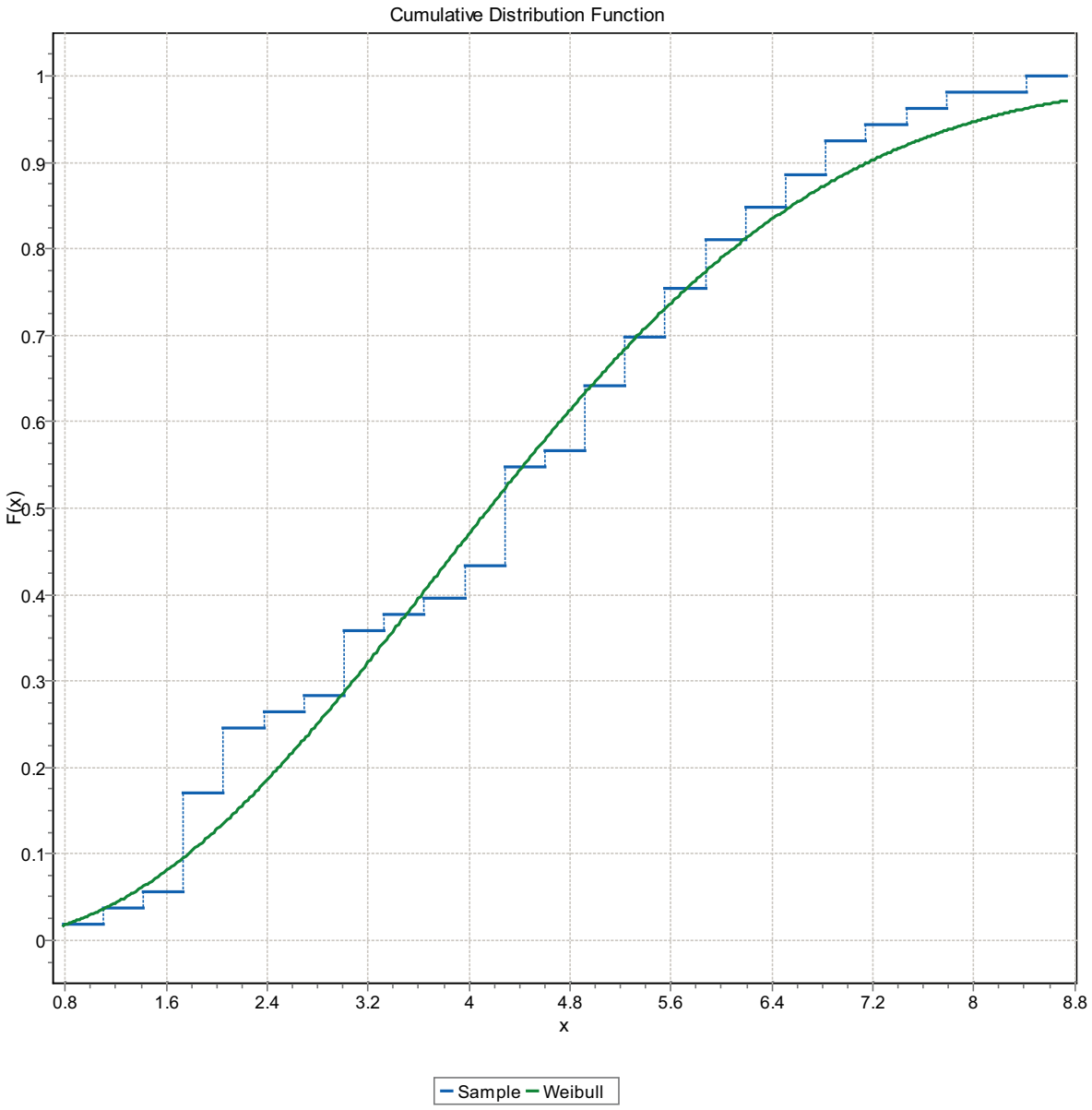

Figure F-108. *CDF, Domain FSM_NE005, 15 m bins, Weibull Distribution.*

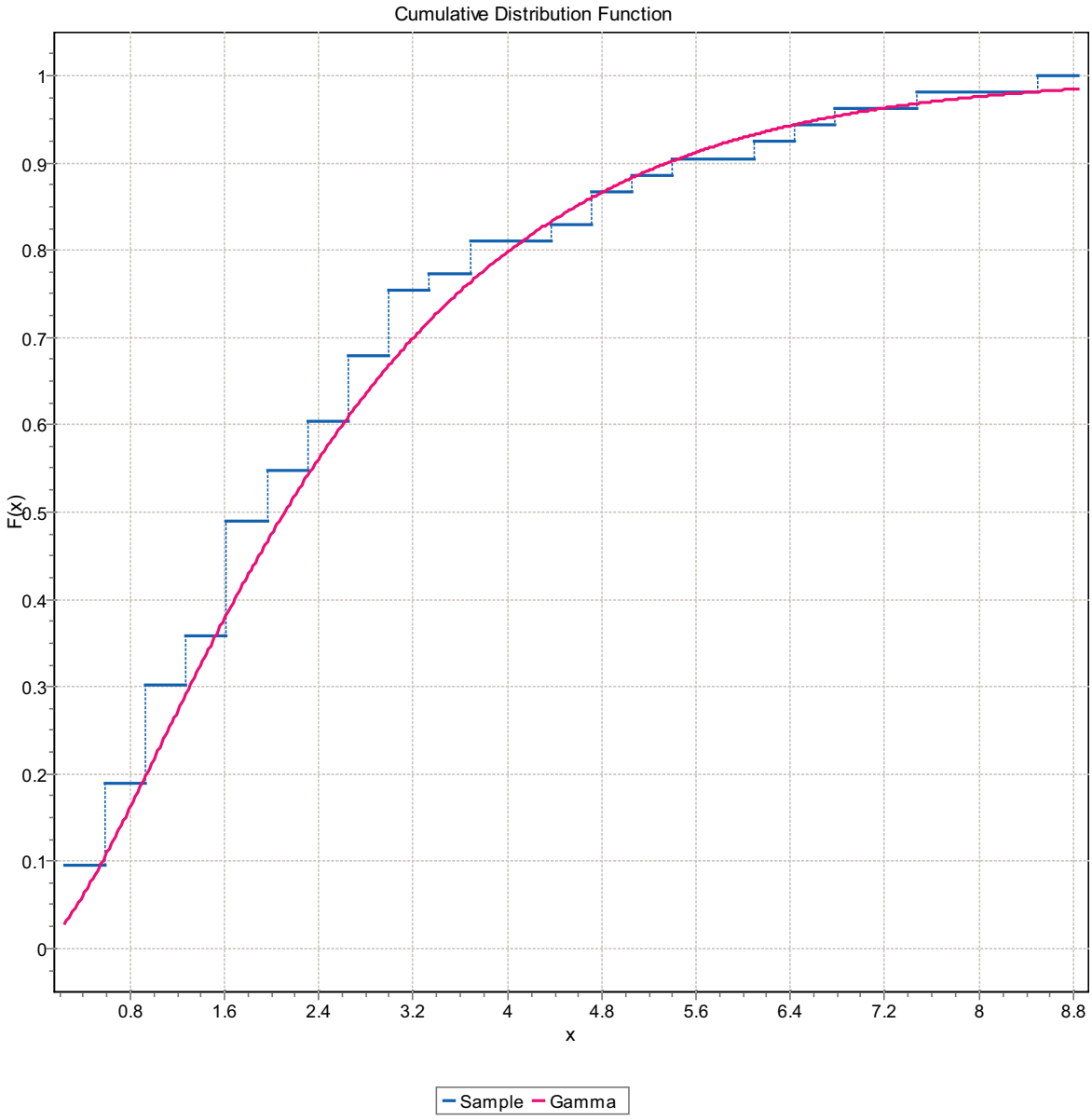

Figure F-109. *CDF, Domain FSM_NE005, 15 m bins, Gamma Distribution.*

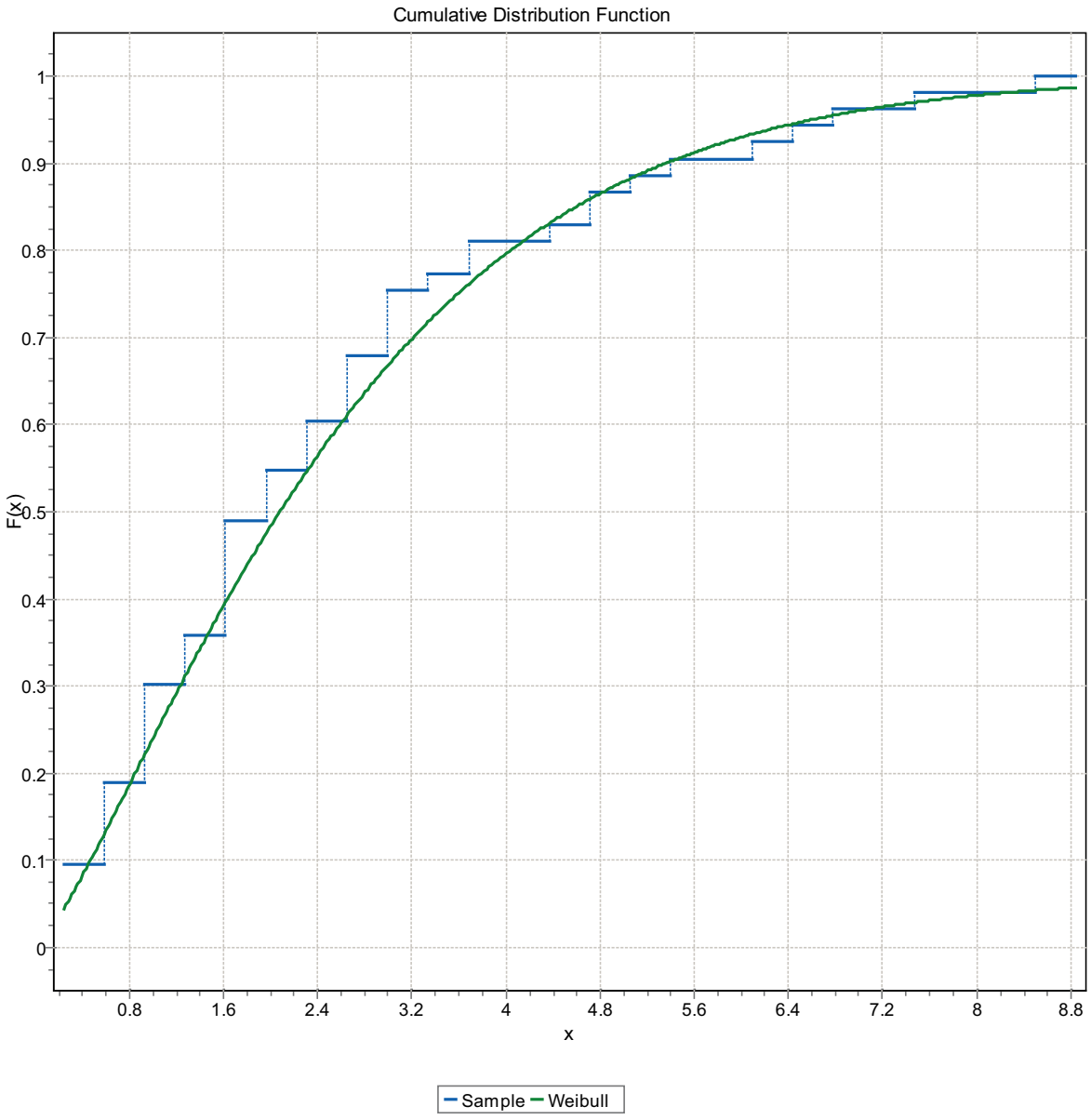

Figure F-110. *CDF, Domain FSM_NE005, 15 m bins, Weibull Distribution.*

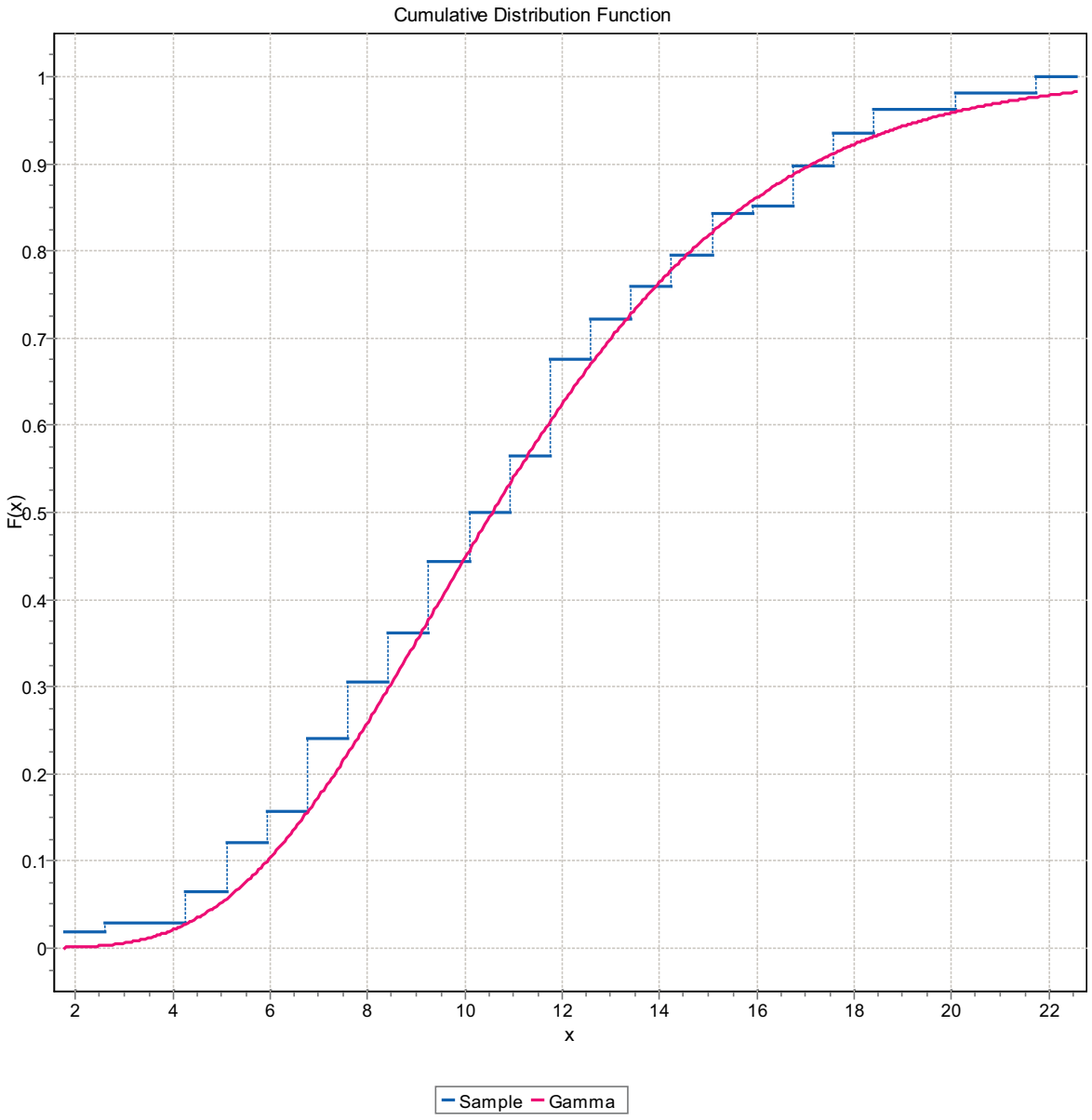

Figure F-111. *CDF, Domain FSM_N, 15 m bins, Gamma Distribution.*

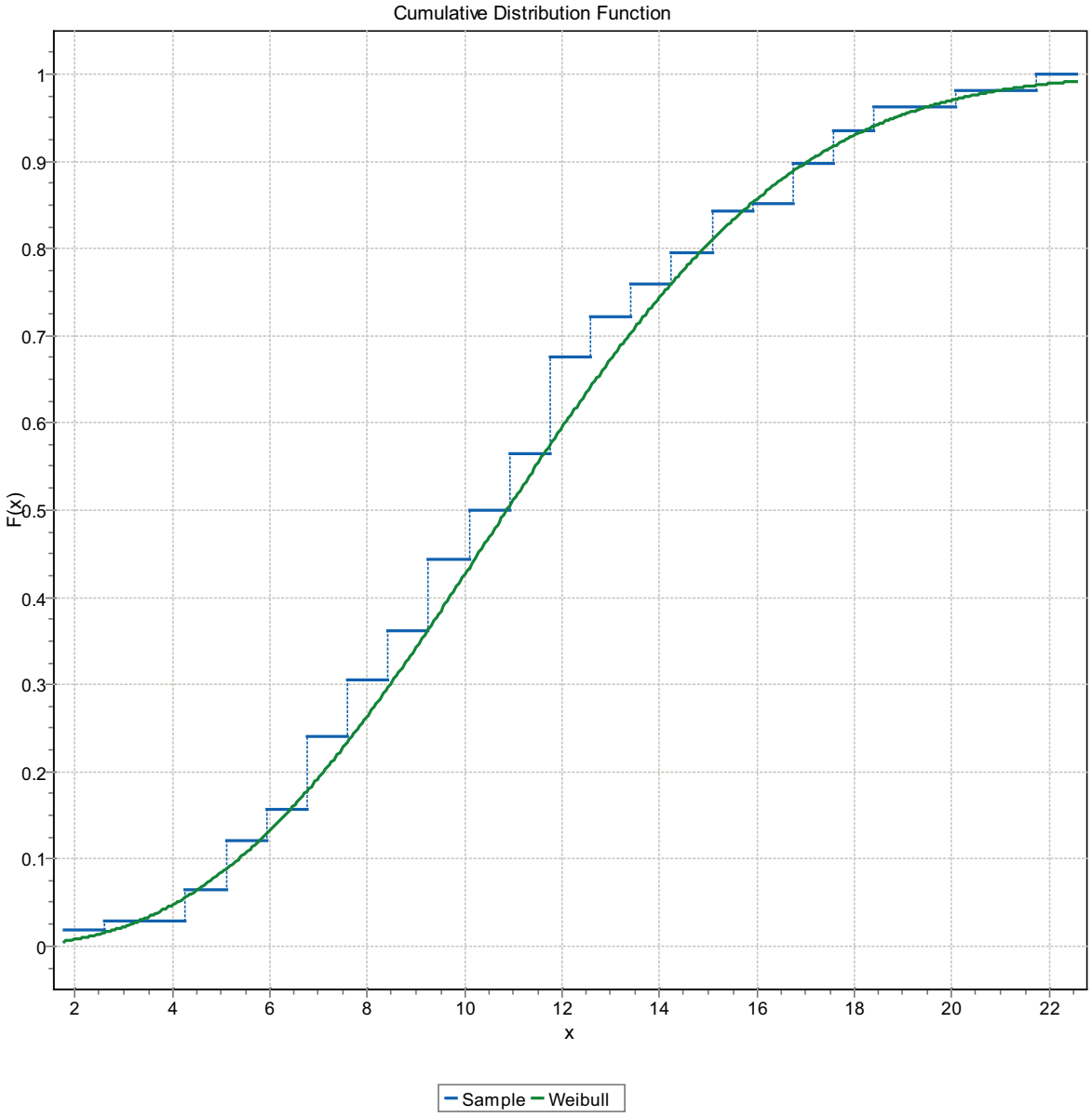

Figure F-112. *CDF, Domain FSM_N, 15 m bins, Weibull Distribution.*

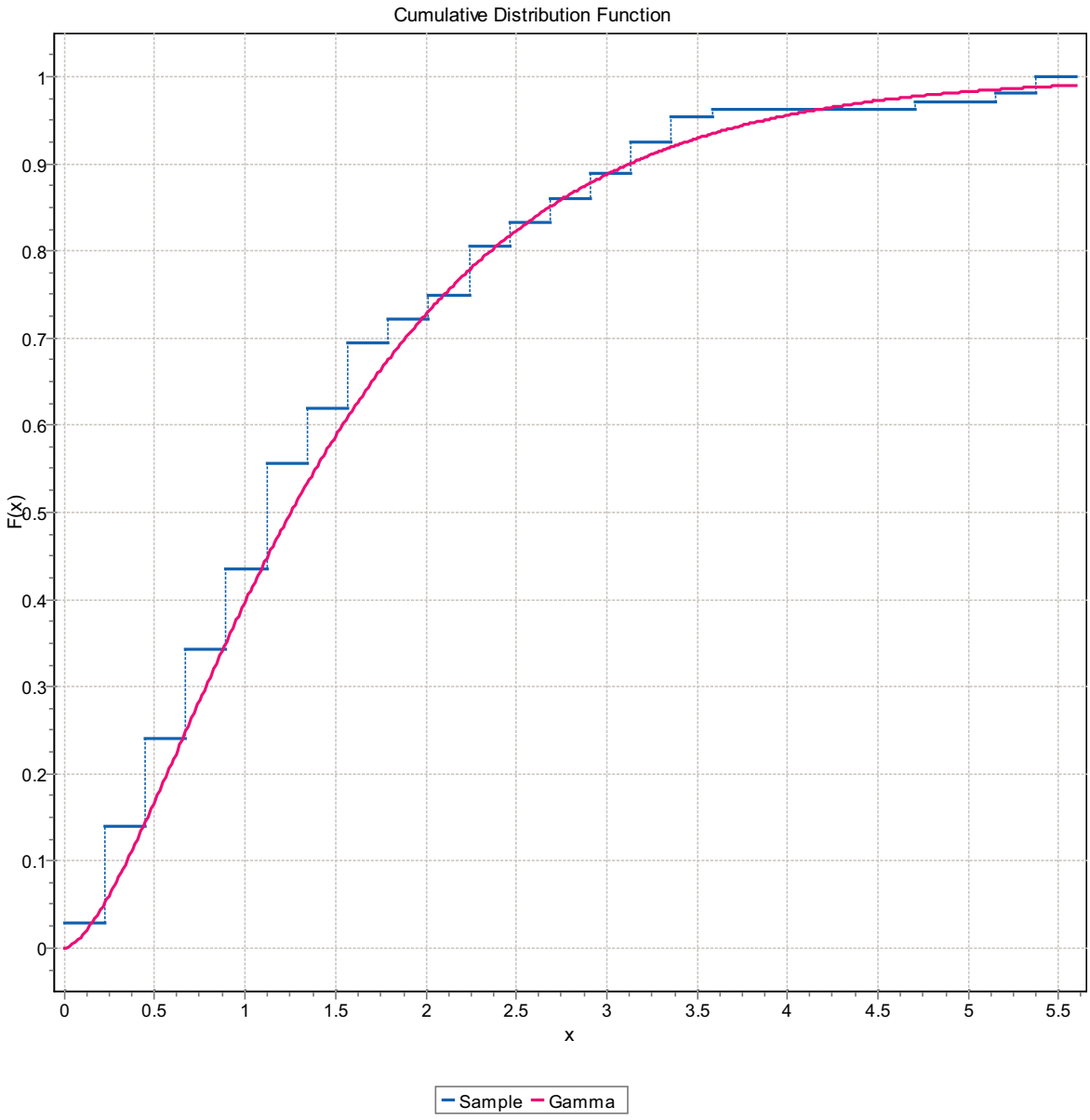

Figure F-113. *CDF, Domain FSM_N, 15 m bins, Gamma Distribution.*

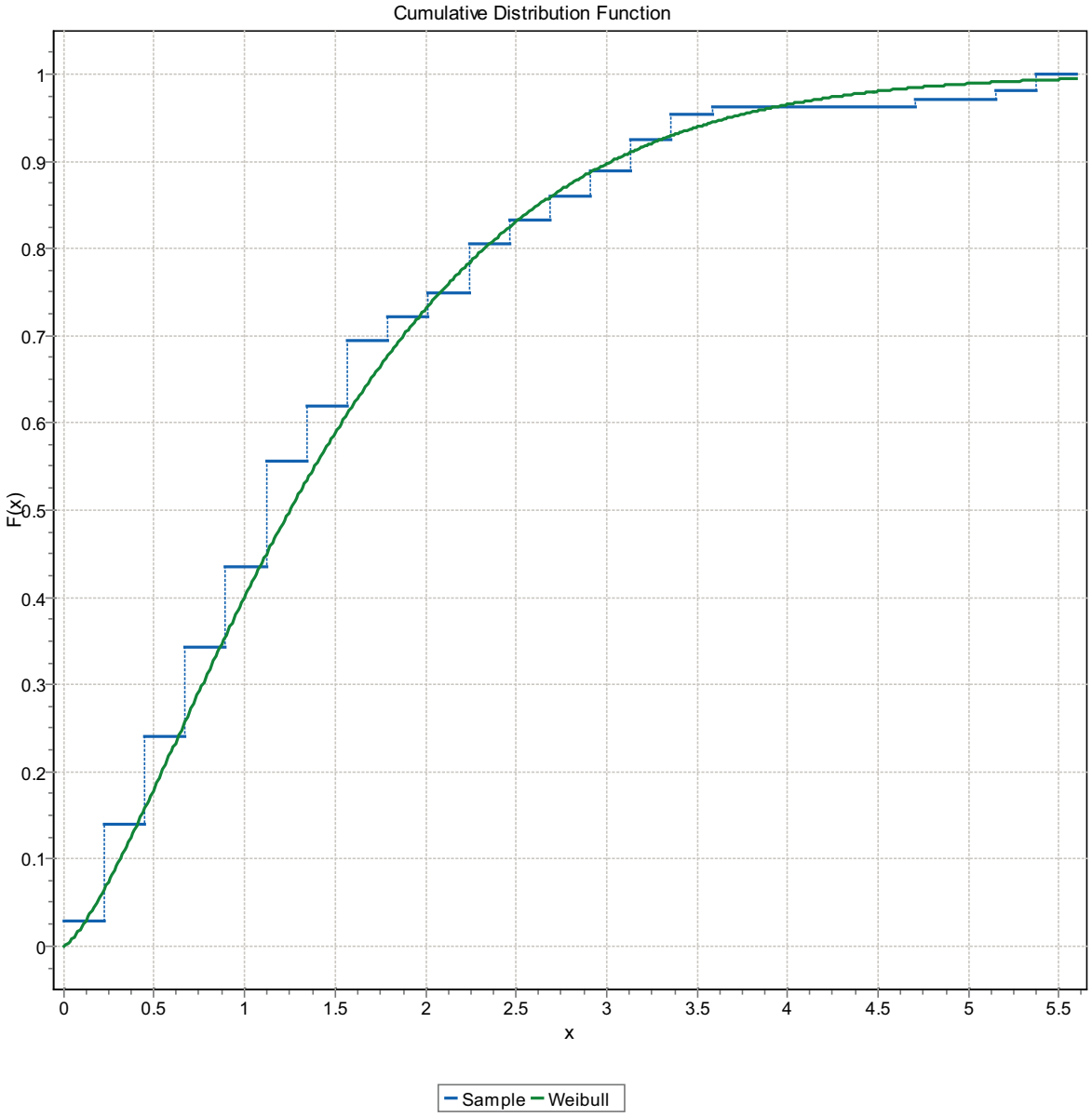

Figure F-114. *CDF, Domain FSM_N, 15 m bins, Weibull Distribution.*

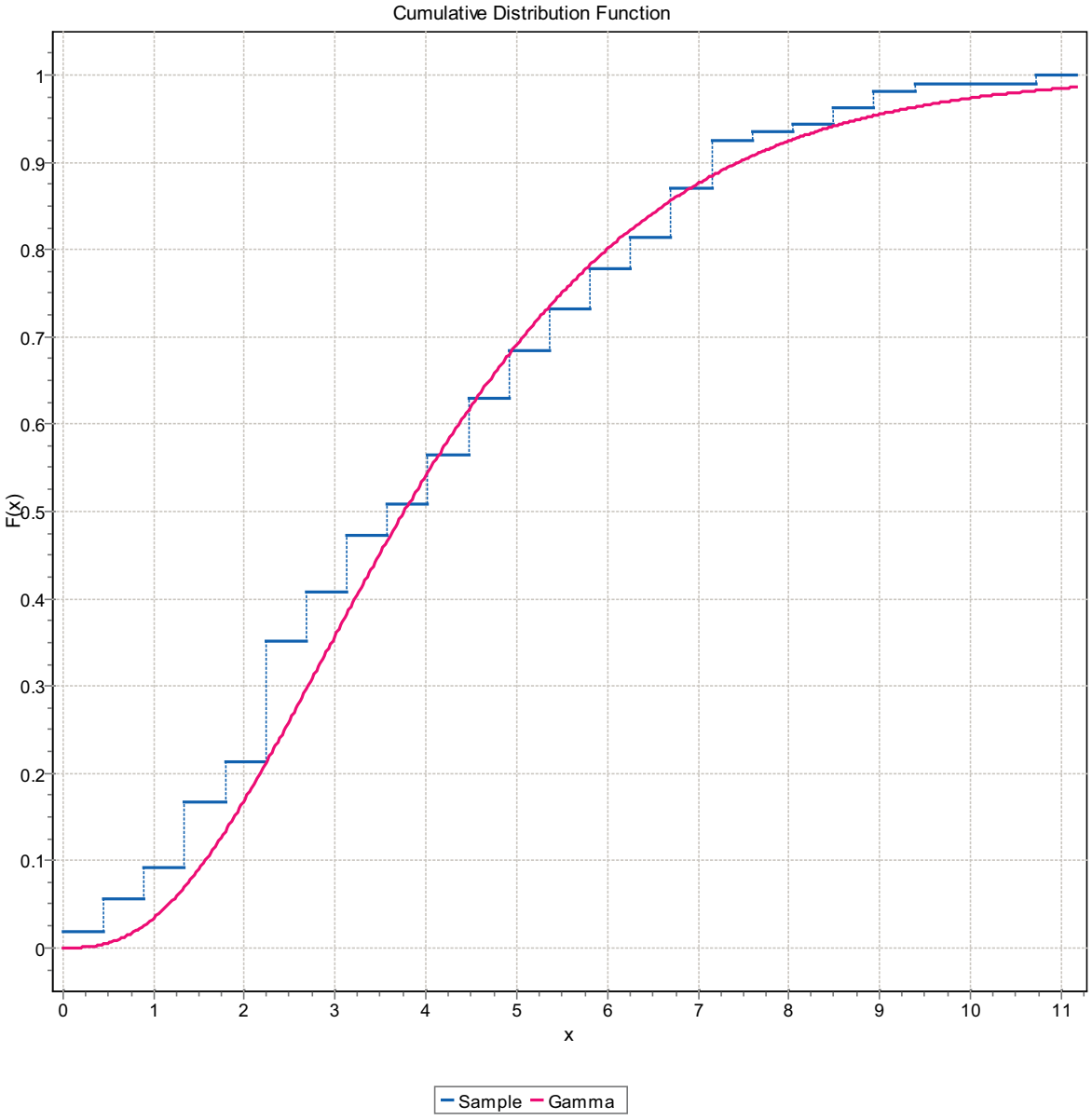

Figure F-115. *CDF, Domain FSM_N, 15 m bins, Gamma Distribution.*

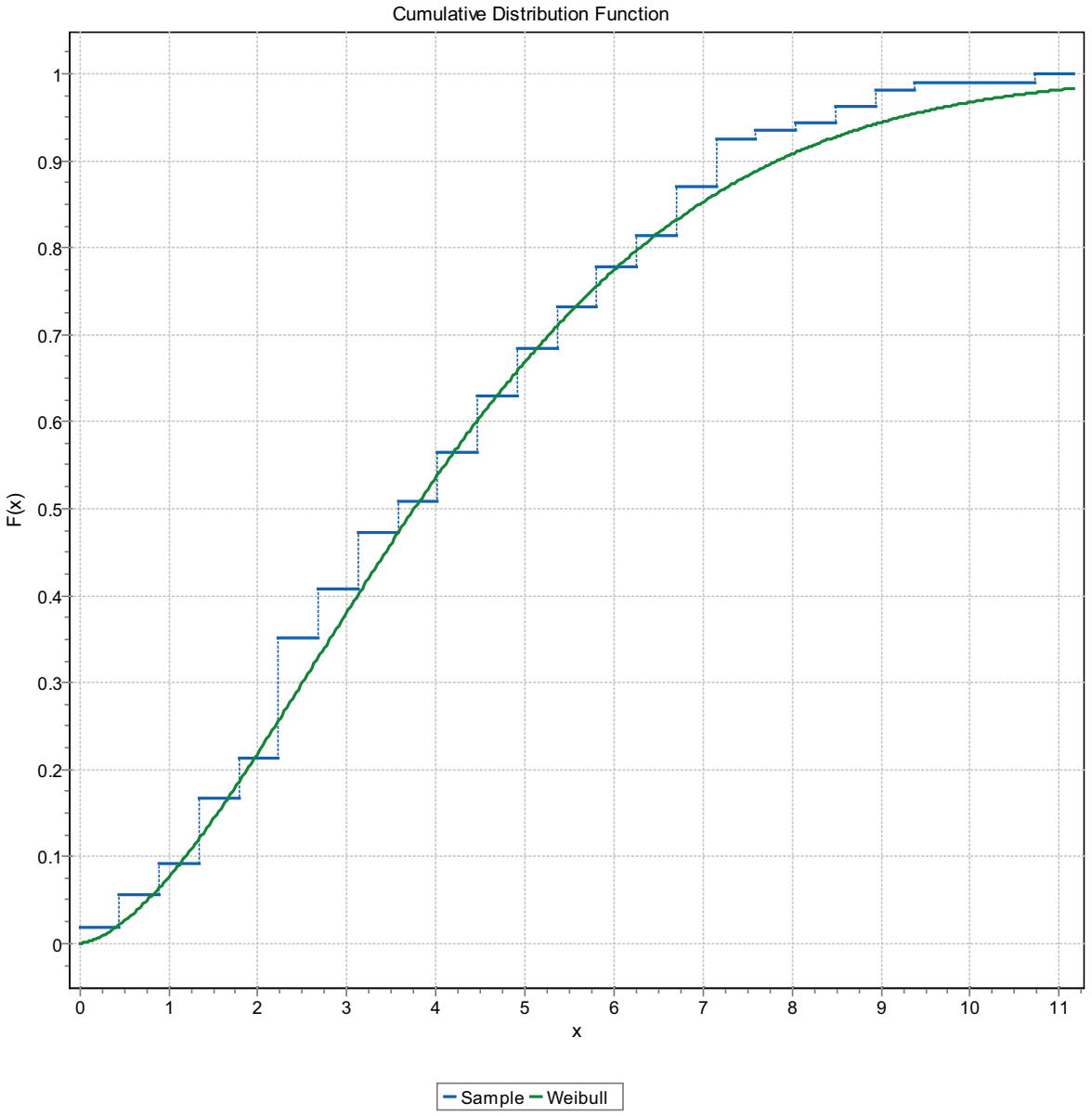

Figure F-116. *CDF, Domain FSM_N, 15 m bins, Weibull Distribution.*

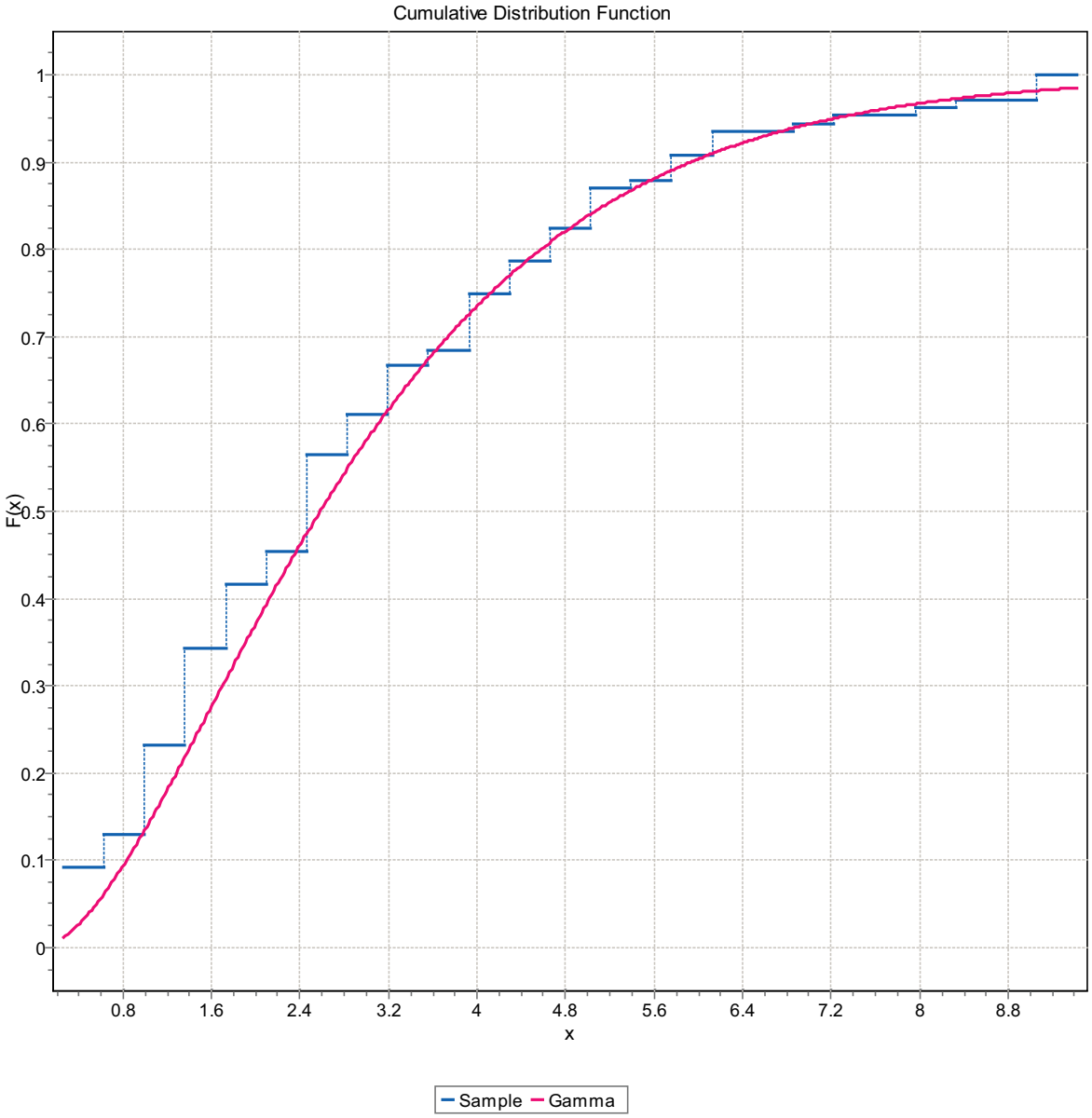

Figure F-117. *CDF, Domain FSM_N, 15 m bins, Gamma Distribution.*

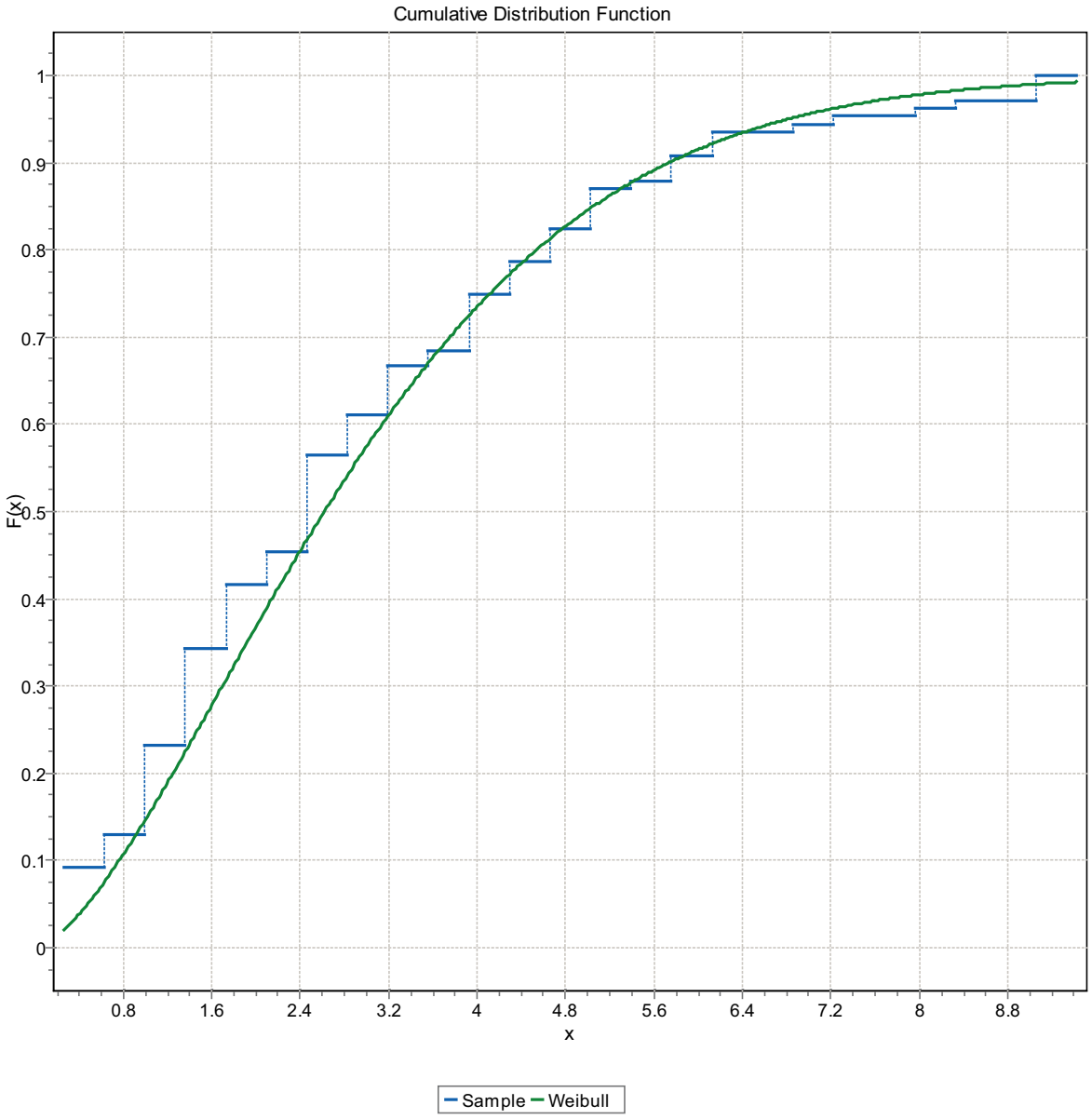

Figure F-118. *CDF, Domain FSM_N, 15 m bins, Weibull Distribution.*

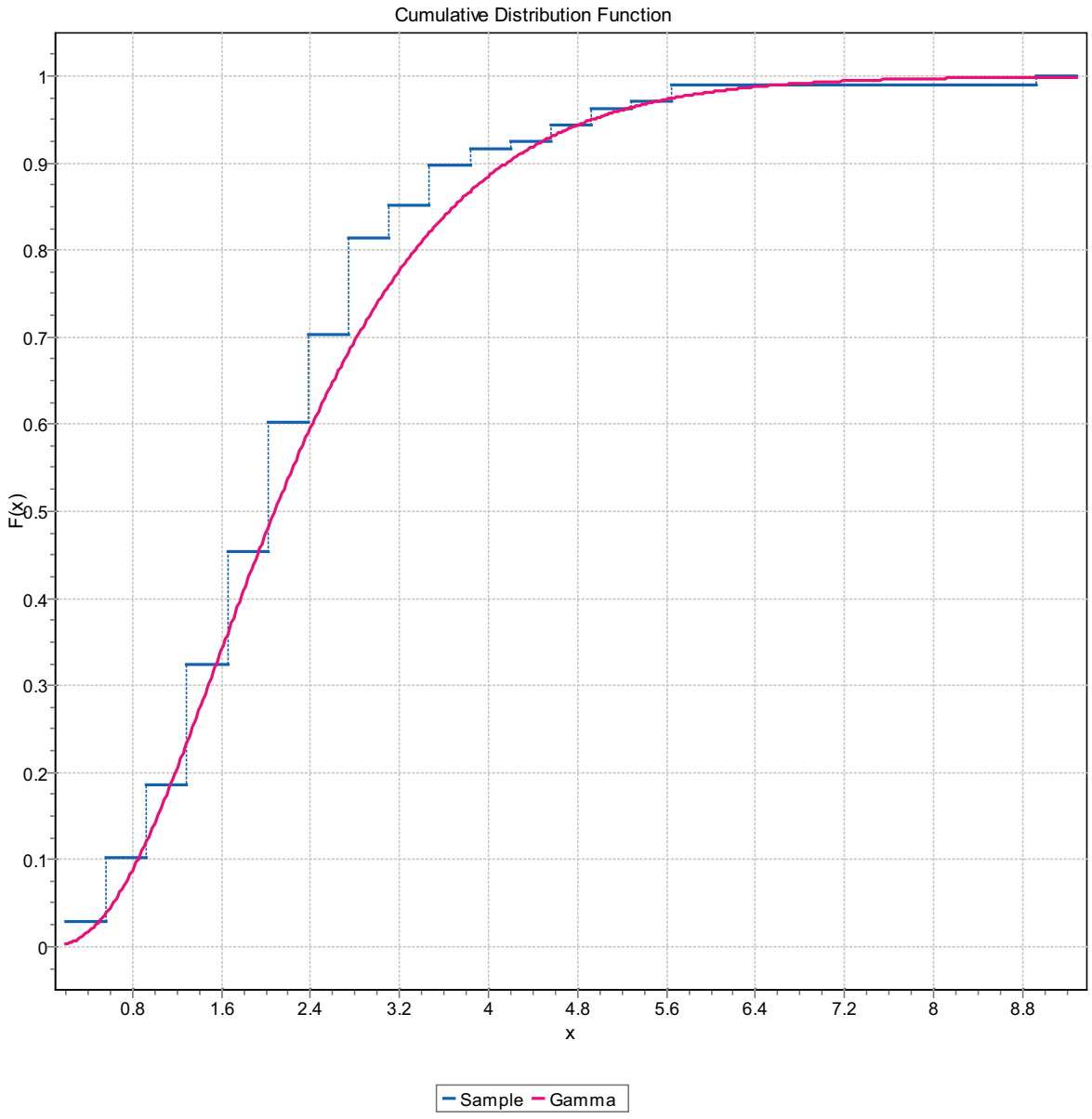

Figure F-119. *CDF, Domain FSM_N, 15 m bins, Gamma Distribution.*

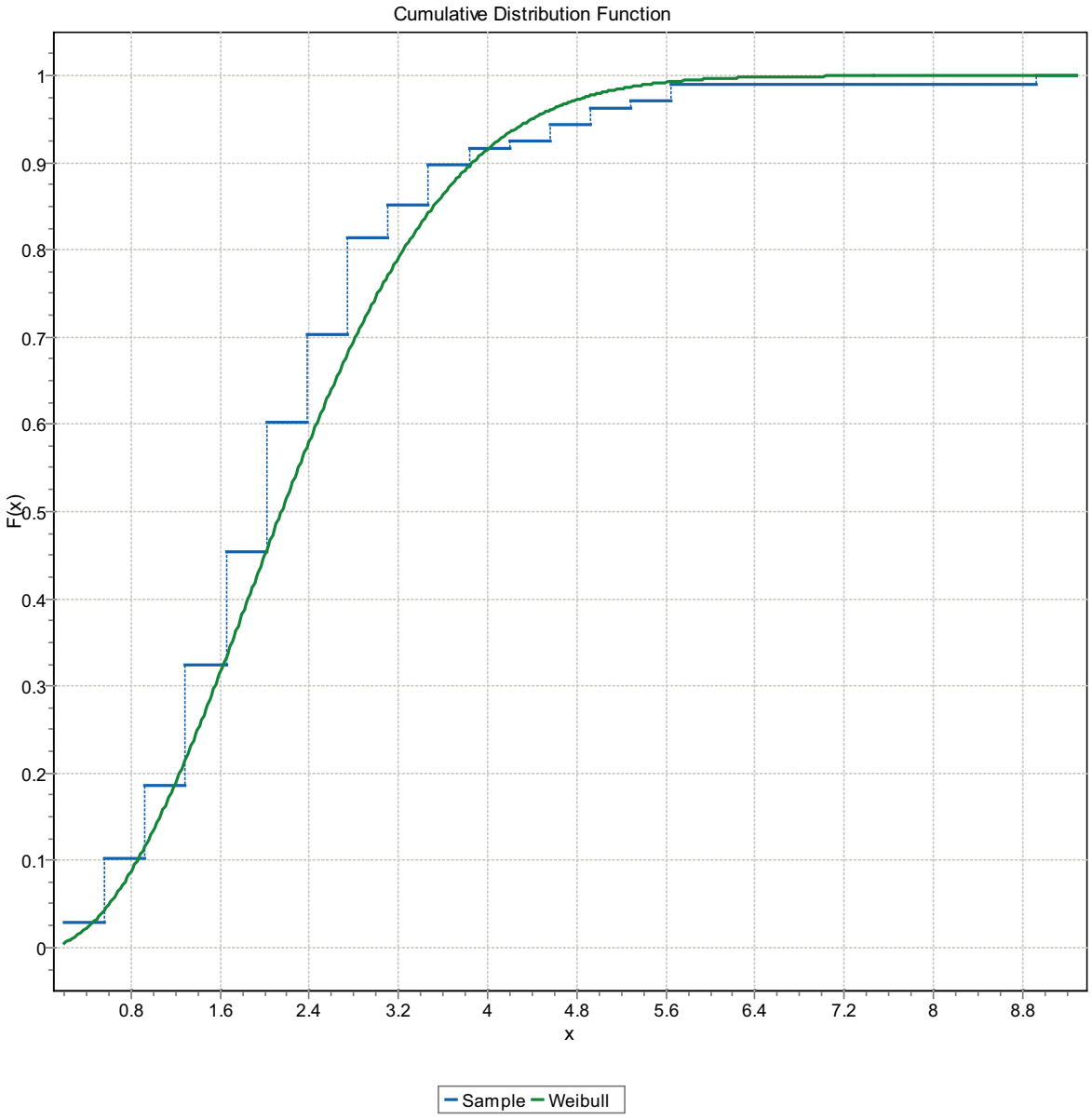

Figure F-120. *CDF, Domain FSM_N, 15 m bins, Weibull Distribution.*

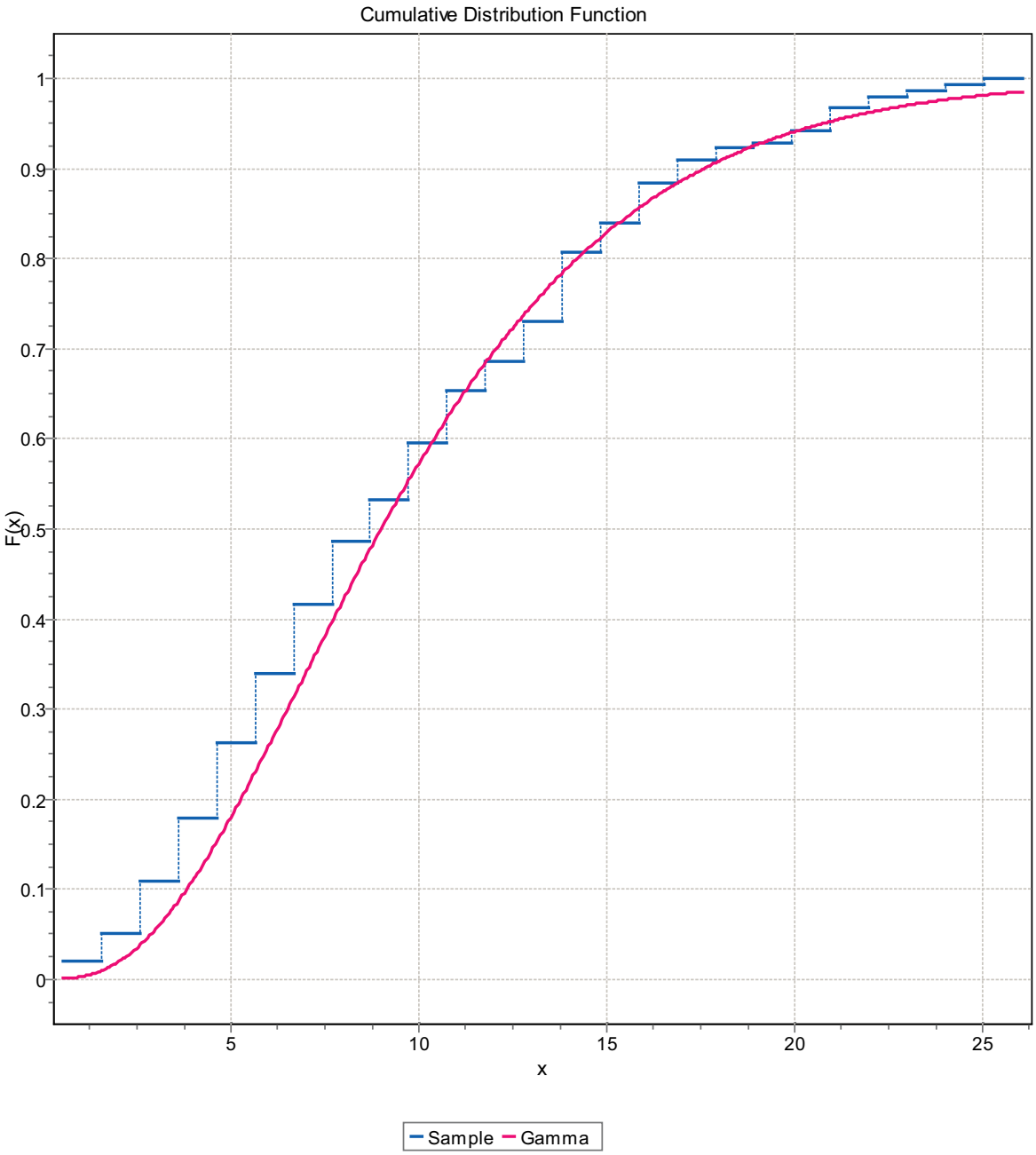

Figure F-121. *CDF, Domain FSM_W, 15 m bins, Gamma Distribution.*

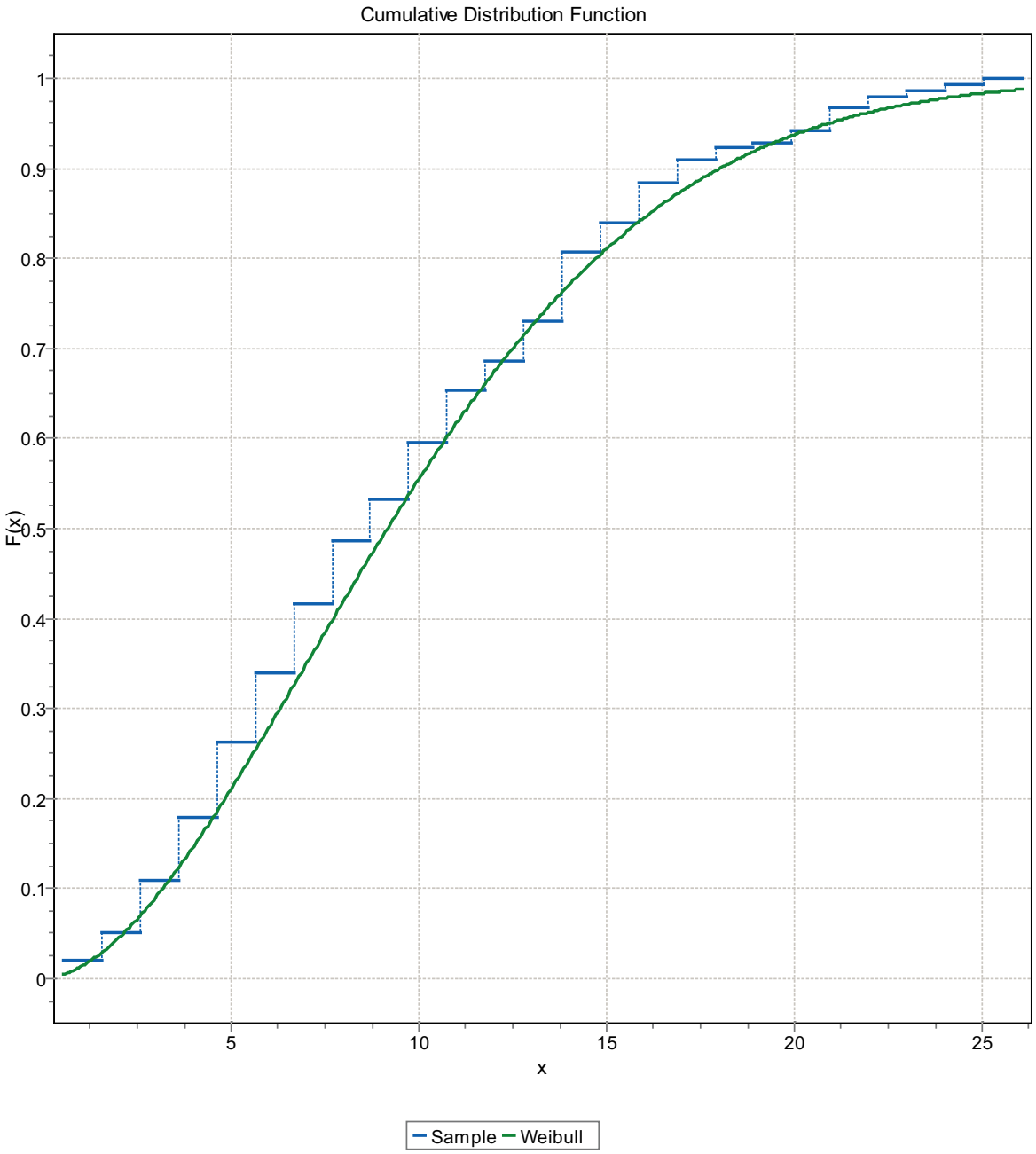

Figure F-122. *CDF, Domain FSM_W, 15 m bins, Weibull Distribution.*

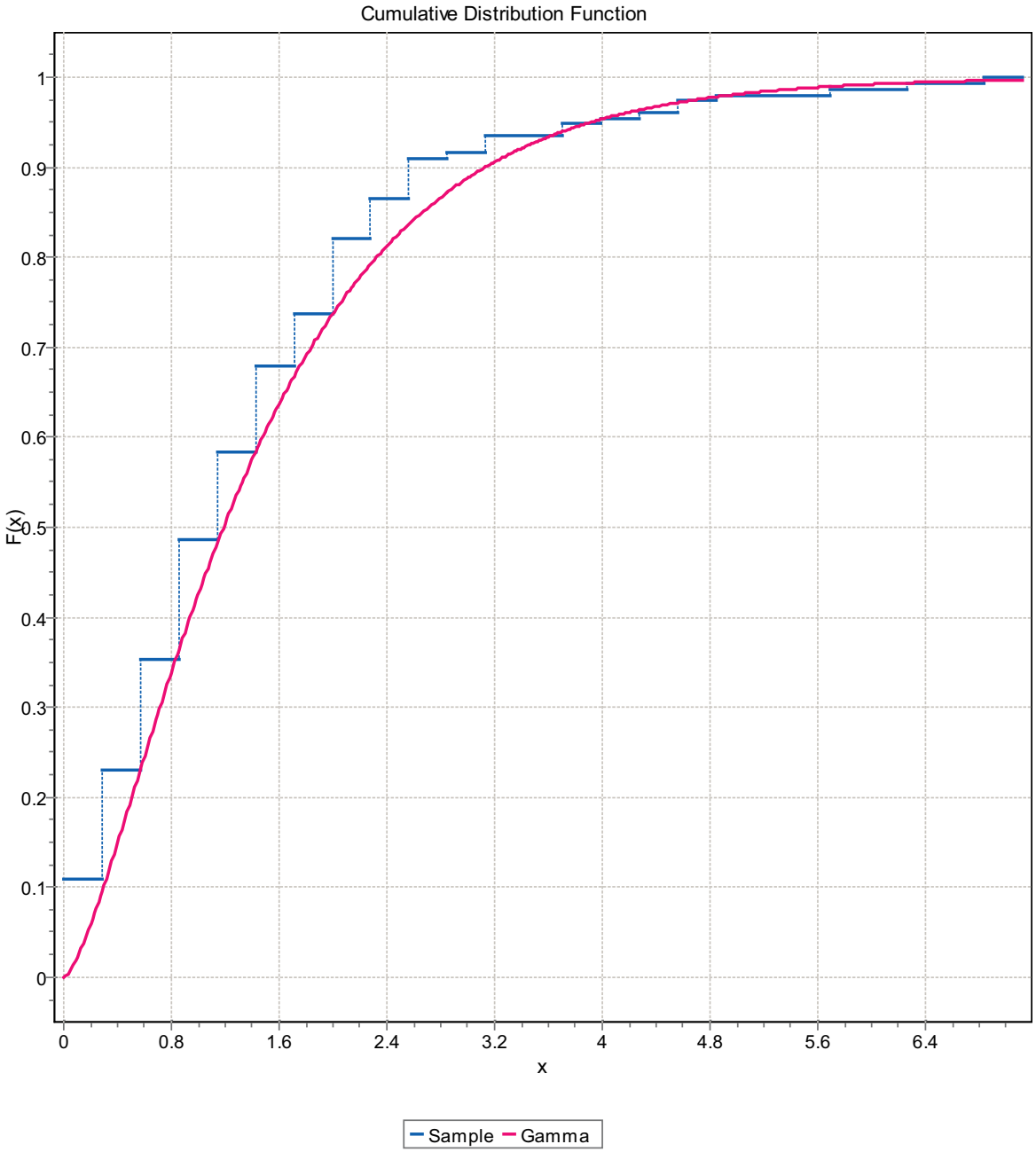

Figure F-123. *CDF, Domain FSM_W, 15 m bins, Gamma Distribution.*

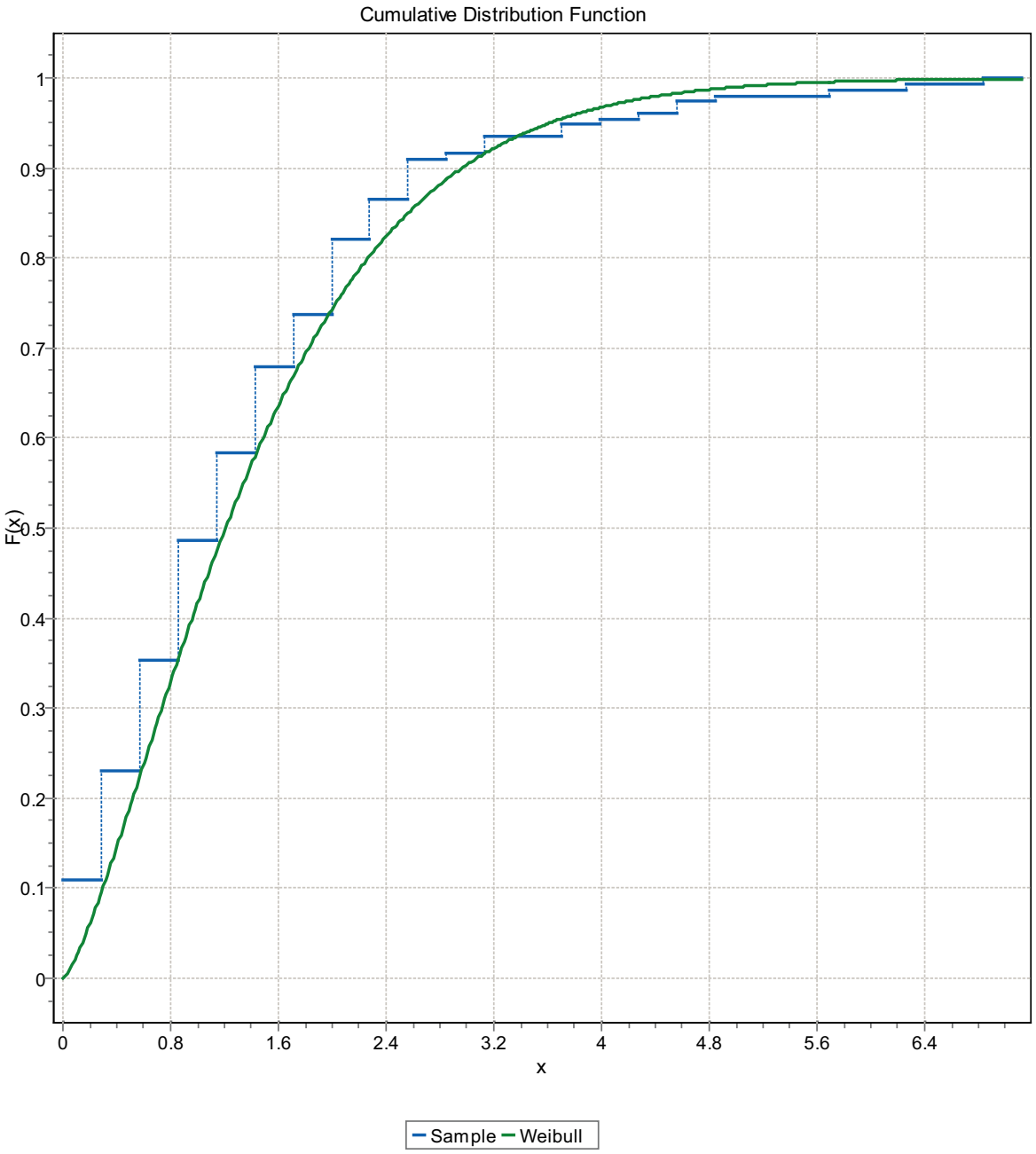

Figure F-124. *CDF, Domain FSM_W, 15 m bins, Weibull Distribution.*

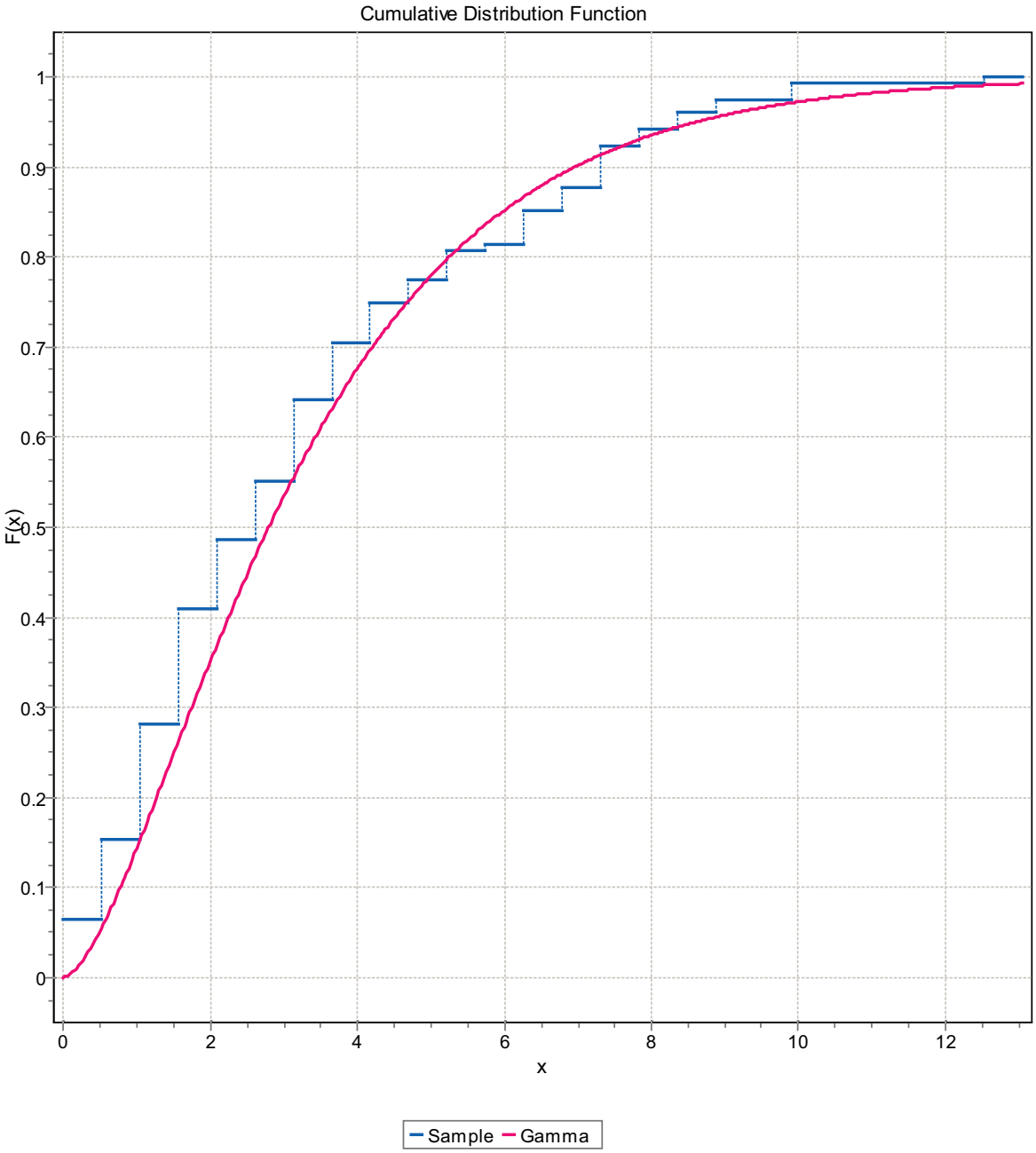

Figure F-125. *CDF, Domain FSM_W, 15 m bins, Gamma Distribution.*

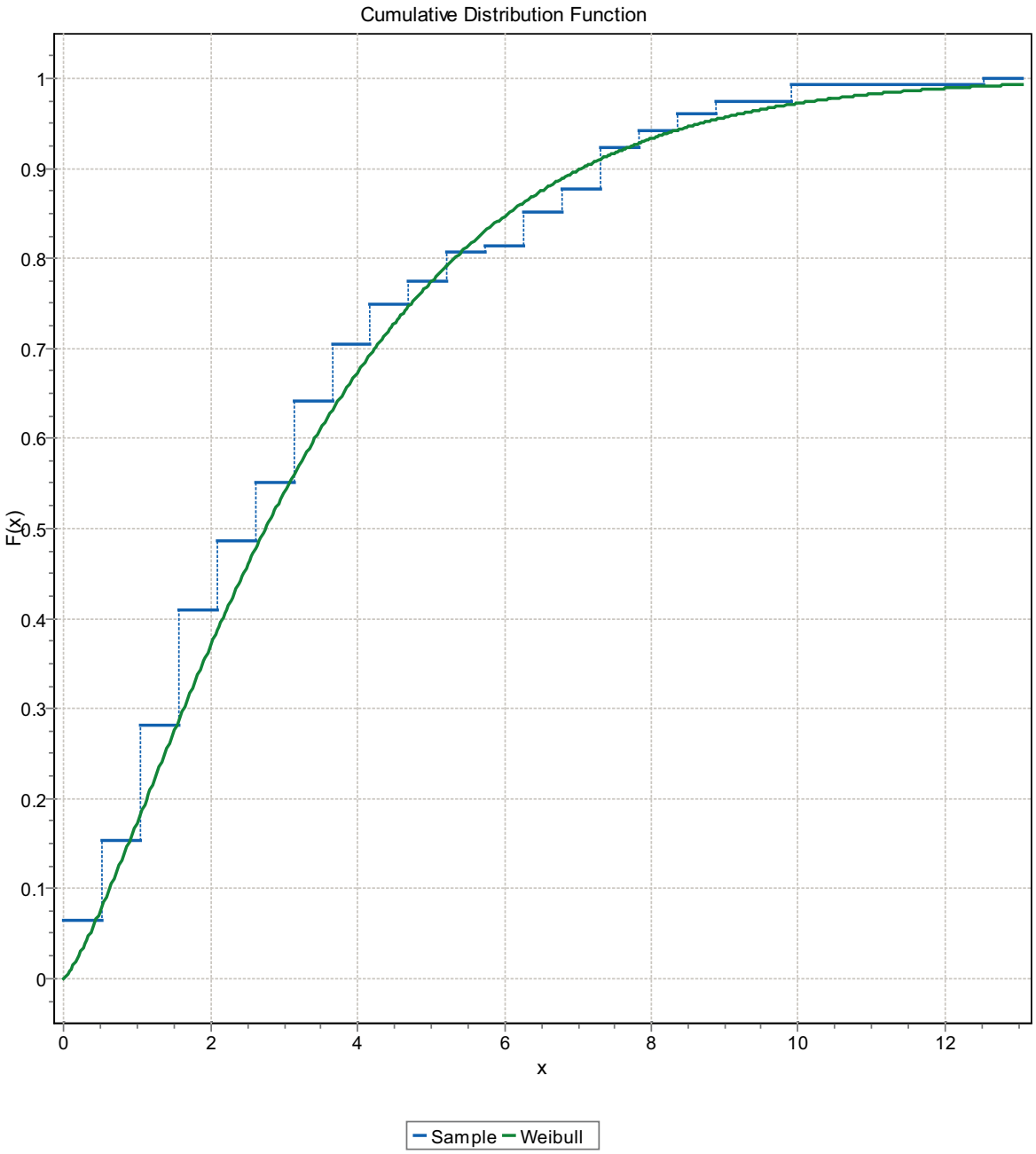

Figure F-126. *CDF, Domain FSM_W, 15 m bins, Weibull Distribution.*

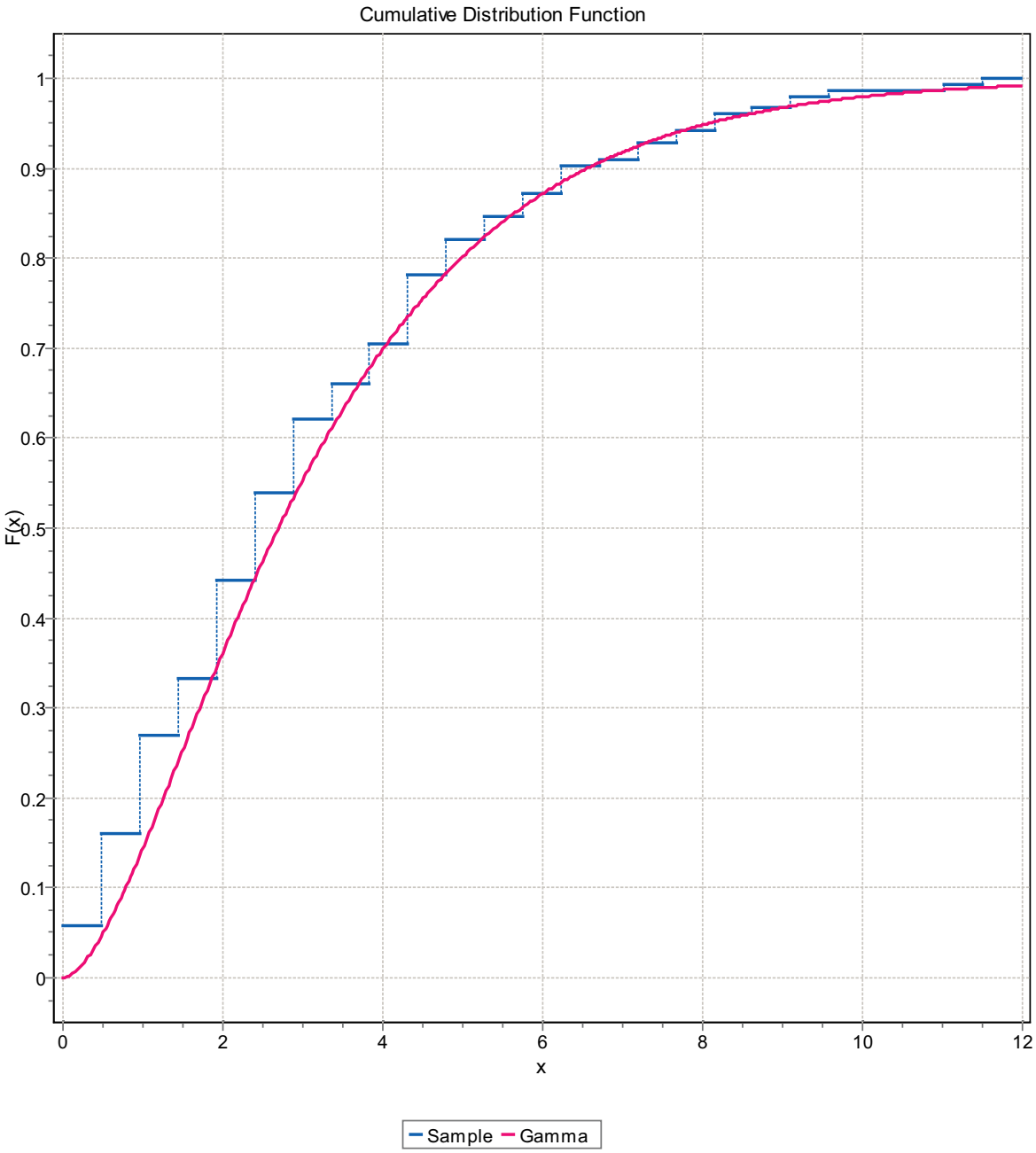

Figure F-127. *CDF, Domain FSM_W, 15 m bins, Gamma Distribution.*

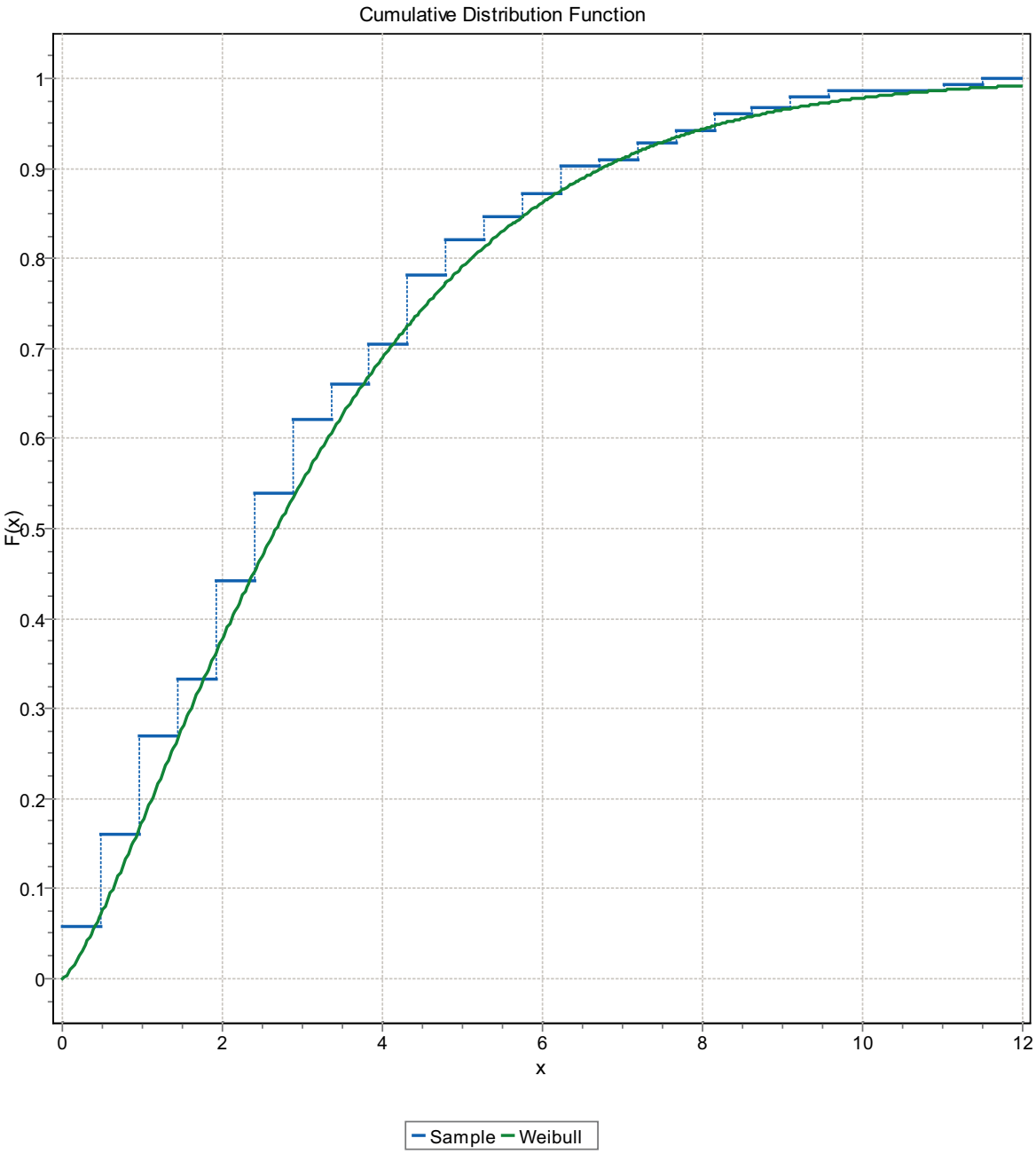

Figure F-128. *CDF, Domain FSM_W, 15 m bins, Weibull Distribution.*

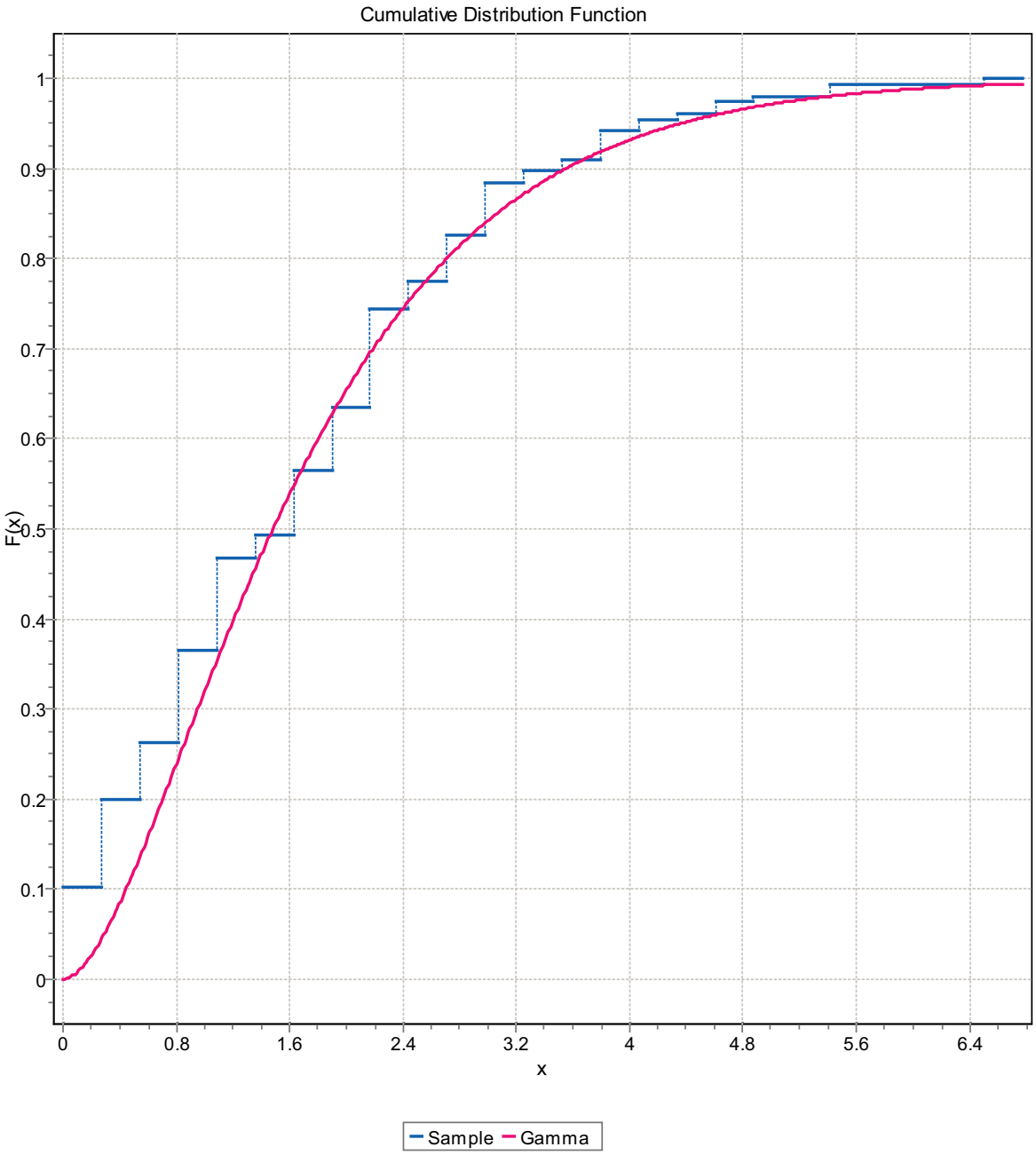

Figure F-129. *CDF, Domain FSM_W, 15 m bins, Gamma Distribution.*

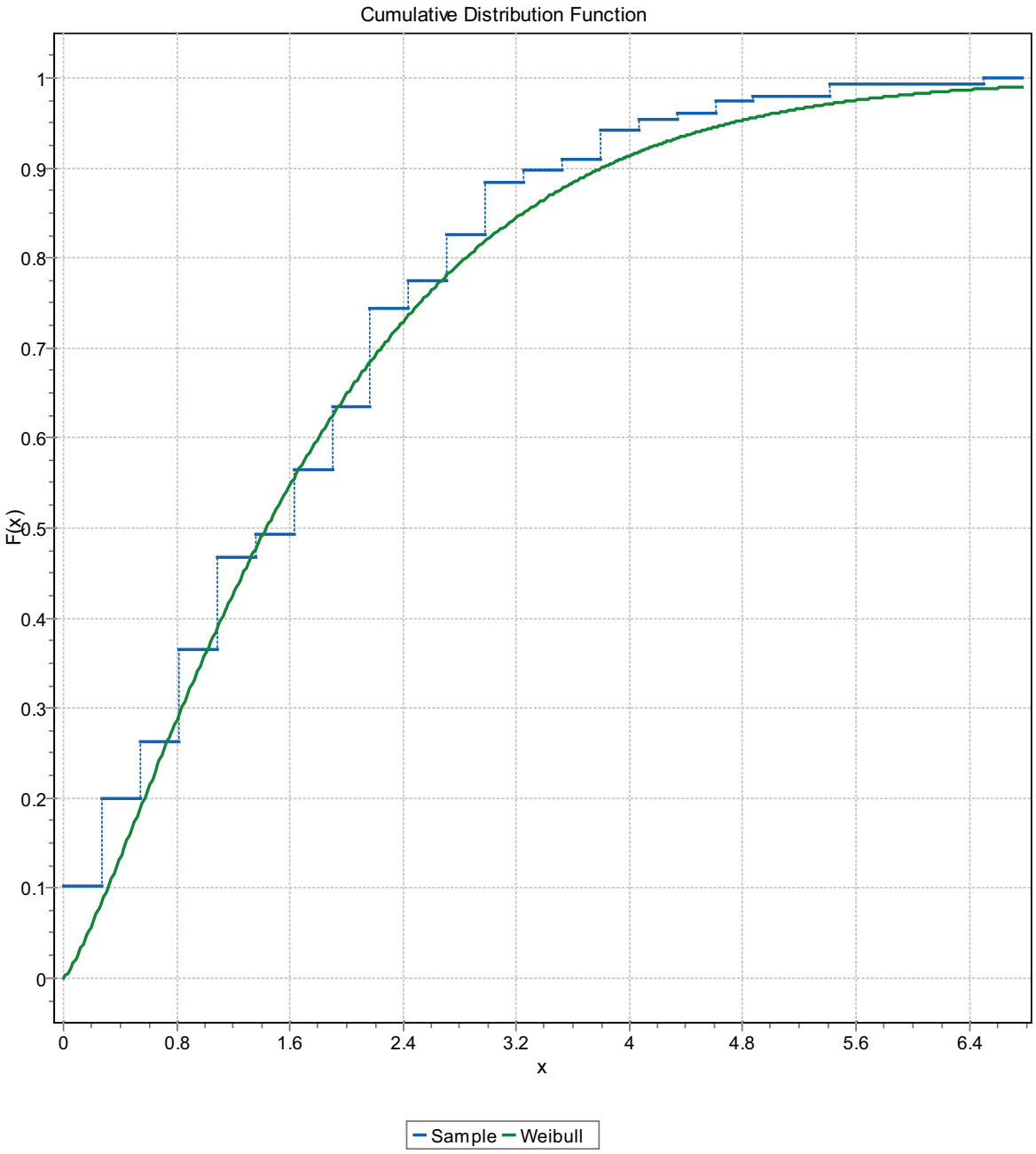

Figure F-130. *CDF, Domain FSM_W, 15 m bins, Weibull Distribution.*

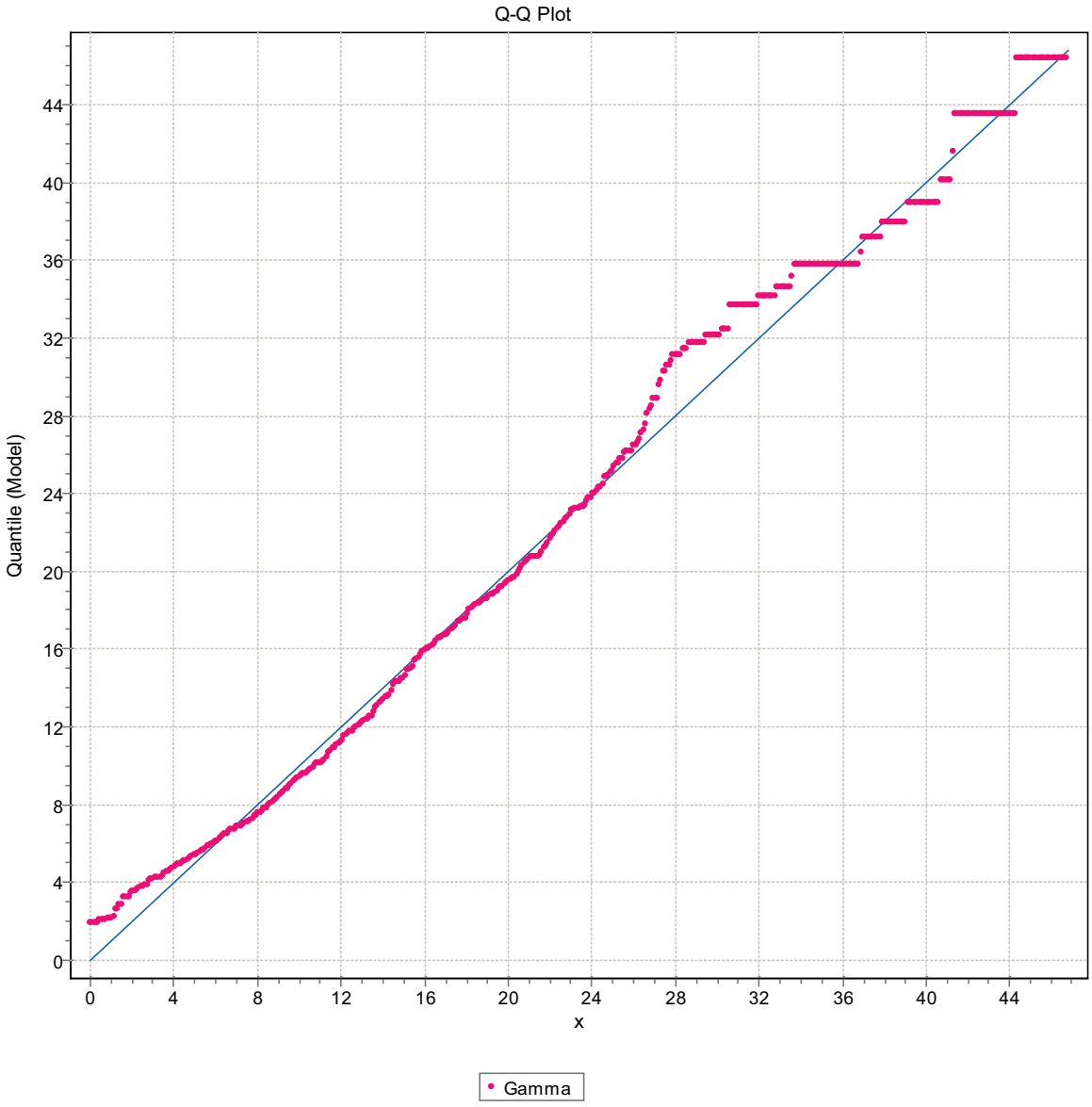

Figure F-131. *Q-Q plot, Domain FSM_EW007, 3 m bins, Gamma Distribution.*

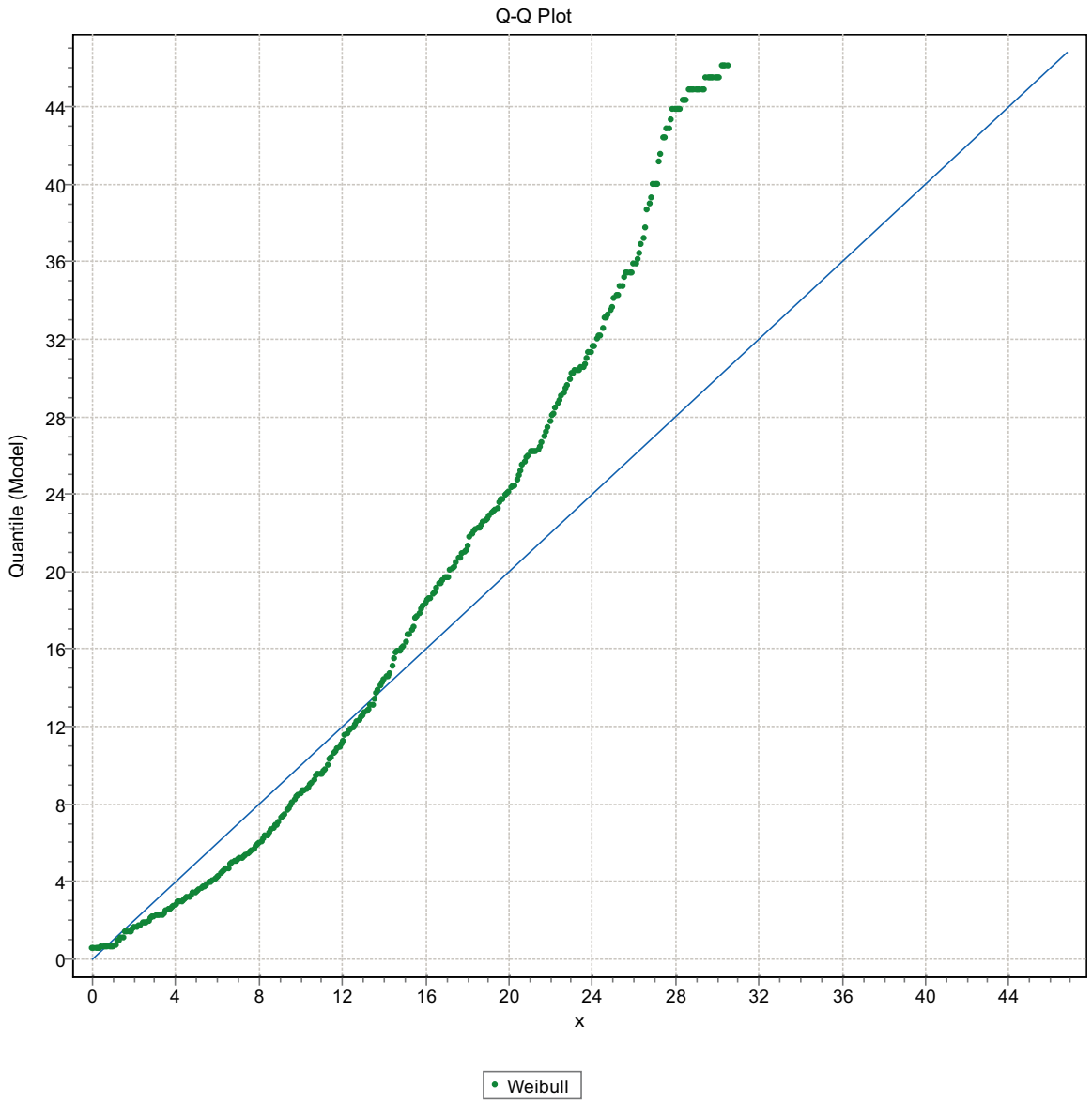

Figure F-132. *Q-Q plot, Domain FSM_EW007, 3 m bins, Weibull Distribution.*

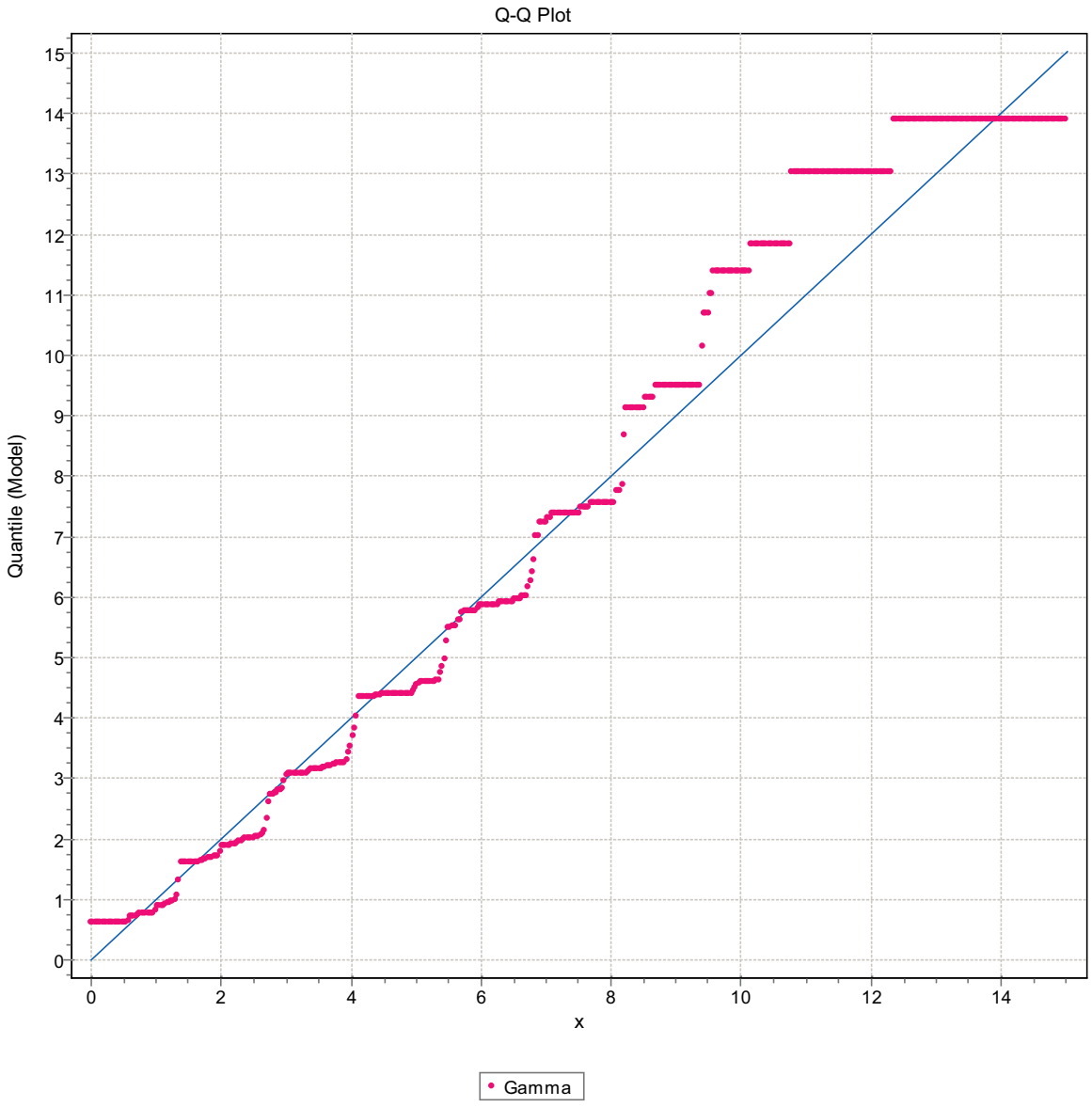

Figure F-133. *Q-Q plot, Domain FSM_EW007, 3 m bins, Gamma Distribution.*

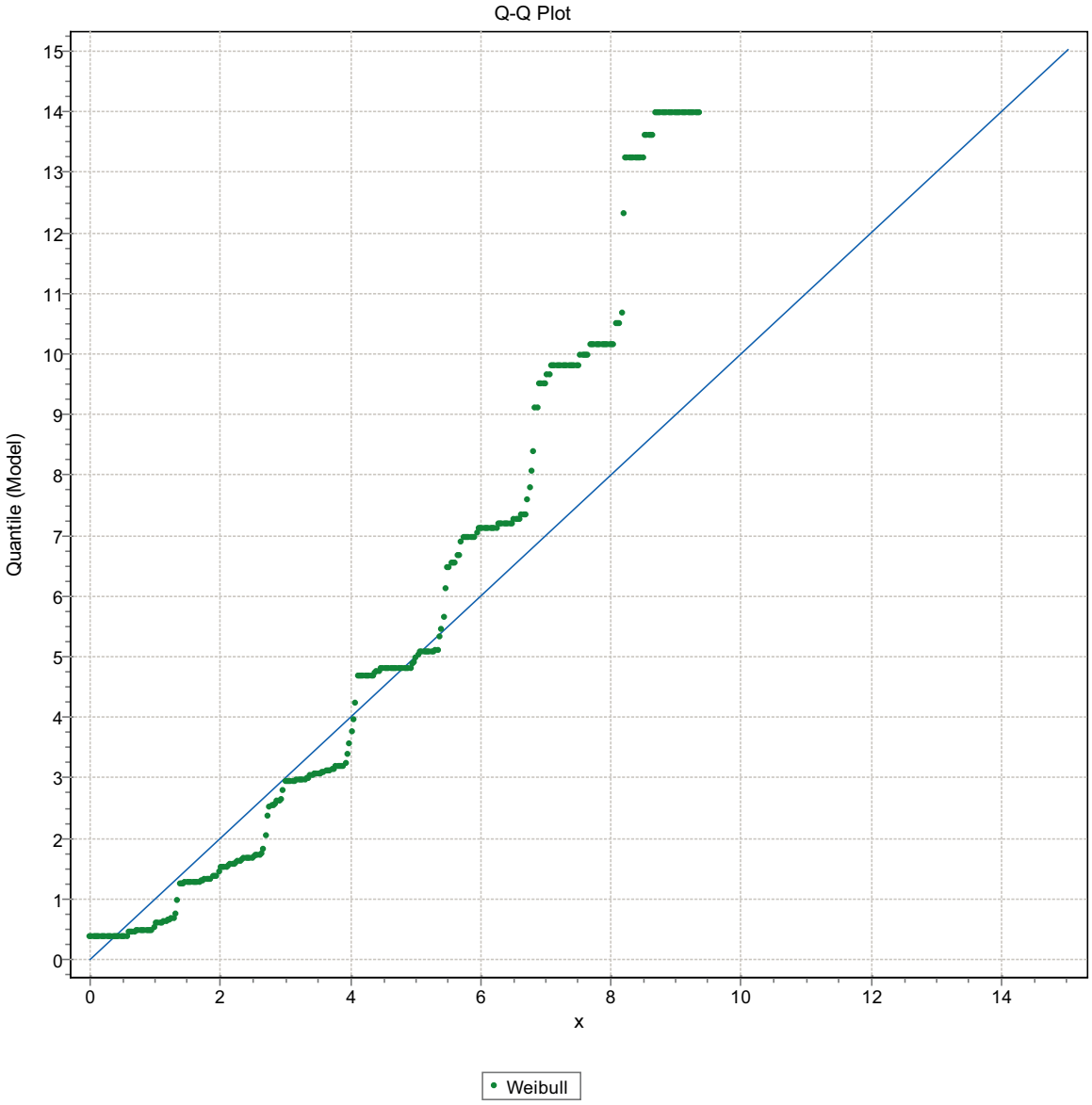

Figure F-134. *Q-Q plot, Domain FSM_EW007, 3 m bins, Weibull Distribution.*

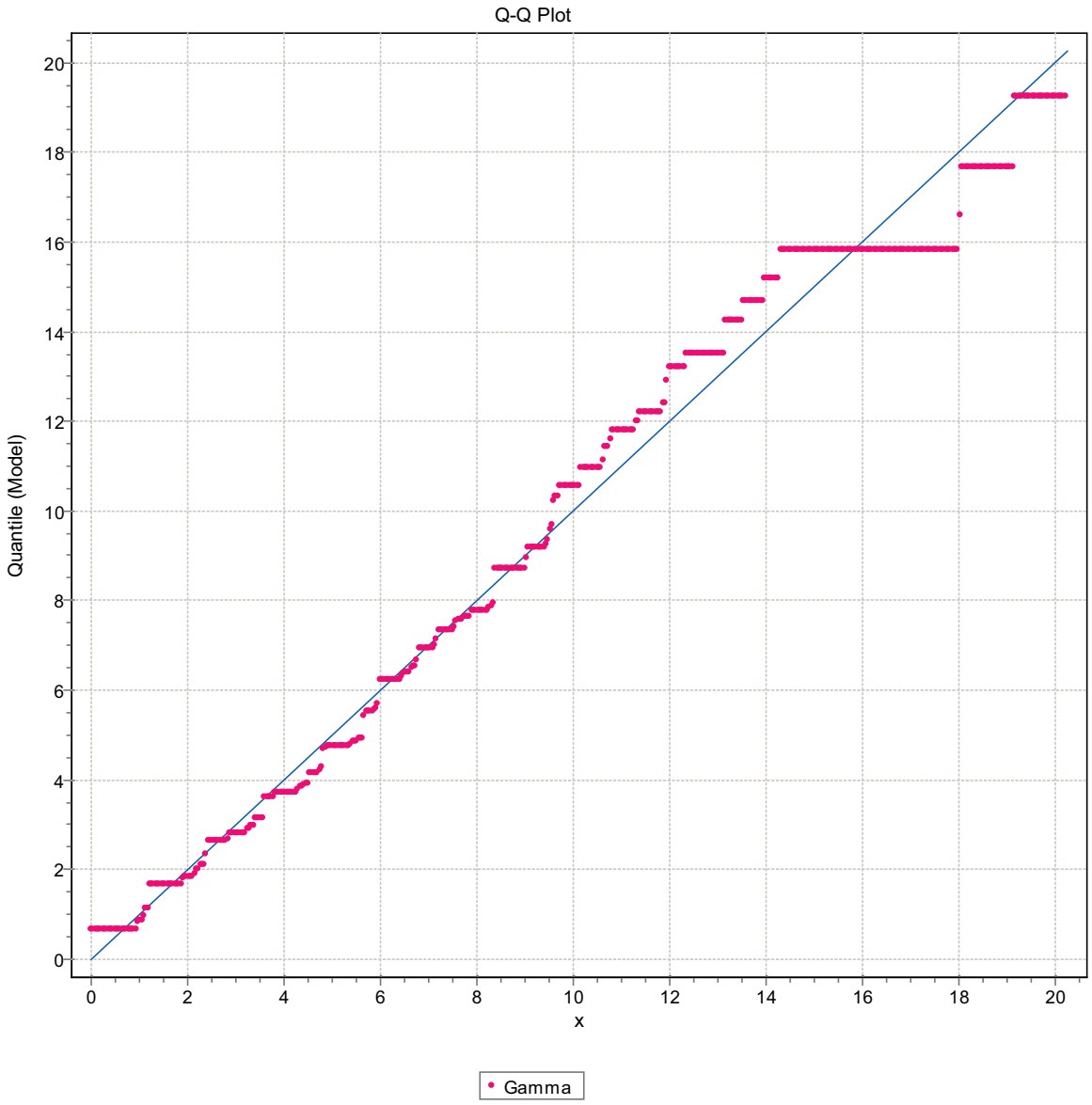

Figure F-135. *Q-Q plot, Domain FSM_EW007, 3 m bins, Gamma Distribution.*

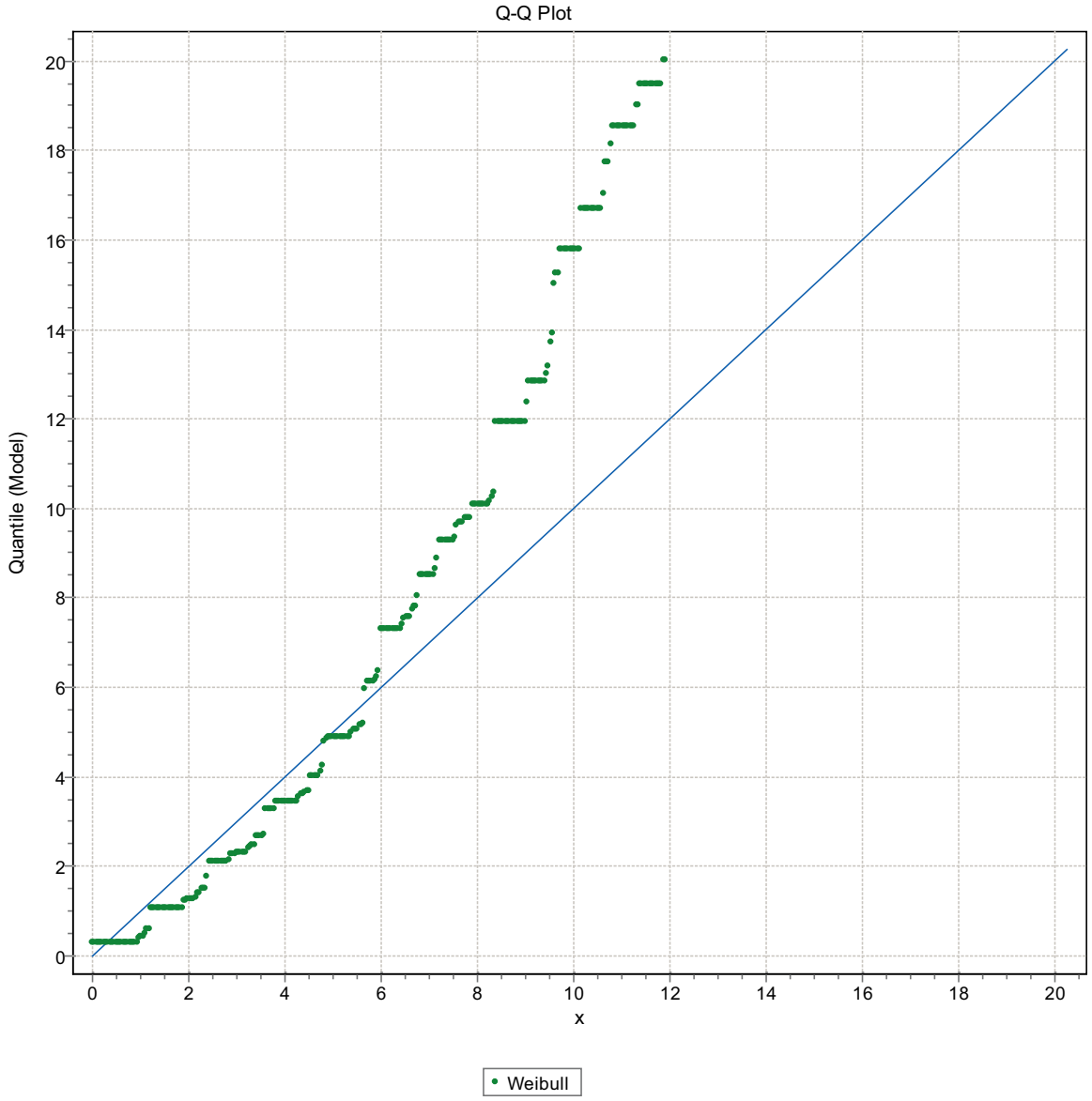

Figure F-136. *Q-Q plot, Domain FSM_EW007, 3 m bins, Weibull Distribution.*

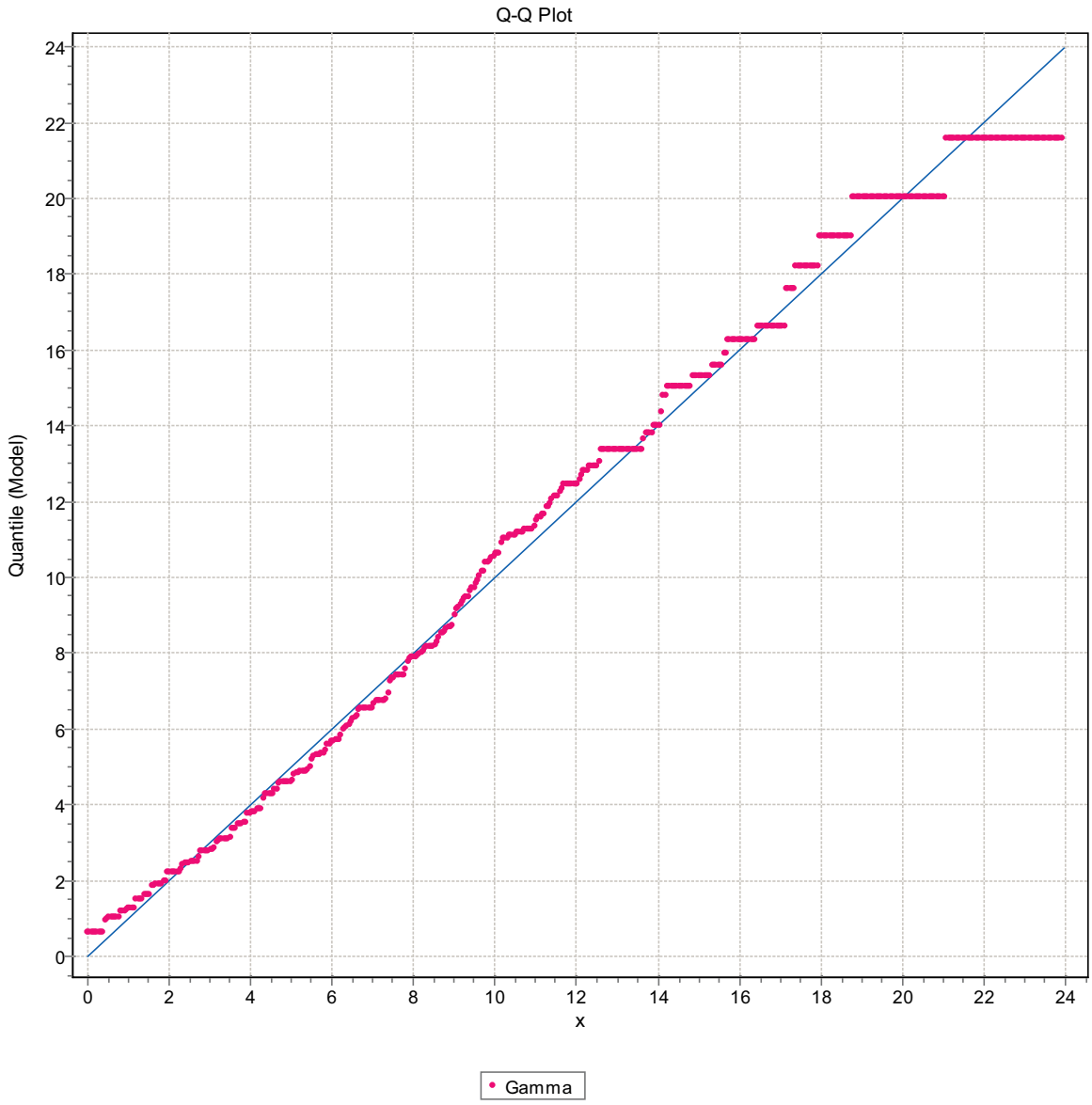

Figure F-137. *Q-Q plot, Domain FSM_EW007, 3 m bins, Gamma Distribution.*

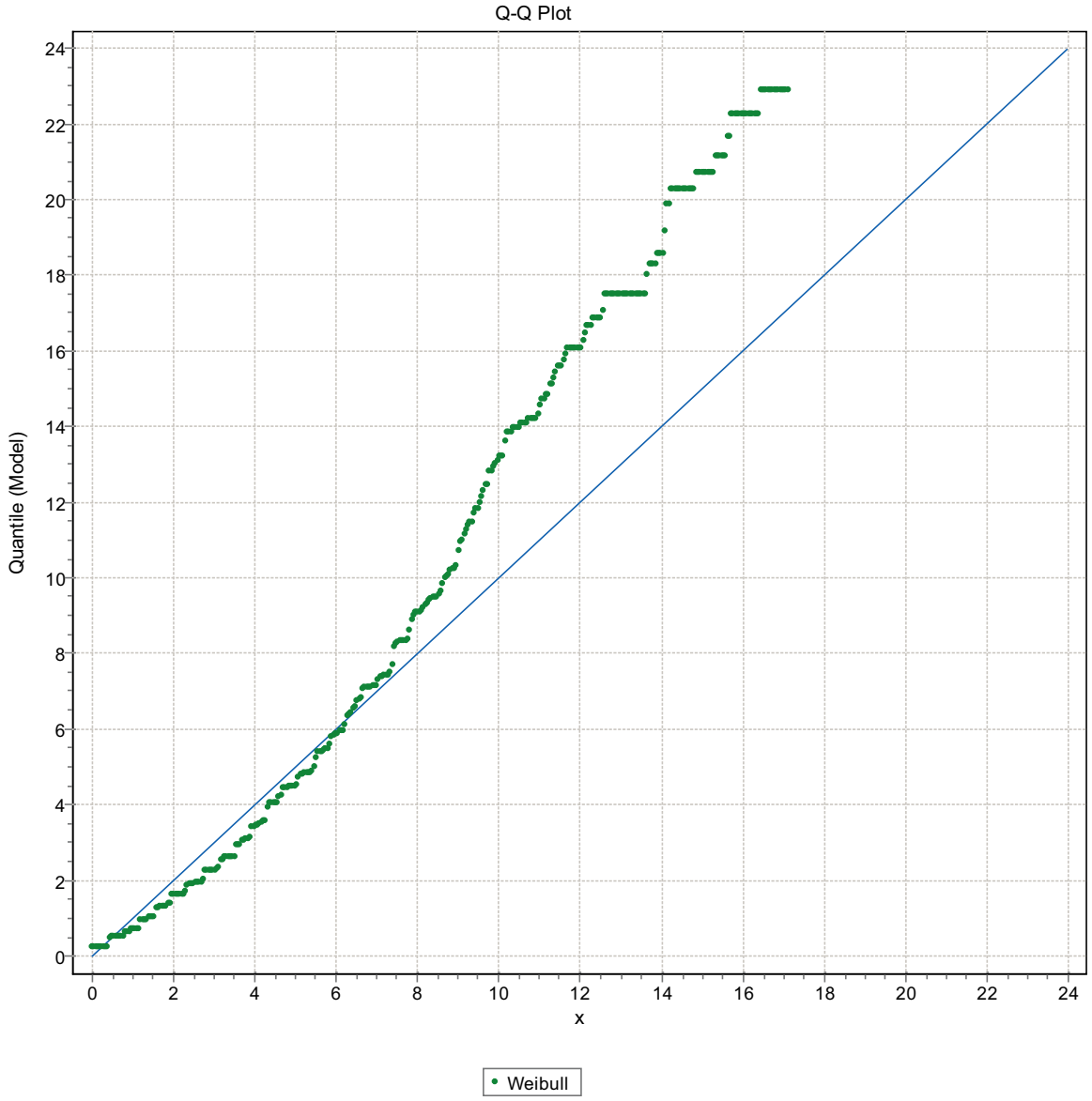

Figure F-138. *Q-Q plot, Domain FSM_EW007, 3 m bins, Weibull Distribution.*

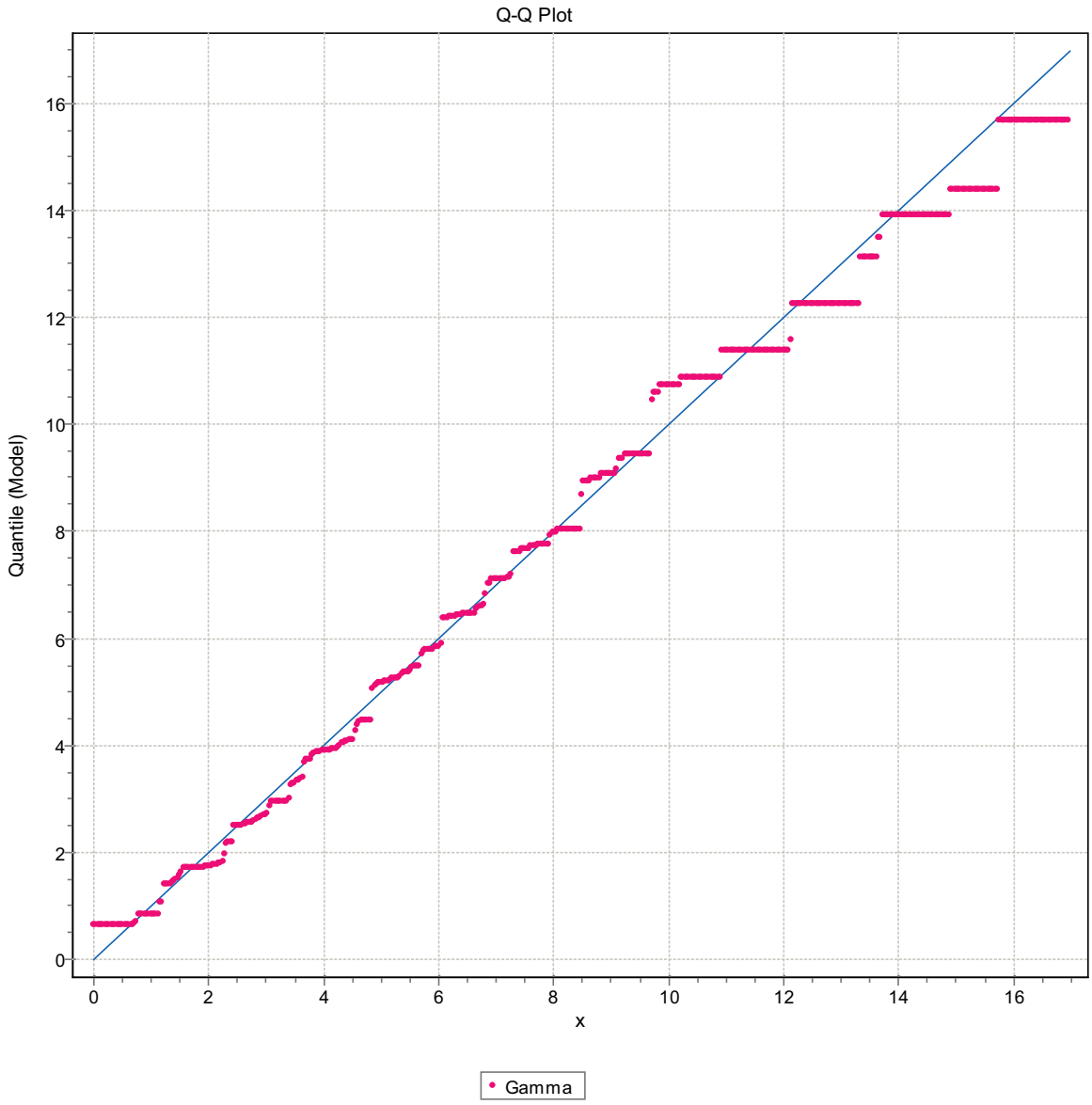

Figure F-139. *Q-Q plot, Domain FSM_EW007, 3 m bins, Gamma Distribution.*

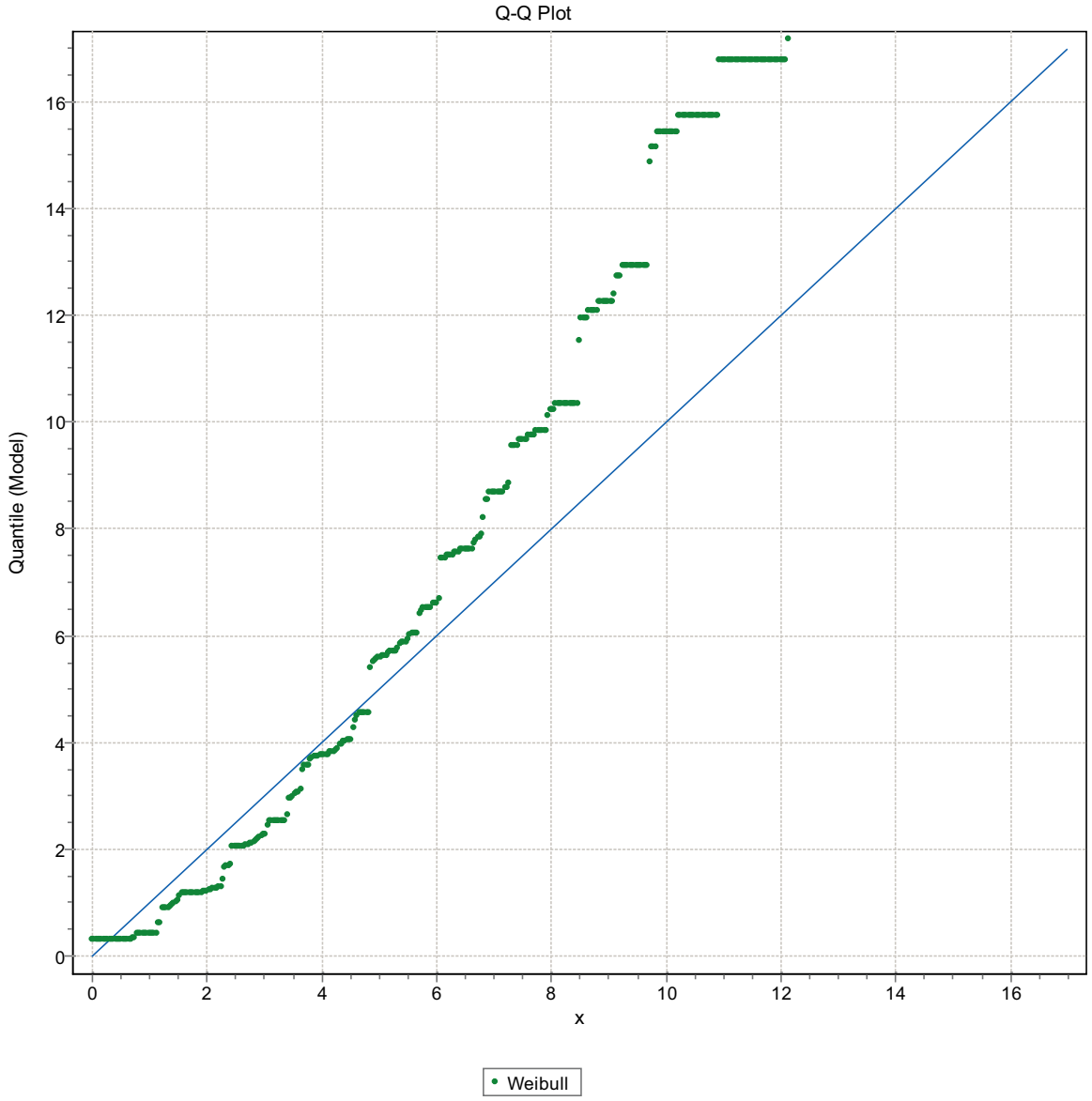

Figure F-140. *Q-Q plot, Domain FSM_EW007, 3 m bins, Weibull Distribution.*

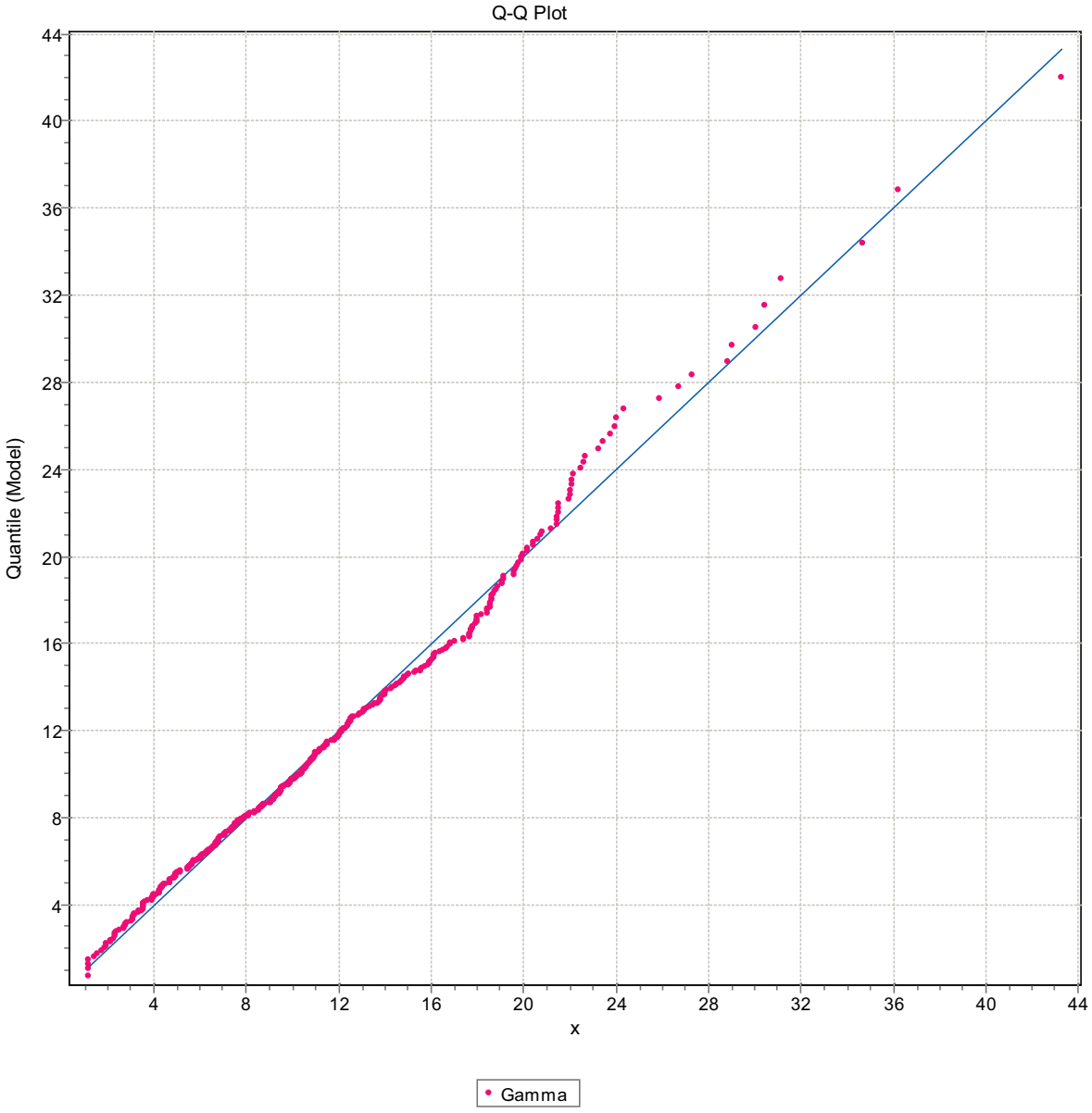

Figure F-141. *Q-Q plot, Domain FSM_NE005, 3 m bins, Gamma Distribution.*

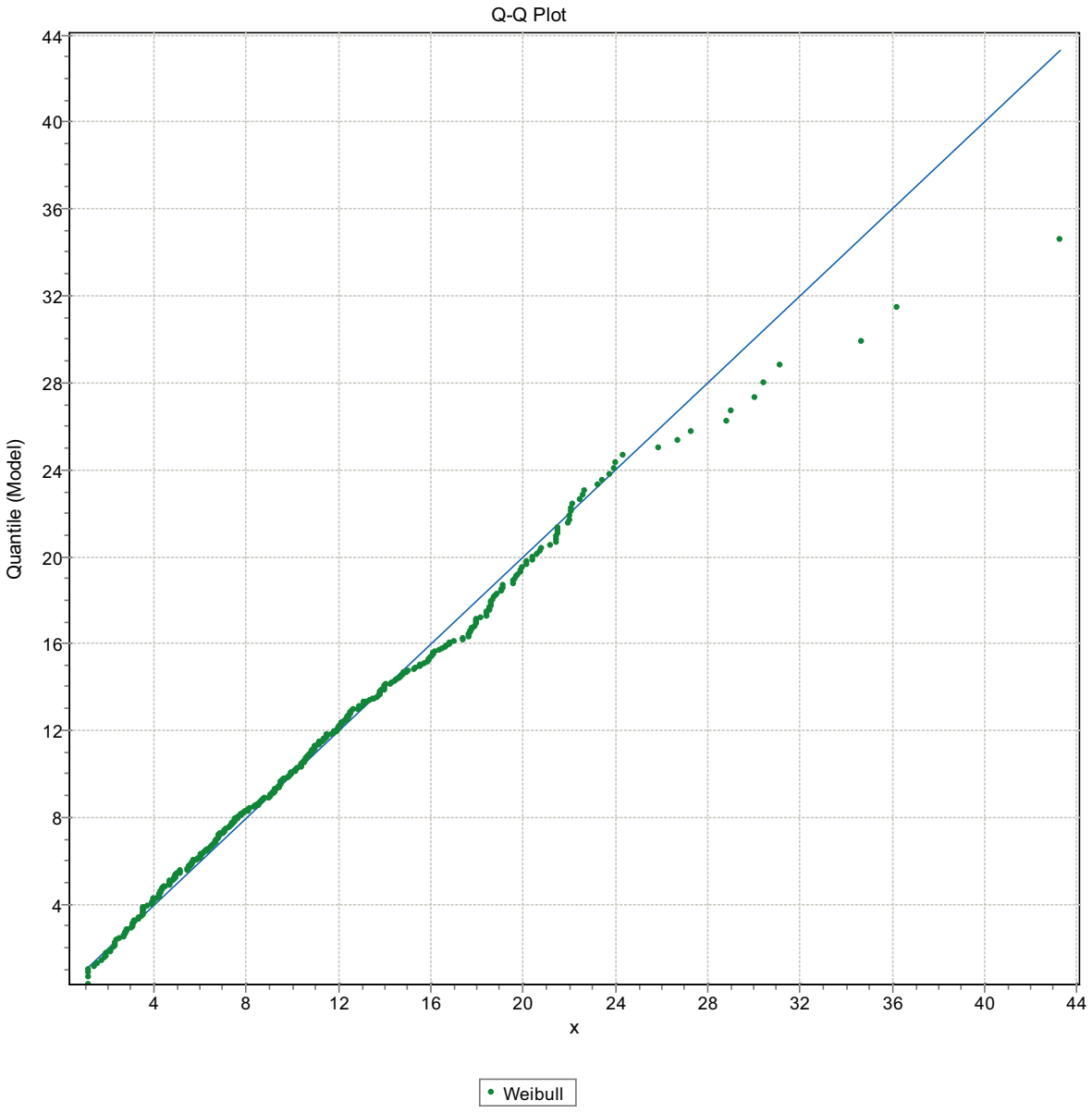

Figure F-142. *Q-Q plot, Domain FSM_NE005, 3 m bins, Weibull Distribution.*

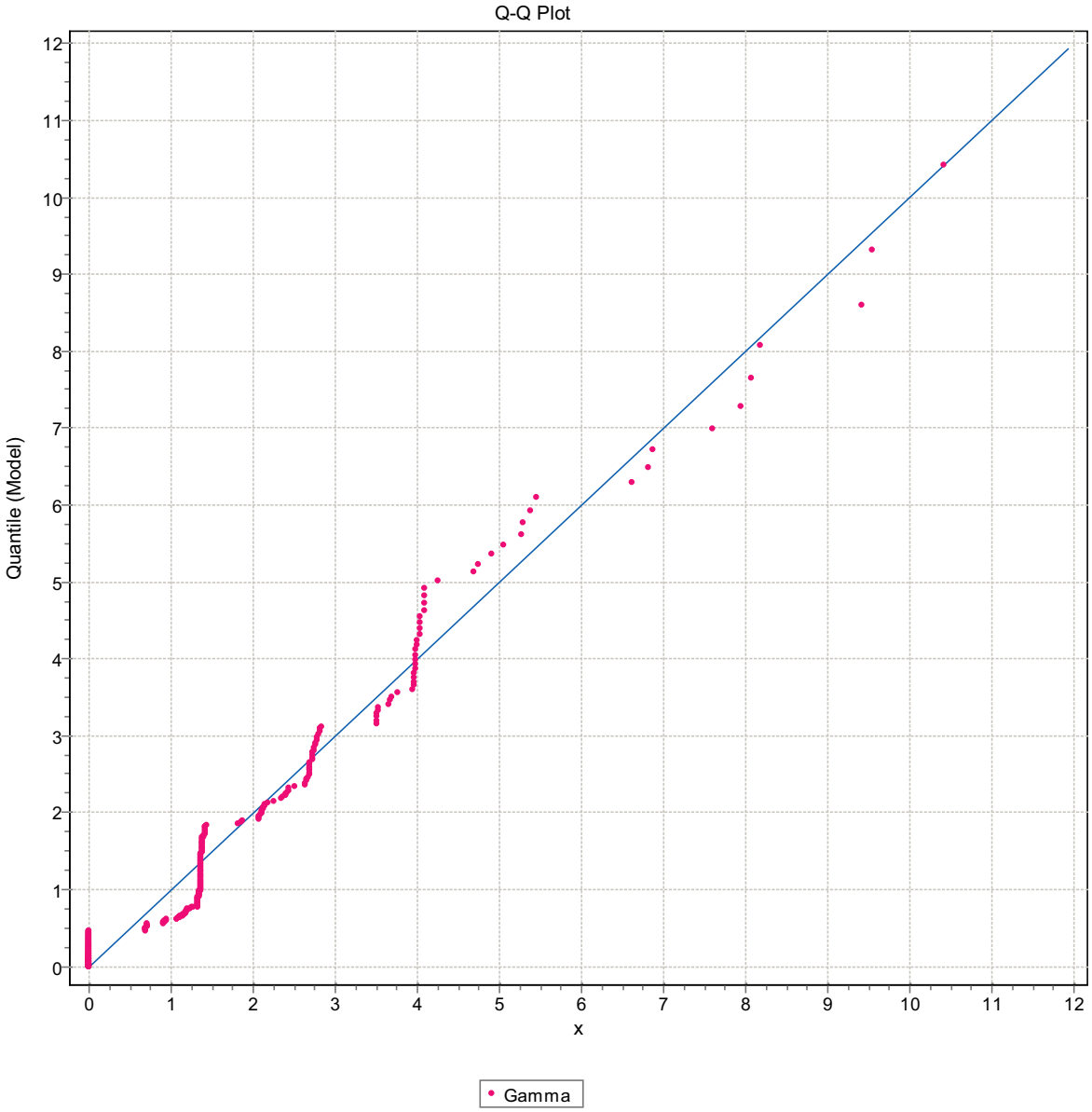

Figure F-143. *Q-Q plot, Domain FSM_NE005, 3 m bins, Gamma Distribution.*

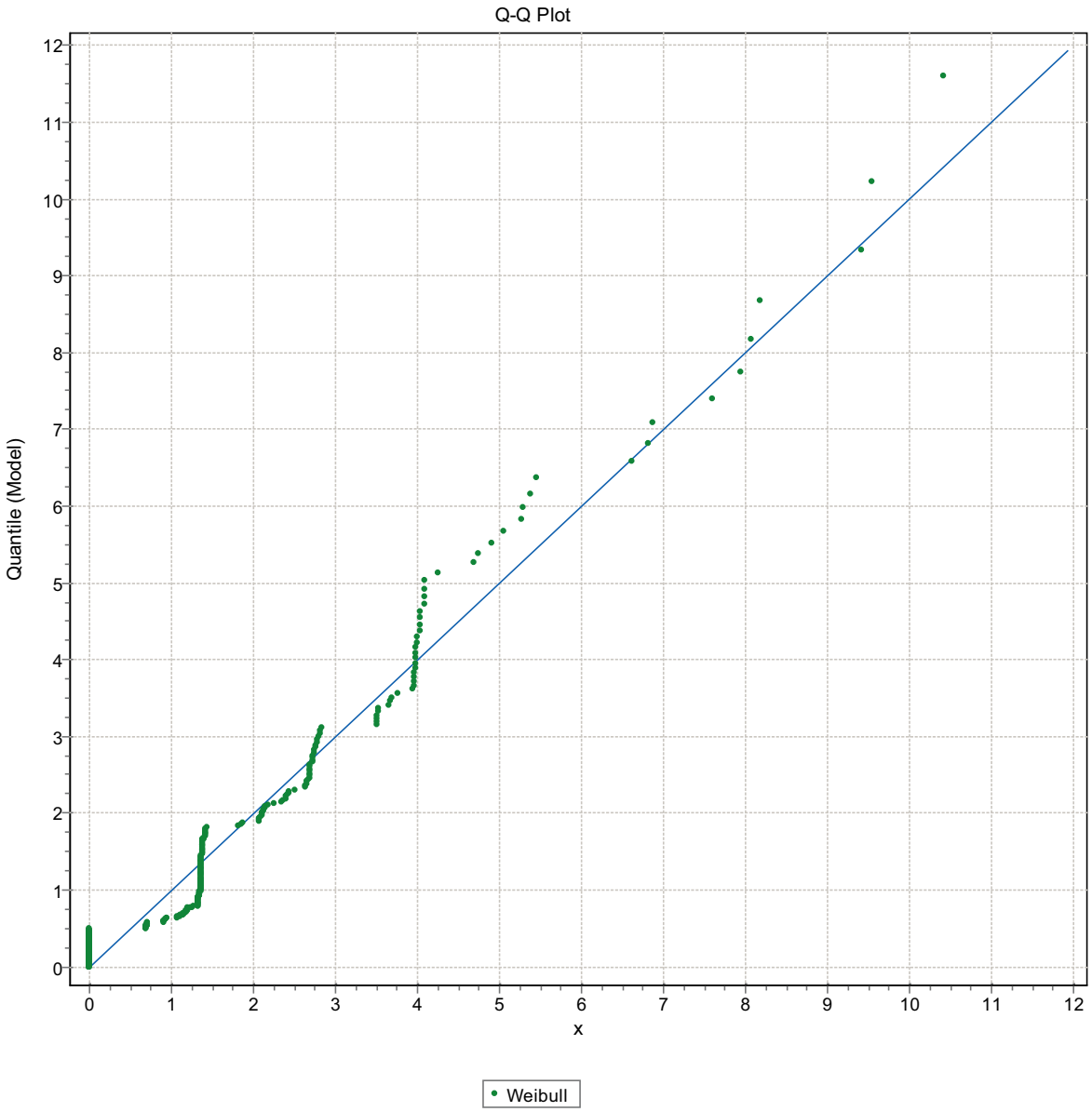

Figure F-144. *Q-Q plot, Domain FSM_NE005, 3 m bins, Weibull Distribution.*

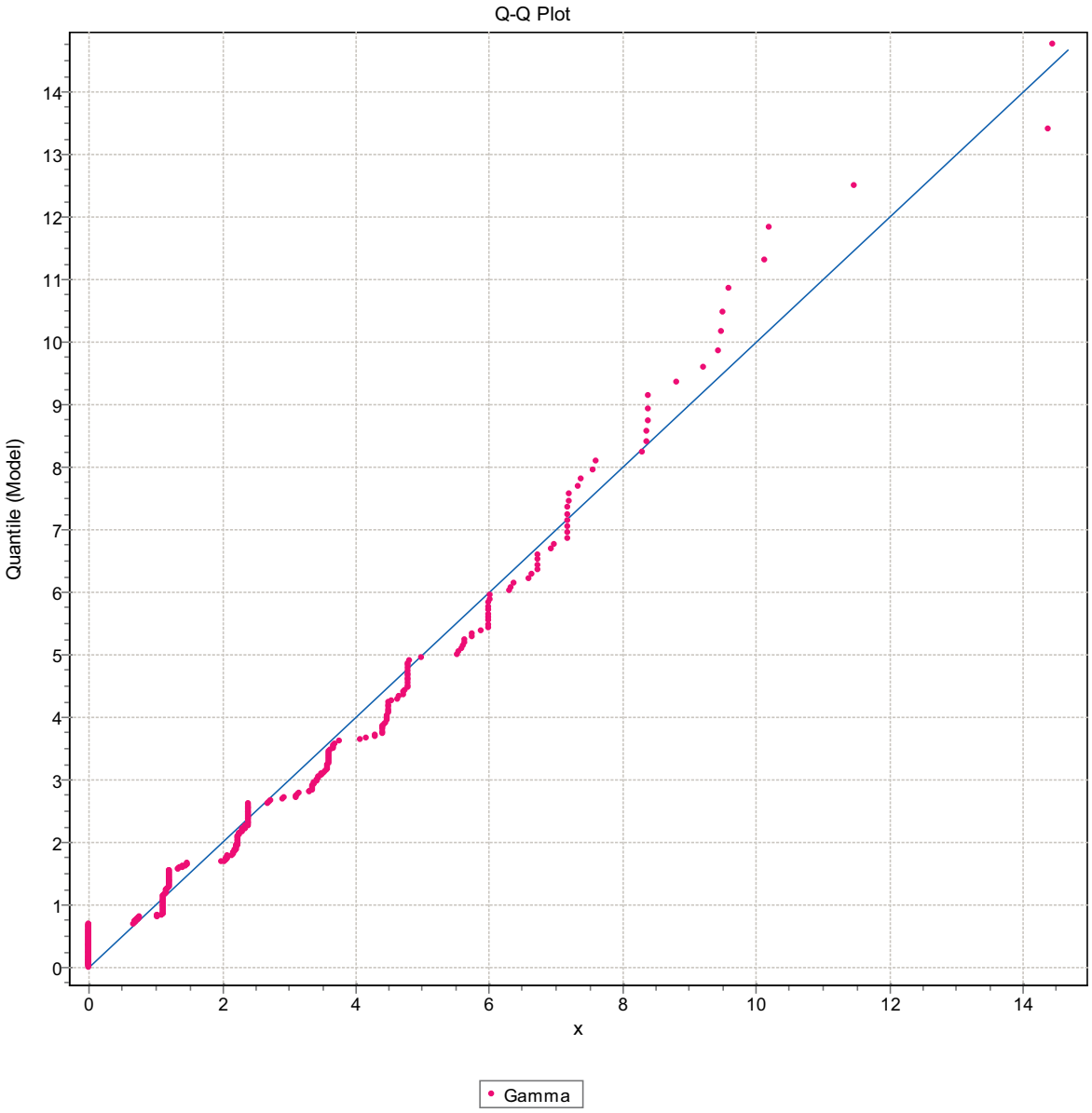

Figure F-145. *Q-Q plot, Domain FSM_NE005, 3 m bins, Gamma Distribution.*

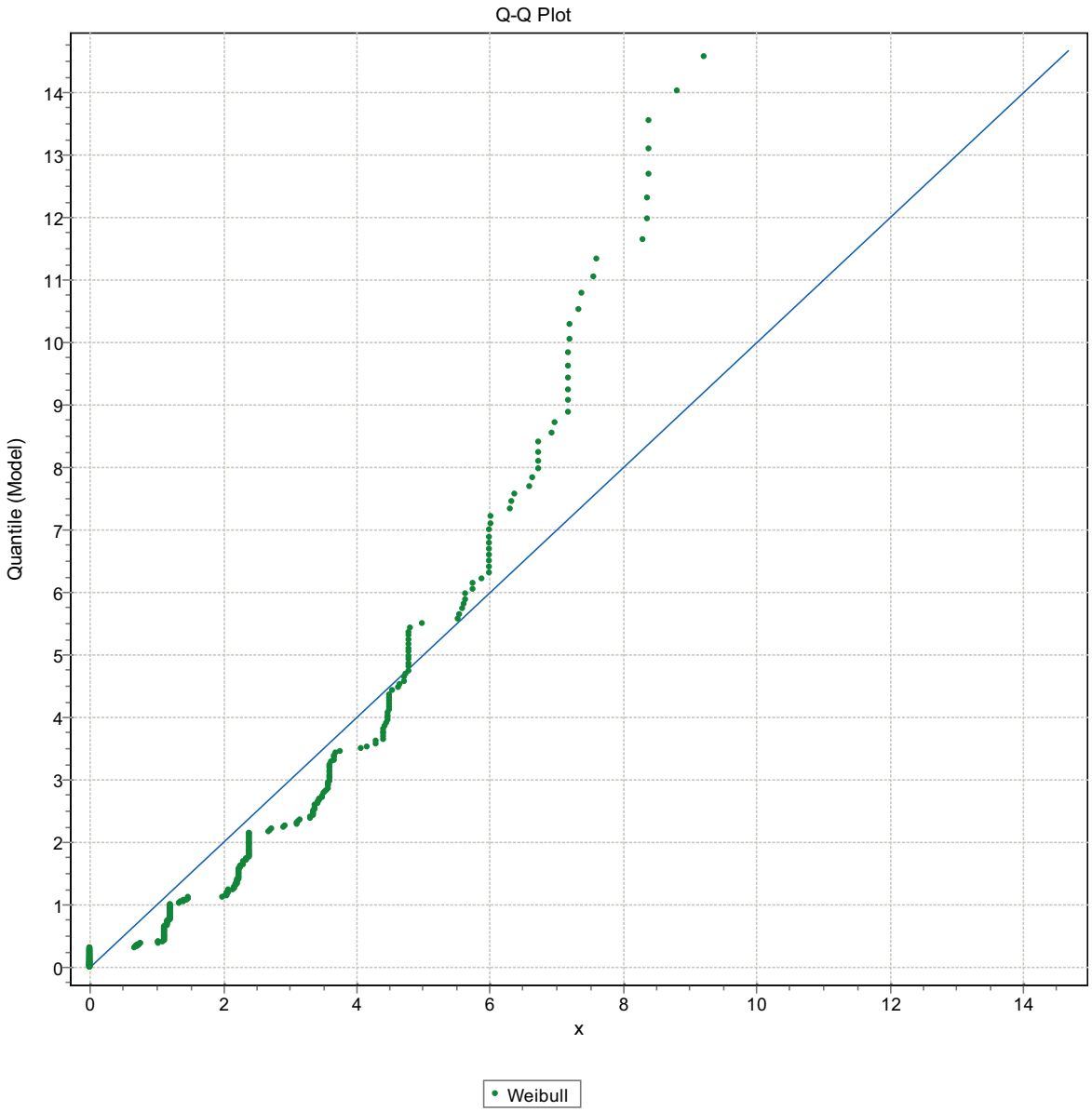

Figure F-146. *Q-Q plot, Domain FSM_NE005, 3 m bins, Weibull Distribution.*

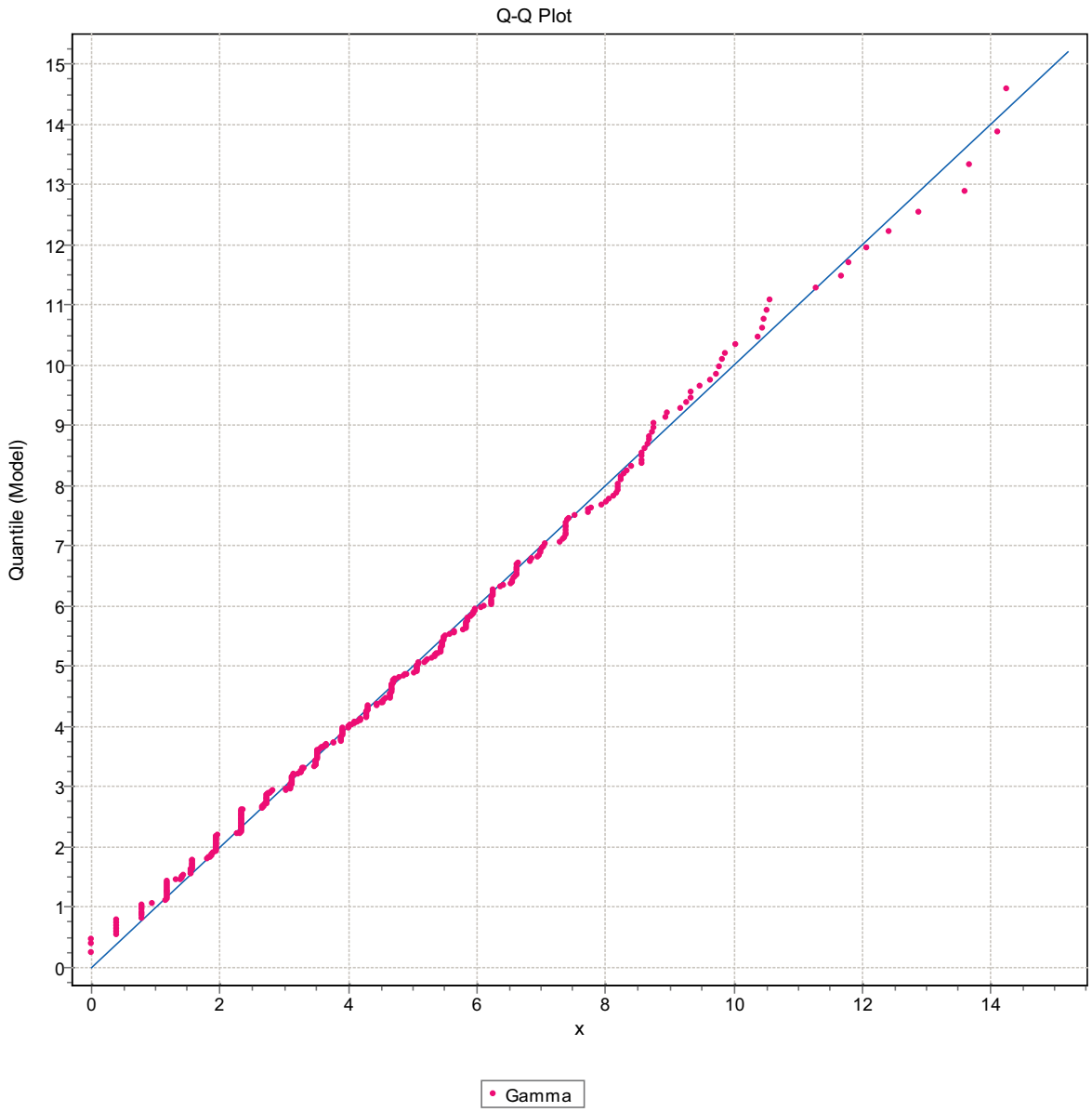

Figure F-147. *Q-Q plot, Domain FSM_NE005, 3 m bins, Gamma Distribution.*

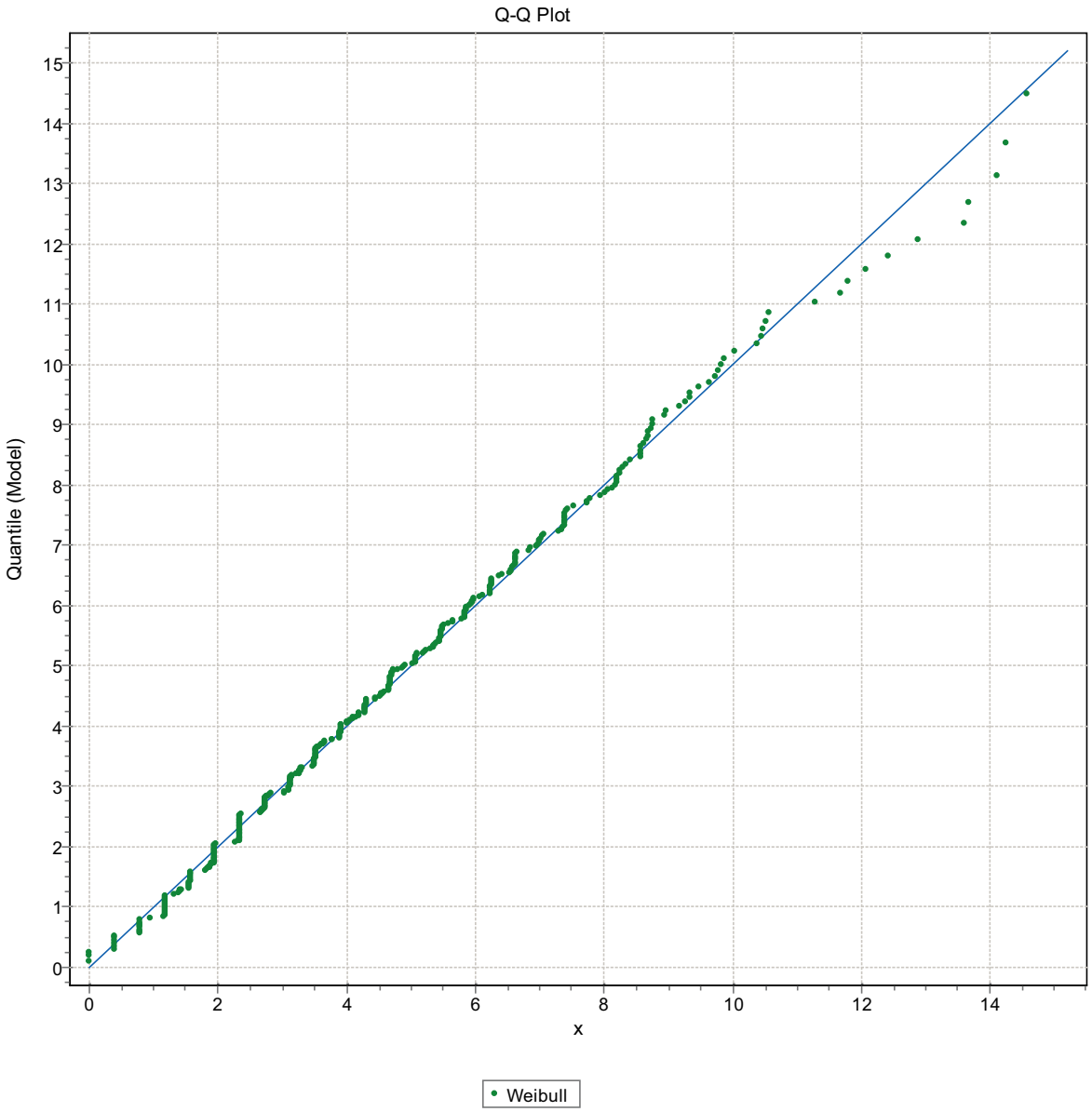

Figure F-148. *Q-Q plot, Domain FSM_NE005, 3 m bins, Weibull Distribution.*

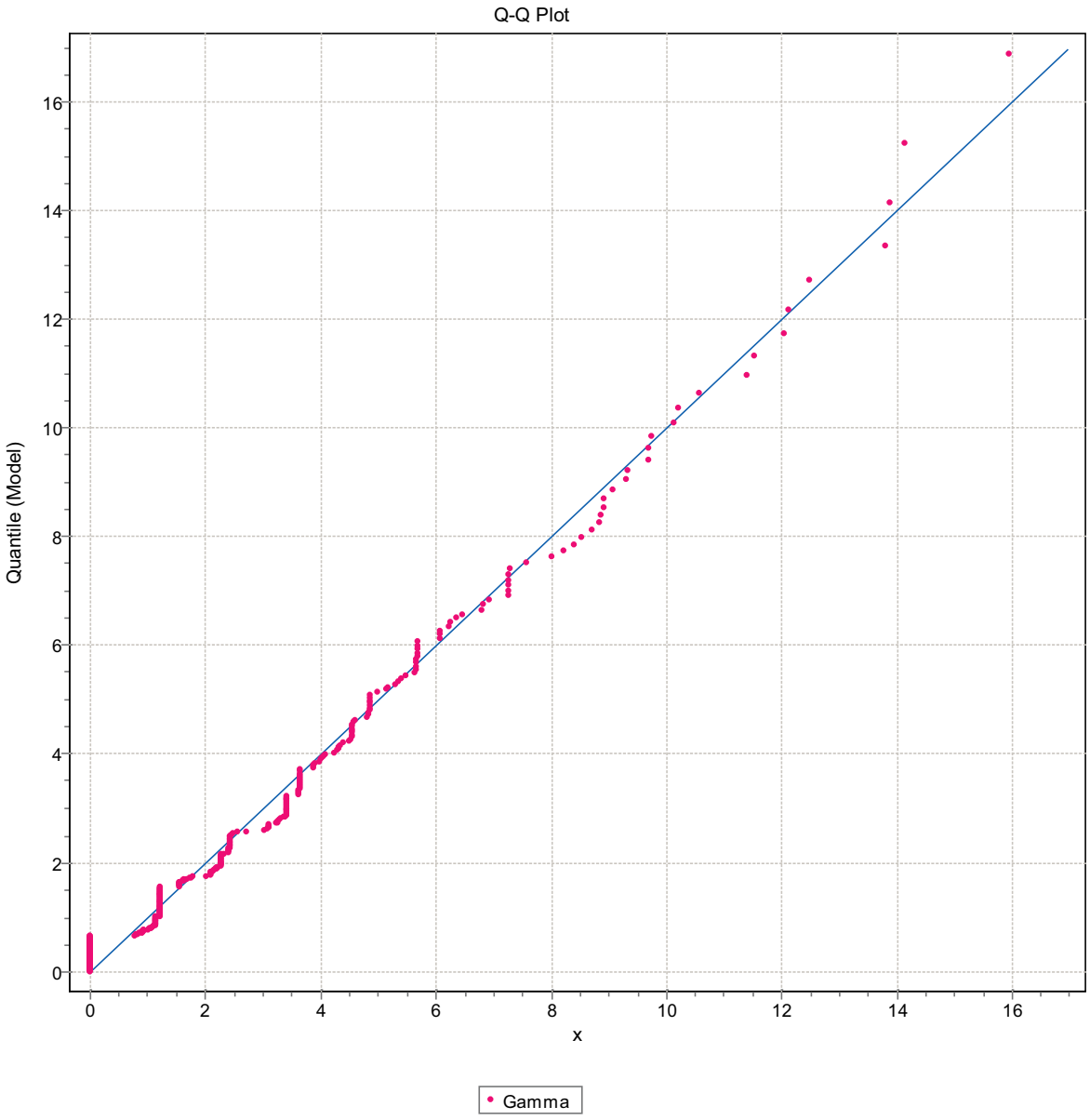

Figure F-149. *Q-Q plot, Domain FSM_NE005, 3 m bins, Gamma Distribution.*

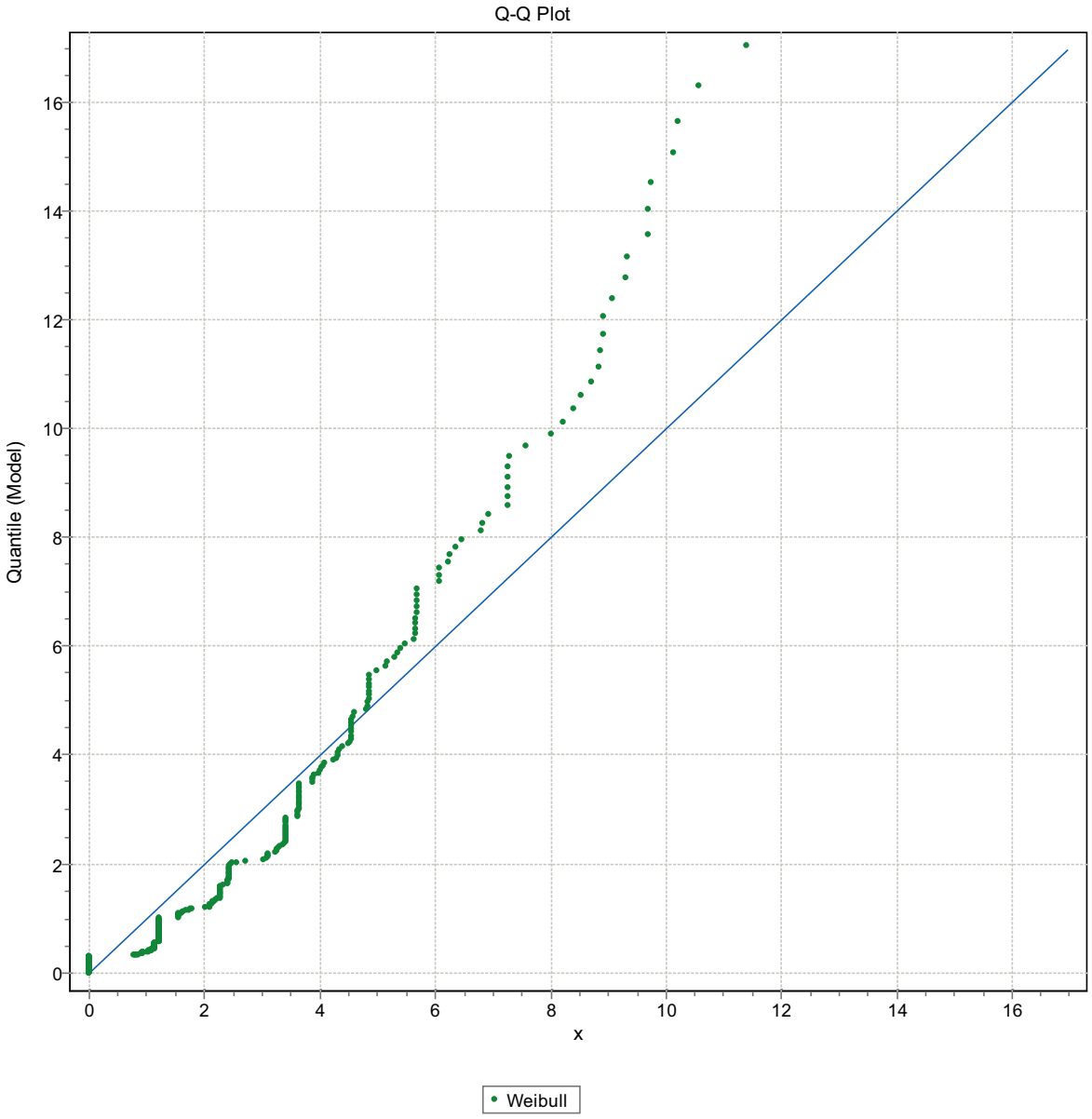

Figure F-150. *Q-Q plot, Domain FSM_NE005, 3 m bins, Weibull Distribution.*

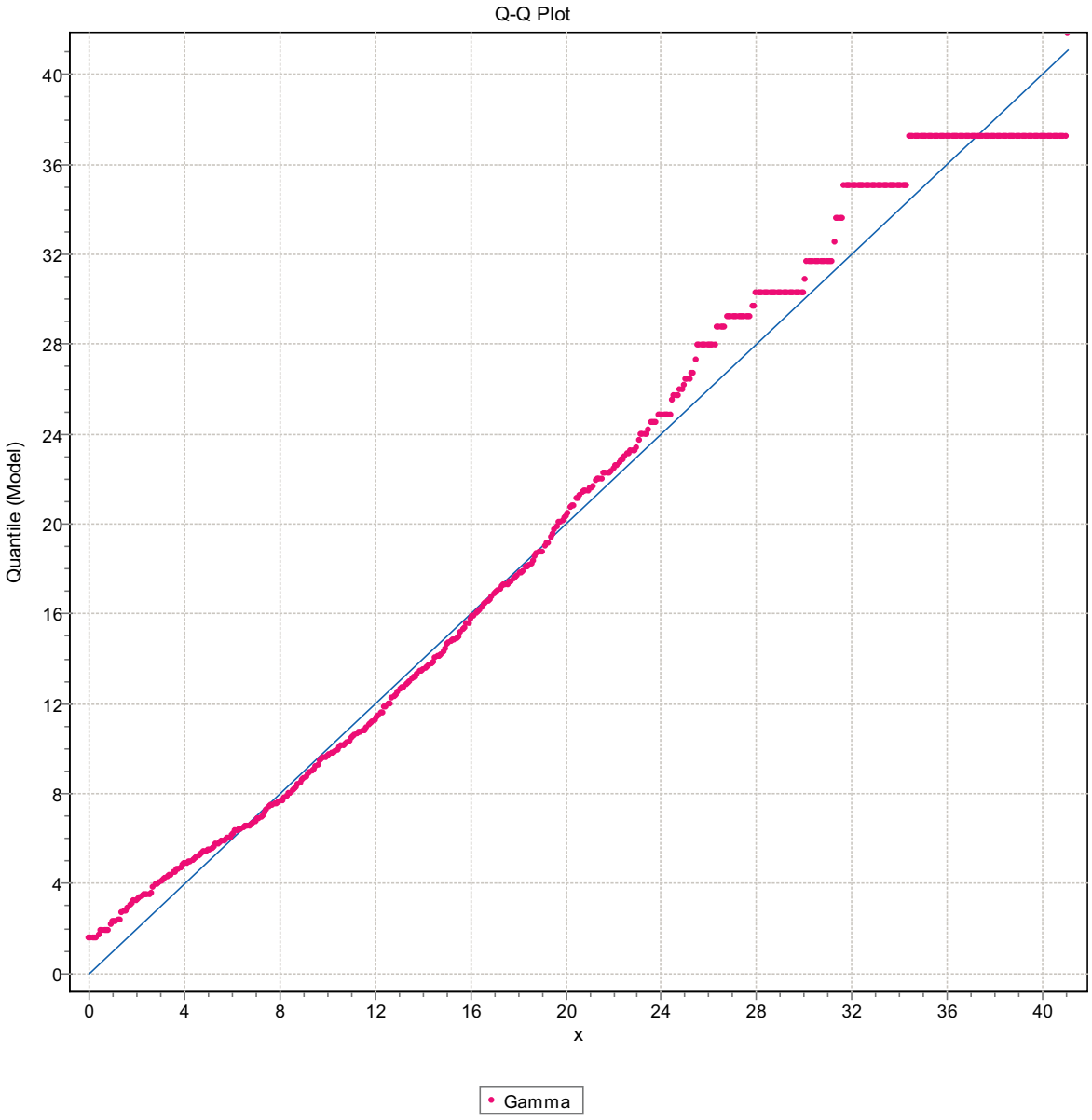

Figure F-151. *Q-Q plot, Domain FSM_N, 3 m bins, Gamma Distribution.*

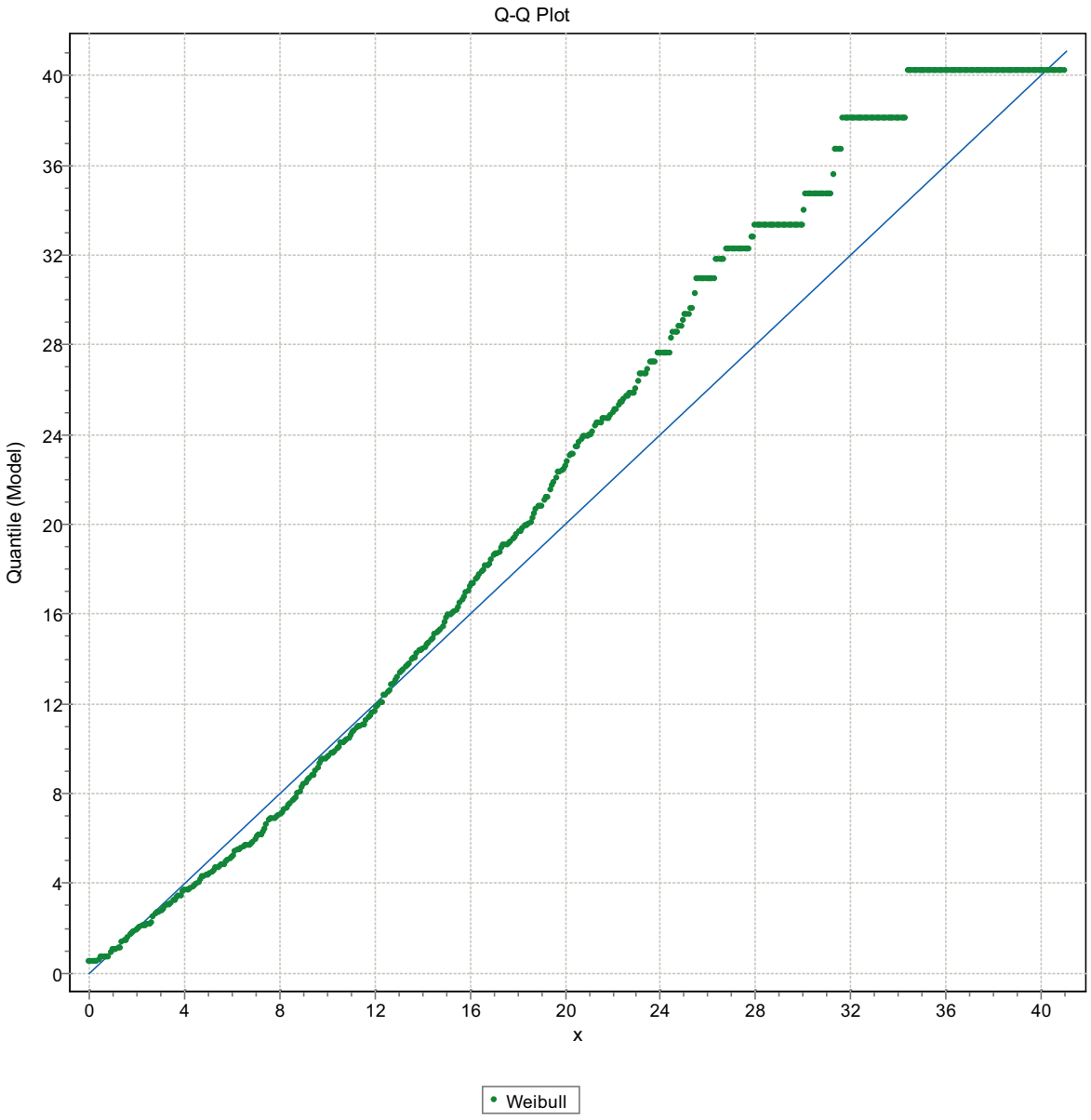

Figure F-152. *Q-Q plot, Domain FSM_N, 3 m bins, Weibull Distribution.*

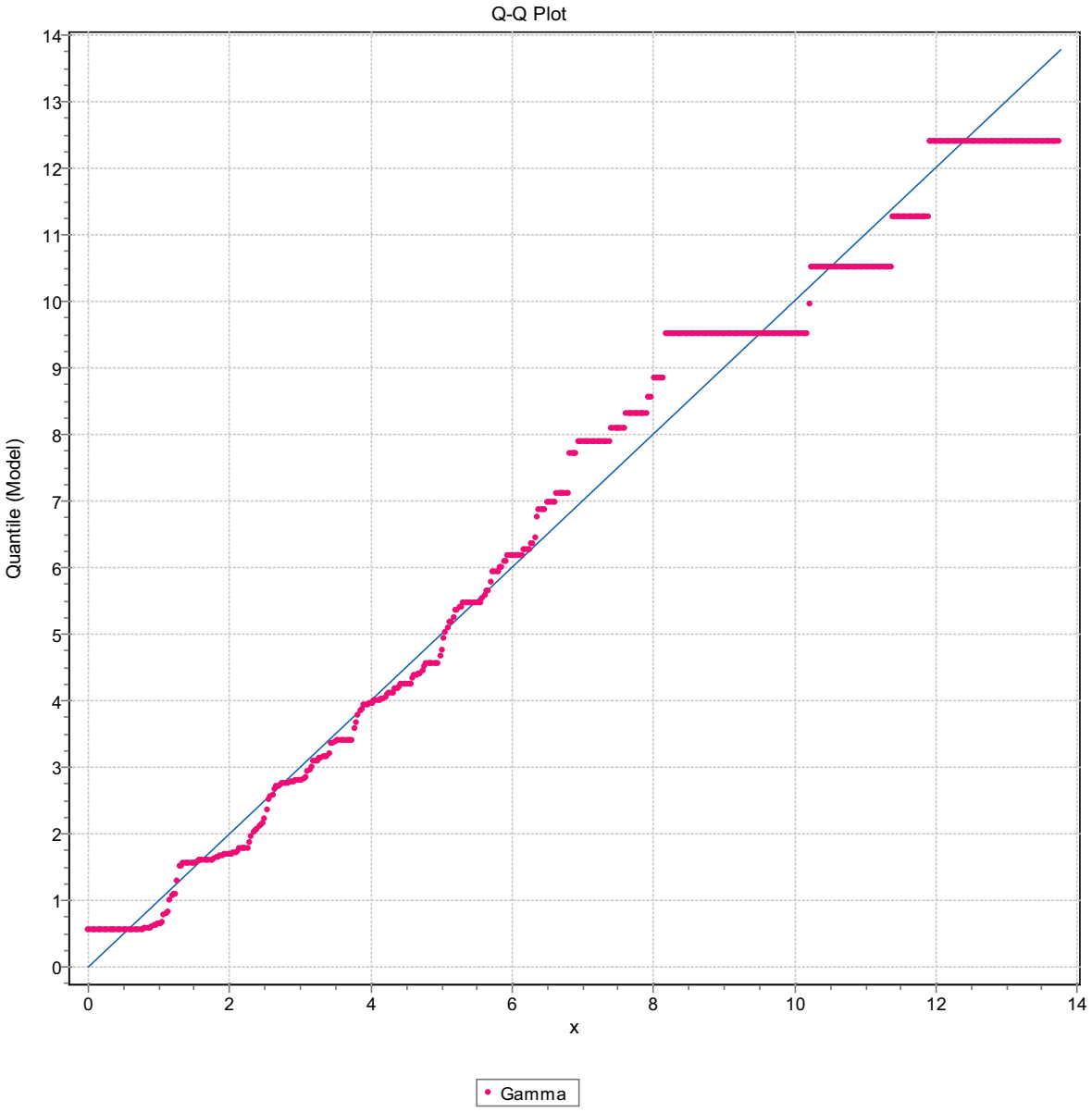

Figure F-153. *Q-Q plot, Domain FSM_N, 3 m bins, Gamma Distribution.*

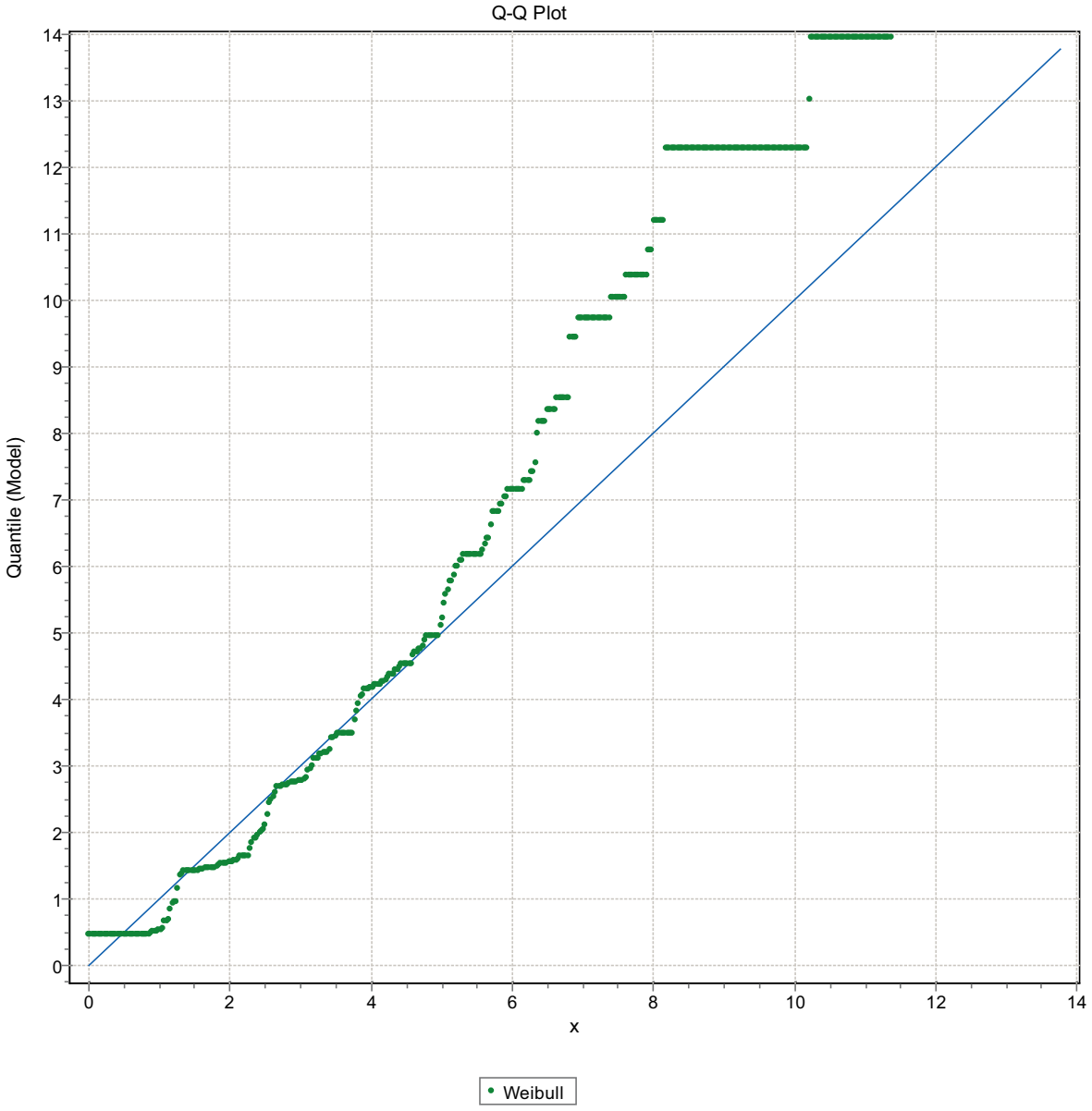

Figure F-154. *Q-Q plot, Domain FSM_N, 3 m bins, Weibull Distribution.*

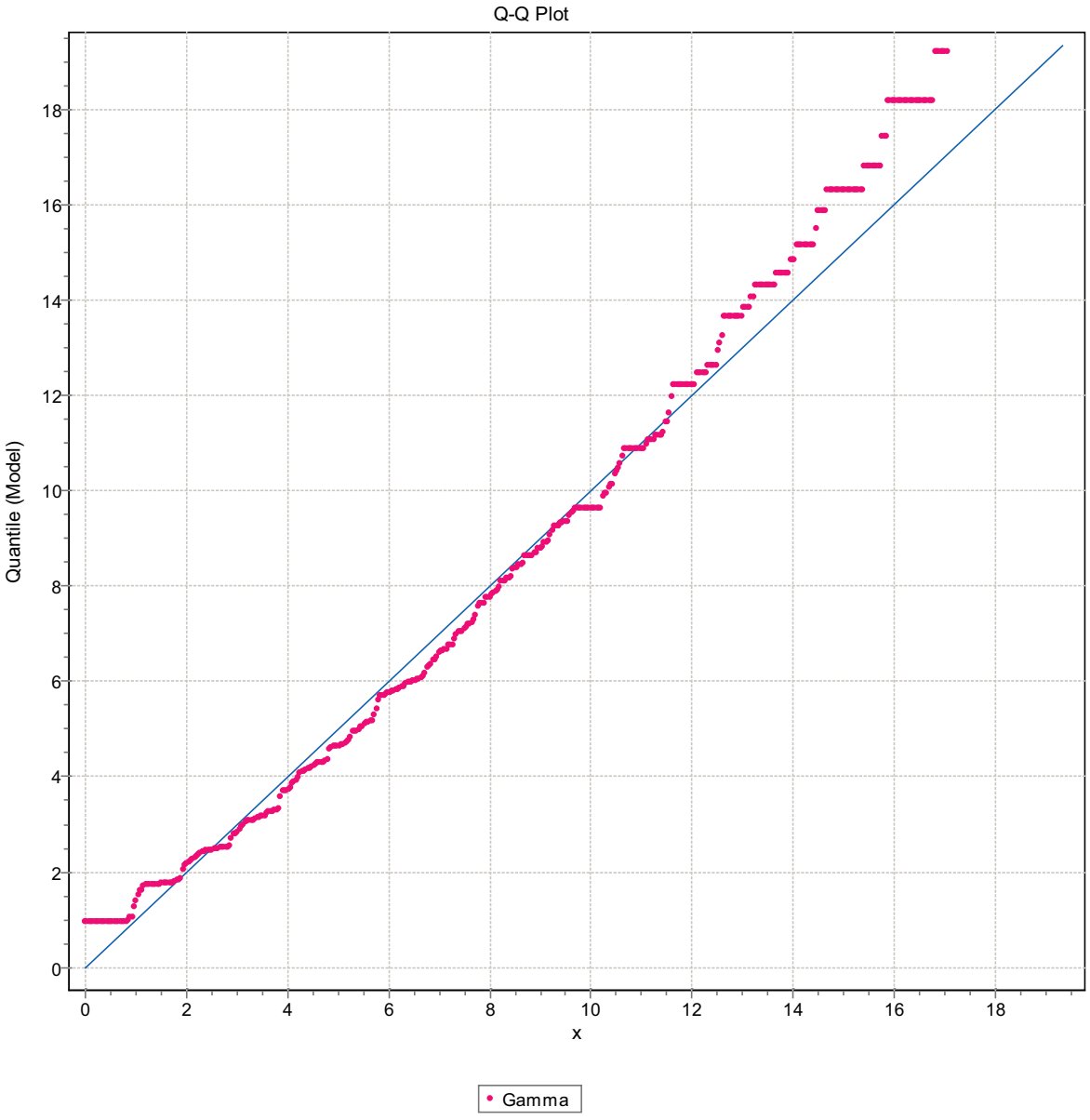

Figure F-155. *Q-Q plot, Domain FSM_N, 3 m bins, Gamma Distribution.*

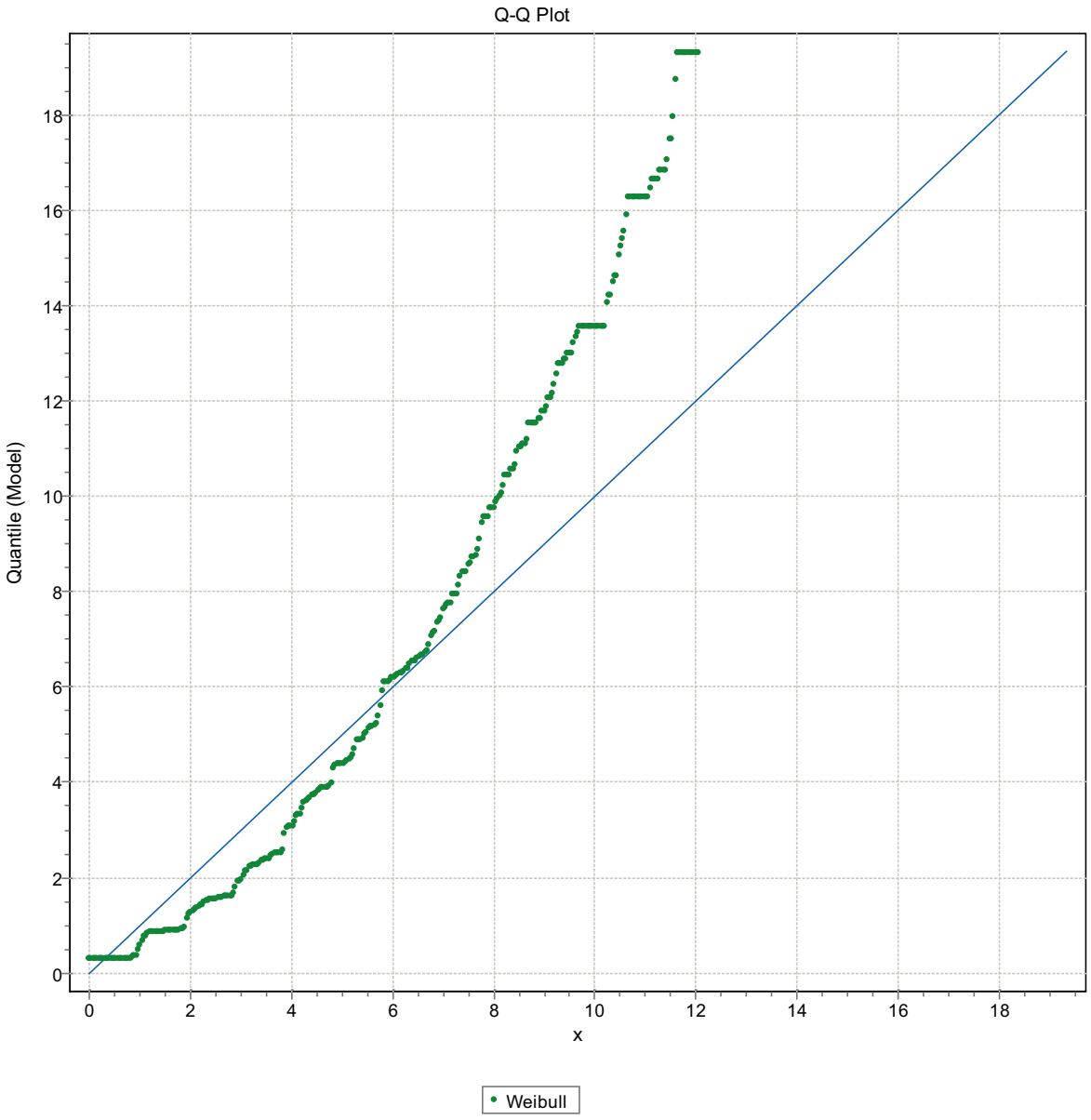

Figure F-156. *Q-Q plot, Domain FSM_N, 3 m bins, Weibull Distribution.*

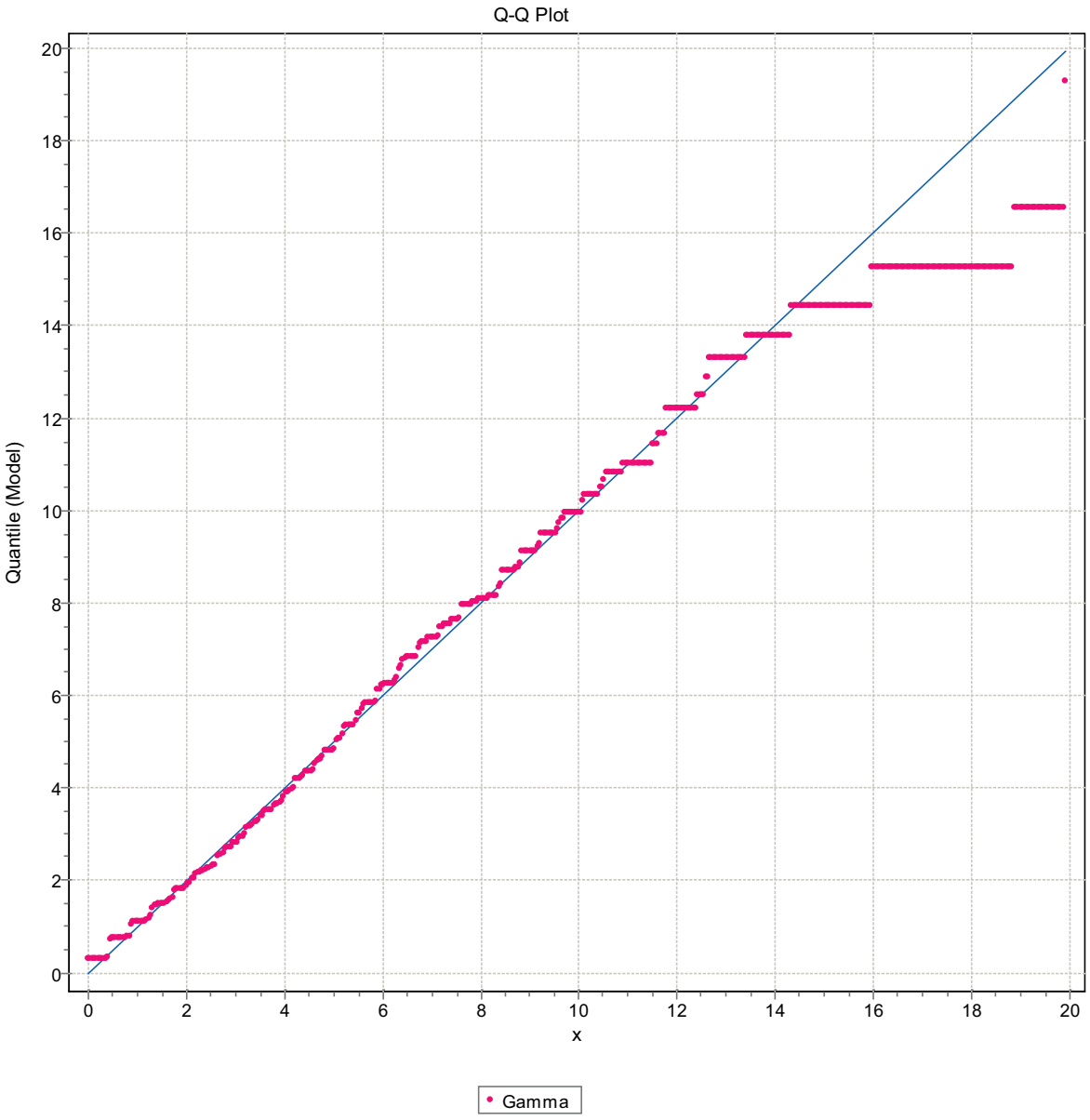

Figure F-157. *Q-Q plot, Domain FSM_N, 3 m bins, Gamma Distribution.*

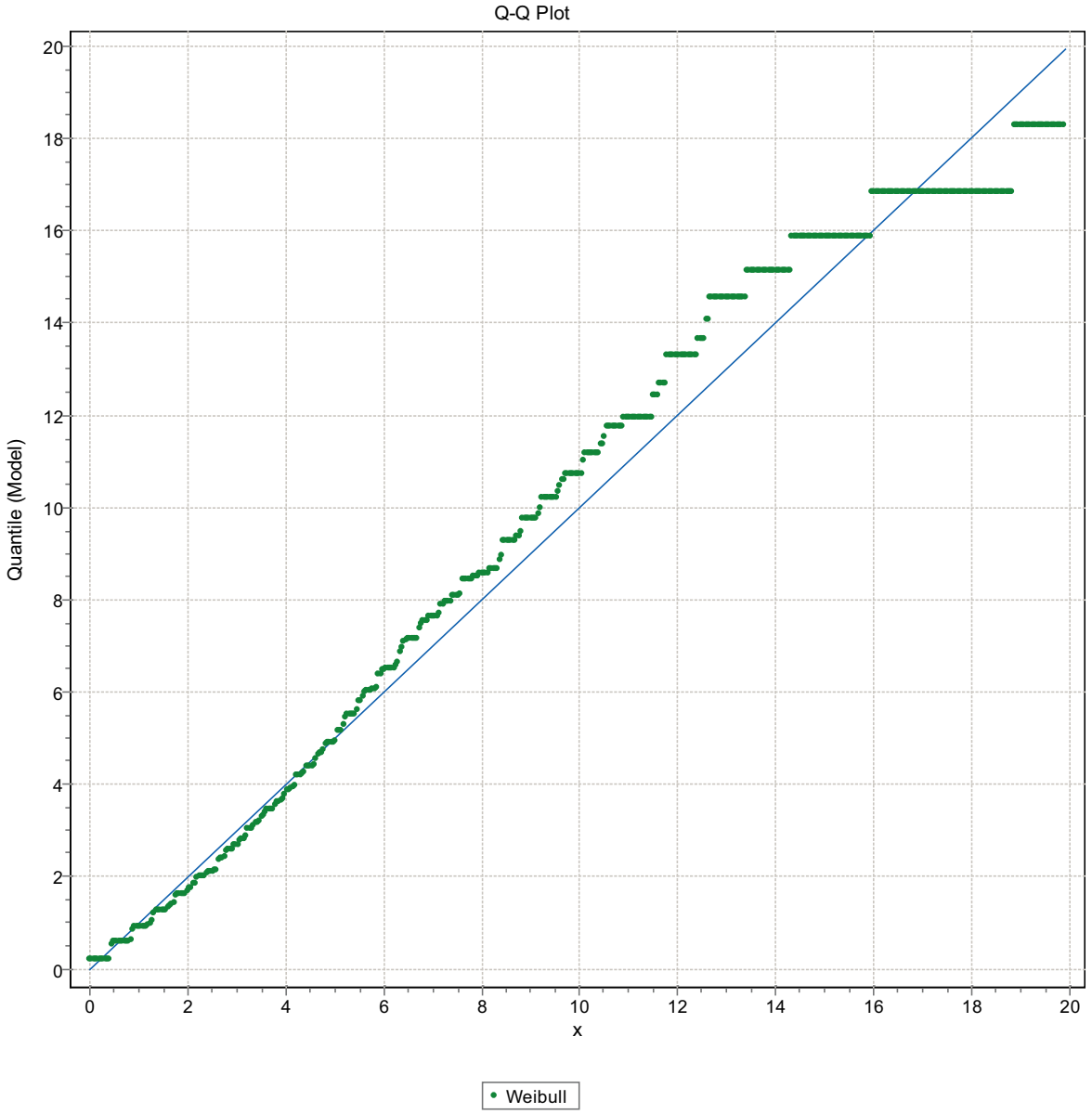

Figure F-158. *Q-Q plot, Domain FSM_N, 3 m bins, Weibull Distribution.*

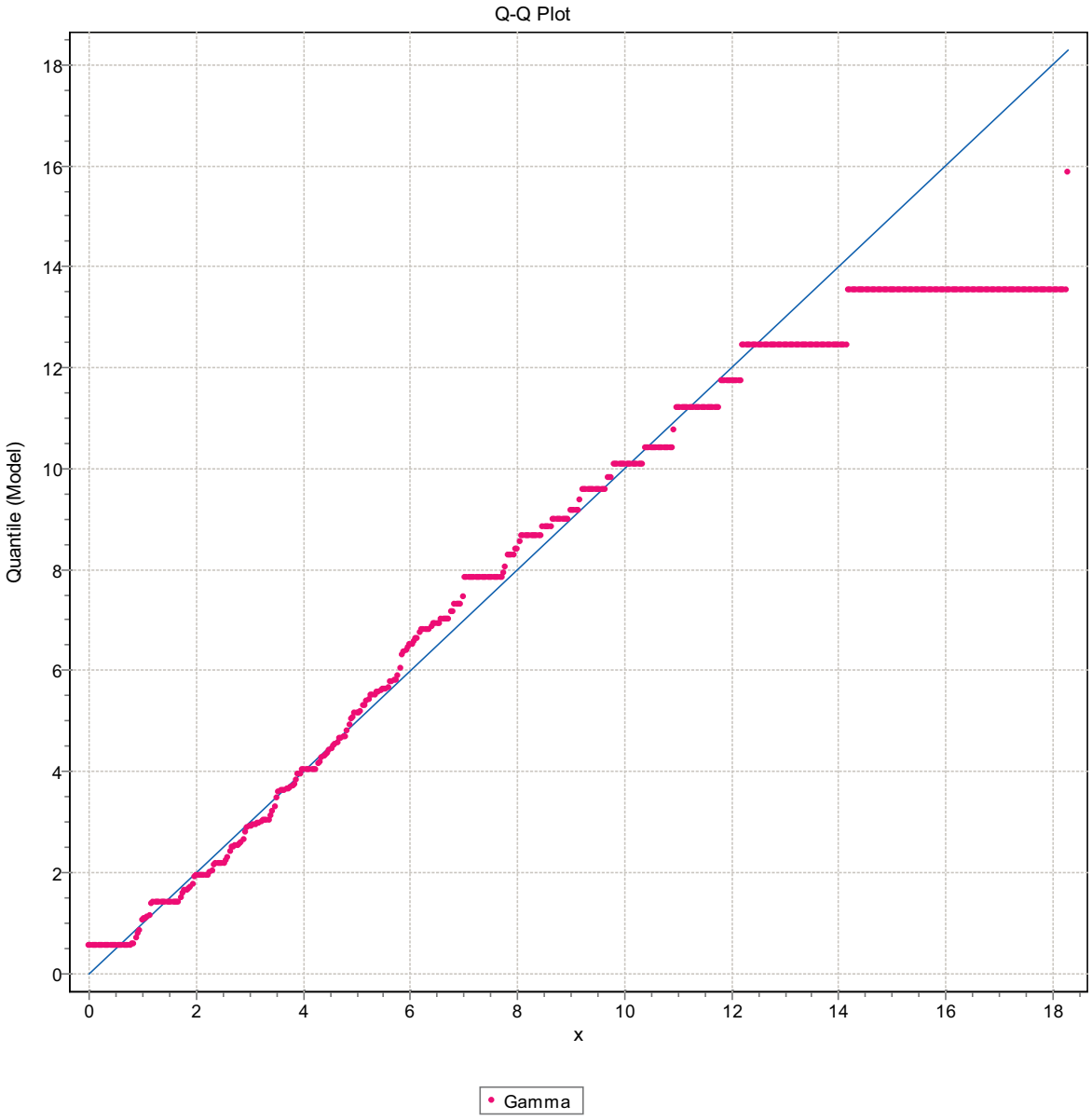

Figure F-159. *Q-Q plot, Domain FSM_N, 3 m bins, Gamma Distribution.*

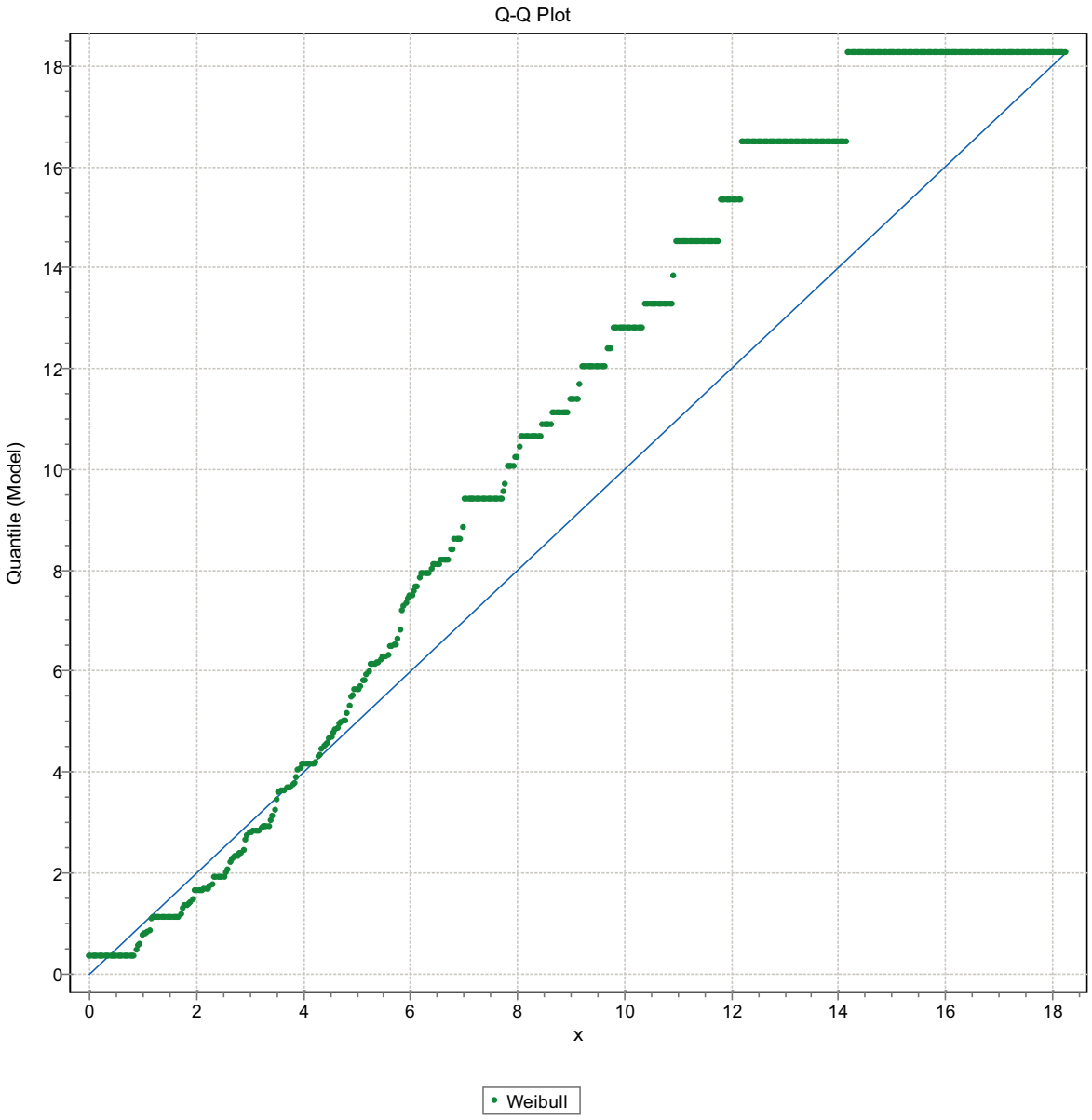

Figure F-160. *Q-Q plot, Domain FSM_N, 3 m bins, Weibull Distribution.*

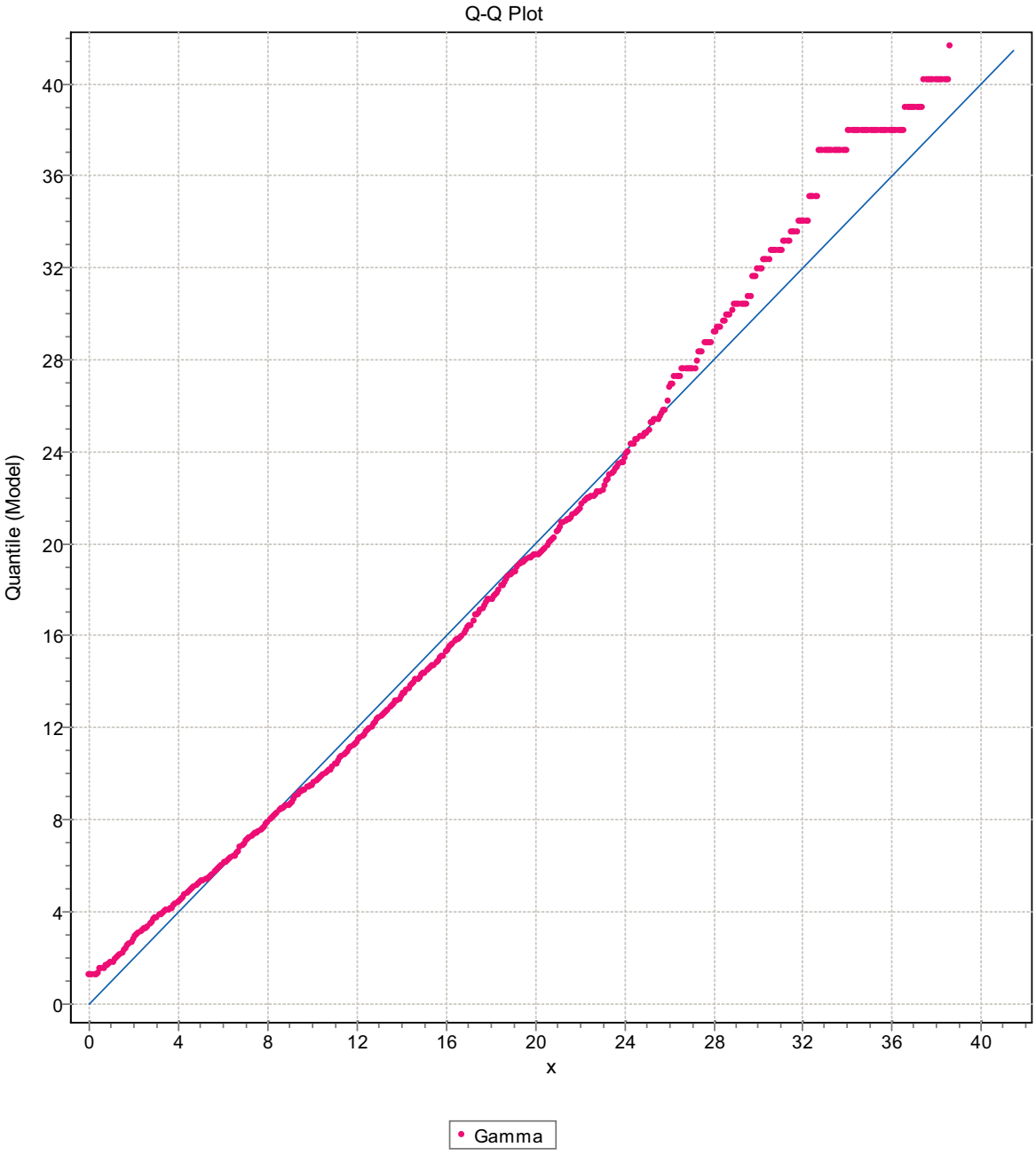

Figure F-161. *Q-Q plot, Domain FSM_W, 3 m bins, Gamma Distribution.*

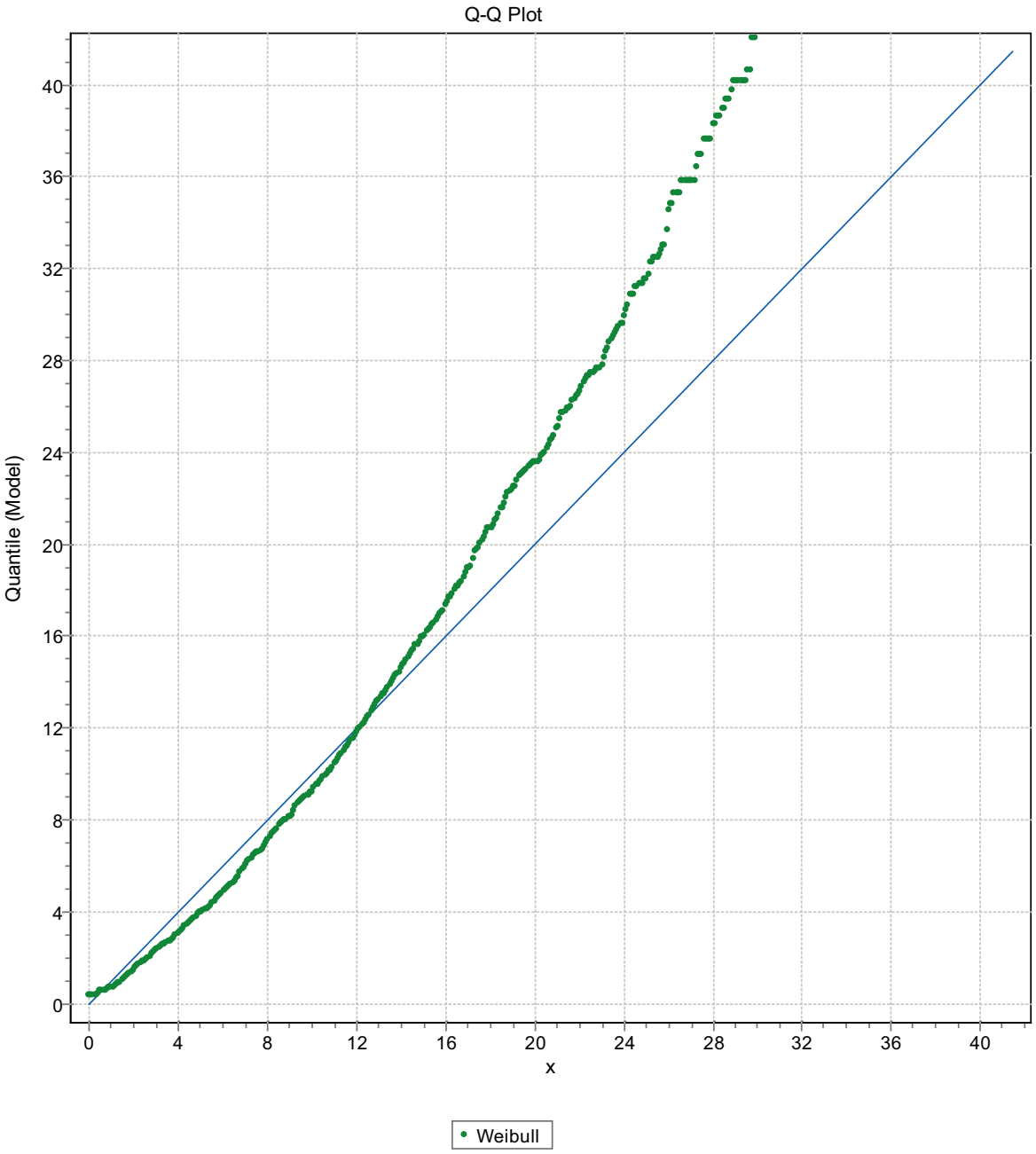

Figure F-162. *Q-Q plot, Domain FSM_W, 3 m bins, Weibull Distribution.*

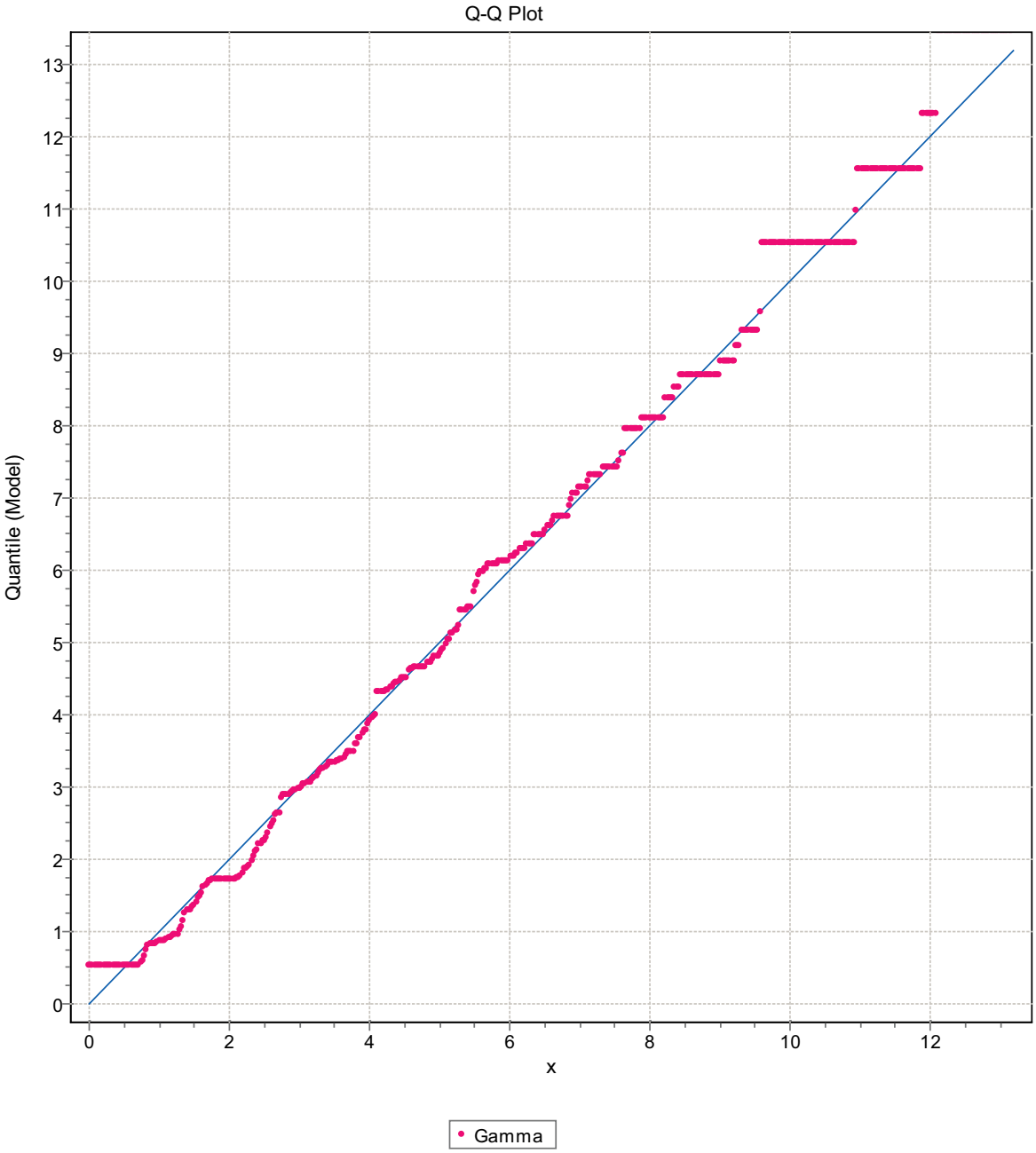

Figure F-163. *Q-Q plot, Domain FSM_W, 3 m bins, Gamma Distribution.*

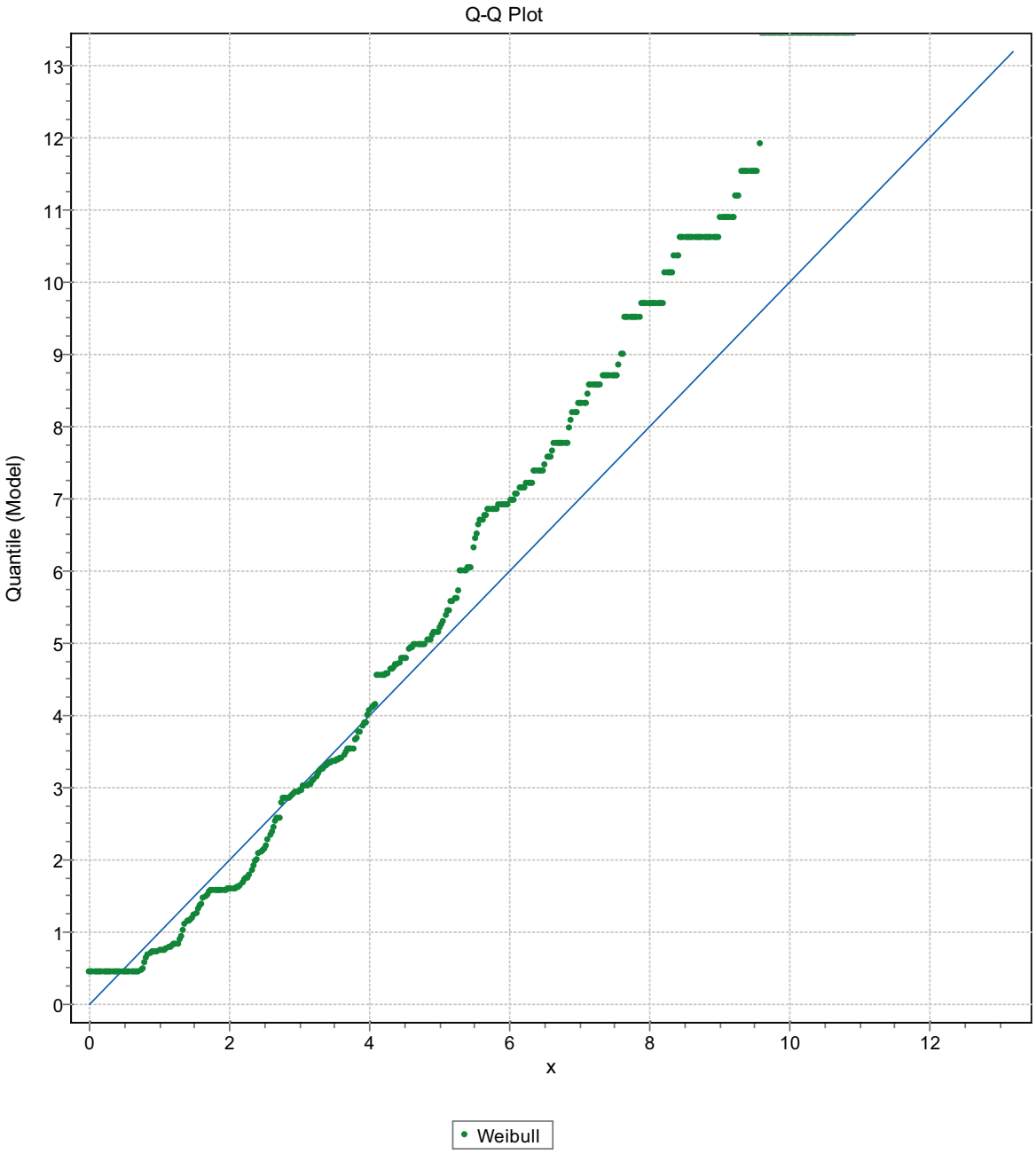

Figure F-164. *Q-Q plot, Domain FSM_W, 3 m bins, Weibull Distribution.*

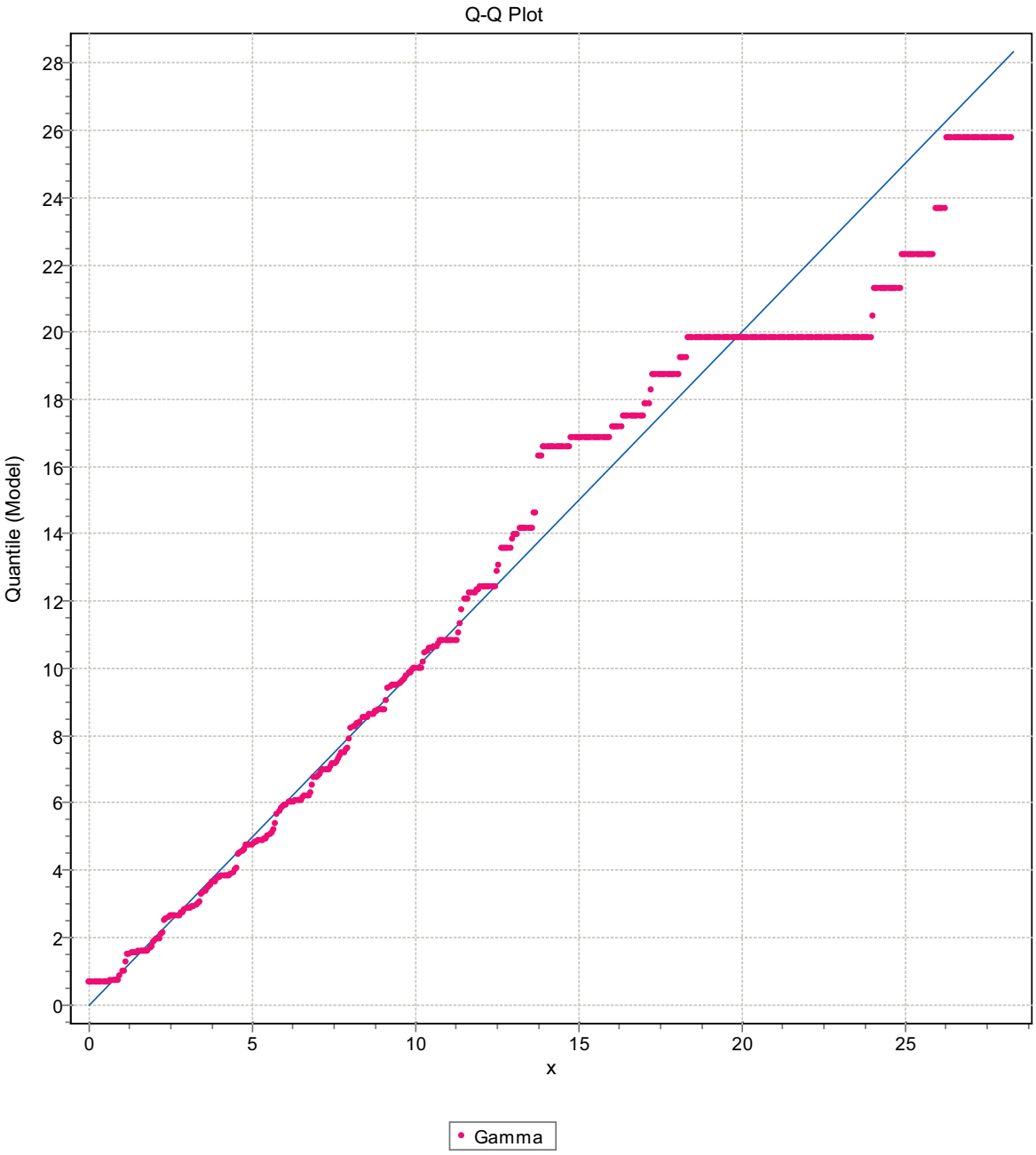

Figure F-165. *Q-Q plot, Domain FSM_W, 3 m bins, Gamma Distribution.*

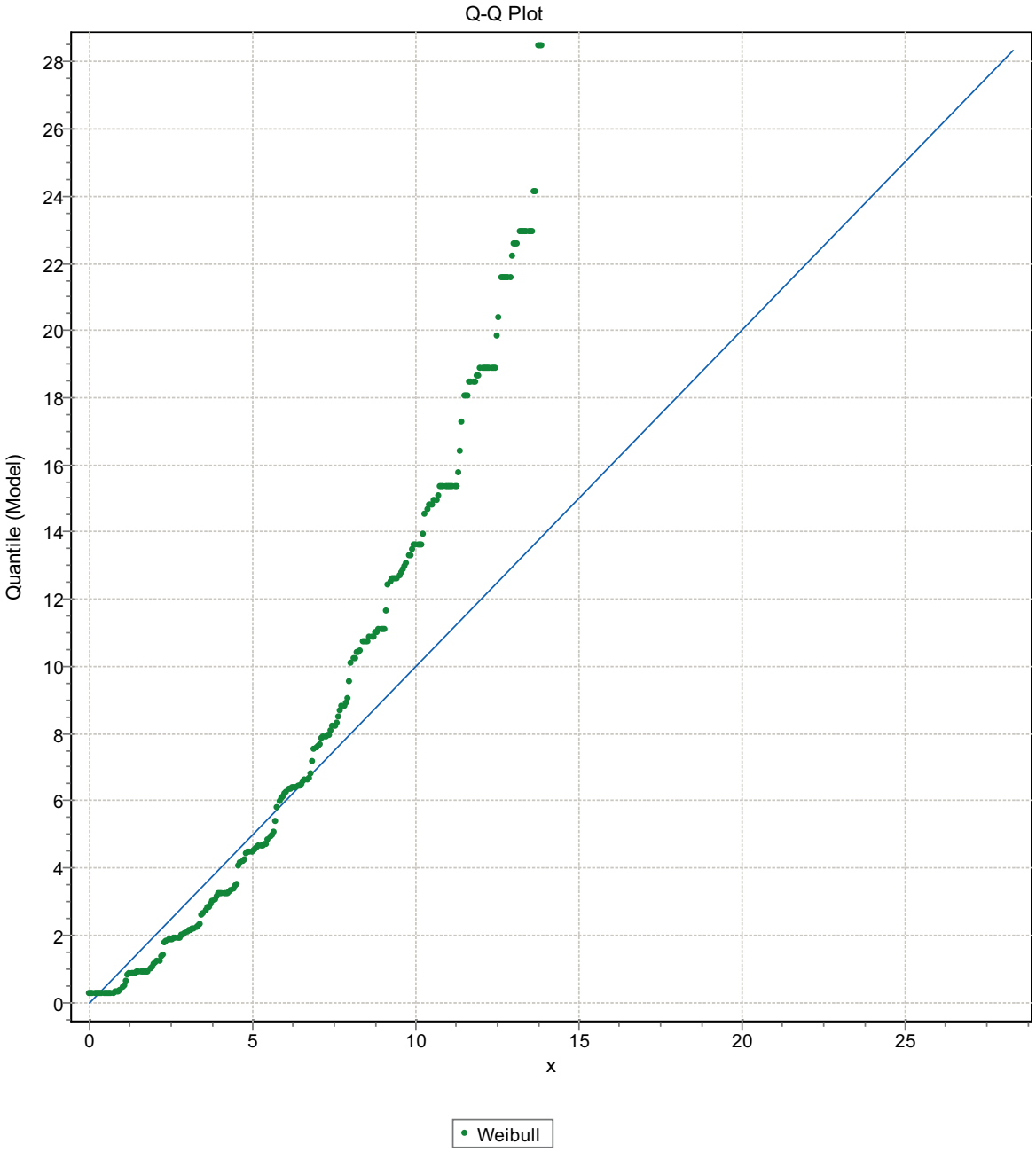

Figure F-166. *Q-Q plot, Domain FSM_W, 3 m bins, Weibull Distribution.*

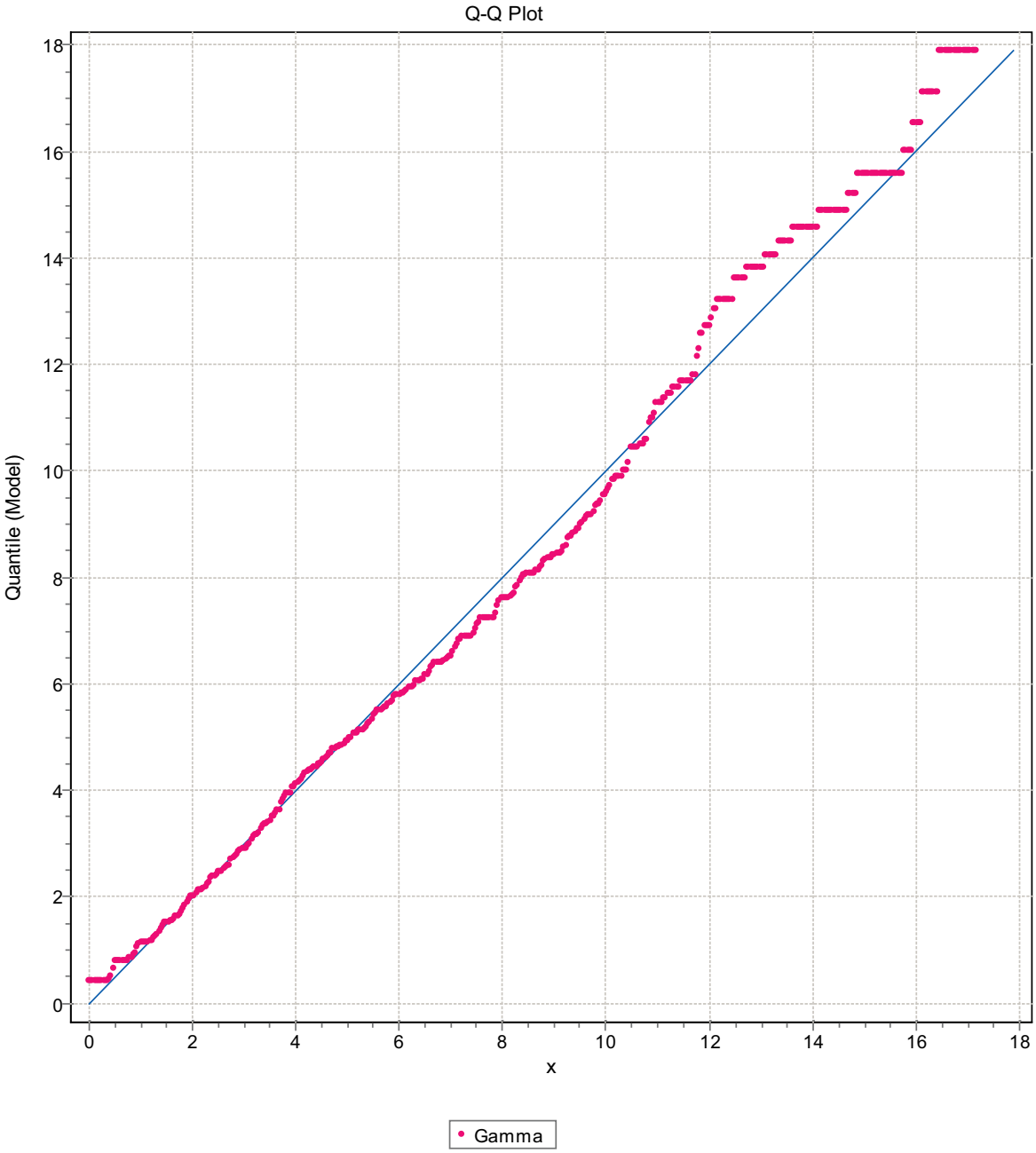

Figure F-167. *Q-Q plot, Domain FSM_W, 3 m bins, Gamma Distribution.*

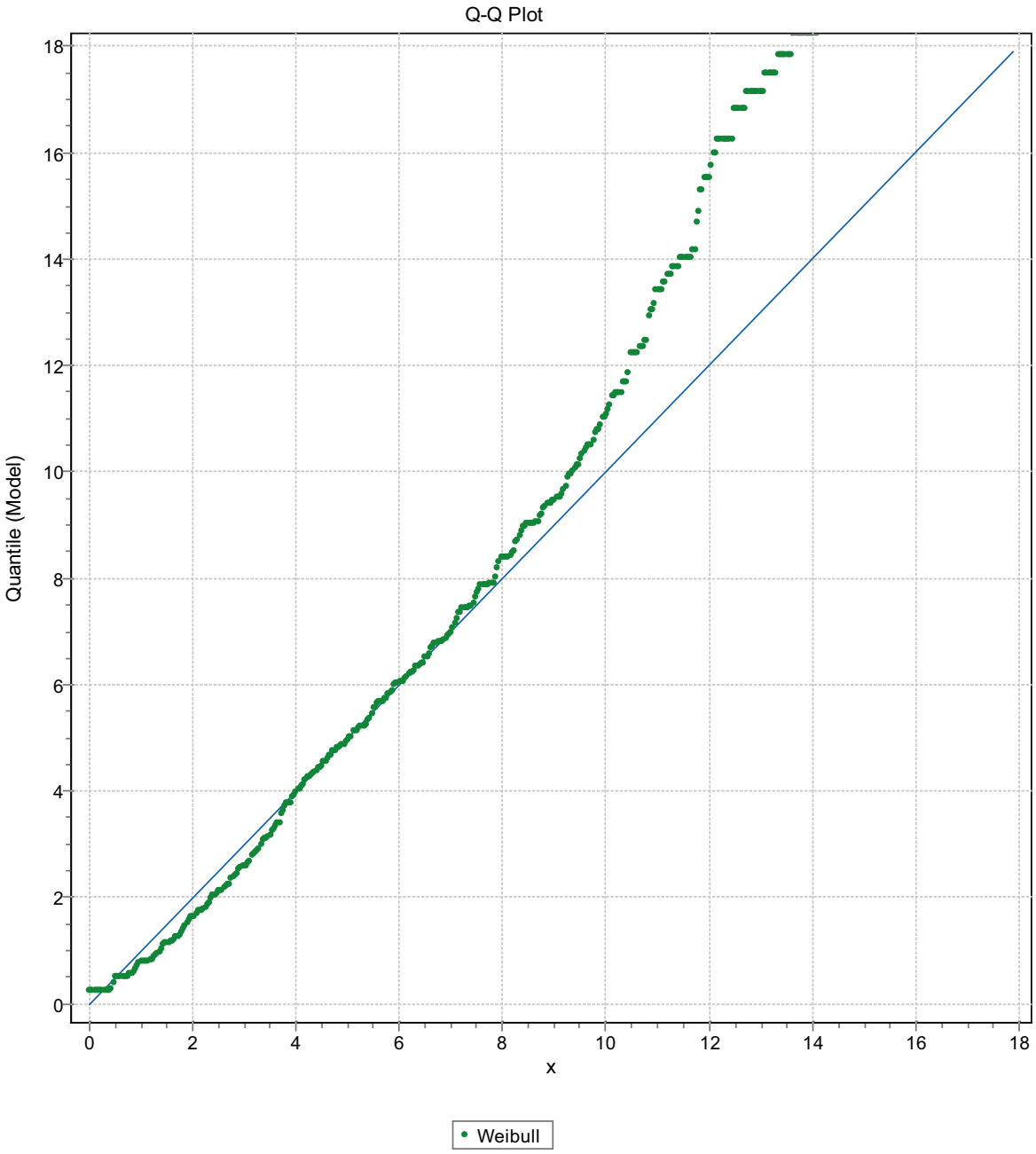

Figure F-168. *Q-Q plot, Domain FSM_W, 3 m bins, Weibull Distribution.*

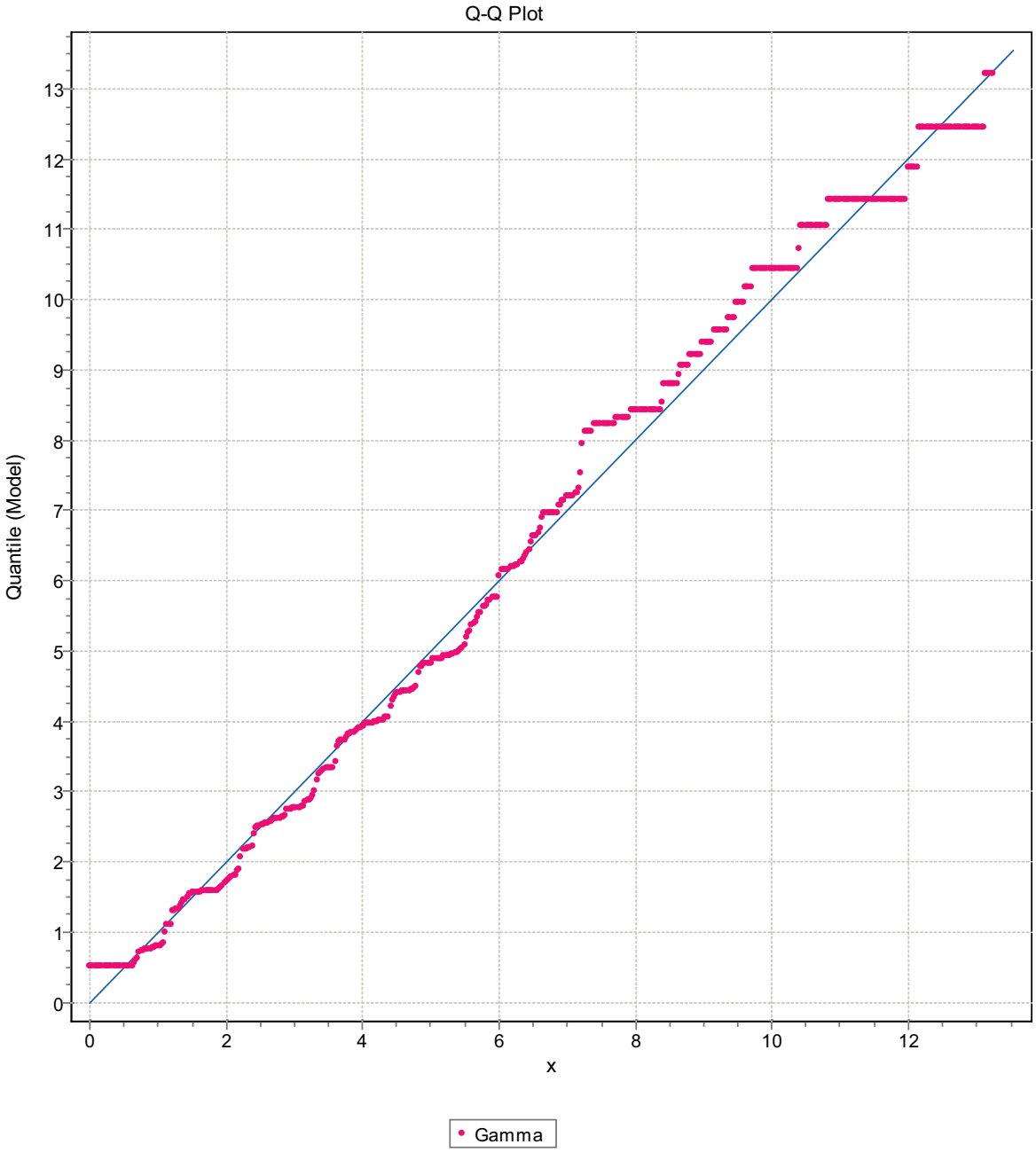

Figure F-169. *Q-Q plot, Domain FSM_W, 3 m bins, Gamma Distribution.*

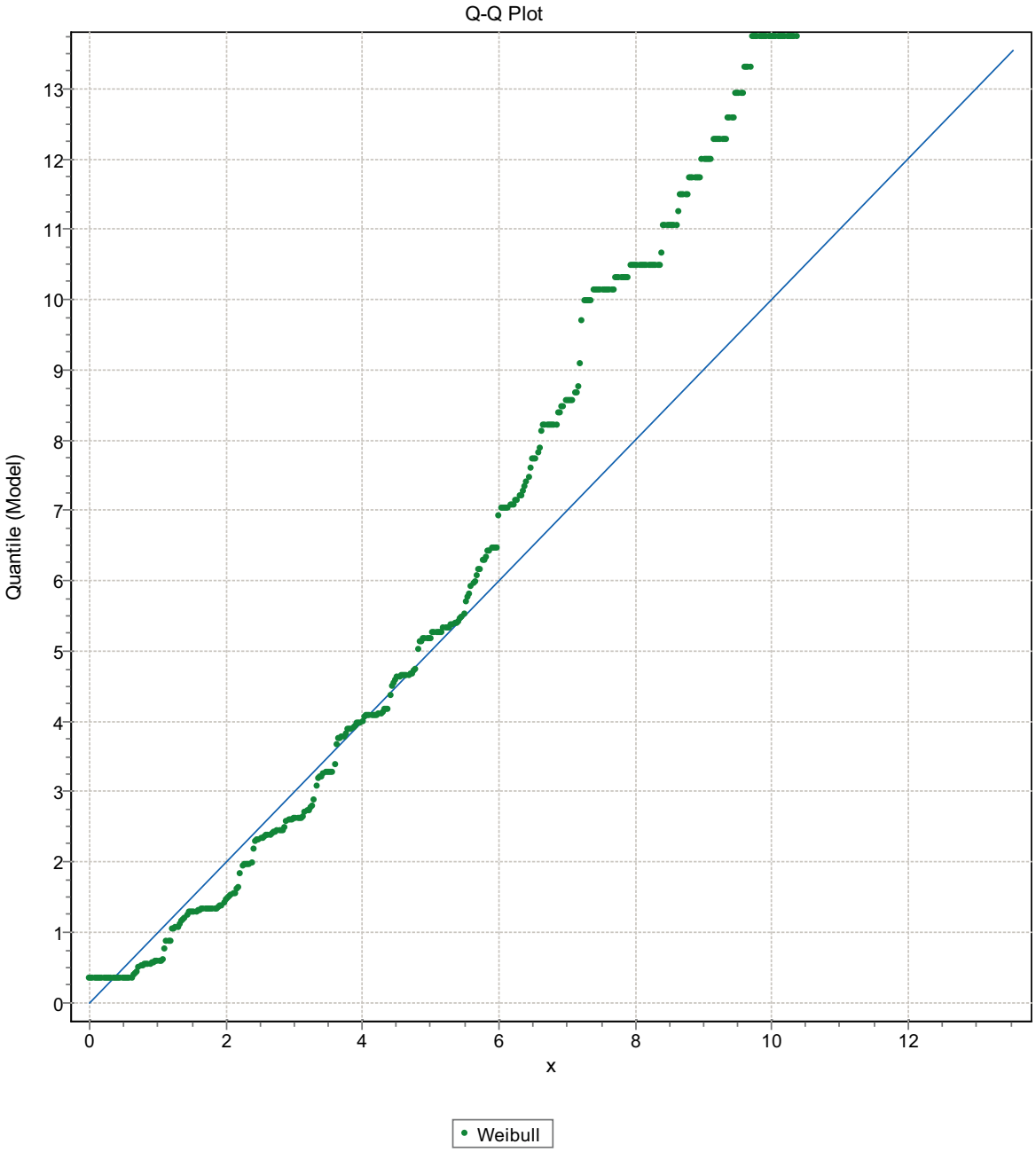

Figure F-170. *Q-Q plot, Domain FSM_W, 3 m bins, Weibull Distribution.*

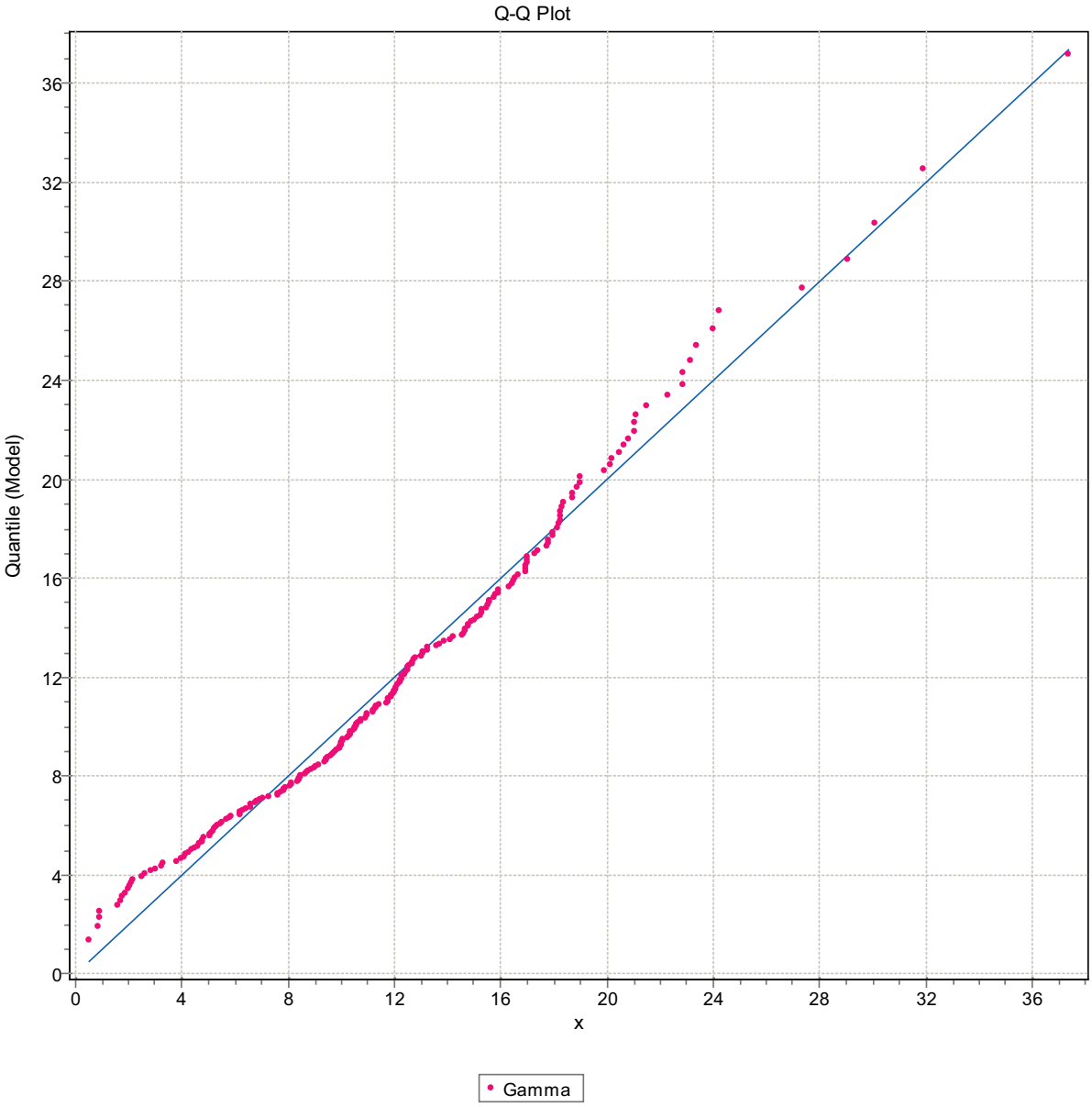

Figure F-171. *Q-Q plot, Domain FSM_EW007, 9 m bins, Gamma Distribution.*

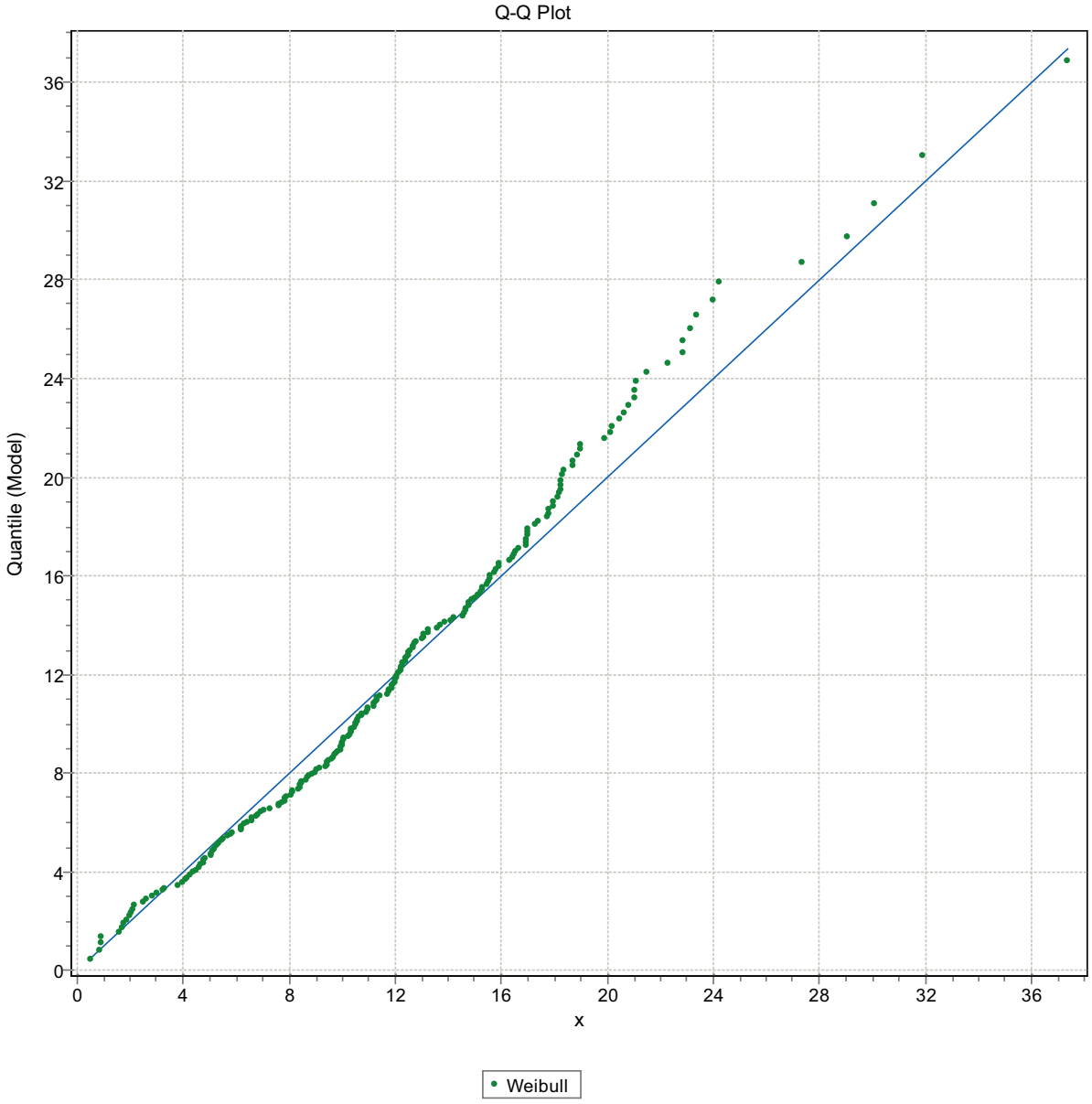

Figure F-172. *Q-Q plot, Domain FSM_EW007, 9 m bins, Weibull Distribution.*

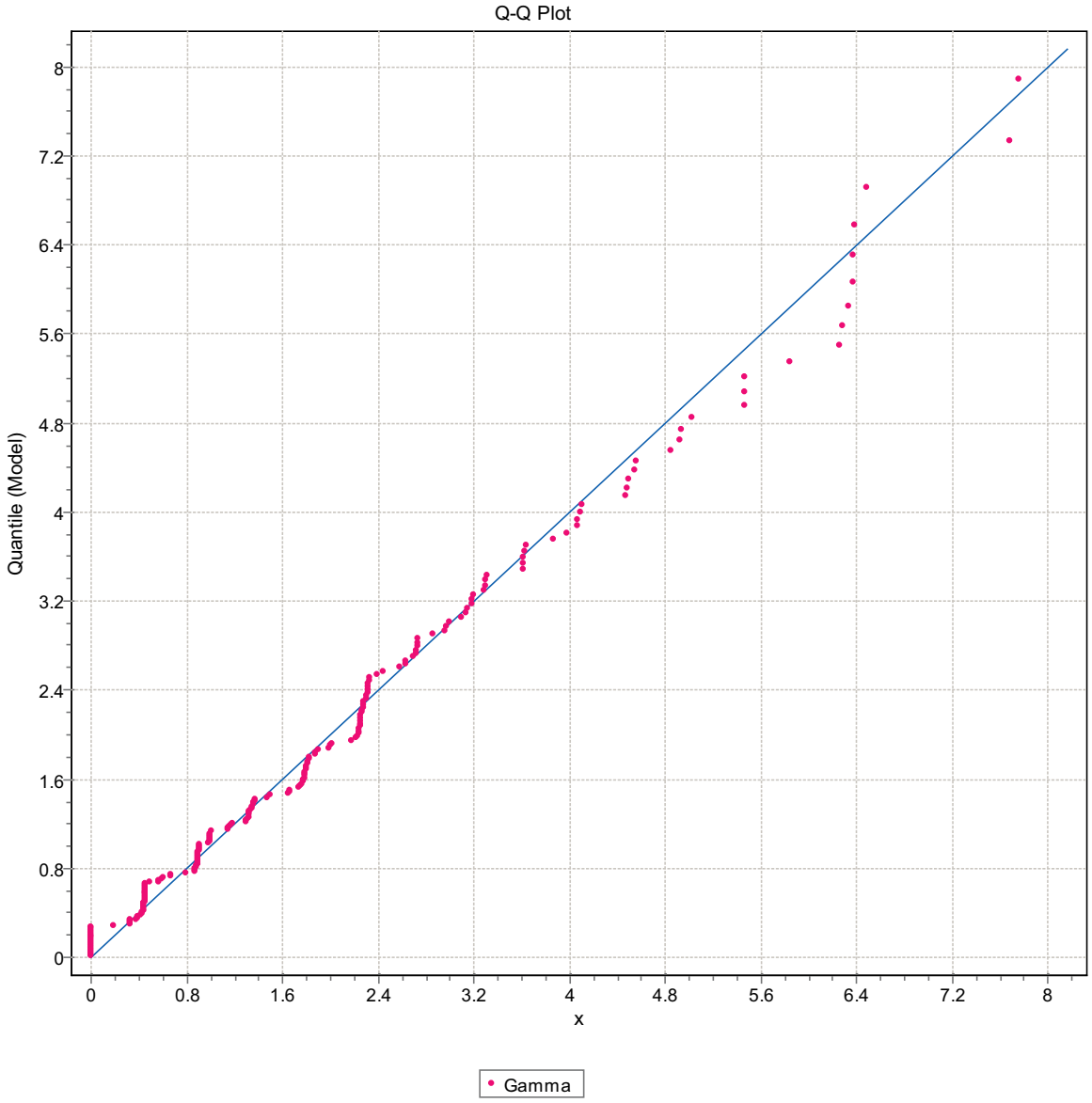

Figure F-173. *Q-Q plot, Domain FSM_EW007, 9 m bins, Gamma Distribution.*

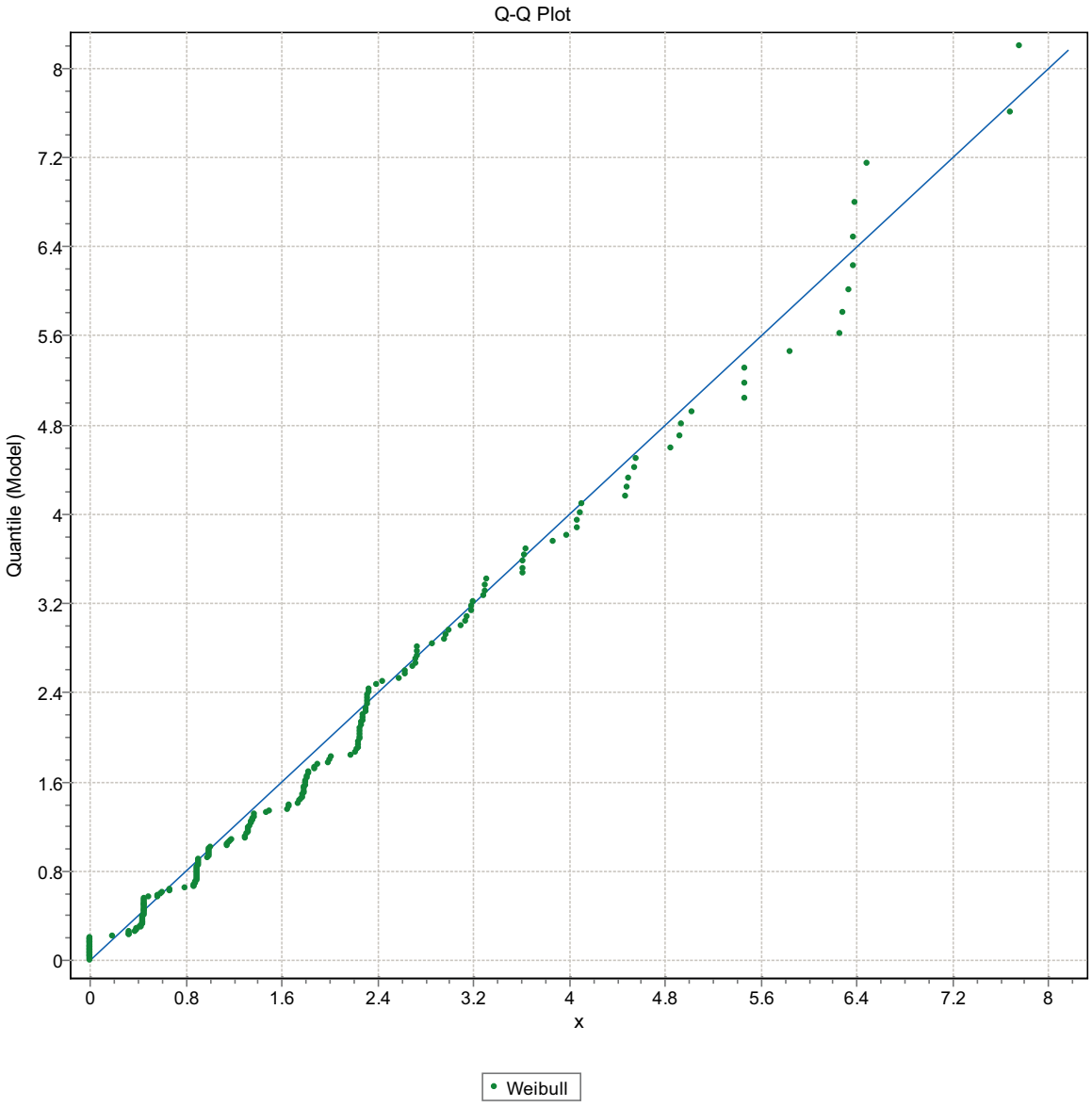

Figure F-174. *Q-Q plot, Domain FSM_EW007, 9 m bins, Weibull Distribution.*

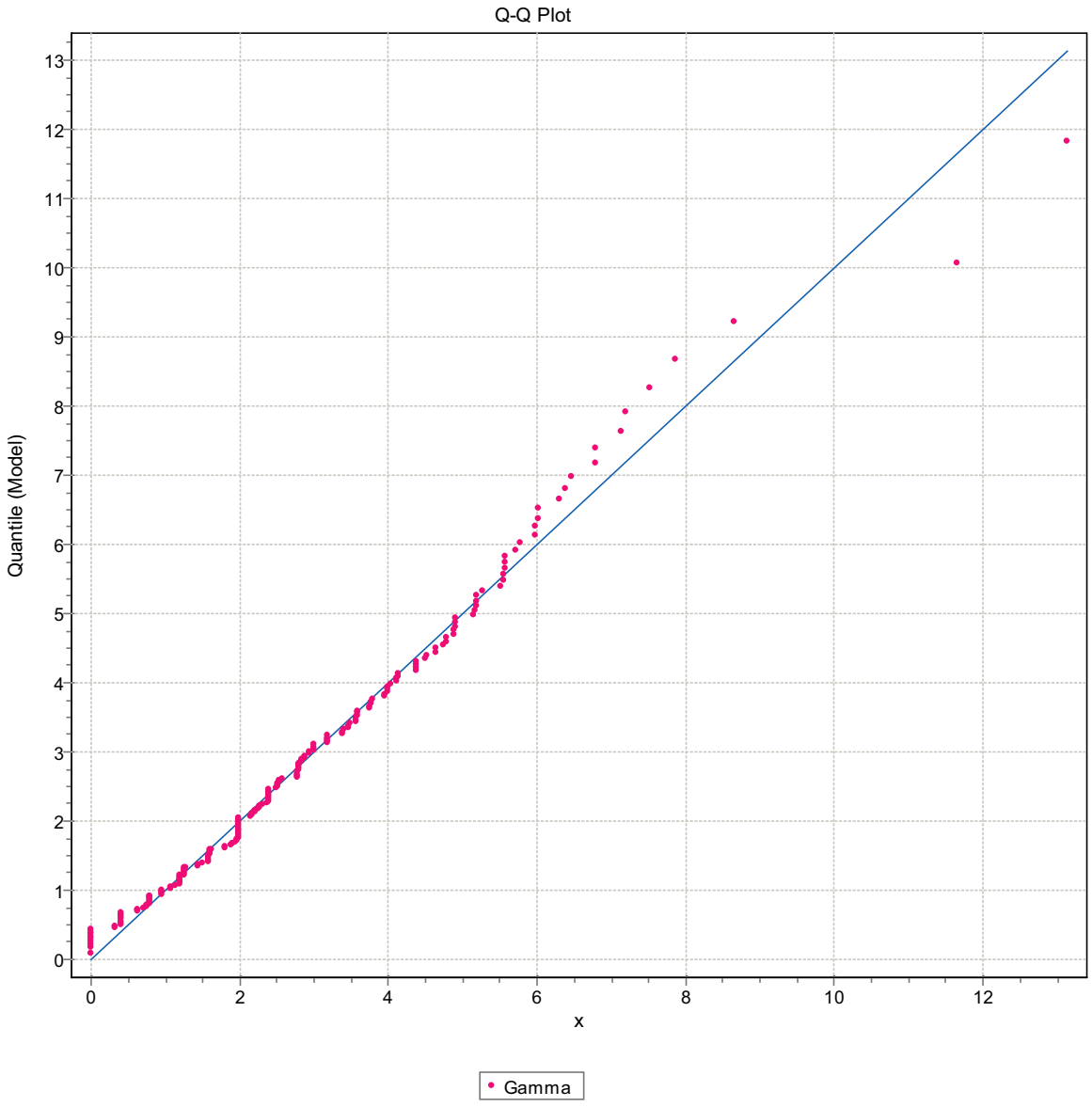

Figure F-175. *Q-Q plot, Domain FSM_EW007, 9 m bins, Gamma Distribution.*

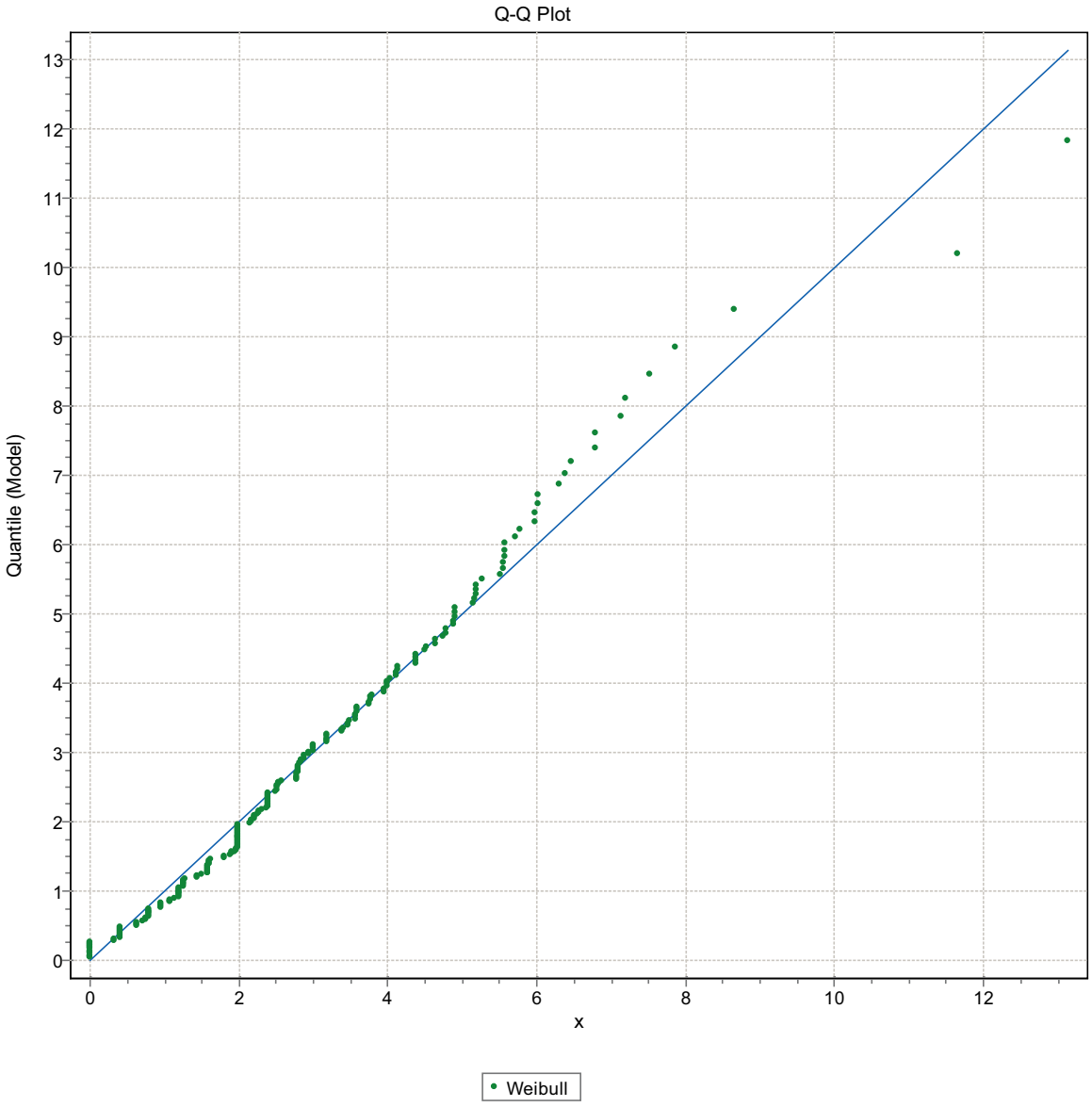

Figure F-176. *Q-Q plot, Domain FSM_EW007, 9 m bins, Weibull Distribution.*

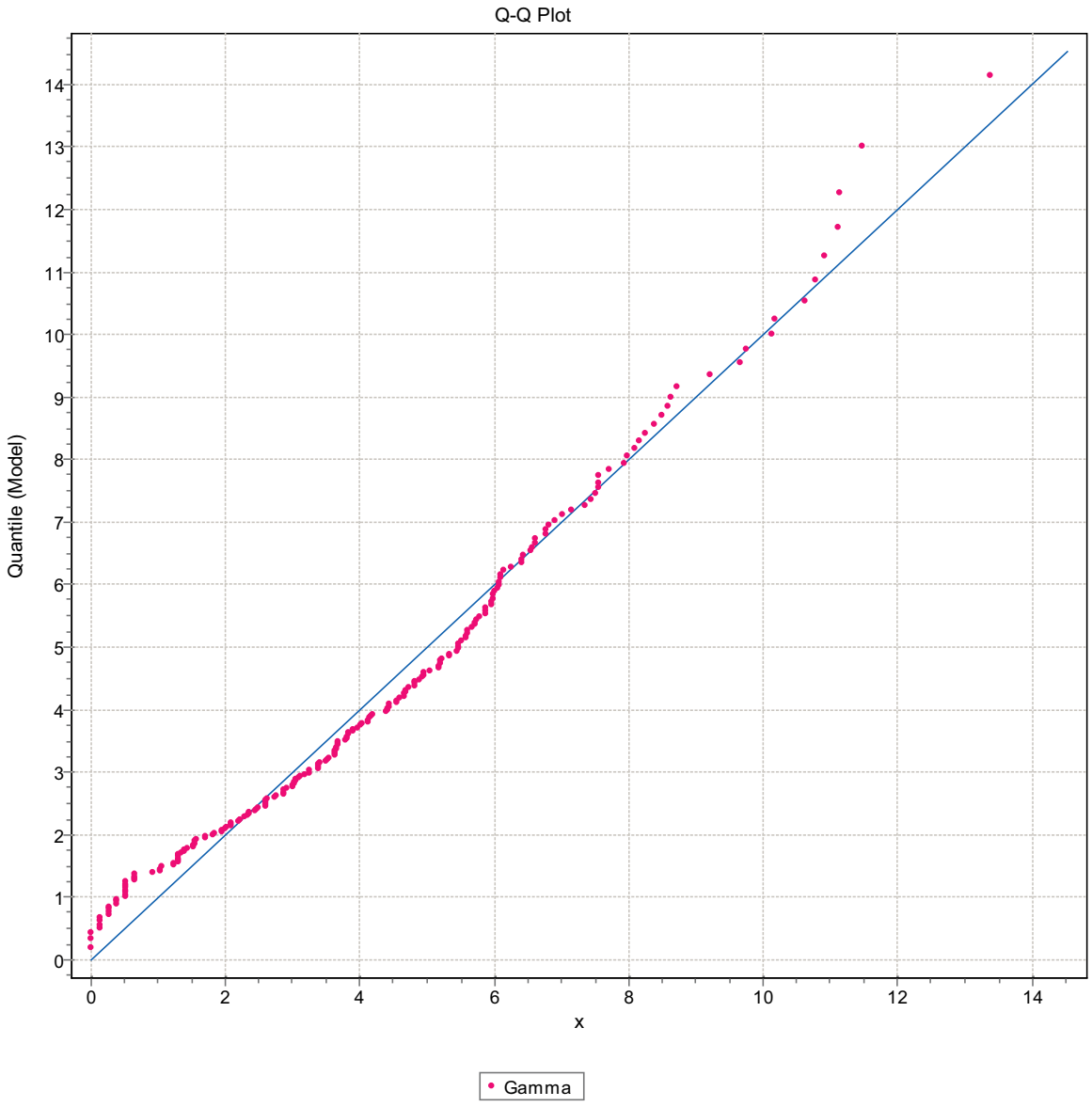

Figure F-177. *Q-Q plot, Domain FSM_EW007, 9 m bins, Gamma Distribution.*

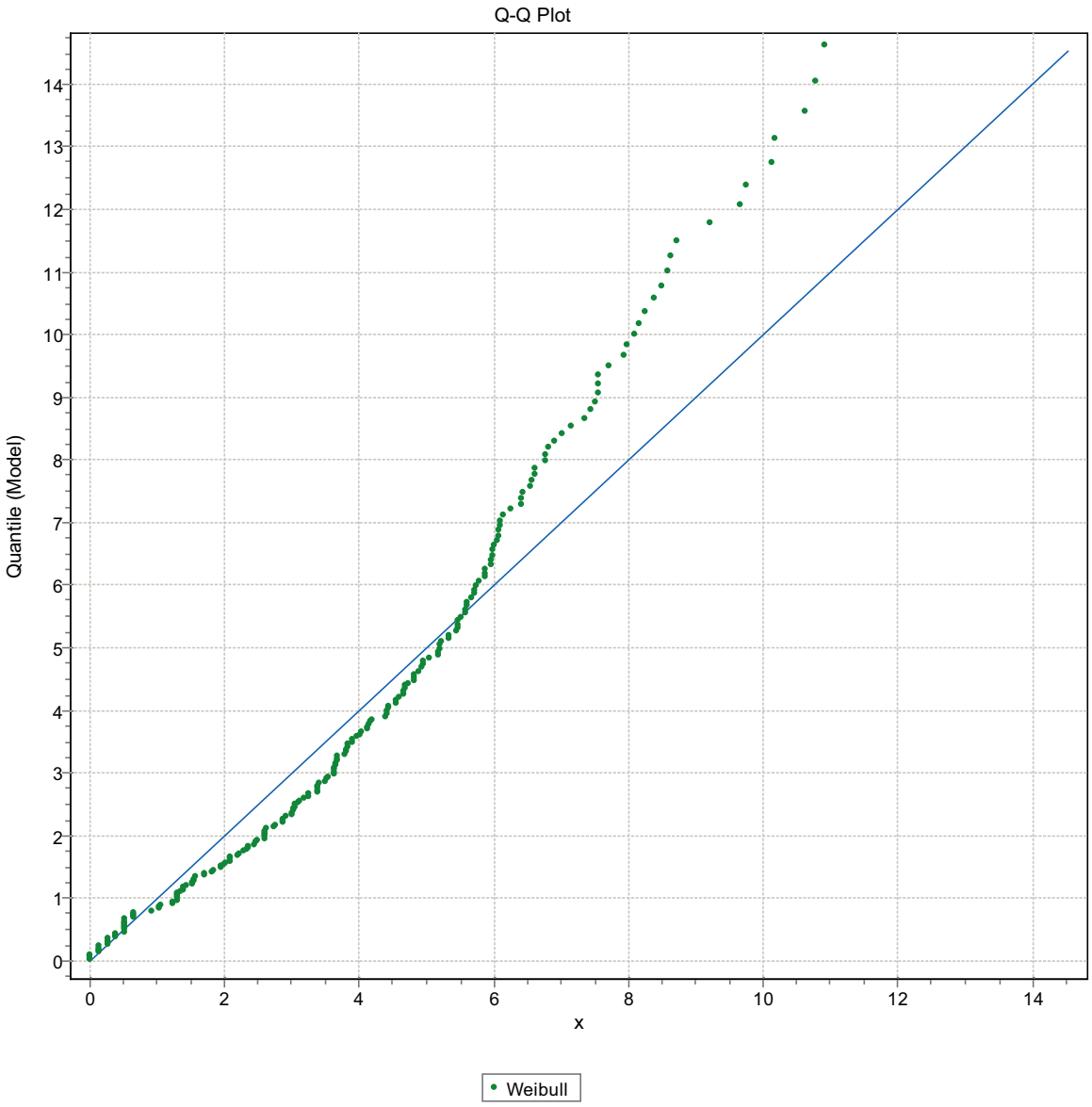

Figure F-178. *Q-Q plot, Domain FSM_EW007, 9 m bins, Weibull Distribution.*

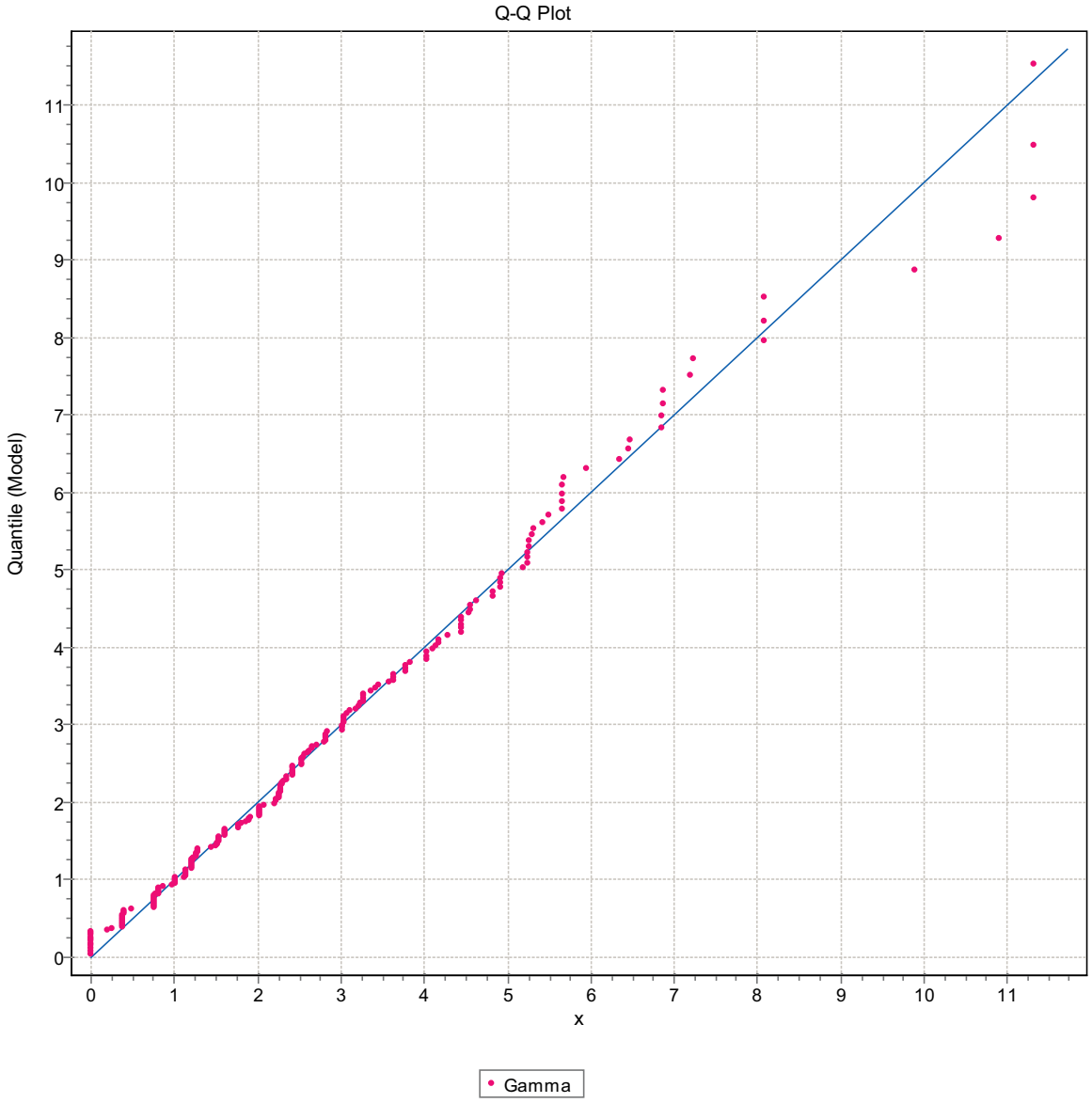

Figure F-179. *Q-Q plot, Domain FSM_EW007, 9 m bins, Gamma Distribution.*

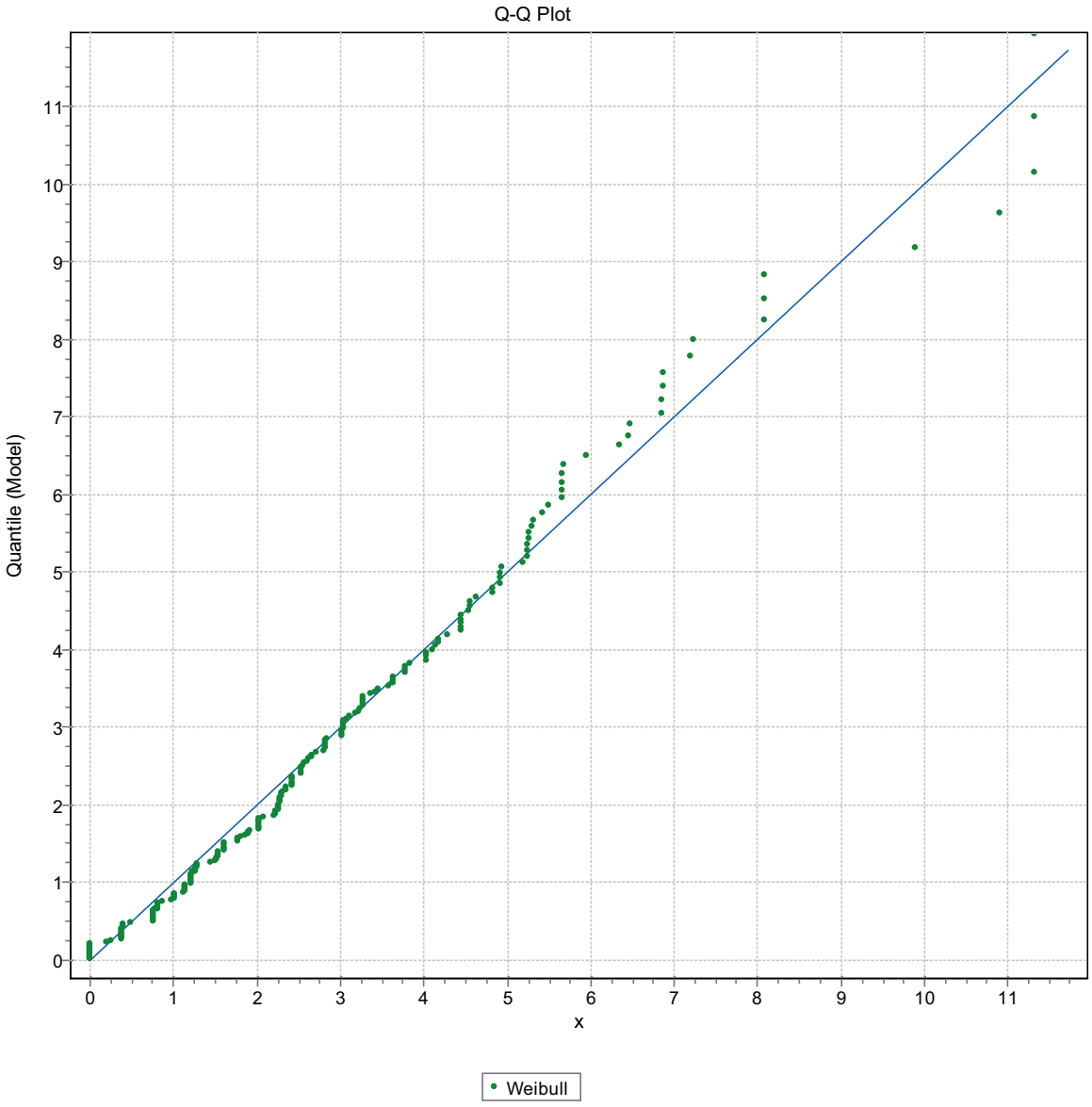

Figure F-180. *Q-Q plot, Domain FSM_EW007, 9 m bins, Weibull Distribution.*

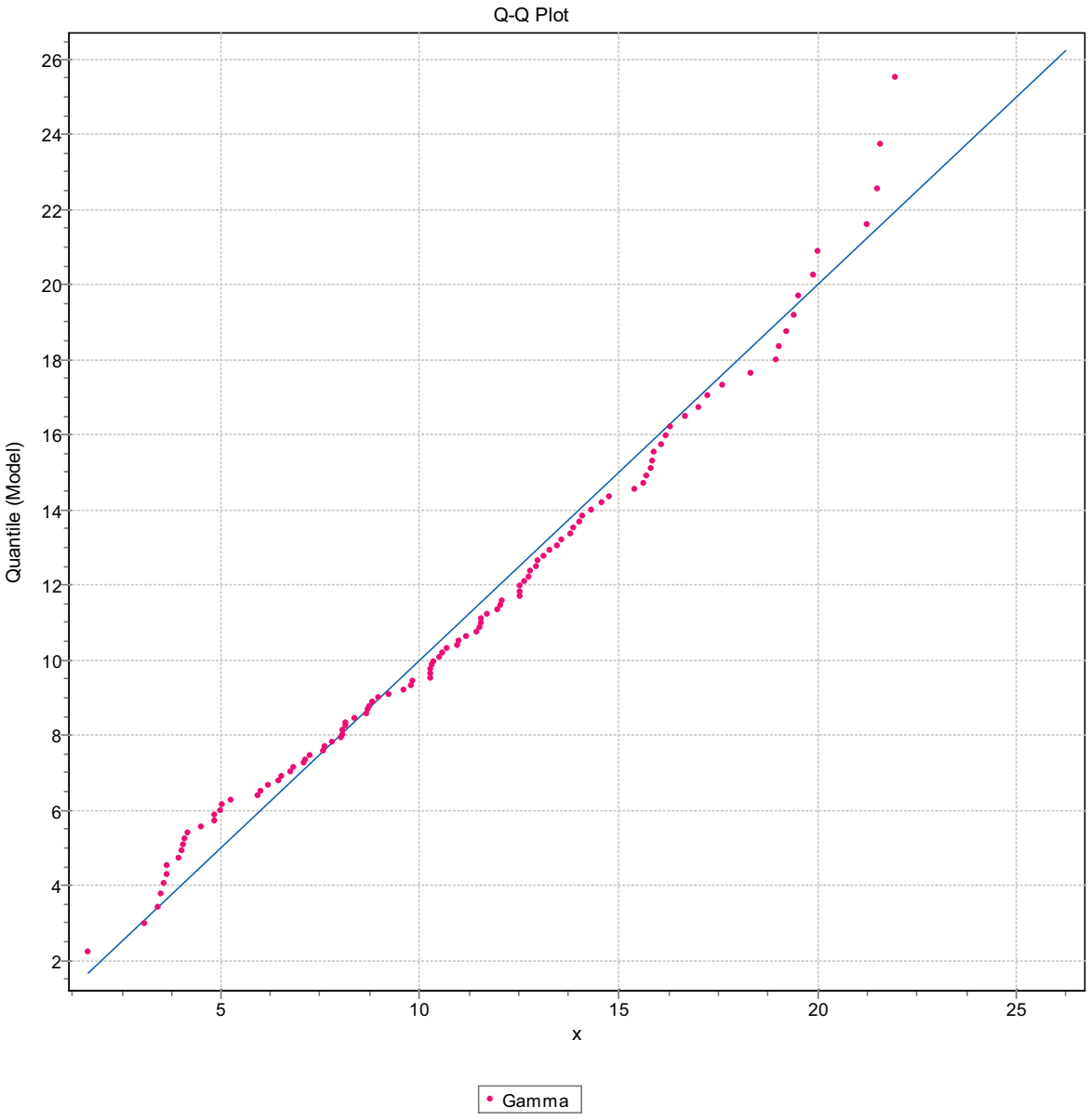

Figure F-181. *Q-Q plot, Domain FSM_NE005, 9 m bins, Gamma Distribution.*

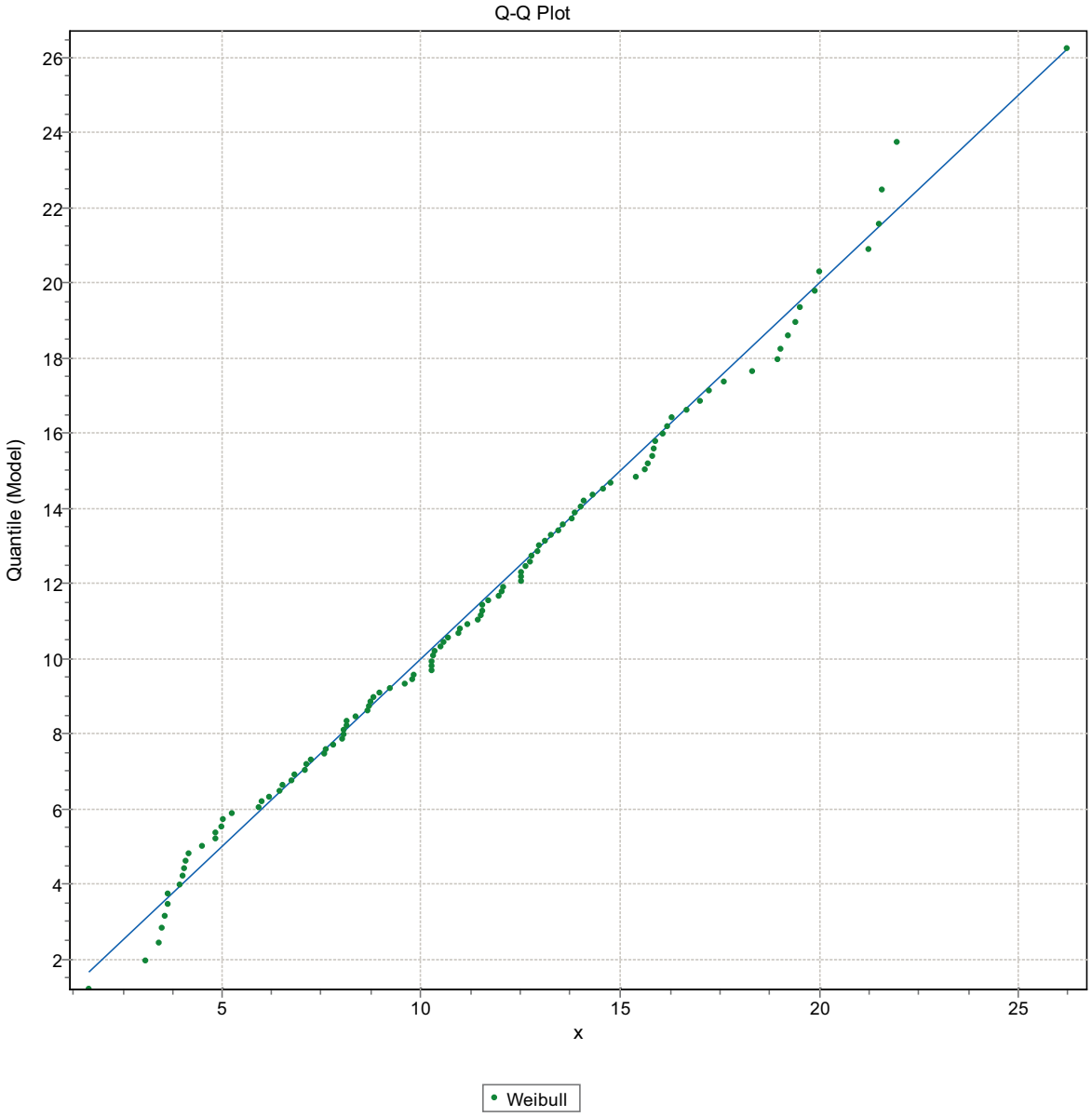

Figure F-182. *Q-Q plot, Domain FSM_NE005, 9 m bins, Weibull Distribution.*

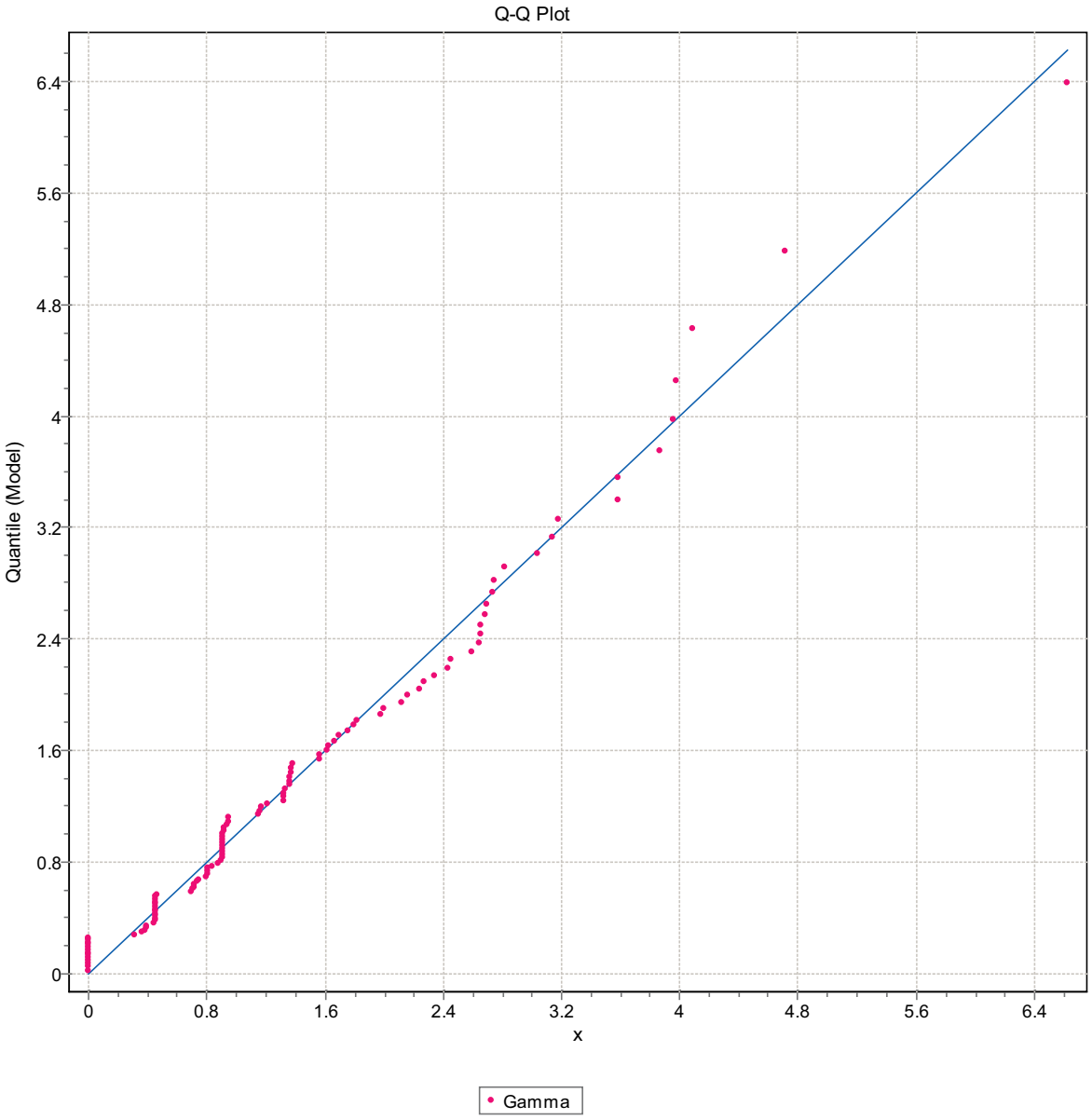

Figure F-183. *Q-Q plot, Domain FSM_NE005, 9 m bins, Gamma Distribution.*

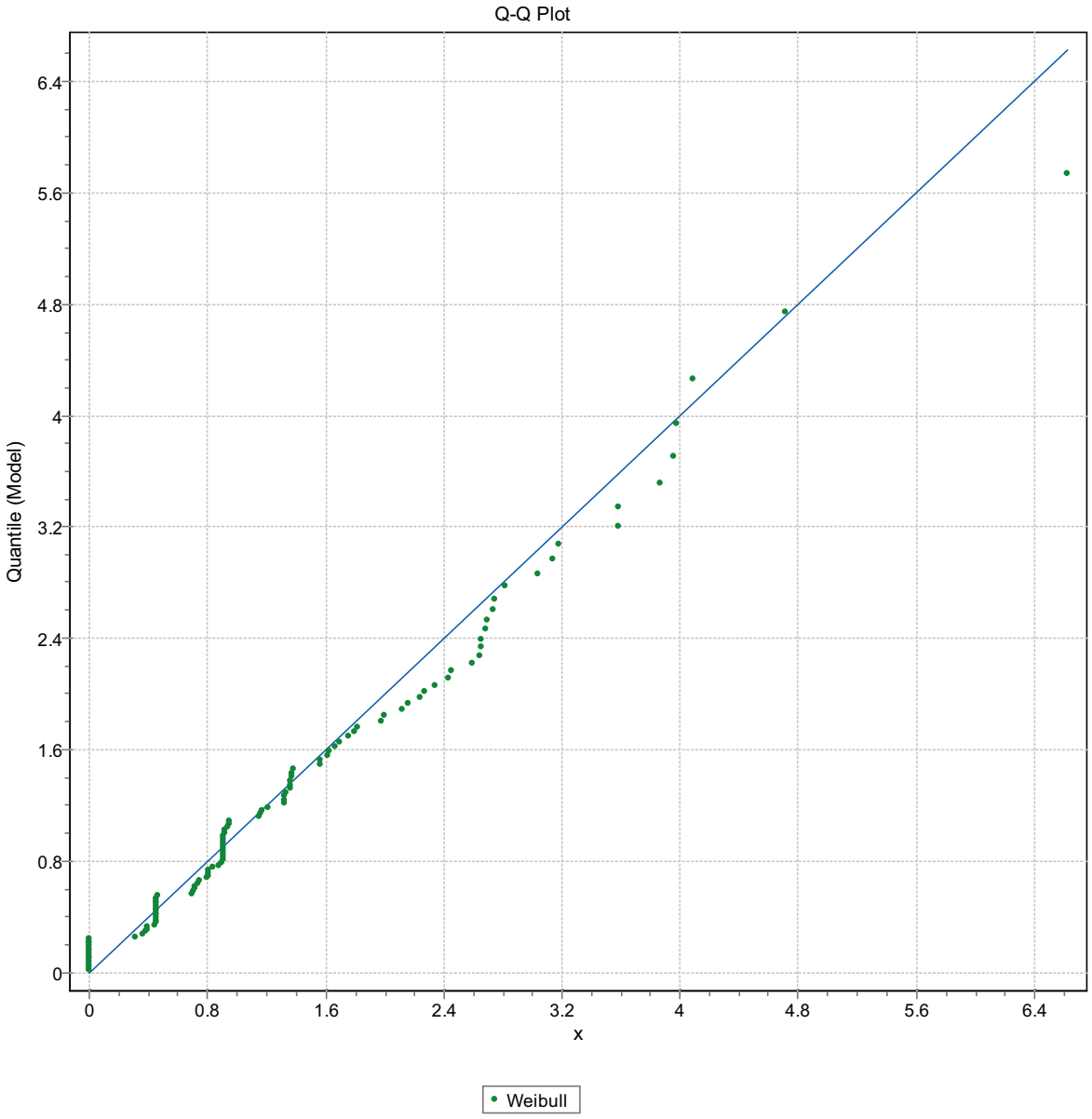

Figure F-184. *Q-Q plot, Domain FSM_NE005, 9 m bins, Weibull Distribution.*

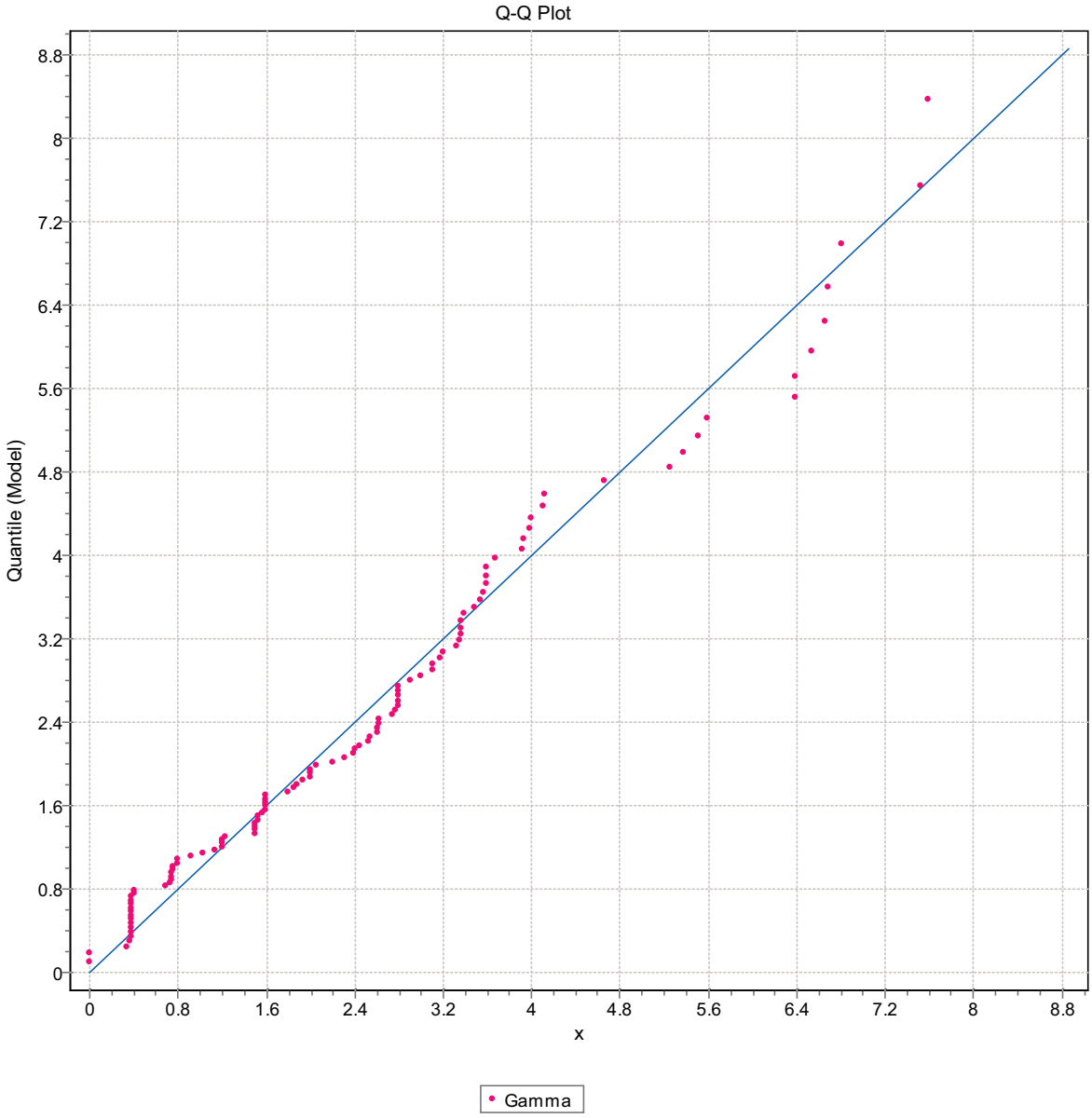

Figure F-185. *Q-Q plot, Domain FSM_NE005, 9 m bins, Gamma Distribution.*

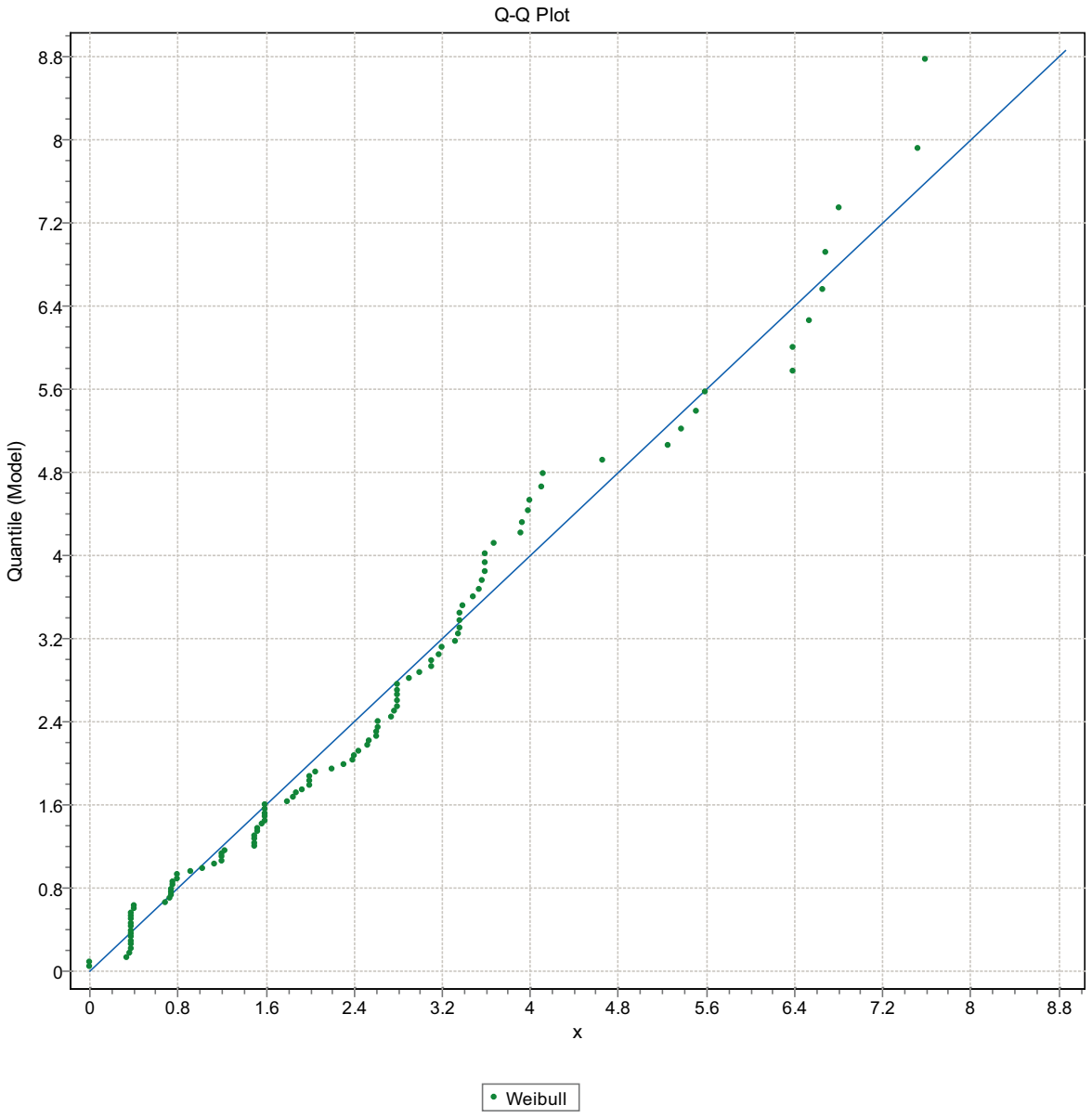

Figure F-186. *Q-Q plot, Domain FSM_NE005, 9 m bins, Weibull Distribution.*

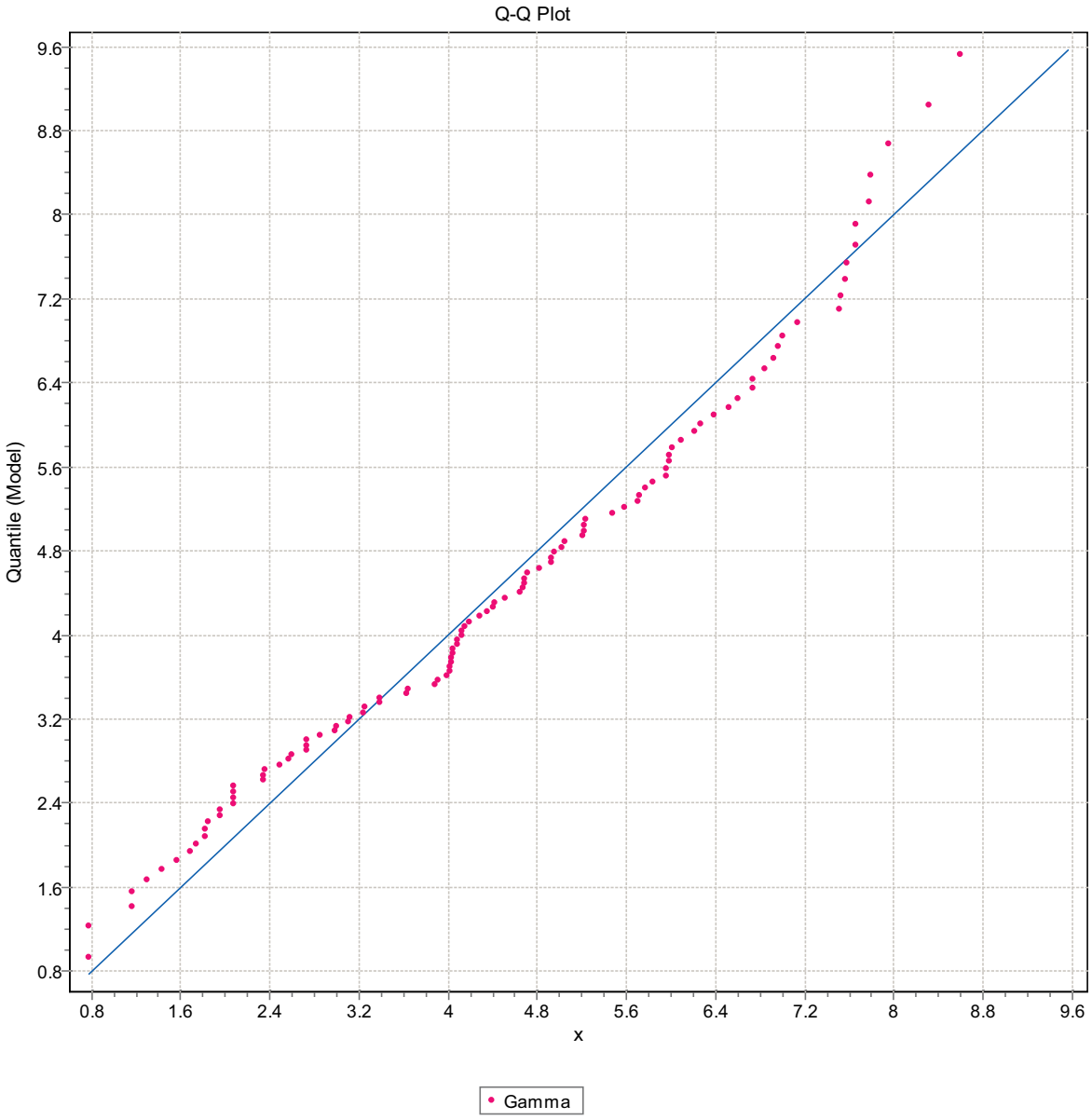

Figure F-187. *Q-Q plot, Domain FSM_NE005, 9 m bins, Gamma Distribution.*

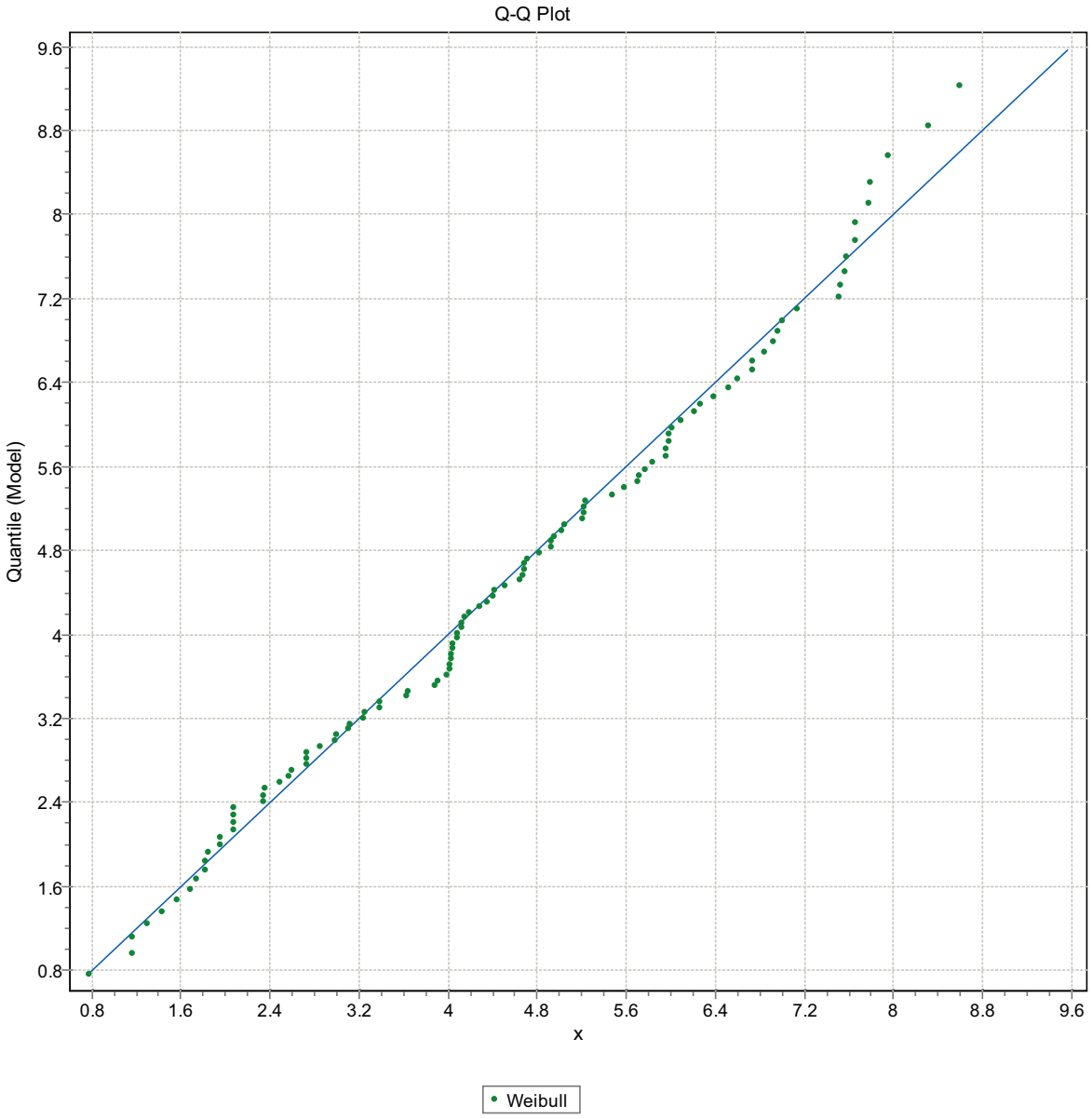

Figure F-188. *Q-Q plot, Domain FSM_NE005, 9 m bins, Weibull Distribution.*

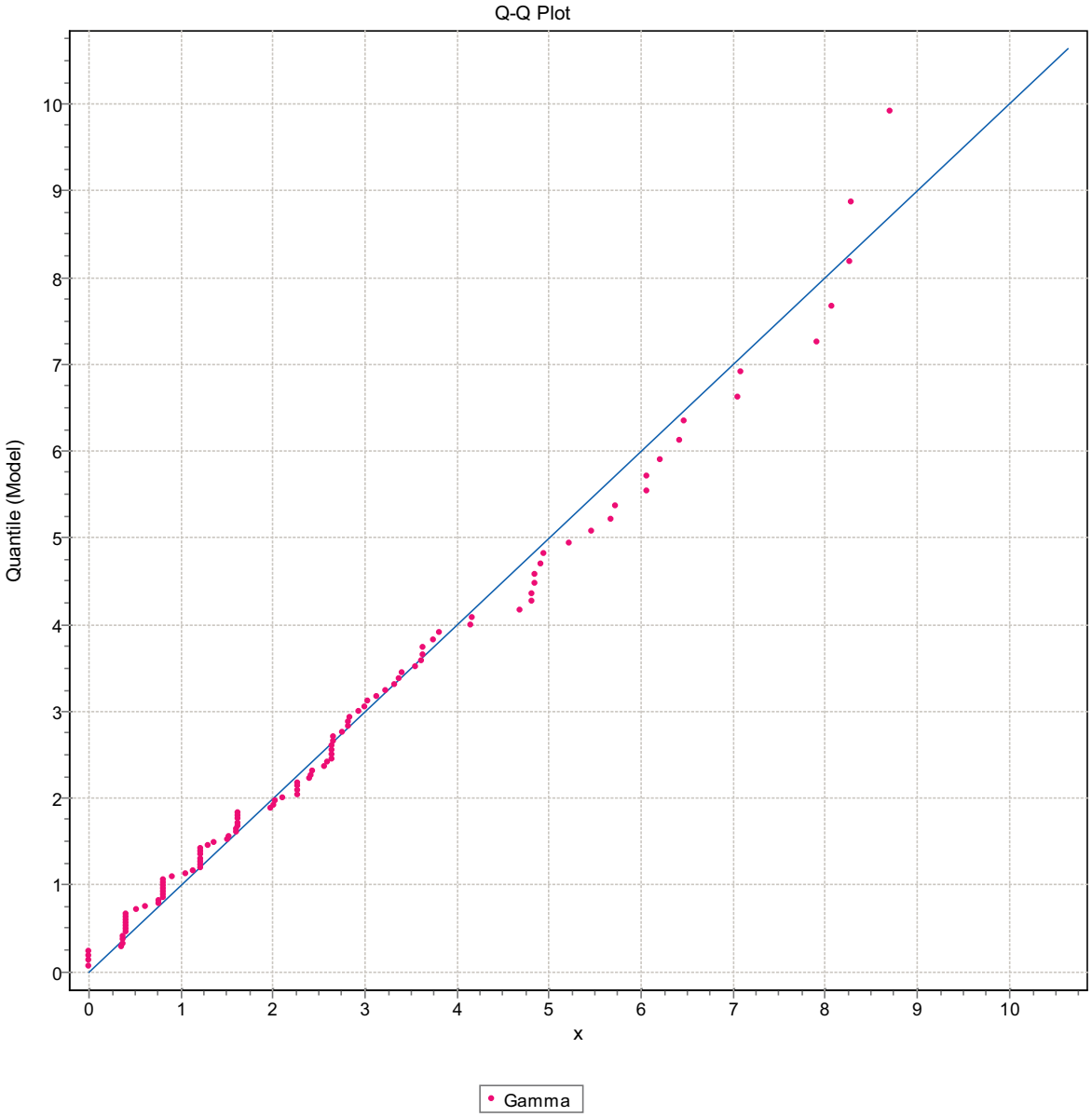

Figure F-189. *Q-Q plot, Domain FSM_NE005, 9 m bins, Gamma Distribution.*

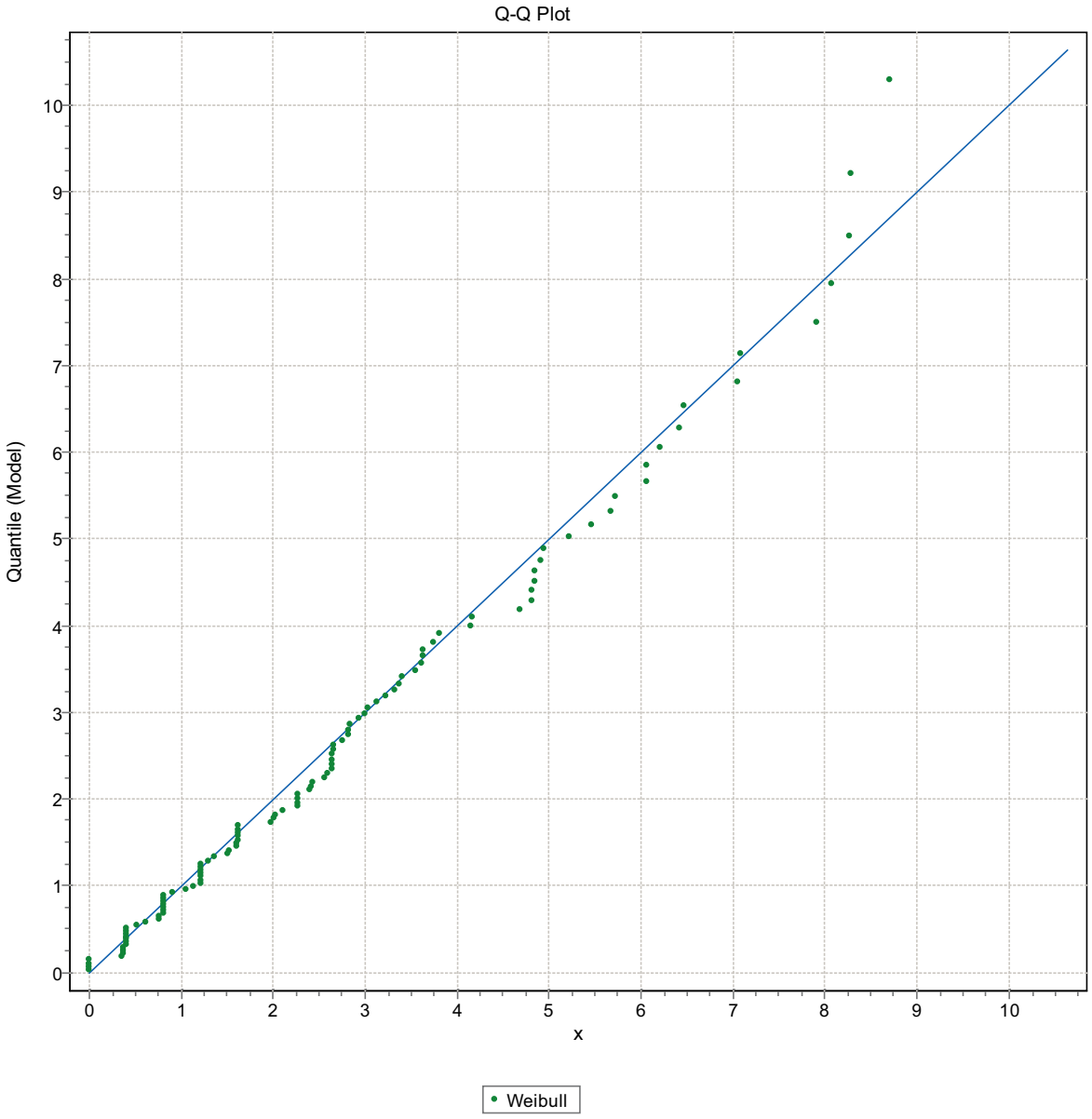

Figure F-190. *Q-Q plot, Domain FSM_NE005, 9 m bins, Weibull Distribution.*

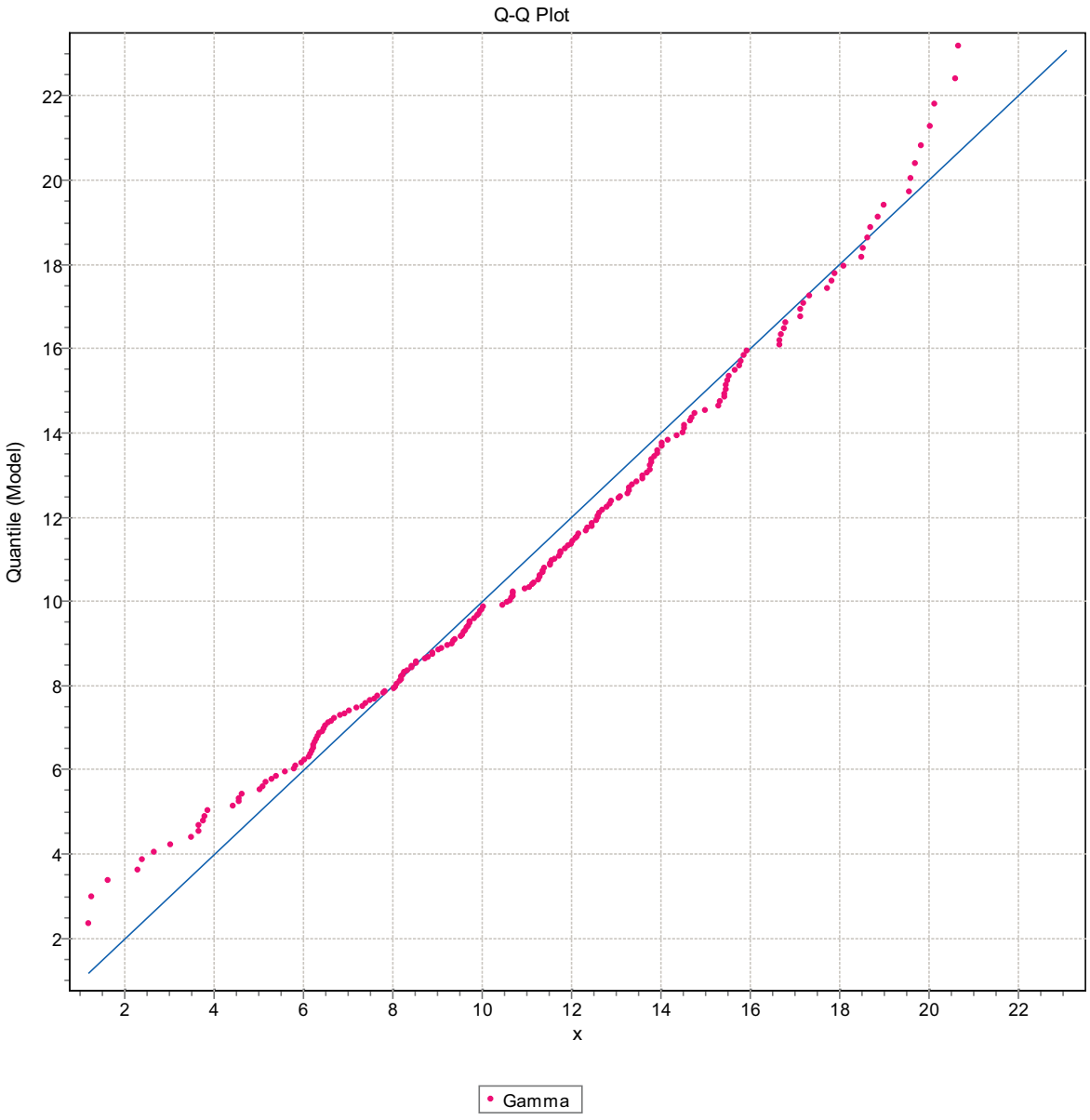

Figure F-191. *Q-Q plot, Domain FSM_N, 9 m bins, Gamma Distribution.*

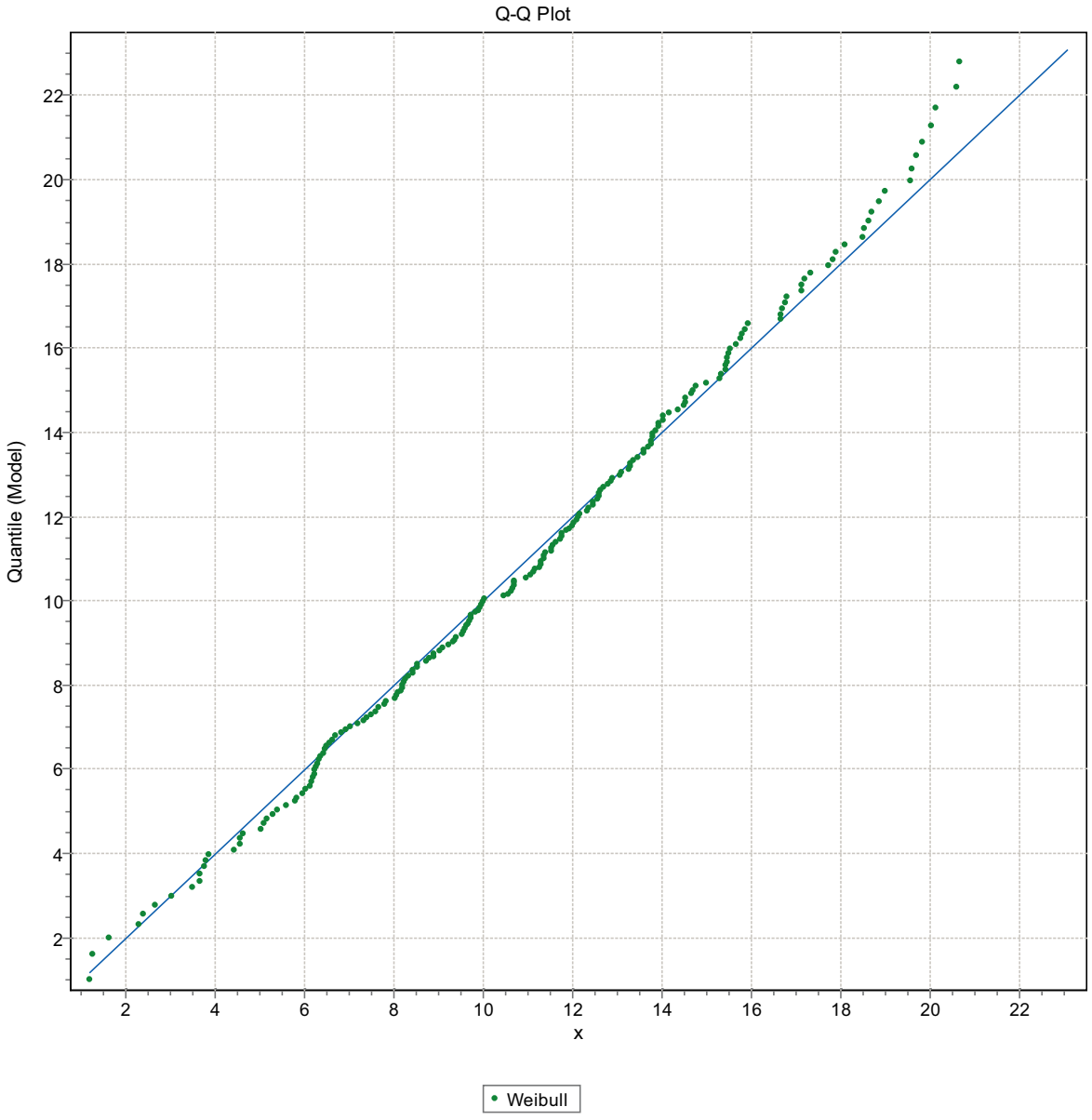

Figure F-192. *Q-Q plot, Domain FSM_N, 9 m bins, Weibull Distribution.*

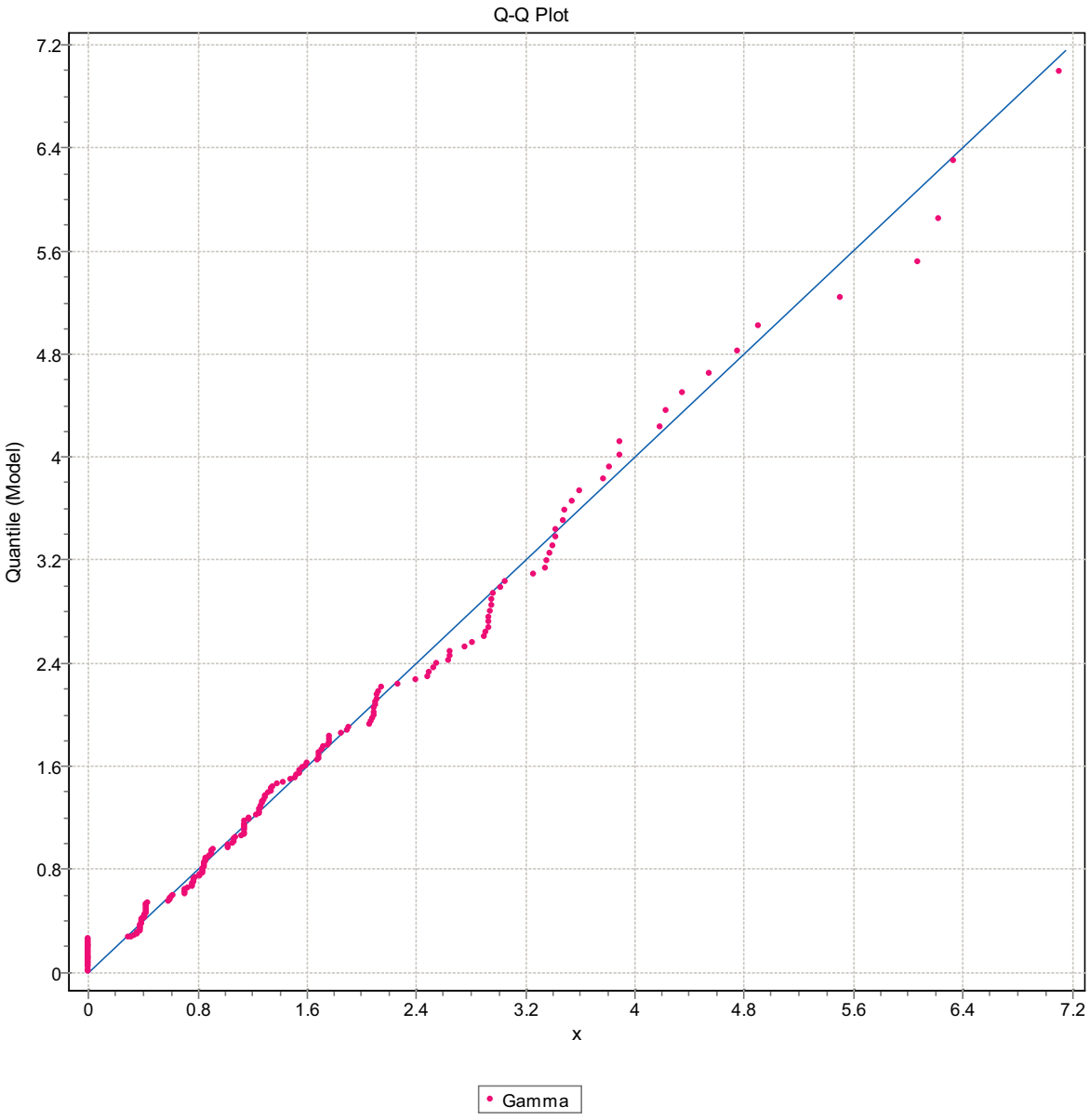

Figure F-193. *Q-Q plot, Domain FSM_N, 9 m bins, Gamma Distribution.*

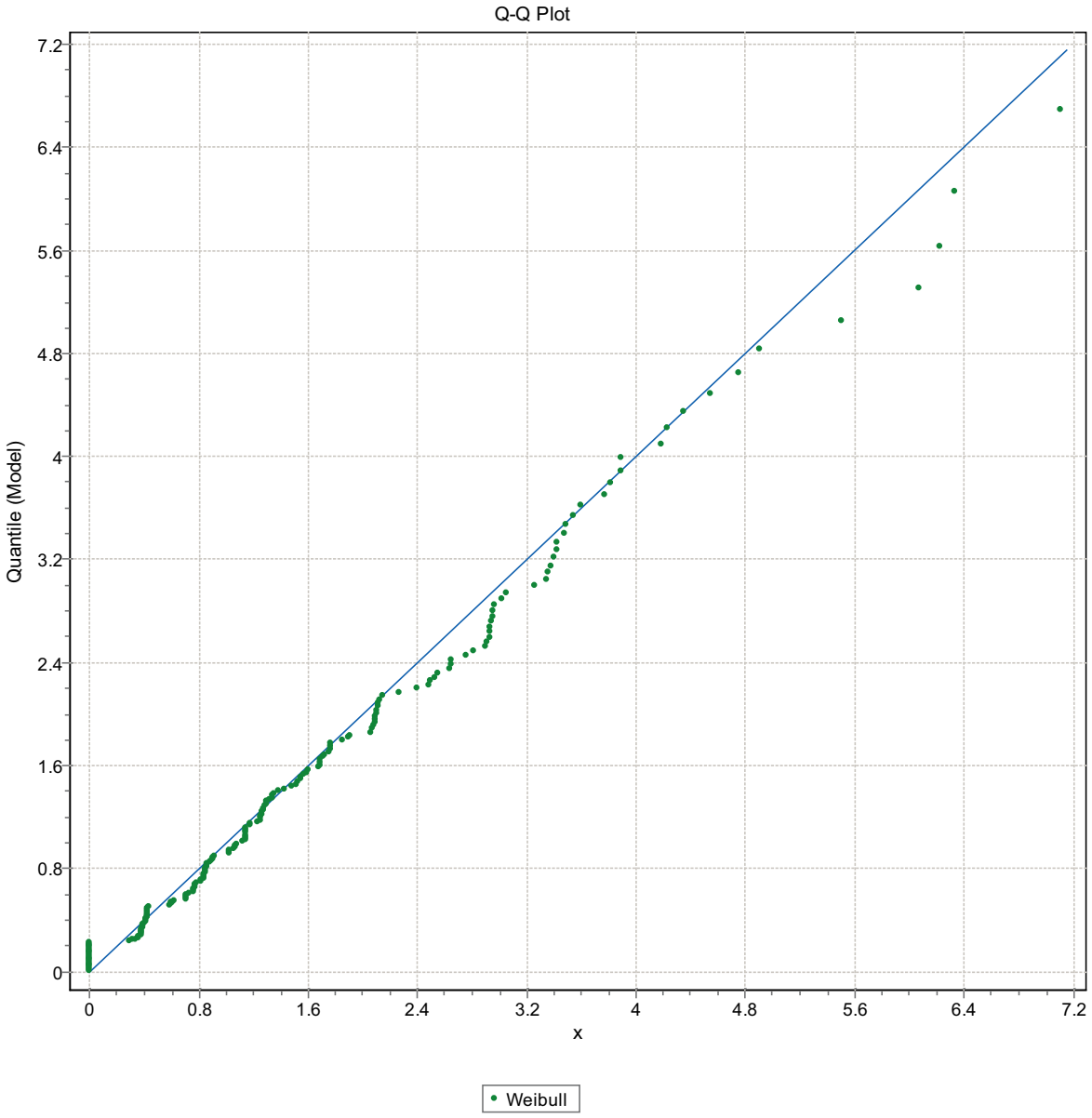

Figure F-194. *Q-Q plot, Domain FSM_N, 9 m bins, Weibull Distribution.*

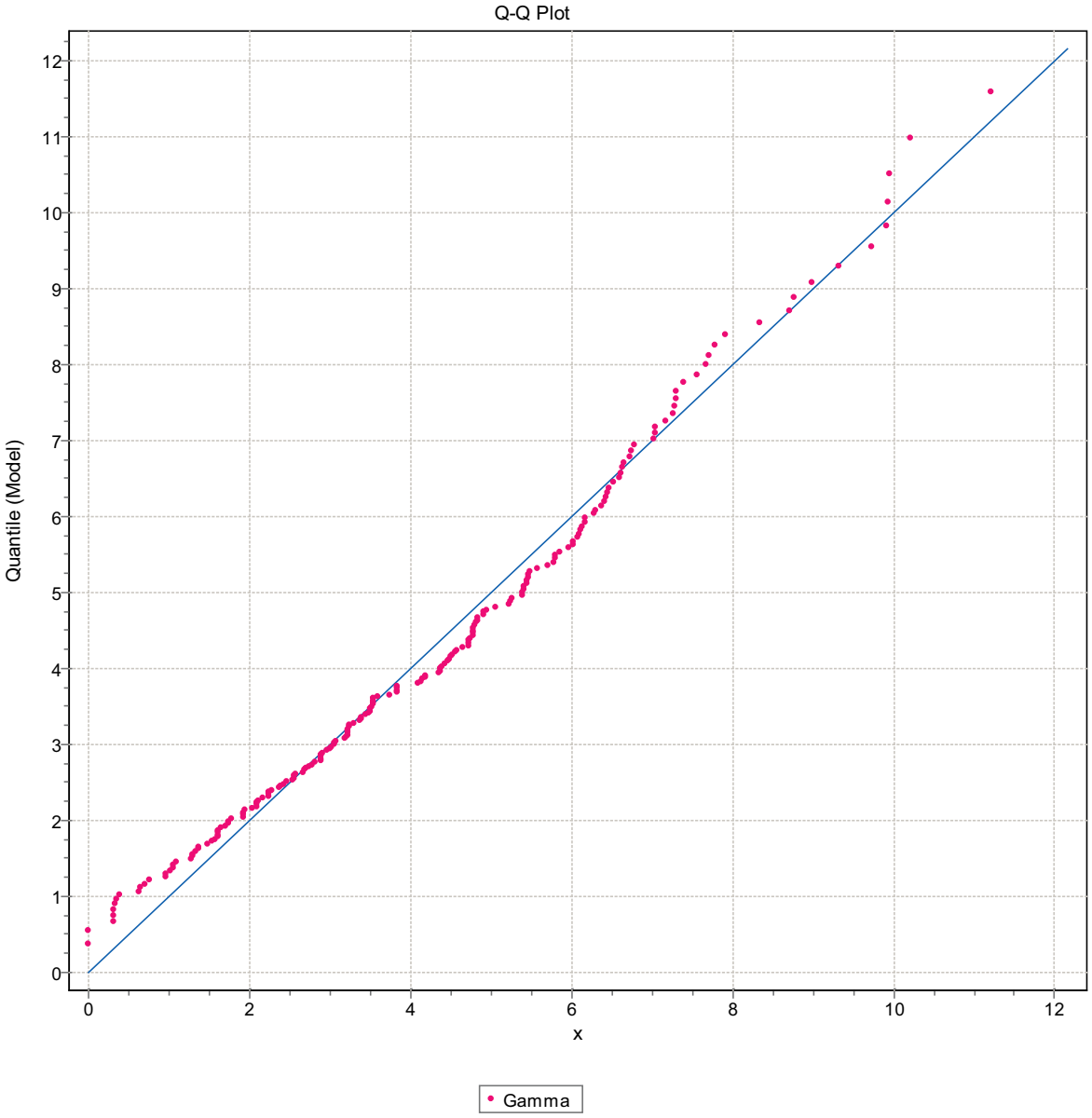

Figure F-195. *Q-Q plot, Domain FSM_N, 9 m bins, Gamma Distribution.*

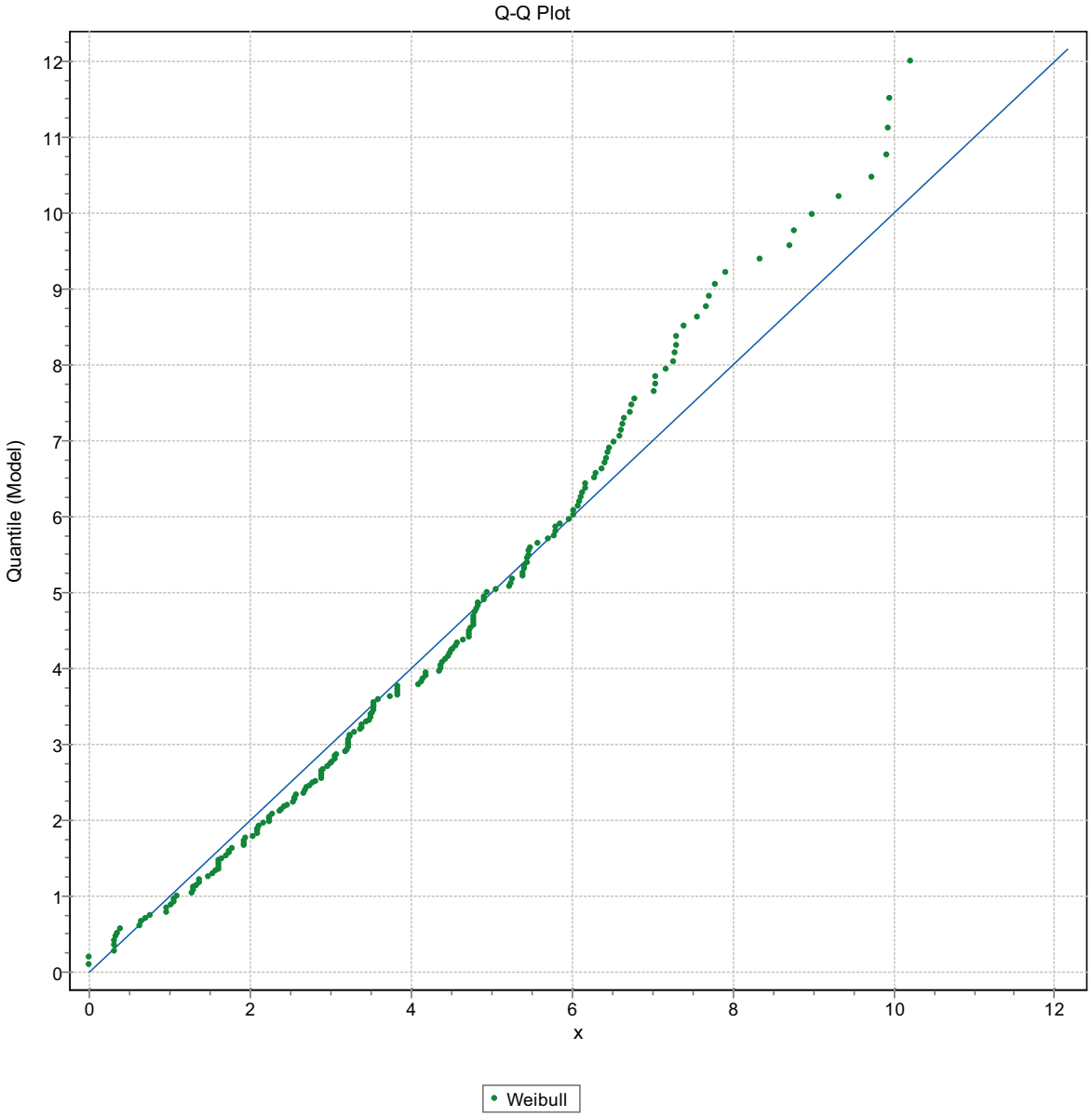

Figure F-196. *Q-Q plot, Domain FSM_N, 9 m bins, Weibull Distribution.*

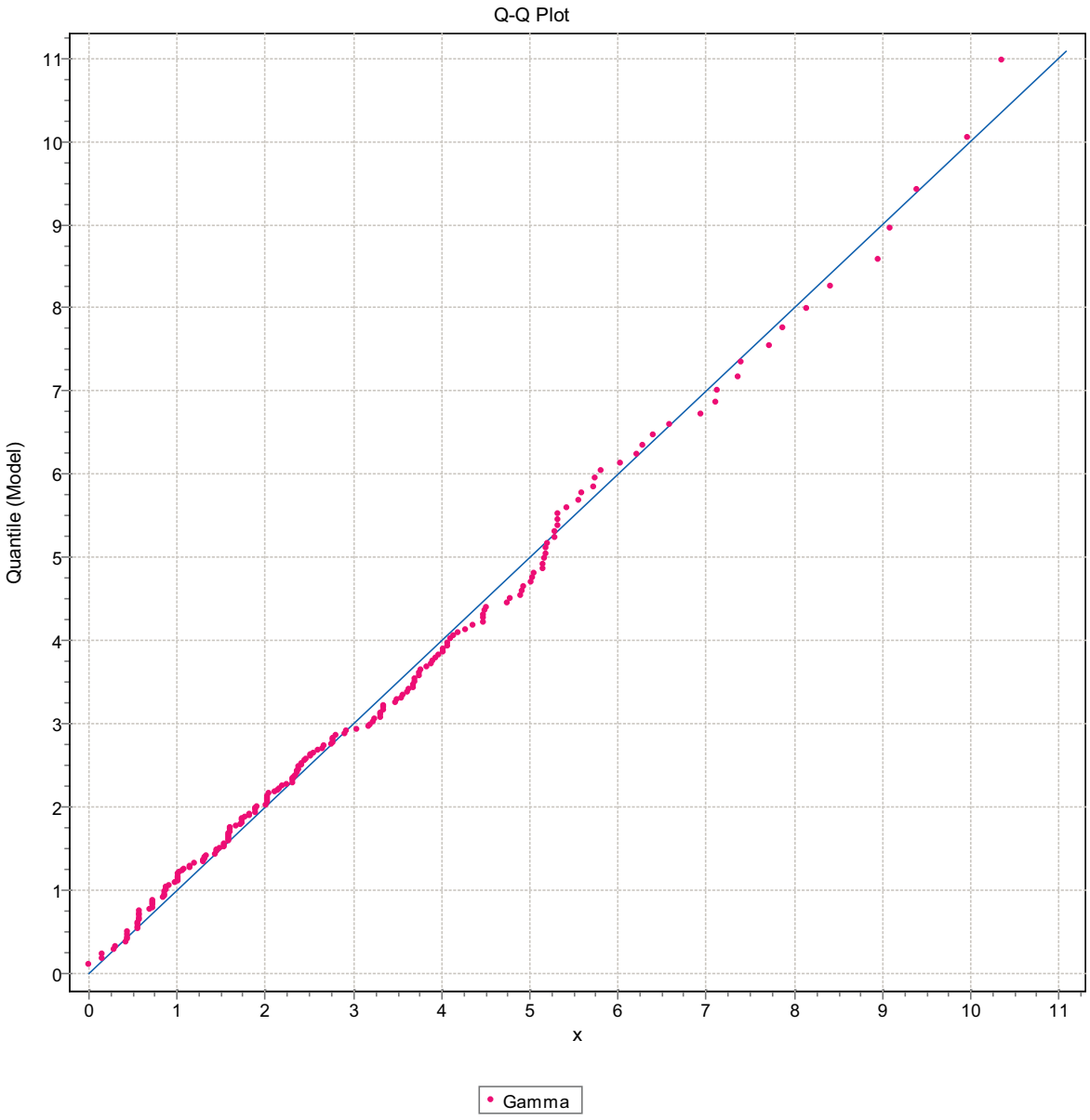

Figure F-197. *Q-Q plot, Domain FSM_N, 9 m bins, Gamma Distribution.*

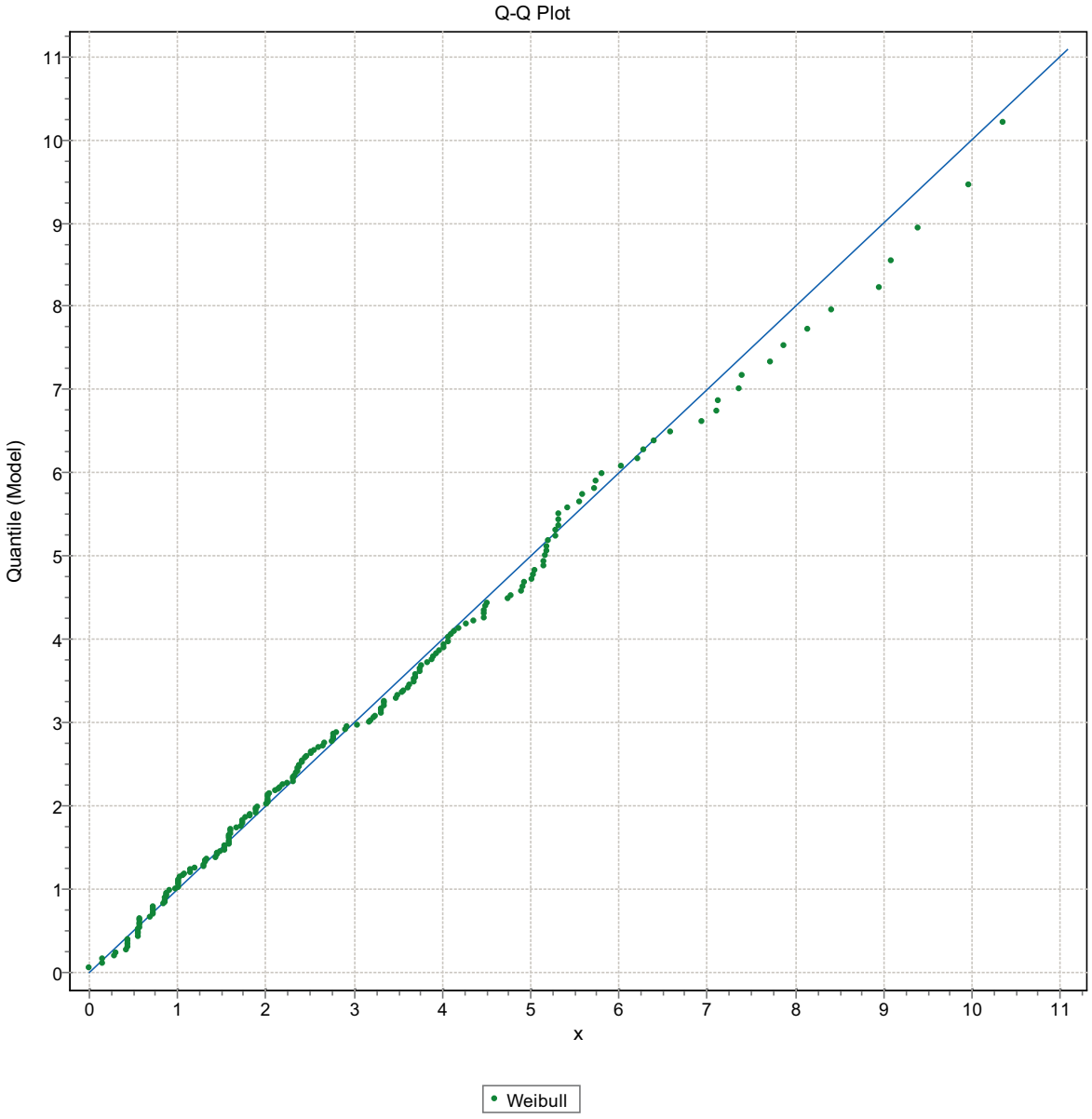

Figure F-198. *Q-Q plot, Domain FSM_N, 9 m bins, Weibull Distribution.*

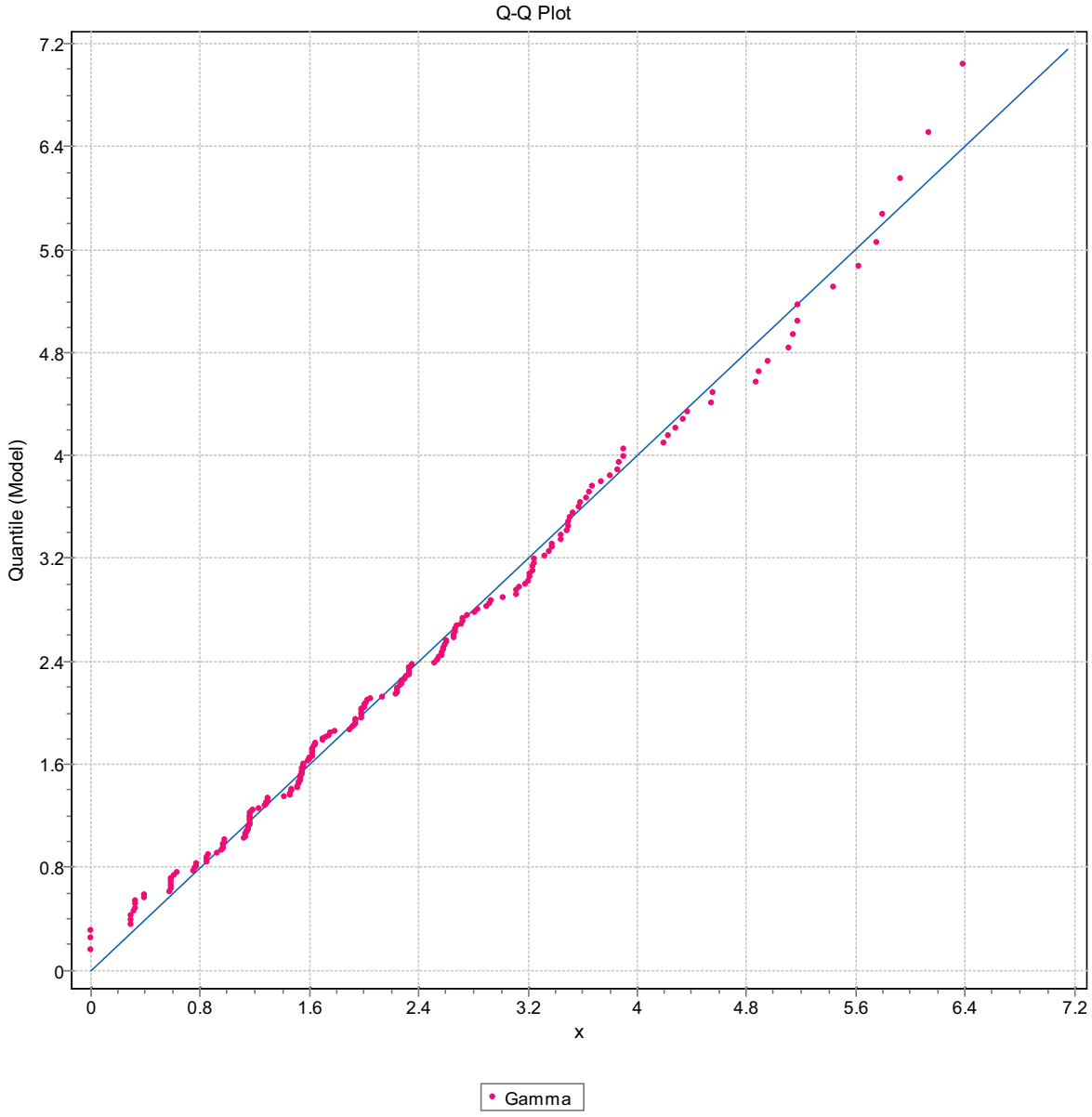

Figure F-199. *Q-Q plot, Domain FSM_N, 9 m bins, Gamma Distribution.*

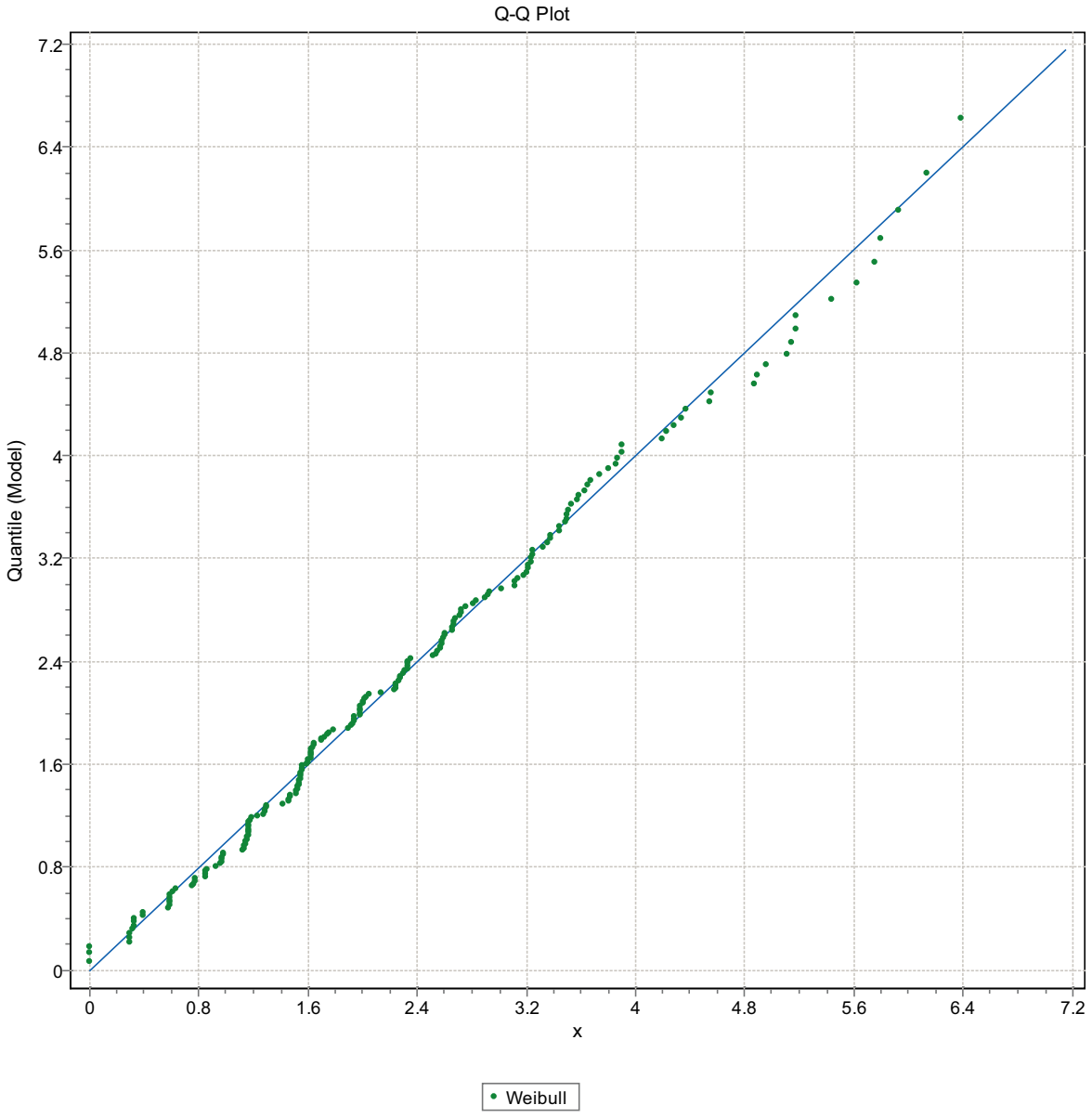

Figure F-200. *Q-Q plot, Domain FSM_N, 9 m bins, Weibull Distribution.*

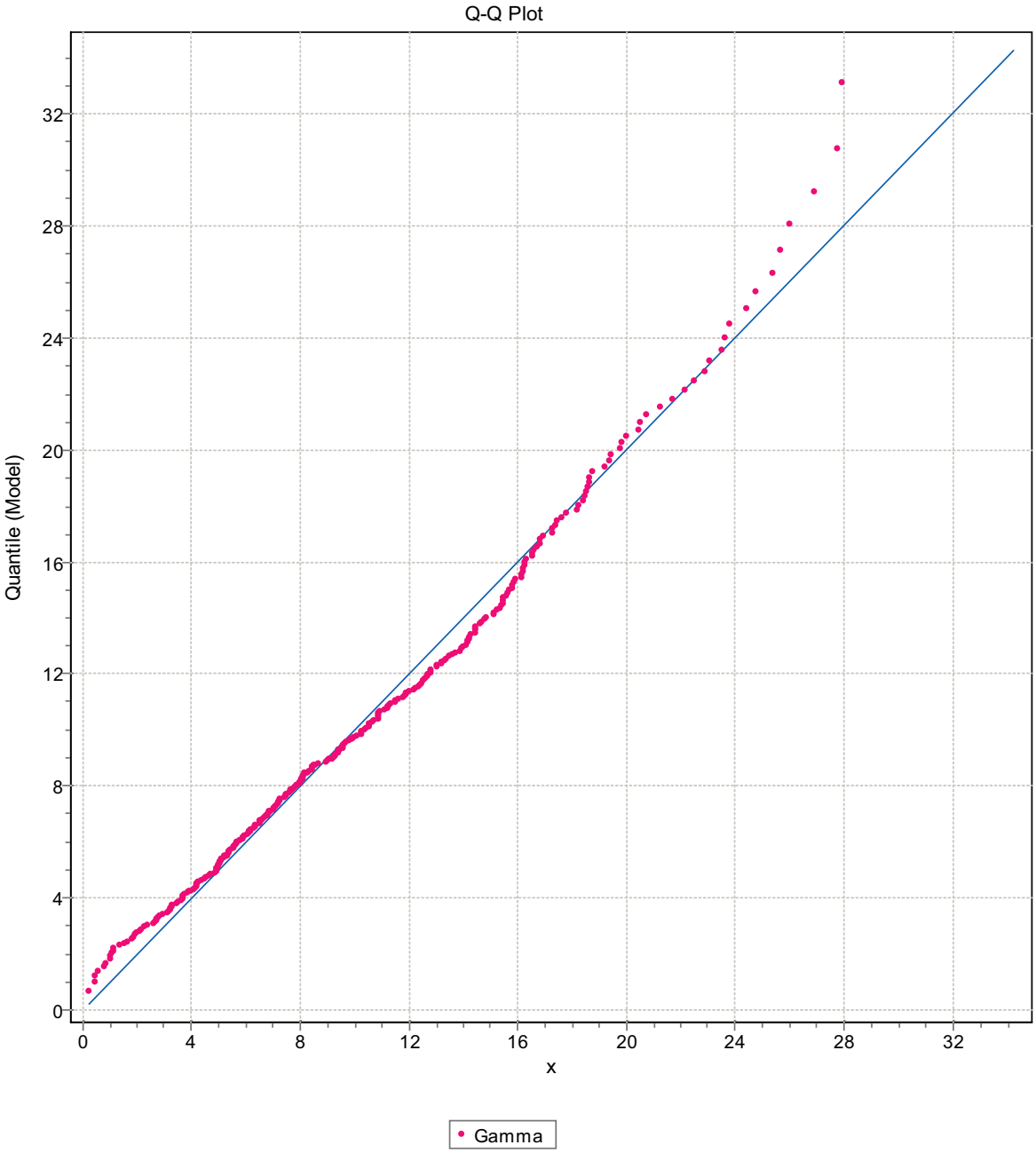

Figure F-201. *Q-Q plot, Domain FSM_W, 9 m bins, Gamma Distribution.*

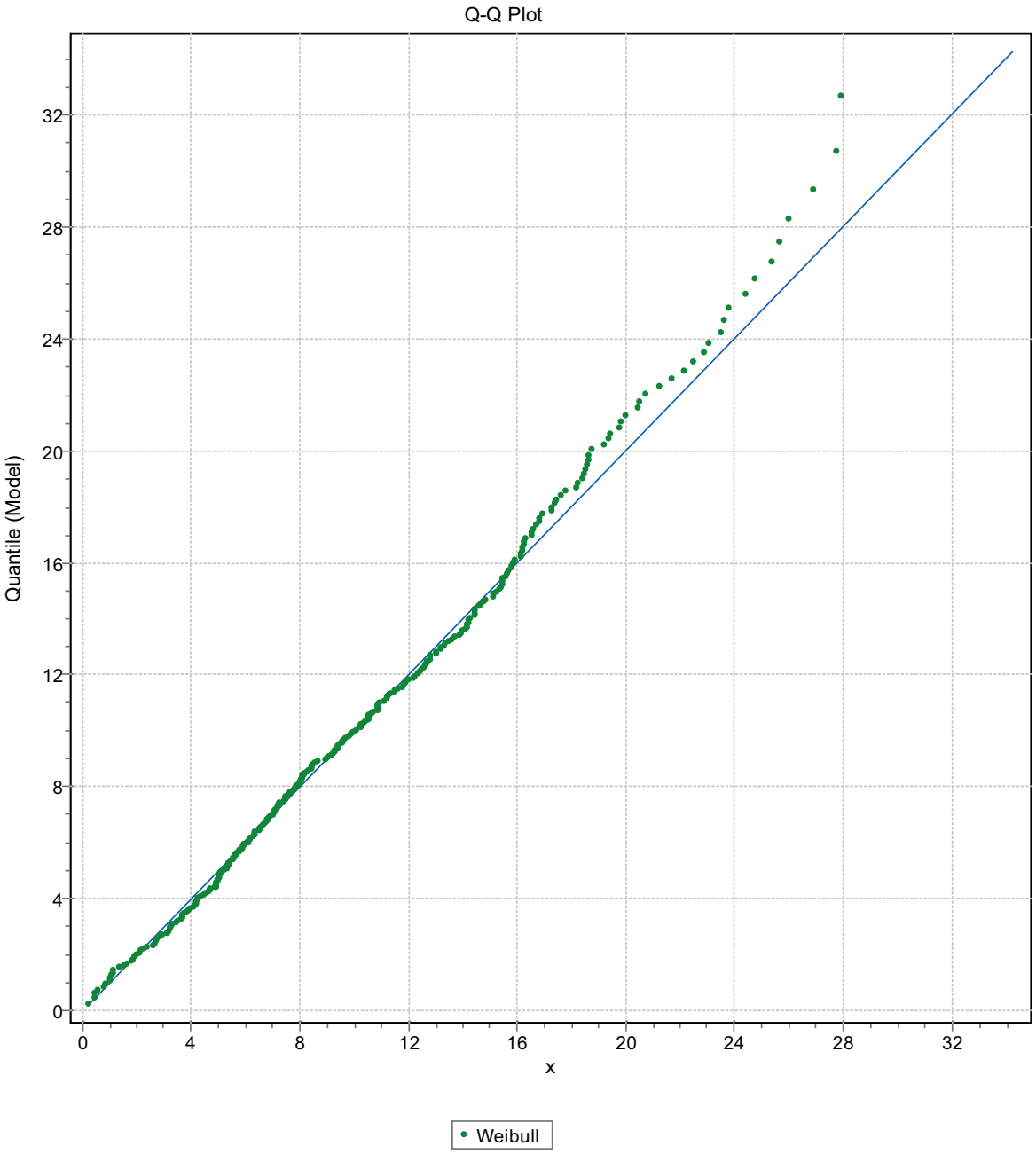

Figure F-202. *Q-Q plot, Domain FSM_W, 9 m bins, Weibull Distribution.*

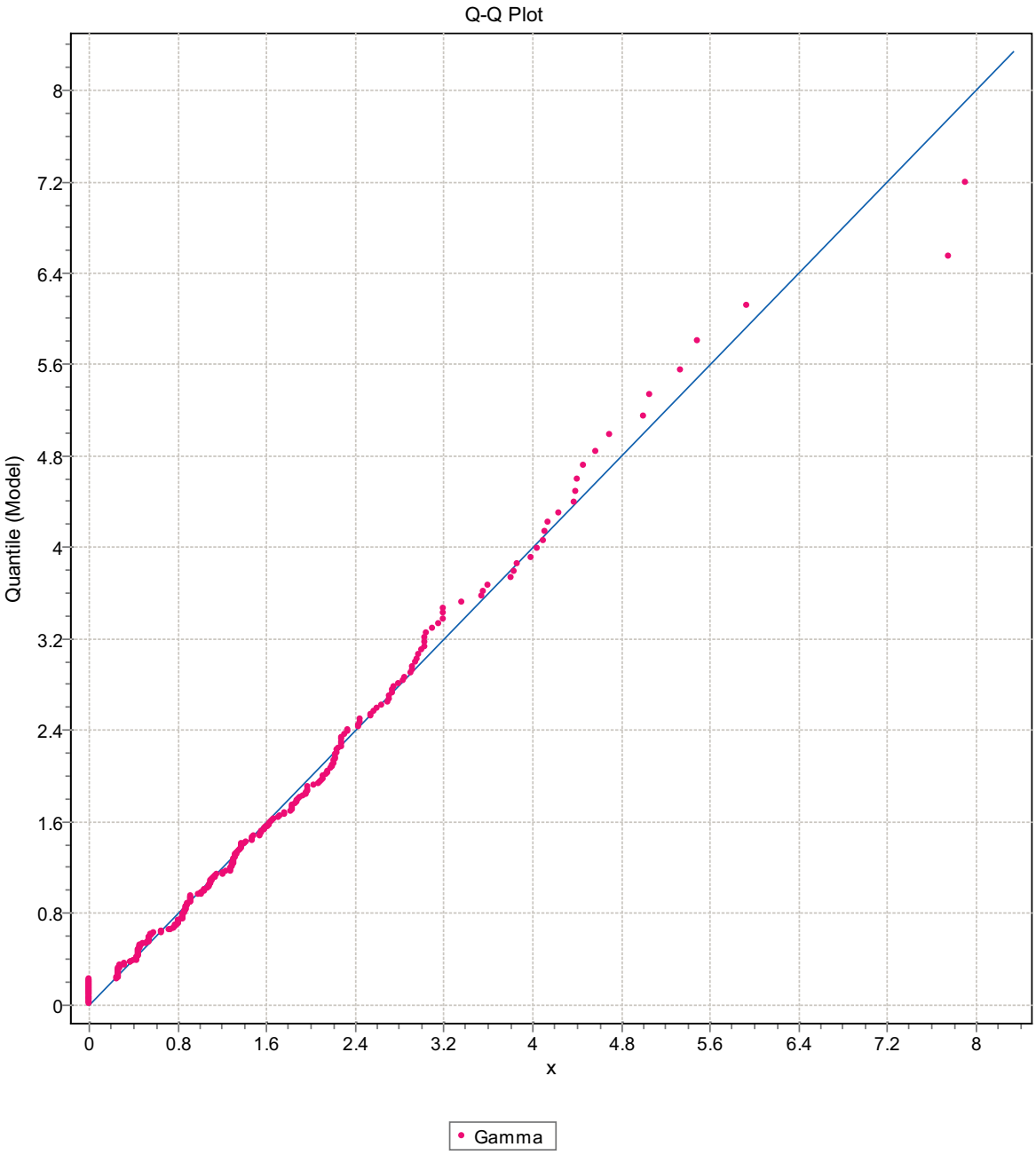

Figure F-203. *Q-Q plot, Domain FSM_W, 9 m bins, Gamma Distribution.*

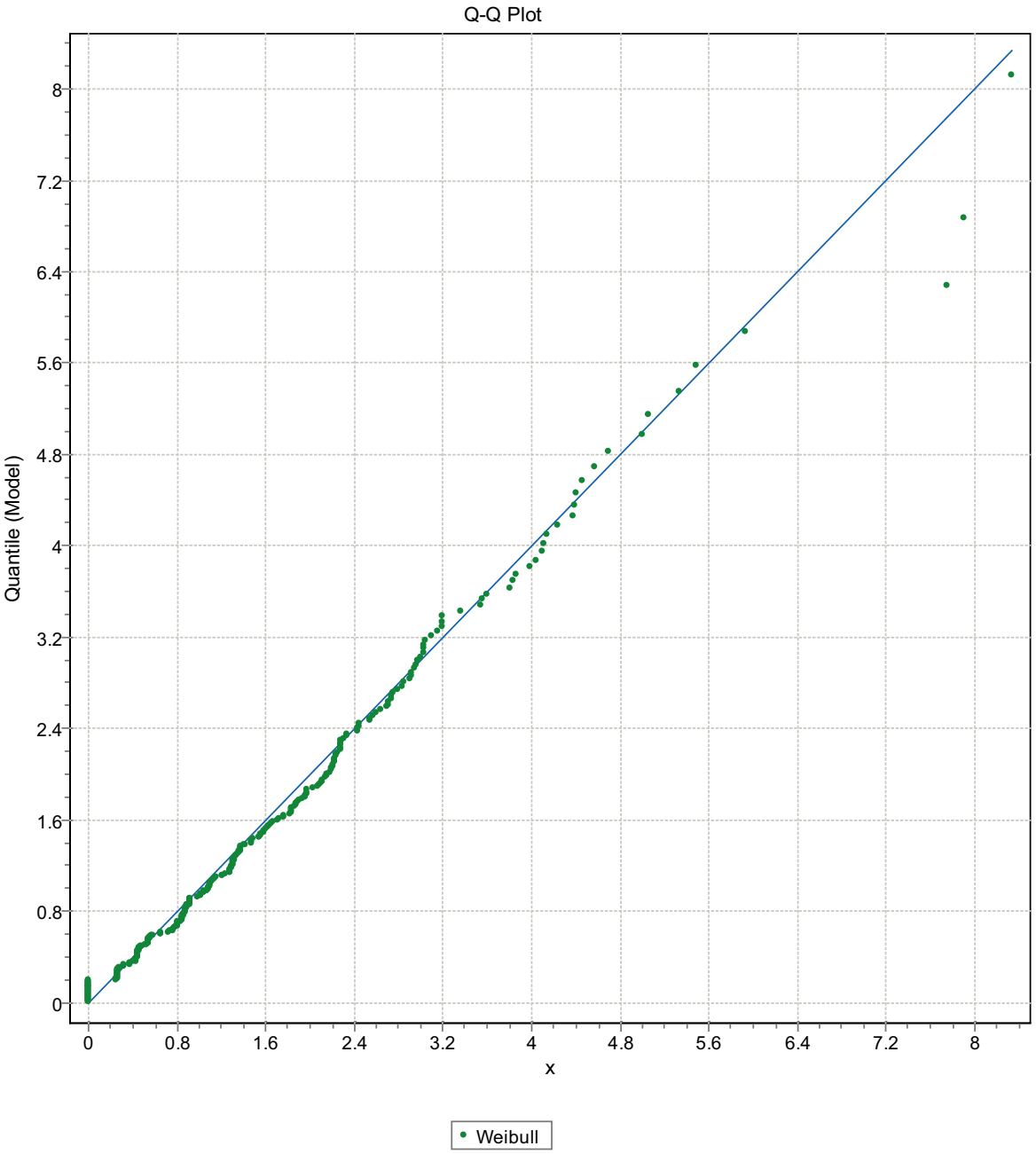

Figure F-204. *Q-Q plot, Domain FSM_W, 9 m bins, Weibull Distribution.*

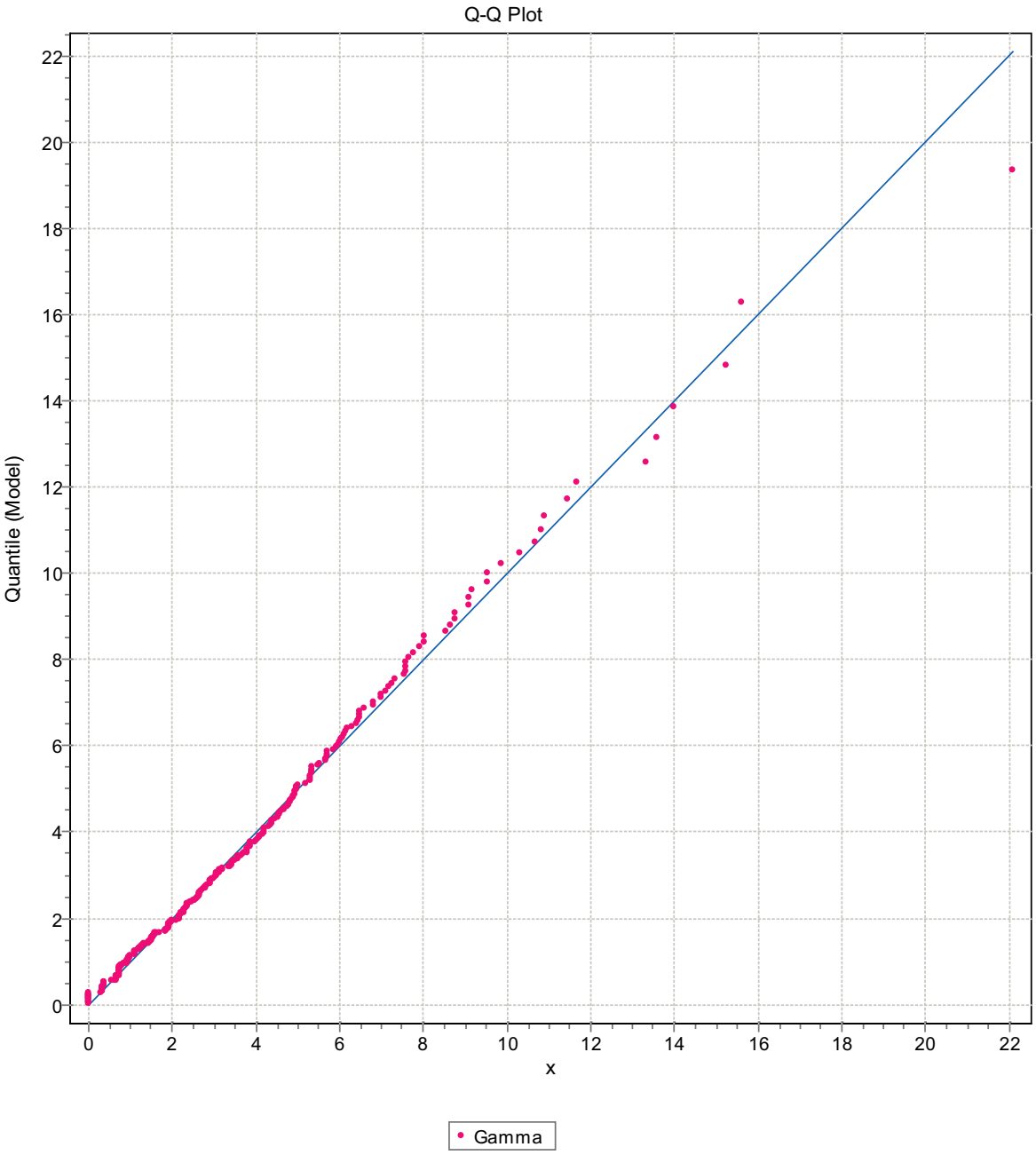

Figure F-205. *Q-Q plot, Domain FSM_W, 9 m bins, Gamma Distribution.*

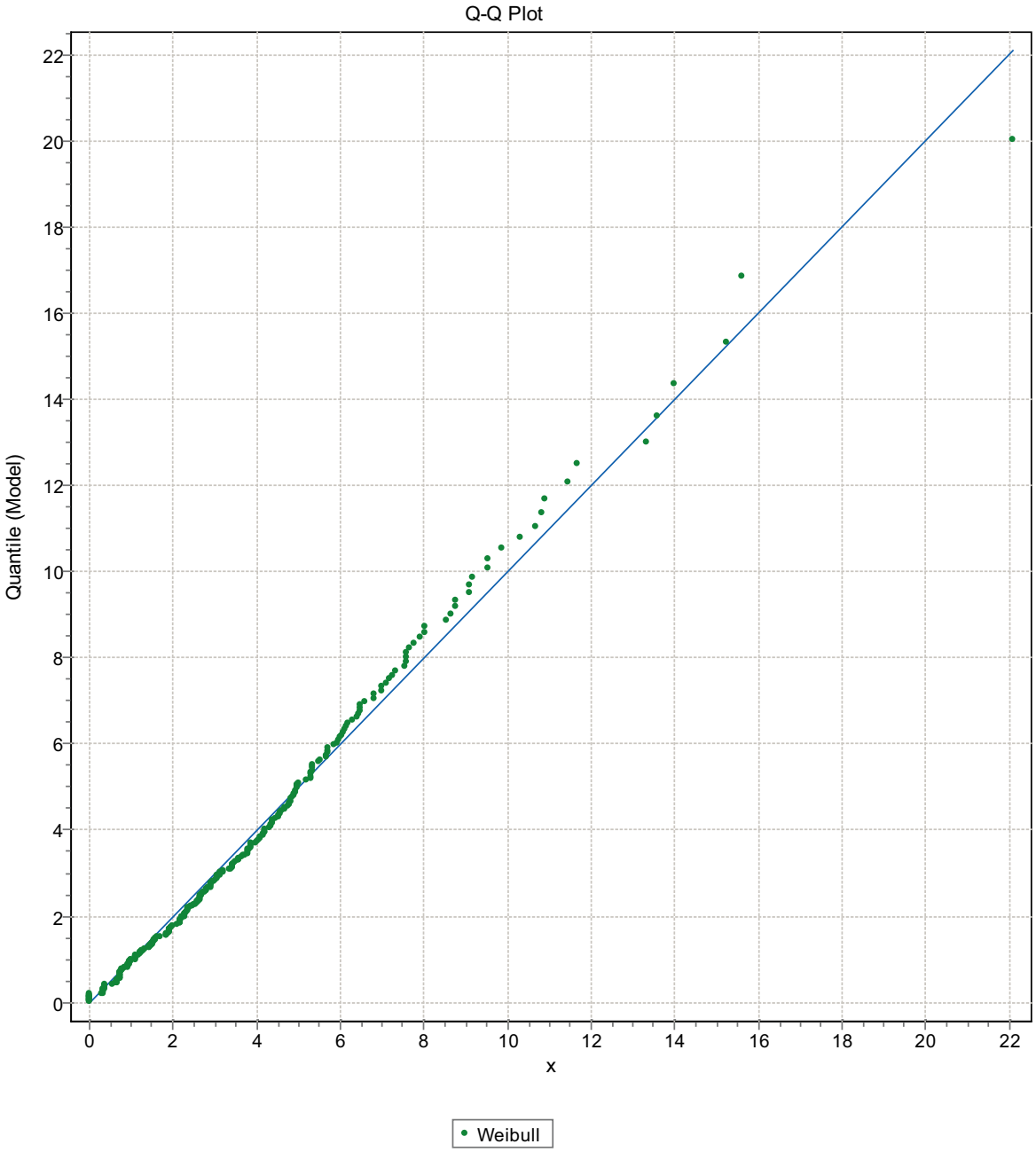

Figure F-206. *Q-Q plot, Domain FSM_W, 9 m bins, Weibull Distribution.*

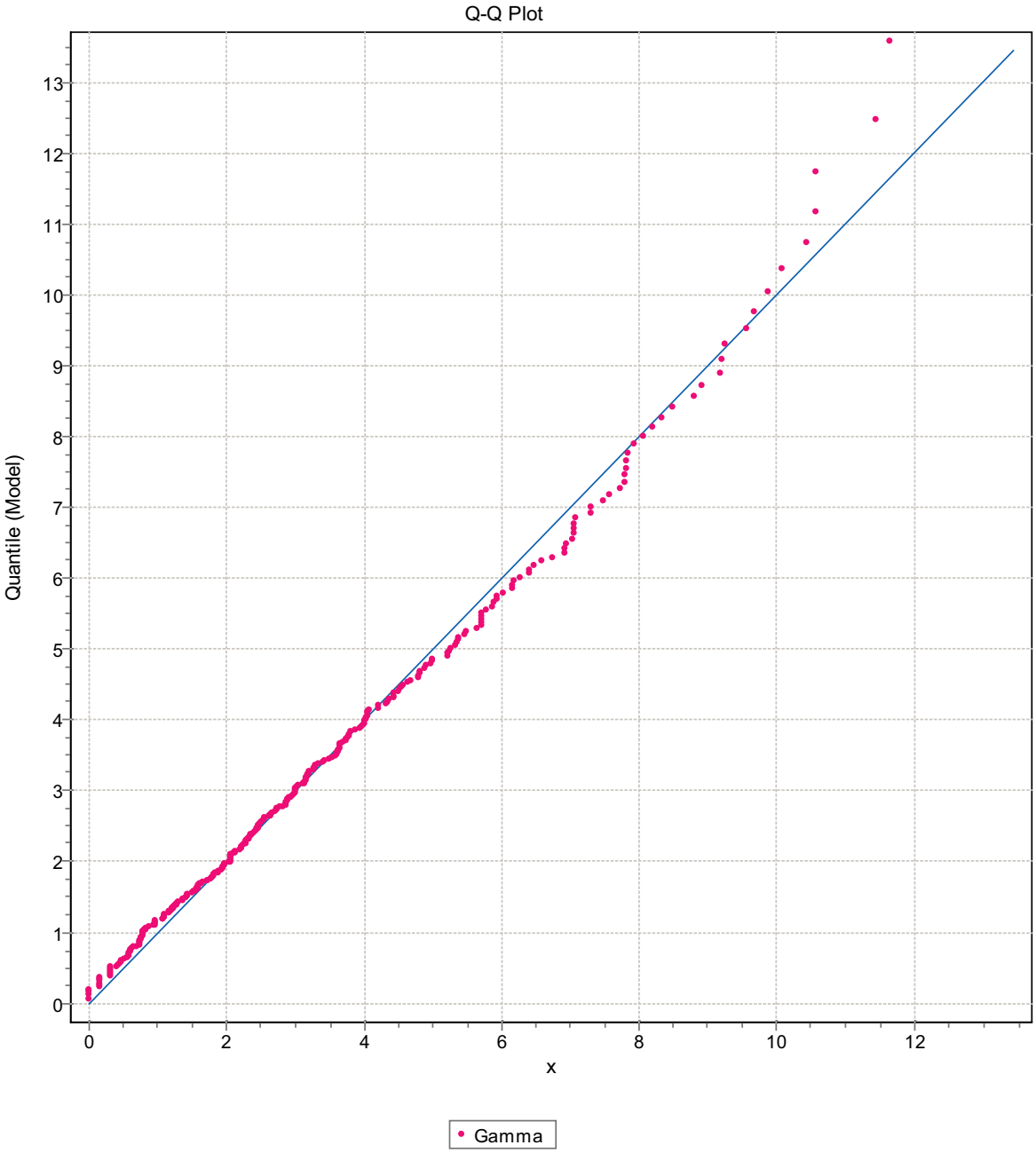

Figure F-207. *Q-Q plot, Domain FSM_W, 9 m bins, Gamma Distribution.*

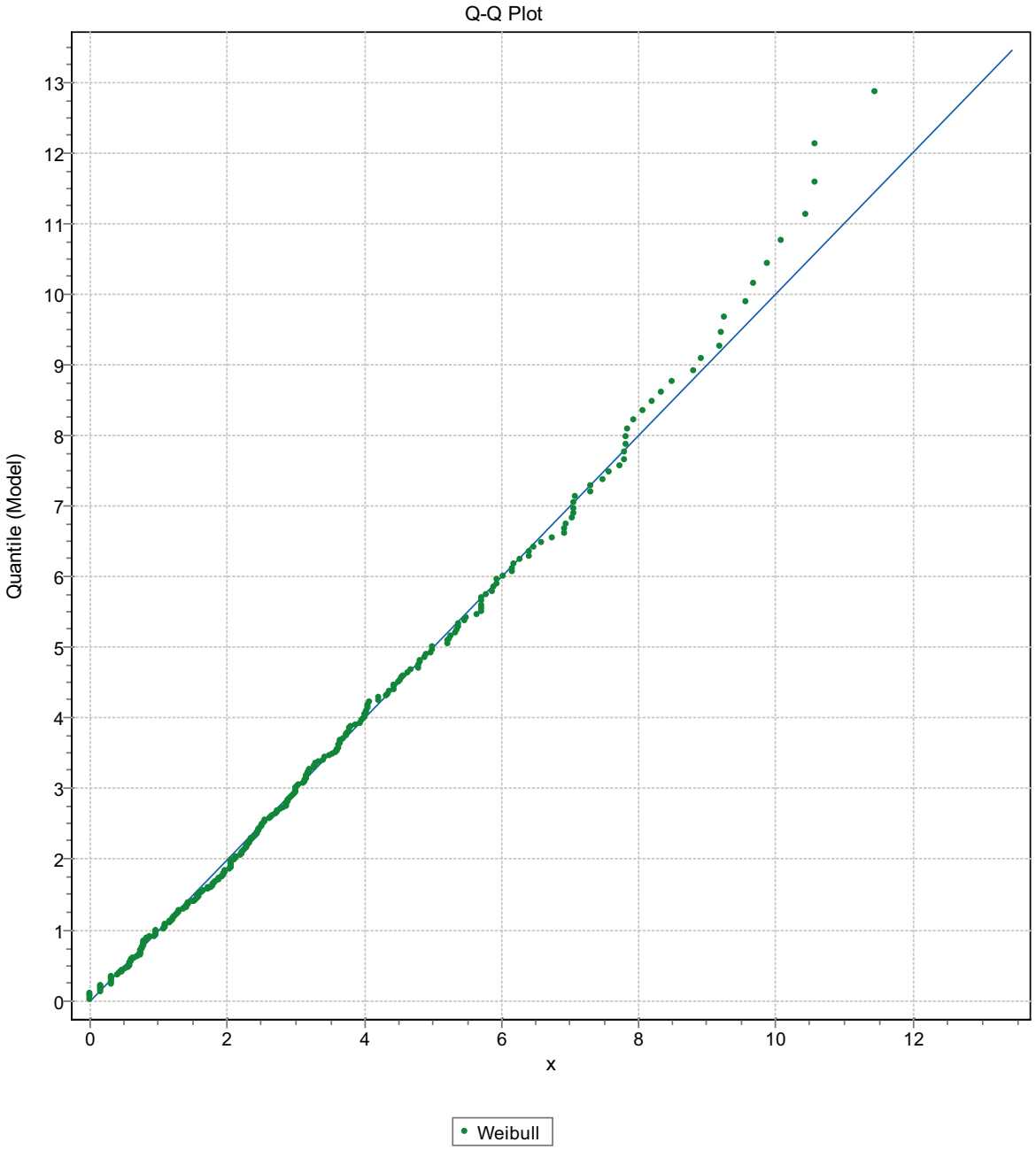

Figure F-208. *Q-Q plot, Domain FSM_W, 9 m bins, Weibull Distribution.*

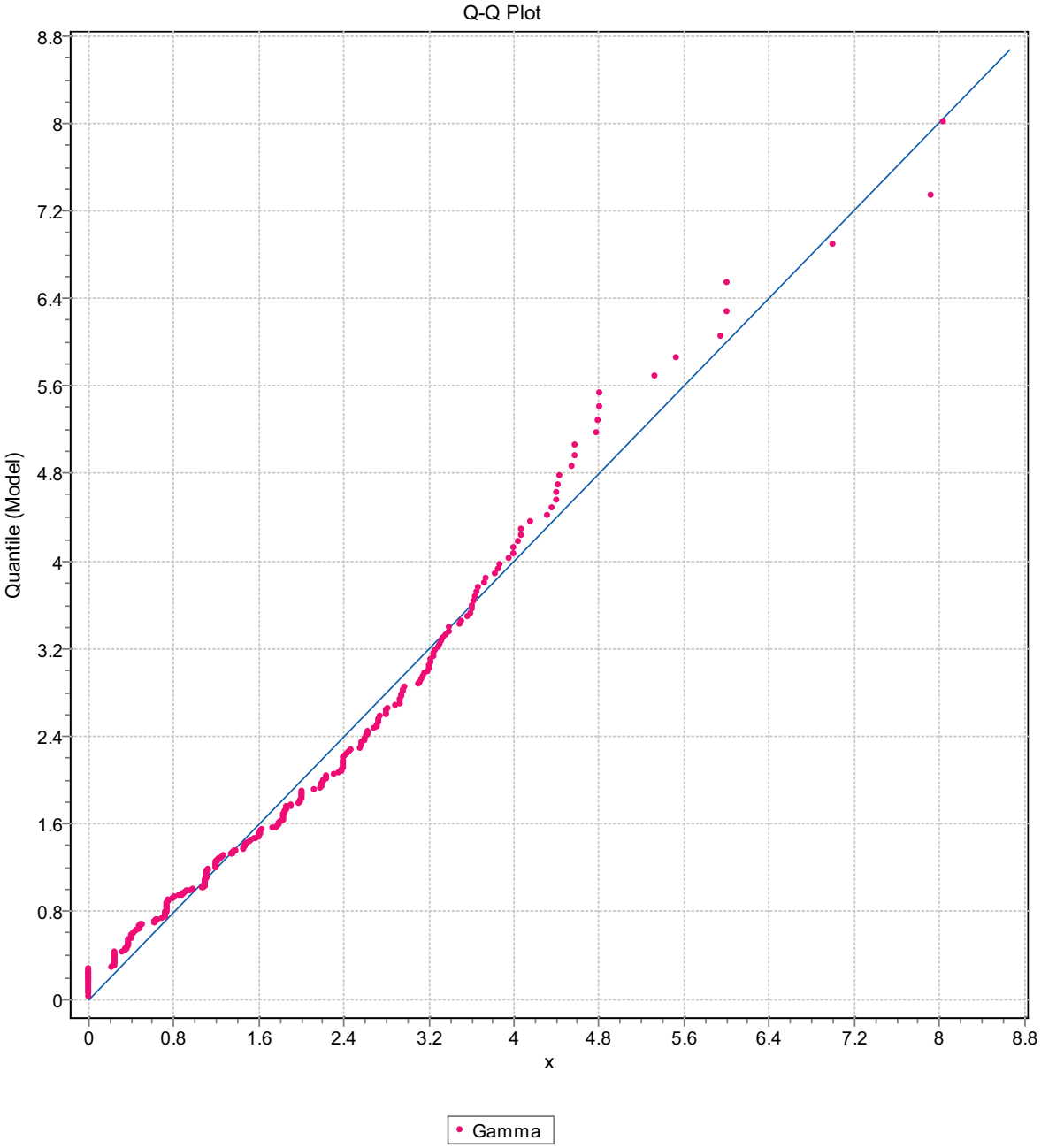

Figure F-209. *Q-Q plot, Domain FSM_W, 9 m bins, Gamma Distribution.*

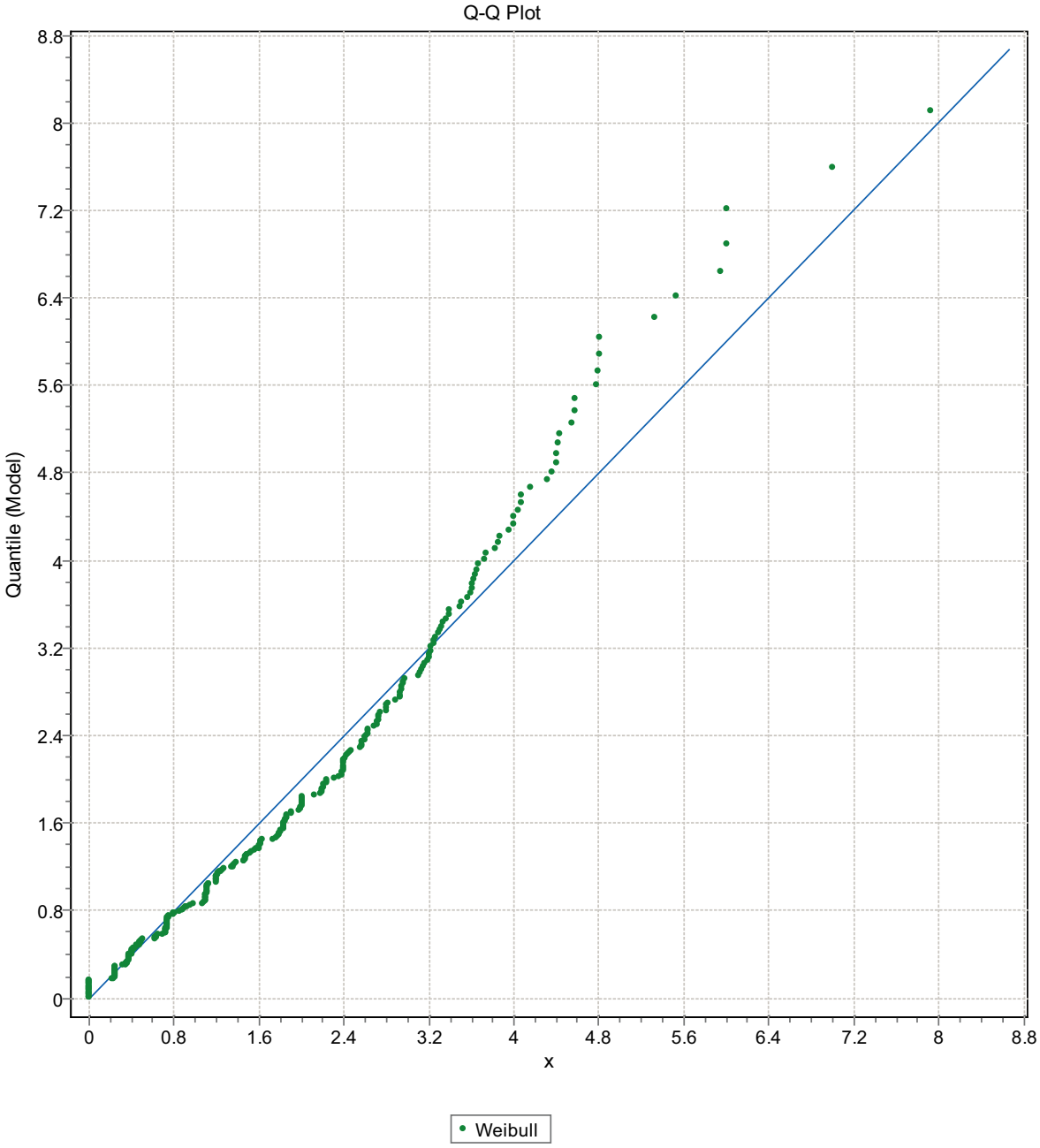

Figure F-210. *Q-Q plot, Domain FSM_W, 9 m bins, Weibull Distribution.*

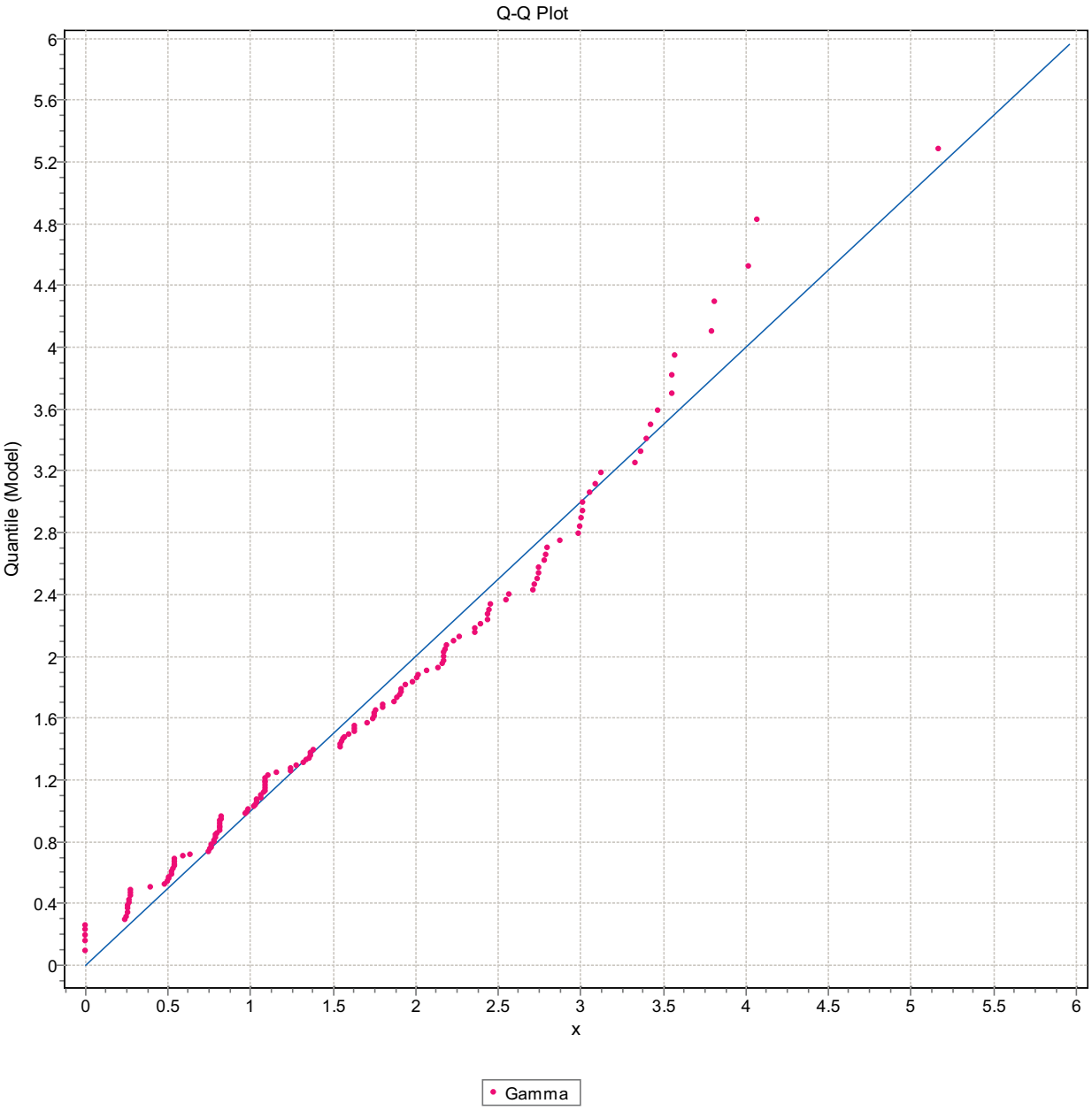

Figure F-211. *Q-Q plot, Domain FSM_C, 15 m bins, Gamma Distribution.*

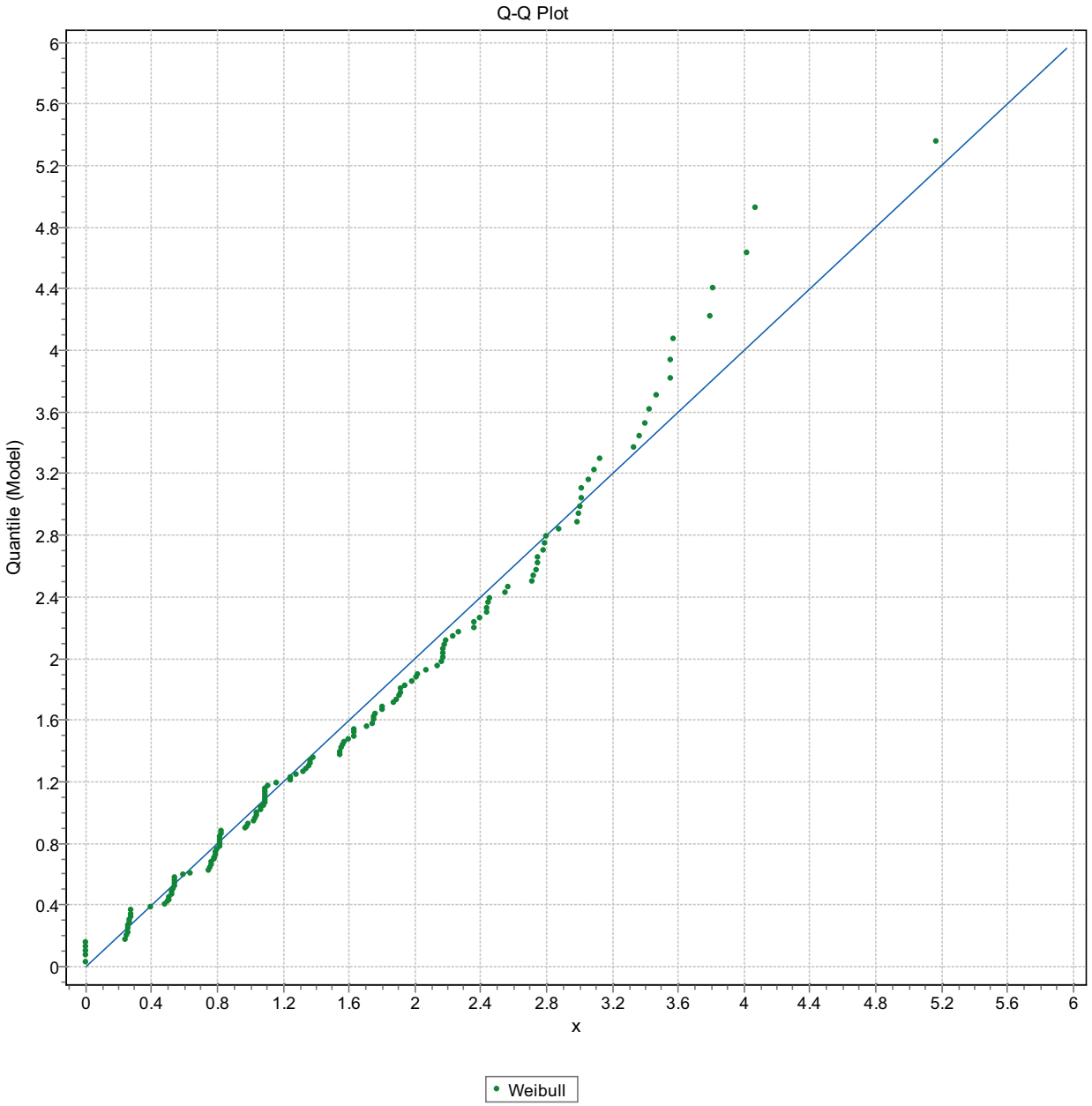

Figure F-212. *Q-Q plot, Domain FSM_C, 15 m bins, Weibull Distribution.*

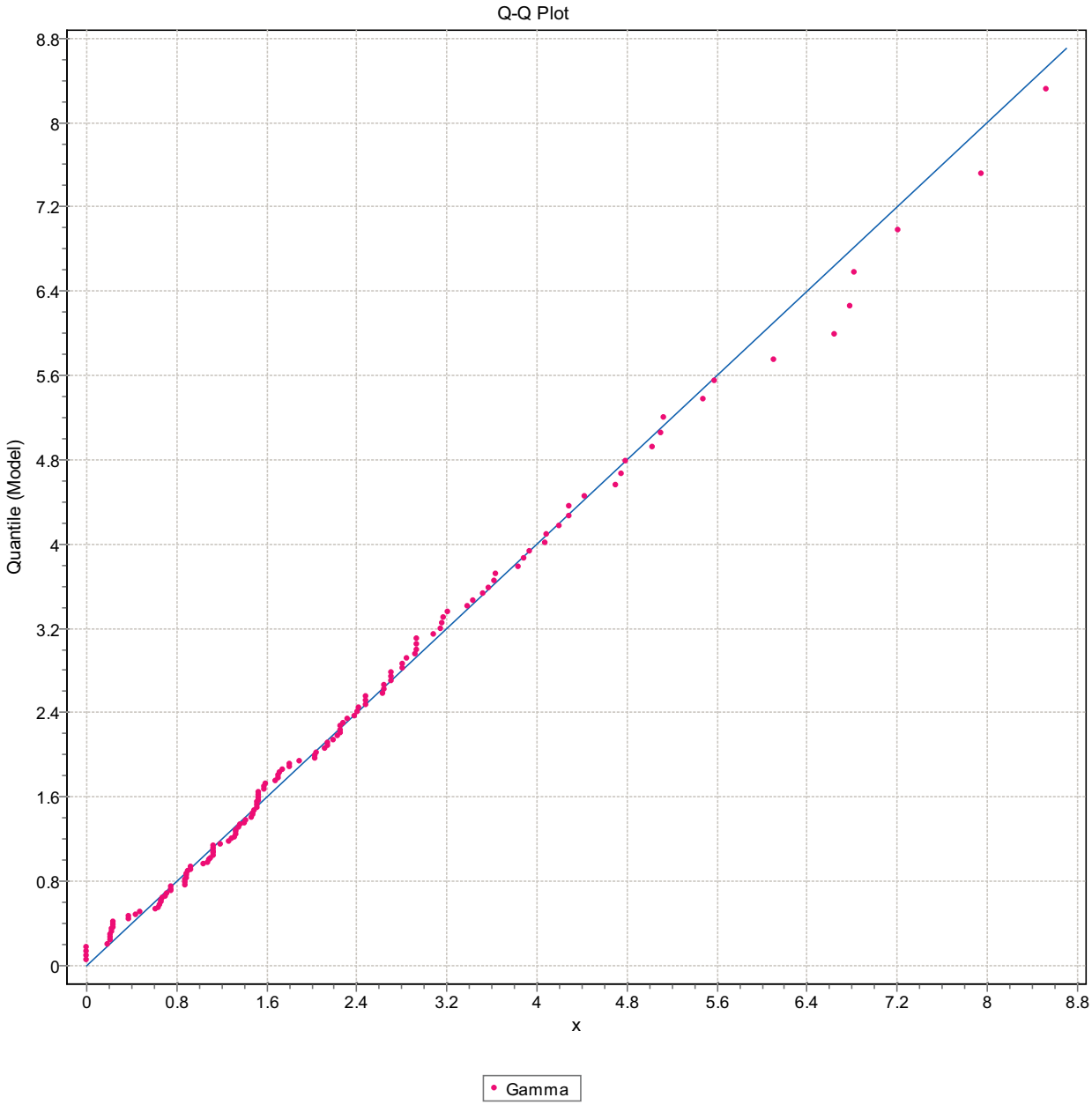

Figure F-213. *Q-Q plot, Domain FSM_C, 15 m bins, Gamma Distribution.*

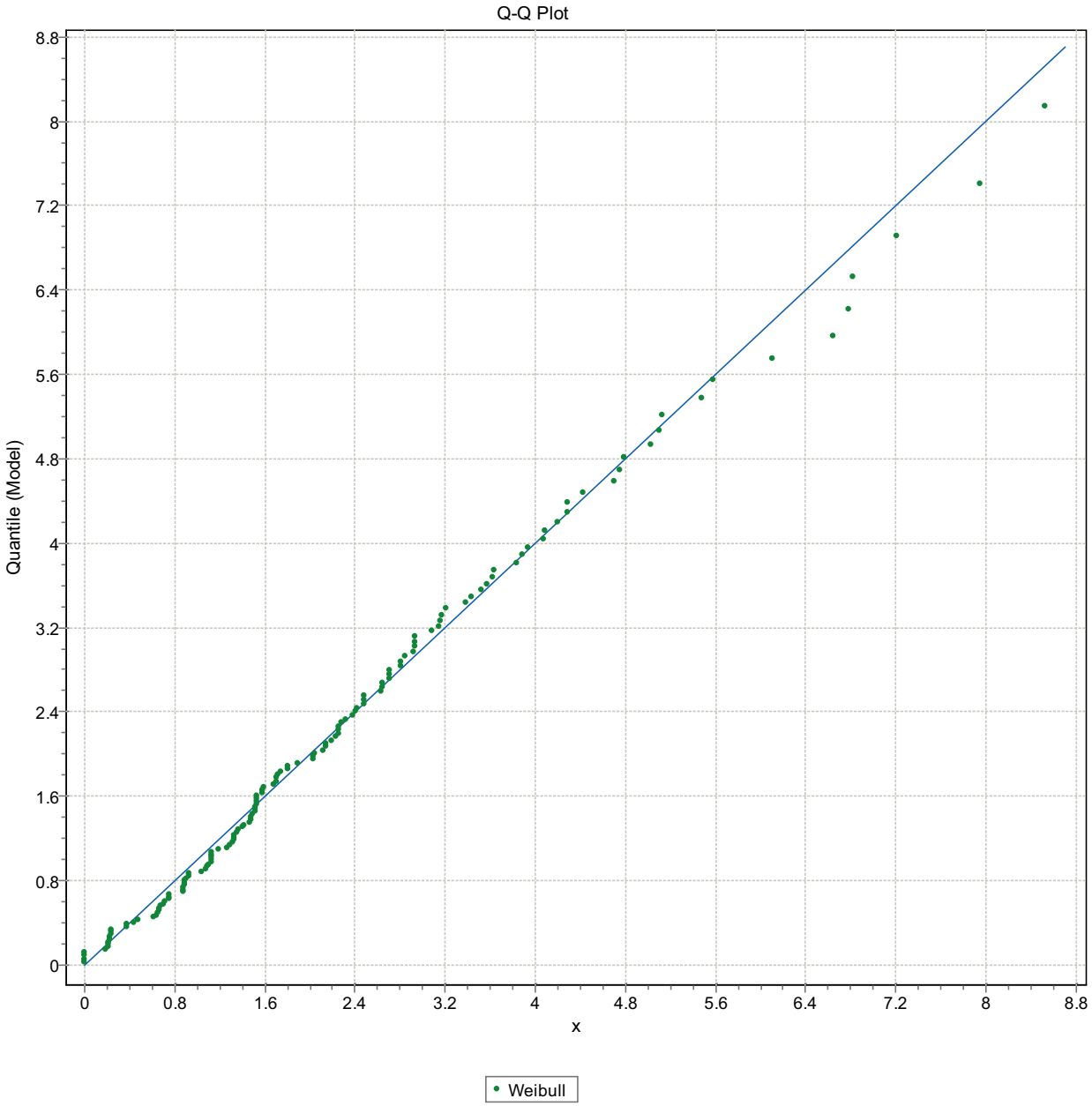

Figure F-214. *Q-Q plot, Domain FSM_C, 15 m bins, Weibull Distribution.*

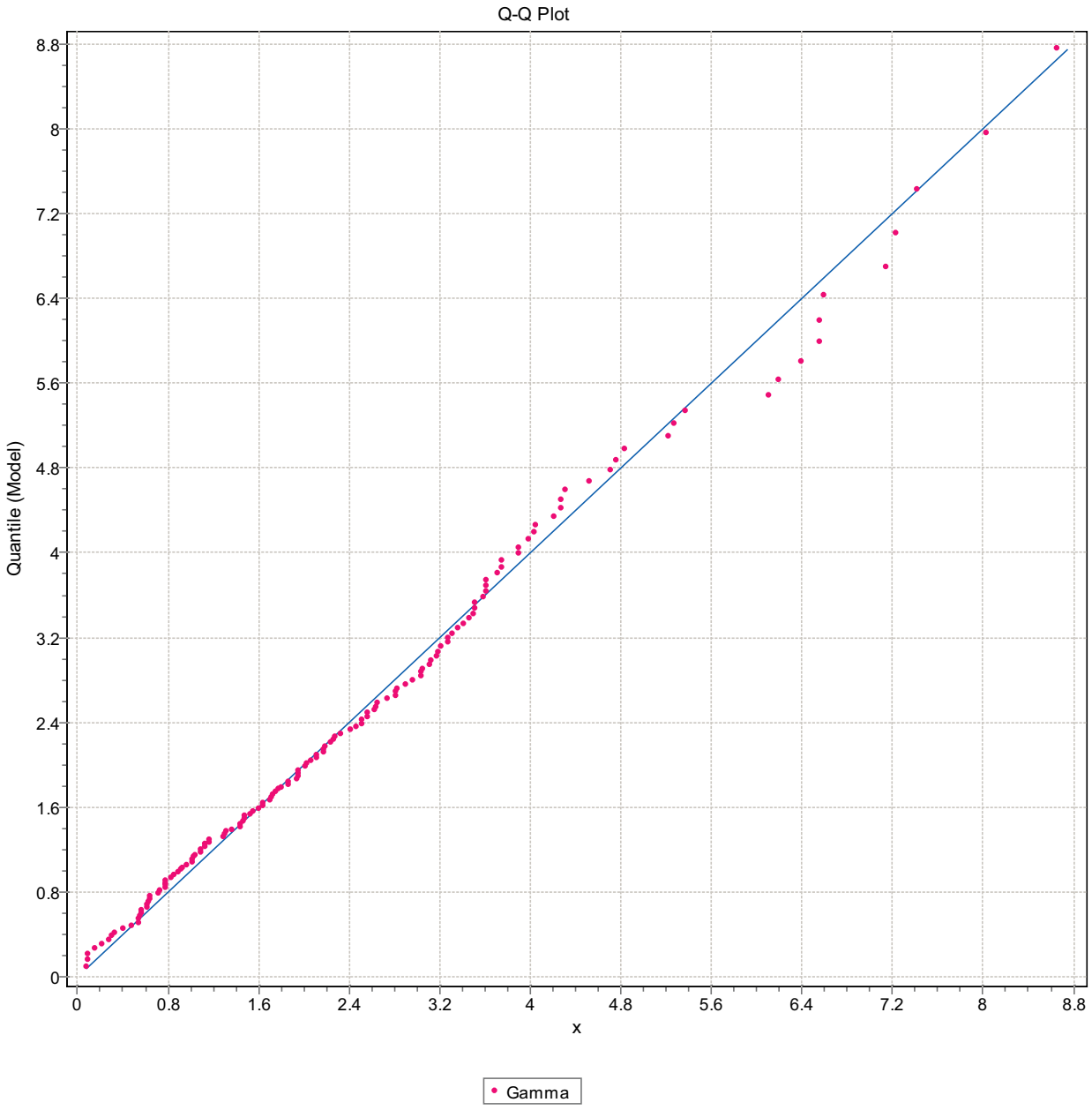

Figure F-215. *Q-Q plot, Domain FSM_C, 15 m bins, Gamma Distribution.*

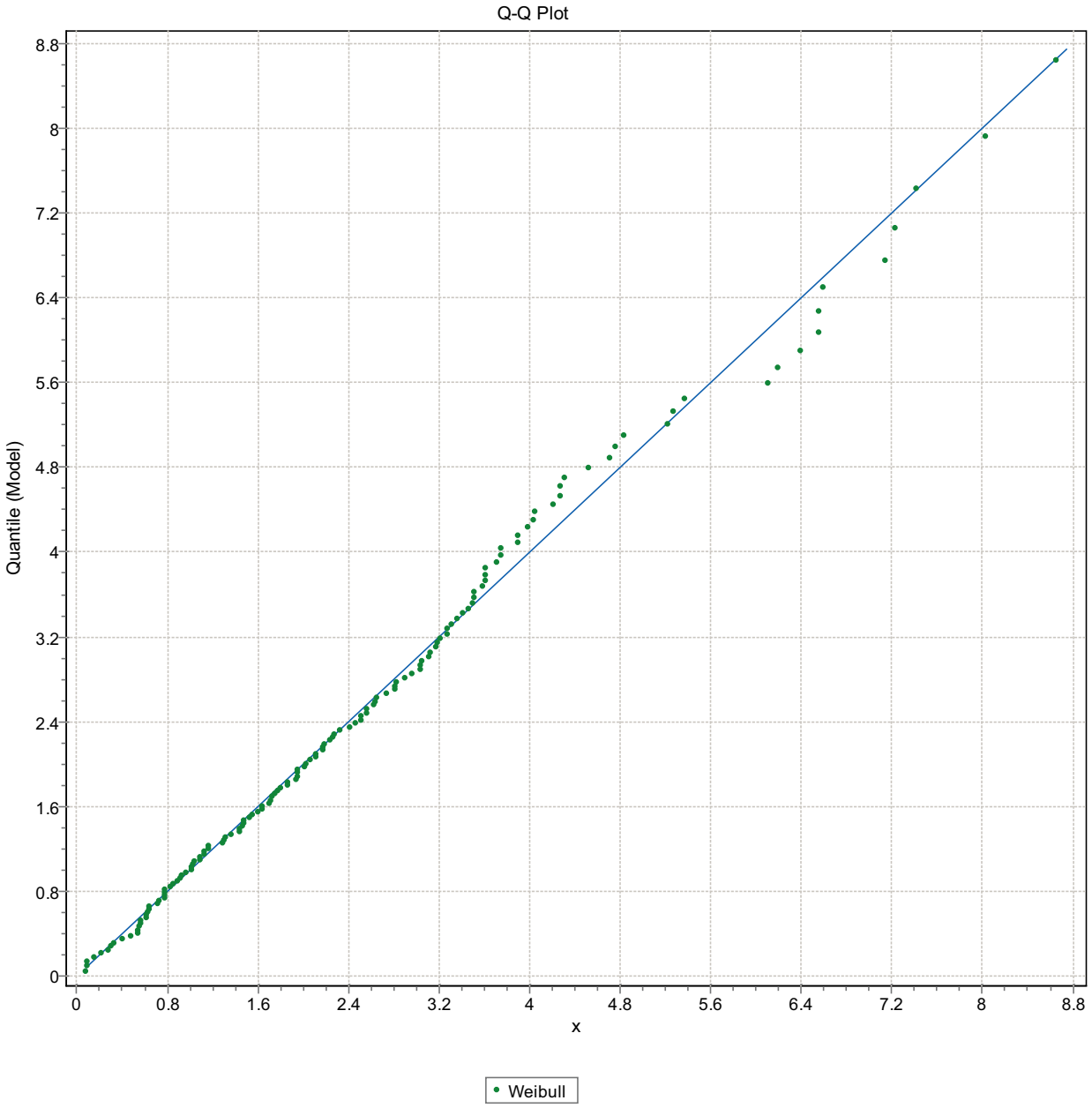

Figure F-216. *Q-Q plot, Domain FSM_C, 15 m bins, Weibull Distribution.*

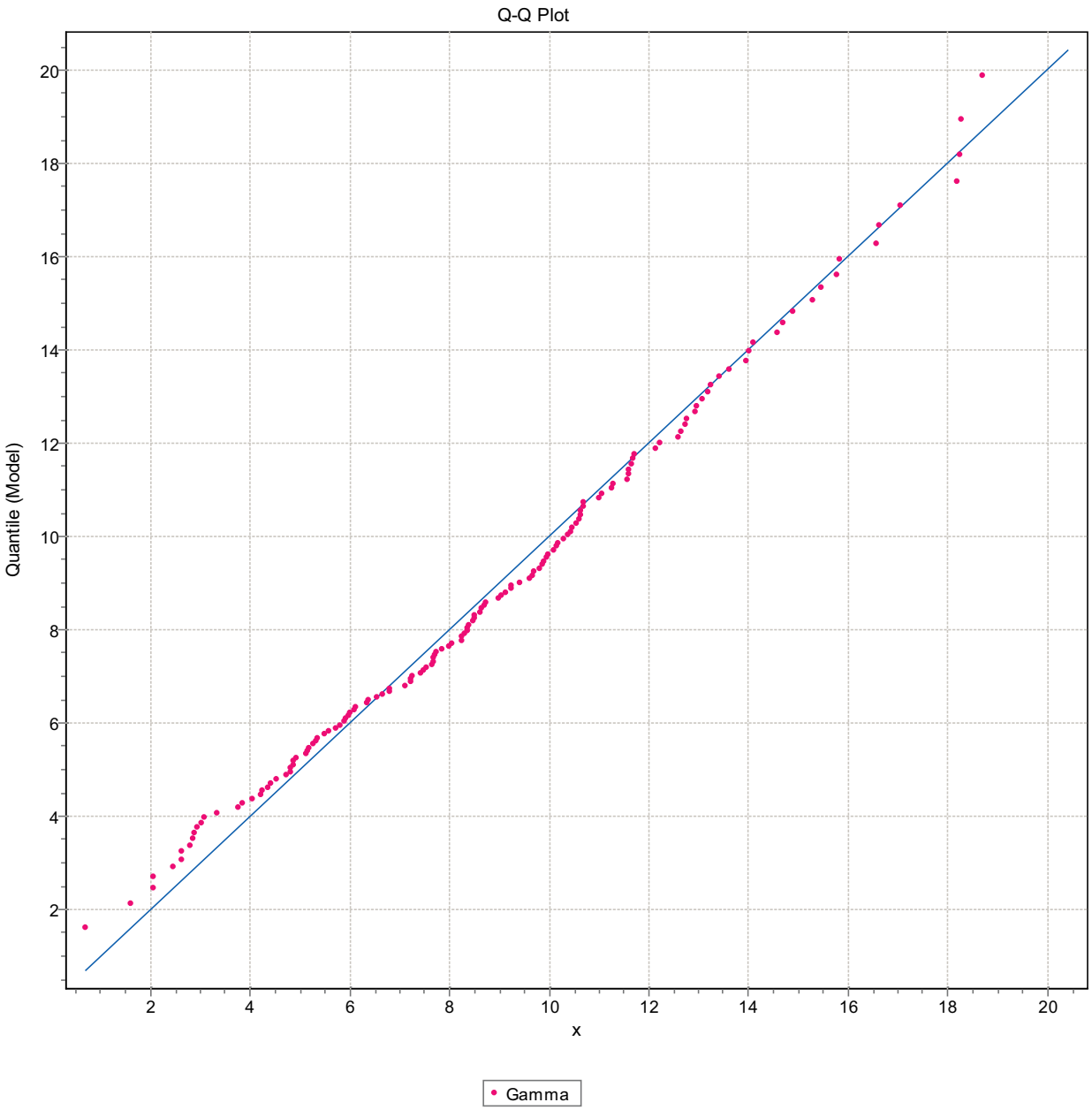

Figure F-217. *Q-Q plot, Domain FSM_C, 15 m bins, Gamma Distribution.*

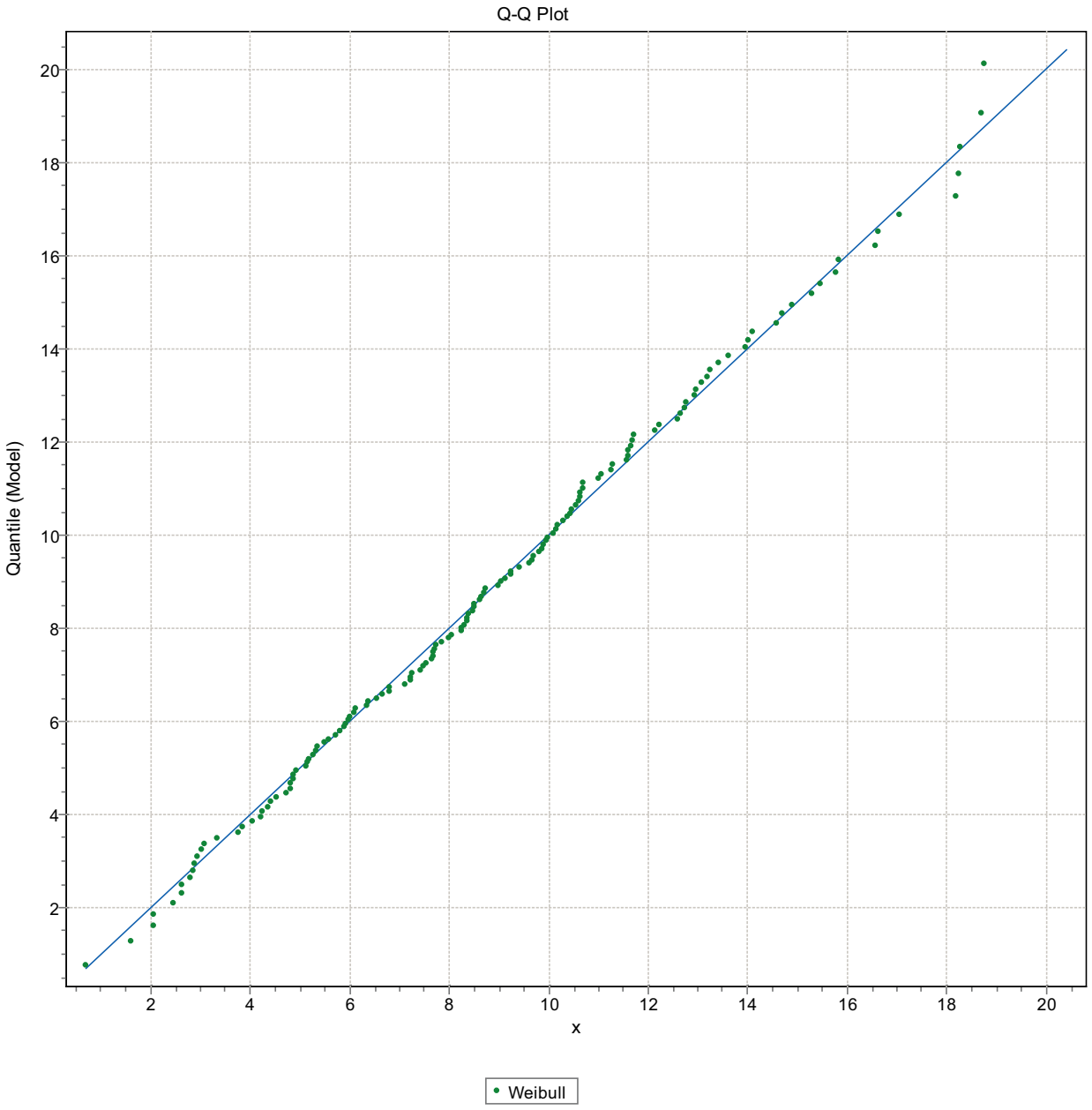

Figure F-218. *Q-Q plot, Domain FSM_C, 15 m bins, Weibull Distribution.*

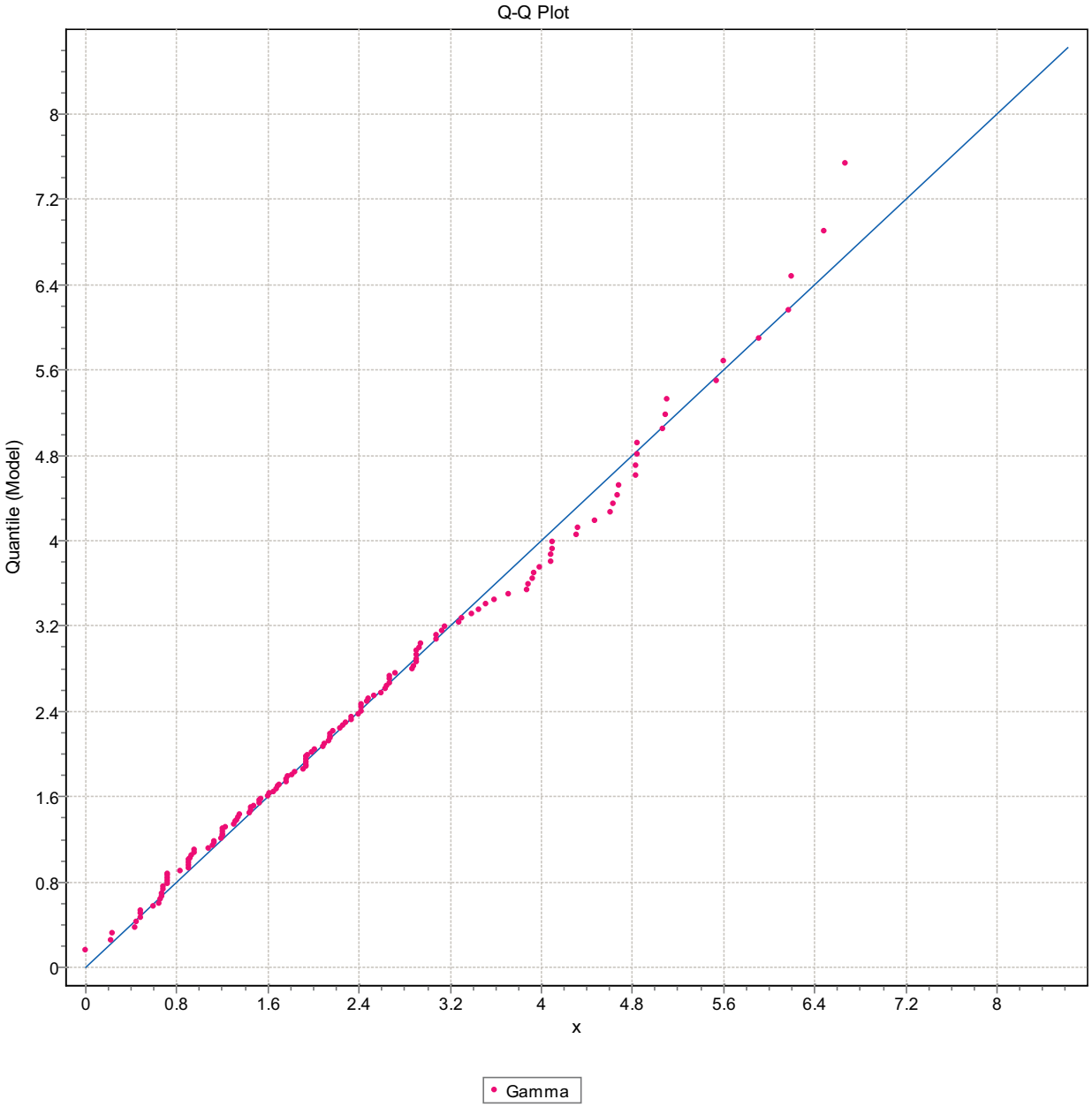

Figure F-219. *Q-Q plot, Domain FSM_C, 15 m bins, Gamma Distribution.*

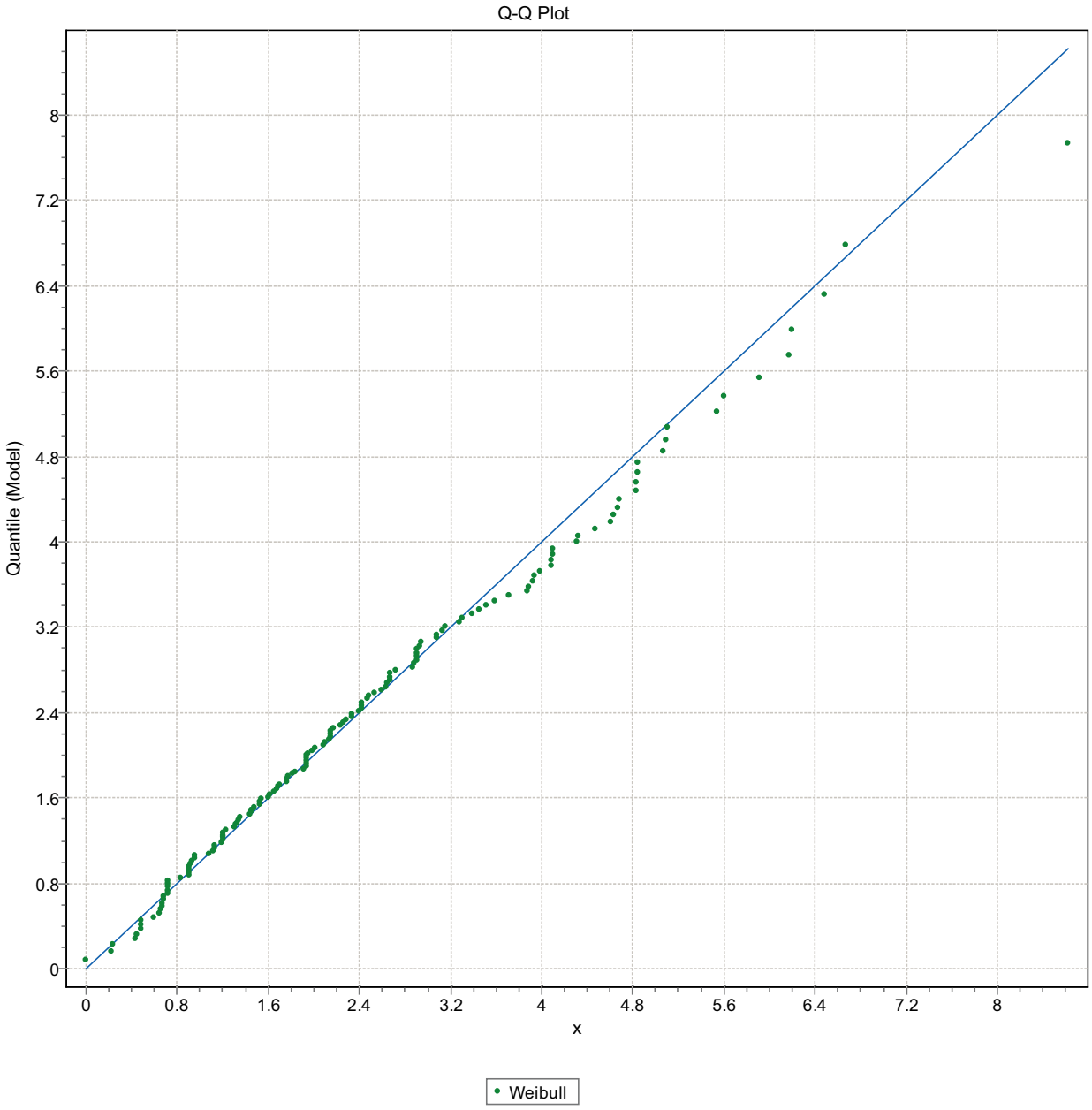

Figure F-220. *Q-Q plot, Domain FSM_C, 15 m bins, Weibull Distribution.*

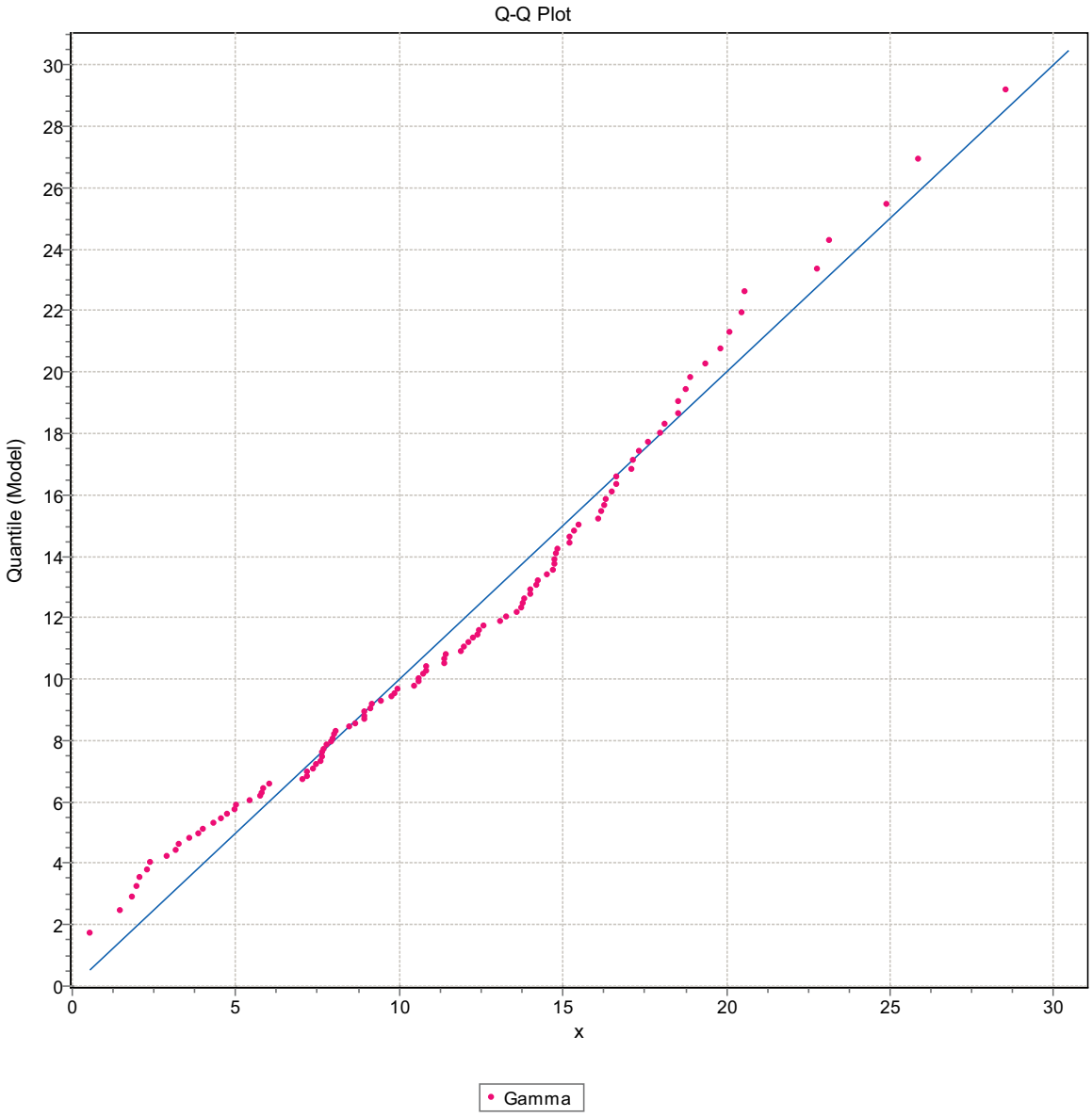

Figure F-221. *Q-Q plot, Domain FSM_EW007, 15 m bins, Gamma Distribution.*

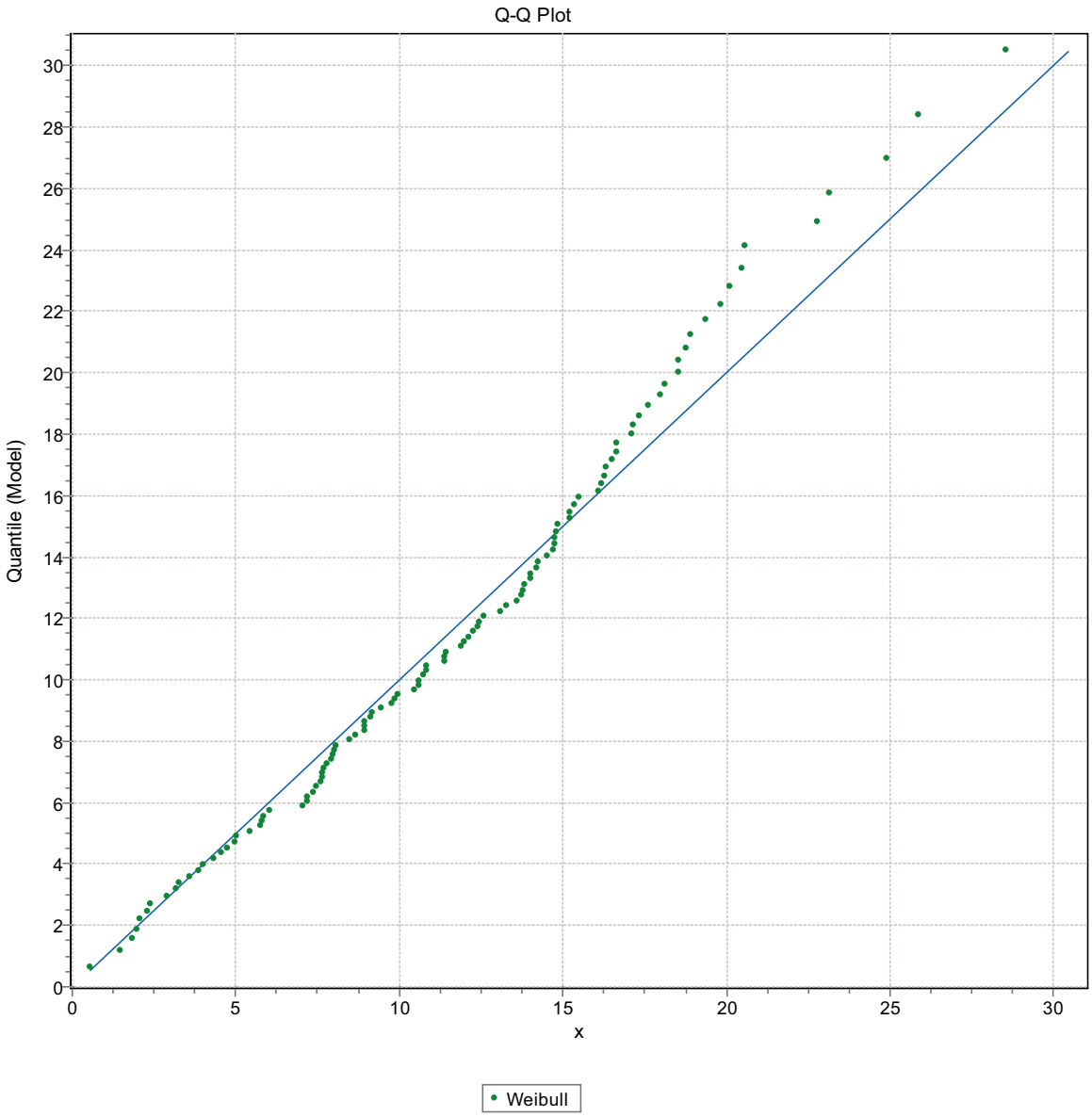

Figure F-222. *Q-Q plot, Domain FSM_EW007, 15 m bins, Weibull Distribution.*

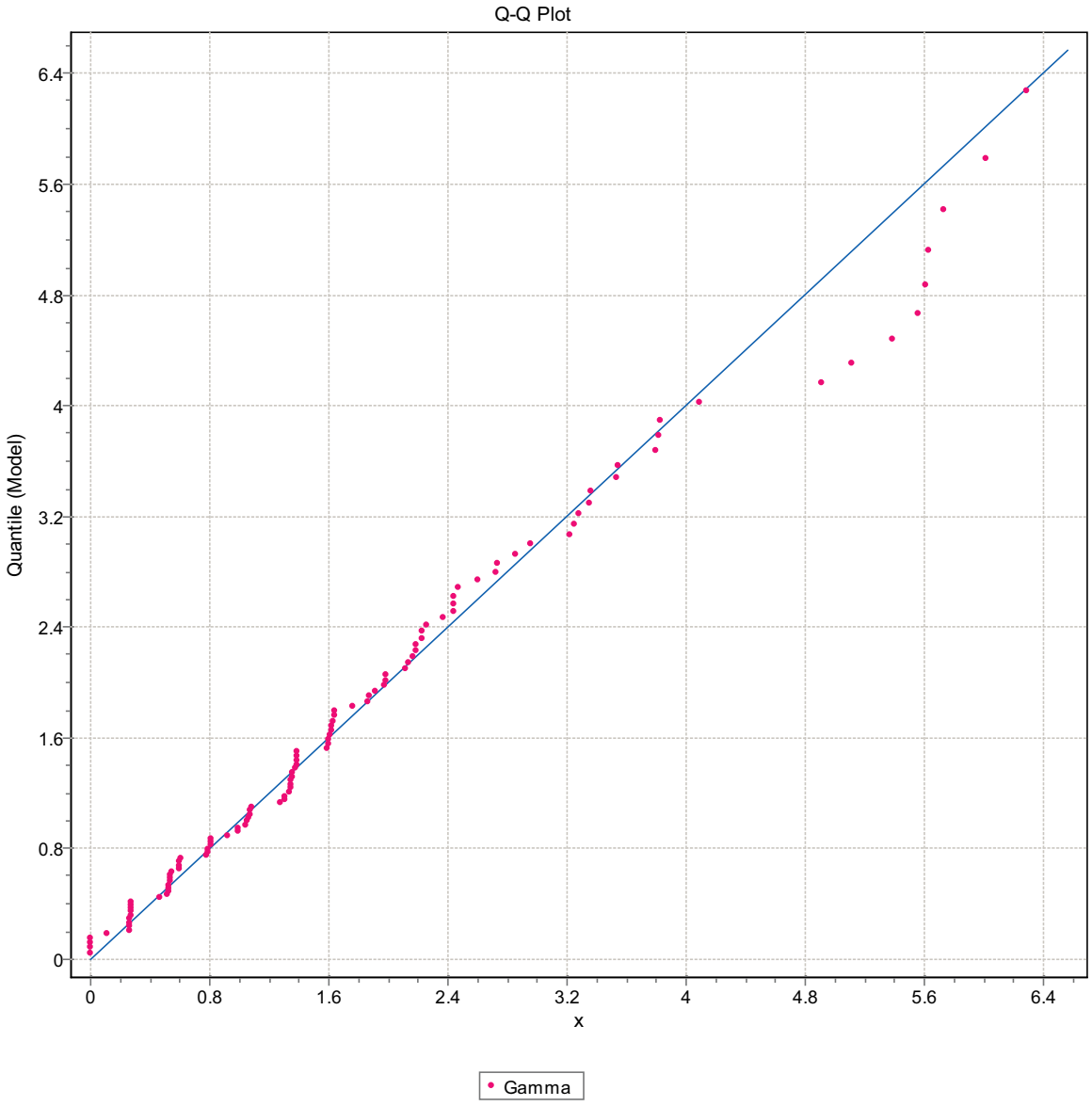

Figure F-223. *Q-Q plot, Domain FSM_EW007, 15 m bins, Gamma Distribution.*

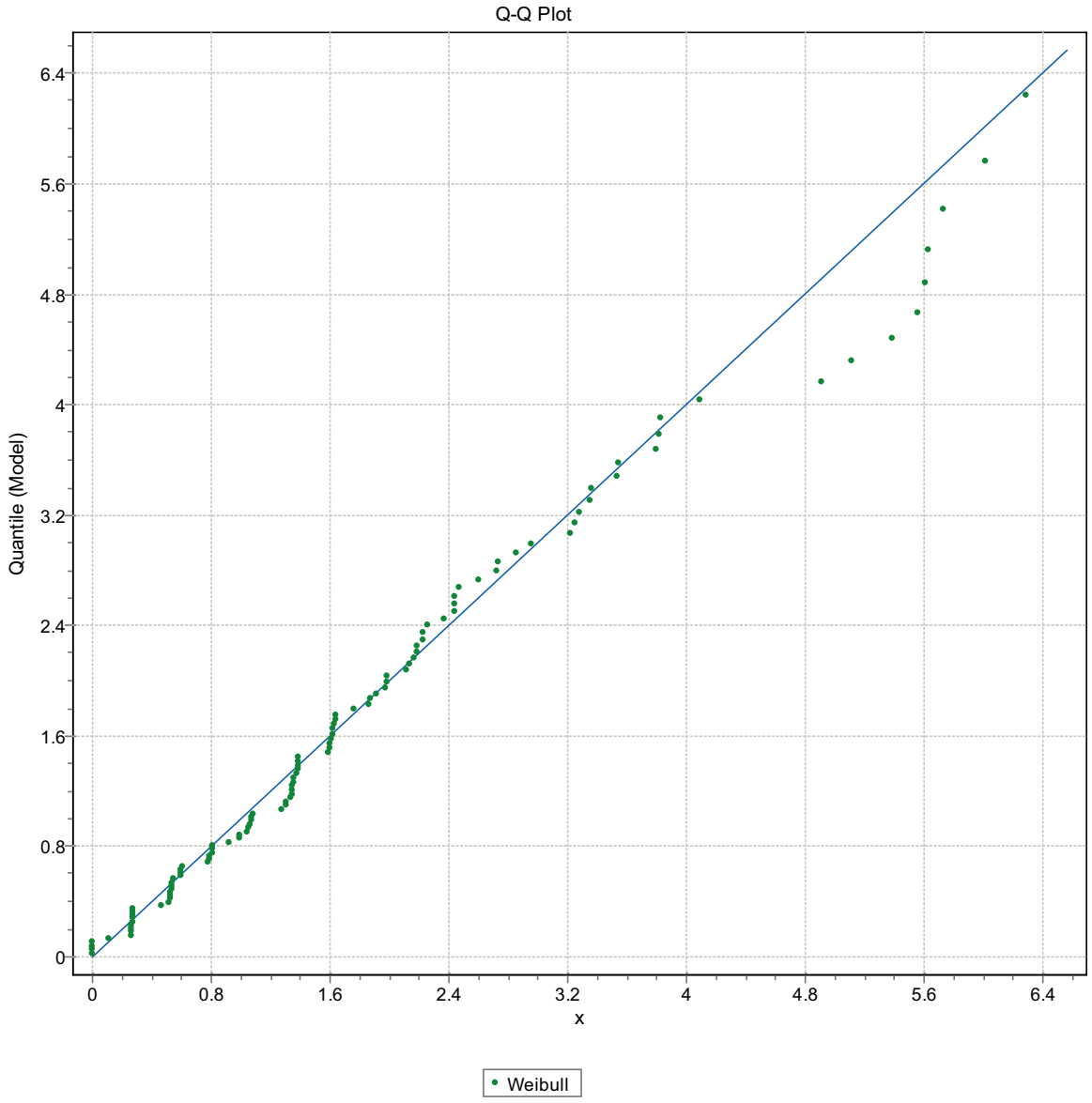

Figure F-224. *Q-Q plot, Domain FSM_EW007, 15 m bins, Weibull Distribution.*

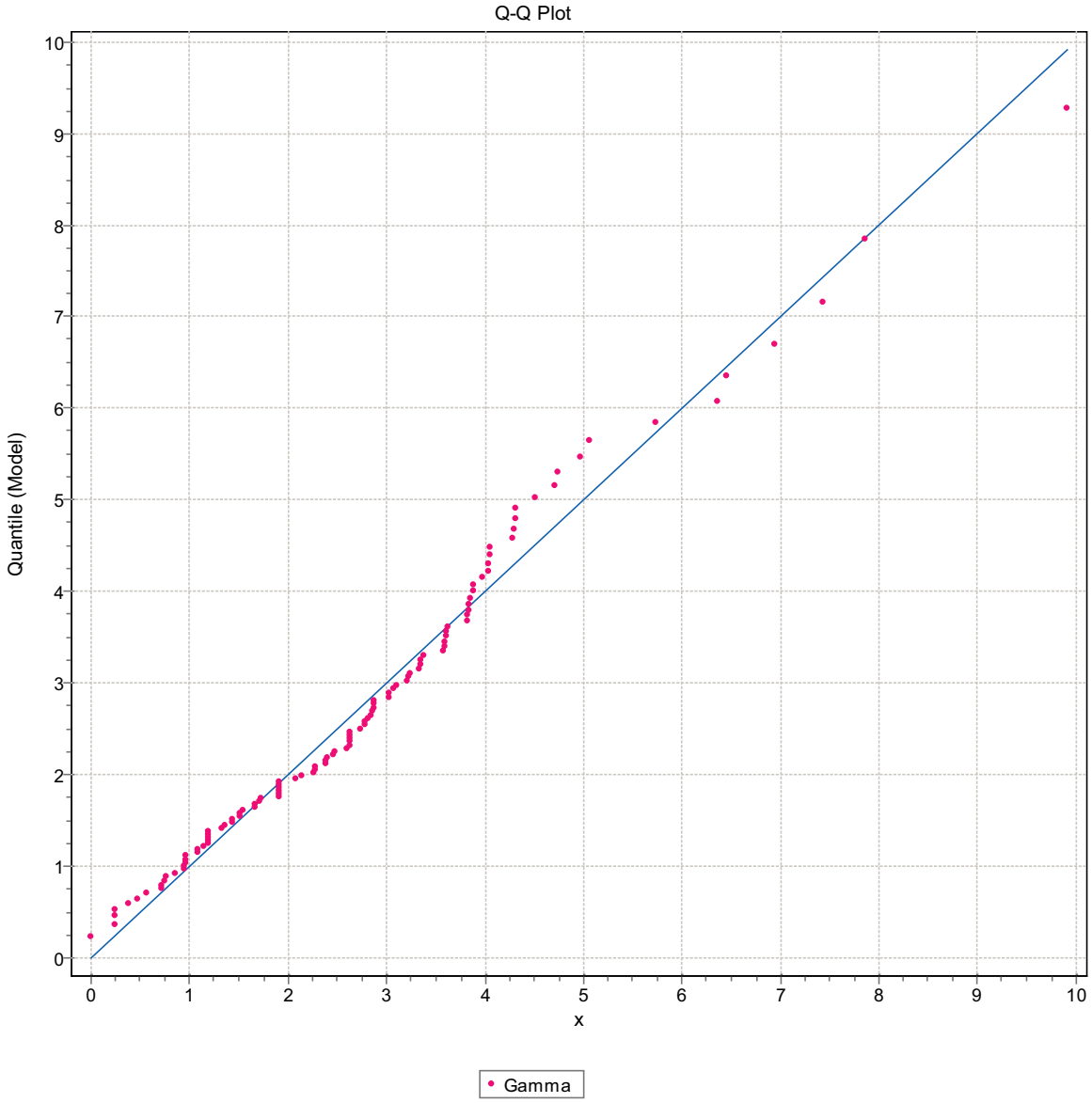

Figure F-225. *Q-Q plot, Domain FSM_EW007, 15 m bins, Gamma Distribution.*

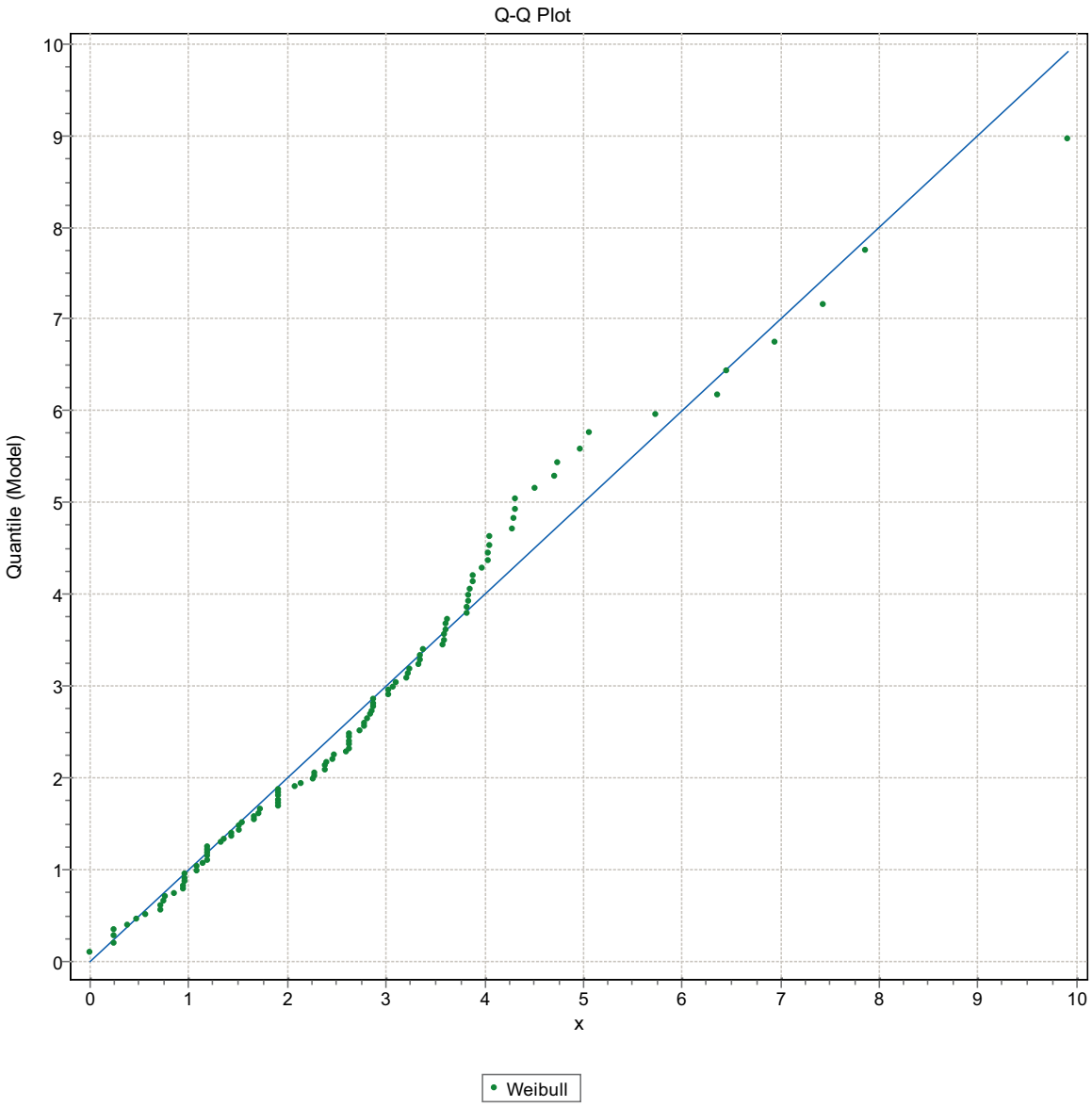

Figure F-226. *Q-Q plot, Domain FSM_EW007, 15 m bins, Weibull Distribution.*

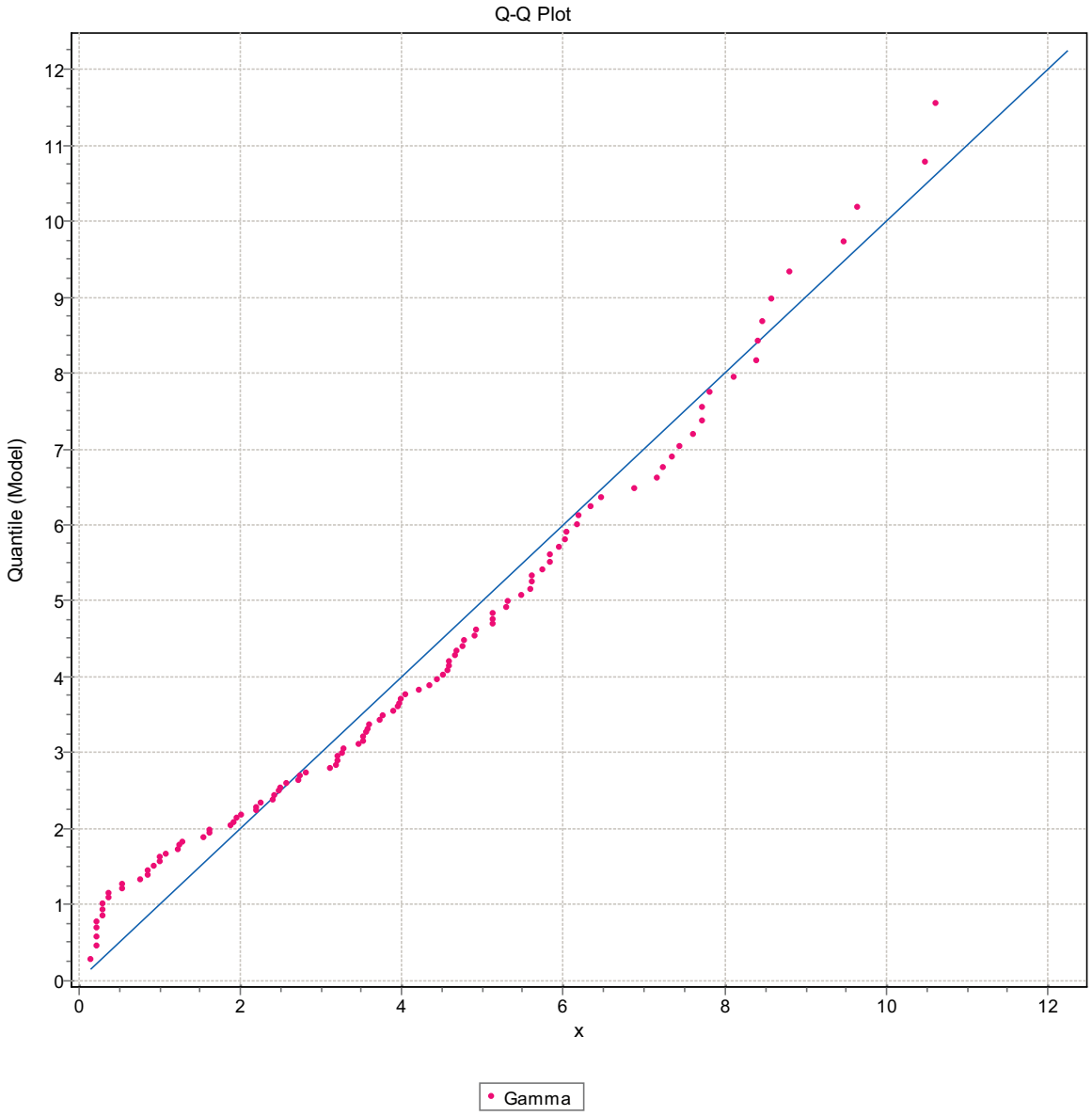

Figure F-227. *Q-Q plot, Domain FSM_EW007, 15 m bins, Gamma Distribution.*

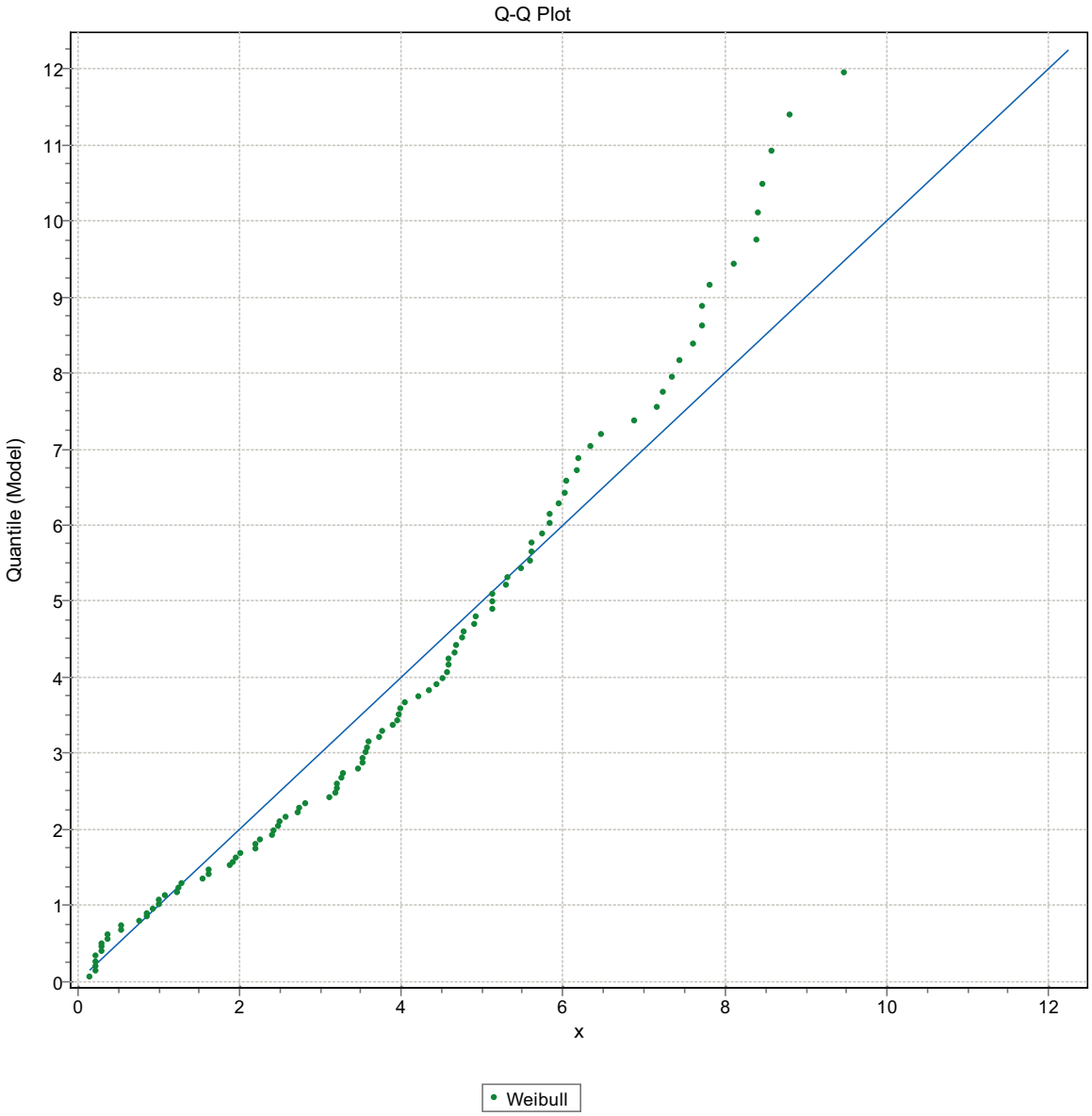

Figure F-228. *Q-Q plot, Domain FSM_EW007, 15 m bins, Weibull Distribution.*

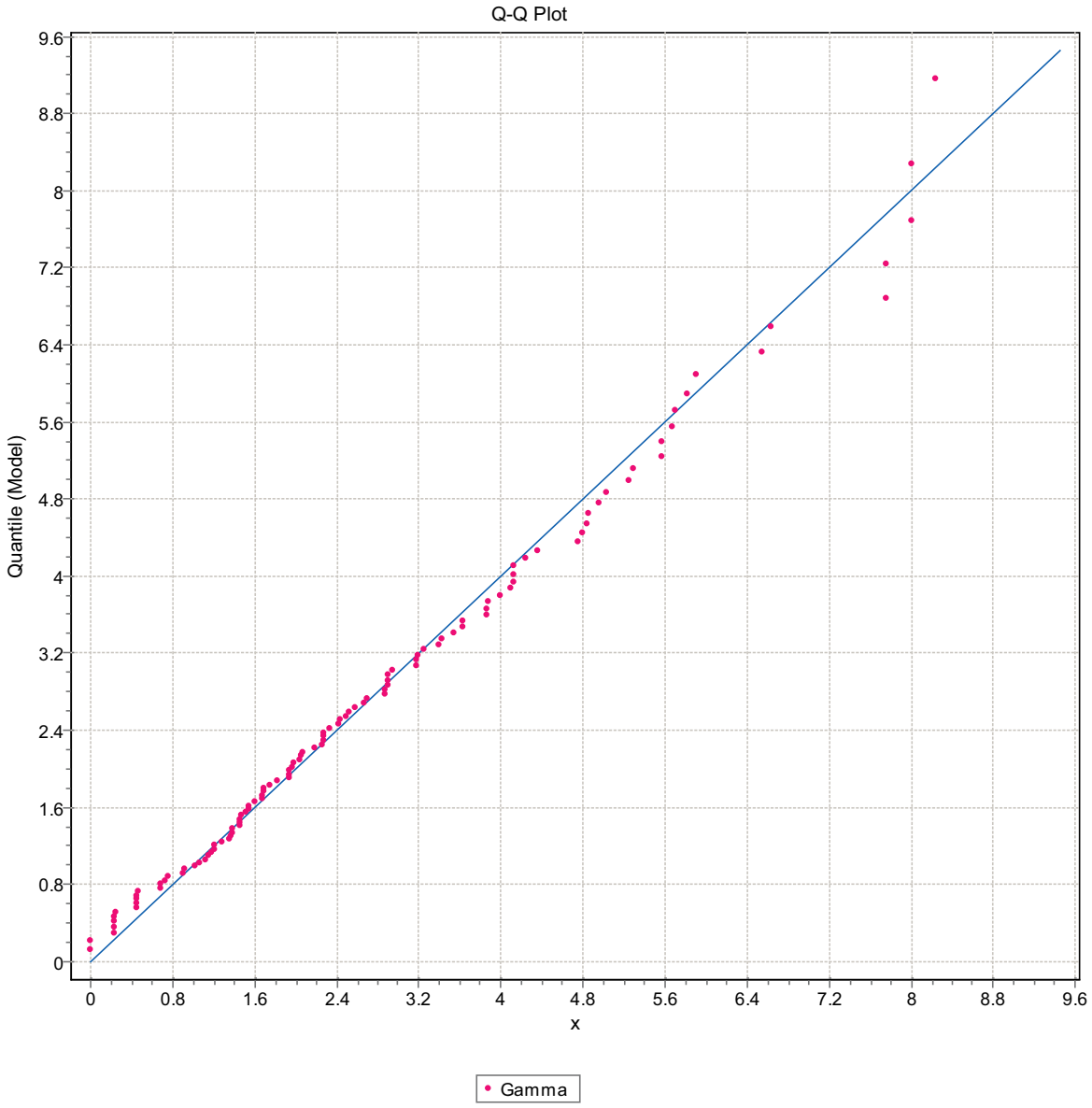

Figure F-229. *Q-Q plot, Domain FSM_EW007, 15 m bins, Gamma Distribution.*

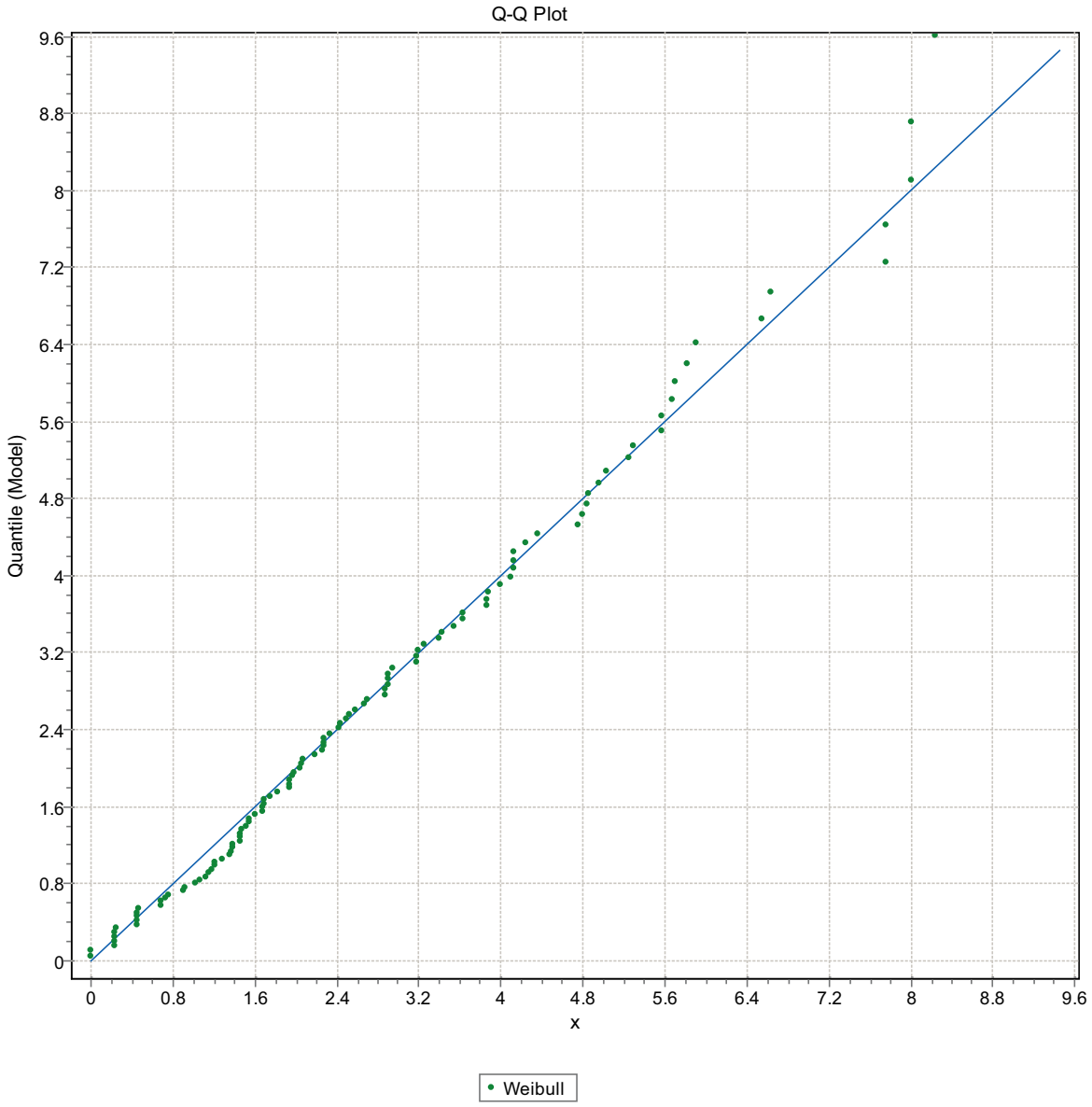

Figure F-230. *Q-Q plot, Domain FSM_EW007, 15 m bins, Weibull Distribution.*

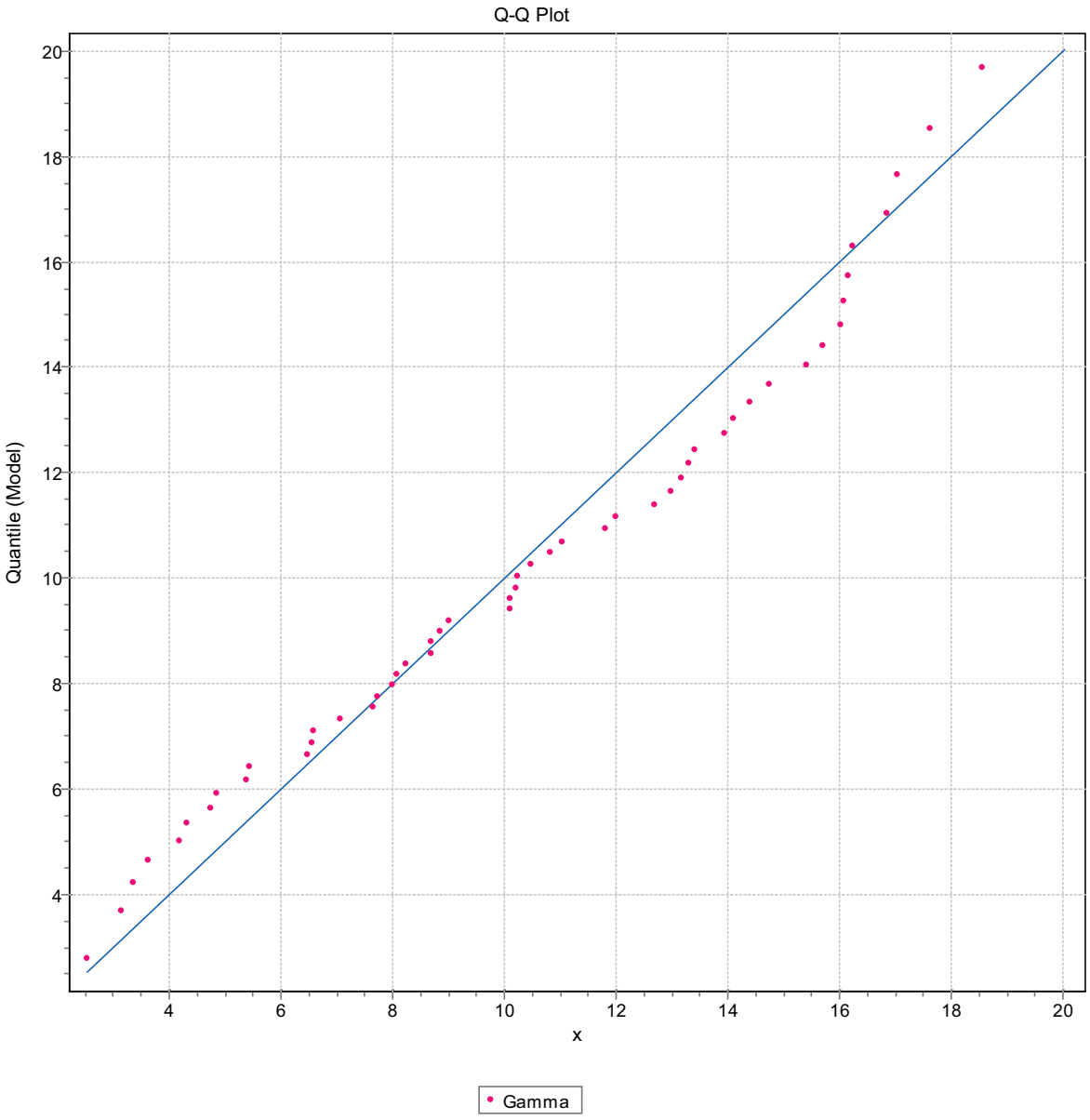

Figure F-231. *Q-Q plot, Domain FSM_NE005, 15 m bins, Gamma Distribution.*

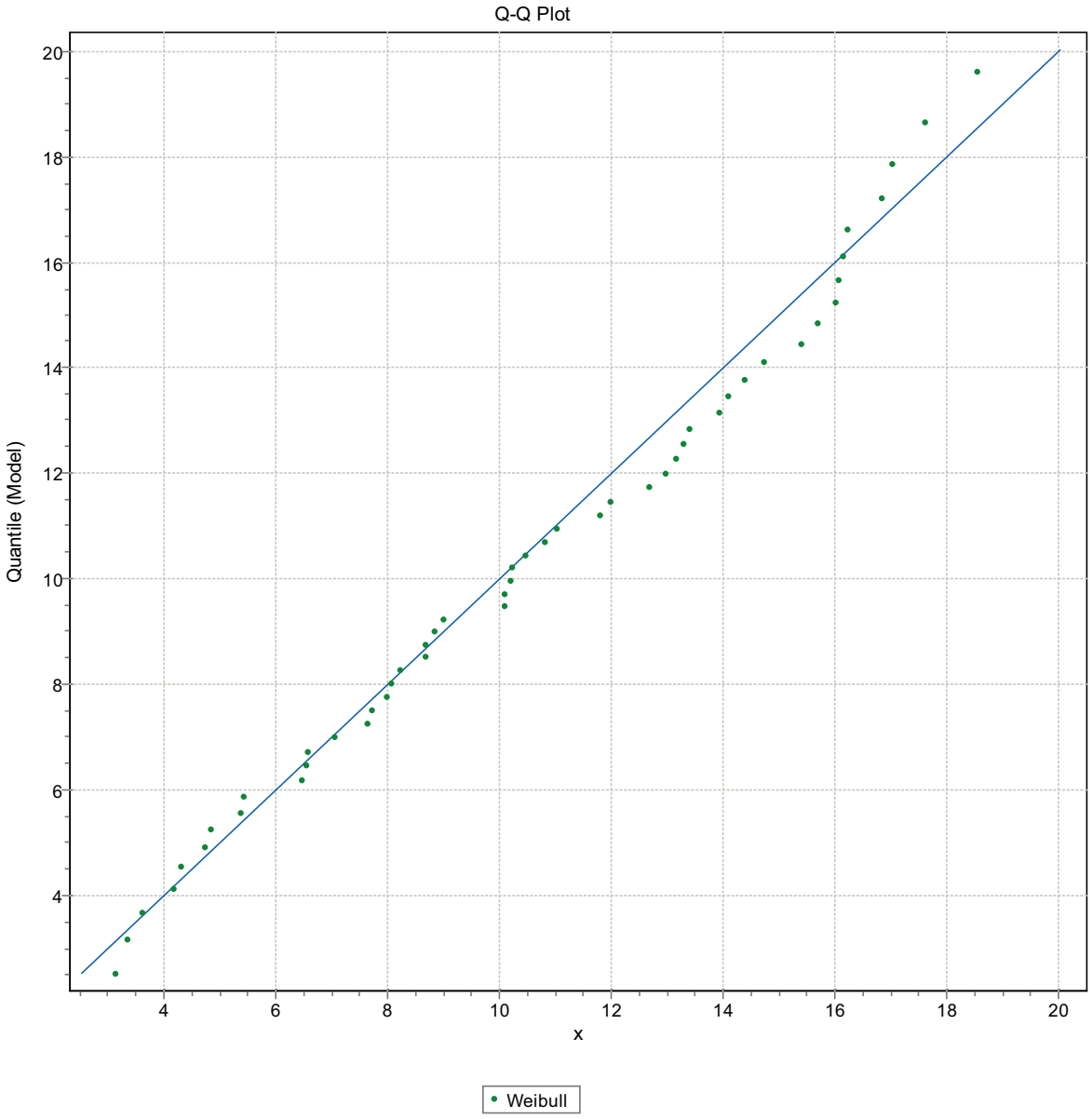

Figure F-232. *Q-Q plot, Domain FSM_NE005, 15 m bins, Weibull Distribution.*

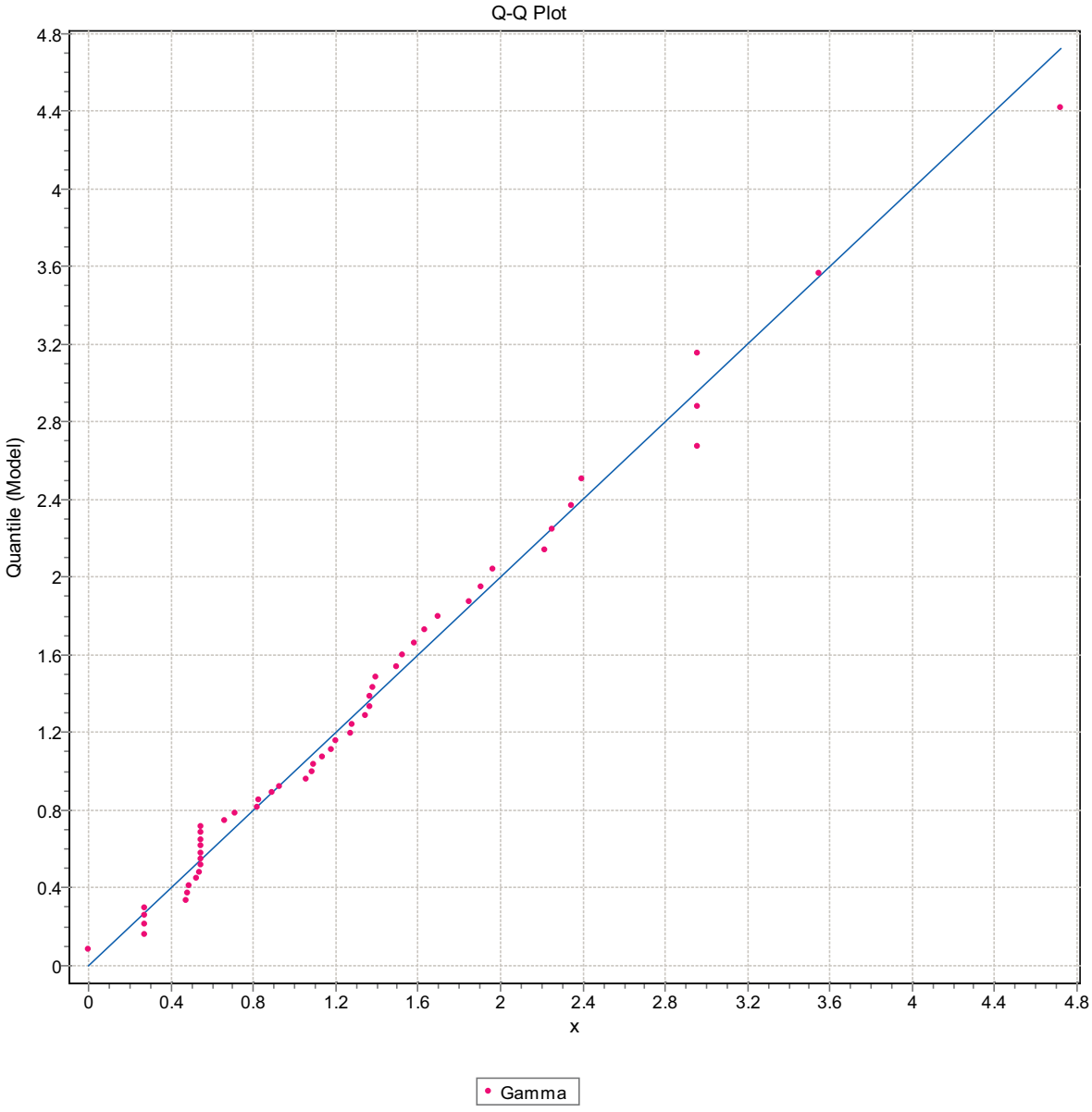

Figure F-233. *Q-Q plot, Domain FSM_NE005, 15 m bins, Gamma Distribution.*

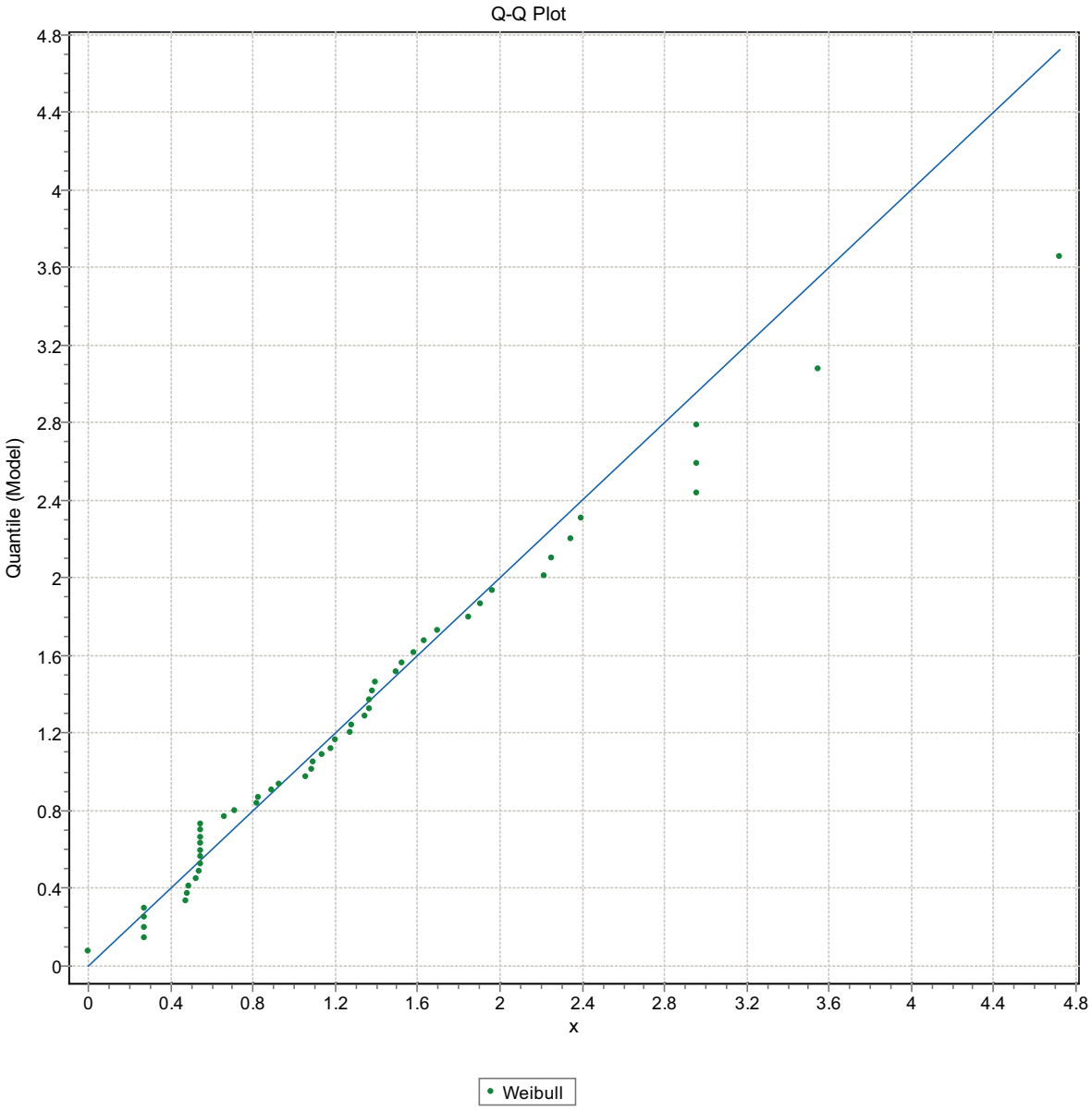

Figure F-234. *Q-Q plot, Domain FSM_NE005, 15 m bins, Weibull Distribution.*

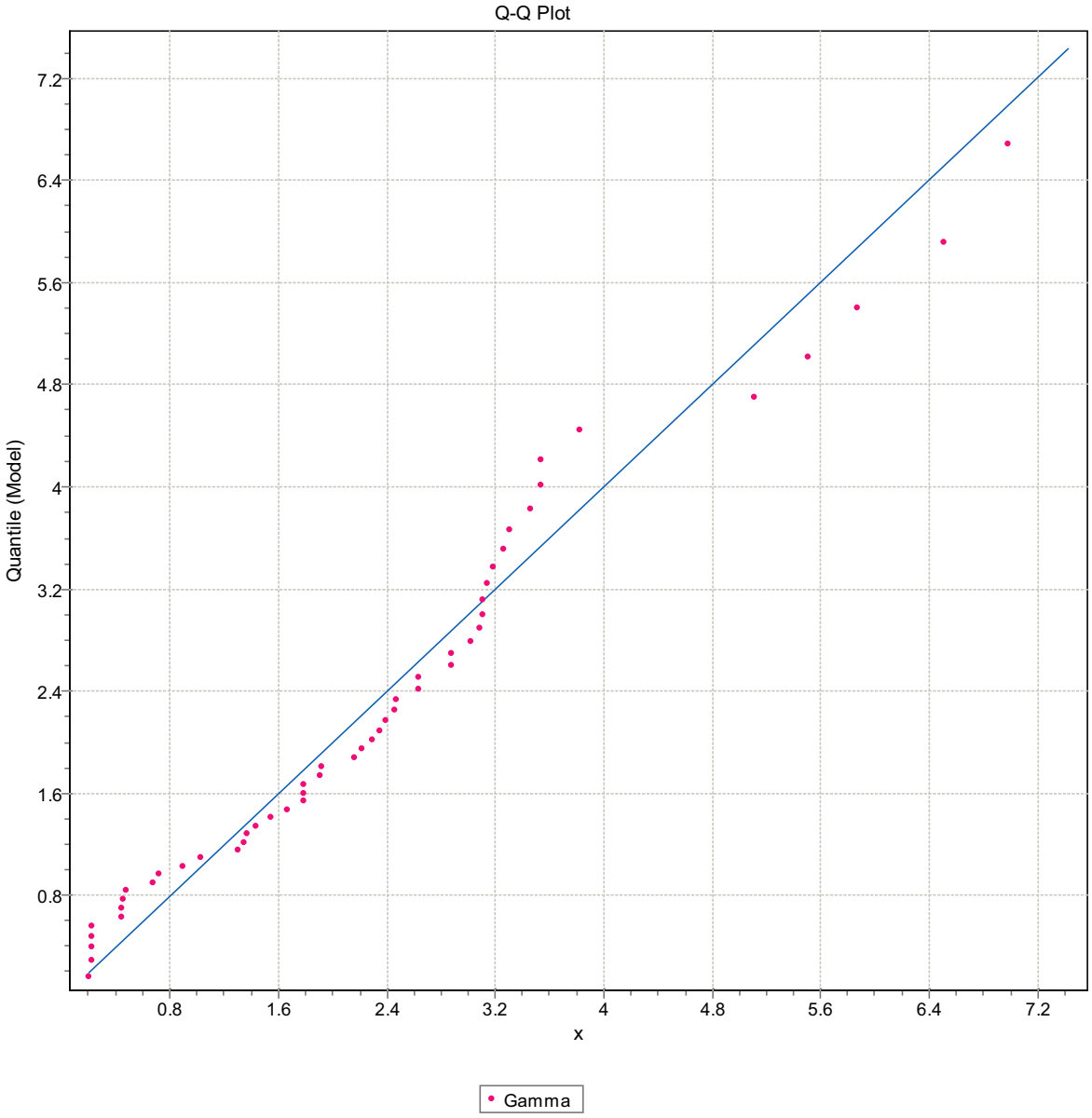

Figure F-235. *Q-Q plot, Domain FSM_NE005, 15 m bins, Gammal Distribution.*

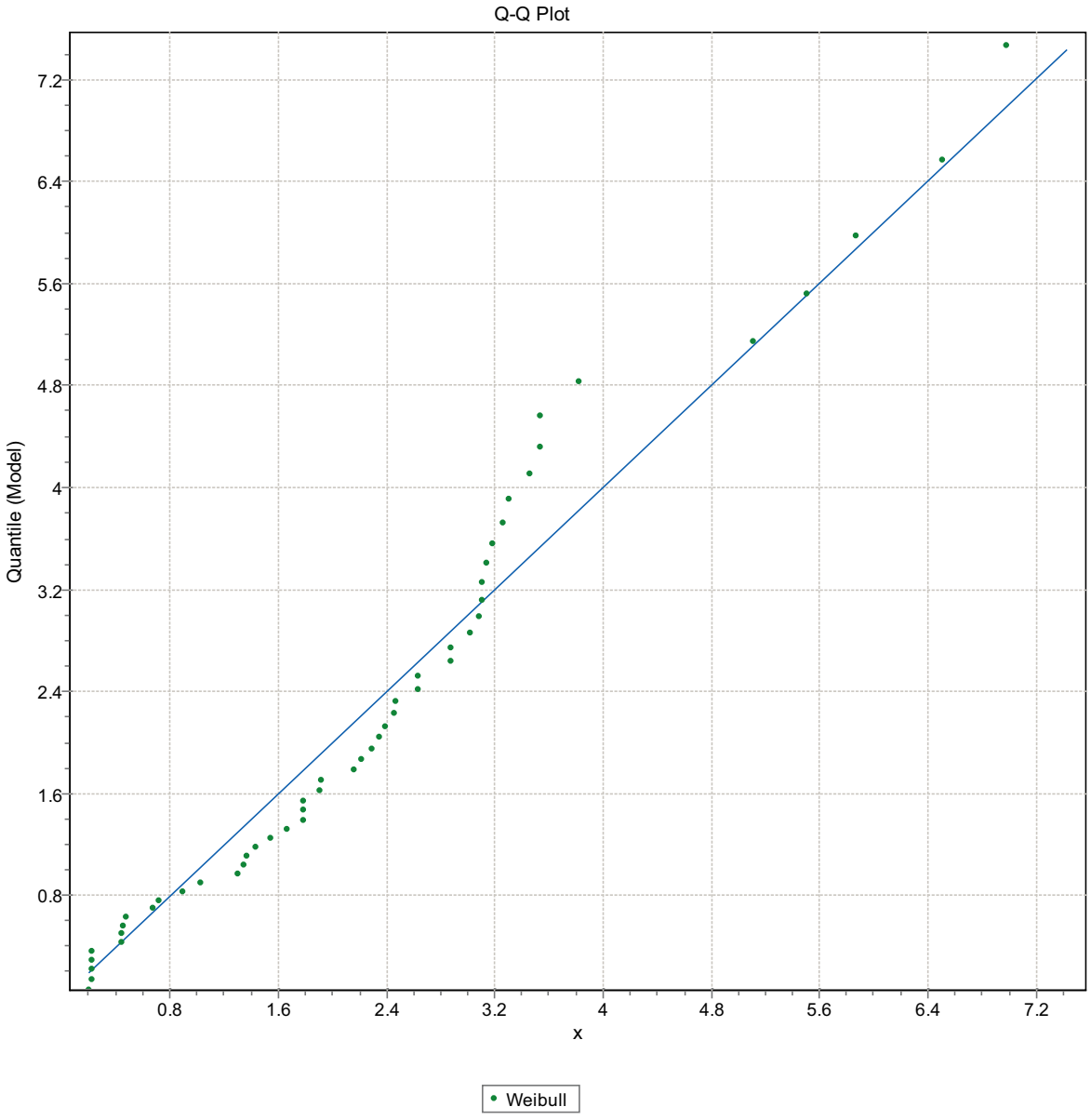

Figure F-236. *Q-Q plot, Domain FSM_NE005, 15 m bins, Weibull Distribution.*

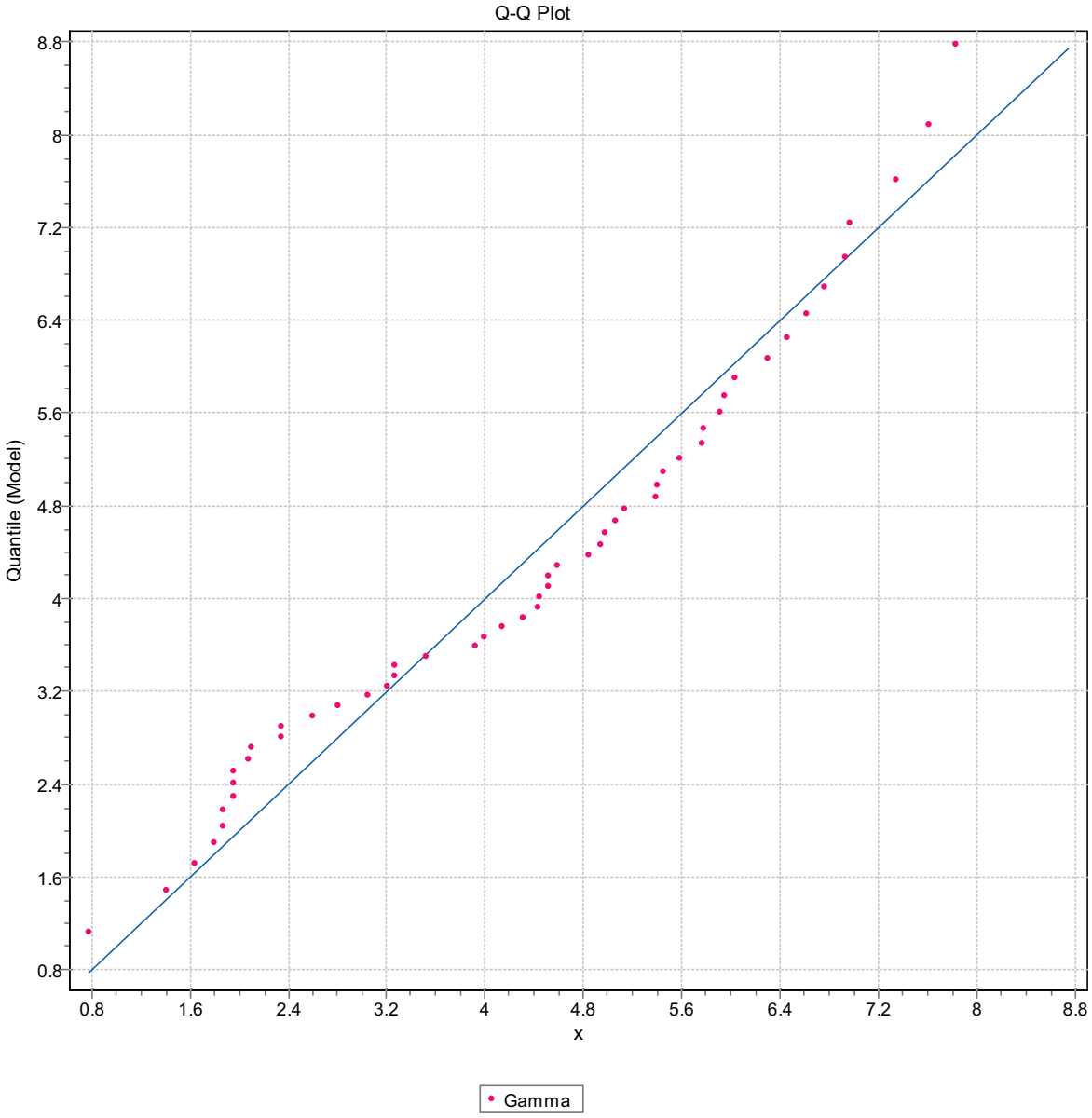

Figure F-237. *Q-Q plot, Domain FSM_NE005, 15 m bins, Gamma Distribution.*

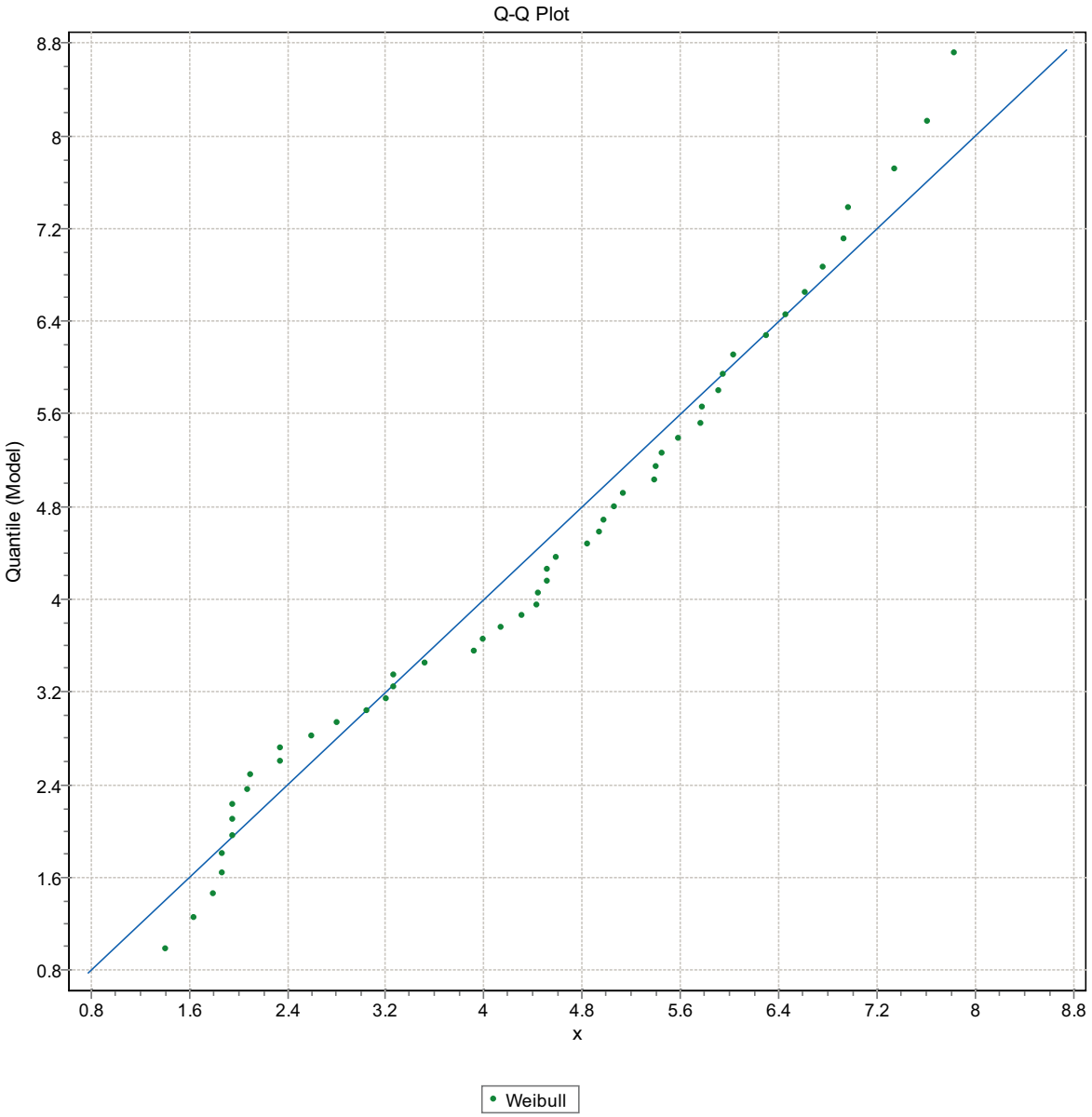

Figure F-238. *Q-Q plot, Domain FSM_NE005, 15 m bins, Weibull Distribution.*

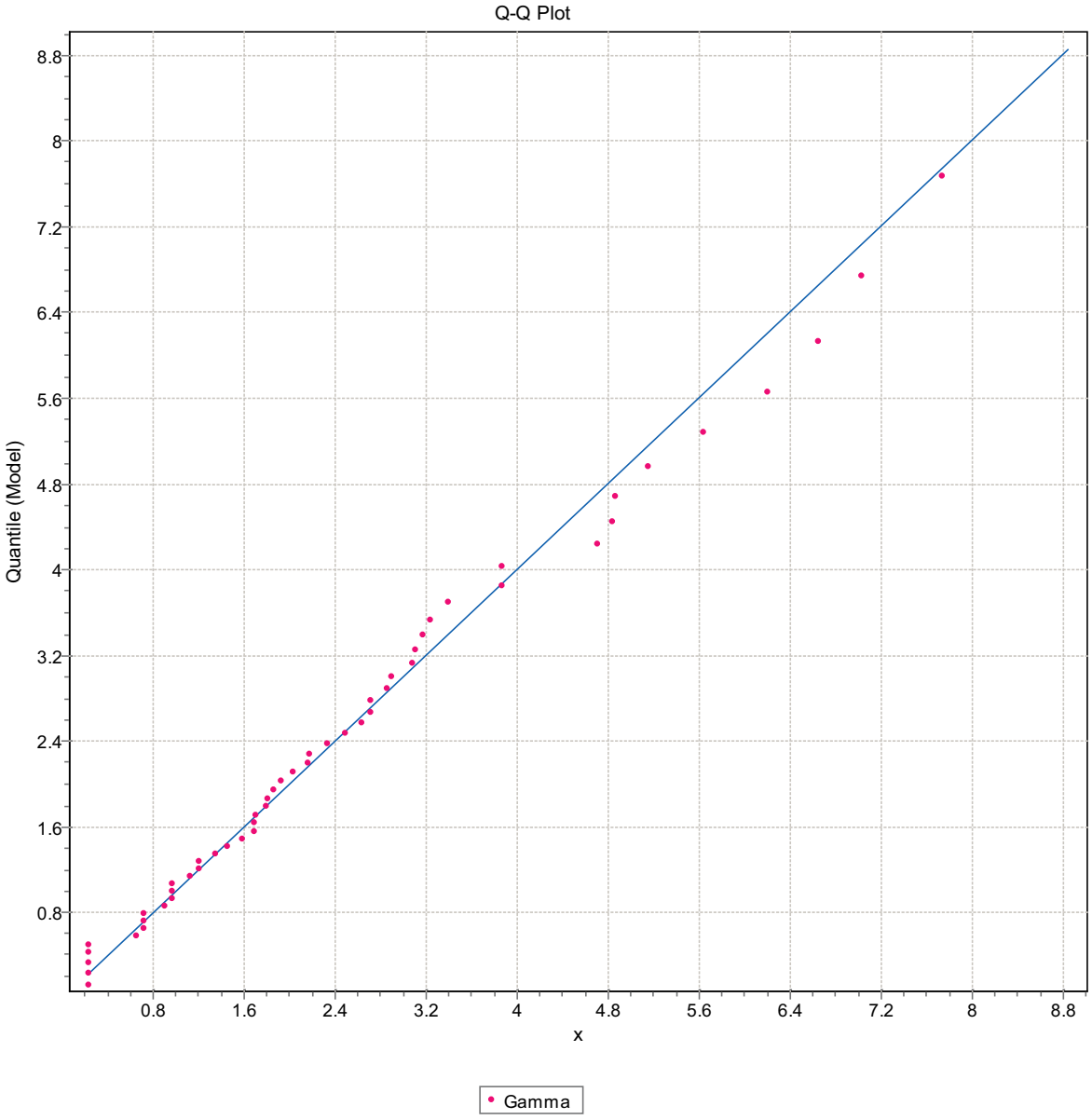

Figure F-239. *Q-Q plot, Domain FSM_NE005, 15 m bins, Gamma Distribution.*

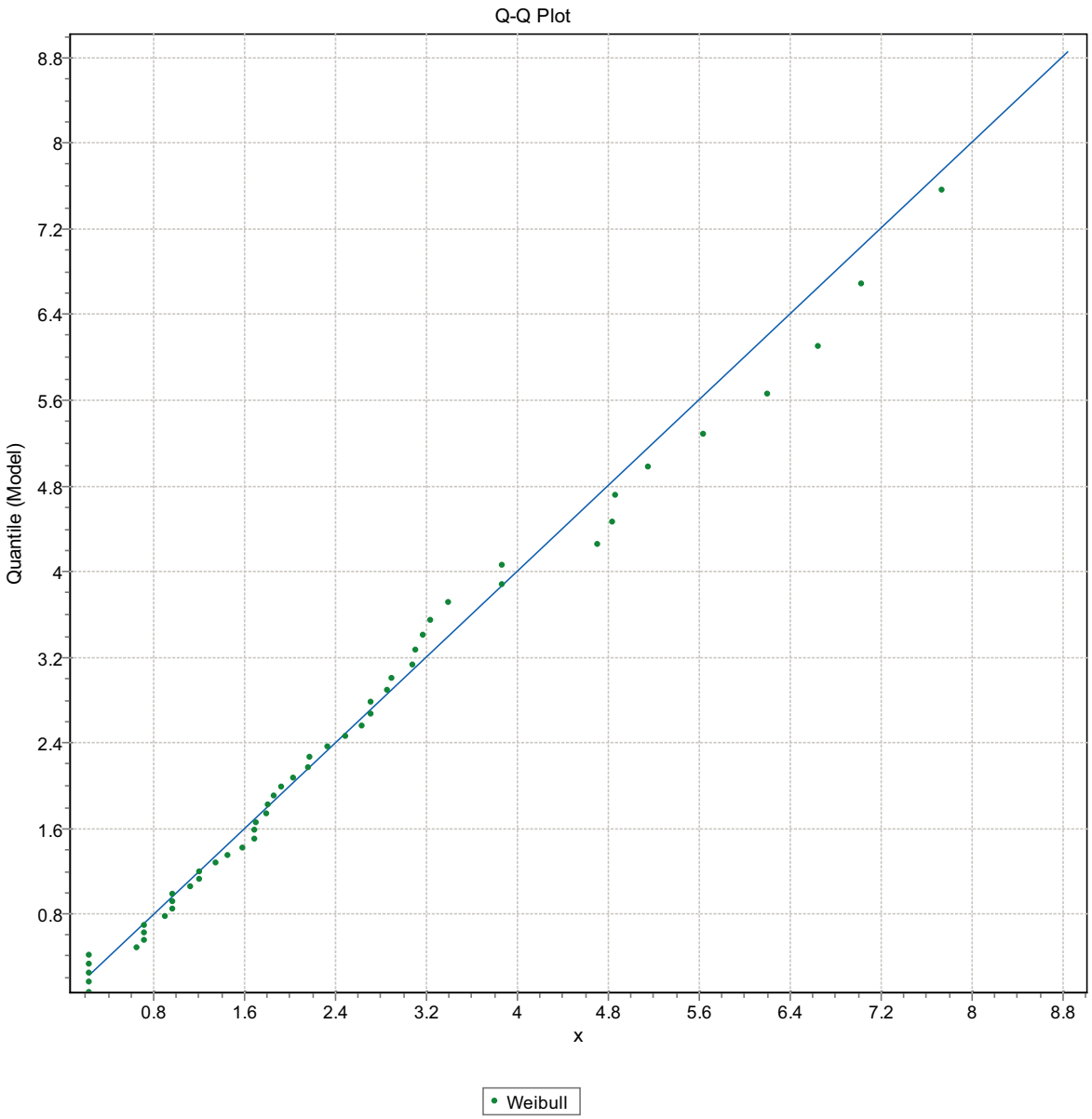

Figure F-240. *Q-Q plot, Domain FSM_NE005, 15 m bins, Weibull Distribution.*

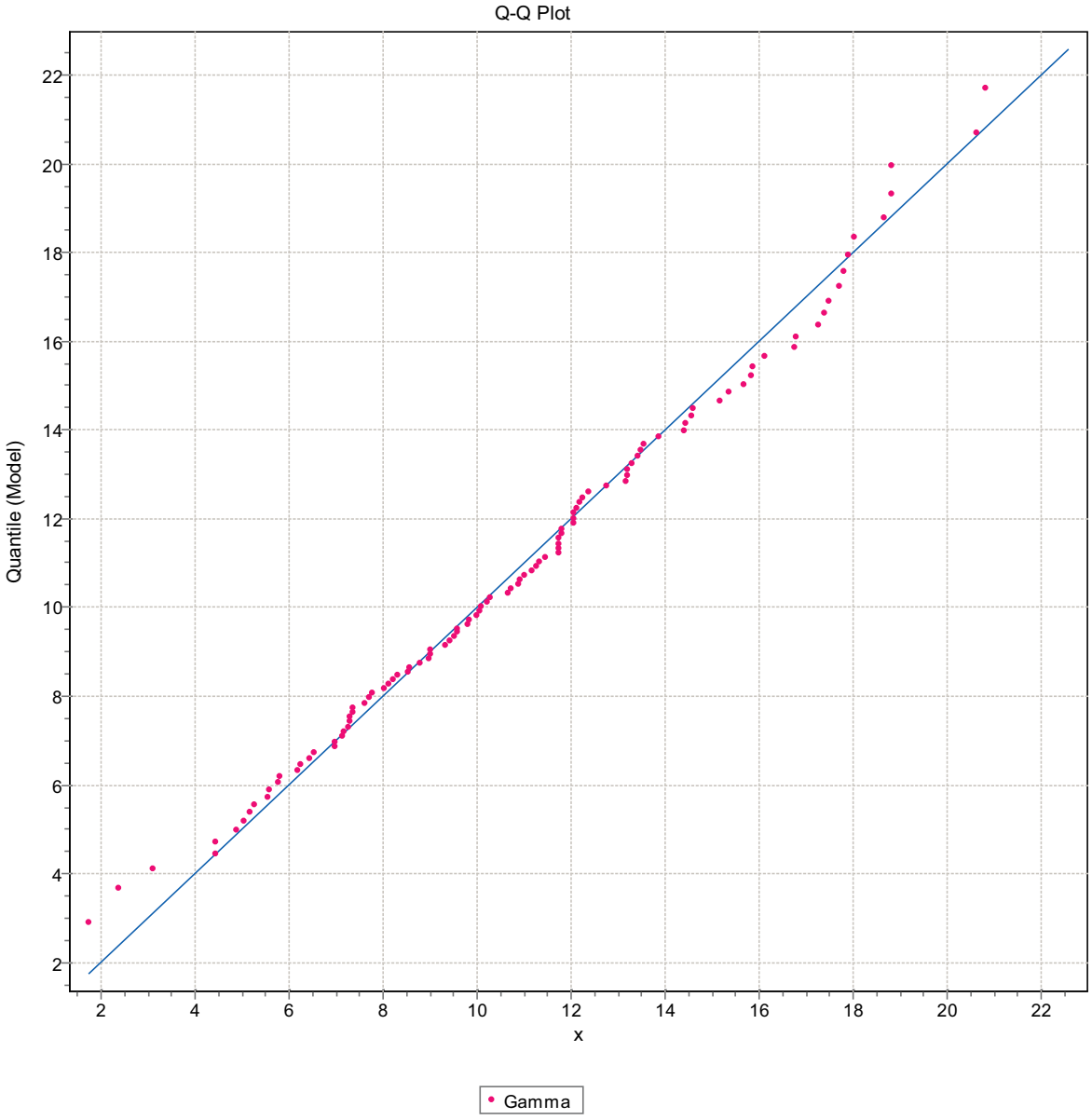

Figure F-241. *Q-Q plot, Domain FSM_N, 15 m bins, Gamma Distribution.*

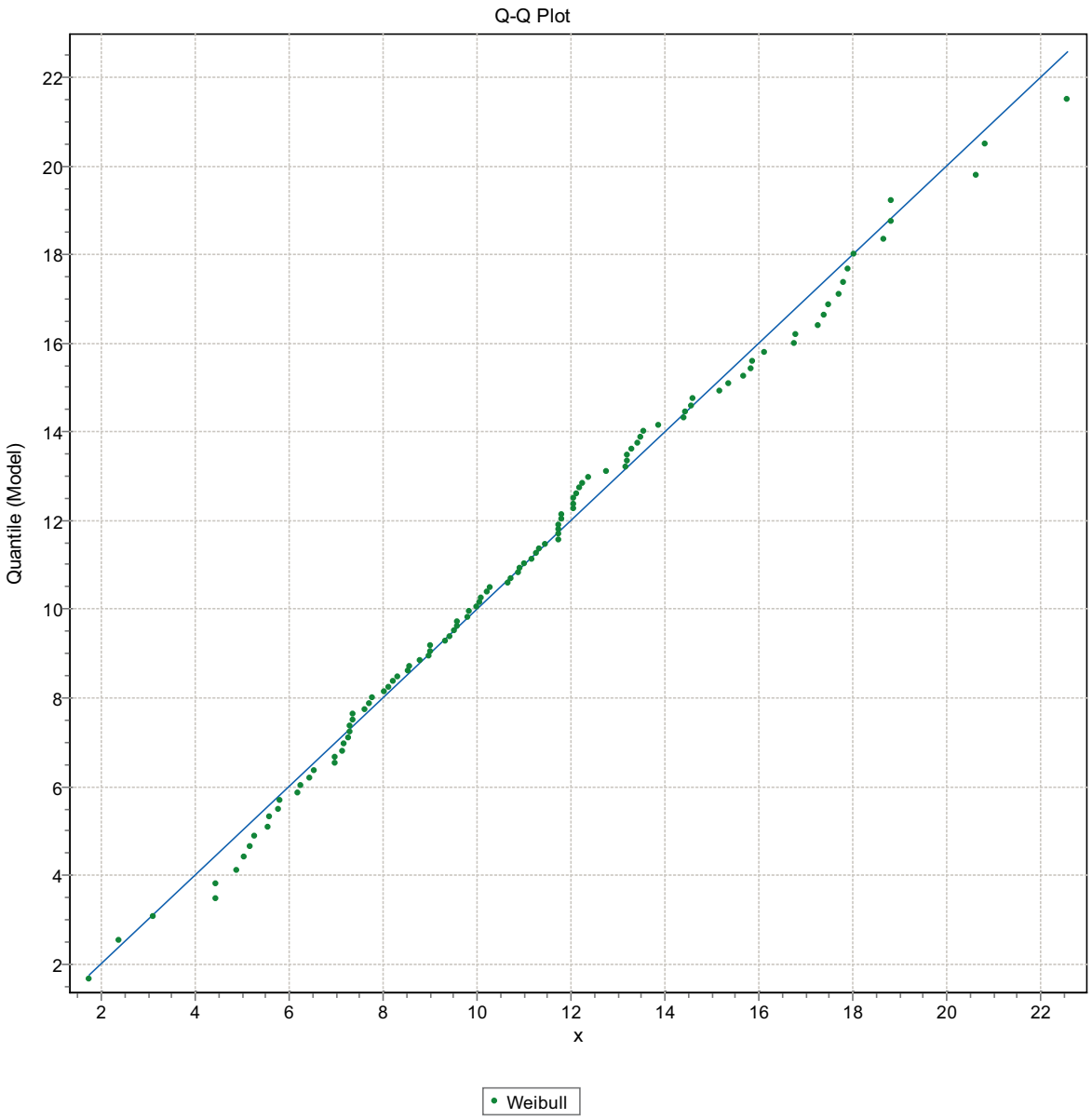

Figure F-242. *Q-Q plot, Domain FSM_N, 15 m bins, Weibull Distribution.*

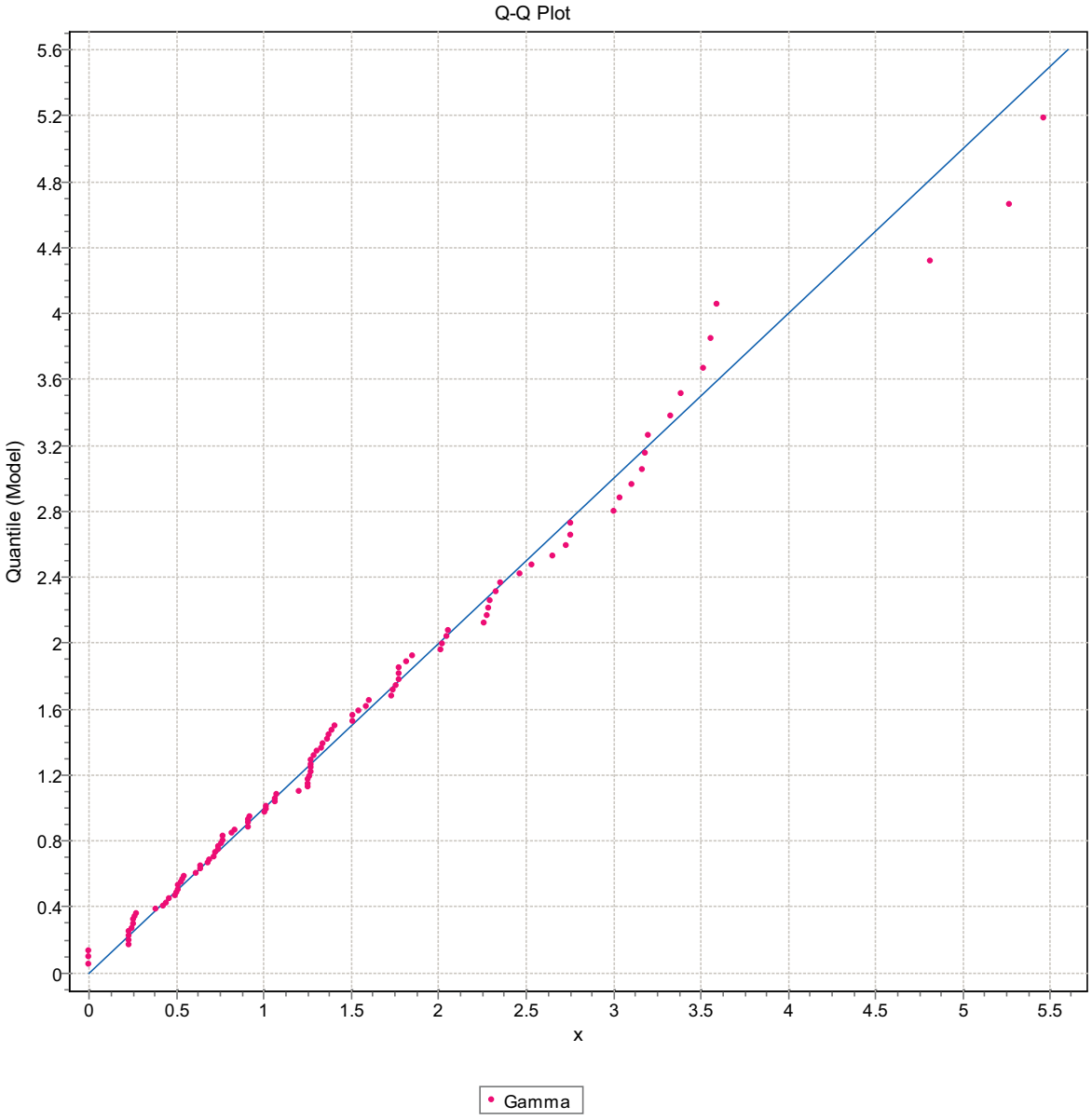

Figure F-243. *Q-Q plot, Domain FSM_N, 15 m bins, Gamma Distribution.*

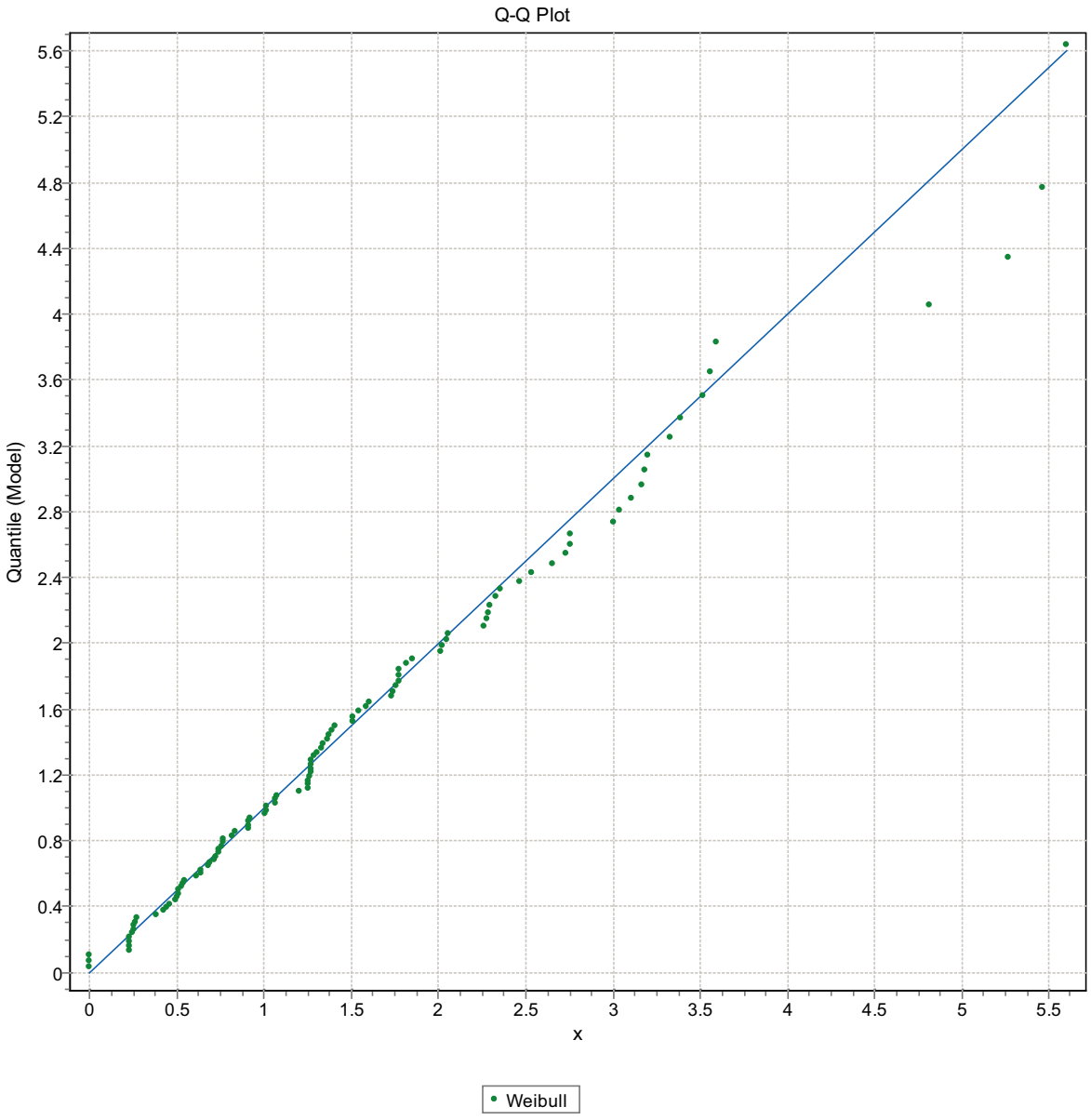

Figure F-244. *Q-Q plot, Domain FSM_N, 15 m bins, Weibull Distribution.*

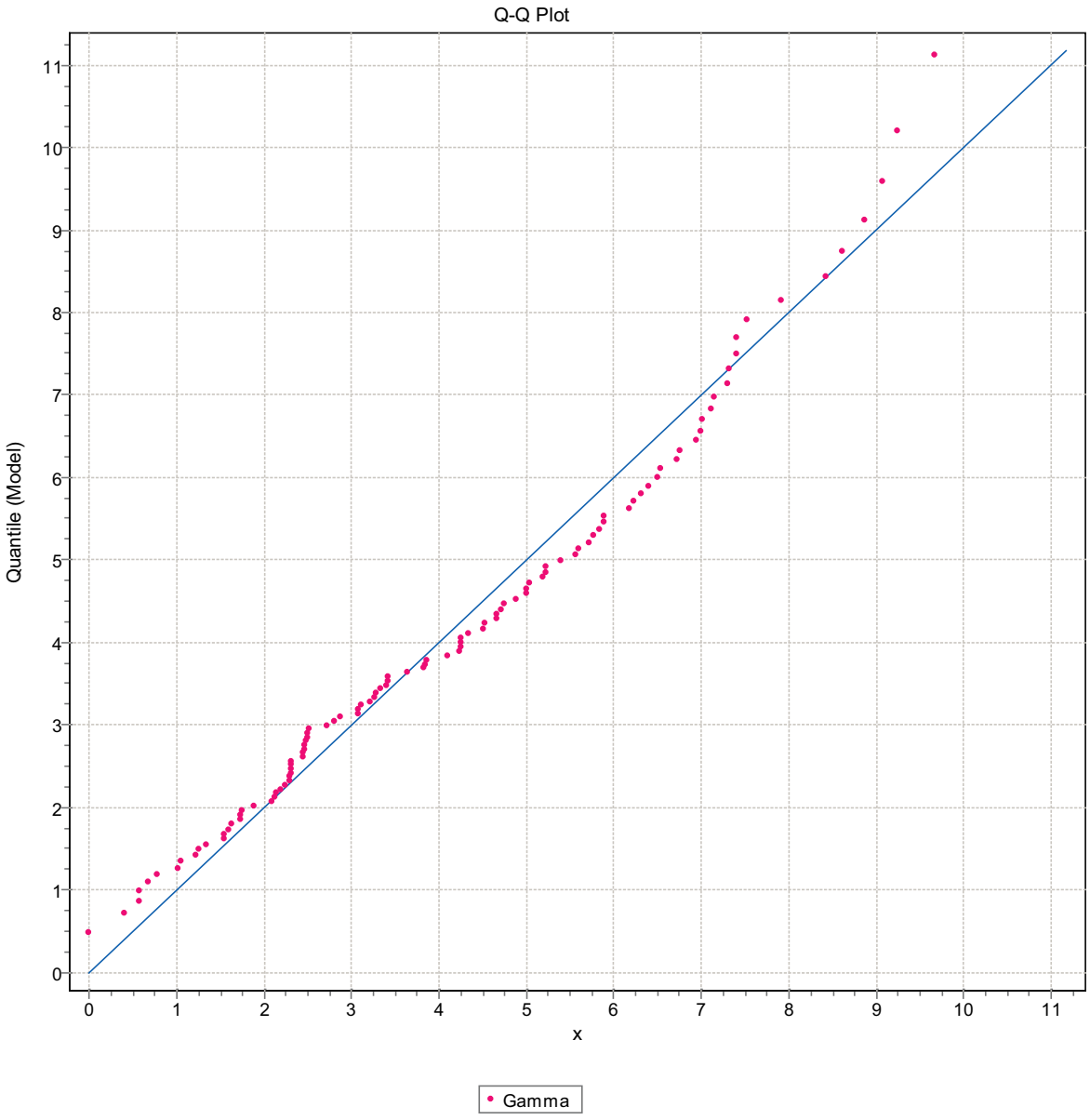

Figure F-245. *Q-Q plot, Domain FSM_N, 15 m bins, Gamma Distribution.*

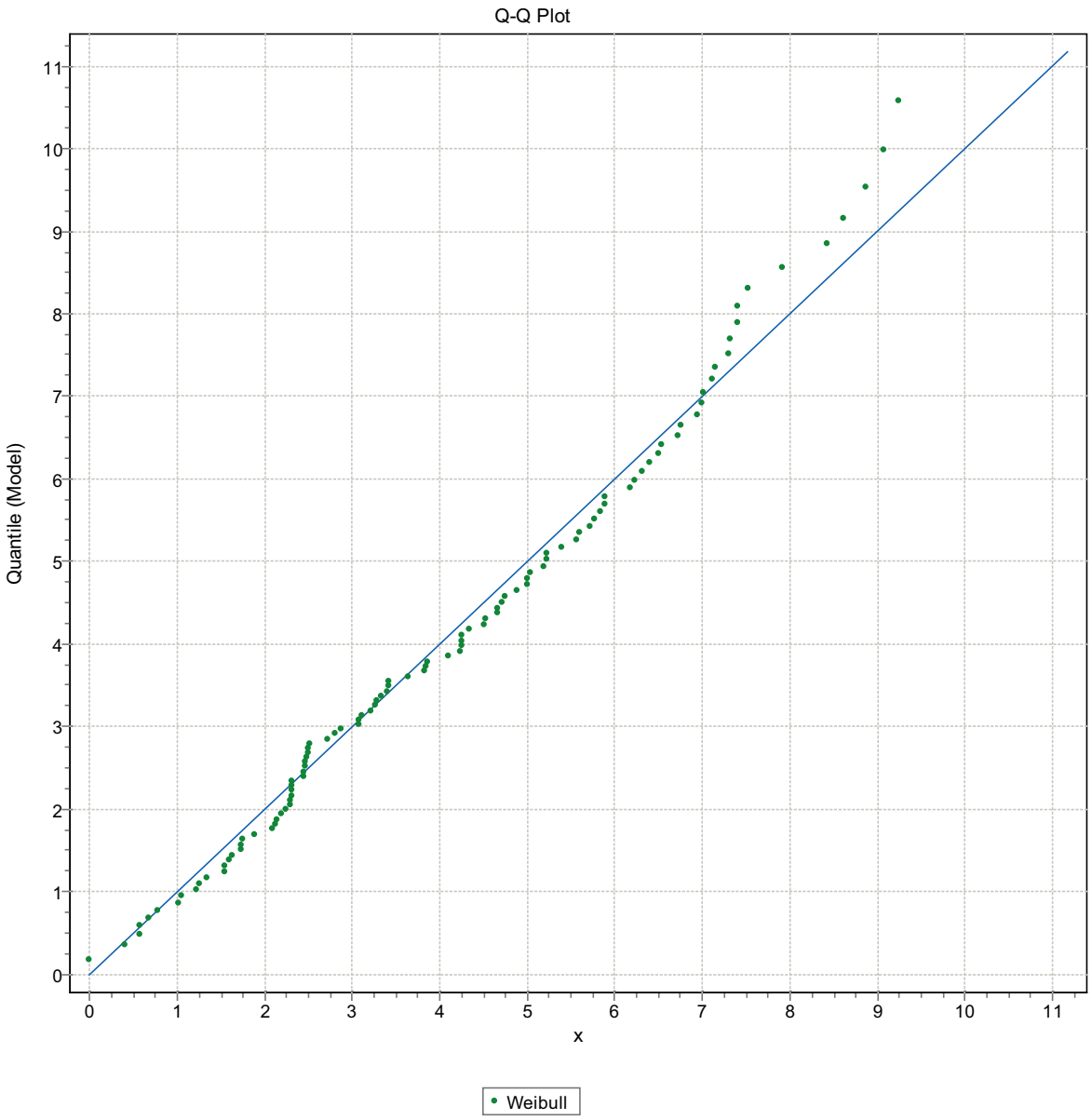

Figure F-246. *Q-Q plot, Domain FSM_N, 15 m bins, Weibull Distribution.*

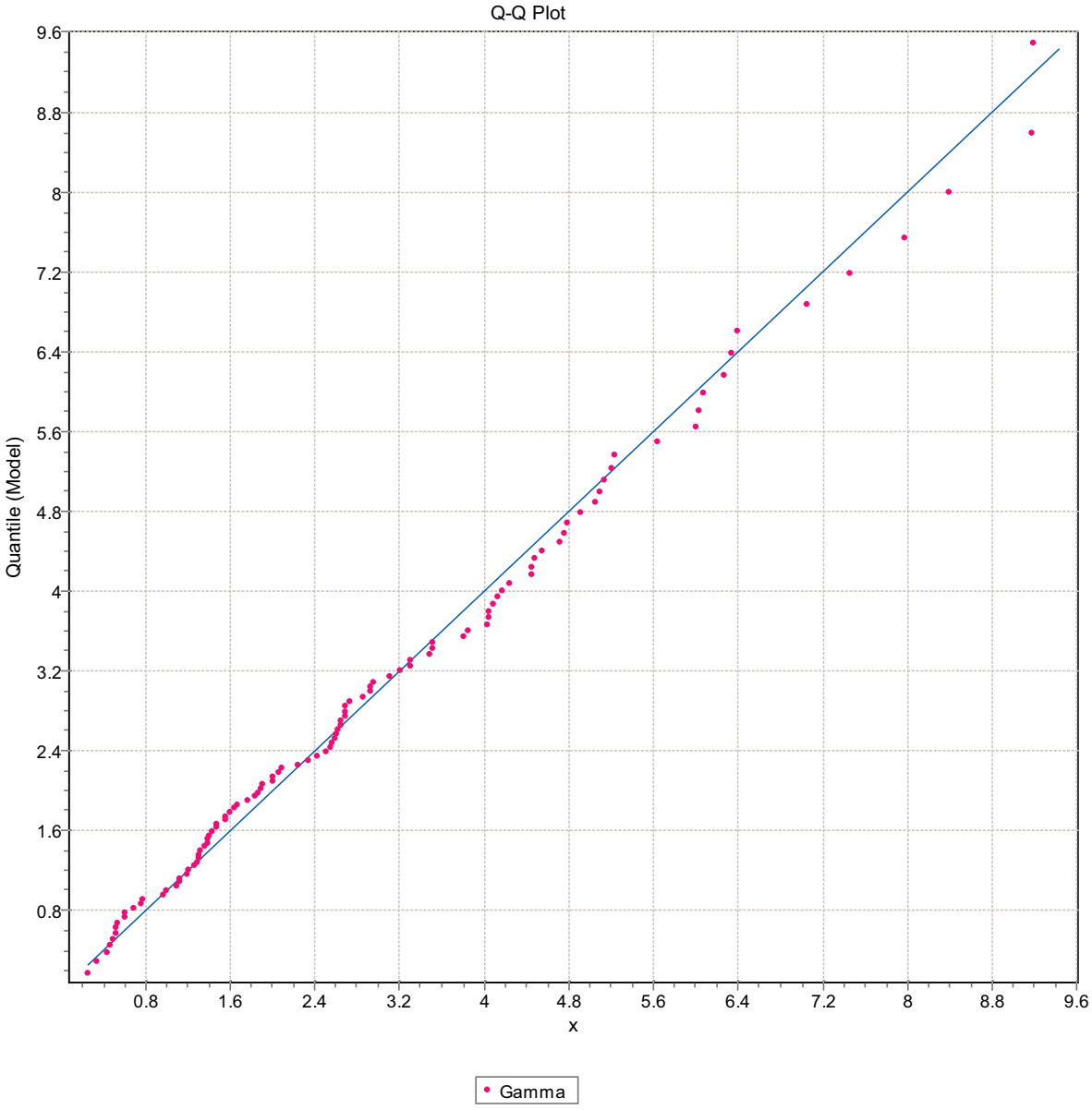

Figure F-247. *Q-Q plot, Domain FSM_N, 15 m bins, Gamma Distribution.*

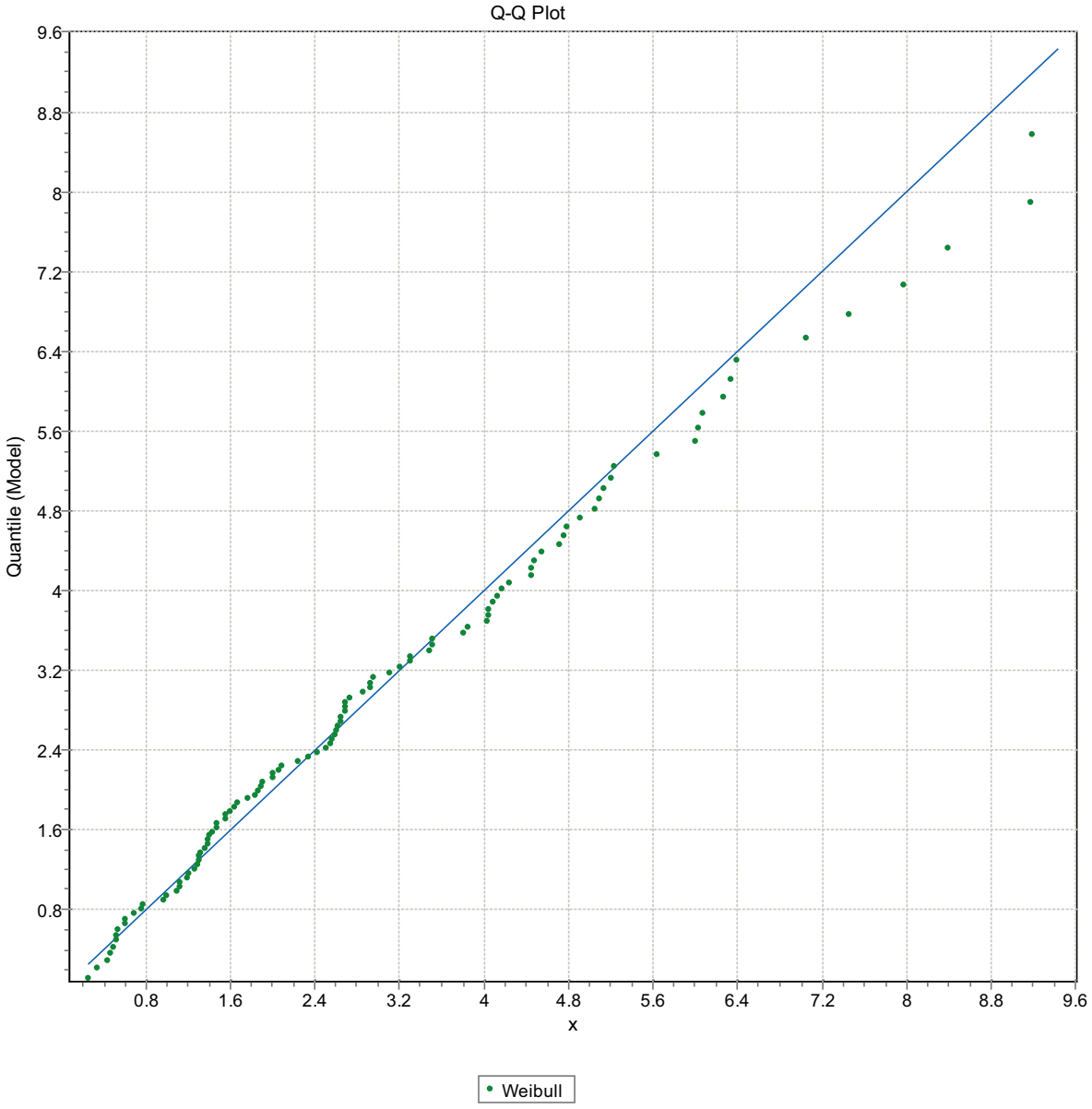

Figure F-248. *Q-Q plot, Domain FSM_N, 15 m bins, Weibull Distribution.*

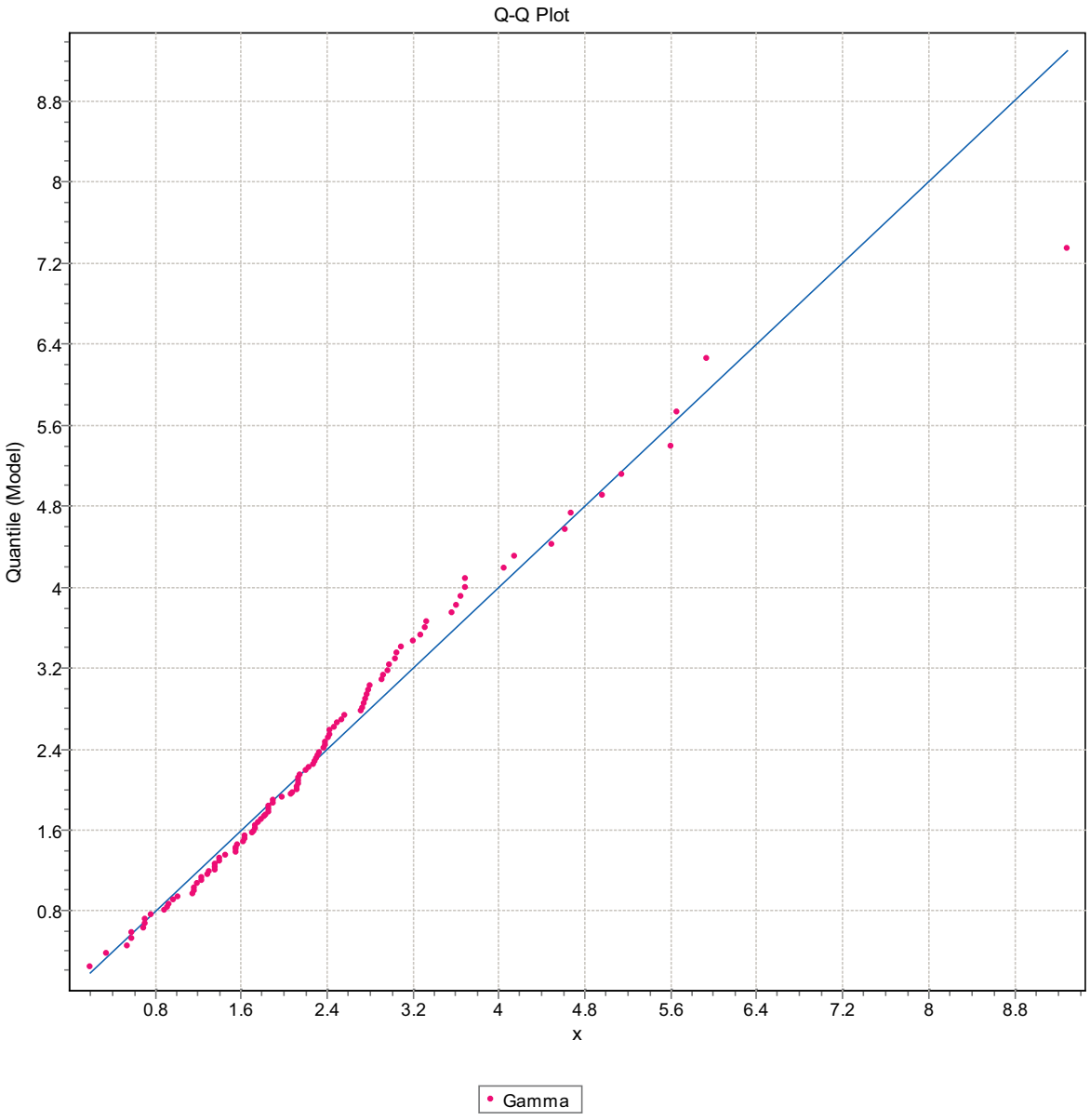

Figure F-249. *Q-Q plot, Domain FSM_N, 15 m bins, Gamma Distribution.*

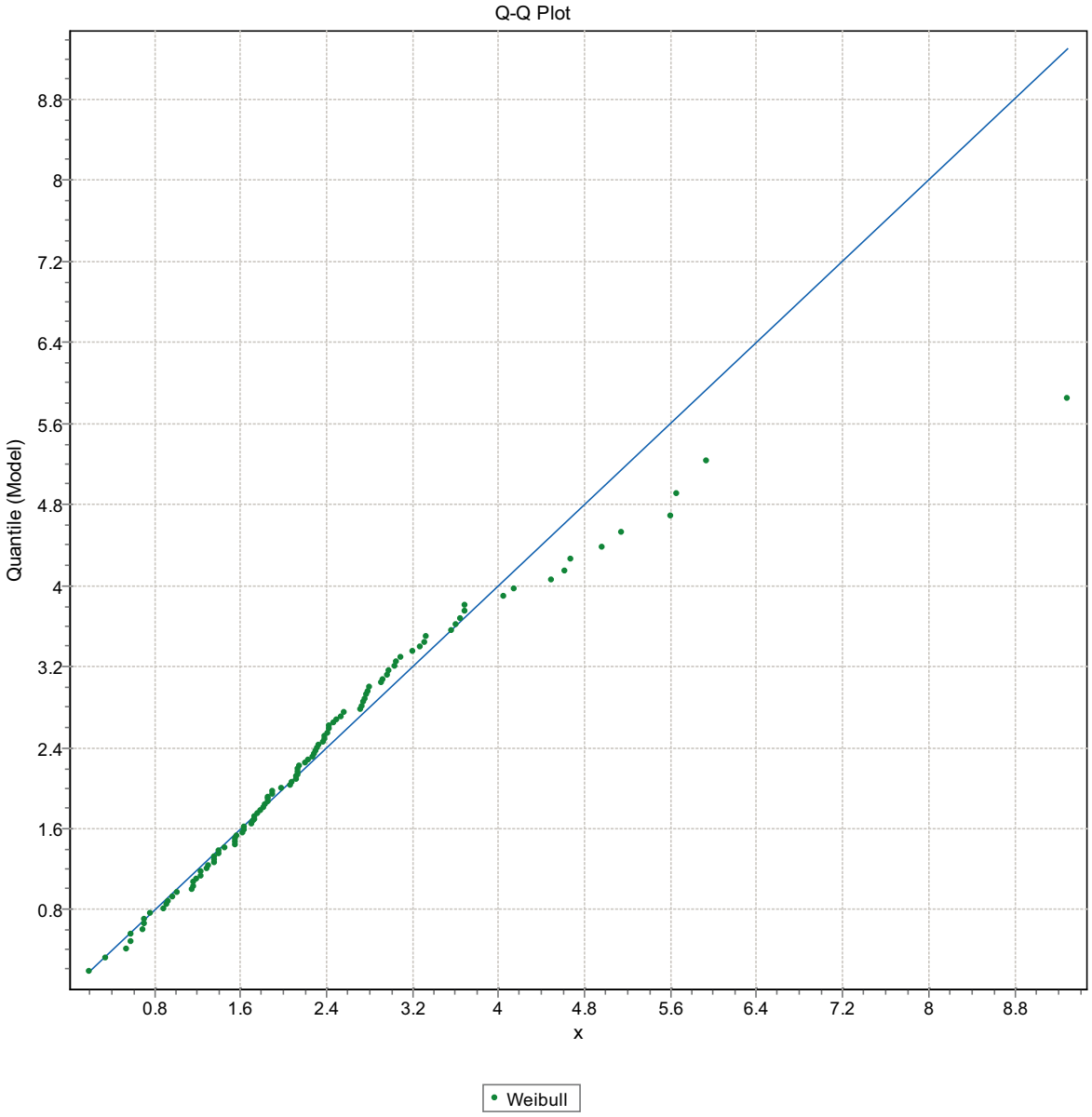

Figure F-250. *Q-Q plot, Domain FSM_N, 15 m bins, Weibull Distribution.*

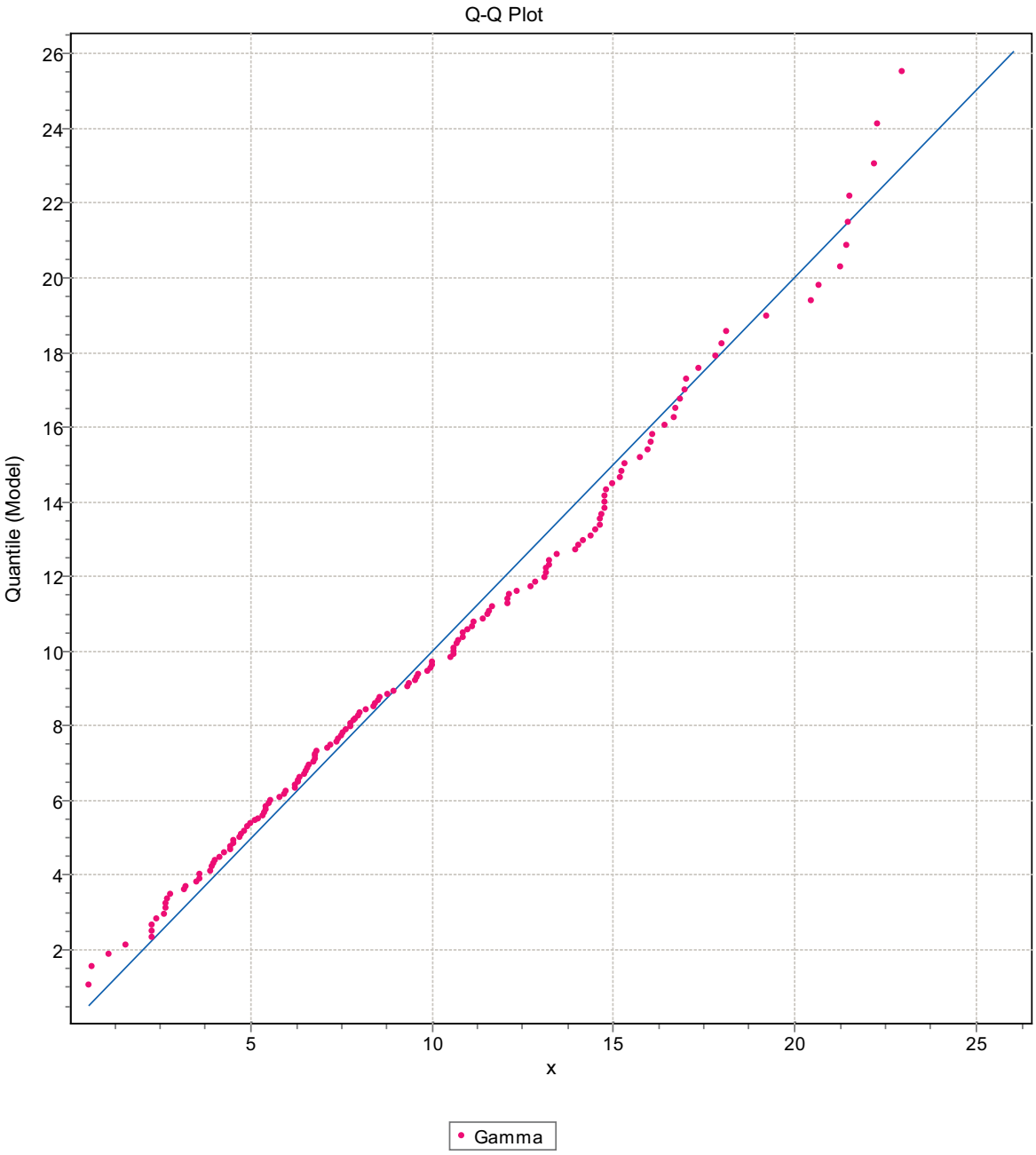

Figure F-251. *Q-Q plot, Domain FSM_W, 15 m bins, Gamma Distribution.*

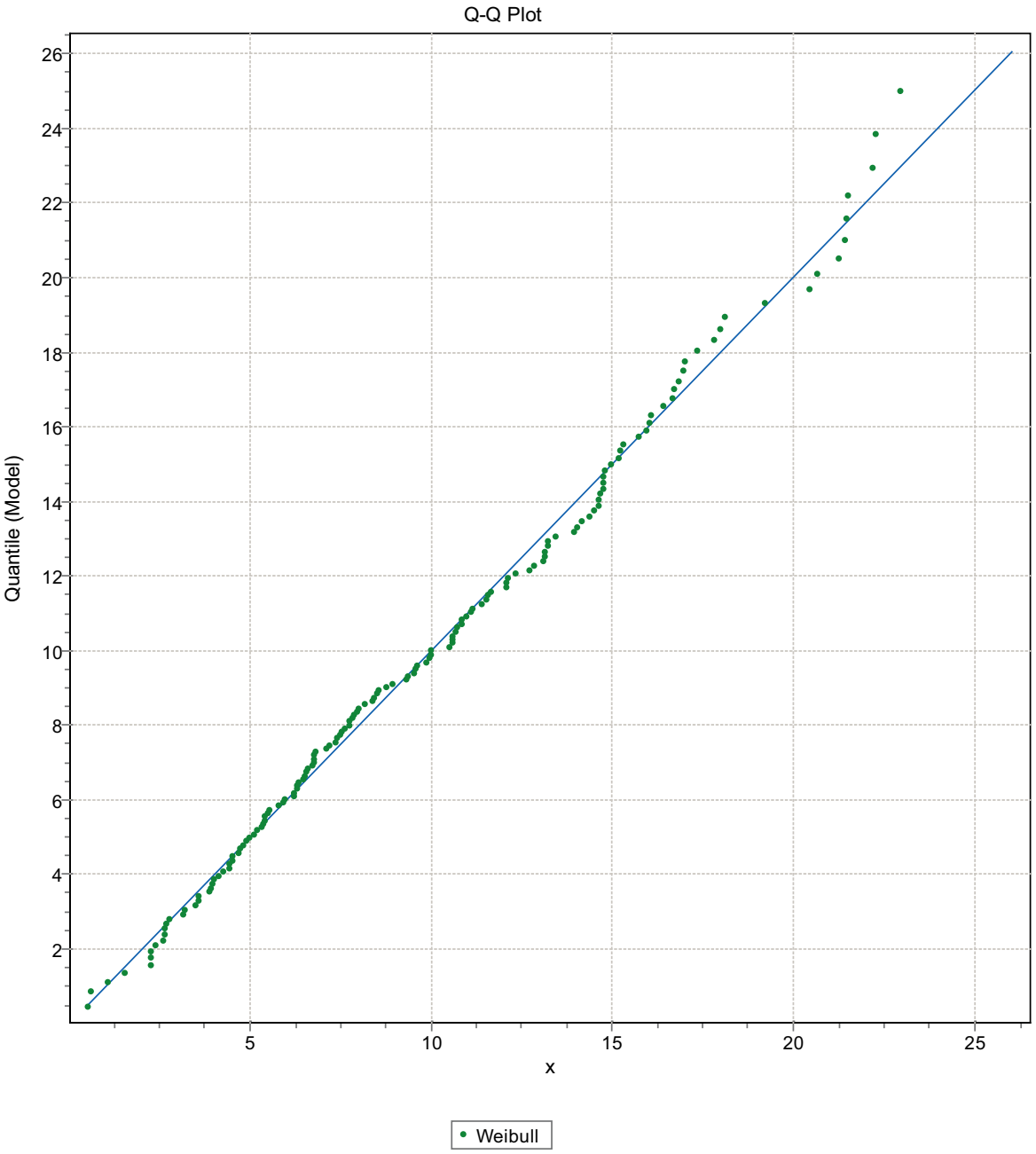

Figure F-252. *Q-Q plot, Domain FSM_W, 15 m bins, Weibull Distribution.*

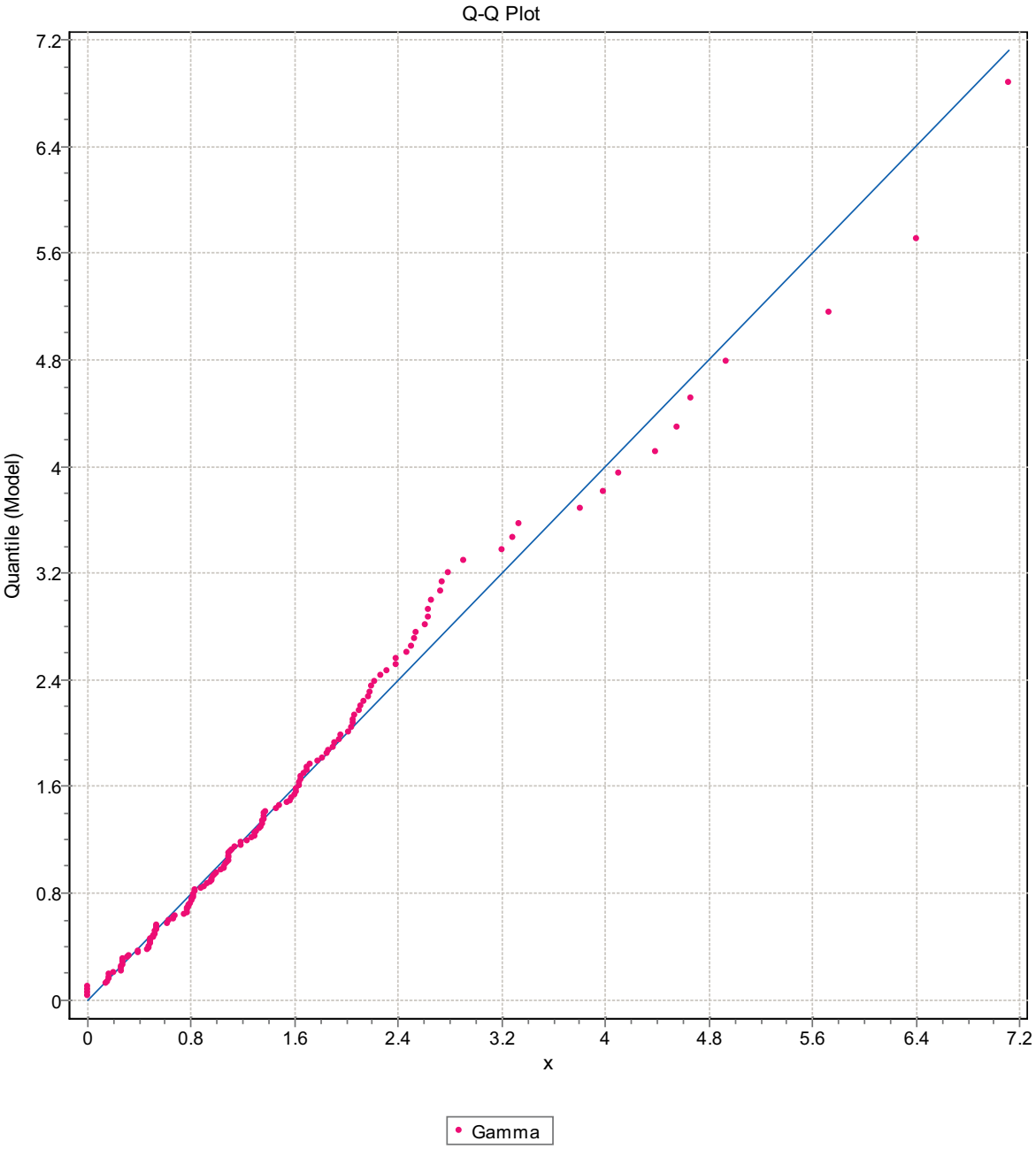

Figure F-253. *Q-Q plot, Domain FSM_W, 15 m bins, Gamma Distribution.*

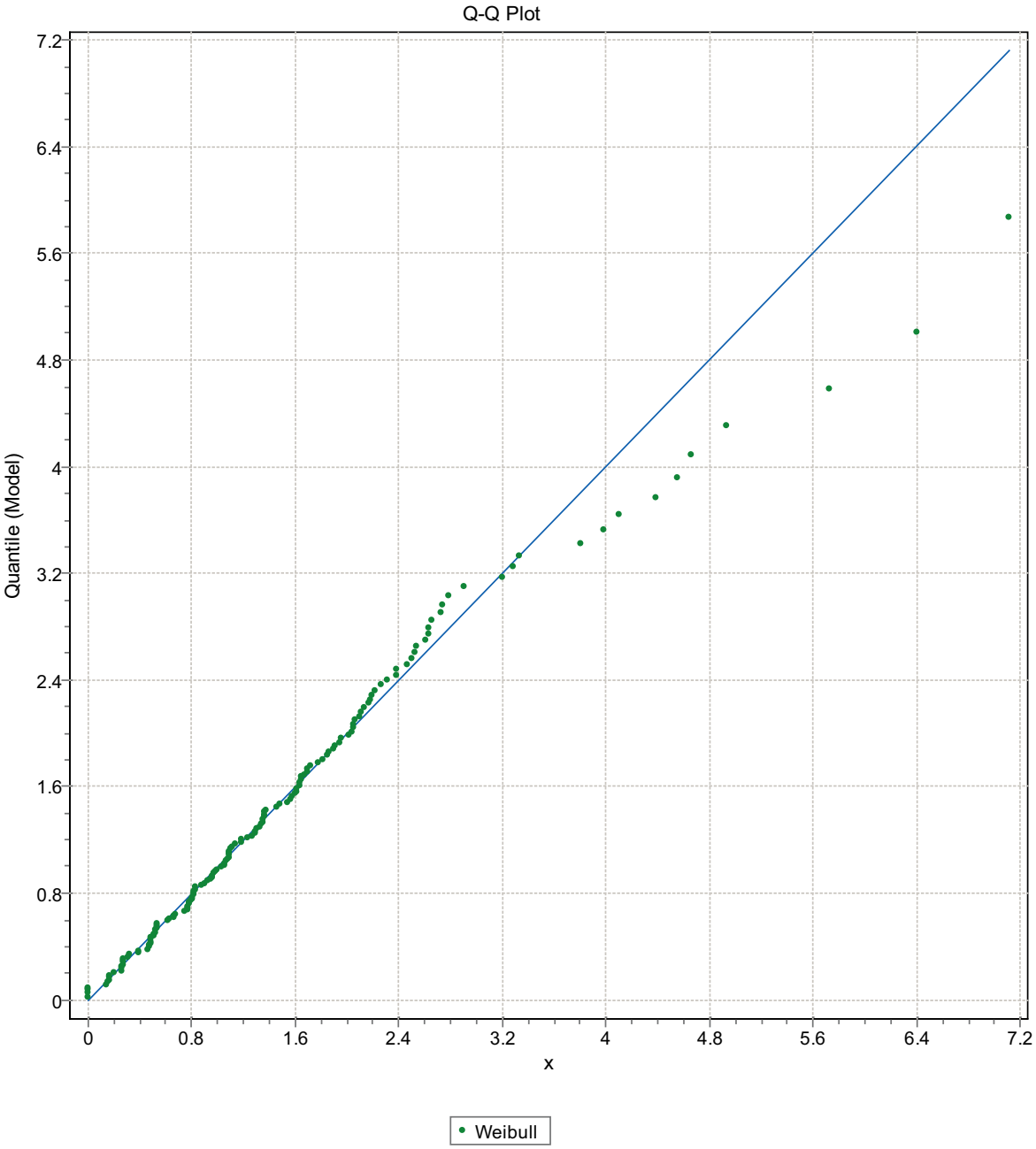

Figure F-254. *Q-Q plot, Domain FSM_W, 15 m bins, Weibull Distribution.*

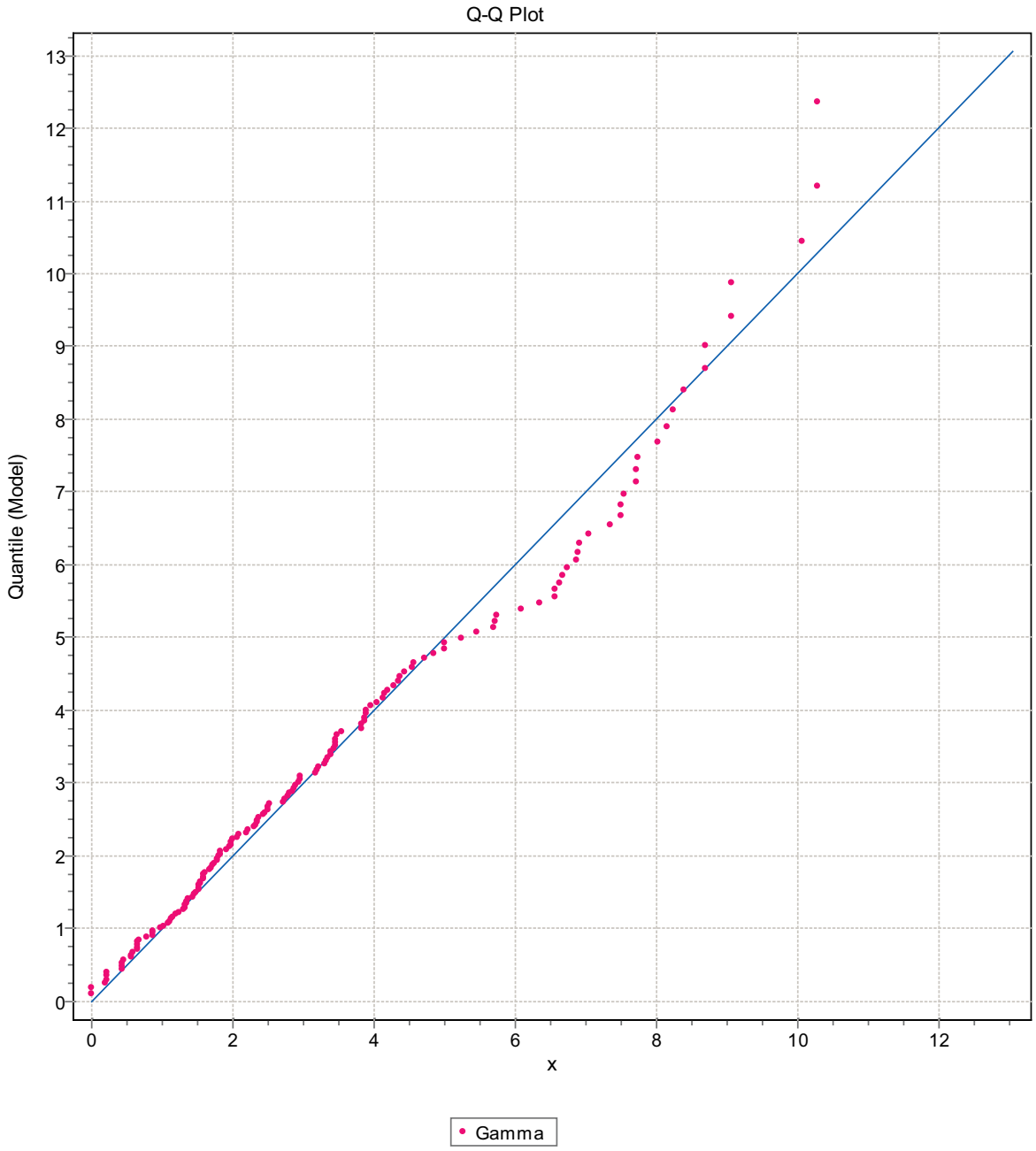

Figure F-255. *Q-Q plot, Domain FSM_W, 15 m bins, Gamma Distribution.*

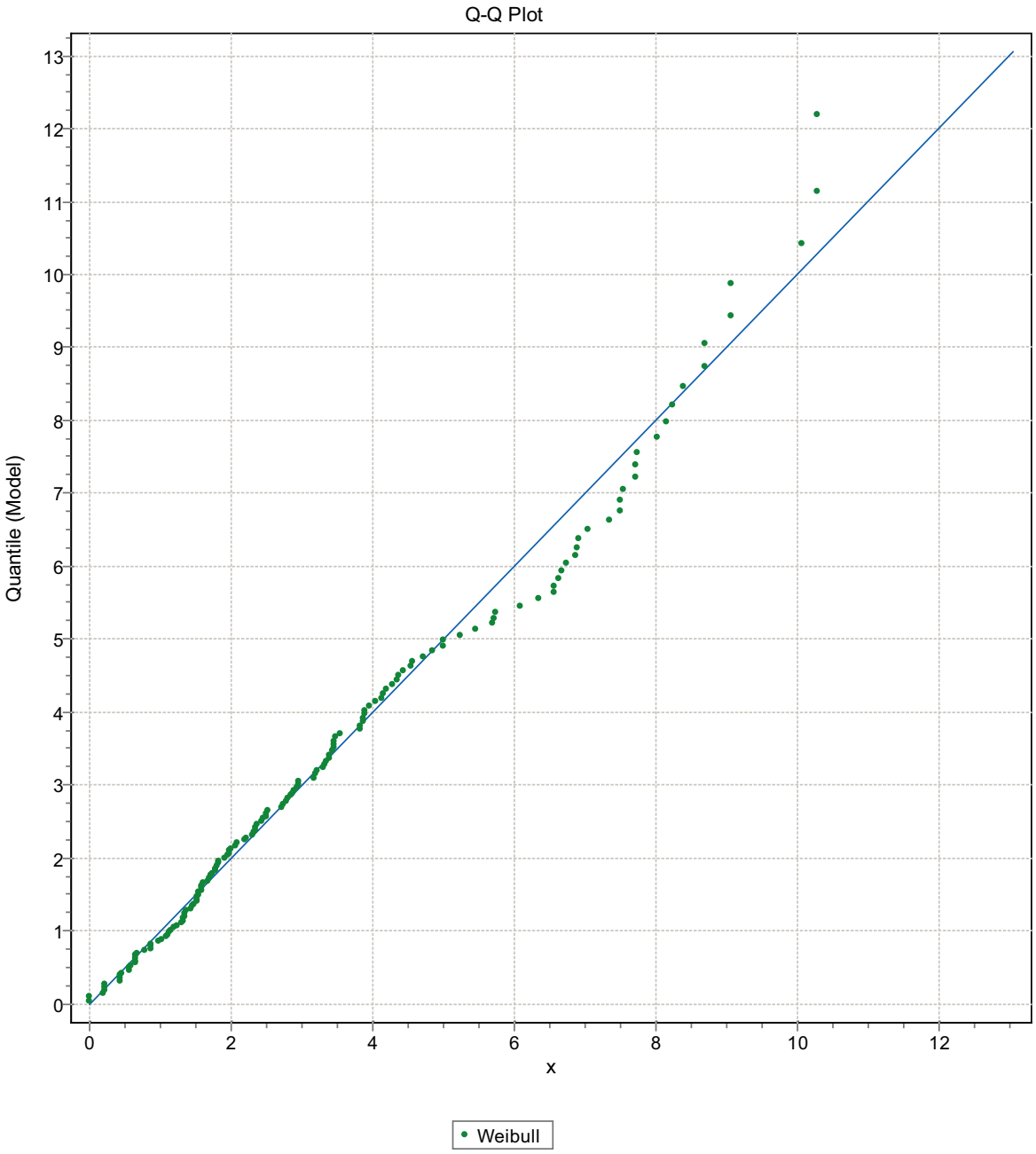

Figure F-256. *Q-Q plot, Domain FSM_W, 15 m bins, Weibull Distribution.*

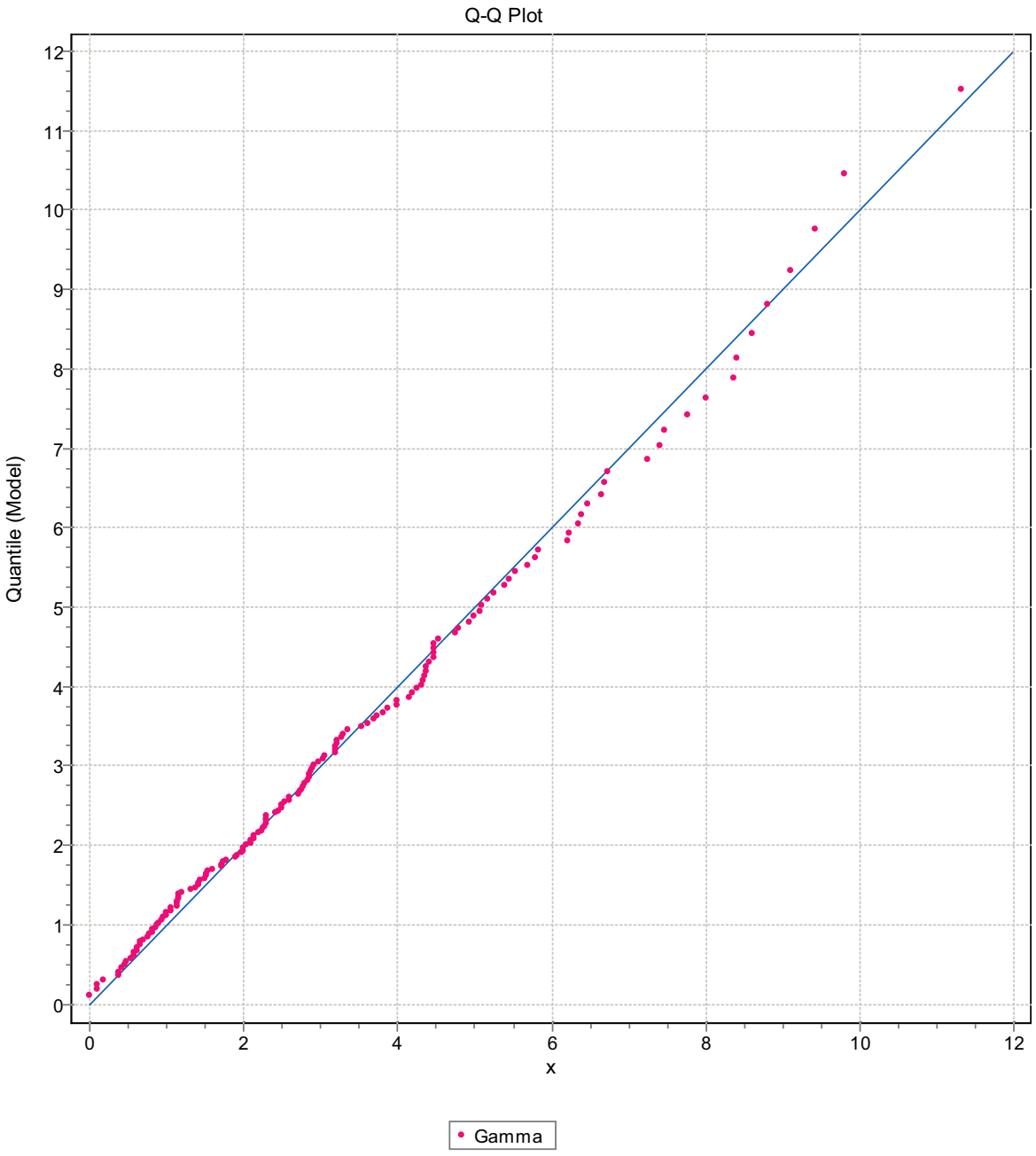

Figure F-257. *Q-Q plot, Domain FSM_W, 15 m bins, Gamma Distribution.*

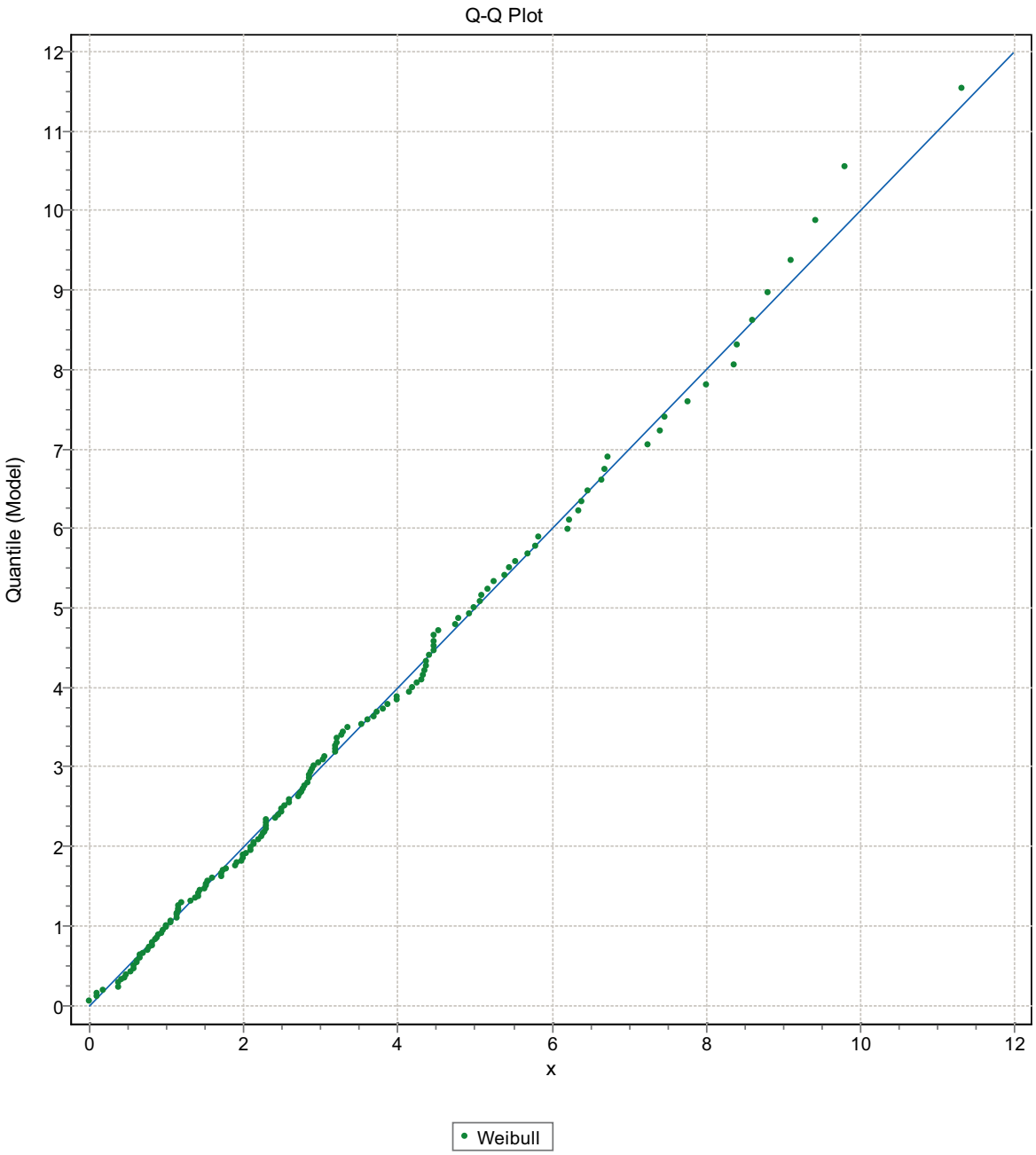

Figure F-258. *Q-Q plot, Domain FSM_W, 15 m bins, Weibull Distribution.*

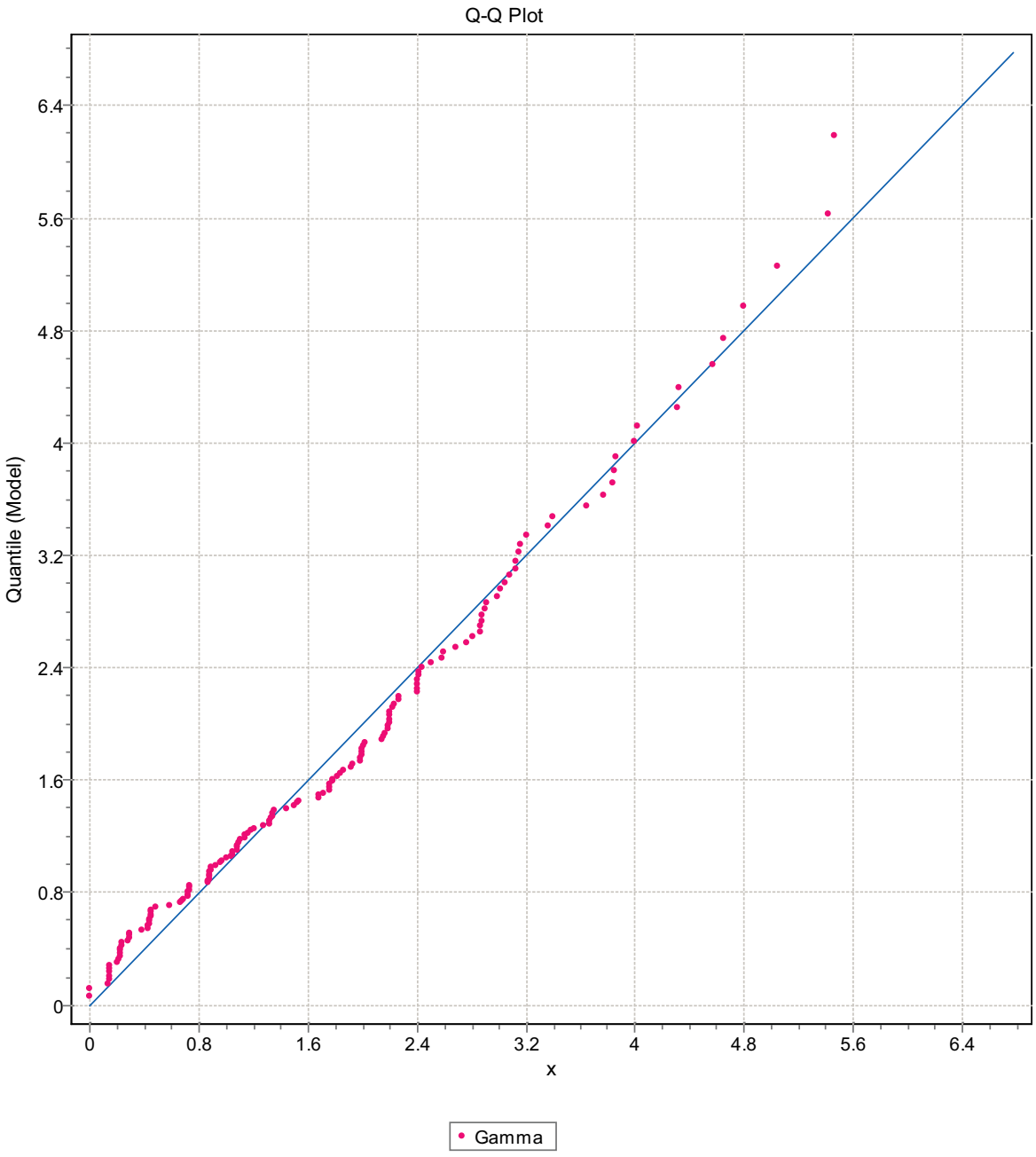

Figure F-259. *Q-Q plot, Domain FSM_W, 15 m bins, Gamma Distribution.*

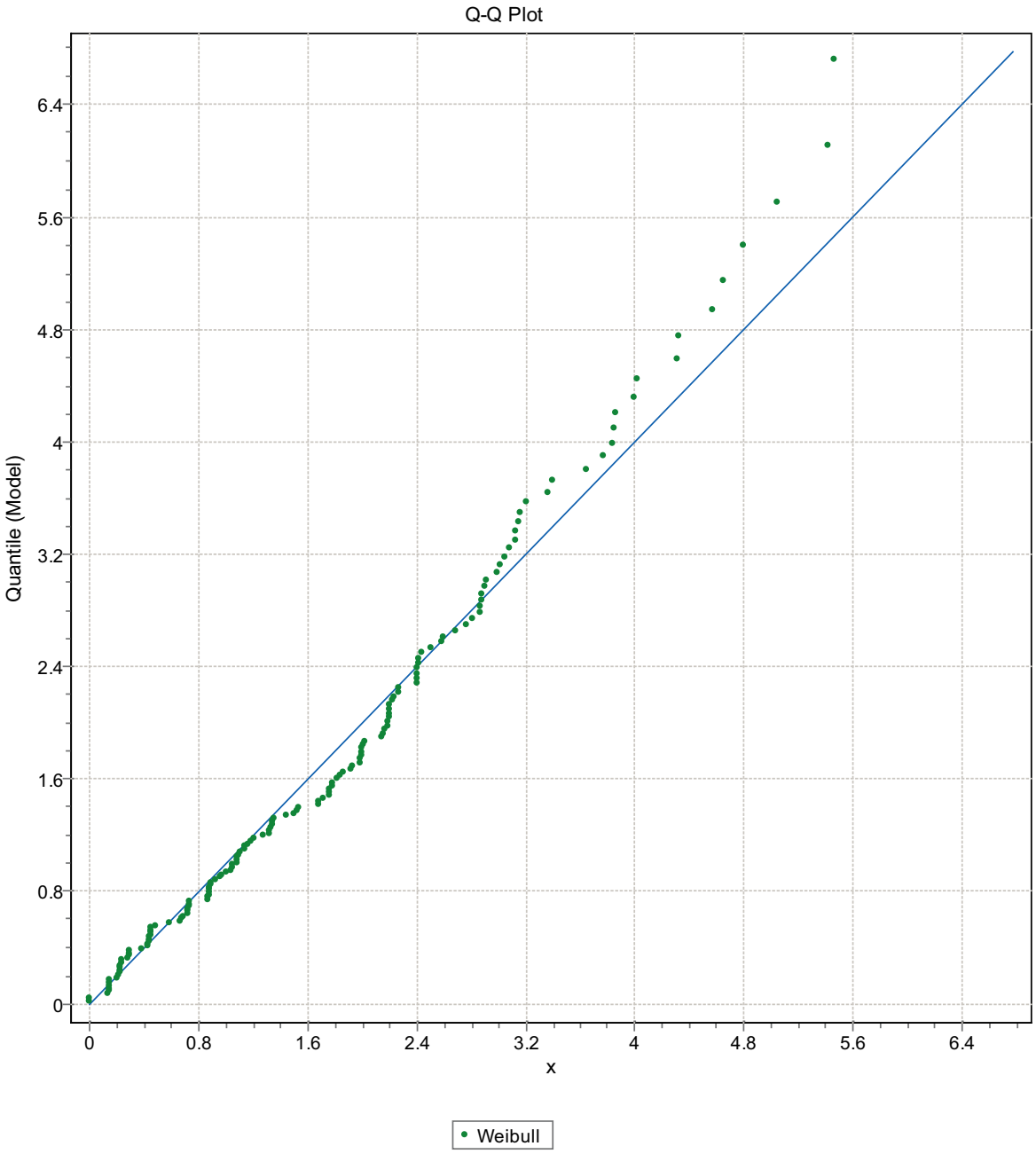

Figure F-260. *Q-Q plot, Domain FSM_W, 15 m bins, Weibull Distribution.*